5/1-7-94 JSC (1)

LBL-PUB-5379
SLAC-418
CALT-68-1869
UCRL-ID-114055
UC-IIRPA-93-01

PEP-II

An Asymmetric *B* Factory

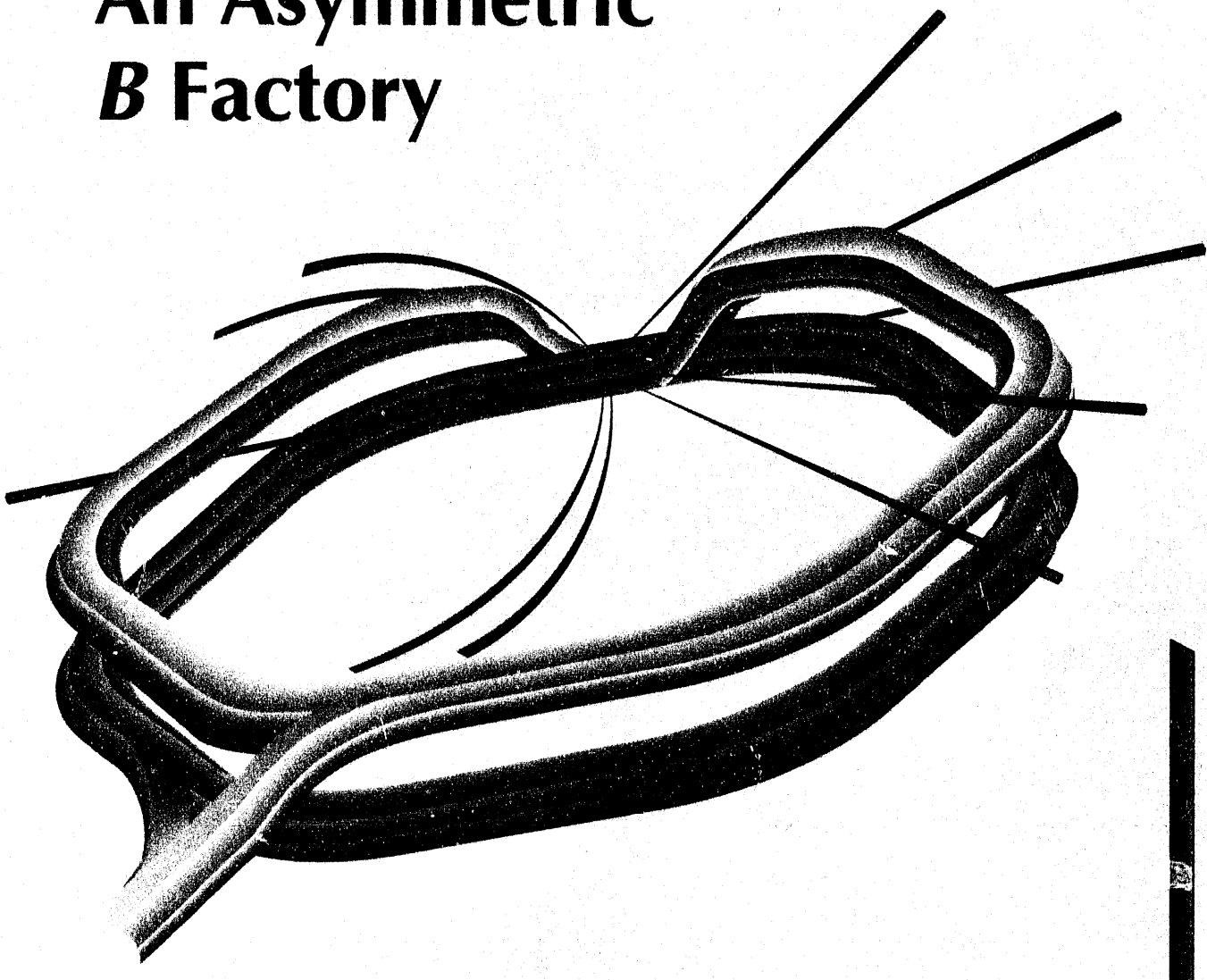

Conceptual Design Report

June 1993

Prepared for the U.S. Department of Energy under contract numbers
DE-AC03-76SF00098, DE-AC03-76SF00515, DE-AC03-81-ER40050, W-7405-Eng-48, and DE-AS03-76ER70285.

PEP-II

An Asymmetric *B* Factory

Conceptual Design Report

June 1993

CONTENTS

1.

OVERVIEW

IT has become increasingly apparent in recent years that systems containing *b* quarks offer unique opportunities for studying the theoretical edifice of particle physics, the so-called "Standard Model." Although measurements with these *b* quark systems offer a host of possibilities, the one that has riveted the attention of the particle physics community worldwide is the potential for understanding the origin of the phenomenon of *CP* violation—a small deviation in Nature's otherwise symmetric order that has been clearly observed but whose origins remain a mystery. The phenomenon of *CP* violation has cosmic consequences; in particular, it played a crucial role in the formation of our Universe. Thus, to understand it is one of the central goals in our quest to comprehend the orderly foundations of the natural world. The program of *CP* violation studies that we envision has great discovery potential; should the measurements disagree with predictions of the Standard Model, the observed pattern of *CP* violation will provide substantial and specific clues as to how the model should be extended.

Capitalizing on recent advances in detector technology and newly acquired information on the properties of the *b* quark, it is now widely accepted that a high-luminosity, asymmetric e^+e^- collider offers an ideal platform for an exhaustive study of *CP* violation. This fact has been forcefully and consistently endorsed by HEPAP (the High Energy Physics Advisory Panel) through its recent deliberations and recommendations. The subpanel on the U.S. High Energy Physics Research Program for the 1990s (the Sciulli Panel, DOE/ER–0453P and the accompanying transmittal letter, April 1990) stated that the physics program of a *B* factory was compelling and recommended that, given a technically sound proposal for construction of a machine, funds for such a facility be sought with high priority. The thrust of the subsequent June 1991 HEPAP transmittal letter was that technically sound designs for a *B* factory had become available (indeed, the original conceptual design for the PEP-based machine, for which this document serves as an update, had successfully undergone a detailed technical review by DOE) and that the funding agencies should seek means for constructing a U.S.-based facility.

The 1992 HEPAP subpanel on the U.S. Program of High Energy Physics Research (The Witherell Panel, DOE/ER-0542P, April 1992) further elucidated the importance of the physics program at a *B* factory. In its section entitled "High Energy Physics in 2002," the subpanel outlines its vision for an exciting and scientifically productive future. A crucial

element of its vision is "a high luminosity asymmetric electron-positron collider—the *B*-factory—completed in the preceding decade and now intensely focused on the study of *B* meson decays in an all-out attack on the origins of *CP* violation." The subpanel's recommendations were given under three budget scenarios. In the middle and upper scenarios, the subpanel recommended "construction of an asymmetric *B*-factory in the existing PEP tunnel at SLAC...," commenting that "The origin of *CP* violation is one of the most fundamental questions in high energy physics today. An asymmetric e^+e^- collider, optimized for operation just above the $B\bar{B}$ threshold, promises to provide the most comprehensive way to address this problem."

While *CP* violation is the main motivation for the construction of a *B* factory, such a facility will also host a very exciting and broad-based program of bottom quark, charm quark, τ, and two-photon physics. Important tests of the Standard Model are possible in this program, and many gaps in our knowledge are sure to be filled in. Because the number and range of distinct topics are very large, an asymmetric *B* factory will be an ideal facility for the training of young physicists, and we envisage more than 200 Ph.D. theses during the lifetime of the program (conservatively estimated at 15 years). The specific machine implementation discussed here has a single interaction region though, in principle, flexibility exists to expand this to two interaction regions, and therefore two detectors, should the user community consider this important enough to provide the extra funds. A parasitic program of synchrotron radiation physics would also be possible with additional funds.

A very large international particle physics community is committed to physics studies at an asymmetric e^+e^- *B* factory. A group of physicists numbering more than 150 Ph.D.'s has been involved with the PEP-based *B* factory (referred to as PEP-II), both in developing the physics arguments and in designing an appropriate detector. This group includes investigators from more than 20 U.S. institutions, as well as physicists from Canada, Europe, Japan, Russia, and Israel. An equal number of physicists are involved in other *B*-factory efforts worldwide.

In early 1989, a group of accelerator and particle physicists from Caltech, LBL, SLAC, and the University of California began a study of the feasibility of an asymmetric e^+e^- collider based on an upgrade of the PEP storage ring at SLAC. A parallel study was conducted to examine in detail the physics capabilities of such a facility and to specify the luminosity required for a broad-based program aimed at understanding the origins of *CP* violation. The feasibility studies indicated that, with appropriate care, PEP could be upgraded to achieve the desired luminosity of 3×10^{33} cm^{-2} s^{-1}. In November 1989, the SLAC Experimental Program Advisory Committee agreed that the PEP-II *B*-factory program was indeed very compelling and encouraged the Directors of SLAC and LBL to move from a feasibility study to a conceptual design phase.

The original conceptual design report (SLAC-372, LBL PUB-5303, UCRL-ID-106426, CALT-68-1715, UC-IIRPA-91-01) was completed in February 1991 and was the basis of the joint SLAC/LBL/LLNL proposal to DOE for construction funding. In March 1991, a DOE Technical Review Committee, under the Chairmanship of Dr. L. Edward Temple, was established to confirm the technical feasibility of the SLAC-based Asymmetric *B* Factory design and to determine the completeness and appropriateness of its cost estimate, schedule, and management plan. The design received the enthusiastic endorsement of the committee, whose judgment was that "there is a high probability of

attaining the physics goals." The cost estimate, schedule, and management plan were also validated by the committee. The PEP-II design described in the conceptual design report thus served as a direct and wholly satisfactory response to the challenge set down by the Sciulli Panel. In the intervening time period, the program of R&D studies on which we have embarked has enabled us to improve and simplify the design of PEP-II. In this updated conceptual design report, we document the present status of the PEP-II design. Given the fact that design changes were made, a new bottom-up cost estimate has been developed. The improvements we have made have resulted in cost savings compared with the original design, and these are reflected in the cost summary presented in Chapter 9.

The goal of the conceptual design was to be a machine that would be both responsive to the physics needs and conservative in its approach to achieving high luminosity. The PEP-II design we propose meets this goal. The facility consists of two independent storage rings, one located atop the other in the PEP tunnel. The high-energy ring, which stores a 9-GeV electron beam, is an upgrade of the existing PEP collider; it reutilizes all of the PEP magnets and incorporates a state-of-the-art copper vacuum chamber and a new radio-frequency system capable of supporting a stored beam of high current. The low-energy ring, which stores 3.1-GeV positrons, will be newly constructed. Its design takes advantage of many of the machine component designs that have already proved successful at PEP.

Our approach to reaching the desired luminosity of 3×10^{33} cm^{-2} s^{-1} is to use, in each ring, high circulating currents (approximately 1–2 A) separated into more than 1600 bunches. An advantage of this approach is that the parameters of individual bunches (current, length, emittance, etc.) are quite conventional and have been demonstrated in numerous successful colliders over many years. Thus, the design challenges are restricted to the high-current and multibunch arenas. These, in turn, are mainly engineering challenges and—although they are by no means easy—they are amenable to standard engineering tools and approaches that assure us that the proposed solutions are workable, reliable, and conservative.

The PEP site offers an ideal location for an asymmetric *B* factory. SLAC has the world's most powerful positron injector, and the availability of the large 2.2-km-circumference tunnel greatly eases the problems associated with handling the intense synchrotron radiation power emitted by the high-current beams. This approach is not unique to the SLAC project; both DESY and KEK moved away from earlier designs that employed small storage rings and adopted machine designs that placed both rings in their large-radius PETRA (2.3 km) and TRISTAN (3 km) tunnels. Moreover, the parameters of the PEP-II high-energy ring match almost perfectly those of the present PEP; the project can benefit from the existing PEP infrastructure so that no conventional construction is required on the SLAC site.

SLAC and LBL have a long and very successful history of design, construction, and operation of e^+e^- storage rings. The original PEP project was a joint endeavor of these two laboratories. The staffs of both laboratories are enthusiastic about the prospect of an upgrade to this facility. Much of the expertise that conceived and built SPEAR and PEP remains within the laboratories, and new additions to the staff [for example, the team that has just completed construction of the Advanced Light Source (ALS) at LBL] have enhanced these strengths. The addition of LLNL as an institutional collaborator further strengthens the team that will build PEP-II.

In summary, we believe that the SLAC site is an ideal location for the construction of an asymmetric *B* factory that will provide the platform for a crucial component of the U.S. high-energy physics base program. The design presented here is flexible and fully capable of meeting the demands of a physics program that will exhaustively examine the question of *CP* violation. As soon as funds are available, we are ready to begin the construction and commissioning of this exciting accelerator facility and then to embark on studying one of the most important topics in high-energy physics today.

2.

INTRODUCTION

ON the following pages, we give an overview of the physics motivation for the PEP-II asymmetric *B* factory. The overview includes a discussion of the advantages of the e^+e^- environment and a menu of the physics achievable at PEP-II. This chapter also offers a justification for the design luminosity for the machine and the asymmetric aspect of the collider, and it outlines a list of constraints on the machine design that arise from the physics goals (that is, tolerable background levels, maximum beam pipe radius, etc.).

2.1 OVERVIEW

We propose to construct PEP-II, a high-luminosity electron-positron colliding-beam accelerator that will operate in the 10-GeV center-of-mass energy ($E_{c.m.}$) regime; the majority of the physics running will be at the $\Upsilon(4S)$ resonance ($E_{c.m.} = 10.58$ GeV). The machine described in the following chapters has the novel feature of unequal beam energies, a configuration we call *asymmetric*. The luminosity goal is 3×10^{33} cm^{-2} s^{-1}; the electron and positron beam energies were chosen to be 9 and 3.1 GeV, respectively.

The main physics motivation for PEP-II is a full and exhaustive study of *CP* violation, using the rich spectrum of *B* meson decays. The goal is not simply to measure, for the first time, *CP* violation in the *B* meson system, but to mount a program sufficiently diverse to examine the more crucial issue of what constitutes the *origin* of *CP* violation. Such a program requires a machine that produces in excess of 10^7 neutral *B* mesons (B^0's) per year. The goal for the machine described in this proposal is 3×10^7 neutral *B* mesons per year.

The 10-GeV region was chosen so as to exploit the copious and exclusive production of *B* mesons at the $\Upsilon(4S)$ resonance; the level of asymmetry was chosen to optimize the measurement of *CP*-violating asymmetries in the decays of the *B* mesons. The full time-evolution of this phenomenon can be exposed by the use of the asymmetry, with the time-evolution measurements providing a comprehensive set of systematic cross-checks for the *CP* violation measurements.

The e^+e^- 10-GeV region has proved to be an ideal environment for the study of *b* quark physics. The $\Upsilon(4S)$ offers special advantages for the study of *B* hadron (meson

and baryon) decays. The production of B hadrons at the $\Upsilon(4S)$ constitutes fully one-third of the available cross section, and the availability of kinematic constraints further permits exceptionally clean isolation of the B physics. The background rejection is sufficient to allow a wide range of B meson decays, even decay modes with small branching fractions (10^{-4}–10^{-5}), to be reconstructed with high efficiencies and large signal-to-noise ratios. These include decay modes of high multiplicity and those that include final state π^0's. The ability to use the sign of the electric charge of both leptons and kaons to establish, accurately and with high efficiency, the difference between a B and a $\overline{B}$ meson is very powerful. These characteristics are especially advantageous for the study of CP violation. Programs at CESR and DORIS have provided a large amount of data for a detailed characterization of the Υ region. This, coupled with the rather simple nature of the e^+e^- environment, makes it possible to simulate the physics processes very reliably. Hence, one can attach considerable confidence to the estimates of the physics capabilities calculated for the B factory. Indeed, as discussed below, the present proposal is based on very detailed modeling of the physics.

Besides bottom quark production, the B factory will produce very large samples of charm quarks and τ leptons. The environment again favors high-efficiency, low-background studies of important physics processes associated with these fundamental constituents. Hence, a B factory is more correctly viewed as a *Heavy Constituent Factory.*

Rounding out the possibilities offered by PEP-II is an exciting program of two-photon physics and the study of the spectroscopy of the Υ resonances. This spectroscopy reflects the underlying strong force that binds the quarks together and offers an opportunity for detailed and essential studies of this fundamental force.

Details of this compelling physics program are given below. As a measure of the power of PEP-II, we have tabulated in Table 2-1 the yields for $B\overline{B}$ and Υ that exist

Table 2-1. Bottom, Υ, charm, and τ yields (1 yr = 10^7 s).

Channel	World sample (April 1993)	B factory $\mathcal{L} = 3 \times 10^{33}$ (per yr)
$B\overline{B}$	$\sim 2 \times 10^6$	3×10^7
$\Upsilon(1S)$	3.5×10^6	5×10^8
$\Upsilon(2S)$	8.5×10^5	2×10^8
$\Upsilon(3S)$	4.9×10^6	1×10^8
D^0	—	6.9×10^7
D^+	—	3.3×10^7
D_s	—	2.3×10^7
$\tau^+\tau^-$	—	2.8×10^7

worldwide today and that will be available in a one-year run at PEP-II. Also tabulated are the annual yields of D mesons and τ pairs expected at PEP-II. The increase in statistical power is itself very impressive; what is not evidenced by the relative numbers is the level of accessibility to crucial physics that can only come with the operation of PEP-II.

PEP-II also offers the opportunity for an exciting parasitic program of synchrotron radiation studies. The very high circulating current will generate x-ray beams of unprecedented brightness, permitting some experiments that will not be accessible even at the next generation of advanced light sources.

The U.S. is currently embarked on the SSC program, which will begin producing physics in the year 2003. The U.S. particle physics program is in great need of additional facilities, particularly in the intervening years, both to maintain a balanced and vibrant program and to keep young people in the field. In this regard, the PEP-II project offers the nation an ideal opportunity. SLAC, with its existing powerful injector and large-circumference machine (PEP), provides a natural site for a high-luminosity asymmetric B factory. PEP-II constitutes an upgrade of the existing SLAC facility, with no conventional construction required. This has the advantage of saving both money and time. With proper financial planning, the U.S. program could have PEP-II operational for physics in 1998. The program has an expected lifetime for exciting physics of at least 15 years. While the SSC challenges the Standard Model by vigorously pursuing an understanding of the Higgs sector, PEP-II would provide a complementary pursuit of the Standard Model through the study of CP violation and the pattern of heavy-constituent decays. The PEP-II physics program is exceedingly diverse, and the number of fully independent physics topics that can be studied is very large. This fact, coupled with the compelling nature of the physics, has brought together a very large community pushing for such a facility. (Based on current attendance at workshops and discussions with members of the worldwide community, we estimate that 300 particle physics Ph.D.'s will work at PEP-II.) The majority of this community has worked on e^+e^- collisions for many years and has a demonstrated ability to produce high-quality physics results. In addition, we envisage PEP-II as providing an exceptional training ground for young physicists: The number of interesting thesis topics far exceeds one hundred.

The rest of this chapter is organized to provide background for the nonspecialist; a more detailed discussion of physics measurements resumes in Section 2.3.4. Section 2.2 discusses the characteristics of the 10-GeV center-of-mass region as seen in e^+e^- collisions. Section 2.3 then discusses the physics motivation, including an outline of the Standard Model (Sections 2.3.1 through 2.3.3), a discussion of how CP asymmetries are measured at the $\Upsilon(4S)$ (Section 2.3.4), a justification of the machine asymmetry and luminosity (Sections 2.3.5 and 2.3.6), a discussion of sensitivity to non–Standard Model explanations for CP violation (Section 2.3.7), and outlines of B physics exclusive of CP violation, together with charm, τ, Υ, and two-photon physics (Sections 2.3.8 through 2.3.12). The chapter concludes with a discussion of the constraints imposed by the physics on the machine design and an outline of the likely scenario for choosing the operating energy of the machine.

2.2 CHARACTERISTICS OF THE 10-GEV REGION—THE UPSILON FAMILY

The cross section for producing hadrons in e^+e^- collisions in the 10-GeV region is shown in Fig. 2-1. The rich resonance structure above the b quark threshold is called the upsilon

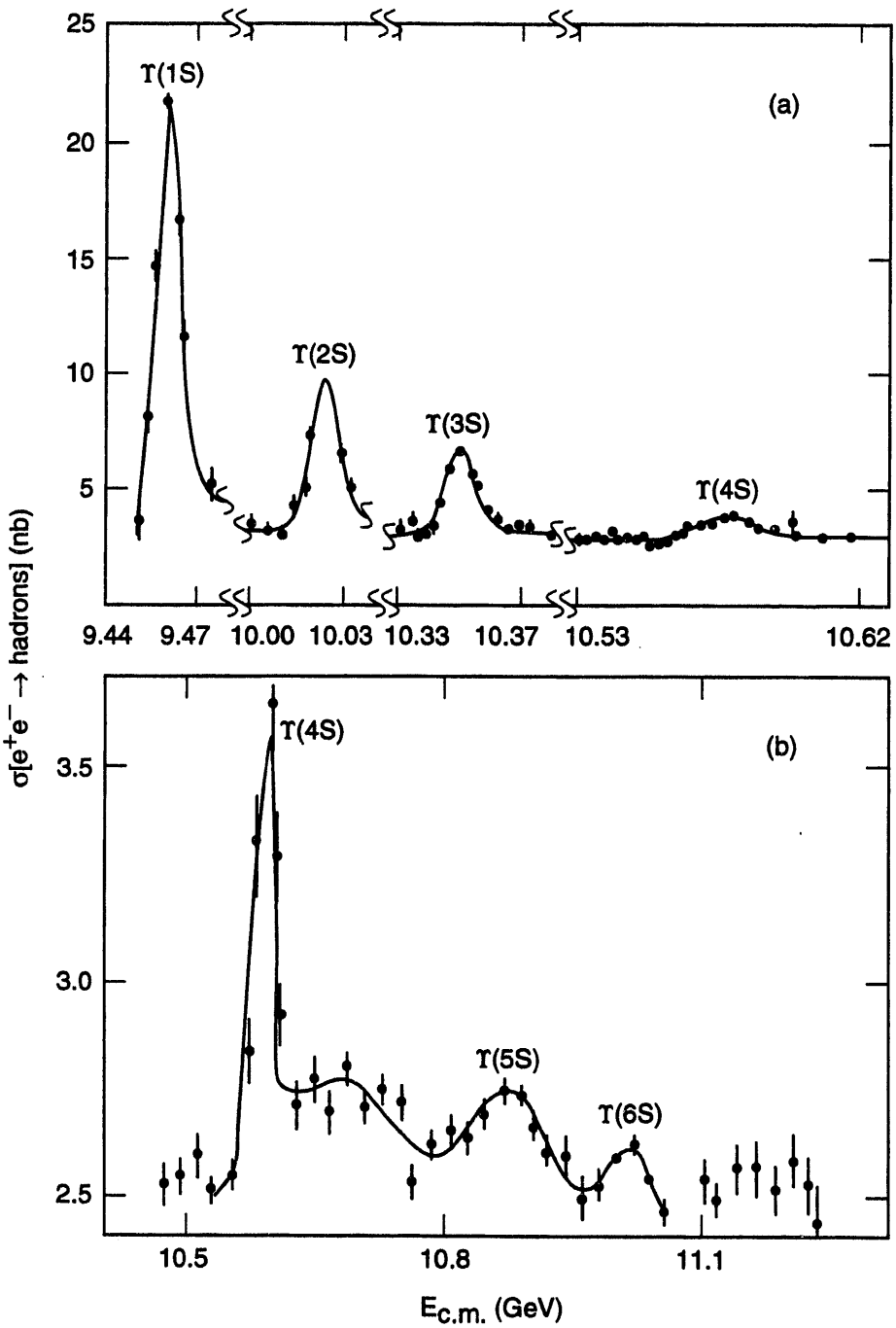

Fig. 2-1. The cross section for the production of hadrons in e^+e^- collisions in the center-of-mass energy region near 10 GeV. The data are characterized by a series of resonances, the Υ family, which herald the onset of the b quark threshold. The data in (a) are from the CUSB detector group; the data in (b) are from the CLEO detector group.

(Υ) system; the first three prominent resonances are the lowest-lying S states of a bound $b\bar{b}$ quark system. These states are analogous to the bound states in an atomic system (such as positronium); in this case, however, it is the strong (color) force that provides the binding

energy for the two constituents. The narrowness of the resonances reflects their stability against strong decays; the states have insufficient energy to decompose into a pair of mesons, each carrying a b quark. The fourth state, $\Upsilon(4S)$, has just sufficient energy to decay to a pair of B mesons (B and $\overline{B}$); this decay totally dominates the disintegration of the $\Upsilon(4S)$. The $\Upsilon(4S)$ is thus an ideal laboratory for the study of B decays, having the following important features:

- The $\Upsilon(4S)$ decays almost exclusively to pairs of B mesons. There are thus no extraneous particles that would provide background and reduce the sensitivity of the measurements.
- Since the $\Upsilon(4S)$ decays to only two particles, the daughter B mesons have a unique momentum in the $\Upsilon(4S)$ center-of-mass frame. In addition, the fraction of all events that contain a $B\overline{B}$ pair is 30%, significantly greater than at higher energies or in proton collisions. These two effects greatly limit contamination from backgrounds from the continuum of physics channels (non-b quarks) that accompany the $\Upsilon(4S)$.
- When the $\Upsilon(4S)$ decays, the two B mesons are coherently produced in a P-wave state. This guarantees that the two B mesons are nonidentical; that is, the one is a B^0 while the other is a $\overline{B}^0$. This feature is particularly advantageous for CP violation studies.
- The multiplicity of hadrons in the $\Upsilon(4S)$ decay is relatively small. When combining particles to reconstruct B meson states, this low multiplicity keeps combinatorial backgrounds at a reasonable level.

The B mesons produced in $\Upsilon(4S)$ decay (B_u, B_d) comprise a b quark and a lighter quark, either an up (u) or down (d) quark. It is also of considerable interest to study the decays of B mesons that contain a strange (s) quark (B_s). These studies must be done at the $\Upsilon(5S)$ resonance (see Fig. 2-1).

The majority of the PEP-II program will be carried out at the $\Upsilon(4S)$. As we have seen, this choice of energy provides a copious source of B_u and B_d mesons. Accompanying the resonant production of B mesons is the so-called continuum physics, the roughly 2.5 nb of cross section that comprises e^+e^- annihilation into pairs of light quarks (u, d, and s), pairs of light leptons (e^+e^- and $\mu^+\mu^-$), pairs of heavy quarks (charm quarks), and pairs of heavy leptons ($\tau^+\tau^-$). The light quark and lepton events are of little interest (save for normalization of the experiment), but the heavy-constituent events are of considerable interest. PEP-II will produce very large samples of these heavy constituents, thereby assuring an interesting and diverse physics program.

2.3 PHYSICS MOTIVATION

We turn our attention now to the details of the particle physics program and how it relates to specifying the goals for PEP-II. We have studied this physics program very extensively and with great attention to detail in a series of workshops and conferences held over the past several years. The interested reader is encouraged to consult the proceedings of these meetings [Hitlin, 1989, 1991, and 1992] for more details. The first meeting covered the full spectrum of available physics (except two-photon physics), whereas the second one

dealt much more extensively with the study of *CP* violation and also covered two-photon physics. The most recent meeting, held at Stanford in 1992, provided a summary of progress during the past year. The machine design goals all come from the *B* physics program and are dominated by the requirements for studying *CP* violation. [A rather similar set of goals arises from the study of B_s mixing, although, in this case, the experiment is done at the T(5S).] Happily, the requirements for the *CP* violation program do not conflict in any way with those of the rest of the physics program.

2.3.1 The Standard Model of Particle Physics

Our understanding of the interactions among Nature's basic building blocks, the quarks and leptons, is described by a theory called the *Standard Model.* This model successfully explains all experimental measurements as they pertain to the three forces seen by the constituents, the strong force, the electromagnetic force, and the weak force. There are no verified experimental anomalies between experiment and the Standard Model—a situation of unprecedented success. However, as a complete model of Nature, the Standard Model has several crucial shortcomings, and most particle physicists believe that it must one day be superseded by a more complete theory. It is widely acknowledged that progress towards this more satisfactory theory will almost certainly have to come from experiment (as opposed to new theoretical insights); the field is therefore greatly in need of verifiable data that is in solid *conflict* with the Standard Model.

Among the unsatisfactory elements of the Standard Model are its inability to predict many important numbers (such as the masses of the constituents, the masses of the force mediators, etc.) and the rather ad hoc (often called "unnatural") manner in which it handles certain essential elements, the leading example being the way particle masses are generated (the Higgs phenomenon). Whereas the well-established phenomenon of *CP* violation has a natural place within the Standard Model, it in no sense has an explanation. One of the strengths of the PEP-II heavy-constituent program is the broad range of measurements that will directly confront the validity of the Standard Model. Many ways can be imagined in which this program could provide the first indication of where the Standard Model fails—in this sense, it provides possibly the best window to new physics of any currently proposed facility. Understanding the Higgs mechanism supplies the justification for the SSC; likewise, understanding the origin of *CP* violation is the central driving force for the construction of PEP-II.

The Standard Model describes the interactions of the building blocks of matter, the six quarks and the six leptons. These spin 1/2 constituents interact via three forces, each of which is mediated by spin 1 force carriers such as the photon (electromagnetic); the Z, W^+, and W^- (weak); and the gluons (strong). With these twelve constituents (and their antiparticles) and the force carriers, all physical phenomena are explainable (we ignore gravity in this discussion). The constituents come in three generations or families. The lightest generation (the up and down quarks, the electron and the electron neutrino) plays a special role in our universe: All stable matter is made up of these four constituents. Yet, for reasons we do not understand (another shortcoming of the Standard Model), Nature has chosen to make two replicas of this lightest generation (see Table 2-2). The clearest distinction among the generations is the increase in mass; the higher the generation, the

Table 2-2. The particles of the Standard Model.

Name	Symbol	Mass (GeV)	Electric charge
	Leptons		
Electron	e^-	0.000511	−1
Electron neutrino	ν_e	0	0
Muon	μ^-	0.106	−1
Muon neutrino	ν_μ	0	0
Tau	τ^-	1.777	−1
Tau neutrino	ν_τ	0	0
	Quarks		
Up	u	0.31	+2/3
Down	d	0.31	−1/3
Charm	c	1.50	+2/3
Strange	s	0.51	−1/3
Top	t	>100	+2/3
Bottom	b	5.0	−1/3
	Carriers of force		
Photon	γ	0	0
	Z^0	92	0
Weak vector bosons	W^+	81	+1
	W^-	81	−1
Gluon	g	0	0
	Higgs		
Higgs	H^0	?	0

larger the constituent masses (save for the neutrinos, which so far appear massless). Hence, the τ lepton is the heaviest charged lepton, the top quark (as yet undiscovered, with a mass in excess of 100 GeV) is the heaviest charge 2/3 quark, and the b quark is the heaviest charge −1/3 quark. Whereas we do not understand the replication of the lowest-lying generation, there is no denying the existence of the second and third generations. Indeed, it is the richness of the quark generations that most likely holds the key to expanding beyond the Standard Model.

2.3.2 The Pattern of Quark Decays—The CKM Matrix

To understand this last statement, we must delve more deeply into the pattern of constituent decays. Here the apparently symmetrical role of the quarks and leptons breaks down. The lepton generations are distinct: No interactions couple them. In any physical process, lepton number is conserved separately *for each generation.* Thus, in the decay of a muon, three particles materialize: a muon neutrino, an electron, and an electron antineutrino. The first-generation lepton number is conserved by the balance of the electron and its antineutrino, while the muon neutrino is needed to balance the second-generation lepton number. This absence of cross-generation coupling appears to be absolute in the lepton sector, but not in the quark sector. Indeed, the *s* and *b* quarks would be entirely stable if they could not couple to quarks of a lower generation. Thus, quark decay involves a coupling of the generations: A *b* quark can cascade down to the charm quark (which is its predominant choice) or, less likely, to the up quark. This intergenerational mixing is summarized by the so-called Cabibbo-Kobayashi-Maskawa (CKM) matrix. This matrix represents the fact that the weak interaction does not couple directly to the quark mass eigenstates; rather, the weak eigenstates (which couple to the *W*'s) are admixtures of the mass eigenstates, the exact admixture being given by the elements of the CKM rotation matrix. The richness of the quark decay spectra is represented by the elements of the matrix:

$$\begin{pmatrix} V_{ud} & V_{us} & V_{ub} \\ V_{cd} & V_{cs} & V_{cb} \\ V_{td} & V_{ts} & V_{tb} \end{pmatrix}$$

The CKM matrix can be completely characterized by four parameters: three real numbers and one complex phase. A commonly used approximate parametrization is that due to Wolfenstein:

$$\begin{pmatrix} 1-\lambda^2/2 & \lambda & A\lambda^3(\rho-i\eta) \\ -\lambda & 1-\lambda^2/2 & A\lambda^2 \\ A\lambda^3(1-\rho-i\eta) & -A\lambda^2 & 1 \end{pmatrix}$$

where A, λ, ρ, and η are real parameters. When $\lambda = 0$, this matrix becomes the unit matrix, and there is no coupling among generations.

If the Standard Model were truly a complete theory of Nature, the CKM mechanism would have arisen naturally in the model, and all the values of the elements of the matrix would be specified. Instead, these numbers must be measured, and self-consistency must be established to check the validity of the model. *It is for this reason that the pattern of quark decays offers a powerful window onto the validity of the Standard Model.* In particular, the heavy-quark decays (those of charm and bottom, which are so profuse and so readily studied at PEP-II) provide a wealth of data for testing the Standard Model.

2.3.3 *CP* Violation in the Standard Model

We will now focus on the phenomenon of *CP* violation. The origin of *CP* violation has been one of the defining mysteries of particle physics since the violation was first discovered in the Nobel Prize–winning work of Cronin, Fitch, and collaborators [Christenson et al., 1964]. While the physical manifestations of this asymmetry are tiny, its ramifications are cosmic. Indeed, without the presence of this phenomenon, we would be hard-pressed to explain the presence of our universe. In the absence of *CP* violation, the equations that govern the behavior of particles created in the Big Bang are matter-antimatter symmetric. Under such circumstances, particle-antiparticle annihilation should have dominated, and no stable universe should have resulted. Yet we find ourselves living in a stable, matter-dominated universe. The tiny anisotropy generated by *CP* violation, the only known physical process that allows for an *absolute* determination of the sign of the electric charge, was sufficient to tip the balance away from total annihilation and permit the creation of a stable universe.

The lack of *CP* symmetry is experimentally well demonstrated in the decays of K mesons. However, an explanation for the origin of the violation remains no more than conjecture; the K meson system provides too limited a set of measurements to fully fix the appropriate CKM parameters or to distinguish between competing models of the mechanism. It is the inclusion of the complex element (the phase η in the Wolfenstein representation) that provides a *mechanism* for *CP* violation in the Standard Model. It should be emphasized that *CP* violation is not a necessary consequence of the Standard Model; it is merely allowed. We have no experimental evidence for or against the idea that this mechanism of *CP* violation is in fact the correct one. Studies of *CP* violation in the decays of the B meson system, unlike those in the K meson system, provide the diversity needed to over-constrain the Standard Model and hence establish once and for all whether this mechanism is correct.

Using the data from K meson measurements and the framework of the Standard Model, predictions for the size of the *CP* asymmetries in B meson decays can be made. Because our understanding of quark decays is not perfect, the size of these *CP*-violating effects cannot be precisely pinpointed; rather, a range of validity is predicted. Despite this uncertainty, for certain decays ($B^0 \to J/\psi K_S$ being the most studied), the Standard Model makes an unambiguous prediction of a large *CP*-violating asymmetry, in the range of 16–60%. (This can be contrasted with the asymmetries in the K meson system, which amount to two parts per thousand.) The physical effect we seek is thus large and easily measured, provided that sufficient events can be accumulated in the appropriate B meson decay modes. The branching fractions for these *CP*-violating decay modes tend to be small (typically 10^{-4}–10^{-5}), hence one needs to produce of the order of 10^7–10^8 B mesons to make statistically significant measurements of *CP* asymmetries. The desire to confront *CP* violation in this complete manner is what leads to the requirement of a very large integrated luminosity.

We shall now explore the range of the Standard Model predictions more quantitatively, because, if we are to fully test the validity of the Standard Model, we need to construct a machine capable of producing sufficient luminosity to cover this range completely. The

CKM matrix is unitary, and therefore the following requirement must hold:

$$V_{ud} V^*_{ub} + V_{cd} V^*_{cb} + V_{td} V^*_{tb} = 0$$

This equation can be viewed as the closure of a triangle (the "Unitarity Triangle") in the complex (ρ,η) plane. Using the Wolfenstein representation, the triangle is as shown in Fig. 2-2. If *CP* violation in the *B* meson system were absent, then η would be zero and the triangle would collapse to a line on the real axis. As we stated above, the Standard Model predicts a range of *CP*-violating asymmetries in *B* decays and therefore a range of allowable angles α, β, and γ. This range is shown in Fig. 2-3 as a function of the *t* quark mass. It is this range of values that we must be capable of measuring if we are to ascertain whether the Standard Model can accommodate *B* meson *CP* asymmetries and whether it is self-consistent. As indicated in Fig. 2-2, α, β, and γ are directly measurable from specific *B* meson decays to *CP* eigenstate final states, respectively indicated by a set of prototypical decays $B_d \rightarrow J/\psi K_s$, $B_d \rightarrow \pi\pi$, and $B_s \rightarrow \rho K_s$.

2.3.4 How *CP* Asymmetries Are Measured

To understand how the asymmetries are measured, we now return to our discussion of the $\Upsilon(4S)$ system and its decay into a $B^0\overline{B}^0$ pair. These *B* mesons are fairly long-lived (the *B* meson lifetime is about 1 ps) and will propagate a measurable distance before they decay. The first *B* (we assume it to be a B^0; the argument is just reversed if it is a $\overline{B}^0$) will decay at time t_1 and, by the coherence referred to earlier, will force the second *B* to be a $\overline{B}^0$. This second *B* meson propagates further in time before it decays at time t_2. However, during the time interval $t_2 - t_1$, the $\overline{B}^0$ can change itself into a B^0 via the phenomenon of mixing. In fact, the Argus Group at DESY [Albrecht et al., 1987] first showed that mixing of neutral B_d mesons is large. Hence, it is possible to end up with either a $B^0\overline{B}^0$ final state or a B^0B^0 final state, depending on whether the second *B* meson has mixed or not. If we now arrange to detect one of the *B*'s decaying to a *CP* self-conjugate eigenstate (like $J/\psi K_s$

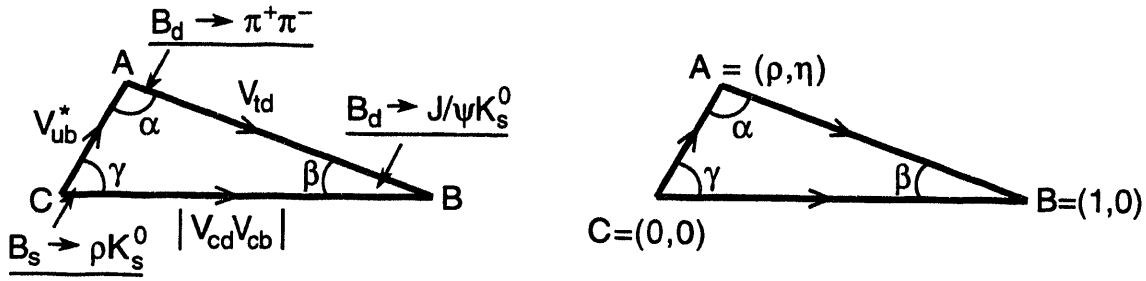

Fig. 2-2. The "Unitarity Triangle," along with definitions of the angles α, β, and γ and the prototypical self-conjugate CP eigenstates that are used to measure these angles. Closure of this triangle in the complex plane represents the unitarity of the CKM matrix. The parameters ρ and η, which appear in the Wolfenstein parametrization of the CKM matrix, are also shown here.

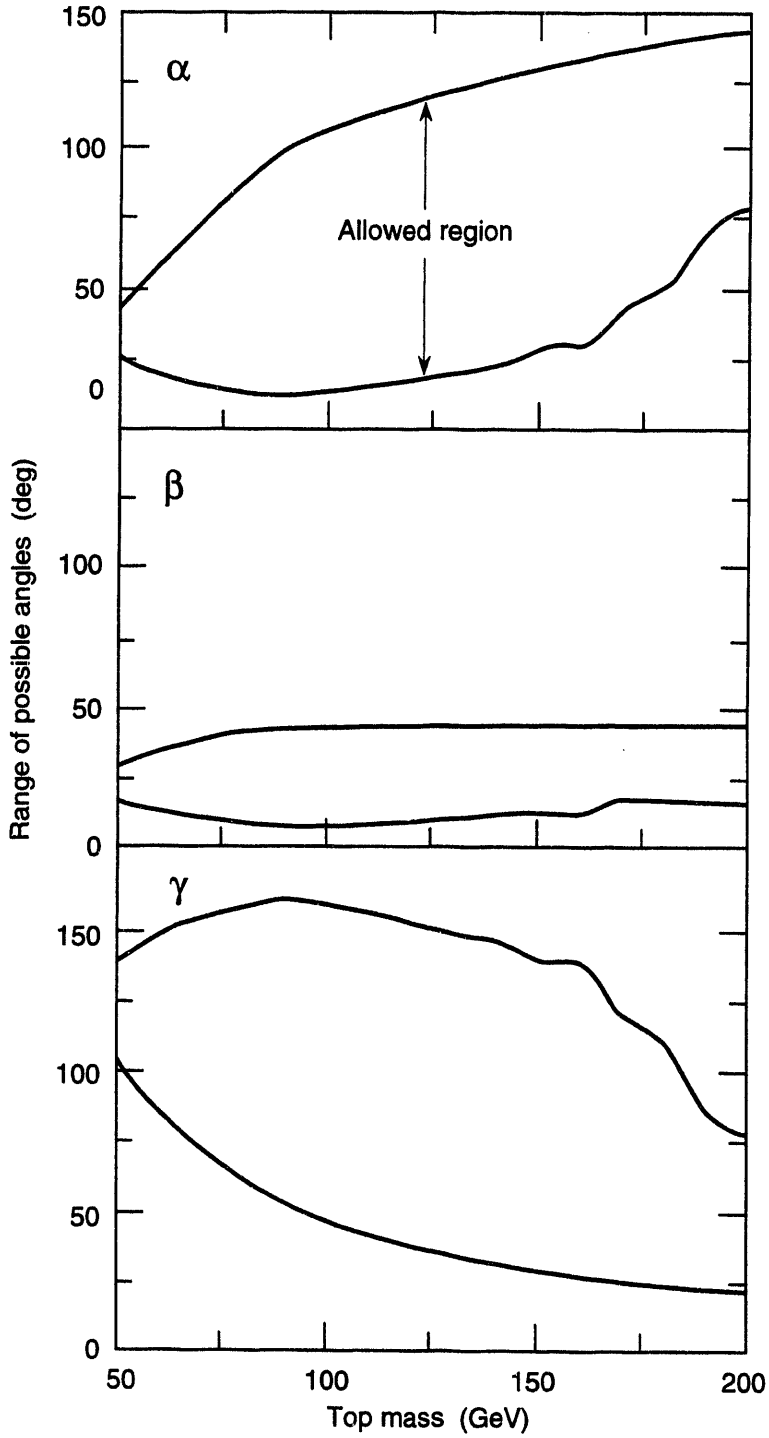

Fig. 2-3. The range of the unitary triangle angles allowed by the Standard Model (under reasonable assumptions for the model parameters), as functions of the top mass, currently thought to be above 100 GeV. Since the allowed range of β is never zero, the Standard Model unambiguously predicts finite asymmetries in decays characterized by sin 2β (like $J/\psi K_S$).

or $\pi\pi$) and the other in a decay that distinguishes between a B^0 and a $\overline{B}^0$ (such as the sign of the charge of a lepton or kaon), it is possible to measure a *CP* asymmetry. The asymmetry arises from the fact that mixing has allowed two separate routes from the initial *B* meson to the final *CP* self-conjugate state (see Fig. 2-4), one without intermediate mixing and the other with mixing. If the interference between these two separate paths is different, depending on whether one starts from a physical B^0 or $\overline{B}^0$, a potentially measurable asymmetry is generated. The decay rate (Γ) of a time-evolved, initially pure $B^0\overline{B}^0$

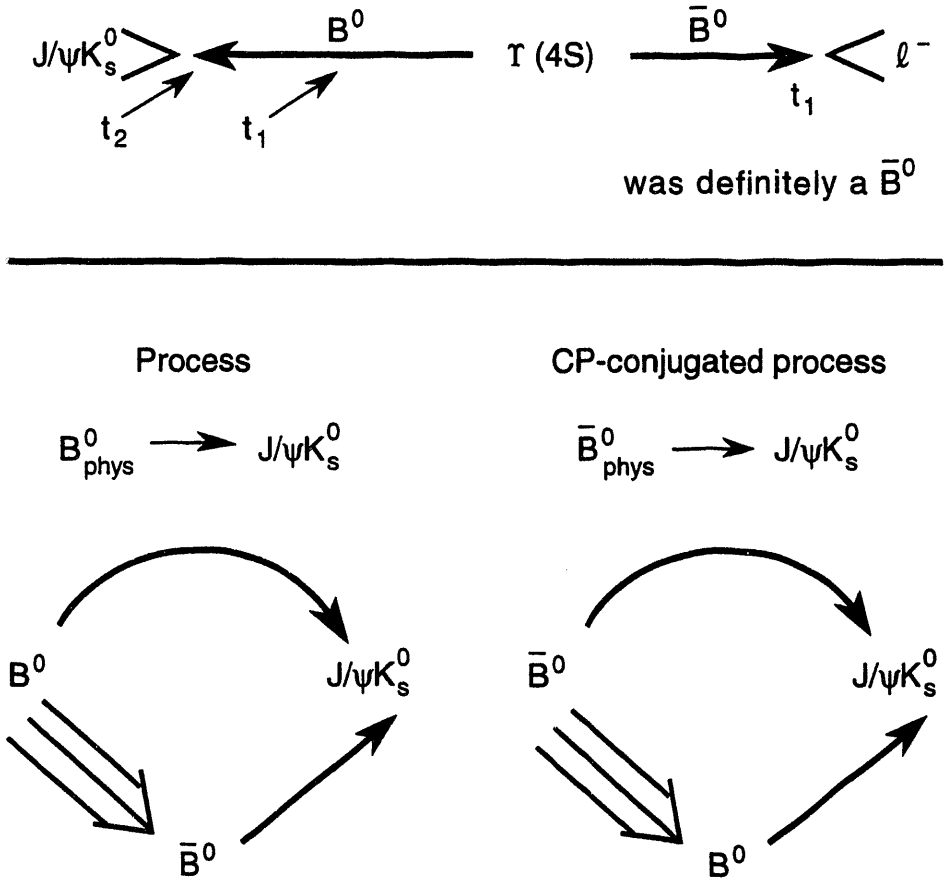

Fig. 2-4. An artist's rendition (upper diagram) of the topology used for measuring CP violation effects at the Υ(4S). One of the neutral B's is reconstructed in a CP self-conjugate state (the J/ψK$_S$), while the identity of the other B (B^0 or $\overline{B}^0$) is established from the sign of the charge of a lepton (or K meson). The lower diagram illustrates how mixing is used to project out the CP violation effects. The B^0 can decay to J/ψK$_S$ (bottom left) via two routes, one direct and one involving mixing. These two amplitudes will interfere, and this interference has a different magnitude when one begins with the CP-conjugated state $\overline{B}^0$ bottom right). Thus, final states involving J/ψK$_S$/B^0 and J/ψK$_S$/$\overline{B}^0$ can be used to measure CP asymmetries.

into a B^0 ($\overline{B}^0$) and a self-conjugate *CP* eigenstate f_{CP} is given by

$$\Gamma(B^0\overline{B}^0 \rightarrow B^0 f_{CP}) \propto e^{-\Gamma\Delta t}\,[1+ \sin 2\phi\ \sin \Delta m(t_2 - t_1)]$$

$$\Gamma(B^0\overline{B}^0 \rightarrow \overline{B}^0 f_{CP}) \propto e^{-\Gamma\Delta t}\,[1- \sin 2\phi\ \sin \Delta m(t_2 - t_1)]$$

where Δm is the $B^0\overline{B}^0$ mass difference, $\Delta t = t_2 - t_1$, and ϕ is α, β, or γ, depending on whether the *CP* eigenstate observed is $J/\psi K_s$, $\pi\pi$, or ρK_s.

There are four different measurable configurations:

$$n_1\text{: } f_B(t_1) f_{CP}(t_2)$$
$$n_2\text{: } f_{CP}(t_1) f_B(t_2)$$
$$n_3\text{: } f_{\overline{B}}(t_1) f_{CP}(t_2)$$
$$n_4\text{: } f_{CP}(t_1) f_{\overline{B}}(t_2)$$

where f_B signifies a B^0 tag, $f_{\overline{B}}$ signifies a $\overline{B}^0$ tag, and f_{CP} signifies a *CP* eigenstate. *CP* violation produces a distribution in $t_2 - t_1$ for n_1 and n_4 that is different from that for n_2 and n_3. In the absence of *CP* violation, the n_i distributions would be exponentials; in the presence of *CP* violation, they are measurably distorted by a sinusoidal oscillation with amplitude $\sin 2\phi$ and frequency Δm, as shown in Fig. 2-5.

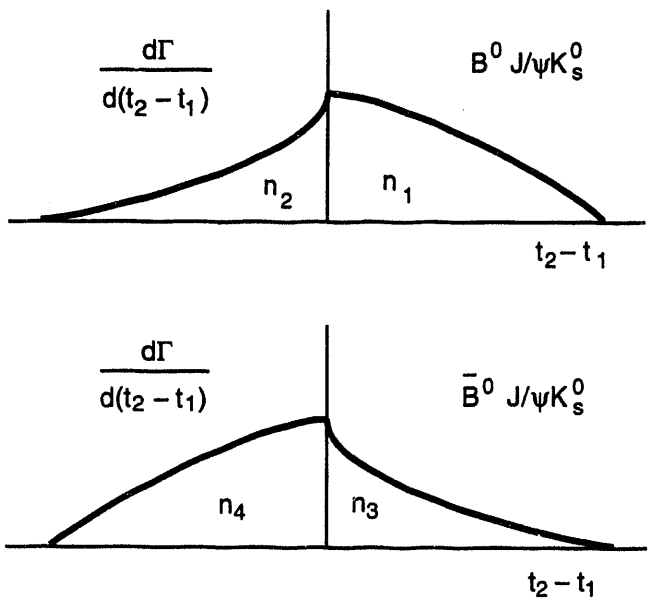

Fig. 2-5. The time-evolved decay distributions that are measured to yield the CP asymmetries. The n_i signify four different final-state topologies, as outlined in the text. It is the distortion of these spectra from exponentials that provides the information for measuring CP violations.

A measurable asymmetry results from a proper summation of the number of events of each type:

$$A_{CP} = (n_2 + n_3 - n_1 - n_4)/(n_1 + n_2 + n_3 + n_4)$$

It is this asymmetry, as well as the detailed time distributions, that will be measured at PEP-II. As seen from Fig. 2-5, the advantage of an asymmetric B factory is the availability of the time-evolving distributions. Not only does this exhibit the CP violation to its fullest extent, but also the four time-evolved spectra provide two pairwise identical distributions, and the sum of the integrals under the four distributions should be zero (another way of saying that the time-integrated asymmetry must be identically zero). These constraints provide a valuable set of cross-checks on the correctness of the measurements.

The asymmetry A_{CP} is directly related to the angles of the Unitarity Triangle, according to

$$A_{CP} = \frac{x_d \sin 2\phi}{(1 + x_d^2)}$$

where ϕ is α, β, or γ, depending on whether the CP eigenstate observed is $J/\psi K_s$, $\pi\pi$, or ρK_s. Here x_d represents the strength of the B^0 mixing (measured to be 0.70), hence the dilution factor relating the measured asymmetry to the unitarity angle is known.

To summarize, then, the experiment involves measuring the time difference between the decay points of the two B mesons produced in the decay of the $\Upsilon(4S)$. In addition, one of the B final states must be established as a CP eigenstate, and the other must be tagged as either a B^0 or a $\overline{B}^0$. Establishing the identity of the two B mesons is readily done; this has a significant impact on the design of the detector but relatively little impact on the design of the accelerator. The time-difference measurement is faithfully represented by the measurement of the difference in the positions of the two decay points of the B mesons; it is the need to measure this difference that is responsible for the energy asymmetry of the accelerator.

2.3.5 Justification for the Energy Asymmetry

As suggested above, the crucial experimental ingredient is the ability to accurately measure the distance between the decay points of two B mesons. With modern vertex detectors using silicon technology, one is able to measure this distance with a resolution of about 50 μm. If a B meson facility is run with equal beam energies, the $\Upsilon(4S)$ is produced at rest in the laboratory, and the two mesons do not propagate very far before they decay. The typical distance between the B meson decay points in this equal-beam-energy geometry would be about 30 μm, a distance too small to discern with today's detectors. The solution to this dilemma, first proposed by Oddone [1987], is to boost the $\Upsilon(4S)$ in the laboratory frame by running the collider with *unequal beam energies*, hence the term asymmetric B factory. The asymmetry denotes the difference in energy between the electron and positron beams. For example, if one chooses 9 and 3.1 GeV for the two beam energies [$E^2_{c.m.} = 4E_{low}E_{high}$; the center-of-mass energy is thus that of the $\Upsilon(4S)$], then the average distance

between the two B meson decays becomes 180 μm. Figure 2-6 shows the results of a detailed simulation (see Hitlin [1989], pp. 69–83) of a measurement of sin 2β, using the CP eigenstate $J/\psi K_s$ and kaons and leptons as tags. The distortion of the exponential decay distributions, arising from CP violation, is readily seen.

The justification for an asymmetry in the beam energy is now clear: It is required to give the $\Upsilon(4S)$ system a sufficient Lorentz boost to provide a measurable $t_2 - t_1$ distribution. But how large does the asymmetry need to be? Figure 2-7 shows a simulation of the measurement error for sin 2β as a function of the energy of the high-energy beam. One sees a precipitous dependence on the asymmetry for energy choices below 8 GeV. To remain safely above this region, and to protect against a less optimal set

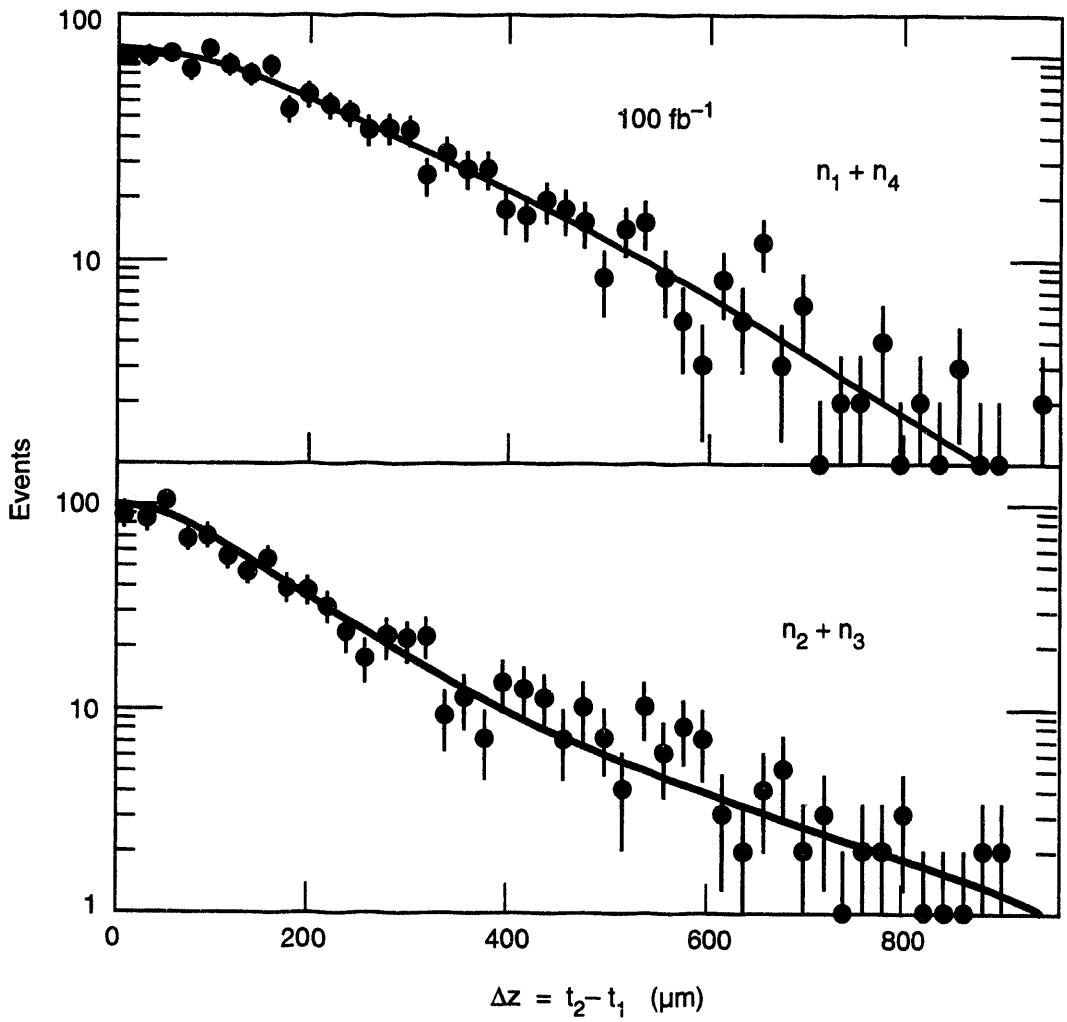

Fig. 2-6. A simulation of the decay length distributions for two classes of events. The upper plot includes events where the first B decays to $J/\psi K_s$ and the second B is tagged as a B^0, or the first B is tagged as a $\overline{B}^0$ and the second B decays to $J/\psi K_s$ (n_1 and n_4); the lower plot has the two complementary topologies (n_2 and n_3). For details, see Hitlin [1989], pp. 69–83. The input value was sin $2\beta = -0.4$; a fit to the data yielded sin $2\beta = -0.408 \pm 0.023$ for the assumed 100 fb^{-1} of data.

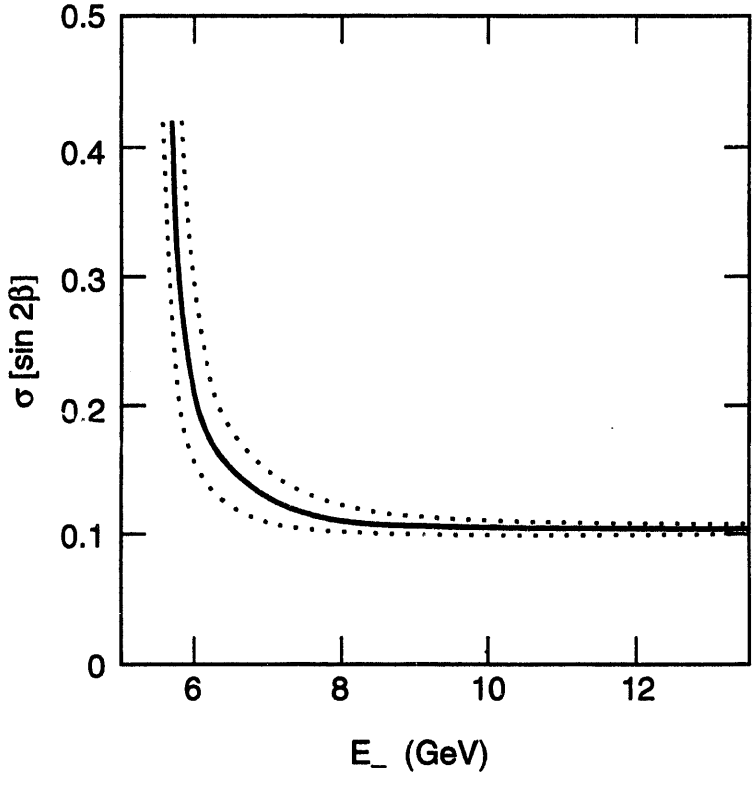

Fig. 2-7. The resolution for measuring sin 2β as a function of the energy of the electron (high-energy) beam. The upper (lower) dotted curve assumes a vertex resolution of 120 μm (50 μm); the solid line assumes 80 μm.

of experimental conditions than those assumed in the simulation, we chose to set the high-energy beam energy at 9 GeV. This choice guarantees the full benefit of the asymmetric geometry.

2.3.6 Justification for the Design Luminosity

We now turn to the issue of what the machine design luminosity ought to be if we are to fully constrain the Standard Model within a reasonable period of time. A decision requires doing very detailed simulations of the measurements of *CP* asymmetries, using a realistic detector. Accordingly, simulations have been performed [Hitlin, 1989 and 1991] for a wide variety of final states. It turns out that it is possible to employ many more B^0 final states than the *CP* self-conjugate ones referred to above. A number of impressive studies have now shown that these final states also have measurable asymmetries, comparable to those expected for $J/\psi K_s$ and $\pi\pi$. These states are those of mixed *CP*, such as $J/\psi K^*$ and $D^{*+}D^{*-}$, as well as states that are not *CP* eigenstates, such as $\rho\pi$ or $a_1\pi$. Figure 2-8 shows the range of sensitivity to the angles α and β for an integrated luminosity of 100 fb^{-1}, using only the *CP* eigenstates $J/\psi K_s$ (for β) and $\pi\pi$ (for α). A data set of this size gives excellent coverage of the range of parameter space allowed by the Standard

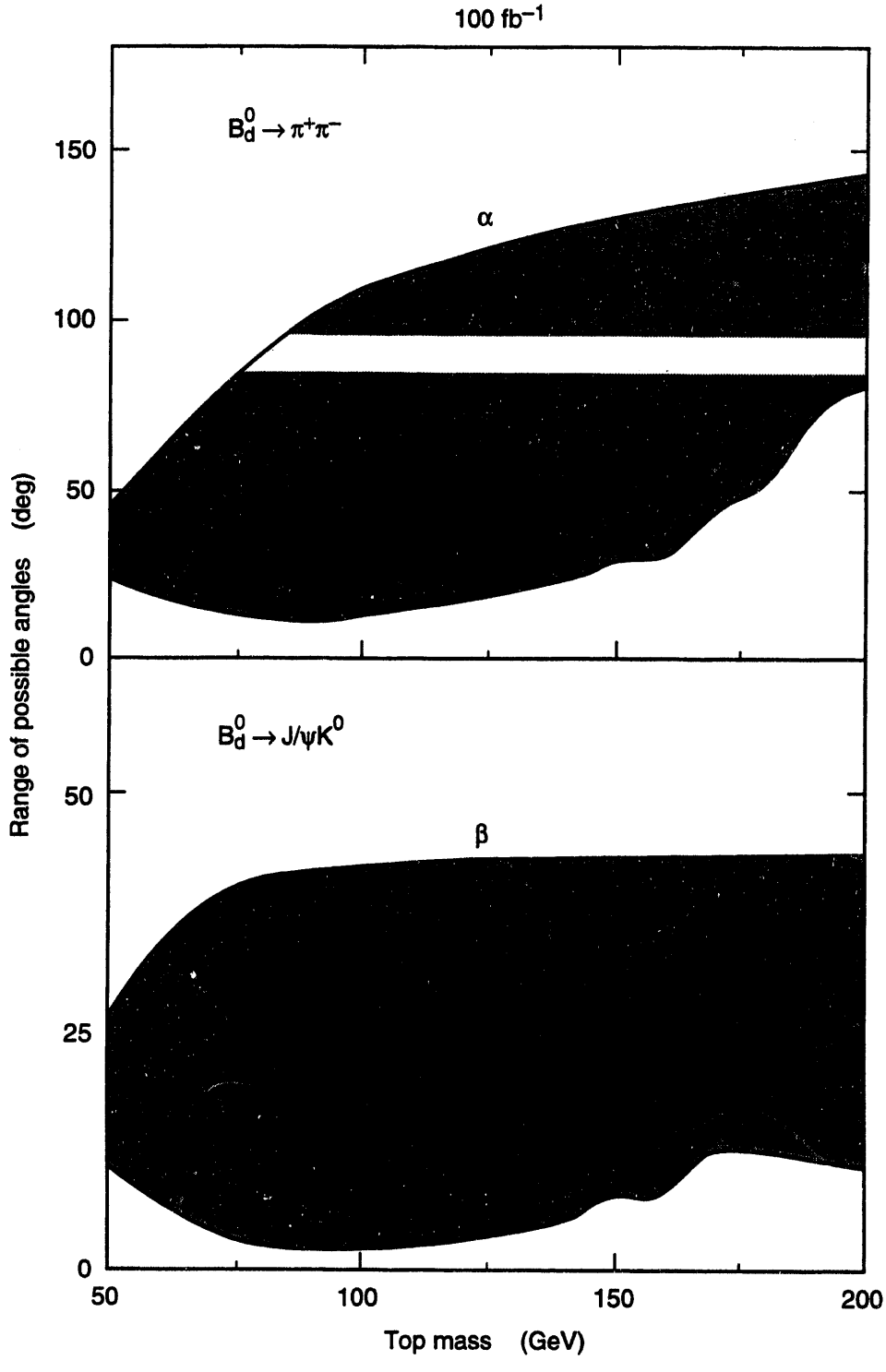

Fig. 2-8. The range of the Standard Model predictions for α and β. The shaded region represents the portion of this range covered (with 3σ precision) by measurements using the CP decay modes $J/\psi K_S$ (for β) and ππ (for α). A data set of 100 fb^{-1} was assumed.

Model. Figure 2-9 shows what can be accomplished using the additional modes in Table 2-3, based upon a data set of 30 fb^{-1}.

It is important to emphasize here that the large integrated luminosities shown in Figs. 2-8 and 2-9 arise from the need to cover essentially the entire range of Standard Model predictions. It is entirely possible that a significant measurement of a *CP* violation asymmetry could be established with far less data. For instance, if the angle β were in the middle of the predicted Standard Model range, $\sin 2\beta = -0.4$, a 3σ measurement would be obtained with only 3 fb^{-1}. Likewise, if the Standard Model were wrong, and $\sin 2\beta$ were positive, a clear indication of such an effect would require relatively little data. It is for "less favorable" scenarios that the high luminosity is necessary.

Based on Figs. 2-8 and 2-9, we have concluded that an accelerator that delivers 30 fb^{-1} per calendar year has spectacular discovery potential and will cover the complete range of Standard Model predictions in a period of a few years. This then becomes the design goal for the collider. To convert this into a design luminosity for PEP-II, we use the "Snowmass convention" that a year has 10^7 seconds, taking into account accelerator and detector efficiencies and the difference between peak and average luminosities. We thus require a peak luminosity of 3×10^{33} cm^{-2} s^{-1} to obtain 30 fb^{-1} in one calendar year.

Information gathered at the $\Upsilon(5S)$ resonance on the angle γ is complementary to the measurements of α and β, but very large samples (several hundred fb^{-1}) are required to match the precision of the measurements done at the $\Upsilon(4S)$. For details, see Hitlin [1989], pp. 84–91. Methods for extracting γ at the $\Upsilon(4S)$ have also been developed (see Hitlin [1992]).

2.3.7 Sensitivity to Nonstandard Origins for *CP* Violation

So far we have restricted ourselves to the use of *CP* asymmetries in the context of verifying the Standard Model. The asymmetries are actually much more powerful: They can provide deep insights in the event that the Standard Model proves to be incorrect.

The simplest statement that can be made is that, a priori, there is no reason to expect the Standard Model range for $\sin 2\beta$ to be any more probable than the rest of the physical range. Establishing that the Standard Model is wrong is therefore very direct and could take relatively little running time, even at luminosities significantly below the design level.

The B^0 meson *CP* laboratory is considerably richer than even this statement would suggest, as has been outlined by Nir and collaborators [1990a, b, and c]. When we make the predictions about *CP* asymmetries discussed above for the Standard Model, we make several essential assumptions. We assume, for instance, that the nontagging B^0 decay has contributions from only one *W*-mediated quark subprocess. Multiple subprocesses (such as penguin contributions) could significantly change the predictions of the Standard Model. (It is fortunate that this assumption is reliable for the prototypical decay $B^0 \to J/\psi K_s$, where contaminations are considered to be below the few percent level.) We also assume that both K-$\overline{K}$ and B-$\overline{B}$ mixing proceed via the Standard Model mechanism of a "box diagram." Both of these assumptions enter the calculations of the asymmetries in a central way. What Nir and collaborators have shown is that experiments performed at PEP-II can, through a specific set of measurements, pinpoint directly which of these underlying

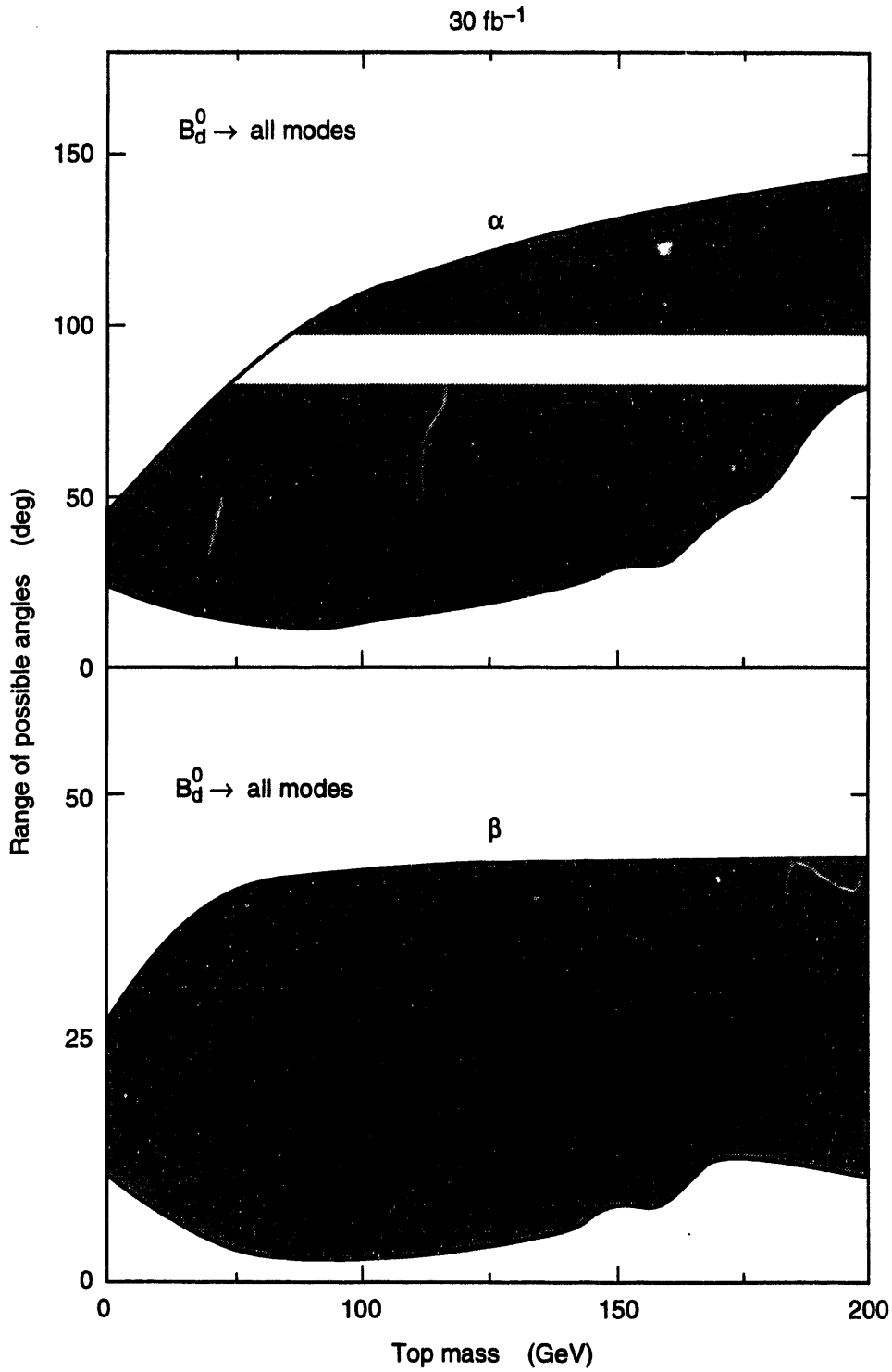

Fig. 2-9. The range of α and β predicted by the Standard Model that can be covered (3σ) by a 30-fb^{-1} data set, using a spectrum of CP decay modes (see Table 2-3).

Table 2-3. Summary of the assumptions used in the simulations of Fig. 2-9 to establish the measurement errors for sin 2α and sin 2β (here generalized as sin 2ϕ). In addition, we have used as input a wrong-sign fraction of 8%, a $B\bar{B}$ cross section of 1.2 nb, and a neutral B fraction of 0.5.

	Mode	Assumed reconstructible branching fraction	Tagging efficiency (%)	Reconstruction efficiency (%)	σ (sin 2ϕ) (30 fb^{-1})
B^0	$\rightarrow J/\psi K_S^0$ [a]	$5 \times 10^{-4} \times 0.12$	45	51[d]	0.09
	$\rightarrow J/\psi K_L^0$ [b]	$5 \times 10^{-4} \times 0.12$	42	34	0.12
	$\rightarrow J/\psi \bar{K}^{*0}$ [c]	$12.5 \times 10^{-4} \times 0.12 \times 0.33$	45	30	0.13
	$\rightarrow D^+D^-$ [a]	$6 \times 10^{-4} \times 0.017$	45	38	0.28
	$\rightarrow D^{*+}D^{*-}$	$16 \times 10^{-4} \times 0.017$	45	21	0.21
	Combined (2β)				0.059
B^0	$\rightarrow \pi^+\pi^-$ [e]	2×10^{-5}	45	35	0.20
	$\rightarrow \rho^{\pm}\pi^{\mp}$ [f]	6×10^{-5}	45	48	0.12
	$\rightarrow a_1^{\pm}\pi^{\mp}$ [f]	$6 \times 10^{-5} \times 0.5$	45	42	0.15
	Combined (2α)				0.083

[a] SLAC-373.
[b] KEK Report 92-3, May 1992.
[c] Assuming decay dominated by a single *CP* eigenstate, and only using the $K^{*0} \rightarrow \pi^0 K_S^0$ mode. I. Dunietz, H. Quinn, A. Snyder, W. Toki, H. Lipkin; Phys. Rev. D 43 2193 (1991).
[d] E. Hyatt, R. Fernholz, D. MacFarlane; BaBar Note 95, Feb. 1993.
[e] SLAC-353.
[f] R. Aleksan, I. Dunietz, B. Kayser, F. LeDiberder; Nucl. Phys. B 361 141 (1991).

assumptions is breaking down. For instance, in the Standard Model, the asymmetry measured in $B^0 \rightarrow J/\psi K_S$ must have the same value as that measured in $B^0 \rightarrow D^+D^-$: If these do not agree, the problem is uniquely with the assumption that K-$\bar{K}$ mixing proceeds via the box diagram. It has also been shown [Nir, 1990c] that in a model in which B-$\bar{B}$ mixing is predominantly due to Z-mediated flavor-changing neutral currents (rather than the familiar box diagram), the predictions for α and β can be completely different from those in the Standard Model; in fact, in this model, the Unitarity Triangle is actually a quadrangle. All these eventualities lead to striking departures from the Standard Model predictions—and they are all readily measurable at PEP-II.

It should also be reiterated that backgrounds in the reconstruction of B mesons in the $\Upsilon(4S)$ environment are small, making it uniquely suited to the reconstruction of a large

number of B^0 decay modes with measurable CP asymmetries, even those of higher multiplicity and those that involve final state π^0's (see Table 2-3). This gives us the ability to make important cross-checks, as well as to reduce the luminosity required for the asymmetry measurements. Our simulations demonstrate that, for all the modes studied, large detection efficiencies are possible, with excellent signal-to-noise ratios.

2.3.8 Other *B* Physics

As outlined in Hitlin [1989], data taken at the $\Upsilon(4S)$ yield a rich B physics program beyond the area of CP violation. The production of several hundreds of millions of B mesons permits a sensitive search for rare and unexpected B decays. These rare decays also provide an important window to violations of the Standard Model. Processes involving penguin diagrams (an example of which is the decay $B^0 \rightarrow K^*\gamma$) will be readily accessible. It may also be possible to observe the decay $B^0 \rightarrow \tau\nu_\tau$, which would yield a measurement of the B decay constant f_B, a fundamental parameter. PEP-II will permit the search for rare decays at the level of 1 part in 10^8.

As pointed out earlier, the patterns of the heavy-quark decays are basic to an understanding of the weak interaction, and they determine directly the elements V_{ij} of the CKM matrix. A wide variety of $b \rightarrow c$ and $b \rightarrow u$ hadronic decays are available for study, as are $b \rightarrow c$ and $b \rightarrow u$ semileptonic decays.

Whereas we have measured mixing in the B_d^0 sector, mixing in the B_s^0 sector has not yet been observed. The mixing is expected to be more rapid: x_s is expected to be in the range 3–20 (compared with x_d, which is 0.70). Observing this mixing is a high-priority measurement. We have simulated a measurement of x_s using same-sign dilepton events observed in the decay of the $\Upsilon(5S)$. Requiring 10% measurement precision, x_s is measurable up to a value of 15 in a run of 30 fb^{-1}. This result assumes that the energy asymmetry at the $\Upsilon(5S)$ would be the same as at the $\Upsilon(4S)$; one gains rapidly in precision by increasing the energy asymmetry. In all likelihood, the $\Upsilon(5S)$ running will be a second-round experiment, following the first round of CP violation measurements done at the $\Upsilon(4S)$. It would seem prudent, then, when moving the energy up to the $\Upsilon(5S)$, to also reoptimize the interaction region geometry to provide a larger asymmetry. The PEP-II design allows for such a change.

2.3.9 Charm Quark Physics

There is a long list of important topics in charm physics accessible at PEP-II by virtue of its high luminosity.

Mixing in the $D^0\overline{D}^0$ system can be measured at a level several times smaller than the Standard Model prediction for this phenomenon. The expected limit on the mixing for a 30 fb^{-1} run at the $\Upsilon(4S)$ is less than 6×10^{-5}, compared with the Standard Model prediction of about 10^{-4} or larger. This means that if the Standard Model prediction is wrong, PEP-II will have adequate sensitivity to establish this fact. The same measurement will yield information about CP violation in D decay, which is expected to be very small in

the Standard Model. In a 30 fb^{-1} run at the $\Upsilon(4S)$, we will be able to search for CP-violating effects in the decays $D^0 \to K^+K^-$ and $D^0 \to \pi^+\pi^-$ at the 1% level. An effect this large would be uncommonly interesting, but is rather unlikely.

As with bottom quark decays, charm quark decays provide valuable input for the CKM matrix. Definitive measurements of both Cabibbo-allowed and Cabibbo-suppressed semileptonic decay modes are possible.

Two new areas of interest in charm physics are the spectroscopy of the $L = 1$ D^{**} meson resonances and charmed baryons. This area of study has recently been initiated by CLEO and ARGUS with small numbers of events. There are 12 D^{**} $L = 1$ states. Because this system is composed of one heavy and one light object (much like the hydrogen atom), the energy levels are sensitive to the details of the long-range (scalar) part of the potential. Mass splittings between the states are due to the spin-orbit interaction, rather than the more familiar spin-spin interaction. A large number of events are required to measure the masses, widths, spins, and splittings in this system. Estimates have been made (see Hitlin [1989], Table 9.1, p. 236) of the number of events that would be observed in these 12 states. For a 30 fb^{-1} run, these numbers range from 700 to 20,000, with typical signal-to-noise ratios of better than 1:1. There is also a rich spectroscopy of charmed baryon states, few of which have been observed. The same 30 fb^{-1} run would yield thousands of these events per mode (see Hitlin [1989], Table 9.2, p. 239), with a signal-to-noise ratio of about 1:1.

2.3.10 Tau Physics

As far as we can discern, the τ lepton is a heavier version of the muon and electron, all three having properties strikingly consistent with the predictions of the Standard Model. The level of certainty of this statement is, however, experimentally not as great in the case of the τ as it is for the two lighter leptons, as our studies of τ decay involve statistical samples many orders of magnitude smaller. There are, in fact, several inconsistencies in the measurements of τ branching fractions. PEP-II will provide an increase in statistical power, relative to present studies, of one to two orders of magnitude, thus allowing much more thorough tests of the sequential lepton hypothesis for the τ.

Many specific measurements have been considered in detail. The limit on the τ neutrino mass (currently less than 30 MeV) can be lowered to a few MeV. The Cabibbo angle in τ decay can be measured far more accurately than the current ±20%. Searches for second-class currents are possible at a level below the expectations of the Standard Model. Rare decays can be searched for at the 10^{-8} level. The structure of the τ-W-ν_τ vertex can be studied in detail. Both τ branching fractions and the τ lifetime can be measured with exquisite precision; these can then be combined to yield absolute decay widths. The precision with which these measurements can be made is summarized in Table 2-4.

2.3.11 Upsilon Physics

Quarkonia, bound states of quark and antiquark, provide us with an excellent testing ground for QCD, both perturbative and nonperturbative. Bottomonium ($b\bar{b}$), the heaviest

Table 2-4. Summary of τ physics measurements.

Physics topic	$\int \mathcal{L}\, dt$ (fb^{-1})	Sensitivity	Backgrounds	Systematics
M_{ν_τ}	100	3 MeV @ 95% CL	None found	1.1 MeV; hadronic mass scale & M_τ
Cabibbo angle	30	0.5%	Small; from $\tau^+\tau^-$	0.4%; from background and cuts
Second-class currents	30	5σ signal if BF = 3×10^{-5}	From $\tau^+\tau^-$	
Rare decays ($\tau^+ \rightarrow \mu^+\mu^+\mu^-$)	100	BF $\leq 3 \times 10^{-7}$ @ 95% CL	Dominantly $\tau^+\tau^-$	
B_e/B_μ	30	0.2%	Dominantly $\tau^+\tau^-$	0.4%; from background
τ lifetime	30	0.14%	1%; from $q\bar{q}$	0.25%; from vertex detector position
Branching frac. ($\tau \rightarrow e\, \nu\, \bar{\nu}$)	30	0.3%	2%; from $q\bar{q}$	0.2%; from background
τ-W-ν_τ structure	30	ρ, η $O(0.1\%)$ ξ, δ $O(1\%)$		

known system, is the most amenable to theoretical interpretation, as both relativistic corrections and higher-order QCD effects are much smaller than in the lighter quarkonia. The spectrum of bottomonium states is very rich, and although many of the states have been observed, a number of important spectroscopic measurements remain to be made. Much of this physics is only accessible with statistical samples of the size to be available at PEP-II.

Among these measurements, we single out a few for illustration. Transitions from the $\Upsilon(3S)$ and $\Upsilon(2S)$ states to the singlet S states (η_b) and to the lowest singlet P state could lead to the discovery of the pseudoscalar and pseudovector states and measurements of the hyperfine splittings. Detailed studies of the known triplet P states are needed. Enhanced studies of hadronic transitions between the Υ family are also much needed. High-statistics studies of radiative transitions will be performed, including searches for nonstandard Higgs particles. The Υ system can yield precise determinations of the strong coupling constant α_s from comparisons of B meson branching fractions to different final states.

These studies require that the machine be run at energies other than that of the $\Upsilon(4S)$. Relatively short runs (5–10 fb^{-1}) easily provide more than sufficient data for these channels. These dedicated runs will be interspersed with $\Upsilon(4S)$ running: The accelerator will have sufficient energy tunability to allow movement among the Υ resonances.

2.3.12 Two-Photon Physics

The study of final states produced in e^+e^- reactions via the two-photon reaction (in contrast to the more prevalent one-photon exchange) has been actively pursued over the last ten years. Two-photon physics is now one of the primary sources of information about meson spectroscopy and QCD, and it serves as a unique laboratory for exotic meson searches. While a second generation of experiments is currently accumulating data, the much higher integrated luminosities available at PEP-II will make it an ideal place to study two-photon physics and will extend the range of results considerably beyond what could otherwise be achieved in the next few years.

The two-photon reaction permits detailed studies of the properties of charge-conjugation $C = +1$ mesons, which are not directly accessible in one-photon annihilation. The environment has many advantages for establishing the quantum numbers of these states; in the special case of spin 1 particles, the TPC group at PEP has demonstrated a unique method for determining the spin and parity of the states. The two-photon reaction probes the quark content of hadrons in a manner different from that of one-photon annihilation. The former has a rate proportional to the fourth power of the quark charges, whereas the latter has a rate proportional to the second power. This enhances sensitivity to the mesons containing up and charm quarks.

Two-photon reactions provide an ideal hunting ground for exotic meson states, those that cannot be formed by pairs of quarks. Such states might include four-quark states, states made from two quarks and a gluon, etc. Here, as with the $C = +1$ mesons, the high luminosity of PEP-II will provide sensitivity to particle masses well above anything current experiments will achieve.

The measurement of exclusive and inclusive hadron production in two-photon reactions allows access to many aspects of QCD that remain difficult to probe in other ways. Reaction rates and kinematic distributions yield important information on the distribution of quarks and gluons inside hadrons. One can probe regions of high Q^2 and large two-photon center-of-mass energy, where reliable perturbative QCD predictions exist. The total cross section yields information about the hadronic nature of the photon, while photon structure-function measurements permit a definitive test of perturbative QCD.

2.4 CONSTRAINTS IMPOSED ON THE ACCELERATOR BY THE DETECTOR

The detector required for this physics program imposes certain constraints on the accelerator design, in addition to those of the energy asymmetry and the required luminosity. The main constraints involve requirements of solid angle coverage, the radius of the beam pipe, and the reduction of backgrounds.

The detector will closely resemble a conventional 4π detector for e^+e^- annihilation, with a stronger than normal emphasis on good charged-particle and photon detection in the forward direction. Sensitivity to *CP* asymmetries suffers significantly if the solid angle for tracking is reduced, for example, from 95% to 85%. This leads to a requirement that the machine components not encroach beyond a ±300-mrad cone, measured relative to the beam direction. This stay-clear region must be maintained to a distance of ±2 m along the beam axis.

One would expect that an experimental program that depends so heavily on vertex detection for its success would require that a layer of vertex detector be at the smallest possible radius. There are many reasons for a small beam pipe radius, such as reducing the cost and improving many physics measurements, but they must be balanced against the fact that the detector backgrounds improve with a larger beam pipe radius. It is therefore fortunate that the measurement of the *CP*-violating asymmetries, which is the experiment motivating the entire facility, does *not* depend critically on this radius. Figure 2-10 shows the relative error on the measurement of sin 2α (using $B^0 \rightarrow \pi\pi$), as a function of the radius of the first vertex detector layer. One sees that providing a beam pipe with a radius

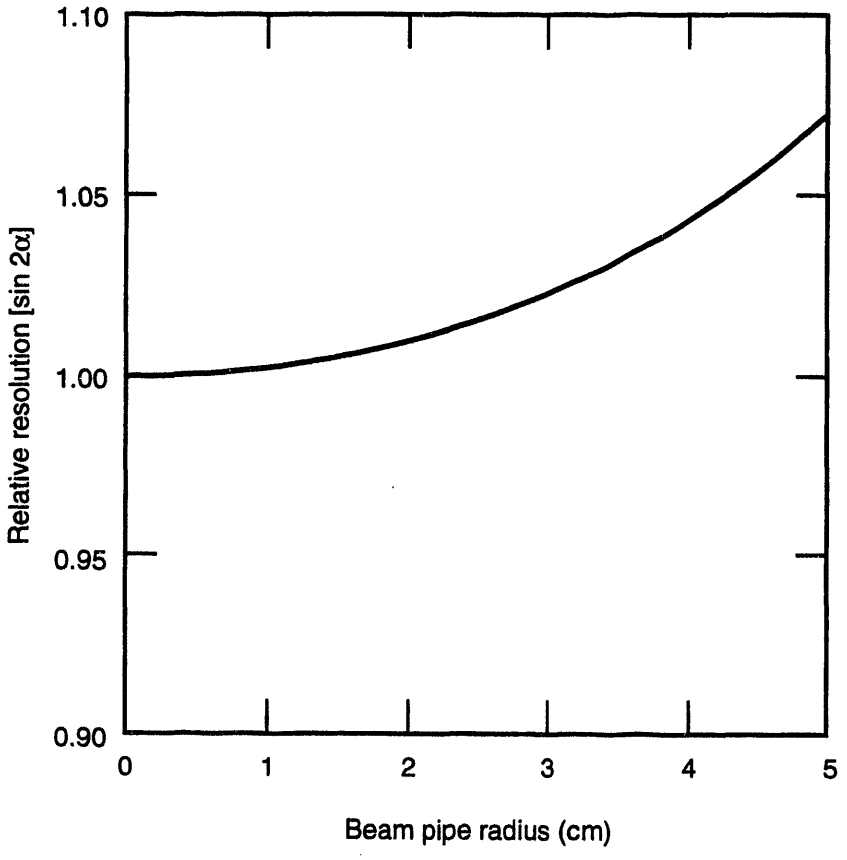

Fig. 2-10. The sensitivity of the measurement error for sin 2α, as a function of the radius of the beam pipe. The resolution worsens slowly as the beam pipe radius (that is, the radius of the first vertex detector layer) increases.

in the region of 2–4 cm maintains resolution close to the best case, assuming an energy asymmetry of 3.1 on 9 GeV. (For B_s mixing, the story is somewhat different: Here it is indeed best to have the smallest possible beam pipe radius.)

Detector backgrounds have two deleterious effects: radiation damage to the devices and unacceptable occupancy levels. We have carefully studied the tolerance level for these two effects on the main elements of the detector. These backgrounds arise from two sources, namely, synchrotron radiation photons and lost particles ($e^{\pm}$)—either direct sources of electrons and positrons or those resulting from photon conversions (independent of whether the photons are from synchrotron radiation or bremsstrahlung). Our detailed synchrotron radiation calculations were based on the appropriate photon spectrum, as generated in the background studies (see Section 4.2). Energy-loss mechanisms in the devices were also accounted for.

Tables 2-5 and 2-6 show the tolerance levels of the silicon vertex detector and the central drift chamber for these sources, as they pertain to detector occupancy and radiation damage. For the silicon, we assumed a radiation limit of 200 krads/yr, and for the occupancy limit, we assumed 10% per μs in four strips [Browder and Witherell, 1991]. For the drift chamber, we took the radiation limit to be 0.5 C/cm of sense wire [Kadyk, 1991], and for the occupancy limit, we used 10% per μs. For the calorimeter, we used the results of recent measurements by Barton et al. [1991]. In this study, irradiation of a CsI(Tl) crystal with ^{60}Co gamma rays to a dose of 100 krad resulted in a 75% reduction in pulse height, along with a modest loss in resolution. In a similar irradiation of a CsI(Na) crystal, the pulse height reduction at a dose of 100 krad was only 10%. (It is unclear at this time whether the behavior is influenced primarily by the dopant material or by the presence of impurities. To better understand the radiation damage limits, such studies are continuing.) We see that, in reality, the calorimeter radiation requirements are less stringent than those for the other two devices.

It is against these criteria that the estimates of backgrounds in Section 4.2 must be measured.

Table 2-5. Silicon vertex detector background limits.

Source	Limit	Flux (particles/cm^2-μs)	Rate (particles/μs)
Synchrotron radiation photons	Occupancy	2	550
	Radiation damage	6	1650
Lost particles ($e^{\pm}$)	Occupancy	1	275
	Radiation damage	0.2	55

Table 2-6. Drift chamber background limits.

Source	Limit	Flux (particles/cm^2-μs)	Rate (particles/μs)
Synchrotron radiation photons	Occupancy	1.0	30,000
	Radiation damage	2.0	60,000
Lost particles ($e^{\pm}$)	Occupancy	0.0003	11 (1st sense wire layer)
	Occupancy	0.0003	28 (middle sense wire layer)
	Radiation damage	0.002	50 (1st sense wire layer)

2.5 RUNNING SCENARIOS

In conclusion, we summarize the machine energy settings that one might anticipate for a balanced physics program.

The physics running will commence on the Υ(4S); indeed, most of the running during the first few years will be at that energy. The main focus of this program will be the study of *CP* asymmetries in B_d meson decays. This provides simultaneous study of a wide range of topics in the areas of *b* quark, *c* quark, τ lepton, and two-photon physics. Open questions at the Υ(1S), Υ(2S), Υ(3S), and Υ(5S) resonances can be addressed by short runs (1–2 months). These runs would be interspersed with the Υ(4S) running.

After sufficient Υ(4S) data have been accumulated to establish the *CP* program, we would contemplate a long (one year or more) dedicated run at the Υ(5S), so as to gain access to a copious source of B_s mesons. There are two separate physics motivations for a major run at the Υ(5S). B_s mixing may have already been observed through integrated dilepton event samples, but a time development analysis is likely to require Υ(5S) running at an increased energy asymmetry. In addition, *CP* violation measurements in B_s decay may prove to be crucial to a full understanding of the phenomenon. For such a dedicated Υ(5S) run, we anticipate a reoptimization of the interaction region to accommodate an increased asymmetry and improved vertex detection, including the possibility of a reduced beam pipe radius. This may also be the natural time to invest in a major luminosity upgrade program.

3.

GENERAL DESCRIPTION AND PARAMETER CHOICES

IN this chapter, we give a general overview of the PEP-II collider. First, we summarize the performance goals of the collider, based on the physics considerations outlined in Chapter 2. Then, we briefly describe a design that meets these requirements. To carry out the physics program of a *B* factory, the luminosity of the facility must be improved by a factor of 15 over that of currently operating e^+e^- colliders. It is clear, of course, that this is a challenging goal, and one that is inherently at odds with maintaining a "conservative" design in all areas. On the other hand, we are convinced that a successful project must take seriously the concept of a "factory," that is, the machine must be designed—insofar as possible—to be highly reliable.

As might be imagined, there are various possible machine configurations that could be considered to achieve our performance goals. Therefore, it is necessary to make certain choices from the outset to focus the design process. Such choices might be based on the advantages (or disadvantages) of a particular site, on the experience and expertise of the design team, or on judgments about the degree of reliability and/or flexibility inherent in particular approaches. To put our parameters in context, we include in this chapter a discussion of the rationale for each of the major choices made in arriving at the PEP-II configuration described in this report.

We have restricted ourselves to consideration of a *B* factory based upon storage ring technology. At the present time, alternative approaches, such as linac-on-linac or linac-on-storage-ring scenarios, are felt to be more speculative than the approach taken here. For example, the technology of high-power, high-repetition-rate, high-brilliance linacs is still in its infancy. Moreover, it does not appear that these alternative approaches offer significant advantages over the more straightforward approach of extrapolating the relatively well-understood performance of storage rings. This outlook is clearly shared by many other groups worldwide that have actively pursued the design of a *B* factory collider, all of whom have based their work on asymmetric storage rings [Funakoshi et al., 1990; Hartill, 1990; Rivkin, 1990; Zholents, 1990].

3.1 DESIGN OVERVIEW

The primary performance goals for the collider, based on the discussion in Chapter 2, are as follows:

- Achieving a peak luminosity of 3×10^{33} cm^{-2} s^{-1} in a reliable fashion
- Operating with an energy asymmetry of about 1:3 in the vicinity of the $\Upsilon(4S)$ resonance, $E_{c.m.} = 10.58$ GeV
- Storing high beam currents (1–2 A) stably and with adequate lifetime
- Maintaining acceptable detector background conditions
- Providing flexibility to accommodate both modifications to the assumed beam-beam interaction parameters and optics changes near the interaction point required by background considerations

The PEP-II design described in this report meets all of these requirements. Key features of the design are summarized below:

- Low β_y^* values at the interaction point
- Head-on collisions
- Flat beams ($\sigma_x/\sigma_y = 25$)
- Many bunches ($k_B = 1658$ in each ring)
- Two rings (9-GeV e^- in the refurbished PEP ring; 3.1-GeV e^+ in a new low-energy ring)
- Low-photodesorption, low-impedance vacuum chambers
- Wigglers to control the emittance and damping time of the low-energy ring
- Single-cell, room-temperature RF cavities
- Feedback systems for controlling multibunch instabilities
- A powerful injection system (the SLC linac)

The PEP-II collider is an upgrade of the existing PEP ("Positron-Electron Project") collider at the Stanford Linear Accelerator Center (SLAC); its major parameters are collected in Table 3-1. To optimize the physics potential of the facility, we have adopted an *asymmetric* design in which a high-energy electron beam of 9 GeV collides with a low-energy positron beam of 3.1 GeV. We thus require a two-ring configuration, where each beam circulates in its own vacuum chamber and is controlled by independent optical elements, except in the interaction region (IR) where the beams collide. The high-energy beam will circulate in the (upgraded) PEP ring; the low-energy beam will circulate in a newly constructed ring.

Both the high-energy ring (HER) and the low-energy ring (LER) are located in the existing PEP tunnel; a site plan for the facility is shown in Fig. 3-1. The tunnel has a hexagonal geometry and accommodates a ring having a circumference of 2200 m. The six straight sections in the PEP tunnel are each 120 m long; this provides generous space not only for the IR but also for the various utility functions (RF, injection, etc.).

Table 3-1. Main PEP-II parameters.

	Low-energy ring	High-energy ring
Energy, E [GeV]	3.1	9.0
Circumference, C [m]	2199.32	2199.32
Emittance, $\varepsilon_x/\varepsilon_y$ [nm·rad]	64.3/2.6	48.2/1.9
Beta function, β_x^*/β_y^* [cm]	37.5/1.5	50.0/2.0
Beam-beam tune shift, $\xi_{0,x}/\xi_{0,y}$	0.03/0.03	0.03/0.03
RF frequency, f_{RF} [MHz]	476	476
RF voltage, V_{RF} [MV]	5.9	18.5
Bunch length, σ_ℓ [cm]	1.0	1.0
Number of bunches, k_B	1658	1658
Bunch separation, s_B [m]	1.26	1.26
Damping time, τ_E/τ_x [ms]	19.8/40.3	18.4/37.2
Total current, I [A]	2.14	0.99
Synch. rad. loss, U_0 [MeV/turn]	1.14	3.58
Luminosity, $\mathcal{L}$ [cm^{-2} s^{-1}]	3×10^{33}	

Because the PEP tunnel was originally sized to house a second (proton) ring, there is ample room for the LER to be mounted above the HER, as illustrated in Fig. 3-2. This design choice, which leads to equal circumferences for the LER and HER, has several advantages. First, it eliminates the need for the major conventional construction that would result if a smaller-circumference LER were chosen. Second, it permits the same number of beam bunches in each ring, thus avoiding possible concerns about coherent beam-beam instabilities. Finally, the large circumference increases the luminosity lifetime, compared with that in a smaller ring, by storing more particles (which are lost at a constant rate in the beam-beam collisions) for a given luminosity. (To take full advantage of the last benefit, it must be possible to fill the large ring quickly. As we will discuss below, the linac injector available at SLAC is ideal for this purpose.)

Reutilizing the PEP tunnel has the added benefit of making many of the installed utilities available for PEP-II, including power and water distribution, cable ways, etc. This is advantageous not only in terms of costs, but also in terms of minimizing the construction time for the facility. We also intend to reuse essentially all of the existing PEP magnets for the HER. This too will yield significant cost and schedule benefits, with no compromise on the performance of PEP-II.

PEP was built to operate at beam energies up to 18 GeV; therefore, its magnet parameters are fully compatible with the requirements for the HER of the PEP-II collider. For example, the PEP bending magnets have a magnetic radius of ρ = 165 m, which at

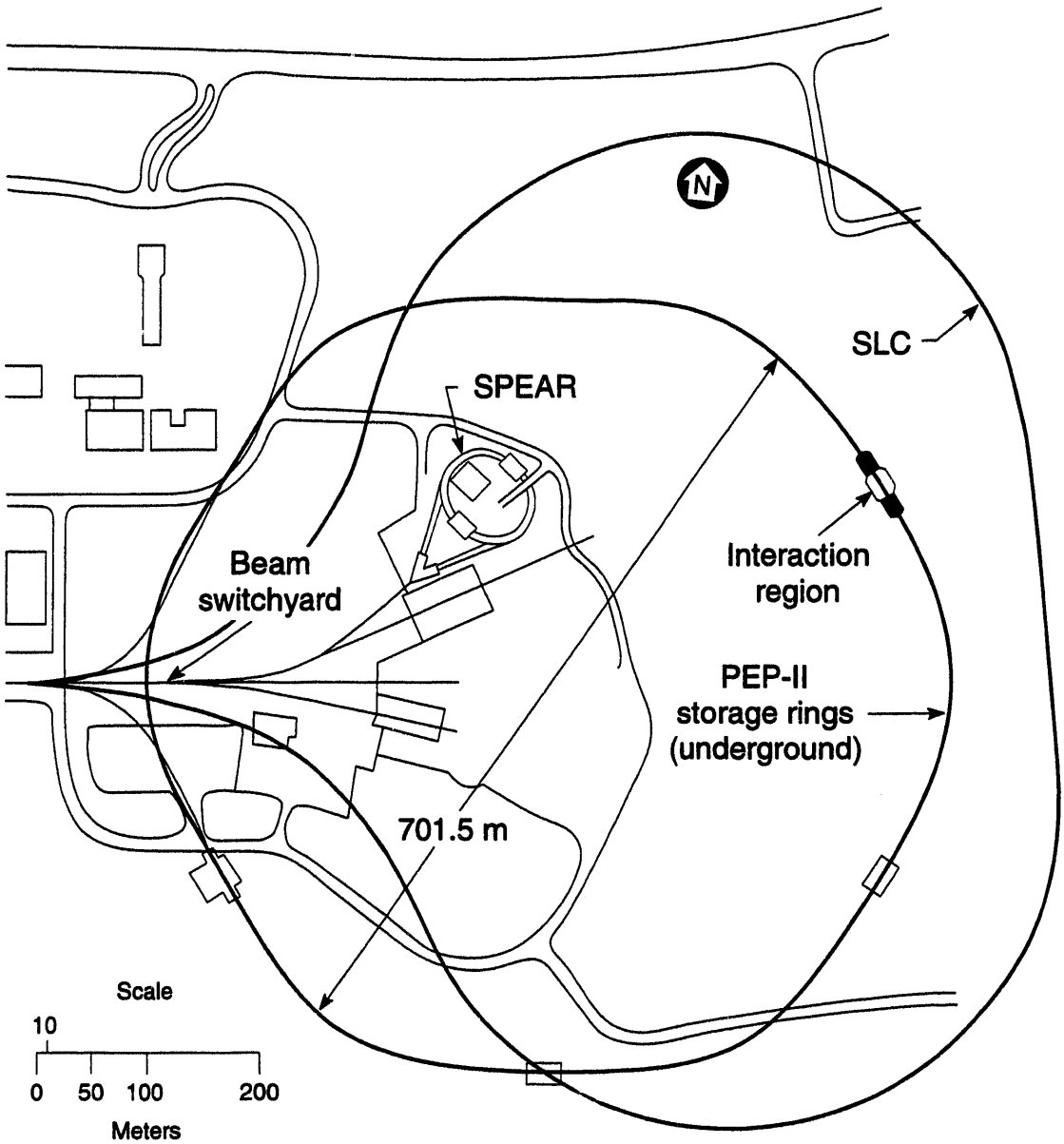

Fig. 3-1. SLAC site plan showing the general configuration of PEP-II. The linac beam enters the rings from the beam switchyard at the left. The SLC arcs are at a different elevation from the PEP tunnel and thus do not intersect it.

9 GeV considerably reduces the synchrotron radiation power emitted by the high-energy beam in PEP-II compared with that from a smaller ring. Thus, we will be able to maintain a high beam current and a suitable asymmetry without prohibitively high synchrotron radiation power losses. The natural emittance required for the PEP-II HER is essentially that of the standard PEP lattice. Moderate adjustments to the emittance, such as might be dictated by beam-beam considerations, can be accommodated either by mismatching the dispersion function or by trimming the phase advance in one or more sextants of the ring.

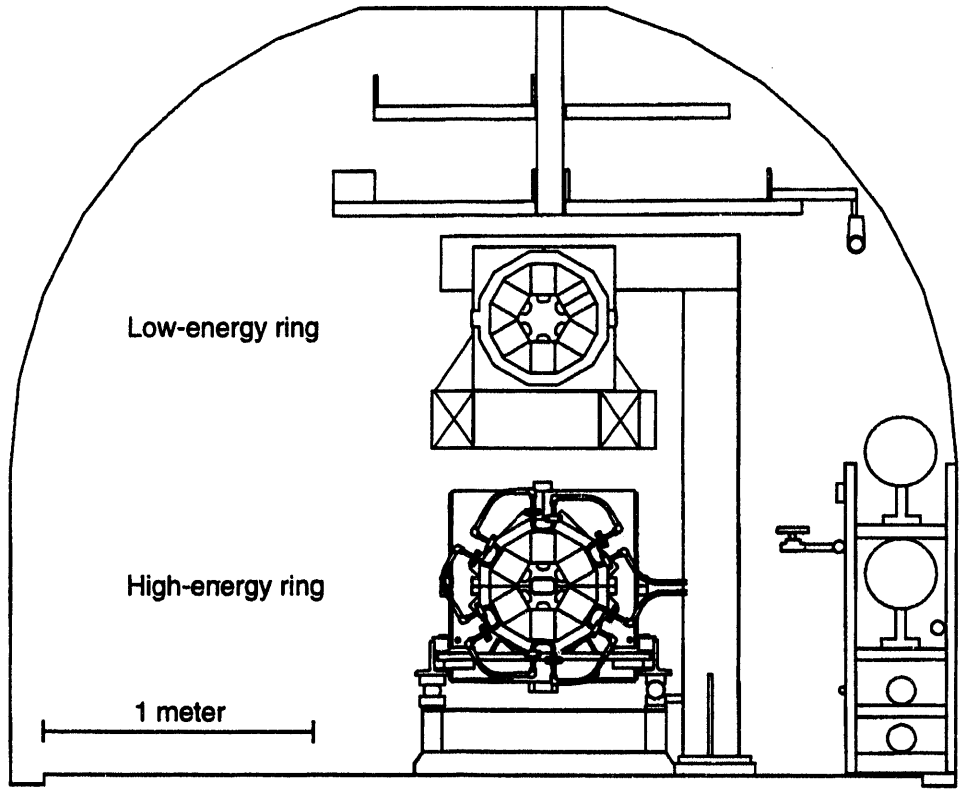

Fig. 3-2. Cross section of the PEP tunnel, showing the locations of the two PEP-II rings and installed utilities.

In the case of the LER, relatively short (0.45 m) bending magnets having a magnetic radius of ρ = 13.75 m are used. Despite this choice, the natural emittance generated in the ring dipoles alone would be considerably lower than the emittance called for in Table 3-1. To handle this, we make use of wigglers in two straight sections to give independent control of emittance and damping times. This approach provides a great deal of flexibility to select the operating parameters of the LER in an optimum fashion.

The injection system for the collider is based upon the existing SLC linac injector, as illustrated in Fig. 3-3. It is assumed here that the SLC experimental program will be completed prior to the time PEP-II becomes operational, although it is likely that the injector complex will still play a part in various R&D activities (for example, as injector for the Final Focus Test Beam or, possibly, for a test section of the so-called Next Linear Collider), in addition to its primary role as the PEP-II injector. Thus, the SLC damping rings and positron-production target will be available for PEP-II. We will see in Chapter 6 that this combination is very powerful and provides an ideal injector for the PEP-II project. With the injection system operating at only 10% of routine SLC intensity, the top-up time for *both* collider rings is about 3 minutes.

To summarize, we note that from many viewpoints the PEP site at SLAC is an ideal location for the construction of an asymmetric *B* factory collider:

- The availability of a large-circumference tunnel offers maximum flexibility in the choice of collider parameters.

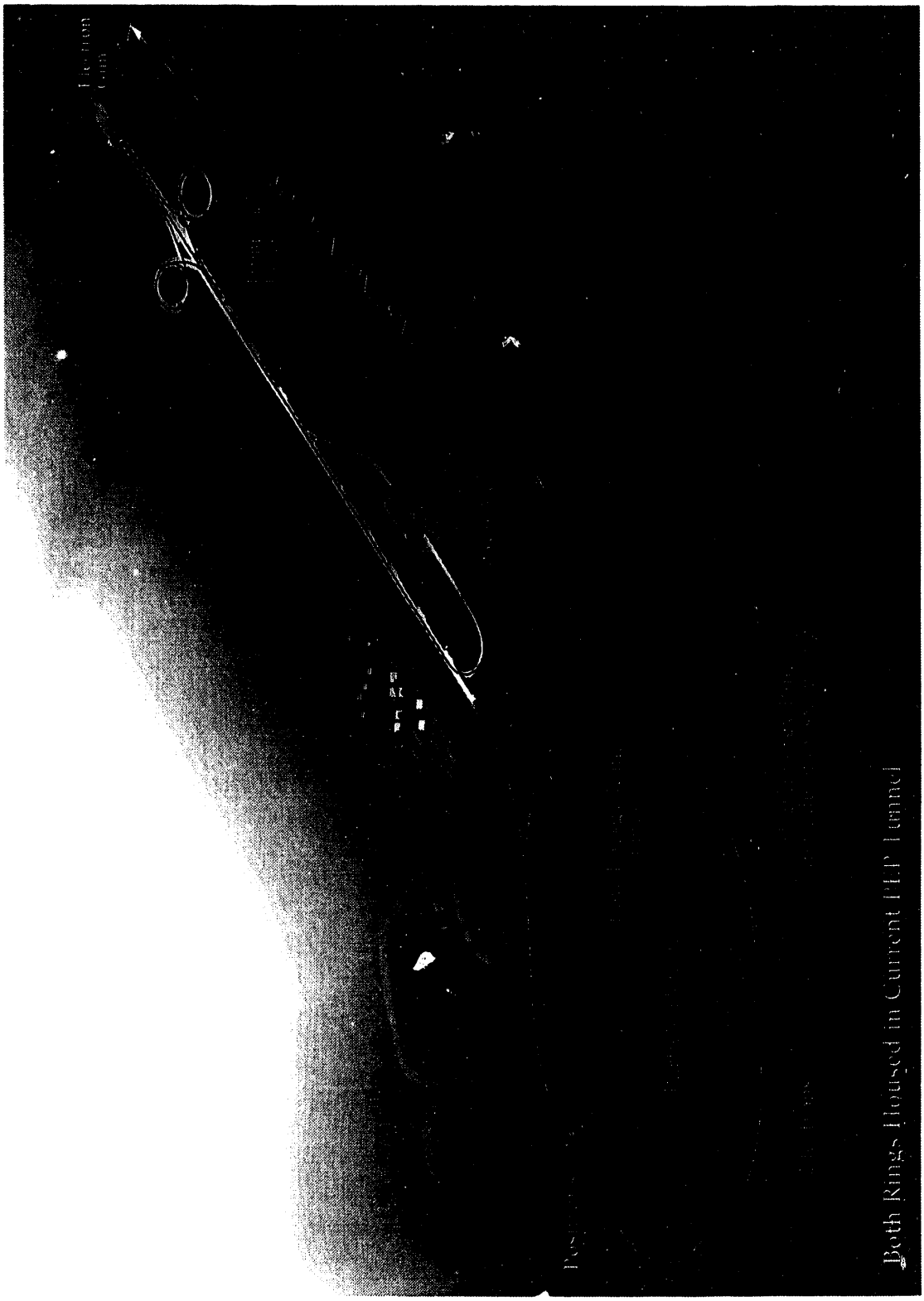

Fig. 3-3. Schematic illustration of PEP-II, showing the existing injector system.

- The existence of a powerful positron injector facilitates rapid commissioning and ensures a high *integrated* luminosity.
- The existing PEP infrastructure permits the rapid construction and commissioning of the facility.

In addition, the considerable accelerator design expertise and engineering strengths of SLAC, LBL, and LLNL will ensure the successful and reliable operation of the facility at its design luminosity.

3.2 LUMINOSITY CONSIDERATIONS

The first four of the key PEP-II design features listed earlier are dictated primarily by the luminosity limitations associated with the beam-beam interaction. The physics issues will be discussed in detail later (in Section 4.4), but here we will introduce the topic in the context of parameter choices for the PEP-II project.

The general expression for luminosity in an asymmetric collider is cumbersome, involving various parameters of both beams at the interaction point (IP). To simplify the choices and to elucidate the general issues of luminosity for any *B* factory, it is helpful to write the luminosity in an energy-transparent way. In this section, we express the luminosity in terms of a single beam-beam tune shift parameter ξ, common to both beams, along with a combination of other parameters taken from *either* the high-energy (e^-) or low-energy (e^+) ring, irrespective of energy.

With a few plausible assumptions (for example, complete beam overlap at the IP and equal beam-beam tune shifts for both beams in both transverse planes), such parameters as energy, intensity, emittance, and the values of the beta functions at the IP nay be constrained to satisfy certain scaling relationships. (Details of this approach are presented in Section 4.4.) It then becomes possible to express luminosity in a simple, energy-transparent form [Garren et al., 1989]:

$$\mathcal{L} = 2.17 \times 10^{34}\, \xi (1 + r) \left(\frac{I \cdot E}{\beta_y^*} \right)_{+,-} \quad \left[\mathrm{cm}^{-2}\, \mathrm{s}^{-1} \right] \tag{3-1}$$

where

- ξ is the maximum saturated dimensionless beam-beam interaction parameter (taken to be the same for both beams, and for both the horizontal and the vertical transverse planes)
- r is the aspect ratio characterizing the beam shape ($r = \sigma_y^*/\sigma_x^*$)
- I is the average circulating current (in amperes)
- E is the energy (in GeV)
- β_y^* is the beta function at the IP (in cm)

The subscript on the combination $(I \cdot E/\beta_y^*)_{+,-}$ means that it may be evaluated with parameter sets taken from either ring.

The scaling relations derived in Section 4.4 were used to produce a self-consistent set of parameters that have been used in this report. After a few basic parameters are chosen, such as the energies, the currents, the aspect ratios, and the lowest beta value at the IP for each ring, most of the other parameters, including the luminosity $\mathscr{L}$, follow. To a certain extent, the choice of which parameters are specified and which are derived is arbitrary. Nonetheless, as discussed below, there are many practical considerations that limit the degrees of freedom in maximizing the luminosity.

Energy. The energies $E_{+,-}$ are not entirely free parameters; they are constrained kinematically. To take advantage of the cross section enhancement at the $\Upsilon(4S)$ resonance, the collider center-of-mass energy must be 10.58 GeV. Precise determination of the decay vertices with a reasonable detector geometry then limits the energy ratio to the range of about 1:3 to 1:5. Simulations of the beam-beam interaction (both our own and those of others [Hirata, 1990]) argue for approximately equal damping times per collision ("damping decrement") in the two rings, which is more easily accomplished when the energy asymmetry is reduced. On the other hand, magnetic separation becomes easier when the energy asymmetry increases. Taken together, these considerations lead to an optimum energy of the high-energy beam of $E \approx 8$–12 GeV, and the corresponding energy of the low-energy beam is thus $E \approx 3.5$–2.3 GeV. For the PEP-II design, we have adopted energies of $E_- = 9$ GeV and $E_+ = 3.1$ GeV.

Beam-beam tune shift. The beam-beam tune shift parameter ξ is not really a free parameter; it is determined intrinsically by the nature of the beam-beam interaction. The range of maximum beam-beam tune shifts achieved in existing equal-energy e^+e^- colliders is $\xi \approx 0.03$–0.07. We chose a moderate value of $\xi = 0.03$ as the basis of our nominal luminosity estimates. (For simplicity, we assume at this point that the ξ values of both beams, in both transverse planes, are equal. Less restrictive assumptions would lead to a parameter dependence similar to that in Eq. 3-1, as discussed in Section 4.4.) Insofar as considerably higher tune-shift values than this have already been observed at PEP—even with multiple IPs—we consider the value of 0.03 to be reasonable for estimating the performance of an asymmetric collider.

One implication of the tune-shift limitation is that increased luminosity must perforce come from decreasing the bunch spacing s_B, that is, increasing the number of bunches. The push towards small bunch spacing has a significant impact on the design of the IR, which must separate the beams sufficiently to avoid unwanted collisions. (As will be discussed in Section 4.4, including the effects of parasitic crossings makes the ξ value we have adopted less conservative.) The close spacing also exacerbates the problem of controlling coupled-bunch beam instabilities, because it increases the bandwidth requirement of the feedback systems.

There is evidence from computer simulations [Krishnagopal and Siemann, 1990] that the maximum achievable ξ may depend on the beam aspect ratio: $\xi = \xi(r)$. This is a controversial issue, now being debated, but it is known that an enhancement in ξ (for round beams) of at best a factor of two can be obtained. As will be discussed below, there are significant difficulties associated with round beams, having nothing to do with the beam-beam interaction, that make this option unattractive even if the tune-shift enhancement proves to be correct.

Beam Aspect Ratio. The aspect ratio r is free to the extent that one can create round beams. However, the physics of the beam-beam interaction is sensitive to the method (coupling resonances, wigglers, etc.) used to make the beams round. Although the use of coupling resonances is a straightforward way to obtain a round beam, it is not clear that applying such a constraint in tune space—where the nonlinear effects of the beam-beam interaction manifest themselves—is the best thing to do. The use of wigglers or phase-plane rotators offers the potential advantage of producing round beams via a noiselike excitation that should not correlate with the subtleties of the nonlinear tune-space behavior.

In the LER, one could imagine the use of wigglers to create a large vertical emittance corresponding to $r = 1$. In the case of the HER, where the synchrotron radiation emission in the horizontal bending magnets is already very large, the addition of sufficient wigglers (in an intentionally created vertically dispersive region) to produce a round beam is nontrivial, although it is certainly conceptually possible. This technique may, however, be impractical from the viewpoint of synchrotron radiation power. Therefore, optics changes (via skew quadrupoles) would likely be the preferable way to create round beams in the HER.

If there is no increase in the beam-beam tune shift, the maximum enhancement from the use of round beams is a factor of two, that is, $r = 1$ gives $(1 + r) = 2$ in Eq. 3-1. (As discussed below, however, the limit on β_y^* is lower in the flat-beam case, so the geometrical gain does not appear to be realizable in practice.) If the tune shift itself increases, a luminosity improvement by another factor of two might result. Such enhancements potentially permit the same luminosity to be reached with a twofold or fourfold decrease in the required beam current.

The fundamental disadvantage of round beams lies in the optics required to focus them. Near the IP, very strong quadrupoles are required. Because of the magnetic separation scheme, at least one of the beams must be off-axis in the quadrupoles, which results in the production of copious synchrotron radiation very close to the detector. In our earlier attempts [LBL, 1989; LBL, 1990] to explore the round-beam case, up to 750 kW of synchrotron radiation power was emitted within a few meters of the IP. To handle this power, and the photon background that comes with it, in such a spatially constrained region appears at best to be very difficult.

Flat-beam optics, in contrast, produce an order-of-magnitude less synchrotron radiation power near the IP. In this case, a masking and cooling scheme is practical, though still difficult. The flat-beam solution we adopted is described in detail in Section 4.2. It is worth noting here that, even taking account of the possible reductions in beam current resulting from the use of round beams, the synchrotron radiation power near the IP in the round-beam case would be at least twice that of the flat-beam solution adopted here.

For the flat-beam case, there are some constraints on how low the aspect ratio can be. In the LER, the need to displace the beam vertically in the IR contributes to vertical emittance. For the HER, there is no such limit. In any case, we are concerned that the independent optics in the two rings could lead to a tilt of the two "ribbon beams" at the IP, such that the luminosity degrades quite substantially. The beam separation scheme gets easier if the aspect ratio of the beams is large (due to the lower angular spread of the beams at the IP), so it is to the designer's advantage to postulate as large a ratio as

possible. The PEP-II design is based upon an assumed aspect ratio of $r = 0.04$; this value, conservative from the standpoint of ensuring a good collision geometry, makes the requirements on beam separation more stringent. (Because the limit associated with the weak LER vertical bends is only $r = 0.001$, we have considerable margin for improvement. This has *not* been taken into consideration in assessing the efficacy of the separation scheme discussed in Section 4.2.)

Beam Intensity. The average beam current I is a relatively free parameter, but not absolutely so. It is determined by various current-dependent coherent effects. The storage rings must accept the chosen currents, given certain impedances in the paths of the beams. There are several intensity-dependent issues with which we must be concerned:

- Longitudinal microwave instability, which causes individual beam bunches to grow both in length and in momentum spread; both the increased bunch length and the increased center-of-mass energy spread can reduce the effective luminosity
- Transverse mode-coupling instability, which limits the maximum current that can be stored in a single beam bunch
- Touschek scattering, which causes particle loss (from large-angle intrabeam scattering) and reduces the beam lifetime
- Coupled-bunch instabilities, which, unless controlled by feedback, can lead to unstable longitudinal or transverse motion and thus to either beam loss or luminosity loss
- Synchrotron-radiation-induced gas desorption, which can lead to very high background gas pressure and thus to beam losses from gas scattering
- Synchrotron radiation heating of the vacuum chamber wall, which can lead to melting of the chamber if the power density is sufficiently high

As will be discussed in Section 4.3, for our chosen parameters, the first three issues listed above are not expected to limit the performance of PEP-II. Based on our present estimates, the issues of most concern to the PEP-II design are coupled-bunch instabilities (driven by parasitic higher-order modes of the RF system) and synchrotron-radiation-induced gas desorption. Means to deal with the former issue are discussed in Sections 5.5 and 5.6. Problems arising from the latter issue require innovations in vacuum chamber design; our approach, based on a copper vacuum chamber, is described in Section 5.2. To provide a safety margin and to permit some room for future improvements, we have considered a maximum beam current of 3 A in the design of the vacuum systems for both the HER and the LER.

Beta Function at the IP. The beta function at the IP, β_y^*, is a free parameter and is easily variable down to a few centimeters, subject to the bunch-length condition $\sigma_\ell \leq \beta_y^*$ that arises from considerations of the beam-beam interaction. (Specifically, we wish to avoid luminosity loss resulting from either the increase in beam size away from the IP or the excitation of synchrobetatron resonances.) As the beta functions are reduced, of course, it becomes difficult to reduce the bunch length accordingly. Either the RF

voltage becomes excessive or the IR optics become unmanageable owing to the increased chromaticity. We have taken a bunch length of $\sigma_\ell = 1$ cm, which then restricts the value of β_y^* to the range of 1–3 cm.

It turns out that, for round-beam optics, the chromaticity tends to be about twice that of flat-beam optics. Thus, whatever chromaticity is tolerable in the round-beam case can be reached equivalently with flat-beam optics in which the β_y^* value has been reduced by a factor of two. This means that, in practice, the factor of two increase in luminosity implied by Eq. 3-1 is largely illusory.

From Eq. 3-1, it is clear that the luminosity is maximized with high currents and low β_y^*. What are the implications regarding these parameters for a luminosity goal of 3×10^{33} cm^{-2} s^{-1}? Following a conservative route, we use a typical low β_y^* of a few centimeters (1.5 cm in the LER, 2 cm in the HER), $\xi \approx 0.03$, and flat beams ($r = 0.04$). These choices imply an average circulating current I of several amperes (2.14 A in the LER, 0.99 A in the HER). As mentioned above, those portions of the vacuum chambers that would be difficult to upgrade later in the project have been designed to handle up to 3 A of beam current.

As a final point, we note that, for the initial phase of the project, we have adopted a design based upon a head-on collision geometry. This configuration has been employed successfully in many colliders and is therefore felt to be a prudent choice. It is possible, however, that detector backgrounds could be reduced by going to a nonzero crossing angle geometry, either one with a small uncorrected crossing angle or one in which the bunches are tilted transversely with respect to their direction of motion (a so-called "crab-crossing" scheme) to avoid the excitation of synchrobetatron resonances. To permit reaching higher luminosity values in the future, therefore, we do not wish to preclude this alternative now. Fortunately, because the separation scheme adopted here operates in the horizontal plane, the proposed layout lends itself quite well to later modification to a nonzero crossing angle scheme. This possibility is *not* part of the present project but could be considered as a future upgrade.

3.3 RF CONSIDERATIONS

There are two important choices to be made in the design of the RF system: frequency and technology (room temperature vs superconducting). The issues involved are discussed below.

3.3.1 Choice of Frequency

The choice of frequency is influenced by a number of intertwined issues. We have already discussed the need for obtaining short bunches, $\sigma_\ell = 1$ cm, to avoid a loss in luminosity. To obtain short bunches, it is necessary to increase the longitudinal focusing of the RF system, which can be accomplished with either additional voltage or higher frequency. Indeed, in the limit where the applied voltage is large compared with the synchrotron radiation energy loss (that is, $\cos \phi_s \rightarrow -1$), the two parameters are essentially equivalent and $\sigma_\ell \propto (V_{RF} f_{RF})^{-1/2}$.

The aperture of the accelerating cavities must be sufficient to avoid reducing the beam lifetime and to avoid introducing excessive transverse beam impedance into the ring. In practice, these constraints limit the choice to only a few frequency "islands" ($f \approx 350$ MHz and 500 MHz) for which high-power ($\approx$1 MW) klystrons are commercially available. Because we must provide 1-cm bunches, we find that—even with equal apertures—the upper frequency range, near 500 MHz, offers lower power and lower cost; it is thus the preferred choice.

To pick the exact frequency, we must bring in additional considerations. The injection system timing requirements are best handled by having the linac and storage ring RF systems phase-locked, which is most easily accomplished if the two frequencies are harmonically related. The advantage of phase-locking the two RF systems is expected to show up primarily in the feedback system requirements. Any phase jitter at injection will initiate oscillations that must be controlled by the longitudinal feedback system. Such injection jitter can easily dominate the feedback system design, in the sense of determining the power required by the system. Because the SLAC linac operates at a frequency of 2856 MHz, the possible harmonically related choices are 357 and 476 MHz. As mentioned, we prefer a higher frequency to reduce the voltage requirement, so we have adopted 476 MHz for the PEP-II RF system.

3.3.2 Choice of Technology

The choice of room-temperature or superconducting RF is also a complicated issue. Given the parameters of PEP-II, superconducting technology would not be of much benefit in reducing the power requirements of the facility. Even for room-temperature cavities, only about one-third of the RF power will be dissipated in the walls, and the power associated with cryogenics for a superconducting RF system would consume a significant fraction of the potential savings. Thus, the choice is not dominated by operating cost considerations.

The potential benefit of a superconducting RF system is that it can provide a high voltage with relatively few cavities. This is important because the most serious beam instabilities in PEP-II (the coupled-bunch instabilities; see Section 4.3) are driven primarily by the higher-order-mode (HOM) impedance of the RF cavities. Reducing the number of cavities lowers the instability growth rates proportionately, which in turn reduces the feedback system power requirement quadratically (unless the power is already limited by injection jitter).

As mentioned, in the case of PEP-II the RF power requirements are dominated by beam loading; that is, the majority of the power put into a cavity goes to the beam itself, even in the case of a room-temperature system. The limit on the number of cavities, then, is dictated by the power-handling capability of the RF input coupler. In the PEP-II HER design, a 20-cavity room-temperature RF system requires about 300 kW per cavity, of which about two-thirds goes into the beam. If the difficulty of designing a reliable high-power input coupler were the same in a superconducting environment as it is in a room-temperature environment, then the number of cavities could possibly be reduced by one-third in the superconducting case. A moderate derating of the input power capability in the (presumably more difficult) superconducting case, however, would lead to roughly equal numbers of cavities in the two scenarios.

A difficulty with superconducting cavities that requires new technology arises from the need to remove the HOM power deposited in the cavity by the high-current beam. For the room-temperature case, solutions for this problem have been demonstrated in test cavities and can be implemented in a reasonably straightforward manner (see Section 5.5). The problem of removing hundreds of kilowatts from the cryogenic environment, however, has not been solved. At present, the Cornell RF group [Padamsee et al., 1990] is working on this problem, and it may be solvable with appropriate R&D.

On balance, superconducting RF technology for a high-luminosity collider seems to require a significantly larger performance extrapolation than does room-temperature technology, and it is not judged by us to be a sufficiently mature platform on which to base a "factory" at present. Therefore, the present proposal is based on a conventional room-temperature RF system, as described in Section 5.5.

3.4 RELIABILITY CONSIDERATIONS

The physics requirements for PEP-II are associated with a large *integrated* (as opposed to peak) luminosity. Therefore, it will be necessary to pay attention to reliability issues from the outset. Several approaches can be used to improve the reliability of the facility:

- Provide safety margins in the initial design parameters
- Design the control system to facilitate failure diagnosis
- Design the hardware in a modular fashion to facilitate repairs
- Maintain adequate spares
- Use a powerful, fully automated injection system to recover quickly from beam loss

All of these approaches will be taken at PEP-II to maximize the machine operational efficiency.

The operational efficiency is defined as the availability of the machine, during scheduled physics running, for collisions that provide usable physics luminosity. The goal for the operational efficiency has been established using the following criteria:

- The machine will deliver 30 fb^{-1} per calendar year
- The machine will operate for 9 months (274 days) per calendar year
- The peak luminosity will be 3×10^{33} cm^{-2} s^{-1}
- Scheduled maintenance will be 2 days per month
- Machine physics will be 4 days per month
- Injection from scratch will occur three times per day

The rest of the injection cycles will be in "top-off" mode, which will provide an equivalent luminosity of 71% of the maximum deliverable luminosity (see Chapter 6). (The 71% efficiency value assumes a 6-minute top-off time, twice the design value, but is

fairly insensitive to this assumption—increasing the top-off time from 6 to 10 minutes, for example, reduces the efficiency to 65%.)

Injection into an empty ring will often occur because of a failure in one of the machine subsystems that is, in principle, preventable. Down-times resulting from these preventable failures will properly be charged against the operational efficiency. There will also be some aspects of lost time, most of which will show up in the injection mode, that are *not* easily attributable to preventable failures. Examples are "green-thumbing" the machine into an unacceptable operating mode (probably requiring a magnet standardization), tuning to reduce excessive backgrounds, etc. For these inevitable problems, we have budgeted 1.5 hours per day of lost collisions.

The above criteria establish for the design staff the appropriate goal for PEP-II operational efficiency—it must be at least 75% to yield the required integrated luminosity of 30 fb^{-1} per year under the conditions described above. While we recognize that it will not be possible to reach this goal immediately, it is clear that highly reliable operation of PEP-II mandates a careful and conservative design approach. This has been our guideline for the design presented here.

4.

COLLIDER DESIGN

IN this chapter, we describe the physics designs of the two storage rings that make up PEP-II. The concepts described here have evolved over the past several years and are based on numerous interactions among the lattice designers, detector designers, and engineering staff. More than has been true for most past colliders, the PEP-II design has, from the outset, focused heavily on the issues of flexibility and reliability. In addition, it was recognized that the success of the PEP-II project, measured in terms of its ability to produce the requisite physics data, would depend on special attention being paid to the machine-detector interface. The issue of background suppression is so central to the project that it quite strongly influenced the lattice design.

In what follows, we first describe the lattice designs themselves and the beam focusing and separation solutions we have adopted. Thereafter, we describe the detailed background and masking studies we have undertaken. The design we have arrived at has considerable safety margin in terms of expected vs tolerable background levels, based on careful and systematic examination of all background sources. Because of the high beam intensity required for PEP-II, it is important to examine the influence of collective effects on the ring performance. These are discussed in Section 4.3. Our choice of many relatively low-current bunches results in there being no single-bunch thresholds that lead to performance limitations. Coupled-bunch instabilities are important, however. We have developed means to deal with this problem by damping the cavity HOMs and by feedback. These solutions are described in Sections 5.5 and 5.6. Beam lifetimes have been examined for both rings and found to be acceptably long. Because we wish to achieve a very high luminosity, we have looked carefully at the performance limitations imposed by the beam-beam interaction. Detailed results of our simulations appear in Section 4.4.

4.1 LATTICE DESIGN

4.1.1 High-Energy Ring

The design of the lattice for the high-energy ring (HER) has been influenced by the following criteria:

- It must meet all the conditions necessary to obtain the desired luminosity of 3×10^{33} cm^{-2} s^{-1}. These conditions require that the beta functions at the collision point be correct; that the emittance, energy spread, and momentum compaction factor be brought to their proper values; and that the dynamic aperture of the ring be adequate.
- It must fit in the PEP tunnel, leaving space for existing services and enough aisle space for the passage of magnet trolleys, etc., and it must have the correct circumference for the chosen RF frequency and harmonic number.
- It must be arranged in the tunnel such that it is easily supported and aligned.
- It should be designed such that existing PEP components and services are used as much as possible (provided that the design is not compromised by doing so).

The lattice we have adopted meets all the criteria outlined above. In Fig. 4-1 we show a layout of the PEP tunnel. The straight sections of the hexagonal ring are labeled according to the clock. (The straight sections have even numbers, and the arcs connecting them are odd-numbered regions.) Figure 4-2 shows the lattice functions of the HER, β_x, β_y, and D_x, starting and ending at the center of the straight section in region 8. (The HER lies in a plane and D_y is zero everywhere.) Collisions take place in the center of the straight section of region 2, which is shown in the center of the figure. In the straight section of region 8 (and also in region 6) the beta functions are seen to be somewhat uneven. This is because these straights are used to adjust the betatron tunes of the lattice. In arcs 5, 7, 9, and 11, the horizontal dispersion function is mismatched. This (controllable) mismatched dispersion function is used to adjust the horizontal emittance of the beam. Region 10 is the injection straight section, where the beta functions are tailored to optimize the injection process. Arcs 1 and 3 have a regular dispersion function to make it easier to match the chromatic properties of the interaction region by adjustment of sextupoles. The design of the lattice is modular, and the individual modules can be adjusted with little or no effect on the remainder of the lattice. The basic modular building blocks of the lattice are regular arcs, dispersion suppressors, and straight sections. Details of each of these lattice modules are discussed below.

4.1.1.1 Choice of Cell Length. Before design can start in earnest, the length of the standard arc cell must be chosen. One obvious choice of cell length would have been to leave the layout of the ring components exactly as it is in PEP, so that PEP essentially becomes the HER. Consideration of this possibility, however, showed that such a layout

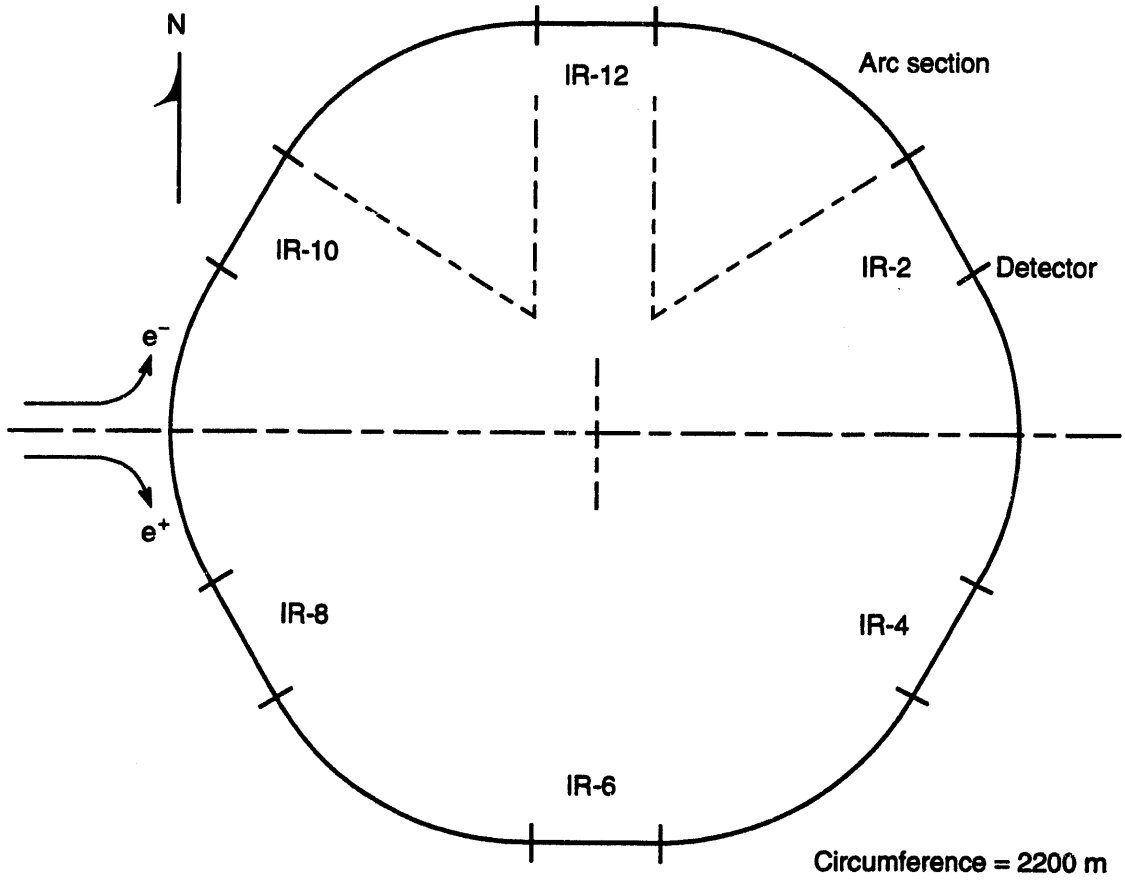

Fig. 4-1. Layout of the PEP tunnel. The numbering system follows the clock, with the straight sections being even numbers; IR = interaction region.

would not suffice and that the cell length would have to be changed. There are three factors that enter:

- The HER is located closer to the tunnel floor than the PEP ring, so that the low-energy ring (LER) can be mounted above it while still providing sufficient space for cable trays, etc. Therefore, the present support structure will have to be replaced.
- The circumference of the ring has been slightly changed to match the new RF frequency chosen for PEP-II. The circumference of PEP was 2200.0004 m, whereas the PEP-II HER circumference will be 2199.318 m. The harmonic number of the HER is 3492, compared with 2592 for PEP.
- The new copper vacuum chambers cannot be fabricated in sections as long as the PEP (aluminum) chambers, so extra space is needed for additional flanges. Therefore, the cell length must be longer than the 14.35 m of the PEP cell.

To accommodate the longer cell, we must remove the short (symmetry) straight sections located at mid-arc in the present PEP lattice. (A half-sextant of PEP was made

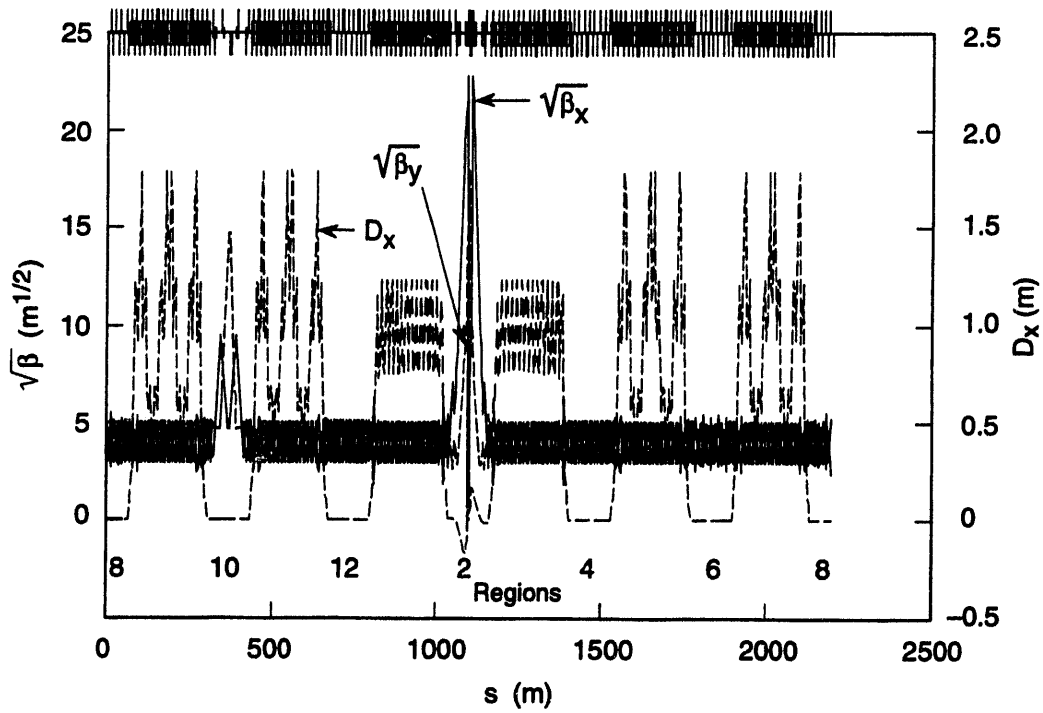

Fig. 4-2. Lattice functions $\sqrt{\beta_x}$, $\sqrt{\beta_y}$, and D_x (horizontal dispersion function) for the complete HER, starting at region 8. The collision region (region 2) is shown in the center of the figure.

up of a long straight section of just over 60 m, followed by an arc section and terminated by a short straight section of about 2.5 m. This short straight section was used as a utility straight and was tailored to the needs of PEP. For PEP-II, however, the utilities are more usefully placed in the long straight sections.)

PEP has 192 main dipole magnets, 16 in each half-arc, 2 per standard FODO cell. Keeping this structure, a range of cell lengths was investigated for two different types of dispersion suppressor. The missing-magnet type of dispersion suppressor was found to be unsuitable for the HER, because the "gap" in the bending makes the central orbit too different from the present PEP central orbit, giving layout problems in the tunnel. A dispersion suppressor consisting of two cells, each of approximately 90° phase shift, gave an acceptable geometry for the beam orbit.

A computer code was developed to plot the deviation of the central orbit of the beam relative to the central orbit of a smooth version of PEP. (A "smooth PEP" consists of straight sections of the appropriate lengths sandwiching an arc of constant radius.) The results of the survey of cell lengths are shown in Fig. 4-3.

In Fig. 4-3, three parameters are plotted as a function of cell length: The straight lines, labeled "mid-arc" and "mid-straight," show the deviation of the orbit from the smooth PEP orbit at the symmetry point (mid-arc) and at the original PEP interaction point (IP, in the center of a long straight section). The curve shows the maximum deviation of the orbit in the arc toward the inside of the smooth PEP orbit. It is seen that a cell length of 15.2 m gives an orbit closest to the original PEP orbit and thus minimizes layout problems in the tunnel. This cell length is also long enough to meet the spatial

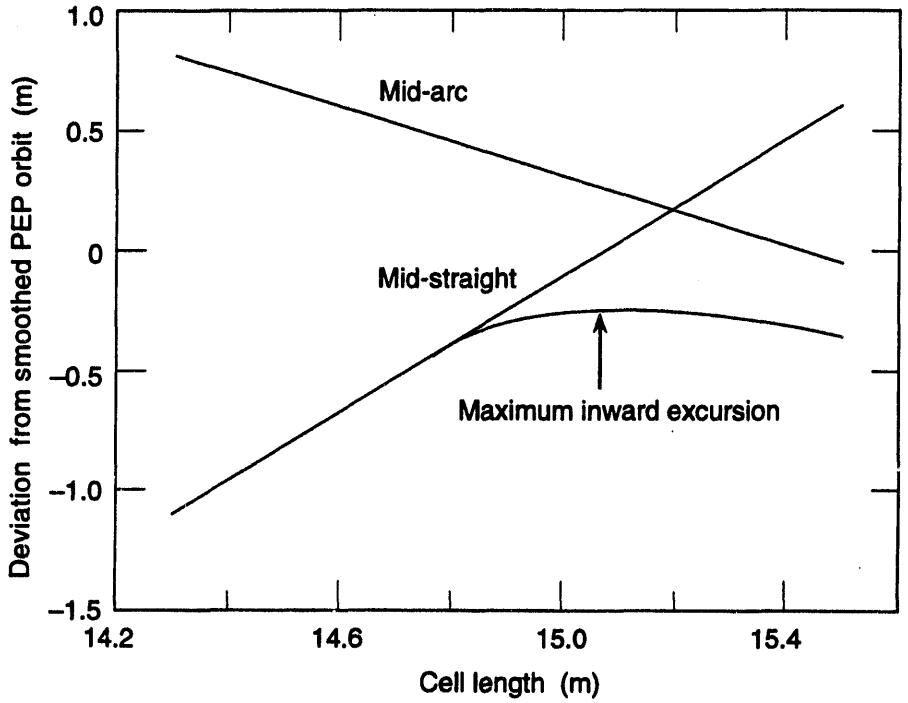

Fig. 4-3. Results of computations to find the optimum length for the regular arc cells. The radial displacement from the smooth PEP orbit is plotted as a function of cell length. The displacement is plotted for mid-straight, mid-arc, and the greatest excursion inside the PEP orbit.

requirements given by mechanical engineering considerations and is thus a good choice on that basis as well.

With this choice of cell length, the long straight sections can be segmented into eight cells of about the same length as the regular arc cells. The various cell lengths of the HER modules are summarized in Table 4-1.

The geometry of a normal sextant of the HER is shown in Fig. 4-4, where the ordinate denotes the radial position of the beam orbit relative to the smooth PEP orbit. The curve

Table 4-1. Lengths of PEP-II lattice modules.

	Cell length (m)	
Module	HER	LER
Arc	15.2	15.191
Straight section	15.419	16.030, 14.608
Dispersion suppressor	15.2	15.191

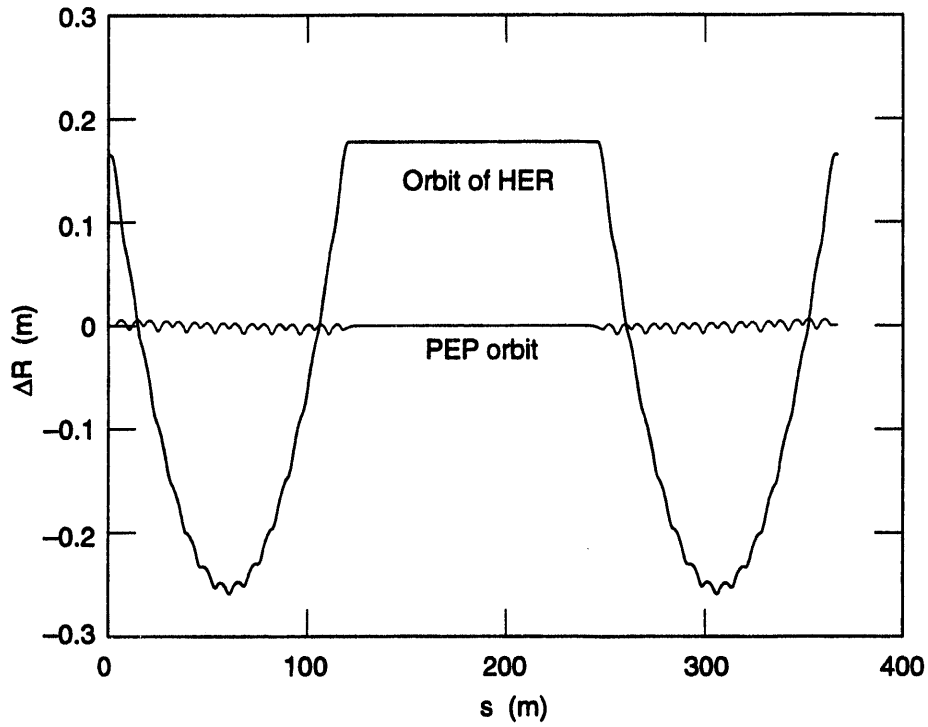

Fig. 4-4. Geometry of the HER orbit in the PEP tunnel relative to that of a smooth PEP orbit. The radial displacement of the orbit is plotted as a function of distance along the orbit from mid-arc to mid-arc. Negative ΔR values correspond to being inside the smooth PEP orbit. A different geometry applies in the special case of the collision sextant (cf. Fig. 4-13).

close to the zero position is the actual PEP orbit, the small wiggles being due to the nonuniform bending in a PEP cell (due in turn to the fact that the dipoles occupy most, but not all, of the length). The other curve shows the deviation of the orbit of the HER from the smooth orbit. At the ends (symmetry points in the arcs), the HER orbit is just under 20 cm outside of the smooth orbit; in the long straight section (center section of the plot), the orbit is again just less than 20 cm outside the PEP orbit; and in the arcs, the orbit comes inside the PEP orbit by about 26 cm. With this layout for the HER, there is enough clearance on the inside for the existing PEP services, and there is enough space in the outer aisle for magnet trolleys to pass.

4.1.1.2 Normal Sextant. A phase shift of 60° per cell was chosen to obtain a beam emittance slightly below the emittance required for the design luminosity. As will be discussed shortly, the emittance can be changed, in a controlled fashion, above and below the design value. The phase advance of 60° per cell is also optimal for the control of the chromatic properties of the lattice by sextupole compensation. The lattice functions for a normal sextant are shown in Fig. 4-5. It can be seen that the lattice is quite well matched; the dispersion function is zero in the straight section and the beta functions are regular throughout, except for a small beating in the dispersion suppressor cells. Beta function

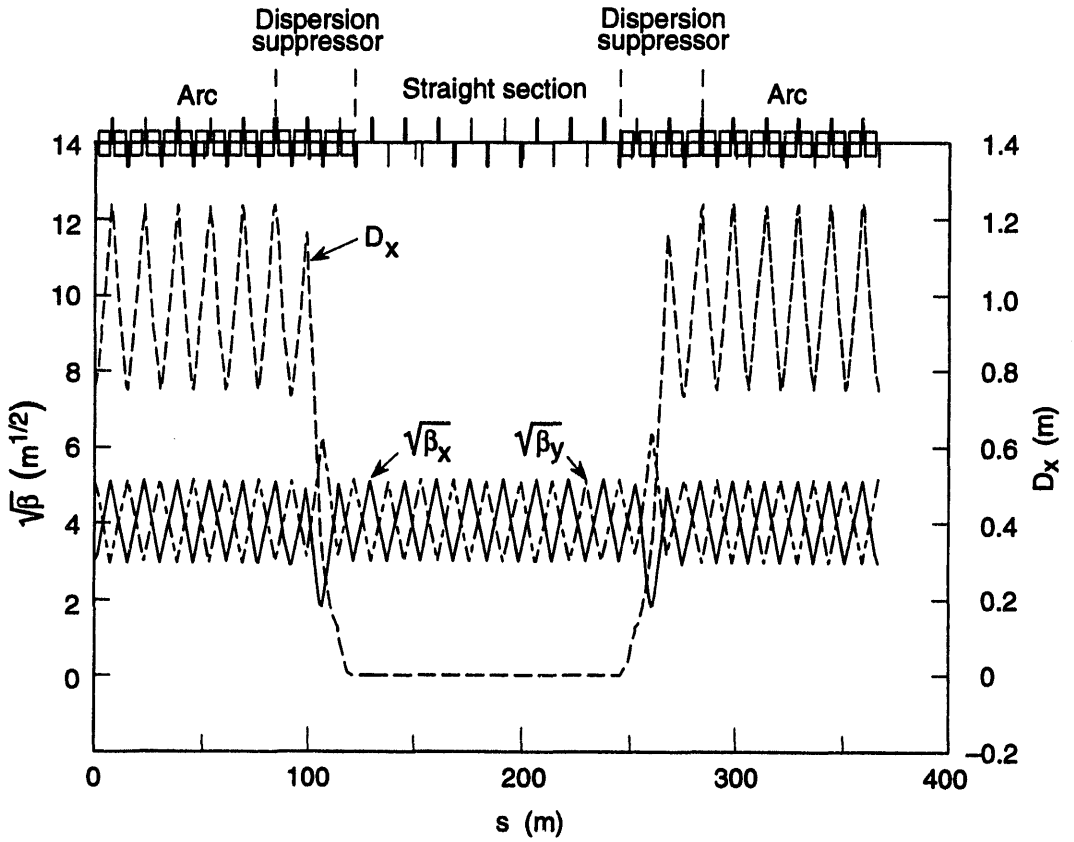

Fig. 4-5. Lattice functions for a normal sextant of the HER, plotted as a function of position in the sextant, from mid-arc to mid-arc. Dispersion is matched to zero in the straight sections.

values are moderate in the straight section, making it a suitable place for locating the RF accelerating cavities.

4.1.1.3 Emittance Control Sextant. The HER beam emittance is controlled by adjusting the dispersion function at the position of the main dipoles, where most of the synchrotron radiation is generated. It is, of course, possible to have a portion of the lattice with a phase shift per cell different from 60°. (As the phase shift per cell decreases, the dispersion function increases and therefore the emittance increases.) Adjustment in this fashion is workable, but has the disadvantage of increasing the momentum compaction factor α. This means that additional RF accelerating voltage would be needed to maintain the desired 1-cm bunch length. Instead of this phase adjustment, we have chosen to use a mismatched dispersion function in the arcs of four of the six sextants. Similar to an orbit bump, the dispersion mismatch is confined to the arc, with the dispersion in the adjoining straight sections remaining at zero. Although the average value of D remains unchanged by this modulation, it is the square of the dispersion function that determines the increase in emittance. Figure 4-6 shows an emittance control sextant that is mismatched sufficiently to increase the emittance from 40 nm rad to 48 nm rad. (In reality, there is no sextant exactly like the idealized version

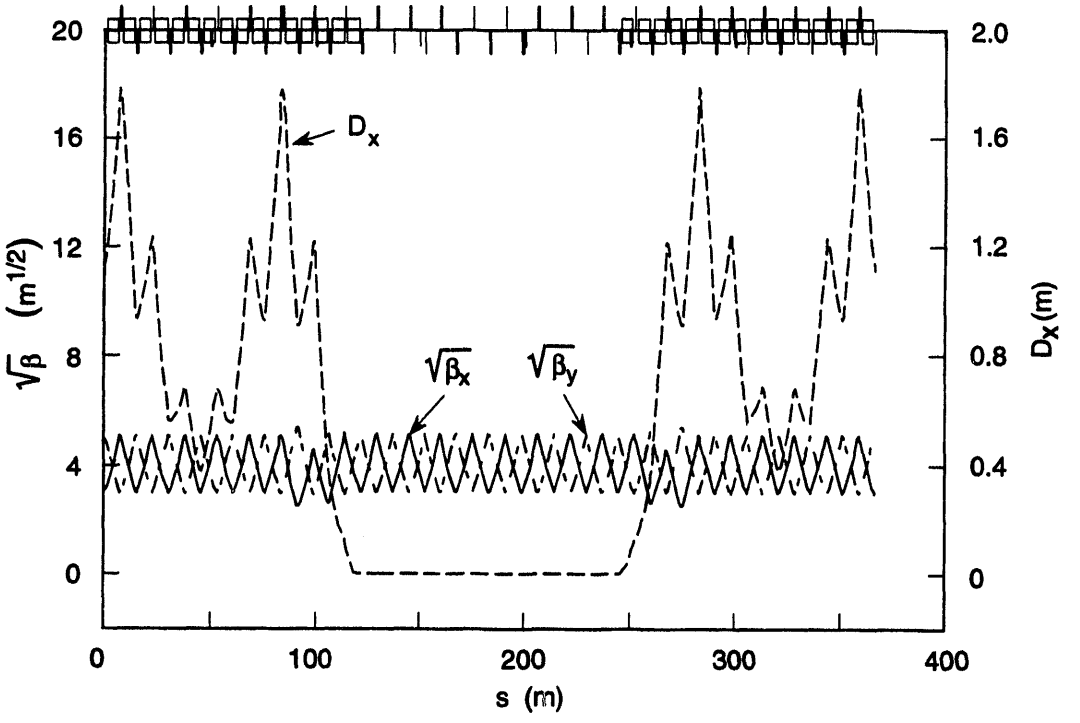

Fig. 4-6. Lattice functions for an emittance control sextant of the HER. The dispersion function mismatch is confined to the arcs, the dispersion function being zero in the straight section.

in Fig. 4-6, because the straights adjoining these arcs are all special.) The modularity of our lattice design allows "plugging in" sections in a mix-and-match manner without having to do any lattice rematching, apart from possibly having to restore the betatron tune.

4.1.1.4 Injection Sextant. As explained in Section 6, we have chosen to inject in the vertical plane, i.e., the injected bunch merges with an already stored bunch in (y,y') phase space. We inject at a location with a high vertical beta function so that the septum thickness is small relative to the 10σ vertical extent of the beam. As shown in Fig. 4-7, the higher β_y value is achieved by means of a one-cell, quarter-wave transformer (after first adding one normal empty cell at each end of the injection straight section). The chromaticity introduced by the high-beta cell is no more than that generated by any other 90° cell.

Two identical kickers, placed 180° apart in vertical betatron phase, are used for injection. A four-magnet DC beam bump is also employed to bring the stored beam closer to the injection septum and thus reduce the kicker performance specifications. The DC bump also controls the angle of the stored beam orbit at the injection septum.

4.1.1.5 Phase Control Sextant. The straight sections of two sextants will be used to change the betatron tune of the HER. Even a single phase-control sextant would probably have enough range to be acceptable, but the choice of two sextants improves the

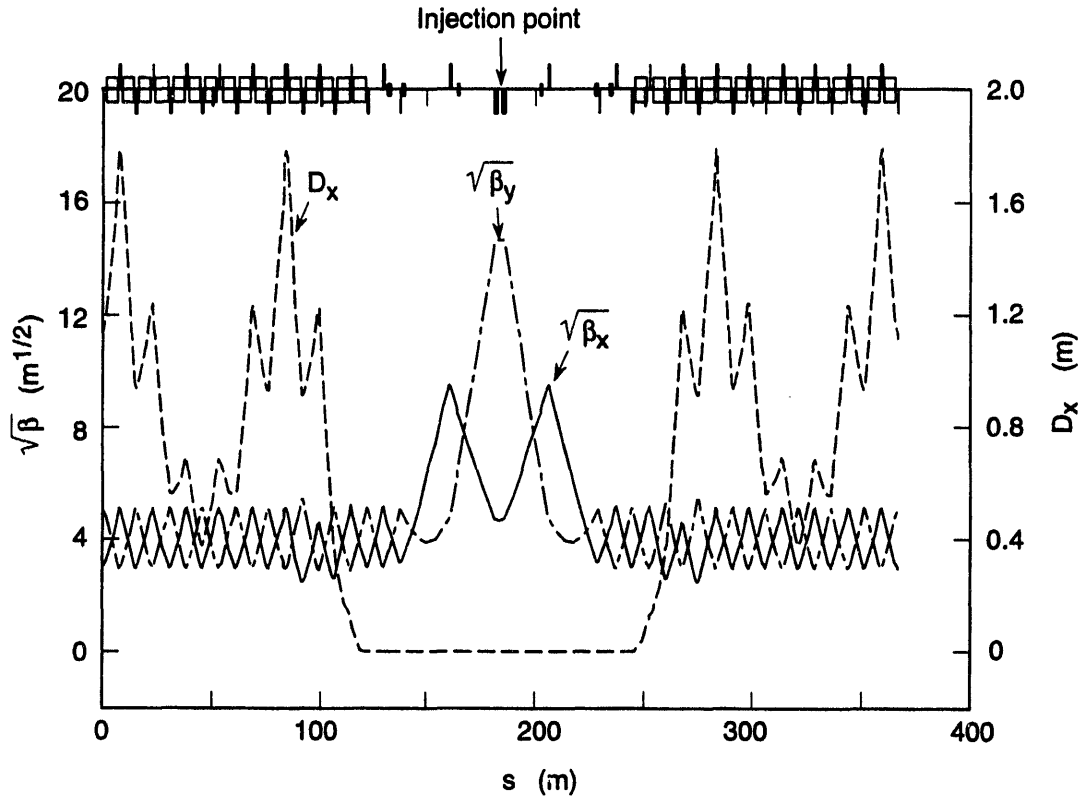

Fig. 4-7. Lattice functions for the injection straight section of the HER. Injection takes place in the vertical plane. The beta functions are transformed to higher values by a long 90° cell that acts as a quarter-wave transformer. The kicker magnets are separated from each other by 180° in vertical betatron phase.

beta functions at the extremes of the required tune range. The phase control straight sections are located in regions 6 and 8. The optical functions of a phase control sextant are shown in Fig. 4-8. (The beta functions in the straight will vary slightly depending on the betatron tune of the HER.)

4.1.1.6 Interaction Region Sextant. The IR sextant is very special and is considerably more complicated than the other sextants. The IR, described in Section 4.1.2, is at its center. The arcs on either side have matched dispersion functions so as to facilitate the correction of chromatic aberrations produced by the IR focusing that gives the β_y^* of 2 cm. Between the IR and the arcs are the matching elements. The matching of the HER is fairly simple owing to the fact that the ring lies in a plane (that is, there are no vertical bends). The lattice functions for the collision sextant and right-hand half-sextant are shown in Figs. 4-9 and 4-10, respectively. In Fig. 4-9 notice the antisymmetry of the dispersion function caused by the S-bend geometry.

Figure 4-11 shows the first 10 m from the interaction point (IP). The dipole B1 initiates the separation of the beams, the separation being augmented by the quadrupole QD1, which is centered on the high-energy beam and deflects and focuses (vertically) the low-energy beam. It also gives considerable vertical "prefocusing" to the high-energy

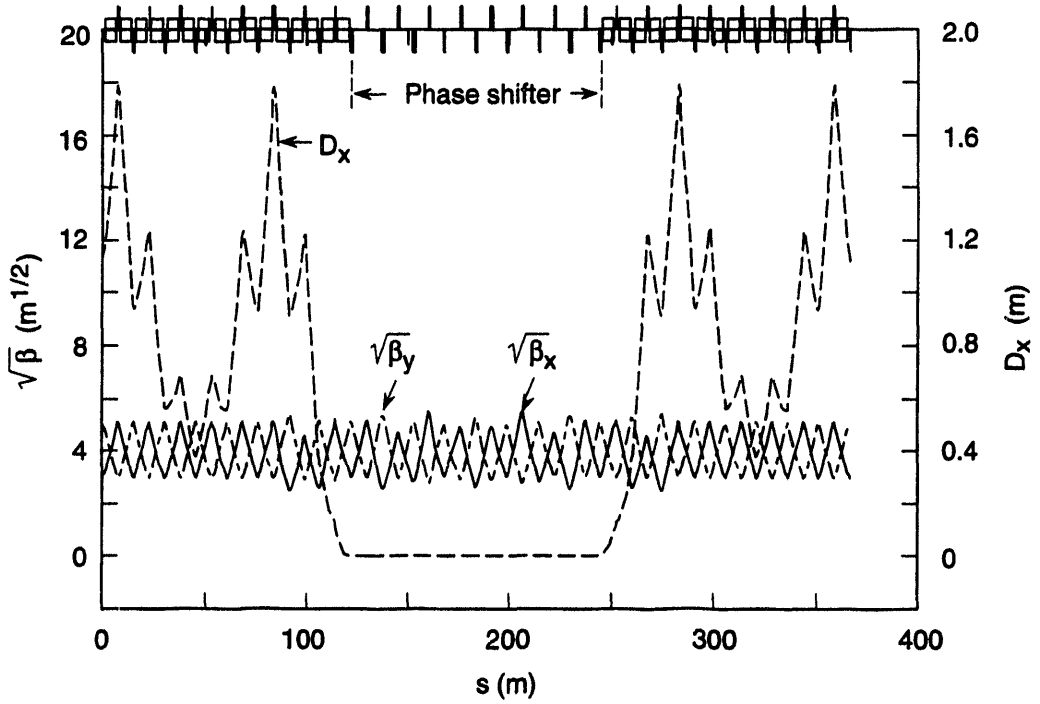

Fig. 4-8. Lattice functions for the phase control sextant of the HER. The beta functions are almost regular in the straight section where the phase shifter is located.

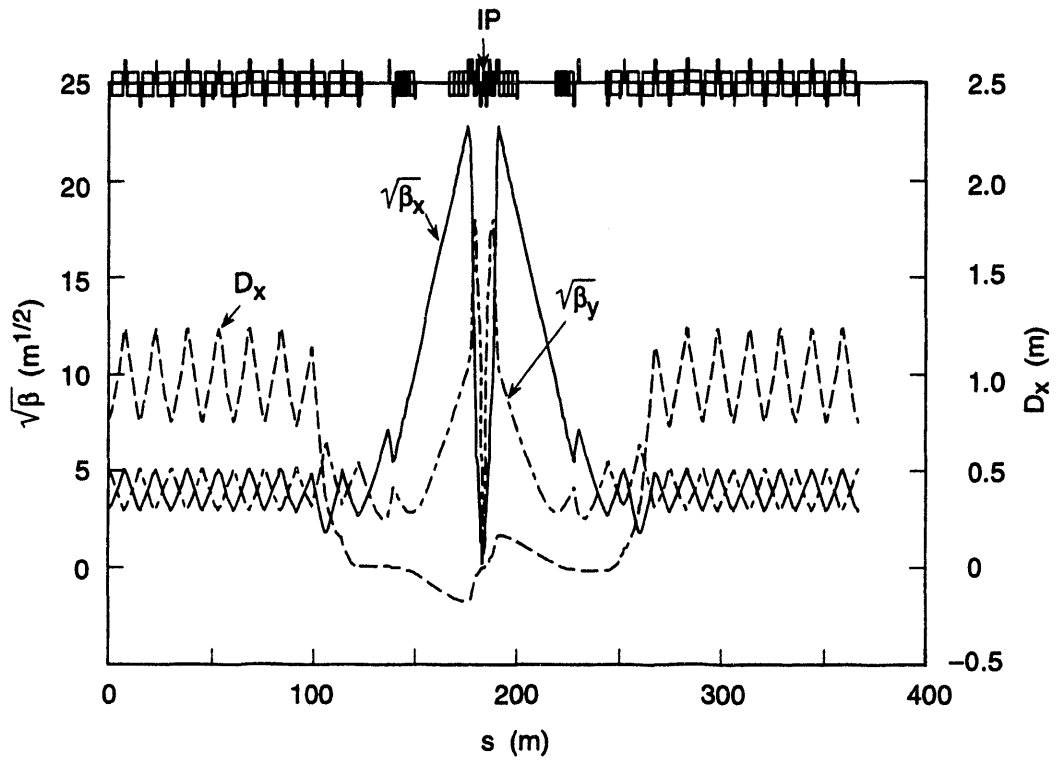

Fig. 4-9. Lattice functions for the collision sextant of the HER. Note the symmetry of the beta functions and the antisymmetry of the dispersion function in the straight section.

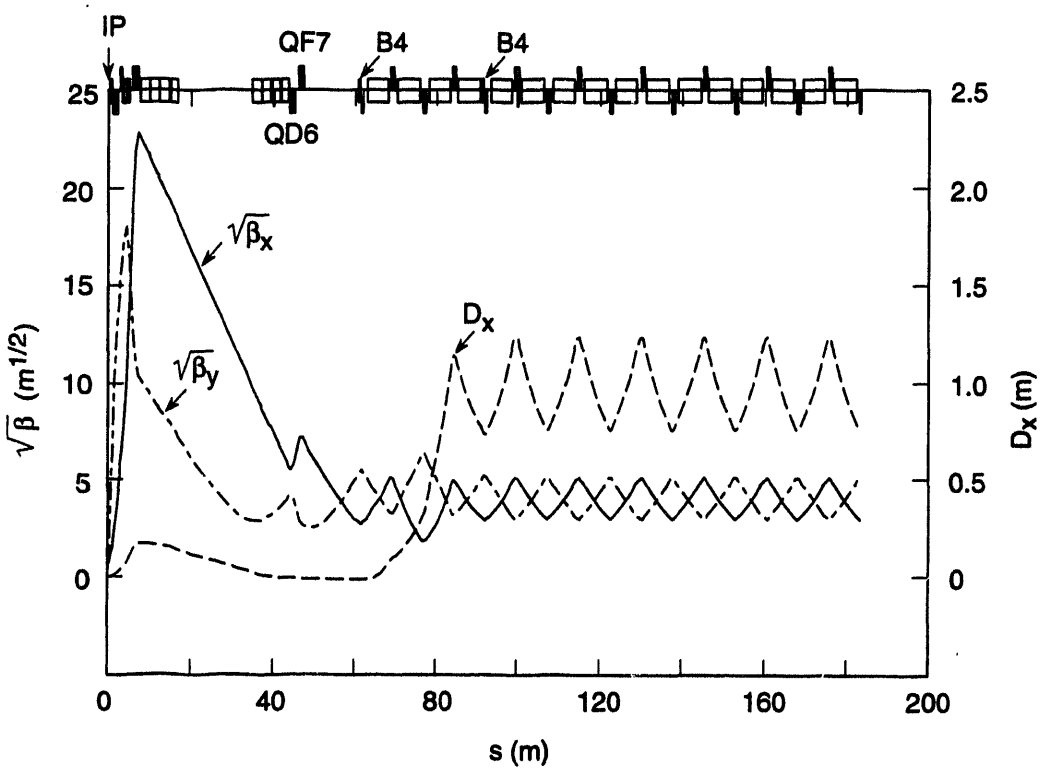

Fig. 4-10. Lattice functions for the right-hand half of the collision sextant of the HER. The B4 magnets that steer the orbit into the arcs are shown here.

beam (at the expense of some horizontal defocusing). Quadrupole QF2 (see Section 5.1.3.4) is a septum quadrupole, affecting the low-energy beam only; the high-energy beam passes through a field-free region.

Upon entering QF2, the low-energy beam is fully separated from the high-energy beam and the HER optical elements are independent of those for the LER. Beyond QF2 is a small permanent-magnet dipole BH1 and the main HER focusing elements QD4 and QF5. Although BH1 has a negligible effect on the optics of the high-energy beam, it serves to deflect the beam orbit sufficiently that the synchrotron radiation from QD4 and QF5 is not pointing directly at the IP, thereby avoiding this potential source of background. As Fig. 4-11 shows, QD4 and QF5 serve to turn over the beta functions coming from the IR and reduce the slope of the dispersion function to near zero. The dispersion function produced by the bending in the IR should be corrected before matching the IR into the arc region. (Strictly speaking, this is not necessary, but to keep the design modular, it is advantageous to insist on it.)

Figure 4-12 shows the 60 m from the IP to the start of the arc (that is, to the entrance of the dispersion suppressor). The dispersion function and its slope are brought to zero by the dipole combination B2 and B3. These are very weak dipoles, each made up of four of the PEP low-field bends. The bending is purposely kept very weak to avoid problems with synchrotron radiation shining into the IR. The dipoles B2 and B3 are followed by a pair of matching quadrupoles QD6 and QF7 that, in conjunction with QD4 and QF5, match the beta functions into the dispersion suppressor.

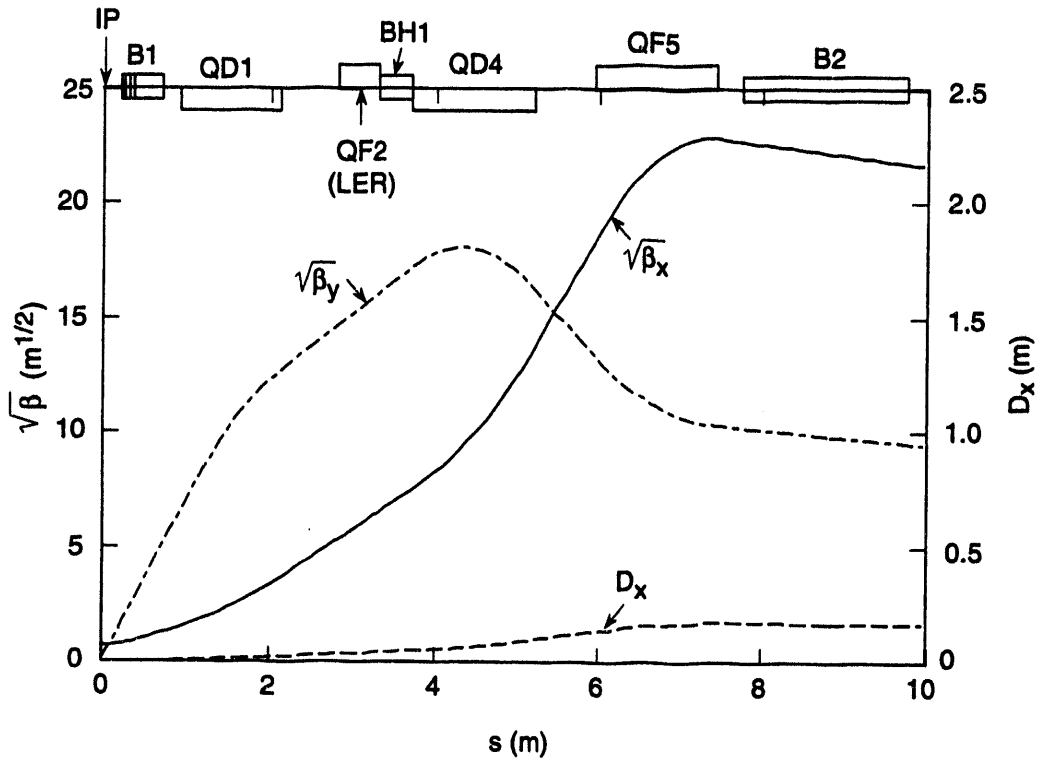

Fig. 4-11. Lattice functions for the first 10 m of the IR straight section of the HER. Elements B1 and QD1 are common to both beams, QD1 providing considerable vertical prefocusing for the high-energy beam. The septum quadrupole QF2 acts only on the low-energy beam; elements beyond QF2 (BH1, QD4, QF5, etc.) affect only the high-energy beam. The QD4 is tilted slightly with respect to the beam axis; this feature, along with the small permanent-magnet dipole BH1, helps avoid synchrotron radiation striking close to the detector beam pipe.

The dispersion suppressors in the arcs adjacent to the IP are slightly different from the others. There is a pair of small dipoles, B4, situated 180° apart in betatron phase (see Fig. 4-10), that match the angles of the orbits from the IP to the arcs. These pairs of dipoles on the two sides of the IP are powered antisymmetrically, as is the B1 dipole. The B4 dipoles make an adjustment to the beam trajectory such that the center of the IP lies at the point where the center of the straight section of a normal sextant would be. The angle of the high-energy beam at the IP is not zero with respect to this line, however. The LER has to match the angle of the low-energy beam to this same angle, 15.4 mrad. The IR geometry is illustrated in Fig. 4-13.

4.1.1.7 Dispersion Suppressors. The HER dispersion suppressors extend over three cells. The main part of the suppressor consists of two cells, each with betatron phase shift close to 90°. However, to obtain a perfect match between the regular cells and the straight section, it is necessary to slightly change the strength of the QF in a third cell (by 1.3% from its value in the regular cells, making the third cell merely a slight variant of a regular cell.) As mentioned, the dispersion suppressors surrounding the IR have

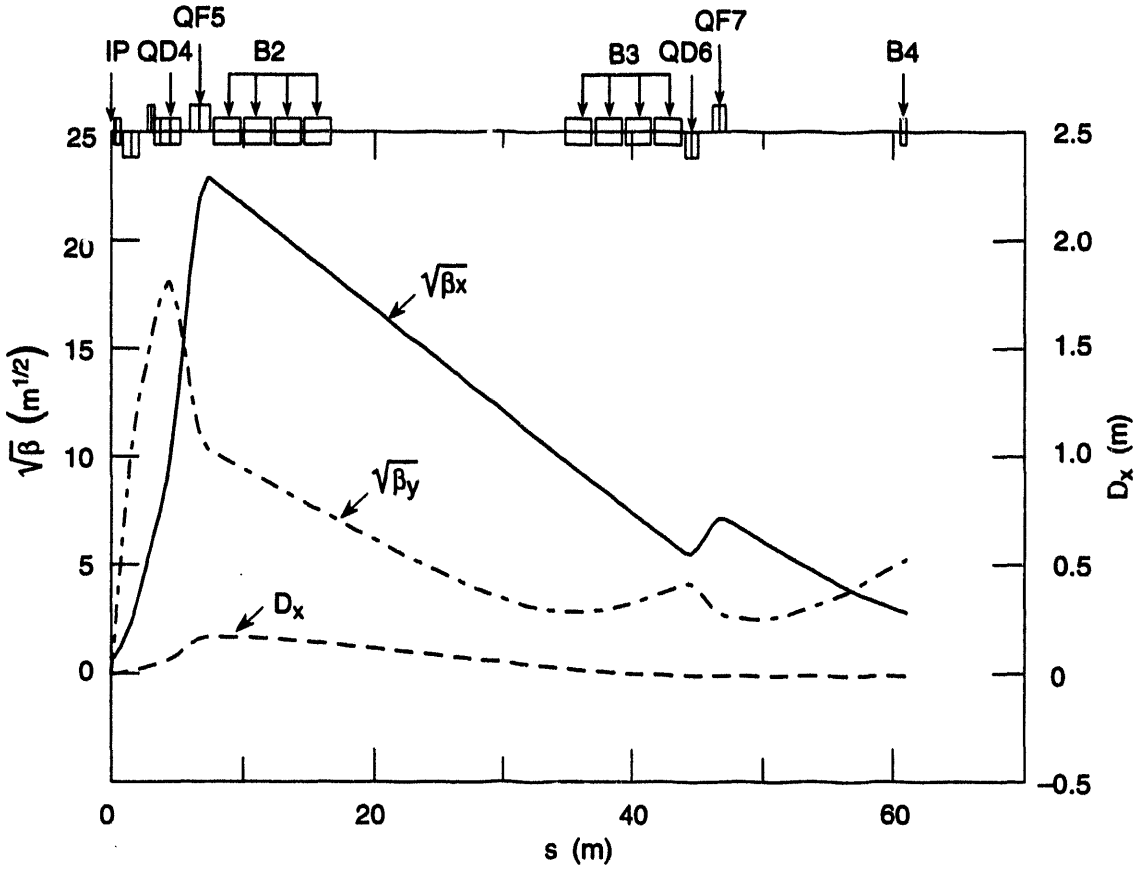

Fig. 4-12. Lattice functions for the first 60 m of the IR straight section of the HER. The weak dipoles B2 and B3 match the dispersion function to zero.

additional dipoles B4 in them to adjust the position of the IP. Dispersion suppressors in the emittance control sextants are the same as those for the normal sextants, but they have their quadrupoles powered differently to produce the dispersion function mismatch in the arcs. The six variables—five quadrupoles in the first two cells plus the QF in the third cell—are sufficient to cover the normal range of emittance control required. To extend the emittance range further, or to radically change the phase shift per cell in the arcs, it would be necessary to independently power the QD in the third cell as well.

To fulfill the requirement of twelve *totally* regular 60° cells (for a possible non-interleaved chromaticity correction scheme), we could tolerate a small beating of the dispersion function in the arcs surrounding the IR. Such a beating would only be about 5%, and would only slightly increase the minimum achievable emittance.

4.1.2 Low-Energy Ring

The LER is designed to satisfy the design parameters discussed in Chapter 3. Key features of the LER include

- Head-on collision optics
- Flat beams with 25:1 horizontal-to-vertical aspect ratio and $\beta_y^* = 1.5$ cm

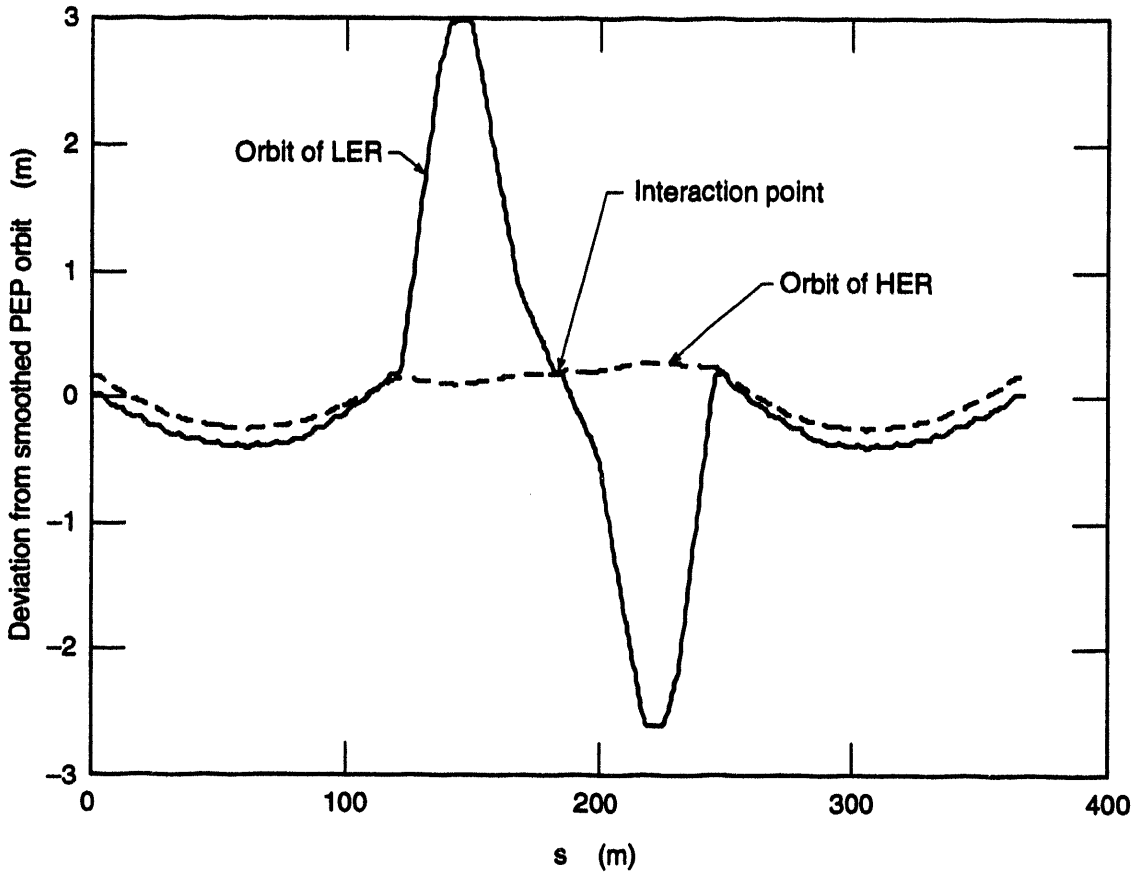

Fig. 4-13. Geometry of the collision sextant, showing how the orbits of the LER and HER deviate from the orbit of PEP. The orbits at the collision point are tilted 15.384 mrad with respect to the straight-section axis.

- Zero dispersion in both planes at the IP
- Bunch separation of 1.26 m
- Beam separation in the IR first horizontally and then vertically
- Wigglers to permit adjustments of emittances and damping times

4.1.2.1 Overall Ring Configuration. The LER has a circumference of 2199.318 m and is designed to operate at 3.1 GeV. As illustrated schematically in Fig. 4-14, the ring has the hexagonal shape of PEP, with six long straight sections and six arcs. One of the long straight sections contains the IR with its low-beta optics; on the opposite side of the ring, the straight section is configured for injection. Two straight sections contain wigglers; two others, one containing the RF cavities, are used for tune adjustment. Figure 4-15 shows the layout and lattice functions of the LER. The beam circulates in a counter-clockwise direction as seen from above the ring. (Note, however, that the optics figures, such as Fig. 4-15, are arbitrarily drawn in the clockwise direction.)

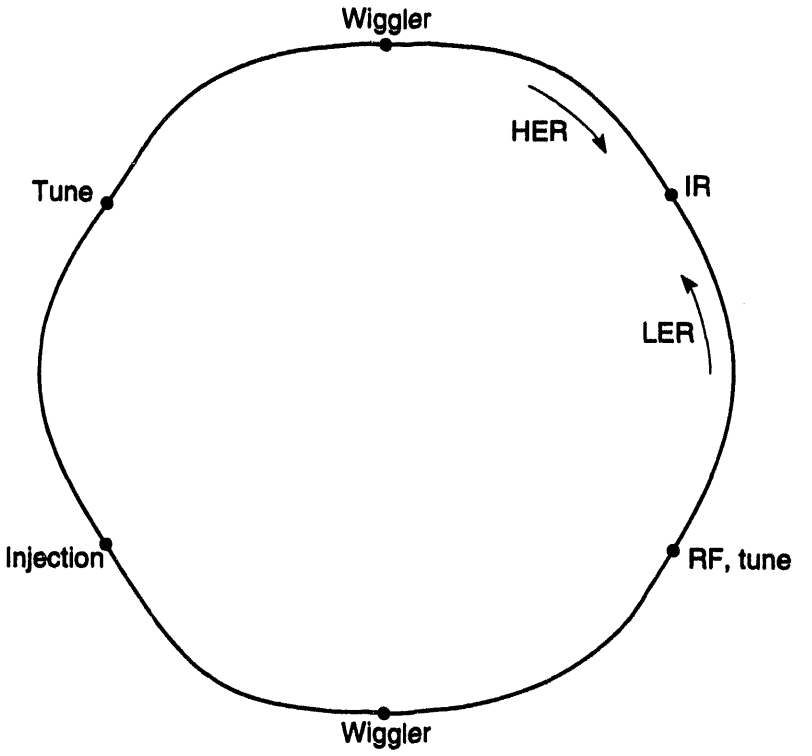

Fig. 4-14. Schematic layout of the LER, which will be located above the HER in the sixfold symmetric PEP tunnel.

The LER is situated 1 m above the HER in the PEP tunnel, except in the IR straight section, where the two beams collide head-on. There are small radial offsets of the two rings in the arcs, and in the RF and injection straight sections, and larger offsets in the IR and wiggler straight sections.

4.1.2.2 Arcs. The LER has six arcs, each built from 16 standard cells in a FODO structure. Two and a half cells in regions 1 and 3—adjacent to the IR—are used for dispersion suppression surrounding the IR straight section. In the arcs located in regions 3, 5, 9, and 11, three and a half cells are used for dispersion suppression surrounding the tune and RF straight sections. The lengths of both the standard cell and the cell in the dispersion suppressor are 15.191 m. The length of each long straight section—measured from the end of the last bending magnet in one arc to the beginning of the first bending magnet in the next arc—is 130.502 m.

The optics of the LER employs mirror symmetry relative to the center of each long straight section. Every arc bending magnet has its azimuthal position centered above the center of the corresponding HER bending magnet. The quadrupoles and sextupoles are located next to the bending magnets, but they alternate their positions from one side of the dipole to the other at each long straight section. This alternating arrangement preserves mirror symmetry about the center of each long straight.

Each FODO half-cell of the LER contains one 0.45-m bending magnet, one 0.43-m quadrupole and one 0.25-m sextupole. The distance between centers of the bending magnet and the quadrupole is 0.555 m and the distance between centers of the quadrupole

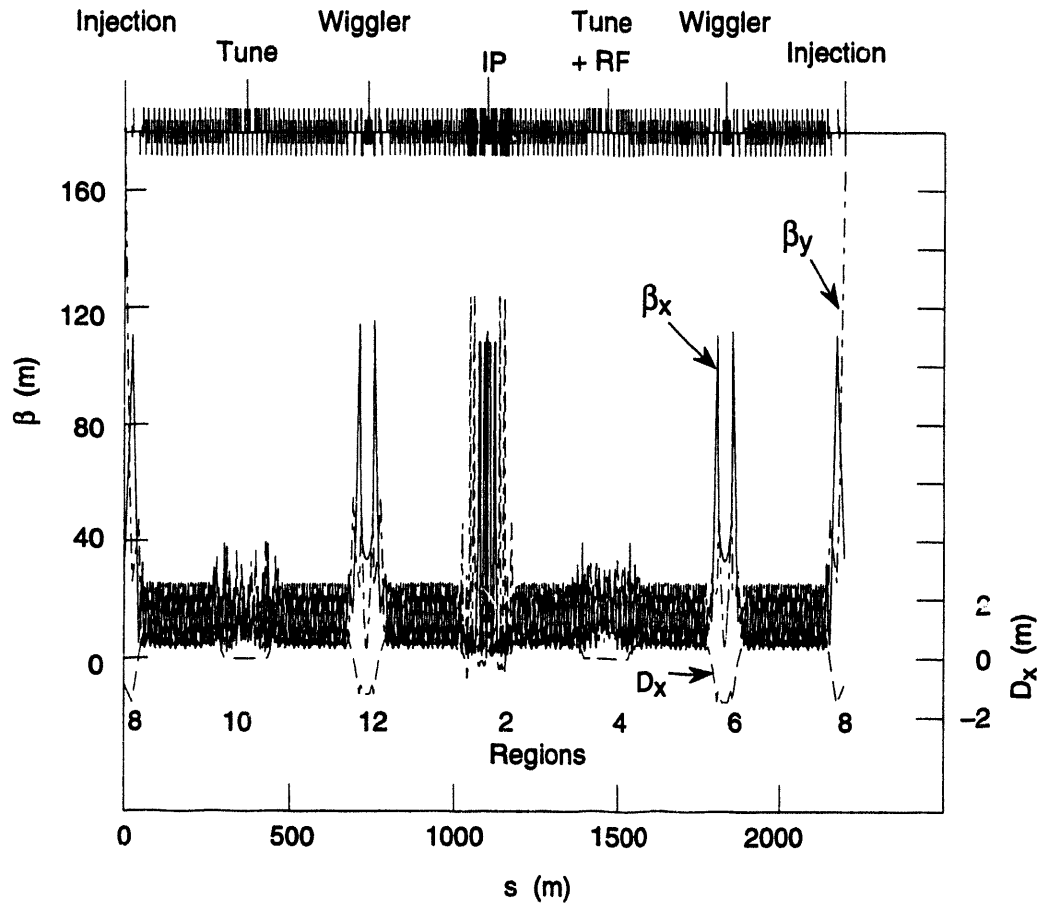

Fig. 4-15. Layout and optics functions for the LER. The lattice for the full ring is shown, starting and finishing at the injection point in the center of region 8. The interaction point (IP) is shown at the center of the figure in region 2. Wiggler magnets are located in regions 6 and 12 and tune control is accomplished in regions 4 and 10. The RF cavities are located in region 4. The layout is shown in the clockwise direction, the low-energy beam circulating anticlockwise from right to left.

and the sextupole is 0.485 m. This proximity of all LER magnetic elements facilitates their being combined into modules for common support and alignment. The long drift spaces between groups of magnetic elements are used to absorb the synchrotron radiation from the bending magnets and to pump (by means of lumped ion pumps) the photodesorbed gas (see Section 5.2). The optics for one cell, shown in Fig. 4-16, are adjusted to give a phase advance of 90° in each transverse plane; hence, four regular cells constitute an achromat. The reason the cell phase advance is higher in the LER than in the HER (where it is 60°) is to avoid having too large a value for the momentum compaction factor α. If α gets too large, a very high RF voltage is required to hold the bunch length to a value compatible with the low value of β_y^*.

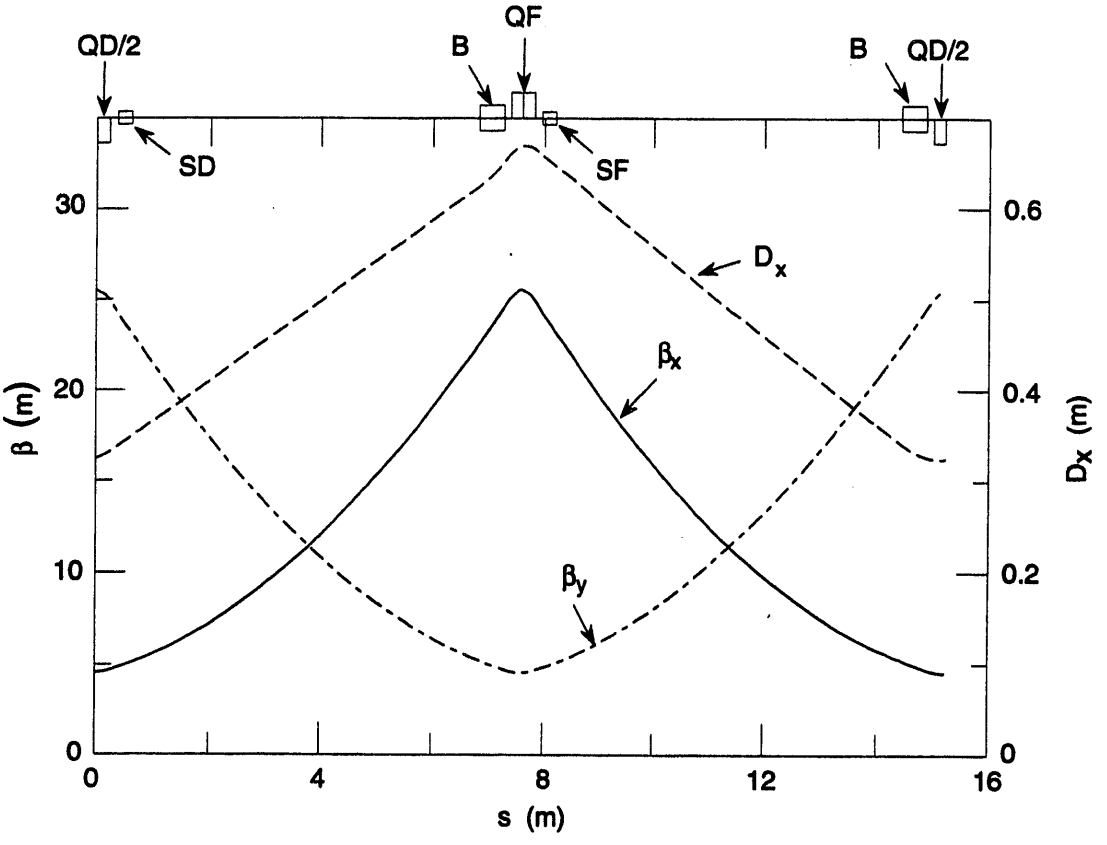

Fig. 4-16. Layout and optics functions for the standard arc cell of the LER. The dipoles B are offset from the center of the half cells so that synchrotron radiation from the beam, traveling from right to left, is absorbed in the longer straight sections between B and QF or B and QD.

4.1.2.3 Dispersion Suppressors. The dispersion suppressor next to the IP straight section is shown in Fig. 4-17. It is bordered on the left by regular cells and on the right by the IP straight section. This suppressor has six bending magnets and five quadrupoles, all but one being placed at the same position as in the regular cell. The last focusing quadrupole of the dispersion suppressor is shifted towards the arc by 4.9874 m. The bending magnets used in the dispersion suppressor are the same as those used in the regular cells, but the magnetic field of the first bend, SB1, is decreased by about 13% relative to the regular cell dipoles and the magnetic field of the last bend, SB2, is increased by the same amount. This is done to bring the orbit of the LER (at the IP) onto the slightly larger radius of the HER. All dispersion suppressor quadrupoles have individually adjustable gradients.

The dispersion suppressor next to a tune or RF section is shown in Fig. 4-18. It is bordered on one side by the regular cells and on the other by the tune section. This suppressor has seven bending magnets and eight quadrupoles, all placed at the same positions as those in the regular cells. All bending magnets are the same as those of the regular cells but all quadrupoles have individual gradients.

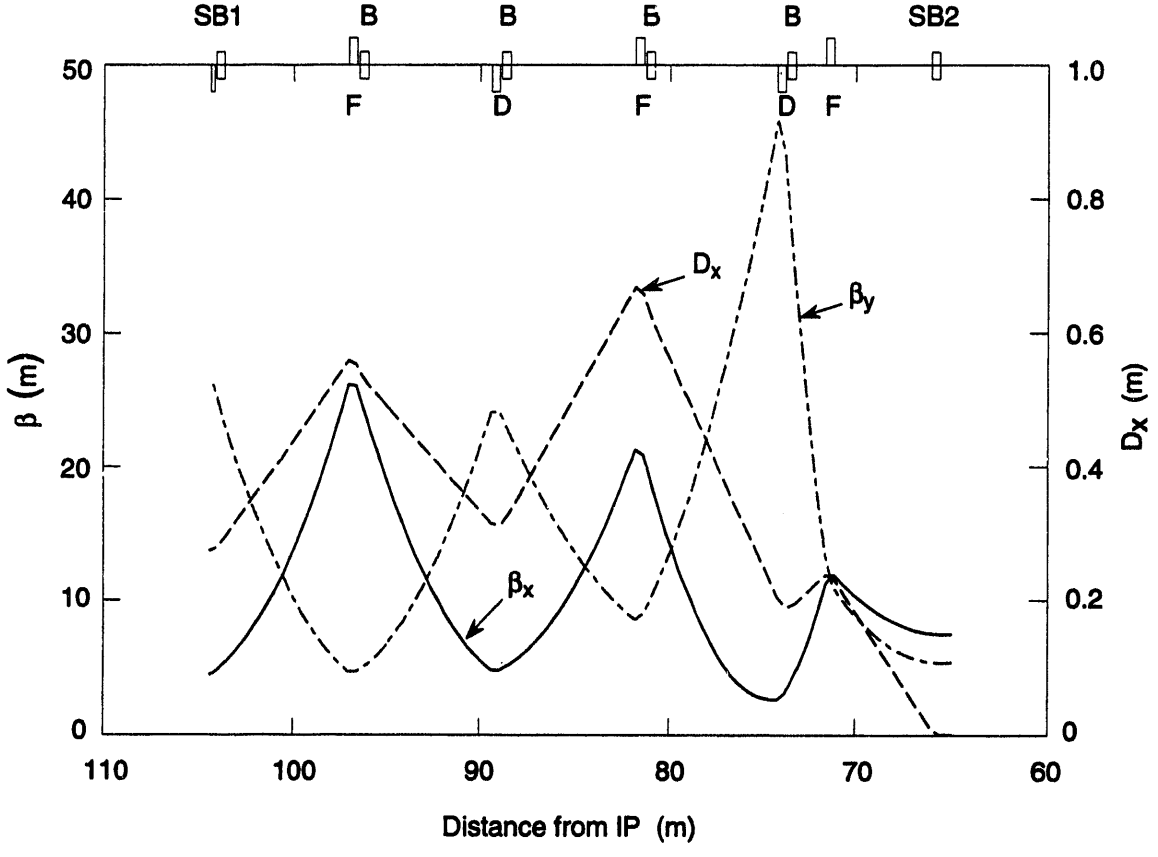

Fig. 4-17. Layout and optics functions for a dispersion suppressor next to the IP section of the LER.

4.1.2.4 Tune and RF Sections. The tune and RF sections of the LER are designed on the same principle. Fifteen equally spaced quadrupoles are placed between the end quadrupoles of the dispersion suppressors. These quadrupoles constitute a FODO type lattice structure, which is used for adjustment of the global betatron tunes over a wide range. The RF section also houses the RF cavities. For convenience in locating the LER and HER cavities, all quadrupoles of the LER in this region are shifted slightly towards the center of the straight section, the distance between them decreasing by 0.1 m.

Figure 4-18 shows the layout and optics functions for the RF section with its adjacent dispersion suppressors. The layout for the tune section is essentially identical to that shown in Fig. 4-18. The plan view of the HER and LER orbits in a tune sextant is shown in Fig. 4-19.

4.1.2.5 Wiggler Straight Sections. Two of the long straight sections contain wiggler magnets, which are used to adjust the emittance of the LER and also to permit the damping time of the LER to be reduced to a value as low as that of the HER, if desired. Figure 4-20 shows the layout and optics of a wiggler straight section. Four blocks of 4-m wigglers are placed in each wiggler straight section in a special bypass. The bypass serves both to deflect the synchrotron radiation away from the main beamline and to increase the dispersion, and its derivative, in the wigglers (which in turn causes a growth

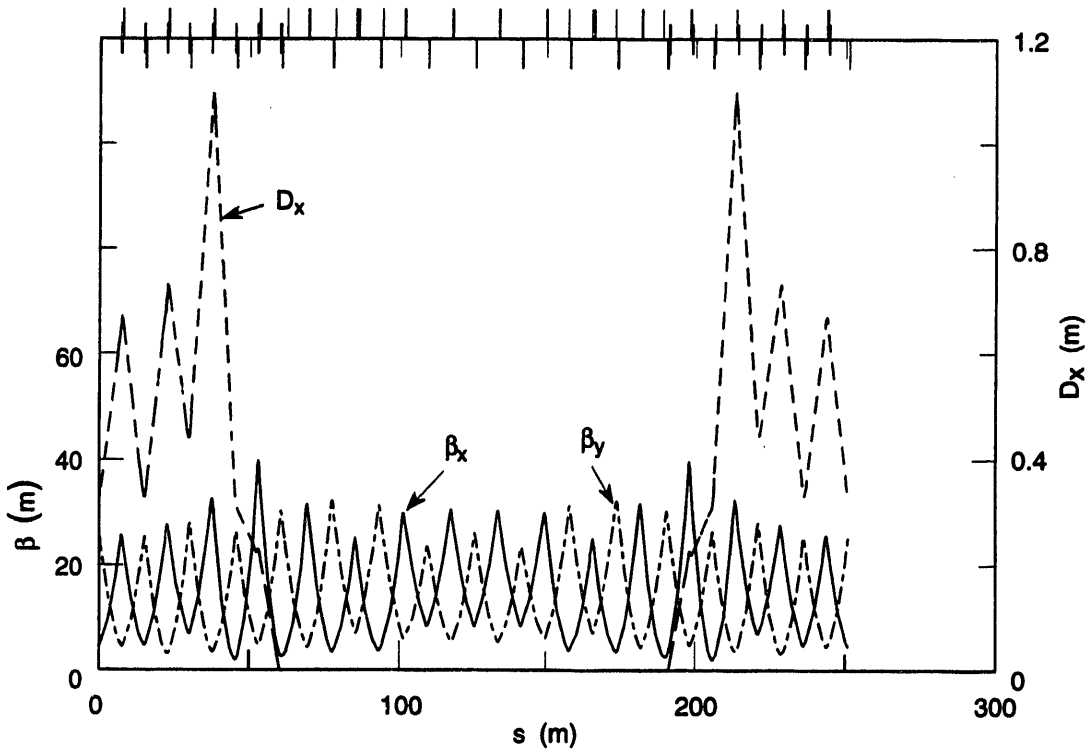

Fig. 4-18. Layout and optics functions for an RF or tune straight section of the LER, with adjacent dispersion suppressors.

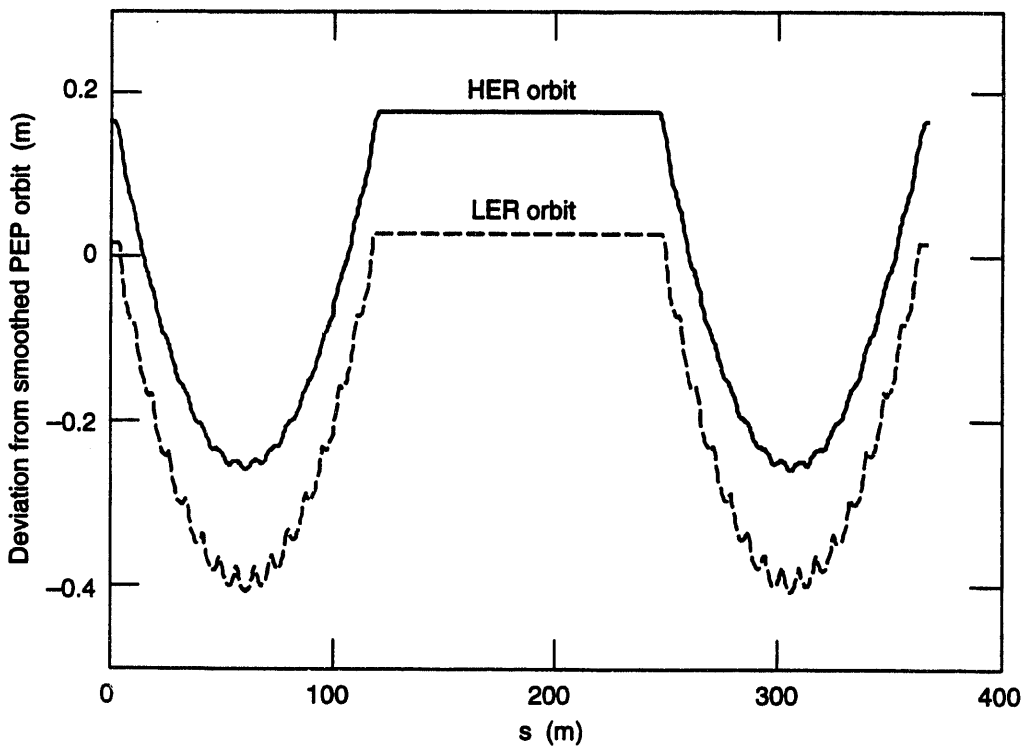

Fig. 4-19. Plot showing the radial offsets of the LER and HER in a tune sextant, with respect to the PEP centerline. The maximum excursions are 41 cm to the inside and 18 cm to the outside of the PEP orbit.

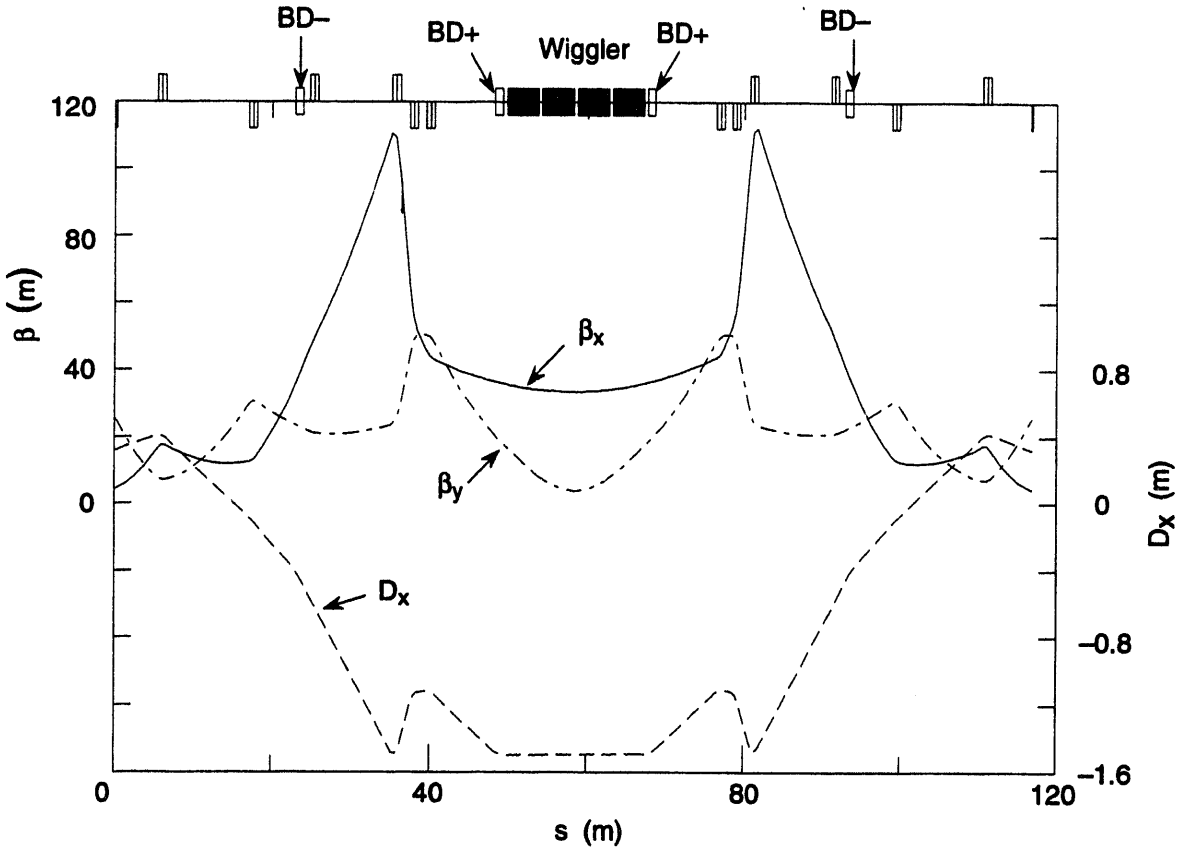

Fig. 4-20. Layout and optics functions for a wiggler straight section of the LER.

of horizontal emittance). A schematic drawing of the bypass and the main beamline in the wiggler section is shown in Fig. 4-21.

The optics shown in Fig. 4-20 corresponds to the case where the damping time in the LER is about the same as that in the HER. Six independent quadrupoles produce a beam waist at the center of the wiggler where the slope of the dispersion function is also zero. These quadrupoles permit adjustment of the horizontal beta function to provide good control over the emittance excitation in the wiggler.

4.1.2.6 Injection Straight Section. The straight section opposite the IR straight section is used for injection into the LER. It is configured in the same way as that of the HER, and has a similar value of β_y (170 m) at the injection point. The layout and optics of this straight section are shown in Fig. 4-22.

4.1.2.7 Interaction Region and Beam Separation. The most difficult part of the design of a collider is that of the IR, and that is especially true in the case of a high-luminosity asymmetric machine. The energies and beta functions of the two rings are different, the bunches are closely spaced, and the synchrotron radiation from the magnetic separation is large. Optics, separation, masking, and experimental detectors must all coexist in a very small region, so that neat, modular designs are elusive or nonexistent.

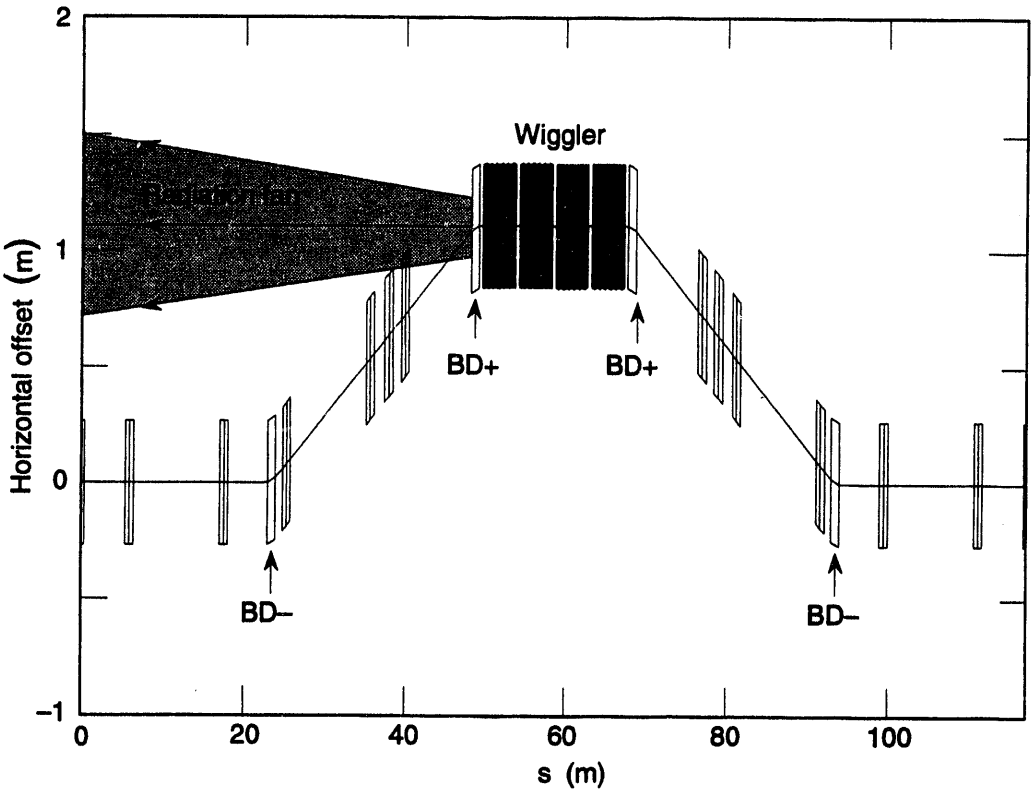

Fig. 4-21. Diagram showing the horizontal offset of the low-energy beam in the wiggler sextants. The low-energy beam travels anticlockwise from right to left in this figure. The bypass causes the radiation fan from the wiggler to be directed outward where it can be absorbed in a dump. The four equally powered dipoles BD+ and BD– create the bump and thereby the dispersion function necessary for increasing the emittance of the beam. The wigglers are wide-aperture devices, with a horizontal gap considerably wider than the pole width to accommodate the fan of synchrotron radiation produced by the strong magnetic field.

As discussed earlier, the scheme adopted for this design is horizontal separation using a separating dipole, B1. The separating dipole is followed by a horizontally defocusing quadrupole, QD1, centered on the high-energy beam, that enhances the beam separation. (These first two optical elements, B1 and QD1, are constructed with permanent-magnet technology because they are immersed in the solenoidal field of the detector.) The other main function of the optics near the IP is to focus both beams as quickly as possible in order to avoid excessively large beta functions and excessively high chromaticity. With the beam separation available in our design, the next focusing element can be a horizontally focusing septum quadrupole acting on the low-energy beam alone. (This element completes the focusing of the low-energy beam as it leaves the IP region.) The high-energy beam is thereafter in an independent beamline where it is focused by a quadrupole doublet, as described in Section 4.1.1.

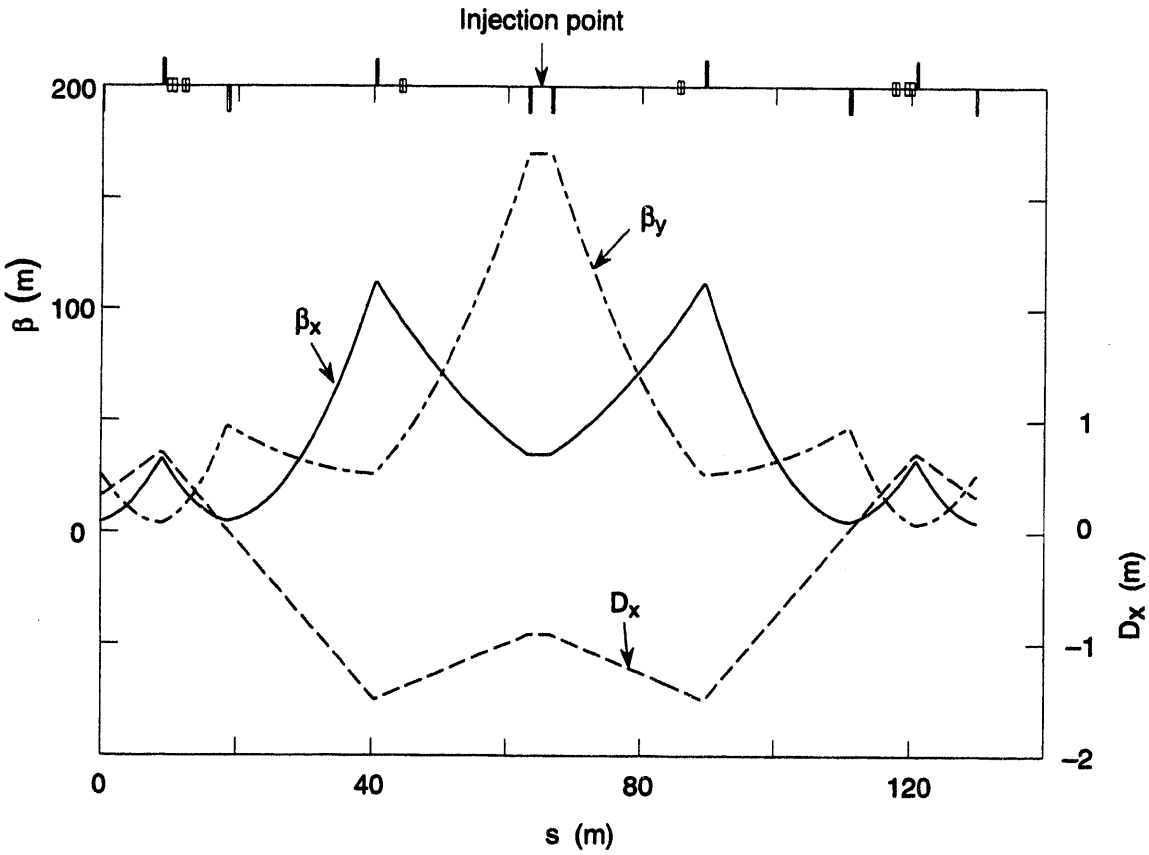

Fig. 4-22. Layout and optics functions for the injection straight section of the LER. The injection point is at the center of the figure, between the horizontally defocusing quadrupoles. The injection straight sections of the LER and HER are similar.

Figure 4-23 shows an anamorphic diagram of the IR in plan view. The horizontal bending pattern is antisymmetric about the IP, which produces an S-bend layout; this geometry is conducive to extracting the synchrotron radiation, as discussed in Section 4.2.2. The separated beams then traverse the septum quadrupole QF2, which focuses the low-energy beam only. Figure 4-24 shows the displacements of the low-energy beam from the IP through the horizontal and vertical separation systems. The low-energy beam is transported from the collision plane to a plane 1 m above it by the action of the three vertical bending magnets BV1, BV2, and BV3.

The optical functions of the LER in the horizontal separation region are shown in Fig. 4-25. The low-energy beam proceeds from a waist at the IP with $\beta_x^* = 37.5$ cm, $\beta_y^* = 1.5$ cm. The first parasitic bunch crossing point occurs 0.63 m from the IP, where the incoming and outgoing beams are just inside of B1 and the beam orbits are separated by $11.8\sigma_x$. The dipole and quadrupole apertures allow for $15\sigma_x$ and $15\sigma_y$ beams (the fully coupled vertical emittance being used to calculate the vertical beam size), plus at least 8 mm for the beam pipe and trim coils, a 2 mm closed-orbit-distortion allowance, and the additional aperture required to clear the synchrotron radiation fans. These factors set the

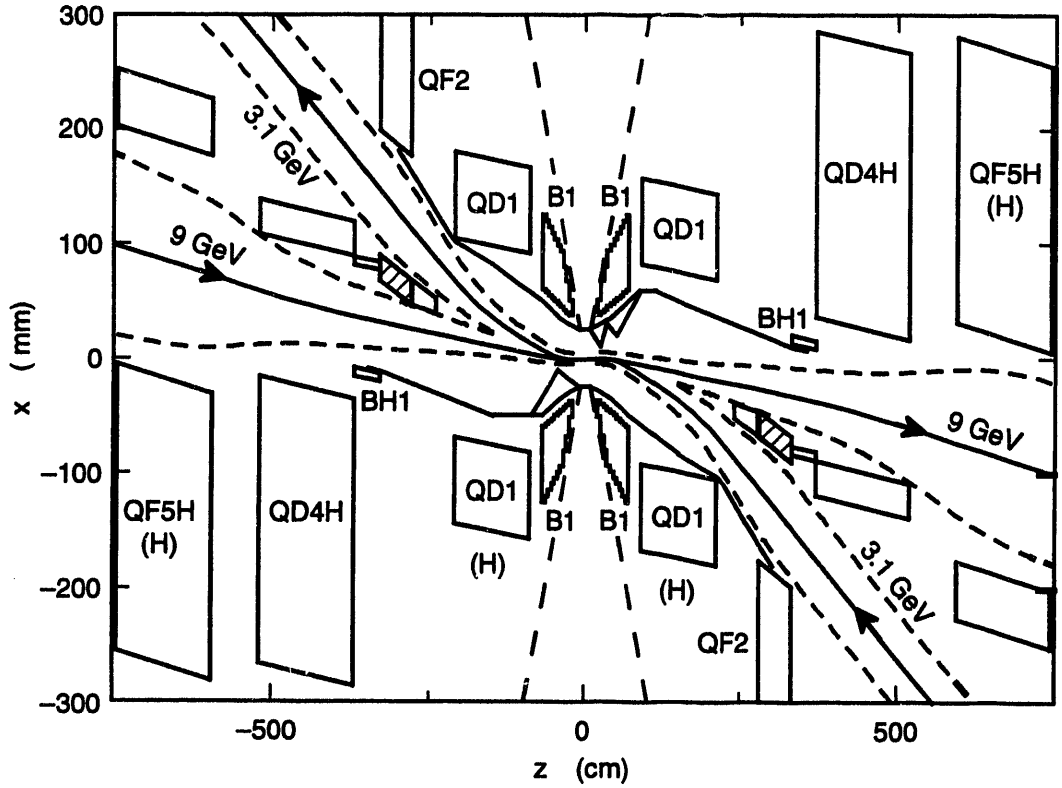

Fig. 4-23. Anamorphic plan view of the IR. Beam trajectories are indicated by thick solid lines, and the $15\sigma_x$ beam-stay-clear envelopes are shown as dashed lines. The horizontal separation is produced by B1 and QD1 with the offsets shown. Quadrupole polarities are indicated, as usual, by the names QF (horizontally focusing) or QD (horizontally defocusing); the labels (H) or (L) denote that the magnet is centered on the high- or low-energy beam orbit.

inner radii for B1 and QD1; the outer radii are controlled by the need to maximize the detector solid angle. The magnet dimensions, and an assumed remanent field of 1.05 T, give the gradient of QD1. The length of QD1 and the gradient of QF2 are then adjusted to achieve the desired optical behavior for the low-energy beam, as shown in Fig. 4-25. It should be noted that QF2 is tilted slightly (and also offset) with respect to the axis of the low-energy beam, in order to maximize the area available for the current sheet septum of the magnet. After a number of iterations, the outcome was a conservative and robust design. It is worth reiterating here that the high-energy beam benefits significantly from the focusing of QD1. Although the primary focusing of the high-energy beam does not take place until farther from the IP in QD4, the β_y value in this quadrupole is held sufficiently low by QD1 that the resultant chromaticity contribution to the HER from the combination of QD1 and QD4 is only 2% higher than that of the corresponding quadrupole at PEP (which was operating at a higher β_y^* of 4 cm).

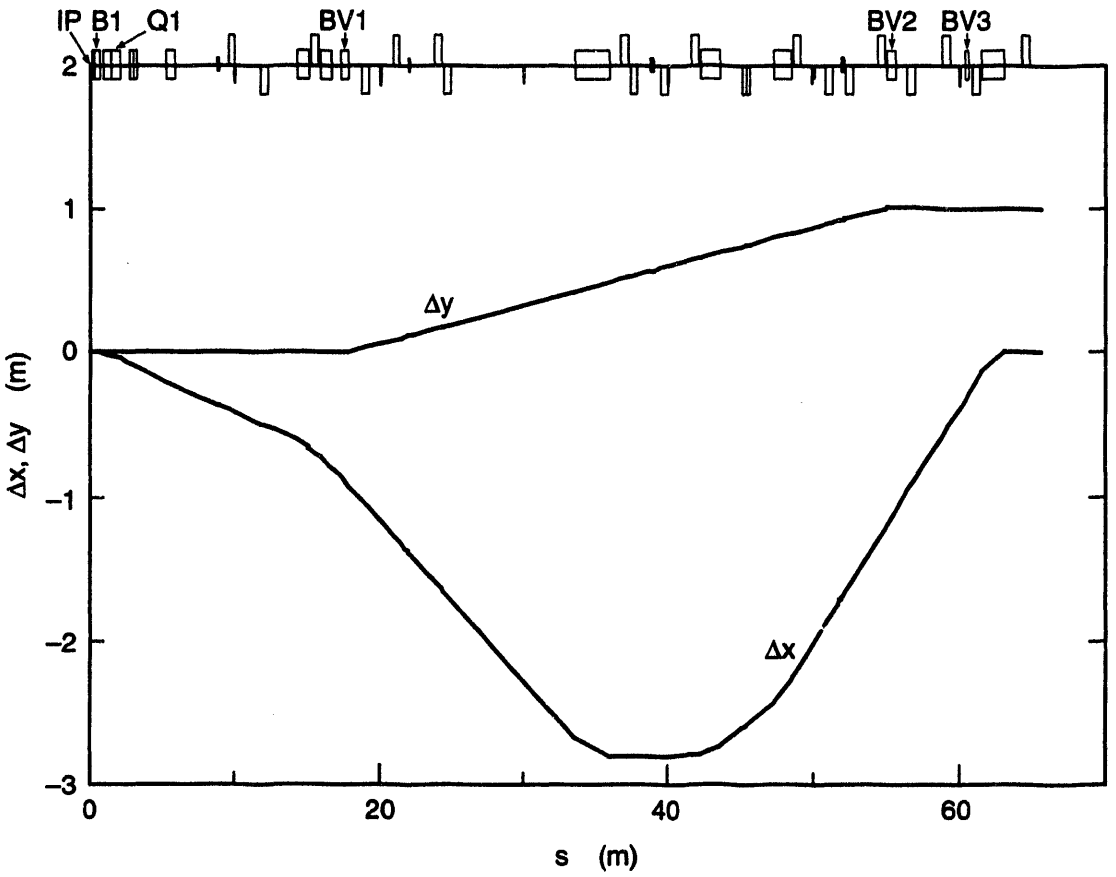

Fig. 4-24. Plot showing the horizontal and vertical displacements of the low-energy beam in the separator system. The dipoles BV1, BV2, and BV3 control the vertical step that brings the LER above the plane of the HER.

With the IP region defined, there remain many design requirements for the rest of the IR straight section:

- There must be a vertical separation region where the LER orbit is raised 1 m above the HER orbit before the rings enter the arc region
- The horizontal separation must be reversed so that the LER optical elements can be placed directly above the HER elements in the arcs
- All lattice functions, including the horizontal and vertical dispersion functions and their derivatives, must be properly matched
- Conditions for local chromaticity correction must be fulfilled

By the term *local chromaticity correction*, we mean that the chromaticity due to the LER quadrupoles QD1 and QF2 is corrected directly in the IP straight section. For this purpose a special scheme of chromaticity correction was implemented; its main principles are demonstrated in Fig. 4-26. Two pairs of sextupole lenses on each side of the IP are used for correction of the chromatic aberrations due to the two QD1 and the two QF2

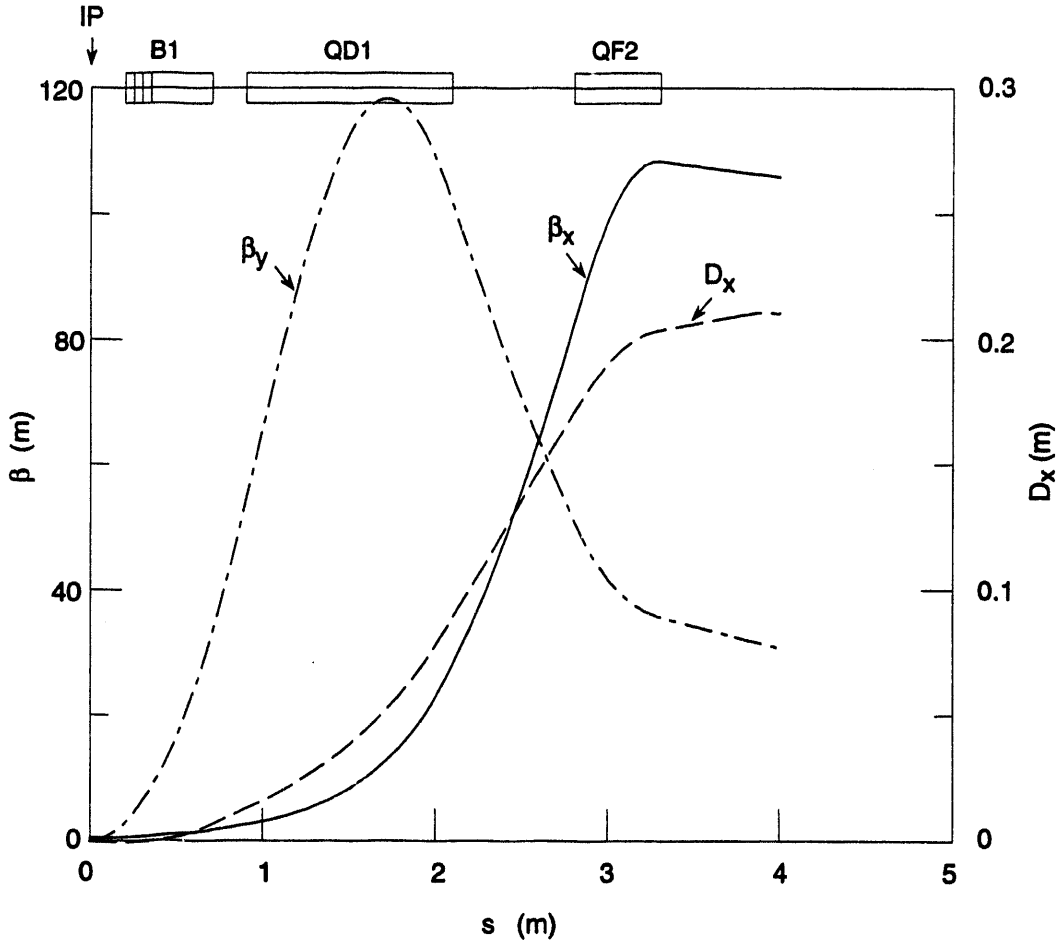

Fig. 4-25. Layout and optics functions for the horizontal separation region of the LER. The dipole B1 and the offset quadrupole QD1 separate the beams. The horizontally focusing quadrupole QF2 is a septum magnet; the high-energy beam passes through a field-free region in the magnet (see Fig. 5-24).

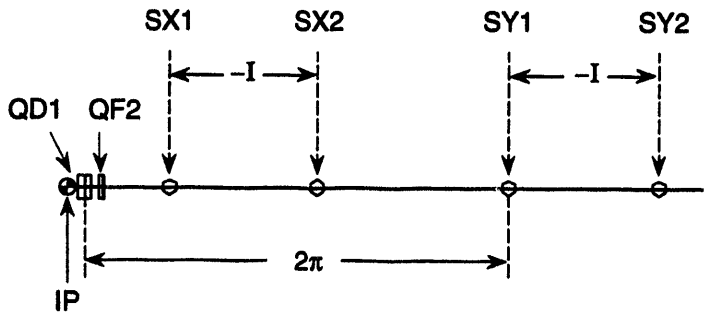

Fig. 4-26. Local chromaticity correction scheme of the LER.

quadrupoles. The sextupole pair SX1-SX2 corrects for the horizontal aberrations; the pair SY1-SY2 simultaneously corrects for the vertical aberrations.

Figure 4-26 shows the main elements of the local chromaticity correction scheme; for clarity, only half of the IR is shown. (The two halves of the IR have symmetry about the IP, focusing and vertical bending being symmetric and horizontal bending being antisymmetric.) The first sextupole of the horizontally correcting pair, SX1-SX2, is close to QF2. The first sextupole of the vertically correcting pair, SY1-SY2 is placed at a position 2π in vertical phase advance from QD1. Sextupole SX2 (SY2) is situated such that the horizontal (vertical) betatron phase advance is π from SX1 (SY1). The transfer matrix between each pair of sextupoles is exactly $-I$, which ensures cancellation of the sextupole-like geometrical aberrations of the individual sextupoles. To maximally decouple the functions of the sextupoles in the horizontal and vertical planes, a high vertical and a low horizontal beta function are created at the locations of SY1 and SY2 and vice versa at the locations of SX1 and SX2. Bending magnets are used to enhance the dispersion function at the sextupoles, the value of D being equal at each sextupole of a pair.

The realization of the local chromaticity correction scheme in the IR straight section is shown in Fig. 4-27. The large horizontal beta function at the exit of QF2 is extended a

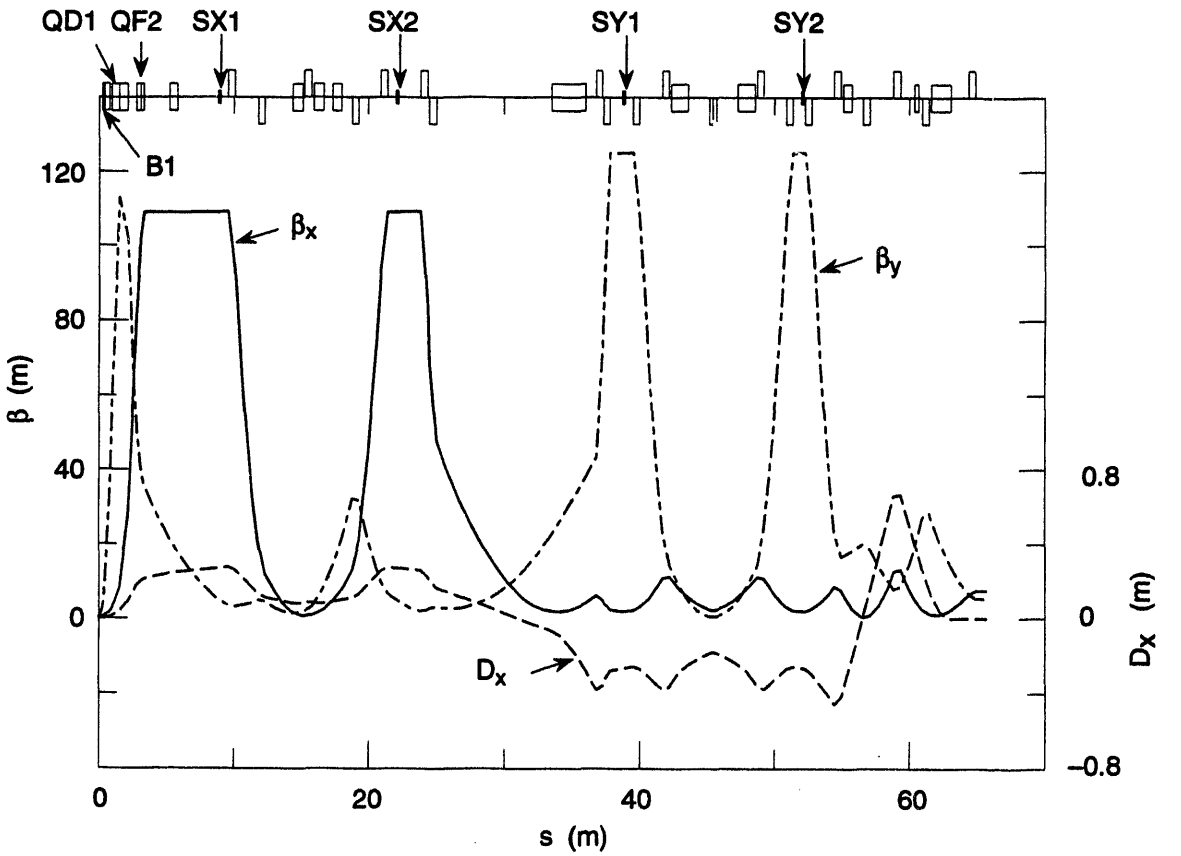

Fig. 4-27. Layout and optics functions of the right half of the IR straight section of the LER. The IP is at the left.

further 3.5 m to allow β_y to decrease to a low value and to allow the dispersion function (generated by B1 and the offset QD1) to increase further; the sextupole SX1 is placed at this position. The next section of the lattice generates the $-I$ transformation between SX1 and SX2. A consequence of the $-I$ transformation is that β_x and β_y have the same values at both SX1 and SX2. The positive value of dispersion at SX2—the same as at SX1—is preserved by the two B3 magnets. The function of the optics between SX2 and SY1 is to interchange β_x and β_y (that is, to obtain a small β_x and a large β_y) to facilitate correction of the vertical chromaticity, and to simultaneously adjust the betatron phase advances in both planes to their correct values. A second $-I$ transformation after SY1 brings β_y to a maximum and β_x to a minimum at SY2. Equal dispersion at SY1 and SY2 is preserved by the two B5 magnets. The remaining part of the optics in this section serves for matching the two beta functions and the two dispersion functions to the values needed for the dispersion suppressor.

Figure 4-28 shows the vertical dispersion function. Vertical dispersion is generated by the first magnet of the vertical step (BV1) and is not fully removed until the third vertical bending magnet BV3. By proper positioning of BV1, the vertical dispersion is made small at SX2, SY1 and SY2. The main cancellation of the vertical dispersion function is done by BV2, which is positioned almost 2π away from BV1 in vertical phase

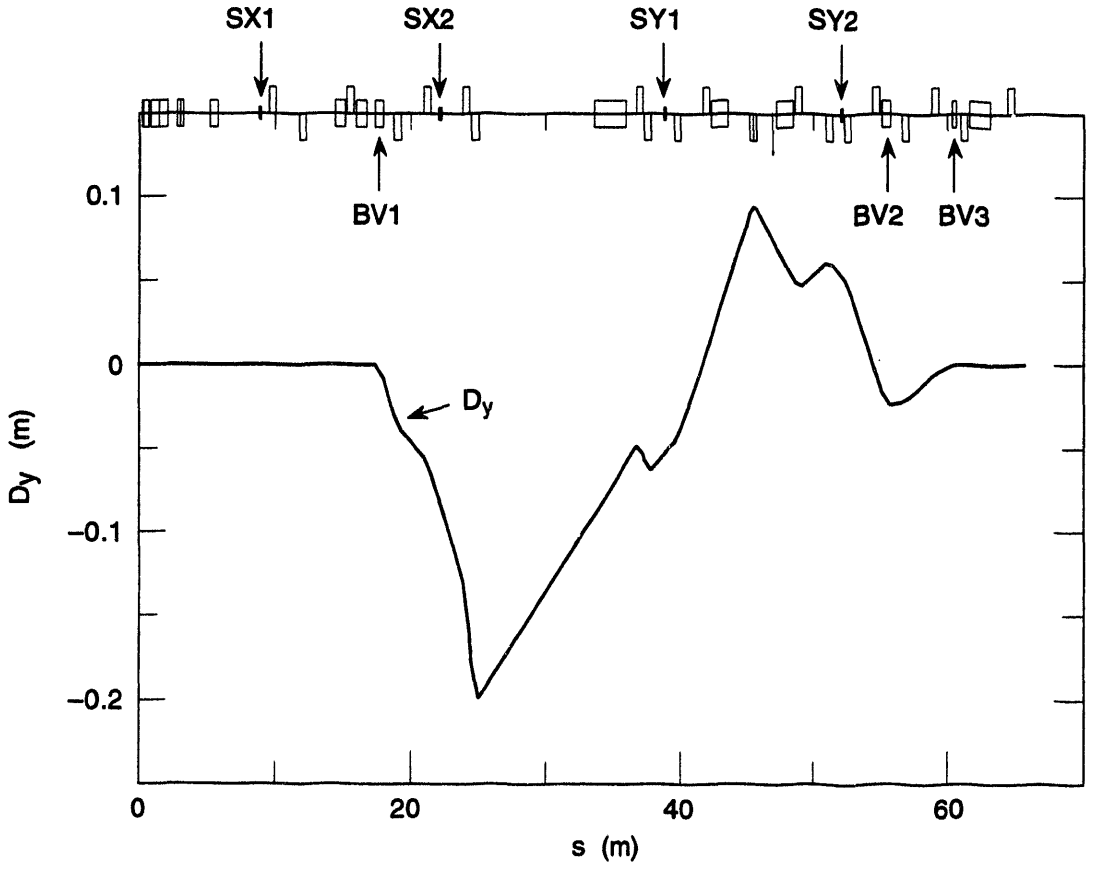

Fig. 4-28. Vertical dispersion function of the right half of the IR straight section.

advance. Vertical bending magnet BV3 acts as a small trim to BV2 to complete both the vertical bending and the cancellation of the vertical dispersion function.

4.1.2.8 Ring Closure. There are two absolute requirements on the rings:

- Their path lengths must be the same and must be equal to the nominal circumference of 2199.318 m
- Their interaction points must coincide

Another important requirement is that the two rings bear a consistent physical relationship to each other to facilitate the construction of support structures and to make alignment reasonably straightforward.

The IR straight sections in both rings, and the wiggler straight sections in the LER, all have bending elements that make the path length greater than the straight-line distance across them. We choose to make the straight-line distance across all straight sections the same in both rings. To achieve this, and to maintain the correct overall path length in both machines, the path lengths in the arcs must be reduced by a small amount, that is, the cell radius in the arcs must be shortened. Because of the antisymmetry of some of the bending in the dispersion suppressors adjacent to the collision straight of the HER, special adjustments must be made in these locations. To align the center of the bends at equal angles with respect to the arc center, small length adjustments are made between each dipole; the IP then falls at the geometric center of the IR straight section. As the dispersion suppressors on each side of the collision straight have individual power supplies, the asymmetry presents no matching problems. The above procedure has been carried out for the HER. The overall path length adjustment was 3.7 mm, which translates into a 19.3-μm change in the length of each half-cell.

The LER requires much more adjustment than the HER, due mainly to the path-length differences in the wiggler straight sections. The overall LER path length adjustment is 0.845 m and the change per half-cell is 4.53 mm. As there is no mixture of symmetrical and antisymmetrical bending in the LER, the correction that was applied to the HER is not necessary. However, in the LER the mixture of vertical and horizontal bending does require special attention. In the region of mixed horizontal and vertical bending, the local coordinate system has to be rolled slightly (a maximum of 1.5 mrad). When this is done, closure is achieved and the IP lies at the geometrical center of the straight section.

Because the LER bending cells have been shortened much more than those in the HER, the LER lies inside the HER by about 14.7 cm. To bring the IP of the LER outwards to coincide with that of the HER, special bends SB1 and SB2 are powered separately from the main string of bending magnets.

4.1.3 Tracking Studies

4.1.3.1 Description of Methods. There are many reasons to require a large dynamic aperture, the main ones being the need for efficient injection and the need for long lifetime under colliding-beam conditions. Evaluating the requirements for these two conditions takes similar, but slightly different, information.

Injection takes place in the vertical plane for both PEP-II rings, so the injection point is vertically displaced relative to the closed orbit. To evaluate the injection aperture we launch particles at the injection location and determine the aperture in terms of transverse position coordinates measured from the closed orbit. For injection we wish to have an aperture that includes the injection point and several rms beam sizes (typically six or more) around the injection point for particles that are within $10\sigma_E$ of the nominal injection energy. For the tracking results evaluated here, we take the horizontal rms beam size σ_x from the natural (uncoupled) horizontal emittance of the ring; the vertical beam size σ_y is taken from the fully-coupled emittance, that is, half the uncoupled horizontal emittance.

To evaluate the aperture for colliding-beam conditions, the one-turn map for the lattice is factored into a normal form, from which the transformations to approximate invariant tori are extracted. Each launch position then corresponds to an invariant action, and the aperture can be represented as an area in transverse action space or amplitude space (amplitude being defined as the square root of twice the action). For colliding-beam conditions, the dynamic aperture should be about 10σ in both transverse planes. (Note that the nominal vertical emittances of both HER and LER lattices are only 4% of the horizontal emittance, so the injection aperture of $10\sigma_y$ fully-coupled corresponds to roughly $36\sigma_y$ of the actual beam.)

Tools. The linear lattices were designed using the well-known MAD program [Iselin, 1991]. Various errors (see Section 4.1.3.2) are then introduced and the "imperfect" lattice is regenerated by the code TRACY [Bengtsson, 1992]. TRACY makes use of multistep symplectic integrators and uses an isomagnetic Hamiltonian model for dipoles, truncated at second-order in the transverse variables. The code incorporates routines to correct the orbit and retune the linear lattice and provides a Pascal interpreter for implementing lattice correction algorithms. The corrected lattice output from TRACY serves as input for DESPOT [Forest et al., 1992], a combination tracking and mapping code where the Hamiltonian for tracking and mapping are guaranteed to be identical.

Powerful nonlinear analysis tools are now available for storage ring design. These serve three important purposes: (i) a cross-check of lattices generated for dynamic aperture studies, to verify that they have the expected linear and nonlinear properties; (ii) the improvement of the design of lattice sections, such as the IR region, so that the magnitudes of higher-order terms are minimized; and (iii) the determination of the source of all terms in the one-turn map, to facilitate decisions regarding modifications of the lattice arrangement and specifications of tolerances. We have used a number of these packages.

Berz [1989] has introduced a set of truncated power series manipulation tools (referred to as "differential algebra" tools). Many others have now implemented this technique in various computer languages. Algebraic capabilities include addition, multiplication, taking inverses, general functions, and concatenation. Lattice maps may be created to arbitrary order, constrained only by computer capability and the user's ability to extract useful information. These tools can be used for general fitting by introducing additional variables when creating the one-turn map.

We have also used a set of Lie algebra tools that are gathered in a package called LIELIB [Forest, 1993], which employs a full range of analytic techniques to evaluate

maps created by the differential algebra codes. These techniques include exponentiation (Dragt-Finn or single-exponent), transformation to a resonance basis, and normal-form analysis. (The result of exponentiating a map is the product of a linear map and a higher-order map defined by a Hamiltonian generator; this form is preferable for interpreting the map, as each monomial in the Hamiltonian corresponds to a distinct aberration. Expressed in a resonance basis, the coefficients can be interpreted as resonance strengths.) Walker [1993] has implemented the method of using the CBH (Campbell-Baker-Hausdorff) theorem in an interactive *Mathematica* program named LAMA to identify the source of terms in the one-turn Hamiltonian mentioned above.

The various codes are used in a complementary manner: DESPOT, with its capabilities to digest complicated lattices, is used to create maps of lattice sections, LIELIB is used to exponentiate them, and LAMA is used to take the resultant Hamiltonian generators and combine them with CBH analysis so that they can be scaled, transformed, and analyzed.

Multiturn trajectory analysis tools are also used to identify the harmonic content of particle motion near the edge of the dynamic aperture. In particular, we have used HARMON [Donald, 1982] for harmonic analysis, and BIGT [Warnock, 1992] for construction of toroidal invariants and Fourier-series maps.

It is not yet possible to track at the edge of the dynamic aperture directly with maps, due to problems associated with the symplectic condition. Ideally, one would modify the one-turn Hamiltonian, extract certain terms or combinations of terms, and see what impact they have on the dynamic aperture. Though the complete Hamiltonian cannot be symplectically tracked, monomial terms can be integrated. By introducing "monomial" elements into the lattice, specific terms in the map can be removed in such a way as to leave the remaining Hamiltonian unchanged. The consequences of these modifications can then be followed by tracking with these monomial elements in the ring. An example of such an approach would be to remove all amplitude-dependent tune shift terms, as it is well known that the magnitude of the amplitude-dependent tune shift is very important for dynamic aperture considerations. These terms will be of equal importance for beam-beam effects, especially tail motion (and thus beam lifetime). It may, therefore, be important that both the HER and LER have the capability to adjust the three linear amplitude-dependent tune shift coefficients.

Error Groups. Errors in the lattices are introduced in three groups:

- Misalignments, dipole and quadrupole roll errors, and dipole strength errors
- Magnetic multipole errors
- Multipoles plus quadrupole and sextupole strength errors

A description of the magnitudes of these errors and how they were derived is given in Section 4.1.3.2. Introduction of the first error group requires orbit correction, and possibly dispersion and coupling correction. The second group requires chromaticity, and perhaps $d\beta/d\delta$ correction. The third group requires tune correction, and possibly beta function correction as well.

4.1.3.2 Magnet Errors. We collect in this section information on the magnitudes of all errors that were assumed in the dynamic aperture studies described in Section 4.1.3.4. The correction strategies used to compensate these errors are described in Section 4.1.3.3. Errors are categorized in this report in four groups:

- Field strength errors
- Roll errors
- Misalignment errors
- Multipole errors

Field Strength Errors. The rms strength errors used in all dynamic aperture studies for both HER and LER are summarized in Table 4-2. These are assumed to arise from nonuniformities in construction, such as variations in magnet length and gap. Because the absolute strengths of dipoles, quadrupoles, and sextupoles are set in the tracking code to yield a proper orbit, tune, and chromaticity, respectively, we exclude systematic strength errors.

Roll Errors. The rms roll errors for both HER and LER are summarized in Table 4-3. Within the detector barrel, both quadrupole and dipole elements in the string B1-Q1-Q1-B1 are taken to have a correlated roll error.

Table 4-2. Field strength errors used in tracking.

Error	Amount
$\Delta B/B$ (dipoles)	0.001
$\Delta K/K$ (quadrupoles)	0.001
$\Delta S/S$ (sextupoles)	0.002

Table 4-3. Magnet roll errors used in tracking.

Error	Amount (μrad)
Dipoles	300
Quadrupoles	500
Sextupoles	500
Detector barrel (B1 and Q1)	300

Misalignment Errors. The arcs consist of a sequence of modules containing a quadrupole, a sextupole, and a BPM, separated by dipoles and drifts. Because alignment between modules is likely to be less accurate (and less important) than alignment within a module, in Table 4-4 we have specified both intramodule and module-to-module misalignments. Dipole misalignments are also included, to allow for the feed-down that results from multipole errors. Errors for the elements in the straight sections are taken to be the same as module-to-module errors, as summarized in Table 4-5.

Because the spacing between wiggler sections (13 cm) is much greater than their magnetic gap (4.5 cm), wigglers in the LER are treated (and will be built) as a series of alternating dipoles. Thus, the dipole errors in Tables 4-2, 4-3, and 4-4 are used for this element.

It is possible that the alignment of those beamline elements within the detector will be difficult, so we have a separate specification for Q1 and B1 misalignments (both horizontal and vertical) of 200 μm.

Table 4-4. Arc misalignment errors used in tracking. All errors apply to both the horizontal and vertical planes.

Error	Amount (μm)
Dipole, rms	1,000
Quadrupole, rms	100
Sextupole, rms	100
BPM, rms	0[a]
Module-to-module	150

[a]The BPM center defines the module location.

Table 4-5. Straight section misalignment errors used in tracking. All errors apply to both the horizontal and vertical planes.

Error	Amount (μm)
Quadrupole, rms	150
Sextupole, rms	150
BPM, rms	150

Multipole Errors. For tracking purposes, we specify both systematic and random errors. For the HER, many of the magnets will be recycled PEP magnets, so the multipole values mainly come from actual magnetic measurements or POISSON calculations. For the LER, we make estimates based upon POISSON calculations, along with assembly simulations, for magnets not yet built.

Dipole field errors (up to sextupole terms) for the HER are based on measurements of PEP magnets; harmonics beyond sextupole are based on modeling the magnets with POISSON. The PEP dipoles were measured at a current of 1250 A, nearly double the PEP-II requirement of 640 A. The bending magnet multipole components are summarized in Table 4-6 in the following manner: n gives half the number of poles of the multipole and b_r corresponds to the magnitude of the magnetic field for the nth component at a reference radius r. Errors are described by giving the magnetic field of the nth harmonic divided by the strength of the magnetic field due to the fundamental (dipole) component, b_n/b_1, at the reference radius. For the HER dipoles, the reference radius is taken to be $r = 3$ cm, the radius at which the measurements were made.

The multipole values used for the LER dipoles are estimates based in part on POISSON calculations for an H-style magnet geometry. Due to its symmetry, an H magnet has no allowed quadrupole component. Field errors b_n/b_1 are given in Table 4-7 at a radius of 3 cm. As noted, these are also the tolerances assumed for the wiggler, which is a series of short dipoles.

Table 4-6. HER bending magnet field errors at r = 3 cm.

n	Systematic (b_n/b_1)	Random (b_n/b_1)
2	-3.9×10^{-5}	4.1×10^{-5}
3	1.0×10^{-5}	3.2×10^{-5}
4	–	3.2×10^{-5}
5	–	6.4×10^{-5}
6	–	8.2×10^{-5}

Table 4-7. LER bending magnet field errors at r = 3 cm.

n	Systematic (b_n/b_1)	Random (b_n/b_1)
3	1.0×10^{-4}	1.0×10^{-4}
5	–	1.0×10^{-4}
7, 9	–	1.0×10^{-5}

In PEP there were three types of regular quadrupoles, with different lengths. For the HER, we use errors based on measurements of a 10% sample of the 740-mm quadrupoles made at a current of 200 A (somewhat higher than the 145 A typical for the HER arc quadrupoles). From POISSON, we do not expect the quadrupoles to saturate at currents below 200 A. In Table 4-8, the magnetic field due to the nth harmonic divided by the strength of the magnetic field due to the fundamental (quadrupole) component, b_n/b_2, is specified at a radius of $r = 4.49$ cm (the radius at which the measurements were taken).

For the majority of the LER quadrupoles, we use an estimate based on the assumption that the machining error of the surface is about 25 μm. For a quadrupole with a 5-cm bore radius, the magnetic field contribution from the nth multipole (b_n) relative to the magnetic field from the quadrupole (b_2) at the pole-tip radius is 5×10^{-4}. In Table 4-9 we

Table 4-8. HER quadrupole field errors at r = 4.49 cm. Values based on PEP measurements.

n	Systematic (b_n/b_2)	Random (b_n/b_2)
3[a]	1.0×10^{-3}	3.2×10^{-4}
4[a]	5.6×10^{-4}	4.5×10^{-4}
5[a]	4.8×10^{-4}	1.9×10^{-4}
6	2.4×10^{-3}	1.7×10^{-4}
10	-3.1×10^{-3}	1.8×10^{-4}
14	-2.6×10^{-3}	7.0×10^{-5}

[a]Unallowed components are randomly skewed.

Table 4-9. Comparison of LER quadrupole fabrication error estimate with measured values from PEP quadrupoles at r = 5 cm.

n	Random (PEP) (b_n/b_2)	Random (Estimate) (b_n/b_2)
3	3.2×10^{-4}	4.5×10^{-4}
4	4.5×10^{-4}	4.1×10^{-4}
5	1.9×10^{-4}	3.6×10^{-4}
6	1.7×10^{-4}	3.3×10^{-4}
10	1.8×10^{-4}	2.2×10^{-4}
14	7.0×10^{-5}	1.4×10^{-4}

compare this estimate with the PEP measurements. For the allowed systematic multipoles we assume a relative field error twice that of the random errors. This is consistent with the measurements of the PEP quadrupoles. The LER quadrupole errors used in the tracking are summarized in Table 4-10; values of b_n/b_2 are at the pole-tip radius of 5 cm.

Since the HER and LER sextupoles are of identical design, we use the same errors for both. Because the multipole errors for the sextupoles are based on a measurement of a single prototype PEP magnet, it is difficult to assign rms values in this case. The values of b_n/b_3 in Table 4-11 are specified at a radius of $r = 5.652$ cm, the radius at which the measurements were taken.

The multipole content of Q1 (Table 4-12) is based on assembly simulations. The first allowed multipole is the $n = 18$ harmonic; random errors are included up to the 15-pole. The reference radius is 8.7 cm, the inner radius of Q1. Since the LER beam is not centered in Q1, feed-down must be computed for it.

The intrinsic multipole content of the B1 magnet is also based on simulations of assembly errors for Q1, as both are permanent magnets and their random assembly errors should be comparable. B1 is made up of 8 permanent magnet segments, so $n = 9$ is the first allowed multipole. The magnetic field due to the nth harmonic is specified in Table 4-13 at $r = 4.9$ cm.

Table 4-10. LER quadrupole field errors evaluated at $r = 5$ cm.

n	Systematic (b_n/b_2)	Random (b_n/b_2)
3[a] – 5[a]	—	5.0×10^{-4}
6, 10, 14	1.0×10^{-3}	5.0×10^{-4}

[a]Unallowed components are randomly skewed.

Table 4-11. HER and LER sextupole field errors (taken from PEP measurements at r = 5.652 cm).

n	Systematic (b_n/b_3)	Random (b_n/b_3)
5[a]	—	2.2×10^{-3}
7[a]	—	1.1×10^{-3}
9	-1.5×10^{-2}	—
15	-1.3×10^{-2}	—

[a]Unallowed components are randomly skewed.

Table 4-12. Q1 multipole field errors at r = 8.7 cm, based on fabrication tolerances.

n	Systematic (b_n/b_2)	Random (b_n/b_2)
3[a]–15[a]	—	2.0×10^{-4}
18	-8.0×10^{-2}	—

[a]Unallowed components randomly skewed.

Table 4-13. B1 multipole field errors at r = 4.9 cm, based on fabrication tolerances.

n	Systematic (b_n/b_1)	Random (b_n/b_1)
2–8	—	2.0×10^{-4}
9	2.48×10^{-2}	2.0×10^{-4}
10–15	—	2.0×10^{-4}

For the Q2 septum quadrupole, there are POISSON estimates for the magnitude of the intrinsic multipoles (neglecting end effects); these are summarized in Table 4-14. The values for the random column in Table 4-14 are difficult to achieve but such values are measurable and, in principle, correctable. (Indeed, such values have been achieved in existing magnets—the values for the PEP IR quadrupoles are lower than 1×10^{-4}.) The reference radius, 4.23 cm, is the inner radius of Q2. Because Q2 is a septum quadrupole, all harmonics are allowed by symmetry. Systematic multipoles are normally oriented; random components are randomly skewed.

The HER septum quadrupoles Q4 and Q5 require careful engineering and construction to achieve multipoles that are corrected to the level that they can be measured. For both magnets, we specify a multipole content of $b_n/b_2 \leq 1 \times 10^{-4}$ for n = 3–15 (at a reference radius of 5.0 cm for Q4 and 8.0 cm for Q5).

4.1.3.3 Correction Strategies. Magnet errors as specified in the previous section often lead to unacceptable errors in the closed-orbit location and linear lattice parameters. This section describes the methods used to correct such errors. In the tracking results reported in Section 4.1.3.4, these methods are not always used, but their effects on the dynamic aperture have been studied for several cases described there. Although some of the correction techniques described in this section are not explicitly included in the description of PEP-II contained in this report, all could be implemented if necessary. We

Table 4-14. LER Q2 multipole field errors at r = 4.23 cm, based on POISSON calculations.

n	Systematic (b_n/b_2)	Random (b_n/b_2)
3	-1.11×10^{-4}	1.0×10^{-4}
4	1.82×10^{-4}	1.0×10^{-4}
5	6.30×10^{-5}	1.0×10^{-4}
6	-5.00×10^{-5}	1.0×10^{-4}
7–15	—	1.0×10^{-4}

would consider the implementation of some of these techniques if it were unambiguously shown that they are necessary. In all cases, such additions would be minor.

Chromaticity. The chromaticity is corrected by slight adjustments of the arc sextupole strengths. In the LER, the chromaticity of the quadrupole doublet on each side of the IP is corrected with special nearby sextupole pairs that are not readjusted to account for magnet errors. For the HER, the sextupoles in each correction sextant are grouped into pairs, members of a pair being 180° apart in betatron phase. Final adjustment is then made to the six pairs of sextupoles of each type—horizontally focusing and vertically focusing—on each side of the IP. In this adjustment, special care is given to the momentum dependence of the beta functions at the IP and at the injection point.

Energy-Dependent Beta Functions. The $d\beta/d\delta$ term is corrected by using additional sextupole families. In each arc of the LER we assume two SF and two SD families (corresponding to the two phases of the 90° FODO cell lattice.) If the sum of the strengths of these families is held constant, the chromaticity correction is unchanged. This yields six knobs in each plane, one from each arc—enough to correct $d\beta/d\delta$ at three locations (which we choose to be the center of the RF straight section, the injection straight section, and the IP). The IR sextupoles provide an additional knob in each plane for $d\beta/d\delta$ adjustment. The HER 60° lattice has three distinct phases in each plane, providing sufficient knobs for $d\beta/d\delta$ correction in this lattice. For the work reported here, $d\beta/d\delta$ is corrected only if the beta function changes by more than 15% for a 0.3% change in δ (that is, $d(\ln\beta)/d\delta$ must be larger than 50), and it is corrected only to this level of accuracy in the simulations.

Tune. The LER and HER both have special sections (shared with the RF straight sections) for tune control. These sections are retuned to restore the tunes to their nominal values prior to tracking with errors.

Beta Functions. Correction of the beta functions is accomplished by analyzing their behavior around the ring. For each arc, the incoming and outgoing $\Delta\beta/\beta$ is analyzed for

amplitude and phase. If the QD and QF quadrupoles are on two strings, they may be tuned such that the incoming and outgoing magnitude and phase of $\Delta\beta/\beta$ are identical (to within measurement limits, taken to be $\Delta\beta/\beta = 0.15$). After this is done, quadrupole families at the entrance and exit of each straight section are adjusted in unison such that the amplitude and phase of $\Delta\beta/\beta$ agree in the adjoining arcs. Finally, the quadrupole families at the entrance and exit of each straight section are adjusted in opposition to obtain a symmetric $\Delta\beta/\beta$ at the center of the straight, and a slope adjusted to be zero.

Dispersion. After the closed orbit is corrected, the dispersion is corrected by minor changes in vertical steering (to minimize the vertical dispersion function) or by minor changes in horizontal steering (to minimize the variation of the horizontal dispersion from its design value).

Horizontal-Vertical Coupling. The HER and LER each contain skew quadrupoles in the RF straight sections to control global coupling. No provision for local coupling control has been made in the present lattices.

4.1.3.4 Dynamic Aperture Studies. Here we present dynamic apertures for each of our design lattices (corresponding to a specific choice of IP beta functions). To the ideal lattices are added various errors. We also briefly examine the effects of including such items as dipole and quadrupole edge effects, kinematic correction terms in the tracking, hard- and soft-edge solenoid fields (with compensation), the IR injection bump, quantum excitation and damping terms, and the effects of parasitic beam-beam collisions. The results are presented for the design energy, which we call "on-energy" and for $10\sigma_E$ from the design energy, which we call "off-energy."

Each lattice—with or without various errors, with or without various correction strategies, and with or without various additional effects—is tracked for 1,024 turns at several amplitudes. These amplitudes are chosen in two distinct ways: (i) all points on a rather large grid extending from –20 to $+20\sigma_x$ and from $0–20\sigma_y$, or (ii) points along various rays emanating from the origin in amplitude space. These rays may be along the horizontal or vertical axis, the diagonal, or some direction in between. Though it is computer intensive, option (i) is preferable as sometimes there exist certain regions of instability in the tracking space that are not identified by method (ii). Also, in method (i) we have identified the horizontal and vertical tunes for all particles that survive the 1,024 turns. This has often enabled us to identify the aperture boundary as corresponding to the location of a particular resonance line. All off-energy tracking includes synchrotron motion.

When quantum excitation and damping are included, we track for 4,096 turns (one transverse damping time). We wish to ensure that our 1,024-turn dynamic aperture without damping is approximately the same as the 4,096-turn aperture with damping.

A launch point is considered stable—that is, inside the dynamic aperture—if it is not lost within the chosen number of turns. A "scraper" aperture is located at a distance several times larger than the physical aperture, typically at about 20 cm. (The reason for this large scraper aperture is that the dynamically stable aperture for machines without errors can be larger than the physical aperture, and we wish to allow for this possibility.

On the other hand, particles that have become unstable, quickly reach very large amplitudes, so the definition of stability does not depend strongly on scraper position.)

HER Tracking. Figure 4-29 shows a plot of the injection coordinate space for the HER bare lattice (that is, the results are plotted based on betatron amplitudes measured at the injection point rather than at the IP). Each numerical entry in the diagrams gives the fractional horizontal tune at that launch point for particles that have survived for 1,024 turns on-energy (Fig. 4-29a) or off-energy ($10\sigma_E$ deviation, see Fig. 4-29b). Figure 4-30 shows similar results for the off-energy case when radiation damping and quantum excitation are included. In this case, particles were tracked for 4,096 turns, or roughly one transverse damping time. Comparison of Figs. 4-29b and 4-30 demonstrates clearly that the tracking results do not depend on the effects of the radiation damping, in the sense that the dynamic apertures are nearly identical in the two cases.

In Fig. 4-31, we plot the HER tracking results of Fig. 4-29a projected into tune space. Each stable amplitude in Fig. 4-29a is plotted as a point in the tune plane, and locations of low-order betatron and synchrobetatron resonance lines are indicated. To examine the influence of the parasitic beam-beam collisions on the tracking, we show in Fig. 4-32 a tune diagram that includes the effect of the first parasitic crossings (those nearest the IP). We find a distortion in the tune footprint, for particles with large horizontal amplitude, associated with the amplitude-dependent tune shift from the parasitic crossings. This effect is discussed in more detail in Section 4.4 in the context of the beam-beam simulations.

As can be seen in Fig. 4-33 for the on-energy HER bare lattice, the influence of the nonlinear effects of the parasitic beam-beam collisions is negligible, that is, tracking with the parasitic crossings included gives only a small reduction in dynamic aperture compared with the bare lattice. Also shown in Fig. 4-33 is the off-energy dynamic aperture of the HER including the effects of the fringing fields of the dipoles in the tracking. Here too, we see that this effect has a negligible impact on the dynamic aperture. We see that the on-energy dynamic aperture at the injection point is quite large. There is a noticeable reduction in aperture for the off-energy case, though the available aperture considerably exceeds our injection requirements. Because the effects of dipole fringe fields (which are not normally considered in the tracking runs) are very minor, they were ignored in subsequent tracking of the HER.

The effects of including the various error groups are illustrated for the HER (both on- and off-energy) in Fig. 4-34. We see that each of the error groups applied separately (misalignments and roll errors, multipole errors, quadrupole and sextupole strength errors combined with multipole errors) gives qualitatively the same reduction in dynamic aperture. The degradation compared with the bare lattice is small in every case. In Fig. 4-35 we show the results of combining all the lattice errors (for three random seeds). In all cases, the resulting dynamic aperture is quite adequate for injection, exceeding our goal of $10\sigma_y$ (fully coupled). The results in Fig. 4-35 correspond to a lattice having a sufficiently well-corrected orbit that no compensation for beta function mismatch, x-y coupling, or residual dispersion is required to obtain a large dynamic aperture.

LER Tracking. The dynamic aperture for the LER bare lattice, plotted at the injection point, is shown in Fig. 4-36. Both on-energy and off-energy ($10\sigma_E$ deviation) particles

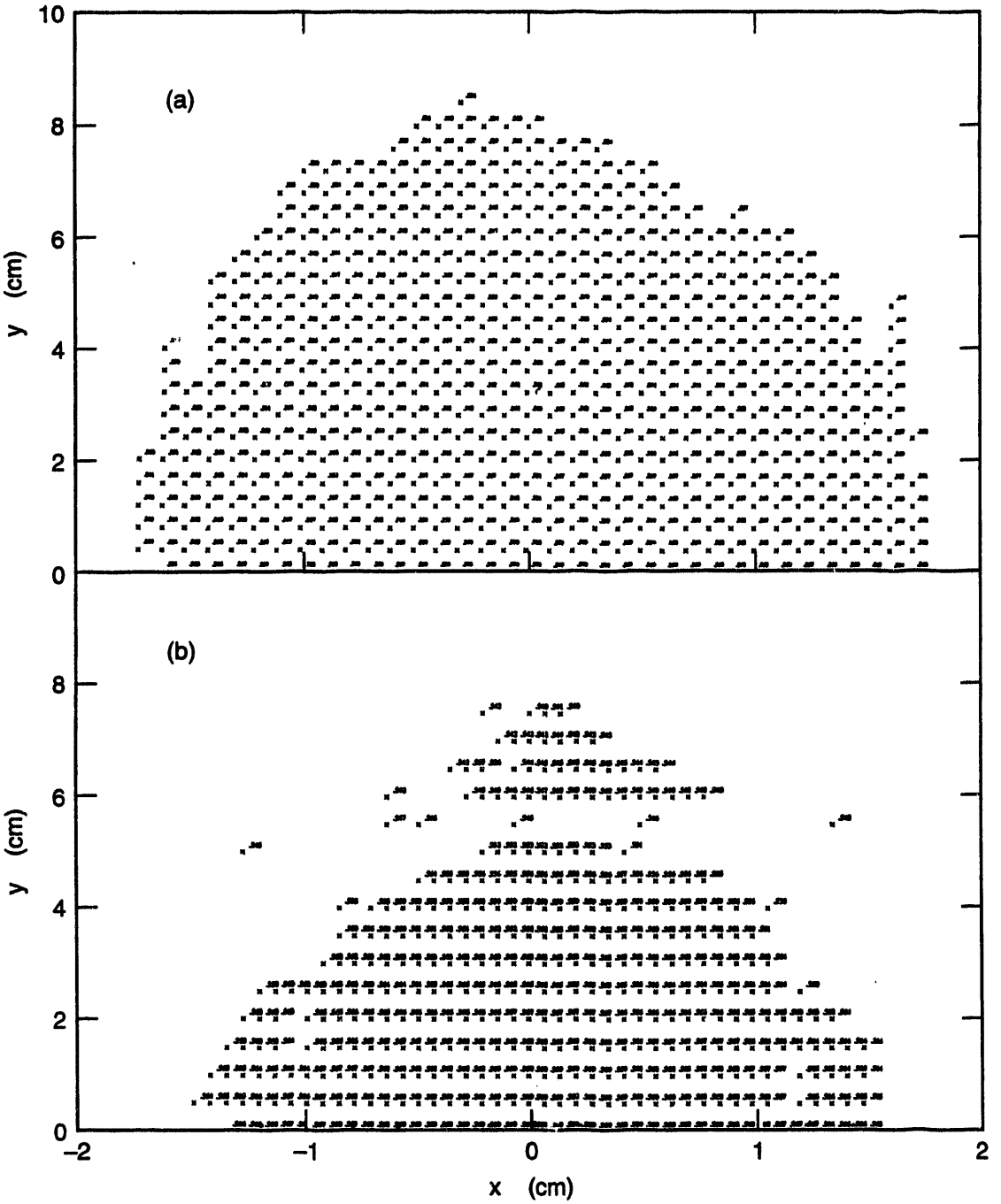

Fig. 4-29. Dynamic aperture of the HER bare lattice for on-energy (a) and off-energy cases. The amplitudes are plotted at the injection point, corresponding to β_x = 20 m and β_y = 215 m. The points denote particles launched at that amplitude that survived for 1,024 turns.

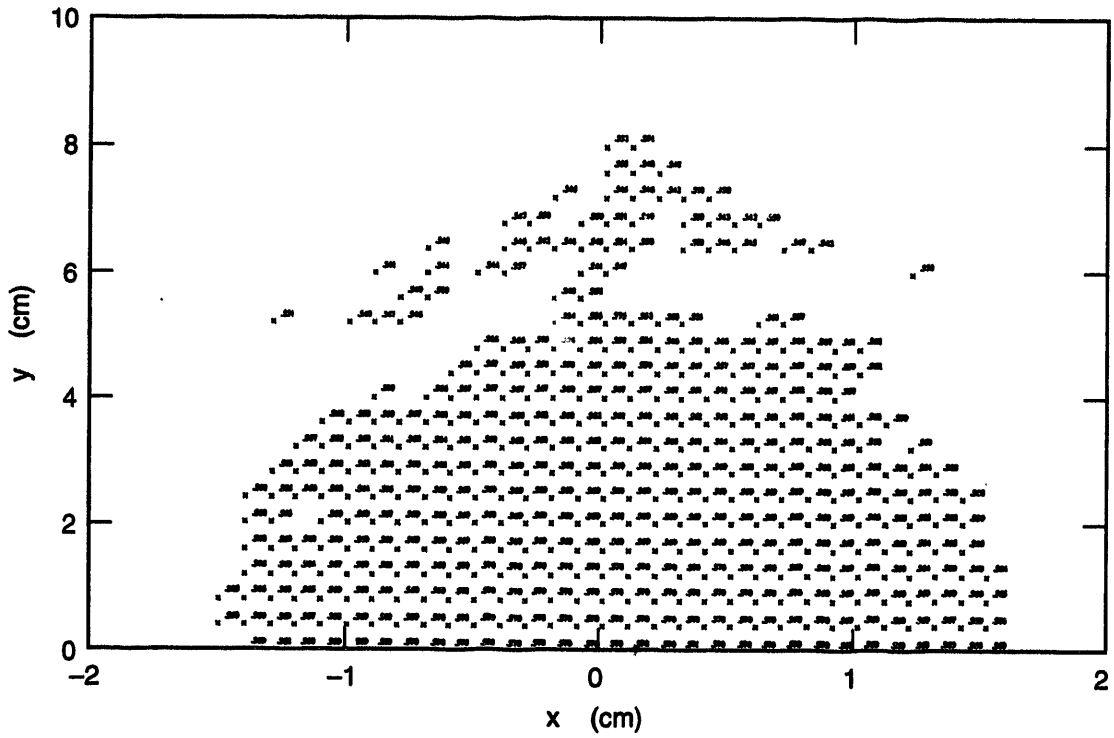

Fig. 4-30. Off-energy dynamic aperture at the injection point for the HER bare lattice, including the effects of radiation damping and quantum excitation. The points denote particles launched at that amplitude that survived for 4,096 turns.

were tracked for 1,024 turns and the fractional horizontal tune values of surviving particles are indicated. The off-energy results (Fig. 4-36b) are projected into the tune plane in Fig. 4.-37. We see a tune footprint that is very similar to that of the HER (cf. Fig. 4-31).

Dynamic aperture results for the off-energy LER lattice, including the effects of parasitic beam-beam collisions and fringe fields, are presented in Fig. 4-38. As for the HER (Fig. 4-33), we find no significant effects from the inclusion of dipole fringe fields in the tracking. The influence of the parasitic beam-beam collisions for the LER is more visible than was the case for the HER, but it is not of consequence.

Figure 4-39 shows the results of LER tracking, both on- and off-energy, with all errors for three random seeds. These results demonstrate that with a well-corrected orbit there is adequate dynamic aperture for injection, even for particles with an energy deviation of $10\sigma_E$. Present tracking results indicate that the vertical dynamic aperture is sensitive to systematic errors in the Q1 quadrupoles (closest to the IP). This is due to the off-axis beam orbit in these magnets, which gives rise to significant feed-down terms from the higher multipoles. Thus, it will be important to construct the Q1 magnets to limit the systematic multipole contributions to the levels specified in Table 4-12. In Fig. 4-40 we replot the data from Fig. 4-39 in terms of invariant amplitudes (corrected by

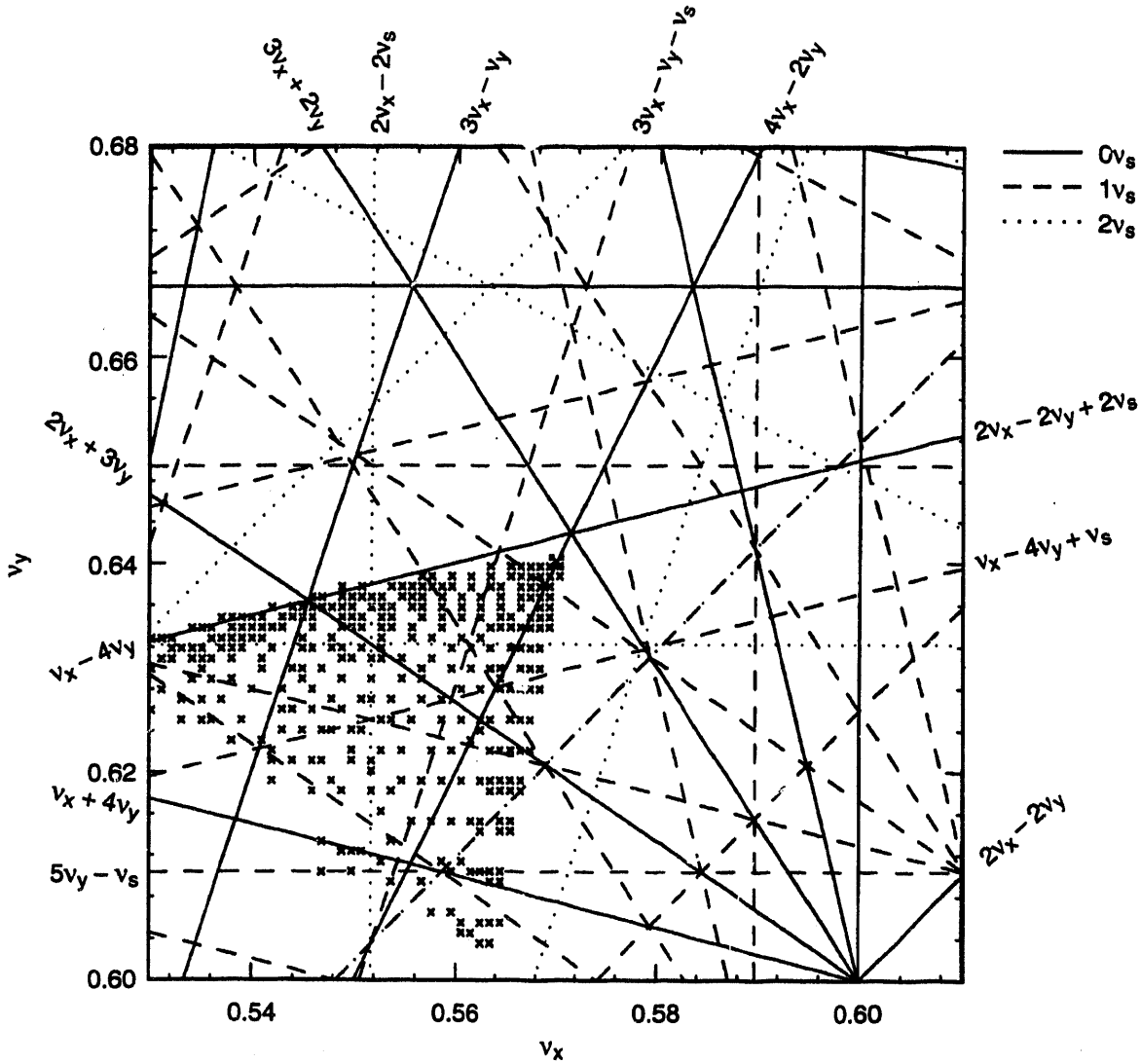

Fig. 4-31. HER on-energy tracking results from Fig. 4-29a projected into tune space. Low-order betatron (solid) and synchrobetatron (dashed and dotted) resonance lines are indicated.

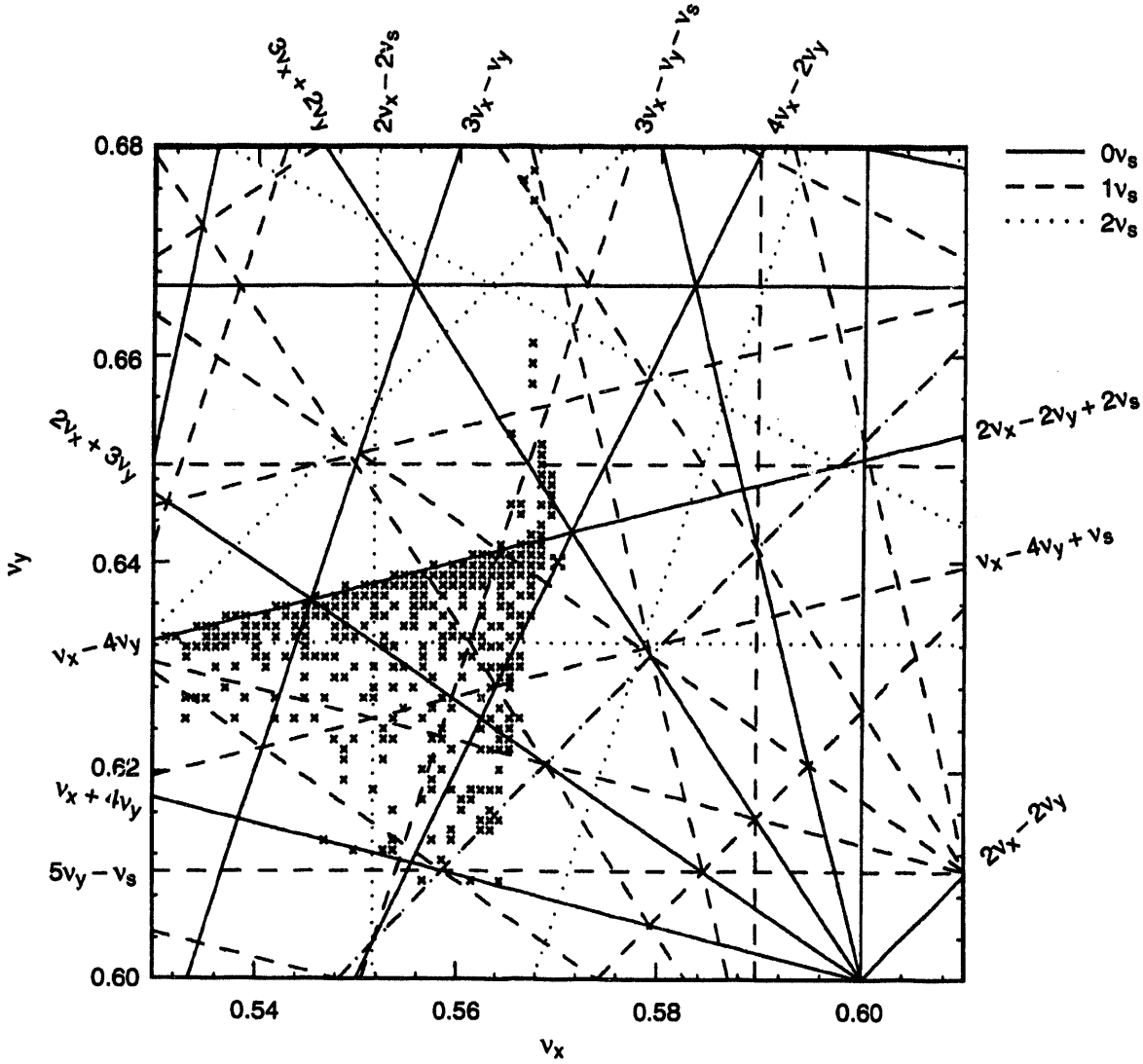

Fig. 4-32. Projection into tune space of HER on-energy tracking results including the effects of the parasitic beam-beam collisions. The tune footprint for large-amplitude particles is distorted compared with that in Fig. 4-31 due to the amplitude-dependent tune shift from the parasitic crossings.

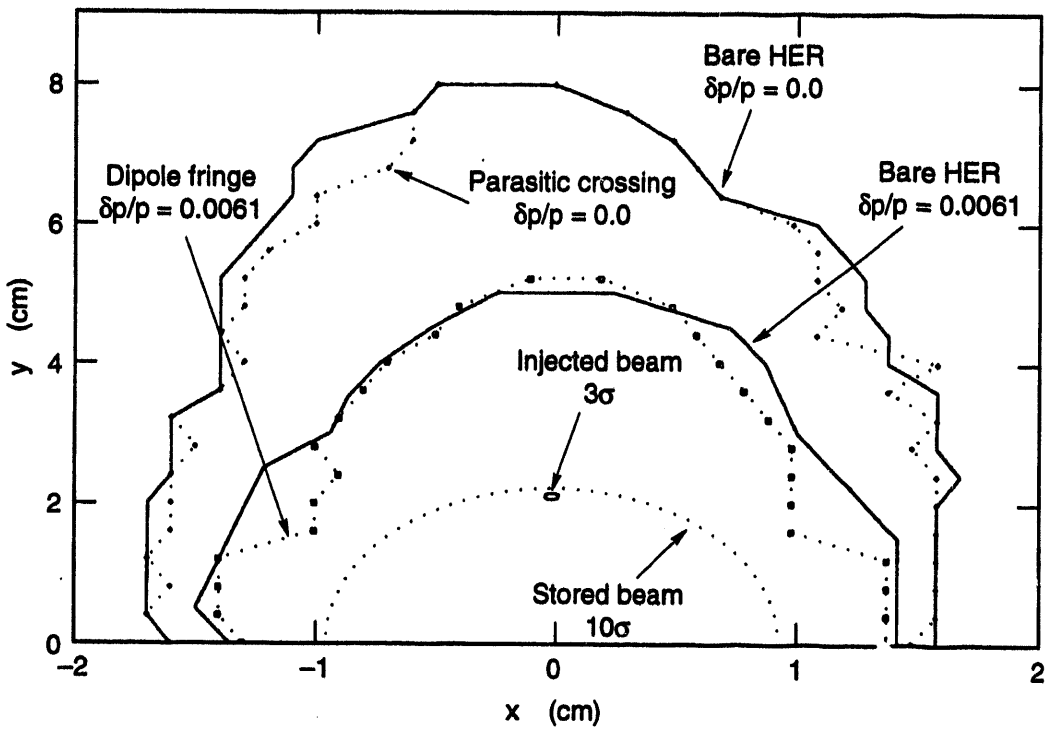

Fig. 4-33. HER bare lattice dynamic aperture at the injection point showing the effects of the parasitic crossings for the on-energy case and the effects of including dipole fringing fields for the off-energy case. Tracking was done for 1,024 turns.

a fourth-order, normal-form analysis). In this presentation, distortions associated with the nonlinearities (changes in beta functions, for example) are eliminated and the dynamical behavior of the various errors sets can be compared on an equal footing.

Tracking Summary. To summarize our present results, we find that the HER and LER lattices considered here have adequate dynamic aperture (greater than 10σ with a $10\sigma_E$ energy deviation) for both injection and stored-beam lifetime. Further work to optimize the chromatic behavior of the rings is now under way.

4.1.3.5 Influence of the Detector Solenoid on the Orbit. The constraints of an asymmetric high-luminosity *B* factory—unequal beam energies and small bunch spacing—imply that both beams cannot be aligned along the magnetic axis of the detector solenoid. Therefore, when the detector solenoid is energized, at least one beam will experience magnetic forces that change its trajectory vertically and horizontally from the nominal (solenoid-off) trajectory. In the case of PEP-II, the beams are separated in the horizontal plane, so the effect of the detector solenoidal field is primarily to shift the beam orbits vertically. We assume a solenoidal field strength of 1 T over a distance of ±2 m around the IP. However, the fringe field of the solenoid has been included when calculating the effect of the detector field on the beam orbits, as this has a significant influence on the results. For the case under study, a magnetic field map was generated

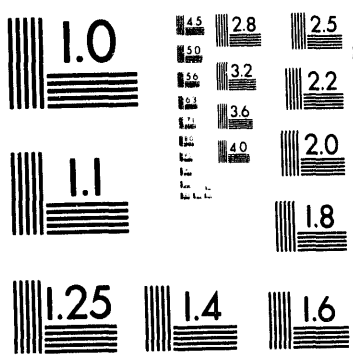
1.0
1.1
1.25
1.4
1.6
1.8
2.0
2.2
2.5
2.8
3.2
3.6
4.0
4.5
5.0
5.6

2 of 7

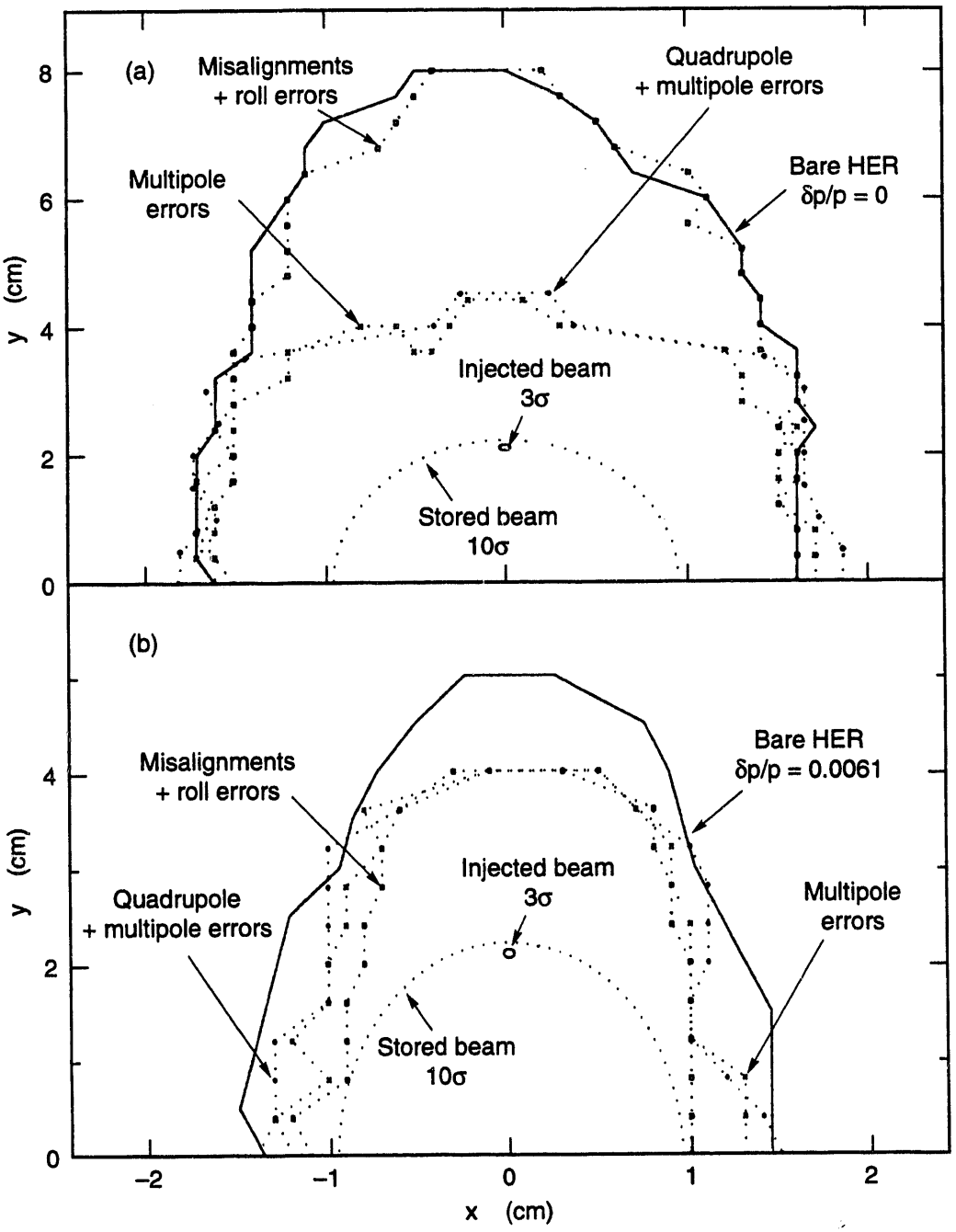

Fig. 4-34. HER dynamic aperture at the injection point (tracked for 1,024 turns), for (a) on-energy and (b) off-energy cases, showing the effects of various combinations of lattice imperfections. Set 1 corresponds to adding only misalignments and roll errors, Set 2 corresponds to only magnetic multipole errors, and Set 3 is the result of combining the multipole errors with strength errors for both quadrupoles and sextupoles.

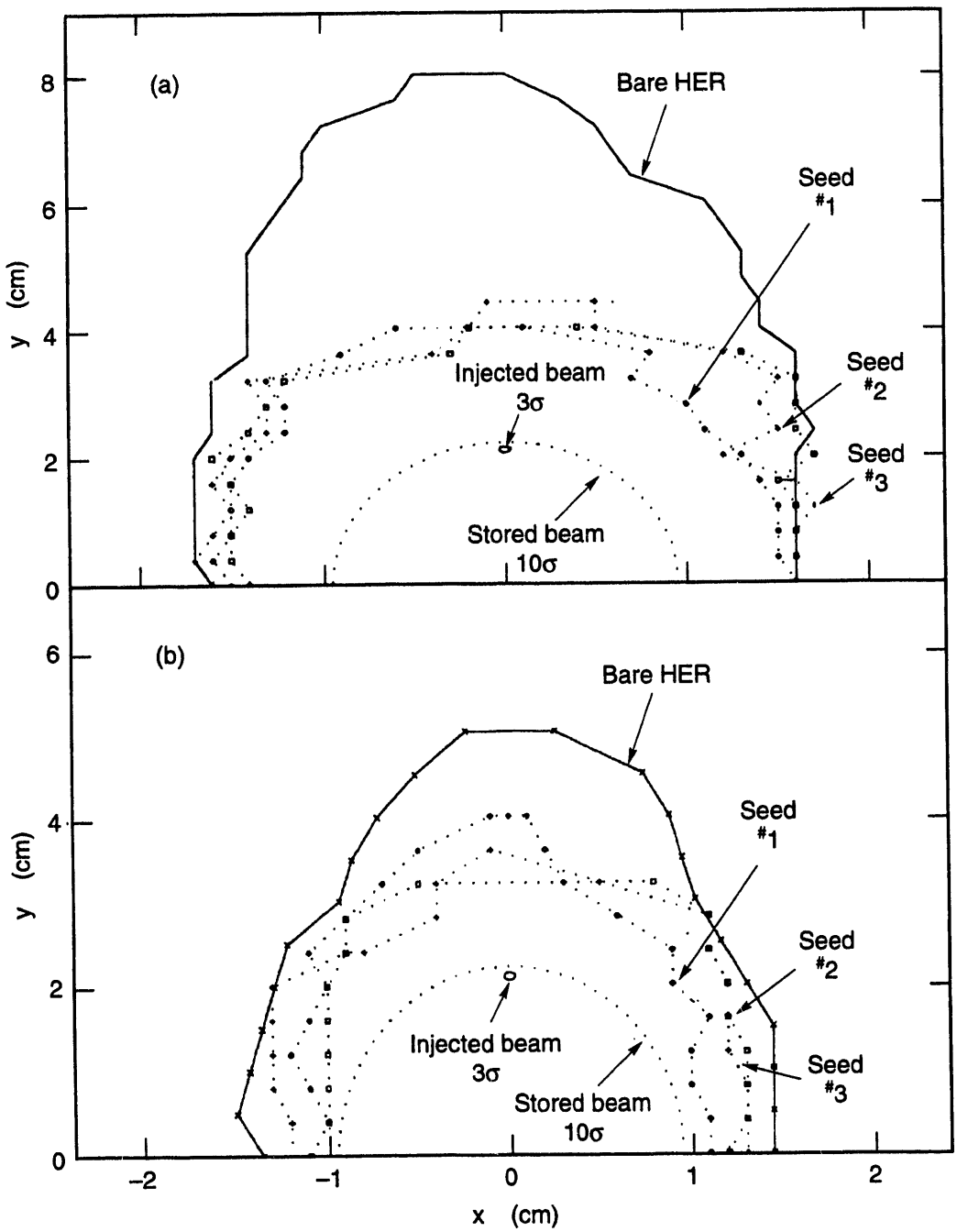

Fig. 4-35. HER dynamic aperture at the injection point (tracked for 1,024 turns), for (a) on-energy and (b) off-energy cases, including the combined effects of all lattice errors (with three random seeds). The 10σ boundary required for injection is indicated.

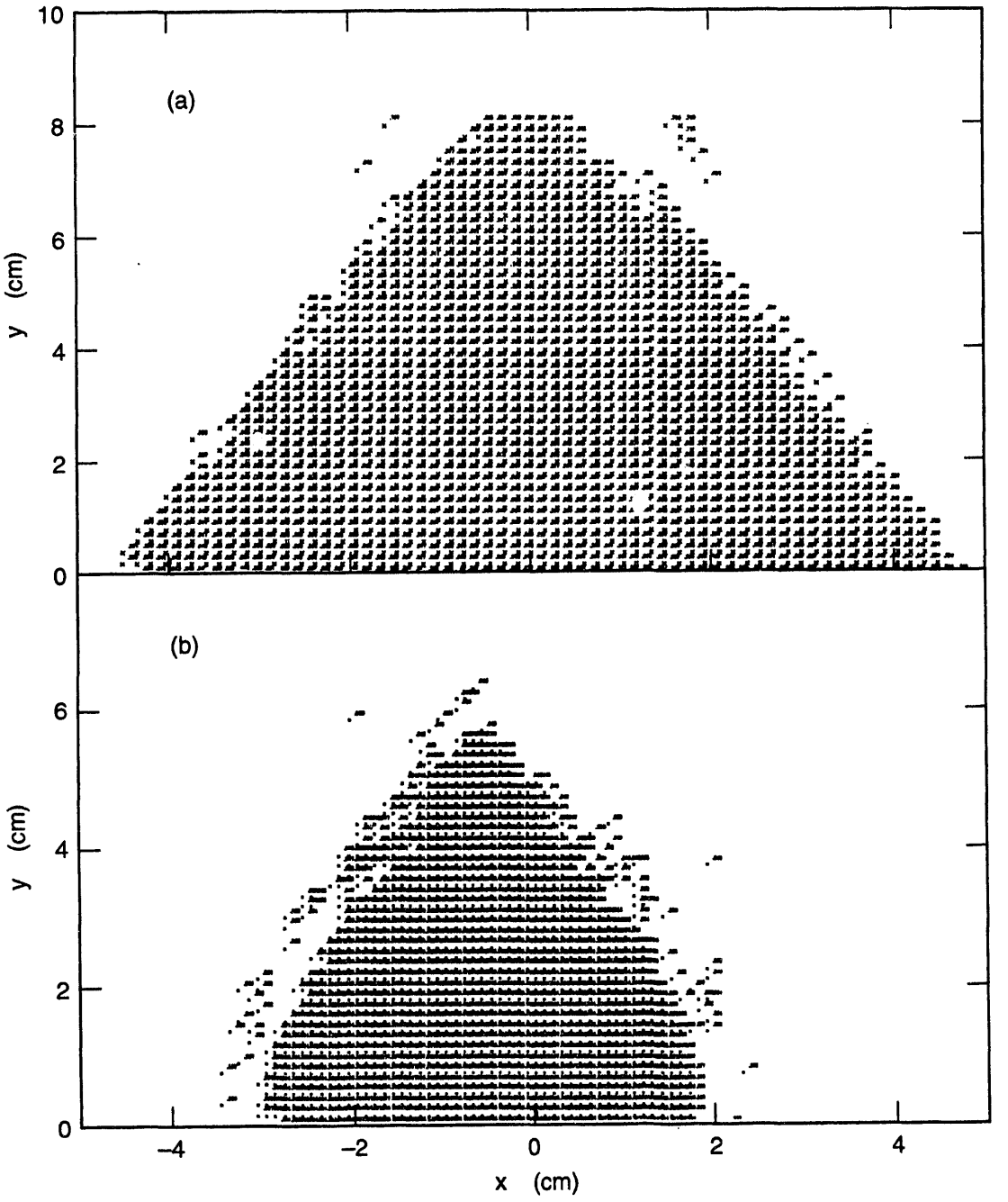

Fig. 4-36. Dynamic aperture of the LER bare lattice for (a) on-energy and (b) off-energy cases. The amplitudes are plotted at the injection point, corresponding to β_x = 40 m and β_y = 170 m. The points denote particles launched at that amplitude that survived for 1,024 turns.

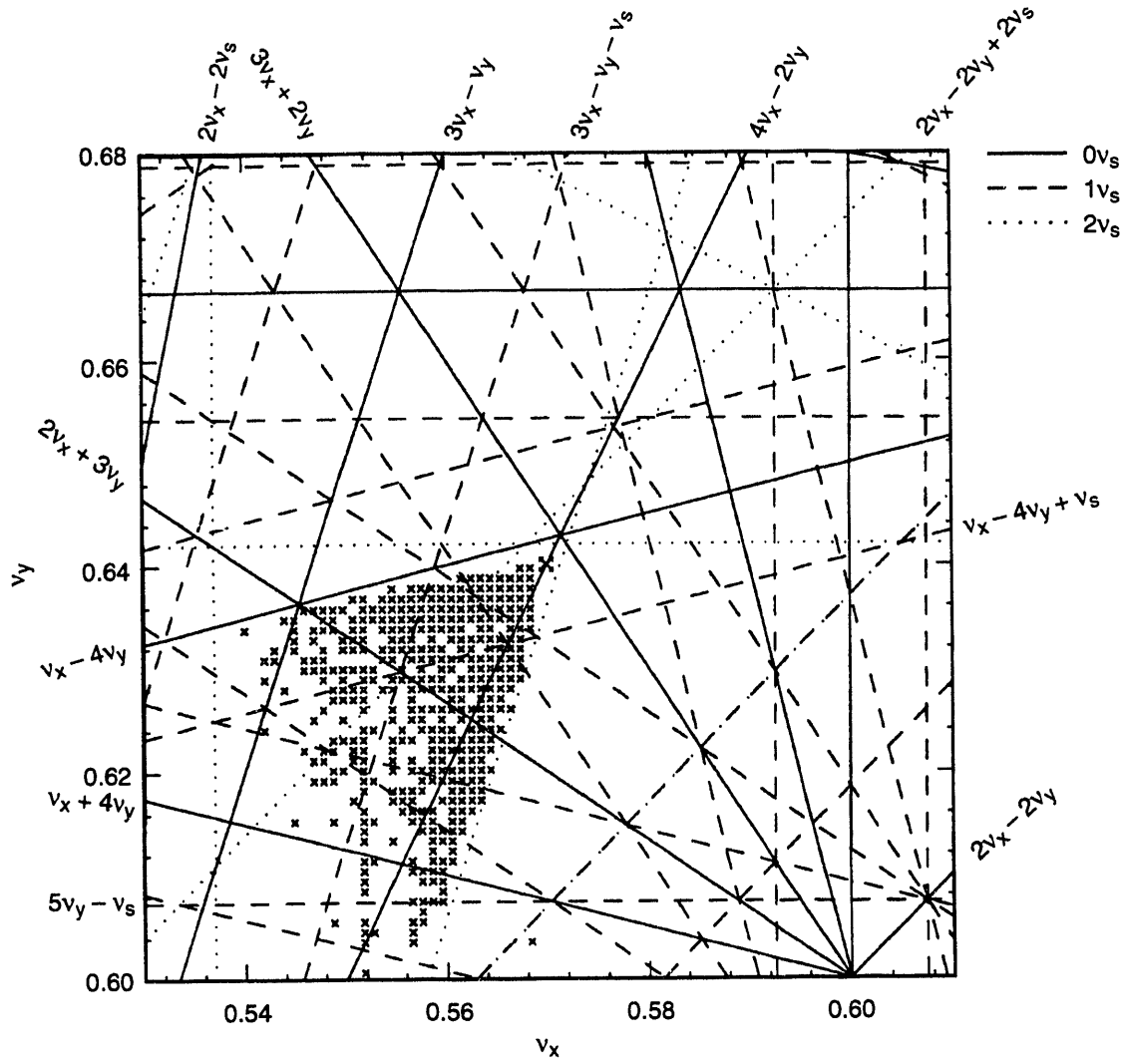

Fig. 4-37. LER off-energy tracking results from Fig. 4-36b projected into tune space. Low-order betatron (solid) and synchrobetatron (dashed and dotted) resonance lines are indicated.

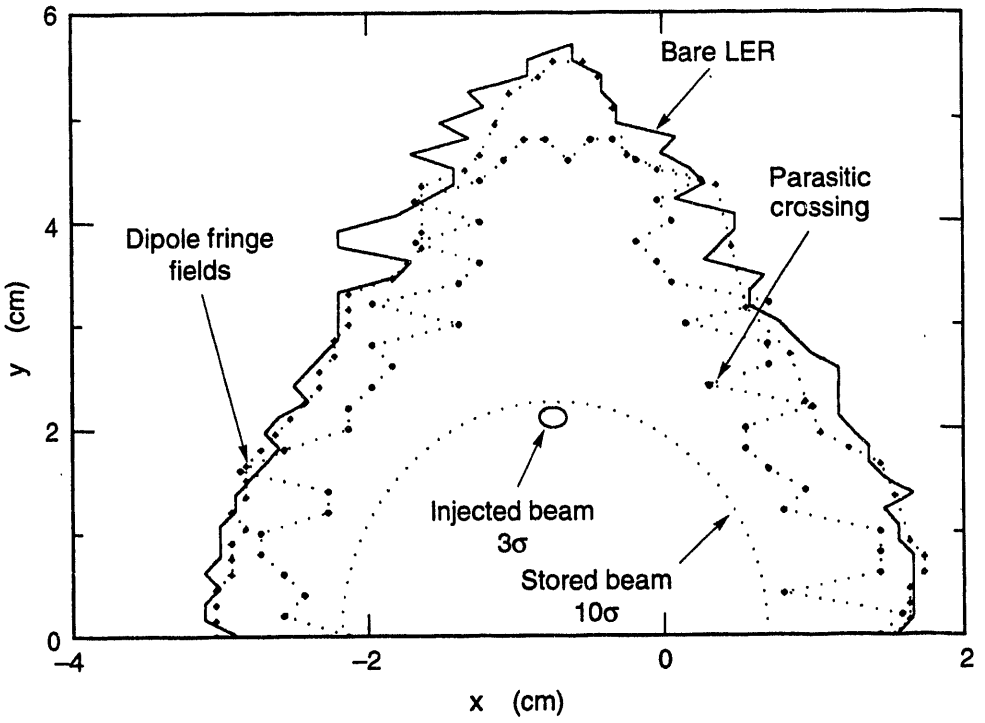

Fig. 4-38. LER bare lattice dynamic aperture at the injection point showing the effects of the parasitic crossings and the effects of including dipole fringing fields for the off-energy case. Tracking was done for 1,024 turns. The 10σ boundary required for injection is indicated.

for a representative PEP-II detector configuration using the program POISSON. The resultant longitudinal component of the field along the solenoid axis is shown in Fig. 4-41. Expansion formulas for both the radial and longitudinal components of the solenoidal field [Glaser, 1956] were used to calculate the magnetic field along the beam trajectories.

To minimize the orbit deviations, the angle of the detector solenoid with respect to the collision axis of the beams is treated as a free parameter. In addition, by differentially powering the trim coil of the Q1 permanent magnet we can add a small dipole field to the quadrupole field, thereby using the trim coil to steer the beams. A 1-mm displacement of the magnetic center of the quadrupole requires a superimposed dipole field of 0.011 T, about 40% of the design value for the Q1 trim coils (see Section 5.1.3.3). Once beyond the Q1 magnet, the two beams enter separate magnetic channels. We allow for ±2 mm of transverse motion of the Q2 and Q4 magnets for further beam steering. The transverse displacement of the magnetic center of these magnets could be achieved either mechanically (by physically moving the magnets) or electrically (by adding trim coils to the magnets); both alternatives are under study.

Because it is easier to resteer the low-energy beam than the high-energy beam, we want the tilt of the solenoid axis with respect to the collision axis to be roughly aligned with the 11.2-mrad entrance and exit angles of the high-energy beam. This minimizes the

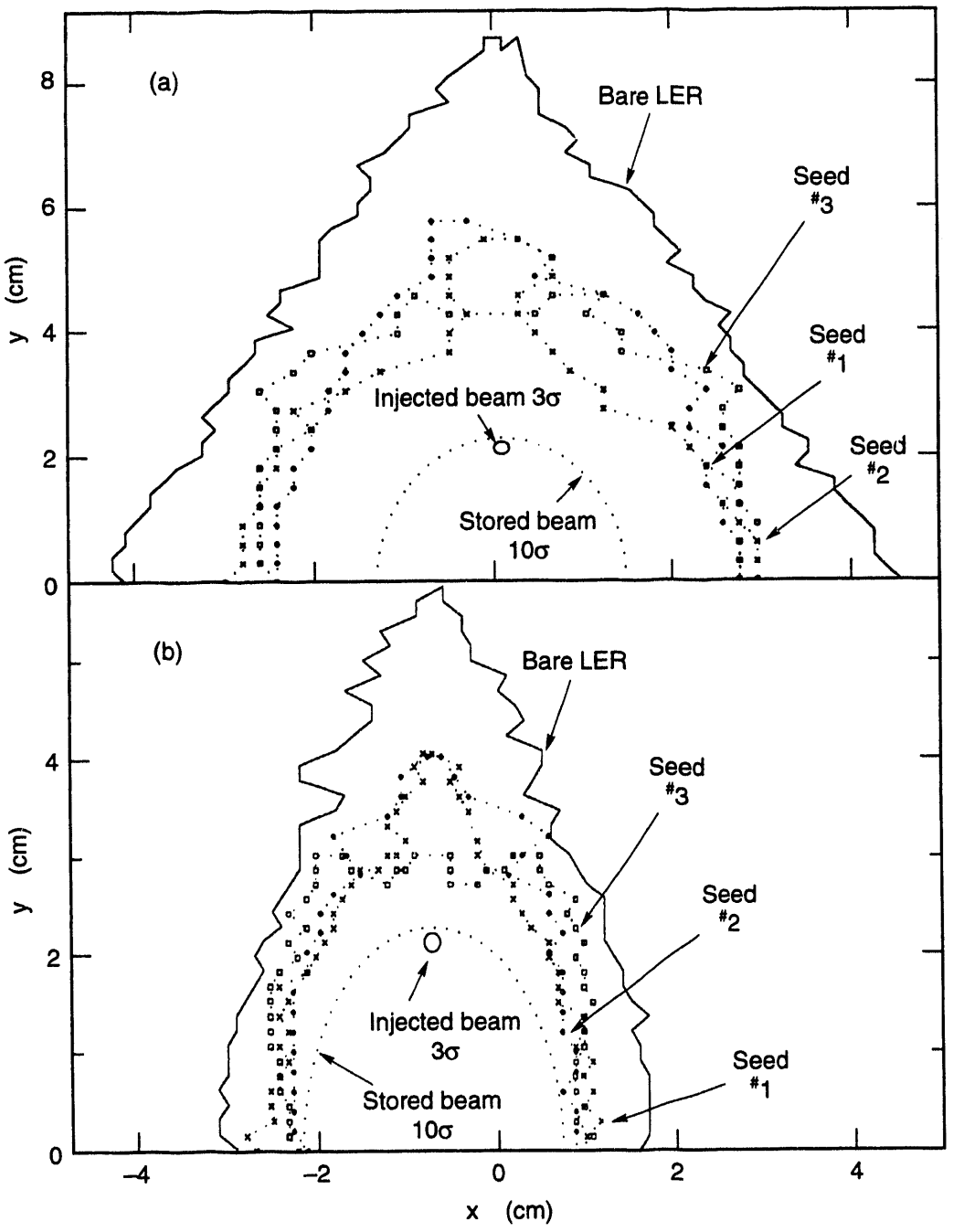

Fig. 4-39. LER dynamic aperture at the injection point (tracked for 1,024 turns), for (a) on-energy and (b) off-energy cases, including the combined effects of all lattice errors (with three random seeds). The 10σ boundary required for injection is indicated.

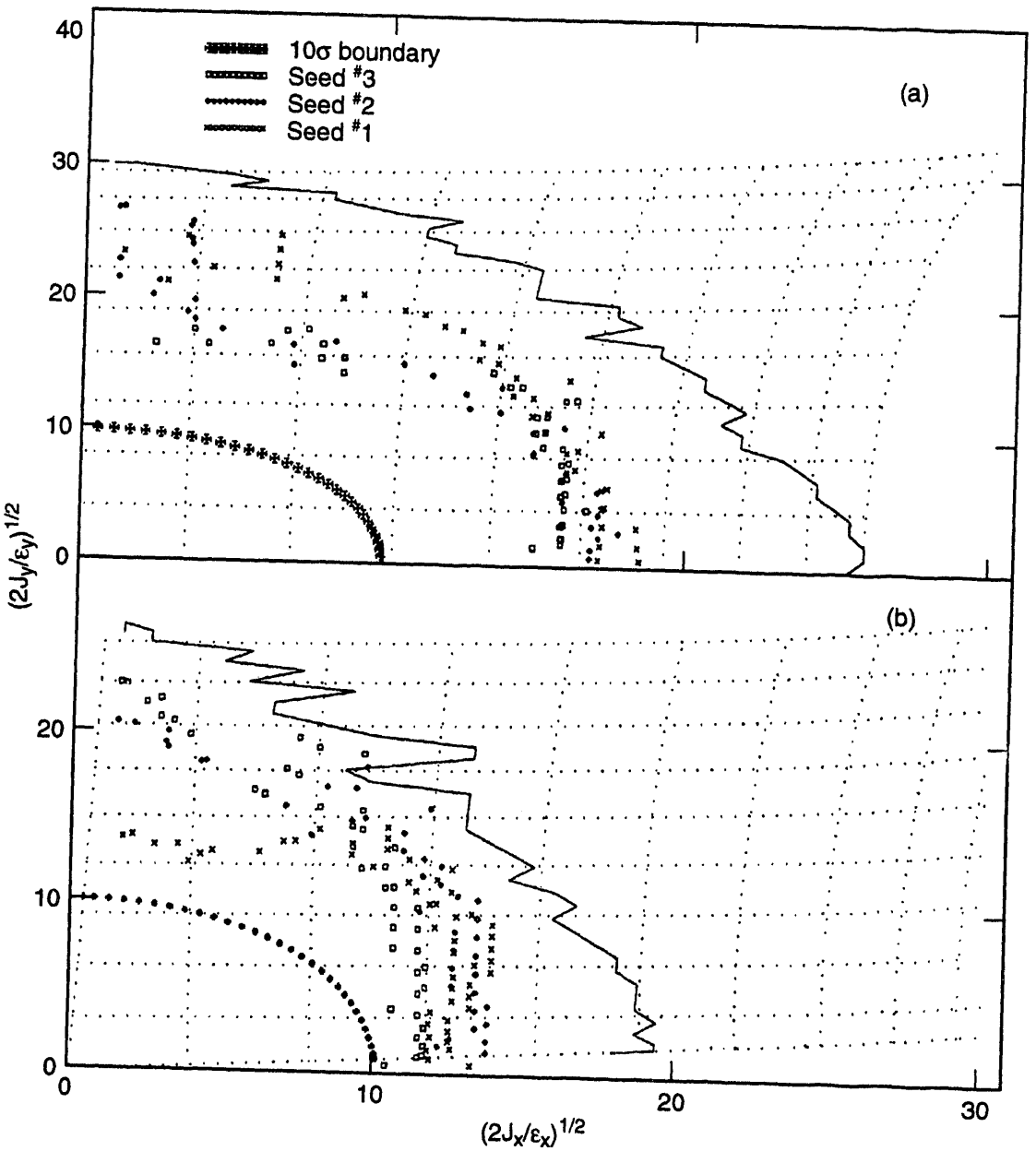

Fig. 4-40. LER dynamic aperture at the injection point (tracked for 1,024 turns), for (a) on-energy and (b) off-energy cases, including the combined effects of all lattice errors (with three random seeds). These results are the same as those shown in Fig. 4-39, but plotted as invariant amplitudes determined by a fourth-order, normal-form analysis. The 10σ boundary required for injection is indicated. Dotted lines indicate the mapping of the coordinate-space grid from Fig. 4-39.

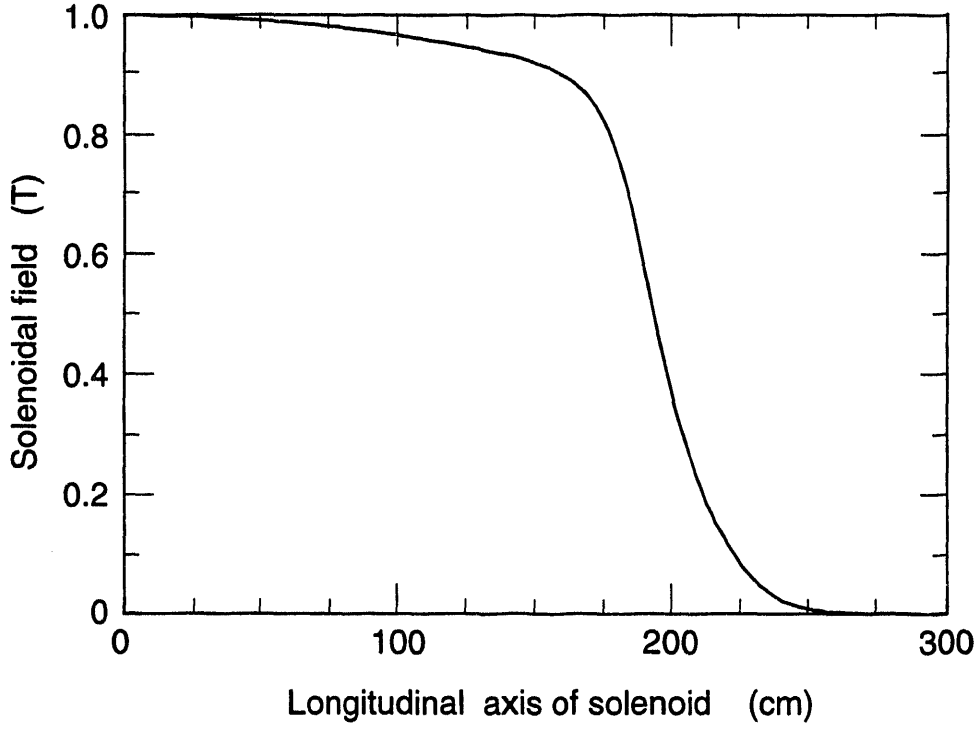

Fig. 4-41. Plot of the solenoidal magnetic field along the longitudinal axis of the detector solenoid.

effect of the solenoid on the stiffer beam. After investigating a range of solenoid tilt angles between 5 and 25 mrad, an angle of 15 mrad was chosen. Figure 4-42 shows the two beamlines and the detector solenoid field orientation. Figure 4-43 shows the effect of the solenoid field on the vertical beam trajectories when no orbit compensation is used. Displacing the magnetic center of the Q1 magnet downward by 0.8 mm and raising the magnetic centers of Q2 and Q4 by 1.4 mm and 0.5 mm, respectively, results in vertical and horizontal beam orbits that deviate by less than 1.5 mm from the nominal (solenoid-off) location, as indicated in Figs. 4-44 and 4-45, respectively. We know that such orbit deviations are acceptable in terms of detector background, because only minor changes in the calculated backgrounds resulted from magnet misalignments of about this magnitude (see Section 4.2.1.6). It should be noted that the above solution represents a fairly broad optimum—changes in tilt angle of ±3 mrad and deviations of ±0.2 mm in the quadrupole magnetic centers do not significantly alter the beam orbits.

4.1.3.6 Compensation of the Optical Effects of the Detector Solenoid. As the effect of the solenoid on the beam scales with the beam energy, we expect the LER optics to be much more affected than the HER optics. A quick comparison between the solenoid field normalized to the LER energy, 1.22 T·m/GeV, and the strongest solenoid (ALEPH) in LEP normalized to its injection energy, 0.5 T·m/GeV, shows that the expected effect on the LER optics is considerably stronger than at LEP. (For LEP, the maximum tilt of the normal modes with respect to the horizontal and vertical axes is about 4° after perfect

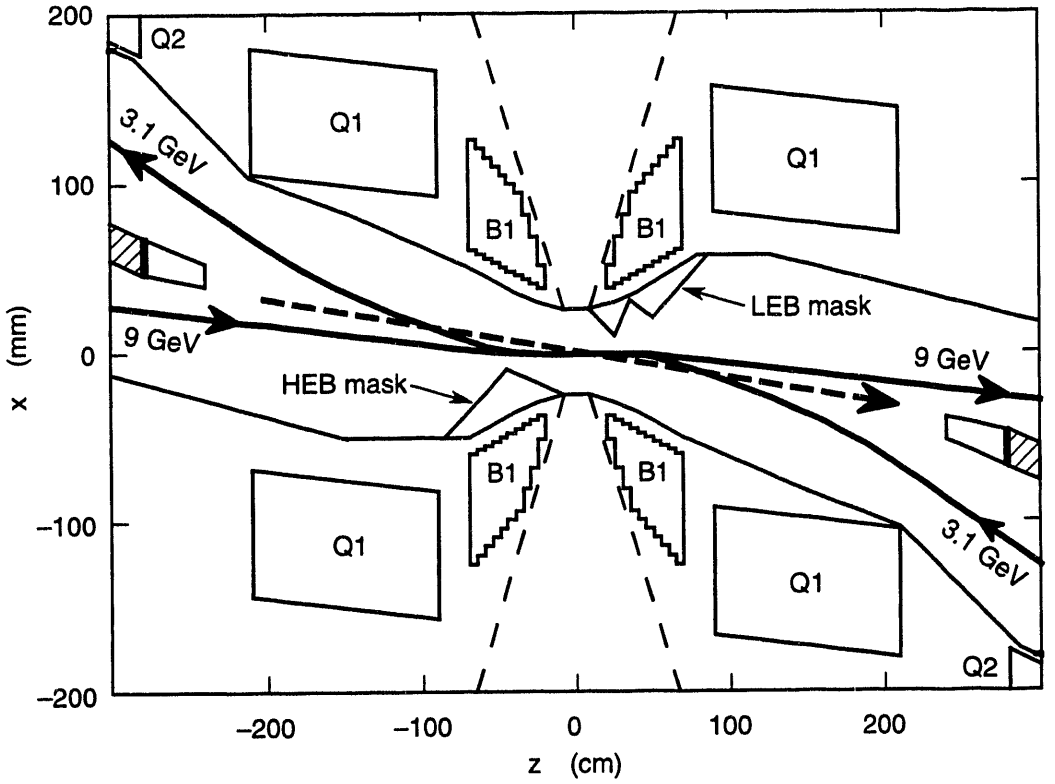

Fig. 4-42. Plan view of the beamlines. The orientation of the detector solenoid axis is indicated by the thick dashed line. The detector solenoid is tilted by 15 mrad with respect to the collision axis.

compensation.) It turns out that the first LER quadrupole, which is located inside the PEP-II detector solenoid, changes the phase advance such that the ends of the solenoid tend to partially compensate the optical effect of the center.

Because a 4×4 symplectic matrix can be generated by a quadratic Hamiltonian in two degrees of freedom, we require ten adjustable parameters to match the transverse optics. In other words, with ten "knobs" we can restore a coupled, mismatched matrix to its original form. These ten knobs are identified with four skew quadrupoles and six normal quadrupoles on each side of the IP. Because the detector solenoid is tilted with respect to the horizontal axis, a residual vertical dispersion must also be compensated, which requires a total of six (rather than four) skew quadrupoles on each side of the IP. Additionally, two pairs of normal quadrupoles are needed to restore the horizontal dispersion.

Evaluation of the transfer matrix was done with special attention to the details of the PEP-II design:

- The solenoid axis is tilted by 15 mrad horizontally with respect to the collision axis
- At the entrance and exit of the solenoid, the beam will sense longitudinal and transverse nonlinear fields (which have been evaluated from the longitudinal field distribution shown in Fig. 4-41)

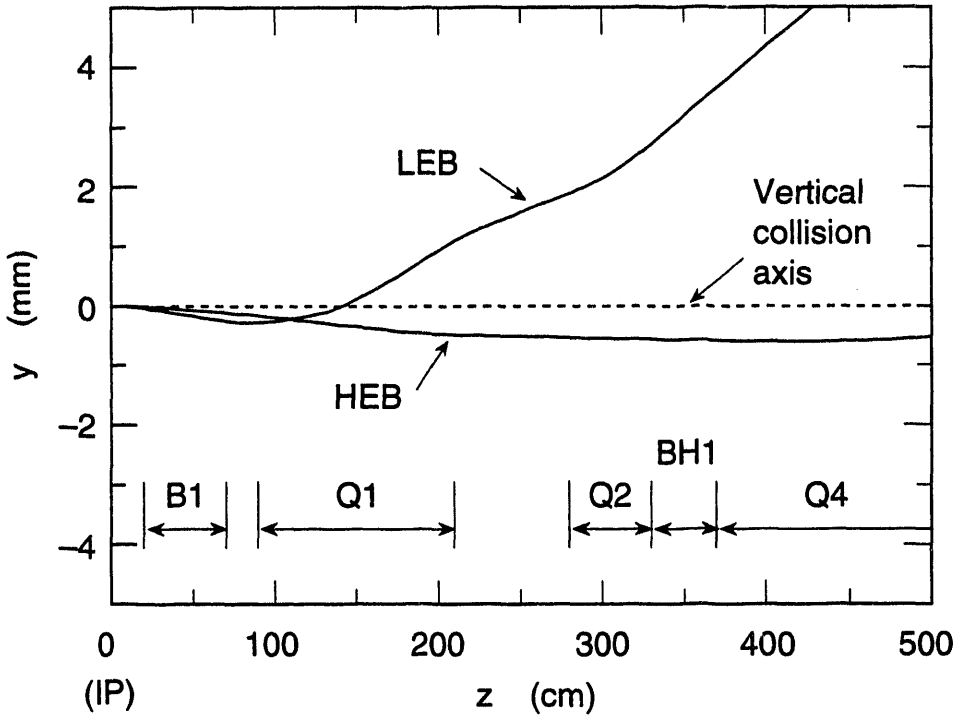

Fig. 4-43. Vertical orbit deviations of the low- and high-energy beams in the presence of the detector solenoidal field with no orbit compensation.

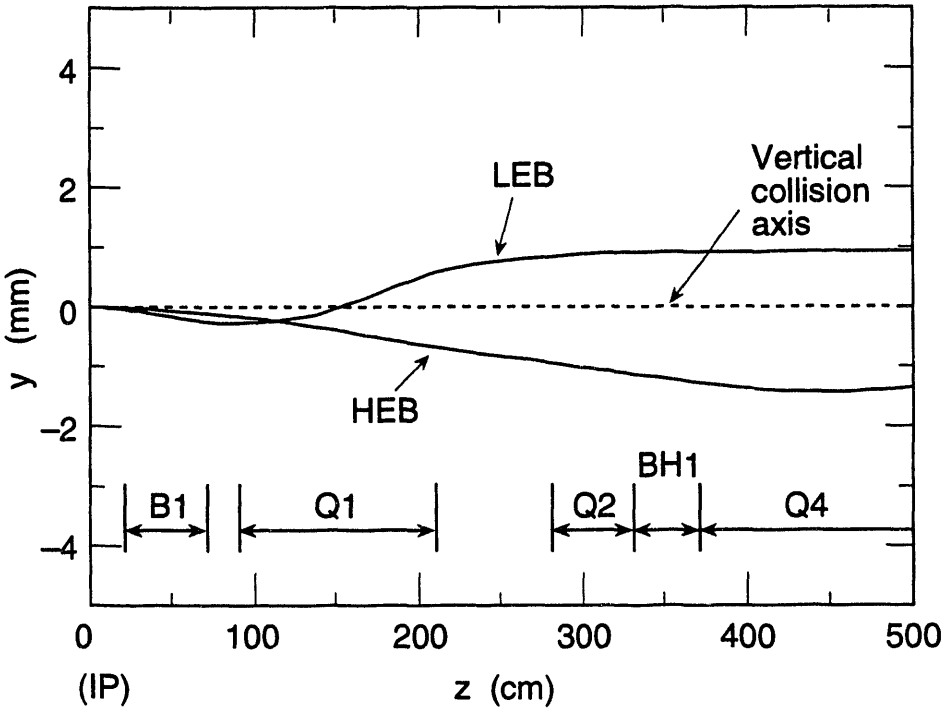

Fig. 4-44. Vertical orbit deviations of the low- and high-energy beams in the presence of the detector solenoidal field with vertical displacements of the magnetic centers of Q1, Q2, and Q4 by –0.8 mm, 1.4 mm, and 0.5 mm, respectively.

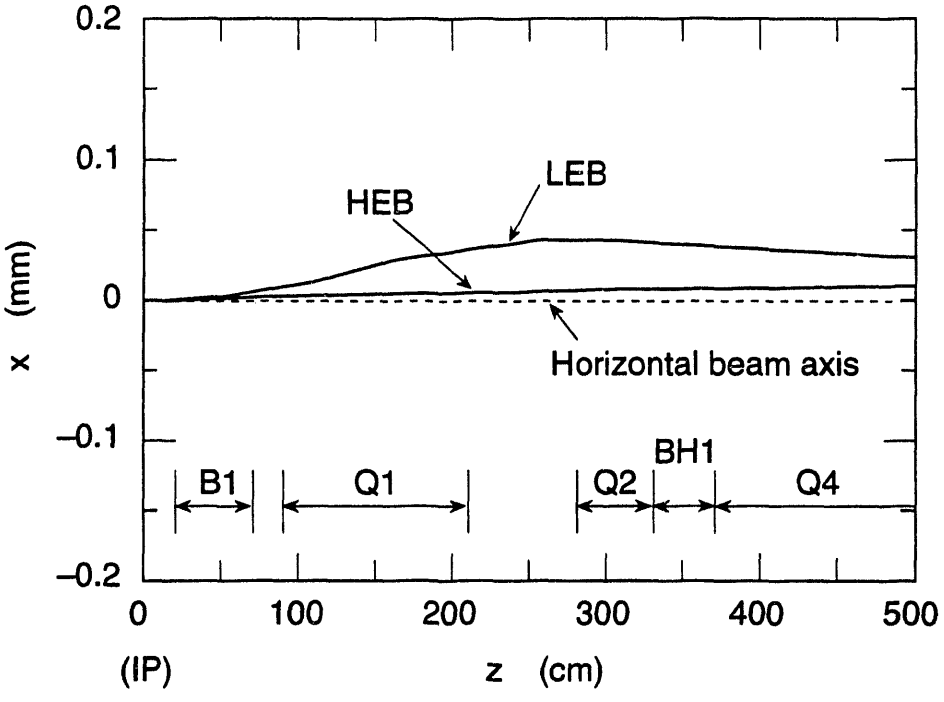

Fig. 4-45. Horizontal orbit deviations of the low- and high-energy beams in the presence of the detector solenoidal field with the same displacements of Q1, Q2, and Q4 used in Fig. 4-44.

- Some quadrupoles and bending magnets are located inside the detector; their fields are superimposed on the magnetic field of the solenoid

The six-dimensional transfer matrix from the IP to the end of the solenoid fringe field has been evaluated by integrating Hamilton's equations using a fourth-order Runge-Kutta method. This linear transfer map was then inserted into the lattice, and the optics code MAD was used to rematch the transfer matrix from the IP to the beginning of the arc to its form without the solenoid. Four skew quadrupoles have been placed at locations of independent phases, $\mu_x \pm \mu_y$, as is suggested by Hamiltonian perturbation theory. The remaining 2 skew quadrupoles are placed at locations with vertical dispersion. For both the LER and the HER, these magnet locations were varied until an optimal solution was achieved. The maximum integrated strength of the tilted quadrupoles is about 10% of the integrated strength of a normal quadrupole. After compensation, the maximum tilt of the normal modes in the LER is less than 5°.

4.1.4 Energy Tunability

Because the IR optics are based on permanent magnet technology and are thus not easily adjustable, some care must be taken to ensure suitable optics flexibility.

The majority of running at PEP-II will be at the Υ(4S) resonance. This is where the *CP* violation physics is done; the remaining physics topics, except for the Υ resonance and B_s mixing studies, are also best done at the Υ(4S). It may nevertheless be desirable to

intersperse short runs (1–3 months) at other resonances, such as the Υ(2S), Υ(3S), and Υ(5S) (see Fig. 2-1). For such studies, these short runs will generate enormous increases (factors in excess of 100; see Table 2-1) over the size of data-sets currently available. In addition to a short run at the Υ(5S), a longer dedicated run (on the order of 30 fb^{-1}) will be needed for studies of B_s mixing; for this, it may well be prudent to reoptimize the IR region, increasing the machine asymmetry and reducing the radius of the first layer of the silicon vertex detector. This experiment is not foreseen early in the program; it will commence after a comprehensive *CP* violation program has been established.

PEP-II has been designed to accommodate this program. The collision energy is tunable over the full range of desired energies. The strategy for covering this range is to change both the electron and positron beam energies such that the angle between the two beams as they exit the B1 magnet is held constant. The maximum change in the energy of the low-energy beam (LEB) is less than 3% relative to the nominal Υ(4S) case. Because this change is within the range of the trim coils of the QD1 magnet, QD1 can track the LEB energy (thereby ensuring proper focusing). The high-energy beam is focused primarily by the QD4 and QF5 electromagnets so it is easy to maintain proper focusing for it. The collision angle at the IP is adjusted to keep deviations from the nominal trajectory of each beam to less than 0.5 mm out to a distance of 5 m. We have assured ourselves that the beam trajectories in this case—as at higher center-of-mass energies—remain within our conservatively defined stay-clear region of $15\sigma + 2$ mm.

PEP-II has been designed to deliver a luminosity of 3×10^{33} cm^{-2} s^{-1} at the Υ(4S). It is, of course, desirable to maintain this maximum luminosity for the short Υ-physics runs; by the very nature of the large increase in statistics these runs will bring, however, moderate reductions in machine luminosity pose no problems.

The luminosity of PEP-II at different center-of-mass energies can be derived in a straightforward way from the scaling of a single-ring circular collider. In going from the Υ(4S) to the Υ(5S), the beam energies must be raised by 2.4%. In a conventional electron-positron collider, most of the RF power is devoted to producing the cavity voltage at the design energy. Above this energy, the voltage required is proportional to the synchrotron radiation loss (the well-known γ^4 law), so the cavity dissipation scales as γ^8. Since the tune shift is proportional to γ, the luminosity scales as γ^7. In the case of PEP-II, the cavity wall losses are less than one-third of the total power; the existing spare capacity can therefore be used to keep the luminosity approximately constant up to the Υ(5S).

In the regime below the nominal energy, and with fixed optics, the beam dimensions are proportional to γ. (In this regime, the RF power needed to restore synchrotron radiation is always less than at the design energy.) The current per beam is then limited by the beam-beam tune shift equation, scaling as γ^3. The luminosity then scales as γ^4. In PEP-II, as in most modern storage rings, the emittance can be optimized by using wigglers or dispersion mismatching. In this case, it is possible to keep the beam dimensions constant as the energy varies. Under these conditions, the luminosity varies as γ^2, giving a 25% reduction in luminosity at the Υ(1S) and correspondingly lower reductions at the Υ(2S) and Υ(3S).

4.2 ESTIMATION OF DETECTOR BACKGROUNDS

The problem of machine-related backgrounds is one of the leading challenges in the PEP-II project: The detector must be sufficiently well protected to prevent either excessive component occupancies or deterioration from radiation damage. In effect, what is required is to achieve background rates similar to those of existing colliders, but at beam currents an order of magnitude higher. There are three primary sources of backgrounds:

- Synchrotron radiation photons produced in the machine magnetic elements
- Off-energy electrons and photons produced in bremsstrahlung interactions with background gas molecules
- Elastically (Coulomb) scattered, off-angle electrons produced in interactions with background gas molecules

These background sources can give rise to primary particles that can either enter the detector directly or generate secondary debris that ultimately reaches the detector.

We have carefully simulated, in great detail, the effects of these backgrounds. It is probably fair to say that the interaction of machine backgrounds and the detector environment has never been so exhaustively studied for any previous accelerator. This level of detail is mandatory in the case of a *B* factory design, because the consequences of underestimating the effects of the background are so serious. Thus, we view the considerations described in this section to be the sine qua non of the PEP-II design.

In what follows, we try to convey the breadth of the considerations and the level of detail that were incorporated in the simulations. Before delving into the details of the calculations, however, it is useful to provide an overview that describes the thrust of our approach to the machine optimization.

The attraction of head-on collisions and magnetic separation of the heteroenergetic beams was discussed in Chapter 3. As indicated there, we believe that this strategy provides the most conservative approach to achieving high luminosity in an asymmetric collider. Magnetic separation (as opposed to using a nonzero crossing angle) does come at a price, however. The separating elements (dipoles and quadrupoles) generate high levels of radiated power and consequently a large flux of synchrotron radiation photons. Two issues thus dominate the optimization of the interaction region (IR) optical design: controlling the resultant backgrounds and effectively managing the absorption of the power. Achieving these goals simultaneously is quite difficult. Indeed, we generated many attractive IR geometries that were ultimately rejected because one or both of these criteria could not be met.

It is also crucial to subject each promising design to the stringent test of a realistic engineering solution for the IR elements (magnets, masks, etc.). Both the limiting of backgrounds and the ability to engineer all the beamline elements in the IR must be demonstrated before the design can be deemed acceptable. We believe that what follows in this section (management of backgrounds) and the detailed engineering considerations for all the IR mechanical elements, covered in Sections 5.1.3 and 5.2.7, represent a robust and completely satisfactory solution.

Our design strategy was to choose the placement and apertures of the IR magnetic elements in such a way as to ensure that most (about 90%) of the radiated power produced close to the interaction point (IP) is absorbed on downstream surfaces far away from the detector. This is the key ingredient in the success of the design, because it ensures that local sources of secondary interactions are greatly limited. Our strategy requires a careful evaluation of all the material required for the machine elements and for their support, as well as a generous space allowance between the radiation fans and any such material. Realistic evaluations of the space required for the IR elements have been based on the detailed engineering designs discussed in Section 5.1.3; appropriate clearances, including an allowance for displacement of the beam orbit, have been incorporated. It has also proved important to provide a low gas pressure (below 1 nTorr) in the section of beam pipe in each ring that immediately precedes the IR.

In addition to paying attention to these engineering details, sufficient care must also be taken with the simulations of the absorption, scattering, and reemission of radiation incident on masks, beam pipe walls, magnets, etc. In our simulations, all primary sources (both electrons and photons) were propagated from their creation to the point where they are intercepted by a machine element. For charged particles, the effects of all magnetic elements were taken into account. The EGS electromagnetic shower simulation code [Nelson et al., 1985] was used to track the debris of the showers. This code includes the material properties appropriate to each intercepting element, the incidence angle and energy of the showering particle, and the geometry of the scatterer (particularly thin, sharp edges or "tips"). The shower process is followed until an inventory, in terms of both energy and number, of all electrons, positrons, and photons hitting each detector element has been established. The appropriate material, geometry, and magnetic effects of the detector are incorporated in establishing this inventory.

In what follows, we turn first to the details of the synchrotron radiation backgrounds (Section 4.2.1), next to the inventory of where all the synchrotron radiation power is deposited (Section 4.2.2), and finally to the consideration of lost-particle backgrounds (Section 4.2.3). We will see that the design we adopted provides a considerable safety margin between the occupancy and radiation-tolerance levels of the detector components (see Section 2.4) and the estimated levels of detector backgrounds.

4.2.1 Synchrotron Radiation Backgrounds

Several sources must be considered in the investigation of synchrotron radiation backgrounds:

- Direct synchrotron radiation (primary masks must be placed to prevent such radiation from striking the detector beam pipe, at the same time keeping the number of photons striking their tips to an acceptable level)
- Photons that scatter through a mask tip
- Sources of synchrotron radiation from elements far upstream of the IP
- Sources of backscattered photons from downstream surfaces

These issues are taken up here, along with a discussion of the calculational procedure used for predicting detector backgrounds. Our conclusions are that synchrotron radiation background rates are 84 times lower than the allowable detector occupancy and ation damage limits.

A detailed tracing of all the synchrotron radiation power must also be undertaken to make sure that no background problems arise from surfaces where the power is absorbed. This study is described in Section 4.2.2.

Separating the unequal-energy beams by the use of bending magnets and offset quadrupoles generates several fans of synchrotron radiation. The geometry of the IR optics, however, is designed to minimize the amount of synchrotron radiation that strikes nearby surfaces. In particular, the "S-bend" geometry of the beamlines (see Fig. 4-46) allows most of the synchrotron radiation generated by magnetic elements upstream of the IP to pass through the detector region without hitting local surfaces.

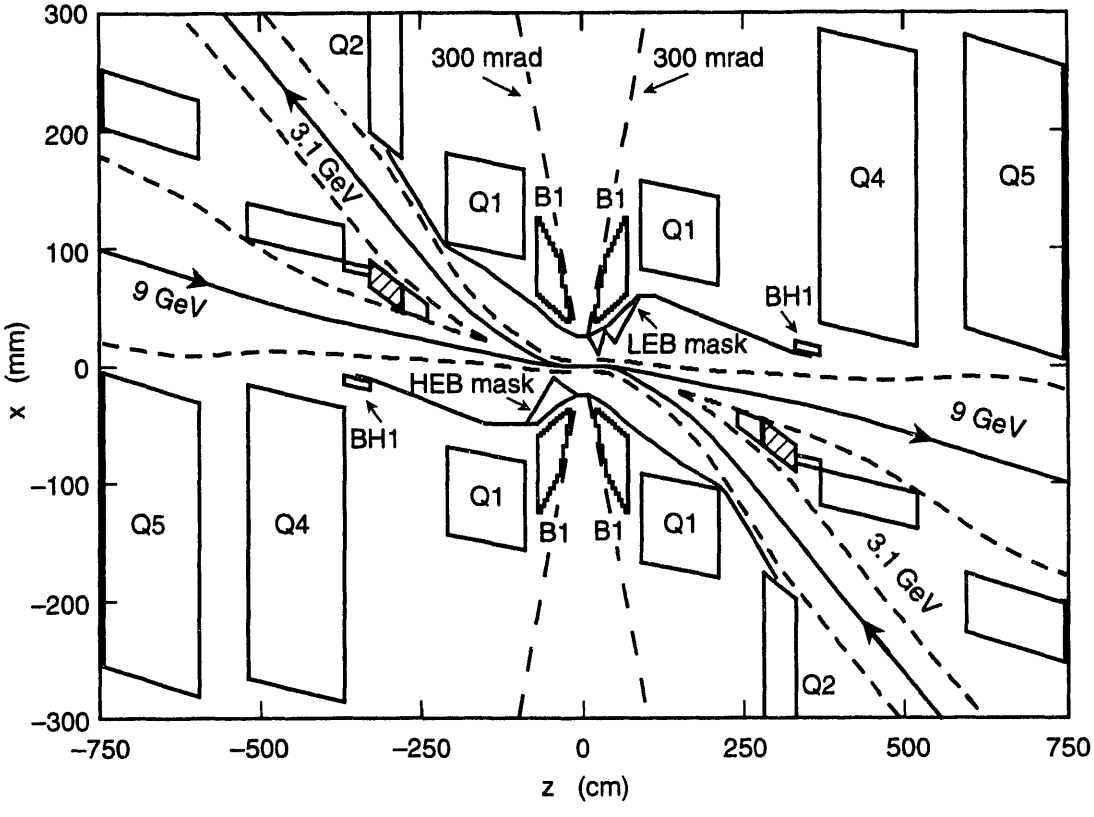

Fig. 4-46. General layout of the interaction region. The vertical scale is highly exaggerated. The dashed lines are the beam-stay-clear envelopes. The masks labeled LEB and HEB shield the detector beam pipe from direct synchrotron radiation. The mask surfaces facing away from the collision point are sloped such that incoming photons striking these surfaces cannot scatter directly onto the detector beam pipe. The cross-hatched regions indicate the septum portion of the Q2 quadrupoles. As discussed in Section 4.1, there is no longer a magnet designated Q3 in the lattice.

For this discussion, synchrotron radiation generated by beam particles is separated into two categories:

- Radiation generated by a beam passing through a bending magnet or an offset quadrupole; this is referred to as *fan radiation.* The intensity and power density of the fan radiation are high, because all of the beam particles contribute.
- Radiation generated by a beam that is on-axis as it travels through a quadrupole; this is referred to as *quadrupole radiation.* The intensity and power density of quadrupole radiation are much lower than for fan radiation, because the radiation is dominated by beam particles that are some distance away from the beam centerline, usually by three or more rms beam widths ($\sigma_{x,y}$).

In general, quadrupole radiation contributes only about 1% of the power generated by fan radiation, and the power is spread out over a much larger surface area. All calculations of detector backgrounds reported here include both fan and quadrupole radiation. Power calculations and estimates of photon power density on surfaces, described in Section 4.2.2, include only fan radiation. The IR has been designed to be compatible with two running conditions for the HER, $\beta_y^* = 2$ cm (the nominal case) or $\beta_y^* = 3$ cm. The 2-cm design has a high-energy beam (HEB) current of 0.99 A; the 3-cm design would require a beam current of 1.48 A. All synchrotron radiation power calculations near the IP, and the detector background calculations reported in this section, use the nominal beam currents for the 2-cm design: 0.99 A for the HEB and 2.14 A for the low-energy beam (LEB). The detector background numbers or radiation power for the 3-cm design can be obtained by multiplying the HEB background numbers by 1.5. For thermal design purposes, we have considered the higher HER beam current, 1.48 A, in specifying the IR mask properties (see Section 5.2.7).

As shown in Fig. 4-46, the HEB is centered in the Q1 quadrupole and the LEB is offset. Because Q1 is horizontally defocusing, this arrangement maximizes the separation of the beams by bending the LEB only. Sufficient separation is available to allow the Q2 quadrupole to be placed close enough to the IP to keep the maximum beta functions of the LEB near 100 m.

The apertures of the separation dipole magnet B1 and the quadrupoles Q1 and Q2 are large enough to accommodate at least 8 mm of radial space for a beam pipe and trim coils, while still maintaining 2 mm of free space between the beam pipe and either the synchrotron radiation fans or the 15σ envelope of the beam. (For determining beam-stay-clear apertures, we use the *uncoupled* horizontal emittance and the *fully coupled* vertical emittance, as discussed in Section 5.2.)

4.2.1.1 Synchrotron Radiation Fans. The LEB generates synchrotron radiation fans as it passes through the Q1 and B1 magnets on its way to the IP. Figure 4-47 shows the LEB radiation fans near the IP. The LEB mask in Figs. 4-46 and 4-47 is designed to prevent any of the synchrotron radiation (either fan or quadrupole) generated by the upstream magnets from directly striking the detector beam pipe. The surfaces of the LEB mask that are struck by the upstream radiation fans (that is, those surfaces facing away from the IP) are sloped such that incoming photons cannot scatter into the detector beam pipe. Fans generated by the two B1 magnets and by the downstream Q1 magnet pass

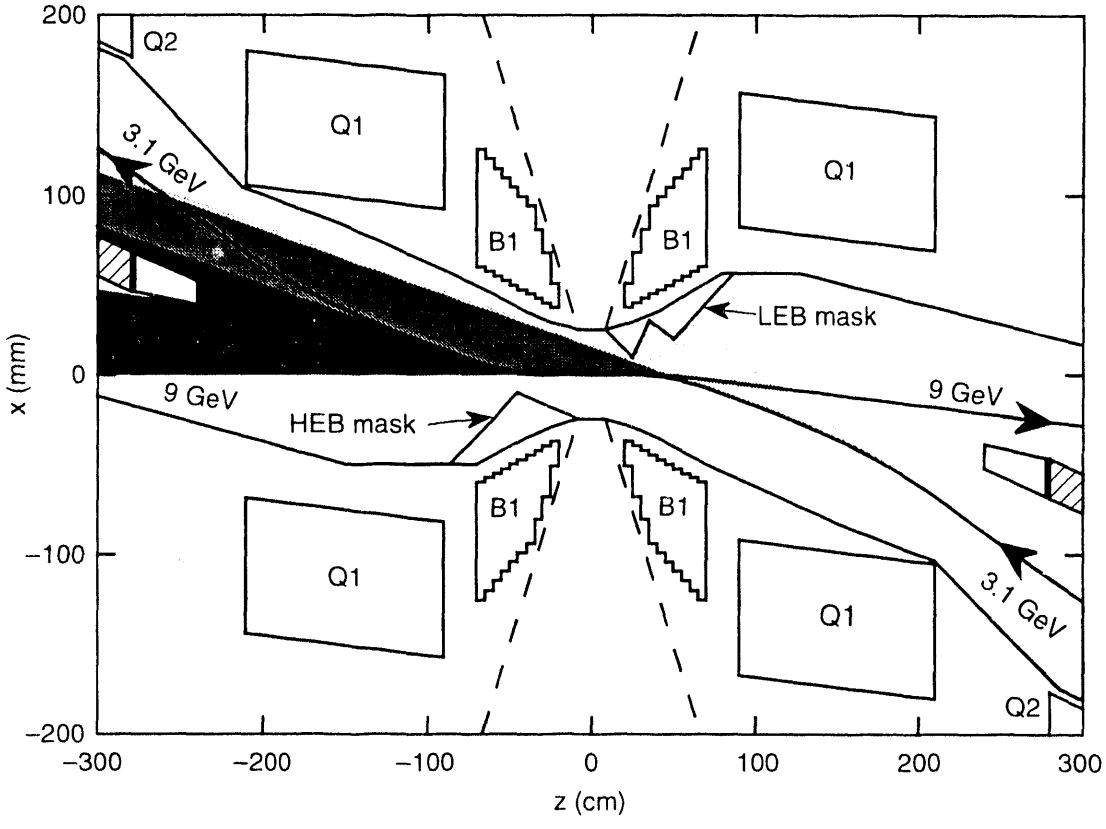

Fig. 4-47. Detail of the IR geometry, showing the radiation fans from the LEB. The density of shading gives an indication of the relative photon intensity from the various radiation fans.

through the IR without striking any surfaces. The first surface that intercepts the B1 fans is the septum mask in front of the Q2 septum quadrupole, located 2.8 m from the IP. This septum mask must be capable of absorbing 3.5 kW of power; a satisfactory design is described in Section 5.2.7. Table 4-15 summarizes some of the properties of the LEB and HEB radiation fans.

The Q4 quadrupole (see Fig. 4-46) is offset from the HEB axis by 10 mm. This produces a fan of bend radiation and deposits about 853 W of power on the HEB mask (see Fig. 4-48). The surface struck by this radiation is sloped such that scattered photons cannot reach the detector beam pipe. The HEB then goes through a horizontal bend magnet BH1. This magnet produces another radiation fan, part of which strikes the downstream Q2 septum mask, depositing 233 W of power. The combined effect of the two bends is to move the HEB axis such that the quadrupole radiation from the upstream Q5 does not strike the IP side of the LEB mask. Thus, no synchrotron radiation photons directly strike the IP side of either the HEB or the LEB mask. The fans of radiation generated by the HEB as it passes through the two B1 magnets do not strike any surfaces in the IP region and are absorbed in a high-power dump that starts at about 17 m from the IP (see Fig. 4-49).

Table 4-15. General properties of the fans of synchrotron radiation generated by the B1 magnets and the offset beams in the quadrupoles within ±5 m of the IP. The values are based on the nominal beam currents of 0.99 A for the HEB and 2.14 A for the LEB.

Magnet	Fan power (kW)	N_γ (10^{10})	ε_{crit} (keV)
LEB:			
Upstream Q2	0.07	1.5	0.4
Upstream Q1	2.88	12.2	2.0
Upstream B1	6.18	11.0	4.8
Downstream B1	6.18	11.0	4.8
Downstream Q1	2.88	12.2	2.0
Downstream Q2	0.07	1.5	0.4
Subtotal	18.3	49	
HEB:			
Upstream Q4	1.11	2.1	4.5
Upstream BH1	0.91	0.9	8.1
Upstream B1	24.0	5.1	40.4
Downstream B1	24.0	5.1	40.4
Downstream BH1	0.91	0.9	8.1
Downstream Q4	1.11	2.1	4.5
Subtotal	52.0	16	
Total	70.3	65	

As can be seen in Table 4-15, most of the synchrotron radiation power is generated by the HEB, and all but 2 kW of this power passes through the IR without striking any local surfaces. A complete inventory of synchrotron radiation power striking various surfaces near the IP is presented in Section 4.2.2.

4.2.1.2 Detector Backgrounds from Synchrotron Radiation. To evaluate detector backgrounds from synchrotron radiation, a series of programs was used. A flow diagram corresponding to the description below is shown in Fig. 4-50. As a first step, a machine lattice file is produced in which magnet positions, lengths, and strengths are specified, as well the position of each beam in each magnet. This information is fed into two programs, MAGBENDS and FINBETAS. The MAGBENDS code produces a beamline geometrical layout and calculates the fan power distribution. The FINBETAS code is used to calculate beta functions, beam sigmas, and beam-stay-clear envelopes for both beams. Information from both of these programs is used to produce pictorial layouts of the IP region. In addition, outputs from these two programs are used to make the input file for SYNC_BKG, an enhanced version of the code QSRAD that was originally

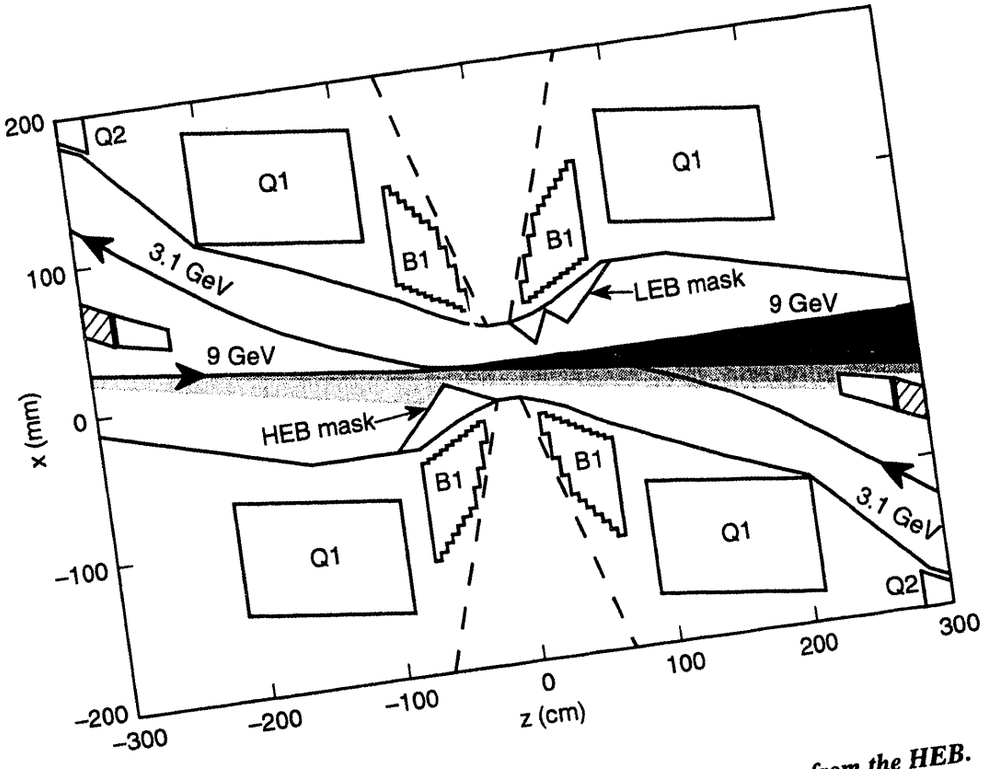

Fig. 4-48. Detail of the IR geometry, showing the radiation fans from the HEB. The density of shading gives an indication of the relative photon intensity from the radiation fans. The tip of the HEB mask is at least 3 mm outside the fan of radiation generated by the HEB as it goes through BH1. A radiation fan from the upstream Q4 magnet strikes the HEB mask.

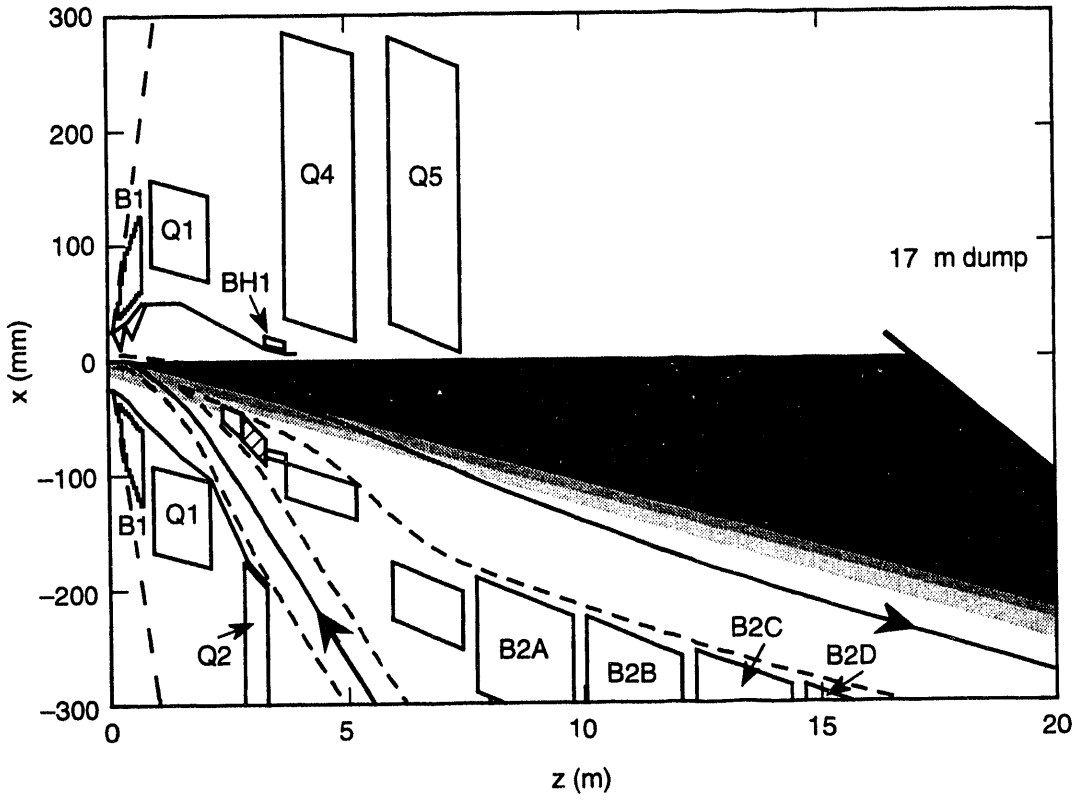

Fig. 4-49. The HEB synchrotron radiation fans from the two B1 magnets. These fans do not strike any surfaces near the IP and are absorbed in a high-power dump that starts at about 17 m from the IP.

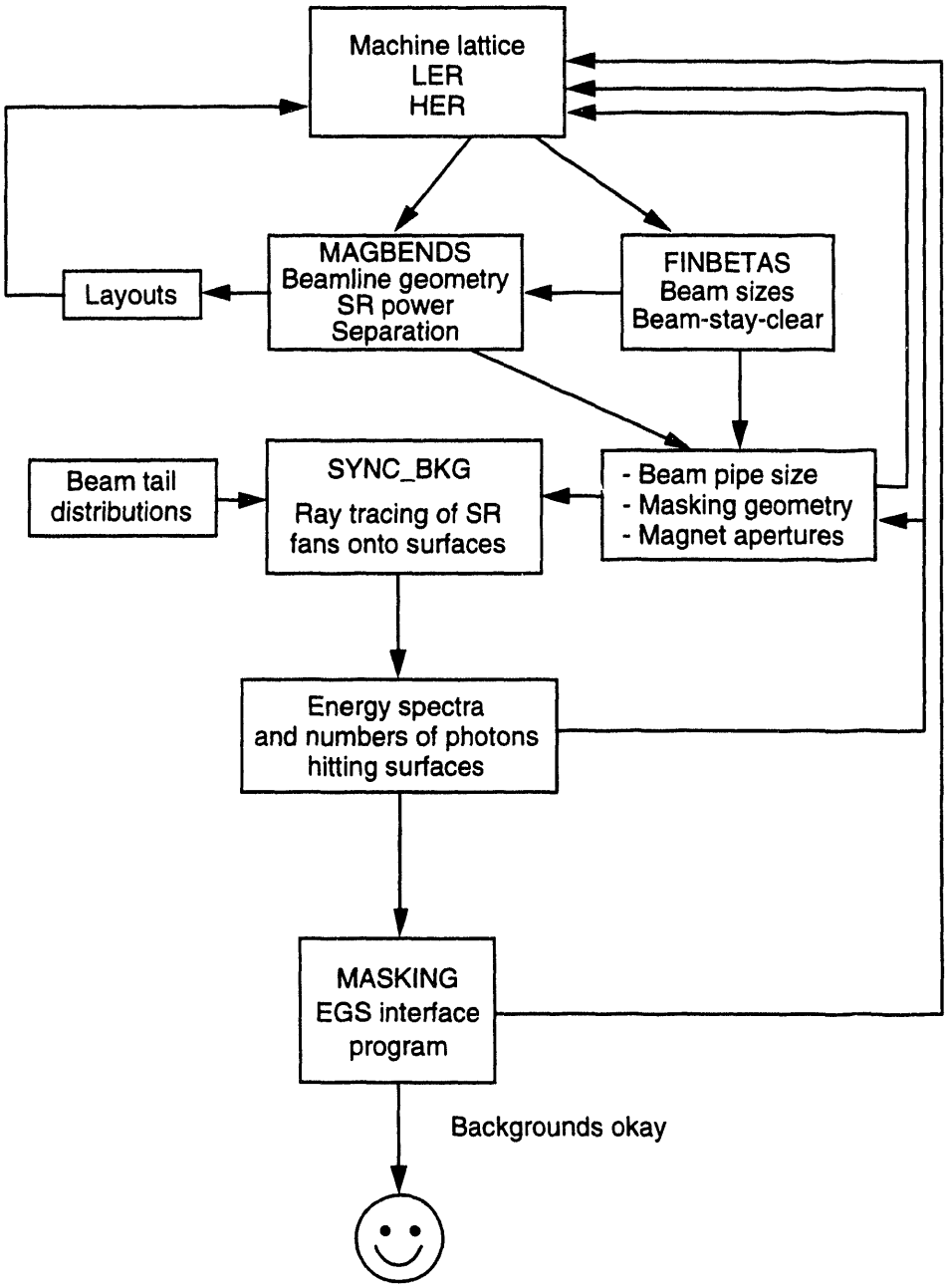

Fig. 4-50. Flow diagram of the procedure for calculating detector backgrounds from synchrotron radiation. At various stages in the procedure, a problem can be uncovered that forces a change in either the lattice or the masking geometry. This is represented by the various arrows returning to the lattice and masking geometry boxes. For any single design, many trips around these internal loops are needed before the design is either accepted or rejected.

written to study synchrotron radiation backgrounds at PEP and that has also been used to model backgrounds at the final focus of the SLC.

The SYNC_BKG program traces rays for the entire beam profile through quadrupoles and produces synchrotron radiation fans that are "scored" on various user-supplied mask surfaces. SYNC_BKG tallies both the number of photons striking each surface and the photon energy distribution. For PEP-II, the masking and beam pipe surfaces are designed so that the only nearby sources of photons that can reach the detector beam pipe are the tips of the LEB and HEB masks.

In addition to the beam pipe and masking geometry, SYNC_BKG also receives information about the transverse profile of the beam. Although its exact shape is not easily predicted, a non-Gaussian beam profile might result from, say, the beam-beam interaction. We include this possibility in our calculations by introducing a second Gaussian that has a larger rms width (σ) and a lower amplitude than that of the nominal beam core. Adding these two distributions together produces a non-Gaussian beam profile, with enhanced particle densities at large amplitudes. This parametrization of the beam tail yields two variables, the amplitude A of the distribution and the scaling factor S for the beam tail width. Figure 4-51 shows the beam distributions and the values of A and S used in this study; these values result from a previous study of synchrotron radiation backgrounds at PEP. To ensure that detector background rates are acceptable under all conditions, the beam-tail distributions are traced out to the limiting aperture of the ring. In the case under study, this means $10\sigma_{x0}$ and $35\sigma_{y0}$. We determined that our masking design is insensitive to the exact beam-tail distribution. Removing the tail distribution completely results in a very small (about 1%) change in detector background rates.

The information from SYNC_BKG is fed into an EGS interface program called MASKING. As indicated in Fig. 4-52, for a given incident photon energy spectrum, this program produces reflected, transmitted, and absorbed photon energy spectra. (A large selection of elements and compounds is available for the intercepting materials.) The EGS package includes K-shell photon fluorescence and Rayleigh scattering, but does not have provision for L-shell fluorescence. (Calculations of L-shell fluorescence suggest only small increases in the synchrotron radiation background rates we have computed.) MASKING uses an infinite-slab geometry to calculate the spectrum of photons that reflect from a surface or that penetrate through materials (for example, a beam pipe). In addition, a finite-slab geometry is available to study tip scattering. The files of reflection, transmission, and absorption coefficients thus produced are collected by another program (PHTALLY) and folded together to produce the background rates for various detector elements. These are displayed in Table 4-16. For comparison, Tables 2-5 and 2-6 indicate the maximum numbers of photons/μs that are permissible in terms of detector occupancy and radiation damage considerations. Figures 4-53 and 4-54 show the photon energy spectra for the HEB and LEB, respectively.

4.2.1.3 Tip Scattering. The scattered photons incident on the detector beam pipe are those that scatter through the tips of the LEB and HEB masks. Figure 4-55 illustrates the mechanism of tip (as opposed to surface) scattering. The tip-scattering effect is modeled by uniformly generating the incident photons along a line perpendicular to the edge of the material. Photons that scatter through the mask tips are then followed and a tally is kept

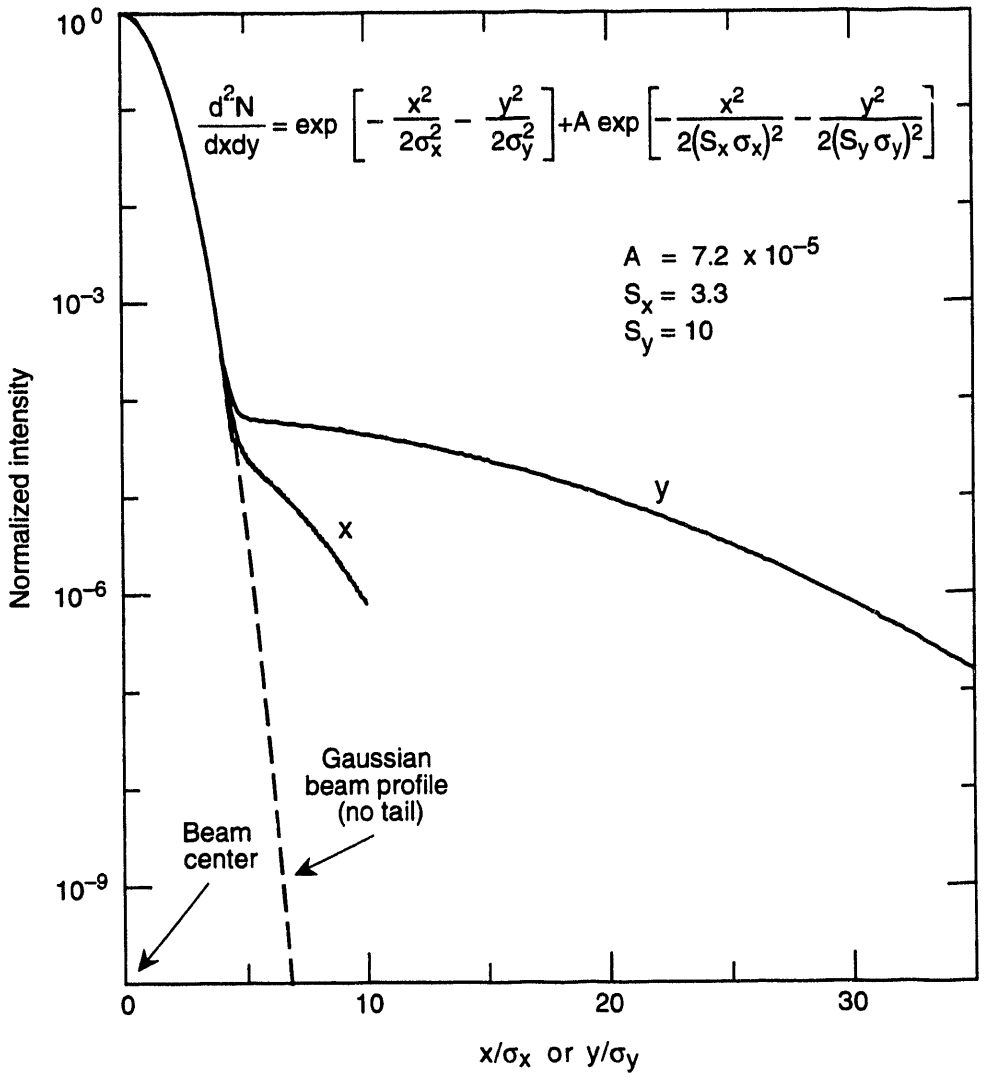

Fig. 4-51. Plot of the beam profiles assumed for the calculation of detector backgrounds due to synchrotron radiation. The integral of the background Gaussian is about 0.25% of the main beam Gaussian.

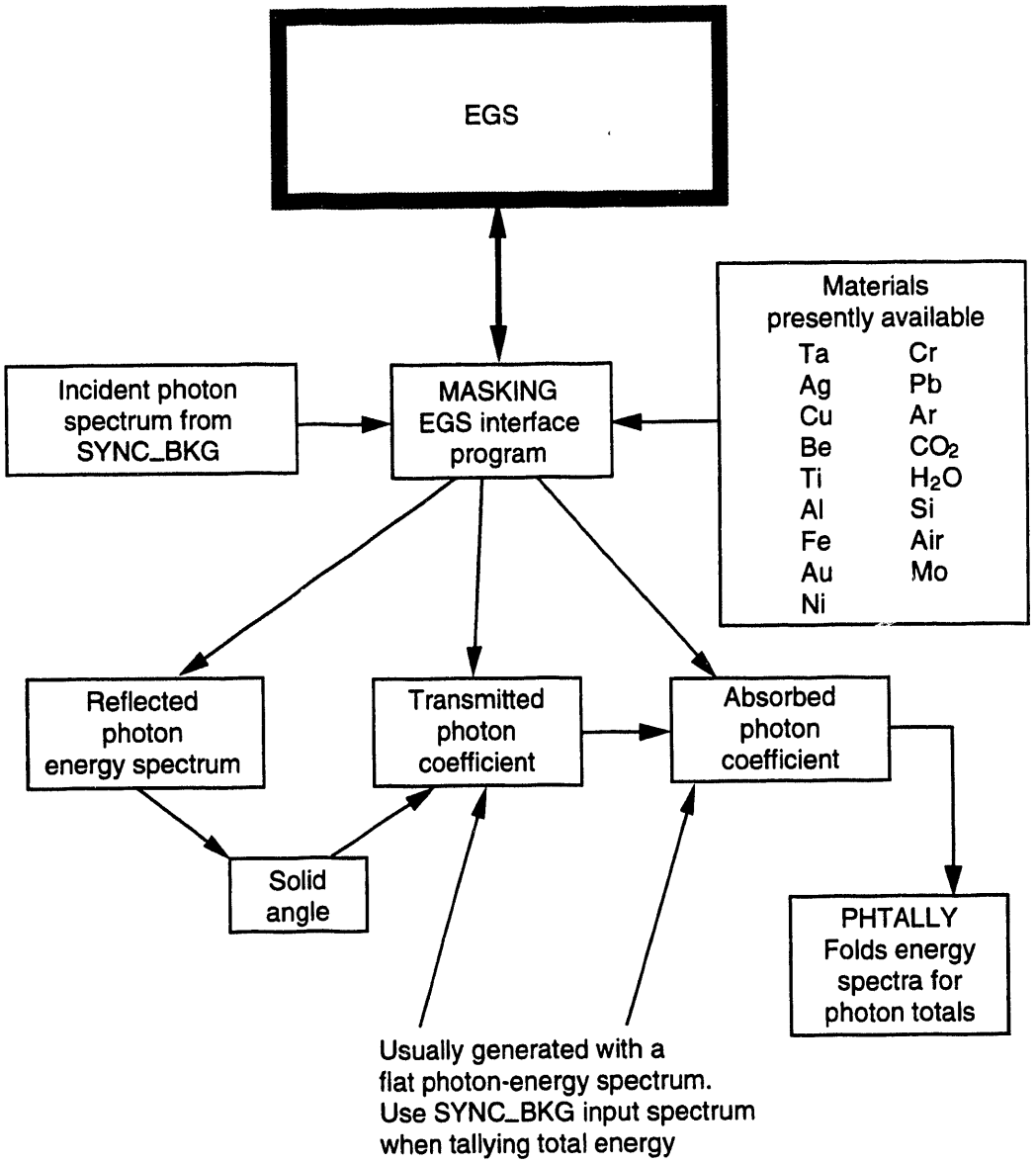

Fig. 4-52. Flow diagram of the procedure for producing reflection, transmission, and absorption coefficients and final photon spectra.

Table 4-16. Synchrotron radiation detector background predictions. The numbers are for each crossing. Multiply by 2.38×10^8 to get photons per second. The energies refer to the total energies of the indicated photons. The beam currents used in these calculations are 0.99 A for the HEB and 2.14 A for the LEB. Beam pipe materials are 25 μm of Cu and 1 mm of Be. The beam pipe inner radius is 2.5 cm with a 17-cm length for the Be section. The average angle of incidence is 75 mrad for the radiation striking the beam pipe from the tip of the HEB mask and 140 mrad for the radiation striking the pipe from the LEB mask tip. Silicon layers are 300 μm thick. The number of photons per crossing penetrating the beam pipe and incident on the first layer of silicon is 0.040. The total energy of these photons is 0.94 keV.

	Incident on Be pipe	Absorbed in first Si layer	Absorbed in second Si layer	Absorbed in third Si layer	Incident on drift chamber
			3.1-GeV beam		
$4 < E_\gamma < 100$ keV:					
Number of photons	0.20	5.5×10^{-4}	2.9×10^{-6}	8.1×10^{-8}	1.3×10^{-10}
Energy (keV)	1.28	4.5×10^{-3}	2.5×10^{-5}	7.1×10^{-7}	1.2×10^{-9}
$4 < E_\gamma < 20$ keV:					
Number of photons	0.20	5.5×10^{-4}	2.9×10^{-6}	8.1×10^{-8}	1.3×10^{-10}
Energy (keV)	1.28	4.5×10^{-3}	2.5×10^{-5}	7.1×10^{-7}	1.2×10^{-9}
			9.0-GeV beam		
$4 < E_\gamma < 100$ keV:					
Number of photons	1.04	0.027	6.9×10^{-4}	5.6×10^{-4}	2.5×10^{-5}
Energy (keV)	16.3	0.43	0.022	0.020	3.2×10^{-3}
$4 < E_\gamma < 20$ keV:					
Number of photons	0.76	0.021	9.4×10^{-5}	8.5×10^{-6}	2.1×10^{-7}
Energy (keV)	8.06	0.17	8.9×10^{-4}	1.3×10^{-4}	3.7×10^{-6}
			Totals		
$4 < E_\gamma < 100$ keV:					
Number of photons	1.24	0.028	6.9×10^{-4}	5.6×10^{-4}	2.4×10^{-5}
Energy (keV)	17.6	0.43	0.022	0.020	3.2×10^{-3}
$4 < E_\gamma < 20$ keV:					
Number of photons	0.96	0.02?	3.8×10^{-5}	8.6×10^{-6}	2.1×10^{-7}
Energy (keV)	9.34	0.17	9.2×10^{-4}	1.3×10^{-4}	3.7×10^{-6}

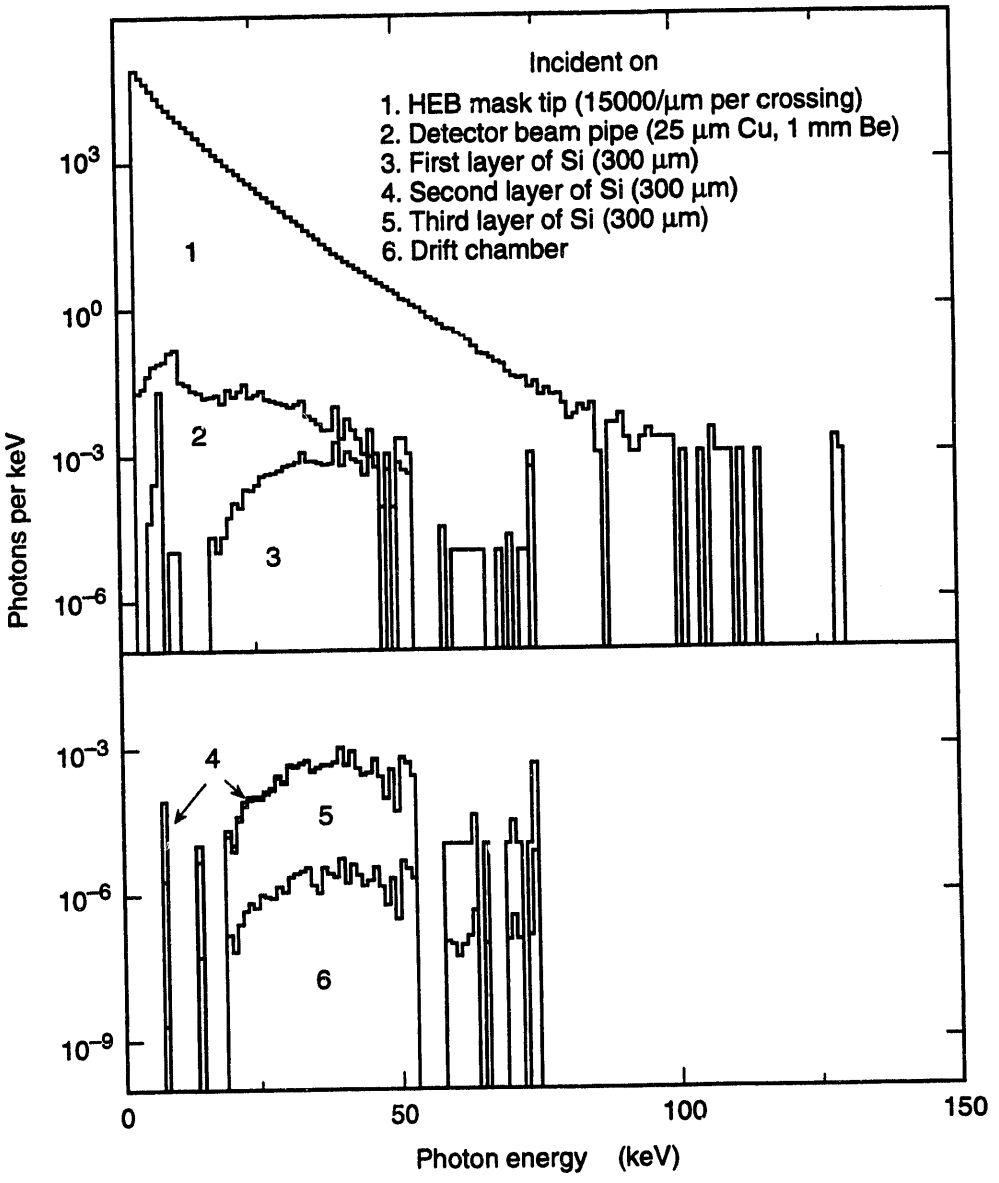

Fig. 4-53. Final photon spectra for the HEB. The initial photon spectrum is incident on the 22 μm of the HEB mask nearest the edge. The second spectrum results from photons that have scattered through the tip of the HEB mask.

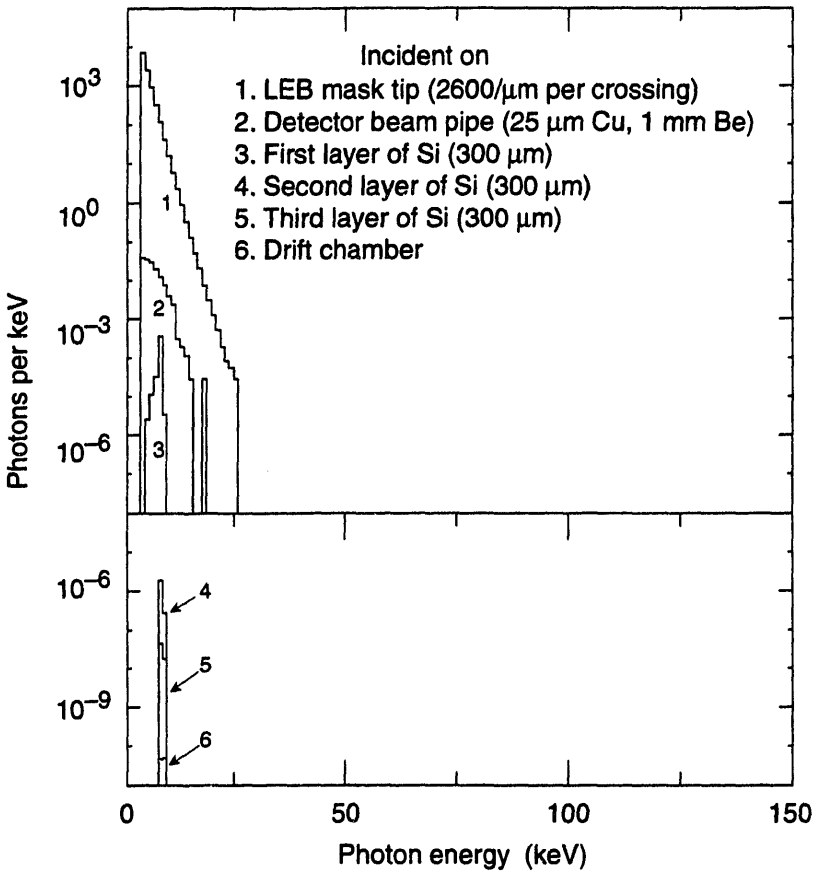

Fig. 4-54. Final photon spectra for the LEB. The initial photon spectrum is incident on the 5 μm of the LEB mask nearest the edge. The second spectrum results from photons that have scattered through the tip of the LEB mask.

of those that reach the detector beam pipe. The energy and the angle of incidence on the detector beam pipe of these photons are recorded, and this information is used to calculate the number and total energy of photons that penetrate the beam pipe and are absorbed in the silicon layers of the detector. Figure 4-56 is a plot of the z position of the intersection of the scattered photons and a cylinder having a 2.5-cm radius.

Figure 4-57 shows a plot of the distribution of photons that scatter through a mask tip of gold, as a function of the distance from the edge of the mask. Half of the scattered photons result from incident photons that are less than 2 μm from the edge. This calculation assumes a perfectly sharp mask edge; however, an actual mask tip will be somewhat rounded. Photons that strike the rounded surface can also reflect directly, as illustrated in Fig. 4-58; indeed, this direct reflection is more likely than tip scattering through the mask. If we assume that the corner of the mask has a 1-μm radius (which is not difficult to achieve), then, for the 9-GeV radiation on the tip of the HEB mask, we can estimate the number of photons per crossing incident on the detector beam pipe from this source of background by taking the product of the number of incident photons/μm (above

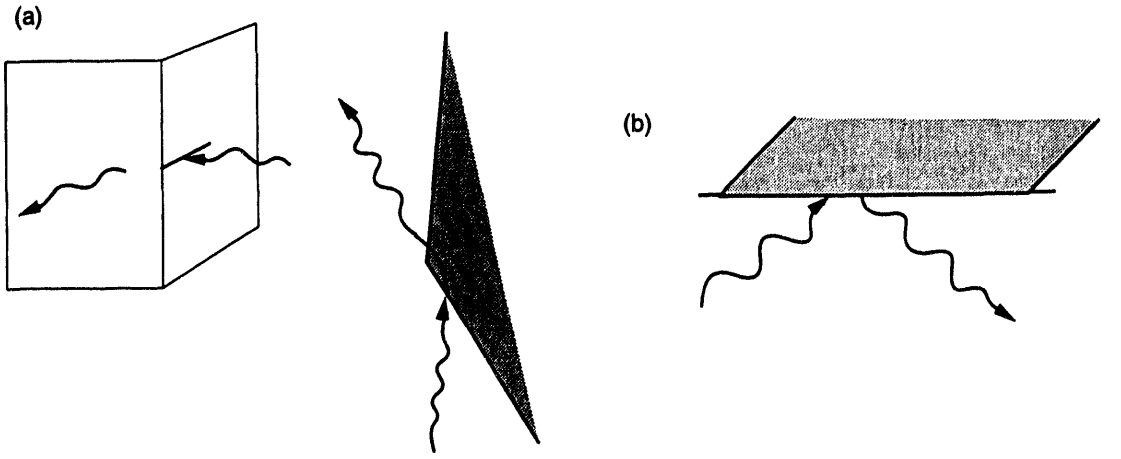

Fig. 4-55. Schematic illustration depicting the mechanisms of (a) tip scattering and (b) reflected scattering from a surface.

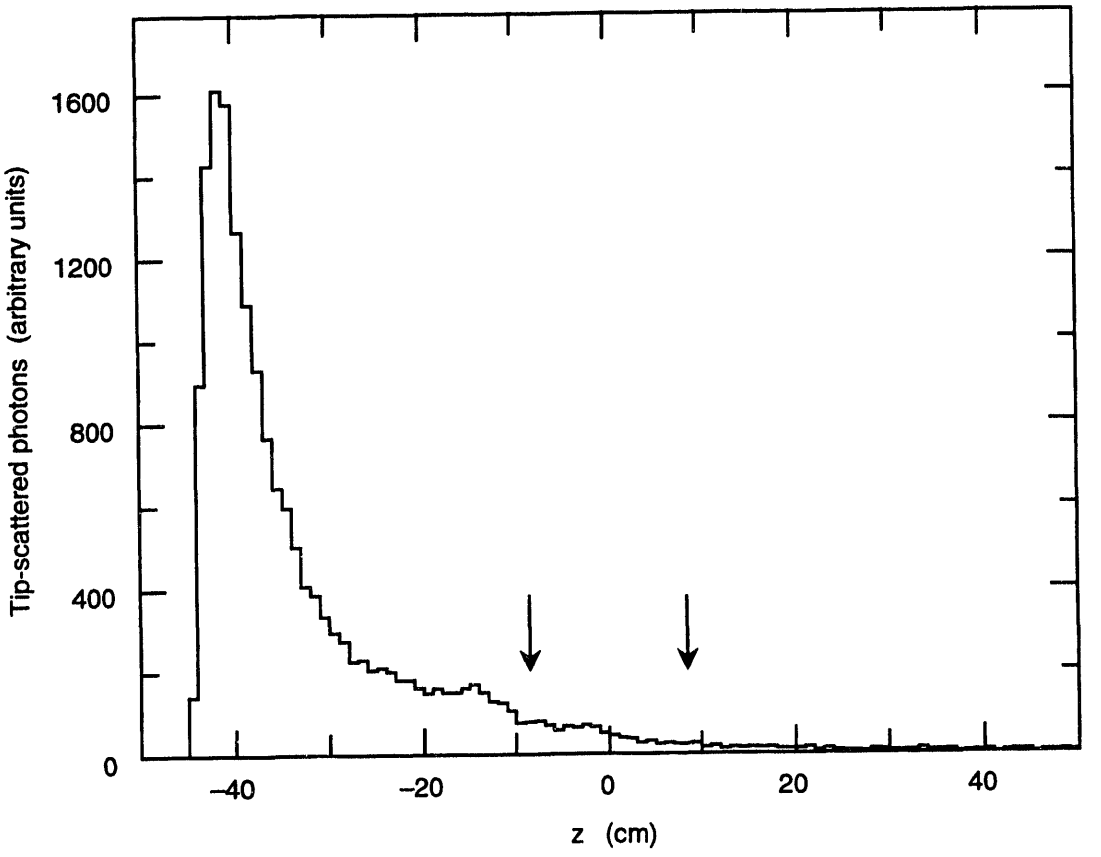

Fig. 4-56. Plot of the z position of photons scattered from the HEB mask tip and striking a cylinder with a 2.5-cm radius. The mask tip is positioned at –45 cm and is 1 cm off the axis of the cylinder. The two arrows encompass the detector beam pipe region.

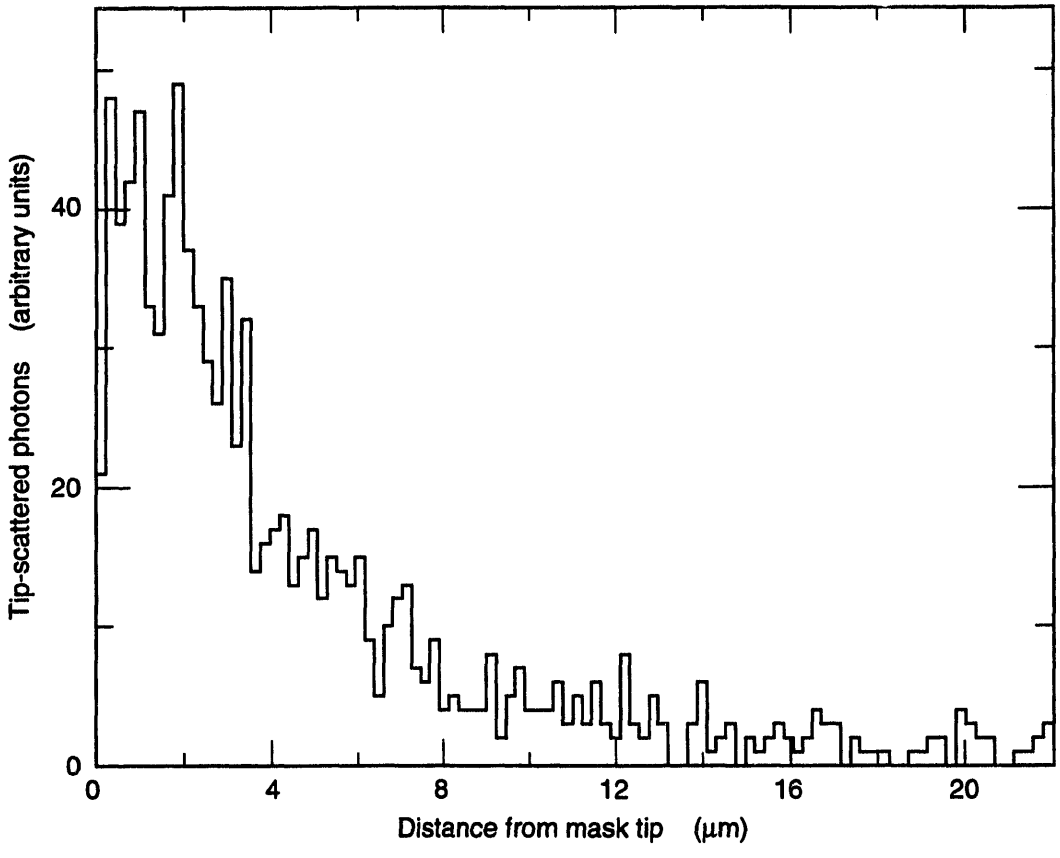

Fig. 4-57. Plot of the distribution of photons that scatter through a gold mask tip, as a function of the incident distance from the mask tip, for the HEB mask.

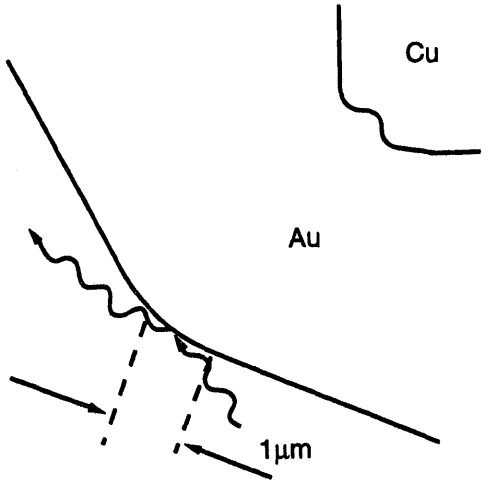

Fig. 4-58. Schematic illustration of direct reflection from a rounded mask tip.

4 keV), the surface-scattering probability of the mask material, and the solid-angle fraction subtended by the detector beam pipe:

$$15000 \text{ photons}/\mu\text{m} \times 0.007 \text{ (for Au)} \times 0.014 = 1.5 \text{ photons per crossing}$$

Similarly, for the 3.1-GeV radiation on the rounded LEB mask tip we have

$$2600 \text{ photons}/\mu\text{m} \times 0.0016 \text{ (for Au)} \times 0.095 = 0.40 \text{ photons/crossing}$$

We therefore find that the background rates from a tip with a 1-μm radius and that from a perfect tip are comparable (see Table 4-16, which assumes a perfect tip).

4.2.1.4 Other Upstream Sources of Synchrotron Radiation

High-Energy Beamline. There is a long, very-low-field (ε_{crit} = 1.2 keV) bending magnet (B2) located 10–15 m from the IP. The radiation fan from this magnet deposits 105 W onto the HEB mask. The septum of the Q2 magnet shadows the downstream LEB mask from this radiation fan. Consequently, the synchrotron radiation fans from B2, and all other HEB magnets upstream of B2, do not contribute to detector backgrounds.

Low-Energy Beamline. In order to maximize the physical space available for the septum of Q2, the magnet has been tilted by 20 mrad and offset by 6 mm with respect to the LEB axis. This tilt and offset together generate a small bend in the beam trajectory, producing 72 W of synchrotron radiation. This power is deposited on the far upstream end of the LEB mask and is not seen by the detector beam pipe. Further upstream, two horizontal bends (with ε_{crit} = 0.6 and 3.1 keV, respectively) deposit 707 W of power on the LEB mask; the rest of these fans are shadowed by the Q2 septum (from which scattered photons cannot reach the detector beam pipe in a single bounce, as discussed below) and by the beam pipe for the incoming LEB. None of the photons from these sources or from any other magnet further upstream strike the detector beam pipe.

4.2.1.5 Downstream Secondary Sources of Synchrotron Radiation. The radiation fans generated by the LEB as it passes through the B1 magnets strike the downstream septum mask in front of the Q2 septum quadrupole. Roughly 5.7×10^9 photons (>4 keV) per crossing strike this mask. Photons that backscatter out of the septum mask have no direct line-of-sight to the detector beam pipe: The HEB mask shields the beam pipe from this source of photons. Nonetheless, the intensity of this photon source is sufficiently high that one must ascertain that photons bouncing off the intervening beam pipe do not cause a background problem.

The mechanism of the "double bounce" of photons onto the detector beam pipe is illustrated in Fig. 4-59a. The simplified geometry shown in Fig. 4-59b permits the calculation of solid-angle fractions for various cylindrical sections of beam pipe between the detector beam pipe and the source. A calculation of the solid-angle fraction of the detector beam pipe seen by each cylindrical section of beam pipe can also be made. Summing the products of these two solid-angle fractions yields the probability that a photon can backscatter from the septum mask and strike the detector beam pipe. The

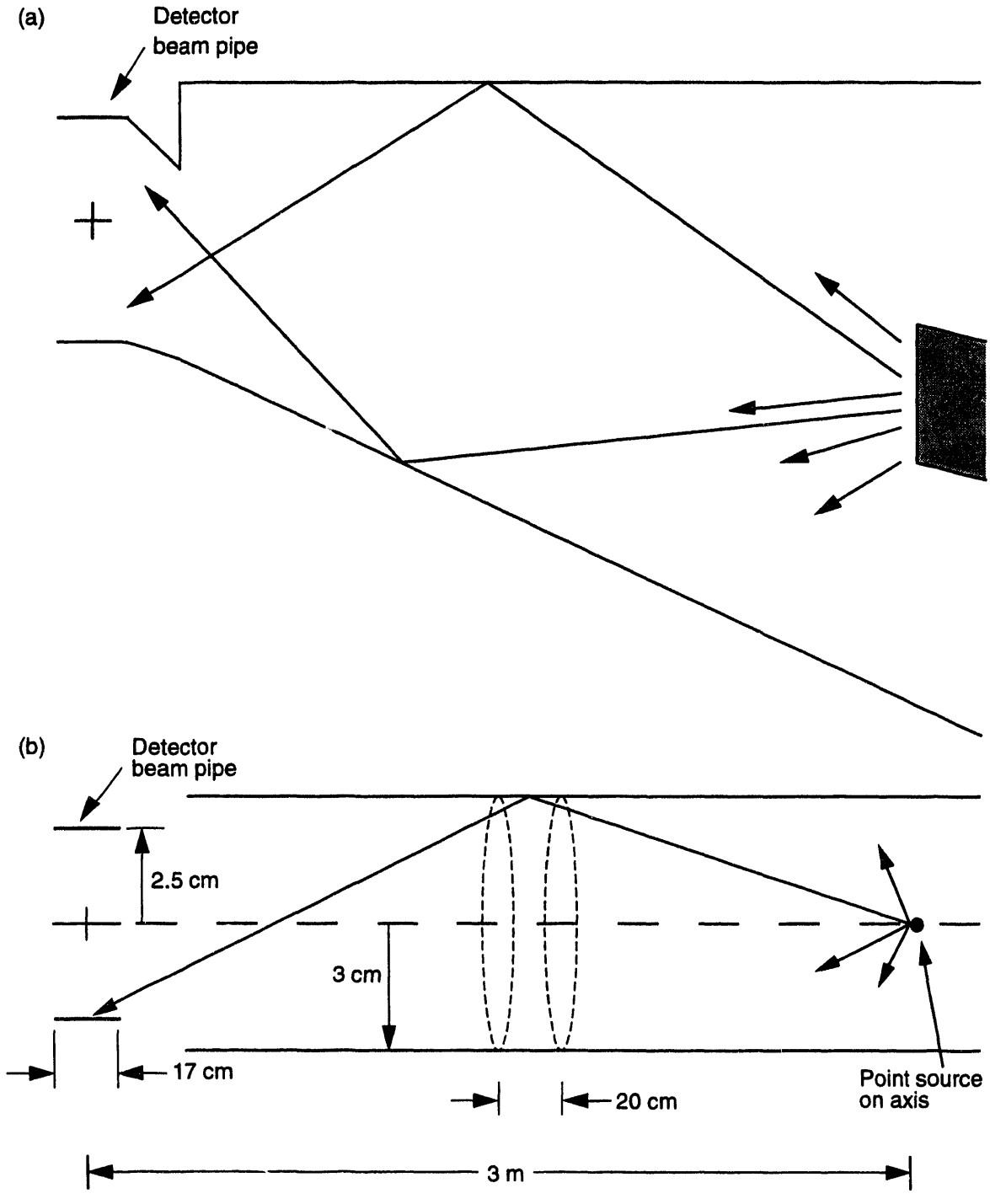

Fig. 4-59. (a) Schematic illustration of photons "double bouncing" to the detector beam pipe from a source of synchrotron radiation, and (b) a simplified geometry for the double-bounce problem. The typical dimensions shown in (b) were used to generate Table 4-17.

solid-angle fractions, along with their products, are displayed in Fig. 4-60; Table 4-17 lists the numerical solid-angle values.

As can be seen, the largest contribution to the solid angle comes from those beam pipe surfaces near the detector beam pipe and near the source. Assuming 5.7×10^9 photons per crossing incident on a copper mask located 2.8 m from the IP, and assuming that the intervening beam pipe is coated with a high-Z element such as gold, then the number of photons per crossing incident on the detector beam pipe is given by the product of the photons per crossing incident on the mask, the reflectivity of the mask material, the solid angle for a double bounce, and the reflectivity of the beam pipe coating:

$$(5.7 \times 10^9) \times 0.026 \text{ (for Cu)} \times (2.7 \times 10^{-6}) \times 0.0024 \text{ (for Au)} = 1.0 \text{ photons per crossing}$$

The HEB mask effectively shields most of the detector beam pipe from photons reflected from the nearby portion of the intervening beam pipe. In addition, care has been taken to ensure that regions of the beam pipe within 50 cm of the source and within 50 cm of the detector beam pipe do not have any line-of-sight to the detector beam pipe. This reduces by two orders of magnitude the probability of backscattered photons striking the detector beam pipe (see Table 4-17). Furthermore, most of the photons that do strike the detector beam pipe have a very small angle of incidence (<25 mrad), which further reduces the probability that photons from this source will penetrate the detector beam

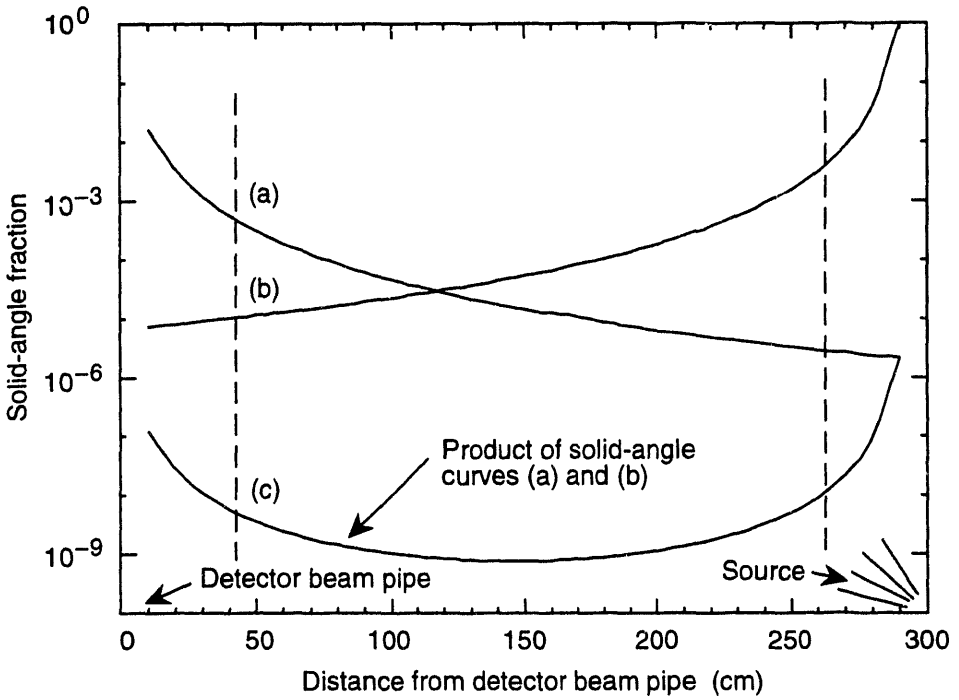

Fig. 4-60. Plot of (a) the solid-angle fraction of detector beam pipe as seen from the main beam pipe, (b) the solid-angle fraction of intervening beam pipe as seen from the source of radiation, and (c) the product of (a) and (b); the abscissa represents the distance from the detector beam pipe.

Table 4-17. Solid-angle (SA) fractions from a double-bounce source. The numbers between the two dashed lines correspond to the double-bounce solid angle for the 1.8 m of beam pipe centrally located between the source and the detector beam pipe.

Distance from detector beam pipe to intervening beam pipe (cm)	SA fraction of detector beam pipe as seen from intervening beam pipe segment (a)	SA fraction of intervening beam pipe segment as seen from source (b)	Product (c)
270	2.64×10^{-6}	0.9557	2.52×10^{-6}
250	3.30×10^{-6}	8.26×10^{-3}	2.73×10^{-8}
230	4.21×10^{-6}	1.55×10^{-3}	6.53×10^{-9}
210	5.49×10^{-6}	5.45×10^{-4}	2.99×10^{-9}
190	7.34×10^{-6}	2.53×10^{-4}	1.86×10^{-9}
170	1.10×10^{-5}	1.37×10^{-4}	1.51×10^{-9}
150	1.45×10^{-5}	8.28×10^{-5}	1.20×10^{-9}
130	2.19×10^{-5}	5.38×10^{-5}	1.18×10^{-9}
110	3.52×10^{-5}	3.69×10^{-5}	1.30×10^{-9}
90	6.20×10^{-5}	2.64×10^{-5}	1.64×10^{-9}
70	1.25×10^{-4}	1.95×10^{-5}	2.44×10^{-9}
50	3.11×10^{-4}	1.48×10^{-5}	4.60×10^{-9}
30	1.18×10^{-3}	1.16×10^{-5}	1.37×10^{-8}
10	1.60×10^{-2}	9.17×10^{-6}	1.47×10^{-7}
		Total	2.73×10^{-6}
		Total for central 1.8 m	2.53×10^{-8}

pipe. Taken together, these factors make double-bounce photons from the septum mask a negligible source of detector background.

Still another possible source of detector background is backscattered photons coming from the dump downstream of the IP in which most of the synchrotron radiation power from the IR is absorbed. These photons may backscatter directly onto the detector beam pipe. To estimate this effect, we assumed that the entire synchrotron radiation power is absorbed in a dump located 17 m from the IP. The solid-angle fraction of the detector beam pipe seen from this source is 2×10^{-8}. (This calculation assumes that there is no intervening LEB mask to shield most of the detector beam pipe.) There are about 5×10^{10} photons (>4 keV) per crossing incident on the dump mask. Taking a reflection

coefficient for the dump mask material of 0.007, we get 7 photons per crossing incident on the detector beam pipe. In reality, the LEB mask shields at least 90% of the detector beam pipe from this source. The small region of detector beam pipe still exposed can be easily shielded by a small lip (about 1 mm) near the edge of the beam pipe. In addition, the very small angle of incidence on the beam pipe (about 2 mrad) eliminates the high-power downstream dump as a possible source of detector background.

4.2.1.6 Sensitivity of Backgrounds to Misalignments. The following misalignments were evaluated for their effects on detector backgrounds:

- Displacing the Q4 magnet ±1 mm in x and y for the HEB
- Displacing the Q2 magnet ±1 mm in x and y for the LEB
- Displacing the Q1 magnet ±1 mm in x and y for both beams
- Displacing Q1, Q4, and Q5 ±5 mm in x for the HEB; this corresponds to a displacement of about 1σ for the beam
- Displacing Q1, Q4, and Q5 ±0.8 mm in y for the HEB; this also corresponds to a displacement of about 1σ for the beam
- Displacing Q1 and Q2 ±2.6 mm in x for the LEB; this corresponds to about a 1σ beam displacement
- Displacing Q1 and Q2 ±0.55 mm in y for the LEB; this also corresponds to a displacement of about 1σ for the beam

The HEB background is the more sensitive to misalignments such as these. We see a threefold increase in the background rate in one direction and a 2.4-fold increase in the opposite direction for a 5-mm displacement in x of Q1, Q4, and Q5. The rest of the misalignment checks produced small (<50%) increases in backgrounds, with some configurations producing rates that are actually below the nominal background rate. None of the above misalignments resulted in synchrotron radiation photons directly striking the detector beam pipe.

4.2.2 Survey of Synchrotron Radiation Power in the Interaction Region

Here we discuss the power levels on all the surfaces near the IP. An extensive analysis of all sources of fan radiation that either travels through, or comes close to, the IP is included. The analysis follows the fan from each source of radiation, and a tally for all surfaces the fan strikes is maintained. Table 4-18 summarizes the power deposited on various surfaces near the IP. The letters in the table that identify the various surfaces are also shown in Figs. 4-61 through 4-64. As mentioned earlier, the power values are calculated using the nominal beam currents: 0.99 A for the HEB and 2.14 A for the LEB.

There are twelve radiation fans, nine of which are produced within 5 m of the IP and three of which originate from upstream bending magnets. The radiation fans can be conveniently separated into four categories: upstream LEB sources, downstream LEB sources, upstream HEB sources, and downstream HEB sources.

Table 4-18. Power on surfaces near the IP. Each surface is identified by letter in Figs. 4-61 through 4-64. Radiation fans that strike a surface do not necessarily overlap; the surface power summary for each surface is the maximum power density for that surface.

	Source	Surface power (W/mm)	Total power (W)
Surface struck:			
a. Beam pipe of Q2, HEB side of septum (2.8–3.3 m)			
	B2	0.2	81
b. HEB septum mask (2.8 m)			
	B1 upstream	1.3	1424
	B1 downstream	2.0	2078
		3.3	3502
c. Beam pipe of Q2, LEB side of septum (2.8–3.3 m)			
	B1 upstream	1.2	600
	B1 downstream	1.3	666
		2.5	1266
d. Beam pipe behind Q2, LEB side of septum (3.3–4.25 m)			
	B1 upstream	2.7	155
	Q1 downstream	0.6	509
		2.7	664
e. HEB mask (0.45 m)			
	B2	1.0	105
	Q4	7.3	854
		8.3	959
f. LEB mask (0.25 m)			
	B6	1.6	620
	B5	0.9	145
	Q2	1.0	72
	Q1	15.0	2775
		17.5	3612
g. LEB septum mask (2.8 m)			
	B2	0.09	73
	Q4	0.73	253
	BH1	1.40	233
		1.49	559[a]
h. Beam pipe of Q2, LEB side of septum			
	B6	0.3	135
i. Beam pipe behind Q2, LEB side of septum (3.3–5.3 m)			
	B6	0.1	123

[a]An additional 62 W of power from B6 strike the edge of this mask.

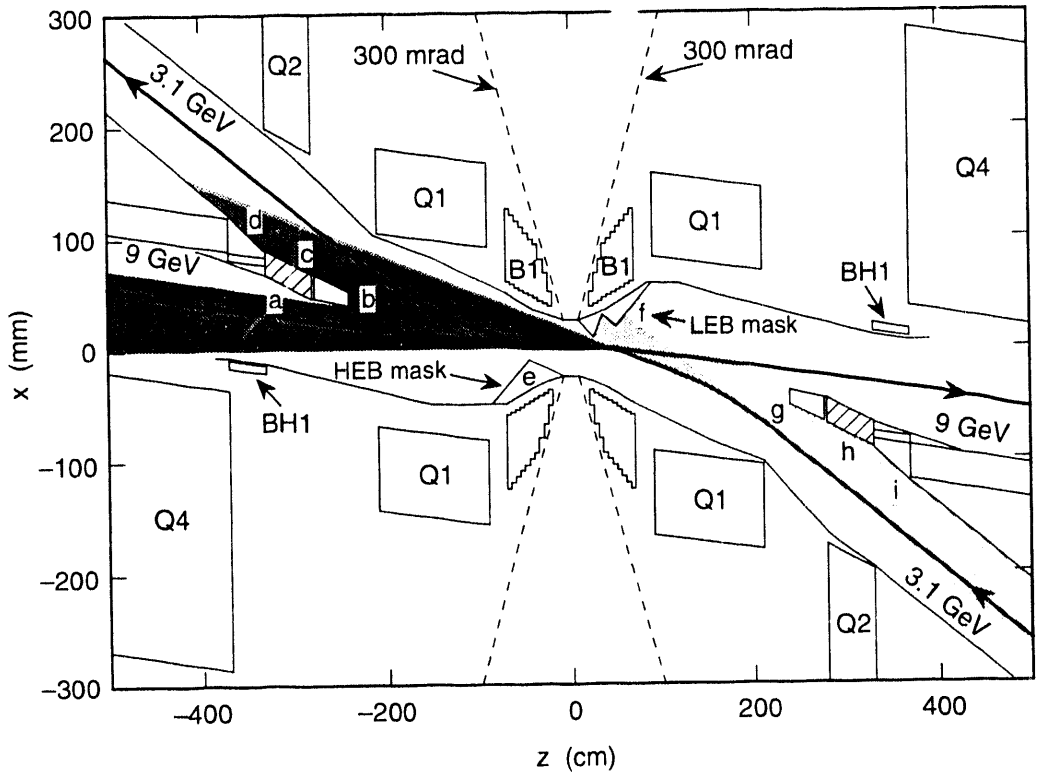

Fig. 4-61. LEB radiation fans produced upstream of the IP. The fan generated by the upstream Q1 magnet is almost entirely absorbed by the LEB mask. The lower-case lettering refers to surfaces in Table 4-18 that are struck by synchrotron radiation.

4.2.2.1 Upstream LEB. These sources of radiation include upstream bending magnets, B5 and B6, and three magnets near the IP: Q2, Q1, and B1. Part of the synchrotron radiation fan from B6 strikes the beam pipe inside the Q2 septum magnet, depositing about 135 W along the 0.5-m magnet length. Some of the remaining B6 fan deposits about 60 W on the side of the septum mask located in front of Q2. The rest of the B6 fan (620 W), the fan from B5 (145 W), the small radiation fan from Q2 (72 W), and essentially all of the Q1 fan strike the LEB mask, depositing a total power of 3.61 kW. The total B1 fan power is 6.2 kW. Some of this fan strikes the beam pipe beyond the downstream Q2 magnet in the LER and deposits 1.6 kW. Another part of the B1 fan deposits 600 W on the beam pipe inside the Q2 magnet. A third part of the B1 fan strikes the HEB septum mask, depositing 1.4 kW, and the rest of the fan (about 2.5 kW) is absorbed in a radiation dump. There are two such radiation dumps in the HER beam pipe, one on each side of the IP and located in the region about 17–24 m away from it. The dump in the upstream part of the HEB beam pipe is referred to as the "high-power upstream dump" (HPUD), and the dump located downstream of the IP is called the "high-power downstream dump" (HPDD). The upstream LEB radiation fans are shown as shaded regions in Fig. 4-61.

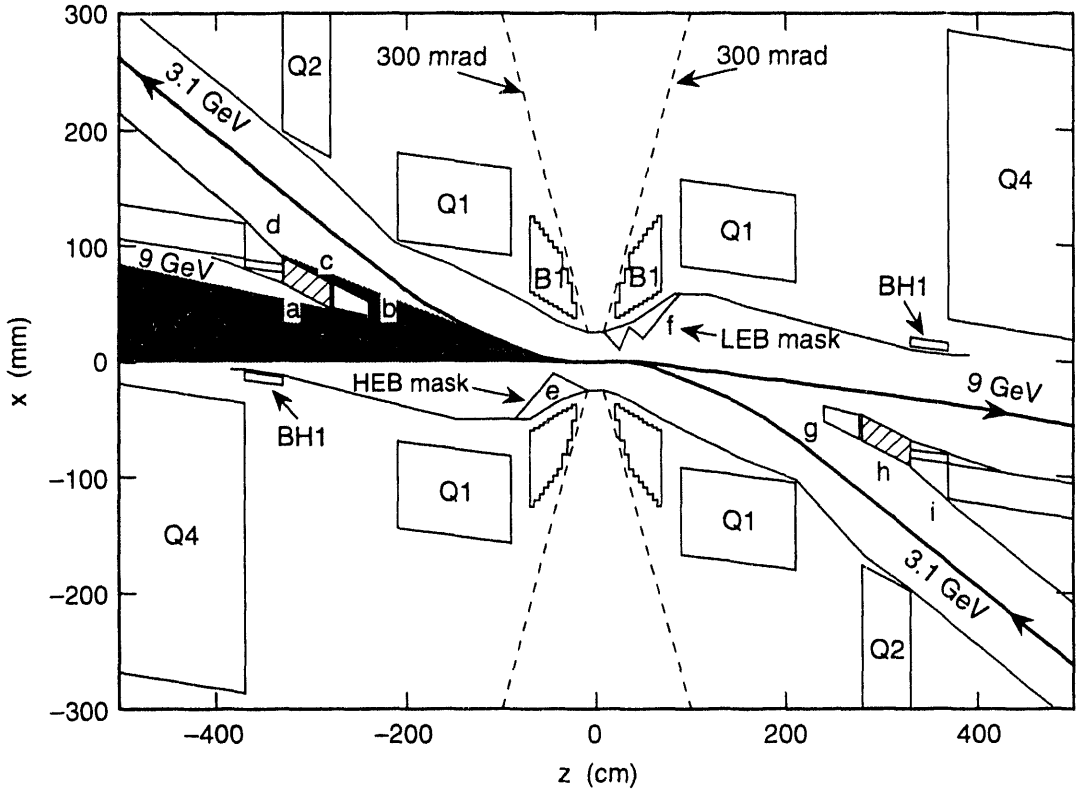

Fig. 4-62. LEB radiation fans produced downstream of the IP. The radiation fan from the downstream B1 magnet overlaps the upstream B1 radiation fan (see Fig. 4-61). The overlapping B1 fans deposit about 3.5 kW of power on the HEB septum mask in front of the Q2 septum.

4.2.2.2 Downstream LEB. Two fans are generated by the downstream elements B1 and Q1. A little over half of the B1 fan (3.3 kW) is absorbed in the HPUD. Most of the remaining B1 fan strikes the HEB septum mask, depositing 2.1 kW of power. The rest of the fan strikes the beam pipe inside the Q2 magnet, leaving 666 W. The Q1 fan deposits 2.9 kW of power along about 4 m of the LER beam pipe, starting at 3.3 m from the IP. Figure 4-62 shows as shaded regions the fans generated by the downstream LEB elements.

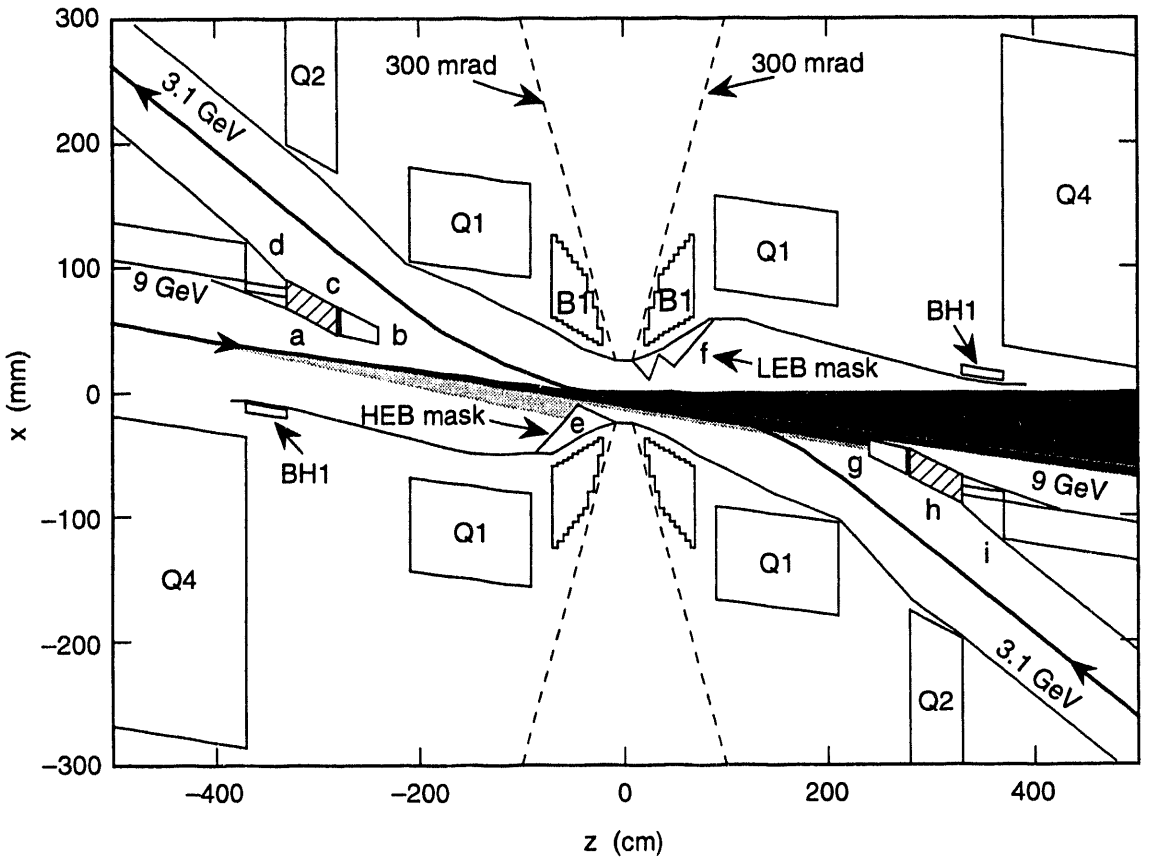

Fig. 4-63. HEB radiation fans produced upstream of the IP. The upstream Q4 fan strikes the HEB mask, depositing about 870 W of power. The remaining Q4 fan and about half of the BH1 fan strike the LEB septum mask in front of Q2, depositing about 500 W of power.

4.2.2.3 Upstream HEB. For the HEB, there are four upstream sources of radiation fans, as shown in Fig. 4-63: A weak radiation fan from B2 (ε_{crit} = 1.2 keV) strikes the beam pipe upstream of Q2 with 51 W of power, the beam pipe inside the Q2 magnet (81 W), the HEB mask (105 W), the LEB septum mask (73 W), and the HPDD (9 W). Part of the Q4 fan (ε_{crit} = 4.5 keV) strikes the HEB mask, depositing 870 W, and the rest (253 W) strikes the LEB septum mask. Part of the BH1 fan strikes the LEB septum mask, depositing 233 W, and the rest (677 W) is absorbed in the HPDD. The B1 fan misses all nearby surfaces and is absorbed in the HPDD.

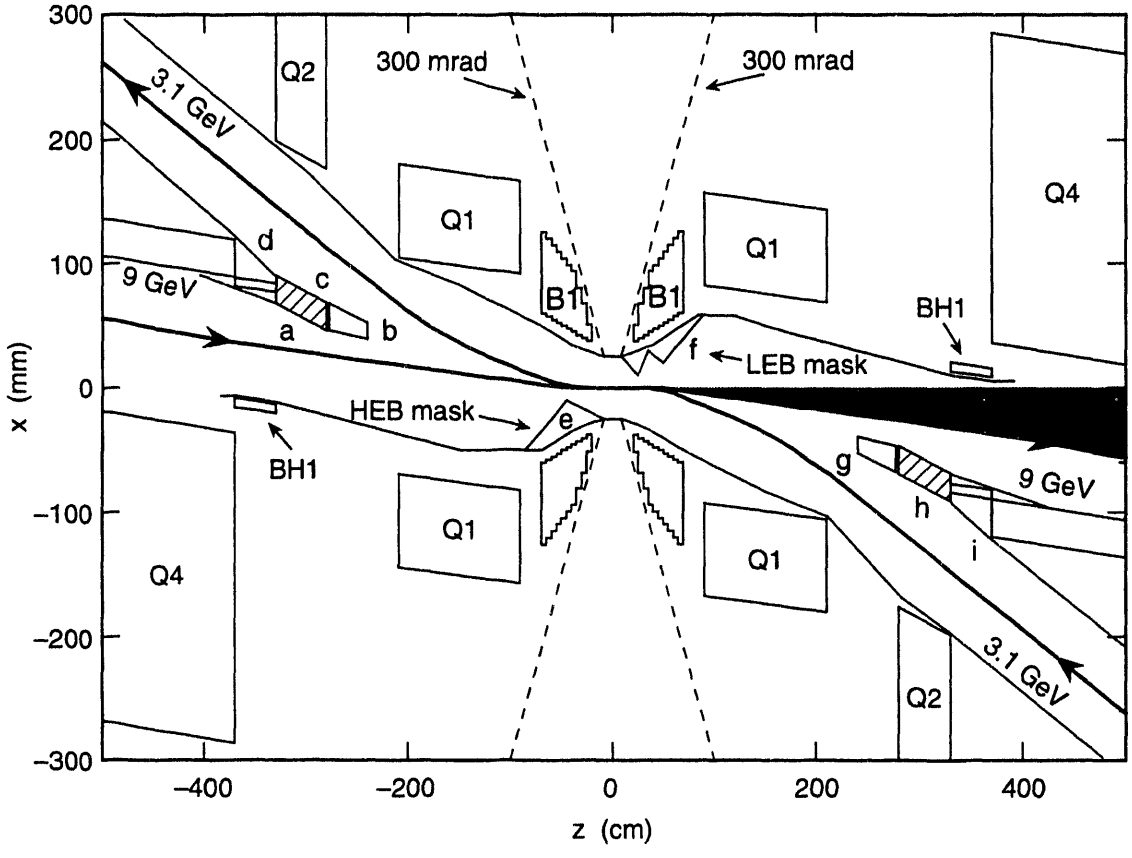

Fig. 4-64. HEB radiation fans produced downstream of the IP. The radiation fan from the downstream B1 magnet overlaps the upstream B1 radiation fan (see Fig. 4-63).

4.2.2.4 Downstream HEB. The three radiation fans from downstream HEB elements B1, BH1, and Q4 miss all nearby surfaces (see Fig. 4-64) and are absorbed in the HPDD. The total amount of power that is absorbed in the HPUD is 5.8 kW, and the HPDD absorbs 50 kW of power. No power is seen in the upstream beamline of the LER.

4.2.2.5 Summary. We find that 80% of the synchrotron radiation power is absorbed in downstream dumps and thus causes no increase in detector background, either from backscattered photons or from beam-gas interactions. Of the remaining 14 kW, 5.8 kW are absorbed in an upstream region of the HER 17 m from the IP, and most of the rest is absorbed on the septum mask at Q2 and on the LEB mask.

4.2.3 Detector Backgrounds from Lost Beam Particles

Bremsstrahlung and Coulomb scattering of beam particles from residual gas molecules in the beam pipe can lead to high-energy electrons and photons striking masks and the beam pipe near the IP. The resulting electromagnetic showers can cause excessive detector occupancy and/or lead to radiation damage. In this section, we discuss the methods used to simulate this process, the rates and locations of lost-particle hits, and the resulting detector backgrounds.

In calculating the rates at which particles strike near the IP due to bremsstrahlung and Coulomb scattering, we simulate both the HER and LER lattices for a distance of 185 m upstream of the IP (halfway around the adjacent arc). Bremsstrahlung scattering produces an electron and a photon whose combined energy is equal to the beam energy. In our simulations, the photon energy is restricted to the range between 2% and 99% of the beam energy—events with a photon energy outside this range contribute less than 1% of the energy deposited near the IP. Coulomb scattering gives an off-axis electron having the full beam energy. In the simulations, we restrict the Coulomb scattering to angles between 0.33 and 500 mrad, because electrons scattered by smaller angles do not hit near the IP.

The analysis was carried out using two codes. DECAY TURTLE [Carey et al., 1982] was used to simulate the interaction of beam particles with the gas and to transport the scattered particles through the ring optics, and EGS was used to simulate the electromagnetic showers produced in the masks and magnets near the IP and in the detector. In DECAY TURTLE, which is a modified version of TRANSPORT [Brown et al., 1977], rays (representing particles) are transported until they either strike an aperture or reach the end of the system (a point well beyond the IP). Rays that strike within 2.25 m of the IP for the HEB, or within 2.1 m of the IP for the LEB, are passed to EGS for a detailed simulation of the shower development.

Our rate estimates are based upon a nominal beamline pressure of 1 nTorr (N_2-equivalent) for a distance of 35–60 m upstream of the IP. Beyond 60 m, that is, in the arcs (where copious synchrotron radiation makes it difficult to maintain this pressure), a pressure of 5 nTorr is assumed. For the HER, we maintain a lower pressure (~0.2 nTorr) from 35 to 3 m upstream of the IP, as discussed in Section 5.2.7.1; for the LER, the region from 15 to 2 m upstream is kept at 0.2 nTorr. For both rings, the pressure close to the IP is taken as 1 nTorr. In the discussion below, we quote the background rates *per microsecond*, since 1 μs is a typical integration time for detector elements. Other measures are employed for radiation damage, namely, rads/yr for the vertex detector and C/cm/yr for the drift chamber.

The number of rays striking near the IP is reduced by suitably placed upstream masks. The masks we consider are elliptical, with half-apertures given by the larger of 1 cm or

$n\sigma_{x,y}$ + 2 mm, where $\sigma_{x,y}$ is the transverse (horizontal or vertical) beam size at the mask location. We employ a graded aperture in this region of the lattice, that is, we use progressively larger apertures as we approach the IP. Thus, we choose n = 15 within 10 m of the IP, n = 12 between 10 and 20 m from the IP, and n = 10 beyond 20 m from the IP.

Suitable mask positions along the beam axis (z position) are selected by examining plots of the trajectories of tracks that strike near the IP. Figure 4-65a shows the trajectories of soft bremsstrahlung rays (particles having between 80% and 98% of the full beam energy) from the HEB that strike either the detector beam pipe or the LEB synchrotron radiation mask ("+x" hits). Masks at the z positions indicated (arrows) will clearly be effective in reducing the rate of these rays. Figure 4-65b shows trajectory plots for soft bremsstrahlung from the LEB striking the detector beam pipe or the HEB synchrotron mask ("–x" hits). The indicated mask locations (arrows) are used to reduce these rays. Similar plots are made for hard bremsstrahlung (particles having 1% to 80% of the full beam energy) and for rays due to Coulomb scattering. The positions and apertures of our chosen masking solution are summarized in Table 4-19.

The masking scheme adopted essentially eliminates rays from the higher-pressure upstream arc regions 60 m from the IP in each ring. Some of the remaining rays—due to soft bremsstrahlung interactions—are illustrated in Figs. 4-66a (+x) and 4-66b (–x). Some of these soft bremsstrahlung rays remain inside the beam-stay-clear envelope until they are well inside the IP region; their rate is controlled by maintaining a low pressure in the region immediately upstream of the IP. The required extent of the low-pressure region in each ring was selected based on an examination of the source points of the rays that deposit energy near the IP. Figure 4-67 shows, for each ring, the distribution of energy incident on the bare beam pipe (the location most effective in producing background in the silicon vertex detector) as a function of upstream distance from the IP where the lost particles were produced. Based on these results, the low-pressure region in the HER is maintained until 3 m from the IP, and that for the LER until 2 m from the IP. The resulting hit rates and energy deposits near the IP are summarized in Table 4-20.

EGS is used to model the effects of rays that strike the detector close to the IP (within 3 m for the HEB and 2 m for the LEB). In this case, the EGS simulation includes not only the geometry and material type of the beam pipe, masks, magnets, and detector components, but the IR optics and detector magnetic fields. The probability of a DECAY TURTLE ray being used in the simulation is determined by its "weight," which includes the effects of the appropriate cross sections for bremsstrahlung and Coulomb interactions and the pressure at the point where the parent ray interacted.

Calculations make use of the OBJEGS interface to EGS [Hearty, 1991], which allows the geometry to be specified in a straightforward, user-friendly way. There is, however, a restriction in OBJEGS that requires our model of the detector and the IR to be constructed from cylinders parallel to, and centered on, the z-axis. Thus, the geometry is specified in terms of the extent in z and the inner and outer radii of each object (see Fig. 4-68). Because the actual synchrotron masks are not cylindrically symmetric, we use two variants of the geometry (details of which are shown in Figs. 4-69a and 4-69b). The +x variant (Fig. 4-69a) is used to model the LEB mask side and the –x variant (Fig. 4-69b) is used to model the HEB mask side. As most stray particles strike near the

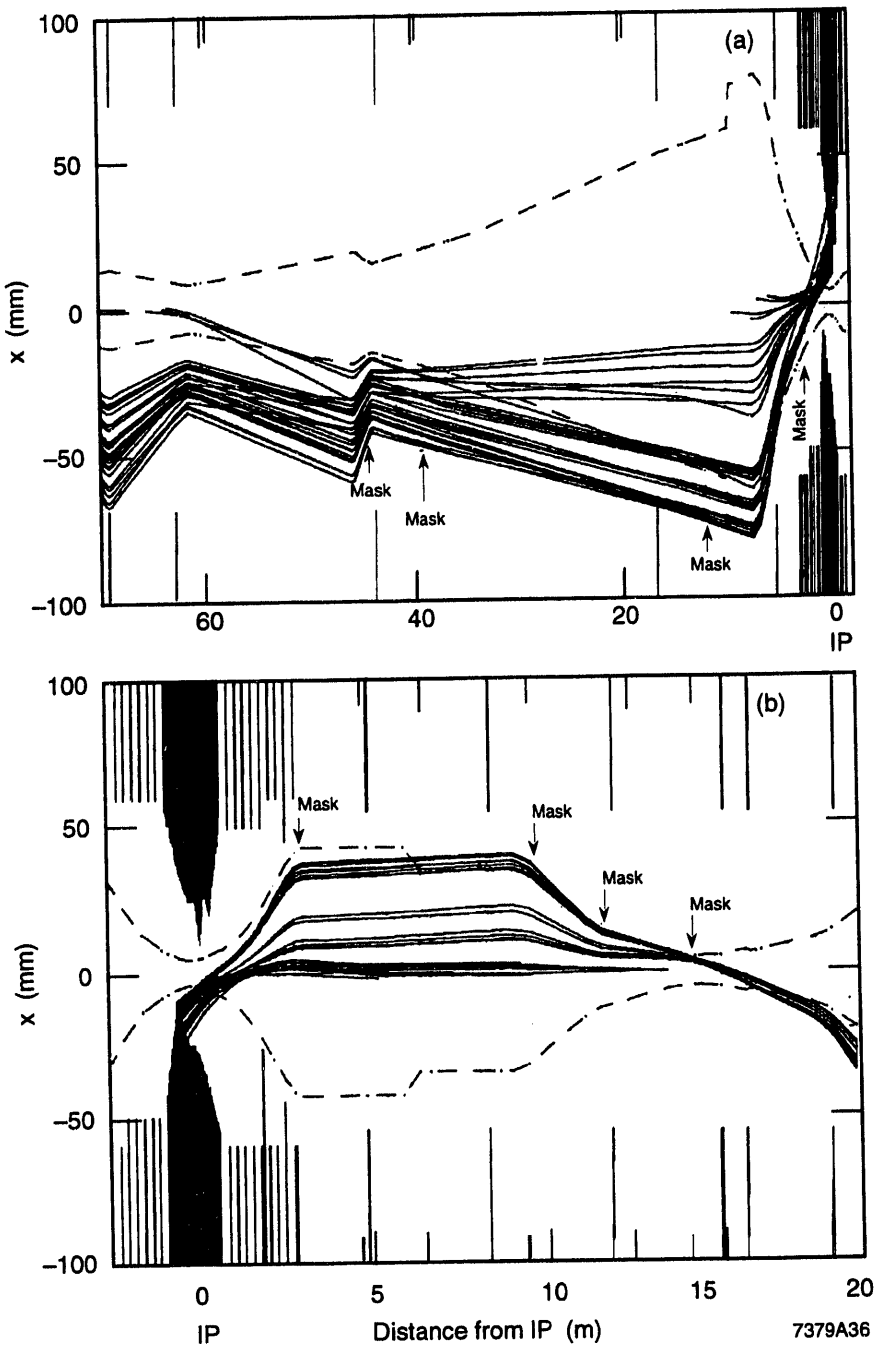

Fig. 4-65. Trajectories of off-energy electrons from soft bremsstrahlung interactions without upstream masking that strike (a) the +x side (side with the LEB synchrotron mask) for the HEB and (b) the –x side for the LEB. The vertical scale gives the distance from the nominal beam trajectory in mm, and the horizontal scale gives the distance from the IP in meters. The vertical lines are the scoring apertures in DECAY TURTLE that approximate the beam pipe aperture. The dashed lines represent the beam-stay-clear envelope; the beam pipe itself and all masks must remain outside this boundary. Arrows indicate locations where masks that would eliminate many of these rays can be placed.

Table 4-19. Elliptical mask locations and apertures.

Beamline	Distance upstream of IP (m)	x aperture (cm)	y aperture (cm)
HEB	44.28	1.55	1.00
HEB	39.45	2.00	1.00
HEB	12.05	5.75	1.87
HEB	2.80	1.96	3.70
LEB	21.80	3.00	1.00
LEB	15.13	1.00	1.00
LEB	12.29	1.30	1.00
LEB	10.06	3.30	1.00
LEB	3.30	4.30	1.90

Table 4-20. Hit rates and (photon + electron) energy deposited near the IP.

Location	LEB rate (hits/μs)	LEB energy deposit (GeV/μs)	HEB rate (hits/μs)	HEB energy deposit (GeV/μs)
$+x$ beam pipe	0.007	0.002	0.074	0.296
$-x$ beam pipe	0.207	0.350	0.0009	0.0003
LEB mask	0.936	0.671	0.157	1.052
HEB mask	0.288	0.731	1.155	6.922

horizontal plane, this approach gives a reasonably accurate model of the masking and detector geometry.

Because the actual layout of the IR and the corresponding model used by DECAY TURTLE are *not* cylindrically symmetric about the z-axis, some procedure for mapping DECAY TURTLE rays to the OBJEGS geometry must be defined. We do this by making the DECAY TURTLE geometry closely follow the EGS geometry in the x-z plane. Masks in DECAY TURTLE are infinite planes perpendicular to the beam axis, with elliptical holes that define their aperture. Hits on the DECAY TURTLE planes are tracked backwards in the OBJEGS geometry until their entrance point is found. An example of this mapping procedure is given in Fig. 4-70.

The EGS calculation determines the number of photons and electrons entering, and the energy deposited in, each object. Electrons are counted *each time* they loop through an object in the solenoid field. For this reason, the drift chamber is divided into a series

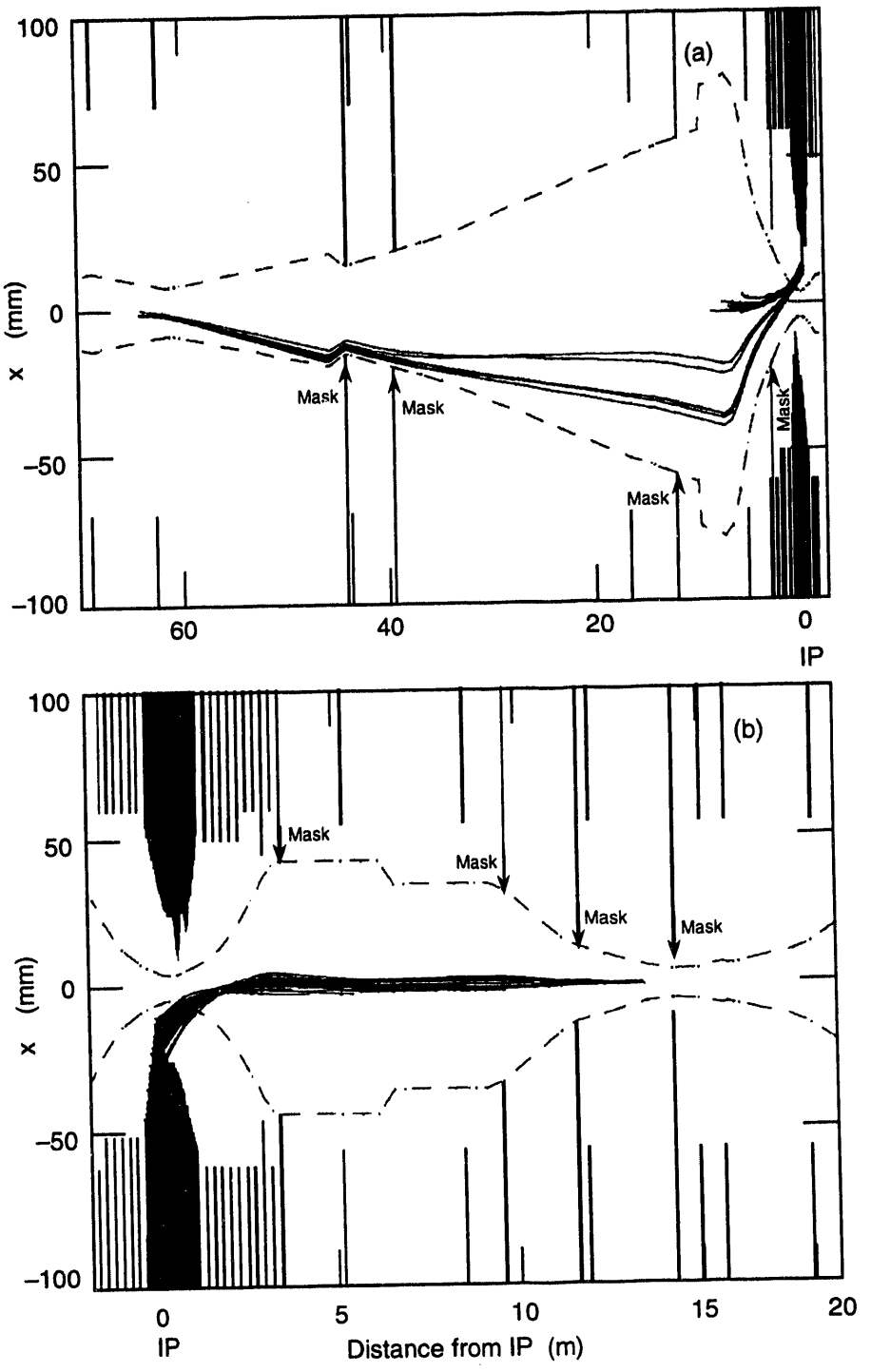

Fig. 4-66. Trajectories of off-energy electrons from soft bremsstrahlung interactions with upstream masking that strike (a) the +x side (side with the LEB synchrotron mask) for the HEB and (b) the –x side for the LEB. The vertical scale gives the distance from the nominal beam trajectory in mm, and the horizontal scale gives the distance from the IP in meters. Note that it is not possible to eliminate rays that remain within the beam-stay-clear aperture (see caption to Fig. 4-65).

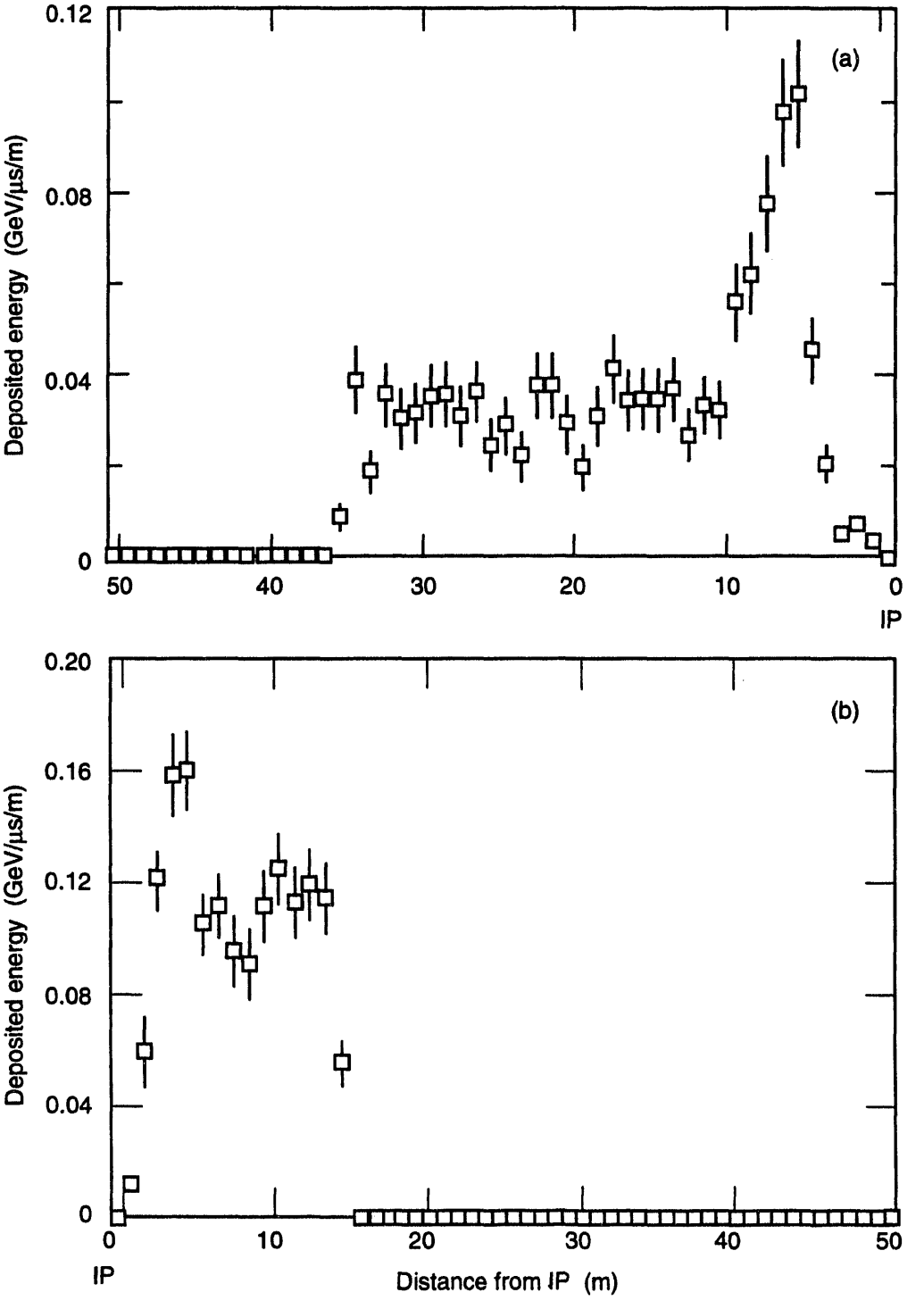

Fig. 4-67. Energy incident on the bare beam pipe as function of the distance from the IP at which the parent beam particle interacted, (a) HEB and (b) LEB. These results are normalized to a beamline pressure of 1 nTorr.

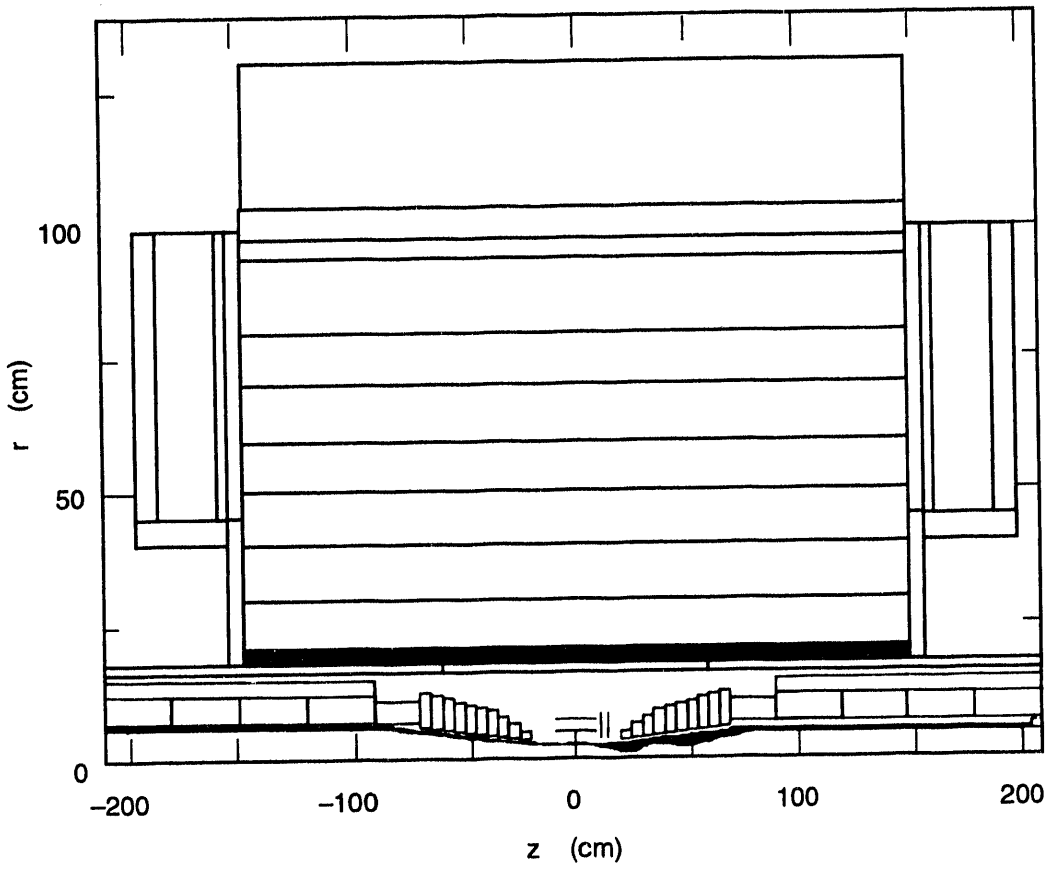

Fig. 4-68. Overview of OBJEGS geometry (corresponding to the LEB synchrotron mask version) used to model the detector and IR optics for the EGS simulations.

of thin cylinders ("scoring layers") so that the number of electron crossings at each radius is counted accurately. Electrons produced by photons in the gas are scored when they subsequently enter a new object (such as a drift chamber scoring layer). For purposes of estimating occupancies, multiple hits closer together than the nominal detector resolution are counted only once.

EGS returns the average energy deposited (E, in MeV) in each device *per ray incident on the IP*. This can be turned into the radiation dose (D, in rads/yr) using the relationship

$$D = (E/M) \times N \times F \tag{4-1}$$

where N is the number of rays that would be incident in a standard operating year (10^7 s), M is the mass of the device in kilograms, and F (= 1.60×10^{-11}) is the conversion factor from MeV/kg to rads. Equation 4-1 yields the expected average dose values, which are tabulated, along with the detector limits, in Table 4-21. (Aside from a very small region of silicon layer 1, less than 1% of its solid angle, the difference between the average and peak dose is about a factor of 3.)

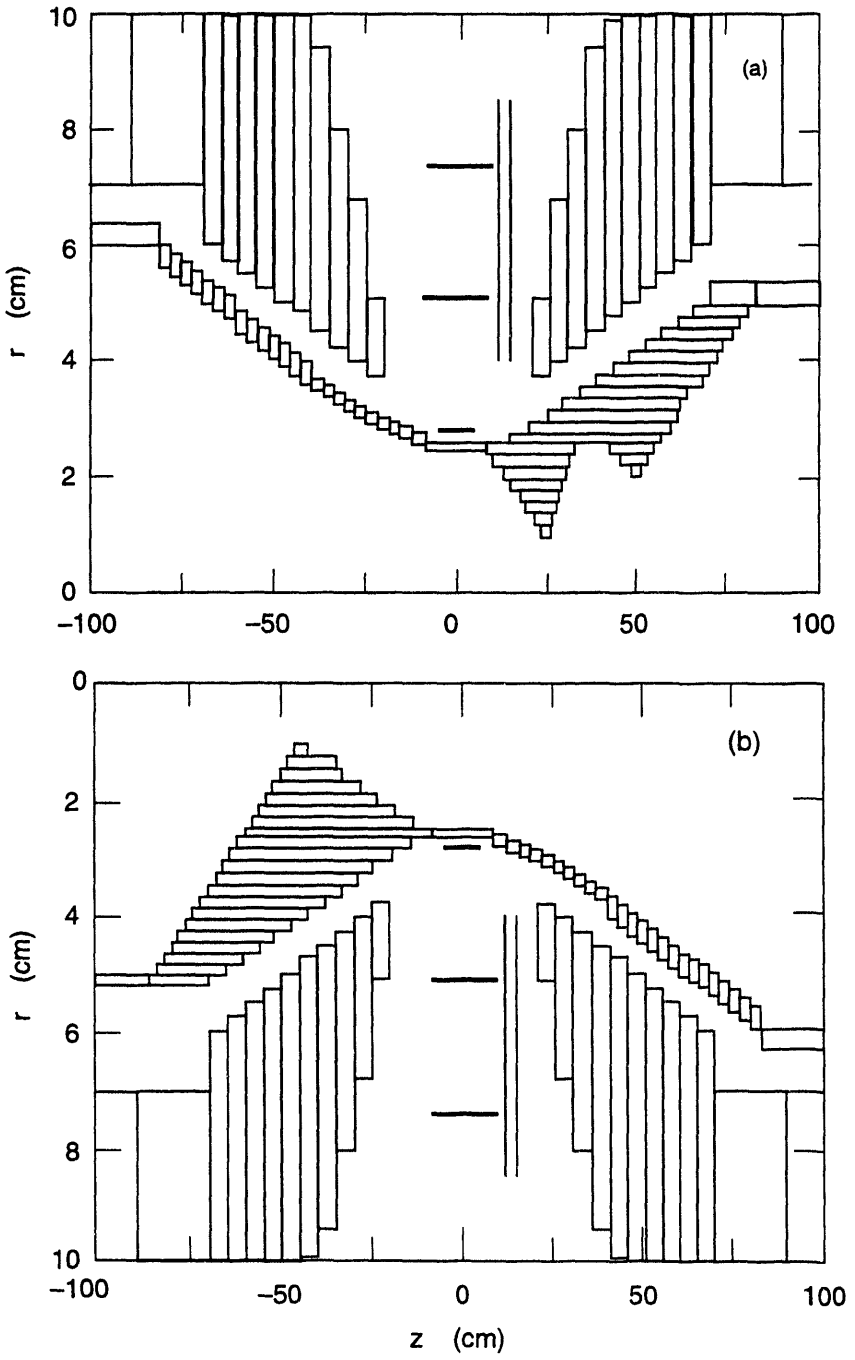

Fig. 4-69. (a) Magnified view of geometry used to model the +x (LEB synchrotron mask) side of the detector and IP; (b) magnified view of geometry used to model the −x (HEB synchrotron mask) side of the detector and IP.

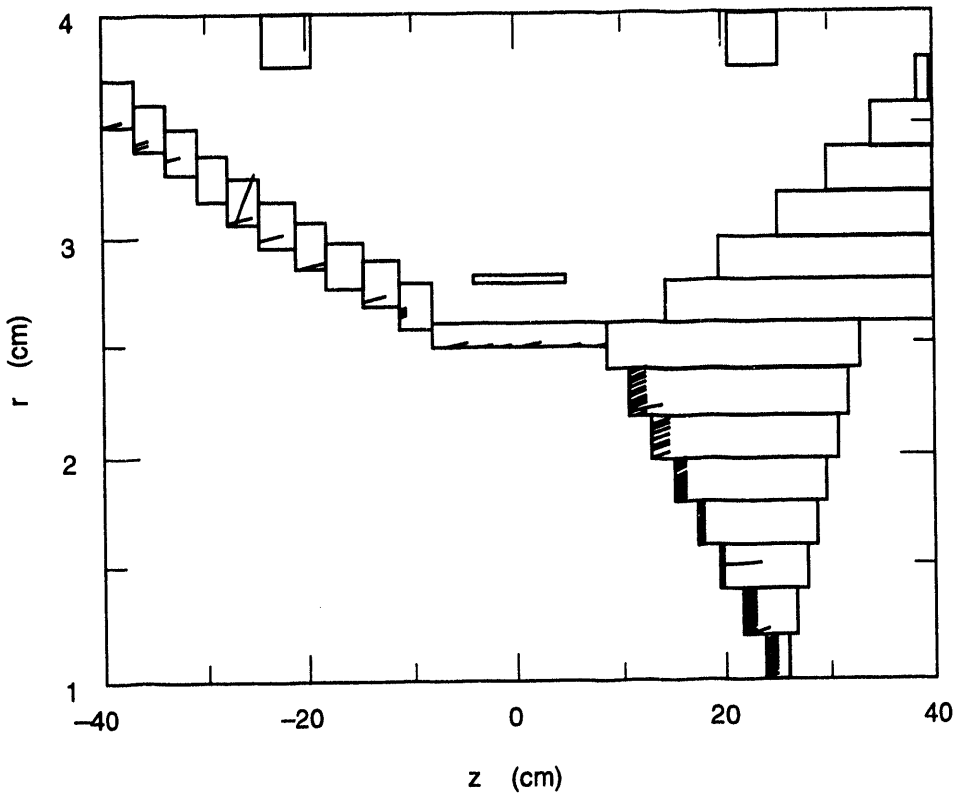

Fig. 4-70. Illustration of DECAY TURTLE to OBJEGS mapping. Lines show how much each ray was moved by the mapping from the point it hit a DECAY TURTLE mask to where it entered the OBJEGS element (see text).

The radiation damage analysis for the drift chamber is somewhat more complex. The appropriate quantity for estimating radiation damage is C/cm. We estimate the average charge per cm deposited on a wire in a year, Q, as follows

$$Q = \kappa\left(eG\frac{E}{E_i}\right)\left(\frac{N}{N_{\text{wire}}L_{\text{wire}}}\right) \tag{4-2}$$

where E is the average energy deposited in the chamber per incident ray, G is the gain (2×10^5), e is the electron charge (1.602×10^{-19} C), E_i is the energy needed to create an ion-pair (30 eV), N is the number of rays incident in a standard operating year, L_{wire} is the length of a signal wire, and N_{wire} is the number of wires. The factor κ corrects for charge deposited in the gas due to electrons created by photons interacting in the wires; it is needed because the effect of the wires themselves is not included explicitly in the EGS simulation. Charge deposited in the wires is not included because, if it is deposited in a signal wire, it does not get amplified (no gas multiplication) and, if it is deposited in a field wire, it does not get collected.

A Monte Carlo integration technique is used to compute κ by determining the average interaction cross section for the photon spectrum incident on the drift chamber as

Table 4-21. Annual radiation dose in silicon vertex detector, drift chamber, and CsI calorimeter.

Device	Average dose (krad/yr)	Acceptable limit[a] (krad/yr)	Safety factor
Silicon layer 1	10	200	20
Silicon layer 2	3.3	200	60
Silicon layer 3	0.8	200	250
CsI calorimeter (first 2 cm)	0.009	20	2200
Drift chamber	0.001[b]	0.1[b]	100

[a]For five-year operating life.
[b]C/cm/yr.

determined by EGS. We find $\kappa \approx 1.3$, which yields a charge deposition of $Q = 1.1 \times 10^{-3}$ C/cm/yr on an average wire. Some wires will receive more than the average dose due to the nonuniform distribution of background hits. There are three factors that concentrate the charge deposition compared with the average value:

- Peaking in ϕ ($\times 2$)
- Limited z range ($\times 1.3$)
- Inner wire-plane radius vs average chamber radius ($\times 1.5$)

There is no evidence of ϕ-z correlations in the simulations. However, the z distribution, though not peaked, only fills about three-quarters of the available range. Applying the above corrections, the worst wire receives about 0.004 C/cm/yr near $\phi = 0$. This is well below the allowed limit of 0.1 C/cm/yr.

Occupancies in the vertex detector, the calorimeter and the drift chamber are summarized in Table 4-22 in terms of the average number of hits per microsecond. The definition of a "hit" depends on the device being considered:

- For the silicon, a hit is defined as one or more electrons in a 50-μm longitudinal strip
- For the drift chamber, a hit is one or more electrons in a 1.9-cm-wide wire cell (the approximate cell size envisioned for the detector)
- For the calorimeter, a hit corresponds to depositing more than 10 MeV in a 5 cm $\times$ 5 cm CsI crystal

Based on the above results, we find that occupancy and radiation dose are well within acceptable limits for the silicon detector, the drift chamber, and the CsI calorimeter. It is worth noting here that vertex detectors based on silicon PIN-diode arrays (pixels) lead to more relaxed requirements for the accelerator. Due solely to geometry, for example, the occupancy limit can be increased to a few hundred particles/cm^2 per microsecond.

Table 4-22. Occupancy in selected detector elements.

Device	Average hits per μs	No. of channels	Occupancy limit[a]
Silicon 1	6	7000	140
Silicon 2	6	13,000	260
Silicon 3	4	18,000	360
Drift chamber (per layer)	0.4	70–300	7–30
Calorimeter	0.8	8000	80

[a]Limit is 2% per strip for silicon, 1% for calorimeter, 10% for drift chamber.

4.2.4 Detector Backgrounds from Bremsstrahlung at the IP

If radiation is produced when a particle in one beam scatters off a particle in the other beam, a process referred to as radiative Bhabha scattering, a particle with an energy much less than the nominal beam energy can result. Such low-energy particles can then be swept into the beam pipe inside the detector and contribute to the background in various detector elements. This process is similar to beam-gas bremsstrahlung, except that it occurs solely at the IP rather than being distributed throughout the beamline. For such events, the rate is proportional to luminosity (as opposed to the proportionality to the product of beam current and gas pressure that characterizes the beam-gas bremsstrahlung rate). We calculate the effects of the radiative Bhabha events using the same tools as for the bremsstrahlung events, that is, DECAY TURTLE is used to find where the particles hit inside the beam pipe, and OBJEGS is then used to generate the showers and to trace the shower debris into the detector elements themselves.

The general features of the radiative Bhabha process can be summarized as follows:

- The rate is large—at the design luminosity, the IP bremsstrahlung rate is roughly equivalent to the beam-gas bremsstrahlung rate in 3000 m of N_2 at 1 nTorr.
- Degraded particles with an energy less than about 1.5–2 GeV hit the beam pipe inside the detector, that is, within about 1.5 m of the IP. Higher-energy particles tend to hit farther from the IP. Particles hitting the end of B1 nearer the IP have very low energies; as they leave the IP they spiral around the 1-T field lines of the detector solenoid. When they enter B1, they see an overall 1.25-T field (the vector sum of the solenoidal field from the detector and the B1 dipole field), inclined at 37° to the horizontal, which guides them into the beam pipe wall.
- Because the generated showers are proportional to energy, the background source term increases with distance away from the IP. However, here the beam pipe is

better shielded and, in addition, the showers are directed away from the unshielded IP region.

- Rates from the HEB and the LEB are similar. Compared with the HEB, the LEB needs to radiate less energy to reach 1.5–2 GeV. Although, on average, the LEB particles have less energy, and hence smaller showers, these particles hit the beam pipe with larger angles and so penetrate somewhat more easily.
- The angular distribution of the degraded beam particles is not much wider than the natural angular spread of the beam, so we neglect the increase.

The main source of detector background comes from shower photons (with energies near the minimum of the absorption cross section) that interact via Compton scattering in the central drift chamber (CDC). The average photon energy is about 1.5 MeV, and about 95% of the photons have energies less than 5 MeV. These photons are not uniformly distributed but are concentrated in azimuth on the side where the degraded beam particles hit, and in z toward the ends of the chamber. Due to the concentration in z, the radiative Bhabha process does not contribute significantly to background in the silicon detectors.

The average energy of the Compton recoil electrons is about half the energy of the photons. These electrons typically spiral around the field lines of the solenoid; some range out, but some have ranges larger than the CDC size. The concentration of energy deposition in the CDC follows the initial photon concentration in azimuth, but the initial concentration in z tends to wash out.

For the actual calculation of the background rate in the CDC, radiative events from the HEB were generated at the IP in DECAY TURTLE and transported through the nearby HEB optical elements (B1 and Q1). Blinov [1988] gives the cross section for the radiative Bhabha process for the case where the minimum momentum transfer is limited by the size of the Gaussian beam.

Masks representing the beam pipe were placed at various z locations and the number of radiated particles hitting the masks was recorded, along with the particle energies and horizontal angles. Smooth fits were made to these distributions and the fits were then used to generate input rays for OBJEGS. To decrease the amount of computer time necessary to get reasonable statistics for energy deposition in the CDC, two techniques were used. First, energy deposition was scored in a layer 20 cm thick, whereas an actual cell is less than 2 cm thick. Second, we made use of a preliminary run in which photons were scored entering the inner wall of the CDC; these photons were then used repeatedly as input rays for a second calculation in order to accumulate photon interactions in the CDC gas.

The result for the HEB is 0.06 MeV/μs absorbed in the CDC, over its full 300-cm length, in the radial region between 20 and 40 cm. In a cell of 2.3 cm^2 transverse area, centered at 21 cm radius, the energy absorption rate is 0.174 eV/μs per cm of wire length. To correct for photon interactions in the wires, we increase the energy absorption by 30%, as discussed in Section 4.2.3. We calculate the average charge per cm deposited in the wires using Eq. 4-7, which yields a value of 0.002 C/cm/yr. Equivalent calculations for the LEB yield a similar value. Next we combine the HEB and LEB contributions,

taking account of the nonuniform distributions in ϕ and z to arrive at the maximum value of the aging parameter. Here we assume that the HEB and LEB distributions are the same. We also take the ϕ and z distributions to be independent, consistent with the OBJEGS results.

In ϕ, the maximum deposition is 3.1 times the average and the minimum is 0.4 times the average. In z we take 1.5 and 0.5 as the maximum and minimum factors for the distribution of energy deposition. (This is much smoother than the photon distribution, for which the factors are 4 and 0.) For the two beams, the ϕ peaks are on opposite sides of the CDC and the z peaks are at opposite ends. Taking the overall ϕ-z peaking factor as 5, the final result is a maximum charge deposition of 0.009 C/cm/yr, or about a factor of 11 below our maximum acceptable level of 0.5 C/cm over a five-year operating lifetime.

We conclude that this background mechanism is at an acceptably low level without any increase in beam pipe shielding. For completeness, we also examined the elastic Bhabha scattering process. We find that it contributes background levels much smaller than the other processes we have considered, and thus conclude that it is not an issue.

4.2.5 Summary

The PEP-II lattice and masking designs produce detector synchrotron radiation backgrounds that are more than 84 times below the specified limits for radiation damage and detector occupancy. The design allows most of the synchrotron radiation to pass through the IR without striking any nearby surfaces. Backgrounds are insensitive to the beam-particle distribution at large amplitudes, making the design insensitive to details of the beam-beam interaction. The primary masks, labeled HEB and LEB in Fig. 4-46, shield the detector beam pipe from direct synchrotron radiation. Detector backgrounds result from photons that scatter through the tips of these masks. A careful analysis of tip-scattered photons using a realistic (rounded) tip edge shows that the background levels are essentially the same as those of a mask with a perfect tip. Sources of synchrotron radiation farther upstream (beyond 5 m) were also investigated. These sources do not increase detector occupancy or radiation damage. A substantial amount of synchrotron radiation power strikes surfaces downstream of the IP. Photons that backscatter from these surfaces were studied and found not to contribute to detector background levels. The sensitivity of detector backgrounds to reasonable beam misalignments (±1 mm) is small (about a factor of two).

We made an exhaustive study of all radiation fans generated near the IP. Care was taken to ensure that all of this miscellaneous synchrotron radiation does not increase detector backgrounds. About 80% of the 70 kW of power is absorbed in downstream dumps far from the IP. This causes no increase in detector backgrounds, either from backscattered synchrotron radiation photons or from beam-gas interactions. To verify that the present IR design is compatible with a $\beta_y^* = 3$ cm configuration for the HER, backgrounds were also examined for that case. All the results reported here remain the same, except that the backgrounds and synchrotron radiation power values associated with the HEB increase by a factor of 1.5 (that is, they scale with the beam current), which is not of concern. As noted earlier, the thermal designs for the IR masks reported in Section 5.2.7 are based on the higher-current case to ensure a conservative solution.

A detailed study of lost-particle backgrounds in the detector was also carried out to simulate the detector backgrounds due to beam-gas interactions at PEP-II. All devices are found to be well within acceptable limits for both average radiation damage and average occupancy, having typical safety factors relative to conservative limits of more than 20 for a five-year operating life. We have also examined the effects of the radiative Bhabha process and find it gives acceptably low backgrounds.

4.3 COLLECTIVE EFFECTS

In Chapter 3 we discussed the alternatives that might be considered in the design of a high-luminosity *B* factory, and indicated the reasons for the choices we have made for PEP-II. The lattice design presented in Section 4.1 is based on these choices. Having fixed these parameters, it is necessary to investigate the influence of the various intensity-dependent effects on the actual performance of the accelerator.

The main parameters we must achieve in PEP-II include:

- Beam energies of 9 GeV (HER) and 3.1 GeV (LER)
- Beam currents of 0.99 A (HER) and 2.14 A (LER)
- Bunch length of 1 cm
- Beam emittances of approximately 50 nm·rad (HER) and 66 nm·rad (LER)
- Beam energy spread of $\sigma_E/E \leq 1 \times 10^{-3}$

In terms of collective effects, the dominant issue is the relatively high beam current that must be supported in each ring. As was discussed briefly in Chapter 3, and as will be covered in more detail in Section 4.4, this constraint is associated mainly with the fact that the beam-beam tune shift parameter is taken to be a design limit, which means that the high luminosity must come mainly from the combined benefits of low beta functions and high currents.

A beam circulating in a storage ring interacts with its surroundings electromagnetically by inducing image currents in the walls of the vacuum chamber and other "visible" structures, such as beam position monitor (BPM) electrodes, kickers, RF cavities, bellows, valves, etc. This interaction leads, in turn, to time-varying electromagnetic fields that act on the beam and can give rise to instabilities. In most electron-positron colliders, single-bunch effects are the primary concern. The current threshold for these effects is defined by the ring impedance at high frequencies, $f > 8$ GHz, which correspond to wavelengths λ comparable to or less than the bunch length, say, $\lambda \leq 4\sigma_\ell$.

The issues with which we must deal for PEP-II fall into the broad categories of single-bunch and multibunch phenomena. Single-bunch phenomena include:

- Longitudinal and transverse single-bunch instabilities
- Beam loss from intrabeam (Touschek) scattering
- Beam loss from beam-beam (Bhabha) scattering
- Higher-order-mode (HOM) heating

Beam-gas scattering, though actually a single-particle effect, can be included in this category, as can the phenomenon of ion trapping in the electron beam.

For the PEP-II, however, the main concern is from coupled-bunch instabilities, where different bunches "communicate" through the narrow-band (high-Q) ring impedances. That is, wakefields deposited in various high-Q resonant objects can influence the motion of following bunches and can cause the motion to become unstable if the beam currents are too high. To effectively couple the bunch motion, HOMs must have a damping time $\tau \approx 2Q/\omega$ longer than the bunch spacing s_B/c. For modes with $Q \leq 100$, this restricts the frequencies $f \leq 8$ GHz. The frequency limit is lower for smaller Q. This effect is one of the most serious issues for the PEP-II design.

For PEP-II, we have opted for a situation in which the nominal beam currents of 0.99 A in the HER and 2.14 A in the LER are distributed in many (1658) bunches. Our reasoning is as follows: The multibunch instabilities are mainly driven by the total beam current, with little regard to how it is distributed in the ring. That is, once the bunch separation is small enough for bunches to fully see wakefields left by preceding bunches, the growth rates are independent of the details of the bunch pattern. Thus, if a high beam current is needed, coupled-bunch instabilities become almost unavoidable. If we choose a relatively small number of bunches to make up the high current, we do little to improve the situation with regard to coupled-bunch instabilities and simply make the single-bunch phenomena harder to manage—in effect requiring the accelerator designers to wage a two-front war. (This usually translates into impedance requirements for the ring that are difficult to meet.) It is true, of course, that the bandwidth requirement of a feedback system to deal with coupled-bunch motion is eased if the bunch spacing increases. However, we do not feel that this is a major limitation (see Section 5.6 for details), and it should not dominate the design decisions.

Given our decision to utilize many bunches, the parameters of the single bunches (emittances, bunch length, intensity) are not unusual—they are in the parameter regime in which PEP and many other colliders have run successfully for many years. This, in turn, means that heroic efforts at impedance reduction are not required to avoid problems with single-bunch effects.

4.3.1 Single-Bunch Issues

In this section, we focus on the issues of single-bunch instability thresholds, beam lifetime, and heating of the chamber due to parasitic HOM losses. We also discuss the issue of ion trapping and the means available to avoid or eliminate it. Before beginning, we digress briefly to define the beam impedances that drive the various instabilities.

4.3.1.1 Impedances. Beam instabilities can occur in either the longitudinal or transverse phase planes. Longitudinal instabilities are driven by voltages induced via interactions of the beam with its environment. The strength of the interaction can be characterized by the ring impedance $Z_{\|}(\omega)$, in ohms, which is defined by

$$V_{\|}(\omega) = -Z_{\|}(\omega)\, I_b(\omega) \tag{4-3}$$

where $V_{\|}(\omega)$ is the longitudinal voltage induced in the beam per turn arising from a modulation of the beam current $I_b(\omega)$ at some particular angular frequency ω.

Transverse instabilities arise from the transverse dipole wakefield, which gives a force that increases linearly with transverse distance from the electromagnetic center of the vacuum chamber and is antisymmetric in sign about that center. The transverse impedance (in Ω/m) is defined by

$$Z_{\perp}(\omega) = \frac{-i\int_0^{2\pi R} F_{\perp}(\omega,s)\,ds}{e\Delta I_b(\omega)} \tag{4-4}$$

where $F_{\perp}$ is the transverse force, integrated over one turn, experienced by a charge e having transverse displacement Δ. Explicitly, $F_{\perp}$ is given by

$$F_{\perp} = e\hat{\theta}(E_{\theta} + B_r) + e\hat{r}(E_r - B_{\theta}) \tag{4-5}$$

In a typical storage ring, the impedance seen by the beam can be loosely characterized as being either broadband or narrow-band. Sharp discontinuities in the vacuum chamber act as local sources of wakefields. These fields have a short time duration, which means that they include many frequency components, and we refer to the corresponding impedance as broadband.

The main contribution to the narrow-band impedance comes from the RF cavities. The approach we have adopted for PEP-II, using a small number of damped RF cavities, serves to substantially reduce the narrow-band impedance. Calculations and measurements with a prototype low-power cavity (see Section 5.5) have confirmed that the strongest HOMs of the damped cavities can be reduced to $Q \leq 70$ without degradation of the fundamental mode. For the impedance estimates we use results of the code URMEL from Corlett [1992], which are in good agreement with the measured HOM spectrum [Byrd, 1993] given in Table 4-23.

The narrow-band longitudinal impedance of a cavity for low frequencies $\omega < \omega_{max}$ may be described as the sum over the modes

$$Z(\omega) = i\sum_{\omega_m<\omega_{max}} k_{\ell}\left[\frac{1}{(\omega-\omega_m)+i(\omega_m/2Q_m)} + \frac{1}{(\omega+\omega_m)+i(\omega_m/2Q_m)}\right] \tag{4-6}$$

For high frequencies $\omega > \omega_{max}$, a broadband high-frequency tail should be added. We can express the overall impedance as a series expansion over $\sqrt{\omega}$:

$$Z(\omega) = -i\frac{L\omega}{c^2} + R_W\sqrt{\omega} + R_{\Omega} + (1+i)Z_{cav}\sqrt{\frac{\omega_0}{\omega}} + \cdots \tag{4-7}$$

where the first term describes an inductive impedance, the second term represents the resistive-wall impedance, the third term corresponds to a constant resistivity, and the last describes the high-frequency impedance tail of the RF cavities. This part of the

Table 4-23. Monopole modes below cutoff.

f (MHz)	k_ℓ (V/pC)	R/Q (Ω)	Q
476	0.1694	113.2	30000
758	0.107	44.97	28
1016	0.000	0.006	246
1285	0.031	7.68	66
1296	0.027	6.57	907
1588	0.025	5.06	178
1821	0.000	0.06	295
2109	0.023	3.52	233
2168	0.000	0.01	201
2253	0.008	1.21	500

impedance rolls off as $\omega^{-1/2}$, in accordance with simulations and the Dôme-Lawson analytic result for a pillbox cavity with attached beam tubes.

The "shunt impedance" of a mode, R_n, gives the peak value of Re $Z(\omega)$ at the resonance. The loss factor of a mode is related to R/Q by

$$k_\ell = \frac{\omega}{2}\left(\frac{R}{Q}\right) \tag{4-8}$$

The total loss factor is given by a convolution of the impedance with the bunch spectrum $\rho(\omega)$:

$$k_{tot} = \frac{2}{cZ_0}\int_{-\infty}^{\infty} Z(\omega)\rho^2(\omega/c)\,d\omega \tag{4-9}$$

According to TBCI, a reentrant RF cavity with the dimensions shown in Fig. 5-93 has a loss factor $k_\ell = 0.515$ V/pC.

The parameter Z_{cav} can be defined by comparing the total loss calculated from Eqs. 4-6 to 4-8 with that given by TBCI. The parameter ω_{max} is somewhat arbitrary, in the sense that results are not sensitive to its value. For $f_{max} = 1260$ MHz, $Z_{cav} = 5.31$ kΩ.

RF Cavity. The wakefield of a cavity with an impedance of the type given by Eqs. 4-6 and 4-7 reproduces the wakefield of a cavity given by TBCI, Fig. 4-71. Indeed, an impedance of this form is actually a general expression that satisfies the conditions of causality and has the correct analytic properties.

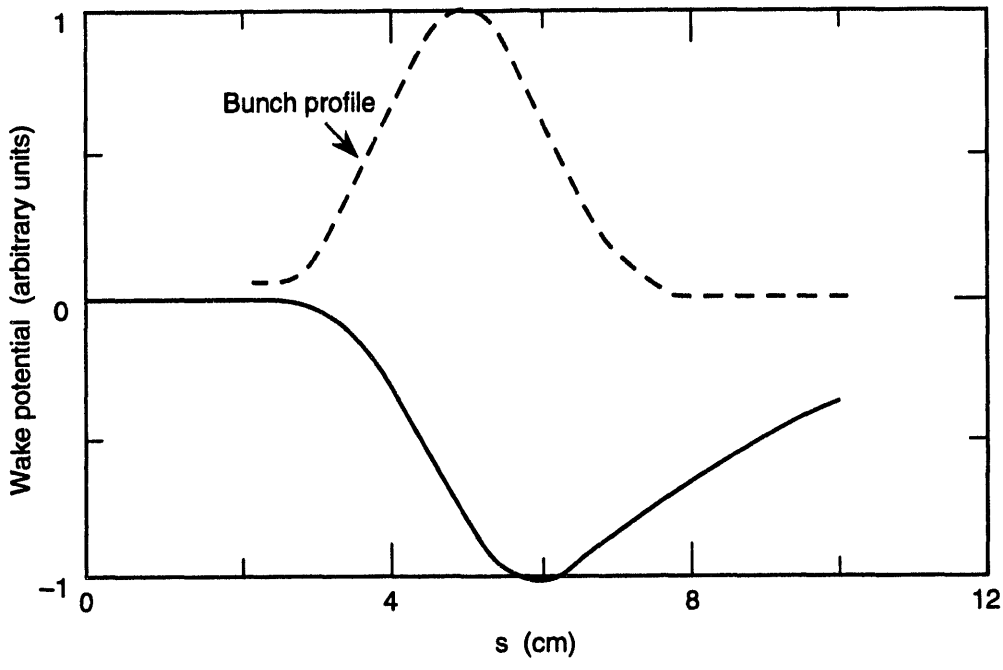

Fig. 4-71. Wakefield of PEP-II RF cavity calculated with TBCI.

The low-frequency limit $\omega \ll \omega_n$ of the narrow-band impedance (Eq. 4-6) is inductive; that is, as $\omega \to 0$,

$$Z(\omega) \to -i\frac{L\omega}{c^2} \tag{4-10}$$

where

$$L = \frac{4\pi}{Z_0}\sum_n \left(\frac{R}{Q}\right)_n \frac{c}{\omega_n} \tag{4-11}$$

(The sum in Eq. 4-11 should not include the fundamental mode of the cavity.) Note that the ratio $(Z/n)_0$ in this limit is independent of frequency and often is used as a single parameter describing the impedance. In our case, $(Z/n)_0 = 9.3\ \text{m}\Omega$ for one RF cavity.

At high frequencies, the narrow-band impedance is capacitive. It rolls off as ω^{-2} and is thus small compared with the high-frequency tail given by Eq. 4-7, which is the quantity relevant for single-bunch stability:

$$\frac{Z(n)}{n} = (1+i)\frac{Z_{\text{cav}}}{n^{3/2}}. \tag{4-12}$$

With Z_{cav} and (Z/n) as given above, this can be written as

$$\frac{Z(n)}{n} = (1+i)\left(\frac{Z}{n}\right)_0 \left(\frac{c}{\omega b_{\text{eff}}}\right)^{3/2} \tag{4-13}$$

where $b_{\text{eff}} = 4.96$ cm. At the bunch frequencies $\omega/c \approx 1/\sigma_\ell$, this is very close to the SPEAR-scaling relationship

$$Z/n \propto \left(\frac{\sigma_\ell}{b}\right)^{1.68} \tag{4-14}$$

where b is taken as an effective beam-pipe radius.

The impedance of the cavities (Eq. 4-12) rolls off as $n^{-3/2}$ and is thus small at high frequencies. Other components of the impedance, such as the resistive-wall impedance

$$\frac{Z(n)}{n} = Z_0\left(\frac{1-i}{2}\right)\frac{\delta}{b} \tag{4-15}$$

where δ is the skin depth, and the inductive impedance of the ring, $Z/n = -iL/c^2$, roll off more slowly and may become important in this high-frequency limit.

Resistive Wall. The PEP-II beam pipe is copper with a roughly elliptical cross section having half-axes of dimension 4.5×2.5 cm in the arcs (total length 6×243.2 m) and round stainless-steel pipe with radius 4.6 cm in the straight sections (total length 6×123.4 m). The average resistive-wall impedance is [J. Corlett, 1992]

$$\left\langle \frac{Z}{n} \right\rangle_{\text{RW}} = (1-i)\frac{2.55}{\sqrt{n}} \tag{4-16}$$

The change in conductivity going from copper to stainless steel produces some additional impedance that can be described as a change of the beam-pipe radius by a skin depth of the stainless-steel pipe, δ_{SS}. This results in an impedance

$$Z \simeq \frac{Z_0}{\pi}\frac{\delta_{SS}}{b} \tag{4-17}$$

which is negligibly small.

At the bunch frequencies $n \approx R/\sigma_\ell = 3.5 \times 10^4$, the resistive-wall impedance is larger than the total impedance of 10 RF cavities by a factor of 1.5, whereas at the bunch spacing frequencies $n \approx s_B/\sigma_\ell = 120$, it is smaller by a factor of 5.5×10^{-3}. Because Eq. 4-16 scales as $\sigma_\ell^{1/2}$, we might expect that SPEAR-scaling will not be valid for the short PEP-II bunches.

The rest of the impedance comes from the many small impedance-generating elements of the ring. A list of some of these elements is given in Table 4-24 for a half-sextant of the ring.

Miscellaneous Elements. The stainless-steel vacuum pipe in the straight sections is connected by two tapers per sextant, or 12 tapers per ring, to the octagonal copper tubes in the arcs. The beam pipe is separated from the vacuum DIP chamber by a slotted 5-mm-thick screen. There are six rows of longitudinal slots in the wall with 10 slots per meter, each slot 9 cm long and 0.2 cm wide. The total number of slots in the HER is about 60,000. Each cell has a shielded bellows at each quadrupole. There are also two

Table 4-24. Average number of the impedance-generating elements in a half-sextant (1/12) of the high-energy ring.

Component	Number of items
Flanges	60
BPMs	12
Vacuum ports	24
Bellows	24
Valves	1
Tapers	1
Slots of DIP screen	3000

vacuum ports per cell at each quadrupole for the lumped vacuum pumps. A 4-button design has been chosen for the BPM, with a button diameter of 1 cm and a 1-mm groove around each button. There are 18 valves in the HER (two valves per sextant at the ends of the arc sections, two valves in each RF section, and two valves in the interaction region). For the impedance estimate, flanges are taken simply as shallow grooves. Additional impedance-generating elements, not included in Table 4-24, include three kickers for the feedback system, several collimators, the injection port, and the various masks in the IR. Some special elements such as diagnostic devices, which are not considered at the present time, may be added later. These will not have a noticeable effect on the total impedance. Details on the vacuum chamber hardware may be found in Section 5.2. We note here that special efforts have been made in designing elements of the vacuum system to have minimum impedance by using shielded bellows, by tapering all shape transitions, by screening the vacuum ports and the pumps, etc.

The impedance of the ring may be estimated as the sum of the impedances of the individual elements. (Any cross-talk between elements tends to decrease the total impedance, making such an estimate conservative.) Most of these elements are discontinuities having resonant frequencies much higher than the frequencies within the bunch spectrum. They give rise, therefore, to a predominantly inductive impedance. This was confirmed by calculating wakefields of these elements with the code TBCI. For example, the wakefield of a shielded bellows, modeled as several shallow tapers, made up from a synchrotron mask and sliding contacts, is shown in Fig. 4-72. The wakefield of a σ_ℓ = 1 cm bunch behaves like the derivative of the bunch density, as is typical for an inductive impedance. The maximum value of the wakefield, $W_{\max}$, is related to the inductance L of the bellows by

$$W_{\max} = \frac{L}{\sigma_\ell^2 \sqrt{2\pi e}} \tag{4-18}$$

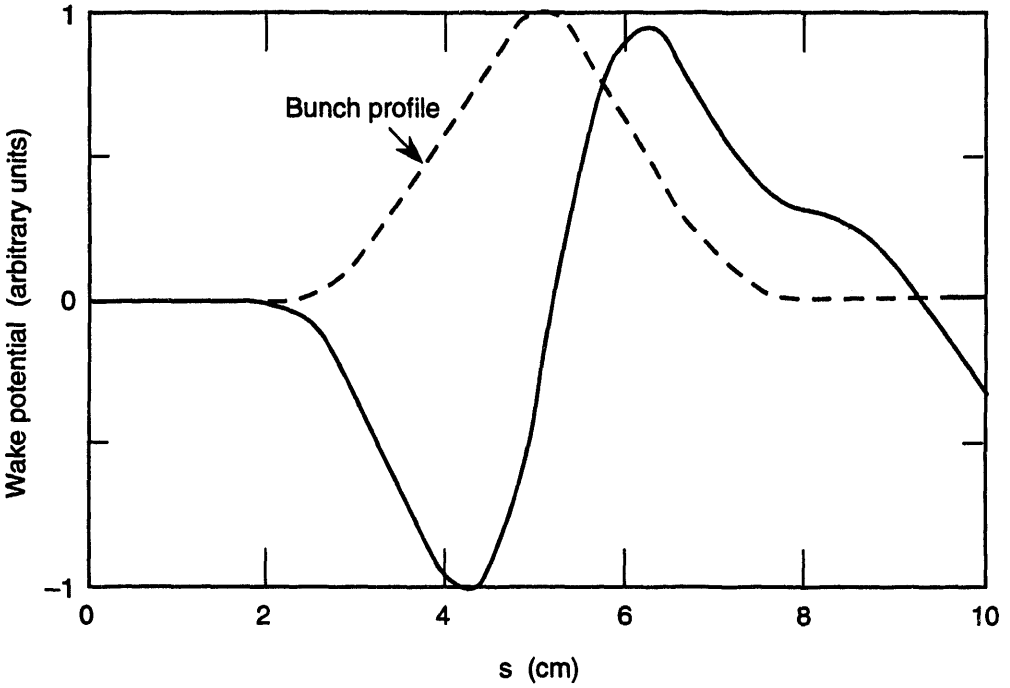

Fig. 4-72. Wakefield of PEP-II shielded bellows calculated with TBCI.

TBCI gives $W_{max} = 0.0121$ cm^{-1}, which correspond to an inductance $L = 0.05$ cm per bellows. Additional impedance is generated by the slots between the sliding fingers of the bellows. The impedance of a rectangular slot having a width w has been found analytically [Kurennoy, 1991] to be

$$\frac{Z(n)}{n} = -\frac{i}{3}\frac{Z_0}{4\pi^2}\frac{w^3}{Rb^2}. \tag{4-19}$$

The total contribution of the 24 slots per bellows, averaged over the azimuth of b, $2.5 < b < 4.5$ cm, is $L = 6 \times 10^{-3}$ cm. The total inductance of a bellows is 5.6×10^{-2} cm, or

$$\frac{Z}{n} = -i\,30\left(\frac{L}{R}\right) = -i\,1.4 \times 10^{-2}\ \Omega \tag{4-20}$$

for 288 bellows in the ring.

For purely inductive elements, the loss factor is zero. Indeed, the loss factor of a bellows given by TBCI is small, $k_\ell = 2.2 \times 10^{-3}$ V/pC per bellows, and strongly depends on the bunch length. We take this loss into account as a constant resistance that would give the same loss

$$R_\Omega = \frac{Z_0\sigma_\ell}{2\sqrt{\pi}}k_\ell = 67.4\ \Omega/\text{ring} \tag{4-21}$$

The loss factor of a hole is a second-order effect (proportional to w^5 and completely negligible). Measurements of the loss factor of a 6-in. PEP valve gave $k_\ell = 0.006$ V/pC,

which corresponds to $R_\Omega = 8.5\ \Omega$ per ring. The loss at PEP-II may be higher by $\sqrt{2}$ due to its shorter bunch length. We can similarly estimate the impedance of the vacuum ports, shielded by ten 14×0.2 cm slots, giving $Z/n = 5 \times 10^{-5}\ \Omega$ for 24 ports in the ring.)

The DIP screen slots can be modeled in the same way, giving a total contribution per ring of $Z/n = -i\ 0.03\ \Omega$.

For an impedance estimate, a flange can be modeled as a shallow cavity with inner and outer radii a, b, where $b - a \ll a$. For small gaps, $g \ll a$, the inductance [Bane, 1988] is

$$L = 2g\left(\frac{b-a}{a}\right) \tag{4-22}$$

If we take $a = 3$ cm for the inner radius, $b = a + 0.1$ cm for the outer radius, and a cavity gap of 0.25 mm, then $Z/n = -i1.1 \times 10^{-3}\ \Omega$ for one ring. TBCI gives the loss factor for such a cavity as $k_\ell = 2.46 \times 10^{-5}$ V/pC. The total contribution of the 576 flanges in one ring is $k_\ell = 0.018$ V/pC.

The impedance of a taper scales with the angle as $\sqrt{2\theta/\pi}$. The angle of the taper should be small compared with the ratio σ_ℓ/b. We chose 10° tapers. Modeling the transitions between straight sections and arcs together as a pair of tapers (the first a taper out, the second a taper in) has also been considered. This approach gives a more realistic result than simply adding the losses of two tapers independently. The loss of a pair of tapers calculated for the azimuthally symmetric pair and then multiplied by the azimuthal filling factor $4.5/(4.5 + 2.5) = 0.643$ is $k_\ell = 2.0 \times 10^{-2}$ V/pC. That gives $k_\ell = 0.125$ V/pC for 12 tapers in a ring, corresponding to $R_\Omega = 29.5\ \Omega$. The s-dependence of the wakefield corresponds to that of an inductive impedance and is similar to the wakefield of a bellows with $W_{\max} = 0.348$ V/pC. The inductance of the 12 tapers is $L = 11.46$ cm and gives

$$\mathrm{Im}\left[\frac{Z(n)}{n}\right] = 1.2 \times 10^{-2}\ \Omega$$

Some elements of the ring, such as feedback kickers and BPMs, have low-Q resonances at high frequencies, of the order of 10 GHz, that give an inductive tail at the bunch frequencies. Measurements of the beam impedance of a button electrode [Jacob et al., 1989] show resonances as summarized in Table 4-25. The low-frequency limit given by these modes, calculated from Eq. 4-11, is

$$\left(\frac{Z}{n}\right)_0 = -i \sum_n \left(\frac{R}{Q}\right)_n \frac{\omega_0}{\omega_n} \tag{4-23}$$

which gives $(Z/n) = 1.9 \times 10^{-7}\ \Omega$ per button. For 144 four-button BPMs, the total impedance is $(Z/n)_0 = 1.1 \times 10^{-4}\ \Omega$. The peak impedance at the resonance frequency of 3.3 GHz is $Z/n = 2.47 \times 10^{-6}\ \Omega$ per button, or $Z/n = 1.42 \times 10^{-3}\ \Omega$ per ring. This is completely negligible in comparison with, say, the resistive-wall impedance, which is $Z/n = 1.36 \times 10^{-2}\ \Omega$ at the bunch frequency $\omega = c/\sigma_\ell$ or $n = R/\sigma_\ell$. Hence, the resonant contribution of the BPMs can be neglected. The impedance of the BPMs, therefore, may be described as purely inductive. The inductance could alternatively be estimated by considering a number of holes with a diameter $w = 1$ mm equal to the diameter of the

Table 4-25. Resonances of a button electrode.

f (GHz)	Q	R_s (Ω)
3.3	17	0.06
16.2	470	0.72
18.3	110	0.46

BPM gap and a total surface area equal to the surface area of the gap. Impedance of such a hole is

$$\frac{Z(n)}{n} = -i\left(\frac{Z_0}{48\pi^2}\right)\left(\frac{w^3}{Rb^2}\right) \tag{4-24}$$

giving $(Z/n) = -i\ 1.3 \times 10^{-4}\ \Omega$ for 144 BPMs. We take this more conservative estimate for the contribution to the total impedance budget.

The total loss factor of the 144 BPMs in the ring due to the resonant modes is $k_\ell = 0.20$ V/pC. It should be mentioned that the contribution of the original PEP BPMs to the loss factor was found to be below the accuracy of the measurements.

The impedance of the three kickers for the longitudinal feedback system can be described [Corlett, 1992] as a $Q = 7$ resonance at $f = 16.2$ GHz, with a shunt impedance of $R = 170\ \Omega$. Other modes have parameters given by the sum of the resonant modes listed in Table 4-26. The total loss factor of the feedback system is $k_\ell = 2.15$ V/pC, and, for comparison, the low-frequency limit is $(Z/n) = 3.4 \times 10^{-3}\ \Omega$.

Coherent synchrotron radiation may produce at its maximum value a noticeable impedance:

$$(Z/n)_{\max} = 300\left(\frac{b}{R}\right) \approx 0.04\ \Omega \tag{4-25}$$

Table 4-26. HOM modes of the PEP-II longitudinal feedback kickers.

f (GHz)	R/Q (Ω)
2.6	9.3
3.1	2.2
3.3	3.5
5.0	1.8

However, the threshold frequency is very high

$$\left(\frac{\omega\sigma_\ell}{c}\right)_{\text{thr}} \approx \left(\frac{\sigma_\ell}{R}\right)\left(\frac{\pi R}{2b}\right)^{3/2} = 37$$

and the effect is suppressed exponentially.

The IR within ±80 cm from the IP has been described as a three-dimensional system of tapers and the impedance has been estimated using TBCI with proper azimuthal averaging. The wakefield found by TBCI corresponds to an inductive impedance with $W_{\text{max}} = 0.62$ V/pC, giving an inductance of $L = 2$ cm and an impedance of $Z/n = 1.8 \times 10^{-3}$ Ω. The loss factor of this portion of the IR is $k_\ell = 0.059$ V/pC or $R_\Omega = 12.5$ Ω.

The impedance of crotches and the injection port must be similar to the impedance of the septa in the SLC damping rings; these have been investigated with MAFIA by Bane [1988] and shown to give an inductive impedance with $L = 2$ cm.

Fabrication errors and misalignments of the sections of the vacuum pipe can give additional impedance. For example, the misalignment Δ of two adjacent sections of beam pipe with a radius b results in a real impedance $(Z_0/\pi)(\Delta/b)$ and a reactive impedance with inductance $L = 6\Delta^2/b$. Five hundred joints with $\Delta = 1$ mm and $b = 5$ cm give an additional inductance of $L = 6$ cm, or $(Z/n)_0 = 0.005$ Ω. Tilting of the slots in the DIP screen by an angle θ with respect with the beam plane increases the impedance of a slot of length l and width w by a factor of $[1 + (l/w)\theta]$. This defines the tolerance of the tilt angle $\theta < w/l \approx 22$ mrad, which does not give substantial fabrication problems.

The total impedance of the ring is the sum of the impedance of the cavities (Eqs. 4-6 and 4-7), the resistive wall (Eq. 4-16), the constant resistance R_Ω representing losses in the mostly inductive components, and the inductive impedance $-i(Z/n)_0$. Contributions of the individual elements to the total inductive impedance $(Z/n)_0$ are given in Table 4-27.

With a "contingency" $Z(n)/n = 0.024$ Ω for the collimators, the total inductive impedance is $Z(n)/n = 0.10$ Ω.

The total longitudinal wake function can be calculated from the longitudinal impedance. It is shown in Fig. 4-73.

Transverse Impedance. The transverse impedance may be estimated as

$$Z_\perp = \frac{Z_\parallel c}{\omega b^2} \tag{4-26}$$

It rolls off with frequency faster than does the longitudinal impedance and is maximum at frequencies close to the cutoff frequency $\omega \approx c/b$.

4.3.1.2 Longitudinal Microwave Instability. The first instability we consider is the longitudinal microwave instability, sometimes referred to as turbulent bunch lengthening. This instability, which has been seen in numerous proton and electron storage rings, is not a "fatal" instability, in the sense that it does not lead to beam loss. Instead, the instability causes an increase in both the bunch length and the momentum spread of a bunched beam. Its threshold (peak) current is given by

Table 4-27. The PEP-II inductive impedance budget.

Component	Impedance (Ω)
BPMs	1.3×10^{-5}
Vacuum ports	5×10^{-5}
Bellows	1.4×10^{-2}
Flanges	1×10^{-3}
Valves	6×10^{-3}
Tapers	1.6×10^{-2}
DIP screen	3×10^{-2}
Feedback system	3.5×10^{-3}
Interaction region	2×10^{-3}
Injection, crotches	3.6×10^{-3}
Total	0.076

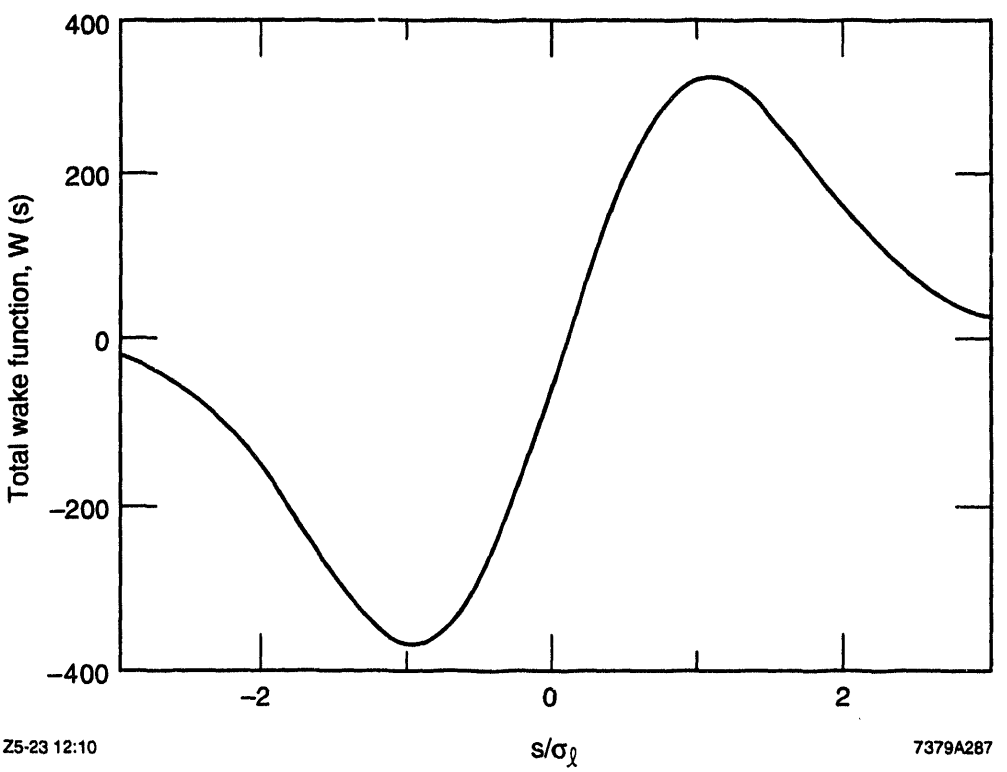

Fig. 4-73. Total longitudinal wakefield for PEP-II HER.

$$I_p = \frac{2\pi|\eta|\,(E/e)\,(\beta\sigma_p)^2}{\left|\frac{Z_{\|}}{n}\right|_{\text{eff}}} \tag{4-27}$$

where $|Z_{\|}/n|_{\text{eff}}$ is the effective broadband impedance of the ring and $\eta = \alpha - 1/\gamma^2$ is the phase-slip factor.

The average bunch current of the LER, 1.3 mA, corresponds to a 113-A peak current for a Gaussian bunch with $\sigma_\ell = 1$ cm. For the LER parameters, $\alpha = 1.31 \times 10^{-3}$, $\sigma_p = (\delta p/p)_{\text{rms}} = 8 \times 10^{-4}$, and $E = 3.1$ GeV, stability requires $|Z/n| \leq 0.144\ \Omega$.

The effective impedance in Eq. 4-27 is defined as the impedance averaged over the bunch spectrum. For short bunches, for which the spectrum is wide compared with the frequency range of the impedance, the relevant parameter is

$$\left|\frac{Z_{\|}}{n}\right|_{\text{eff}} = \frac{\int [Z(n)/n]\,\rho^2(n)\,dn}{\int \rho^2(n)\,dn} \tag{4-28}$$

The main contribution to this integral comes from low frequencies, which are irrelevant to single-bunch stability. Therefore, to properly estimate the effective impedance for single-bunch stability, the integration should be performed starting with the harmonic number n_m corresponding to a wavelength comparable to or smaller than the bunch length. Figure 4-74 depicts $|Z/n|_{\text{eff}}$ and a plot of Re $Z(n)/n$ vs Im Z/n for different values of n_m. In the left column, $n_m = 300$ and the value of the effective impedance is of the order of $2\ \Omega$. The middle column is for $n_m = 3500$, which corresponds to including a maximum wavelength equal to the RF wavelength. The right column in Fig. 4-74 corresponds to a maximum wavelength of $20\sigma_\ell$. This limit already gives acceptable effective impedance. The Z/n at high frequencies is always within the area of stability allowed by Landau damping. A calculation with $n_m = 10500$ (or $20\sigma_\ell$) gives $|Z(n)/n| = 0.185\ \Omega$. It agrees well with the SPEAR-scaling [Chao and Gareyte, 1976] estimate of

$$\left(\frac{Z}{n}\right)_0 \left(\frac{\sigma_\ell}{b}\right)^{1.68} \tag{4-29}$$

with $(Z/n)_0 = 2.4\ \Omega$ for the beam pipe radius $b = 4.6$ cm. This appears consistent with PEP bunch lengthening measurements, which can be described with SPEAR scaling and the parameter $(Z/n)_0 = 3\ \Omega$. However, SPEAR scaling, which can be expected in the situation when the impedance is dominated by the RF cavities, i.e., for long bunches, may be invalid for shorter bunches, as was mentioned above. Figure 4-75 shows the dependence of the effective impedance on the bunch length.

To estimate the growth from the longitudinal microwave instability, we must assume a value for the broadband impedance of the ring. For the PEP-II HER, this value—usually dominated by the RF system in a high-energy storage ring—is expected to be lower than the value of $|Z/n|_0 = 3\ \Omega$ obtained from measurements at PEP [Rivkin, 1987].

The equivalent broadband contribution to the impedance seen by the beam can be estimated, for a given RF system, following the approach of Zisman et al. [1986].

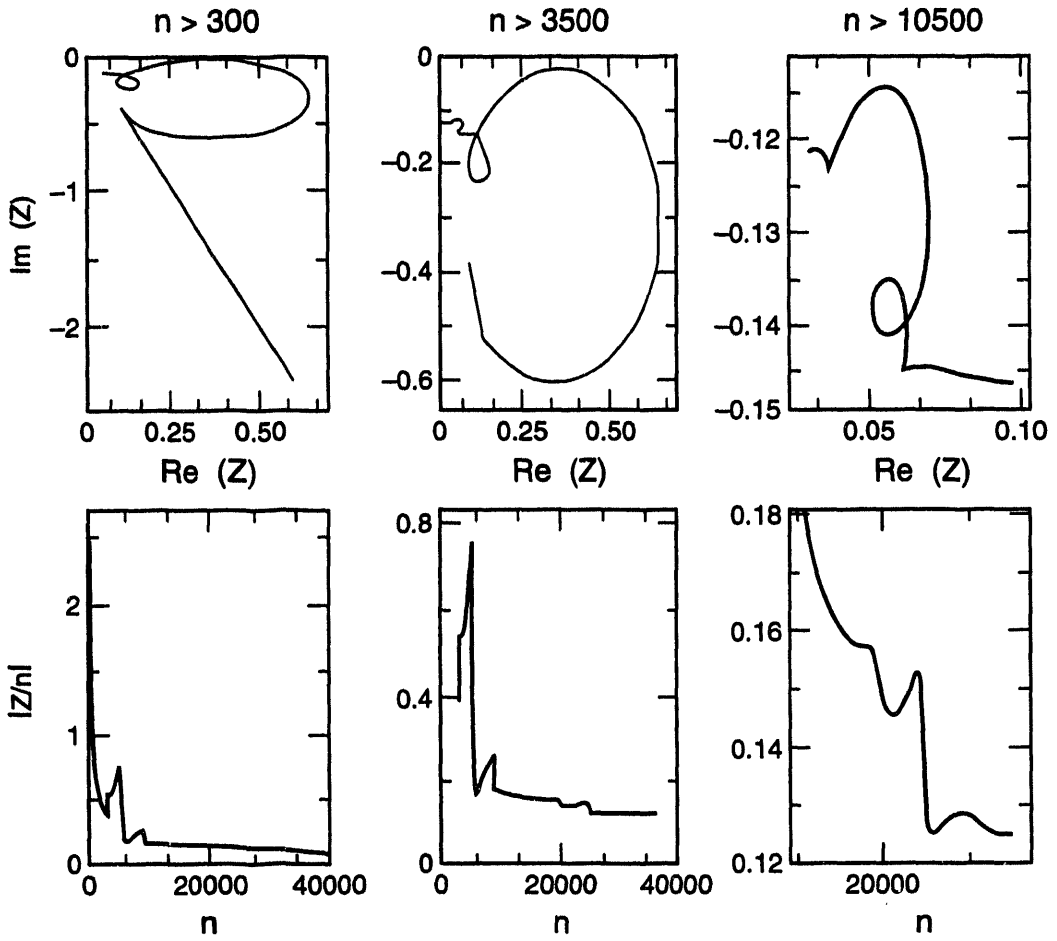

Fig. 4-74. (Upper) Plot of real vs imaginary impedance of PEP-II for various assumptions about n = ω/ω₀. (Lower) Plot of absolute value of Z/n for various values of low-frequency cutoff n.

Basically, this involves estimating the frequency shift that would be induced in a long beam bunch by the aggregate of the many cavity HOMs, and then determining the strength of a $Q = 1$ broadband resonator that would produce the same effect. That is, we take

$$\left|\frac{Z_{\|}}{n}\right|_{\mathrm{BB,RF}} = \sum_{\mathrm{HOMs}} \left|\frac{Z_{\|}}{n}\right|_j = \sum_j \left(\frac{R_s\,\omega_0}{Q\,\omega_R}\right)_j \tag{4-30}$$

where R_s, ω_R, and Q are the shunt impedance, resonant angular frequency, and quality factor, respectively, of the jth HOM, and ω_0 is the particle (angular) revolution frequency. With this approach, we find that the present PEP RF system contributes an equivalent broadband component of $|Z/n| \approx 0.026\ \Omega$/cell. Applying the same prescription to the PEP-II RF cavity (described in Section 5.5) yields an equivalent broadband contribution of $|Z/n| \approx 0.01\ \Omega$ for the first few trapped modes.

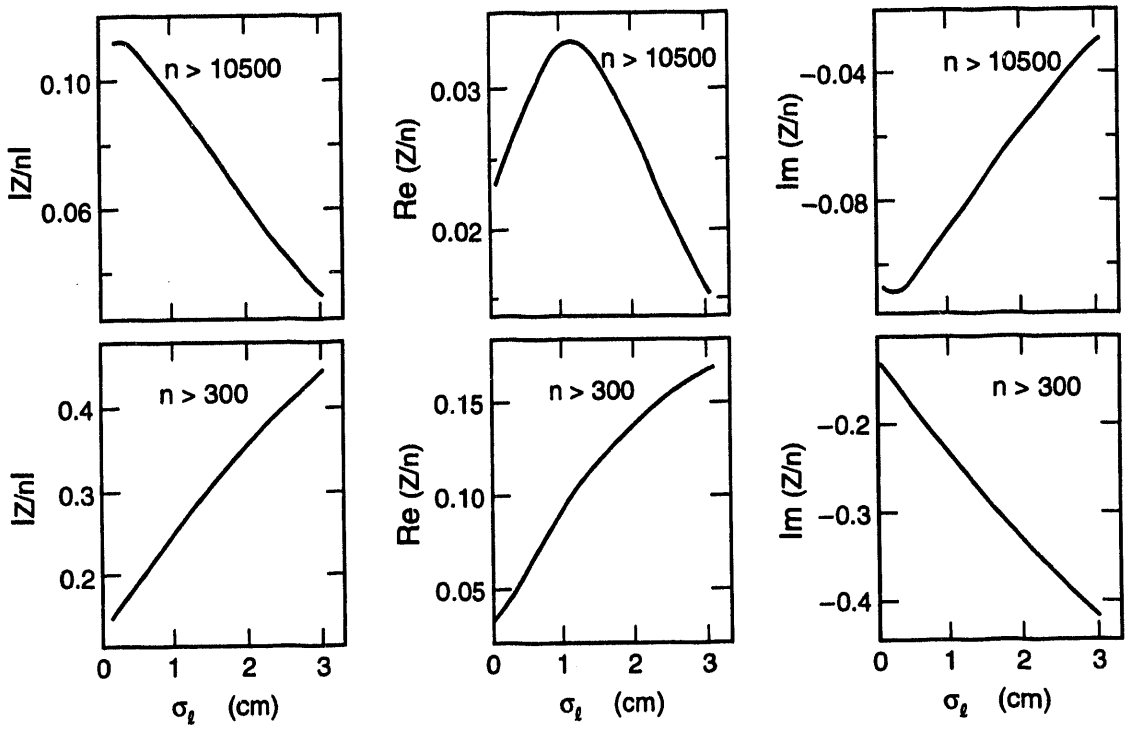

Fig. 4-75. Plots of the absolute value of Z/n (left column), the real part of Z/n (center column) and the imaginary part of Z/n (right column) vs bunch length. The upper row corresponds to a high cutoff frequency (wavelengths of the order of the bunch length); the lower row corresponds to a very low cutoff frequency.

A more significant gain is made by producing the required voltage and providing the required power to the beam (to replenish the losses to synchrotron radiation) with many fewer RF cells than the 120 used now at PEP. In the design described in Section 5.5, the voltage is provided by only 20 RF cells in the HER or 10 cells in the LER. This decrease in the number of cells reduces, by about a factor of six, the broadband impedance in the ring that stems from the RF system (estimated in PEP to be about two-thirds of the total). Thus, we expect to reduce the RF contribution to the broadband impedance to about 0.3 Ω. Clearly, however, the broadband impedance from the other components in the beam path (valves, bellows, BPMs, etc.) must contribute to the total seen by the beam, and there will be additional hardware in the PEP-II rings (for example, feedback kickers) that will have an effect.

The PEP chamber has a broadband impedance of about 1 Ω, and it is prudent, for now, to take the larger value to account for those impedance-producing components that have not been considered yet. With this in mind, for simulations with ZAP, which uses the SPEAR scaling approach (Eq. 4-28), we have adopted a total broadband impedance $|Z/n|_0 = 1.5\ \Omega$ (half that of PEP), which is consistent with the calculated $|Z/n|_{\text{eff}} = 0.18\ \Omega$ for the average beam pipe radius of 3.3 cm. As we will see, even this fairly conservative assumption does not lead to any difficulties in the parameter regime in which the PEP-II rings are designed to operate.

To maintain bunch lengths in both rings that are short compared with the small β^* value of 1.5 cm in the LER, we adopt an RF voltage in the HER of 18.5 MV. As shown in Fig. 4-76a, this voltage gives an rms bunch length of $\sigma_\ell = 1$ cm at the required single-bunch current of 0.6 mA. For the LER (see Fig. 4-76b), a 1-cm bunch at the design current of 1.3 mA can be obtained with a voltage of 5.9 MV.

The expected bunch lengthening beyond threshold is shown in Fig. 4-77a for the HER, based on the threshold formula given in Eq. 4-27. We remain well below the threshold at the required single-bunch current of 0.6 mA. The situation for the LER is shown in Fig. 4-77b; again we are well below threshold at the nominal 1.3 mA/bunch value. The curves in Figs. 4-77a and 4-77b are based on the so-called SPEAR-scaling ansatz, mentioned earlier. It is worth noting here that we have estimated the natural momentum spread of the low-energy beam to be 8×10^{-4}. This relatively large value is associated with the significant amounts of "extra" synchrotron radiation (generated in the wigglers) needed to achieve the proper emittance and to preserve the ability to reach equal damping decrement if need be.

Because the collider must be able to accommodate some energy variability, we have also considered the effects of moderate changes from the nominal operating energies of 9 GeV (HER) and 3.1 GeV (LER). In Fig. 4-78, we show the energy dependence of the microwave threshold current at the specified operating voltages for the two rings. The steepness of these curves is mainly due to the increase in natural momentum spread with energy (see Eq. 4-27). The dependence of the threshold current on voltage is shown for several different energies in Figs. 4-79a (HER) and 4-79b (LER). The preference for higher voltage is a consequence of the decrease in effective impedance as the bunch length decreases.

In our calculations we have ignored the effect of potential-well distortion, which—for short bunches—is predicted to reduce the bunch length; this effect is expected to be minor.

From these estimates, we conclude that there are no problems associated with the longitudinal microwave instability, provided the low-frequency broadband impedance of each ring can be kept at or below 1.5 Ω.

4.3.1.3 Transverse Mode-Coupling Instability. Because the ring is large, we must also consider the transverse mode-coupling instability, which is known [Zisman et al., 1988] to limit the single-bunch current in PEP. This instability arises when the imaginary part of the transverse impedance $Z_\perp$ couples the frequency of the $m = 0$ and $m = -1$ synchrotron sidebands. For long bunches, the threshold is expected to scale as

$$I_b = \frac{4\,(E/e)\,\nu_s}{\left\langle \mathrm{Im}\,(Z_\perp)\,\beta_\perp \right\rangle R} \frac{4\sqrt{\pi}}{3}\,\sigma_\ell \qquad (4\text{-}31)$$

where ν_s is the synchrotron tune, $\beta_\perp$ is the beta function at the location of the impedance, and R is the average ring radius. Although the transverse impedance is expected to decrease for very short bunches [Zisman 1990a], we are operating in a regime where the mode-coupling threshold is more or less independent of bunch length. For the impedance presently expected for the HER, a simple scaling from measured PEP data based on

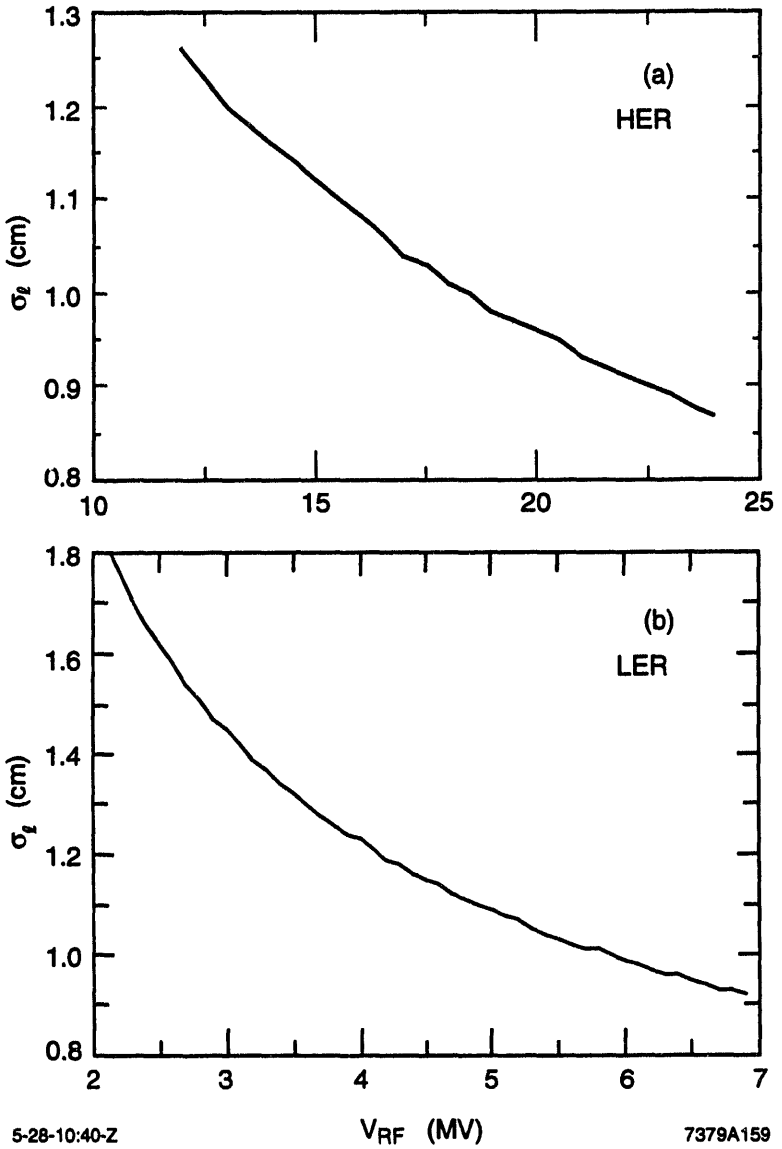

Fig. 4-76. Plot of (a) HER and (b) LER bunch lengths as a function of RF voltage. A 1-cm bunch requires V_{RF} = 18.5 MV in the HER and V_{RF} = 5.9 MV in the LER.

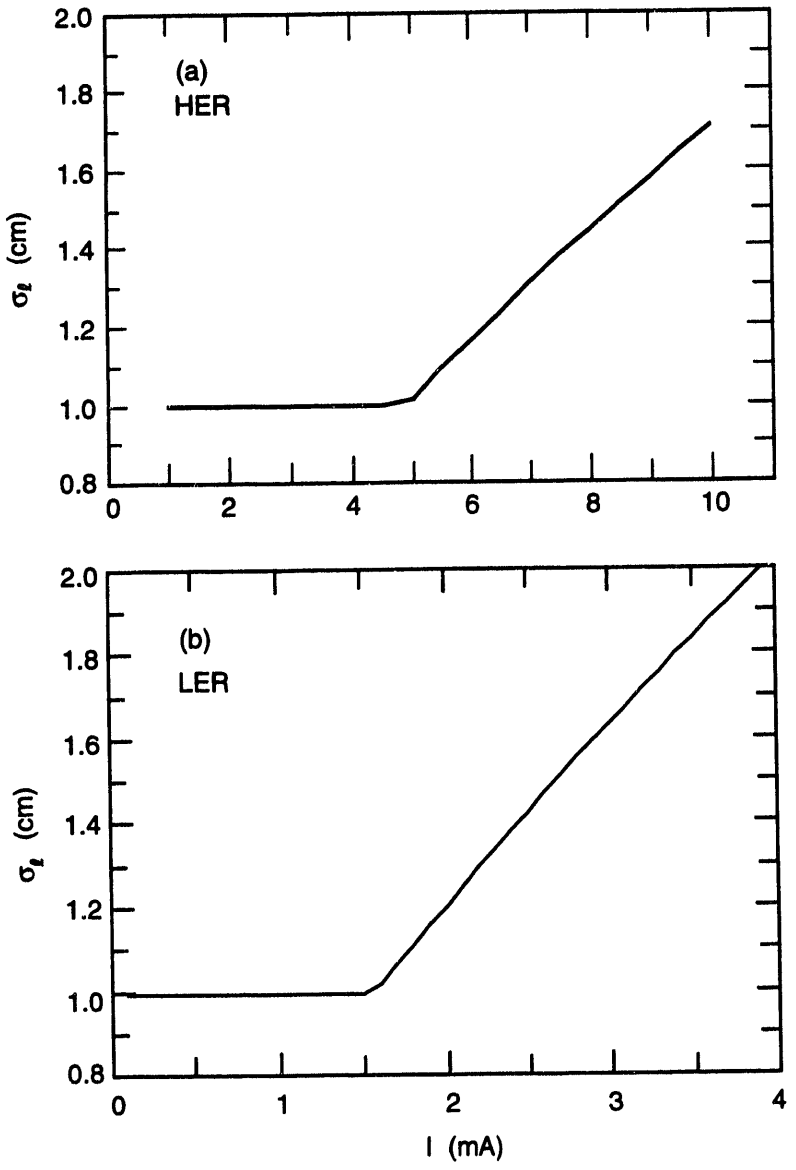

Fig. 4-77. Plot of (a) HER and (b) LER bunch lengths as a function of current, showing the onset of bunch lengthening. Even above threshold, the bunch length increases only slowly with current.

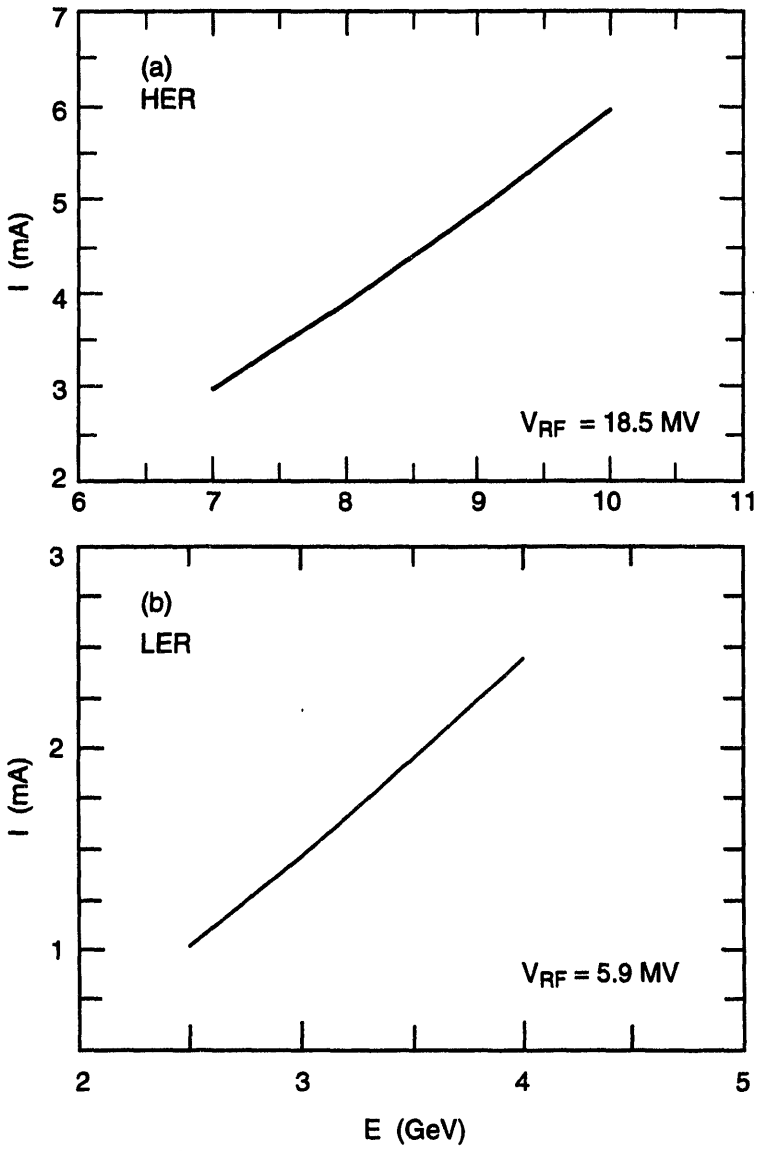

Fig. 4-78. Plot of the microwave threshold current in (a) the HER and (b) the LER as a function of energy, for V_{RF} = 18.5 MV (HER) and V_{RF} = 5.9 MV (LER). The required single-bunch currents of 0.6 mA (HER) and 1.3 mA (LER) are below the instability threshold in this energy range.

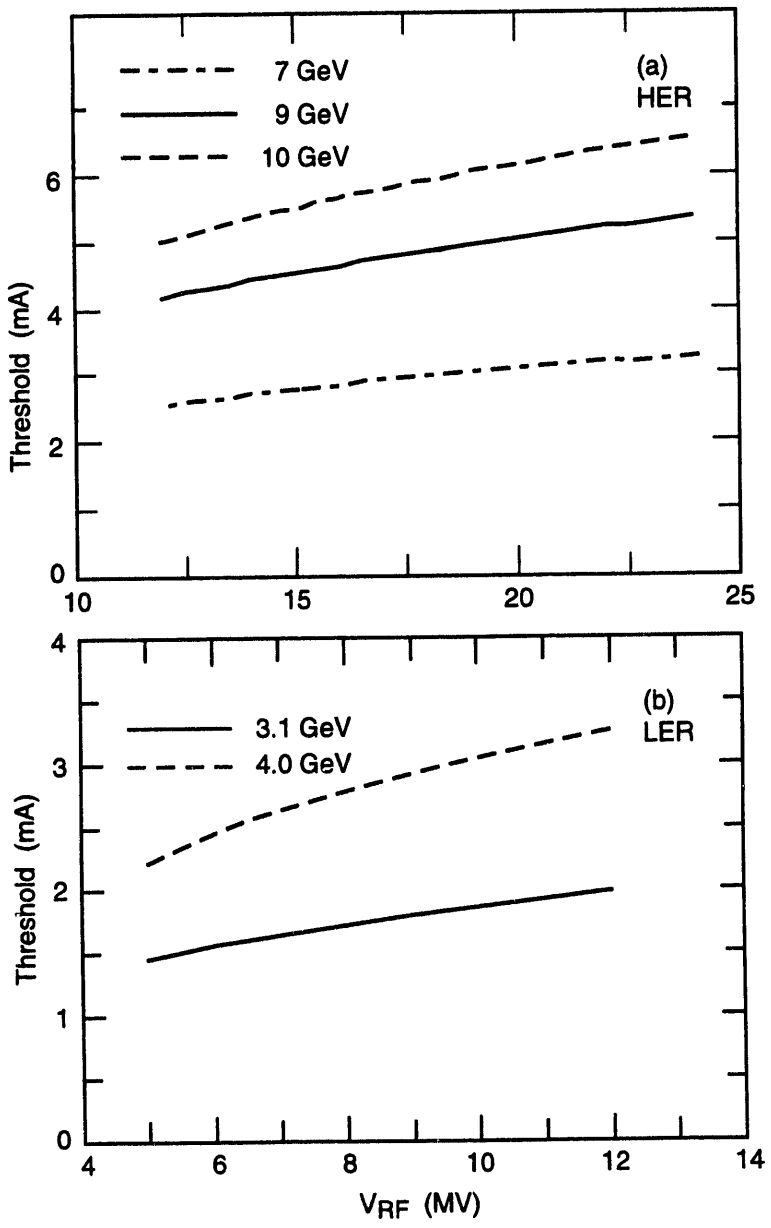

Fig. 4-79. Plot of the microwave threshold current in (a) the HER and (b) the LER as a function of RF voltage, for several beam energies. For the HER, the threshold current is well beyond the required 0.6 mA. For the LER, the threshold current approaches the required operating value of 1.3 mA only for the lowest voltage.

Eq. 4-31, shown in Table 4-28, suggests that the transverse mode-coupling threshold should be somewhat higher for PEP-II than for PEP, even though both the HER and LER will have a lower beam energy than did PEP. The scaled threshold value for the LER, about 10 mA/bunch, is well beyond the required single-bunch current of 1.3 mA and should pose no problem.

To estimate the transverse mode-coupling threshold in each ring more reliably, we used the code MOSES [Chin, 1988]. Initially, we considered a Q = 1 resonator impedance having a cutoff frequency of 1 GHz and a transverse impedance of 0.5 MΩ/m. The calculations take into account the effect of bunch lengthening at high currents, which is ignored in the simple scaling arguments presented in Table 4-28. The threshold currents, corresponding to the crossing of the mode m = 0 and mode m = –1 frequencies, are 37 mA for the HER (Fig. 4-80a) and 8.8 mA for the LER (Fig. 4-80b), in good agreement with the scaling estimates.

Because the RF cavities are no longer expected to be the dominant impedance source, we have also considered the situation in which the transverse impedance comes mainly from the arc vacuum chamber hardware. In this case, the cutoff frequency for $Z_\perp$ increases to 1.9 GHz, and the strength of the impedance (weighted by the fraction of the circumference that consists of arc chambers, roughly 70%) increases to about 1.3 MΩ/m. For these parameters, MOSES predicts the transverse thresholds to be 6.5 mA for the HER and 2.2 mA for the LER.

Table 4-28. Scaling comparison for transverse mode-coupling threshold.

	Low-energy ring	PEP	High-energy ring
E [GeV]	3.1	14.5	9.0
$\beta_\perp$ [m]	20	87	20
R [m]	350	350	350
ν_s [10^{-2}]	3.7	4.6	5.3
$Z_\perp$ [MΩ/m]	0.5	0.8	0.5
Relative factor[a]	1.2	1	5.0
Observed [mA]	—	8.5	—

[a] Factor $= \dfrac{E\nu_s}{Z_\perp \beta_\perp R}$

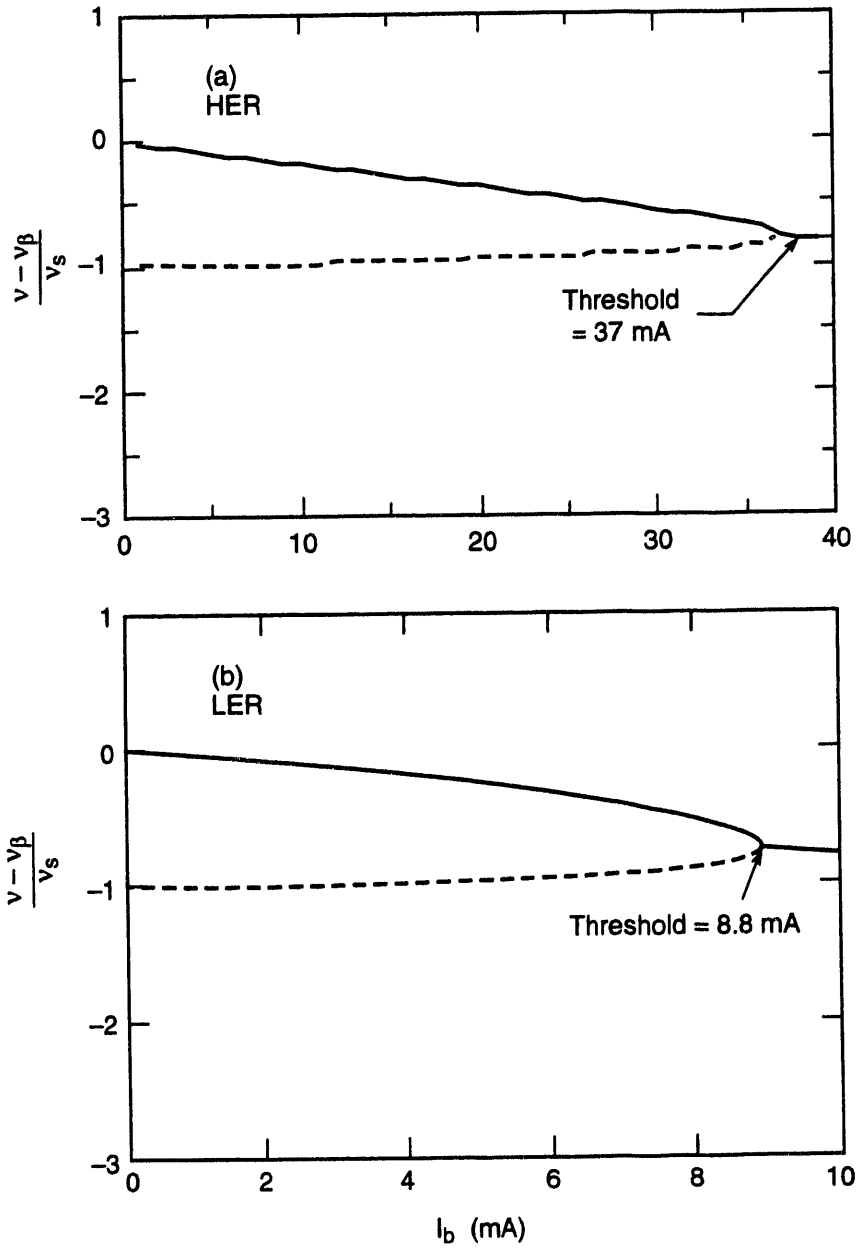

Fig. 4-80. Calculation of transverse mode-coupling instability threshold for (a) the HER, assuming $Z_\perp = 0.5$ MΩ/m and (b) the LER, assuming $Z_\perp = 0.5$ MΩ/m. The instability sets in when the $m = 0$ and $m = -1$ frequencies merge. This calculation represents a limitation in the horizontal plane; the vertical limitation is lower (see text).

To put these results in context, we note that the maximum allowable single-bunch current in the PEP-II rings is 1.8 mA, corresponding to 3 A in 1658 bunches. Thus, the transverse mode-coupling instability is not expected to limit the performance of PEP-II.

Although the RF cavities are not the dominant contributors to the transverse impedance, it is still best to "hide" them in a low-beta region of the ring. This should be more easily accomplished in the PEP-II HER than in PEP, because the total length of RF structure will be considerably shorter. Indeed, it would be possible, in principle, to adapt the focusing of the RF straight sections to permit very low beta functions in both planes.

4.3.1.4 Intrabeam Scattering. Although we are considering beams of fairly high energy, the requirements for relatively short bunches and relatively high peak currents make emittance growth from intrabeam scattering (IBS) a possible concern. IBS collisions occur because, in the bunch rest frame, not all particles are moving in the same direction. In general, the temperatures in the transverse phase planes (x and y) are higher than in the longitudinal plane. This results in small-angle multiple scattering occurring mainly in such a way as to transfer momentum from the transverse to the longitudinal plane. However, in dispersive regions of the lattice, this momentum change results in the excitation of a betatron oscillation and thus gives rise to an increase in horizontal emittance.

To be sure this is not a concern, we performed calculations on each of the rings at the lowest energy now being considered: 7 GeV for the HER and 2.5 GeV for the LER. In the HER case, our estimates indicate that no growth is expected. In the LER case, the lower beam energy enhances the IBS growth rates, and the single-bunch current is higher than for the high-energy beam, so we might expect an observable growth. However, in the LER these aspects are compensated by the larger transverse emittance values. Thus, even here we predict no emittance growth from intrabeam scattering.

4.3.1.5 Beam and Luminosity Lifetime. For a high-energy electron beam, there are four main processes that lead to beam loss: Touschek and gas scattering for the single beams, and Bhabha ($e^+e^- \rightarrow e^+e^-$) and radiative Bhabha ($e^+e^- \rightarrow e^+e^-\gamma$) interactions for the beams in collision. For single beams at PEP-II, the first of these effects is not generally important, but the second one is. For the colliding beams, the radiative Bhabha interactions dominate the luminosity lifetime. Lifetimes presented in this section are quoted as mean (that is, $1/e$) values.

Touschek Scattering. The Touschek scattering mechanism is related to the IBS mechanism described above. The main difference is that we are concerned now with large-angle, single-scattering events that change the scattered particle's momentum sufficiently to make it fall outside the momentum acceptance of the accelerator.

The limit on the tolerable momentum deviation from the design value can come from several sources. There is a longitudinal limit from the potential well ("RF bucket") provided by the RF system. Particles deviating in momentum from the nominal value by more than this amount do not undergo stable synchrotron oscillations and are lost. There can also be a transverse limit on momentum acceptance, arising from the excitation of a betatron oscillation when the Touschek scattering event takes place in a dispersive region of the lattice. For large momentum deviations ($\delta p/p \approx$ several percent), the resultant

betatron oscillation can either hit the vacuum chamber wall elsewhere in the lattice (physical aperture limit) or exceed the dynamic aperture of the machine. Because the lifetime for Touschek scattering increases approximately as $(\Delta p/p)^3$, where $(\Delta p/p)$ is the limiting momentum acceptance value, there is the potential for a strong degradation if the acceptance is too low.

For detector background reasons, we envision the possibility of installing collimators in the arcs that would restrict the particle amplitudes to about $10\sigma_x$ motion. To see how this affects the various lifetimes, ZAP has been modified to include this possibility.

The RF voltage in the HER, selected to be 18.5 MV so as to produce short beam bunches, actually provides too large an acceptance ($\Delta p/p$ = 1%) compared with the estimated limitation from the physical aperture ($\Delta p/p$ = 0.7%). This is not beneficial to the lifetime, since it results in a higher bunch density and thus a higher collision probability; this is the price we must pay to obtain short bunches. Fortunately, the Touschek lifetime is not a major concern in this parameter regime, as shown in Fig. 4-81a. At 9 GeV, a Touschek lifetime of 870 hours is predicted for the HER based on the physical aperture limit. If a 10σ limit is applied, the Touschek lifetime is still 188 hours.

In the LER, the physical momentum acceptance limit, $\Delta p/p \approx 1.3\%$, is the same as that of the RF bucket. Although the energy is lower than in the HER, the large acceptance makes the Touschek lifetime about 270 hours, and thus not of concern. With a 10σ aperture restriction, the lifetime becomes 65 hours, which is still quite comfortable. We see (Fig. 4-81b) that a 10σ aperture becomes quite noticeable at the lower energies, where the lifetime drops to below 10 hours.

Gas Scattering. Gas scattering involves collisions with residual gas nuclei present in the vacuum chamber. Such collisions can be either elastic or inelastic (bremsstrahlung). In the former case, particle loss results from the excitation of a betatron oscillation that exceeds the physical or dynamic aperture of the ring; in the latter case, the loss results from a momentum change that exceeds the momentum acceptance of the ring (see discussion above).

The HER must accommodate 0.99 A of circulating beam to reach a luminosity of 3×10^{33} cm^{-2} s^{-1}. This high beam current will give a large desorbed-gas load, and substantial pumping speed is needed to maintain a background gas pressure below 10 nTorr in the ring. The PEP-II vacuum system is designed to produce a pressure of less than 5 nTorr under these conditions, so we base our lifetime estimates on this value (N_2 equivalent).

For the HER (see Fig. 4-82a), the estimated lifetime from gas scattering—dominated by the bremsstrahlung process—is 6 hours at a pressure of 5 nTorr. This beam loss process is much more severe in its effects than the Touschek scattering process; therefore, we have placed great emphasis (see Section 5.2) on a vacuum system design capable of maintaining a good pressure in the presence of a large gas load from synchrotron-radiation desorption. It is worth noting here that our lifetime estimates are somewhat pessimistic in that they are based on a fixed gas pressure. In reality the pressure will decrease as the beam current decreases, making the lifetimes longer than the values quoted here.

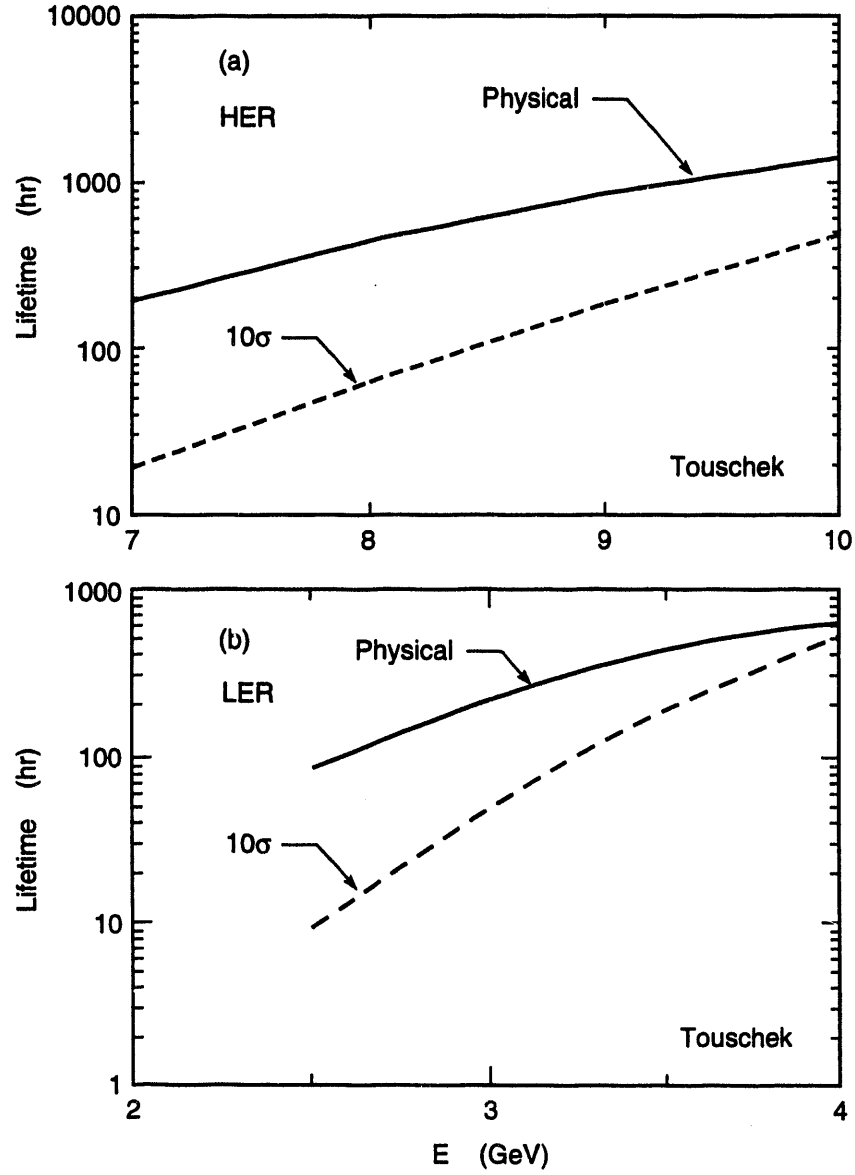

Fig. 4-81. Plot of Touschek lifetime as a function of beam energy in (a) the HER and (b) the LER. The solid line corresponds to taking the physical aperture of the vacuum chamber as the transverse limitation; the dashed line assumes a 10σ aperture restriction in the injection straight section.

For the LER at a gas pressure of 6 nTorr (N_2 equivalent), the lifetime is roughly equally matched between elastic scattering and bremsstrahlung losses (see Fig. 4-82b); the overall beam lifetime is 2.7 hours. Even for the LER, special care must be taken in the design of the vacuum chamber; this topic is discussed in Section 5.2.

Luminosity Lifetime. A potentially important contribution to beam lifetime is the loss of particles due to interactions between the individual particles in the two beams. In

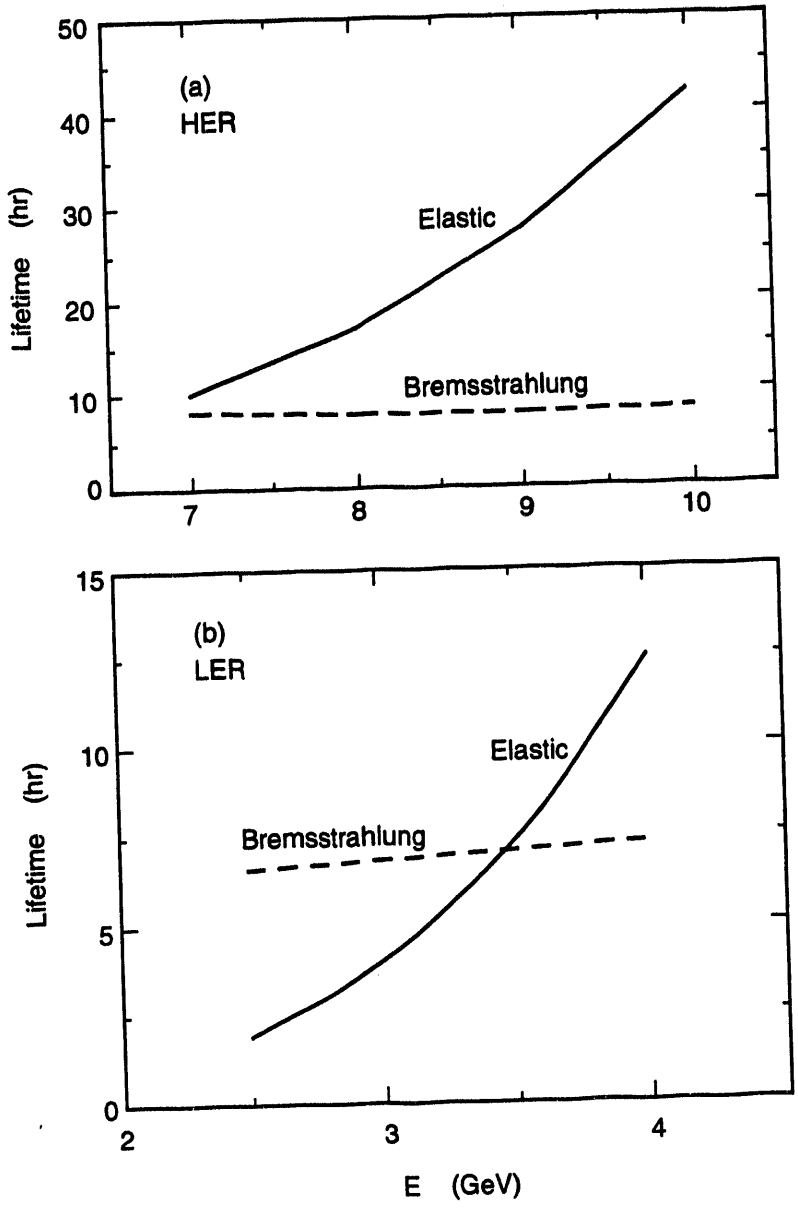

Fig. 4-82. Plot of gas-scattering lifetime as a function of beam energy for (a) the HER and (b) the LER. For the elastic scattering (solid line), an aperture restriction of 10σ was taken in each plane, with the vertical σ being calculated with the fully coupled vertical emittance. An average pressure of 5 nTorr (N_2 equivalent) was assumed for the HER and 6 nTorr for the LER.

particular, we consider the loss of particles due to $e^+e^- \rightarrow e^+e^-$ and $e^+e^- \rightarrow e^+e^-\gamma$ interactions that scatter beam particles outside the accelerator acceptance.

If the e^+e^- cross section leading to loss of a particle from beam i is σ_i, then the loss rate depends on the luminosity according to

$$\frac{dN_i}{dt}(t) = -\sigma_i \mathcal{L}(t) \tag{4-32}$$

Each beam may consist of a number of bunches (not including gaps), n_{bi} with a number of particles per bunch, $N_{bi}(t)$. The subscript b is used to indicate that this is a quantity for a single bunch, and the subscript i refers to the beam (i = +,–). The total number of particles in a given beam is $N_i = n_{bi}N_{bi}$. We introduce the notation $N_{0,i} \equiv N_i(0)$, and we also use $\mathcal{L}_0 \equiv \mathcal{L}(0)$ to denote quantities evaluated at $t = 0$.

To determine the beam and luminosity lifetimes for the processes of interest, we need to know how the luminosity depends on the beam currents. This dependence is determined to some extent by the operation of the storage ring. We adopt here a conservative model that assumes that the bunch sizes do not vary with time. Then the luminosity is given by

$$\mathcal{L}(t) = \frac{N_{b+}(t)N_{b-}(t)n_{bi}f_i}{2\pi\sqrt{\left(\sigma_{x,+}^{*2} + \sigma_{x,-}^{*2}\right)\left(\sigma_{y,+}^{*2} + \sigma_{y,-}^{*2}\right)}} \tag{4-33}$$

The $\sigma_{x,\pm}^*$ and $\sigma_{y,\pm}^*$ in this equation are the transverse rms spot sizes at the interaction point (IP). All time-dependent terms are explicitly indicated. It is assumed that the bunches are distributed such that all bunches meet opposing bunches at the IP (that is, bunches meet bunches and gaps meet gaps), hence $n_{b+}f_+ = n_{b-}f_-$ is the bunch collision frequency. Here, f_i is the revolution frequency for beam i. We also assume that any modifications to the above formula from considerations such as finite bunch lengths and nonzero crossing angles are time independent.

Equations 4-32 and 4-33 lead to two coupled differential equations in the beam currents:

$$\begin{aligned} \frac{dN_+}{dt} &= -k\sigma_+ N_+ N_- \\ \frac{dN_-}{dt} &= -k\sigma_- N_+ N_- \end{aligned} \tag{4-34}$$

where

$$k \equiv \frac{\mathcal{L}_0}{N_{0,+}N_{0,-}} \tag{4-35}$$

The solution is

$$N_+(t) = N_{0,+}\frac{1-r}{e^{Gt}-r}$$

$$N_-(t) = N_{0,-}\frac{1-r}{1-re^{-Gt}} \tag{4-36}$$

where

$$G \equiv \mathcal{L}_0\left(\frac{\sigma_+}{N_{0,+}} - \frac{\sigma_-}{N_{0,-}}\right) \tag{4-37}$$

and

$$r \equiv \frac{N_{0,+}\sigma_-}{N_{0,-}\sigma_+} \tag{4-38}$$

The $1/e$ beam lifetimes are given by

$$\tau_+ = \frac{1}{G}\ln\left[e + r(1-e)\right]$$

$$\tau_- = -\frac{1}{G}\ln\left[\frac{1}{r}(1-e+re)\right] \tag{4-39}$$

The time-dependence of the luminosity is

$$\mathcal{L} = \mathcal{L}_0 e^{Gt}\left(\frac{1-r}{e^{Gt}-r}\right)^2 \tag{4-40}$$

We define the luminosity lifetime τ to be the time it takes the luminosity to reach $1/e$ of its initial value:

$$\tau = \frac{1}{G}\ln\left\{\frac{e}{2}\left[(1-r)^2 + 2r/e + (1-r)\sqrt{(1-r)^2 + 4r/e}\right]\right\} \tag{4-41}$$

The more important mechanism of the two Bhabha processes considered here is loss due to bremsstrahlung ($e^+e^- \rightarrow e^+e^-\gamma$) of a photon, which can change the energy of a beam particle sufficiently to put it outside the energy acceptance of the accelerator. An excellent approximation for the cross section to lose a particle from beam i due to bremsstrahlung is [Altarelli and Buccella, 1964]

$$\sigma_{\text{brems } i} \approx \frac{16\alpha r_e^2}{3}\left[\left(\ln\frac{E_{\text{c.m.}}^2}{m_e^2}-\frac{1}{2}\right)\left(\ln\frac{E_i}{k_{\min i}}-\frac{5}{8}\right)+\frac{1}{2}\left(\ln\frac{E_i}{k_{\min i}}\right)^2-\frac{3}{8}-\frac{\pi^2}{6}\right] \quad (4\text{-}42)$$

In this expression, $k_{\min i}$ is the minimum energy of a radiated photon that causes loss of a particle from beam i. Thus, $k_{\min i}/E_i$ can be taken as the fractional energy aperture of the machine for beam i. This cross section depends slowly on the energy aperture and on $E_{\text{c.m.}}$.

Table 4-29 shows the bremsstrahlung beam loss cross section for PEP-II calculated according to Eq. 4-42. The fractional energy aperture is limited by the transverse aperture rather than by the RF voltage—we have used a value corresponding to ten times the rms energy spread of the beam.

We note that the large circumference of the PEP-II rings (2200 m) helps to produce a comfortably large luminosity lifetime from this source. Even if future upgrades result in a higher luminosity, we do not have a problem. For example, suppose we anticipate a luminosity of 1×10^{34} cm^{-2} s^{-1}. As a "worst case," suppose further that this gain is achieved at the same beam currents as in our nominal design, either by reaching higher tune shifts or by focusing more strongly. In this case, the luminosity lifetime is inversely proportional to the luminosity, so 12.6 hours at 3×10^{33} cm^{-2} s^{-1} becomes 3.8 hours at 1×10^{34} cm^{-2} s^{-1}. This would still be acceptable, although it would then be comparable to the beam-gas luminosity decay rate.

Another loss mechanism, typically not as important as the bremsstrahlung considered above, is the loss due to Bhabha ($e^+e^- \rightarrow e^+e^-$) scattering at sufficiently large angles to escape the acceptance of the machine. To a good approximation for the small angles and high energies that we consider, the cross section to lose a particle from beam i is

$$\sigma_{\text{Bhabha } i} \approx \frac{8\pi\alpha^2}{E_{\text{c.m.}}^2}\frac{E_j}{E_i}\left(\frac{1}{\theta_{\min x;i}^2}+\frac{1}{\theta_{\min y;i}^2}\right) \quad (4\text{-}43)$$

Table 4-29. Bremsstrahlung luminosity lifetime calculation.

Parameter	Symbol	High-energy ring	Low-energy ring
Fractional energy aperture	f_E	0.0061	0.0081
Min. energy in brems. integral [MeV]	$k_{\min}$	55.1	25.1
Brems. cross section for particle loss [cm^2]	$\sigma_{e^+e^-\gamma}$	3.0×10^{-25}	2.8×10^{-25}
Bremsstrahlung beam lifetime [hr]	$\tau_{\text{Br}\,i}$	14.8	34.4
Bremsstrahlung luminosity lifetime [hr]	τ_{Br}	12.6	

where $\theta_{\min x,y;i}$ is the minimum horizontal or vertical scattering angle in the laboratory frame leading to particle loss, and $j = (-,+)$. Cross sections in units of GeV^{-2} may be converted to cm^2 by multiplying by 3.89×10^{-28} GeV^2 cm^2.

Table 4-30 summarizes the calculation for the PEP-II design. For the minimum angles, we have made our usual assumption that the limiting aperture is 10σ (using the uncoupled horizontal and the fully coupled vertical beam sizes). Because the Bhabha cross section to lose a beam particle is substantially smaller than the cross section in our earlier bremsstrahlung loss example, this is not a significant lifetime consideration.

We conclude that the luminosity lifetime from $e^+e^- \rightarrow e^+e^-$ and $e^+e^- \rightarrow e^+e^-\gamma$ will not be a significant limitation for PEP-II at a luminosity of $\mathcal{L} = 3 \times 10^{33}$ cm^{-2} s^{-1}. Even at a luminosity of 1×10^{34} cm^{-2} s^{-1}, the large circumference (and hence large number of particles per unit of beam current) of the PEP-II rings ensures that these sources of beam loss will not seriously degrade the lifetime.

4.3.1.6 Higher-Order-Mode Losses. A complete specification of the thermal loading in the vacuum chamber must take into account the localized heating of beamline components due to the absorption of power generated by the beam in the form of HOM losses. We estimate the HOM power as

$$P_{\mathrm{HOM}} = 1.6 \times 10^{-10} N_b I k_\ell \ [\mathrm{kW}] \tag{4-44}$$

where N_b is the number of particles per bunch, I (in A) is the total current, and k_ℓ (in V/pC) is the loss factor for the ring due to its impedance. For the PEP-II design parameters, the HOM power in the HER is given by [PEP 90a]

$$P_{\mathrm{HOM}} = 4.3\, k_\ell \ [\mathrm{kW}] \tag{4-45}$$

The equivalent value for the LER is

$$P_{\mathrm{HOM}} = 20\, k_\ell \ [\mathrm{kW}] \tag{4-46}$$

Table 4-30. Bhabha luminosity lifetime calculation.

Parameter	Symbol	High-energy ring	Low-energy ring
Minimum angle in Bhabha integral [rad]	$\theta_{\min x}$	3.17×10^{-3}	4.22×10^{-3}
Minimum angle in Bhabha integral [rad]	$\theta_{\min y}$	1.12×10^{-2}	1.49×10^{-2}
Bhabha cross section for beam loss [cm^2]	$\sigma_{e^+e^-}$	1.73×10^{-28}	8.16×10^{-28}
Bhabha beam lifetime [hr]	$\tau_{\mathrm{Bh}\,i}$	26000	12000
Bhabha luminosity lifetime [hr]	τ_{Bh}	10064	

The loss factor is defined as

$$k_\ell = \frac{1}{\pi}\int_0^\infty Z(\omega)\, e^{-(\omega\sigma_\ell/c)^2} d\omega \tag{4-47}$$

Based on the impedance values estimated here, the total loss factor of the LER with 10 RF cavities is k_ℓ = 11.2 V/pC. Of this, the RF cavities give 5.15 V/pC, the ring components give 3.25 V/pC, and the resistive wall gives 2.8 V/pC.

The HOM power deposition in the LER is then found from Eq. 4-46 to be P = 225 kW. For the HER there are 10 additional RF cavities that contribute an additional loss factor of 5.15 V/pC. The HOM power for the HER is then P = 70 kW. To be conservative, we double these $P_{\rm HOM}$ values in determining RF parameters, that is, we use $P_{\rm HOM}$ = 150 kW for the HER and $P_{\rm HOM}$ = 450 kW in the LER. The total HOM loss in the IR from both beams is P = 1.2 kW. This is very small compared with the power deposited by the synchrotron radiation (about 75 kW).

We estimate the ohmic losses (power deposition per unit length) from a beam with k_B bunches in the ring as

$$\frac{dP}{dz} = k_B f_0 \left(\frac{e^2}{2\pi b}\right)\frac{N_b^2}{\sigma_\ell^{3/2}}\sqrt{\frac{2}{\sigma Z_0}}\,\Gamma(3/4) \tag{4-48}$$

For the beryllium pipe at the IP, $\sigma = 3.1 \times 10^5\ \Omega^{-1}\ \mathrm{cm}^{-1}$ and b = 2.5 cm. For the two beams with parameters k_B = 1658, f_0 = 136 kHz, $N_b = 2.75 \times 10^{10}$ (HER) and 5.91×10^{10} (LER), we find dP/dz = 0.70 W/cm.

The estimate shows also that the HOM power will be absorbed mostly outside of the interaction region. The wakefields generated outside of, but absorbed within, the IR deposit very little energy because the average loss factor per unit length outside of the IR (excluding RF cavities) is much smaller than that of the IR. This contribution may be dominated by the wakefields generated at the crotches far away from the IP.

Energy deposition could be enhanced substantially if there were trapped modes in the IR, provided their wavelengths were multiples of the bunch spacing. We have tried to find the trapped modes in a structure that reproduces the real IR structure within ±25 cm from the IP and then is continued with straight pipes, using the code MAFIA. We failed to find any trapped modes [Ko, 1990]. This is not surprising in an open structure such as the PEP-II IR.

4.3.1.7 Ion Clearing. The trapping of positively charged ions produced by collisions between electrons of the beam and background gas molecules has degraded the performance of many electron storage rings. The production rate for the total ring is 1.3×10^9 ions per turn at an average pressure of 5 nTorr. The linear theory of ion trapping is quite simple. When an electron beam bunch passes near an ion, the ion experiences a restoring force toward the beam axis. This force results in a change in the transverse velocity of the ion. Between bunch passages, the transverse velocity produces a change in the transverse position of the ion. This pattern is repeated for each passage of an electron bunch.

To estimate the ion motion, it is useful to consider [Villevald, 1993] the transverse charge density of the electron beam as a Gaussian profile with rms width and height σ_x and σ_y, respectively. The equation of vertical motion for an ion in the electron bunch may be written as

$$\ddot{y} + \hat{\Omega}_y^2 \, y = 0 \tag{4-49}$$

where

$$\frac{\hat{\Omega}_y^2}{c^2} = \frac{2\hat{I}}{I_p A \sigma_y (\sigma_x + \sigma_y)} \tag{4-50}$$

with $\hat{I}$ the peak current of the bunch, c the speed of light, $I_p = m_p c^3/e = 3.1 \times 10^7$ A the Budker current of a proton, and A the ion mass number. The bunch cross section varies around the ring, but, for purposes of estimation, we can take $\sigma_x = 0.1$ cm, $\sigma_y = 0.02$ cm, an ion mass of 20, and a peak current 130 A. These parameters give $\hat{\Omega}_y = 4 \times 10^8$ rad/s. The bunch length τ and the bunch spacing Δt are 30 ps and 4.2 ns, respectively. Since both the quantities $\hat{\Omega}_y \tau$ and $\hat{\Omega}_y^2 \tau \, \Delta t$ are much less than one radian, we can neglect the bunch structure of the beam and describe the ion motion as occurring in the potential well of a continuous electron beam. Figure 4-83 shows the depth of the potential well for a

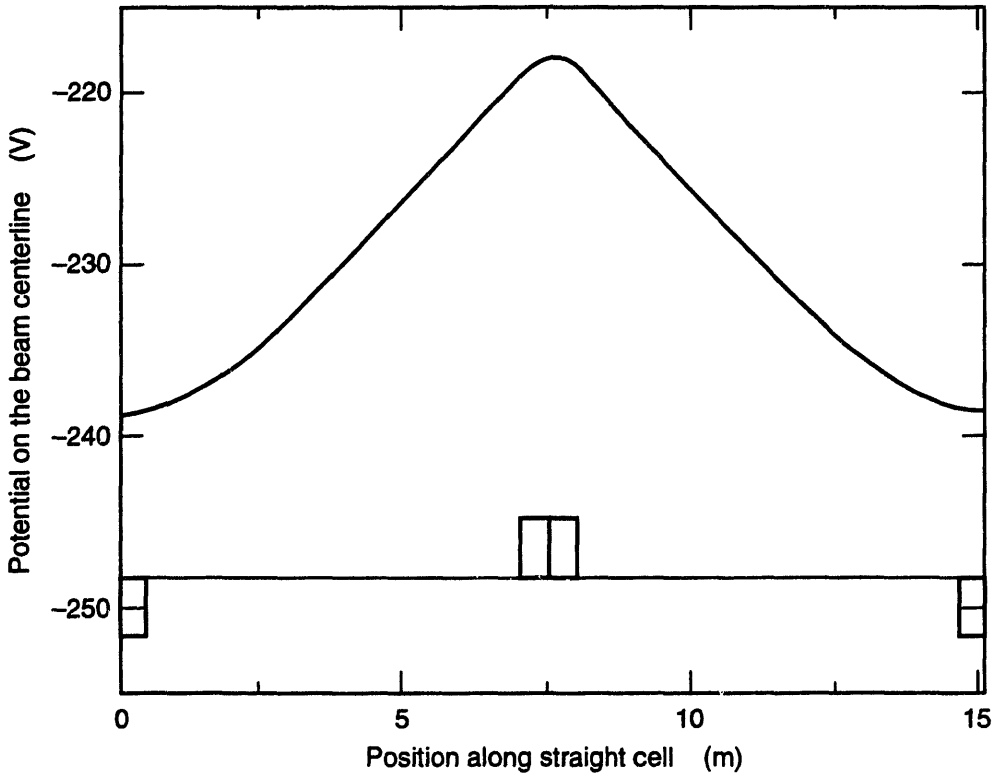

Fig. 4-83. Depth of potential well for a singly charged ion in the HER straight section.

singly charged ion along the straight section lattice cell. The average transverse ion motion can be obtained from Eq. 4-49 by replacing the peak current in Eq. 4-50 by the average current $I = 0.99$ A. The ion effectively sees a continuous electron beam and oscillates with an average frequency of $\Omega_y = 3.3 \times 10^7$ rad/s. The same analysis applied to the horizontal ion motion gives $\Omega_x = 1.5 \times 10^7$ rad/s. For a continuous bunched beam in the HER, ions will be trapped unless measures are taken to remove them.

The best known approach to avoiding ion trapping is to leave a gap in the electron bunch train. This gap need be only a few percent of the total ring circumference, so that only a small increase in the single-bunch current is necessary to achieve the same luminosity obtained for the continuous bunch train. An ion will be linearly unstable whenever the gap satisfies the following condition:

$$\left|\cos\left[\Omega_{x,y}\left(T_0 - \Delta T\right)\right] - \frac{\Omega_{x,y}\,\Delta T}{2}\sin\left[\Omega_{x,y}\left(T_0 - \Delta T\right)\right]\right| > 1 \qquad (4\text{-}51)$$

where T_0 is the revolution period and ΔT is the gap length. For $T_0 = 7.3$ μs, the phase advance of ion oscillation during the passage of the bunch train is given by $\Omega_{x,y}(T_0 - \Delta T) \approx 170$ rad and stability is sensitive to small parameter variations. For a particular combination of current, beam cross section, and ion mass, the ion would perform nearly an exact number of half-integer oscillations during the passage of the bunch train. This would result in violation of the instability condition, Eq. 4-51. Therefore there will be locations along the ring where ions can be trapped (see Fig. 4-84). The typical width of each of these zones is of the order of a few centimeters. These locations shift along the beam orbit as the current decays and/or the beam cross section changes. The ratio of the total length of stability zones to the ring circumference has been calculated as a function of gap length from Eq. 4-51 and is plotted in Fig. 4-85, which shows the percentage of ions trapped in stability zones as a function of gap length for various ion masses (for the average current in the HER of 0.99 A). The design length of the HER gap is 88 bunches or 5% of the ring circumference. This choice gives a total length of the transverse stability zones of the order of 18% of the circumference for a typical ion mass number of $A = 20$; a longer gap doesn't change this percentage drastically.

The majority of the ions are expected to leave the stable zones due to longitudinal motion caused by variation of the depth of the beam potential well with azimuth (due to variation of the transverse beam sizes σ_x and σ_y, as shown in Fig. 4-83) and, for nonzero transverse amplitude, due to the cross-field force. A time of the order of 2–3 revolution periods is enough for the ion to drift from the stability zone and become transversely unstable.

A worst case would occur when an ion is both transversely and longitudinally stable and the zone of stability coincides with the minimum of the beam potential well, that is, when ions are generated at the QD location (see Fig. 4-83). The typical width of the stability zone near the minimum of the beam potential well varies from $w = 18$ cm for hydrogen ($A = 2$) to $w = 85$ cm for carbon dioxide ($A = 44$). Ions will accumulate in these zones from one turn to another. The frequencies of the trapped ions should be within the frequency range

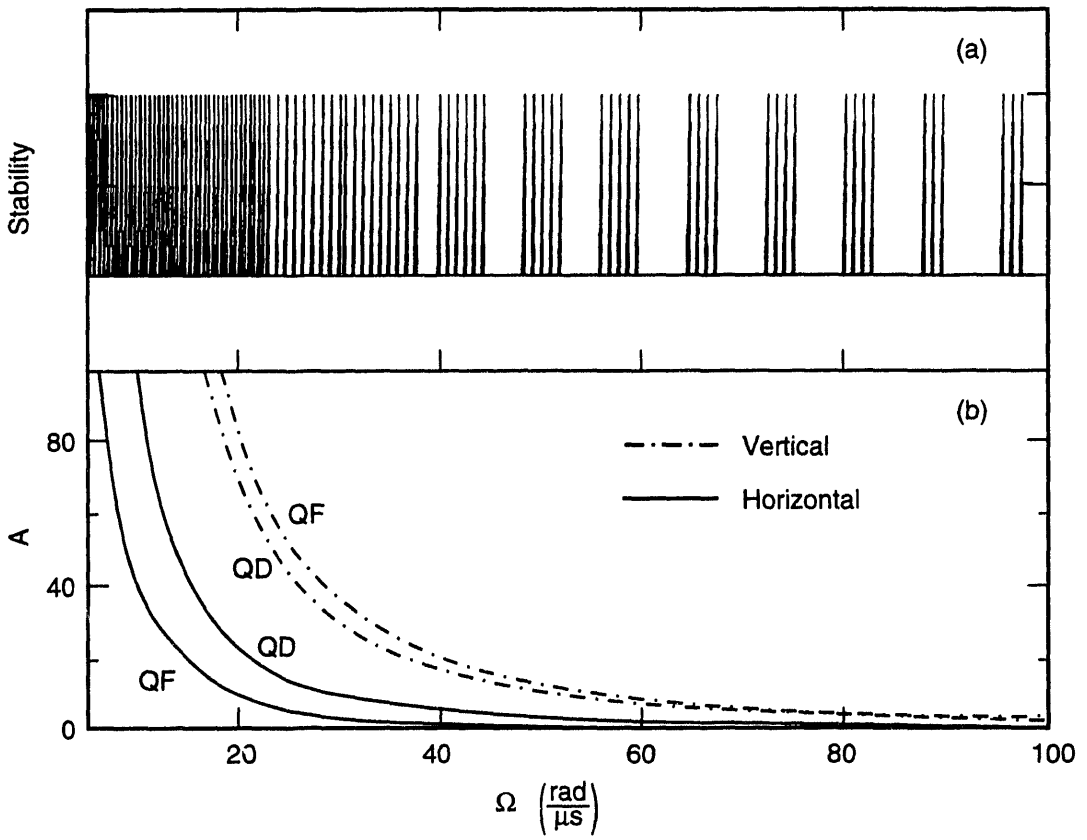

Fig. 4-84. (a) Stable zones for ion trapping, plotted as a function of ion frequency. (b) Frequencies for different masses at QF and QD locations.

$$\frac{\Delta\Omega_{x,y}}{\Omega_{x,y}} = \frac{2}{\Omega_{x,y}\,T_0}\cot^{-1}\left(\frac{\Omega_{x,y}\,\Delta T}{2}\right) \tag{4-52}$$

For heavy ions, A ≈ 44, and a gap length $\Delta T/T = 0.05$, we find $\Omega\Delta T \gg 1$ and $\Delta\Omega/\Omega$ very small, about 3×10^{-3}.

The number of accumulated ions in a stable zone is limited by two effects that change the ion frequency: the space charge of the trapped ions and the amplitude dependence of the frequency Ω. The space-charge effect produces a frequency shift Eq. 4-52 when the ion linear density is

$$\Delta N_i^{st} = 2\,\frac{N_e}{cT_0}\,\frac{\Delta\Omega_y}{\Omega_y} \tag{4-53}$$

where $N_e = 4.5 \times 10^{13}$ is the total number of electrons in the HER. Therefore, the number of ions trapped in this stable zone is $w\Delta N_i^{st}$ ions. The total number of the stability zones coinciding with the bottom of the beam potential well cannot exceed the number of lattice cells in the HER: $n_{\text{cell}} = 144$, so the maximum number of trapped ions is

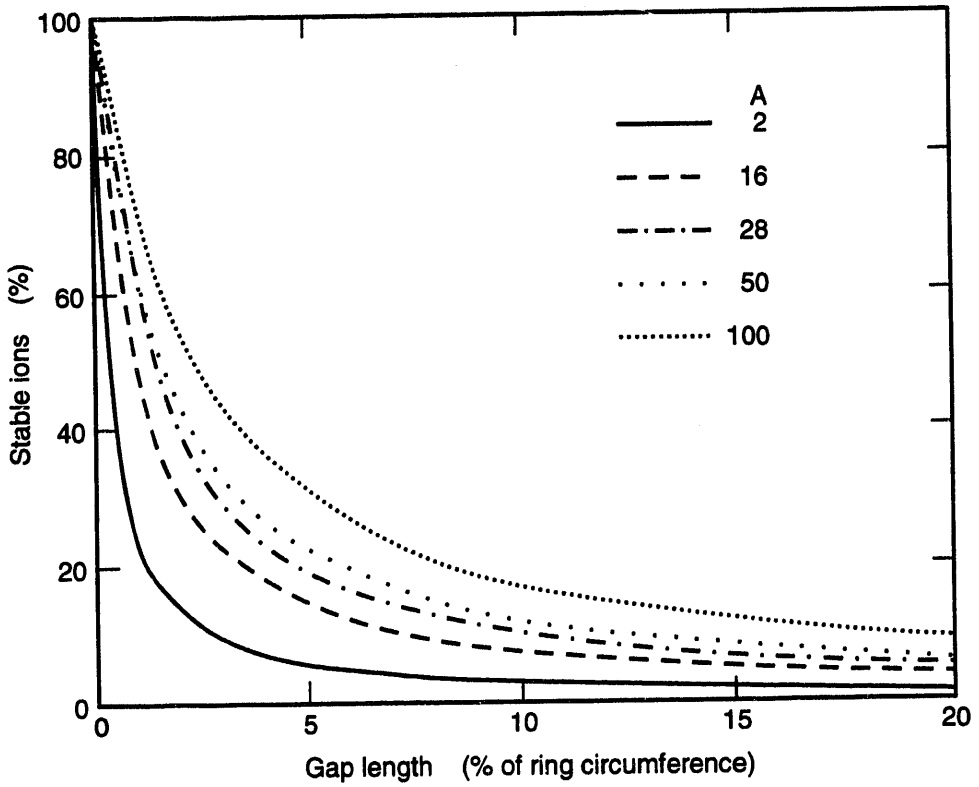

Fig. 4-85. Percentage of circumference that gives stable ion motion as a function of the length of the ion-clearing gap.

$$N_i^{st} = \Delta N_i^{st}\, wn_{\text{cell}} \tag{4-54}$$

For hydrogen $N_i^{st} = 1.3 \times 10^8$ and for carbon dioxide $N_i^{st} = 1.3 \times 10^{10}$.

The accumulation of these ions is a relatively slow process, taking 10^3–10^4 turns. During this time, the number of trapped ions will also decrease due to fluctuations of the beam current and transverse beam size. In reality, the number of trapped ions is also less than that given by Eq. 4-54 because the straight-section cells, dispersion-suppressor cells, and arc cells are not all identical. We see that the number of trapped hydrogen ions is much lower than the total number of ions produced during the revolution period of the HER, $N_i = 1.3 \times 10^9$. However, the number of trapped heavy ions ($A = 44$) is significant.

There is an additional reduction in the number of trapped ions due to the dependence of the ion frequency on ion amplitude a_y. For example,

$$\Omega_y = \Omega_y^0 \left[1 - \left(\frac{a_y}{4\sigma_{y,e}}\right)^2\right] \tag{4-55}$$

An amplitude $a_y/\sigma_{y,e} = 0.22$ corresponds to a frequency shift $\Delta\Omega/\Omega \approx 3 \times 10^{-3}$. Such a shift reduces the total number of stable ions by an order of magnitude, making their effect small compared with that of single-turn ions. The maximum betatron tune shift generated

by trapped heavy ions is

$$\Delta\nu_y^{st} = \frac{N_i^{st}}{2\pi}\frac{1}{\gamma}\frac{r_e\hat{\beta}_y}{\hat{\sigma}_y(\hat{\sigma}_y + \hat{\sigma}_x)} \tag{4-56}$$

For a beam current $I = 0.99$ A in the HER, $\hat{\beta}_y = 2500$ cm, $\gamma = 1.8 \times 10^4$ (the relativistic factor), and beam sizes at the QD locations of $\hat{\sigma}_x = 0.07$ cm, $\hat{\sigma}_y = 0.022$ cm, the tune shift is 0.04 and the betatron tune spread due to the trapped ions is of the order of $\delta\nu_y^{st} = 0.03$. In reality, the effect is even larger, because the distribution function of trapped ions is expected to be narrower than the distribution function of the electron beam (see Fig. 4-86) [Tavares, 1992], which increases the tune shift by a factor of two. However, only a small number of electrons, about 0.25%, experience a tune shift of this magnitude (which is still less than the tune shift given by the beam-beam interaction).

In considering the effects of unstable ions, it is convenient to divide them into two groups. The first group we refer to as "single-turn" ions, that is, ions accumulated during the passage of the previous bunch train. The total number of single-turn ions is

$$N_i = N_e\frac{T_0}{\tau_i} = 1.3 \times 10^9 \tag{4-57}$$

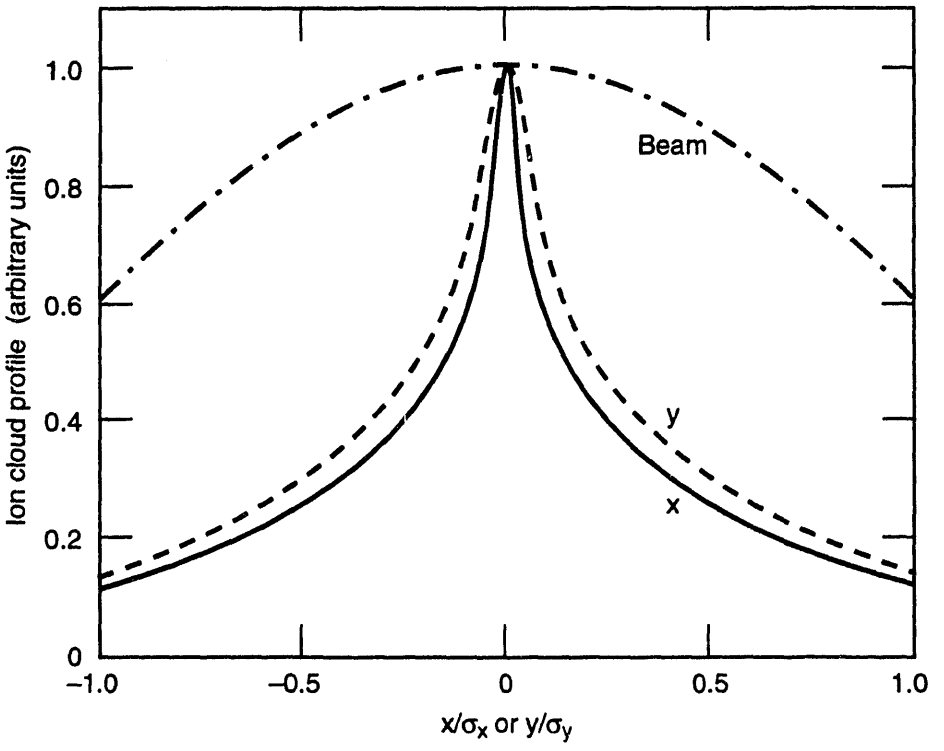

Fig. 4-86. Calculated distribution of trapped ions compared with beam dimensions.

where $\tau_i = 0.25$ s is the total ionization time. These ions cannot be removed by lumped clearing electrodes. Single-turn ions produce a betatron tune spread from bunch to bunch. Indeed, there are no single-turn ions at the head of the bunch train, whereas the number of single-turn ions for the last bunch of the train is given by Eq. 4-57. The bunch-to-bunch betatron tune spread is given by

$$\Delta\nu_y = \frac{N_i}{2\pi}\frac{1}{\gamma}\frac{r_e\langle\beta_y\rangle}{\sigma_y(\sigma_y+\sigma_x)} = 0.002 \tag{4-58}$$

for the HER current of $I = 0.99$ A and $\langle\beta_y\rangle = 1.5 \times 10^3$ cm the beta function averaged over the ring circumference. This tune spread is unavoidable even with clearing electrodes.

The second category of unstable ions involves "many-turn" ions, that is, ions generated and trapped during many previous turns. During the time of the gap passage, these ions reach large amplitudes, so we need to consider nonlinear theory in analyzing their behavior. Generally speaking, the amplitude dependence of the ion oscillation frequency may result in nonlinear resonances. The resonance condition is

$$k\Omega_{x,y} = n\omega_0 \tag{4-59}$$

where ω_0 is the revolution frequency and k and n are integers. For $\Omega_{x,y} \approx 3 \times 10^7$ rad/s, $\omega_0 = 8.6 \times 10^5$ rad/s, and $k = 1$, the order of the resonance is $n \approx 35$. Resonances of such high order are suppressed strongly. Therefore, a linearly unstable ion remains unstable at large amplitudes. This statement has been confirmed by computer simulations in which it was shown that the betatron tune shift due to many-turn ions is

$$\Delta\hat{\nu}_y \approx \Delta\nu_y \frac{q}{1-q} \tag{4-60}$$

where $\Delta\nu_y$ is the tune shift due to single-turn ions, given by Eq. 4-58, and the parameter q is proportional to the atomic number A

$$q \equiv \frac{\sigma_x^2}{c^2\Delta T^2}\frac{A\pi m_p c^2}{eIZ_0} = 6.8 \times 10^{-4} A \tag{4-61}$$

with $I = 0.99$ A and $Z_0 = 377\ \Omega$ (the impedance of free space). The tune-shift value obtained from Eq. 4-60 is small in comparison with the shift due to single-turn ions for our design current.

The nonlinear field of the single-turn ion cloud results in a betatron tune spread given by

$$\delta\nu_y = \frac{\partial\nu_y}{\partial\varepsilon_y}\varepsilon_y = \frac{3\varepsilon_y}{32}\frac{e}{\gamma m_e c^2}\oint_C \beta_y^2(s)\frac{\partial^3 E_y}{\partial y^3}\,ds \tag{4-62}$$

With $\varepsilon_y = 1.93 \times 10^{-9}$ m·rad, E_y the electric field of the ion cloud (for the cloud of single-turn ions, $\partial^3 E_y/\partial y^3 = -2$ kV/cm), and C the ring circumference, we find $\delta\nu_y = -0.002$.

Figure 4-87 shows the horizontal and vertical "bunch-to-bunch" betatron tune spread induced by single-turn ions as a function of HER current. Although these ions cannot be removed by lumped clearing electrodes, this is not necessary because the tune spread from them is well below the corresponding value due to the beam-beam interaction.

The betatron tune spread due to the trapped heavy ions (Eq. 4-56) is of the order of the beam-beam tune shift. Hence, ion clearing might be necessary near the horizontally defocusing quadrupoles in the arcs and straight sections.

A closely related possible problem in PEP-II is that of cross-talk between the DIPs and the beam, a phenomenon observed at CESR. The effect at CESR is believed to be related to the penetration of the electrostatic field through the slots of the screen [Sagan and Welch, 1992]. Such an effect scales with the slot width w and the thickness of the screen as $w^2 e^{-\pi d/w}$. Simulations with POISSON (see Fig. 4-88) show that, for PEP-II parameters, the field at the beam is reduced to 0.012 V/cm—a negligible amount—with 5.5 kV on the DIPs.

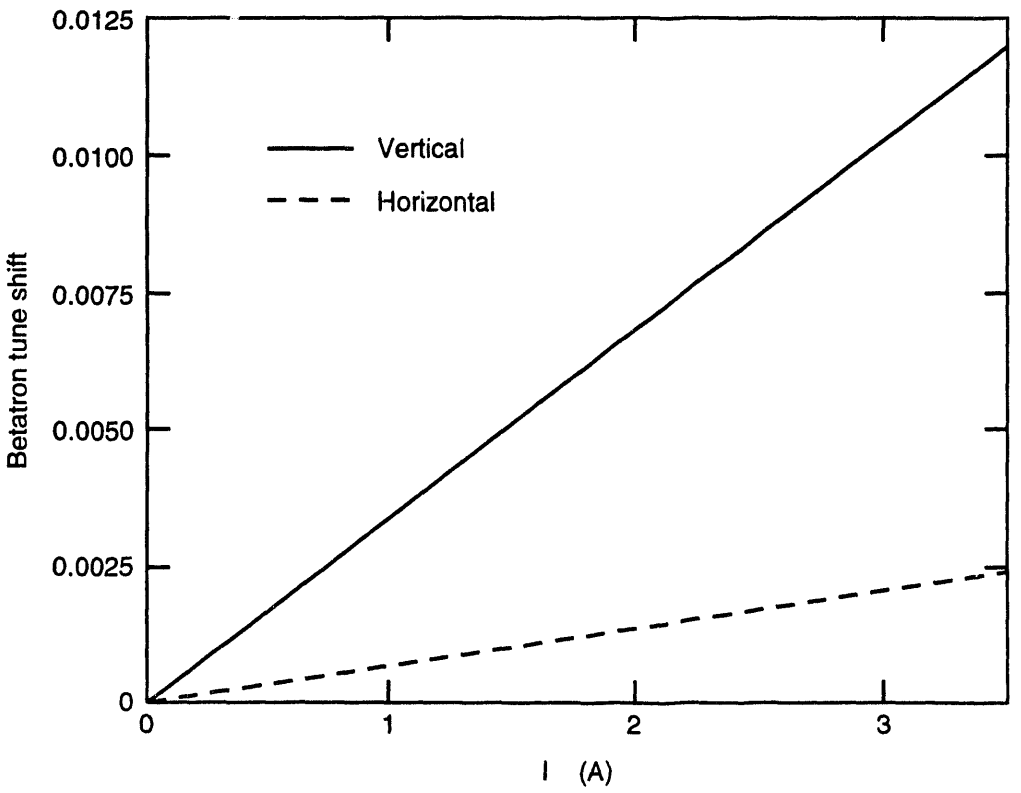

Fig. 4-87. Betatron tune spread due to trapped ions.

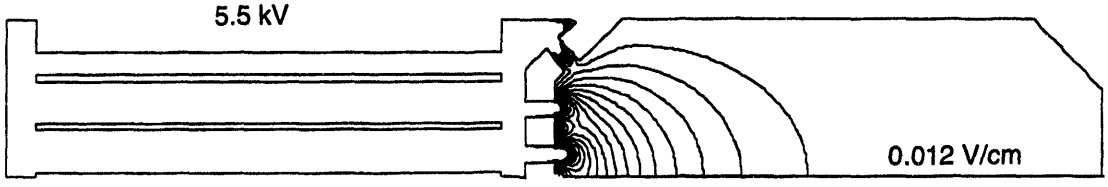

Fig. 4-88. Calculated electric field in beam chamber due to high-voltage on DIPs. A voltage of 5.5 kV in the pump chamber produces an electric field of only 0.012 V/cm at the beam location.

4.3.2 Coupled-Bunch Instabilities

As mentioned earlier, wakefields in high-Q resonant structures in a storage ring cause different beam bunches to interact. In general, such high-Q resonances result from the HOMs of the RF cavities. For certain values of relative phase between bunches, the coupled-bunch motion can grow and become unstable, leading to beam loss. In addition to the relative phase between bunches, the instabilities are characterized by their motion in longitudinal (synchrotron) phase space. Longitudinally, the $a = 0$ mode (corresponding to no motion) cannot be unstable, so the lowest longitudinal instabilities are characterized by $a = 1$ (dipole) synchrotron motion. In the *transverse* case, the $a = 0$ motion can also become unstable (referred to as "rigid-dipole" motion).

In the case of PEP-II, we require a relatively large number of RF cells, both to generate the voltage needed to produce the short bunches and to replace the beam power lost to synchrotron radiation each turn. Combined with the required very high average beam currents, the substantial RF system can produce extremely rapid growth of coupled-bunch instabilities. In the cases studied here, the most severe growth comes from the lowest modes, that is, $a = 1$ longitudinally and $a = 0$ transversely.

We have estimated the growth rates for both longitudinal and transverse instabilities for typical PEP-II parameters, that is, 1746 bunches having a total current of 0.99 A (HER) or 2.14 A (LER). This bunch number, which ignores the gap for clearing ions, is necessary for calculations performed with ZAP in the frequency domain.

Two different cases, based on the cavity design described in Section 5.5, were studied:

Case A: Undamped cavities; 20 cells (HER) or 10 cells (LER)

Case B: As in A, but with HOMs damped to $Q = 70$; 20 cells (HER) or 10 cells (LER)

In Case A, we examined the behavior of a standard PEP-II cavity with no HOM damping. This cavity has a high shunt impedance for the fundamental while having reasonable values for the HOMs. Case B represents what happens when the higher-order RF modes of the single-cell system are heavily de-Qed by external means, such as the waveguides described in Section 5.5.

Predictions of longitudinal growth times (for the fastest-growing mode) for both RF scenarios considered are summarized in Tables 4-31 and 4-32. The undamped cavity

Table 4-31. Longitudinal coupled-bunch growth times for the PEP-II HER (9 GeV; τ_E = 18.4 ms) at a beam current of 0.99 A.

(A) Undamped	
$\tau_{a=1}$	0.06 ms
$\tau_{a=2}$	2.0 ms
(B) Damped to Q = 70	
$\tau_{a=1}$	7.7 ms
$\tau_{a=2}$	363 ms

(Case A) gives a = 1 growth times below 0.1 ms. Substantial de-Qing (Case B) does help slow down the growth considerably, to times on the order of 8 ms. Note that the feedback system power required to counteract these instabilities will scale as the square of the growth rate, so the change associated with damping the cavity HOMs is very significant.

Although not shown in Tables 4-31 and 4-32, we have also observed that the fundamental mode of the RF system is capable of causing instability for selected coupled-bunch normal modes. This problem is handled via feedback on the cavity itself, as described in Sections 5.5 and 5.6. Transverse results, summarized in Tables 4-33 and 4-34, are similar to those for the longitudinal case. Here, too, we find for Case A that the two lowest synchrotron modes, a = 0 and a = 1, have growth times much shorter than the radiation damping time. We again note the benefits of substantial de-Qing (Case B) in slowing down the growth rates to more manageable levels. For Case A, it is the RF HOMs that dominate the predicted instability growth times for both a = 0 and a = 1

Table 4-32. Longitudinal coupled-bunch growth times for the PEP-II LER (3.1 GeV; τ_E = 19.8 ms) at a beam current of 2.14 A.

(A) Undamped	
$\tau_{a=1}$	0.03 ms
$\tau_{a=2}$	1 ms
(B) Damped to Q = 70	
$\tau_{a=1}$	3.8 ms
$\tau_{a=2}$	180 ms

Table 4-33. Transverse coupled-bunch growth times for the PEP-II HER (9 GeV; τ_x = 37.2 ms) at a beam current of 0.99 A.

(A) Undamped	
$\tau_{a=0}$	0.20 ms
$\tau_{a=1}$	3.2 ms
(B) Damped to Q = 70	
$\tau_{a=0}$	4.5 ms
$\tau_{a=1}$	122.0 ms

synchrotron modes. For Case B, however, the growth of the instability is driven exclusively by the resistive-wall impedance for a = 0 modes (though the cavity HOMs still dominate the growth time for the a = 1 modes). Thus, the transverse feedback system power requirements are determined by the resistive-wall instability, as discussed in Section 5.6.2.

Although the feedback system design (Section 5.6) is based on detailed simulations of the multibunch growth rates, the simple estimates made here already justify the effort that has gone into designing an effective HOM damping system for the RF cavities (described in Section 5.5).

Table 4-34. Transverse coupled-bunch growth times for the PEP-II LER (3.1 GeV; τ_x = 40.3 ms) at a beam current of 2.14 A.

(A) Undamped	
$\tau_{a=0}$	0.1 ms
$\tau_{a=1}$	1.4 ms
(B) Damped to Q = 70	
$\tau_{a=0}$	1.1 ms
$\tau_{a=1}$	21.4 ms

4.3.3 Summary of Findings

Total beam current limitations in both rings will depend upon the ability of the vacuum system to maintain an acceptable pressure, about 5 nTorr, in the presence of 1–2 A of circulating beam. Neither bunch lengthening and widening due to the longitudinal microwave instability (which places a limit on the allowable broadband impedance), nor current limitations arising from the transverse mode-coupling instability are predicted to be constraints in the multibunch scenario considered here.

We have seen here that the performance of both high- and low-energy rings is likely to be limited mainly by coupled-bunch instabilities. Our choice of specially designed single-cell RF cavities helps to reduce the longitudinal HOM impedance by permitting the voltage to be produced with relatively few cells and by permitting the cavity HOMs to be effectively damped. Feedback systems able to deal with the remaining growth have been designed; they are described in Section 5.6.

4.4 BEAM-BEAM ISSUES

As discussed in Chapter 3, the desire to achieve high luminosity leads one naturally to specify high currents and/or small beam sizes. These tend to make the beam-beam interaction stronger, which, in turn, may lead to beam blowup, coherent oscillations, or fast particle losses that could defeat the purpose of the initial specification.

If the beam-beam interaction is sufficiently weak, the beams behave as if there were no collisions, and the performance is controlled by the single-beam parameters of the two rings. This condition implies a relative simplicity in the operation of the collider, because the two beams are effectively decoupled. The price one must pay for this simplicity is that, in order to achieve a specified luminosity, the weakness of the beam-beam interaction must be compensated by using large beam currents distributed over many bunches, or over few bunches with a large beam emittance. Either of these approaches can become a problem for other aspects of the design, such as the vacuum system or RF system, and can also lead to various kinds of beam instabilities.

If the beam-beam interaction is significant, the dynamical beam parameters generally deviate from their nominal values. A strong beam-beam interaction naturally tends to imply a high luminosity, but it entails the potential for the problems mentioned above. In addition, the operation becomes relatively more complicated because the two beams are effectively coupled.

Obviously, the desired luminosity performance of the collider implies specifications on the dynamical quantities. The nominal quantities, on the other hand, imply specifications on the individual rings. If the beam-beam dynamics were well understood, it would be possible to translate specifications from dynamical to nominal quantities, and then to proceed to the design of the two rings individually. Unfortunately, our understanding is incomplete. This is particularly true for asymmetric colliders, which involve the additional complication of having two separate rings. Furthermore, all beam-beam simulation tools in existence take nominal parameters as input and produce dynamical quantities as output. Therefore, the understanding obtained from beam-beam

simulations proceeds, in some sense, "in reverse." In practice, therefore, the only way to arrive at a specification of nominal beam parameters is to proceed by iterations.

The basic strategy we adopt for PEP-II is to choose values for the nominal quantities (including the beam-beam parameters ξ_0) to achieve a certain (nominal) luminosity, and then to verify by simulations that the dynamical behavior is close to nominal. If the dynamical results are substantially different from the nominal expectations, we change the nominal parameters and try again until an acceptable solution is found.

As mentioned earlier in this report, the key figure-of-merit for PEP-II (or any other particle "factory") is high integrated luminosity. This implies that a proper design must have good operational reliability and high average luminosity. This last requirement implies high peak luminosity, long beam lifetime, and the capability for rapid injection; the first two requirements are almost always in conflict.

The bulk of the beam-beam studies carried out to date, which are summarized here, have set a priority on demonstrating the feasibility of attaining or exceeding a short-time-average luminosity of 3×10^{33} cm^{-2} s^{-1}. In this section, we present one set of parameters that strikes a balance between the conflicting requirements mentioned above. This solution is not necessarily unique or optimal, but it is an existence proof that such a value for the luminosity is an achievable goal. The short-time-average luminosity is determined by the dynamics of the beam core, while the beam lifetime is determined by the long-time dynamics of the tails of the beam. Since high peak luminosity is a necessary (but not sufficient) condition for good average luminosity, we have mainly focused our efforts on the dynamics of the beam core. Preliminary results from studies of beam-tail distributions (see Section 4.4.5) indicate acceptable beam lifetimes.

A complete set of beam-beam studies would need to address a large number of issues, such as those arising from the energy and lattice asymmetries, multibunch coherent effects, magnet nonlinearities, multiple parasitic collisions, injection transients, and beam lifetime calculations. Such a task is beyond the reach of any single tool available today, so one must necessarily resort to various approximations; the studies summarized here are no exception. For this reason we cannot, in general, interpret our results quantitatively. However, we do believe that qualitative comparisons between results for different parameter values provide us with valid guidance with regard to desirable or undesirable changes in these parameters. This philosophy underlies the interpretation of our beam-beam studies, particularly multiparticle simulations.

In summary, although substantial work remains to be done, we are confident that the solution we propose here will lead to a productive *B* factory, and we further expect that improved solutions can be found by modest modifications of various parameters.

4.4.1 Nominal and Dynamical Beam Quantities

In the absence of the beam-beam interaction, the beam parameters are determined by the lattice, the energy, and the RF parameters of each ring. In particular, this is true of the emittances and therefore the beam sizes at the interaction point (IP). From these one can compute the beam-beam parameters and the resultant luminosity in the limit that the beam-beam interaction does not change them; the quantities calculated in this limit are referred to here as *nominal* and are indicated by a subscript 0. As an example of our

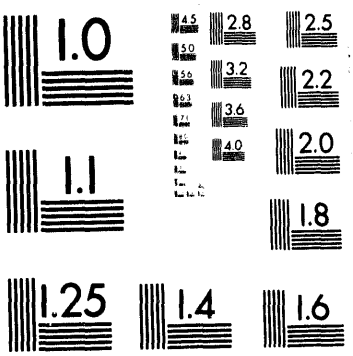
1.0
1.1
1.25
1.4
1.6
1.8
2.0
2.2
2.5
2.8
3.2
3.6
4.0
4.5
5.0
5.6
6.3
7.1

3 of 7

notation, the nominal vertical beam size at the IP, $\sigma^*_{0y,+}$ and beam-beam parameter $\xi_{0y,+}$ of the positron beam, and the nominal luminosity $\mathcal{L}_0$ are given by

$$\sigma^*_{0y,+} = \sqrt{\varepsilon_{0y,+}\beta^*_{y,+}} \tag{4-63a}$$

$$\xi_{0y,+} = \frac{r_0 N_- \beta^*_{y,+}}{2\pi\gamma_+ \sigma^*_{0y,-}\left(\sigma^*_{0x,-} + \sigma^*_{0y,-}\right)} \tag{4-63b}$$

$$\mathcal{L}_0 = \frac{N_+ N_- f_c}{2\pi\sqrt{\left(\sigma^{*2}_{0x,+} + \sigma^{*2}_{0x,-}\right)\left(\sigma^{*2}_{0y,+} + \sigma^{*2}_{0y,-}\right)}} \tag{4-63c}$$

where $\beta^*_{y,+}$ and $\varepsilon_{0y,+}$ are the vertical beta function at the IP and the nominal emittance of the positron beam, the $N_\pm$ are the numbers of particles per bunch, r_0 is the classical electron radius, and f_c is the bunch collision frequency. We assume here that the bunches collide head-on, that they have elliptical Gaussian transverse profiles with common axes, and that they have lengths comparable to or smaller than their transverse beta functions. In this case, the so-called "hourglass" reduction effect is small [Furman, 1991a]. There are three more beam-beam parameters, whose expressions are obtained from the above by the replacements $x \leftrightarrow y$ and/or $+ \leftrightarrow -$. If the bunches are evenly spaced by a distance s_B, the bunch collision frequency is, in the relativistic limit, $f_c = c/s_B$, where c is the speed of light.

Once the beams are brought into collision, the emittances inevitably deviate from their nominal values and, as a result, so do all quantities involving the beam sizes, including the beam-beam tune shift and the luminosity. These are the *dynamical* quantities, denoted without the subscript 0; the dynamical quantities corresponding to those in Eqs. 4-63 above are given by

$$\sigma^*_{y,+} = \sqrt{\varepsilon_{y,+}\beta^*_{y,+}} \tag{4-64a}$$

$$\xi_{y,+} = \frac{r_0 N_- \beta^*_{y,+}}{2\pi\gamma_+ \sigma^*_{y,-}\left(\sigma^*_{x,-} + \sigma^*_{y,-}\right)} \tag{4-64b}$$

$$\mathcal{L} = \frac{N_+ N_- f_c}{2\pi\sqrt{\left(\sigma^{*2}_{x,+} + \sigma^{*2}_{x,-}\right)\left(\sigma^{*2}_{y,+} + \sigma^{*2}_{y,-}\right)}} \tag{4-64c}$$

In this discussion, we assume that the beam-beam interaction does not induce coherent oscillations or a relative displacement of the closed orbits at the IP. This is discussed in greater detail when we describe our simulation results in Section 4.4.4.

4.4.2 Transparency Symmetry

The fact that an asymmetric collider necessarily consists of two rings enlarges the beam dynamics parameter space considerably relative to a single-ring, symmetric collider. The bunches in the two rings see different RF systems, different lattice functions, and different magnetic fields. Even the simplest beam-beam dynamics study requires, at a minimum, the specification of the following quantities:

- Two values for the number of particles per bunch, $N_{\pm}$
- Six beam sizes (two transverse and one longitudinal for each beam)
- Four beta functions at the IP (one vertical and one horizontal for each beam)
- Six tunes
- Two sets of damping decrements

In general, the four beam-beam parameters are different, as can be seen from Eq. 4-63.

Because no asymmetric e^+e^- colliders exist at present, and because the consequences of the beam-beam interaction are not completely understood for intense beams, it has been argued [Garren, 1989; Chin, 1989, 1990] that a cautious approach would be to require that the beam dynamics of an asymmetric collider resemble as closely as possible the dynamics of a symmetric one. In this way, the design can draw upon the valuable experience gained from single-ring colliders. This is the so-called "transparency symmetry" condition; it is reached by imposing constraints on the parameters of the two rings according to the following:

(i) Pairwise equality of nominal beam-beam parameters: $\xi_{0x,+} = \xi_{0x,-}$ and $\xi_{0y,+} = \xi_{0y,-}$

(ii) Pairwise equality of nominal beam sizes: $\sigma^*_{0x,+} = \sigma^*_{0x,-}$ and $\sigma^*_{0y,+} = \sigma^*_{0y,-}$

(iii) Equality of damping decrements of the two rings

(iv) Equality of the tune modulation amplitudes due to synchrotron oscillations: $(\sigma_\ell \nu_s/\beta^*_{x,y})_+ = (\sigma_\ell \nu_s/\beta^*_{x,y})_-$, with σ_ℓ the bunch length and ν_s the synchrotron tune

These conditions have been arrived at by a combination of analytic arguments and by trial and error in simulations. It has been shown that, in certain cases, the predicted performance is better when the above conditions are satisfied than when they are badly violated [Chin, 1989, 1990]. From the theoretical perspective, however, the status of this transparency symmetry is not completely settled: It has been argued, from general principles, that the *global* beam-beam limit (understood to mean maximum integrated luminosity at a fixed overall cost) in an asymmetric collider can only be reached under asymmetric conditions [Tennyson, 1990]. However, it is possible that this beam-beam limit can be achieved only at the price of relinquishing too much flexibility and therefore operational reliability, or of undesirably tight tolerances. Furthermore, it is not known at present how different the luminosity at the beam-beam limit would be compared with what could be achieved in a given transparent-symmetric design. On the other hand, by demanding that the dynamics of the two beams be identical, a single-particle Hamiltonian

analysis in the linear-lattice approximation leads to a more restrictive set of transparency conditions than those above [Krishnagopal and Siemann, 1990b]. This analysis implies that the tunes, emittances, beta functions, beam-beam parameters, and bunch lengths of the two beams must be pairwise equal. The only freedom left over is a trade-off between energy and bunch current such that $(N\gamma)_+ = (N\gamma)_-$.

In any case, the design of PEP-II must strike a compromise among competing requirements from different areas of the design. This compromise requires accommodating certain constraints, such as those arising from single-particle nonlinear dynamics, synchrotron radiation masking, etc., that affect an idealized optimization of the beam-beam interaction. As a result of this compromise, the present design of PEP-II satisfies exactly only conditions (i) and (ii) above. However, as will be discussed later in this section, we have also carried out studies in which condition (i) is violated [Eden and Furman, 1993a]. These studies show that the dynamics behaves smoothly as the nominal beam-beam parameters move away from equality. The PEP-II design allows enough flexibility to accommodate such a departure from condition (i), within a certain range, should further research indicate the need. For now, however, we have adopted the approximate transparency symmetry as a prudent starting point in the design.

An important practical implication of the constraints above is that they reduce considerably the parameter space and hence simplify the design. A mathematical advantage of transparency symmetry is that the luminosity can be very simply and conveniently expressed in terms of a single beam-beam parameter. First, we note that condition (ii) above implies that there is a single nominal beam-aspect ratio r,

$$\left(\frac{\sigma_{0y}^*}{\sigma_{0x}^*}\right)_+ = \left(\frac{\sigma_{0y}^*}{\sigma_{0x}^*}\right)_- \equiv r \tag{4-65}$$

and that the expression for the nominal luminosity simplifies to

$$\mathcal{L}_0 = \frac{N_+ N_- f_c}{4\pi\sigma_{0x}^*\sigma_{0y}^*} \tag{4-66}$$

By combining conditions (i) and (ii), we have [Garren, 1989; Chin, 1990; Furman, 1991b]

$$\frac{\beta_{x,-}^*}{\beta_{x,+}^*} = \frac{\beta_{y,-}^*}{\beta_{y,+}^*} = \frac{(EI)_-}{(EI)_+} \tag{4-67}$$

where I = total beam current (assuming no gaps). One also finds that there is a single beta-function ratio (rather than two) and a single nominal emittance ratio:

$$\frac{\beta_{y,+}^*}{\beta_{x,+}^*} = \frac{\beta_{y,-}^*}{\beta_{x,-}^*} \equiv r_\beta \quad \text{and} \quad \frac{\varepsilon_{0y,+}}{\varepsilon_{0x,+}} = \frac{\varepsilon_{0y,-}}{\varepsilon_{0x,-}} \equiv r_\varepsilon \tag{4-68}$$

so that the beam-size ratio becomes

$$r = \sqrt{r_\varepsilon r_\beta} \tag{4-69}$$

The nominal beam-beam tune shift parameters are related to r_β and r_ε by

$$\frac{\xi_{0y}}{\xi_{0x}} = \sqrt{\frac{r_\beta}{r_\varepsilon}} = \frac{r_\beta}{r} \tag{4-70}$$

and the nominal luminosity is

$$\mathcal{L}_0 = K(1+r)\xi_{0y}\left(\frac{EI}{\beta_y^*}\right)_{+,-} \tag{4-71}$$

where the subscript +,– means that the expression in parentheses can be taken from either beam, because of Eq. 4-67. The constant K is

$$\begin{aligned} K &= \frac{1}{2er_0mc^2} \\ &= 2.17\times 10^{34}\ \left[\mathrm{cm^{-2}\,s^{-1}}\right]\cdot\left[\frac{\mathrm{cm}}{\mathrm{GeV\cdot A}}\right] \end{aligned} \tag{4-72}$$

where mc^2 is the rest energy of the electron and e is its charge. Therefore, if we express the energy E in GeV, the current I in A, and the beta function in cm, we obtain

$$\mathcal{L}_0 = 2.17\times 10^{34}\ (1+r)\xi_{0y}\left(\frac{EI}{\beta_y^*}\right)_{+,-}\quad \left[\mathrm{cm^{-2}\ s^{-1}}\right] \tag{4-73}$$

Note that ξ_{0y} cannot be varied independently of the other parameters, since it is related to them through Eqs. 4-69 and 4-70. It is also worth commenting that Eq. 4-73 can be rewritten, if desired, in terms of horizontal, rather than vertical, parameters by making the replacements $y \rightarrow x$ and $r \rightarrow 1/r$.

In contrast, the nominal aspect ratio r, the beta function ratio r_β, and the nominal emittance ratio r_ε are free parameters, except that they are related by Eq. 4-69.

If, in addition to the transparency symmetry condition (i), we impose the extra requirement that *all four* beam-beam parameters should be equal, that is

$$\xi_{0x,+} = \xi_{0y,+} = \xi_{0x,-} = \xi_{0y,-} \equiv \xi_0$$

as we will in our simulations presented below, then one finds the additional equality $r = r_\beta = r_\varepsilon$ or, explicitly,

$$\frac{\sigma_{0y,+}^*}{\sigma_{0x,+}^*} = \frac{\sigma_{0y,-}^*}{\sigma_{0x,-}^*} = \frac{\beta_{y,+}^*}{\beta_{x,+}^*} = \frac{\beta_{y,-}^*}{\beta_{x,-}^*} = \frac{\varepsilon_{0y,+}}{\varepsilon_{0x,+}} = \frac{\varepsilon_{0y,-}}{\varepsilon_{0x,-}} = r \tag{4-74}$$

The formula for the luminosity reads the same as the previous case, Eq. 4-73, except that now the beam-beam parameter carries no index *y*.

4.4.3 Physics of the Simulation Codes

For our simulations, we employ two distinct codes (one by H. Yokoya and another, called "TRS," by Tennyson [1989]) that are similar, but not identical. Each of these codes represents a beam bunch by a collection of many (we have used up to 256) "superparticles." Initially, these superparticles have a Gaussian distribution in phase space. At the IP, the rms beam sizes σ_x and σ_y are calculated from the superparticle distribution at every turn. Although the shape of the distribution deviates from Gaussian as time progresses, for the purposes of computing the beam-beam kick, it is a good approximation (for the range of parameters of interest to us) to retain the Gaussian shape, albeit with time-dependent σ_x and σ_y. From these distributions, the beam-beam force on each superparticle of the opposing bunch is computed by means of the well-known expression for the transverse electric field in terms of the complex error function [Bassetti and Erskine, 1980]. Deviations from a Gaussian shape are monitored; if the dynamic distribution were to differ substantially from Gaussian, one would have reason to doubt the results, owing to the lack of self-consistency. The importance of allowing for, and consistently treating, non-Gaussian distributions has been emphasized [Krishnagopal and Siemann, 1991]. At present, it appears that such an extension implies a significant complication in the tracking codes and a major increase in the computer time needed. This work remains to be carried out in the future to confirm that, in this parameter regime, our present predictions are not significantly modified.

Each beam is transported through the rest of the machine by a linear matrix; that is, no lattice nonlinearities are considered. Synchrotron radiation and damping are included and are represented by localized kicks. The RF system is also represented by a localized kick. Typically, the beams are tracked for three to five damping times to verify that an equilibrium situation has been reached. (For the specific set of parameters studied here, we have verified that five damping times is long enough to yield stable results and that three damping times is often adequate.)

The electromagnetic fields produced by relativistic particles are Lorentz-contracted into a thin disk perpendicular to the direction of motion. As a consequence, the force on a single particle due to the opposing bunch is, to a good approximation, strictly transverse; longitudinal forces can be neglected. (Indeed, the integrated longitudinal force is *exactly* zero in the case when the beta function is constant during the collision.) What cannot be neglected, however, is the fact that the opposing bunch has a finite longitudinal extent.

Near the IP, the vertical beta function is small and the betatron phase of a particle changes rapidly. Consequently, the net force due to the opposing bunch (that is, the beam-beam interaction) is distributed over a wide range of betatron phase. Because most beam-beam limiting phenomena are resonant in nature, this feature, called phase averaging, is important and must be incorporated into beam-beam calculations and simulations [Krishnagopal and Siemann, 1990a].

Phase averaging thus emphasizes the importance of the longitudinal extent of the beam-beam interaction. A Hamiltonian analysis that includes this feature predicts resonance strengths that are smaller than those calculated by models in which the beam-beam interaction is approximated by a single kick (impulse approximation). This also implies that resonance overlap, and the stochastic motion that results from it, set in at higher currents than would be estimated in the impulse approximation.

In the simulation results presented here, we allow for phase averaging by dividing the bunch longitudinally into several slices. Typically, five slices are used, although spot-checks with nine slices have sometimes been made. Both codes distribute the slices evenly along the length of the bunch and symmetrically about its center. However, the slices farthest away from the center are located in different places in the two codes. In Yokoya's code, the outermost slices are located at a distance $s = \pm 2\sigma_\ell$ from the bunch center, regardless of the number of slices. In TRS, the corresponding outermost distance is $s = \pm[1 + (n - 3)/12]\sigma_\ell$, where n is the total number of slices. Thus, the two codes have identical slicing algorithms only when 15 slices are used; for fewer slices, TRS code concentrates the slices closer to the center of the bunch than does Yokoya's code. As the bunches pass through each other during the collision, the beta functions seen by the different slices are different, since the slices collide at points away from the IP. In the neighborhood of the IP, we take the s-dependence of the beta functions to correspond to that of a drift.

Besides the distinctions discussed above, the codes also differ in technical details having to do with the way certain quantities are averaged from turn to turn in order to smooth out statistical fluctuations associated with the relatively small number of superparticles.

The lattice design described in Section 4.1 has head-on collisions at the IP, with magnetic separation of the beams. However, the beams go into their own vacuum pipes only after traveling about 3 m away from the IP; as a result, they experience several grazing collisions on their way into and out of the IP. There are four such "parasitic" crossings on either side of the IP. These parasitic crossings couple the dynamics of all bunches, so a completely faithful simulation of the PEP-II beam-beam dynamics would require 1658 bunches per ring, along with a gap equivalent to 88 bunches. Since this is an impractical requirement for any present-day simulation, we make two simplifying approximations: (i) We consider only the first parasitic crossing on either side of the IP and (ii) we use only one bunch per ring, which is "reused" (so that this bunch collides three times per turn—two parasitic crossings plus the main collision at the IP—with the same partner in the other beam).

The first approximation is quite reasonable, since, as discussed in more detail below, the effect of the first parasitic crossing overwhelms all the others. The second approximation rests on the sensible assumption that, in reality (or in a faithful simulation), the particle distributions are not expected to differ much from bunch to bunch, especially when the bunches interact at a distance, as is the case at the parasitic crossings.

Given the complicated process that is being simulated, it is natural to test the predictions of the simulation codes against known experimental results. As an example, we have studied the particular PEP configuration summarized in Table 4-35 with Yokoya's code. We find that the luminosity prediction agrees with the measured value to

Table 4-35. PEP parameters used in simulation comparison.[a]

Betatron tunes	
Horizontal	21.2962
Vertical	18.2049
Beta functions at IP	
Horizontal [m]	1.342
Vertical [m]	0.053
Dispersion at IP	
Horizontal [m]	0.00049
Emittances	
Horizontal [nm·rad]	99.6
Vertical [nm·rad]	3.96
Synchrotron tune	0.043
Beam current [mA]	18.85
Nominal beam-beam parameter, ξ_0	
Horizontal	0.04653
Vertical	0.04653
Luminosity	
Nominal [$cm^{-2}\,s^{-1}$]	5.07×10^{31}
Observed [$cm^{-2}\,s^{-1}$]	4.80×10^{31}
Simulation [$cm^{-2}\,s^{-1}$]	4.34×10^{31}

[a] Data from E. Bloom and M. Donald.

within 10%. In fact, the simulation result is actually slightly *pessimistic,* since it is 10% below the observed luminosity. We also predict from the simulations that there will be no saturation of the dynamic beam-beam tune-shift parameter ξ up to a beam current of 30 mA—again in agreement with experimental observations. Calculations for other PEP configurations yield more or less equivalent agreement with the observed luminosities.

We have also tested TRS for the case of PEP, for a different configuration from that above, including the effect of the parasitic crossings in the arcs. The comparison with experiment is summarized in Fig. 4-89. In this comparison, too, we find reasonable agreement with experiment. Again, we note that the code tends to underestimate the luminosity.

Insofar as the simulation results in both cases are consistent in trend with the actual PEP observations, we feel that the predictions derived from these codes are reasonable guides for the design of PEP-II. Implied in this statement is the assumption that there is

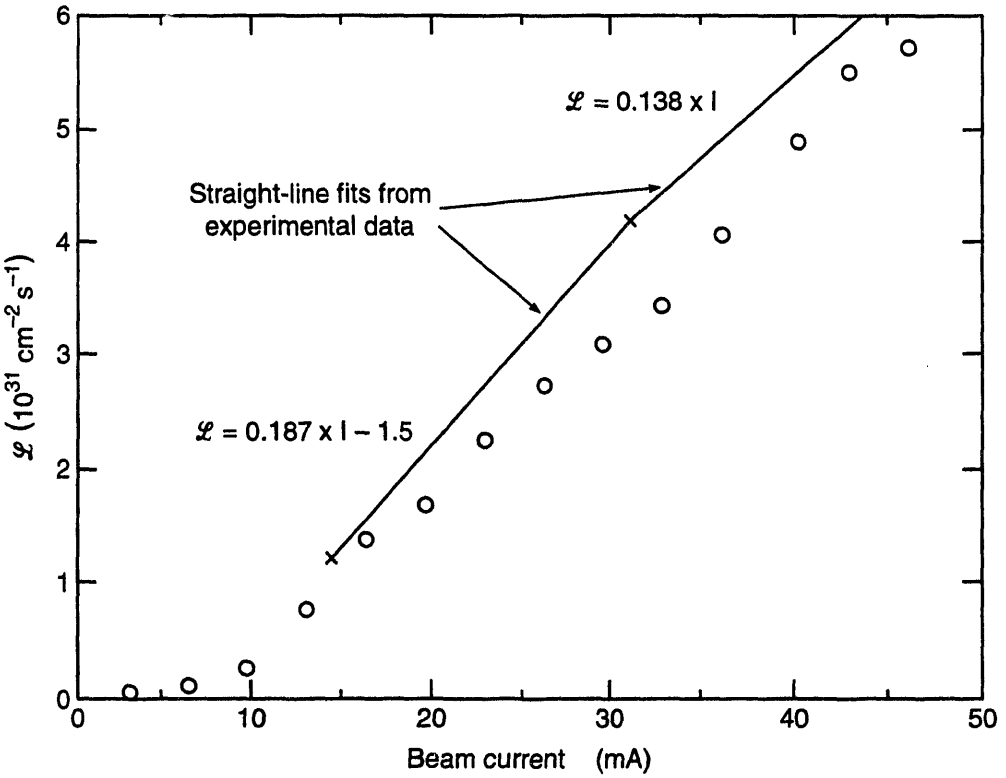

Fig. 4-89. Plot of observed luminosity at PEP and the simulation results from TRS. The tune values used in the simulation were slightly different from those used in the experiment itself; preliminary results show that the agreement improves when the tunes are the same.

no new physics that enters into the beam-beam interaction due to the asymmetric collisions. At the present time, we have every reason to believe that this assumption is valid.

4.4.4 Beam Dynamics Studies

The primary parameters that determine the strength of the beam-beam interaction are the four nominal beam-beam parameters, $\xi_{0x,\pm}$ and $\xi_{0y,\pm}$. If these are small enough, and if the working point of the ring is not too close to the integer tunes, ξ_0 is equal to the nominal tune spread induced by the beam-beam interaction. We adopt, as a starting point, the fully symmetric condition

$$\xi_{0x,+} = \xi_{0y,+} = \xi_{0x,-} = \xi_{0y,-} = 0.03 \tag{4-75}$$

The specification of $\xi_0 = 0.03$ is intended to be conservative, insofar as existing machines have already achieved substantially higher values of ξ_0 [Rice, 1989, 1990; Seeman, 1985]. As mentioned, this strategy of setting the beam-beam interaction to be

reasonably weak has the desirable consequence that the beam behavior will be close to nominal. This has the advantage of preserving operational flexibility, because the closer to nominal the beam-beam dynamics is, the more controllable is the machine performance. (Clearly, in an operating collider, the machine parameters will be adjusted to maximize the luminosity. The idea here is not to limit the machine performance, but rather to leave room for subsequent improvements.)

As mentioned earlier in this section, most of our beam-beam studies carried out to date have set a priority on demonstrating the feasibility of attaining or exceeding a dynamical luminosity value of 3×10^{33} cm^{-2} s^{-1}. We have studied first the short-time-average luminosity, which is determined by the dynamics of the beam core. This is studied quite effectively with "weak-strong" and "strong-strong" simulations involving a few hundred macroparticles per bunch tracked for several damping times, neglecting all lattice nonlinearities. Previous experiments and simulations for CESR [Jackson and Siemann, 1990] provide justification for the linear-lattice approximation since they show that magnet nonlinearities do not affect the core dynamics significantly once a good working point is adopted. On the other hand, the dynamics of the beam tails, relevant to beam lifetime, might be expected to be more sensitive to nonlinearities.

Specifically, the focus of our simulations has been to try to answer the following questions:

- Can a region of the tune plane be found such that the dynamics is close to nominal (that is, relatively small beam blowup)?
- Is the orbit separation between the two beams at the parasitic collisions large enough?
- Is the value of 0.03 for the beam-beam parameter conservative enough? How does the dynamics behave for $\xi = 0.05$?
- How do the beams behave during the first few damping times following injection?
- How do they behave after injection is complete but the beams are still separated by the injection orbit bump?
- How sensitive is the dynamics to changes in the asymmetry of the design?

Our basic strategy is first to choose nominal parameters and then to verify that the beam-beam interaction does not cause significant deviations from them. If the beam dynamics is substantially different from nominal (for example, if beam blowup is too large or beam lifetime too short), we change the nominal parameters and try again until an acceptable solution is found. In more detail, this strategy is divided into several steps:

(*i*) *Set nominal parameters.* Our design goal is a nominal luminosity of $\mathcal{L}_0 = 3 \times 10^{33}$ cm^{-2} s^{-1}. From this requirement and other considerations, a complete set of parameters for both rings can be derived (see Appendix A). For the purposes of this section, however, we show only an abbreviated list in Table 4-36. Further, because the collider design has evolved in parallel with the simulation study, some of the final parameters in Appendix A differ slightly from those in this section. The parameters indicated in Table 4-36, however, are the values used in the simulation study.

In Table 4-36, E is the beam energy, s_B is the bunch spacing, and f_c is the bunch collision frequency at the IP ($f_c = c/s_B$); V_{RF}, f_{RF}, and ϕ_s are the RF voltage, frequency,

Table 4-36. Main PEP-II parameters used in the beam-beam simulation studies.

	LER (e^+)	HER (e^-)
$\mathcal{L}_0$ [$cm^{-2}\,s^{-1}$]	3×10^{33}	
C [m]	2199.32	2199.32
E [GeV]	3.1	9.0
s_B [m]	1.26	
f_c [MHz]	238.000	
V_{RF} [MV]	9.5	18.5
f_{RF} [MHz]	476.000	476.000
ϕ_s [deg]	170.6	168.7
α	1.5×10^{-3}	2.41×10^{-3}
ν_s	0.050	0.052
σ_ℓ [cm]	1.0	1.0
σ_E/E	1.00×10^{-3}	0.616×10^{-3}
N [a]	5.630×10^{10}	2.586×10^{10}
I [A]	2.147	0.986
ε_{0x} [nm·rad]	61.27	45.95
ε_{0y} [nm·rad]	2.451	1.838
β_x^* [m]	0.375	0.500
β_y^* [m]	0.015	0.020
σ_{0x}^* [μm]	151.6	151.6
σ_{0y}^* [μm]	6.063	6.063
τ_x [turns]	5,014	5,014
τ_y [turns]	5,014	5,014

[a]These values for N do not take into account the existence of the ion-clearing gap, that is, they assume 1746 equally spaced bunches.

and synchronous phase, respectively; α is the momentum compaction factor; ν_s is the synchrotron tune; σ_ℓ is the rms bunch length; and τ_x, τ_y are the horizontal and vertical damping times, respectively. The other parameters are the emittances ε, beta functions β, and nominal rms beam sizes σ_0 at the IP.

The parameter values in Table 4-36 are consistent with Eq. 4-75 and our stated luminosity goal, as can be easily verified. The values do not, however, correspond exactly to the requirements of transparency symmetry, on account of the difference in the amplitudes of the tune modulation:

$$\left(\frac{\sigma_\ell \nu_s}{\beta_x^*}\right)_+ = 1.33\times 10^{-3}\,, \qquad \left(\frac{\sigma_\ell \nu_s}{\beta_x^*}\right)_- = 1.04\times 10^{-3}$$
$$\left(\frac{\sigma_\ell \nu_s}{\beta_y^*}\right)_+ = 3.33\times 10^{-2}\,, \qquad \left(\frac{\sigma_\ell \nu_s}{\beta_y^*}\right)_- = 2.60\times 10^{-2} \tag{4-76}$$

(*ii*) *Select a working point.* Usually, only the primary collisions at the IP are considered in this step. The choice of tunes can be made quite effectively with "weak-strong" beam-beam simulations, in which the high-energy beam is forced to remain undisturbed while the low-energy beam is studied dynamically. (For PEP-II, we are confident that this approximation is reasonable, because more realistic "strong-strong" simulations show that there is little or no beam blowup for the high-energy beam in our design.) This more approximate type of simulation has the advantages that it is relatively fast and that the effects of resonances, such as synchrotron sidebands, are clearly seen (thus allowing, in principle, a theoretical understanding of the underlying beam dynamics). The main figure-of-merit that we use in this study is the beam blowup factor of the low-energy beam.

A tune scan is presented in Fig. 4-90, which shows the vertical and horizontal beam blowup factors of the low-energy beam for each working point scanned [Tennyson, 1991b] (the tunes shown are the "bare lattice" tunes). This tune scan was actually carried out for an earlier design, called APIARY 6.3D, and it *does* include the effect of the parasitic collisions. From the limited perspective of the beam-beam studies presented in this section, the APIARY 6.3D design differs from the present design basically in two ways: (a) the beta functions at the IP of the high-energy ring in the current design are 2/3 as large as they were in APIARY 6.3D and (b) the normalized separation between the beam orbits at the first parasitic crossing, $d/\sigma_{0x,+}$, is ~55% larger in the current design than it was in APIARY 6.3D. The beam-beam parameters and nominal luminosity are the same in the two designs, and the synchrotron tunes are almost the same. Since the parasitic collisions were shown to be weak relative to the IP collisions for APIARY 6.3D [Eden and Furman, 1992a, 1992b; Chin, 1991a; Tennyson, 1991a], and they are even weaker in the current design, as shown below, the tune scan in Fig. 4-90 is still relevant for the current design. Figure 4-91 shows the same portion of the tune plane, with resonance lines through sixth order. The beam-beam interaction causes a tune spread because particles of different betatron amplitude experience different tune shifts. This causes the beam to have a characteristic "footprint" (see Fig. 4-92) that extends diagonally upward from the working point.

For the beam-beam simulations, we have adopted, as suggested by the results in Fig. 4-90, a working point with fractional tunes $\nu_x = 0.64$ and $\nu_y = 0.57$ (both beams). Several existing colliders operate in this region of the tune plane, just above the half-integer [Rice, 1989, 1990; Seeman, 1985], which has the advantage of reduced sensitivity to closed-orbit errors. As our results (presented below) show, this working point is quite acceptable, and we are confident that an optimal working point can be found close to our current choice. Because of the asymmetry of the machine design, it is possible that the optimal working point will be different for the two rings; an optimization study along these lines will be carried out in the near future.

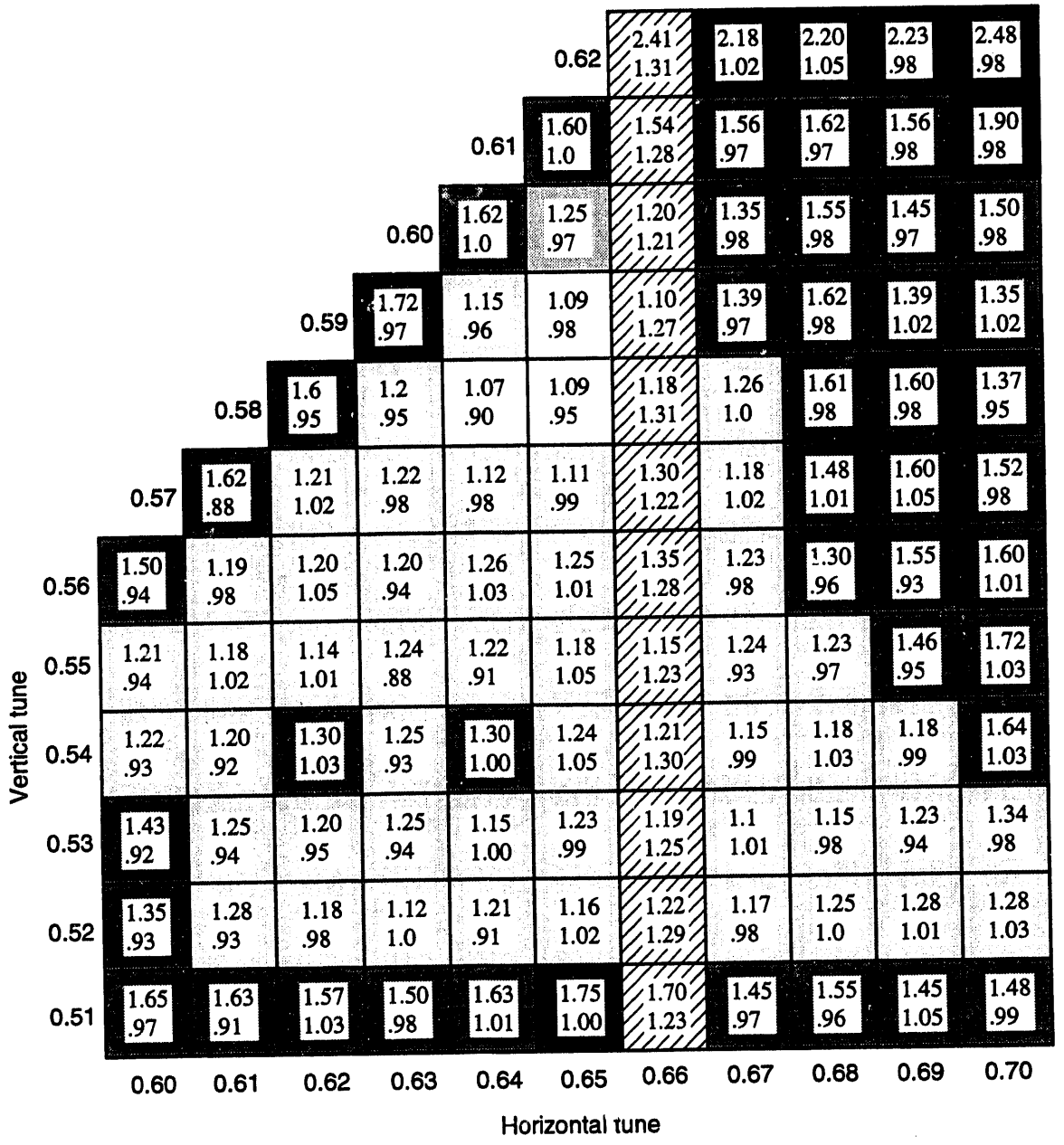

Fig. 4-90. Low-energy beam blowup factors (σ/σ_0) for various working points for the earlier PEP-II design APIARY 6.3D, including parasitic collisions. The numbers in each box are the vertical and horizontal blowup factors at that particular working point. The shading in each box is indicative of the blowup: the darker the shading, the larger the vertical blowup. The cross-hatched boxes indicate horizontal blowup >20%.

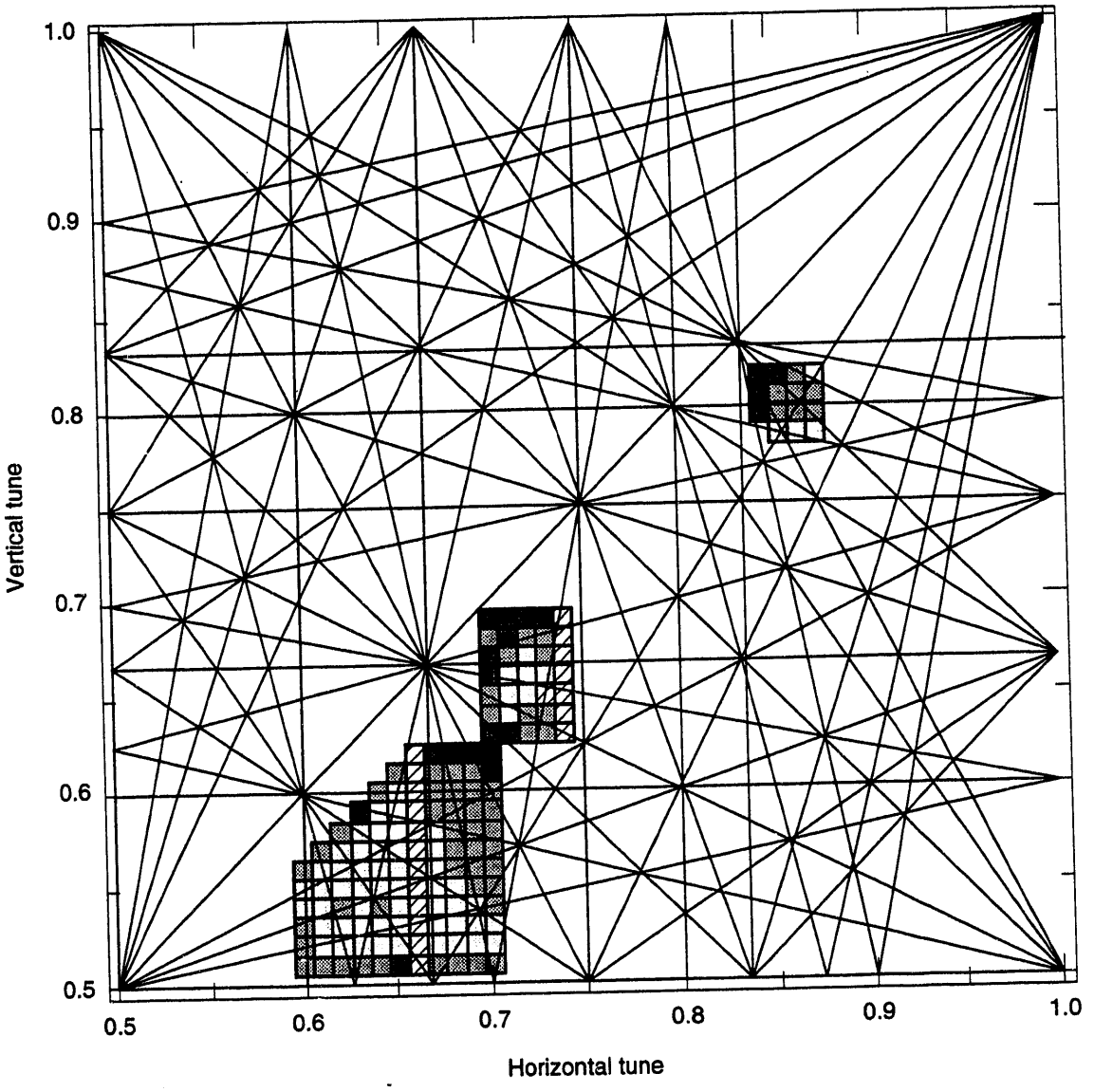

Fig. 4-91. Tune plot with even-order resonance lines through sixth order. This is the same portion of the tune plane as in the previous figure.

We will refer again to results for the earlier designs APIARY 6.3D [Furman, 1991] and APIARY 7.5 [Eden and Furman, 1992] in other subsections below. From the beam-beam perspective, there are only two differences between the present and previous designs: the beta functions of the HER are now smaller than before, and the normalized beam separation at the first parasitic collision is larger. The beam currents and emittances are adjusted such that the beam-beam parameters and nominal luminosity remain unchanged. A comparison is presented in Table 4-37.

(iii) Verify the behavior of the beam-beam interaction. The next step is to check that the beam-beam interaction remains reasonably weak in the fully coupled beam-beam calculations. This is done with "strong-strong" simulations, in which both beams are

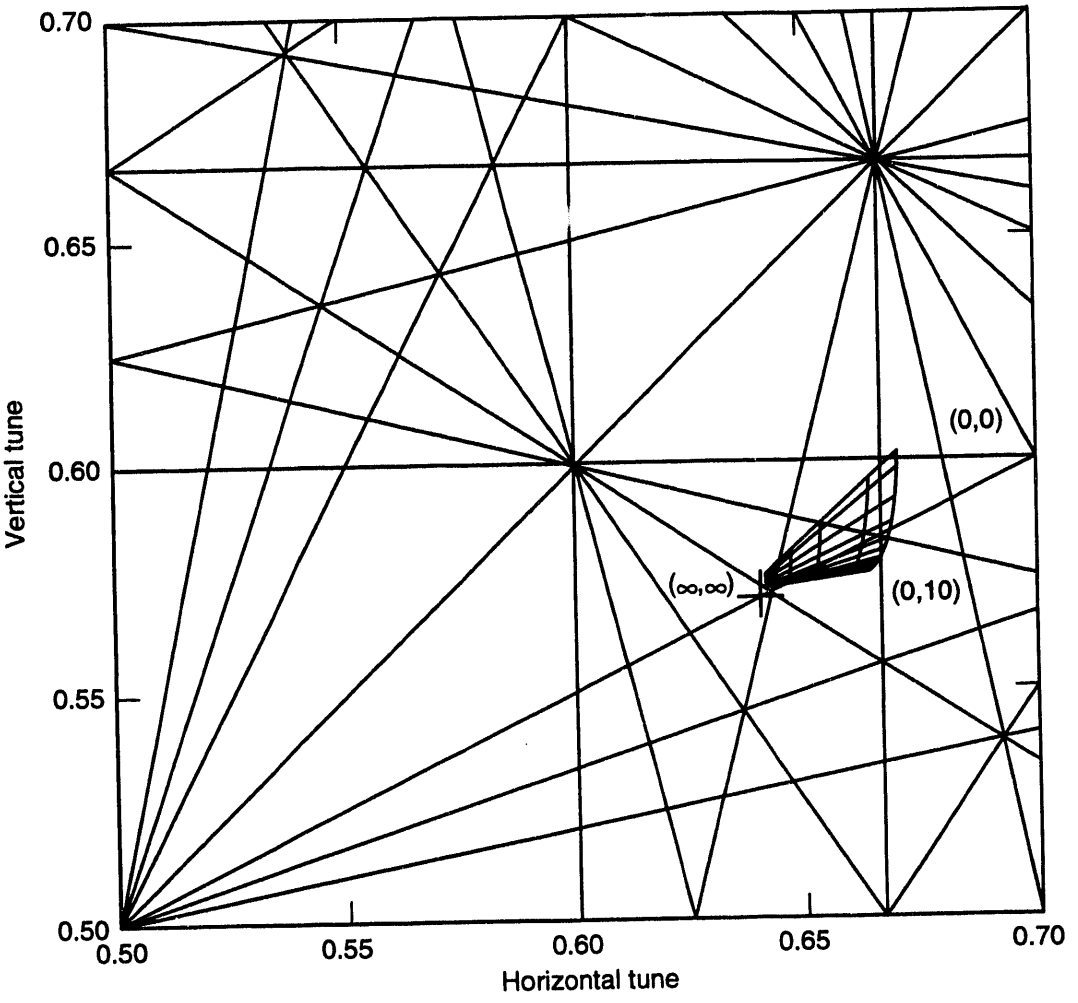

Fig. 4-92. Tune plot and beam footprint. The tune plane shows the working point (cross) and the beam footprint caused by the beam-beam tune spread. The lines in the footprint correspond to particles with amplitudes with constant σ_x or constant σ_y, at 0, 1, 2, 3, 4, 5, 6, 8 and 10σ. The particle closest to the working point has the largest amplitude, $10\sigma_x$ and $10\sigma_y$. The particle furthest away is at the center of the bunch and is labeled (0,0).

allowed to vary dynamically according to their mutual beam-beam interaction. During the initial stage, the study is done with only the primary collisions at the IP. This type of simulation is time consuming, but it is necessary because it is the only way to compute dynamical quantities, such as actual beam blowup and luminosity, and because it can reveal coherent oscillations, closed-orbit distortion, and particle losses. As a check on the robustness of our chosen parameters and working point, we have considered values of ξ_0 much higher than the nominal value of 0.03 in the simulations. This is shown in Fig. 4-93, which gives the calculated blowup factors of all four beam sizes vs ξ_0, and Fig. 4-94, showing the corresponding luminosities. In both Figs. 4-93 and 4-94, we maintain the equality of all four ξ_0 values (which are varied by simply increasing the

Table 4-37. Comparison between the current design and two earlier versions.

	Current design		APIARY 7.5		APIARY 6.3D	
	LEB	HEB	LEB	HEB	LEB	HEB
$\mathcal{L}_0$ [cm^{-2} s^{-1}]	3×10^{33}		3×10^{33}		3×10^{33}	
ξ_{0x}	0.03		0.03		0.03	
ξ_{0y}	0.03		0.03		0.03	
β_x^* [m]	0.375	0.50	0.375	0.75	0.375	0.75
β_y^* [m]	0.015	0.02	0.015	0.03	0.015	0.03
σ_{0x}^* [μm]	152		186		186	
σ_{0y}^* [μm]	6.1		7.4		7.4	
I [A]	2.1	1.0	2.1	1.5	2.1	1.5
d [mm] [a]	3.5		3.5		2.8	
d/σ_{0x} [a]	11.8	14.3	9.6	14.4	7.6	11.5

[a] d is the beam separation at the first parasitic collision, and d/σ_{0x} is the separation normalized to the local horizontal beam size.

number of particles per bunch). In general, the two codes predict reasonably similar dynamical behavior. (The discrepancy at large ξ_0 is probably related to the different ways the two codes handle coherent oscillations, which are significant at such extreme parameter values.)

Because the various beam sizes change differently, the dynamical beam-beam parameters also become different from each other. This means that the transparency symmetry is inherently broken by the dynamics, although not to a great extent.

(iv) Verify that the results are maintained when parasitic crossings are included. Although the beams collide head-on at the IP, the bunches experience grazing collisions on their way into and out of the region within about ±3 m of the IP, where both beams travel in a common pipe. We must assess the effect of these parasitic crossings on the performance. This is done with strong-strong simulations. Parasitic crossings have a potentially detrimental effect on beam blowup, because they induce odd-order resonances and horizontal-vertical coupling. Taken together, these effects make it harder to find an optimum working point in the tune plane.

There are four parasitic crossings symmetrically located on either side of the IP. All of them occur in the horizontal plane. For the purposes of studying the beam-beam dynamics, the first parasitic crossing (that is, the one closest to the IP on either side) overwhelms the others on account of the relatively small separation, together with the large vertical beta function. The strength of the long-range beam-beam kick at this first parasitic crossing is much greater than those of all the remaining crossings combined. This fact, discussed in more detail below, justifies our considering only this first parasitic

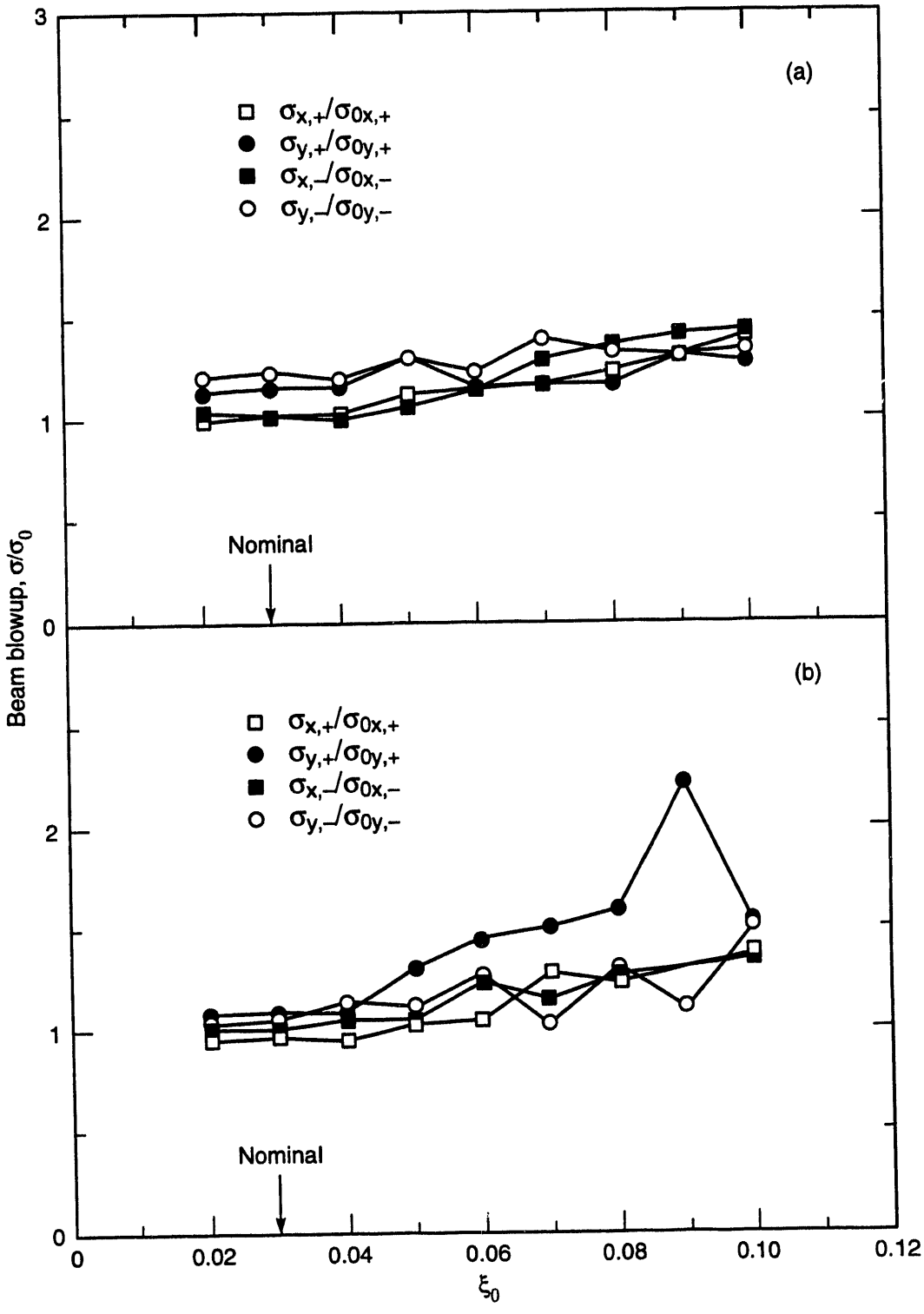

Fig. 4-93. Beam blowup factors vs ξ_0 (IP collisions only). These are the results for the dynamical beam size over nominal beam size for both beams, from both simulation codes: (a) Yokoya's and (b) TRS. The parameter ξ_0 is increased by increasing the number of particles per bunch in both beams, with fixed nominal emittance.

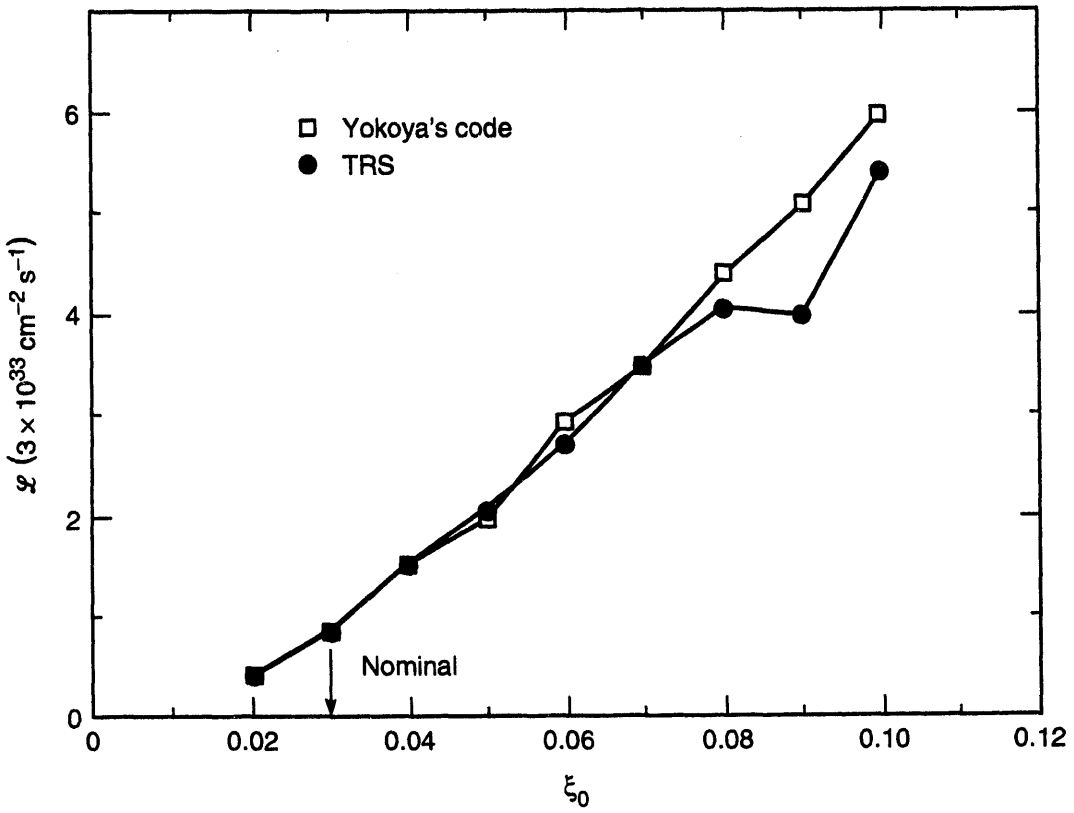

Fig. 4-94. Luminosity vs ξ_0 corresponding to the blown-up beam sizes in Fig. 4-93 (IP collisions only).

crossing in our present calculations. Table 4-38 shows the relevant parameters for the primary and the first parasitic crossing for PEP-II.

In Table 4-38, Δs is the distance from the IP to the parasitic crossing point along the beam trajectory; $2\pi\Delta\nu_x$ and $2\pi\Delta\nu_y$ are the phase advances from the IP to the parasitic crossing; d is the (horizontal) separation between the two closed orbits at the parasitic crossing; and d/σ_{0x} is a measure of the extent of the overlap between the two bunches at the parasitic crossing point. The nominal emittances and number of particles per bunch are listed in Table 4-36. The parasitic crossings induce a tune shift and an amplitude-dependent tune spread in the particles due to the mutual interaction of the two bunches. It can be shown that the incoherent beam-beam parameters of a particle at the center of the positron bunch from a single parasitic interaction point are, to lowest-order approximation, given by [Tennyson, 1991a]

$$\xi_{0x,+}^{(PC)} = -\frac{r_0 N_- \beta_{x,+}}{2\pi\gamma_+ d^2}$$

$$\xi_{0y,+}^{(PC)} = +\frac{r_0 N_- \beta_{y,+}}{2\pi\gamma_+ d^2} \qquad (4\text{-}77)$$

Table 4-38. PEP-II nominal parameters at the IP and first parasitic crossing.

	LER (e^+)		HER (e^-)	
Δs [cm] [a]	63			
d [mm] [a]	3.50			
	IP	First PC	IP	First PC
$\Delta\nu_x$ [a]	0	0.1645	0	0.1432
$\Delta\nu_y$ [a]	0	0.2462	0	0.2449
β_x [m]	0.375	1.43	0.500	1.29
β_y [m]	0.015	26.46	0.020	19.85
α_x	0	−1.68	0	−1.26
α_y	0	−41.99	0	−31.49
σ_{0x} [μm]	151.6	296.3	151.6	243.8
σ_{0y} [μm]	6.063	254.6	6.063	191.0
$\sigma_{0x'}$ [mrad]	0.404	0.404	0.303	0.303
$\sigma_{0y'}$ [mrad]	0.404	0.404	0.303	0.303
d/σ_{0x}	0	11.81	0	14.35
ξ_{0x}	0.03	−0.000224	0.03	−0.000152
ξ_{0y}	0.03	+0.004133	0.03	+0.002326
$\xi_{0x,\mathrm{tot}}$ [b]	0.0296		0.0297	
$\xi_{0y,\mathrm{tot}}$ [b]	0.0383		0.0347	

[a]The first PC occurs at a distance Δs and at a phase advance $\Delta\nu$ from the IP. At this point the nominal orbits are separated horizontally by a distance d.

[b]The total nominal beam-beam parameter is defined to be $\xi_{0,\mathrm{tot}} \equiv \xi_0^{(\mathrm{IP})} + 2\xi_0^{(\mathrm{PC})}$.

with the corresponding expressions for the electron bunch obtained by exchanging the indices + and − in Eq. 4-77. Here $\beta_{x,y}$ are the beta functions at the parasitic crossing location. The negative sign in the expression for $\xi_{0x,+}^{(\mathrm{PC})}$ arises from the fact that the horizontal force is a decreasing function of separation at the parasitic crossing. Using the numerical values for the parameters given in Table 4-38, we obtain

$$\xi_{0x,+}^{(\mathrm{PC})} = -0.00022, \qquad \xi_{0x,-}^{(\mathrm{PC})} = -0.00015$$
$$\xi_{0y,+}^{(\mathrm{PC})} = +0.0041, \qquad \xi_{0y,-}^{(\mathrm{PC})} = +0.0023 \tag{4-78}$$

which shows that the first parasitic crossings together contribute a vertical tune shift of approximately 0.008 to the nominal IP tune shift of 0.03 in the positron beam. The remaining parasitic crossings contribute negligibly to the tune shifts.

A tune shift by itself is not detrimental, since it can be compensated by a shift in the working point. However, as mentioned above, the amplitude dependence causes a tune spread, which is more problematic. This spread, which can be calculated by appropriate numerical integration [Tennyson, 1991a; Siemann, 1993], causes a distortion of the beam footprint, as shown in Fig. 4-95. Such a distortion makes it more difficult to find a good working point; for our present simulation purposes, we have maintained the original working point, $\nu_x = 0.64$, $\nu_y = 0.57$.

As implied by the above, the parasitic crossings produce horizontal-vertical coupling that can cause beam blowup. Obviously if the separation d were large enough, all effects of the parasitic crossings would disappear altogether. To assess this effect, we have carried out simulations in which we vary the separation d and keep all other parameters

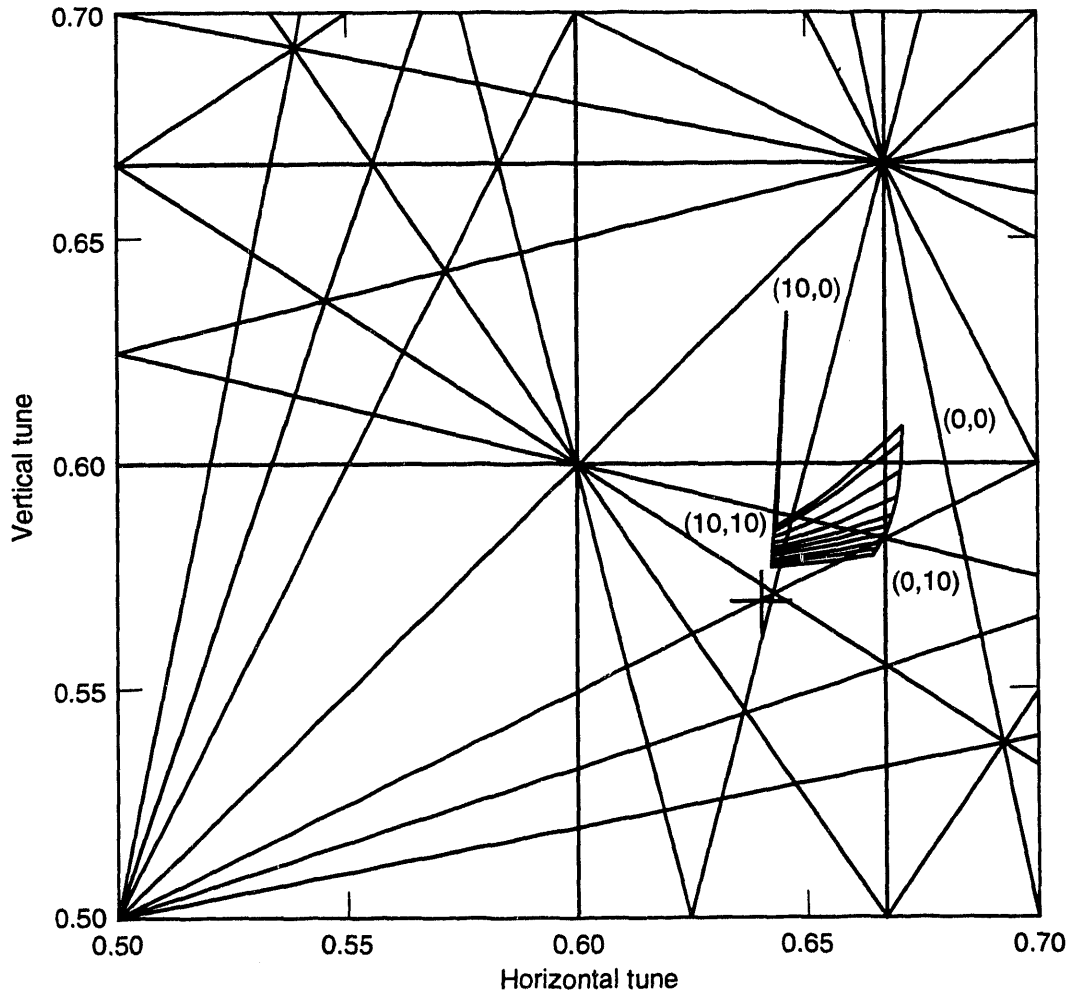

Fig. 4-95. Beam footprint of the LEB, including the effect of the parasitic crossings. The large-amplitude distortion of the footprint produced by the long-range collision is apparent (see Fig. 4-92 for a comparison). The lines in the footprint correspond to particles with constant amplitude (vertical and horizontal) at 0, 1, 2, 3, 4, 5, 6, 8 and 10σ.

fixed. Figure 4-96 shows the beam blowup factors vs $d/\sigma_{0x,+}$ for $\xi_0 = 0.03$, obtained with TRS. Figure 4-97 shows the vertical beam blowup factors for the LEB from both codes for $\xi_0 = 0.03$ and 0.05. Figure 4-98 shows the corresponding luminosity vs $d/\sigma_{0x,+}$ for $\xi_0 = 0.03$ and 0.05. This larger value of ξ_0 is obtained by increasing the number of particles per bunch by a factor of 5/3, at fixed nominal emittance.

The lack of smoothness in the blowup curves as $d/\sigma_{0x,+}$ increases, particularly for $\xi_0 = 0.05$, is almost certainly due to resonance effects. Indeed, as d varies, the cores of the two beams sample different areas of the tune plane on account of the d-dependence of the long-range beam-beam parameter, Eq. 4-77. This effect can be compensated by appropriate changes of the bare-lattice working points of the two beams. Simulations with such tune-compensation have been carried out, and they indeed show smoother blowup curves [Eden and Furman, 1993b].

As mentioned above, there are four parasitic collisions on either side of the IP. Table 4-39 summarizes the relevant parameters for all collisions, including the IP. In this table, s is the distance from the IP where the collision takes place and d is the separation between the beam orbits at that location (in all cases the separation is purely horizontal). The nominal beam-beam parameters ξ_0 of a particle at the center of the bunch are computed according to Eq. 4-77.

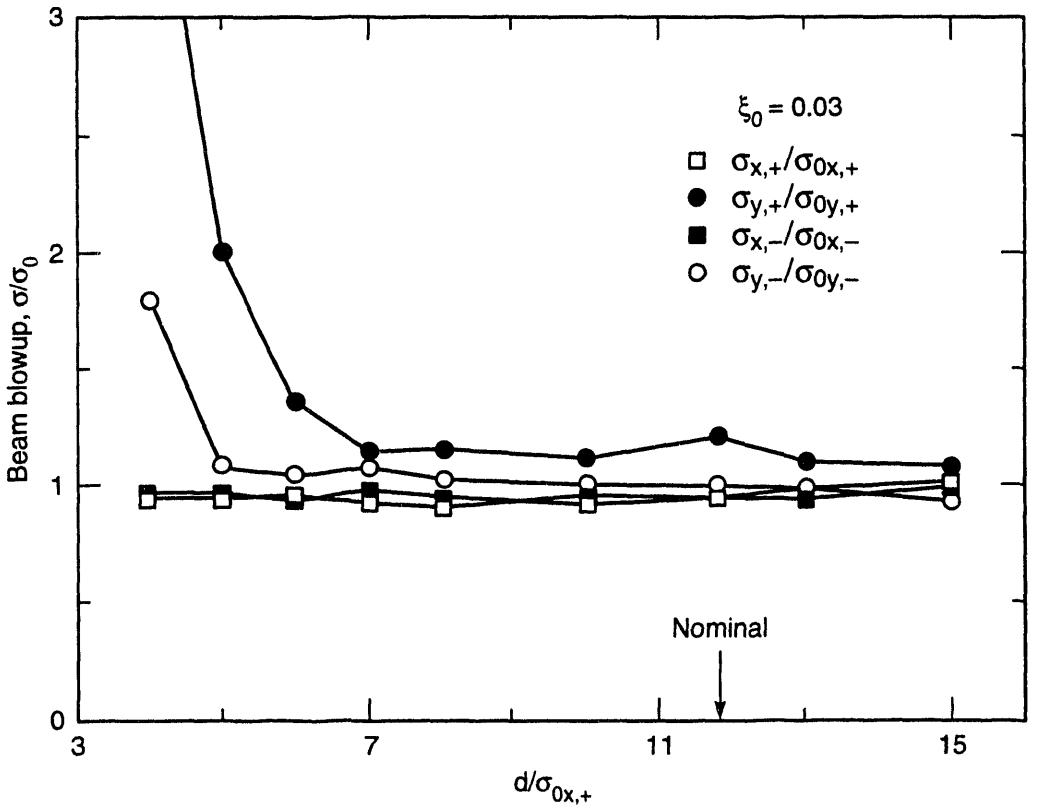

Fig. 4-96. Beam blowup factors vs $d/\sigma_{0x,+}$ for both beams obtained with TRS for $\xi_0 = 0.03$. The nominal beam separation at the parasitic collision, indicated by the arrow, corresponds to $d/\sigma_{0x,+} = 11.8$.

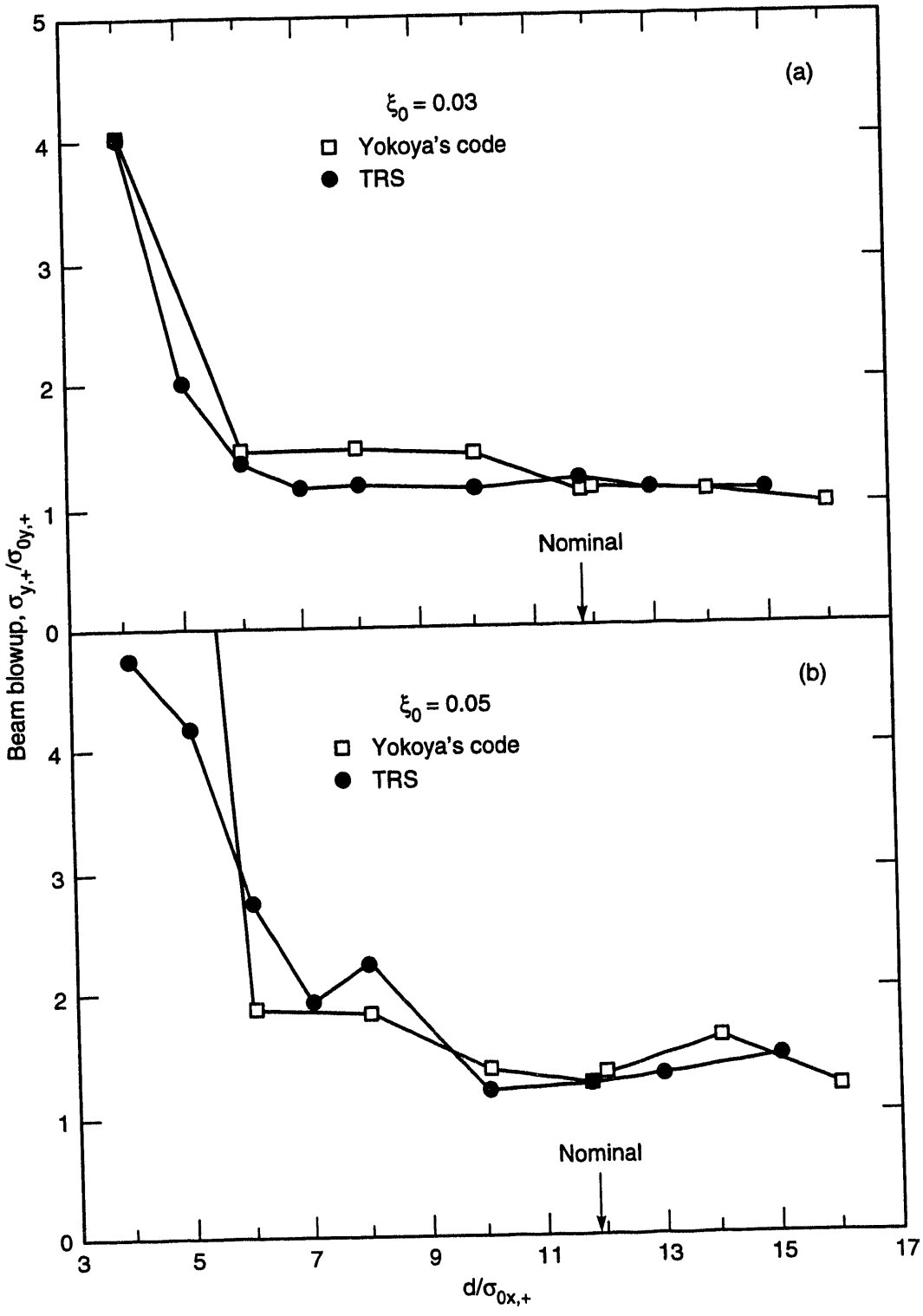

Fig. 4-97. Vertical beam blowup factor for the low-energy (positron) beam vs $d/\sigma_{0x,+}$ for (a) $\xi_0 = 0.03$ and (b) $\xi_0 = 0.05$. The nominal beam separation at the parasitic crossing, indicated by the arrow, corresponds to $d/\sigma_{0x,+} = 11.8$. The remaining three beam sizes are not shown because they exhibit blowup (or contraction) factors of 10% or less in all cases, except at very low values of $d/\sigma_{0x,+}$.

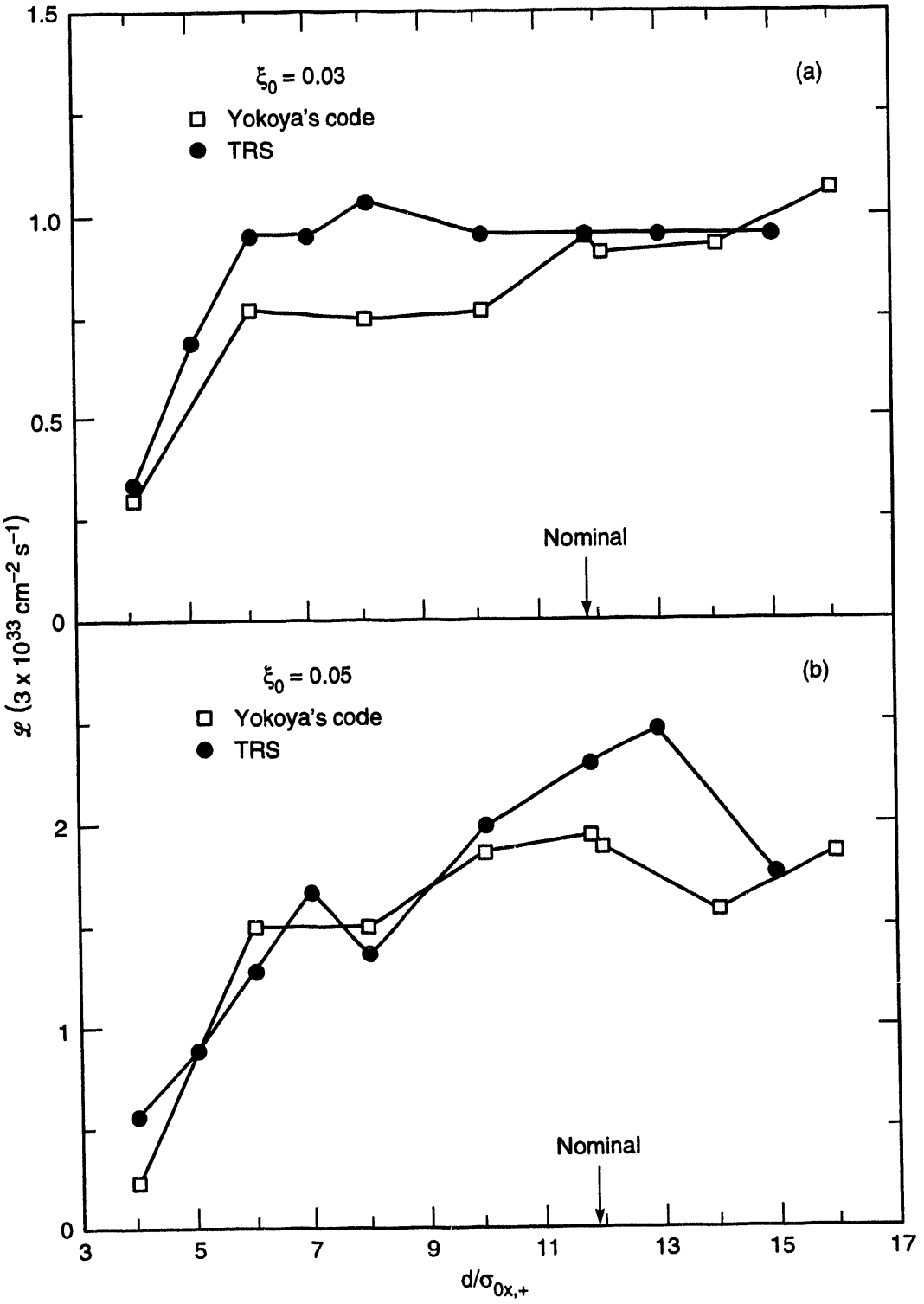

Fig. 4-98. Luminosity vs $d/\sigma_{0x,+}$ for (a) $\xi_0 = 0.03$ and (b) $\xi_0 = 0.05$, corresponding to the blown-up beam sizes shown in Fig. 4-97. Note that, for $\xi_0 = 0.05$, the nominal value of the luminosity is 8.3 $\times 10^{33}$ cm^{-2} s^{-1}.

Table 4-39. Parameters at the IP and all four parasitic crossings.

LER (e^+)				
s (m)	d (mm)	d/σ_{0x}	ξ_{0x}	ξ_{0y}
0.0 (IP)	0.0	0.0	+0.030000	+0.030000
0.63	3.498	11.8	–0.000224	+0.004133
1.26	17.651	33.2	–0.000028	+0.000648
1.89	39.114	39.3	–0.000020	+0.000167
2.52	71.879	38.4	–0.000021	+0.000026
HER (e^-)				
s (m)	d (mm)	d/σ_{0x}	ξ_{0x}	ξ_{0y}
0.0 (IP)	0.0	0.0	+0.030000	+0.030000
0.63	3.498	14.3	–0.000152	+0.002326
1.26	17.651	43.0	–0.000017	+0.000365
1.89	39.114	60.3	–0.000009	+0.000139
2.52	71.879	73.3	–0.000006	+0.000053

The simulation studies presented above indicate that the effect of the parasitic collisions on beam blowup becomes negligible compared with that from the IP when the relative separation $d/\sigma_{0x,+}$ is $\gtrsim 7$. Because the parasitic collisions beyond the first have $d/\sigma_{0x,+} \geq 33.2$, we are confident that their contribution to beam blowup is insignificant. (To account for the combined beam-beam tune shifts of the additional parasitic crossings, a small adjustment of the working point may be needed.)

It is likely that the only significant effect of the parasitic collisions beyond the first would be to excite a coherent dipole mode in the beams. However, because the combined beam-beam tune shifts of these additional parasitic crossings are small, this coherent dipole mode is likely to be insignificant except when the working point is very close to an integer or half-integer, a situation that will be avoided.

4.4.5 Beam Tail Simulations

The beam-beam problem is usually studied in two regimes: the core particles and the tail particles. The two regimes are very different in terms of their physics issues and their effects on machine performance. From an operational point of view, the core particles determine the luminosity, whereas the tail particles determine the lifetime and influence detector backgrounds (both aspects being critical to successful operation).

Compared with the core-particle problem, the tail problem has not been well studied, either with analytical calculations or simulations. The reason for the lack of simulation

results is that particles are rarely in the tail. Even though the number of particles moving into the tail is large enough to degrade the beam lifetime, it is not large enough to provide a tail distribution with satisfactory statistical accuracy in a typical beam-beam simulation with a few hundred superparticles. That is, a simulation with a huge number of particle-turns would be required to give a single tail distribution, which prevents this problem from being studied systematically by standard beam-beam codes.

To avoid this limitation, a new simulation code has been developed by Irwin [1992]. Instead of tracking billions of particle-turns in the core, we concentrate on the particles that are evolving into the tail. To do this, an imaginary boundary is drawn in normalized amplitude space to separate about 100 particles (out of 1000 particles) moving in the tail. Then, we continue tracking the particles and randomly save the coordinates of particles that are above the boundary, until 1000 particle coordinates have been saved. Meanwhile, the coordinate information for any particles that move up across the boundary is also saved. At this point, we track 1000 particles outside the boundary. During the tracking, any particle that drops below the boundary will be reinserted above it by using new coordinates from the crossing information saved previously. After sufficient tracking time (a few damping times), a second boundary (at larger amplitudes) is created and 100 particles outside the second boundary are evolved into 1000 particles. This process can be repeated a few times to keep tracking particles that are going into the tail. Each time we increase the boundary amplitude, we gain a factor of 10 for the number of particles in the tail.

The results of the Irwin code have been compared with the results of conventional tracking for 6 billion particle-turns. Excellent agreement has been achieved, using only 2% of the particle-turns of the conventional tracking code. This indicates that the new simulation code is a very powerful tool for studying beam-tail distributions.

The code features six-dimensional phase-space tracking, one interaction point with asymmetric beam parameters, a linear arc transport with energy-dependent phase advance and beta functions, parasitic crossings, and a multiple-slice beam-beam kick at the interaction point. It has been developed to meet the requirements of PEP-II performance studies.

Figure 4-99 shows the results of a simulation for the PEP-II LER in which the strong bunch is segmented into five slices. An equivalent of about 70 billion particle-turns was simulated. The results show that synchrotron motion is important in the beam-tail distribution. The parasitic crossings do not appear to affect the distribution very much. However, they do change the large amplitude tail by a small amount, which has an impact on lifetime. Figure 4-100 compares the beam distributions in the vertical plane with and without parasitic crossings. The distributions split at large amplitudes. Based on these data, the lifetime can be estimated: For a two-hour lifetime, a $16.5\sigma_y$ physical aperture in the vertical plane is required without parasitic crossings, and a $22\sigma_y$ physical aperture is required with parasitic crossings. (For comparison, we note that the dynamic aperture of the LER exceeds 35σ in the vertical plane, as shown in Section 4.1.3.3.)

More work will be carried out to check various effects, such as different working points and lattice nonlinearities. Our goal is to identify possible problems, rather than to predict the actual operational performance of PEP-II.

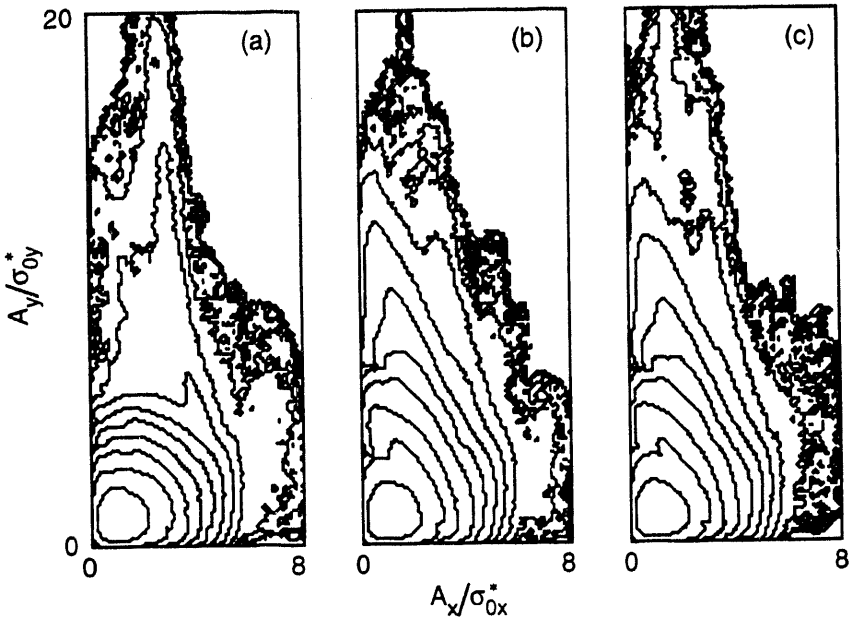

Fig. 4-99. Beam distributions from simulation: (a) without synchrotron motion; (b) with synchrotron motion; (c) with synchrotron motion and parasitic crossings. The horizontal and vertical axes scales are A_x/σ^*_{0x} and A_y/σ^*_{0y}, where $A = \sqrt{2J\beta}$ is the amplitude.

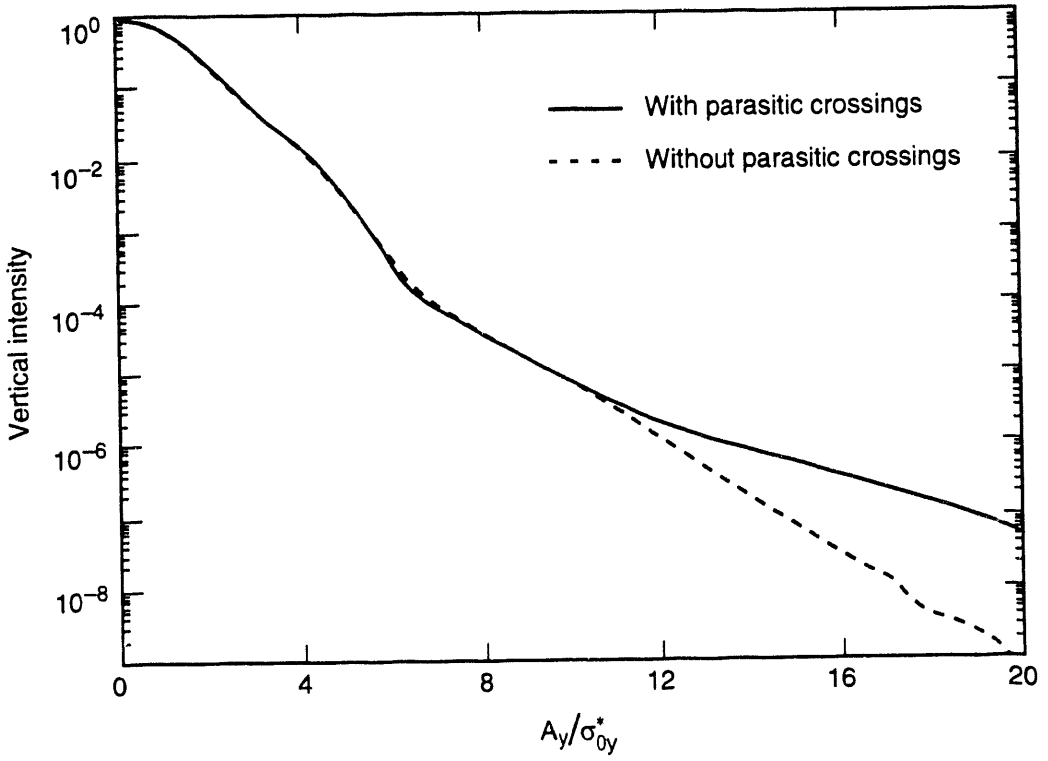

Fig. 4-100. Vertical beam distribution with and without parasitic crossings for the low-energy beam.

4.4.6 Injection Simulations

In this section, we present a summary of an assessment of beam-beam effects during injection into the empty machine. Most present and past e^+e^- colliders have found it necessary—or at least very useful for the smoothness of injection—to avoid collisions during the filling process by injecting the beams while they are separated at the IP. While this requirement has not proved universal, we should assume, at least for now, that PEP-II will require this.

The beam separation is achieved by means of a temporary orbit bump in the interaction region. In a simplified description, the injection process can be divided up into four stages:

(1) Turn on the orbit bumps in the empty rings

(2) Fully inject one beam into its ring

(3) Fully inject the other beam into its ring

(4) Bring the beams into collision by turning off the orbit bumps

Section 4.4.6.1 addresses step (3) of this process. The simulations focus on the transient effects of the dynamics for the first several damping times following the injection of the first 20% batch of positrons, assuming that the electron ring is fully filled. In Section 4.4.6.2 we look at the transition between steps (3) and (4), that is, we assume that all injection transient effects have died down and that both beams have reached full current and the emittances their nominal, steady-state values, but that the orbit bump is still turned on [Furman, 1993]. In this regime, we compare the pros and cons of a vertical and a horizontal orbit bump.

4.4.6.1 Transient Effects at the Beginning of the Injection Process. An extensive study of beam-beam effects during the injection process, including the influence of the parasitic crossings, has been carried out for the earlier designs APIARY 6.3D and APIARY 7.5 [Chin, 1991b, 1992]. In those studies, it was found that the strong parasitic beam-beam interaction in the initially proposed horizontal injection scheme induces a significant beam blowup in the vertical size of the injected beam, although it does not lead to particle loss.

We have only studied the case in which injection takes place into the low-energy ring while the high-energy beam is already fully stored. This configuration is expected to be the most unfavorable case with respect to the dynamics, since our beam-beam studies show that it is the low-energy beam that blows up preferentially.

In the APIARY 6.3D design, bunches were injected horizontally with an offset of $8\sigma_{ix}$, where σ_{ix} is the uncoupled horizontal beam size of the *stored* beam at the injection point. The injected beam travels around the ring oscillating horizontally for the first several damping times. When the injected beam arrives at the first parasitic crossing, where the two nominal orbits for the APIARY 6.3D configuration were separated horizontally by about $7.6\sigma_{0x,+}$, it may approach the stored beam far more closely than the nominal separation, or it may even strike it head-on. Due to the large vertical beta function ($\beta_{y,+} \approx 25$ m), the vertical beam-beam tune shift at the first parasitic crossing can become of the order of unity. Computer simulation results show that the vertical beam

size reaches its peak value (about 11 times the nominal storage ring beam size) very quickly, within approximately 300 turns; the beam blowup then damps gradually in the following few radiation damping times. No particle loss was found in the simulation.

The simulations show that the horizontal beam size also blows up, to about three times the nominal stored-beam value, but much more slowly (roughly one radiation damping time). A detailed investigation of the time evolution of the horizontal phase-space distribution shows that the injected beam is sheared into an elongated shape, and eventually spreads out over a circular annulus in horizontal phase space, due to horizontal kicks from the other beam. This leads to a rapid damping of the horizontal baricentroid motion even though the particle amplitudes themselves have not yet been significantly damped. The process would likely be enhanced if the amplitude-dependent tune shifts due to lattice nonlinearities were taken into account.

Although the resultant performance of the horizontal injection scheme in the APIARY 6.3D design would have been acceptable, we have explored two alternative injection schemes in an attempt to seek a solution that entails less blowup of the injected beam. One such scheme is to inject beams vertically instead of horizontally. Obviously, this scheme prevents the injected beam from approaching the other beam at the first parasitic crossing more closely than the nominal separation distance between the two stored-beam orbits. Another scheme is horizontal injection, but with vertical separation at both the IP and the first parasitic crossing (produced by a bumped orbit during the injection process). Simulation results for both of these schemes show substantial reduction of the blowup of the injected beam sizes. No particle loss was found in either case.

Based on these results, we adopted a vertical injection scheme for the intermediate design, APIARY 7.5. Because the two beams cannot get any closer at the parasitic collision point than the nominal (stored-beam) separation distance, the beam-beam kick is weaker on average than during steady-state colliding-beam operation. However, the parasitic beam-beam interaction, being a collision of the two beams at large amplitude in phase space, still tends to shear the injected beam into an elongated shape in vertical phase space. The process is accelerated as the coherent vertical oscillation of the injected beam damps away, because the distance between the two beams gets shorter on average. This behavior, schematically illustrated in Fig. 4-101, is a peculiar point that contrasts with the horizontal injection case (in which the parasitic beam-beam interaction becomes *weaker* as the horizontal coherent oscillation of the injected beam damps away). Obviously, the parasitic beam-beam interaction in both cases approaches the same strength in the steady state.

Although the present design has a substantially larger beam separation at the first parasitic collision and smaller long-range beam-beam parameters for the LEB compared with our earlier designs, we have retained the vertical injection scheme. In this way, we are certain to avoid potentially adverse effects from close encounters of the beams at the parasitic crossing points during injection.

The main storage ring and injection parameters of the present design are listed in Table 4-40; the numbers in square brackets are the values of the corresponding parameters at the time of injection. As in previous simulations, we consider only the first parasitic crossing (that closest to the IP) on either side, because it overwhelms the others.

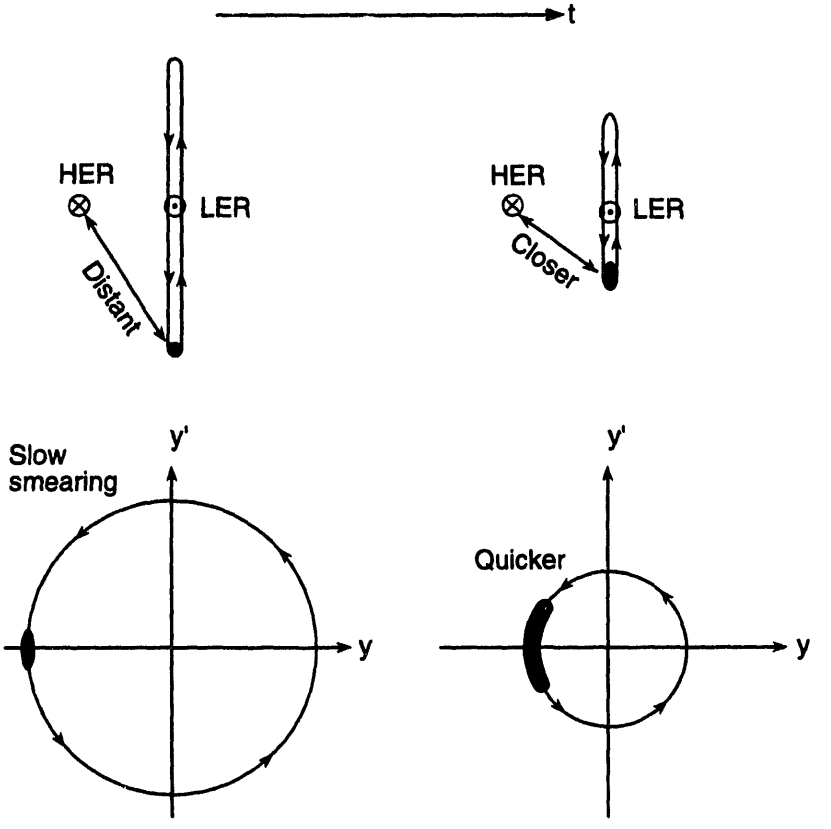

Figure 4-101. Schematic illustration of the parasitic beam-beam interaction during the vertical injection process.

A bunch with 20% of the nominal single-bunch current is injected into the LER with a vertical displacement $22\sigma_{iy}$ from the stored-beam orbit, where σ_{iy} is the nominal (stored-beam) vertical beam size of the LER at the injection point. We assume that the phase advance between the injection point and the first parasitic crossing point is 2π times an integer. The fractional tunes of the working point are taken as $\nu_x = 0.64$ and $\nu_y = 0.57$ for both beams.

Figure 4-102 shows the rms sizes of the injected beam, in units of the nominal stored-beam sizes, versus the turn number after injection. The evolution of the baricentroid motion of the injected beam is shown in Fig. 4-103. The largest turn number, 20000, corresponds to about four radiation damping times. We see that the vertical beam size reaches its peak value of $\sim 3\sigma_{0y}$ very quickly, within approximately 1000 turns. The beam blowup then damps out gradually in the following few radiation damping times. Horizontally, the injected beam converges monotonically toward its equilibrium size due to radiation damping. At an early stage of the simulation, the injected beam is sheared into an elongated shape. This elongated shape closes to a circular annulus after approximately 8000 turns, that is, roughly two damping times. Accordingly, the vertical baricentroid position settles down at the origin as shown in Fig. 4-103. No particle loss from the 200 superparticles was found during the simulation. The high-energy beam sizes, which are not plotted here, show practically no change from their nominal values.

Table 4-40. PEP-II parameters used in the injection simulation studies of the LER. Parameters in brackets are those of the injected beam at the time of injection; the other values correspond to the nominal stored beams.

	LER (e^+)		HER (e^-)	
E [GeV]	3.1		9.0	
C [m]	2200		2200	
$\tau_x = \tau_y$ [turns]	5014		5040	
I_b [mA]	[0.246]		0.565	
σ_ℓ [cm]	1.0		1.0	
ε_{0x} [nm·rad]	61.3 [8.24]		45.9	
ε_{0y} [nm·rad]	2.45 [8.24]		1.84	
d [mm]	3.50			
	IP	First PC	IP	First PC
β_x [m]	0.375	1.43	0.50	1.29
β_y [m]	0.015	26.46	0.02	19.85
σ_{0x} [μm]	152 [56]	296 [109]	152	244
σ_{0y} [μm]	6.06 [11.1]	255 [467]	6.06	191
d/σ_{0x}	0	11.8 [25.2]	0	14.4
A_x/σ_{0x}	10		10	
A_y/σ_{0y}	36		36	

We conclude from these results that the vertical injection scheme is quite comfortable in terms of the beam-beam dynamics. It leads to very little beam blowup and to no particle losses (to the extent that these simulations are able to predict).

4.4.6.2 Simulations with Displaced Beams at Full Current. In this section, we summarize simulation results corresponding to the state reached after injection is complete but the beams are still separated. If the beams are slowly brought into collision in step (4) of the injection process, the results presented in this section also allow a rough understanding of what would happen during this beam-collapsing process. One implicit assumption that is necessary for the relevance of these simulations to the beam-collapsing process is that the time scale for switching off the orbit bumps is longer than a few damping times. If the beam-collapsing process is fast (on the order of one damping time or less), our simulations are probably relevant only to the static situation existing before step (4) is taken. We are also assuming that multibunch coherent beam-beam instabilities are not excited in the separated state or during the beam-collapsing process.

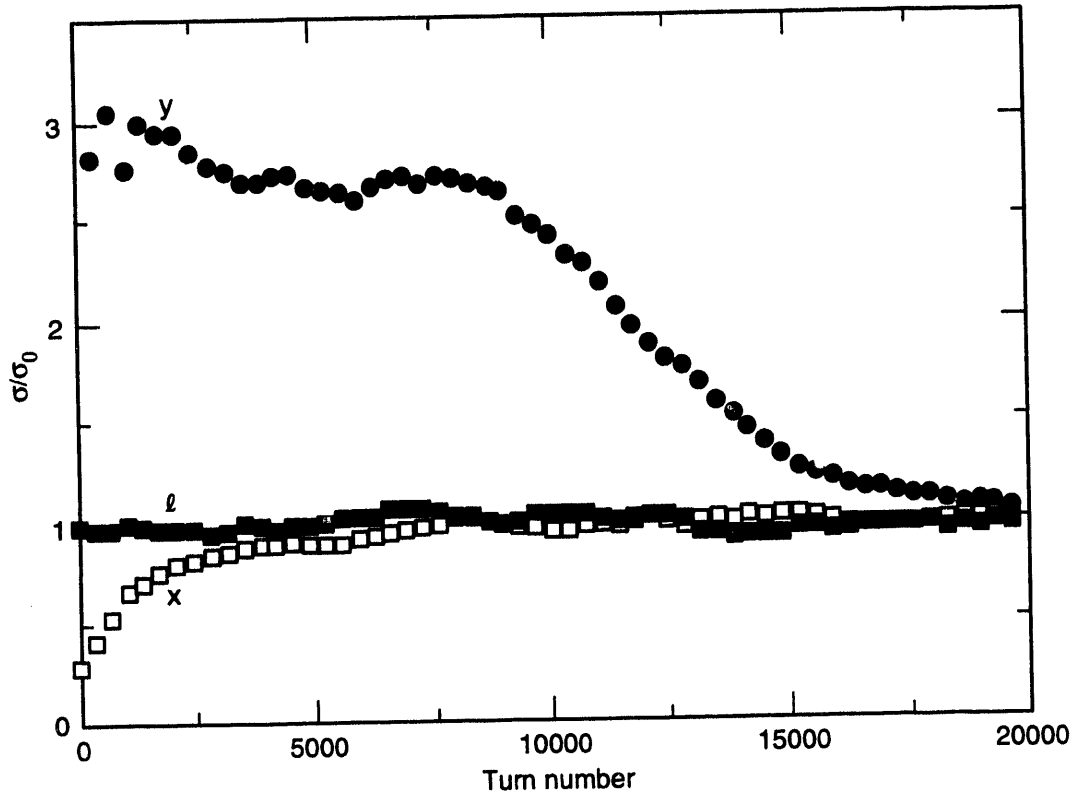

Figure 4-102. Time evolution of the injected beam sizes of the LEB, in units of the nominal stored-beam sizes, during the vertical injection process.

The results below are in the form of beam blowup, σ/σ_0, plotted versus d_x/σ_{0x} or d_y/σ_{0y} for horizontal or vertical separation, respectively, where σ_{0x} and σ_{0y} are the nominal, steady-state, rms beam sizes at the IP, and d_x or d_y is the orbit separation at the IP in either case. In the horizontal separation case, we varied d_x while keeping d_y fixed, and vice versa for the vertical case. We assume that the beam separation is implemented by a closed-orbit bump that is symmetric about the IP and whose elements (orbit bump magnets) are outside the region encompassing the IP and the first parasitic collision points (however, see the discussion below). Since there are no focusing elements between the IP and the first parasitic collisions, the closed orbits inside this region are parallel-displaced from the nominal orbits. As a result, the orbit separation at each parasitic collision is related to that at the IP by simple geometry as follows:

$$\text{Horizontal separation case:} \quad \begin{cases} d_{IP} = d_x & (d_y = 0, \text{ fixed}) \\ d_{PC1} = d_0 + d_x & (d_y = 0, \text{ fixed}) \\ d_{PC2} = d_0 - d_x & (d_y = 0, \text{ fixed}) \end{cases} \tag{4-79}$$

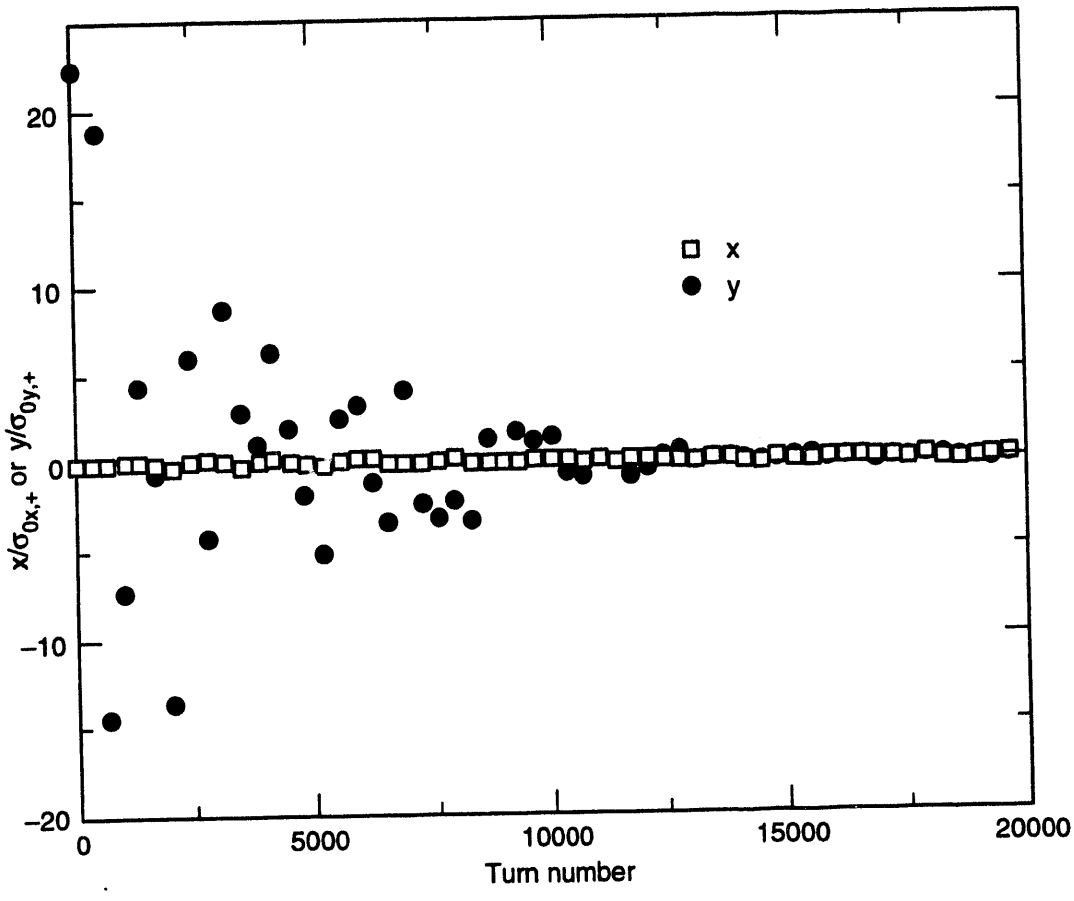

Figure 4-103. Time evolution of the baricentroid positions of the injected low-energy beam, in units of the nominal stored-beam sizes, during the vertical injection processes.

$$\text{Vertical separation case:} \quad \begin{cases} d_{IP} = d_y & (d_x = 0, \text{ fixed}) \\ d_{PC1} = d_y & (d_x = d_0, \text{ fixed}) \\ d_{PC2} = d_y & (d_x = d_0, \text{ fixed}) \end{cases} \tag{4-80}$$

where d_0 is the nominal orbit separation at the first parasitic collision ($d_0 = 3.5$ mm). Parasitic collisions beyond the first were not considered, even though the horizontal-separation alternative would almost certainly demand that they be included in a faithful simulation. The simulation was run with the code TRS at the working point (0.64, 0.57).

In the horizontal-separation alternative, Eq. 4-79 shows that, as the beams are displaced, one of the parasitic collisions (called PC2) gets stronger while the other one (PC1) gets weaker. The collision at the IP also gets weaker. As one can see in Fig. 4-104, beam blowup is not significant provided the separation at the IP is such that $d_x/\sigma_{0x} \lesssim 5$–10. In this regime, the parasitic collisions are still well separated (for an IP separation $d_x/\sigma_{0x} = 5$, the parasitic collision separations are $d_{PC2}/\sigma_{0x,+} = 9.25$ and

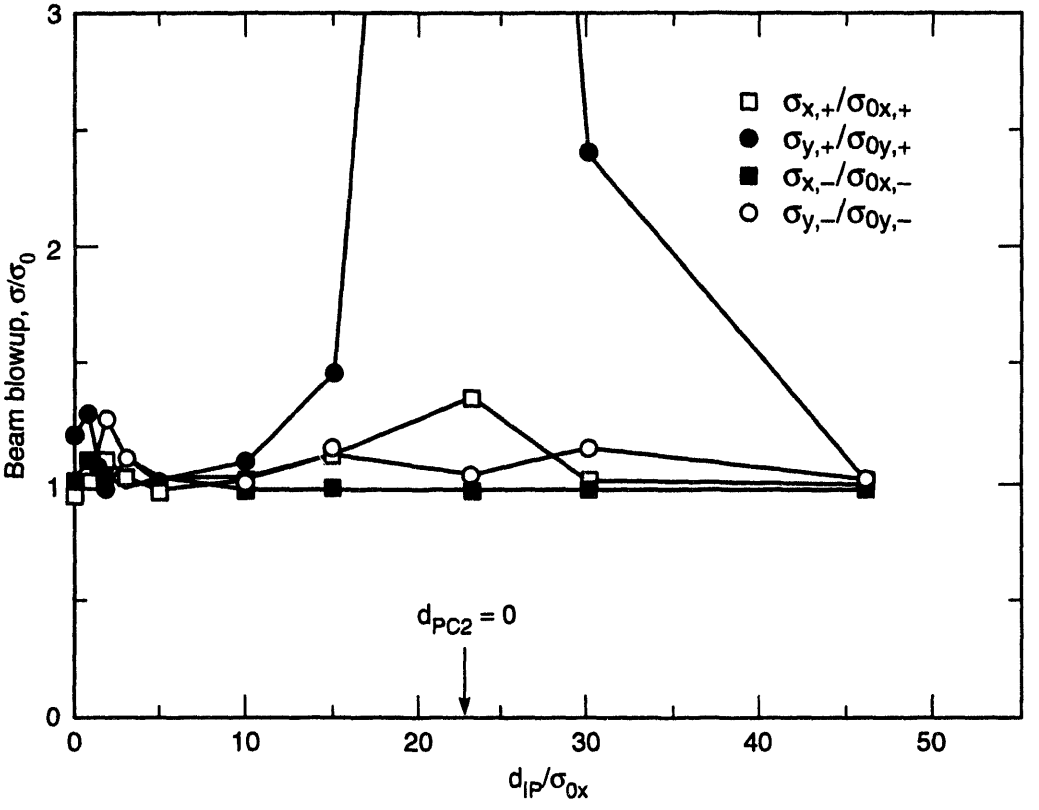

Fig. 4-104. Beam blowup as a function of horizontal beam separation at the IP. As the beam separation at the IP increases, the separation at one of the parasitic collisions (called PC1) increases, while the separation at the other (PC2) decreases. The arrow indicates the separation at which there is a head-on collision at PC2.

$d_{PC1}/\sigma_{0x,+} = 14.4$; the nominal head-on case has $d_x = 0$ and $d_{PC2}/\sigma_{0x,+} = d_{PC1}/\sigma_{0x,+} = 11.8$). However, as one might expect, when the IP separation is so large that the beams collide head-on at the PC2 location (indicated by the arrow labeled "$d_{PC2} = 0$" in the plot), the beam blowup is very large and the simulations also show particle loss. As the beams are further separated, they eventually become so far apart that there are effectively no beam-beam collisions (the last point in the plot, at the unrealistically large separation $d_x/\sigma_{0x} = 46.2$, is such that $d_{PC2}/\sigma_{0x,+} = 11.8$ and $d_{PC1}/\sigma_{0x,+} = 35.4$, and one sees that, indeed, there is no beam blowup).

In the vertical-separation case, as implied by Eq. 4-80, the beams are always more separated than nominal. The results are shown in Fig. 4-105. The LEB blowup becomes substantial (~75%) when $d_y/\sigma_{0y} \gtrsim 1$, and it does not come back down to nominal (that is, unity) until the separation is $d_y/\sigma_{0y} \gtrsim 10$–12, corresponding to $d_y \gtrsim \sigma_{0x}/2$.

The simulations above assume that only the first parasitic collisions and the IP come into play. However, the traditional (and simplest) closed-orbit bump is implemented by means of two kicking elements of opposite sign, separated by a distance such that the intervening phase advance is

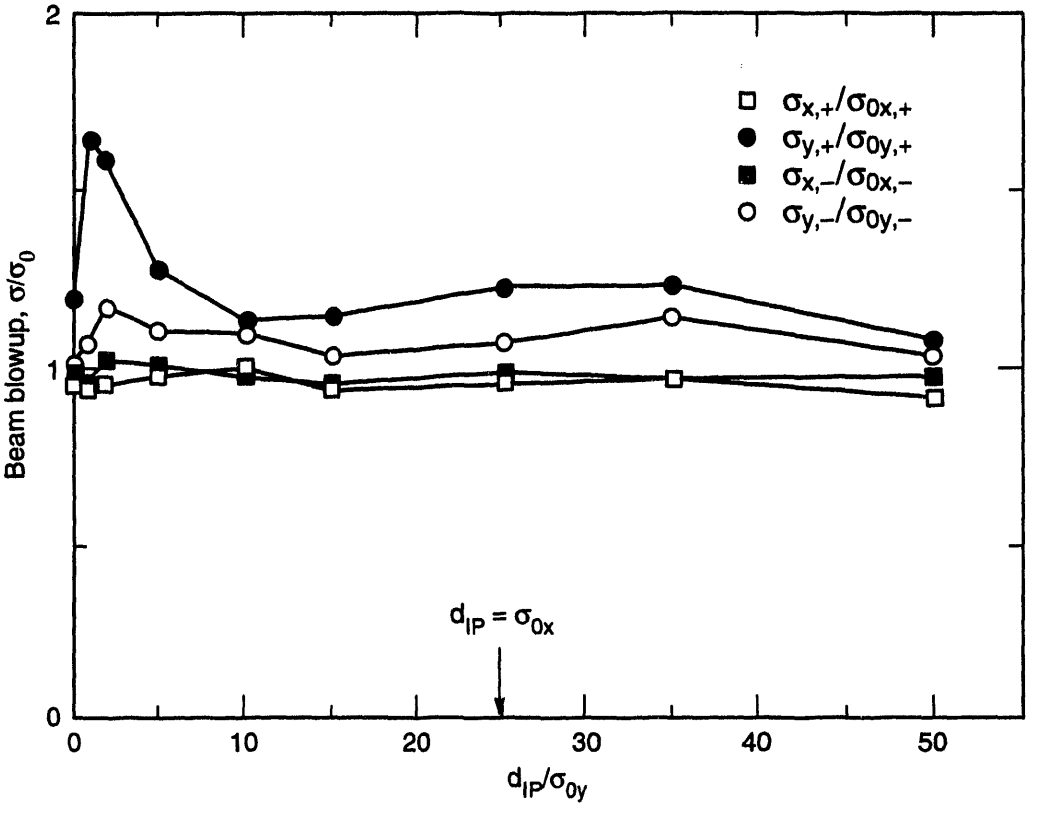

Fig. 4-105. Beam blowup as a function of vertical beam separation. As the beam separation at the IP increases, so does the separation at both PCs. The arrow indicates the point at which the vertical separation equals the nominal horizontal beam size.

$$\Delta\mu = \pi/2, 3\pi/2, 5\pi/2, \ldots \tag{4-81}$$

The PEP-II lattice is such that even the first option, $\Delta\mu = \pi/2$, implies that the bump elements must be located at a distance $\gtrsim$2.5 m from the IP. This is true for both rings, whether the separation is vertical or horizontal. This means that all four parasitic collisions on either side of the IP would be encompassed by such an orbit bump. Of course, it is, in principle, possible to separate beams by means of a more elaborate orbit bump, or a bump that is not closed. Either alternative entails complications.

Thus, if the beams are separated horizontally, the simulations above indicate that the closed-orbit bump must be tightly constrained by the lattice functions and phase advances of all the parasitic collision locations, while there is no such constraint in the vertical-separation case. If an orbit bump encompassing only the IP and the first parasitic collisions could be designed, a horizontal separation $3 \lesssim d_x/\sigma_{0x} \lesssim 10$ would seem to be adequate. (If $d_x/\sigma_{0x} \lesssim 3$, the bump would probably not be very effective, and if $d_x/\sigma_{0x} \gtrsim 10$, the adverse effects of the parasitic collisions could become quite severe.) Realistically, the orbit bump must encompass all parasitic collisions; therefore, care must

be taken in its design so that the beams do not come too close to each other at any parasitic collision point in the separated state.

The conclusion is that vertical separation is favored over horizontal on account of the diminished adverse effects from the parasitic collisions: When the beams are vertically separated, the dynamics is essentially determined by the main collision at the IP. All parasitic collisions, especially the "outer" ones, have negligible effect. A vertical separation $d_y \gtrsim (1\text{–}2)\sigma_{0x}$ is probably adequate for smooth injection. Note that, as a practical matter, it is σ_{0x} that determines the scale for the falloff of the beam blowup, whether the separation is horizontal or vertical. This implies that the orbit separation must be at least a few times σ_{0x} in magnitude (whether it is vertical or horizontal) for it to be effective. This conclusion is consistent with PEP [Chin, 1991b] and CESR [Billing, 1993] experience.

The horizontal-separation alternative does have the advantage that the simulations show no significant beam blowup when the beams are slowly brought into collision. In the vertical-separation case, on the other hand, the simulations show beam blowup of ~75% in the vertical dimension when the beam centers approach to within a distance $d_y \approx (1\text{–}2)\sigma_{0y}$. With the large PEP-II beam-stay-clear specifications, this temporary beam blowup is not a concern.

Based upon these results, a vertical injection scheme with a vertical orbit bump has been adopted for PEP-II.

4.4.7 Discussion

4.4.7.1 Effects of the Primary Parasitic Collisions: the d/σ_0 Rule. Our simulation results show that, if only the IP were considered, the PEP-II design would show behavior quite close to nominal from the beam-beam perspective, implying that the design is conservative in this sense. Limited tune scans, within the approximations embodied by our simulation methods, show that there is plenty of room to operate in the tune plane. Indeed, Fig. 4-94 shows that nominal behavior for the luminosity would persist up to values of ξ_0 significantly larger than 0.03 for the working point chosen. However, the parasitic crossings cause a preferential blowup in the vertical size of the low-energy beam that tends to limit the range of parameters for which nominal behavior prevails. Even so, Fig. 4-98a shows that the effect of the parasitic collisions is to reduce the luminosity by only ~5% from its design value for $\xi_0 = 0.03$. For the higher value of $\xi_0 = 0.05$, shown in Fig. 4-98b, the luminosity degradation from its nominal value, $\mathcal{L}_0 = 8.33 \times 10^{33}$ cm^{-2} s^{-1}, is more significant, although its absolute dynamical value, $\mathcal{L} \lesssim 7 \times 10^{33}$ cm^{-2} s^{-1}, is more than twice the PEP-II design goal.

Another way to achieve the higher-than-nominal value $\xi_0 = 0.05$ is to decrease the emittances by a factor of 3/5 at fixed bunch current. The resultant nominal luminosity in this case is a factor of 5/3 larger, that is, $\mathcal{L}_0 = 5 \times 10^{33}$ cm^{-2} s^{-1}. The beam sizes are a factor of $\sqrt{3/5}$ smaller, and the normalized parasitic separation is thus $d/\sigma_{0x,+} = \sqrt{5/3} \times 11.8 = 15.2$. A simulation for this case is shown in Fig. 4-106; the beam blowup reduces the luminosity to a dynamical value $\mathcal{L} \gtrsim 4 \times 10^{33}$ cm^{-2} s^{-1}.

By comparing the two cases at $\xi_0 = 0.05$, Figs. 4-97b and 4-106, one can see that the first one is more "effective" in increasing the luminosity from its nominal value of

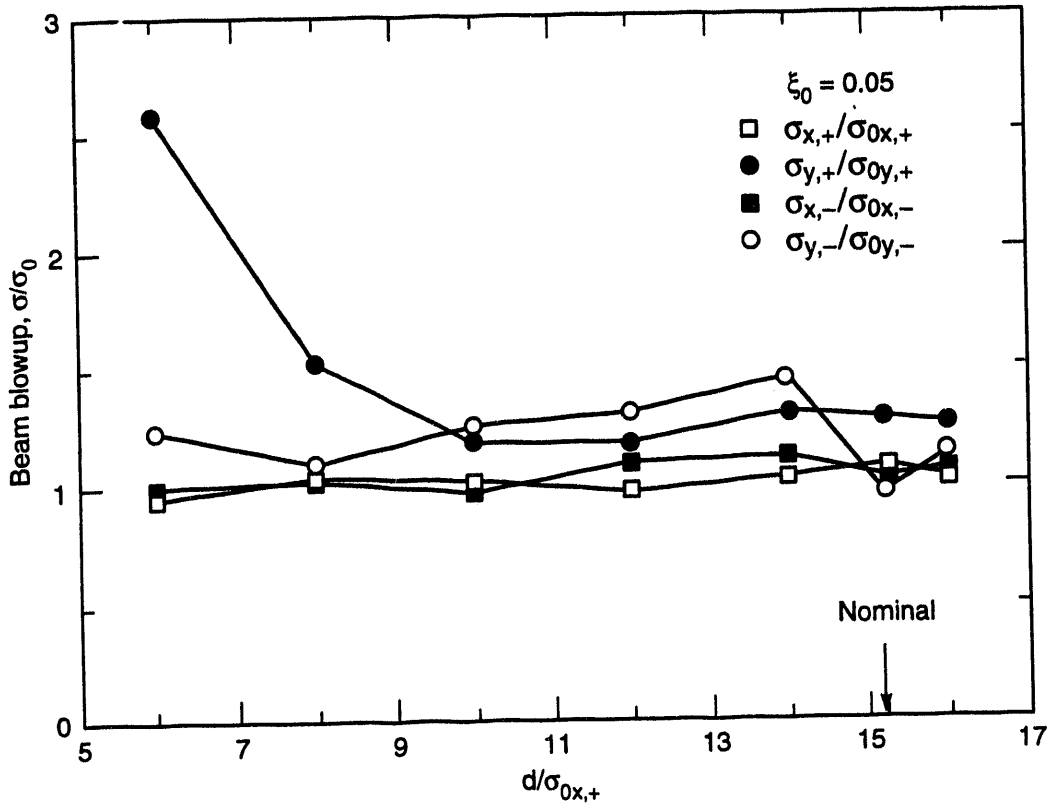

Fig. 4-106. Beam blowup factors vs $d/\sigma_{0x,+}$ for $\xi_0 = 0.05$. This value of ξ_0 is achieved by decreasing the nominal emittances by a factor of 3/5 at fixed bunch current. The corresponding nominal luminosity is 5×10^{33} cm^{-2} s^{-1}. The beam blowup reduces it to a dynamical value $\mathcal{L} \gtrsim 4 \times 10^{33}$ cm^{-2} s^{-1}.

3×10^{33} cm^{-2} s^{-1}, while the second is "safer." The greater effectiveness of the first method is due to the fact that $\mathcal{L}$ depends quadratically on N but only linearly on ε_0^{-1}. The second method is safer in the sense that the actual value of $d/\sigma_{0x,+}$, which is 15.2 in this case, is further away from the onset of significant blowup ($d/\sigma_{0x,+} \approx 9$) than in the first case, for which the actual separation value is 11.8.

All simulation cases show that, if the parasitic collision separation is sufficiently small, there is an onset of substantial beam blowup. This means that a local beam-beam limit has been reached. By examining all of our simulation cases summarized in this report and all previous studies [Chin, 1991a; Tennyson, 1991a, 1991b; Eden and Furman, 1992a, 1992b, 1993a, 1993b], we can state an approximate rule-of-thumb for this beam-beam limit, the *"d/σ_0 rule"*:

- for $\xi_0 = 0.03$, the onset of significant beam blowup occurs when $d/\sigma_{0x,+} \lesssim 7$
- for $\xi_0 = 0.05$, the onset occurs when $d/\sigma_{0x,+} \lesssim 9$

Obviously, this rule has been obtained within the context of our approximations and is thus of limited validity. In particular, it is valid only at a good working point. Nevertheless, it is consistent with similar results obtained from simulations for the

DAΦNE collider [Biscari, 1992], and is in rough agreement with the experience for minimum pretzel separation in existing machines such as CESR [Rice, 1990] and LEP [Goddard, 1992]. (In these last two cases, the constraint on d/σ_0 pertains more to beam lifetime than to core blowup, however.) We take this rule as a qualitatively valid guide for comparative assessments.

The two previous designs, APIARY 6.3D and APIARY 7.5, had nominal values $d/\sigma_{0x,+} = 7.6$ and 9.6, respectively, while the current design has $d/\sigma_{0x,+} = 11.8$. (We always use the beam size of the LEB for normalization purposes, because it is larger than the beam size of the HEB at the first parasitic crossing point and therefore gives a lower value for d/σ_{0x}.) Thus, the PEP-II design is quite safe in this respect—the large value for $d/\sigma_{0x,+}$ ensures that the parasitic collisions are effectively weak so that the dynamics of the beam core is dominated by the primary collision at the IP.

4.4.7.2 Larger Bunch Spacing. It is possible to weaken the parasitic collisions even more by operating PEP-II with a larger bunch spacing. In this case, the natural divergence of the closed orbits provides larger beam separation at the parasitic collisions. For example, one can increase the bunch spacing s_B by 50%, from 1.26 m to 1.89 m, by filling every third RF bucket rather than every second bucket (the RF wavelength is $\lambda_{RF} = 63$ cm). In this case, the first parasitic collision occurs at a distance $\Delta s = 94.5$ cm from the IP instead of 63 cm. In order to maintain ξ_0 and $\mathcal{L}_0$ at their original values of 0.03 and 3×10^{33} cm^{-2} s^{-1}, respectively, we require that the number of particles *per bunch* and nominal emittances of both beams be increased by 50%. The total beam current remains unchanged but the beam separation at the new parasitic crossing point is $d = 10.1$ mm instead of 3.5 mm. Because of intervening focusing elements, $d/\sigma_{0x,+}$ is not the same as before: The new value is $d/\sigma_{0x,+} = 20.1$ instead of 11.8, which implies a much weaker parasitic collision. Simulations for the previous designs APIARY 6.3D and APIARY 7.5 [Eden and Furman, 1992a, 1992b] show that the beam blowup is slightly less for the $s_B = 1.89$ m case than for the $s_B = 1.26$ m case at the nominal value of $d/\sigma_{0x,+}$. What is more important is that the "comfort factor" is significantly larger, since the value of 20.1 for $d/\sigma_{0x,+}$ is much larger than the rule-of-thumb threshold value of 7. Although we have not carried out these simulations for the current design, it is clear that the same conclusion about the beam blowup would be valid.

If the bunches are injected every third bucket but the emittances and bunch currents have their nominal values instead of being 50% larger, then the first parasitic collision is such that $d/\sigma_{0x,+} = 24.6$ and therefore it is truly negligible. In this case, the beam-beam parameter at the IP is still $\xi_0 = 0.03$, but the luminosity is $\mathcal{L}_0 = 2 \times 10^{33}$ cm^{-2} s^{-1}. This operating configuration could be used as a comfortable initial stage in the commissioning of the machine. Table 4-41 shows a comparison of the nominal case with the two alternatives with $s_B = 1.89$ m.

4.4.7.3 Unequal Beam-Beam Parameters. As mentioned earlier, the transparency symmetry in the PEP-II design is not obeyed exactly by the damping decrements or the synchrotron tunes. We have therefore felt motivated to explore consequences of breaking the symmetry in the beam-beam parameters as well. To this end, we carried out simulations [Eden and Furman, 1993a] for the two previous designs, APIARY 6.3D and APIARY 7.5, for unequal beam-beam parameters in two cases:

Table 4-41. Comparison of primary parameters for the nominal case with two options with larger bunch spacing.

	Nominal spacing		s_B = 1.89 larger N		s_B = 1.89 nominal N	
	LEB	HEB	LEB	HEB	LEB	HEB
s_B [m]	1.26		1.89		1.89	
$\mathcal{L}_0$ [cm^{-2} s^{-1}]	3×10^{33}		3×10^{33}		2×10^{33}	
ξ_0	0.03		0.03		0.03	
N [10^{10}]	5.6	2.6	8.4	3.9	5.6	2.6
I [A]	2.1	1.0	2.1	1.0	1.4	0.66
ε_{0x} [nm·rad]	61	46	92	69	61	46
ε_{0y} [nm·rad]	2.5	1.8	3.7	2.8	2.5	1.8
d [mm]	3.5		10.1		10.1	
d/σ_{0x}	11.8	14.3	20.1	20.4	24.6	24.8

Approach A: we set $\xi_{0x,+} = \xi_{0y,+} \equiv \xi_{0+}$ and $\xi_{0x,-} = \xi_{0y,-} \equiv \xi_{0-}$ with $\xi_{0+} \neq \xi_{0-}$

Approach B: we set $\xi_{0x,+} = \xi_{0x,-} \equiv \xi_{0x}$ and $\xi_{0y,+} = \xi_{0y,-} \equiv \xi_{0y}$ with $\xi_{0x} \neq \xi_{0y}$

In both cases, we maintained the pairwise equality of the rms beam sizes at the IP and kept the luminosity fixed at its nominal value, $\mathcal{L}_0 = 3 \times 10^{33}$ cm^{-2} s^{-1}. Other constraints were in effect. In Approach B, the transparency-symmetry constraint on the beam-beam parameters is respected, as explained in Section 4.4.2, but this is not the case in Approach A. The simulation results showed that:

- In both approaches, only the vertical beam blowup is significant, and this blowup behaves smoothly as the beam-beam parameters move away from full equality
- In Approach A, the dynamics favors (that is, beam blowup is less for) $\xi_{0+} \approx 0.024$, $\xi_{0-} \approx 0.04$ over $\xi_{0+} = \xi_{0-} = 0.03$
- In Approach B, the dynamics favors $\xi_{0y} \approx 0.023$, $\xi_{0x} \approx 0.04$ over $\xi_{0x} = \xi_{0y} = 0.03$

In both cases, the dynamical value of the luminosity is slightly increased from the values corresponding to $\xi_{0x,+} = \xi_{0y,+} = \xi_{0x,-} = \xi_{0y,-} = 0.03$. We have every reason to believe that qualitatively similar results apply to the current design. We conjecture that, if the beam-beam parameters were chosen according to the preference expressed by the dynamics, the operation of the machine would perhaps be smoother and more reliable. Of course, there are implications for other areas of the design associated with these changes. Table 4-42 shows values for selected parameters of PEP-II in two examples with unequal beam-beam parameters. Both sets are within the operational reach of the machine. We note that, in both examples, the total current of the LEB is higher than the nominal value.

Table 4-42. Two examples of modified sets of basic parameters based on different choices for the nominal beam-beam parameters, compared with the nominal specification. The nominal luminosity is $\mathcal{L}_0 = 3 \times 10^{33}$ cm^{-2} s^{-1} for all three cases.

	Nominal		Approach A		Approach B	
	LEB	HEB	LEB	HEB	LEB	HEB
ξ_{0x}	0.03	0.03	0.025	0.04	0.04	0.04
ξ_{0y}	0.03	0.03	0.025	0.04	0.025	0.025
σ_{0x} [μm]	152		144		141	
σ_{0y} [μm]	6.06		5.75		9.0	
$r \equiv \sigma_{0y}/\sigma_{0x}$	0.04		0.04		0.06	
d/σ_{0x}	11.8	14.3	12.4	15.1	12.7	15.5
I [A]	2.1	1.0	2.8	0.74	2.5	1.2

4.4.7.4 Pairwise-Equal Beta Functions. As mentioned in Section 4.4.2, a single-particle Hamiltonian analysis leads to a more restrictive set of transparency conditions than those we have adopted [Krishnagopal and Siemann, 1990b]. Motivated by this analysis, we have gone through the exercise of running one simulation case for a modified PEP-II design that satisfies this more restricted symmetry. In this particular example, we have set the beam-beam parameters and the nominal luminosity to their PEP-II nominal values of 0.03 and 3×10^{33} cm^{-2} s^{-1}, respectively, and we have chosen the beta functions at the IP to be $\beta^*_{x,+} = \beta^*_{x,-} = 50$ cm and $\beta^*_{y,+} = \beta^*_{y,-} = 2$ cm. An immediate consequence of going to this configuration is that the total current in the LEB increases to 2.9 A (which is still within the PEP-II design specification). Table 4-43 shows other basic parameters for this modified case, and Fig. 4-107 shows the results for the beam blowup as a function of the beam separation at the first parasitic collision.

In this case, one sees that the beam blowup curves behave symmetrically and tend to rise more gently as the parasitic separation decreases than in the nominal case (Fig. 4-96). However, for the nominal value of the separation, the simulation results for *both* cases show that the dynamical value of the luminosity is within a few percent of 3×10^{33} cm^{-2} s^{-1}.

4.4.7.5 Other Alternatives Studied. In the same spirit of examining departures from the nominal parameters, we also studied the two earlier designs. Specifically, we looked at (a) making $\beta^*_{x,+}$ and $\beta^*_{y,+}$ larger than nominal and (b) making $\sigma_{\ell,+}$ smaller than nominal. The object of both changes was to try to bring transparency condition (iv) closer to being satisfied. Simulations for both cases indicated slightly better luminosity performance. The penalty in case (a) is an increase in the LEB current, and in case (b) an increase in the required RF voltage and a change in the momentum compaction factor.

4.4.7.6 Simulation Parameters. As mentioned in Section 4.4.3, in all the simulation results with TRS presented above we used five damping times and 256 superparticles,

Table 4-43. Modified main PEP-II parameters used in a beam-beam simulation with pairwise-equal beta functions.

	LER (e^+)	HER (e^-)
$\mathcal{L}_0$ [$cm^{-2}\ s^{-1}$]	3×10^{33}	
ξ_{0x}	0.03	0.03
ξ_{0y}	0.03	0.03
ν_x	0.64	0.64
ν_y	0.57	0.57
ν_s	0.052	0.052
σ_ℓ [cm]	1.0	1.0
σ_E/E	1.00×10^{-3}	0.616×10^{-3}
N [a]	7.507×10^{10}	2.586×10^{10}
I [A]	2.862	0.986
β_x^* [m]	0.5	0.5
β_y^* [m]	0.02	0.02
σ_{0x}^* [μm]	175	175
σ_{0y}^* [μm]	7	7
Parameters at the first parasitic collision		
d/σ_{0x}	12.4	12.4
ξ_{0x}	–0.0002	–0.0002
ξ_{0y}	+0.003	+0.003

[a]These values for N do not take into account the existence of the ion-clearing gap.

and represented thick-lens beam-beam effects by using five slices. In order to save computer time, in some cases (typically tune scans) we used fewer superparticles or ran the simulation for only three damping times. In general, for $\xi_0 = 0.03$, the results are qualitatively the same. As an example of these kinds of comparisons, we present below a spot-check with more superparticles. Figure 4-108 shows results with 256 and with 1024 superparticles for the vertical blowup of the LEB, for the nominal design case. The curve with 256 superparticles is taken from Fig. 4-96. One can see that there is essentially no difference in the two cases.

4.4.8 Conclusions

Our results show that, without the parasitic crossings, the beam dynamics performance of the machine is quite close to nominal, up to values of ξ_0 substantially higher than the

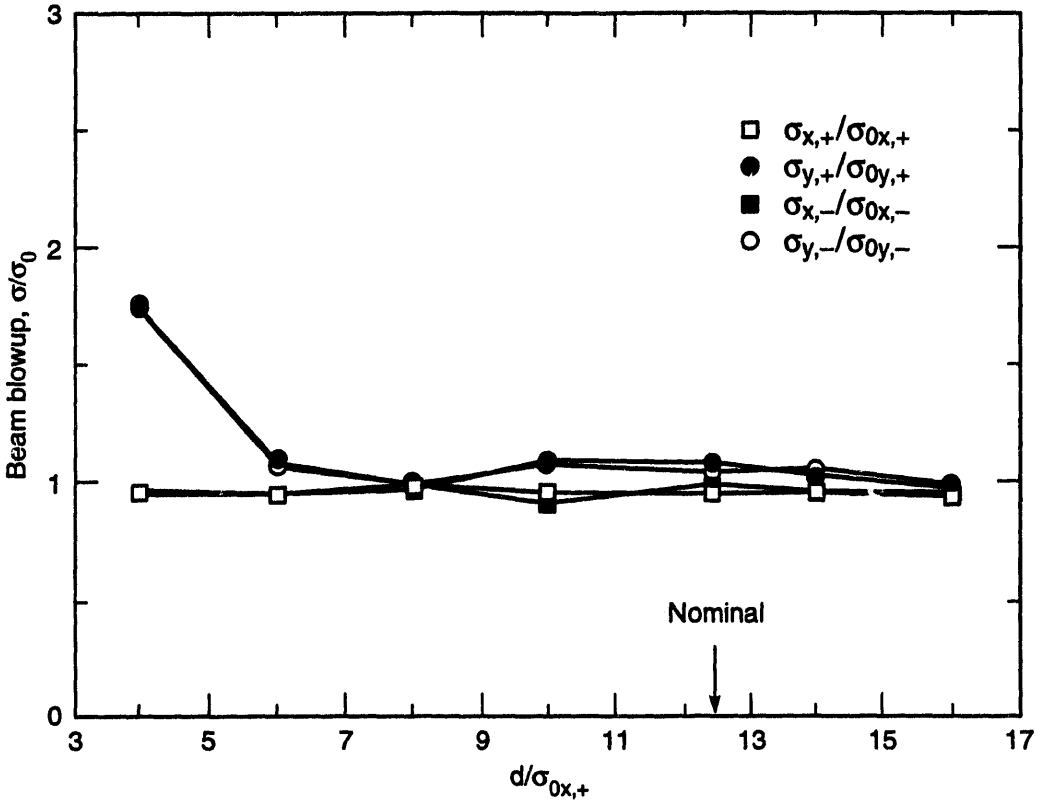

Fig. 4-107. Beam blowup factors vs $d/\sigma_{0x,+}$ for a beam-beam simulation (using TRS) with pairwise-equal beta functions. This should be compared with the nominal case, shown in Fig. 4-96.

design specification of 0.03. The parasitic crossings introduce a horizontal-vertical coupling due to the large value of the vertical beta function. This has the effect of increasing the vertical size of the low-energy beam, with a corresponding lowering of the luminosity. However, because the other three transverse beam sizes are not changed much, the luminosity degrades no more than 5% from its nominal value for $\xi_0 = 0.03$. For $\xi_0 = 0.05$, the relative degradation is larger, of the order of 15%; however, since the nominal luminosity is larger in this case ($\mathcal{L}_0 = 8.3 \times 10^{33}$ cm^{-2} s^{-1}), the *absolute* value of the luminosity is about 7×10^{33} cm^{-2} s^{-1}, which exceeds the PEP-II design specification.

The calculated results for the value of $\xi_0 = 0.05$ were achieved by increasing the bunch currents by a factor of 5/3 from the nominal values at fixed emittance. Another way of achieving $\xi_0 = 0.05$ is to decrease the emittances by a factor of 3/5 at fixed bunch current. In this case, because of the reduced beam size, the parasitic collisions have an increased normalized separation, namely $d/\sigma_{0x,+} = 15.2$ instead of a nominal value of 11.8. The expected luminosity in this case is $\mathcal{L}_0 = 5 \times 10^{33}$ cm^{-2} s^{-1}, but the beam blowup leads to a dynamical value of $\mathcal{L} \gtrsim 4 \times 10^{33}$ cm^{-2} s^{-1}. This second mode of operation with $\xi_0 = 0.05$ is somewhat more easily accomplished than the first as a result of the lower beam-current requirements and the larger parasitic collision separation.

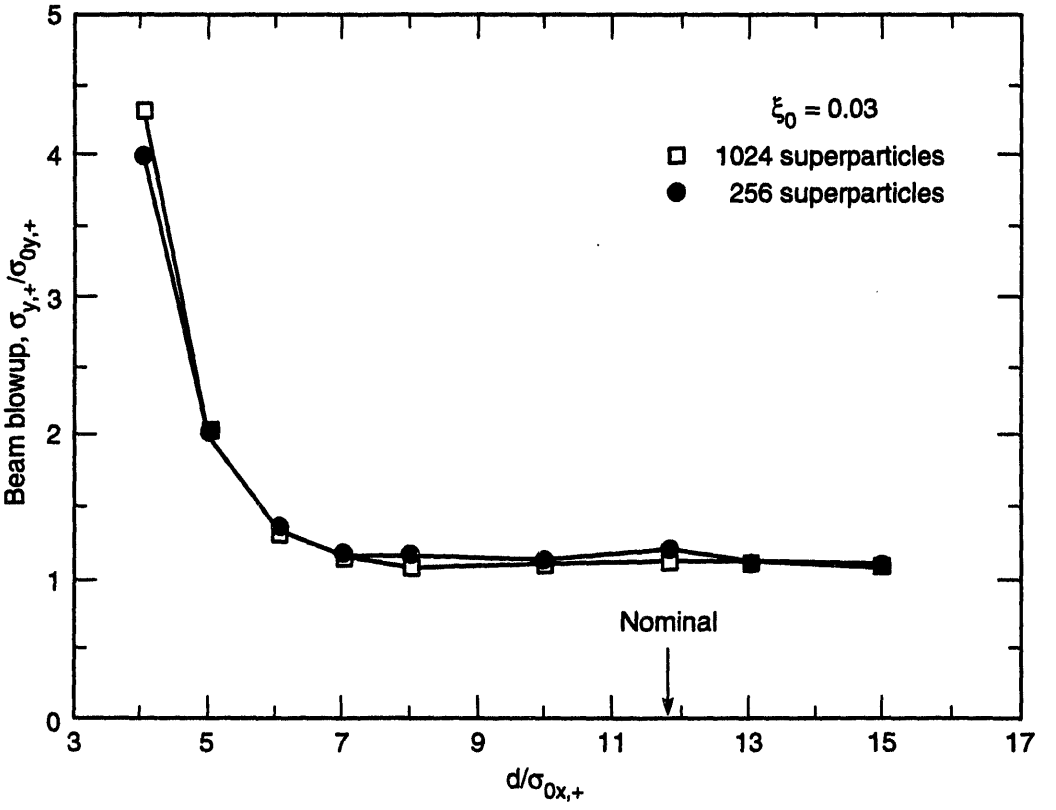

Fig. 4-108. Comparison of simulation results with TRS for 256 vs 1024 superparticles per bunch. The vertical blowup factor of the LEB is plotted vs $d/\sigma_{0x,+}$ for the nominal design case. The curve with 256 superparticles is taken from Fig. 4-96.

Our simulations for luminosity performance, based on studies of the dynamics of the beam core, suggest a simple rule-of-thumb for the effective weakness of the parasitic collisions: Once a good working point has been found, the parasitic collisions are effectively weak when $d/\sigma_{0x,+} \gtrsim 7$ for $\xi_0 = 0.03$ (or $d/\sigma_{0x,+} \gtrsim 9$ for $\xi_0 = 0.05$). Obviously, a prudent approach dictates choosing a design value for $d/\sigma_{0x,+}$ larger than 7; all our evidence to date confirms that the nominal separation value of 11.8 for PEP-II will be quite comfortable.

The influence of parasitic crossings beyond the first one is quite weak. (To take account of these collisions may require a very small adjustment of the working point.) They may induce a coherent dipole oscillation in the beams, but this instability should be easily avoided by a suitable choice of working point.

In general, from the perspective of beam-beam dynamics, we conclude that the energy asymmetry of PEP-II presents no qualitatively new problems compared with those arising in single-ring colliders.

Although our studies show completely acceptable luminosity performance of the nominal design, we have explored to some extent how this performance varies as some parameters take on values that are different from, but close to, nominal. Obviously these

changes would have implications for other areas of the design, or for the operation of the machine. Three such variations are:

- Increase the bunch spacing from $2\lambda_{RF} = 1.26$ m to $3\lambda_{RF} = 1.89$ m, with a concomitant increase in emittances and bunch currents, so that the total beam current, nominal beam-beam parameters, and nominal luminosity remain unchanged
- Adopt unequal beam-beam parameters according to two approaches: (A) make the beam-beam parameters of the LEB different from those of the HEB, but keep the horizontal and vertical parameters equal for each beam; (B) make the beam-beam parameters equal in the two beams, but horizontal parameters different from vertical
- Set the beta functions at the IP pairwise equal

Because the luminosity performance is already quite close to nominal, these alternatives do not improve the performance more than a few percent for $\xi_0 = 0.03$. Thus, the advantage of making these changes may only be in further weakening the effect of the parasitic collisions compared with the nominal design.

Beam-beam simulations of the injection process show that the vertical injection scheme with vertical beam displacement is quite comfortable, since it induces a temporary beam blowup of only a factor of three, which is easily accommodated within the physical aperture.

The lifetime is an important issue that we are just beginning to study. This is the most difficult and expensive part of beam-beam simulations. Preliminary results show that, in the absence of machine nonlinearities, the beam lifetime is comfortably long. (Thus far, we have not included magnet nonlinearities in the simulation studies.) Because magnet nonlinearities are more important at the tails of the beam than at the core, they are unlikely to affect the luminosity performance of PEP-II. However, their influence on the beam lifetimes may be significant and should be estimated.

Based on our results, and the possibilities for improvement described above, we are convinced that the PEP-II design with a luminosity of 3×10^{33} cm^{-2} s^{-1} is quite comfortable. While important issues remain to be studied in more detail, such as beam lifetimes, optimal choice of working point, and effects of magnet nonlinearities on beam dynamics performance, we are confident that our solution will meet and has margin to exceed its luminosity goals.

5.

COLLIDER COMPONENTS

IN Chapter 4 we presented the physics design of PEP-II. The parameters we have adopted to achieve a luminosity of 3×10^{33} cm^{-2} s^{-1}, and the beam separation scheme we have arrived at (driven mainly by background considerations), impose many requirements on the various technical components of the project. In this chapter, we describe these technical components, paying particular attention to those aspects that are most crucial to reaching the high luminosity we have specified. In general, the challenges to be met are associated with the high beam currents that must be stored in the two rings, 0.99 A in the high-energy ring (HER) and 2.14 A in the low-energy ring (LER). In all cases, we have designed the hardware to have adequate operating margin to ensure reliability, and we have employed proven design concepts wherever possible.

In Section 5.1 we describe the magnets and supports. In the case of the HER, nearly all of these magnets are existing PEP magnets, but we describe them briefly for completeness. Though the LER magnets will be newly constructed, they are based (with the exception of the dipoles) on proven PEP designs and are therefore straightforward to design and build. Magnets in the interaction region (IR), however, are technically quite challenging and are the key to the successful implementation of the beam separation scheme; these are described in Section 5.1.3.

The vacuum systems for the two rings are described in Section 5.2. The design challenges here are to provide a low background gas pressure in the face of copious synchrotron-radiation-induced photodesorption and to manage the high thermal loads associated with many megawatts of synchrotron radiation power. We have adopted a copper chamber for our design, based on its desirable properties in both these regards. In this section, we also describe the design and cooling for the various IR hardware components, such as the synchrotron radiation masks, the beam dumps, and the vertex detector beam pipe.

The other technically challenging aspects of the PEP-II design include the RF cavities (Section 5.5) and the feedback system (Section 5.6). The RF cavities must be designed to dissipate approximately 150 kW of power and to permit the effective damping of dangerous higher-order modes (HOMs) to Q values of about 70. This damping is accomplished with an innovative design in which three waveguides are attached to the body of the room-temperature cavity to remove the HOM power. The feedback system utilizes a bunch-by-

bunch approach that is designed to handle the full bunch repetition rate of 238 MHz; the system employs a novel digital processing scheme that is very flexible and can accommodate both injection and colliding-beam conditions. Detailed simulations of system performance and tests of a portion of the system at SPEAR have demonstrated the efficacy of the design.

The remaining design aspects covered in Chapter 5—survey and alignment (Section 5.3), power supplies (Section 5.4), instrumentation and electronics (Section 5.7), and control system (Section 5.8) are relatively straightforward. Here too we have paid attention to providing flexibility and reliability in all components to ensure that PEP-II will indeed function as a "factory."

5.1 MAGNETS AND SUPPORTS

The magnet system in PEP-II provides the guide fields that bend and focus the charged particles, electrons in the HER and positrons in the LER. In the case of the HER, the lattice is designed to make use of most of the existing PEP magnets. The LER is an entirely new ring for which all magnets must be newly constructed.

Because PEP was designed to operate at 18 GeV, whereas the PEP-II HER has a nominal energy of 9 GeV, the PEP magnets are very conservatively designed for their new function. As discussed in Section 7.2, it is prudent to inspect the magnets when they are removed from the tunnel; as needed, the magnet coils will be refurbished to ensure their reliability for long-term PEP-II service. In addition, some of the magnets will be measured after reassembly to ensure that their fields remain the same.

We plan to reuse all of the PEP dipoles and quadrupoles for the PEP-II HER. Because the HER lattice uses more quadrupoles than did PEP, additional magnets must be fabricated. In the case of the dipoles, we need 192 regular bending magnets and an additional 16 PEP low-field bending magnets, for a total of 208 PEP dipoles; four short LER-style dipoles will also be used, making a grand total of 212 dipoles for the HER. All 144 sextupoles are available from PEP. For completeness, however, we describe the existing PEP magnets briefly in Section 5.1.1.

The quadrupole and sextupole magnets for the LER are designed to have the same aperture as the present PEP magnets. This is justified because the required beam-stay-clear aperture in the LER is almost identical to that of the HER, as discussed in Section 5.2.2. Basing the LER designs on PEP magnets minimizes the engineering and design efforts required, because the already-optimized pole profiles of the PEP magnets can be used without modification. The LER dipoles are much shorter than the PEP dipoles (0.45 m compared with 5.4 m for PEP) and will not be based on that pole profile. Design details for the LER magnets are presented in Section 5.1.2.

5.1.1 HER Magnets

As mentioned above, most of the magnets for the HER are existing PEP magnets. The only exception is the quadrupoles. Additional quadrupoles are needed for the HER because the FODO focusing structure (see Section 4.1) will be maintained throughout the straight sections, except for the IR-2 straight that houses the detector.

5.1.1.1 Dipoles. The main parameters of the laminated PEP dipoles are summarized in Table 5-1 for conditions corresponding to the nominal PEP-II operating energy of 9 GeV. Physical dimensions of the magnet are shown in Fig. 5-1. Each magnet has a magnetic length of 5.4 m (212.607 in.) and weighs 7.4 tons. The coils, located above and below the midplane, are constructed of water-cooled aluminum, insulated with Mylar and fiberglass tape and vacuum potted in a radiation-hardened alumina-based epoxy. All dipoles will be disassembled and will have their coil insulation inspected and refurbished to ensure reliable service in PEP-II. After reassembly, a sample of magnets will be remeasured to ensure the constancy of their magnetic properties. To provide horizontal orbit correction, backleg windings are employed. Windings from a pair of dipoles on either side of a focusing quadrupole will be ganged together to form a single corrector.

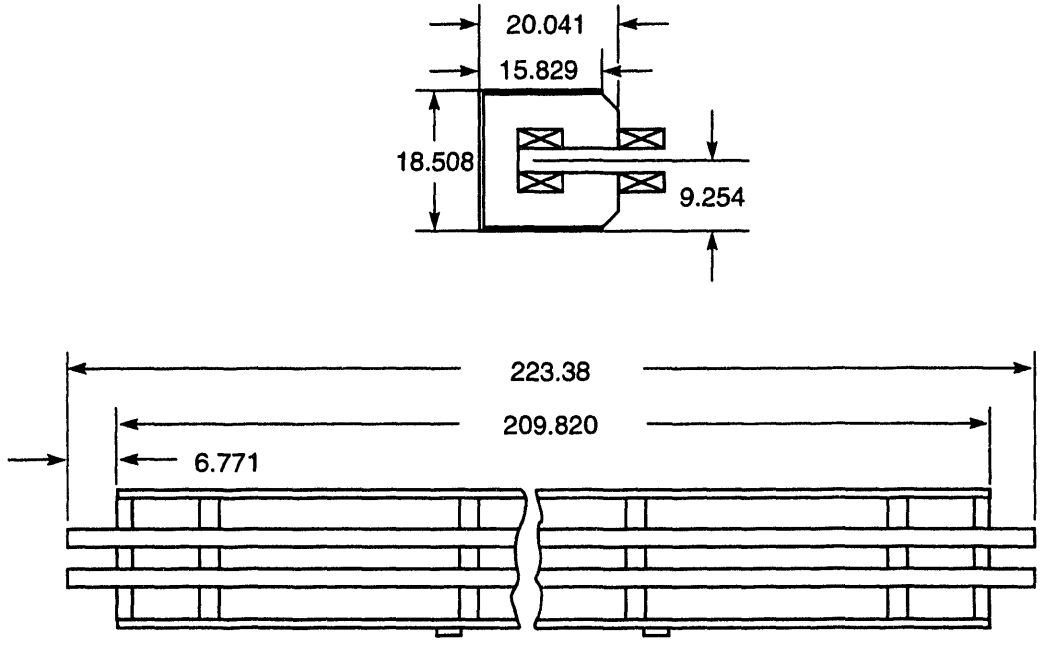

Fig. 5-1. End and side views of the HER bending magnet. Dimensions are given in inches.

Table 5-1. HER dipole parameters.

Magnet designation	2.8C212	2.8H17	5.8H85	5.8H80
Lattice designation	B	B4	B3	B2
Number of magnets	192	4	8	8
Field @ 9 GeV [T]	0.1819	0.0904	0.0216	0.0216
Integrated field @ 9 GeV [T·m]	0.9824	0.0407	0.0466	0.0431
Pole width [in.]	8.425	7.5	5.9	5.9
Gap height [in.]	2.787	2.787	5.875	5.875
Core length [in.]	209.820	14.930	79.085	72.685
Magnetic length [in.]	212.607	17.717	84.960	78.560
Width of useful field, 0.1% [in.]	4.725	4.00	3.15	3.15
Lamination height [in.]	15.433	16	13.38	13.38
Lamination width [in.]	18.19	17.8	10.47	10.47
Packing factor, minimum [%]	98	98	NA	NA
Core weight [lb]	14,168	2,000	1,500	1,500
Amp·turns @ 9 GeV	5,121	2,544	1,280	1,280
Turns	8	36	2	2
Pancakes per pole	1	1	1	1
Conductor dimensions [in.]	2.4 × 0.7	2.0 × 0.3125	2.4 × 0.7	2.4 × 0.7
Cooling hole diameter [in.]	0.25	0.1875	0.25	0.25
Conductor cross section [in.^{2}]	1.63	0.60	1.63	1.63
Current @ 9 GeV [A]	640.1	70.7	640.1	640.1
Resistance @ 40°C [mΩ]	5.1	7.2	0.4	0.4
Power @ 9 GeV [kW]	2.08	0.04	0.15	0.15
Voltage drop @ 9 GeV [V]	3.6	0.5	0.2	0.2
Coil weight [lb]	585	200	40	40
Number of water circuits	1	1	1	11
Water flow rate [gpm]	0.8	0.3	1.4	1.4
Water pressure drop [psi]	150	100	50	50
Temperature rise [°C]	5.3	0.4	0.4	0.4
Total power, magnets and bus [kW]	399.4	0.1	1.2	1.2
Total voltage, magnets and bus [V]	691.2	2.0	1.9	1.9
Total system water requirements [gpm]	144.4	1.4	11.0	11.4

5.1.1.2 Quadrupoles. As with the dipole magnets, all existing PEP quadrupoles will be reused for the HER. Altogether, 270 magnets are required for the PEP-II HER, of which 200 are available from PEP. The additional magnets will be fabricated using the same pole-tip profile developed for PEP, thus avoiding the need to develop a new design. Dimensions of a typical quadrupole magnet are shown in Fig. 5-2. The electrical characteristics of the existing quadrupoles, together with the new magnets, are summarized in Table 5-2. As is the case for the dipoles, the conductor for the quadrupoles is an aluminum extrusion. The insulating procedure used for the dipoles, employing Mylar, fiberglass tape, and alumina-loaded epoxy, will also be used for the quadrupole magnets.

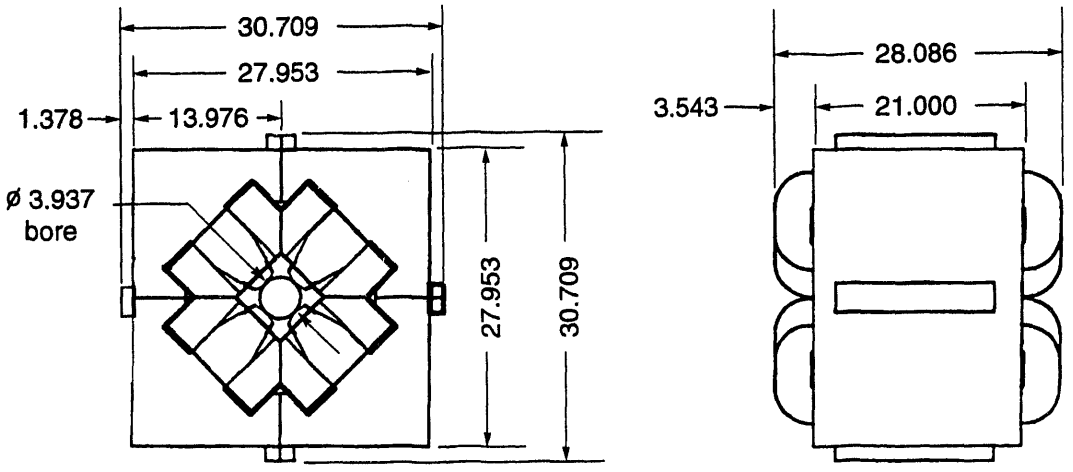

Fig. 5-2. End and side views of an HER quadrupole magnet. Dimensions are given in inches.

Table 5-2. HER quadrupole parameters. The column heads indicate whether the magnets are refurbished PEP quadrupoles or newly constructed magnets.

	PEP	PEP	PEP	New	PEP	PEP
Magnet designation	4Q22	4Q40	4Q40	4Q18	4Q40	4Q40
Lattice designation	QD	QD6	QDI	QDO	QDOI	QDP1
Number of magnets	54	2	2	14	2	2
Operating gradient [T/m]	7.33	7.89	1.95	8.83	2.98	4.06
Pole-tip field @ operating gradient [T]	0.366	0.394	0.097	0.441	0.149	0.203
Gradient-length product [T]	4.03	7.89	1.95	3.97	2.98	4.06
Inscribed radius [in.]	1.968	1.968	1.968	1.968	1.968	1.968
Minimum gap [in.]	1.457	1.457	1.457	1.457	1.457	1.457
Core length [in.]	19.69	37.40	37.40	15.75	37.40	37.40
Magnetic length [in.]	21.65	39.37	39.37	17.72	39.37	39.37
Lamination height [in.]	13.98	13.98	13.98	13.98	13.98	13.98
Lamination width [in.]	13.35	13.35	13.35	13.35	13.35	13.35
Packing factor, minimum [%]	98	98	98	98	98	98
Core weight [lb]	2898	5506	5506	2318	5506	5506
Amp-turns per pole @ 9 GeV	7280	7837	1935	8770	2965	4032
Turns per pole	57	57	57	57	57	57
Pancakes per pole	1	1	1	1	1	1
Conductor cross-sectional area [$in.^2$]	0.197	0.197	0.197	0.197	0.197	0.197
Conductor dimensions [in.]	0.5×0.5	0.5×0.5	0.5×0.5	0.5×0.5	0.5×0.5	0.5×0.5
Cooling hole diameter [in.]	0.25	0.25	0.25	0.25	0.25	0.25
Current @ 9 GeV [A]	128	137	34	154	52	71
Resistance @ 40°C [mΩ]	82	127	127	72	127	127
Power @ 9 GeV [kW]	1.3	2.4	0.2	1.7	0.3	0.6
Voltage drop @ 9 GeV [V]	10.5	17.5	4.3	11.1	6.6	9.0
Coil weight [lb]	282	438	438	248	438	438
Number of water circuits	1	2	1	1	1	1
Water flow rate [gpm]	0.5	1.2	0.4	0.6	0.4	0.4
Water pressure drop [psi]	150	150	150	150	150	150
Temperature rise [°C]	9.8	7.7	1.4	11.7	3.2	5.9
Total power (magnets and bus) [kW]	72.4	4.8	0.3	23.9	0.7	1.3
Total voltage [V]	567	35	9	156	13	18
Magnet system water requirements [gpm]	28	2	1	8	1	1

Table 5-2. HER quadrupole parameters. The column heads indicate whether the magnets are refurbished PEP quadrupoles or newly constructed magnets (continued).

	PEP	New	PEP	New	PEP	New
Magnet designation	4Q40	4Q18	4Q40	4Q18	4Q40	4Q18
Lattice designation	QDP3	QDP3	QDP5	QDP5	QDP7	QDP7
Number of magnets	2	2	2	2	2	2
Operating gradient [T/m]	4.02	8.94	4.00	8.89	3.99	8.88
Pole-tip field @ operating gradient [T]	0.201	0.447	0.200	0.444	0.199	0.444
Gradient-length product [T]	4.02	4.02	4.00	4.00	3.99	3.99
Inscribed radius [in.]	1.968	1.968	1.968	1.968	1.968	1.968
Minimum gap [in.]	1.457	1.457	1.457	1.457	1.457	1.457
Core length [in.]	37.40	15.75	37.40	15.75	37.40	15.75
Magnetic length [in.]	39.37	17.72	39.37	17.72	39.37	17.72
Lamination height [in.]	13.98	13.98	13.98	13.98	13.98	13.98
Lamination width [in.]	13.35	13.35	13.35	13.35	13.35	13.35
Packing factor, minimum [%]	98	98	98	98	98	98
Core weight [lb]	5506	2318	5506	2318	5506	2318
Amp-turns per pole @ 9 GeV	3999	8887	3974	8832	3964	8819
Turns per pole	57	57	57	57	57	57
Pancakes per pole	1	1	1	1	1	1
Conductor cross-sectional area [in.^{2}]	0.197	0.197	0.197	0.197	0.197	0.197
Conductor dimensions [in.]	0.5×0.5	0.5×0.5	0.5×0.5	0.5×0.5	0.5×0.5	0.5×0.5
Cooling hole diameter [in.]	0.25	0.25	0.25	0.25	0.25	0.25
Current @ 9 GeV [A]	70	156	70	155	70	155
Resistance @ 40°C [mΩ]	127	72	127	72	127	72
Power @ 9 GeV [kW]	0.6	1.8	0.6	1.7	0.6	1.7
Voltage drop @ 9 GeV [V]	8.9	11.3	8.9	11.2	8.9	11.2
Coil weight [lb]	438	248	438	248	438	248
Number of water circuits	1	1	1	1	1	1
Water flow rate [gpm]	0.4	0.6	0.4	0.6	0.4	0.6
Water pressure drop [psi]	150	150	150	150	150	150
Temperature rise [°C]	5.8	12.0	5.7	11.8	5.7	11.8
Total power (magnets and bus) [kW]	1.3	3.5	1.2	3.5	1.2	3.5
Total voltage [V]	18	23	18	22	18	22
Magnet system water requirements [gpm]	1	1	1	1	1	1

Table 5-2. HER quadrupole parameters. The column heads indicate whether the magnets are refurbished PEP quadrupoles or newly constructed magnets (continued).

	PEP	PEP	PEP	PEP	New	New
Magnet designation	4Q29	4Q29	4Q29	4Q29	4Q18	4Q18
Lattice designation	QDSO1	QDSO1E	QDSO2	QDSO2E	QDSOL	QDSOR
Number of magnets	1	4	1	4	1	1
Operating gradient [T/m]	5.33	5.62	5.35	5.66	8.61	8.61
Pole-tip field @ operating gradient [T]	0.266	0.281	0.267	0.283	0.430	0.430
Gradient-length product [T]	3.89	4.10	3.91	4.13	3.87	3.87
Inscribed radius [in.]	1.968	1.968	1.968	1.968	1.968	1.968
Minimum gap [in.]	1.457	1.457	1.457	1.457	1.457	1.457
Core length [in.]	26.77	26.77	26.77	26.77	15.75	15.75
Magnetic length [in.]	28.74	28.74	28.74	28.74	17.72	17.72
Lamination height [in.]	13.98	13.98	13.98	13.98	13.98	13.98
Lamination width [in.]	13.35	13.35	13.35	13.35	13.35	13.35
Packing factor, minimum [%]	98	98	98	98	98	98
Core weight [lb]	3941	3941	3941	3941	2318	2318
Amp-turns per pole @ 9 GeV	5297	5585	5317	5623	8550	8550
Turns per pole	57	57	57	57	57	57
Pancakes per pole	1	1	1	1	1	1
Conductor cross-sectional area [in.^{2}]	0.197	0.197	0.197	0.197	0.197	0.197
Conductor dimensions [in.]	0.5×0.5	0.5×0.5	0.5×0.5	0.5×0.5	0.5×0.5	0.5×0.5
Cooling hole diameter [in.]	0.25	0.25	0.25	0.25	0.25	0.25
Current @ 9 GeV [A]	93	98	93	99	150	150
Resistance @ 40°C [mΩ]	100	100	100	100	72	72
Power @ 9 GeV [kW]	0.9	1.0	0.9	1.0	1.6	1.6
Voltage drop @ 9 GeV [V]	9.3	9.8	9.4	9.9	10.8	10.8
Coil weight [lb]	345	345	345	345	248	248
Number of water circuits	1	1	1	1	1	1
Water flow rate [gpm]	0.5	0.5	0.5	0.5	0.6	0.6
Water pressure drop [psi]	150	150	150	150	150	150
Temperature rise [°C]	7.1	7.8	7.1	7.9	11.1	11.1
Total power (magnets and bus) [kW]	9	39	9	40	1.6	1.6
Total voltage [V]	1	39	9	40	11	11
Magnet system water requirements [gpm]	0	2	0	2	1	1

Table 5-2. HER quadrupole parameters. The column heads indicate whether the magnets are refurbished PEP quadrupoles or newly constructed magnets (continued).

	New	New	New	New	PEP	PEP
Magnet designation	4Q18	4Q18	4Q18	4Q18	4Q22	4Q22
Lattice designation	QDS11	QDS11E	QDS12	QDS12E	QDS1L	QDS1R
Number of magnets	1	4	1	4	1	1
Operating gradient [T/m]	8.61	9.37	9.79	9.41	7.98	8.01
Pole-tip field @ operating gradient [T]	0.430	0.468	0.489	0.470	0.399	0.400
Gradient-length product [T]	3.87	4.22	4.41	4.24	4.39	4.41
Inscribed radius [in.]	1.968	1.968	1.968	1.968	1.968	1.968
Minimum gap [in.]	1.457	1.457	1.457	1.457	1.457	1.457
Core length [in.]	15.75	15.75	15.75	15.75	19.69	19.69
Magnetic length [in.]	17.72	17.72	17.72	17.72	21.65	21.65
Lamination height [in.]	13.98	13.98	13.98	13.98	13.98	13.98
Lamination width [in.]	13.35	13.35	13.35	13.35	13.35	13.35
Packing factor, minimum [%]	98	98	98	98	98	98
Core weight [lb]	2318	2318	2318	2318	2898	2898
Amp-turns per pole @ 9 GeV	8550	9309	9728	9352	7925	7960
Turns per pole	57	57	57	57	57	57
Pancakes per pole	1	1	1	1	1	1
Conductor cross-sectional area [in.^{2}]	0.197	0.197	0.197	0.197	0.197	0.197
Conductor dimensions [in.]	0.5×0.5	0.5×0.5	0.5×0.5	0.5×0.5	0.5×0.5	0.5×0.5
Cooling hole diameter [in.]	0.25	0.25	0.25	0.25	0.25	0.25
Current @ 9 GeV [A]	150	163	171	164	139	140
Resistance @ 40°C [mΩ]	72	72	72	72	82	82
Power @ 9 GeV [kW]	1.6	1.9	2.1	1.9	1.6	1.6
Voltage drop @ 9 GeV [V]	10.8	11.8	12.3	11.9	11.4	11.5
Coil weight [lb]	248	248	248	248	282	282
Number of water circuits	1	1	1	1	1	1
Water flow rate [gpm]	0.6	0.6	0.6	0.6	0.5	0.5
Water pressure drop [psi]	150	150	150	150	150	150
Temperature rise [°C]	11.1	13.1	14.3	13.2	11.6	11.7
Total power (magnets and bus) [kW]	1.6	7.7	2.1	7.8	1.6	1.6
Total voltage [V]	11	47	12	47	11	11
Magnet system water requirements [gpm]	1	2	1	2	1	1

Table 5-2. HER quadrupole parameters. The column heads indicate whether the magnets are refurbished PEP quadrupoles or newly constructed magnets (continued).

	PEP	PEP	PEP	PEP	New	New
Magnet designation	4Q22	4Q22	4Q22	4Q22	4Q18	4Q18
Lattice designation	QDS21	QDS21E	QDS22	QDS22E	QDS2L	QDS2R
Number of magnets	1	4	1	4	1	1
Operating gradient [T/m]	7.19	7.72	7.17	7.71	8.68	8.76
Pole-tip field @ operating gradient [T]	0.359	0.386	0.358	0.385	0.434	0.438
Gradient-length product [T]	3.95	4.25	3.94	4.24	3.90	3.94
Inscribed radius [in.]	1.968	1.968	1.968	1.968	1.968	1.968
Minimum gap [in.]	1.457	1.457	1.457	1.457	1.457	1.457
Core length [in.]	19.69	19.69	19.69	19.69	15.75	15.75
Magnetic length [in.]	21.65	21.65	21.65	21.65	17.72	17.72
Lamination height [in.]	13.98	13.98	13.98	13.98	13.98	13.98
Lamination width [in.]	13.35	13.35	13.35	13.35	13.35	13.35
Packing factor, minimum [%]	98	98	98	98	98	98
Core weight [lb]	2898	2898	2898	2898	2318	2318
Amp-turns per pole @ 9 GeV	7140	7672	7119	7656	8621	8701
Turns per pole	57	57	57	57	57	57
Pancakes per pole	1	1	1	1	1	1
Conductor cross-sectional area [$in.^2$]	0.197	0.197	0.197	0.197	0.197	0.197
Conductor dimensions [in.]	0.5×0.5	0.5×0.5	0.5×0.5	0.5×0.5	0.5×0.5	0.5×0.5
Cooling hole diameter [in.]	0.25	0.25	0.25	0.25	0.25	0.25
Current @ 9 GeV [A]	125	135	125	134	151	153
Resistance @ 40°C [mΩ]	82	82	82	82	72	72
Power @ 9 GeV [kW]	1.3	1.5	1.3	1.5	1.7	1.7
Voltage drop @ 9 GeV [V]	10.3	11.1	10.3	11.1	10.9	11.0
Coil weight [lb]	282	282	282	282	248	248
Number of water circuits	1	1	1	1	1	1
Water flow rate [gpm]	0.5	0.5	0.5	0.5	0.6	0.6
Water pressure drop [psi]	150	150	150	150	150	150
Temperature rise [°C]	9.4	10.9	9.4	10.9	11.3	11.5
Total power (magnets and bus) [kW]	1.3	6.0	1.3	5.9	1.7	1.7
Total voltage [V]	10	44	10	44	11	11
Magnet system water requirements [gpm]	1	2	1	2	1	1

Table 5-2. HER quadrupole parameters. The column heads indicate whether the magnets are refurbished PEP quadrupoles or newly constructed magnets (continued).

	PEP	PEP	PEP	PEP	PEP	PEP
Magnet designation	4Q22	4Q22	4Q22	4Q22	4Q22	4Q22
Lattice designation	QDS31	QDS31E	QDS32	QDS32E	QDS3L	QDS3R
Number of magnets	1	4	1	4	1	1
Operating gradient [T/m]	7.33	7.33	7.33	7.33	7.33	7.33
Pole-tip field @ operating gradient [T]	0.366	0.366	0.366	0.366	0.366	0.366
Gradient-length product [T]	4.03	4.03	4.03	4.03	4.03	4.03
Inscribed radius [in.]	1.968	1.968	1.968	1.968	1.968	1.968
Minimum gap [in.]	1.457	1.457	1.457	1.457	1.457	1.457
Core length [in.]	19.69	19.69	19.69	19.69	19.69	19.69
Magnetic length [in.]	21.65	21.65	21.65	21.65	21.65	21.65
Lamination height [in.]	13.98	13.98	13.98	13.98	13.98	13.98
Lamination width [in.]	13.35	13.35	13.35	13.35	13.35	13.35
Packing factor, minimum [%]	98	98	98	98	98	98
Core weight [lb]	2898	2898	2898	2898	2898	2898
Amp-turns per pole @ 9 GeV	7280	7280	7280	7280	7280	7280
Turns per pole	57	57	57	57	57	57
Pancakes per pole	1	1	1	1	1	1
Conductor cross-sectional area [$in.^2$]	0.197	0.197	0.197	0.197	0.197	0.197
Conductor dimensions [in.]	0.5×0.5	0.5×0.5	0.5×0.5	0.5×0.5	0.5×0.5	0.5×0.5
Cooling hole diameter [in.]	0.25	0.25	0.25	0.25	0.25	0.25
Current @ 9 GeV [A]	128	128	128	128	128	128
Resistance @ 40°C [mΩ]	82	82	82	82	82	82
Power @ 9 GeV [kW]	1.3	1.3	1.3	1.3	1.3	1.3
Voltage drop @ 9 GeV [V]	10.5	10.5	10.5	10.5	10.5	10.5
Coil weight [lb]	282	282	282	282	282	282
Number of water circuits	1	1	1	1	1	1
Water flow rate [gpm]	0.5	0.5	0.5	0.5	0.5	0.5
Water pressure drop [psi]	150	150	150	150	150	150
Temperature rise [°C]	9.8	9.8	9.8	9.8	9.8	9.8
Total power (magnets and bus) [kW]	1.3	5.4	1.3	5.4	1.3	1.3
Total voltage [V]	11	42	11	42	11	11
Magnet system water requirements [gpm]	1	2	1	2	1	1

Table 5-2. HER quadrupole parameters. The column heads indicate whether the magnets are refurbished PEP quadrupoles or newly constructed magnets (continued).

	PEP	PEP	PEP	New	PEP
Magnet designation	4Q29	4Q40	4Q40	4Q18	4Q40
Lattice designation	QF	QF7	QFI	QFO	QFOI
Number of magnets	60	2	2	16	2
Operating gradient [T/m]	5.48	5.96	1.92	8.83	4.08
Pole-tip field @ operating gradient [T]	0.274	0.298	0.096	0.441	0.204
Gradient-length product [T]	4.00	5.96	1.92	3.97	4.08
Inscribed radius [in.]	1.968	1.968	1.968	1.968	1.968
Minimum gap [in.]	1.457	1.457	1.457	1.457	1.457
Core length [in.]	26.77	37.40	37.40	15.75	37.40
Magnetic length [in.]	28.74	39.37	39.37	17.72	39.37
Lamination height [in.]	13.98	13.98	13.98	13.98	13.98
Lamination width [in.]	13.35	13.35	13.35	13.35	13.35
Packing factor, minimum [%]	98	98	98	98	98
Core weight [lb]	3941	5506	5506	2318	5506
Amp-turns per pole @ 9 GeV	5450	5923	1905	8770	4054
Turns per pole	57	57	57	57	57
Pancakes per pole	1	1	1	1	1
Conductor cross-sectional area [in.^{2}]	0.197	0.197	0.197	0.197	0.197
Conductor dimensions [in.]	0.5×0.5	0.5×0.5	0.5×0.5	0.5×0.5	0.5×0.5
Cooling hole diameter [in.]	0.25	0.25	0.25	0.25	0.25
Current @ 9 GeV [A]	96	104	33	154	71
Resistance @ 40°C [mΩ]	100	127	127	72	127
Power @ 9 GeV [kW]	0.9	1.4	0.1	1.7	0.6
Voltage drop @ 9 GeV [V]	9.6	13.2	4.3	11.1	9.1
Coil weight [lb]	345	438	438	248	438
Number of water circuits	1	1	1	1	1
Water flow rate [gpm]	0.5	0.4	0.4	0.6	0.4
Water pressure drop [psi]	150	150	150	150	150
Temperature rise [°C]	7.5	12.7	1.3	11.7	6.0
Total power (magnets and bus) [kW]	55.0	2.8	0.3	27.3	1.3
Total voltage [V]	575	26	9	178	18
Magnet system water requirements [gpm]	28	1	1	9	1

Table 5-2. HER quadrupole parameters. The column heads indicate whether the magnets are refurbished PEP quadrupoles or newly constructed magnets (continued).

	PEP	New	PEP	New	PEP	PEP
Magnet designation	4Q40	4Q18	4Q22	4Q18	4Q22	4Q22
Lattice designation	QFP2	QFP4	QFP6	QFP8	QFS11	QFS11E
Number of magnets	4	4	4	4	1	4
Operating gradient [T/m]	4.29	9.46	7.61	9.22	9.48	8.06
Pole-tip field @ operating gradient [T]	0.214	0.473	0.380	0.461	0.474	0.403
Gradient-length product [T]	4.29	4.26	4.19	4.15	5.22	4.43
Inscribed radius [in.]	1.968	1.968	1.968	1.968	1.968	1.968
Minimum gap [in.]	1.457	1.457	1.457	1.457	1.457	1.457
Core length [in.]	37.40	15.75	19.69	15.75	19.69	19.69
Magnetic length [in.]	39.37	17.72	21.65	17.72	21.65	21.65
Lamination height [in.]	13.98	13.98	13.98	13.98	13.98	13.98
Lamination width [in.]	13.35	13.35	13.35	13.35	13.35	13.35
Packing factor, minimum [%]	98	98	98	98	98	98
Core weight [lb]	5506	2318	2898	2318	2898	2898
Amp-turns per pole @ 9 GeV	4259	9403	7561	9163	9423	8005
Turns per pole	57	57	57	57	57	57
Pancakes per pole	1	1	1	1	1	1
Conductor cross-sectional area [$in.^2$]	0.197	0.197	0.197	0.197	0.197	0.197
Conductor dimensions [in.]	0.5x0.5	0.5x0.5	0.5x0.5	0.5x0.5	0.5x0.5	0.5x0.5
Cooling hole diameter [in.]	0.25	0.25	0.25	0.25	0.25	0.25
Current @ 9 GeV [A]	75	165	133	161	165	140
Resistance @ 40°C [mΩ]	127	72	82	72	82	82
Power @ 9 GeV [kW]	0.7	2.0	1.5	1.9	2.3	1.6
Voltage drop @ 9 GeV [V]	9.5	11.9	10.9	11.6	13.6	11.6
Coil weight [lb]	438	248	282	248	282	282
Number of water circuits	1	1	1	1	1	1
Water flow rate [gpm]	0.4	0.6	0.5	0.6	0.5	0.5
Water pressure drop [psi]	150	150	150	150	150	150
Temperature rise [°C]	6.6	13.4	10.6	12.7	16.4	11.9
Total power (magnets and bus) [kW]	2.8	7.9	5.8	7.5	2.2	6.5
Total voltage [V]	38	48	44	46	14	46
Magnet system water requirements [gpm]	2	2	2	2	1	2

Table 5-2. HER quadrupole parameters. The column heads indicate whether the magnets are refurbished PEP quadrupoles or newly constructed magnets (continued).

	PEP	PEP	PEP	PEP	New	New
Magnet designation	4Q22	4Q22	4Q22	4Q22	4Q18	4Q18
Lattice designation	QFS12	QFS12E	QFS1L	QFS1R	QFS21	QFS21E
Number of magnets	1	4	1	1	1	4
Operating gradient [T/m]	9.48	8.08	9.76	9.80	11.77	10.55
Pole-tip field @ operating gradient [T]	0.474	0.404	0.488	0.490	0.588	0.527
Gradient-length product [T]	5.22	4.44	5.37	5.39	5.30	4.75
Inscribed radius [in.]	1.968	1.968	1.968	1.968	1.968	1.968
Minimum gap [in.]	1.457	1.457	1.457	1.457	1.457	1.457
Core length [in.]	19.69	19.69	19.69	19.69	15.75	15.75
Magnetic length [in.]	21.65	21.65	21.65	21.65	17.72	17.72
Lamination height [in.]	13.98	13.98	13.98	13.98	13.98	13.98
Lamination width [in.]	13.35	13.35	13.35	13.35	13.35	13.35
Packing factor, minimum [%]	98	98	98	98	98	98
Core weight [lb]	2898	2898	2898	2898	2318	2318
Amp-turns per pole @ 9 GeV	9423	8025	9696	9742	11695	10479
Turns per pole	57	57	57	57	57	57
Pancakes per pole	1	1	1	1	1	1
Conductor cross-sectional area [$in.^2$]	0.197	0.197	0.197	0.197	0.197	0.197
Conductor dimensions [in.]	0.5×0.5	0.5×0.5	0.5×0.5	0.5×0.5	0.5×0.5	0.5×0.5
Cooling hole diameter [in.]	0.25	0.25	0.25	0.25	0.25	0.25
Current @ 9 GeV [A]	165	141	170	171	205	184
Resistance @ 40°C [mΩ]	82	82	82	82	72	72
Power @ 9 GeV [kW]	2.3	1.6	2.4	2.4	3.0	2.4
Voltage drop @ 9 GeV [V]	13.6	11.6	14.0	14.1	14.8	13.3
Coil weight [lb]	282	282	282	282	248	248
Number of water circuits	1	1	1	1	1	1
Water flow rate [gpm]	0.5	0.5	0.5	0.5	0.6	0.6
Water pressure drop [psi]	150	150	150	150	150	150
Temperature rise [°C]	16.4	11.9	17.4	17.6	20.7	16.6
Total power (magnets and bus) [kW]	2.2	6.5	2.4	2.4	3.0	9.8
Total voltage [V]	14	46	14	14	15	53
Magnet system water requirements [gpm]	1	2	1	1	1	2

Table 5-2. HER quadrupole parameters. The column heads indicate whether the magnets are refurbished PEP quadrupoles or newly constructed magnets (continued).

	NEW	NEW	NEW	NEW	PEP	PEP
Magnet designation	4Q18	4Q18	4Q18	4Q18	4Q29	4Q29
Lattice designation	QFS22	QFS22E	QFS2L	QFS2R	QFS31	QFS31E
Number of magnets	1	4	1	1	1	4
Operating gradient [T/m]	11.75	10.53	11.68	11.74	5.61	6.16
Pole-tip field @ operating gradient [T]	0.588	0.526	0.584	0.587	0.280	0.308
Gradient-length product [T]	5.29	4.74	5.26	5.28	4.10	4.49
Inscribed radius [in.]	1.968	1.968	1.968	1.968	1.968	1.968
Minimum gap [in.]	1.457	1.457	1.457	1.457	1.457	1.457
Core length [in.]	15.75	15.75	15.75	15.75	26.77	26.77
Magnetic length [in.]	17.72	17.72	17.72	17.72	28.74	28.74
Lamination height [in.]	13.98	13.98	13.98	13.98	13.98	13.98
Lamination width [in.]	13.35	13.35	13.35	13.35	13.35	13.35
Packing factor, minimum [%]	98	98	98	98	98	98
Core weight [lb]	2318	2318	2318	2318	3941	3941
Amp-turns per pole @ 9 GeV	11678	10465	11605	11666	5575	6117
Turns per pole	57	57	57	57	57	57
Pancakes per pole	1	1	1	1	1	1
Conductor cross-sectional area [in.^{2}]	0.197	0.197	0.197	0.197	0.197	0.197
Conductor dimensions [in.]	0.5x0.5	0.5x0.5	0.5x0.5	0.5x0.5	0.5x0.5	0.5x0.5
Cooling hole diameter [in.]	0.25	0.25	0.25	0.25	0.25	0.25
Current @ 9 GeV [A]	205	184	204	205	98	107
Resistance @ 40°C [mΩ]	72	72	72	72	100	100
Power @ 9 GeV [kW]	3.0	2.4	3.0	3.0	1.0	1.2
Voltage drop @ 9 GeV [V]	14.8	13.3	14.7	14.8	9.8	10.8
Coil weight [lb]	248	248	248	248	345	345
Number of water circuits	1	1	1	1	1	1
Water flow rate [gpm]	0.6	0.6	0.6	0.6	0.5	0.5
Water pressure drop [psi]	150	150	150	150	150	150
Temperature rise [°C]	20.7	16.6	20.4	20.6	7.8	9.4
Total power (magnets and bus) [kW]	3.0	9.7	3.0	3.0	1.0	4.6
Total voltage [V]	15	53	15	15	10	43
Magnet system water requirements [gpm]	1	2	1	1	0	2

Table 5-2. HER quadrupole parameters. The column heads indicate whether the magnets are refurbished PEP quadrupoles or newly constructed magnets (continued).

	PEP	PEP	PEP	PEP	NEW	NEW
Magnet designation	4Q29	4Q29	4Q29	4Q29	4Q60	4Q60
Lattice designation	QFS32	QFS32E	QFS3L	QFS3R	QD4	QF5
Number of magnets	1	4	1	1	2	2
Operating gradient [T/m]	5.62	6.16	5.61	5.62	7.37	6.00
Pole-tip field @ operating gradient [T]	0.281	0.308	0.281	0.281	0.369	0.300
Gradient-length product [T]	4.10	4.50	4.10	4.10	11.556	9.403
Inscribed radius [in.]	1.968	1.968	1.968	1.968	1.968	1.968
Minimum gap [in.]	1.457	1.457	1.457	1.457	1.457	1.457
Core length [in.]	26.77	26.77	26.77	26.77	60.72	60.72
Magnetic length [in.]	28.74	28.74	28.74	28.74	61.70	61.70
Lamination height [in.]	13.98	13.98	13.98	13.98	10.5	10.5
Lamination width [in.]	13.35	13.35	13.35	13.35	10.5	10.5
Packing factor, minimum [%]	98	98	98	98	98	98
Core weight [lb]	3941	3941	3941	3941	5465	5465
Amp-turns per pole @ 9 GeV	5579	6123	5577	5579	7339	5961
Turns per pole	57	57	57	57	12	12
Pancakes per pole	1	1	1	1	1	1
Conductor cross-sectional area [$in.^2$]	0.197	0.197	0.197	0.197	0.197	0.197
Conductor dimensions [in.]	0.5x0.5	0.5x0.5	0.5x0.5	0.5x0.5	0.5x0.5	0.5x0.5
Cooling hole diameter [in.]	0.25	0.25	0.25	0.25	0.25	0.25
Current @ 9 GeV [A]	98	107	98	98	611.6	497
Resistance @ 40°C [mΩ]	100	100	100	100	43.8	43.8
Power @ 9 GeV [kW]	1.0	1.2	1.0	1.0	16.4	10.8
Voltage drop @ 9 GeV [V]	9.8	10.8	9.8	9.8	26.8	21.8
Coil weight [lb]	345	345	345	345	125	125
Number of water circuits	1	1	1	1	4	4
Water flow rate [gpm]	0.5	0.5	0.5	0.5	4.8	4.8
Water pressure drop [psi]	150	150	150	150	50	50
Temperature rise [°C]	7.8	9.4	7.8	7.8	13	8.6
Total power (magnets and bus) [kW]	1.0	4.6	1.0	1.0	32.8	21.6
Total voltage [V]	10	43	10	10	54	44
Magnet system water requirements [gpm]	0	2	0	0	9.6	9.6

5.1.1.3 Sextupoles. For chromaticity correction in the PEP-II HER, 144 sextupoles are required; all are from PEP. The nominal operating point of the HER is quite similar to that of PEP, and since the sextupoles were designed for 18-GeV operation, they have ample margin for any reasonable HER operating parameters. The dimensions of the sextupole are shown in Fig. 5-3, and the electrical characteristics for the various sextupole types at the nominal HER energy are summarized in Table 5-3. Coil design and insulation are the same as for the dipoles and quadrupoles, discussed above.

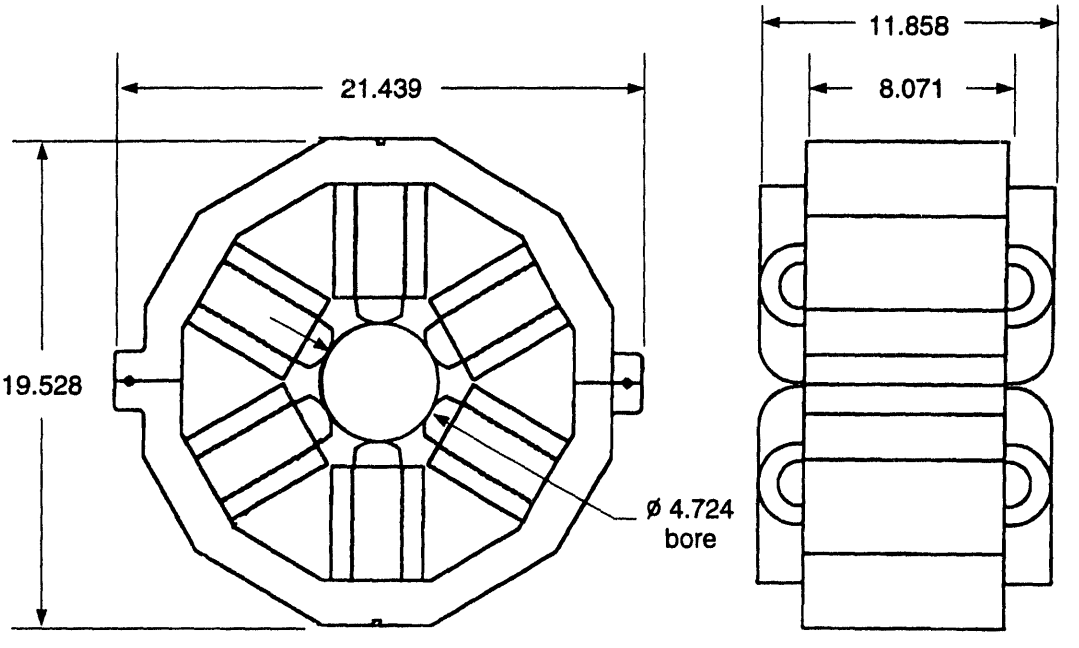

Fig. 5-3. End and side views of a PEP/HER sextupole magnet. Dimensions are given in inches.

Table 5-3. HER sextupole parameters.

Magnet designation	10 SD	10 SF	10 SD	10 SF	10 SD	10 SF
Lattice designation	SD	SF	SD6	SF6	SD5	SF5
Number of magnets	48	48	1	1	1	1
Operating gradient [T/m^2]	79.654	42.029	61.903	96.006	60.042	54.908
Pole-tip field @ operating gradient [T]	0.143	0.076	0.111	0.173	0.108	0.099
Integrated strength @ 9 GeV [T/m]	10.40	5.49	8.08	12.54	7.84	7.17
Aperture inscribed radius [in.]	2.362	2.362	2.362	2.362	2.362	2.362
Core length [in.]	8.071	8.071	8.071	8.071	8.071	8.071
Magnetic length [in.]	10.041	10.041	10.041	10.041	10.041	10.041
Core weight [lb]	170	170	170	170	170	170
Amp turns per pole	2269	1197	1763	2735	1710	1564
Turns per pole	24	24	24	24	24	24
Pancakes per pole	1	1	1	1	1	1
Square conductor dimensions [in.]	0.375	0.375	0.375	0.375	0.375	0.375
Cooling hole diameter [in.]	0.125	0.125	0.125	0.125	0.125	0.125
Conductor cross-sectional area [in.^{2}]	0.127	0.127	0.127	0.127	0.127	0.127
Current @ 9 GeV [A]	94.5	49.9	73.5	114.0	71.3	65.2
Coil length/pole [ft]	49.6	49.6	49.6	49.6	49.6	49.6
Resistance @ 40°C [mΩ]	31	31	31	31	31	31
Power @ 9 GeV [kW]	0.3	0.1	0.2	0.4	0.2	0.1
Voltage drop @ 9 GeV [V]	3.0	1.6	2.3	3.6	2.2	2.0
Coil weight [lb]	44	44	44	44	44	44
Number of water circuits	1	1	1	1	1	1
Water flow rate [gpm]	0.2	0.2	0.2	0.2	0.2	0.2
Water pressure drop [psi]	150	150	150	150	150	150
Temperature rise [°C]	5.9	1.6	3.6	8.6	3.3	2.8
Total magnet power [kW]	20.1	5.6	0.3	0.8	0.3	0.3
Total voltage [V]	145.0	74.8	2.3	3.6	2.2	2.0
Total system water requirements [gpm]	13.0	13.0	0.4	0.4	0.4	0.4

Table 5-3. HER sextupole parameters (continued).

Magnet designation	10 SD	10 SF	10 SD	10 SF	10 SD	10 SF
Lattice designation	SD4	SF4	SD6	SF6	SD5	SF5
Number of magnets	1	1	1	1	1	1
Operating gradient [T/m^2]	105.073	11.618	61.903	96.006	60.042	54.908
Pole-tip field @ operating gradient [T]	0.189	0.021	0.111	0.173	0.108	0.099
Integrated strength @ 9 GeV [T/m]	13.72	1.52	8.08	12.54	7.84	7.17
Aperture inscribed radius [in.]	2.362	2.362	2.362	2.362	2.362	2.362
Core length [in.]	8.071	8.071	8.071	8.071	8.071	8.071
Magnetic length [in.]	10.041	10.041	10.041	10.041	10.041	10.041
Core weight [lb]	170	170	170	170	170	170
Amp turns per pole	2993	331	1763	2735	1710	1564
Turns per pole	24	24	24	24	24	24
Pancakes per pole	1	1	1	1	1	1
Square conductor dimensions [in.]	0.375	0.375	0.375	0.375	0.375	0.375
Cooling hole diameter [in.]	0.125	0.125	0.125	0.125	0.125	0.125
Conductor cross-sectional area [in.^{2}]	0.127	0.127	0.127	0.127	0.127	0.127
Current @ 9 GeV [A]	124.7	13.8	73.5	114.0	71.3	65.2
Coil length/pole [ft]	49.6	49.6	49.6	49.6	49.6	49.6
Resistance @ 40°C [mΩ]	31.29	31.29	31.29	31.29	31.29	31.29
Power @ 9 GeV [kW]	0.49	0.01	0.17	0.41	0.16	0.13
Voltage drop @ 9 GeV [V]	3.9	0.4	2.3	3.6	2.2	2.0
Coil weight [lb]	44	44	44	44	44	44
Number of water circuits	1	1	1	1	1	1
Water flow rate [gpm]	0.18	0.18	0.18	0.18	0.18	0.18
Water pressure drop [psi]	150	150	150	150	150	150
Temperature rise [°C]	10.3	0.1	3.6	8.6	3.3	2.8
Total magnet power [kW]	1.0	0.0	0.3	0.8	0.3	0.3
Total voltage [V]	3.9	0.4	2.3	3.6	2.2	2.0
Total system water requirements [gpm]	0.4	0.4	0.4	0.4	0.4	0.4

Table 5-3. HER sextupole parameters (continued).

Magnet designation	10 SD	10 SF	10 SD	10 SF	10 SD	10 SF
Lattice designation	SD4	SF4	SD6A	SF6A	SD5A	SF5A
Number of magnets	1	1	1	1	1	1
Operating gradient [T/m^2]	105.073	11.618	150.104	75.742	60.042	107.835
Pole-tip field @ operating gradient [T]	0.189	0.021	0.270	0.136	0.108	0.194
Integrated strength @ 9 GeV [T/m]	13.72	1.52	19.60	9.89	7.84	14.08
Aperture inscribed radius [in.]	2.362	2.362	2.362	2.362	2.362	2.362
Core length [in.]	8.071	8.071	8.071	8.071	8.071	8.071
Magnetic length [in.]	10.041	10.041	10.041	10.041	10.041	10.041
Core weight [lb]	170	170	170	170	170	170
Amp turns per pole	2993	331	4276	2158	1710	3072
Turns per pole	24	24	24	24	24	24
Pancakes per pole	1	1	1	1	1	1
Square conductor dimensions [in.]	0.375	0.375	0.375	0.375	0.375	0.375
Cooling hole diameter [in.]	0.125	0.125	0.125	0.125	0.125	0.125
Conductor cross-sectional area [in.^{2}]	0.127	0.127	0.127	0.127	0.127	0.127
Current @ 9 GeV [A]	124.7	13.8	178.2	89.9	71.3	128.0
Coil length/pole [ft]	49.6	49.6	49.6	49.6	49.6	49.6
Resistance @ 40°C [mΩ]	31.29	31.29	31.29	31.29	31.29	31.29
Power @ 9 GeV [kW]	0.49	0.01	0.99	0.25	0.16	0.51
Voltage drop @ 9 GeV [V]	3.9	0.4	5.6	2.8	2.2	4.0
Coil weight [lb]	44	44	44	44	44	44
Number of water circuits	1	1	1	1	1	1
Water flow rate [gpm]	0.18	0.18	0.18	0.18	0.18	0.18
Water pressure drop [psi]	150	150	150	150	150	150
Temperature rise [°C]	10.3	0.1	20.9	5.3	3.3	10.8
Total magnet power [kW]	1.0	0.0	2.0	0.5	0.3	1.0
Total voltage [V]	3.9	0.4	5.6	2.8	2.2	4.0
Total system water requirements [gpm]	0.4	0.4	0.4	0.4	0.4	0.4

Table 5-3. HER sextupole parameters (continued).

Magnet designation	10 SD	10 SF	10 SD	10 SF	10 SD	10 SF
Lattice designation	SD4A	SF4A	SD6A	SF6A	SD5A	SF5A
Number of magnets	1	1	1	1	1	1
Operating gradient [T/m^2]	150.104	13.659	150.104	75.742	60.042	107.835
Pole-tip field @ operating gradient [T]	0.270	0.025	0.270	0.136	0.108	0.194
Integrated strength @ 9 GeV [T/m]	19.60	1.78	19.60	9.89	7.84	14.08
Aperture inscribed radius [in.]	2.362	2.362	2.362	2.362	2.362	2.362
Core length [in.]	8.071	8.071	8.071	8.071	8.071	8.071
Magnetic length [in.]	10.041	10.041	10.041	10.041	10.041	10.041
Core weight [lb]	170	170	170	170	170	170
Amp turns per pole	4276	389	4276	2158	1710	3072
Turns per pole	24	24	24	24	24	24
Pancakes per pole	1	1	1	1	1	1
Square conductor dimensions [in.]	0.375	0.375	0.375	0.375	0.375	0.375
Cooling hole diameter [in.]	0.125	0.125	0.125	0.125	0.125	0.125
Conductor cross-sectional area [in.^{2}]	0.127	0.127	0.127	0.127	0.127	0.127
Current @ 9 GeV [A]	178.2	16.2	178.2	89.9	71.3	128.0
Coil length/pole [ft]	49.6	49.6	49.6	49.6	49.6	49.6
Resistance @ 40°C [mΩ]	31.29	31.29	31.29	31.29	31.29	31.29
Power @ 9 GeV [kW]	0.99	0.01	0.99	0.25	0.16	0.51
Voltage drop @ 9 GeV [V]	5.6	0.5	5.6	2.8	2.2	4.0
Coil weight [lb]	44	44	44	44	44	44
Number of water circuits	1	1	1	1	1	1
Water flow rate [gpm]	0.18	0.18	0.18	0.18	0.18	0.18
Water pressure drop [psi]	150	150	150	150	150	150
Temperature rise [°C]	20.9	0.2	20.9	5.3	3.3	10.8
Total magnet power [kW]	2.0	0.0	2.0	0.5	0.3	1.0
Total voltage [V]	5.6	0.5	5.6	2.8	2.2	4.0
Total system water requirements [gpm]	0.4	0.4	0.4	0.4	0.4	0.4

Table 5-3. HER sextupole parameters (continued).

Magnet designation	10 SD	10 SF	10 SD	10 SF	10 SD	10 SF
Lattice designation	SD4A	SF4A	SD1A	SF1A	SD2A	SF2A
Number of magnets	1	1	1	1	1	1
Operating gradient [T/m^2]	150.104	13.659	130.921	17.952	150.104	86.190
Pole-tip field @ operating gradient [T]	0.270	0.025	0.236	0.032	0.270	0.155
Integrated strength @ 9 GeV [T/m]	19.60	1.78	17.10	2.34	19.60	11.26
Aperture inscribed radius [in.]	2.362	2.362	2.362	2.362	2.362	2.362
Core length [in.]	8.071	8.071	8.071	8.071	8.071	8.071
Magnetic length [in.]	10.041	10.041	10.041	10.041	10.041	10.041
Core weight [lb]	170	170	170	170	170	170
Amp turns per pole	4276	389	3730	511	4276	2455
Turns per pole	24	24	24	24	24	24
Pancakes per pole	1	1	1	1	1	1
Square conductor dimensions [in.]	0.375	0.375	0.375	0.375	0.375	0.375
Cooling hole diameter [in.]	0.125	0.125	0.125	0.125	0.125	0.125
Conductor cross-sectional area [in.^{2}]	0.127	0.127	0.127	0.127	0.127	0.127
Current @ 9 GeV [A]	178.2	16.2	155.4	21.3	178.2	102.3
Coil length/pole [ft]	49.6	49.6	49.6	49.6	49.6	49.6
Resistance @ 40°C [mΩ]	31.29	31.29	31.29	31.29	31.29	31.29
Power @ 9 GeV [kW]	0.99	0.01	0.76	0.01	0.99	0.33
Voltage drop @ 9 GeV [V]	5.6	0.5	4.9	0.7	5.6	3.2
Coil weight [lb]	44	44	44	44	44	44
Number of water circuits	1	1	1	1	1	1
Water flow rate [gpm]	0.18	0.18	0.18	0.18	0.18	0.18
Water pressure drop [psi]	150	150	150	150	150	150
Temperature rise [°C]	20.9	0.2	15.9	0.3	20.9	6.9
Total magnet power [kW]	2.0	0.0	1.5	0.0	2.0	0.7
Total voltage [V]	5.6	0.5	4.9	0.7	5.6	3.2
Total system water requirements [gpm]	0.4	0.4	0.4	0.4	0.4	0.4

Table 5-3. HER sextupole parameters (continued).

Magnet designation	10 SD	10 SF	10 SD	10 SF	10 SD	10 SF
Lattice designation	SD3A	SF3A	SD1A	SF1A	SD2A	SF2A
Number of magnets	1	1	1	1	1	1
Operating gradient [T/m^2]	2.000	90.062	130.921	17.952	150.104	86.190
Pole-tip field @ operating gradient [T]	0.004	0.162	0.236	0.032	0.270	0.155
Integrated strength @ 9 GeV [T/m]	7.84	11.76	17.10	2.34	19.60	11.26
Aperture inscribed radius [in.]	2.362	2.362	2.362	2.362	2.362	2.362
Core length [in.]	8.071	8.071	8.071	8.071	8.071	8.071
Magnetic length [in.]	10.041	10.041	10.041	10.041	10.041	10.041
Core weight [lb]	170	170	170	170	170	170
Amp turns per pole	57	2566	3730	511	4276	2455
Turns per pole	24	24	24	24	24	24
Pancakes per pole	1	1	1	1	1	1
Square conductor dimensions [in.]	0.375	0.375	0.375	0.375	0.375	0.375
Cooling hole diameter [in.]	0.125	0.125	0.125	0.125	0.125	0.125
Conductor cross-sectional area [in.^{2}]	0.127	0.127	0.127	0.127	0.127	0.127
Current @ 9 GeV [A]	2.4	106.9	155.4	21.3	178.2	102.3
Coil length/pole [ft]	49.6	49.6	49.6	49.6	49.6	49.6
Resistance @ 40°C [mΩ]	31.29	31.29	31.29	31.29	31.29	31.29
Power @ 9 GeV [kW]	0.00	0.36	0.76	0.01	0.99	0.33
Voltage drop @ 9 GeV [V]	0.1	3.3	4.9	0.7	5.6	3.2
Coil weight [lb]	44	44	44	44	44	44
Number of water circuits	1	1	1	1	1	1
Water flow rate [gpm]	0.18	0.18	0.18	0.18	0.18	0.18
Water pressure drop [psi]	150	150	150	150	150	150
Temperature rise [°C]	0.0	7.5	15.9	0.3	20.9	6.9
Total magnet power [kW]	0.0	0.7	1.5	0.0	2.0	0.7
Total voltage [V]	0.1	3.3	4.9	0.7	5.6	3.2
Total system water requirements [gpm]	0.4	0.4	0.4	0.4	0.4	0.4

Table 5-3. HER sextupole parameters (continued).

Magnet designation	10 SD	10 SF	10 SD	10 SF	10 SD	10 SF
Lattice designation	SD3A	SF3A	SD1	SF1	SD2	SF2
Number of magnets	1	1	1	1	1	1
Operating gradient [T/m^2]	60.042	90.062	104.863	5.674	105.073	78.654
Pole-tip field @ operating gradient [T]	0.108	0.162	0.189	0.010	0.189	0.142
Integrated strength @ 9 GeV [T/m]	7.84	11.76	13.70	0.74	13.72	10.27
Aperture inscribed radius [in.]	2.362	2.362	2.362	2.362	2.362	2.362
Core length [in.]	8.071	8.071	8.071	8.071	8.071	8.071
Magnetic length [in.]	10.041	10.041	10.041	10.041	10.041	10.041
Core weight [lb]	170	170	170	170	170	170
Amp turns per pole	1710	2566	2987	162	2993	2241
Turns per pole	24	24	24	24	24	24
Pancakes per pole	1	1	1	1	1	1
Square conductor dimensions [in.]	0.375	0.375	0.375	0.375	0.375	0.375
Cooling hole diameter [in.]	0.125	0.125	0.125	0.125	0.125	0.125
Conductor cross-sectional area [in.^{2}]	0.127	0.127	0.127	0.127	0.127	0.127
Current @ 9 GeV [A]	71.3	106.9	124.5	6.7	124.7	93.4
Coil length/pole [ft]	49.6	49.6	49.6	49.6	49.6	49.6
Resistance @ 40°C [mΩ]	31.29	31.29	31.29	31.29	31.29	31.29
Power @ 9 GeV [kW]	0.16	0.36	0.48	0.00	0.49	0.27
Voltage drop @ 9 GeV [V]	2.2	3.3	3.9	0.2	3.9	2.9
Coil weight [lb]	44	44	44	44	44	44
Number of water circuits	1	1	1	1	1	1
Water flow rate [gpm]	0.18	0.18	0.18	0.18	0.18	0.18
Water pressure drop [psi]	150	150	150	150	150	150
Temperature rise [°C]	3.3	7.5	10.2	0.0	10.3	5.7
Total magnet power [kW]	0.3	0.7	1.0	0.0	1.0	0.5
Total voltage [V]	2.2	3.3	3.9	0.2	3.9	2.9
Total system water requirements [gpm]	0.4	0.4	0.4	0.4	0.4	0.4

Table 5-3. HER sextupole parameters (continued).

Magnet designation	10 SD	10 SF	10 SD	10 SF	10 SD	10 SF
Lattice designation	SD3	SF3	SD1	SF1	SD2	SF2
Number of magnets	1	1	1	1	1	1
Operating gradient [T/m^2]	60.042	90.272	104.863	5.674	105.073	78.654
Pole-tip field @ operating gradient [T]	0.108	0.162	0.189	0.010	0.189	0.142
Integrated strength @ 9 GeV [T/m]	7.84	11.79	13.70	0.74	13.72	10.27
Aperture inscribed radius [in.]	2.362	2.362	2.362	2.362	2.362	2.362
Core length [in.]	8.071	8.071	8.071	8.071	8.071	8.071
Magnetic length [in.]	10.041	10.041	10.041	10.041	10.041	10.041
Core weight [lb]	170	170	170	170	170	170
Amp turns per pole	1710	2572	2987	162	2993	2241
Turns per pole	24	24	24	24	24	24
Pancakes per pole	1	1	1	1	1	1
Square conductor dimensions [in.]	0.375	0.375	0.375	0.375	0.375	0.375
Cooling hole diameter [in.]	0.125	0.125	0.125	0.125	0.125	0.125
Conductor cross-sectional area [in.^{2}]	0.127	0.127	0.127	0.127	0.127	0.127
Current @ 9 GeV [A]	71.3	107.2	124.5	6.7	124.7	93.4
Coil length/pole [ft]	49.6	49.6	49.6	49.6	49.6	49.6
Resistance @ 40°C [mΩ]	9	31.29	31.29	31.29	31.29	31.29
Power @ 9 GeV [kW]	0.05	0.36	0.48	0.00	0.49	0.27
Voltage drop @ 9 GeV [V]	0.6	3.4	3.9	0.2	3.9	2.9
Coil weight [lb]	44	44	44	44	44	44
Number of water circuits	1	1	1	1	1	1
Water flow rate [gpm]	0.18	0.18	0.18	0.18	0.18	0.18
Water pressure drop [psi]	150	150	150	150	150	150
Temperature rise [°C]	1.0	7.6	10.2	0.0	10.3	5.7
Total magnet power [kW]	0.1	0.7	1.0	0.0	1.0	0.5
Total voltage [V]	0.6	3.4	3.9	0.2	3.9	2.9
Total system water requirements [gpm]	0.4	0.4	0.4	0.4	0.4	0.4

Table 5-3. HER sextupole parameters (continued).

Magnet designation	10 SD	10 SF
Lattice designation	SD3	SF3
Number of magnets	1	1
Operating gradient [T/m^2]	60.042	90.272
Pole-tip field @ operating gradient [T]	0.108	0.162
Integrated strength @ 9 GeV [T/m]	7.84	11.79
Aperture inscribed radius [in.]	2.362	2.362
Core length [in.]	8.071	8.071
Magnetic length [in.]	10.041	10.041
Core weight [lb]	170	170
Amp turns per pole	1710	2572
Turns per pole	24	24
Pancakes per pole	1	1
Square conductor dimensions [in.]	0.375	0.375
Cooling hole diameter [in.]	0.125	0.125
Conductor cross-sectional area [in.^{2}]	0.127	0.127
Current @ 9 GeV [A]	71.3	107.2
Coil length/pole [ft]	49.6	49.6
Resistance @ 40°C [mΩ]	31.29	31.29
Power @ 9 GeV [kW]	0.16	0.36
Voltage drop @ 9 GeV [V]	2.2	3.4
Coil weight [lb]	44	44
Number of water circuits	1	1
Water flow rate [gpm]	0.18	0.18
Water pressure drop [psi]	150	150
Temperature rise [°C]	3.3	7.6
Total magnet power [kW]	0.3	0.7
Total voltage [V]	2.2	3.4
Total system water requirements [gpm]	0.4	0.4

5.1.2 LER Magnets

All magnets for the LER will be newly constructed. However, the beam-stay-clear aperture requirements for the LER are sufficiently similar to those of the HER (and PEP) that it is justifiable to use the same magnet aperture dimensions. (It is worth noting here that a review of the anticipated gas loads in both the HER and the LER indicates very little difference between the two; this argues for the choice of a vacuum chamber of similar aperture in the two rings.)

The main benefit of keeping the same magnet aperture is that the new LER magnets can take advantage of the well-proven pole-tip profiles developed for PEP and PETRA (using the computer program POISSON); that is, the magnets can be very similar to PEP magnets, with only the external dimensions changed to reflect the lower field requirements at the nominal 3.1-GeV operating point. In this way, we substantially reduce our R&D and engineering costs.

The design of the new magnets will be optimized by minimizing the sum of the installed capital cost plus ten years of operating cost at the design energy. This means that prudent attention is paid to reducing power consumption. Despite this, the LER magnets use proportionately more power than the PEP/HER magnets. This comes about because the PEP magnets were optimized for 18-GeV operation, where the power consumption is higher than at 9 GeV.

5.1.2.1 Dipoles. The LER dipole design was dictated by several considerations. First, the LER magnets must be mounted above the HER. To minimize the weight that must be rigidly supported, it is important to reduce the size of the dipoles considerably, compared with the PEP design. Second, the problems with synchrotron-radiation-induced gas desorption are eased considerably if the dipole is kept short enough to permit its synchrotron radiation fan to exit the magnet completely (as discussed in detail in Section 5.2). Finally, the lattice parameters of the LER call for a relatively high emittance and short damping times compared with what would result from a low-field bending magnet lattice. Although we have chosen to provide wigglers to adjust these parameters, the choice of a short, higher-field dipole helps to reduce the demands on the wigglers and to spread the synchrotron radiation power around more of the ring.

The LER arc dipole magnet physical dimensions are shown in Fig. 5-4. The key

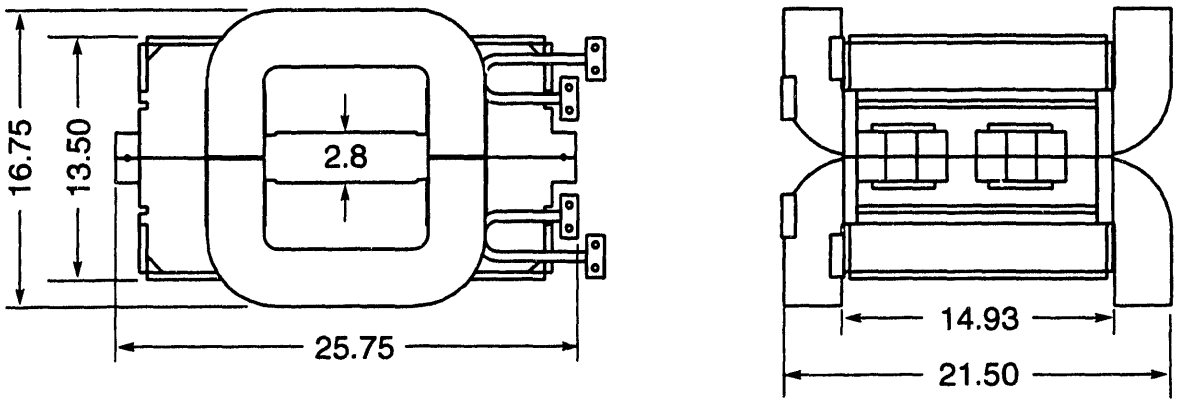

Fig. 5-4. End and side views of the LER bending magnet. Dimensions are given in inches.

dimensions are the core length of 14.92 in. and the gap of 2.8 in. The electrical properties of the LER dipole at its nominal operating energy of 3.1 GeV are summarized in Table 5-4.

To reduce production costs and to maximize magnet-to-magnet uniformity, the main ring magnets for the LER are of laminated construction. The dipole magnets will be constructed of one-piece laminations, 1/16-in. thick, punched from a decarburized, annealed, low-carbon steel sheet, such as Armco special magnet steel. This material—which has been used successfully for many accelerator applications, including those at PEP and Fermilab—exhibits high saturation induction, modest coercive force, and low remanent field. The estimated steel weight to manufacture the required 222 bending magnets is 250 tons.

Laminations will be punched with built-in fiducials to provide convenient external references for alignment, as discussed in Section 5.3. In addition, for reasons explained below, new witness marks will be introduced into the die at each heat-change to ensure magnet uniformity. Particular attention will be paid to the wear on the die. The vendor will be required to keep track of the number of laminations punched between die sharpenings and to provide SLAC with sample laminations on a regular basis, so that in-house inspections can be made to ensure that undue wear (>0.0005 in.) has not taken place on the critical surfaces (thereby producing out-of-tolerance laminations).

The vendor responsible for stacking the laminations will be required to deburr and then stack them, using laminations from consecutive heats. If this is done, the pattern generated by the witness marks will be obvious upon visual inspection. If the observed pattern is regular, the core will be acceptable, whereas an irregular pattern will indicate a lack of quality control on the part of the manufacturer and will be sufficient cause for rejecting the magnet core.

Laminations will be rotated after stacking each (approximately) 4-in. segment of the core. In this way, errors due to the slight variation in the thickness of the laminations will be eliminated. (This thickness error, referred to as "crowning," is well known to occur in flat rolled sheet due to curvature in the rollers caused by forces generated during the production of the sheet.) The precise number of laminations that are stacked before performing such a rotation, which can only be determined when the number of heats is known, will be sufficient to ensure that the regular periodicity of the witness marks is retained.

The magnets operate at low fields, well below saturation, and thus are more sensitive to core length than to the density of the lamination packing. Therefore, to maximize magnet-to-magnet reproducibility, particular attention will be paid to the length of the core (rather than its packing factor).

The magnet end-plates will be manufactured by numerically controlled mills and will contain the necessary holes for mounting coil retainers and other such devices. Angle plates welded to both the end-plates and the laminations will provide the torsional rigidity necessary to stabilize the cores and prevent twisting or bending.

Magnet coils will be of water-cooled aluminum, extruded from billets using porthole dies to provide continuous lengths up to several thousand feet. This technique obviates the need to make joints in the coil, thus eliminating the possibility of leaks. The length of a typical coil is about 150 ft, so there will be minimal waste at the end of each reel of conductor. The estimated weight of one dipole, including coils, is 2200 lb.

Table 5-4. LER dipole parameters.

Magnet designation	2.8H18	2.8H40	2.8H24	2.8H29	2.8H24	2.8H98
Bending angle [deg]	1.875	3.657	0.321	2	1.329	6.925
Lattice designation	B	B1	B2	B3	B4	B5
Number of magnets	192	8	2	4	2	2
Field [T]	0.752	0.660	0.097	0.481	0.400	0.500
Integrated field [T·m]	0.338	0.660	0.058	0.361	0.240	1.250
Pole width [in.]	8	8	8	8	8	8
Gap height [in.]	2.87	2.8	2.8	2.8	2.8	2.8
Core length [in.]	14.85	36.57	20.82	26.73	20.82	95.63
Magnetic length [in.]	17.72	39.37	23.62	29.53	23.62	98.43
Width of useful field, 0.1% [in.]	4.00	4.00	4.00	4.00	4.00	4.00
Lamination height [in.]	6.75	6.75	6.75	6.75	6.75	6.75
Lamination width [in.]	23	23	23	23	23	23
Packing factor, minimum [%]	98	98	98	98	98	98
Core weight [lb]	1,306	4,903	1,832	2,352	1,832	8,415
Amp·turns	21,804	18,665	2,731	13,614	11,308	14,142
Turns	36	36	36	36	36	36
Pancakes per pole	1	1	1	1	1	1
Conductor dimensions [in.]	0.5×0.5	0.5×0.5	0.5×0.5	0.5×0.5	0.5×0.5	0.5×0.5
Cooling hole diameter [in.]	.0.1875	0.1875	0.1875	0.1875	0.1875	0.1875
Conductor cross section [in.^{2}]	0.22	0.22	0.22	0.22	0.22	0.22
Conductor length/pole [ft]	202	352	238	273	238	687
Current [A]	605.68	518.47	75.87	378.18	314.12	392.83
Resistance @ 40°C [mΩ]	24.4	42.5	28.7	33.0	28.7	82.9
Power [kW]	4.47	11.42	0.08	2.36	1.42	6.39
Voltage drop [V]	7.4	20	1.1	6.2	4.5	16.3
Coil weight [lb]	104	182	122	140	122	353
Number of water circuits	2	4	1	2	2	2
Water flow rate, total [gpm]	1.3	1.92	0.4	1.1	1.2	0.7
Water pressure drop [psi]	150	150	150	150	150	150
Temperature rise [°C]	13.2	22.6	0.8	8.2	4.6	36.4
Total power (magnets and bus) [kW]	858	91.2	0.2	9.4	2.8	18.2
Total voltage (magnets and bus) [V]	1420	160	2	25	9	33
Total system water requirements (gpm)	248	15	1	4	2	1

Table 5-4. LER dipole parameters (continued).

Magnet designation	2.8H49	2.8H28	2.8H12	2.8H59
Bending angle [deg]	4.973	1.5	0.166	10.048
Lattice designation	B6	B7	B8	B9
Number of magnets	4	2	2	2
Field [T]	0.718	0.451	0.100	1.209
Integrated field [T·m]	0.898	0.271	0.030	1.814
Pole width [in.]	8	8	8	8
Gap height [in.]	2.8	2.8	2.8	2.8
Core length [in.]	46.41	20.82	9.01	56.26
Magnetic length [in.]	49.21	23.62	11.81	59.06
Width of useful field, 0.1% [in.]	4.00	4.00	4.00	4.00
Lamination height [in.]	16	6.75	6.75	6.75
Lamination width [in.]	23	23	23	23
Packing factor, minimum [%]	96	98	98	98
Core weight [lb]	4,084	1,832	793	4,950
Amp·turns	20,313	3.1	2,825	34,199
Turns	36	36	36	96
Pancakes per pole	1	1	1	1
Conductor dimensions [in.]	0.5×0.5	0.5×0.5	0.5×0.5	0.5×0.5
Cooling hole diameter [in.]	0.1875	0.1875	0.1875	0.1875
Conductor cross section [in.^{2}]	0.22	0.22	0.22	0.22
Conductor length/pole [ft]	392	238	167	1202
Current [A]	564.24	0.09	78.47	356.24
Resistance @ 40°C [mΩ]	47.2	28.7	20.2	145.0
Power [kW]	7.52	0.00	0.06	9.20
Voltage drop [V]	13.3	0.0	0.8	25.8
Coil weight [lb]	201	122	86	617
Number of water circuits	2	2	2	4
Water flow rate, total [gpm]	0.9	1.2	1.4	2.1
Water pressure drop [psi]	150	150	150	150
Temperature rise [°C]	31.6	0.0	0.2	16.8
Total power (magnets and bus) [kW]	30	0.0	1.2	18.4
Total voltage (magnets and bus) [V]	53	0.0	2	52
Total system water requirements (gpm)	4	2	3	4

5.1.2.2 Quadrupoles. The standard LER quadrupole has a length of 17.0 in. and a bore diameter of 3.937 in.; its physical dimensions are shown in Fig. 5-5. The electrical properties of the quadrupoles corresponding to the nominal energy are summarized in Table 5-5.

The LER quadrupoles will be constructed, and the laminations handled, in the same manner described for the dipole magnets, except that they will use four-piece construction. The anticipated weight of steel is larger than that for the dipoles, about 550 tons, thus requiring more heats (about eight rather than five).

The design will include numerically machined end-plates with predrilled holes to mount the beam position monitors. These end-plates will be used to sandwich the laminations together. As with the dipoles, angles welded to the corners of the laminations will provide the required torsional rigidity and stiffness. Four cores, fitted with water-cooled aluminum coils approximately 180 ft long and extruded by the same technique as used for the bending magnets, will be bolted together to form one quadrupole weighing an estimated 2000 lb.

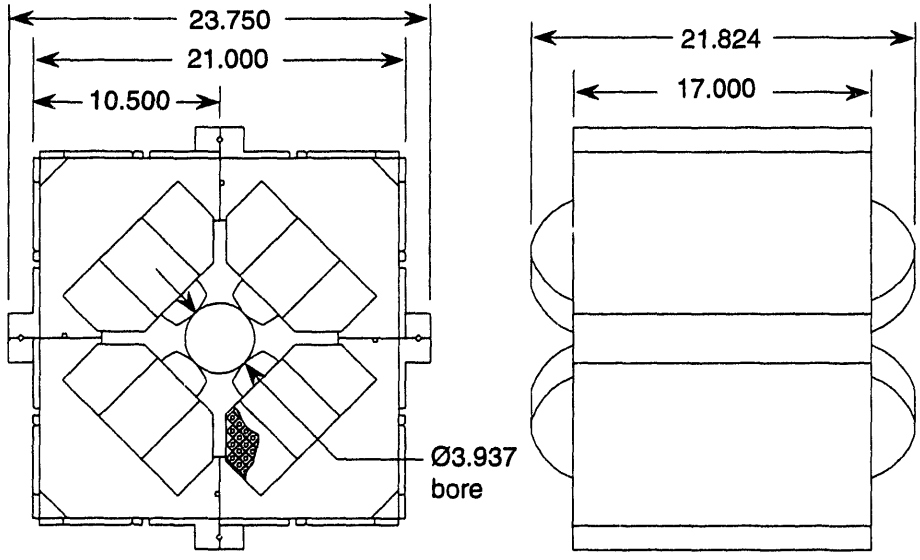

Fig. 5-5. End and side views of an LER quadrupole magnet. Dimensions are given in inches.

Table 5-5. LER quadrupole parameters.

Magnet designation	4Q17	4Q17	4Q17	4Q40	4Q40	4Q40
Location in ring	Arc	Arc	R2	R2	R2	R2
Lattice designation	QF	QD	IQF1	IQD2	IQF3	IQD4
Number of magnets	74	80	2	2	2	2
Operating gradient [T/m]	4.55	4.50	7.12	5.04	4.53	5.05
Pole-tip field @ operating gradient [T]	0.227	0.225	0.356	0.252	0.226	0.253
Gradient length product [T]	1.96	1.93	3.06	5.04	4.529	5.05
Inscribed radius [in.]	1.968	1.968	1.968	1.968	1.968	1.968
Minimum gap [in.]	1.457	1.457	1.457	1.457	1.457	1.457
Core length [in.]	15.95	15.95	15.95	38.39	38.39	38.39
Magnetic length [in.]	16.93	16.93	16.93	39.37	39.37	39.37
Lamination height [in.]	11.88	11.88	11.88	13.98	13.98	13.98
Lamination width [in.]	10.50	10.50	10.50	13.35	13.35	13.35
Packing factor, minimum [%]	98	98	98	98	98	98
Core weight [lb]	1786	1786	1786	6142	6142	6142
Amp·turns per pole	4521	4467	7075	5006	4500	5022
Turns per pole	37	37	37	56	56	56
Pancakes per pole	1	1	1	1	1	1
Conductor cross-sectional area [in.^{2}]	0.198	0.198	0.198	0.198	0.198	0.198
Cooling hole diameter [in.]	0.25	0.25	0.25	0.25	0.25	0.25
Conductor dimensions [in.]	0.5×0.5	0.5×0.5	0.5×0.5	0.5×0.5	0.5×0.5	0.5×0.5
Conductor length/pole [ft]	176	176	176	476	476	476
Current [A]	122	121	191	89	80	90
Resistance @ 40°C [mΩ]	47	47	47	127	127	127
Power [kW]	0.70	0.69	1.72	1.02	0.82	1.02
Voltage drop [V]	5.8	5.7	9.0	11.4	10.2	11.4
Coil weight [lb]	81.4	81.4	81.4	220.2	220.2	220.2
Number of water circuits	1	1	1	1	1	1
Water flow rate [gpm]	0.7	0.7	0.7	0.4	0.4	0.4
Water pressure drop [psi]	150	150	150	150	150	150
Temperature rise [°C]	3.80	3.71	9.32	9.43	7.62	9.49
Total magnet power [kW]	52.0	54.8	3.4	2.0	1.6	2.0
Total magnet water requirements [gpm]	51.9	56.1	1.4	0.8	0.8	0.8

Table 5-5. LER quadrupole parameters (continued).

Magnet designation	4Q17	4Q40	4Q40	4Q40	4Q40	4Q17
Location in ring	R2	R2	R2	R2	R2	R2
Lattice designation	IQF5	IQF6	IQD7	IQF8	IQD9	IQD10
Number of magnets	2	2	2	2	2	4
Operating gradient [T/m]	10.35	5.20	5.98	9.80	7.31	7.12
Pole-tip field @ operating gradient [T]	0.517	0.260	0.299	0.490	0.365	0.356
Gradient length product [T]	4.45	5.20	5.98	9.80	7.31	3.06
Inscribed radius [in.]	1.968	1.968	1.968	1.968	1.968	1.968
Minimum gap [in.]	1.457	1.457	1.457	1.457	1.457	1.457
Core length [in.]	15.95	38.39	38.39	38.39	38.39	15.95
Magnetic length [in.]	16.93	39.37	39.37	39.37	39.37	16.93
Lamination height [in.]	11.88	13.98	11.88	13.98	13.98	11.88
Lamination width [in.]	10.50	13.35	10.50	13.35	13.35	10.50
Packing factor, minimum [%]	98	98	98	98	98	98
Core weight [lb]	1786	6142	4299	6142	6142	1786
Amp·turns per pole	10285	5163	5942	9739	7261	7079
Turns per pole	37	56	56	56	56	37
Pancakes per pole	1	1	1	1	1	1
Conductor cross-sectional area [in.^{2}]	0.198	0.198	0.198	0.198	0.198	0.198
Cooling hole diameter [in.]	0.25	0.25	0.25	0.25	0.25	0.25
Conductor dimensions [in.]	0.5×0.5	0.5×0.5	0.5×0.5	0.5×0.5	0.5×0.5	0.5×0.5
Conductor length/pole [ft]	176	476	476	476	476	176
Current [A]	278	92	106	174	130	191
Resistance @ 40°C [mΩ]	47	127	127	127	127	47
Power [kW]	3.63	1.08	1.43	3.85	2.14	1.72
Voltage drop [V]	13.1	11.7	13.5	22.1	16.5	13.1
Coil weight [lb]	81.4	220.2	220.2	220.2	220.2	81.4
Number of water circuits	1	2	2	4	2	1
Water flow rate [gpm]	0.7	1.2	1.2	3.5	1.2	0.7
Water pressure drop [psi]	150	150	150	150	150	150
Temperature rise [°C]	19.69	3.45	4.57	4.22	6.82	9.33
Total magnet power [kW]	7.3	2.2	2.9	7.7	4.3	6.9
Total magnet water requirements [gpm]	1.4	2.4	2.4	6.9	2.4	2.8

Table 5-5. LER quadrupole parameters (continued).

Magnet designation	4Q17	4Q17	4Q17	4Q40	4Q17	4Q17
Location in ring	R2	R2	R2	R2	R2	R2
Lattice designation	IQF11	IQD12	IQD13	IQF14	IQD15	IQF16
Number of magnets	4	2	2	2	2	2
Operating gradient [T/m]	11.75	10.46	7.04	8.25	5.87	19.21
Pole-tip field @ operating gradient [T]	0.587	0.523	0.352	0.413	0.293	0.960
Gradient length product [T]	5.05	4.50	3.03	8.25	2.52	8.26
Inscribed radius [in.]	1.968	1.968	1.968	1.968	1.968	1.968
Minimum gap [in.]	1.457	1.457	1.457	1.457	1.457	1.457
Core length [in.]	15.95	15.95	15.95	38.39	15.95	15.95
Magnetic length [in.]	16.93	16.93	16.93	39.37	16.93	16.93
Lamination height [in.]	11.88	11.88	11.88	13.98	11.88	11.88
Lamination width [in.]	10.50	10.50	10.50	13.35	10.50	10.50
Packing factor, minimum [%]	98	98	98	98	98	98
Core weight [lb]	1786	1786	1786	6142	1786	1786
Amp·turns per pole	11670	10388	6991	8200	5834	19084
Turns per pole	37	37	37	56	37	37
Pancakes per pole	1	1	1	1	1	1
Conductor cross-sectional area [in.^{2}]	0.198	0.198	0.198	0.198	0.198	0.198
Cooling hole diameter [in.]	0.25	0.25	0.25	0.25	0.25	0.25
Conductor dimensions [in.]	0.5×0.5	0.5×0.5	0.5×0.5	0.5×0.5	0.5×0.5	0.5×0.5
Conductor length/pole [ft]	176	176	176	476	176	176
Current [A]	315	281	189	146	158	516
Resistance @ 40°C [mΩ]	47	47	47	127	47	47
Power [kW]	4.68	3.71	1.68	2.73	1.17	12.51
Voltage drop [V]	14.8	13.2	8.9	18.6	7.4	24.3
Coil weight [lb]	81.4	81.4	81.4	220.2	81.4	81.4
Number of water circuits	2	2	1	2	1	4
Water flow rate [gpm]	2.0	2.0	0.7	1.2	0.7	5.9
Water pressure drop [psi]	150	150	150	150	150	150
Temperature rise [°C]	8.72	6.91	9.10	8.70	6.33	8.02
Total magnet power [kW]	18.7	7.4	3.4	5.5	2.3	25.0
Total magnet water requirements [gpm]	8.2	4.1	1.4	2.4	1.4	11.9

Table 5-5. LER quadrupole parameters (continued).

Magnet designation	4Q17	4Q17	4Q17	4Q17	4Q17	4Q17
Location in ring	R2	R2	IR DS	IR DS	IR DS	IR DS
Lattice designation	IQD17	IQF18	QF1	QD2	QF3	QD4
Number of magnets	2	2	2	2	2	2
Operating gradient [T/m]	10.54	8.89	7.07	6.33	5.18	3.46
Pole-tip field @ operating gradient [T]	0.527	0.444	0.354	0.316	0.259	0.173
Gradient length product [T]	4.53	3.82	3.04	2.72	2.23	1.49
Inscribed radius [in.]	1.968	1.968	1.968	1.968	1.968	1.968
Minimum gap [in.]	1.457	1.457	1.457	1.457	1.457	1.457
Core length [in.]	15.95	15.95	15.95	15.95	15.95	15.95
Magnetic length [in.]	16.93	16.93	16.93	16.93	16.93	16.93
Lamination height [in.]	11.88	11.88	11.88	11.88	11.88	11.88
Lamination width [in.]	10.50	10.50	10.50	10.50	10.50	10.50
Packing factor, minimum [%]	98	98	98	98	98	98
Core weight [lb]	1786	1786	1786	1786	1786	1786
Amp·turns per pole	10469	8834	7027	6291	5147	3436
Turns per pole	37	37	37	37	37	37
Pancakes per pole	1	1	1	1	1	1
Conductor cross-sectional area [in.^{2}]	0.198	0.198	0.198	0.198	0.198	0.198
Cooling hole diameter [in.]	0.25	0.25	0.25	0.25	0.25	0.25
Conductor dimensions [in.]	0.5×0.5	0.5×0.5	0.5×0.5	0.5×0.5	0.5×0.5	0.5×0.5
Conductor length/pole [ft]	176	176	176	176	176	176
Current [A]	283	239	190	170	139	93
Resistance @ 40°C [mΩ]	47	47	47	47	47	47
Power [kW]	3.76	2.68	1.70	1.36	0.91	0.41
Voltage drop [V]	13.3	11.2	8.9	8.0	6.5	4.4
Coil weight [lb]	81.4	81.4	81.4	81.4	81.4	81.4
Number of water circuits	2	2	1	1	1	1
Water flow rate [gpm]	2.0	2.0	0.7	0.7	0.7	0.7
Water pressure drop [psi]	150	150	150	150	150	150
Temperature rise [°C]	7.02	5.00	9.19	7.37	4.93	2.20
Total magnet power [kW]	7.5	5.4	3.4	2.7	1.8	0.8
Total magnet water requirements [gpm]	4.1	4.1	1.4	1.4	1.4	1.4

Table 5-5. LER quadrupole parameters (continued).

Magnet designation	4Q17	4Q17	4Q17	4Q17	4Q17	4Q17
Location in ring	IR DS	R4	R4	R4	R4	R4
Lattice designation	QF5	QDT4	QFT4	QDT3	QFT3	QDT2
Number of magnets	2	1	2	2	2	2
Operating gradient [T/m]	4.55	1.88	3.29	3.57	4.14	3.48
Pole-tip field @ operating gradient [T]	0.227	0.094	0.165	0.178	0.207	0.174
Gradient length product [T]	1.96	0.81	1.42	1.53	1.78	1.50
Inscribed radius [in.]	1.968	1.968	1.968	1.968	1.968	1.968
Minimum gap [in.]	1.457	1.457	1.457	1.457	1.457	1.457
Core length [in.]	15.95	15.95	15.95	15.95	15.95	15.95
Magnetic length [in.]	16.93	16.93	16.93	16.93	16.93	16.93
Lamination height [in.]	11.88	11.88	11.88	11.88	11.88	11.88
Lamination width [in.]	10.50	10.50	10.50	10.50	10.50	10.50
Packing factor, minimum [%]	98	98	98	98	98	98
Core weight [lb]	1786	1786	1786	1786	1786	1786
Amp-turns per pole	4518	1870	3270	3542	4113	3460
Turns per pole	37	37	37	37	37	37
Pancakes per pole	1	1	1	1	1	1
Conductor cross-sectional area [in.^{2}]	0.198	0.198	0.198	0.198	0.198	0.198
Cooling hole diameter [in.]	0.25	0.25	0.25	0.25	0.25	0.25
Conductor dimensions [in.]	0.5×0.5	0.5×0.5	0.5×0.5	0.5×0.5	0.5×0.5	0.5×0.5
Conductor length/pole [ft]	176	176	176	176	176	176
Current [A]	122	51	88	96	111	94
Resistance @ 40°C [mΩ]	47	47	47	47	47	47
Power [kW]	0.70	0.12	0.37	0.43	0.58	0.41
Voltage drop [V]	5.7	2.4	4.2	4.5	5.2	4.4
Coil weight [lb]	81.4	81.4	81.4	81.4	81.4	81.4
Number of water circuits	1	1	1	1	1	1
Water flow rate [gpm]	0.7	0.7	0.7	0.7	0.7	0.7
Water pressure drop [psi]	150	150	150	150	150	150
Temperature rise [°C]	3.80	0.65	1.99	2.34	3.15	2.23
Total magnet power [kW]	1.4	0.1	0.7	0.9	1.2	0.8
Total magnet water requirements [gpm]	1.4	0.7	1.4	1.4	1.4	1.4

Table 5-5. LER quadrupole parameters (continued).

Magnet designation	4Q17	4Q17	4Q17	4Q17	4Q17	4Q17
Location in ring	R4	R4	R4	R3	R3	R3
Lattice designation	QFT2	QDT1	QFT1	QF1	QD1	QF2
Number of magnets	2	2	2	1	1	1
Operating gradient [T/m]	4.83	4.04	4.90	4.16	5.58	4.38
Pole-tip field @ operating gradient [T]	0.242	0.202	0.245	0.208	0.279	0.219
Gradient length product [T]	2.08	1.74	2.11	1.79	2.40	1.88
Inscribed radius [in.]	1.968	1.968	1.968	1.968	1.968	1.968
Minimum gap [in.]	1.457	1.457	1.457	1.457	1.457	1.457
Core length [in.]	15.95	15.95	15.95	15.95	15.95	15.95
Magnetic length [in.]	16.93	16.93	16.93	16.93	16.93	16.93
Lamination height [in.]	11.88	11.88	11.88	11.88	11.88	11.88
Lamination width [in.]	10.50	10.50	10.50	10.50	10.50	10.50
Packing factor, minimum [%]	98	98	98	98	98	98
Core weight [lb]	1786	1786	1786	1786	1786	1786
Amp·turns per pole	4801	4011	4871	4137	5544	4348
Turns per pole	37	37	37	37	37	37
Pancakes per pole	1	1	1	1	1	1
Conductor cross-sectional area [in.^{2}]	0.198	0.198	0.198	0.198	0.198	0.198
Cooling hole diameter [in.]	0.25	0.25	0.25	0.25	0.25	0.25
Conductor dimensions [in.]	0.5×0.5	0.5×0.5	0.5×0.5	0.5×0.5	0.5×0.5	0.5×0.5
Conductor length/pole [ft]	176	176	176	176	176	176
Current [A]	130	108	132	112	150	118
Resistance @ 40°C [mΩ]	47	47	47	47	47	47
Power [kW]	0.79	0.55	0.82	0.59	1.06	0.65
Voltage drop [V]	6.1	5.1	6.2	5.3	7.1	5.5
Coil weight [lb]	81.4	81.4	81.4	81.4	81.4	81.4
Number of water circuits	1	1	1	1	1	1
Water flow rate [gpm]	0.7	0.7	0.7	0.7	0.7	0.7
Water pressure drop [psi]	150	150	150	150	150	150
Temperature rise [°C]	4.29	3.00	4.42	3.19	5.72	3.52
Total magnet power [kW]	1.6	1.1	1.6	0.6	1.1	0.6
Total magnet water requirements [gpm]	1.4	1.4	1.4	0.7	0.7	0.7

Table 5-5. LER quadrupole parameters (continued).

Magnet designation	4Q17	4Q17	4Q17	4Q17	4Q17	4Q17
Location in ring	R3	R3	R3	R3	R3	R6
Lattice designation	QD2	QF3	QD3	QF4	QD4	QFW1
Number of magnets	1	1	1	1	1	2
Operating gradient [T/m]	4.95	4.84	4.12	4.77	4.55	2.52
Pole-tip field @ operating gradient [T]	0.247	0.242	0.206	0.239	0.227	0.126
Gradient length product [T]	2.13	2.08	1.77	2.05	1.96	1.08
Inscribed radius [in.]	1.968	1.968	1.968	1.968	1.968	1.968
Minimum gap [in.]	1.457	1.457	1.457	1.457	1.457	1.457
Core length [in.]	15.95	15.95	15.95	15.95	15.95	15.95
Magnetic length [in.]	16.93	16.93	16.93	16.93	16.93	16.93
Lamination height [in.]	11.88	11.88	11.88	11.88	11.88	11.88
Lamination width [in.]	10.50	10.50	10.50	10.50	10.50	10.50
Packing factor, minimum [%]	98	98	98	98	98	98
Core weight [lb]	1786	1786	1786	1786	1786	1786
Amp·turns per pole	4917	4810	4097	4744	4520	2505
Turns per pole	37	37	37	37	37	37
Pancakes per pole	1	1	1	1	1	1
Conductor cross-sectional area [in.^{2}]	0.198	0.198	0.198	0.198	0.198	0.198
Cooling hole diameter [in.]	0.25	0.25	0.25	0.25	0.25	0.25
Conductor dimensions [in.]	0.5×0.5	0.5×0.5	0.5×0.5	0.5×0.5	0.5×0.5	0.5×0.5
Conductor length/pole [ft]	176	176	176	176	176	176
Current [A]	133	130	111	128	122	68
Resistance @ 40°C [mΩ]	47	47	47	47	47	47
Power [kW]	0.83	0.79	0.58	0.77	0.70	0.22
Voltage drop [V]	6.3	6.1	5.2	6.0	5.7	3.2
Coil weight [lb]	81.4	81.4	81.4	81.4	81.4	81.4
Number of water circuits	1	1	1	1	1	1
Water flow rate [gpm]	0.7	0.7	0.7	0.7	0.7	0.7
Water pressure drop [psi]	150	150	150	150	150	150
Temperature rise [°C]	4.50	4.31	3.12	4.19	3.80	1.17
Total magnet power [kW]	0.8	0.8	0.6	0.8	0.7	0.4
Total magnet water requirements [gpm]	0.7	0.7	0.7	0.7	0.7	1.4

Table 5-5. LER quadrupole parameters (continued).

Magnet designation	4Q17	4Q17	4Q17	4Q17	4Q17	4Q17
Location in ring	R6	R6	R6	R6	R6	R8
Lattice designation	QDW2	QFW3	QFW4	QDW5	QFW6	QDI
Number of magnets	2	2	2	2	2	2
Operating gradient [T/m]	1.64	3.92	0.28	2.02	3.58	0.66
Pole-tip field @ operating gradient [T]	0.082	0.196	0.014	0.101	0.179	0.033
Gradient length product [T]	0.70	1.69	0.12	0.87	1.54	0.28
Inscribed radius [in.]	1.968	1.968	1.968	1.968	1.968	1.968
Minimum gap [in.]	1.457	1.457	1.457	1.457	1.457	1.457
Core length [in.]	15.95	15.95	15.95	15.95	15.95	15.95
Magnetic length [in.]	16.93	16.93	16.93	16.93	16.93	16.93
Lamination height [in.]	11.88	11.88	11.88	11.88	11.88	11.88
Lamination width [in.]	10.50	10.50	10.50	10.50	10.50	10.50
Packing factor, minimum [%]	98	98	98	98	98	98
Core weight [lb]	1786	1786	1786	1786	1786	1786
Amp·turns per pole	1628	3895	283	2009	3553	654
Turns per pole	37	37	37	37	37	37
Pancakes per pole	1	1	1	1	1	1
Conductor cross-sectional area [in.^{2}]	0.198	0.198	0.198	0.198	0.198	0.198
Cooling hole diameter [in.]	0.25	0.25	0.25	0.25	0.25	0.25
Conductor dimensions [in.]	0.5×0.5	0.5×0.5	0.5×0.5	0.5×0.5	0.5×0.5	0.5×0.5
Conductor length/pole [ft]	176	176	176	176	176	176
Current [A]	44	105	8	54	96	18
Resistance @ 40°C [mΩ]	47	47	47	47	47	47
Power [kW]	0.09	0.52	0.00	0.14	0.43	0.01
Voltage drop [V]	2.1	5.0	0.4	2.6	4.5	0.8
Coil weight [lb]	81.4	81.4	81.4	81.4	81.4	81.4
Number of water circuits	1	1	1	1	1	1
Water flow rate [gpm]	0.7	0.7	0.7	0.7	0.7	0.7
Water pressure drop [psi]	150	150	150	150	150	150
Temperature rise [°C]	0.49	2.82	0.01	0.75	2.35	0.08
Total magnet power [kW]	0.2	1.0	0.0	0.3	0.9	0.0
Total magnet water requirements [gpm]	1.4	1.4	1.4	1.4	1.4	1.4

Table 5-5. LER quadrupole parameters (continued).

Magnet designation	4Q17	4Q17	4Q17	4Q17	4Q17	
Location in ring	R8	R8	R8	R10	R10	
Lattice designation	QFI	QDOI	QFOI	QDT4A	QFT4A	
Number of magnets	2	2	2	1	2	2
Operating gradient [T/m]	1.47	2.34	4.17	1.88	3.29	3.57
Pole-tip field @ operating gradient [T]	0.074	0.117	0.208	0.094	0.165	0.178
Gradient length product [T]	0.63	1.01	1.79	0.81	1.42	1.53
Inscribed radius [in.]	1.968	1.968	1.968	1.968	1.968	1.968
Minimum gap [in.]	1.457	1.457	1.457	1.457	1.457	1.457
Core length [in.]	15.95	15.95	15.95	15.95	15.95	15.95
Magnetic length [in.]	16.93	16.93	16.93	16.93	16.93	16.93
Lamination height [in.]	11.88	11.88	11.88	11.88	11.88	11.88
Lamination width [in.]	10.50	10.50	10.50	10.50	10.50	10.50
Packing factor, minimum [%]	98	98	98	98	98	98
Core weight [lb]	1786	1786	1786	1786	1786	1786
Amp·turns per pole	1464	2323	4138	1870	3270	3542
Turns per pole	37	37	37	37	37	37
Pancakes per pole	1	1	1	1	1	1
Conductor cross-sectional area [in.^{2}]	0.198		0.198	0.198	0.198	0.198
Cooling hole diameter [in.]	0.25		0.25	0.25	0.25	0.25
Conductor dimensions [in.]	0.5×0.5	0.5×0.5	0.5×0.5	0.5×0.5	0.5×0.5	0.5×0.5
Conductor length/pole [ft]	176	176	176	176	176	176
Current [A]	40	63	112	51	88	96
Resistance @ 40°C [mΩ]	47	47	47	47	47	47
Power [kW]	0.07	0.19	0.59	0.12	0.37	0.43
Voltage drop [V]	1.9	3.0	5.3	2.4	4.2	4.5
Coil weight [lb]	81.4	81.4	81.4	81.4	81.4	81.4
Number of water circuits	1	1	1	1	1	1
Water flow rate [gpm]	0.7	0.7	0.7	0.7	0.7	0.7
Water pressure drop [psi]	150	150	150	150	150	150
Temperature rise [°C]	0.40	1.00	3.19	0.65	1.99	2.34
Total magnet power [kW]	0.1	0.4	1.2	0.1	0.7	0.9
Total magnet water requirements [gpm]	1.4	1.4	1.4	0.7	1.4	1.4

Table 5-5. LER quadrupole parameters (continued).

Magnet designation	4Q17	4Q17	4Q17	4Q17	4Q17	4Q17
Location in ring	R10	R10	R10	R10	R10	R5
Lattice designation	QFT3A	QDT2A	QFT2A	QDT1A	QFT1A	QF1
Number of magnets	2	2	2	2	2	1
Operating gradient [T/m]	4.14	3.48	4.83	4.04	4.90	4.16
Pole-tip field @ operating gradient [T]	0.207	0.174	0.242	0.202	0.245	0.208
Gradient length product [T]	1.78	1.50	2.08	1.74	2.11	1.79
Inscribed radius [in.]	1.968	1.968	1.968	1.968	1.968	1.968
Minimum gap [in.]	1.457	1.457	1.457	1.457	1.457	1.457
Core length [in.]	15.95	15.95	15.95	15.95	15.95	15.95
Magnetic length [in.]	16.93	16.93	16.93	16.93	16.93	16.93
Lamination height [in.]	11.88	11.88	11.88	11.88	11.88	11.88
Lamination width [in.]	10.50	10.50	10.50	10.50	10.50	10.50
Packing factor, minimum [%]	98	98	98	98	98	98
Core weight [lb]	1786	1786	1786	1786	1786	1786
Amp·turns per pole	4113	3460	4801	4011	4871	4137
Turns per pole	37	37	37	37	37	37
Pancakes per pole	1	1	1	1	1	1
Conductor cross-sectional area [in.^{2}]	0.198	0.198	0.198	0.198	0.198	0.198
Cooling hole diameter [in.]	0.25	0.25	0.25	0.25	0.25	0.25
Conductor dimensions [in.]	0.5×0.5	0.5×0.5	0.5×0.5	0.5×0.5	0.5×0.5	0.5×0.5
Conductor length/pole [ft]	176	176	176	176	176	176
Current [A]	111	94	130	108	132	112
Resistance @ 40°C [mΩ]	47	47	47	47	47	47
Power [kW]	0.58	0.41	0.79	0.55	0.82	0.59
Voltage drop [V]	5.2	4.4	6.1	5.1	6.2	5.3
Coil weight [lb]	81.4	81.4	81.4	81.4	81.4	81.4
Number of water circuits	1	1	1	1	1	1
Water flow rate [gpm]	0.7	0.7	0.7	0.7	0.7	0.7
Water pressure drop [psi]	150	150	150	150	150	150
Temperature rise [°C]	3.15	2.23	4.29	3.00	4.42	3.19
Total magnet power [kW]	1.2	0.8	1.6	1.1	1.6	0.6
Total magnet water requirements [gpm]	1.4	1.4	1.4	1.4	1.4	0.7

Table 5-5. LER quadrupole parameters (continued).

Magnet designation	4Q17	4Q17	4Q17	4Q17	4Q17	4Q17
Location in ring	R5	R5	R5	R5	R5	R5
Lattice designation	QD1	QF2	QD2	QF3	QD3	QF4
Number of magnets	1	1	1	1	1	1
Operating gradient [T/m]	5.58	4.38	4.95	4.84	4.12	4.77
Pole-tip field @ operating gradient [T]	0.279	0.219	0.247	0.242	0.206	0.239
Gradient length product [T]	2.40	1.88	2.13	2.08	1.77	2.05
Inscribed radius [in.]	1.968	1.968	1.968	1.968	1.968	1.968
Minimum gap [in.]	1.457	1.457	1.457	1.457	1.457	1.457
Core length [in.]	15.95	15.95	15.95	15.95	15.95	15.95
Magnetic length [in.]	16.93	16.93	16.93	16.93	16.93	16.93
Lamination height [in.]	11.88	11.88	11.88	11.88	11.88	11.88
Lamination width [in.]	10.50	10.50	10.50	10.50	10.50	10.50
Packing factor, minimum [%]	98	98	98	98	98	98
Core weight [lb]	1786	1786	1786	1786	1786	1786
Amp·turns per pole	5544	4348	4917	4810	4097	4744
Turns per pole	37	37	37	37	37	37
Pancakes per pole	1	1	1	1	1	1
Conductor cross-sectional area [in.^{2}]	0.198	0.198	0.198	0.198	0.198	0.198
Cooling hole diameter [in.]	0.25	0.25	0.25	0.25	0.25	0.25
Conductor dimensions [in.]	0.5×0.5	0.5×0.5	0.5×0.5	0.5×0.5	0.5×0.5	0.5×0.5
Conductor length/pole [ft]	176	176	176	176	176	176
Current [A]	150	118	133	130	111	128
Resistance @ 40°C [mΩ]	47	47	47	47	47	47
Power [kW]	1.06	0.65	0.83	0.79	0.58	0.77
Voltage drop [V]	7.1	5.5	6.3	6.1	5.2	6.0
Coil weight [lb]	81.4	81.4	81.4	81.4	81.4	81.4
Number of water circuits	1	1	1	1	1	1
Water flow rate [gpm]	0.7	0.7	0.7	0.7	0.7	0.7
Water pressure drop [psi]	150	150	150	150	150	150
Temperature rise [°C]	5.72	3.52	4.50	4.31	3.12	4.19
Total magnet power [kW]	1.1	0.6	0.8	0.8	0.6	0.8
Total magnet water requirements [gpm]	0.7	0.7	0.7	0.7	0.7	0.7

Table 5-5. LER quadrupole parameters (continued).

Magnet designation	4Q17	4Q17	4Q17	4Q17	4Q17	4Q17
Location in ring	R5	R9	R9	R9	R9	R9
Lattice designation	QD4	QF1A	QD1A	QF2A	QD2A	QF3A
Number of magnets	1	1	1	1	1	1
Operating gradient [T/m]	4.55	4.16	5.58	4.38	4.95	4.84
Pole-tip field @ operating gradient [T]	0.227	0.208	0.279	0.219	0.247	0.242
Gradient length product [T]	1.96	1.79	2.40	1.88	2.13	2.08
Inscribed radius [in.]	1.968	1.968	1.968	1.968	1.968	1.968
Minimum gap [in.]	1.457	1.457	1.457	1.457	1.457	1.457
Core length [in.]	15.95	15.95	15.95	15.95	15.95	15.95
Magnetic length [in.]	16.93	16.93	16.93	16.93	16.93	16.93
Lamination height [in.]	11.88	11.88	11.88	11.88	11.88	11.88
Lamination width [in.]	10.50	10.50	10.50	10.50	10.50	10.50
Packing factor, minimum [%]	98	98	98	98	98	98
Core weight [lb]	1786	1786	1786	1786	1786	1786
Amp·turns per pole	4520	4137	5544	4348	4917	4810
Turns per pole	37	37	37	37	37	37
Pancakes per pole	1	1	1	1	1	1
Conductor cross-sectional area [in.^{2}]	0.198	0.198	0.198	0.198	0.198	0.198
Cooling hole diameter [in.]	0.25	0.25	0.25	0.25	0.25	0.25
Conductor dimensions [in.]	0.5×0.5	0.5×0.5	0.5×0.5	0.5×0.5	0.5×0.5	0.5×0.5
Conductor length/pole [ft]	176	176	176	176	176	176
Current [A]	122	112	150	118	133	130
Resistance @ 40°C [mΩ]	47	47	47	47	47	47
Power [kW]	0.70	0.59	1.06	0.65	0.83	0.79
Voltage drop [V]	5.7	5.3	7.1	5.5	6.3	6.1
Coil weight [lb]	81.4	81.4	81.4	81.4	81.4	81.4
Number of water circuits	1	1	1	1	1	1
Water flow rate [gpm]	0.7	0.7	0.7	0.7	0.7	0.7
Water pressure drop [psi]	150	150	150	150	150	150
Temperature rise [°C]	3.80	3.19	5.72	3.52	4.50	4.31
Total magnet power [kW]	0.7	0.6	1.1	0.6	0.8	0.8
Total magnet water requirements [gpm]	0.7	0.7	0.7	0.7	0.7	0.7

Table 5-5. LER quadrupole parameters (continued).

Magnet designation	4Q17	4Q17	4Q17	4Q17	4Q17	4Q17
Location in ring	R9	R9	R9	R11	R11	R11
Lattice designation	QD3A	QF4A	QD4A	QF1A	QD1A	QF2A
Number of magnets	1	1	1	1	1	1
Operating gradient [T/m]	4.12	4.77	4.55	4.16	5.58	4.38
Pole-tip field @ operating gradient [T]	0.206	0.239	0.227	0.208	0.279	0.219
Gradient length product [T]	1.77	2.05	1.96	1.79	2.40	1.88
Inscribed radius [in.]	1.968	1.968	1.968	1.968	1.968	1.968
Minimum gap [in.]	1.457	1.457	1.457	1.457	1.457	1.457
Core length [in.]	15.95	15.95	15.95	15.95	15.95	15.95
Magnetic length [in.]	16.93	16.93	16.93	16.93	16.93	16.93
Lamination height [in.]	11.88	11.88	11.88	11.88	11.88	11.88
Lamination width [in.]	10.50	10.50	10.50	10.50	10.50	10.50
Packing factor, minimum [%]	98	98	98	98	98	98
Core weight [lb]	1786	1786	1786	1786	1786	1786
Amp·turns per pole	4097	4744	4520	4137	5544	4348
Turns per pole	37	37	37	37	37	37
Pancakes per pole	1	1	1	1	1	1
Conductor cross-sectional area [in.^{2}]	0.198	0.198	0.198	0.198	0.198	0.198
Cooling hole diameter [in.]	0.25	0.25	0.25	0.25	0.25	0.25
Conductor dimensions [in.]	0.5×0.5	0.5×0.5	0.5×0.5	0.5×0.5	0.5×0.5	0.5×0.5
Conductor length/pole [ft]	176	176	176	176	176	176
Current [A]	111	128	122	112	150	118
Resistance @ 40°C [mΩ]	47	47	47	47	47	47
Power [kW]	0.58	0.77	0.70	0.59	1.06	0.65
Voltage drop [V]	5.2	6.0	5.7	5.3	7.1	5.5
Coil weight [lb]	81.4	81.4	81.4	81.4	81.4	81.4
Number of water circuits	1	1	1	1	1	1
Water flow rate [gpm]	0.7	0.7	0.7	0.7	0.7	0.7
Water pressure drop [psi]	150	150	150	150	150	150
Temperature rise [°C]	3.12	4.19	3.80	3.19	5.72	3.52
Total magnet power [kW]	0.6	0.8	0.7	0.6	1.1	0.6
Total magnet water requirements [gpm]	0.7	0.7	0.7	0.7	0.7	0.7

Table 5-5. LER quadrupole parameters (continued).

Magnet designation	4Q17	4Q17	4Q17	4Q17	4Q17	4Q17
Location in ring	R11	R11	R11	R11	R11	R12
Lattice designation	QD2A	QF3A	QD3A	QF4A	QD4A	QFW1A
Number of magnets	1	1	1	1	1	2
Operating gradient [T/m]	4.95	4.84	4.12	4.77	4.55	2.52
Pole-tip field @ operating gradient [T]	0.247	0.242	0.206	0.239	0.227	0.126
Gradient length product [T]	2.13	2.08	1.77	2.05	1.96	1.08
Inscribed radius [in.]	1.968	1.968	1.968	1.968	1.968	1.968
Minimum gap [in.]	1.457	1.457	1.457	1.457	1.457	1.457
Core length [in.]	15.95	15.95	15.95	15.95	15.95	15.95
Magnetic length [in.]	16.93	16.93	16.93	16.93	16.93	16.93
Lamination height [in.]	11.88	11.88	11.88	11.88	11.88	11.88
Lamination width [in.]	10.50	10.50	10.50	10.50	10.50	10.50
Packing factor, minimum [%]	98	98	98	98	98	98
Core weight [lb]	1786	1786	1786	1786	1786	1786
Amp-turns per pole	4917	4810	4097	4744	4520	2505
Turns per pole	37	37	37	37	37	37
Pancakes per pole	1	1	1	1	1	1
Conductor cross-sectional area [in.^{2}]	0.198	0.198	0.198	0.198	0.198	0.198
Cooling hole diameter [in.]	0.25	0.25	0.25	0.25	0.25	0.25
Conductor dimensions [in.]	0.5x0.5	0.5x0.5	0.5x0.5	0.5x0.5	0.5x0.5	0.5x0.5
Conductor length/pole [ft]	176	176	176	176	176	176
Current [A]	133	130	111	128	122	68
Resistance @ 40°C [mΩ]	47	47	47	47	47	47
Power [kW]	0.83	0.79	0.58	0.77	0.70	0.22
Voltage drop [V]	6.3	6.1	5.2	6.0	5.7	3.2
Coil weight [lb]	81.4	81.4	81.4	81.4	81.4	81.4
Number of water circuits	1	1	1	1	1	1
Water flow rate [gpm]	0.7	0.7	0.7	0.7	0.7	0.7
Water pressure drop [psi]	150	150	150	150	150	150
Temperature rise [°C]	4.50	4.31	3.12	4.19	3.80	1.17
Total magnet power [kW]	0.8	0.8	0.6	0.8	0.7	0.4
Total magnet water requirements [gpm]	0.7	0.7	0.7	0.7	0.7	1.4

Table 5-5. LER quadrupole parameters (continued).

Magnet designation	4Q17	4Q17	4Q17	4Q17	4Q17
Location in ring	R12	R12	R12	R12	R12
Lattice designation	QDW2A	QFW3A	QFW4A	QDW5A	QFW6A
Number of magnets	2	2	2	2	2
Operating gradient [T/m]	1.64	3.92	0.28	2.02	3.58
Pole-tip field @ operating gradient [T]	0.082	0.196	0.014	0.101	0.179
Gradient length product [T]	0.70	1.69	0.12	0.87	1.54
Inscribed radius [in.]	1.968	1.968	1.968	1.968	1.968
Minimum gap [in.]	1.457	1.457	1.457	1.457	1.457
Core length [in.]	15.95	15.95	15.95	15.95	15.95
Magnetic length [in.]	16.93	16.93	16.93	16.93	16.93
Lamination height [in.]	11.88	11.88	11.88	11.88	11.88
Lamination width [in.]	10.50	10.50	10.50	10.50	10.50
Packing factor, minimum [%]	98	98	98	98	98
Core weight [lb]	1786	1786	1786	1786	1786
Amp·turns per pole	1628	3895	283	2009	3553
Turns per pole	37	37	37	37	37
Pancakes per pole	1	1	1	1	1
Conductor cross-sectional area [in.^{2}]	0.198	0.198	0.198	0.198	0.198
Cooling hole diameter [in.]	0.25	0.25	0.25	0.25	0.25
Conductor dimensions [in.]	0.5×0.5	0.5×0.5	0.5×0.5	0.5×0.5	0.5×0.5
Conductor length/pole [ft]	176	176	176	176	176
Current [A]	44	105	8	54	96
Resistance @ 40°C [mΩ]	47	47	47	47	47
Power [kW]	0.09	0.52	0.00	0.14	0.43
Voltage drop [V]	2.1	5.0	0.4	2.6	4.5
Coil weight [lb]	81.4	81.4	81.4	81.4	81.4
Number of water circuits	1	1	1	1	1
Water flow rate [gpm]	0.7	0.7	0.7	0.7	0.7
Water pressure drop [psi]	150	150	150	150	150
Temperature rise [°C]	0.49	2.82	0.01	0.75	2.35
Total magnet power [kW]	0.2	1.0	0.0	0.3	0.9
Total magnet water requirements [gpm]	1.4	1.4	1.4	1.4	1.4

5.1.2.3 Sextupoles. The LER sextupole physical dimensions are shown in Fig. 5-6. These magnets have a length of 8.071 in. and a bore of 4.724 in. Their electrical properties, corresponding to the nominal energy, are summarized in Table 5-6.

The LER sextupoles will be identical to the present PEP short (8-in.) sextupoles. This will permit us to interchange magnets between the LER and HER, if necessary, and minimizes the required number of spares. Manufacturing techniques will be the same as those described above for the LER dipoles and quadrupoles, although the anticipated steel requirement of about 50 tons will come from only a single heat. For this reason, witness marks will not be needed for the sextupoles. Laminations will still be reversed periodically, however, to account for the crowning referred to above.

Table 5-6. LER sextupole parameters.

Magnet designation	4.5S	4.5S	4.5S	4.5S
Lattice designation	SF1	SD1	SX	SY
Number of magnets	72	72	4	4
Operating gradient [T/m^2]	25.62	45.60	113.75	186.13
Pole tip field @ operating gradient [T]	0.046	0.082	0.205	0.335
Integrated strength [T/m]	7.53	13.40	33.43	54.70
Aperture inscribed radius [in.]	2.362	2.362	2.362	2.362
Core length [in.]	8.071	8.071	8.071	8.071
Magnetic length [in.]	10.041	10.041	10.041	10.041
Core weight [lb]	170	170	170	170
Amp·turns per pole	730	1299	3240	5302
Turns per pole	24	24	24	24
Pancakes per pole	1	1	1	1
Conductor cross-sectional area [in.^{2}]	0.127	0.127	0.127	0.127
Cooling hole diameter [in.]	0.125	0.125	0.125	0.125
Conductor dimension [in.]	0.375	0.375	0.375	0.375
Current [A]	30.4	54.1	135.0	220.9
Resistance @ 40°C [mΩ]	31	31	31	31
Power [kW]	0.03	0.09	0.57	1.53
Voltage drop [V]	1.0	1.7	4.2	6.9
Coil weight [lb]	44	44	44	44
Number of water circuits	1	1	1	1
Water flow rate [gpm]	0.2	0.2	0.2	0.2
Water pressure drop [psi]	150	150	150	150
Temperature rise [°C]	0.6	1.9	12.0	32.2
Total magnet power [kW]	2.1	6.6	2.3	6.1
Total voltage [V]	68.5	121.9	16.9	27.6
Total system water requirements [gpm]	13.0	13.0	0.7	0.7

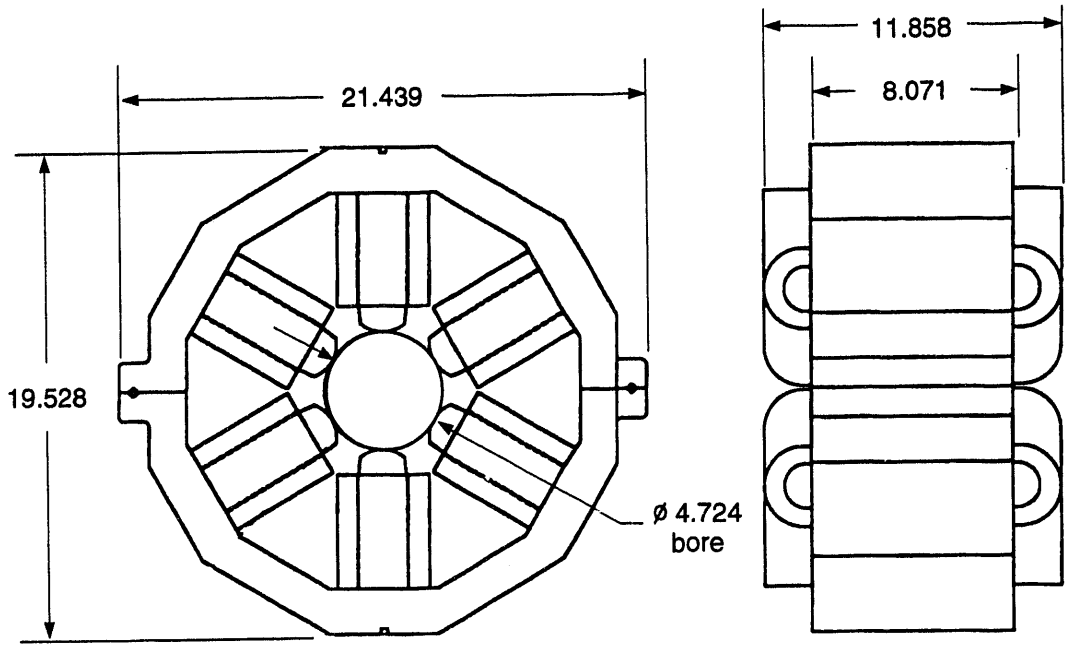

Fig. 5-6. End and side views of the LER sextupole magnet. Dimensions are given in inches.

5.1.3 Interaction Region Magnets and Supports

5.1.3.1 Permanent Magnets. Only the final focusing quadrupoles, Q1, and the magnetic separation dipoles, B1, are located within 2 m of the interaction point (IP). At these close distances, they will be inside the detector and immersed in its solenoidal magnetic field. The only viable magnet technologies for such an environment are superconducting or permanent magnets. A conventional electromagnet with iron pole tips would have its iron saturated and its field distorted by the detector field. For the IR magnets, required field strengths and apertures are within the reach of modern rare-earth–cobalt (REC) alloys, and superconducting technology is not demanded. For PEP-II, the choice of a permanent-magnet design was based on the following characteristics of such magnets:

- Their interaction with the external detector solenoid is minimal. Because magnetized REC is a magnetically hard material with little free magnetic moment left over to interact with external fields, it is magnetically transparent with a permeability μ near the μ_0 of free space. In the standard Halbach configuration [Halbach, 1981] these magnet assemblies project little external field to generate forces between the detector solenoid and the REC assembly.
- They avoid the complexity, cost, and reliability problems inherent in cryogenic operation.
- They are compact and avoid cryogenic plumbing and cryostats, both of which would significantly reduce the detector acceptance solid angle.

- They are nearly free of fringe fields that could otherwise complicate particle tracking in the detector.
- They avoid the safety aspects of superconducting systems; they will not quench—a possible advantage in a high-current storage ring.

There are also drawbacks to our choice of permanent magnet technology. Foremost among these is the fact that permanent magnets offer only a limited adjustment capability. In our design, we have added trim windings on all permanent magnets in the IR to alleviate this lack of flexibility. Other issues include the following:

- The field quality of a REC magnet depends on accurate magnetization of its constituent blocks; special techniques and equipment must be developed to measure block magnetization, and to assemble and adjust blocks.
- Strong demagnetizing external fields and high temperatures must be avoided if field quality is to be preserved. Quadrupole and dipole fields are assembled from sector-shaped REC blocks arrayed in a circle around the magnet aperture [Halbach, 1981]. Each block is magnetized in an appropriate direction so that the magnetic field varies approximately as $\cos(N\theta)$ around the bore, where $N = 1$ for dipoles, $N = 2$ for quadrupoles, etc. The optimal compromise between the number of blocks, M, and the field quality is to use $M = 16$ for a quadrupole and $M = 8$ for a dipole. These configurations are shown in Fig. 5-7.

The magnetic and mechanical properties of the PEP-II IR magnets are summarized in Table 5-7.

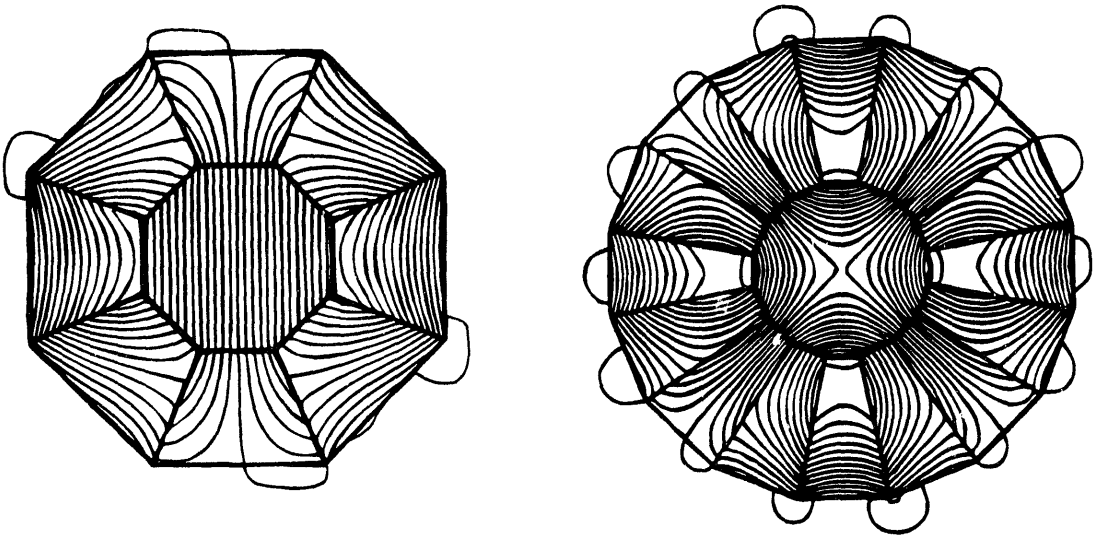

Fig. 5-7. Field lines for an 8-block permanent magnet dipole (left) and a 16-block quadrupole (right).

Table 5-7. Magnetic and mechanical dimensions for the IP permanent magnets.

	$B(r_1)$ [T]	Gradient [T/m]	r_1 [cm]	r_2 [cm]	L [cm]	Weight [kg]
B1	0.80	—	4.9[a]	9.7[a]	50.0	98
Q1	0.89	10.64	8.7	16.6	120.0	633

[a]B1 is tapered; r_1 and r_2 values are averages.

For quadrupoles ($N = 2$), the magnetic field at the aperture radius, $B(r_1)$, is related to the inner and outer radii, r_1 and r_2, by

$$B(r_1) = 2C_N B_r \left(1 - \frac{r_1}{r_2}\right) \tag{5-1}$$

where B_r is the remanent field of the permanent magnet material and

$$C_N = \frac{\cos^N\left(\frac{\pi}{M}\right)\sin\left(\frac{N\pi}{M}\right)}{\frac{N\pi}{M}} \tag{5-2}$$

Whereas Q1 is built up from 24 identical 5-cm-thick slices, B1 is a tapered magnet. The transverse field on axis for this magnet can be computed as the superposition of fields from each separate slice [Bowden, 1991]:

$$B_y(0,0,z) = \sum_{i=1}^{10} B_i(z - z_i) \tag{5-3}$$

For a slice $2l$ thick with remanent field B_r,

$$B_i(z - z_i) = B_r\left[\frac{1}{2}\ln\left(\frac{\sqrt{\bar{z}^2 + r_2^2} + \bar{z}}{\sqrt{\bar{z}^2 + r_1^2} + \bar{z}}\right) + \frac{1}{4}\left(\frac{\bar{z}}{\sqrt{\bar{z}^2 + r_2^2}} - \frac{\bar{z}}{\sqrt{\bar{z}^2 + r_1^2}}\right)\right]\Bigg|_{\bar{z} = z - z_i + l}^{\bar{z} = z - z_i - l} \tag{5-4}$$

Figure 5-8 shows the transverse field on axis for B1.

Choice of Material. The PEP-II magnets will be assembled from Sm_2Co_{17}, a material having a high remanent field ($B_r = 1.05$ T). Figure 5-9 shows the B-H curves of some of these materials. Commercial grades of Sm_2Co_{17} are available.

The B-H relation for a candidate material, R26HS (see Table 5-8), shows a linear $\mu_r \approx 1$ for the entire second quadrant. An external demagnetizing H field must actually

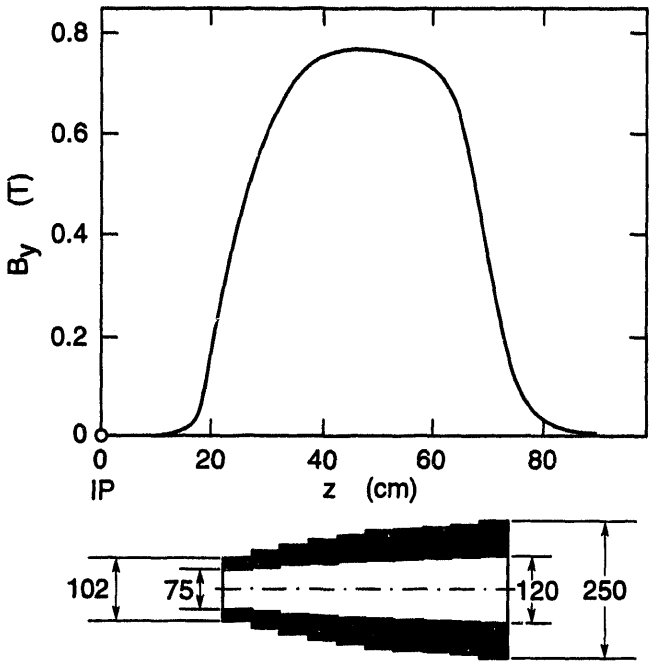

Fig. 5-8. Transverse field on axis for the tapered B1 dipole magnet. Dimensions are in mm.

exceed B_r/μ_0 of the material before nonlinearities and hysteresis develop, causing permanent demagnetization of the material. For lower external fields, simple linear superposition of fields holds. Since the detector axial solenoidal field is nearly orthogonal to the transverse field of the beamline magnets, the two fields are not expected to interact. The high Curie temperature of Sm_2Co_{17} allows this material to be used at temperatures up to 500°C, and its low temperature coefficient should preserve field quality. Lastly, the chosen material has good radiation-resistance properties [Luna, 1989], so its performance is not expected to degrade in the relatively harsh environment of the PEP-II IR.

Table 5-8. Properties of R26HS magnetic material.

Material	B_r [T]	Temperature coefficient [%/°C]	Curie temperature [°C]	Density [g/cm^3]
R26HS	1.05	–0.03	820	8.4

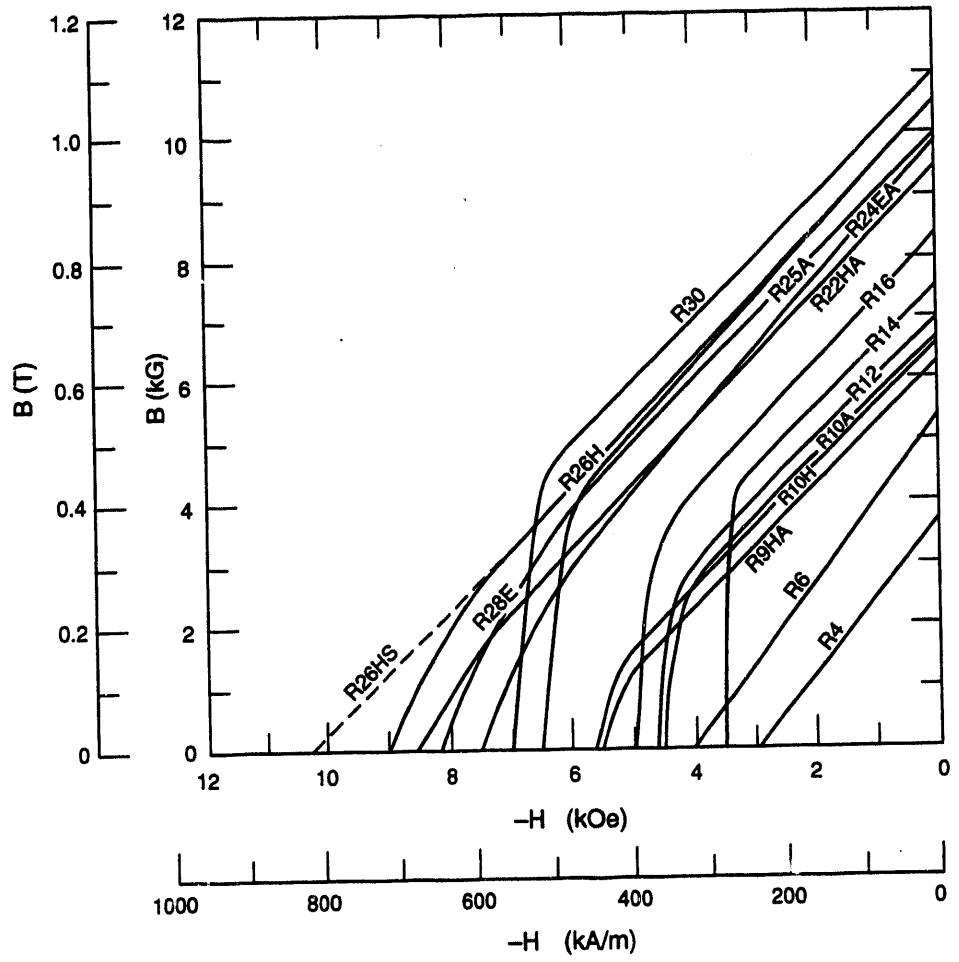

Fig. 5-9. B-H curves for various permanent-magnet materials.

Permanent Magnet Assembly. Both the B1 dipoles and the Q1 quadrupoles will be built up from "pineapple-ring" shaped slices of permanent magnet blocks held in alignment on a common beam pipe mandrel. Individual trapezoidal blocks of Sm_2Co_{17} are collared together between aluminum rings to restrain the magnetic hoop forces. For the 5-cm-thick slices of Q1, these hoop forces are approximately 200 lb.

Taken together, fabrication of the IR magnets will involve nearly one thousand precisely machined and magnetized blocks of Sm_2Co_{17}. The field quality of the resulting magnets depends critically on their precise magnetization. The magnitude, direction, and uniformity of the magnetization **M** will therefore be held to tight tolerances inside each block. In addition, variations can, to some degree, be accommodated by selective assembly and adjustment of final block positions. In any case, block magnetization will be measured before assembly. Even perfectly magnetized individual blocks do not produce simple, uniform **B** fields. Figure 5-10 shows the **B** field pattern for two typical uniform magnetizations of a block. The **B** field is related to block magnetization by

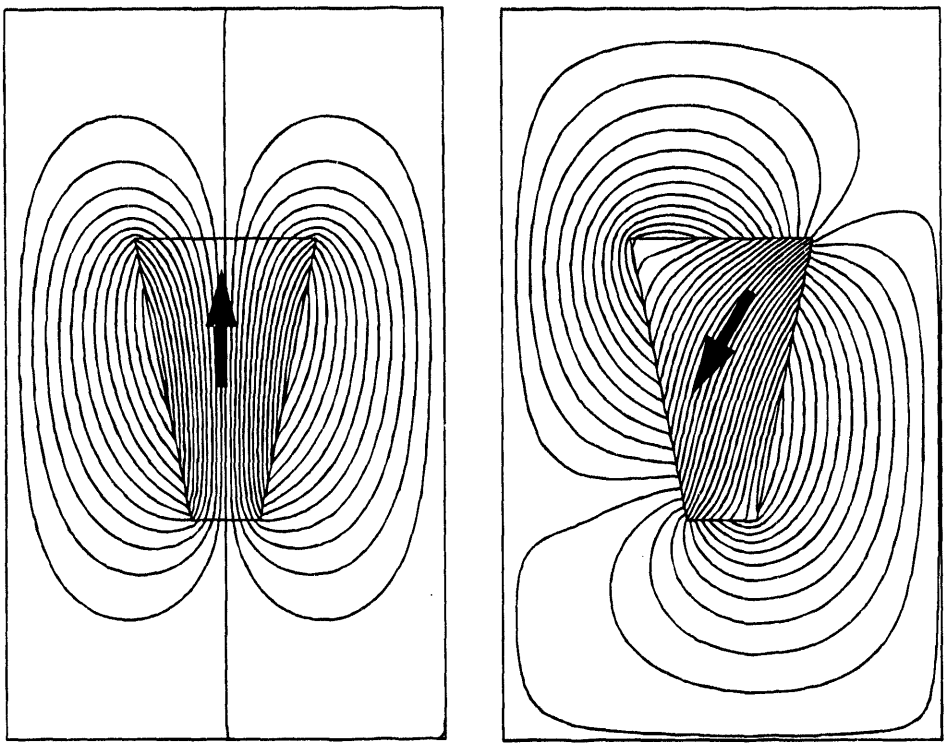

Fig. 5-10. Field patterns for two typical uniform magnetizations of permanent-magnet-material blocks.

$$\mathbf{B}(\mathbf{r}) = \mu_0 \mathbf{M}(\mathbf{r}) + \frac{\mu_0}{4\pi}\left[\int_S \mathbf{M}\cdot\mathbf{n}\,\frac{(\mathbf{r}-\mathbf{r}')}{|\mathbf{r}-\mathbf{r}'|^3}\,da' - \int_V \nabla\cdot\mathbf{M}\,\frac{(\mathbf{r}-\mathbf{r}')}{|\mathbf{r}-\mathbf{r}'|^3}\,dV\right] \qquad (5\text{-}5)$$

If the block has perfectly uniform magnetization ($\nabla\cdot\mathbf{M} = 0$), then **B** and **M** differ only by a surface integral over the shape of the block. Using the above relation, the internal magnetization field of a block can be inspected by making measurements of **B** over its surface. Figure 5-11 illustrates this inspection procedure.

A simple jig will be used to determine the coordinate frame and measurement points on the surface at which the normal component of **B** is measured. These data will then be used to calculate the magnitude and direction of **M** inside the block. Estimates of the uniformity of **M** can also be computed. If magnetic tolerances can be tightly held by this inspection procedure, it would greatly reduce the magnetic trimming involved in the final assembly of the magnet.

Rare-earth permanent-magnet blocks with strength and magnetic direction tolerances of ±2% and ±2°, respectively, were achieved in production 8 years ago [Herb, 1985]. The large number of blocks required for each Q1 (384) makes it practical to sort and selectively assemble blocks to optimize the field quality. Grouping blocks with similar magnetic errors in the same axial slice of the magnet reduces the unwanted field harmonics associated with random magnetic errors. By this means, random multipole strengths can be held at or below 1×10^{-3} of the quadrupole field at the magnet bore radius. Remaining field errors

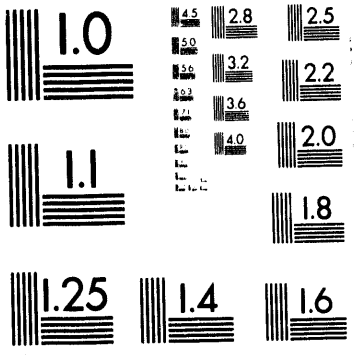
1.0
1.1
1.25
1.4
1.6
1.8
2.0
2.2
2.5
2.8
3.2
3.6
4.0
4.5
5.0
5.6

4 of 7

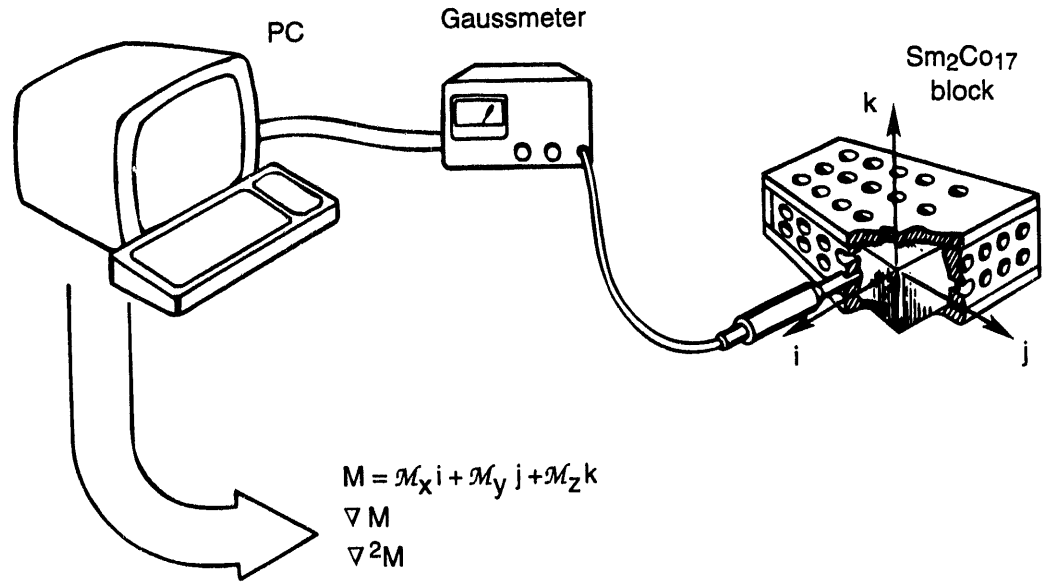

Fig. 5-11. Schematic representation of a procedure to inspect permanent-magnet blocks before assembly.

will be corrected by addition of small shim pieces of Sm_2Co_{17} at appropriate locations around the outer circumference of each slice [Bowden, 1993]. An algorithm for systematically calculating these correction shims has been developed, based on Halbach [1981b].

Each slice of either B1 or Q1 will have the same angular orientation as its neighbors. North poles will be adjacent to north poles and south poles adjacent to south poles. This slice-to-slice juxtaposition of like poles will generate internal axial repulsion forces of 3000 lb in the case of Q1. These forces are carried by the beam pipe mandrel and clamping flanges at each end of the magnet.

Permanent magnets have already been successfully applied to storage rings at SLAC [Spencer, 1985] and elsewhere [Herb, 1987]. We consider the technology to be a mature one, well suited to this application.

5.1.3.2 IP Support Barrel. PEP-II poses difficult support and alignment problems for the final magnetic elements near the IP. Bunch spacing is only 1.26 m and requires magnetic separation of the two beams to begin at ±20 cm from the collision point. The final quadrupoles are completely buried inside the detector. Previous storage rings have placed the equivalent magnets on separate individual supports, cantilevered in from the detector entrance. Unfortunately, such a support is difficult to make rigid, and the relative alignment of the magnets is not easily measurable once they are installed.

As shown in Fig. 5-12, for PEP-II we intend to avoid this limitation by using a single support "barrel" through the detector, from one end to the other, to carry all magnets. In addition to carrying the beam separation dipoles B1 and the final permanent-magnet quadrupoles, Q1, the support barrel carries the central vertex detector. Other equipment carried inside the barrel includes the water-cooled masks that shield the detector from the

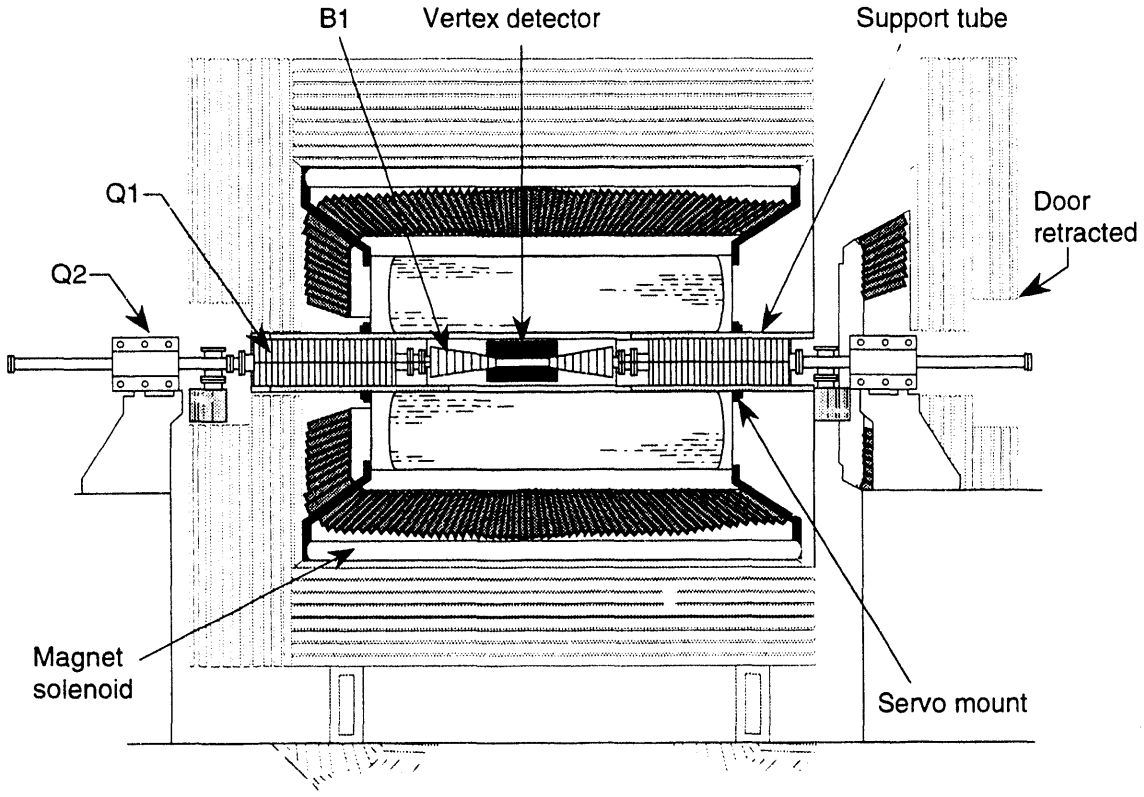

Fig. 5-12. Tube or barrel to support the permanent magnets, beam pipe, and vertex detector inside the drift chamber.

HEB and LEB synchrotron radiation fans (see Sections 4.2 and 5.2.7), radial ion pumps, and BPMs. Plumbing and cabling for this equipment passes through the barrel, while vertex detector cabling is carried on the outside.

Our choice of a single support barrel has two important advantages over previous designs:

- Magnetic elements on each side of the IP are directly connected by a rigid structure that maintains their relative alignment
- All components can be preassembled and aligned in the barrel outside the detector, where precise and effective survey techniques can be employed

Barrel Mounts. The barrel is supported from the detector drift chamber end-plates. These support locations are approximately at the quarter-points of the barrel, thus balancing end and midpoint deflections. This reduces deflection nearly 50-fold compared with a simple end support, and raises the natural frequency of the structure by a factor of 7. The barrel rests on roller cams (consisting of a spherical roller that bears on a shaft with 1.5-mm eccentric journals; see Fig. 5-13) at each end of the drift chamber. Two roller cams locate the barrel axis at one end, and three roller cams fix the axis and roll at the other

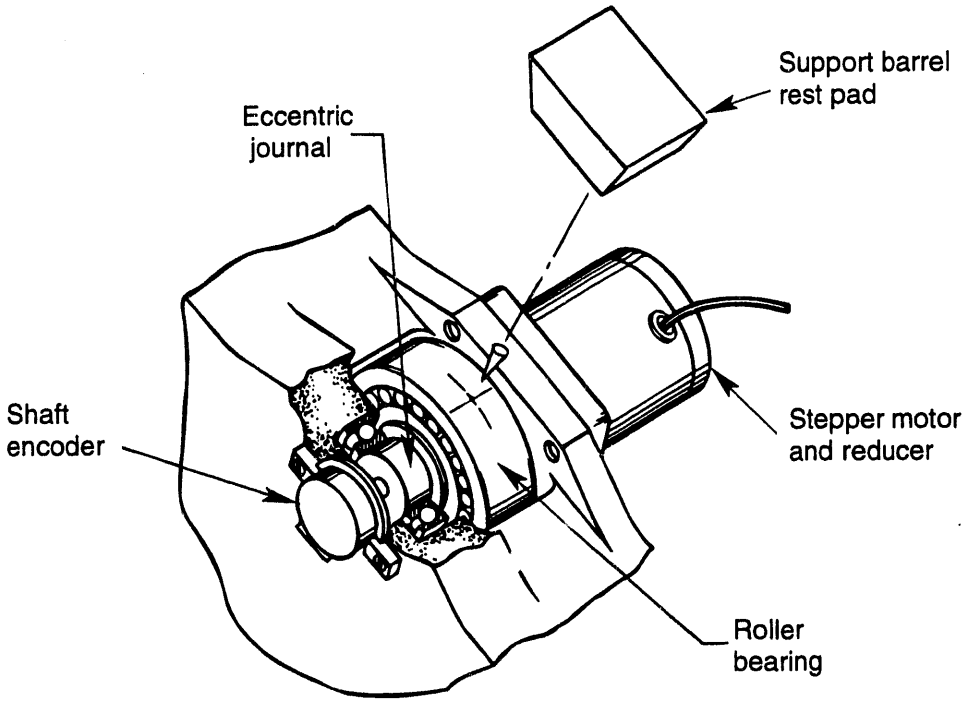

Fig. 5-13. Detail of roller cam for supporting and adjusting the support barrel.

end, as shown in Fig. 5-14. During operation, only the eccentric shaft rotates, displacing the outer bearing race. The race remains in fixed contact with its barrel support pad, so no sliding motions are involved; only rolling motion occurs. All five roller cams are driven by stepper motors through gear reducers, allowing five-axis remote positioning of the barrel; that is, the barrel position can be adjusted by ±1.5 mm in x and y, along with pitch, roll, and yaw, during beam operation.

With this technique, positioning of the support barrel to an accuracy of a few microns is practical. Because excursions are cyclic and naturally limited by cam lift, no limit switches are needed to protect against damage. Except for a fixed z restraint at one end, the barrel mount is fully kinematic and free of any over-constraints that might distort internal alignment. A similar remote-positioning mount design has been used successfully for the final triplets in the SLC interaction region [Bowden and Putallaz, 1985].

Barrel Construction. The support barrel consists of three separable sections. The two outboard ends, which carry the heavy quadrupoles, are made from 0.75-in.-wall nonmagnetic stainless-steel pipe. Access ports and magnet mounting points will be machined into the walls. The middle barrel section is of sandwich construction, with carbon-fiber facings and a foam core. This section must be nearly transparent to radiation and insensitive to thermal distortion. During installation, when the loaded barrel (3500 lb) must be temporarily supported from its end points, fiber stresses reach a maximum of 8000 psi at the midspan of the carbon tube. Figure 5-15 shows the barrel construction details.

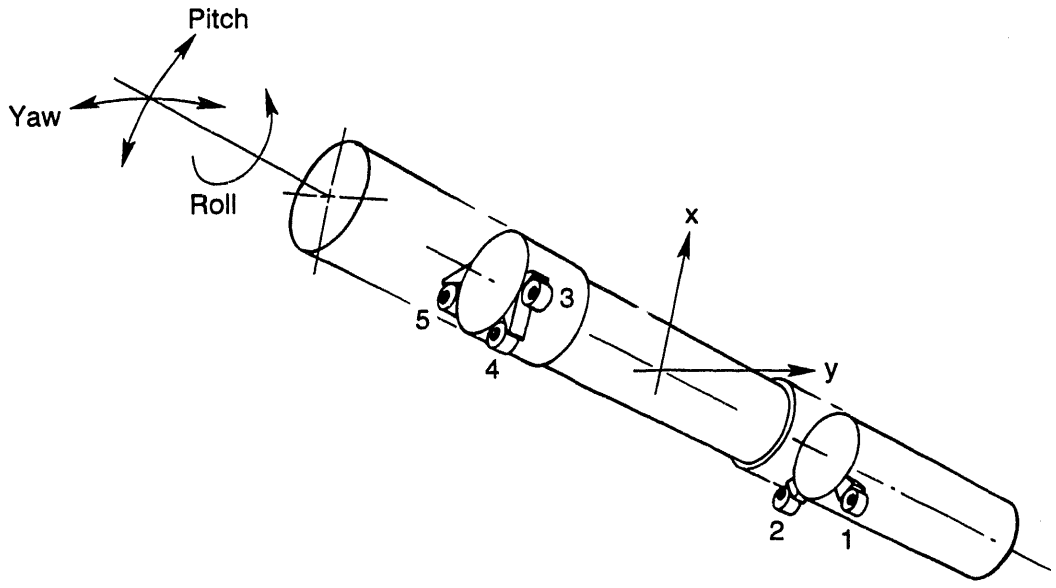

Fig. 5-14. View of the support barrel, showing its five remotely adjusted roller cams.

The most damaging thermal distortion is bending of the barrel due to transverse temperature gradients. Expansion of the warmer top of the barrel and contraction of the cooler bottom would cause the barrel to arch upward, as shown in Fig. 5-16. Because carbon fibers shorten slightly with increasing temperature (see Table 5-9), the center barrel section can be compensated to approximately zero expansion, either by balancing the fiber pitch helix angle against the high expansion coefficient of the resin matrix, or by cladding the fiber layers (which have a negative expansion coefficient) with a thin (say, 10-μm) layer of a material having a positive expansion coefficient, such as aluminum. Because the two outer stainless-steel ends of the barrel are only about one-third of the total length L, it should be possible to hold the total distortion δ (defined in Fig. 5-16), below 25 μm per °C. In addition to the protection afforded by our fabrication method and materials, the

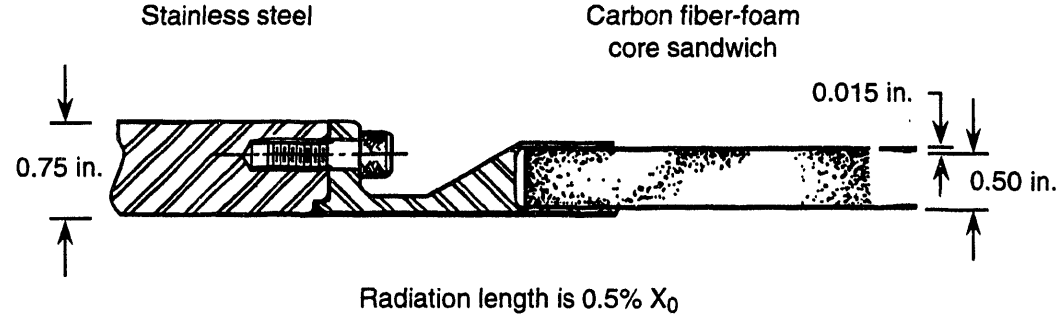

Fig. 5-15. Detail of joint between the thin inner section of the support barrel and the outer stainless-steel section.

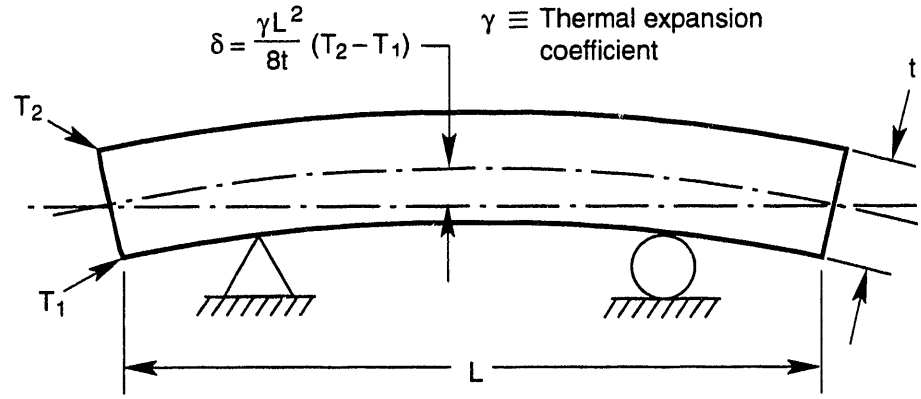

Fig. 5-16. Curvature of support barrel resulting from a temperature difference between its top and bottom.

barrel will be well sealed from natural convection by the detector, and water cooling of local heat sources will prevent asymmetric heating from causing temperature differences greater than 1°C.

Ground Motion. Because PEP-II consists of two independent storage rings, microseismic ground motion could possibly interfere with beam collisions. The spectrum of ground motion measured at SLAC [Bowden, 1985] is shown in Fig. 5-17, along with its amplitude distribution. Most ground motion is found in the 1- to 10-Hz band, whereas the barrel resonant frequency is about 30 Hz; therefore, no strong coupling will occur. The vertical beam-spot size is 6 μm in PEP-II, about 100 times the amplitude of the average microseismic noise. Quadrupole amplification will use up some, but not all, of the available margin. Further, because the barrel ensures a smooth fundamental-mode response to the vibration modes, the relative motions of the quadrupoles will be much smaller than the vibration amplitude of the barrel itself. Previous measurements at SLAC of mechanical noise from cooling-water flow have shown that this source usually does not make a significant contribution. Thus, we conclude that mechanical vibration will not be a serious problem for the barrel support.

Table 5-9. Thermal expansion coefficients and deflection of the materials that make up the 4.35-m barrel.

Material	γ [$\Delta L/L$ per °C]	δ [μm per °C]
Stainless steel	1.7×10^{-5}	113.0
Aluminum	2.3×10^{-5}	153.0
Carbon fiber 0°	-5.6×10^{-7}	−3.7
Carbon fiber 90°	3.6×10^{-5}	235.0

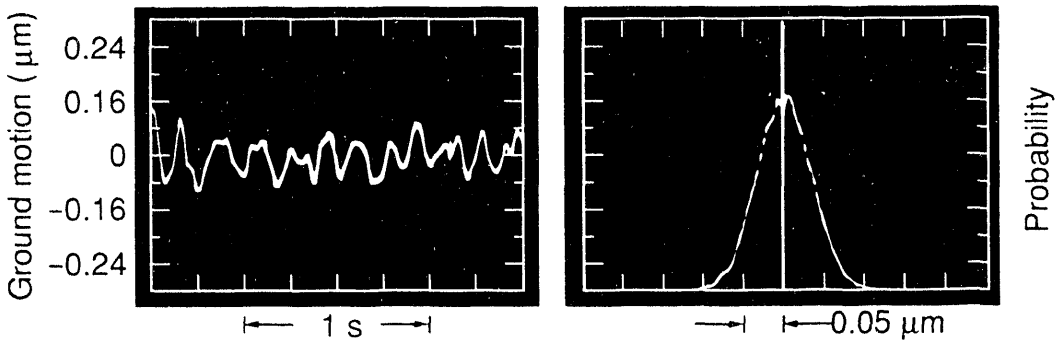

Fig. 5-17. Ground motion measured at SLAC.

Barrel Assembly and Component Alignment. The technical difficulties of assembling 4 m of heavy and delicate beamline equipment in a close-fitting support barrel has already been solved for the SLC final triplets, as demonstrated in Fig. 5-18.

Figure 5-19 is a cross section through half the support barrel length. The barrel assembly separates into three independent modules. The center section, made of carbon-fiber tube, houses the central vertex detector and the B1 deflection dipoles. This central section will be built up in the laboratory as part of the physics detector complex. For commissioning the storage rings in the absence of the detector, there is the option for a simple temporary substitute aluminum tube carrying only the B1 magnets and beam diagnostics instrumentation.

The two outboard stainless steel tubes carry the Q1 quadrupoles. Magnet mounts are installed and adjusted from the outside of the barrel. Magnets are clamped near their ends by shimmed bolts through the barrel wall, as shown in Fig. 5-19. Bolts work in four opposing pairs. The position of one bolt in each pair is fixed by a replaceable shim washer. The opposing bolt preloads the magnet mount through a spring-loaded pusher. The amount of preload is set by a second shim under this bolt. Adjustment of the alignment is made by changing shim thicknesses. Whenever a fixed bolt shim is changed, the corresponding preload shim is changed to maintain the nominal preload. In this way, forces and deflections are held constant during the alignment procedure. Adjustment of one magnet position does not affect another, and the tightening torque on the support bolts does not affect magnet position. When this technique was used on the SLC final triplets, alignment by shim changes converged in two iterations. This method is well-matched to modern survey procedures based on computer-linked theodolites and sophisticated survey software, of the type described in Section 5.3.

Final joining of the three sections into a complete barrel will be done on an assembly/alignment stand capable of supporting and aligning each barrel section independently. To bolt together the vacuum flange between Q1 and B1, the Q1 magnet will be temporarily supported through access windows in the support barrel. Then the support barrel can be pulled back on rollers, like a sleeve, opening access to the beam pipe vacuum flange. After leak checking, the stainless steel barrel is rolled forward and bolted to the flange of the central carbon tube.

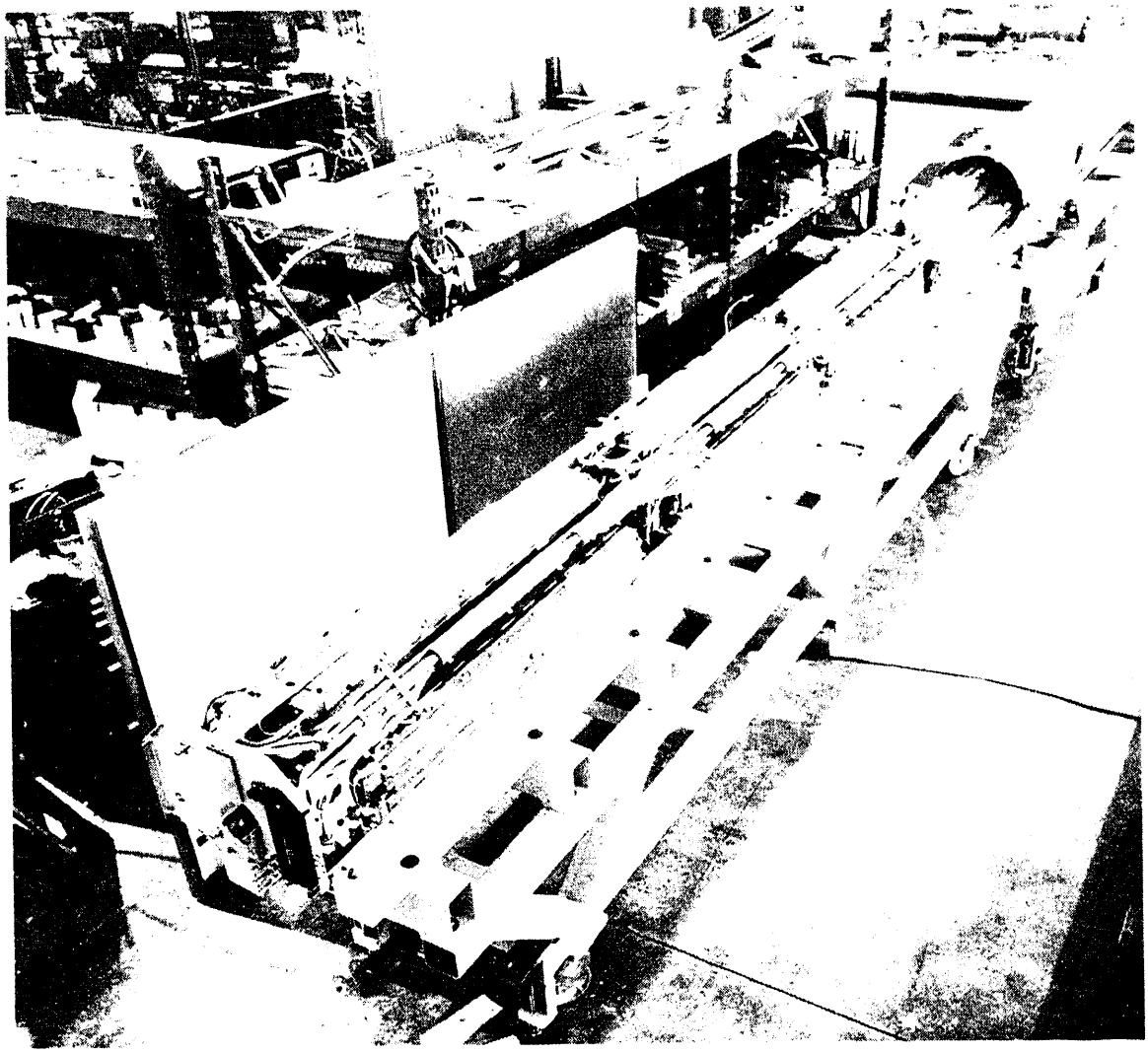

Fig. 5-18. Illustration showing the assembly technique for the SLC final focus triplet barrel.

A major reason for building all IR components into a common support barrel is to allow prealignment of beamline components prior to assembly into the detector. Once hidden inside the detector, magnets cannot easily be surveyed from the outside. The support barrel allows this alignment to be done in the laboratory under optimal conditions; Fig. 5-20 illustrates the procedure.

During alignment, the barrel will be supported in mounts identical to those to be used on the actual detector. In this way, all deflections are accurately reproduced. Access ports for either directly viewing magnet fiducials or attaching extended targets are provided on the support barrel. Magnet survey is done with computer-linked theodolites using many redundant observations to obtain a strongly over-constrained fit on the relative positions of all fiducials. A length standard is set in clear view of all theodolite locations. The raw survey data consist of precision-encoded angle measurements. All measurements are then computer processed to reconstruct the relative magnet positions. The overall resolution of

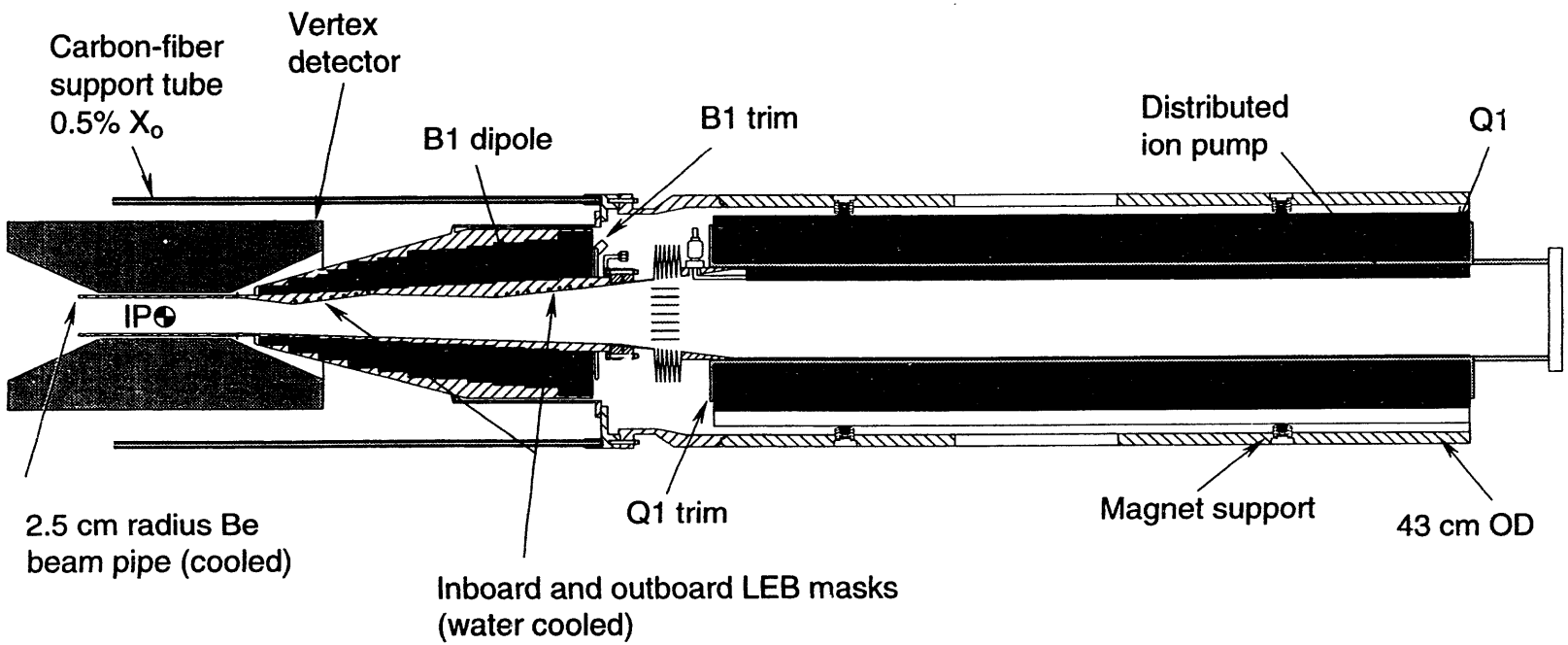

Fig. 5-19. Section through PEP-II IR barrel, showing magnet-positioning technique.

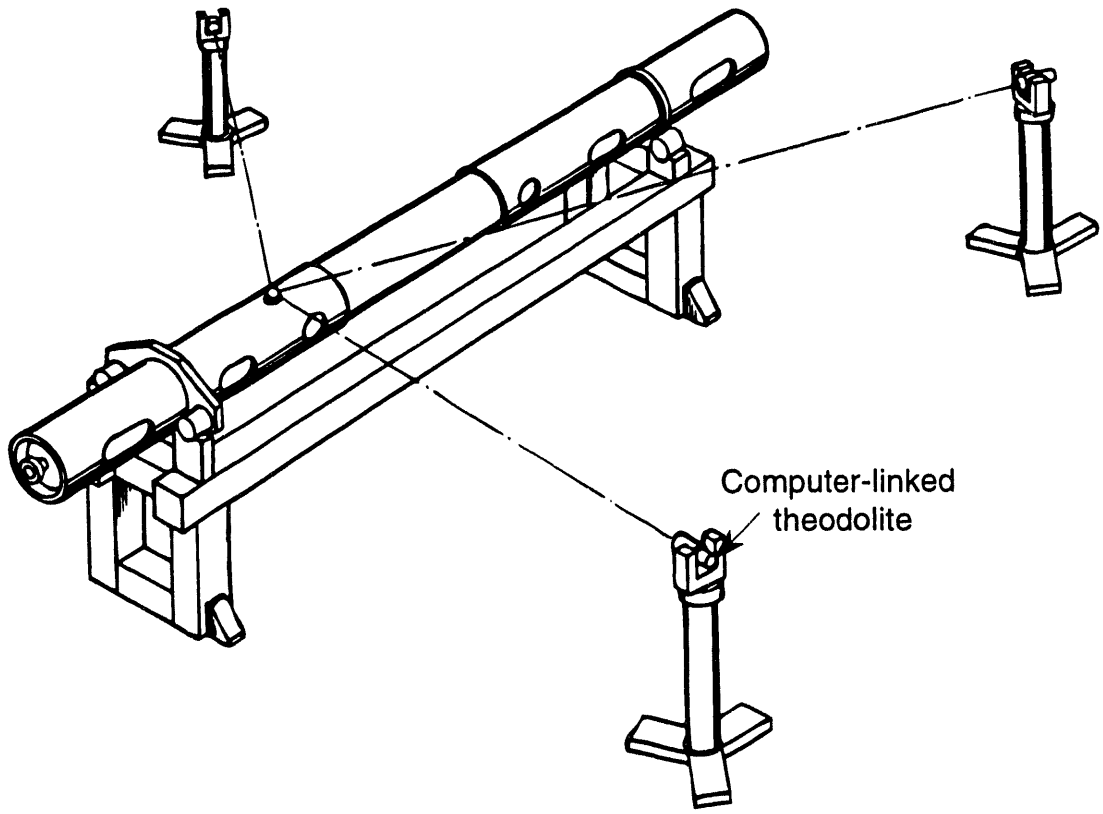

Fig. 5-20. Illustration of a method for prealigning elements inside the support barrel before installation in the detector.

such a modern system is 50 μm over 5 m. Positioning the barrel components with respect to the rest of the storage ring is straightforward. After installation into the detector, barrel-end fiducials will be clearly visible from the standard survey stations used to align other external beamline components. Furthermore, the remote positioning mounts will allow fine adjustment of the barrel position during beam operation.

5.1.3.3 Permanent-Magnet Trim Coils. To tune the collider beam optics and to permit shifting of the ring energies to reach different Υ resonances, Q1 and B1 will require trim coils with a 3% adjustment range. These coils, which line the bores of the permanent magnets, must be of compact design because small increases in the magnet aperture require large increases in the outer diameter of the permanent-magnet assembly to recover the lost strength.

For Q1, a set of four uniform-current-density coils are wound directly on the beam pipe. Coils are 30° wide to cancel the field of the first allowed higher multipole (octupole). The coil consists of 8 turns of 5-mm-square water-cooled copper conductor. A current of 203 A in 8 turns gives the required field of 0.0255 T at the mean trim coil radius. Figure 5-21 shows a section through the coil and a typical plan view. At 203 A, the total four-coil power is 3.8 kW at 19 V. Water cooling will be center tapped at the midpoint of

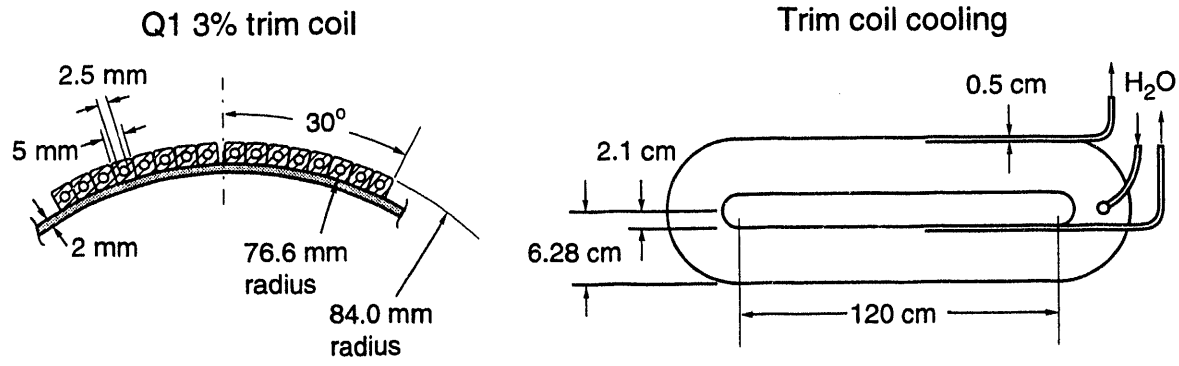

Fig. 5-21. Cross section (left) and plan view (right) of the permanent-magnet trim coils.

each coil, forming two parallel cooling flows to reduce temperatures and pressure drops. Based on a 75-psi pressure drop, water flow is about 2 L/min/coil and the water temperature rise is about 7.5°C. For turbulent flow ($R_c = 1.7 \times 10^4$), the wall-film heat transfer coefficient is about 13 W/in.$^2 \cdot$ °C. This gives a modest 0.5°C temperature difference between the conductor and the water.

5.1.3.4 Septum Quadrupole (Q2). The septum quadrupoles, Q2, are the last magnets before the separate high- and low-energy beam trajectories merge into (diverge from) a common vacuum beam pipe on their way into (out of) the IP. They are located ±2.8 m from the IP and are the first storage ring magnets beyond the detector solenoid. The Q2 magnets must vertically focus the 3.1-GeV LEB while providing a low-field bypass channel for the adjacent 9-GeV HEB.

Figure 5-22 shows the 15σ beam envelopes for the two beams at the inboard face of Q2 (the face closest to the IP). Because the quadrupole aperture of Q2 is separated from the field-free bypass channel for the HEB by only 2.18 cm, a current septum must be introduced between the two regions. In addition to accommodating the two beam envelopes, a clear aperture ("fan stay-clear") must also be provided for the fan of synchrotron radiation generated in the magnets that bend the two beams onto a common collision axis at the IP. This fan (whose power is 49 kW at a beam current of 0.99 A, as discussed in Section 4.2) extends out from the collision axis by 12 mrad.

The required septum quadrupole presents two special challenges:

- An asymmetric magnet having a pure quadrupole field in the magnet aperture, and a low-field bypass channel only 2.18 cm to the side, must be designed magnetically
- A very compact, high-current-density septum having adequate cooling capacity must be designed

Solutions to both of these challenges are presented below.

Magnetic Design. Design requirements for Q2 are summarized in Table 5-10. In any magnet structure, the net flux crossing a surface of infinite extent, such as the midplane of a quadrupole, is zero. The additional field introduced by the asymmetry of the Q2 coil

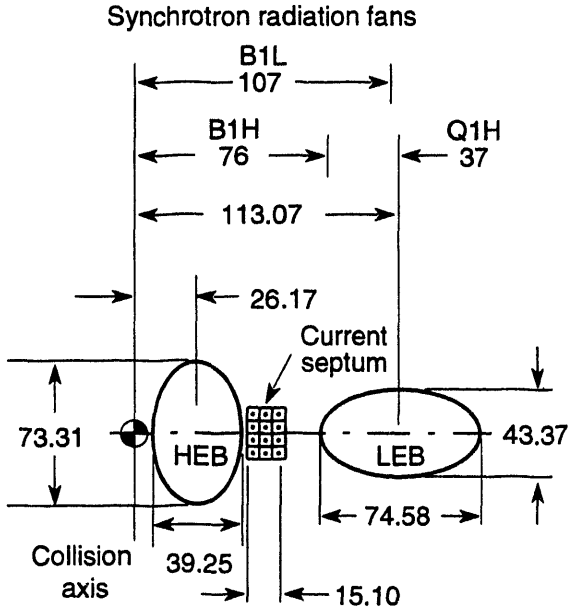

Fig. 5-22. Beam-stay-clear envelopes and locations of synchrotron radiation fans at the inboard face of Q2. All dimensions are in mm.

positions must be shunted across the midplane by iron flux returns. This preserves the high-quality quadrupole field in the magnet aperture as well as the zero field in the adjacent bypass channel. Figure 5-23 shows the flux pattern for the present septum quadrupole design with its iron return paths; the field in the yoke is below 1.1 T everywhere. A small 10-A trim coil is added to the backleg yoke opposite the septum to compensate for the small $\int H \cdot dl$ imbalance between backlegs. Except for the septum conductor on the left side, the Q2 magnet shown in Fig. 5-23 differs little from a conventional warm-iron quadrupole design. Figure 5-24 shows a mechanical layout for the Q2 magnet; its design specifications are summarized in Table 5-11.

Pole tips are shimmed, using the Poisson program MIRT, to compensate for the proximity of the current septum. Deviations from a pure hyperbola amount to 0.5 mm at most. Table 5-12 gives the relative multipole field strengths normalized to the quadrupole field ($n = 2$) at the full aperture radius, r_0. The quadrupole gradient within the ellipse corresponding to 2/3 of the beam-stay-clear aperture (roughly $10\sigma_x$ or $10\sigma_y$) remains within $\pm 2 \times 10^{-3}$ of its nominal value.

Table 5-10. Q2 design parameters.

Magnet length [cm]	50
Gradient [T/m]	11.5
Bypass channel field [T]	≤ 0.01
Multipole field contamination at 2/3 aperture	5×10^{-4}
Trim range	0–110%

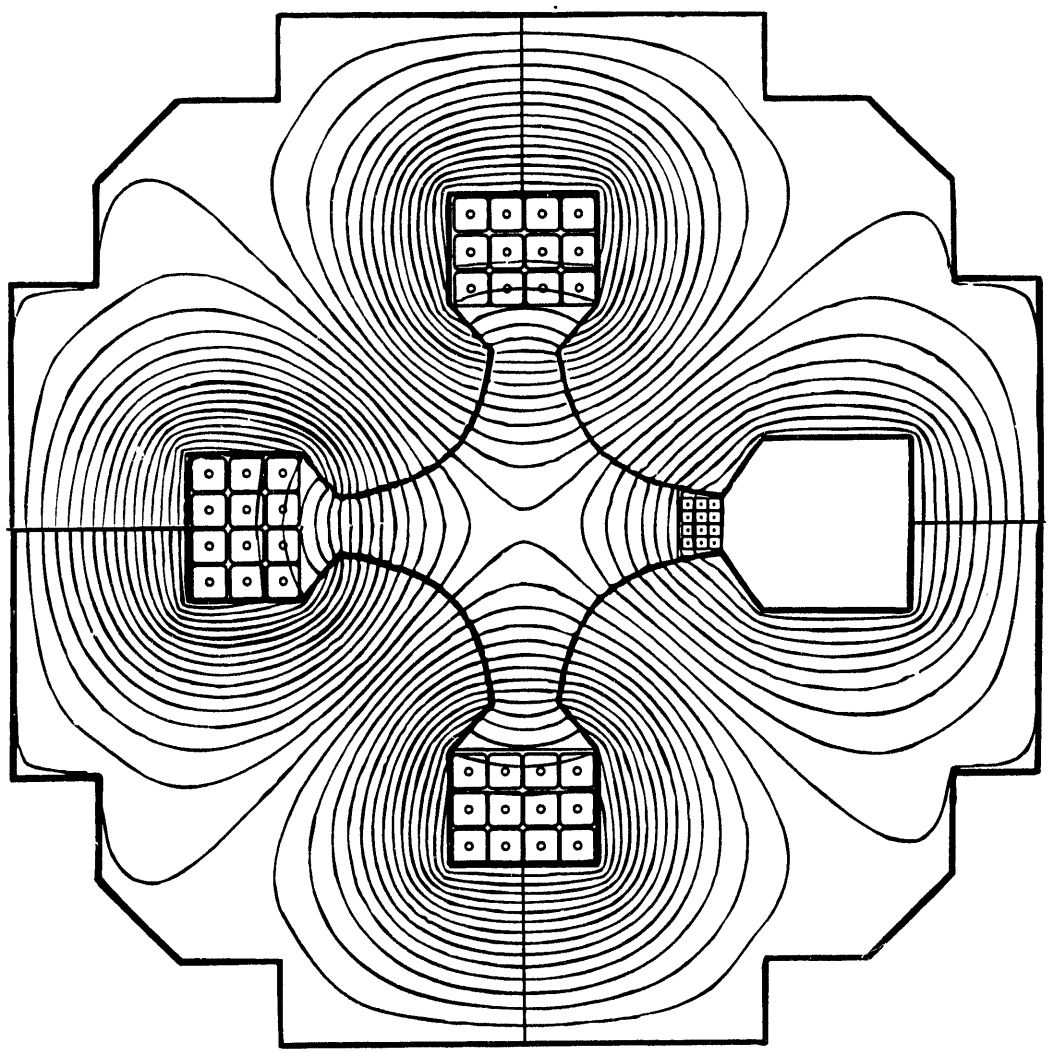

Fig. 5-23. Flux pattern for Q2.

As well as producing a high-quality quadrupole field in the LEB aperture, Q2 must also leave a low-field bypass channel for the HEB. Figure 5-25 shows the residual midplane dipole field in the HEB bypass channel. Because the separation between HEB and LEB beamlines grows as they recede from the IP, the field plotted here (at the front face of Q2) is the maximum field experienced by the HEB. The field on the HEB diminishes as the beam moves closer to the outboard end of Q2 where it is at a greater distance from the current septum.

Thermal Design. To examine the septum cooling issue, we consider the enlargement of the septum region shown in Fig. 5-26. Although the six conductors of the upper septum half are wired in series electrically, their cooling is handled with separate, parallel hydraulic circuits. Coolant streams traverse the length of the septum only once. Each conductor is separated from its neighbors by a 0.4-mm-thick insulation layer. For precise conductor

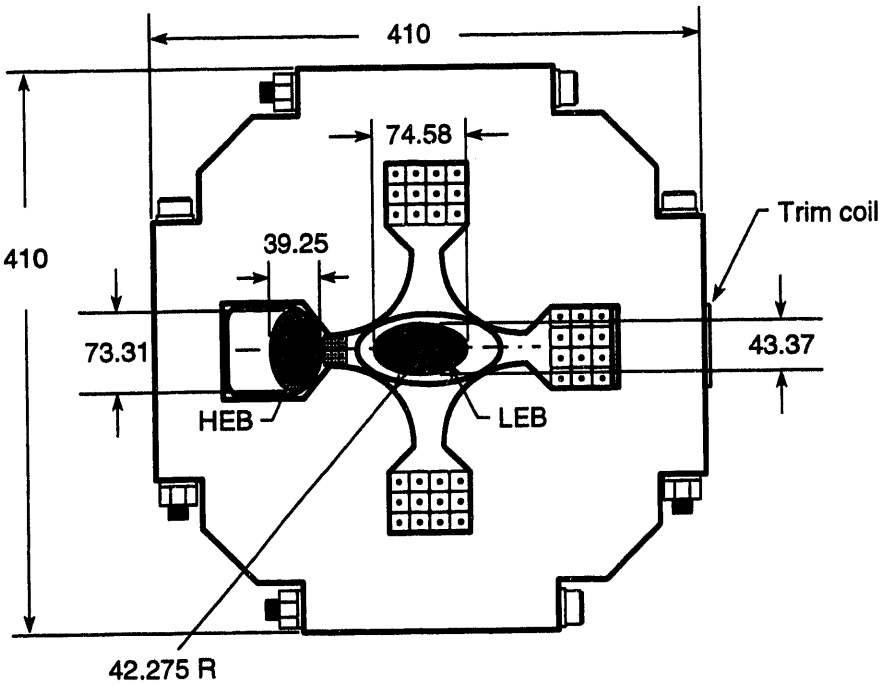

Fig. 5-24. Q2 mechanical layout.

location and mechanical integrity, the entire septum will be built as a single vacuum-impregnated assembly as outlined by Roman [1965]. The current density for the *net* copper cross section is 8.5 kA/cm^2 at the full 8200 A·turns. Starting from a water pressure drop of 75 psi and 70-cm-long conductors, Table 5-13 summarizes the septum thermal parameters.

By using parallel cooling, the total temperature rise can be held to about 15°C for the short length of these conductors. On the right side of Q2 (see Fig. 5-23) the two conventional coils are wound from six turns of 0.5-in.-square copper conductor having a

Table 5-11. Q2 specifications.

Pole-tip inscribed radius, r_0 [cm]	4.23
Gradient [T/m]	11.5
Length [cm]	50
Current [A]	1367
No. of turns	6
Peak field in iron pole [T]	0.9
Septum current density [kA/cm^2]	8.5[a]
Total power [kW]	27.0
Estimated weight [lb]	1000

[a]For net copper cross section.

Table 5-12. Q2 relative multipole field coefficients at r_0 = 4.23 cm.

n	b_n/b_2
1	-0.33×10^{-4}
2	1.00
3	-1.11×10^{-4}
4	1.82×10^{-4}
5	0.63×10^{-4}
6	-0.50×10^{-4}

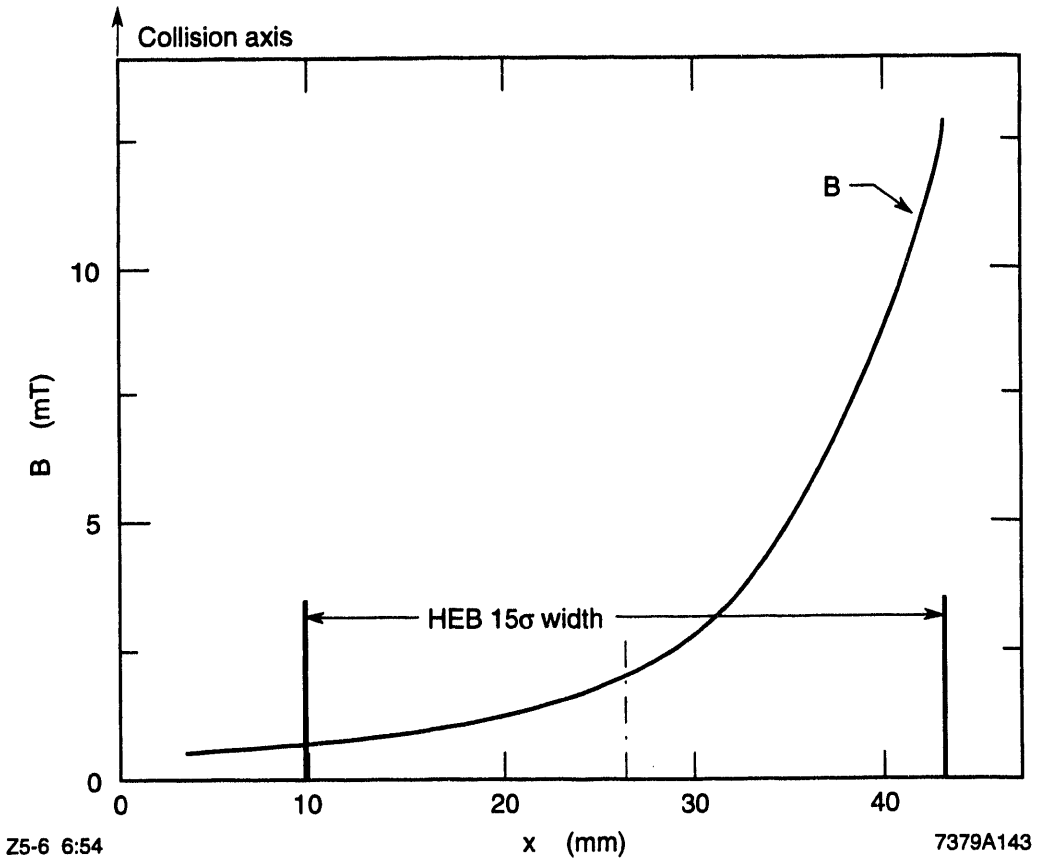

Fig. 5-25. Fringe field in the Q2 bypass channel at inboard end of magnet.

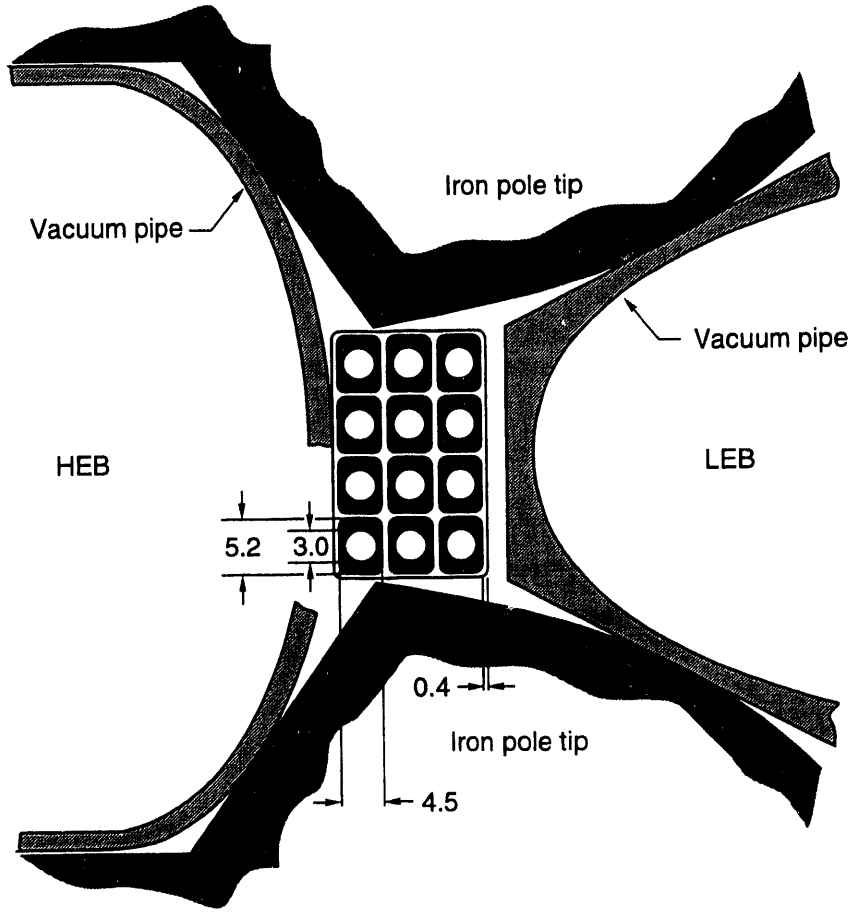

Fig. 5-26. Q2 current septum. Dimensions are in mm.

Table 5-13. Q2 septum thermal parameters.

Water pressure drop [psi]	75
Conductor length [cm]	70
Water velocity, v [m/s]	10
Water flow per conductor [cm^3/s]	70
Water temperature rise [°C]	5.54
Reynolds no., Re	65000
Prandtl no., Pr	2.8
Film coefficient, h^a [W/°C· cm^2]	5.28
Film ΔT [°C]	4.66

[a] $h = 0.023\ Re^{-0.2}\ Pr^{-2/3} v \rho c_p$.

0.25-in.-diameter cooling hole. These coils carry a current density of 1.05 kA/cm^2. This conductor size will also be used to complete the other halves of the two coils that include the septum (those coils that energize the left-hand poles in Fig. 5-23) by lap-splicing conductors at the ends of the magnet. The high-current-density septum will dissipate 19.5 kW and the other coils will add about 7.5 kW. Thus, total power dissipation amounts to 27 kW, which sets the total terminal voltage at about 20 V.

A perspective view of the Q2 magnet is shown in Fig. 5-27. The vacuum pipe is cut away to reveal the water-cooled synchrotron radiation septum mask (see Section 5.2.7.4). This specially machined vacuum pipe will be fabricated from GlidCop, as it must conduct 700 W of synchrotron radiation power from the bore of Q2 to water cooling tubes brazed to the outside. The y-shaped weldment will support the crotch mask and its associated ion pumps. By mounting the septum mask and its cooling supports with a false screen floor in the pump throat, the entire mask subassembly can be removed without disturbing the quadrupole or the y-shaped vacuum pipe. At full current, the septum bears a sideward magnetic force of 460 lb, repelling it from the quadrupole bore. By mounting the septum to a bridge rail along the HEB vacuum pipe, this load can be returned to the magnet iron.

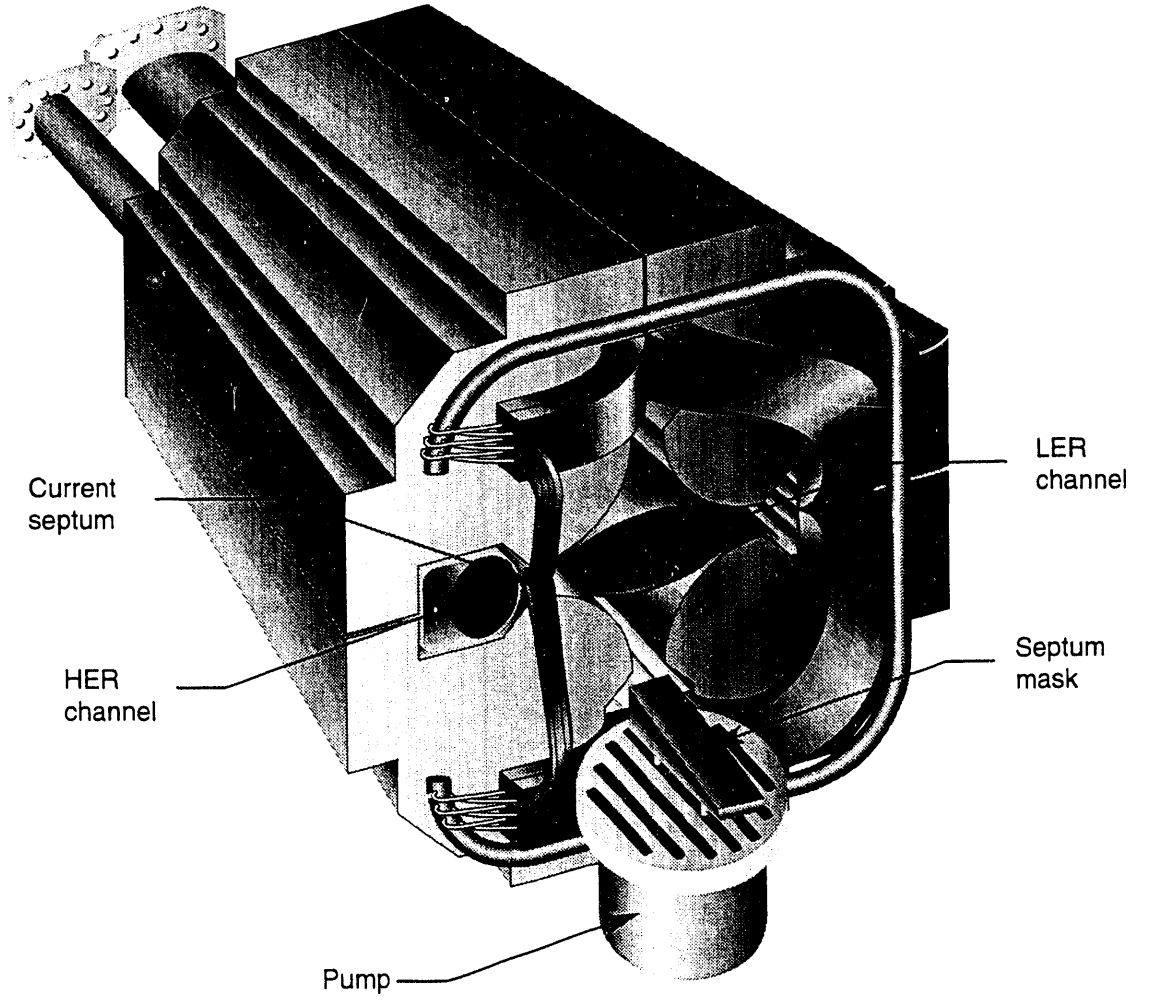

Fig. 5-27. Q2 and vacuum pipe assembly.

5.1.4 Magnetic Measurements

Five stations will be constructed for magnetic measurements, each having a computer. The computer will serve for data storage and data handling, and will also permit a comparison between the new magnetic measurements made on the refurbished PEP magnets and the original data taken at the time of their manufacture. A standardization procedure for each particular type of magnet will be stored in the computer so that it can be performed automatically prior to the commencement of measurements. The software will also prompt the operators to enter serial numbers, attach cables and water hoses, etc. Variables such as water flow, terminal voltage, and temperature rise will all become part of the database. This will ensure quality control and provide a complete pedigree for each magnet.

The choice of five stations will permit us to handle the five different types of magnets: HER dipoles, HER quadrupoles, LER dipoles, LER quadrupoles, and HER/LER sextupoles. This number of stations is perceived to be a minimum, based on the number of magnets to be tested and their different configurations. In particular, the HER dipoles present a challenge, owing to their 5.4-m length. The long coil required for these magnetic measurements will be unique. The LER bends are only 0.45 m long, so a relatively short coil can be used. Both HER and LER quadrupoles could be measured at a single station, but it is prudent to have a degree of redundancy and to avoid the possibility of bottlenecks. Because the HER and LER sextupoles are identical, the same station will be used, irrespective of the final destination of the magnet.

Magnetic measurements will be conducted using standard rotating-long-coil techniques. This method gives the integrated strength of the magnet, either $\int B \cdot dl$ or $\int G \cdot dl$, including end effects. In the case of quadrupoles, the rotating-coil measurement is a convenient way of determining the magnetic center, since a zero dipole signal occurs at this location. This measurement will provide a convenient check on the accuracy of the external fiducials built into the laminations at the time of stamping. Furthermore, the rotating-coil technique permits a determination of the higher-multipole content of the field, which is the true measure of magnet quality. Measurements will be conducted at different current settings, corresponding to the operating energies envisioned. This will provide a polynomial fit that will permit the magnets to be set accurately at any required field strength.

Magnetic tolerances for both the HER and the LER are similar to those for PEP and can be summarized as follows: The sum of all higher multipoles over the required beam-stay-clear region should be less than 0.1% of the main field component of the magnet over this same region.

5.1.5 Supports

Considerable thought has been given to the support and alignment of the two PEP-II rings. Because of the large mass of the PEP components, which are to be reused in the HER, the HER will be mounted below the LER. A side elevation of the standard HER and LER cells and a cross-sectional view of the PEP tunnel are shown in Figs 5-28 and 5-29, respectively. An artist's conception of the overall layout of the two rings is shown in Fig. 5-30.

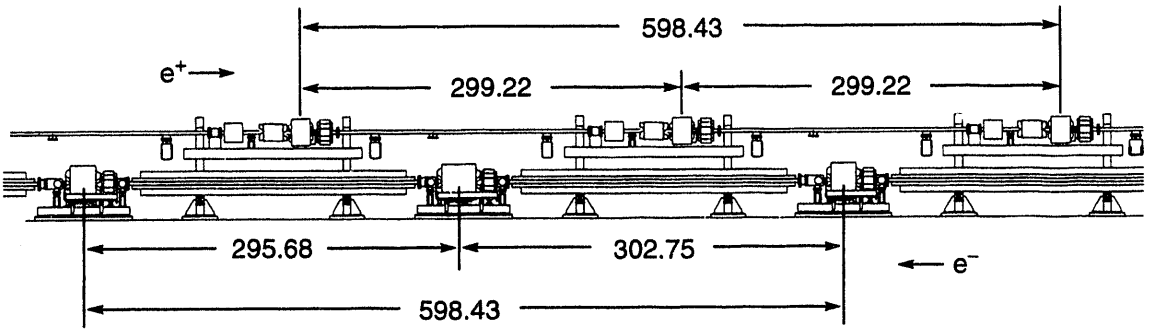

Fig. 5-28. Side elevation of standard HER and LER cells.

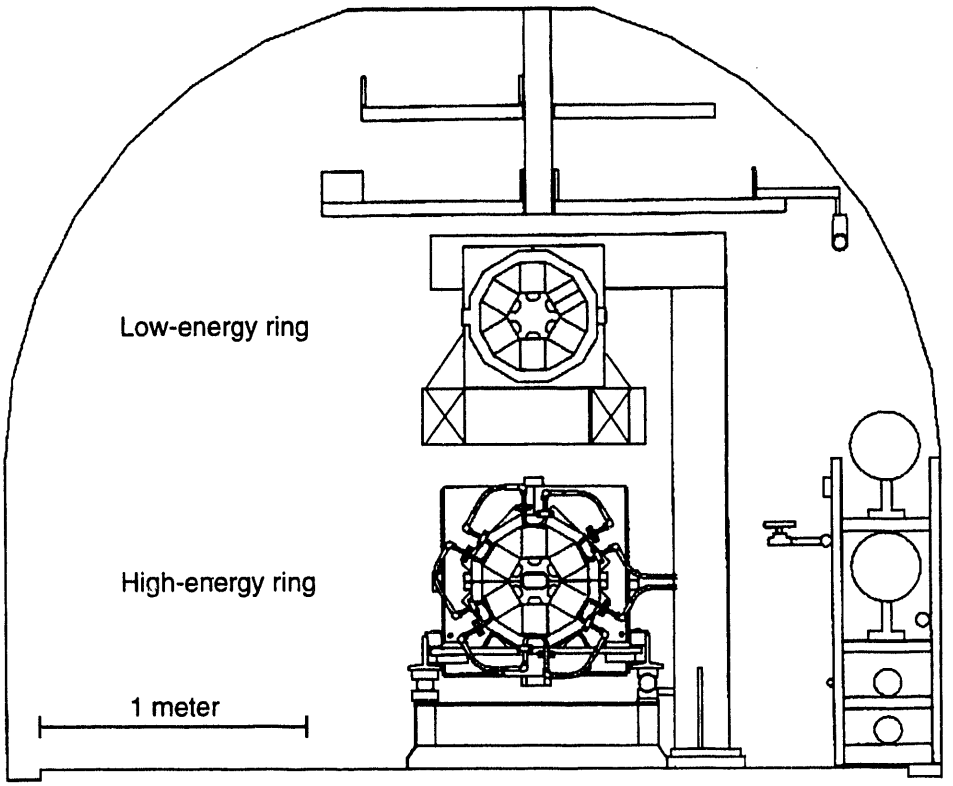

Fig. 5-29. Cross-sectional view of the PEP tunnel, showing the locations of utilities and the high- and low-energy rings.

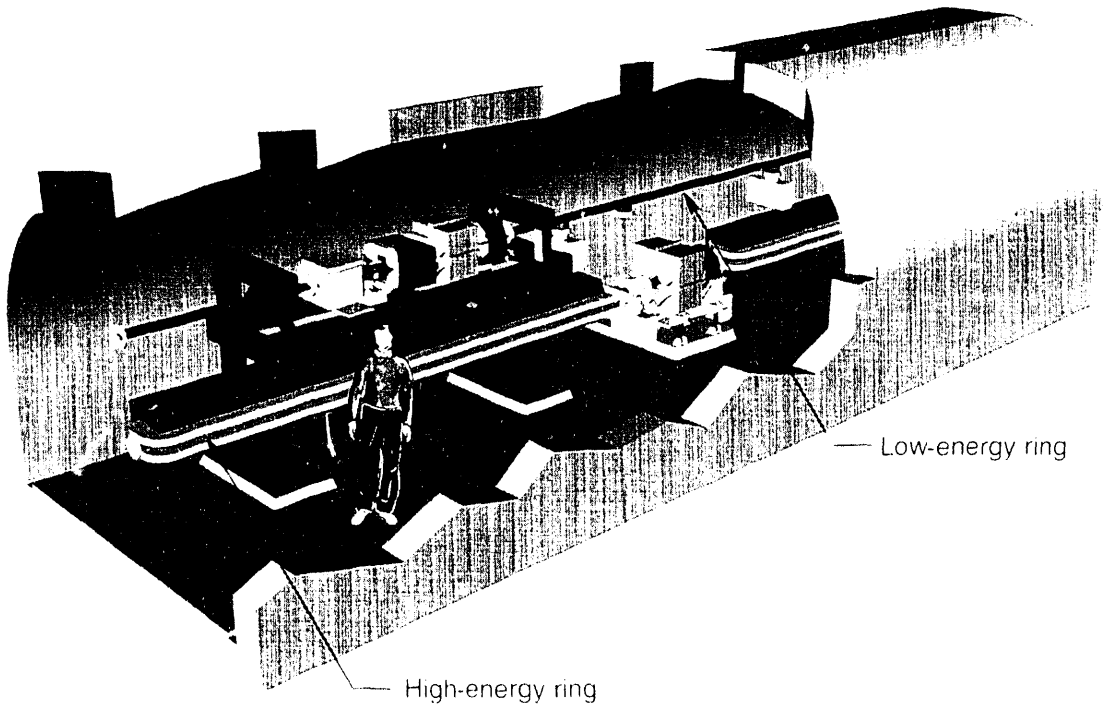

Fig. 5-30. Artist's conception of the high- and low-energy rings in the PEP tunnel.

Once the PEP tunnel has been emptied, a rough alignment procedure (see Section 5.3) will locate the anchors for the lower legs of the support structures. These support structures will be placed close to the quarter-points of the HER dipole magnets, as was done in PEP, to maintain the alignment and minimize sag and twist of these long laminated magnets. The four feet necessary to adjust and maintain the alignment of the bending magnets will be mounted on these horizontal legs.

To facilitate installation, the quadrupole-sextupole pairs for the HER will be mounted on a rigid frame and aligned in a temperature-controlled facility using high-precision optical benches. In this manner, component-to-component misalignment is kept to a minimum. The vacuum spool piece for this section will be installed along with the vacuum chamber support, which must be capable of locating and fixing the associated beam position monitor with an accuracy of about 0.1 mm with respect to the magnetic center of the adjacent quadrupole. This requirement justifies our plan to prealign the individual components on a monolithic, stress-relieved frame that will avoid costly in-field alignment (which historically has proved to be more expensive and less accurate than prealignment in the laboratory).

In the tunnel, precision alignment will locate the base support on which the frame for the quadrupole-sextupole pair rests. This base will have dowel pins identical to those at the alignment stations. Thus, when the magnetic components and base are taken to the tunnel, these pins will enable us to place the frame accurately. Although the base itself will be provided with adjustments having six degrees of freedom, we believe that it will be unnecessary to provide individual adjustment for all the quadrupole-sextupole frame

components. The technique outlined here has been employed successfully at SLAC on several other projects, including PEP, the damping rings, the SLC arcs, and the final focus beamline.

After the main components of the HER ring are in place, the LER components will be installed above them. Once again, we will take the approach of using a raft or strong frame and prealigning the LER components in the laboratory. Because of their smaller size and lighter weight, we expect to be able to support and align the magnetic components of an entire half-cell (including a sextupole, a quadrupole, a bending magnet, and either a steering magnet or beam position monitor, together with the vacuum chamber and associated pumps) on one raft. As with the HER, the raft itself will be provided with six degrees of controlled freedom. We believe that it will be unnecessary to provide easy adjustments for individual raft components.

To facilitate alignment, the LER will be suspended above the HER such as to leave about an 8-in. component-free zone between the two rings for unobstructed line-of-sight. As discussed in Section 5.1.3, extensive ground-motion measurements were made at SLAC prior to building the SLC, because that accelerator was expected to be very sensitive to small, steady-state ground motions or noise. These measurements indicated which site-wide excitation frequencies are a problem. Magnet supports will be designed to avoid unwanted resonances.

Because the two rings are independently supported, at different heights in the tunnel, it is clear that changes in temperature within the tunnel can cause relative motion between them. Fortunately, time constants for such motion will be slow, of the order of hours, and steering corrections can be made in the IR to compensate for the resultant beam drifts.

5.2 VACUUM SYSTEM

The vacuum system of the PEP-II collider presents a technical challenge beyond that of any existing electron-positron collider. Each subsystem must meet demanding design criteria to satisfy the overall system requirements. These subsystems for the high-energy (electron) and low-energy (positron) rings (HER and LER, respectively) include vacuum chambers, pumps, cooling, and special components, such as bellows, beam position monitors (BPMs), and valves.

For PEP-II, the HER and LER will have circulating beam currents of 0.99 and 2.14 A, respectively, to reach the design luminosity of 3×10^{33} cm^{-2} s^{-1}. We refer to these as the *nominal* currents. The nominal beam currents are at least an order of magnitude beyond the typical values for today's colliders and, as such, present an appreciable challenge to the vacuum system designer. To provide for possible upgrades, and for luminosity "breathing room," we also specify a *maximum allowable* current in each ring of 3 A. Because the vacuum system is generally difficult to upgrade after the collider is operating, we have chosen to design for the 3-A capability from the outset.

5.2.1 General Issues and System Requirements

A well-designed vacuum system is the key to providing a suitable beam environment. In particular, the chamber design should have the following attributes:

- Adequate beam-stay-clear aperture for injection and for stored-beam lifetime
- Low impedance to avoid beam instabilities and to minimize higher-order-mode (HOM) power dissipation
- Sufficient pumping speed to maintain a low pressure in the face of substantial synchrotron-radiation-induced gas desorption
- Sufficient cooling to safely dissipate the heat load associated with both synchrotron radiation and HOM losses
- Capability to shield external ring components from synchrotron radiation

Most of these requirements are fairly obvious and do not differ from those of existing colliders. The main distinction in the case of PEP-II is associated with the required beam currents, which are much higher than those in present-day colliders.

Depending on the magnitude of the dynamic gas load due to photodesorption, the chamber could have a conventional elliptical or octagonal shape, or it could exploit differential pumping via an antechamber arrangement. In the PEP-II parameter regime, use of a conventional chamber shape is acceptable, provided that the material is chosen to have a low photodesorption coefficient. If the chamber material is suitably chosen, the chamber walls will also serve as the primary shield for the synchrotron radiation that would otherwise damage magnets and other beamline components. Basically, this consideration implies the use of a high-Z material such as copper or stainless steel, rather than the more easily fabricated aluminum. (If aluminum were chosen, the shielding would have to be provided by an additional layer of material—for example, lead—to absorb the radiation passing through the chamber walls. While this is possible, it is an undesirable complication.)

Included as integral parts of the chamber are several special sections and components, such as shape transitions, pumping ports, bellows, and BPMs. The high peak and average beam currents in PEP-II demand that the electromagnetic environment presented by the vacuum chamber and its special components satisfy a strict impedance budget for the ring. It is known that the present PEP vacuum chamber would provide a sufficiently low broadband impedance ($|Z/n| \approx 1\ \Omega$) to be acceptable for the PEP-II HER [Rivkin, 1987; Zisman, 1990b]. Thus, we are assured that standard care in the design of the vacuum chamber will permit us to reach our impedance goal.

The pumping system of the collider must maintain the specified operating pressure under conditions of a large dynamic photodesorption gas load caused by the intense synchrotron radiation bombardment of the chamber walls. (In high-energy, high-current electron rings, thermal outgassing is generally a small contribution to the gas load that mainly determines the base pressure in the absence of beam.) In addition to handling the gas load during routine operation, the pumping must also be sufficient to allow for rapid initial commissioning (cleaning) of the vacuum chamber. The *system requirements* for the vacuum system during collider operation are as follows:

- ≤10 nTorr in the arcs
- ~3 nTorr in the straight sections
- ~1 nTorr in the two half straight sections upstream of the detector
- ~0.5 nTorr base pressure due to thermal outgassing under no-beam (static load) conditions

(Note that pressure requirements are quoted here as N_2-equivalent values.) We have generally designed the vacuum systems to reach these goals even at the maximum allowable beam current of 3 A. Thus, at the nominal operating currents, we expect to do better than the requirements listed above. In this sense, the design is conservative and should operate very reliably. Clearly, the additional pumping capability will be of great benefit in reducing the conditioning time for the system.

An electron beam circulating in a storage ring subjects the vacuum chamber walls to copious synchrotron radiation. As the incident area of the radiation fan is small, the associated thermal flux is generally high enough to require considerable cooling of the chamber wall. The chamber cooling system is designed to remove the heat safely, despite high power densities. As is typical, cooling is accomplished by water flowing in channels outside the chamber. In addition to ensuring the mechanical stability of the chamber under thermal loads that could reach 10 MW in the HER, maintaining the chamber wall at a relatively low temperature serves to reduce the gas load due to thermal desorption.

5.2.2 Determination of Vacuum Chamber Aperture

The size requirements of the beam chambers are determined by the beam emittances and energy spreads and by the optical functions of the HER and LER lattices. To ensure adequate quantum lifetime, the chamber was designed to accommodate the *uncoupled* horizontal emittance and the *fully coupled* vertical emittance. It is also desirable to keep the cross section of the chamber constant throughout the arc sections to minimize the impedance contributions from shape transitions. Consequently, we considered the maximum values of the beta functions in determining the chamber sizes.

For determining the required chamber aperture, we took the uncoupled emittance value for each ring to be at least twice the value required for the nominal operating configuration. This will provide considerable flexibility to adjust the ring parameters as dictated by operational needs. Thus, the HER chamber was designed for 100 nm·rad uncoupled horizontal emittance, and the LER chamber was designed for 200 nm·rad. In the absence of wigglers, the relative energy spread of the beam in the HER should be close to its natural value of 6.1×10^{-4}. To be conservative, we took a value of 1×10^{-3} for estimating the required chamber size. For the LER, we envision that the natural energy spread from the arcs will be increased by means of wigglers to a value closer to 1×10^{-3}, which we again adopted as a design specification for evaluating aperture requirements. Since the HER optics are similar to PEP, the closed-orbit allowances were taken to be the same as those adopted for the original PEP design; these values were also assumed for the LER.

Emittance and beta function values used to evaluate the required apertures for the HER and LER are summarized in Table 5-14.

The horizontal beam-stay-clear half-aperture in the arcs is evaluated as

$$\mathrm{BSC}_x = 10\sqrt{\varepsilon_{x0}\hat{\beta}_x + \hat{D}^2\left(\frac{\sigma_E}{E}\right)^2} + \mathrm{COD}_x \tag{5-6}$$

Similarly, the vertical beam-stay-clear aperture in the arcs is

$$\mathrm{BSC}_y = 10\sqrt{\varepsilon_{y0}\hat{\beta}_y} + \mathrm{COD}_y \tag{5-7}$$

Using the values in Table 5-14, and including allowances for fabrication and mechanical positioning errors, we obtain the minimum chamber (inner) half-apertures:

HER: $\mathrm{BSC}_x \times \mathrm{BSC}_y = 45\ \mathrm{mm} \times 25\ \mathrm{mm}$

LER: $\mathrm{BSC}_x \times \mathrm{BSC}_y = 45\ \mathrm{mm} \times 25\ \mathrm{mm}$

The HER chamber dimensions can be accommodated by the present PEP magnets.

Table 5-14. Parameters used to evaluate vacuum chamber dimensions for the high- and low-energy ring arcs.

Beam parameter	HER	LER
Max. uncoupled horizontal emittance, ε_{x0} [nm·rad]	100	200
Max. fully coupled vertical emittance, ε_{y0} [nm·rad]	50	100
Max. horizontal beta in arcs, $\hat{\beta}_x$ [m]	26	26
Max. vertical beta in arcs, $\hat{\beta}_y$ [m]	28	26
Max. dispersion, $\hat{D}$ [m]	1.8	1.1
Max. energy spread, σ_E/E	1×10^{-3}	1×10^{-3}
Horizontal closed-orbit allowance, COD_x [mm]	10	10
Vertical closed-orbit allowance, COD_y [mm]	5	5

5.2.3 Synchrotron Radiation and Vacuum

As mentioned earlier, two design issues follow from the copious production of synchrotron radiation in a high-intensity storage ring: (i) heating of the vacuum chamber walls owing to the high thermal flux and (ii) radiation-induced gas desorption (both photodesorption and thermal desorption). In this section, we quantify these effects and evaluate their impact on collider performance. As we shall see, despite the difficulties associated with the high beam currents in the PEP-II storage rings, handling the large synchrotron radiation power is amenable to standard engineering solutions in a beam chamber of elliptical or octagonal cross section, without requiring a more exotic approach based on an antechamber design.

5.2.3.1 Wall Heating. At the design luminosity of 3×10^{33} cm^{-2} s^{-1}, each ring will contain a beam current more than an order of magnitude higher than that typical in existing high-energy storage rings; the associated heat load is, therefore, quite high. The technical difficulty lies not in removing the total synchrotron radiation power per se, but rather in handling the concentrated linear thermal flux. Thus, contrary to intuition, a small-circumference ring is more difficult to cool and pump than a large ring. (If a very small circumference were chosen for the LER, management of the high linear thermal flux would be considerably more difficult than in the HER, despite the fact that the total synchrotron radiation power would be much lower in the LER.) By adopting a design in which the LER has a circumference equal to that of the HER, such concerns are eliminated (except for the damping wiggler regions, which are discussed in Section 5.2.6, below).

To estimate the heat load, we start from the well-known expression [Sands, 1970] for the synchrotron radiation power (in kW) emitted by an electron beam in uniform circular motion:

$$P_{SR} = \frac{88.5\, E^4 I}{\rho} \tag{5-8}$$

where E is the total energy (in GeV), I is the total beam current (in A), and ρ is the bend radius of the dipoles (in meters). The linear power density (in W/cm) radiated along the circumferential path length is given by

$$P_L = \frac{10 P_{SR}}{2\pi\rho} = \frac{885\, E^4 I}{2\pi\rho^2} \tag{5-9}$$

For a 9-GeV beam in the HER (ρ = 165 m) at the maximum allowable current of 3 A, we find from Eq. 5-9 a linear power density of P_L = 102 W/cm. At the nominal operating current of 0.99 A (corresponding to the design luminosity of 3×10^{33} cm^{-2} s^{-1}), the linear power density is reduced to 34 W/cm. In reality, the arcs are not exactly circular in either ring—the dipoles in each cell are connected by short straight sections a few meters in length. These straight regions tend to spread out the radiation flux. Consequently, Eq. 5-9 gives the maximum value of the linear power density anywhere in the arcs.

The peak power density in the LER arcs occurs in the straight section downstream from the bending magnet, where the effect of geometry reduces the power density more than one would calculate using Eq. 5-9. For the 3.1-GeV beam in the LER (ρ = 13.75 m), at the maximum current of 3 A, the linear power density is 45.7 W/cm. At the nominal operating current of 2.14 A, the linear power density is reduced to 32.6 W/cm.

The vertical (half)-angular spread (in radians) of the synchrotron radiation fan containing ~85% of the radiation is given approximately by

$$\psi \approx \frac{m_0 c^2}{E} = \frac{1}{\gamma} \tag{5-10}$$

For a 9-GeV beam, ψ = 0.06 mrad, while for the 3.1-GeV LER beam, ψ = 0.17 mrad. Although it is not strictly true (see Section 5.2.6), we assume the power to be uniformly distributed over this angular extent. Including the finite size and angular divergence of the electron beam, the height of the vertical band illuminated by the synchrotron radiation fan is

$$h = 2\left[\sigma_y^2 + d^2\left(\sigma_{y'}^2 + \psi^2\right)\right]^{1/2} \tag{5-11}$$

where σ_y is the rms beam height, $\sigma_{y'}$ is the rms angular spread, and d is the tangential distance from the beam orbit to the chamber wall. The value for d can be calculated from the geometry shown in Fig. 5-31, where $w/2$ is the transverse distance from the beam orbit to the outer wall of the vacuum chamber. In bend regions,

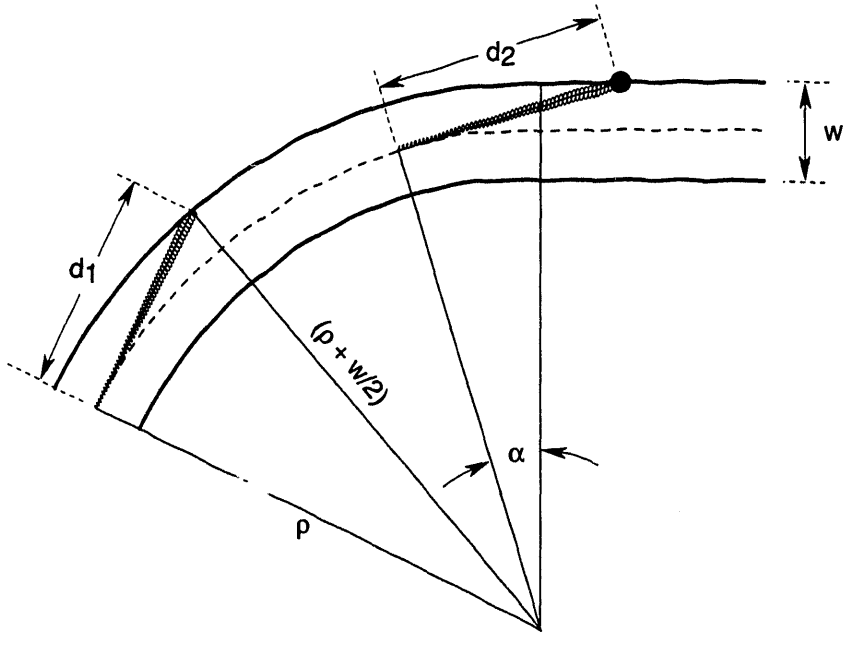

Fig. 5-31. Geometry of the synchrotron radiation fan hitting the vacuum chamber wall in curved and straight pipe sections (not to scale).

$$d_1 = \sqrt{\left(\rho + \frac{w}{2}\right)^2 - \rho^2} \tag{5-12}$$

while in the straight regions between bend fields,

$$d_2 = \frac{\left(\frac{w}{2}\right)}{\sin\alpha} + \rho \tan\left(\frac{\alpha}{2}\right) \tag{5-13}$$

For the HER, with a chamber half-width of 4.5 cm and a 165-m bending radius, we find that $d_{1,\max} = 3.85$ m, with a maximum angle of incidence given by $\alpha = d_1/\rho = 23$ mrad.

To be conservative in estimating the power density, we have ignored the contribution to the height of the synchrotron radiation fan from the finite beam emittance; that is, we take $\sigma_y = \sigma_{y'} = 0$ in Eq. 5-11, and we assume that all the radiation falls between $\pm\psi$. Thus, the minimum height of the illuminated strip is $h = 2\psi d = 0.44$ mm. The corresponding maximum thermal flux density in the HER, at a beam current of 3 A, is then $P_A = P_L/h = 2.3$ kW/cm^2. Tables 5-15a and 5-15b summarize both the nominal-current and maximum-current cases for the LER and HER, respectively, compared with values from PEP.

Table 5-15a. Comparison of radiation loads in PEP and the PEP-II LER. For PEP an aluminum chamber is used; the PEP-II estimates assume a copper chamber and are computed as described by Alexandrov et al. [1990].

		PEP-II	
Parameter	PEP	LER nominal current	LER maximum current
Magnetic radius [m]	165.00	13.75	13.75
Bending magnet field [T]	0.3033	0.7544	0.7544
Energy [GeV]	15.00	3.11	3.11
Current [mA]	200	2140	3000
Total synchrotron power [kW]	5,436	1,290	1,810
Peak chamber wall linear flux [W/cm]	52	33	46
Beam divergence, 2θ [mrad]	0.07	0.33	0.33
Min. tangential distance, d [m]	4.06	2.06	2.06
Max. angle of incidence, α [mrad]	24.6	32.7	32.7
Minimum beam height [mm]	0.28	0.68	0.68
Wall heat load [kW/cm^2]	1.89	0.48	0.67

Table 5-15b. Comparison of radiation loads in PEP and the PEP-II HER. For PEP an aluminum chamber is used; the PEP-II estimates assume a copper chamber.

Parameter	PEP	PEP-II HER nominal current	PEP-II HER maximum current
Magnetic radius [m]	165.0	165.0	165.0
Bending magnet field [T]	0.3033	0.1820	0.1820
Energy [GeV]	15.00	9.00	9.00
Current [mA]	200	1000	3000
Total synchrotron power [kW]	5,436	3,519	10,557
Chamber wall linear flux [W/cm]	52.4	33.9	101.8
Beam divergence, 2θ [mrad]	0.07	0.11	0.11
Min. tangential distance, d [m]	4.06	3.85	3.85
Max. angle of incidence, α [mrad]	24.6	23.4	23.4
Minimum beam height [mm]	0.28	0.44	0.44
Wall heat load [kW/cm^2]	1.89	0.77	2.31

In addition to the synchrotron radiation heating, we must also consider the heat loads from HOM losses. These were estimated in Section 4.3.1.6 to be 70 and 225 kW for the HER and LER, respectively. For safety, we have doubled these estimates to account for presently unidentified impedances. This power will be distributed roughly uniformly around the ring, leading to an additional 0.6-W/cm thermal load for the HER and 2 W/cm for the LER. For the LER, this value is only about 4% of the peak synchrotron radiation load in the arcs, so HOM heating represents only a small additional burden for the cooling subsystem. In the HER, the additional heat load from HOM losses is only about 1% of that from synchrotron radiation.

5.2.3.2 Gas Desorption. The gas load in electron storage rings arises from two processes: thermal outgassing and synchrotron-radiation-induced photodesorption. Thermal outgassing is common to all vacuum systems and occurs in the absence of synchrotron radiation; that is, it contributes mainly to the base pressure of a ring in the absence of circulating beam. In all high-energy electron storage rings, thermal outgassing is negligible when compared with the dynamic gas load from photodesorption. Thus, the gas load due to synchrotron radiation actually determines the operating pressure of the ring.

To estimate the desorption rate, we follow the approach of Gröbner et al. [1983]. After taking the spectrum of the synchrotron radiation photons into account, we can express the photon flux in the spectral interval $(0, x)$ in the form

$$\dot{N}(x) = \frac{\sqrt{3}\, r_e}{e\hbar c} F(x)\, E\, I \tag{5-14}$$

where

$$x = \frac{\varepsilon}{\varepsilon_{\text{crit}}} = \frac{\varepsilon}{\left(\frac{3\hbar c}{2}\right)\left(\frac{\gamma^3}{\rho}\right)} \tag{5-15}$$

with ε being the photon energy and $\varepsilon_{\text{crit}}$ being the critical energy of the radiation in the dipoles. In practical units,

$$\varepsilon_{\text{crit}} = 2.218\, \frac{E^3}{\rho} \ \text{[keV]} \tag{5-16}$$

$F(x)$ is the integral over the modified Bessel function:

$$F(x) = \int_0^x \int_u^\infty K_{5/3}(y)\, dy\, du \tag{5-17}$$

For large values of x, $F(x) \rightarrow 5.23$. After rearranging terms and inserting appropriate values for the constants, we obtain a photon production rate of

$$\dot{N} = 8.08 \times 10^{20}\, E\, I \ \text{[photons/s]} \tag{5-18}$$

where E is in GeV and I is in A.

At the design current of 0.99 A, the synchrotron radiation load in the HER is 7.3×10^{21} photons per second, or a maximum of 7.1×10^{18} photons/s/m. As the minimum height of the synchrotron radiation fan in the HER is only 0.44 mm, the maximum photon flux on the walls is 1.6×10^{18} photons/cm^2/s. By contrast, the maximum photon flux on the walls of the LER chamber is 7.35×10^{17} photons/cm^2/s. For later use in computing the photon dose on the chamber walls, we note that in the HER, 1 A·hr corresponds to 2.5×10^{22} photons/m.

Gas molecules are desorbed from the walls in proportion to the photon flux; that is, the number of molecules produced per incident photon is

$$\dot{N}_{\text{Mol}} = 8.08 \times 10^{20}\, E\, I\, \eta \ \text{[molecules/s]} \tag{5-19}$$

The ideal gas law relates the number of molecules to a gas load in Torr·L by a conversion factor of 3×10^{-20} Torr·L/molecule. In these units, the effective gas load due to photodesorption is found to be

$$Q_{\text{gas}} = 24.2\ E\, I\, \eta \ \text{[Torr·L/s]} \tag{5-20}$$

The photodesorption coefficient η is a property of the chamber that depends on several factors:

- Chamber material
- Material fabrication and preparation
- Amount of prior exposure to radiation
- Photon angle of incidence
- Photon energy

In light of these complexities, it seems better to regard η as an effective engineering value that accounts for the differential illumination of the chamber walls by both direct (beam-produced) and diffusely scattered (secondary) photons, rather than considering the photodesorption coefficient to be a fundamental material property. Using a single value of η in Eq. 5-20 yields only a rough estimate of the actual dynamic gas load but one that is nonetheless useful in setting the scale of the engineering task, as well as in choosing the chamber material.

5.2.3.3 Choice of Chamber Material. Experimental measurements [Gröbner et al., 1983; Foerster et al., 1990; Ueda et al., 1990; Mathewson et al., 1990] for well-exposed samples of aluminum, stainless steel, and oxygen-free, high-conductivity (OFHC) copper indicate minimum values of η ranging from less than 2×10^{-6} for copper and stainless steel up to 2×10^{-5} for aluminum. Although the gas-scattering lifetimes in storage rings with lower critical photon energies than PEP-II suggest that aluminum chambers may eventually develop an effective $\eta \approx 10^{-6}$, we believe a more reliable design procedure is to adopt copper or stainless steel as the chamber material, despite their higher cost per kilogram. Because the data of Ueda et al. indicate that clean, machined, oxygen-free copper can attain $\eta = 2 \times 10^{-6}$, we have chosen this value as the design basis. Such a low photodesorption coefficient allows us to design the PEP-II vacuum chamber with a conventional elliptical or octagonal shape, instead of being driven to adopt an antechamber design that is more difficult and expensive to fabricate. The apparent cost disadvantage of copper or stainless steel vis-à-vis aluminum is more than offset by the relative simplicity of the chamber shape, by the reduction in the amount of pumping needed, and by the shortening of the vacuum commissioning time.

As shown below, copper and stainless steel also have the considerable advantage of being self-shielding and thus can protect the magnets and other hardware from radiation damage caused by the hard component of the synchrotron radiation. The need for lead shielding, which would be required to accompany an aluminum chamber, is completely eliminated. In that the chamber walls are subjected to very high thermal loads, copper, with its excellent thermal conductivity, appears to be the preferred material, despite the paucity of experience in building large copper vacuum chambers.

For a copper chamber with a desorption coefficient of $\eta = 2 \times 10^{-6}$, the dynamic gas load is

$$Q_{\text{gas}} = 4.84 \times 10^{-5}\ E\,I \quad [\text{Torr·L/s}] \tag{5-21}$$

In Tables 5-16a and 5-16b, we use Eq. 5-21 to estimate the gas loads in the low- and high-energy rings. Maintaining a pressure of 10 nTorr in the LER requires a total pumping speed of 96,000 L/s at the maximum allowable current of 3 A. To put this requirement into perspective, we note that it is less than one-tenth of the pumping speed (per meter of ring circumference) installed on the ALS ring at LBL [LBL, 1986].

5.2.3.4 Evaluation of Gas Load Profile. To proceed beyond the estimates of the previous section to an engineering design of the vacuum system, it is necessary to specify the actual distribution of radiation along the arc, $\dot{N}(s)$, taking into account the presence of short straight sections between the dipoles. Following the prescription of Alexandrov et al. [1990], we computed the power distributions shown in Figs. 5-32a and 5-32b for the HER and LER, respectively.

Naively, one might think to compute the distributed gas load in the arcs by applying Eq. 5-20 directly to the profiles given in Fig. 5-32, with the adopted value of η. This procedure would, however, neglect the strong variation in η with material exposure. From a typical set of data, such as that reproduced in Fig. 5-33 [Foerster et al., 1990], we observe that, for large exposures, η tends to follow a power-law dependence on dose; that is,

$$\eta \propto (It + t_0)^{-p} \tag{5-22}$$

Table 5-16a. Comparison of vacuum loads in PEP and the PEP-II LER.

Parameter	PEP	PEP-II LER nominal current	PEP-II LER maximum current
Gas load [Torr·L/s/mA]	5.5×10^{-6}	1.6×10^{-7}	1.6×10^{-7}
Total photon gas load [Torr·L/s]	1.1×10^{-3}	3.4×10^{-4}	4.8×10^{-4}
Assumed desorption coefficient, η	1.5×10^{-5}	2.0×10^{-6}	2.0×10^{-6}
Photon gas load [Torr·L/m/s]	1.1×10^{-6}	2.4×10^{-7}	3.3×10^{-7}
Operating pressure required [nTorr]	10	10	10
Thermal desorption coef. [Torr·L/s/cm^2]	1.0×10^{-11}	1.0×10^{-11}	1.0×10^{-11}
Total perimeter of ring [m]	2200	2200	2200
Calculated thermal load [Torr·L/m/s]	2.6×10^{-8}	2.4×10^{-8}	2.4×10^{-8}
Total calculated thermal load [Torr·L/s]	5.8×10^{-5}	5.3×10^{-5}	5.3×10^{-5}
Total gas load [Torr·L/s]	1.2×10^{-3}	3.9×10^{-4}	5.3×10^{-4}

Table 5-16b. Comparison of vacuum loads in PEP and the PEP-II HER.

Parameter	PEP	PEP-II HER nominal current	PEP-II HER maximum current
Gas load [Torr·L/s/mA]	5.5×10^{-6}	4.3×10^{-7}	4.3×10^{-7}
Total photon gas load [Torr·L/s]	1.1×10^{-3}	4.3×10^{-4}	1.3×10^{-3}
Assumed desorption coefficient, η	1.5×10^{-5}	2.0×10^{-6}	2.0×10^{-6}
Photon gas load [Torr·L/m/s]	1.1×10^{-6}	4.1×10^{-7}	1.2×10^{-6}
Operating pressure required [nTorr]	10	5	10
Thermal desorption coef. [Torr·L/s/cm^2]	1.0×10^{-11}	1.0×10^{-11}	1.0×10^{-11}
Total perimeter of ring [m]	2200	2200	2200
Calculated thermal load [Torr·L/m/s]	2.6×10^{-8}	2.5×10^{-8}	2.5×10^{-8}
Total calculated thermal load [Torr·L/s]	5.8×10^{-5}	5.5×10^{-5}	5.5×10^{-5}
Total gas load [Torr·L/s]	1.2×10^{-3}	4.9×10^{-4}	1.4×10^{-3}

where I is the beam current, t is the exposure time, and p is between 0.4 and 0.7 (depending on choice of material and preparation). The constant t_0 is chosen to yield the correct initial value of η. Assuming that $p = 0.6$ for copper, we can compute a local value of $\eta(s)$ along the beamline. Then the gas load at position s is given by a generalization of Eq. 5-20:

$$Q_{\text{gas}}(s) = \eta(s)\dot{N}(s) \tag{5-23}$$

The effect of the differential exposure of the chamber is to level the gas load along the beamline and thus to require more pumping capacity than would be needed if Q_{gas} were a constant multiple of the photon flux. By assuming that the value of η is 2×10^{-6} where $\dot{N}(s)$ assumes its *maximum* value, we compute the gas load along a half-cell of the arc as shown in Fig. 5-34. This gas profile becomes a system specification for the vacuum engineer.

Using the data of Ueda et al. [1990], we have estimated that for copper with an initial desorption rate of 10^{-3} molecules/photon, the sections of the chamber will reach $\eta \approx 2 \times 10^{-6}$ after a photon exposure of about 100 A·hr. Based on the pumping scheme described in Section 5.2.4, the vacuum-conditioning scenario can be computed as a function of the initial photodesorption rate. Such calculations are displayed in Fig. 5-35.

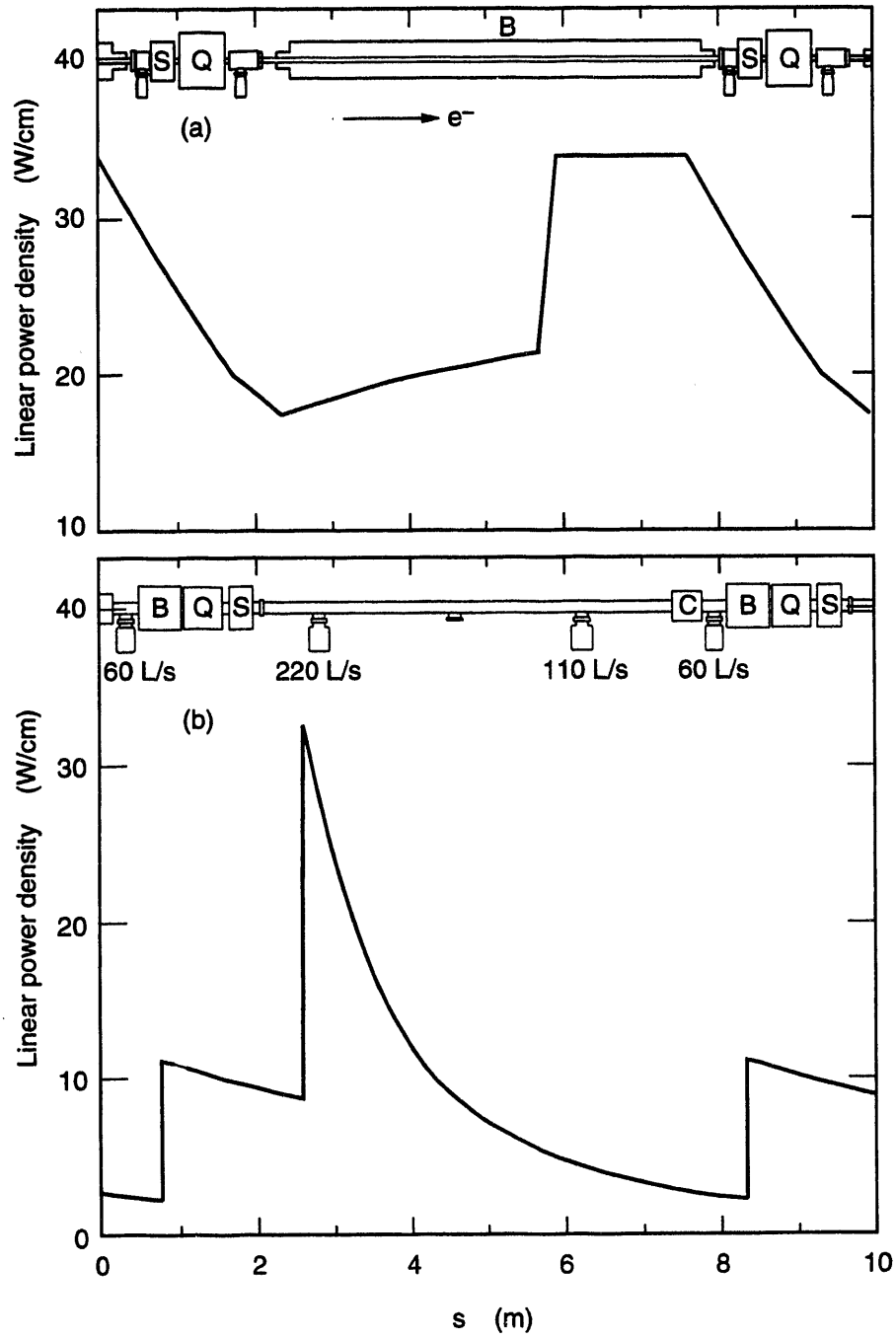

Fig. 5-32. (a) Radiation power distribution along a half-cell of the HER arc at the design current of 0.99 A. (b) Radiation power distribution along a half-cell of the LER arc at the design current of 2.14 A.

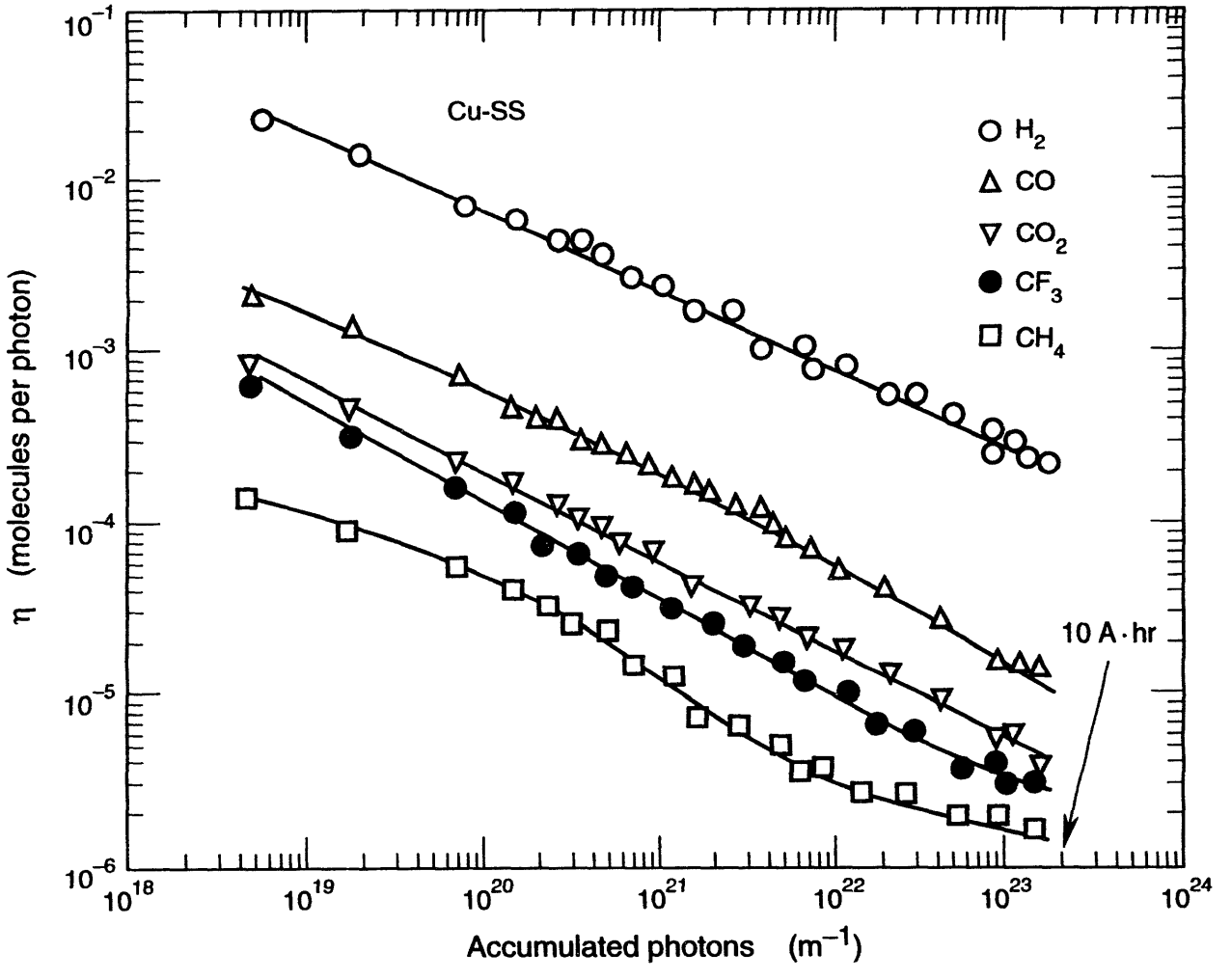

Fig. 5-33. Data from Foerster et al. [1990] showing the variation of the photodesorption coefficient η with material exposure.

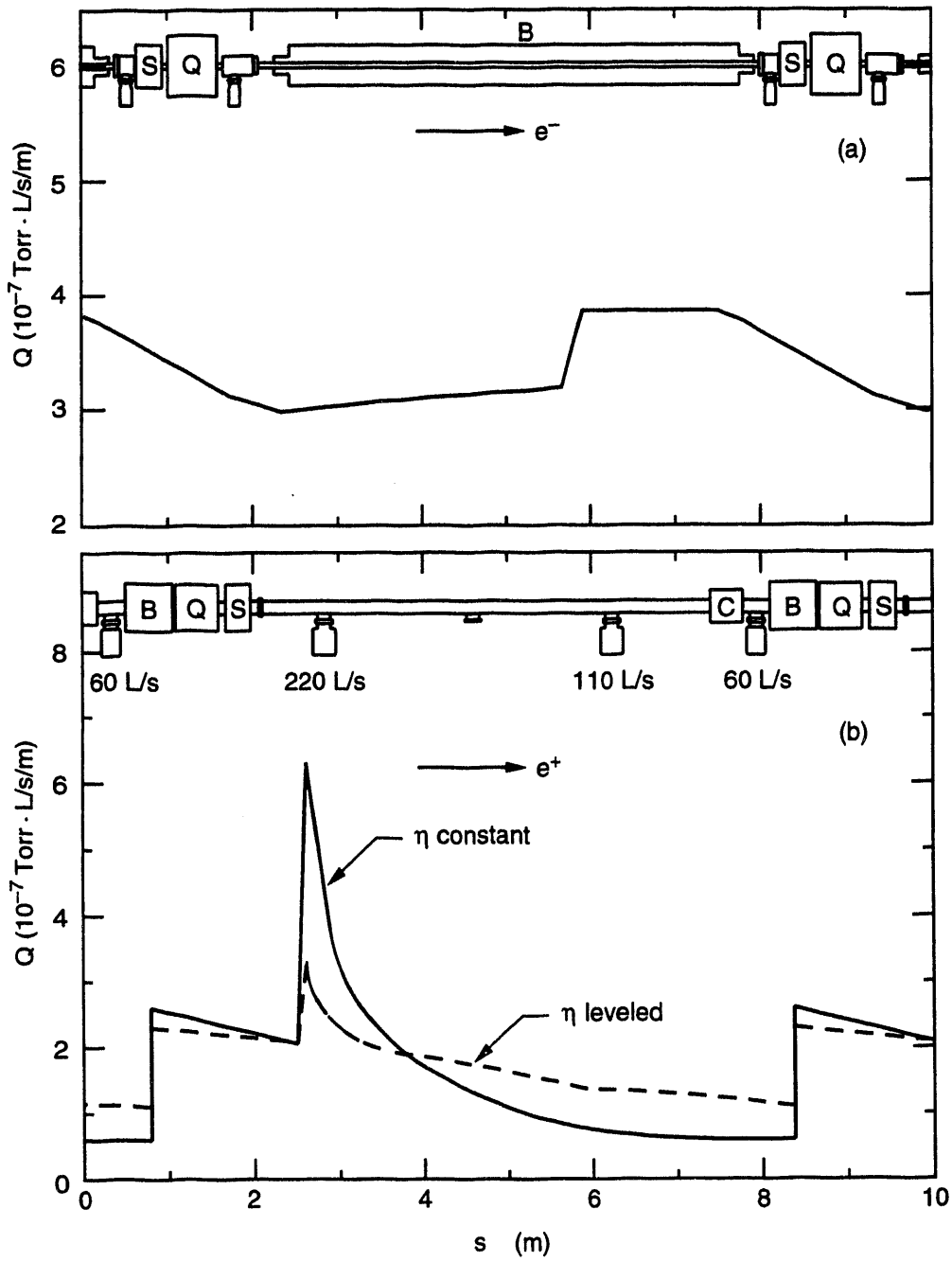

Fig. 5-34. (a) Gas load along a half cell of the arc in the HER at the design current of 0.99 A. The desorption coefficient was assumed to scale with the power profile and was normalized such that $\eta = 2 \times 10^{-6}$ molecules/photon at the location of maximum power. A contribution of 10% from reflected photons was included in the estimate of the gas load. (b) Gas load along an arc in the LER for two assumptions regarding the desorption coefficient: (i) constant value of $\eta = 2 \times 10^{-6}$ molecules/photon (solid line), and (ii) "leveled" photodesorption accounting for the variation in exposure along the arc (dashed line). In the latter case, $\eta = 1 \times 10^{-6}$ at the peak power density.

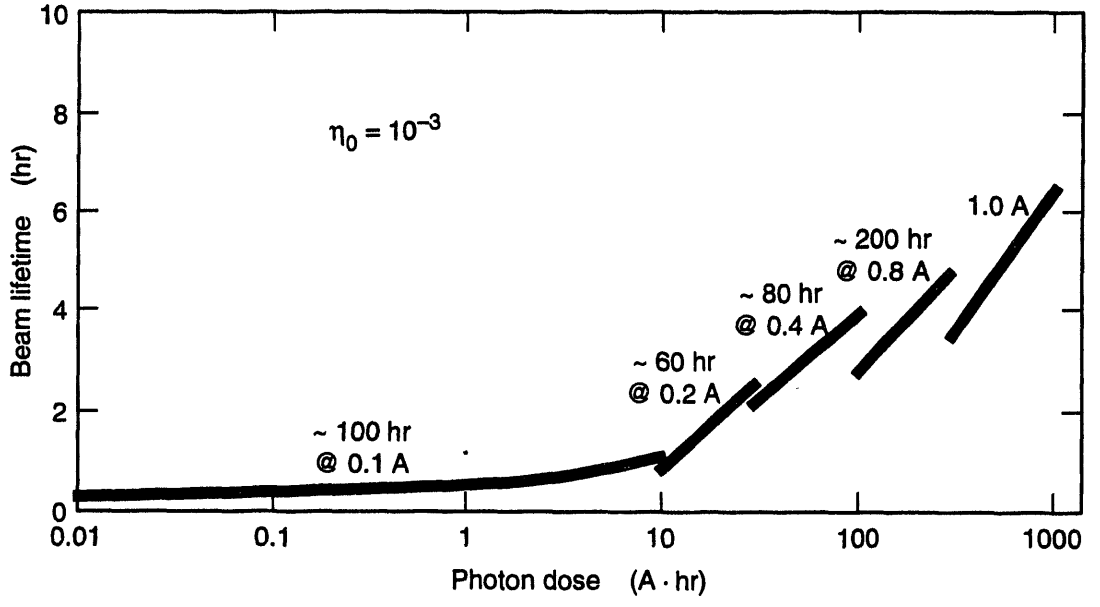

Fig. 5-35. Calculated beam lifetime in the HER as a function of exposure during initial commissioning of the collider.

5.2.3.5 Validation Test Program. The data of Ueda et al., on which the above calculations are based, were taken with a photon beam incident normal to the surface and having $\varepsilon_{crit} = 4.5$ keV. In the HER, the critical energy is nearly 10 keV and photons will strike the surface at a shallow angle. The data of Foerster et al. [1990], though taken at a shallow angle, used a photon beam of $\varepsilon_{crit} = 500$ eV and were not generally carried to such large exposures as to actually observe photodesorption coefficients as low as 10^{-6}. Therefore, our design assumption of $\eta \approx 2 \times 10^{-6}$ must be viewed as an extrapolation of existing experimental data. Although designing the pumping system to handle a photodesorption coefficient of roughly 2×10^{-6} from a copper chamber represents a reasonable extrapolation of that data, it was nonetheless considered prudent to carry out a series of validation experiments using the specific alloys, photon incidence angles, and preparation procedures that will actually be employed in the PEP-II design. Fortunately, appropriate photon sources with which to make measurements on short sections of test chamber are available at several laboratories in the U.S., Europe, and Japan.

Our photodesorption test program is being carried out at the National Synchrotron Light Source (NSLS) in collaboration with H. Halama and C. Foerster of BNL. The experimental setup is located on the U10 beamline of the VUV ring, an area that has previously been used [Foerster et al., 1990] for an extensive series of tests of the photodesorption properties of various materials. The experimental procedures we follow are closely similar to those described in the literature [Foerster et al., 1990; Ueda et al., 1990; Gröbner et al., 1983; Mathewson et al., 1990]. As the U10 beamline includes a built-in swivel point, the exposures can be conducted at the appropriate shallow angle. In our investigations, the test chamber is connected to the beamline through a rectangular duct of calibrated vacuum conductance and is pumped by a calibrated pump with a speed

S_i for the ith molecular species. Exposures are made to white light directly from the source, that is, without employing intervening monochromators or filters. The beam width and height, defined by horizontal and vertical collimators, are adjusted to restrict the area of exposure solely to the test sample. A residual-gas analyzer is used to determine the relative abundance of the principal gas species desorbed (H_2, CH_4, CO, and CO_2).

The primary quantity measured is the specific pressure rise for each molecular species, $\Delta P_i/I$ (averaged over the test chamber), as a function of photon exposure. These data are of most direct relevance to the engineering design of the PEP-II vacuum system. For photons generated over a horizontal angle θ, the average photodesorption of the ith species is

$$\eta_i = \frac{G\, S_i\, (\Delta P_i / I)}{(\dot{N}/I\theta)} \tag{5-24}$$

We began the experimental validation program with a series of measurements of the desorption properties of 1-m copper bars mounted in a stainless-steel test chamber. Copper materials tested included samples of pure copper and of high-purity copper alloys, including one with silver and a dispersion-strengthened copper material. Except for two samples (one of C10100 copper and one of dispersion-strengthened copper material) that were machined before cleaning, all test samples were cleaned and tested with "as received" manufactured surfaces. Also, samples from several vendors having identical materials specifications were tested in order to examine manufacturing differences.

Bar samples of all materials were prepared and baked at LLNL for 48 hours at 200°C prior to shipment to BNL. At NSLS the samples were again baked for 48 hours at 200°C on the beamline prior to testing. In some cases, glow-discharge cleaning was applied when the desorption rate was assumed to be constant, resulting in about a factor of three lower rate of desorption for CO.

A test chamber, fabricated from pure copper (C10100) sheet and baked at 200°C, was also studied. This yielded a desorption coefficient for CO of 2×10^{-6} molecules per photon at 7×10^{23} accumulated photons. In a subsequent run, the vessel was oriented to a new surface and baked as before, but glow-discharge conditioned before the start of the run. As shown in Fig. 5-36, a value of $\eta = 6 \times 10^{-7}$ molecules per photon was achieved for CO at 7×10^{23} accumulated photons. Summing the results for the four measured gases, H_2, CO_2, CO, and CH_4, gave a nitrogen equivalent value of $\eta = 2 \times 10^{-6}$ molecules per photon, thus validating our design value. Additionally, and most importantly, the curves for each species were continuing to drop, indicating that lower values for the desorption coefficient can be achieved.

Initial results of our test program have been presented at vacuum workshops at Cornell (January 1992) and at The Hague [Foerster et al., 1992). Our measurements show that desorption coefficients of $\eta = 10^{-6}$ molecules per photon can be obtained, though not necessarily under exactly the same conditions as would occur at PEP-II.

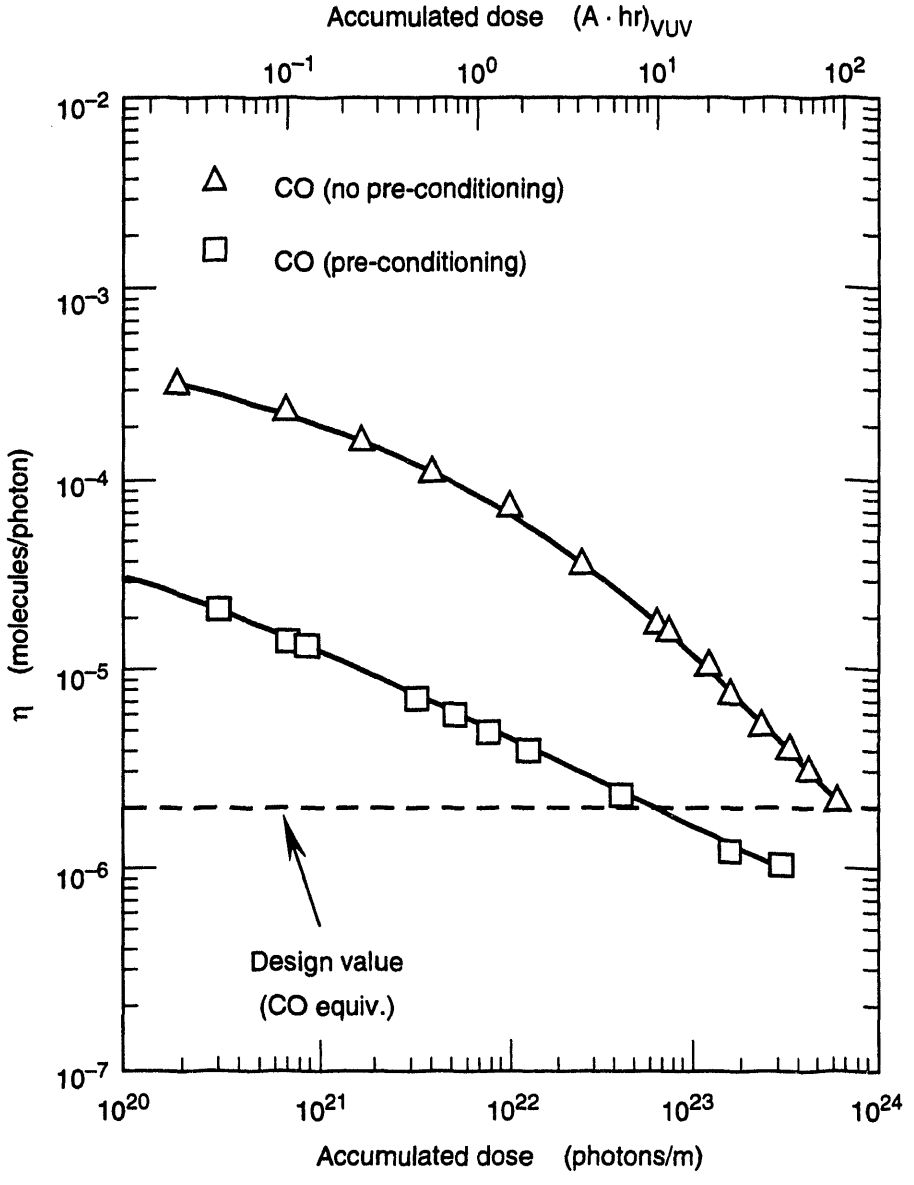

Fig. 5-36. Photodesorption yield measured at NSLS VUV ring for a fabricated copper chamber. The dose in A·hr (based on VUV ring parameters) is shown on the top scale. "Pre-conditioning" refers to performing an argon glow-discharge cleaning prior to exposing the chamber to photons.

Although the VUV ring produces large integrated photon exposures in a relatively short time, the critical energy of the radiation, as mentioned above, is only 500 eV, compared with a critical energy of about 10 keV for the PEP-II HER. For this reason, we plan to measure the dependence of the photodesorption efficiency on photon energy with subsequent exposures of two 3-m copper test chambers on the XRAY ring at NSLS (which provides radiation with a critical energy of 5 keV). One chamber will be fabricated from copper sheet having an octagonal cross section, and a second chamber will be fabricated from the actual extrusion expected to be used in the PEP-II HER.

5.2.3.6 Shielding of Synchrotron Radiation. The PEP-II HER, running at an energy of 10 GeV, generates the synchrotron radiation spectrum shown in Fig. 5-37a. (It has been contemplated that the PEP-II HER might also run at 12 GeV, though this is not part of the present design, in which case it would produce the harder spectrum shown in Fig. 5-37b.) Some of this radiation may escape and deposit energy in the surrounding material. This was originally pointed out during the design of PEP [Nelson et al., 1975] and subsequently verified by measurements both at PEP and at PETRA. Of most concern to PEP-II is magnet insulation. Other materials, such as wire insulation and cooling-water hoses, are even more sensitive to radiation, but they will be more distant from the beam.

Radiation damage to magnets depends strongly on the type of material used in the potting compound. PEP magnets, which will be used for the PEP-II HER, are insulated with an epoxy whose composition is given in Table 5-17. It is estimated that this epoxy

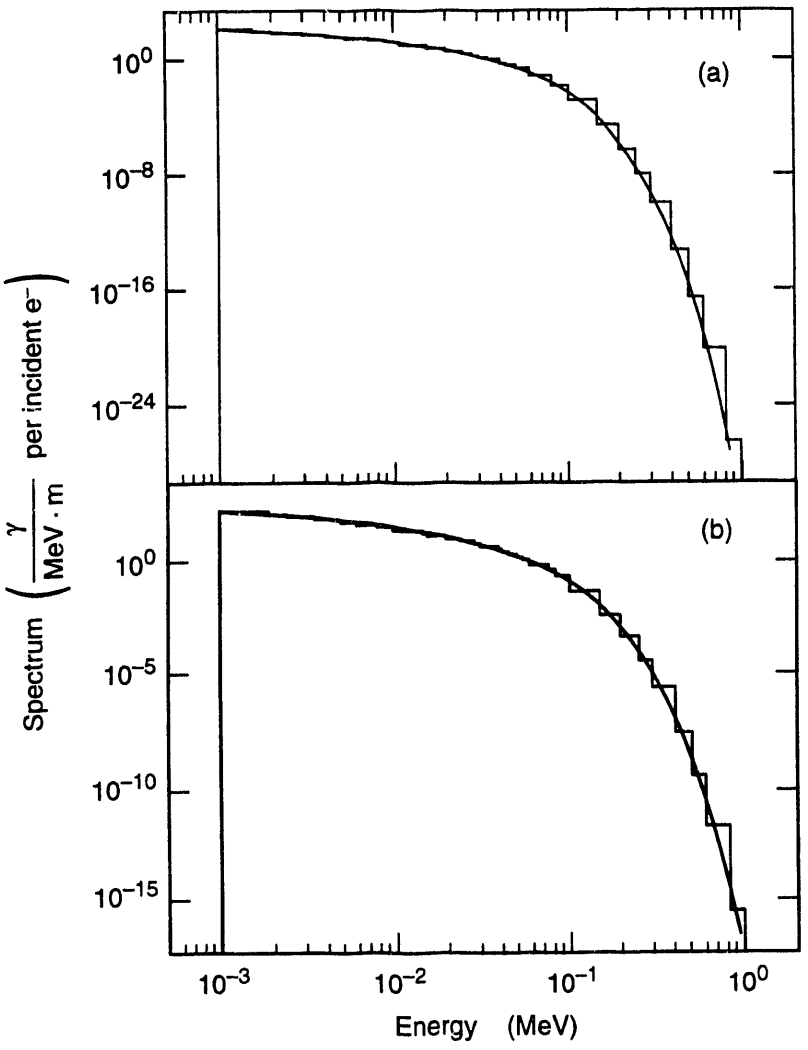

Fig. 5-37. Synchrotron radiation spectrum produced by (a) 10-GeV operation and (b) 12-GeV operation at PEP-II; solid line, analytic; histogram, EGS sampled spectrum.

Table 5-17. Chemical makeup and mass of the epoxy used in the PEP magnets.

Material	Composition	Mass[a] (g)
DER 332—epichlorohydrin + bisphenol A	$C_{21}H_{24}O_4$	851
DER 732—epichlorohydrin-polyglycol	$(C_3H_6O)_n\,C_6H_{10}O_3$	1049
NMA—nadic methyl anhydride	$C_9H_8O_3$	1832
Aluminum oxide	Al_2O_3	4252

[a]Weight fractions of the elements in the epoxy (for EGS4 purposes) are hydrogen, 2.6%; oxygen, 38.4%; carbon, 30.7%; aluminum, 28.3%.

compound should tolerate doses of the order of 10^{10} rads without degradation of its properties. However, the exact damage threshold is not known, so we rely upon other sources to set a criterion. CERN used 3×10^9 rads as the dose criterion for the LEP magnets [CERN 85-02, 1985]. They note that using fiberglass insulation tape gives a factor of ten higher tolerance to radiation damage (up to the 10^{10}-rad region). To be conservative, we have elected to use 3×10^9 rads as a criterion for the PEP-II magnet insulation. Stated another way, the criterion will be 10^8 rads/yr; this should give a magnet lifetime of 30 years or more. (Here, we ignore doses already received by the magnets from PEP running to date. These exposures are small compared with the doses expected from PEP-II operation.)

To estimate the annual radiation dose, we take 3.0 A for a 7200-hr operating year, giving roughly 22,000 A·hr/yr. The radiation strikes the wall at a 23-mrad angle of incidence. The absorbed dose D must remain below 2.0×10^{-19} rads/electron, corresponding to 10^8 rads/yr. This criterion is used when considering output from the program EGS4, which gives synchrotron radiation fluence, energy deposited, or dose (using appropriate conversion factors) per circulating electron. Various user codes built upon EGS4 have been developed specifically to study such problems. These codes all generate the synchrotron radiation spectrum both analytically and from a sampling algorithm, with scoring done in the regions outside the beam pipe. A fluence-to-dose conversion, using the surface dose numbers of Rogers [1984], modified for the SLAC epoxy compound, is performed within the code each time the epoxy region is entered. Details of the calculations can be found in Jenkins et al. [1990].

Calculations are based on the configuration of the present PEP-II HER, assuming (to be conservative) an operating energy of 10 GeV. Only the HER is considered because synchrotron radiation will not penetrate the beam pipe of the LER, which is assumed to operate at an energy of 4 GeV for our estimates.

For this study, the cutoff energies used in the EGS4 simulation were 1 keV (photons) and 1 MeV (electrons). Upper energies for both electrons and photons were 10 MeV,

which is adequate because the spectra are essentially zero above a few MeV for a 10-GeV electron energy. The photon spectrum was sampled uniformly within an energy range from 0.1 ε_{crit} to 10 ε_{crit}. A weight was carried along with each photon (and its progeny) for scoring purposes. The final results were later normalized per circulating beam electron.

The PEP-II HER vacuum chamber geometry is described in Section 5.2.4. The chamber material used for these calculations is copper, and the exact chamber geometry is used.

To summarize the results of our calculations, for typical vacuum chamber configurations, a copper chamber 0.5 cm thick (required for structural reasons) is more than adequate, as shown in Fig. 5-38.

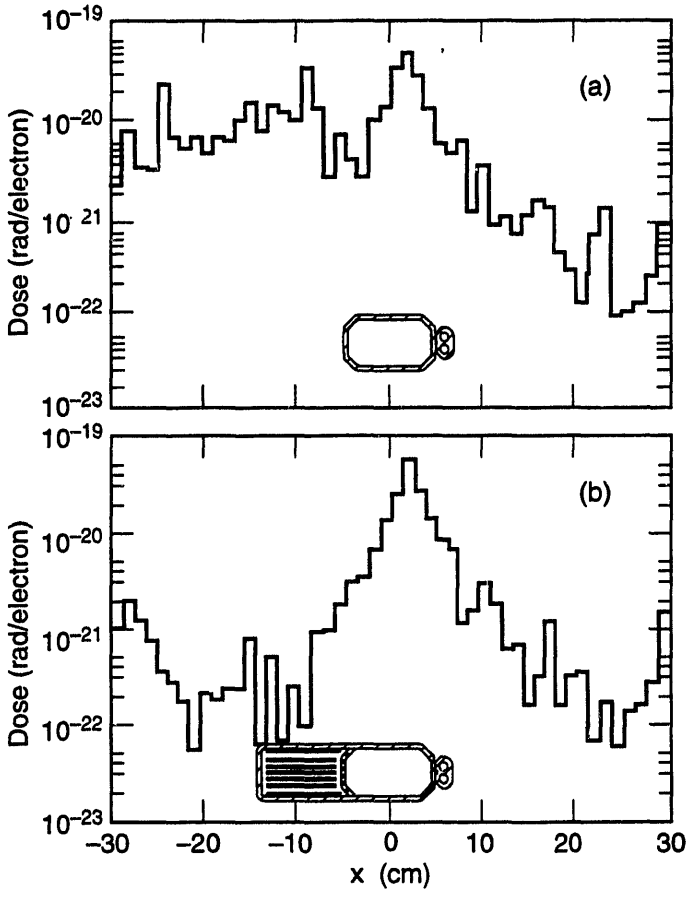

Fig. 5-38. Radiation dose to the magnet windings through two configurations of a 0.5-cm-thick copper vacuum chamber with no liner, computed for 10-GeV operation. The radiation dose limit corresponds to 2 $\times 10^{-19}$ rads/electron, well above the calculated values.

5.2.4 HER Vacuum System

The configuration of the HER is shown schematically in Fig. 5-39. Figure 5-40 shows both the high- and low-energy rings in the tunnel, with the LER positioned above the HER. The circumference of each ring is 2200 m, and both ring geometries have been adjusted to fit in the existing PEP tunnel, as described in Section 4.1.

The vacuum system for the HER is designed to handle the large gas loads anticipated from photon-induced gas desorption and to carry away the large amount of power deposited on the outer chamber wall by the synchrotron radiation. The pressure requirements—quoted as N_2-equivalent values—were described in Section 5.2.1.

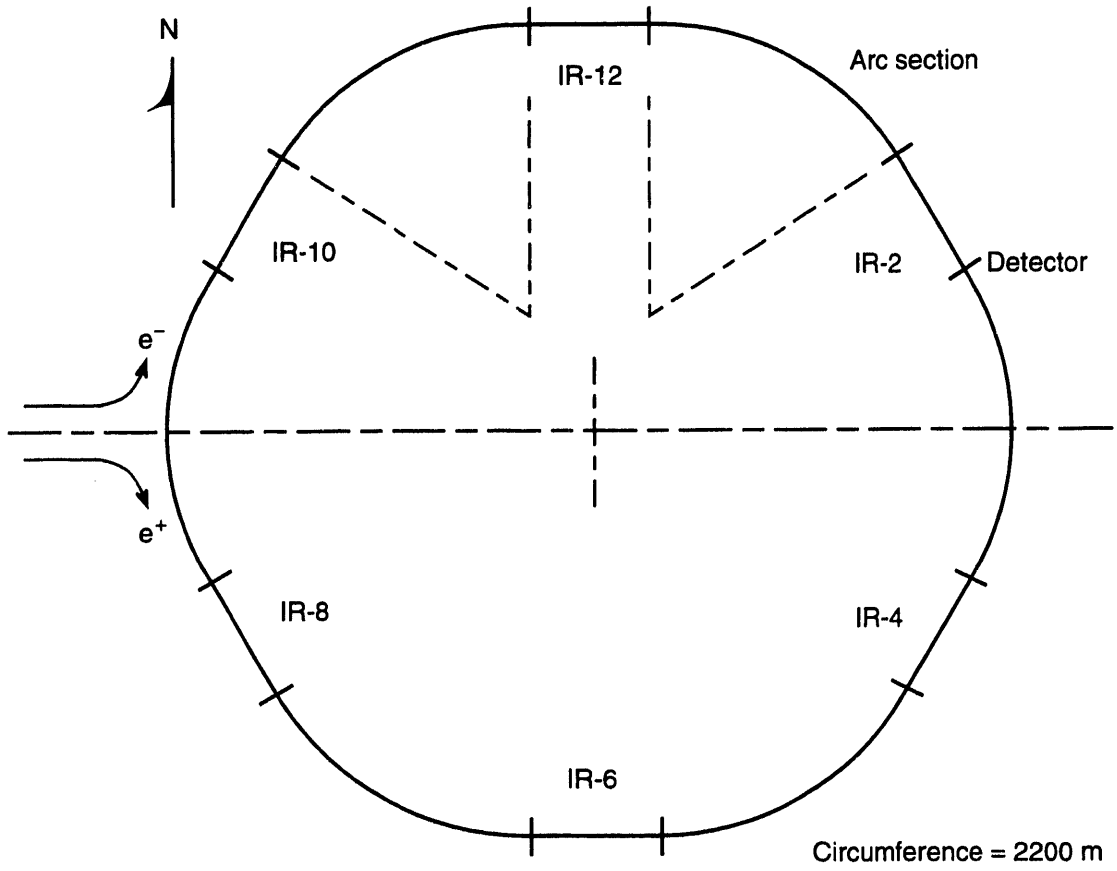

Fig. 5-39. Schematic of the PEP-II storage ring layouts.

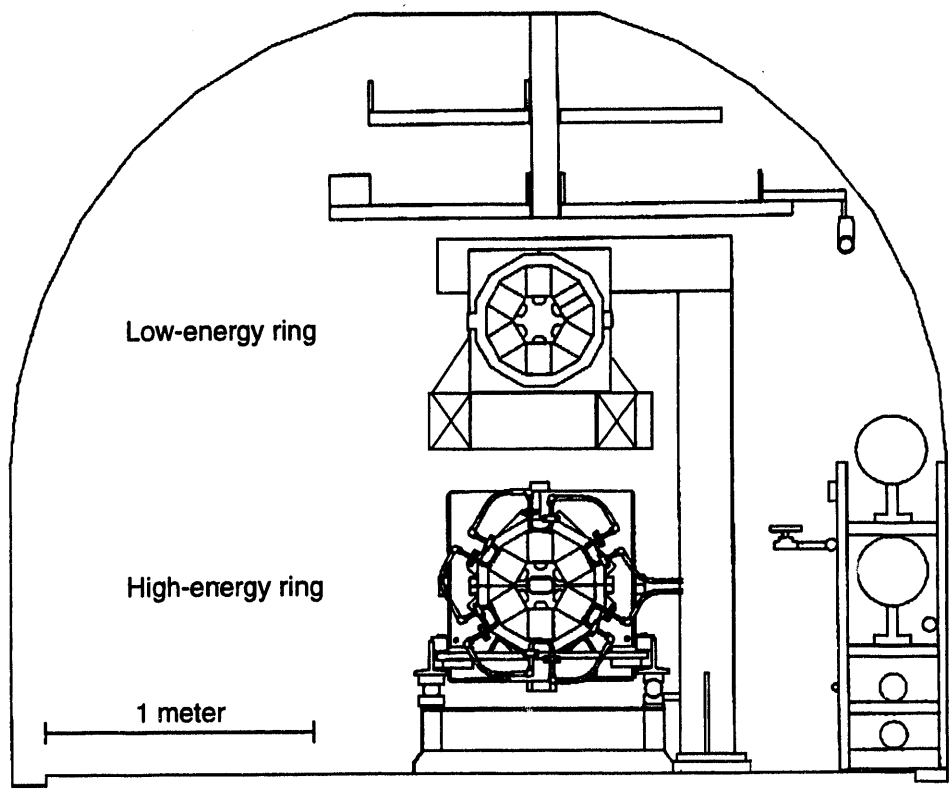

Fig. 5-40. Cross section of the PEP tunnel, showing the arrangement of the high- and low-energy rings of PEP-II.

The HER, illustrated in Fig. 5-41, contains 40 empty FODO cells grouped in five straight sections (the remaining straight section houses the interaction region) and 96 regular FODO cells in the arcs. As discussed above, copper was chosen for the vacuum chamber in the arcs because of its low photon-induced gas desorption coefficient, its high thermal conductivity, and its large absorption coefficient (which obviates the need for adding lead shielding). Vacuum chambers in the straight sections will be fabricated from stainless steel.

5.2.4.1 System Overview.

Arc Sections. Each arc section consists of four dispersion suppressor cells and 12 regular cells, each 15.2 m long, giving an overall arc length of 243.2 m. The magnet arrangement in each of the regular cells consists of a defocusing quadrupole (QD) with sextupole, a dipole, a focusing quadrupole (QF) with sextupole, and finally a second dipole. A beam position monitor (BPM) is located at each QD. The cell vacuum chamber is constructed of four sections of extruded copper in order to facilitate fabrication and assembly in the PEP tunnel. Chamber sections are joined at the ends with 10-in.-diameter, stainless-steel Conflat flanges. A bellows is located near each quadrupole to accommodate thermal expansion during operation and to facilitate installation and servicing.

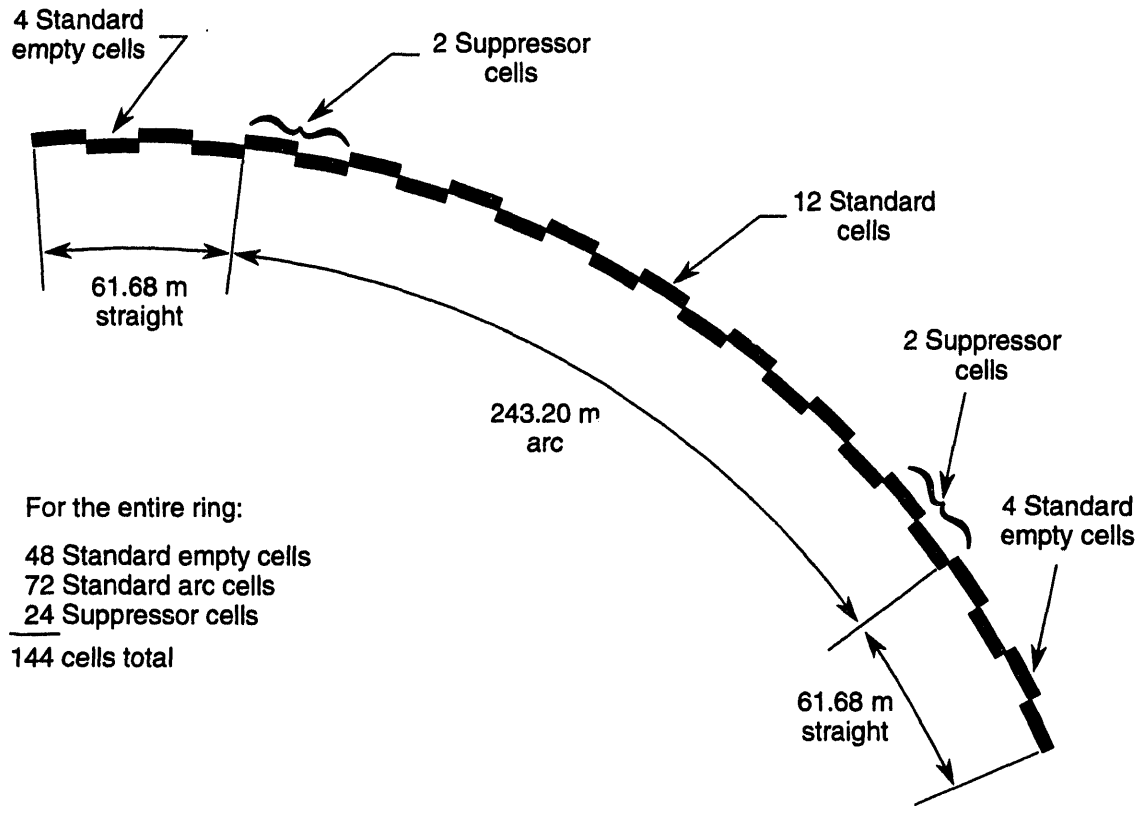

Fig. 5-41. Schematic of one sextant of the PEP-II HER.

Different vacuum chamber cross sections will be used through the dipoles and quadrupoles, as shown in Figs. 5-42 and 5-43. The chamber running through the quadrupoles is octagonal, to maximize conductance. Its outside dimensions are 100 mm wide by 60 mm high, with a uniform wall thickness of 5 mm. The chamber through the dipole magnet includes a passage for distributed ion pumps (DIPs), which is separated from the main beam chamber by a slotted screen. The pumping passage for the DIPs has an inner size of 84 mm wide by 50 mm high. Slots in the screen between pump and beam passages are designed to provide an overall conductance of about 1400 L/s/m. Both the beam tube and the pumping channel will be fabricated from UNS C10100, high-purity, oxygen-free, high-conductivity copper. A double-holed cooling bar attached to the outer wall of the beam tube carries away the heat produced by synchrotron radiation hitting the chamber wall. The bar will be fabricated from UNS C10300, an oxygen-free copper alloy having a thermal conductivity of 93% International Annealed Copper Standard. Discrete ("lumped") ion pumps are provided at each of the pumping plenums adjacent to the quadrupoles, as shown in Fig. 5-44; pressure gauges and pumpdown connections are also located there.

Should the need arise, 180°C water can be circulated through the cooling bar, to provide in situ baking to 150°C without opening the chambers. The additional thermal expansion will be accommodated by the bellows. Bakeout will reduce the initial outgassing rate and thus allow for base pressures in the 0.5-nTorr range, if needed.

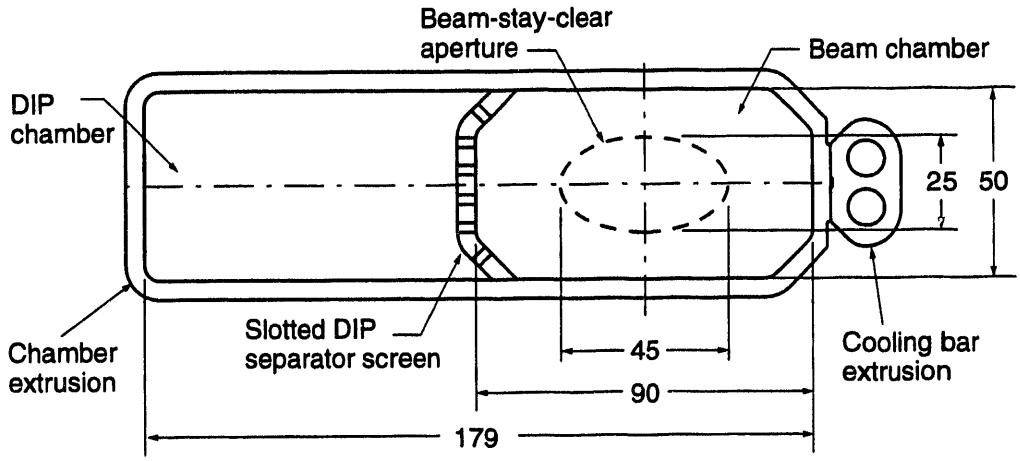

Fig. 5-42. HER vacuum chamber cross section at a dipole; dimensions are in millimeters.

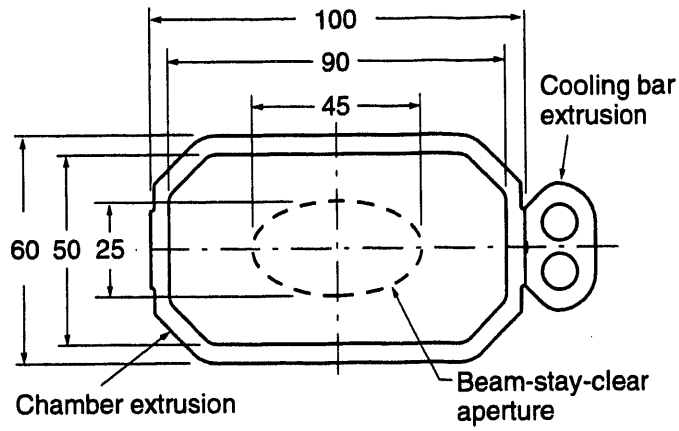

Fig. 5-43. HER vacuum chamber cross section at a quadrupole ; dimensions are in millimeters.

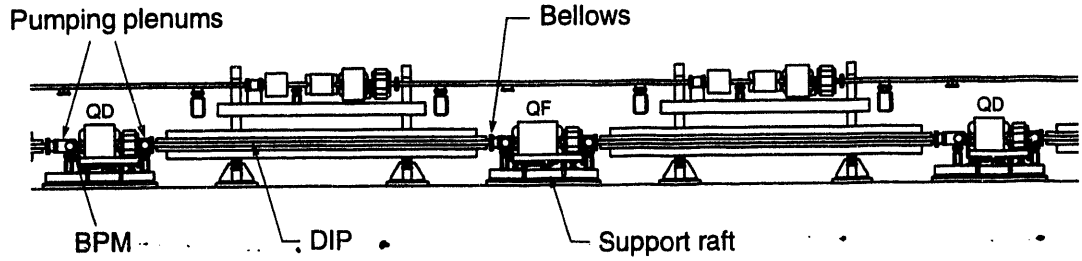

Fig. 5-44. Typical HER arc cell, with DIPs in the dipole magnet and lumped ion pumps in the pumping plenums on either side of the quadrupoles.

Straight Sections. A standard cell in the straight sections is 15.419 m in length, and contains no dipoles. The vacuum pipe is a made from 3.75-in. OD 316L stainless-steel tubing, sized to clear the 100-mm bore of the quadrupole magnets. Because there are no dipole magnets and hence no distributed ion pumps, larger lumped ion pumps are used to produce the 3-nTorr average pressure required. A diagram of a straight-section cell is shown in Fig. 5-45.

Various straight sections contain the injection septum, RF cavities, beam collimators, and optical monitors. Each special component will have its own individual requirements for the vacuum system, and each will require a custom interface.

In situ baking, if needed, will be accomplished using resistive heaters and insulation wrapped around the stainless-steel beam pipe. This can be done without disturbing the vacuum chamber integrity.

5.2.4.2 Analysis.

Thermal Analysis. As discussed in Section 5.2.3.1, one of the main challenges in designing the vacuum system is to adequately handle the high thermal flux densities incident on the vacuum chamber outer wall due to the synchrotron radiation. The peak linear flux in the HER reaches 102 W/cm, which corresponds to a flux density of 2.3 kW/cm^2. Finite-element analysis of a dipole chamber subjected to this high flux shows that the peak local temperature reaches 68°C above the cooling-water temperature. Furthermore, the average temperature of the entire chamber reaches about 25°C above the cooling-water temperature, as shown in Fig 5-46a. This 43°C difference between peak and average chamber temperature produces a 12,000-psi compressive stress in the region near the incident radiation. (The stress arises because the local hot spot is trying to expand but is forced to follow the bulk expansion of the cooler chamber.) Figure 5-46b shows this high axial compressive stress. Note that this stress arises every time the HER is filled with a 3-A beam. We assume a worst-case scenario for thermal analysis of 10,000 maximum-current fills over the life of the machine. The chamber is subjected to cyclic fatigue loading from the stress. The effect of this cyclic loading on the chamber depends largely on the temper of the copper and the residual stresses in the chamber.

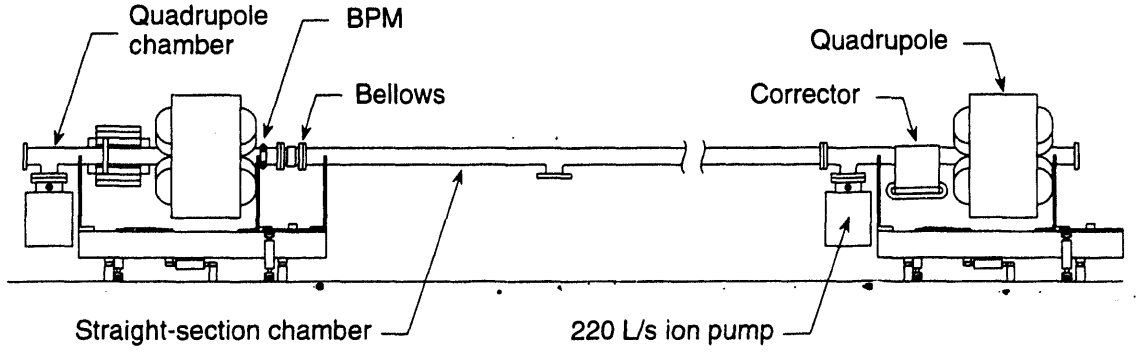

Fig. 5-45. Side view of HER straight-section vacuum chamber.

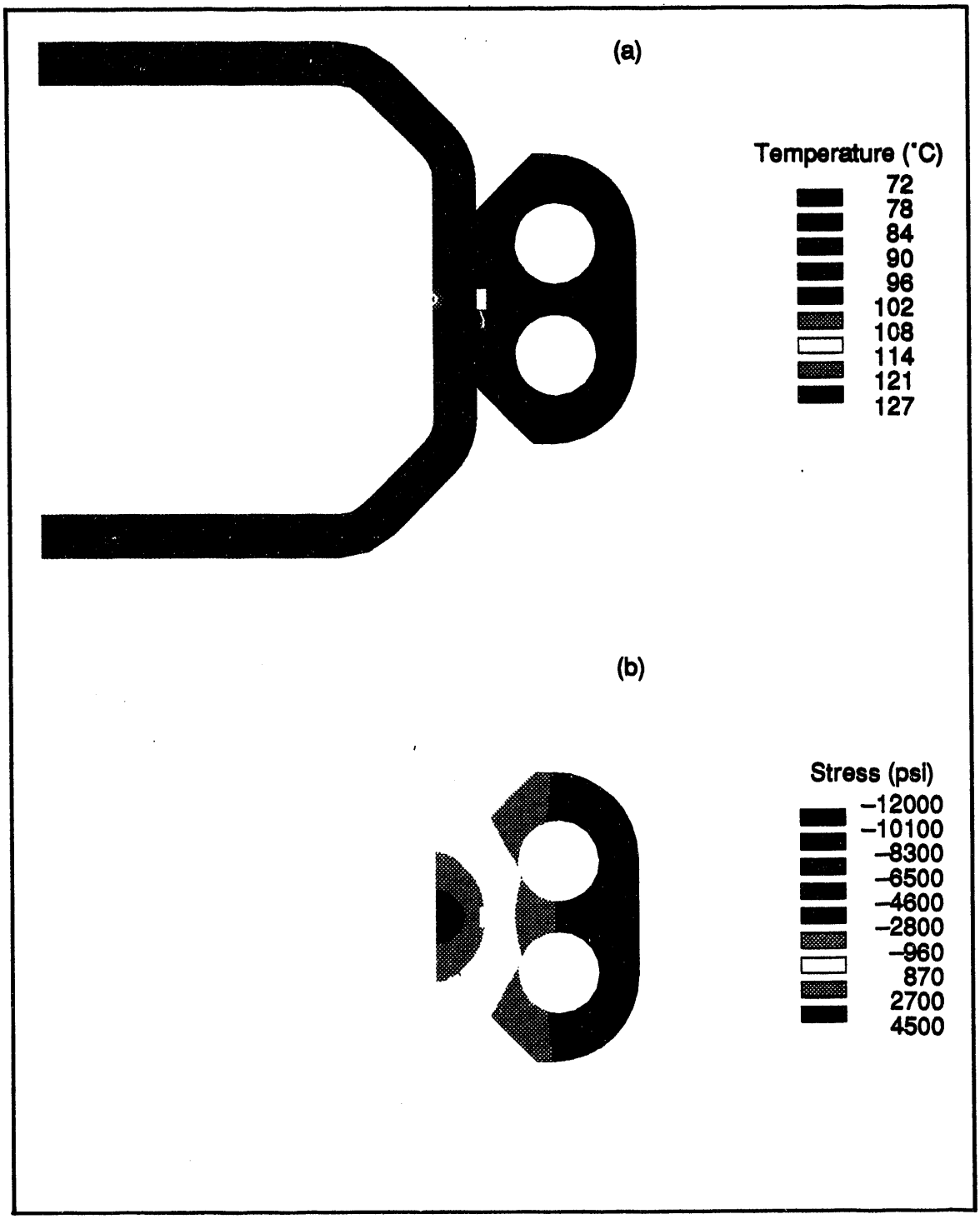

Fig 5-46. (a) Temperature distribution and (b) axial stress distribution in heated region of PEP-II HER bending magnet vacuum chamber with cooling bar, for an incident linear power density of P_L = 102 W/cm. The bulk temperature of the cooling water was 59 °C, which corresponds to the maximum expected outlet temperature.

As detailed in Section 5.2.4.3, the chambers will be extruded and drawn to a half-hard temper, the cooling bar will be electron-beam welded in place, then the chamber will be bent to the correct radius. Manufacturing data for the drawn, half-hard-temper C10100 copper shows that, under a cyclic compressive loading of 12,000 psi, the material will not yield and will not develop fatigue-related cracking for at least 10^8 cycles. Furthermore, as long as the stresses remain compressive, any cracks will not propagate through the material. Therefore, to avoid potential fatigue cracking, further assembly processes must neither remove the half-hard temper of the original drawn material, nor produce additional stresses in the region of high thermal stress. Electron-beam welding tests have shown that, indeed, temper is not affected in the high-stress zone, and thus that the cyclic thermal loading can be absorbed by the copper chamber.

The above analysis assumes a high rate of heat convection to the cooling water. To produce the convection, water will flow through each passage at 3.5 gpm, or 10 ft/s. Water inlet temperature is 30°C, and the total temperature rise through a half-cell water circuit is 29°C. By routing the cooling water in the chambers to take advantage of the variable heating from the synchrotron radiation, we maintain the peak chamber temperature below 118°C, which minimizes any loss of strength associated with elevated temperatures.

Bakeout Heat Transfer. If the HER chambers must be baked in situ to reduce the operating vacuum pressure, 180°C water will be run through the cooling channels. Finite-difference analysis of the natural convection from the heated chamber shows that, with no insulation at all, the chamber loses only 5 kW per half-cell, and the minimum wall temperature is 165°C. Water flow rate and velocity for the bakeout are the same as for normal operation.

Thermal Expansion. During operation and bakeout, the arc chambers expand due to the increased temperature. Because the dipole chambers are bent in an arc, this expansion is not exactly in a line, but has some lateral component. Furthermore, during an operation the asymmetric temperature distribution across the dipole chamber, shown above (Fig. 5-46a) increases the radius of curvature by 4%, producing an additional lateral offset of the chamber. Table 5-18 details these values.

Two features are included in the vacuum system to accommodate these dimensional changes. First, a bellows is added every half-cell to allow the neighboring chambers to expand. The bellows is designed to compress as the chambers expand, even during an in

Table 5-18. Thermal expansion of HER arc half-cell.

	Operation	Bakeout
Expansion along beamline [mm]	3.6	16.9
Lateral offset [mm]	0.1	0.32
Rotation at bellows [mrad]	0.01	0.06

situ bakeout, so no special procedures are needed to prepare for bakeout expansion. They also allow for the (very small) rotation of the chambers because the expansion occurs around a large radius. Second, the chamber supports are designed to flex as the chambers expand. The supports carry the weight and seismic loads of the chambers, while still allowing adequate flexure along the beamline.

Vacuum Analysis. The main issue in designing a pumping scheme for the HER arcs is the high, variable gas load produced by the synchrotron radiation. The pumps must adequately pump this gas load through relatively low-conductance beam pipes. We have adopted a design based entirely on sputter-ion pumps. These provide sufficient pumping speed to attain the required pressures and are very reliable, causing minimal operational interference. Unlike non-evaporable getters (NEGs) or titanium sublimation pumps (TSPs), there is no need for regeneration or filament replacement.

Distributed ion pumps (DIPs) are installed in the dipole vacuum chambers to provide the bulk of the pumping needed. Detailed calculations have been completed to optimize the DIP design to provide maximum pumping speed in the 0.18-T field of the dipole magnets. Furthermore, lumped differential ion (DI) pumps are installed on either side of the quadrupole to pump the quadrupole chamber and to serve as holding pumps when the beam and DIPs are off. To improve conductance to these pumps, a plenum surrounds the beam pipe in this region. The plenum is slotted to provide conductance while minimizing changes in the beam pipe cross section.

Analysis of the vacuum system was carried out using a finite-volume analysis program developed for this application. Variable gas loads, chamber conductances, and pump sizes were all included in the model to ensure that the results adequately simulated the system. The calculation assumes a minimum photodesorption coefficient, scaled with incident power, of 2×10^{-6} molecules per photon. As expected, the results show that the average pressure is strongly dependent on the pumping speed of the DIPs. Furthermore, the quadrupole chamber pressure profile is limited by the conductance of the chamber cross section. Figure 5-47 shows the calculated pressure profile for a half-cell with an optimized DIP pumping speed of 165 L/s/m and two 60-L/s differential ion pumps, one at each end of the quadrupole chamber.

Using the above-mentioned pumping configuration, the average pressure for a half-cell is 8.8 nTorr at 3 A, which is slightly below the design value of 10 nTorr for the arcs. This value provides some margin if the DIP speed turns out to be somewhat lower in practice or if the chambers produce more gas than expected. Also, each pump plenum has sufficient conductance to accommodate two additional differential ion pumps, which could make up for reduced DIP pumping or increased gas load. Table 5-19 shows the pumping configurations we are considering, along with the average pressure while running at the nominal 0.99-A beam current and the average holding pressure. We can implement either of these, depending on actual running conditions.

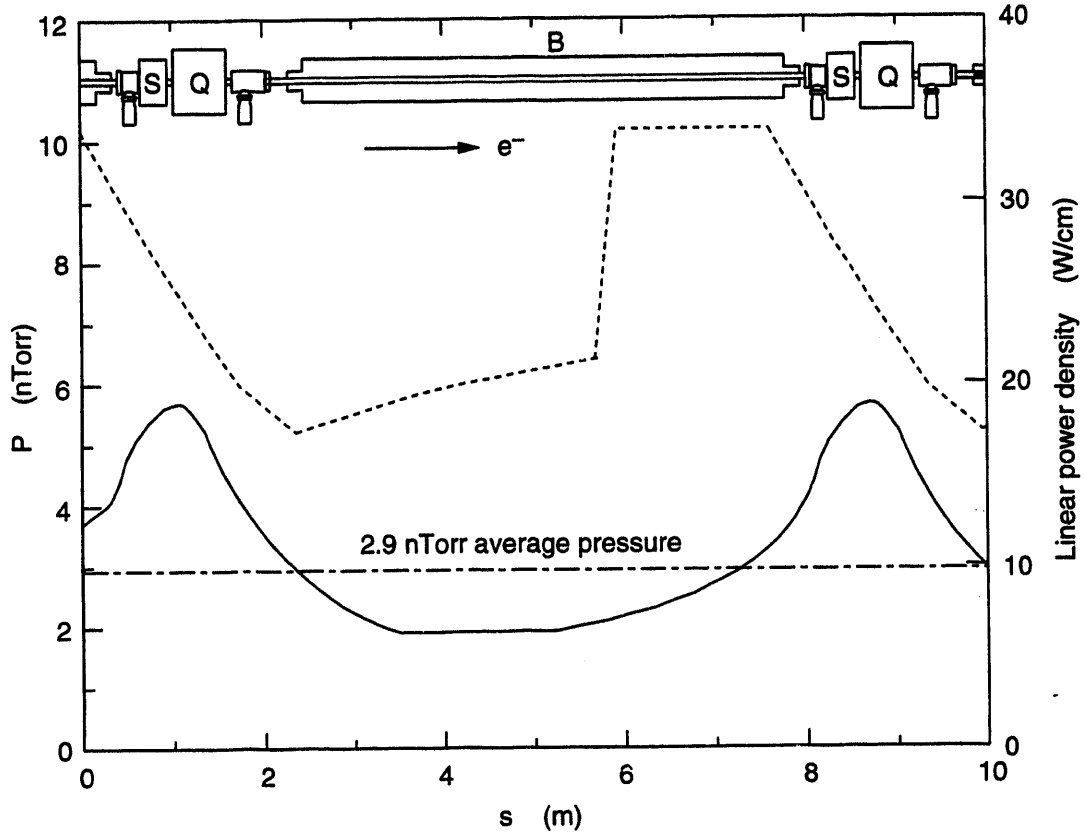

Fig 5-47. Pressure profile for an HER arc half-cell (solid line), shown with power distribution (dashed line).

Table 5-19. Vacuum pumping scenarios for HER arcs at nominal 0.99-A beam current.

	Design configuration	Alternative configuration[a]
Beam current [A]	1.0	1.0
DIP speed [L/s/m]	165	120
Upstream pump speed [L/s]	60	110
Downstream pump speed [L/s]	60	60
Running pressure [nTorr]	2.9	3.4
Holding pressure[b] [nTorr]	1.3	1.1

[a] Alternative is based on a more pessimistic estimate of DIP speed.

[b] With DIPs off.

5.2.4.3 Arc Chamber Design.

Dipole Chamber. The dipole chamber (Fig. 5-48) consists of an extruded copper chamber and cooling bar, the DIPs, a screen that separates the beam and DIP channels, and two Conflat-type end flanges. The chamber will be extruded in full lengths, with no press stops, from UNS C10100 copper, while the cooling bar will be extruded from UNS C10300 copper. These are both drawn to achieve their final shape and to produce a minimum half-hard temper. The pieces are then cleaned and electron-beam welded together. After welding, the subassembly is stretch-formed to its correct radius, then the ends are machined and the part recleaned. The slots in the separator screen are machined, then the screen is bent to its correct cross section and cleaned. The screen is then pulled into the chamber and electron-beam welded into place. Meanwhile, the DIP modules have been fabricated, cleaned, and assembled. They are pulled into the dipole chamber and connected. Finally, the end flanges are TIG-brazed onto the ends of the chamber.

This optimized fabrication sequence is the result of significant design, analysis, and testing of each of the components and fabrication processes. This is summarized in the descriptions below.

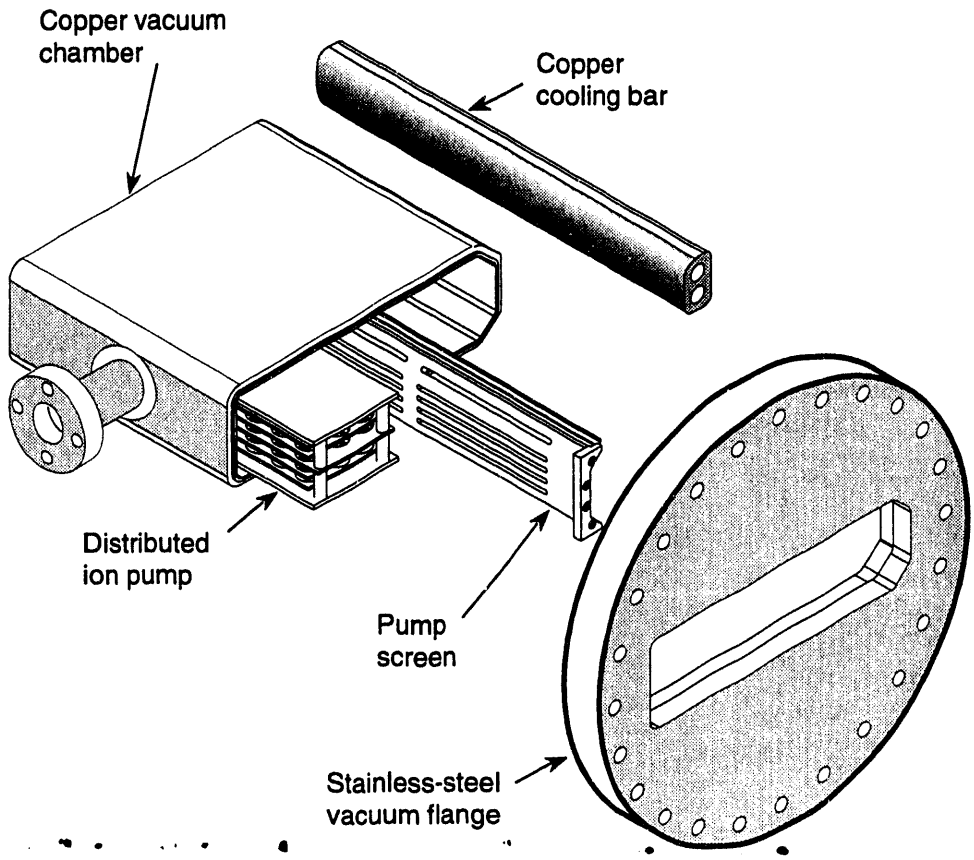

Fig. 5-48. Isometric view of the end of a typical HER arc dipole chamber.

Chamber Extruding. Although various bent sheet-metal fabrication designs were investigated, extrusion is the preferred fabrication method. A one-piece chamber extrusion eliminates all longitudinal vacuum welds, which affords a more accurate and dependable chamber. Three extrusion cross sections will be used (see Fig. 5-49), one each for the dipole and quadrupole chambers and a third for the cooling bar that runs along the outside radius of both chambers. A curved screen will be pulled into the dipole chamber to separate the beam and DIP passages. (If aluminum were used instead of copper, the cooling passages and separator screen could all be extruded into one complex, multiport extrusion. However, copper is needed for the arc chambers to provide the required shielding and low photodesorption coefficient. Because of machine capacity limitations and the flow characteristics of copper during the extrusion process, such a multihole extrusion cannot be fabricated.) We have worked closely with copper extruders to optimize the extrusion shapes and tolerances to ensure the best possible results. Furthermore, prototype chambers have been extruded and delivered to SLAC for

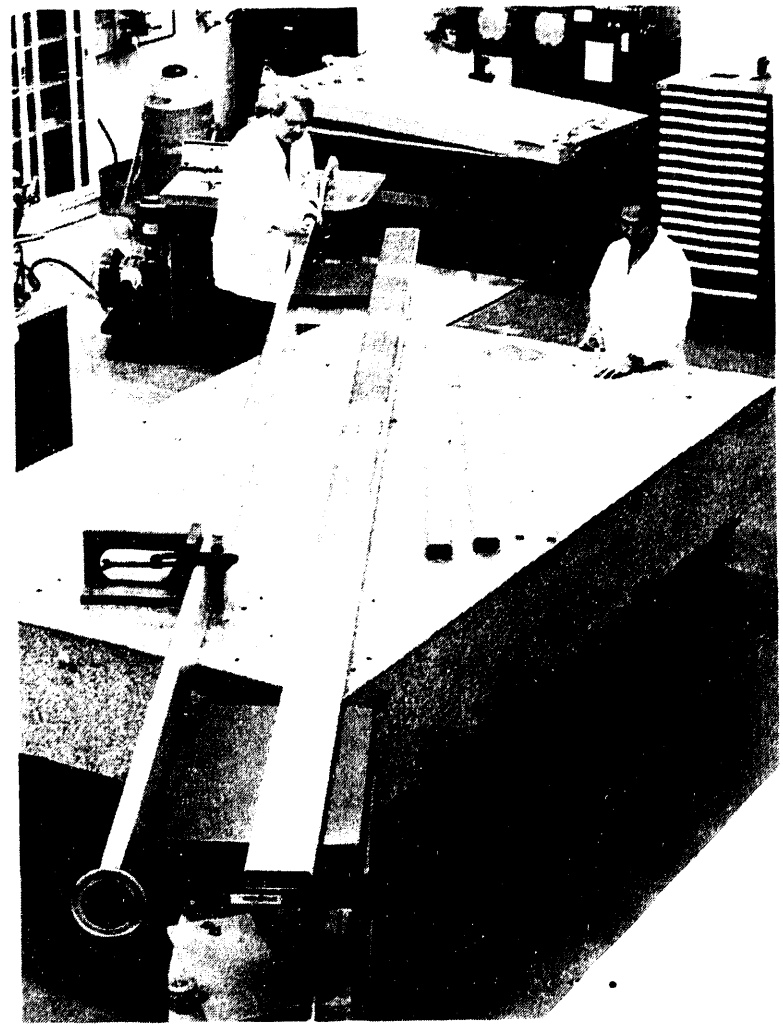

Fig 5-49. Photograph of prototype dipole chamber (long) and quadrupole chamber (short) extrusions being dimensionally inspected at SLAC.

analysis and testing. Recent dimensional, chemical, and material testing has shown that these extrusions exceed our requirements for dimensional stability, material quality, and physical properties. We are currently setting up a photodesorption test at BNL to confirm the manufacturer's data, as well as our earlier test data on similar material.

Electron-Beam Welding. As noted above, the selection of C10100 copper as the material for the arc vacuum chamber makes it necessary to join the cooling bar and DIP separator screen to the beam chamber. The joining process must minimize the heat input to the chamber, be compatible with ultrahigh-vacuum (UHV) standards, and be economically feasible. Several methods were considered to accomplish this task, including bolting, gluing, soldering, brazing, and welding. Low-temperature soldering, brazing, and electron-beam welding were further evaluated as viable options. However, low-temperature solders cannot withstand the thermal stresses, are brittle at room temperature, and outgas unacceptably in UHV systems. Although brazing produces joint geometries that are attractive for UHV applications, the elevated temperature that must be employed destroys the temper and strength of the material being brazed. As detailed in Section 5.2.4.2 above, stress analysis shows that the surface where synchrotron radiation is incident (and some distance into the wall) must be kept half-hard so as to be able to withstand the compressive stress caused by the synchrotron radiation.

Electron-beam joining satisfies all application criteria of cleanliness, strength, and low heat input. Therefore, we will use two electron-beam welds (in each case) to join the cooling bar and the DIP screen to the chamber—one weld from above and one from below. The cooling-bar welds are kept as shallow and narrow as possible, with a void at the cooling-bar midplane that is not welded. Analysis shows that the small void does not affect the temperature distribution significantly, yet provides a needed weld-spike gas vent at the root of the weld, which reduces weld porosity. The cooling bars are chamfered to reduce the required weld depth. The reduction in contact area actually spreads out and reduces the peak stresses by averaging the high temperature over a larger area. This weld joint design and the electron-beam welding procedure were further optimized by test-welding short beam chambers. The chambers were then sectioned and examined to obtain hardness, structural, and quality data. Figure 5-50 shows a micrograph of a typical weld joint. Test results show minimal annealing near the heat-affected zone next to the weld recast, retention of the half-hard temper in the areas of synchrotron radiation incidence, low levels of porosity, and a good weld-depth-to-width ratio. The remaining two-thirds (3.3 mm) of the wall thickness is unaffected by the weld, retaining its half-hard temper and strength.

For the DIP screen welds, the electron beam will be defocused to produce a weld that fuses 75% of the screen width and that is just deep enough to provide good attachment. Testing has shown that this method eliminates the possibility of missing the screen with the welder beam, and thus causing vacuum leaks.

These tests have shown that the selection of the electron-beam welding process will reliably join the chamber, cooling bar, and separator screen together, and maintain the material properties needed.

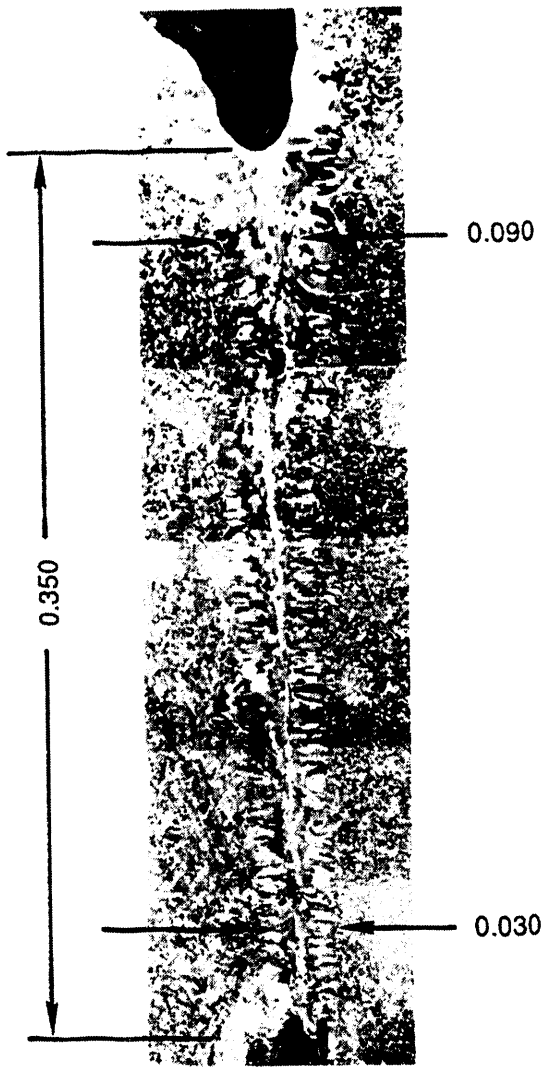

Fig. 5-50. Micrograph of electron-beam weld of the cooling bar to the dipole chamber.

Stretch Forming. The dipole chambers must be bent to conform to the nominal 165-m radius of the beam orbit. At this radius, the angle of incidence for synchrotron radiation on the bend chamber wall is 23 mrad. The thermal analysis discussed above (Section 5.2.4.2) indicates that, in order to stay below PEP-II limits for power density at maximum current, the chambers must be bent sufficiently uniformly that the angle of incidence does not exceed 26 mrad; this determines the tolerance on the bending radius.

We have successfully tested two bending techniques, use of a pin press and use of a stretch-forming apparatus, with 2.4-m test chambers. One chamber was bent to a 36.6-m radius using the pin press with long shoes. The technique gives a satisfactory bend but is tedious and time consuming, and results in a series of small "kinks" that could potentially exceed the maximum allowable incidence-angle criterion. This chamber was

subsequently baked at 200°C and exhibited no noticeable relaxation of curvature or other dimensional changes.

Two additional chambers were bent by stretch forming. In this technique, the chambers are stretched axially to their yield point and then, while in the yield condition, are bent over a form of the appropriate radius. Stretch forming has several advantages. It is fast, it produces a smooth continuous bend, and (because the stretching raises the stress in the entire chamber to its yield point) it results in the lowest possible residual stresses after fabrication is completed. Furthermore, it actually releases the residual stresses left in the chamber from the welding. This, in turn, ensures the lowest operating thermal stresses. Clearly, this method is superior for our application. We have designed and built a stretch-forming apparatus (see Fig. 5-51) and have used it to bend the first 6-m-long prototype extruded chamber to well within the required tolerance.

Cusil TIG Brazing. The dipole and quadrupole chambers will be connected by Conflat-type vacuum flanges. The flanges will be fabricated from 316LN stainless steel and will be joined to the C10100 copper chambers. Typically, the dissimilar joint would be made using an intermediate copper piece that is brazed to the stainless-steel flange and then gas-tungsten arc-welded (GTAW) to the copper chamber. However, this involves a separate piece, an expensive braze joint, and an additional vacuum joint. An alternative

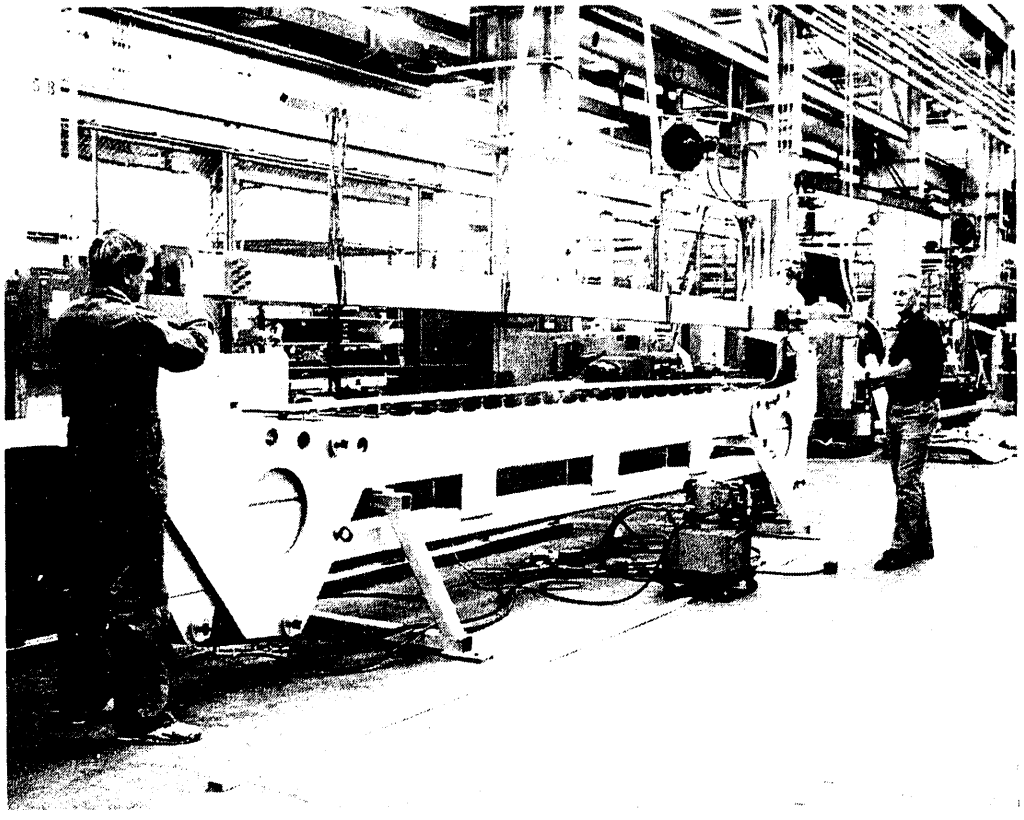

Fig. 5-51. Photograph of HER dipole chamber during stretch-forming at SLAC.

joining method is a single dissimilar-metal weld. Two welding configurations are being investigated.

The first configuration is a two-pass GTAW weld. The first pass deposits a nickel weld bead onto the copper chamber wall, then the second pass overlays this with Inconel wire. This process produces extremely strong, ductile welds, but requires significant heating of both pieces, with the associated thermal distortion. Also, the weld quality is sensitive to variations in the relative dilution of the various base metals.

The second weld configuration is technically a braze joint, which uses a tungsten inert-gas (TIG) torch as a heat source. The TIG torch heats, but does not melt, the two base metals, then Cusil braze wire is deposited into the joint. Preliminary weld tests show that this TIG-braze is stronger than the copper base metal, yet as ductile as the stainless steel. UHV vacuum-tight welds have been made on prototype flange joints and have survived high-temperature cycling under vacuum (see Fig 5-52). Ongoing tests are now quantifying weld-joint strength at room temperature and at 200°C.

In parallel with the welding research, finite-element stress analysis is being used to optimize the weld-joint geometry and location. The weld joint brings together not only dissimilar materials, but dissimilar shapes as well. This produces stress concentrations near the corners of the rectangular beam chamber. Initial finite-element analysis results show that the local stress is high, but manageable. Further analysis and joint design optimization is now under way.

Cleaning. To achieve the desired vacuum environment for the beam, cleanliness during all phases of the fabrication process is of paramount concern. Care must be taken to ensure that no fabrication process contaminates vacuum components after cleaning. Weld joints and machining processes must all be designed to produce cleanable parts that reflect good vacuum design practices.

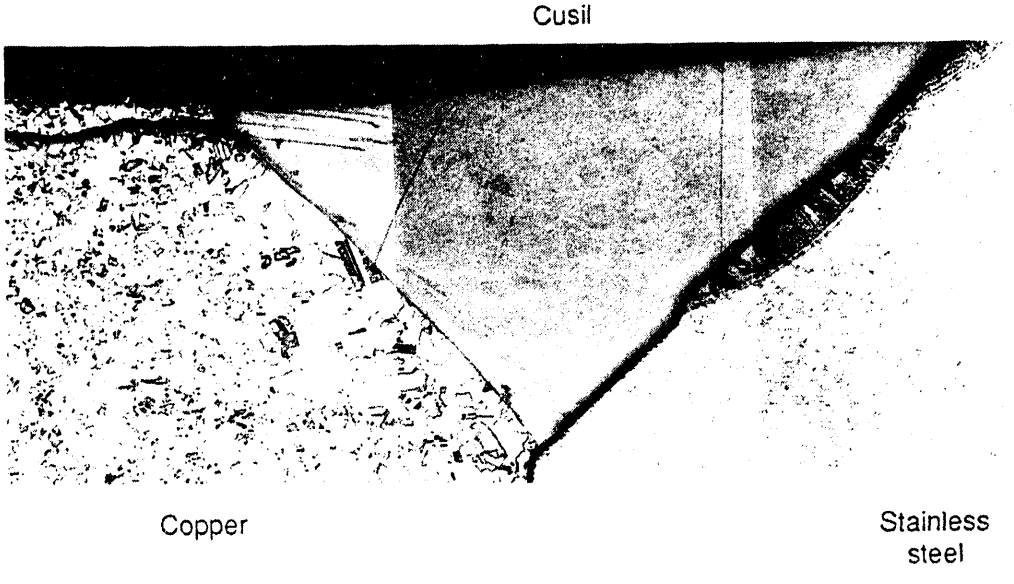

Fig. 5-52. Micrograph of a Cusil TIG braze.

To ensure this, all parts will be cleaned before assembly using existing SLAC cleaning processes and procedures. The process for cleaning stainless-steel parts is summarized in Table 5-20. The copper chambers and other copper parts will be cleaned in a separate process, outlined in Table 5-21.

Finally, following chemical cleaning, all parts will be assembled in a clean-room setting. Nylon gloves will be used when handling parts, and further fabrication, such as welding, brazing, and assembling, will be done using UHV-clean techniques.

DIP Design and Testing. As discussed in Section 5.2.4.2 above, the UHV environment in the HER arcs is attained using a combination of DIPs and discrete differential-ion pumps. The DIPs have been designed to maximize the available pumping using the 0.18-T HER dipole field, which is just over half of the 0.3-T field used in PEP. Our design is expected to provide an average pumping speed of 165 L/s/m, which is more than sufficient to provide the required 10-nTorr pressure at the maximum beam current of 3 A.

To achieve this pumping speed, a plate-type DIP has been chosen. The five-plate stainless-steel anode, shown in Fig. 5-53, contains four rows of pump cells, 1.8 cm in diameter, that intercept the dipole magnetic flux. The flux varies from 0.18 T at the magnet pole center to about 0.10 T at the edges. Theoretically, the cell diameter should increase as the field diminishes to maintain the same pumping speed per cell. We have elected to maintain a uniform cell diameter, however, in order to maximize the total number of cells in the pump. This approach maximizes the overall pumping speed, even though not all cells are pumping at maximum efficiency. Furthermore, the cells are arranged in staggered lines to produce a hexagonal close-packed pattern, which improves the cell-area density to 68%.

Table 5-20. Process for chemical cleaning of austenitic stainless steel.

Vapor degrease in hot 1,1,1 trichloroethane vapor for 5 minutes
Rinse in cold running tap water for 1 minute
Alkaline soak clean for 5 minutes at 180°F
Rinse in cold running tap water for 2 minutes
Pickle in Prepalloy and nitric acid (25 vol-%) at 100°F
Rinse in cold running tap water for 2 minutes
Alkaline soak clean for 5 minutes
Rinse in cold running tap water for 2 minutes
Immerse in room-temperature nitric acid (25–30 vol-%) for 2 minutes
Rinse in cold running tap water for 2 minutes
Rinse in cold de-ionized water for 2 minutes
Rinse in 150°F de-ionized water for 2 minutes
Rinse in isopropyl alcohol at 115°F
Dry in oven at 150°F
Wrap in lint-free paper and food-grade aluminum foil

Table 5-21. Process for chemical cleaning of OFE copper.

Vapor degrease in 1,1,1 trichloroethane for 5 minutes
Alkaline soak clean in Enbond Q527 cleaner at 180°F for 5 minutes
Rinse in cold tap water for 2 minutes
Immerse in room-temperature hydrochloric acid (50%) for 1 minute
Bright dip to produce desired surface finish
Rinse in cold tap water for 2 minutes
Immerse in room-temperature potassium cyanide for 15–20 seconds
Rinse in cold tap water for 1 minute
Rinse in cold de-ionized water for 30 seconds
Rinse in 150°F de-ionized water for 30 seconds
Immerse in isopropyl alcohol at 115°F for 30 seconds
Blow dry with dry nitrogen gas
Dry in oven at 150°F
Wrap openings in lint-free tissue and food-grade aluminum foil

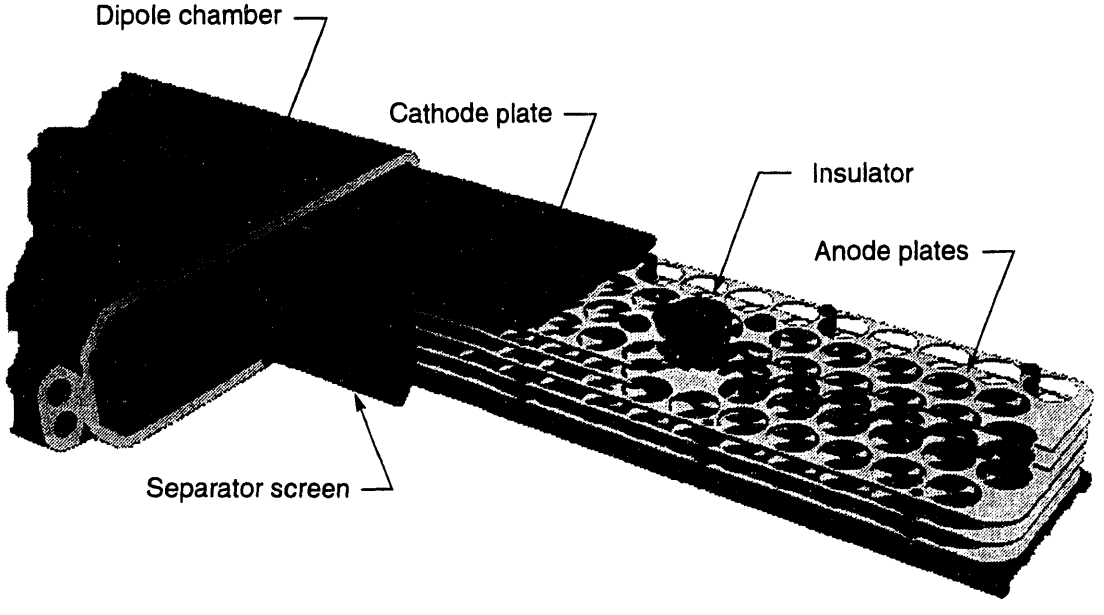

Fig. 5-53. CAD model of HER DIP module.

Beryllium-copper contact fingers between the titanium cathode and chamber wall provide conduction cooling for the cathode plates. These spring contacts, spaced along the length of the cathode, are designed to remove the heat flux of 0.01 W/cm^2 generated by the cathodes. The cathode plates have been shaped to provide the necessary stiffness to carry the contact spring force.

A formed, slotted screen, which separates the beam passage from the pump passage, provides RF continuity for the beam yet allows high conductance between the two passages. The screen contains six rows of slots on a pitch of 10 cm; each slot is 0.25 cm high by 9 cm wide, providing a calculated conductance of 1400 L/s/m. Where possible, slots in the screen have been aligned with the spaces between the anode plates to improve the overall conductance of the pump-screen combination. The height of the slot was selected to keep the contribution to beam impedance to a negligible level, and the height-to-depth ratio of 0.52 for the slot was chosen to minimize the effects of RF interference during operation.

We plan to validate the distributed ion pumping calculations by testing a series of DIP modules in a test stand using a PEP-II dipole magnet to simulate actual ring conditions. The test stand, now nearing completion at LLNL, will test various pump parameters, including cell diameter, cell arrangement, spacing between plates, magnetic field strength and uniformity, and anode voltage.

Test anodes will have five or seven plates, and the separator screen will contain either six or eight lines of slots to match the anode geometry. Initial testing will begin with N_2 gas. However, the final design will be tested with CO, CO_2, H_2, CH_4, and H_2/CO gas mixtures. We also intend to test a DIP module design from NSLS to provide a comparison and calibration with the production PEP-II design.

Tests by Laurent [1992] have shown that, in practice, DIP pumping speed can match theoretical calculations. However, this agreement with theoretical performance is contingent on maintaining extreme cleanliness during fabrication and assembly. Therefore, we will fabricate and clean all parts using the cleaning procedures described above. Then, all stainless-steel parts will be baked at 900°C for four hours, the titanium cathodes will be baked at 800°C for four hours, and the copper parts will be baked at 200°C for 24 hours. Following baking, all parts will be stored and assembled in a clean environment.

Quadrupole Chamber. The quadrupole chamber is actually a combination of elements. Pumping plenums for the two lumped differential ion pumps are included as part of this chamber, as are the BPMs, located at every QD magnet (one per cell). Each quadrupole chamber also includes a bellows to accommodate the thermal expansion of the dipole chambers. Finally, inside the pumping plenums, low-angle masks shield the downstream bellows and flanges from synchrotron radiation. This entire unit is supported by the same raft that supports the quadrupole and sextupole magnets, as shown in Fig. 5-54.

Although the pieces of the quadrupole chamber perform various functions, they are all integrated into a single assembly. Indeed, a single extrusion spans the entire quadrupole chamber, and the various components, such as the masks, BPM, and pumping plenums, register into, and weld onto, this extrusion. This approach ensures maximum

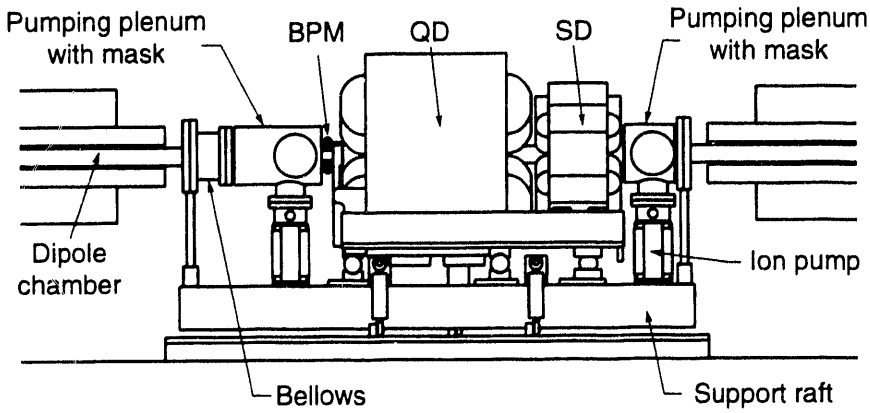

Fig. 5-54. Layout of HER arc quadrupole chamber.

accuracy for the positions of the BPM and masks, both of which must be precisely located.

The quadrupole chamber will be fabricated using the same techniques as the dipole chamber: An extruded chamber and a cooling bar are electron-beam welded together, and the stainless-steel flanges are TIG-brazed with Cusil. The pumping plenums, masks, and bellows will be assembled using conventional techniques, such as GTAW and hydrogen-furnace brazing. Below is a description of the various parts of the quadrupole chamber, their design criteria, and the present state of the development work.

BPM Design and Testing. Approximately 150 BPMs will be installed in each PEP-II storage ring. They will be located adjacent to the QD quadrupole in each cell, 96 in the arc sections, 40 in the straight sections, with some special BPMs in the IR. The design we have chosen (see Fig. 5-55) is based on a BPM feedthrough used in Sincrotrone Trieste, ESRF, APS, and other machines. Small ports will be welded into the quadrupole chamber pump cell, and the feedthroughs will be connected to the chamber by mini-Conflat flanges. The miniflange-mounted feedthrough assembly integrates a ceramic insulator, a 1-cm-diameter metallic button, and a type-N connector in an electrically smooth 50-Ω unit. This design is simple, reliable, and easily replaceable in the field. As noted, the synchrotron radiation masks in the pumping cell absorb radiation that would otherwise strike the BPM. The masks are water cooled and thermally isolated so that movement of the BPM unit is minimal.

The BPM will be fabricated such that the location of its electrical centerline is within ±0.004 in. (±0.1 mm) of its mechanical centerline. The unit will be calibrated using a technique used in the SLC and the ALS whereby each button is pulsed and the response of the other buttons is measured. This technique eliminates the need for expensive calibration fixtures and may be repeated in the tunnel should a problem be suspected. The BPM will be located within ±0.010 in. (±0.25 mm) of the quadrupole axis. The BPM position will be surveyed to within 0.002 in. (0.05 mm) and the measured offset entered into the project database. The BPM support will be designed to maintain long-term positional stability with respect to the quadrupole within ±0.001 in. (±0.025 mm).

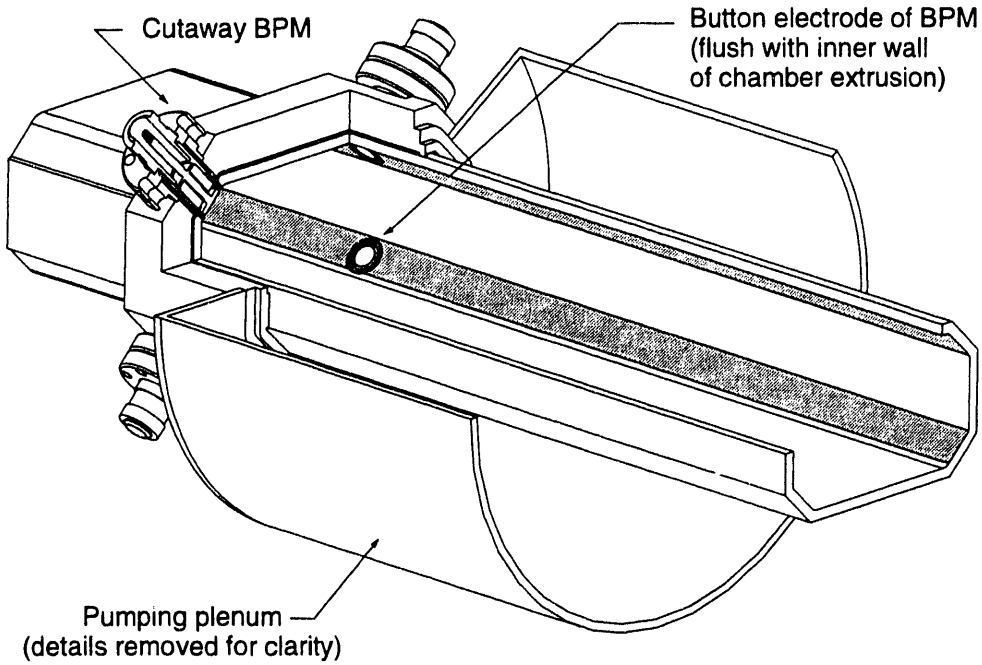

Fig. 5-55. CAD model of an HER arc BPM, integrated with the pumping plenum and quadrupole chamber extrusion.

Prototype feedthroughs are on order from two manufacturers for electrical bench tests and mechanical lifetime testing. A prototype BPM has been fabricated and is being prepared for installation in the SLAC linac for testing with electron and positron beams.

Bellows Design and Testing. The bellows (see Fig. 5-56) allows for the expansion of the vacuum chambers, while still providing a uniform chamber cross section to reduce the impedance seen by the beam to less than 0.05 Ω. Furthermore, it serves as the capstone for the cell—it is the last piece installed and the first removed should servicing be needed. The bellows provides sufficient room to maneuver the large and heavy vacuum chambers into place.

As discussed in Section 5.2.4.2, the chamber expands by different amounts depending on the operational mode of the machine. Table 5-22 summarizes these different operational modes, the corresponding compression requirements for the bellows, and the number of cycles for each of the compressions for which the bellows is designed.

Part of the bellows assembly is a bellows shield, which isolates the welded bellows shape from the beam chamber and ensures that the beam sees a beam pipe of uniform cross section. This shielding is done with prestressed cantilevered beryllium-copper spring fingers that slide along the inside of the beam passage as the bellows is being compressed. RF testing of this finger design is now being performed at LBL. Preliminary results show that the impedance of the bellows shield is as low as that of the chamber itself and that the finger shape will not lead to HOM power losses from the beam. The fingers are designed to maintain a relatively high contact pressure of 0.20

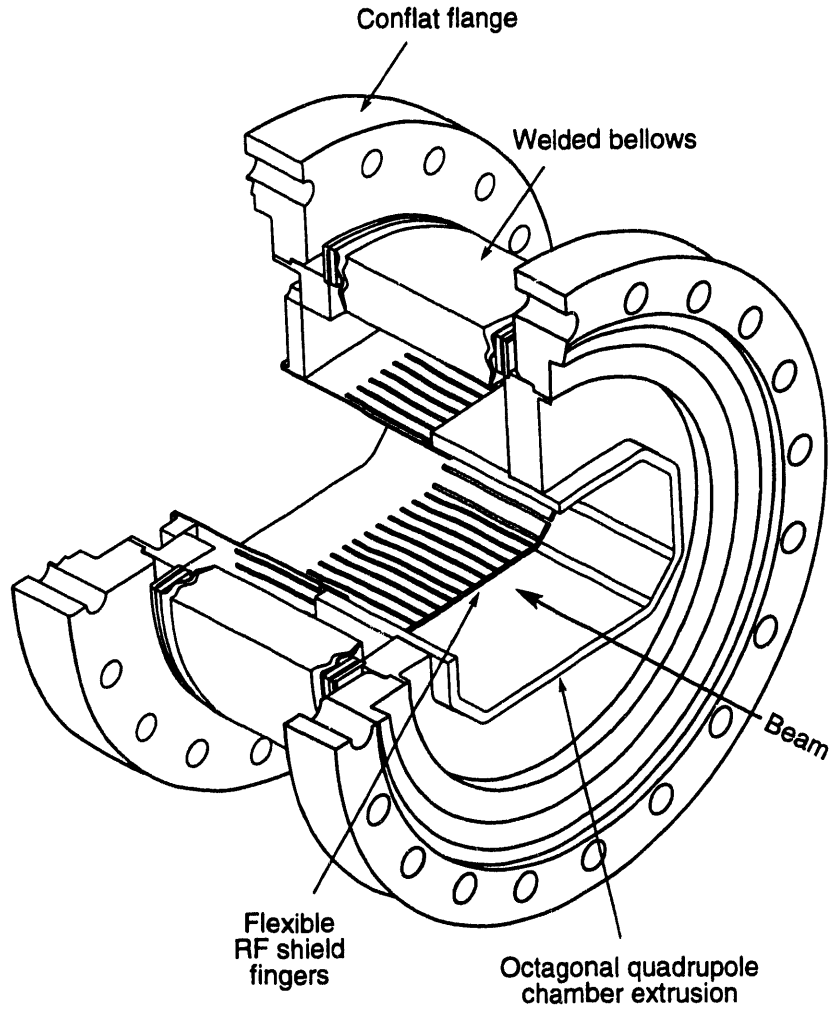

Fig 5-56. CAD illustration of the HER arc bellows, showing inner RF shield.

Table 5-22. Compression requirements for HER arc bellows.

Operational mode	Bellows compression (in.)	Number of cycles
Installation	1.0	100
Nominal (0.99-A beam)	0.09	100,000
Max. design (3.0-A beam)	0.2	100,000
150°C in situ bakeout	0.65	10

pounds per finger, despite any lateral offset introduced into the bellows assembly. Fatigue testing of the sliding contact joint will determine the optimal surface finish and plating material to eliminate both galling and the potential for cold-welding in the UHV environment.

Mask Design. Each quadrupole chamber pumping plenum contains one mask, which shields the neighboring flanges and bellows from the synchrotron radiation (see Fig. 5-57). (The thin bellows fingers and RF gaskets at the flange joints cannot be sufficiently cooled to preclude overheating, so the masks must protect them from damage.) The masks are independently cooled, and thermally and mechanically isolated from the rest of the chamber. The slope of the upstream face of the mask is only 3°, so the maximum linear thermal flux on it is 225 W/cm, compared with a maximum of 102 W/cm on the chamber wall (at 3-A beam current). Finite-element analysis shows that, although the maximum temperature of the mask reaches 90°C, and the local temperature at the point of incidence of the radiation exceeds 180°C, the peak stresses are low. This is because the mask is free to expand as it heats and is not constrained by cooler parts of the chamber. Thermally isolating the mask from the neighboring chamber ensures that it is not a heat source that could locally distort the chamber. This is especially important for the mask shielding the BPM, a component that requires high thermal and mechanical stability.

The masks protrude into the beam chamber by as much as 4.5 mm. Although they stay well outside the beam-stay-clear aperture, they would give an asymmetry to the

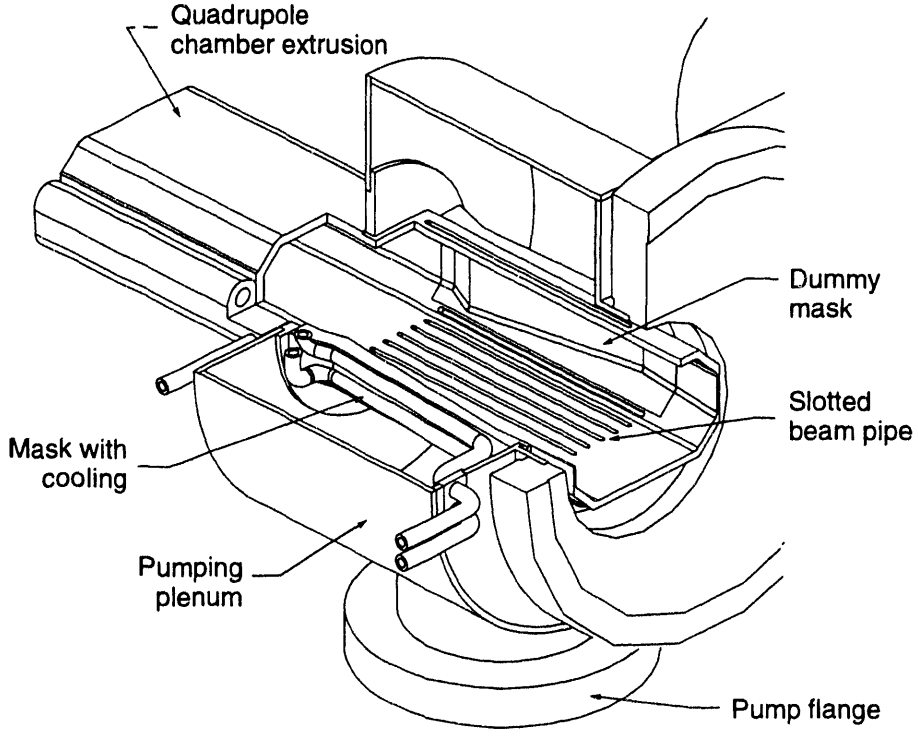

Fig 5-57. Mask and symmetrical dummy mask inside a typical pumping plenum chamber. Note slotted beam pipe for improved vacuum conductance to pump.

chamber. To restore transverse symmetry, dummy masks will be added to the opposite side of the chamber.

Supports. The quadrupole and dipole vacuum chambers sit on supports that mount to the quadrupole magnet support raft. Thus, the vacuum chambers maintain close alignment with respect to the quadrupole magnets of each cell. As discussed above, the BPM position must be tightly maintained, thus the support for the BPM provides rigidity to hold position, despite the weight of the vacuum pumps, transient loads, and thermal expansion of the chamber at operating temperature. (These loads exert up to 500 pounds of force on the support.)

The two remaining supports, one supporting the opposite end of the quadrupole chamber and the second supporting the dipole chamber across the bellows from the BPM, must also provide vertical and lateral rigidity, but must flex axially to accommodate the thermal expansion of the chamber. These supports will be modeled after the original SLAC flex plates, which have been supporting the disk-loaded linac waveguides for 30 years. This support consists of two stainless-steel sheets that are pretensioned by a copper-alloy plate that is cooled in liquid nitrogen, inserted between the sheets, then allowed to warm to room temperature. The resulting prestress produces a support that is extremely rigid laterally and rotationally, yet free to flex along the beamline.

5.2.4.4 Straight Section Design

Standard Chambers. Although the six straight sections of the HER contain all of the nonstandard equipment for the machine, there is still a "standard" cell, consisting of a focusing and defocusing quadrupole, whose centers are spaced 7.709 m apart. The beam pipe consists of 3.75-in.-diameter 316L stainless-steel tubing, sized to clear the 100-mm bore of the quadrupole magnets. As in the arc cells, each QD has an associated BPM. A bellows at each quadrupole takes up the thermal expansion of the chambers, and two pump cells complete the layout of the straight section half-cell.

The other components used in the straight sections are generally adaptations of the corresponding items used in the arcs. The BPM uses identical electrodes, but will be installed in round tubing instead of the octagonal arc chamber. The bellows will be designed using the same sliding-finger RF shield, and incorporating the same criterion for maximum compression at bakeout as in the arcs. However, for the straight sections, they will be modified to fit the 3.75-in. tubing. The pump chambers will be modified slightly to accommodate the round tubing and will also be fitted with different pumps to better handle the particular pumping requirements of the straights (see below). Because there is no synchrotron radiation produced in the straight sections, local masking is not needed at every pump cell. Instead, discrete masks will be placed at three places along the straight section to intercept the low-angle radiation coming from the last bend magnet of the arcs. For the same reason, cooling of the chamber is not needed.

Vacuum Analysis. There are two significant differences between the arcs and the straight sections—in the straights there is little or no synchrotron radiation and there are no dipole bending magnets. Thus, the vacuum design of the arcs, based on the use of distributed ion pumps in the dipoles to provide the bulk of the pumping, cannot easily be

transferred to the straights. A different approach is required, which considers only the thermal gas desorption from the stainless-steel chamber walls and which counts only on discrete ion pumps to maintain the required pressure.

Because of the symmetry of the vacuum system in the straight sections, the pressure curve can be modeled analytically, using the following formula:

$$P_x = q_D B\left[\left(\frac{L}{S_p}\right)+\left(\frac{x}{C}\right)-\frac{x^2}{(2CL)}\right] \tag{5-25}$$

This quadratic equation models the pressure curve as an inverted parabola, which reaches its peak value midway between pumps. Parameters used to evaluate the straight section pressure profile are summarized in Table 5-23.

The values in Table 5-23 correspond to the use of two 220-L/s ion pumps in each cell, one at each quadrupole magnet. With this configuration, the average pressure is

$$\begin{aligned} P_{\text{av}} &= \left(q_D \frac{BL}{C}\right)\left(\frac{C}{S_p}+\frac{1}{3}\right) \\ &= 2.4 \text{ nTorr} \end{aligned} \tag{5-26}$$

This is below the 3-nTorr design pressure for the straight sections. A plot of the pressure profile for a half-cell is shown in Fig. 5-58.

Table 5-23. Parameters used in evaluation of straight section pressure profile.

Thermal outgassing rate, q_D [Torr·L/s/cm^2]	1.0×10^{-11}
Perimeter of beam chamber, B [cm]	28.9
Half-length of a half-cell, L [cm]	385
Pumping speed[a], S_p [L/s]	100
Chamber conductance, C [L/s]	24.8

[a]For half-length of half-cell.

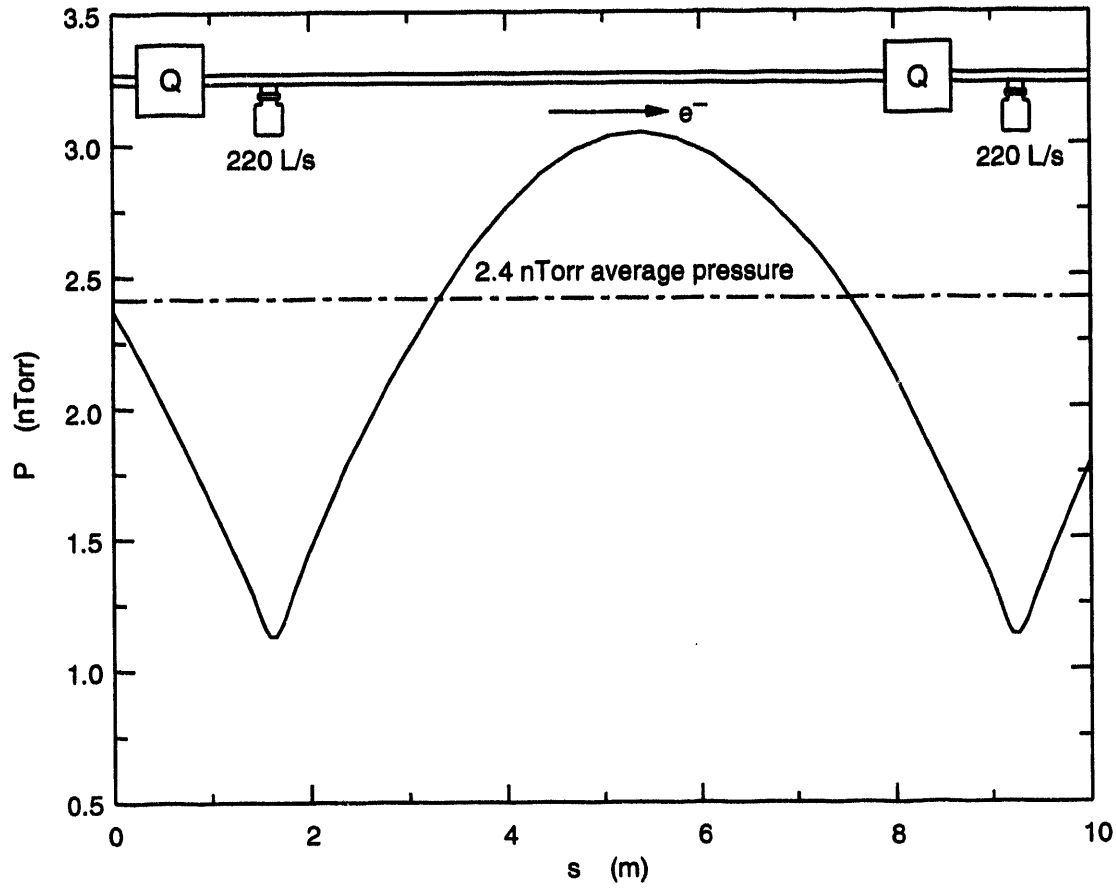

Fig. 5-58. Pressure profile of HER straight section half-cell.

5.2.5 LER Vacuum System

5.2.5.1 System Overview. The LER vacuum system concept is considerably different from that of the HER. Optimization of the LER magnetic lattice, and differences in the bending magnet design have resulted in extensive differences in the arc vacuum system. Nonetheless, the design has been optimized to take advantage of the fabrication techniques developed for the HER vacuum chambers. Operating pressure requirements for the LER are the same as those for the HER. However, due to the lower beam energy, the LER heat loads are lower, making the thermal design less demanding than that of the HER.

All pumping in the LER is by means of lumped sputter-ion pumps. To provide stable argon pumping speed (in case of small air leaks), one pump in each cell will have "differential cathodes" (of titanium and tantalum). An evaluation was done on the use of TSPs and NEG pumps, which potentially provide high pumping speed at low pressures and at somewhat lower cost. Calculations showed that the gas loads in the PEP-II LER arcs would require frequent regeneration of either type of pump. For PEP-II, the loss of operational time during regeneration was considered an undesirable feature and the risk

of lost beam time due to accidents during the frequent regenerations was judged unacceptable. Ion pumps, in contrast, are very reliable and many of them are available from PEP for reuse. It is expected that some combination of TSPs and NEG pumps will be used in special sections of the machine where gas loads are not so high and where very low pressure must be maintained.

The periodic layout of the magnet lattice in the LER is similar to that of the HER—the cells of the two rings are the same length and stacked one atop the other, as shown in Fig. 5-59. Major differences between the two rings, however, are the length and placement of the dipoles. A standard FODO cell in the LER contains the following magnetic elements: (1) focusing quadrupole, (2) focusing sextupole, (3) drift, (4) corrector, (5) dipole, (6) defocusing quadrupole, (7) defocusing sextupole, (8) drift, (9) corrector, and (10) dipole. Alternate arcs are mirror-symmetric both for the magnet lattice and vacuum chambers, reflected about an axis from the interaction point at IR-2 to the injection point in IR-8; that is, the pattern on one side is sextupole-quadrupole-dipole and on the other is dipole-quadrupole-sextupole.

As in the HER, copper was chosen as the most suitable material for fabrication of the arc vacuum chambers. In the straight sections, where the synchrotron radiation is minimal, the vacuum chambers will be fabricated from 316L stainless-steel tubing. Experience from SPEAR and PEP has demonstrated the wisdom of installing a large vacuum system with flanged rather than welded interconnections. Standard stainless-steel Conflat flanges with copper gaskets will be used, as these have proved very reliable in the past. The inner dimensions of the vacuum chamber accommodate the beam-stay-clear region required by beam dynamics and allow for the unavoidable errors in fabrication and mechanical positioning. The cross section (Fig. 5-60) was made as large as would fit in a composite magnet pole profile in order to minimize the synchrotron radiation linear power density and to maximize vacuum conductance.

As in the HER, HOM losses will be kept to a minimum by keeping a uniform chamber cross section where possible. Gently tapered transitions smoothly blend the unavoidable shape changes. Pumping ports on the beam chamber are shielded by screens. Copper contact rings between the flanges provide a smooth electrical path and eliminate RF losses. In the interest of reducing the number of different components, the LER and HER vacuum systems will be standardized wherever possible. For example, the isolation valves, pump-out valves, vacuum gauges, and ion pumps with their associated controllers will be the same type in both rings.

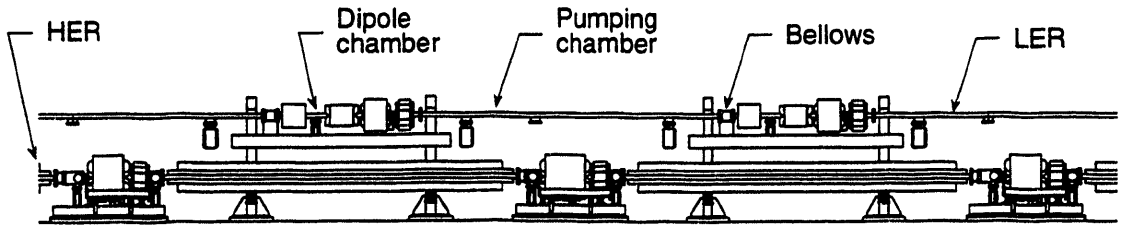

Fig. 5-59. Illustration of standard arc cells, showing the LER above the HER.

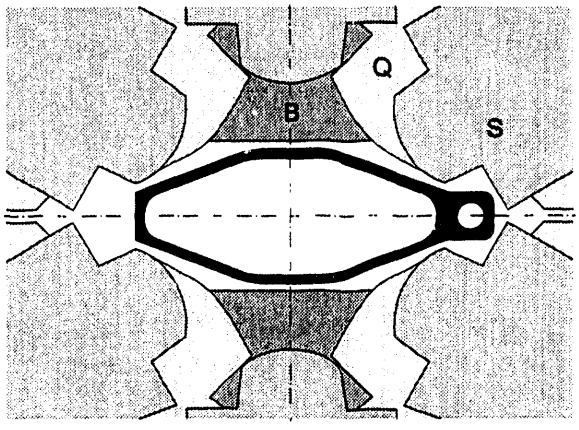

Fig. 5-60. Cross section of the LER vacuum chamber in the arcs; dimensions are in millimeters.

5.2.5.2 Analysis. At a beam energy of 3.1 GeV, the critical energy of the synchrotron radiation is 4.9 keV. In this photon-energy regime, almost all the power is absorbed on the inside wall of the vacuum chamber. With a nominal stored-beam current of 2.14 A, the total power radiated in the arcs is 1288 kW, or 13.4 kW per cell. The power distribution in Fig. 5-61 shows that the peak linear power flux, 33 W/cm, is deposited approximately 1.6 m beyond the exit of the dipole magnet; thereafter, the power decreases rapidly along the cell. A maximum design energy of 3.5 GeV with a 3-A stored-beam current was assumed for the thermal design. With these parameters, the peak linear power density is 73 W/cm, which results in a calculated thermal stress of 1,000 psi and a wall temperature at the point of peak-power incidence of about 80°C.

A series of finite-element calculations has been completed using the maximum design values for synchrotron radiation power. The temperature differential across the water-cooled metal wall of the chamber was calculated to be 26°C, with a 21°C rise across the surface film in the water. At the required flow rate of 10 gpm, the bulk temperature rise per cell is 11°C.

Within each cell, low-conductivity water (LCW) from the supply header will flow out, in both directions, from the center of the cell through an LER dipole and quadrupole chamber in series and then to the return header. A flow switch will be installed to monitor for low flow.

A second consequence of synchrotron radiation is photodesorption. The gas load produced by this mechanism is plotted in Fig. 5-34b, assuming a value for the photodesorption coefficient of $\eta = 1 \times 10^{-6}$ molecules per photon at the maximum value of P_{SR}. As a result of leveling (see Section 5.2.3.4), the photodesorption coefficient used in the pressure profile calculations varied from 1×10^{-6} molecules per photon at the peak to 4.3×10^{-6} molecules per photon at the point of minimum P_{SR}. These leveled values are in good agreement with values measured in the NSLS desorption tests [Foerster et al., 1992]. The arrangement of sputter-ion pumps in the arc cells is shown in the layout of Fig. 5-59. The total installed pumping speed per cell for machine startup is 780 L/s (two 220-L/s pumps, two 110-L/s pumps, and two 60-L/s pumps). (The pumping chamber

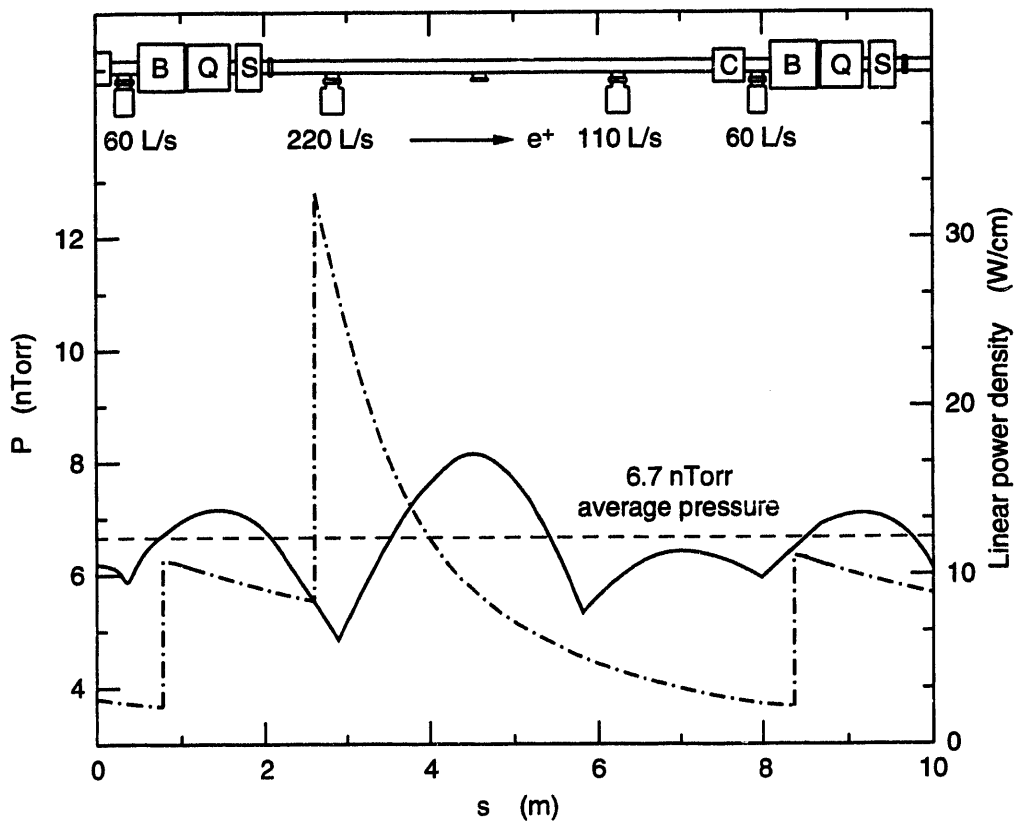

Fig. 5-61. Plot of synchrotron radiation linear power density and vacuum pressure along LER arc cell for the nominal beam energy and current.

will have an extra port to permit additional pumping if required to reach 3-A operation.) The pressure distribution calculated with this configuration is included in Fig. 5-61. Based on the above estimate of the desorption coefficient, the average pressure in the arcs during nominal operation at 3.1 GeV and 2.14 A stored beam current will be 6.7 nTorr, which is below the design requirement.

In the straight sections, the design pressure of 3 nTorr will be maintained by installing 220-L/s sputter-ion pumps at intervals of 7.7 m (that is, two per cell). Based on SLAC experience, we have assumed a thermal outgassing rate of 1×10^{-11} Torr·L/s/cm^2. For the region immediately upstream of the interaction region, 220-L/s pumps will be installed at intervals of 3.85 m to obtain an operating pressure of 1 nTorr. With this pump arrangement, the average pressure around the LER circumference is 6 nTorr. This pressure was used in the lifetime estimate discussed in Section 4.3.

5.2.5.3 Arc Chamber Design. Each arc region vacuum system consists of sixteen standard cells of dipole vacuum chambers with a 4-m-long straight pumping chamber between magnet groups. The layout of one standard cell is shown in Fig. 5-59. There are six beam chamber components per cell: dipole chamber, pumping chamber, bellows, dipole chamber with BPM, pumping chamber, and bellows. The length of the dipole was

chosen such that all of the synchrotron radiation it produces strikes the vacuum chamber wall downstream from the magnet (see Fig. 5-61), where lumped vacuum pumps can be easily located to remove the desorbed gas. Distributed ion pumps inside the dipole are thus unnecessary. (Indeed, for a ring which such a low dipole packing factor, distributed pumping in the dipoles would be ineffective.) As is typical of storage rings, the beam chamber, which is of continuous cross section throughout the arc, is vacuum-conductance limited.

The arc chambers are made from a single-wall copper extrusion such as that illustrated in Fig. 5-60, with an extruded copper cooling bar electron-beam welded to the outer wall of the beam passage. The adopted cross section gives a small incident angle between the synchrotron radiation and the vacuum chamber wall, thereby lowering the linear power density to very modest values. The 2.36-m-long dipole chamber, shown in Fig. 5-62, passes through the sextupole, quadrupole, dipole, and corrector magnets. It is rigidly attached to the support girder between the sextupole and quadrupole, at the location of the BPM. (Only alternate dipole chambers in the cell will contain a BPM, those near the QD magnets.) Flex plates at the ends of the chamber will hold the lateral position while allowing thermal expansion. A screened pumping port is provided between the quadrupole and dipole. At the flange joints, RF seal rings will provide continuity along the inner surface of the vacuum chamber. The outer wall of the vacuum chamber will be tapered away from the beam so that synchrotron radiation does not strike the vacuum flanges or RF seals.

Nearly all of the synchrotron radiation power is absorbed in the 5.01-m pumping chamber, which is located immediately downstream of the dipole. The design, shown in Fig. 5-63, uses a water-cooled, extruded copper beam chamber identical to that used in the dipole chamber, with end flanges for interconnection. A bellows module at the downstream end of the pumping chamber provides the necessary space for installation

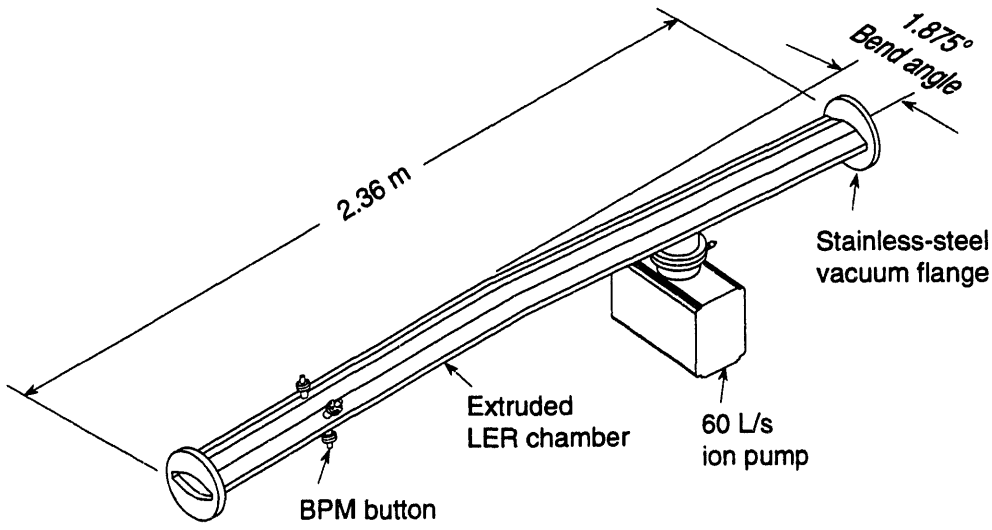

Fig. 5-62. Illustration of LER dipole vacuum chamber.

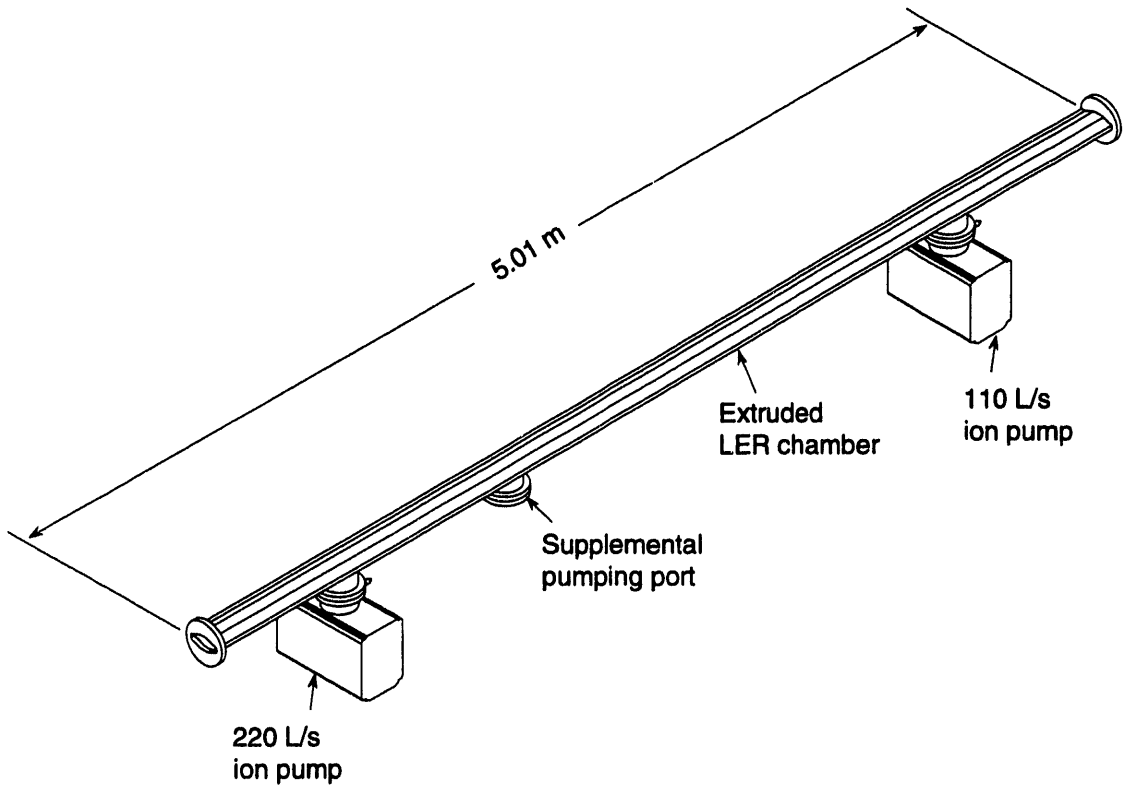

Fig. 5-63. Illustration of LER pumping chamber.

and accommodates thermal expansion. To facilitate connection to the dipole chamber, a flex-joint at the upstream end of the pumping chamber allows angular compliance in the flange joint. A strong-back support structure is envisioned for the pumping chamber to support the weight of the ion pumps and to protect the long slender extrusion from damage. Connections to the LCW system are external to the vacuum system, thus eliminating water-to-vacuum welds that might develop leaks.

The arc vacuum system will be equipped to accommodate an in situ bakeout to 150°C. Hot water at 180°C, circulated through the LCW system, will supply the heat. Testing done for PEP [Winch, 1977; Jurow, 1976] showed that spacing the vacuum chamber away from the magnet poles to create an air gap provides sufficient insulation. Finite-element analysis of the PEP-II vacuum chambers shows that, for a copper chamber (which conducts even better than an aluminum PEP chamber), the desired bakeout temperature is reached without requiring thermal insulation of the vacuum chambers. The existing PEP hot-water bakeout system will be upgraded for PEP-II operation.

The LER BPM assembly will be similar to that of the HER. The BPM feedthrough assemblies are identical to those of the HER but are mounted directly on the dipole chamber extrusion via individual flanged ports, as shown in Fig. 5-64. BPMs will be calibrated using the same noninvasive technique as in the HER, and will be rigidly mounted to the quadrupole magnet to the same level of accuracy as in the HER.

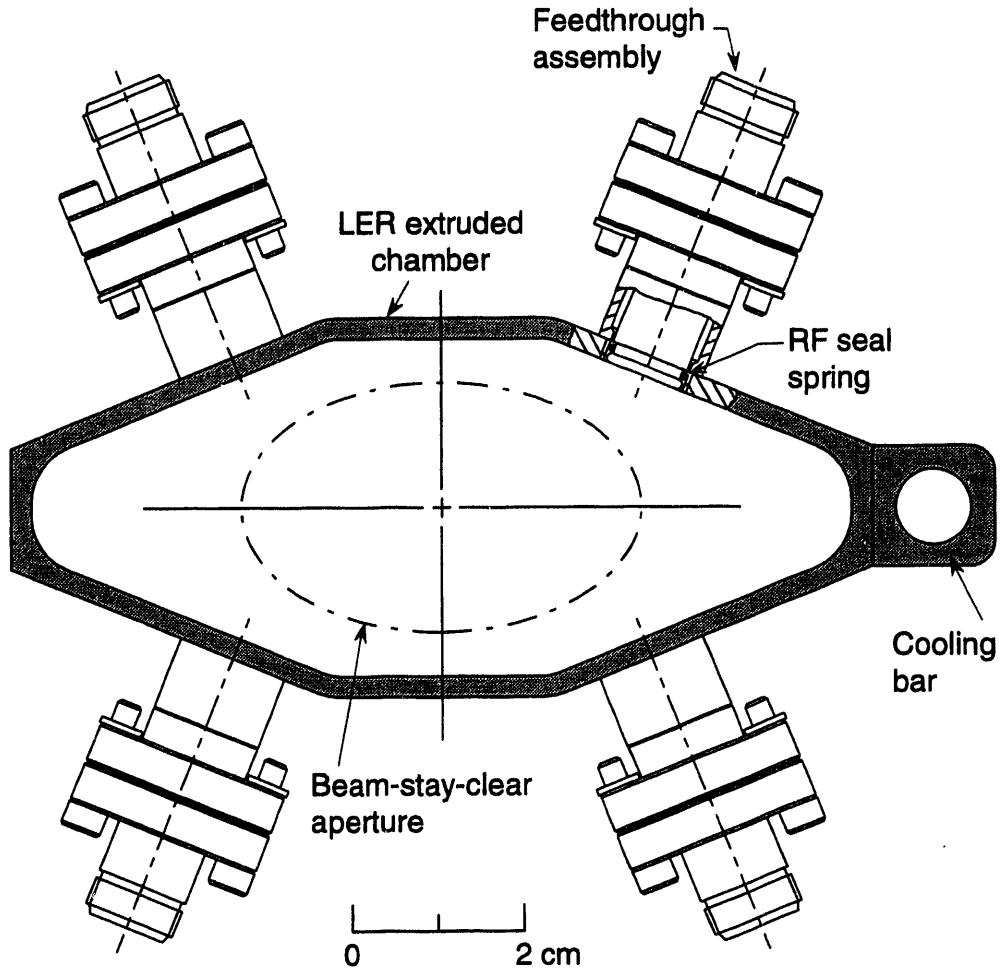

Fig. 5-64. Cross section of LER arc dipole chamber showing BPM configuration.

The basic bellows concept shown in Fig. 5-65 is identical to that for the HER, except for a mask located upstream from the bellows to mask it (and associated vacuum flanges) from synchrotron radiation. The bellows is located in the region with lowest power density, so the linear flux on the mask is very small.

5.2.5.4 Straight Sections. Each of the six straight sections has a length corresponding almost exactly to eight standard cells. Included in these sections are the RF cavities, the injection septa, beam pickups and kickers, horizontal and vertical beam collimators, and BPMs. One of the straight sections houses the common interaction region for PEP-II and thus has a unique layout. There are also 28 empty FODO cells in the ring. The beam pipe in the LER straight sections, made from standard 3.75-in.-OD stainless-steel tubing,

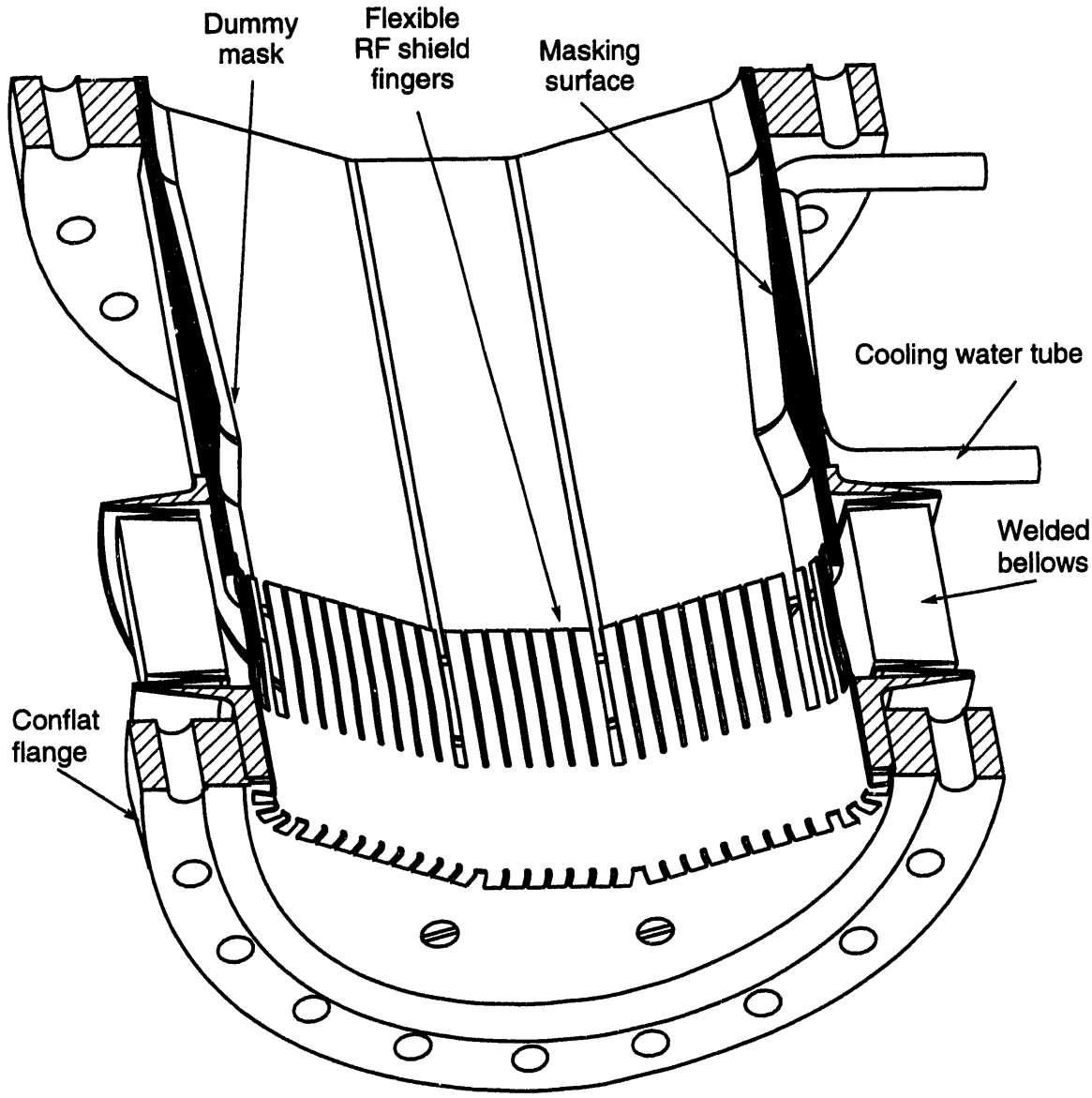

Fig. 5-65. Perspective of LER arc bellows.

along with the bellows, BPMs, and supports, will be essentially identical to components in the HER straight sections. The pumping configuration will be consistent with that designed for the HER. All-metal, RF-sealed, 100-mm-bore isolation valves are located in the straight sections at the end of each arc. To protect the RF cells in the event of an accidental vent to air, and to facilitate their conditioning, additional valves are also provided to isolate them. Isolation valves will also be installed on either side of the interaction region at ±5.2 m from the IP.

5.2.6 Radiation from Wigglers

To provide acceptable beam-beam tune shifts, the natural emittance of the LER must be increased considerably beyond that resulting from the arc dipoles alone. In addition, we have discussed in earlier reports [LBL, 1989; LBL, 1990] the potential advantages of having equal damping decrements in the high- and low-energy rings to minimize the effects of the energy asymmetry on the beam-beam interaction. For these reasons, wigglers will be used to create additional energy loss and control the beam emittance in the LER.

The damping decrement for a storage ring can be written as

$$\lambda = \frac{T_0}{\tau_x} = \frac{U_0}{2E} \tag{5-27}$$

from which it is clear that, for equal damping decrements, the required synchrotron radiation energy loss per turn for the high- and low-energy rings must simply scale proportionately to the beam energy in the ring.

In the high-energy lattice (ρ = 165 m; E = 9 GeV), the total energy loss, which is dominated by the normal bends, is U_0 = 3.58 MeV/turn. For equal damping decrements, then, we need an energy loss in the LER of

$$U_{0,+} = U_{0,-}\frac{E_+}{E_-} = 3.58\left(\frac{3.1}{9.0}\right) = 1.24 \quad \text{[MeV/turn]} \tag{5-28}$$

In the LER, we have a bend radius of ρ = 13.75 m. The energy loss from the horizontal bends can be estimated as

$$U_0 = 0.0885\,\frac{E^4}{\rho} \quad \text{[MeV/turn]} \tag{5-29}$$

giving U_0 = 0.59 MeV/turn, that is, only about half of the requisite amount. (To create the matched damping decrement from the bending magnets alone would require a bend radius of 6.75 m, which would be, at best, inconvenient in terms of thermal power density.) In addition to the contribution from the horizontal bends, we must take account of the synchrotron radiation emission in the horizontal and vertical bends used to steer the low-energy beam from the IP into the arc sections (which lie above the plane of the HER). The energy loss from all of the magnets in the IR can be calculated from

$$U_{0,V} = 1.266 \times 10^{-3} E^2 \sum_i B_i^2 L_i \quad \text{[MeV/turn]} \tag{5-30}$$

where E is in GeV, B_i is the dipole field in T, and L_i is the bend length in meters of the ith magnet. This gives a total contribution of 0.12 MeV/turn. Thus, the lattice itself contributes a total energy loss of 0.71 MeV/turn from the bending and separation magnets.

To reach equal damping decrements, then, we must produce an additional energy loss of 0.53 MeV/turn. This will be accomplished by including wiggler magnets in two of the

LER straight sections. As already mentioned, these wigglers also serve as a means of emittance adjustment for the LER; this adjustment works by creating a dispersion "bump" at the wiggler locations. By locating the wigglers in shallow chicanes off the principal axis of the straight section, the rms dispersion in the wiggler can be controlled externally to the wiggler. This additional degree of freedom extends the range of allowable wiggler characteristics. It also allows us to project the radiation into a distant photon dump and to spread the wiggler radiation along the side walls of the dump beamline.

Four wiggler sections, with six periods of l_W = 0.67 m, are included in each of two utility straight sections, as discussed in Section 4.1. The total length of wigglers is thus 32 m and the magnetic length is 19.2 m. A schematic drawing of the layout is shown in Fig. 5-66. For a wiggler composed of alternating-field dipoles, the total radiated power in MeV/turn is again given by Eq. 5-30. A wiggler field of B = 1.51 T is therefore needed to provide the additional 0.53 MeV/turn to fully equalize the damping decrements.

At the nominal current of 2.14 A, each wiggler will produce about 0.6 MW of synchrotron radiation power, with a critical energy of 9.6 keV. Most of this power will be dealt with externally to the ring vacuum chamber in specially designed photon beam dumps. However, some of the power will be deposited on the side walls of the vacuum chamber in the vicinity of the wiggler. To compute the power density at the dump and on the walls, we must estimate the angular distribution of the radiation. A precise description of radiation from a nonsinusoidally varying wiggler in the near field is not given in the literature, but we can modify the far-field description for standard wigglers given by Kim [1986] and apply it to segments of the wiggler to evaluate the resultant vacuum system requirements [Barletta and Garren, 1990].

Denoting the horizontal angle by θ and the vertical angle by ψ, we can write the power density in W/mrad^2 as

$$\frac{dP}{d\Omega}(\theta,\psi) = \frac{21\gamma^2}{16\pi K} U_{0,w}\, I\, N_W\, G(K)\, f_K(\gamma\theta,\gamma\psi) \qquad (5\text{-}31)$$

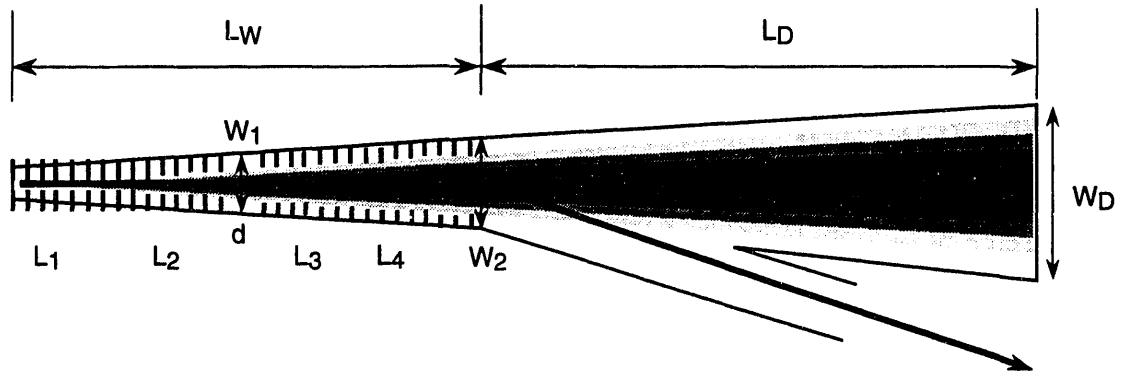

Fig. 5-66. Schematic representation of the vacuum chamber in the region of the LER damping wigglers.

where $U_{0,w}$ is the synchrotron radiation loss in one wiggler period, I is the beam current in A, N_W is the number of wiggler periods, and G and f_K are universal functions. For the bend-drift configuration, $U_{0,w}$ is given by Eq. 5-30, where the wiggler magnetic length is substituted for L_i. For a standard wiggler, K is the usual wiggler parameter defined (for B in T and λ in cm) by

$$K = 0.934 \; B_w \lambda_w \tag{5-32}$$

The normalization factor $G(K)$ is

$$G(K) = K \frac{\left(K^6 + \frac{24}{7}K^4 + \frac{16}{7}\right)}{\left(1 + K^2\right)^{7/2}} \tag{5-33}$$

For $K \gg 1$, $G(K) \rightarrow 1$; moreover, the angular distribution is sharply cut off in the wiggler bend plane. In the limit $K \rightarrow \infty$, the normalized angular distribution function $f_K(\gamma\theta, \gamma\psi)$ is given by

$$f_K(\gamma\theta, \gamma\psi) = \sqrt{1 - (\gamma\theta/K)^2} \left\{ \frac{1}{\left[1 + (\gamma\psi)^2\right]^{5/2}} + \frac{5\,(\gamma\psi)^2}{7\left[1 + (\gamma\psi)^2\right]^{7/2}} \right\} \tag{5-34}$$

From Eq. 5-34 one sees that the radiation is spread over a horizontal angle $2\theta_w$, where

$$\theta_w = \frac{K}{\gamma} \tag{5-35}$$

For the bend-drift configuration, θ_w is the bend angle in a single dipole. In that case Eq. 5-35 becomes the defining relation for an effective K value, K_{eff}. Given this K_{eff}, we apply the formalism for the standard wiggler. In the nonbend (vertical) plane, the rms angle of the radiation is

$$\psi_w = \left(\frac{\varepsilon_y}{\beta_y} + \frac{0.63}{\gamma^2} \right)^{1/2} \tag{5-36}$$

At 3.1 GeV, the second term in Eq. 5-36 is dominant, and $\psi_w \approx 1/\gamma = 0.13$ mrad to a good approximation. At the nominal operating current of 2.14 A, each wiggler generates 35 kW/m. The opening half-angle of the radiation is 15 mrad. Therefore, if the vacuum chamber is to intercept less than 20% of the radiation generated (to avoid an impractically high power loading on the crotch and on the side walls), the enclosure needs to be quite wide. By integrating Eq. 5-31 over ψ for K_{eff}, one can determine the power density on the side walls of the enclosure.

With regard to pumping requirements, there is a weak trade-off between increasing the static load from widening the chamber and minimizing the dynamic load by avoiding the photon fan. In the wiggler region, which occupies only 1.5% of the circumference of the ring, we have relaxed the required operating pressure to 10 nTorr.

The broad radiation fan suggests the use of a tapered stainless-steel chamber, as illustrated in Fig. 5-66. The photodesorption coefficient of the chamber is assumed to be 2×10^{-6}. The width W_1 should be as narrow as possible to maintain a practical quadrupole design. With this constraint in mind, the required pumping, which ranges from less than 5 L/s/m in L_2 to about 30 L/s/m in L_4, is obtained for W_1 = 24 cm and W_2 = 40 cm. The corresponding thermal loads range from less than 0.1 to 1.3 kW/m, respectively, on each side wall of the wiggler enclosure.

From Eq. 5-31, we can estimate that, at 2.14 A, the power density in the forward direction will be 1.0×10^5 W/mrad^2. We also find that 80% of the radiation is emitted into 7.7 mrad^2. Hence, we can compute the distance from the end of the wiggler to the photon dump, such that the power density is limited to a maximum value of 1 kW/cm^2. The distance from the wiggler to the dump, L_D, can be foreshortened by tilting the dump at an angle of about 15° with respect to the vertical. For a tilted dump, L_D should be about 27 m. Although roughly 10% of the power will actually be deposited on the walls of the wiggler chamber, we estimate the gas load at the dump assuming that all the power is incident there. We find that, for a copper dump with a photodesorption coefficient of 2×10^{-6}, the gas load at the dump is $Q_{\text{dump}} = 7.4 \times 10^{-5}$ Torr·L/s.

By considering the flared vacuum chamber from the wiggler to the dump to be a long, differentially pumped manifold, we can allow the pressure at the dump to rise to a much higher value than that required in the beam pipe. At the dump, the maximum horizontal extent of the radiation fan is 1.3 m, whereas the vertical extent of the radiation is only 1.3 cm. To lower the conductance of the photon channel, we take the chamber height to be 8 cm; baffles will also be added as needed to reduce the vacuum conductance into the wiggler straight section to 250 L/s.

The minimum total pumping of the dump plus photon channel is obtained by choosing the pressure at the dump to be 30 nTorr. This pressure requires 2000 L/s of pumping at, or near, the dump. This could be provided, for example, by installing large titanium sublimation pumps. Distributed pumping of 50 L/s/m along the photon channel reduces the pressure to 10 nTorr at the exit of the wiggler. More novel approaches, such as having the radiation fan strike NEG panels, are under study [Halama and Guo, 1990].

A C-frame bending magnet 5 m downstream from the wiggler exit bends the positron beam out of the radiation fan and into the straight beamline. The crotch can thereby be located away from the radiation fan of the wiggler. The straight beam pipe leaving the crotch is a special section of stainless-steel pipe, with a restricted aperture of less than 3 cm. Lumped ion pumps, providing 80 L/s of pumping speed in the region starting 10 m beyond the crotch and extending 5 m downstream of it, will reduce the pressure to 3 nTorr. At this point, a transition section will match the beam pipe dimensions to the standard straight-section vacuum chamber cross section.

5.2.7 Interaction Region Considerations

The interaction region is the heart of the entire PEP-II facility. Because the detector is located in the IR, and because the separation of the two beams takes place here, there are a number of special requirements and special constraints that must be accommodated by the hardware. The design issues that must be considered are mainly those associated with

the need to protect the detector from backgrounds. As discussed in Section 4.2, various masks are used in this region to protect the detector components and other sensitive equipment from the synchrotron radiation emitted as the beams are being magnetically separated, and these masks perforce intercept some of the synchrotron radiation power. The issues that we consider here include:

- Local pumping to deal with the photodesorption from those mask and beam pipe surfaces hit by the synchrotron radiation fans
- Cooling of the detector beam pipe masks to remove the synchrotron radiation power
- Cooling of the septum masks that shield the septum quadrupole (Q2) from the high-power synchrotron radiation fans
- Cooling of the very thin beam pipe in the center of the detector to remove the power due to wall-current and HOM heating

5.2.7.1 Local Pumping. The pressure requirements inside the detector in the region upstream of the permanent-magnet quadrupoles are set by beam-gas bremsstrahlung events leading to lost beam particles. Within about ±20 cm of the IP, the limitation arises from electron-nucleus events leading to spurious triggers. For beam-gas interactions, we would like a pressure of 0.2 nTorr or lower outboard of the upstream Q1 magnet (for each beam). Very near the IP, estimates based on calculations [Lightbody and O'Connel, 1988] indicate that some tens of nanotorr should suffice, although measurements with Mark II at PEP suggest a more stringent limit. For PEP-II, a precise calculation requires more knowledge of the detector and trigger design than is now available, so the simple estimates must suffice.

Pumping inside the detector is provided by DIPs inside the permanent-magnet Q1 quadrupoles. It seems feasible to provide pumps with 150-L/s effective speed, including the conductance of the RF screen required to isolate the pump structure from the beam [Hartwig and Kouptsidis, 1974]. The principal gas load comes from photodesorption by the synchrotron radiation hitting the HEB and LEB masks inside the B1 magnets. To estimate the magnitude of the gas load, we use a desorption coefficient of 2×10^{-6} molecules/photon and a thermal outgassing coefficient of 1×10^{-11} Torr·L/s/cm^2. With these parameters, it will be possible to achieve the desired pressures.

As mentioned, maintaining a low pressure in the HER and LER straight sections that contain the interaction region is critical in order to reduce detector backgrounds. Guided by the background estimates discussed in Section 4.2, we have taken a design goal of 0.2 nTorr (N_2-equivalent) for estimating the amount of pumping needed in the "source" regions upstream of the IP (about 35 m for the HER and 15 m for the LER).

The incoming straight section of the HER has a photodesorption gas load associated mainly with the high-power upstream dump (HPUD, see Section 5.2.7.9). About 6 kW of synchrotron radiation from the low-energy beam impacts the wall in the upstream HER straight section at this dump, which begins 17 m from the IP. Assuming a photodesorption coefficient of 2×10^{-6} molecules per photon, the gas load will be 4.5×10^{-7} Torr·L/s/m in the vicinity of the dump. If this gas load were produced within the beam chamber, it would be necessary to provide about 2300 L/s/m of pumping along the

dump to reduce the pressure to 0.2 nTorr. For this reason, we have considered an alternative approach—using a differentially pumped antechamber.

The arrangement we envision is shown schematically in Fig. 5-67. The duct connecting the antechamber to the beam chamber has a height of 1.1 cm and a length of 30 cm. Cooling along the duct entrance and exit provides fault protection in case of beam orbit shifts. In this arrangement, most of the gas load is removed in the antechamber by TSPs that provide a pumping speed of 1200 L/s/m (just after pump regeneration). Gas that leaks into the beam chamber through the long, low-conductance duct is pumped by two rows of NEG modules. Although rows of virgin NEG modules will pump CO and CO_2 at 700 L/s/m just after regeneration, we assume a maximum pumping speed of 350 L/s/m to account for degradation due to exposures to air early in the commissioning history of the collider. As both the NEGs and TSPs have speeds that vary with time, the upstream HER straight section pressure will not remain constant but will be bounded by the values indicated in Fig. 5-68. These curves determine the required regeneration time for the NEGs to be about 2 months and that for the TSPs to be about 1 week.

The LER gas load is due mainly to photodesorption associated with the horizontal and vertical separation magnets that guide the low-energy beam into the IP. To handle the thermal load and provide sufficient pumping to achieve the desired operating pressure, a differentially pumped antechamber design similar to the chambers for the HER dumps will be used. The IR straight section bending magnets are relatively short, 0.5 to 1.2 m in length, so the radiation produced in them first strikes the vacuum chamber wall downstream of the magnet. At these locations, the synchrotron radiation fans will pass through slots in the beam chamber wall to be absorbed on a water-cooled outer wall. The absorber surfaces will be sloped so as to limit the maximum linear power density to 10 W/mm. A combination of TSPs and 400-L/s sputter-ion pumps (obtained from PEP) will be used to achieve the desired operating pressures in the LER upstream straight section.

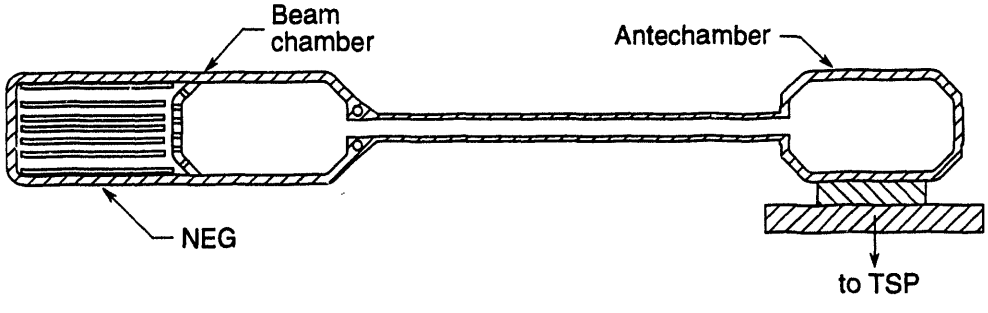

Fig. 5-67. Schematic of differentially-pumped beam chamber in HER beamline upstream of the IP.

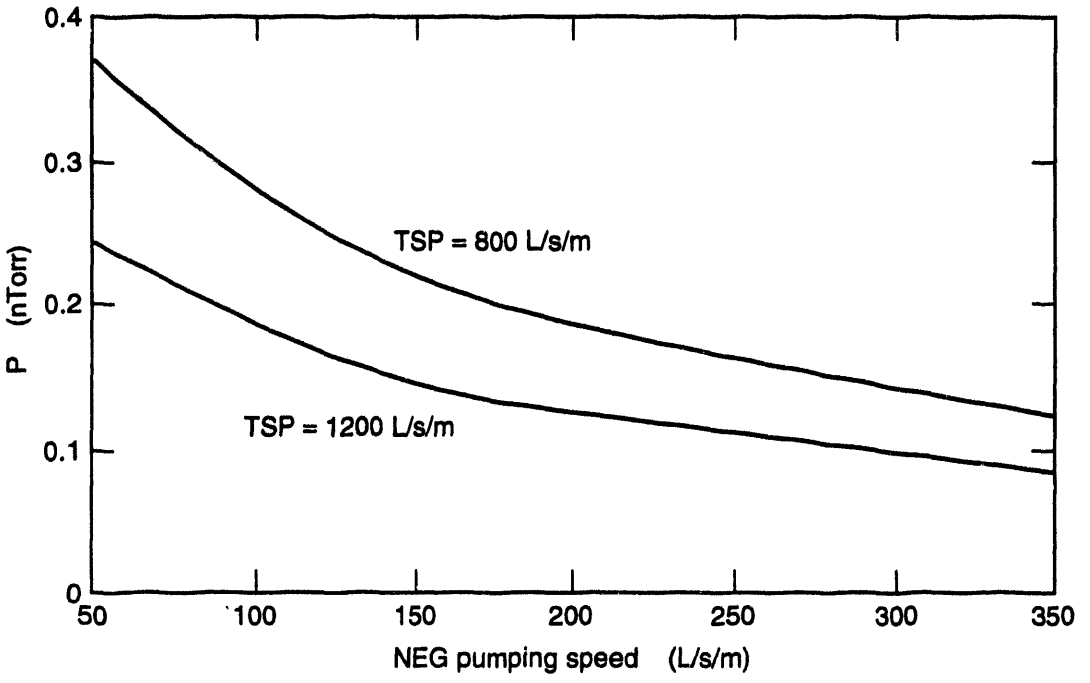

Figure 5-68. Pressure in beam chamber as a function of NEG pumping speed for two TSP pumping speeds. The TSP curves shown bound the expected range of pumping speed that will be covered between regenerations.

5.2.7.2 Synchrotron-Radiation-Absorbing Surfaces Near the IP. Areas in and around the IP where synchrotron radiation energy is deposited are indicated schematically in Fig. 5-69. These areas include the masks to protect the two septa, and the masks to stop radiation from impinging on the walls of the vertex chamber and portions of the walls of the vacuum chambers leading to and from the IP. All of these are considered in the following sections; a more detailed description of the masks can be found in the note by Lisin [1993]. Because reliability is crucial to the operation of PEP-II, it is important that the masks in the interaction region be designed conservatively. Below we estimate the power from the high-energy beam based on a beam current of 1.48 A, rather than the nominal 0.99 A. This will accommodate β_y^* in the HER up to 3 cm. The HEB septum mask will be discussed first as it sees the most severe conditions and therefore poses the greatest design challenge.

HEB Septum Mask. It is important that the vacuum walls of the septa in the two Q2 magnets be protected from incident synchrotron radiation. The septum on the incoming HEB side (left side in Fig. 4-46) sees synchrotron radiation generated by the low-energy beam as it passes through both of the B1 magnets. The HEB septum mask, located just inboard of the septum, intercepts some of the synchrotron radiation from the B1 magnets. Characteristics of those portions of the B1 synchrotron radiation fans that hit the mask are summarized in Table 5-24.

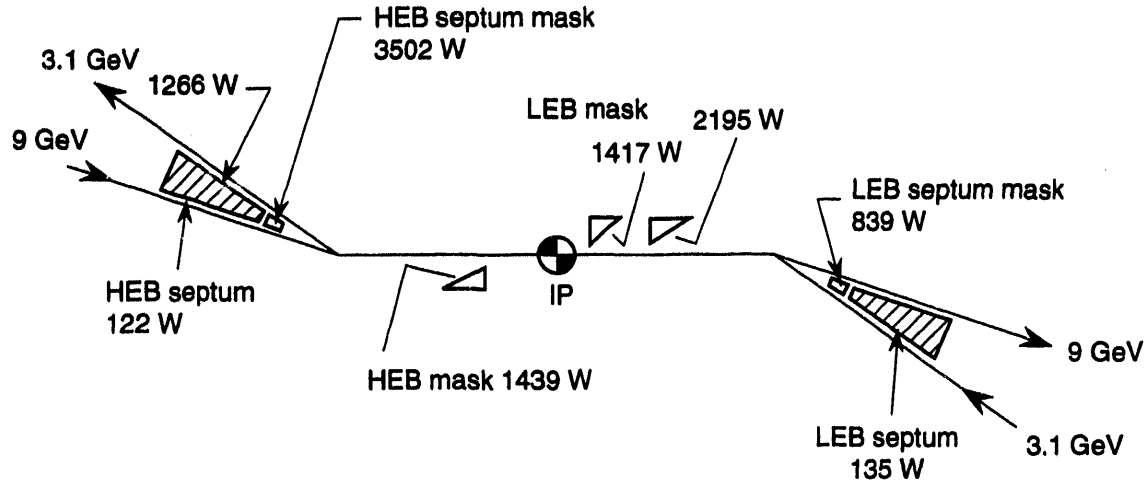

Fig. 5-69. Synchrotron radiation absorption in the vicinity of the interaction region. Power values correspond to a nominal beam current of 2.14 A in the LER and a 1.48-A beam current (compatible with a 3-cm vertical beta function at the IP) in the HER.

As shown in Fig. 4-47, the fans from the two B1 magnets overlap, so their heat inputs are additive. This results in a total power deposition in the HEB septum mask of 3502 W and a linear power density (normal to the radiation fan) of 168 W/mm. Table 5-24 shows the contribution from each source. The table also lists the synchrotron radiation fan height for a zero-emittance beam, which we take for design purposes.

A linear heat flux of 168 W/mm in a narrow stripe would result in excessive temperature and stresses, so the surface on which the synchrotron radiation is incident must be sloped relative to the radiation fan. In this case, we must create the slope by rotating the surface of the mask about an axis that lies in the plane of the radiation fan and is normal to the direction of the fan. Such a rotation avoids having the photons hit the leading edge of the mask, which cannot be adequately cooled. The central portion of the mask must have a very shallow slope in order to be able to absorb the very intense linear heat deposition rate of a narrow fan, while the mask must be sufficiently tall to intercept the fan from a more diffuse beam. The slopes at the ends of the mask can be much

Table 5-24. Synchrotron radiation power on the HEB septum mask.

Source	Power (W)	Normal linear flux (W/mm)	Fan height (mm)
HEB side B1	2078	102	0.67
LEB side B1	1424	66	1.02
Total	3502	168	—

steeper than that of the central portion, because the synchrotron radiation power density is lower with a broad fan. A slope of 1:50 in the central portion is sufficiently flat to give a reasonable heat flux through the body of the mask and across the metal-to-water interface with a 0.67-mm-high fan. With such a slope, the fan is absorbed over a length of 34 mm. The steeper ends are designed to give the same heat flux through the body of the mask and across the metal-to-water interface as for a zero-emittance beam striking the 1:50 slope. The central 1:50 sloping portion is extended to a total length of 137 mm to cover a 1 mm vertical steering error. The total length of the mask is approximately 390 mm.

Figure 5-70 shows the HEB septum mask geometry. The lightly shaded area represents the synchrotron radiation fans streaming from right to left. The tip of the mask lies below the plane of the fans and sees no radiation. As the absorbing plane rises, it intersects the bottom surfaces of the fans at about 180 mm from its leading edge. The next 34-mm section (more heavily shaded area) absorbs the synchrotron radiation. The last 180-mm section lies above the plane of the fans and sees no synchrotron radiation. To coincide with the beam-stay-clear boundaries, the sides of the mask are angled such that the mask is 14.5 mm wide at its tip and 22 mm wide at the septum end. The corner of the septum is located 46 mm from the collision axis.

Figure 5-71 shows the mask configuration used for the thermal analysis. The cooled surface is scalloped so that cooling tubes can be brazed to it. The use of scallops gives the maximum possible contact surface between the mask body and the cooling tubes. Three 6.3-mm (1/4-in.) OD cooling tubes, slightly flattened at the 14.5-mm-wide end, fit into the scallops. (Three tubes are used, rather than a single large passage, to give a greater convective heat transfer area.) Cooling water flows through the three tubes in parallel.

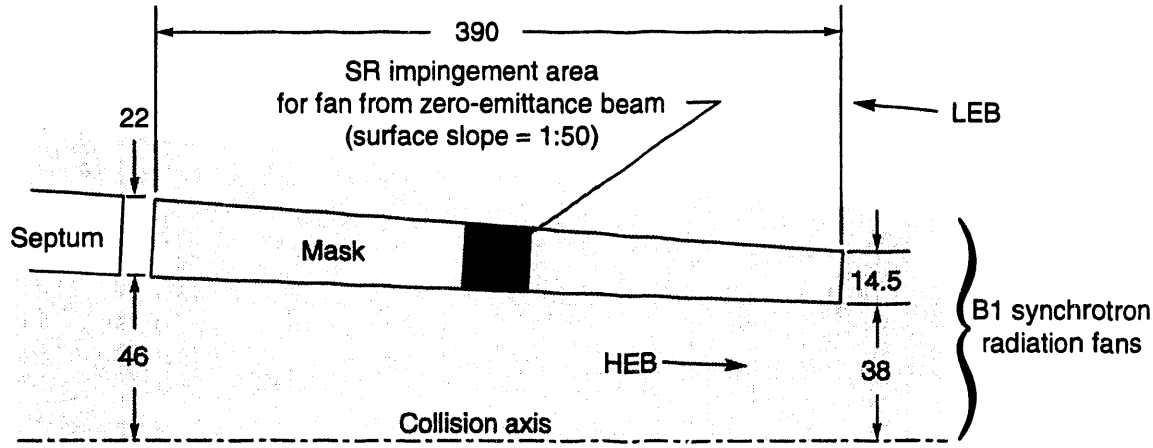

Fig. 5-70. HEB septum mask geometry (plan view). The incident synchrotron radiation fans from the B1 magnets originate approximately 2.2 and 3.1 m away from the mask surface.

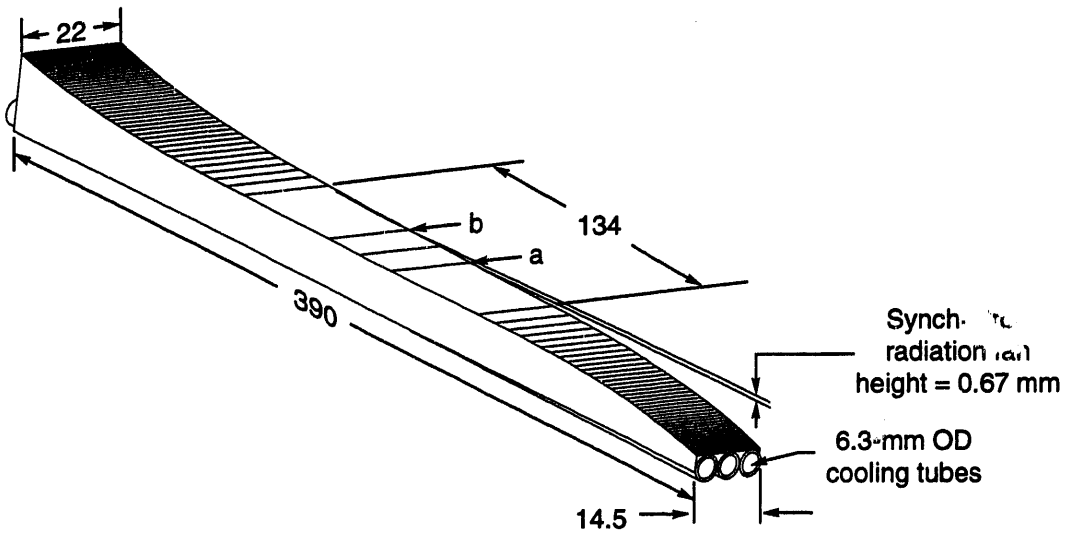

Fig. 5-71. Heat transfer model of HEB septum mask. The total power deposited is 3502 W. Synchrotron radiation from a centered, zero-emittance beam strikes the mask between points a and b.

The HEB septum mask design is summarized below:

- Geometry as shown in Fig. 5-71
- Three cooling tubes, 6.3-mm OD × 1- thickness
- Cooling water flows through the tub rallel, at a velocity of 4.6 m/s; total flow required is 15 L/min (4 gpm)
- Cooling water bulk temperature rise of 3.3°C
- Heated-surface-to-cooling-tube distance of 8 mm
- Mask body made of a dispersion-strengthened copper such as GlidCop AL-15
- Maximum metal temperature of 310°C for 20°C inlet water
- Maximum thermal stress of less than 40,000 psi

The above parameters are based on two-dimensional spread-sheet calculations of temperatures and hand calculations of stresses. Comparisons with earlier analyses of similar designs indicate that hand-calculated stress values are higher than those found from a full three-dimensional thermal and stress analysis using ANSYS. To avoid operational problems, thermocouples will be mounted at several locations along the mask to protect against excessive temperatures; the thermocouples may also prove useful to sense vertical beam position.

LEB Septum Mask. As on the incoming HEB side, the septum on the incoming LEB side (the right side of Fig. 4-46) must be protected from synchrotron radiation. The radiation fans that hit the front of the LEB septum mask are generated by the high-energy

beam as it passes through B2, Q4, and BH1 (see Fig. 4-48). Characteristics of the fans that hit the LEB septum mask face are listed in Table 5-25.

The B2 fan extends over the entire width of the septum. The Q4 fan extends across approximately half of the septum and the BH1 fan across the other half (that is, the Q4 and BH1 fans do not overlap). Therefore, half the septum sees a linear power density normal to the fan of 60 W/mm and the other half sees 113 W/mm. The total power deposited is 839 W. (An additional 62 W coming from B6 on the LEB side strikes the edge of the mask.)

Compared with the HEB septum mask, the LEB septum mask must handle about one-fourth of the total power and has a maximum linear heat flux only two-thirds as much on half its surface (and one-third as much on the other half). The fan heights are essentially the same. The LEB septum mask surface on which the synchrotron radiation is incident will again have to be sloped. Although the heat flux is appreciably lower on half the mask, it is still too high in this region to be absorbed by a sharp corner. Therefore, the mask face will be sloped about an axis lying in the plane of the fan, as is the case for the HEB septum mask. The lower power absorbed by the LEB septum mask means that it could be sloped slightly more steeply than the HEB septum mask, making it shorter.

LEB Mask. The LEB mask (see Fig. 4-47) has two surfaces on which synchrotron radiation is incident. We refer to these as the "inboard" surface (nearer the IP) and the "outboard" surface (farther from the IP). Both the inboard and outboard mask surfaces prevent synchrotron radiation generated by the low-energy beam as it passes through Q1 from striking the vertex detector vacuum chamber wall; the outboard surface of the mask additionally intercepts the synchrotron radiation fans generated in Q2, B5, and B6. Figure 5-72 shows the LEB mask geometry. Table 5-26 lists the characteristics of the synchrotron radiation fans that strike the mask.

The outboard surface is struck by 1358 W of synchrotron radiation power in a fan of 0.5-mm height, 72 W in a fan of 0.8-mm height, plus 765 W in a fan of 4.5-mm height. The total power deposited on the outboard surface is thus 2195 W. The Q1 and Q2 fans do not overlap, but the B5 and B6 fans overlap both the Q1 and Q2 fans. The inboard surface is struck by 1417 W of radiation in a fan that is 0.49 mm high. The small portion of the Q1 fan that is not intercepted by the LEB mask (see Fig. 4-61) flies harmlessly past

Table 5-25. Synchrotron radiation power on the LEB septum mask.

Source	Power (W)	Normal linear flux (W/mm)	Fan height (mm)
HEB side B2	110	7	1.58
HEB side Q4	379	53	0.76
HEB side BH1	350	106	0.73
Total	839	60 or 113	—

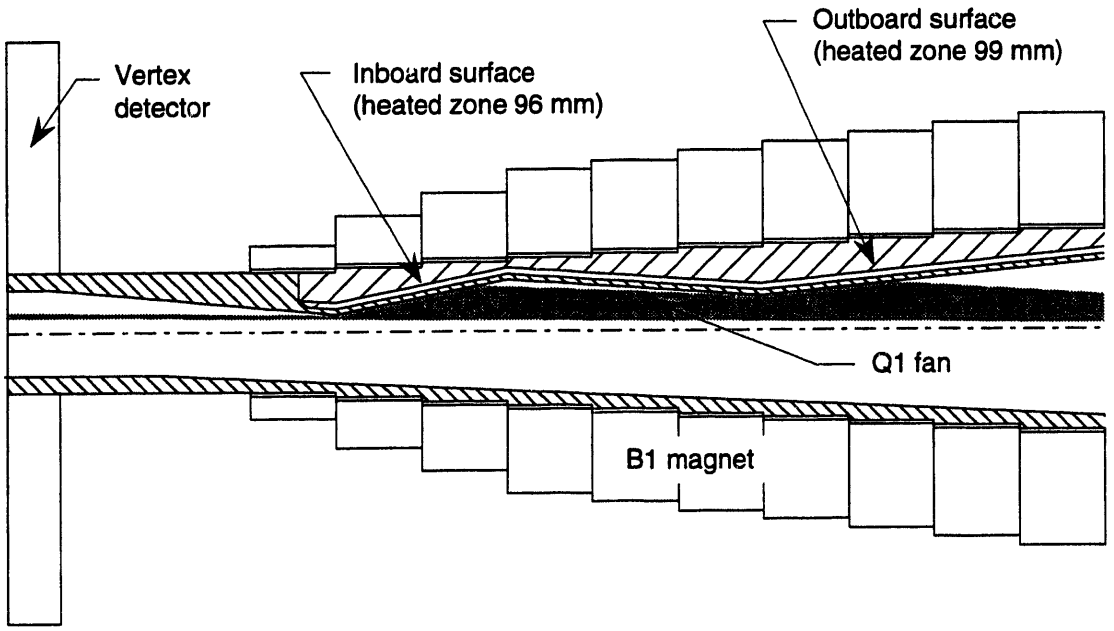

Fig. 5-72. LEB mask geometry, top view, showing zones heated by Q1 synchrotron radiation fan.

Table 5-26. Synchrotron radiation power on the LEB mask.

Incident on	Power (W)	Normal linear flux (W/mm)	Fan height (mm)
Outboard surface			
B5 and B6	765	9.4	4.5
Q2	72	10	0.8
Q1	1358	91.7 (max)	0.5
Total	2195	—	
Maximum	—	101.1	—
Inboard surface			
Q1	1417	71.0 (max)	0.5

the IR and is deposited on the wall of the outgoing LEB vacuum chamber beyond Q2; its intensity is sufficiently low that its energy deposition can be ignored.

The linear power density normal to the fans striking the mask is sufficiently high that the walls on which the synchrotron radiation is incident must be sloped. The outboard surface has a slope of 1:6.7, and the inboard surface has a slope of 1:5; these slopes result in surface linear fluxes of 15 and 14 W/mm, respectively. The slopes are created by rotating about an axis perpendicular to the plane of the fan to gain full advantage of the heat spreading normal to the plane of the fan. The slopes were chosen to be as flat as possible while still precluding the possibility of scattered radiation entering the vertex chamber after only one bounce. Fortunately, the slopes constrained in this way are still sufficiently flat to reduce the surface linear flux to levels that can be readily handled.

Both surfaces of the mask will be cooled by the same water passages. Two parallel water passages are milled into the body of the LEB mask/vacuum chamber straddling the horizontal centerline, as shown in Fig. 5-73. Water is supplied at the outboard end of the mask. The incoming water flowing through the passages removes the heat deposited by the synchrotron radiation fan. Two similar passages, located approximately ±90° away, are used to return the water to the outboard end of the mask. Transverse flow passages to connect the incoming and outgoing passages are milled into the mask body at its inboard end. The outflowing water removes most of the heat generated by scattered radiation, HOM losses, and resistive losses. A total water flow rate of 7.3 L/min (2 gpm) gives a velocity of 4.6 m/s (15 fps) and results in a bulk water temperature rise of 6.8°C. The water temperature rise due to the other heat sources is small and has been ignored.

Heat transfer and stress analyses of the model described above indicate that stresses are sufficiently high to require the use of a dispersion-strengthened copper. Results of a two-dimensional spread-sheet calculation of temperatures and hand calculations of stresses (assuming a zero-emittance beam) are summarized below:

- Cooling water flow rate — 7.3 L/min (2 gpm)
- Inlet water temperature — 20°C
- Outlet water temperature — 26.8°C
- Metal temperature drop (max.) — 70°C
- Film temperature drop (max.) — 37°C
- Maximum metal temperature — 134°C
- Maximum thermal stress — <40,000 psi

The above stresses appear to be reasonably conservative for a material like GlidCop AL 15, which has a fatigue strength of 48,000 psi at 10,000 cycles even after brazing at 800°C.

A more detailed analysis, using a three-dimensional thermal and stress code, will be performed to verify the design.

HEB Mask. The HEB mask prevents synchrotron radiation generated by the incoming high-energy beam as it passes through B2 and Q4 from striking the vertex detector vacuum chamber wall. Table 5-27 lists the characteristics of the fans that strike the mask.

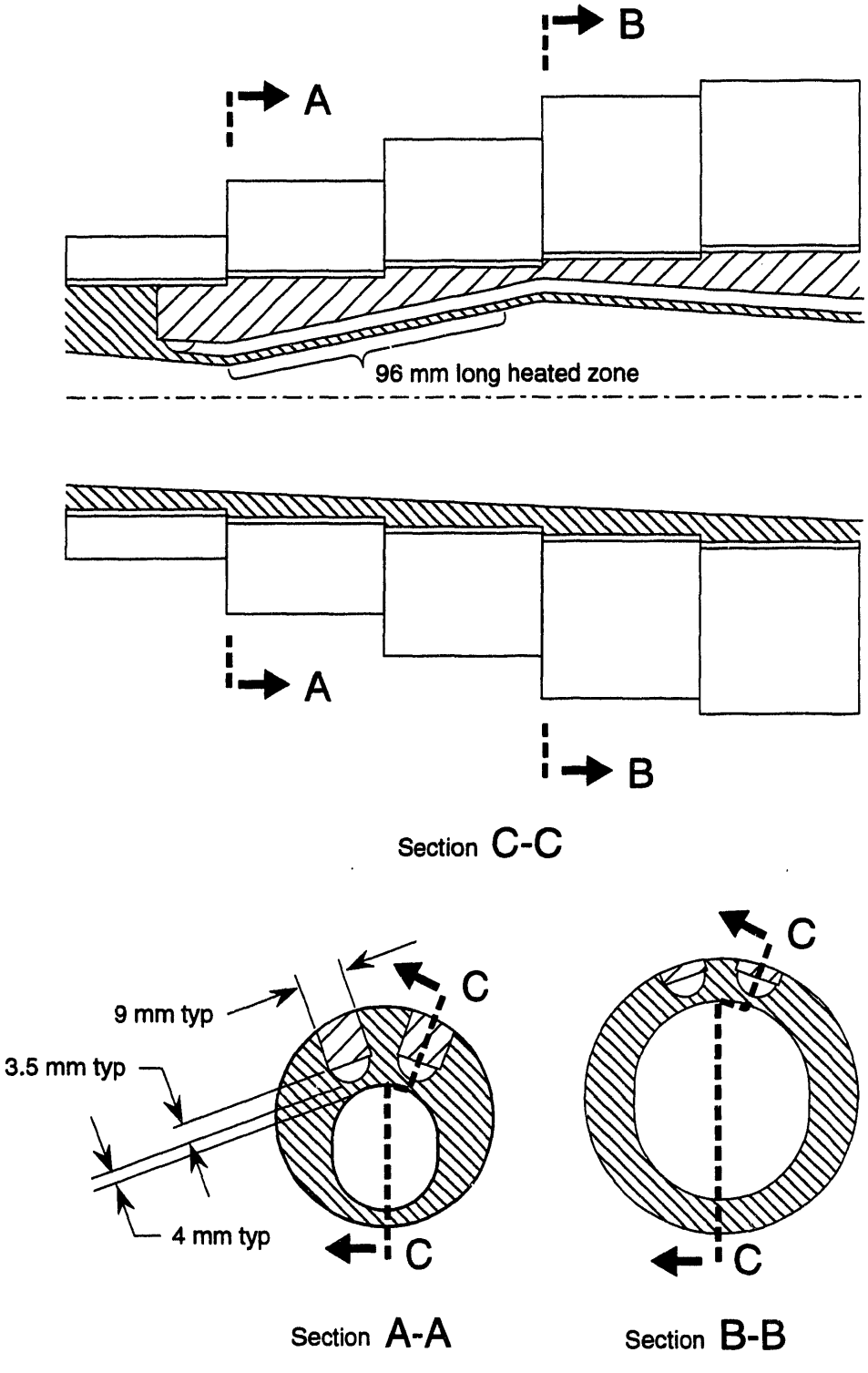

Fig. 5-73. Heat transfer model of LEB mask. Only inboard surface (see Fig. 5-83) and incoming cooling channels shown.

Table 5-27. Synchrotron radiation power on the HEB mask.

Source	Power (W)	Normal linear flux (W/mm)	Fan height (mm)
HEB side B2	158	13	0.94
HEB side Q4	1281	96	0.43
Total	1439	109	—

The effects of the two fans are additive—the total power deposited in the mask is 1439 W, and the linear power density normal to the fan is 109 W/mm. As for the LEB mask, the normal linear flux is undesirably high, so the mask surface must be sloped. A slope of 1:8.5 was chosen so that no scattered radiation can enter the vertex chamber after only one bounce. Such a slope reduces the surface flux to a level that can be readily handled. The total combined surface linear flux is 13 W/mm.

Because the surface linear power density on the HEB mask is comparable to that on the surface of the LEB mask, a cooling arrangement like that used for the LEB mask is adequate and will be employed.

Vacuum Chamber Thermal Issues. The septum side of the incoming HEB vacuum chamber absorbs radiation generated by the high-energy beam as it passes through B2. The total power incident on this wall is only 122 W, and the surface linear power density is 0.3 W/mm. The septum side of the incoming LEB vacuum chamber also sees a small amount of synchrotron radiation (135 W) generated by the LEB passing through B6. These low-intensity heat sources do not require special cooling arrangements.

Portions of the same synchrotron radiation fans that hit the HEB septum mask (see above) continue through the LEB exit chamber (see Fig. 4-62). The surface linear power densities are 1.2 and 1.3 W/mm for a total of 2.5 W/mm. A water-cooling line will be attached to the wall of the vacuum chamber to remove this heat. Heat removal in this area will not be a problem, of course, as the surface linear heat flux is considerably lower than that being handled in the arc vacuum chambers.

Vertex Detector Vacuum Chamber. The vertex detector vacuum chamber must be designed to be compatible with the detector requirements. This means that it must have the following features:

- It must be as transparent as possible to outgoing particles and photons from the collisions over a length of 170 mm
- It must have as small an outside diameter as possible
- It must have an inside diameter of 50 mm or less

Because heat deposited in the chamber by HOM heating and resistive heating will be about 200 W, the vertex detector vacuum chamber must also be cooled.

Beryllium was chosen for the chamber wall material because of its low Z and relatively high strength. The possibility of a beryllium tube cooled only at its ends was considered, but a double-walled tube with a cooling fluid in the annular space was found to be a more transparent and more efficiently cooled design. An illustration of the chamber concept is shown in Fig. 5-74. The ends of the beryllium tubes are brazed to stainless-steel ends. A spacer ring between the inner and outer tubes at each end maintains concentricity between the tubes to form an annular cooling passage 2 mm wide. The stainless-steel ends are welded to the spacer ring to seal the ends of the passage. Stainless-steel-to-beryllium joining technology that was used in the construction of the SLD beryllium vertex chamber will be used. Figure 5-75 is a photograph of the SLD chamber using such joining technology.

The outer wall thickness of the vertex detector chamber pipe is 0.4 mm, and its inner wall has a thickness of 0.8 mm. Both will withstand a pressure of about 50 atm. Coolant pressure will be considerably lower than this, so the safety margin is substantial. Indeed, the thickness was chosen primarily to make the chamber more rugged and to minimize chances of damage in handling.

Helium, hydrogen, and water were all considered as possible coolants. Although helium is not quite as good a coolant as either water or hydrogen, the fact that it is inert led to its being the coolant of choice. Beryllium and water appear to be compatible, but some beryllium would certainly enter the water and be carried by it. Concern about leaks and spills, and the resulting possibility of contamination, thus ruled out water. Hydrogen should be compatible with beryllium, but was ruled out because of its flammability.

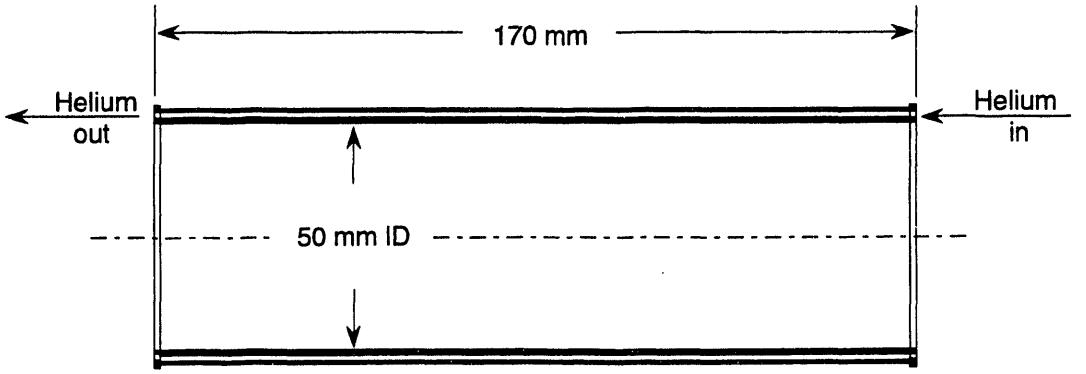

Overall length, 170 mm
Inner tube thickness, 0.8 mm
Outer tube thickness, 0.4 mm
Gap between tubes, 2 mm

Fig. 5-74. Design for the double-walled beryllium vacuum chamber for the vertex detector. Helium at 2 atm is used as the coolant.

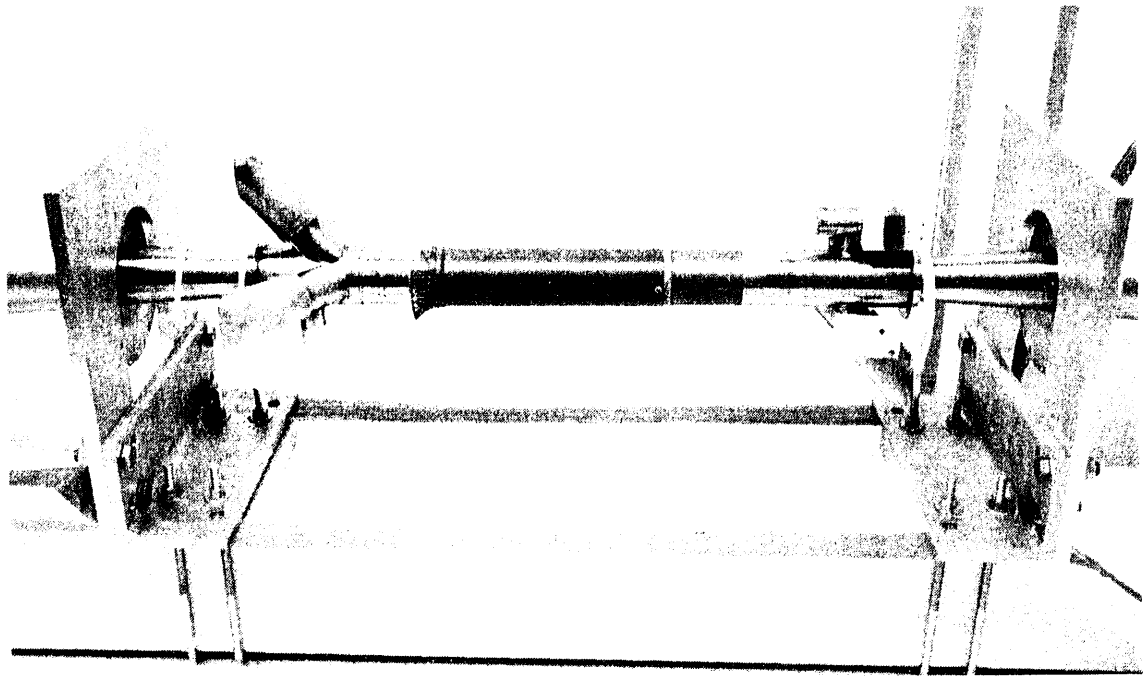

Fig. 5-75. Photograph of SLD vertex chamber.

Helium pressurized to 2 atm is quite adequate as a coolant. A flow of 22 g/s (Mach number = 0.2) gives a helium temperature rise of 1.1°C and a film temperature drop of 2°C for a 200-W heat input. Thermal stresses are quite low at these temperature differences. At least twice as much heat could be removed by the above flow should it prove necessary. Furthermore, the wall thicknesses adopted would allow the use of higher-pressure helium in the event that still more heat needed to be removed. Thus, the vertex chamber beam pipe is very reliably and conservatively designed for use in PEP-II.

5.2.7.3 High-Power Beam Dumps. There are several radiation sources close to the IP where the majority of the synchrotron radiation power is generated—the B1 dipoles and offset Q1 quadrupoles. Although both the HEB and LEB liberate considerable power in this region, the proximity of the sources to the IP means that most of the upstream synchrotron radiation fans (and nearly all of the downstream fans) pass through the detector area without hitting anything. To absorb the power, special dump areas are installed on both the upstream and downstream sides of the IP. The high-power downstream dump (HPDD), located in the HER outgoing beam pipe, absorbs the power generated by the HEB going through the IR (about 75 kW). The high-power upstream dump (HPUD) is the repository of about 6 kW of power generated by the LEB. Because those portions of the B1 fans from the LEB that do not strike the septum mask actually exit the IP area in the HER pipe, this dump too is located in the HER, but in the "upstream" portion (as seen by the HEB). Clearly heat removal per se will not be a problem for either the HPDD or HPUD, as the total power values are moderate. Nonetheless, the power densities are high enough to require special attention.

High-Power Downstream Dump. The synchrotron radiation fans generated by the high-energy beam (dominated by the contributions from the two B1 magnets) carry about 75 kW of power. To keep detector backgrounds low, and to allow the synchrotron radiation fans to spread, the bulk of the HEB radiation fan is dumped at a location 17–24 m away from the IP, just beyond the downstream string of B2 magnets in the HER (see Fig. 4-49). We refer to this area as the high-power downstream dump. Locating the HPDD at 17 m avoids congestion in the B2 area and allows flexibility in the design of the B2 magnets. Furthermore, at a distance of 17 m from the IP, the fans have spread out vertically to σ_y = 2 mm (assuming a zero-emittance beam), a size sufficient to ease the challenges of thermal management.

The HPDD vacuum chamber has an antechamber design, with sufficient differential vacuum pumping to maintain the required low pressure in the beam chamber. The synchrotron radiation fan passes through a slot in the beam chamber wall and is absorbed on a water-cooled outer wall in the antechamber. At 17 m, the linear power density normal to the synchrotron radiation fans is 375 W/mm, which is unmanageably high. However, if the absorbing surface has an initial slope of 1:40 relative to the fan, and the slope gradually steepens as the fan power density decreases, the radiation can be absorbed over a length of about 7 m, and the maximum linear power density can be held to an easily manageable value of about 10 W/mm.

High-Power Upstream Dump. We must also deal with the power carried by synchrotron radiation fans created by the low-energy beam passing through the IR. In this case, the total power that escapes the IP area is only 5.8 kW—much reduced compared with that from the high-energy beam. Furthermore, because of the lower beam energy, the vertical spreading (which goes as $1/\gamma$) will be even greater than for the HEB. Here too, the synchrotron radiation fans will be absorbed by a water-cooled dump (the HPUD) starting at about 17 m upstream of the IP in the HER.

5.3 SURVEY AND ALIGNMENT

The primary goal of the survey and alignment activity for PEP-II is to align the lattice components along a "smooth" curve. This should be done in such a way that the rms deviations of components from this curve do not exceed 150 μm and that the resulting circumference is within 5 mm of its design value. Overall tolerances for the alignment of the various ring components are summarized in Table 5-28. As can be seen from this table, the most important alignment criterion is the *relative* accuracy requirement. Consequently, long-period systematic effects on the measurements and computations are unimportant. This means that we need not be concerned about effects like geoid undulations, deflections of the vertical, earth tides, site-wide water table changes, etc.

Modern computer-aided methods and procedures, which have been tested and proved at SLC, HERA, and LEP, will be applied to perform the alignment. While great care and attention to procedural detail will be required to achieve relative alignment tolerances of 150 μm, much more demanding alignment projects are either ongoing at SLAC or have been successfully completed in the recent past. Magnet-to-magnet deviations obtained for the SLC arcs were 100 μm, despite the fact that, unlike the PEP-II rings (each of which

Table 5-28. PEP-II alignment tolerances.

Global tolerances	
Horizontal and vertical positioning of quadrupoles (rms) [mm]	1.5
Horizontal and vertical positioning of sextupoles (rms) [mm]	1.5
Horizontal and vertical positioning of dipoles (rms) [mm]	4
Roll angle of quadrupoles (rms) [mrad]	1
Roll angle of sextupoles (rms) [mrad]	1
Roll angle of dipoles (rms) [mrad]	0.3
Circumference [mm]	5
Component-to-component tolerances	
Sextupole-to-quadrupole within a module (rms) [mm]	0.10
Horizontal and vertical positioning of quadrupoles and sextupoles in injection line [mm]	0.5
Smoothness tolerance	
Quadrupole-sextupole pair to quadrupole-sextupole pair (rms) [mm]	0.15

lies in a single horizontal plane and exhibits no roll) the SLC beamlines transition continuously through pitch and roll ranges of –4° to +6° and –10° to +15°, respectively. The Final Focus Test Beam (FFTB), now under construction at SLAC, has conventional alignment tolerances of 30 μm. This requirement is truly unprecedented and calls for new techniques, including the application of both laser tracker and portable hydrostatic level technology. PEP-II will benefit directly from the hardware, software, procedure, and experience base gained on these SLAC projects.

The specific alignment tasks that are required include the following, each of which is taken up in a subsequent section:

- Support the component fiducialization effort
- Align modules and girder components in the alignment laboratory
- Perform "blue-line" survey of anchor-bolt positions for supports
- Rough-align the supports
- Rough-align the components
- Final-align (smooth) the components
- Align the interaction region components
- Perform quality control surveys

5.3.1 Preliminary Considerations

Before expanding on specific tasks, some fundamental alignment requirements must be introduced.

5.3.1.1 Fiducialization. The virtual magnetic axis of each component must be related to external fiducial features. Since the fiducialization error is budgeted as part of the overall alignment error, it should be kept very small. Otherwise, it will dominate the alignment error budget, thereby eliminating most of the allowable error margin for the positioning of the fiducial relative to the traverse monuments. In general, the fiducialization error should be kept below 50 μm to ensure a successful alignment.

Because the LER is located above the HER, there is inadequate space to mount alignment equipment on top of the HER magnets. As it is impractical to place permanent alignment fiducials on the tops of magnets, we plan to incorporate reference grooves in the magnet laminations that will allow alignment reference fixtures to be mounted on the aisle side of the components.

PEP-II will use a very versatile fiducial system based on 1.5-in. spheres. Fixtures and components will be built to accept special magnetic cups that can hold a variety of fiducials housed in spheres. Cutaway spheres with a center "bull's-eye" are used for triangulation measurements, a retro-reflector mounted in a sphere is used for electronic distance and laser-tracker observations, and simple spheres are ideal for optical-tooling measurements. The sphere fiducials and cups are commercially available and have proved very effective at CEBAF and on the SLAC FFTB project. Figure 5-76 shows a PEP quadrupole fixture that has been upgraded with magnetic cups. One cup is occupied by a triangulation target, the other by a retro-reflector.

5.3.1.2 Coordinate System. Before performing the survey and alignment procedure, we must first define a coordinate system in which all measurements will be reported. For a machine of this size, the fact that the local shape of the earth is not planar but somewhat spherical must be taken into consideration. If the primary datum of the coordinate system is defined such that it coincides with the center of the ring, then, at least to a first approximation, the machine is built in a common tangential plane. This means that the horizontal direction with respect to gravity is also "horizontal" in the layout coordinate system, within the required accuracy. However, this horizontal plane is inclined with respect to the common SLAC coordinate system. With this in mind, the PEP-II alignment coordinate system (see Fig. 5-77) will have the following attributes:

- Right-handed system
- Primary datum at the center of the HER
- *Y*-axis parallel to gravity at datum point, positive up
- *Z*-axis perpendicular to *Y*, in the plane formed by the linac and gravity vector, with the downstream direction of the linac defined as positive
- *X*-axis perpendicular both to *Y* and *Z*

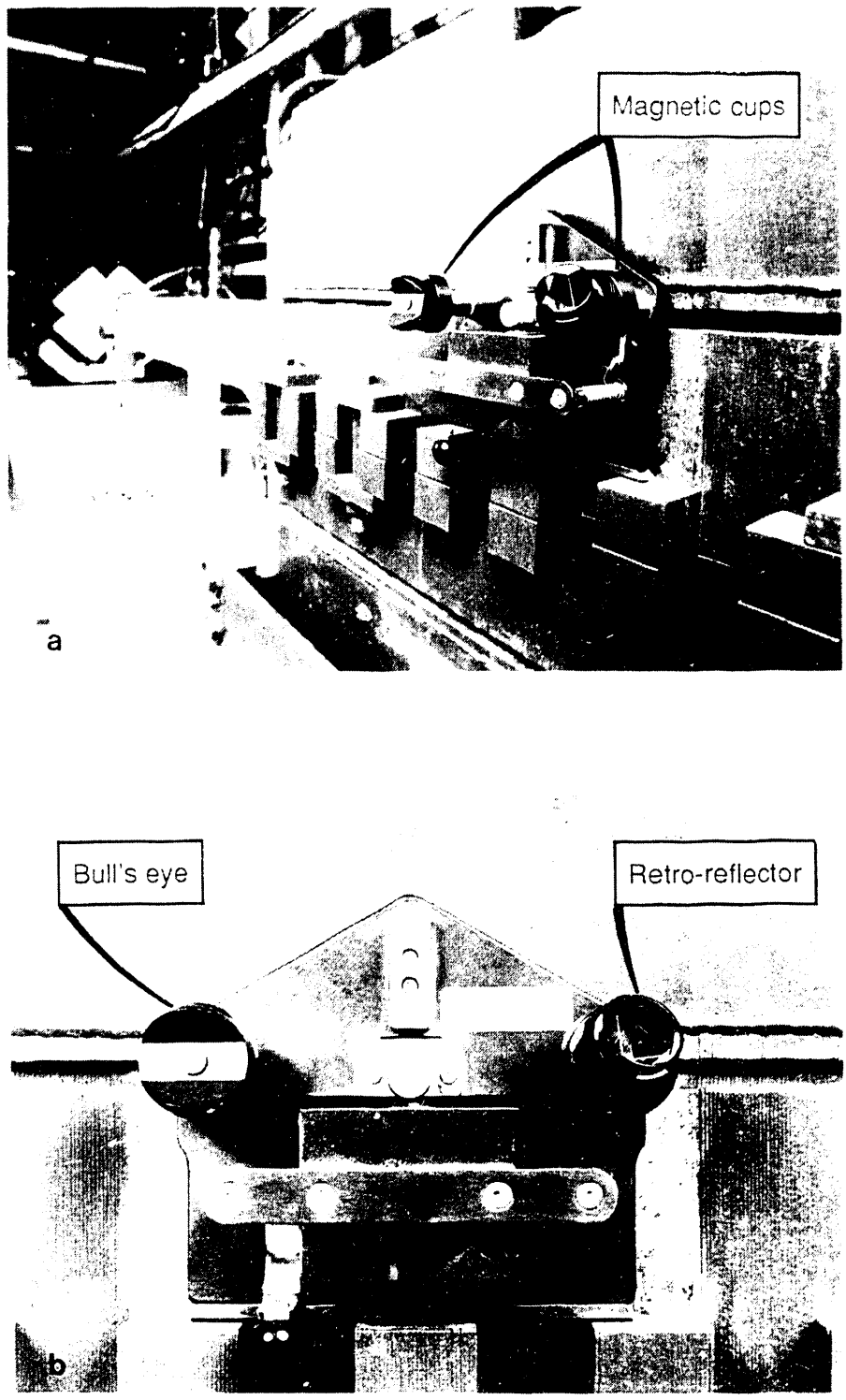

Fig. 5-76. (a) PEP quadrupole fixture upgraded with magnetic cups. (b) Close-up showing "bull's-eye" triangulation target and distance meter retro-reflector.

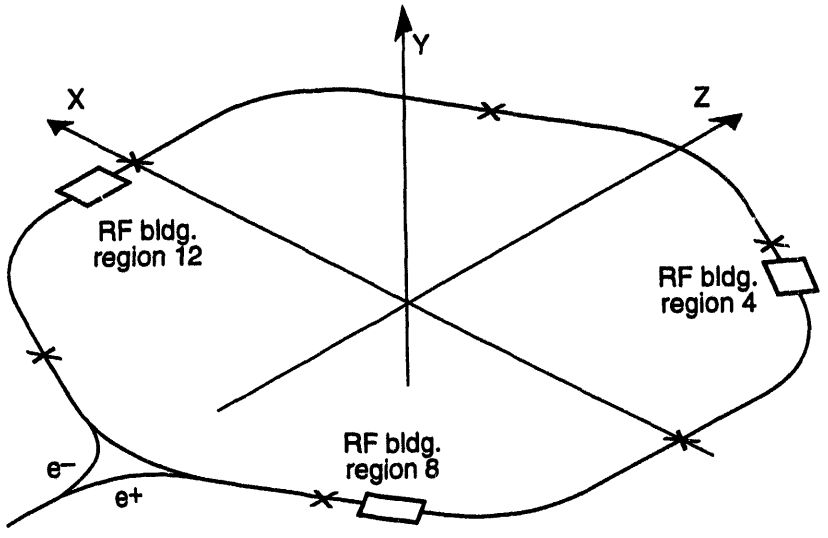

Fig. 5-77. Artist's rendition of the PEP-II coordinate system.

A rotation matrix and translations will be defined to perform transformations between the local PEP-II coordinate system, as defined above, and the global SLAC coordinate system. The elements of this transformation can be found in Fig. 6-15.

5.3.1.3 Control Networks. Computer simulations show that the global tolerances for lattice component positioning can be met without the supporting framework of a surface network. Figure 5-78 shows error ellipses from a free-net simulation of an unsupported tunnel traverse over the existing PEP monuments. However, this assumes many weeks access to the entire ring and linac east end to measure the complete tunnel-control traverse and linac connection in one survey. A surface-net connection to the linac could reduce required linac access to a few shifts and provide great scheduling flexibility. Furthermore, the tunnel network could then be measured in pieces, from one surface connection point to another, without requiring global access. Since the survey shafts already exist and the required Global Positioning System (GPS) receivers could be borrowed from the SSC, an accurate surface net could be determined very economically.

To start the project, the existing 102 PEP horizontal-control monuments, spaced at intervals of 22 m around the ring, will be resurveyed and used to control the layout and installation of supports. Distances between monuments will be measured with a Kern ME-5000 distance meter. Directions will be measured with digital electronic theodolites. Interfaced laptop computers running SLAC data-collection software will control the observation process. Observations are always made to at least two monuments ahead and back to provide a highly redundant and overlapping data set. The software statistically tests the data sets in the field to ensure distance and directional consistency to 0.1 mm and 1 arc-second, respectively. Data transfer, processing, reporting, and archiving are fully automated and performed on the SLAC GEONET system, now the standard at DOE physics labs.

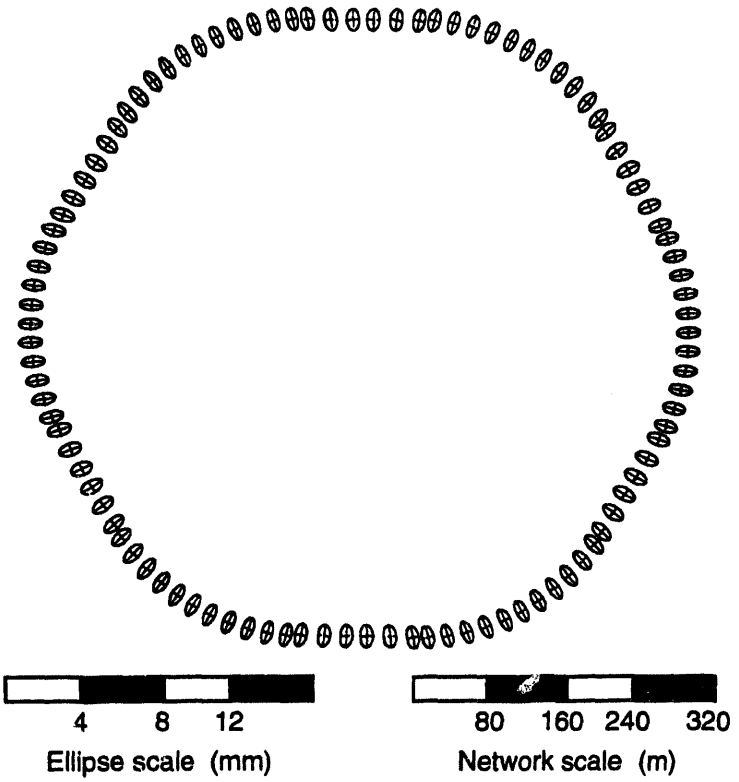

Fig. 5-78. Error ellipses from PEP tunnel traverse free-network simulation.

Before precise magnet positioning begins, the monument net will be made more dense—to a spacing of 7.6 m, or two monuments per cell—and surveyed again. The monuments will split the distance between neighboring HER and LER quadrupoles to optimize magnet survey geometry for both rings. Figure 5-79 shows monument positions and a typical triangulation observation plan. Floor monuments will be styled after the three-dimensional "reference cups" used successfully at CEBAF and the ALS at LBL. The cups will accept the same 1.5-in. spheres described in Section 5.3.1.1. Because distances, directions, and offsets can be measured directly to the cup, the effort to center tripods over monuments is greatly reduced and accuracy is enhanced. Furthermore, three-dimensional mapping with theodolites is facilitated because each monument carries an accurate elevation as well as horizontal position. The traverse configuration will be modified to accommodate interaction-hall bridging and subsequent alignment of interaction region components.

Most vertical control measurements will be performed using differential leveling techniques with precise Wild N3 tilting levels and dual-scale Invar rods. However, the fact that the PEP tunnel lies in a horizontal plane makes a liquid-leveling system practical. We will therefore service and modify the existing PEP liquid-leveling system for use as a master reference in the ring tunnel. Level wells will be installed on both sides of each IR hall and at the center of each arc section. The tie to the linac and the SLAC-wide elevation datum must be made using differential leveling.

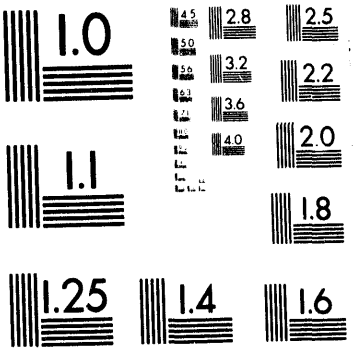
1.0
1.1
1.25
1.4
1.6
1.8
2.0
2.2
2.5
2.8
3.2
3.6
4.0
4.5
5.0
5.6
6.3
7.1
8.0
9.0

5 of 7

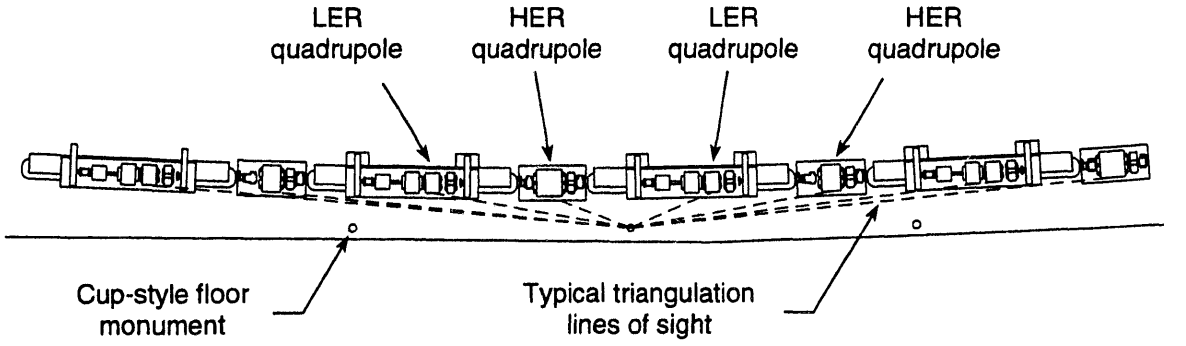

Fig. 5-79. Typical monument locations and triangulation observation plan.

5.3.2 Survey and Alignment Tasks

5.3.2.1 Girder and Module Alignment in the Laboratory. The quadrupole-sextupole pairs in the HER will be aligned with each other in the laboratory and thereafter treated as a module; that is, their relative alignment will not be adjusted in the tunnel. The dipole-quadrupole-sextupole modules on each LER girder will also become a laboratory-aligned unit whose relative alignment will not be adjusted in the field. Figure 5-80 is a schematic of a module alignment bay configured for highly automated operations using the SLAC Industrial Measurement System (SIMS). The SIMS software can control the observing sequence, statistically test the data sets and the coordinates determined therefrom, calculate required component moves, and generate a module survey report. In the bay, three theodolites will be mounted on pillars whose three-dimensional positions have been accurately determined. A module will be brought to the bay and placed on supports exactly like those to be used in the tunnel. The theodolites will be used to quickly triangulate three-dimensional positions of raft and component fiducials in an arbitrary "bay coordinate" system. The bay system will then be transformed to a system defined by the raft fiducials so that all positions and adjustments can be reported in that system.

5.3.2.2 Blue-Line Survey. In preparation for the installation of the support systems, a "blue-line" survey will be performed to lay out the anchor-bolt positions. A file of layout coordinates will be computed from the lattice and the support design information. An electronic-theodolite–distance-meter combination, known as a "total station," interfaced with a laptop computer, will be used to conduct the work. After setting up the total station on top of one monument and sighting another, the computer will generate the distance and angle to the desired layout point and transmit them to the total station display screen. The instrument operator directs an assistant holding a retro-reflector to the proper line while the screen displays the difference between the distance to the reflector and the desired point. An accuracy of 5 mm, which is more than sufficient, can be easily achieved. All points thus laid out will be checked from a second monument and the results stored in an output file.

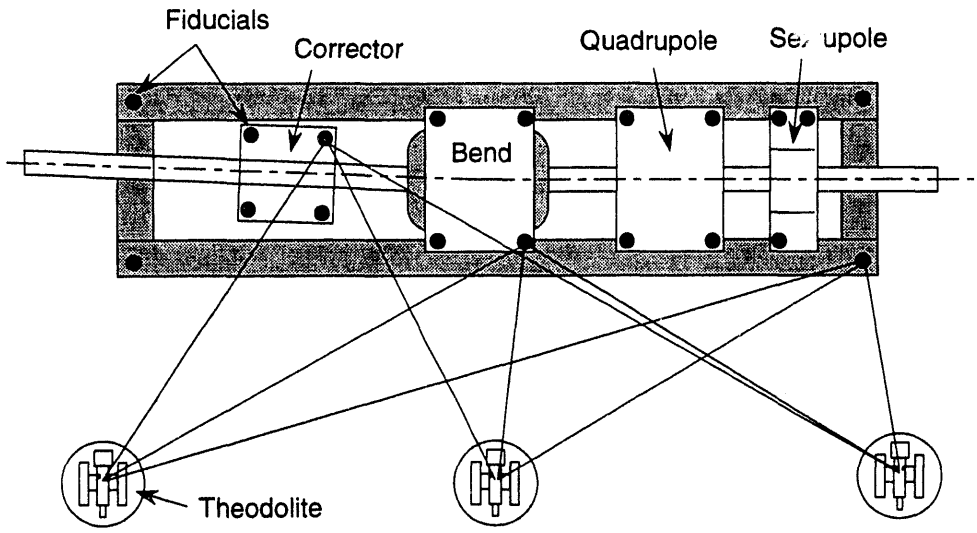

Fig. 5-80. Laboratory module alignment by triangulation.

5.3.2.3 Rough Alignment of Supports. After the blue-line survey, the anchors and support systems will be installed, but with the anchor bolt nuts only hand tight. All baseplates, C-frames, and other supports will be keyed and designed to "stack up" accurately with laboratory aligned modules. Rough alignment fiducial fixturing will key to the supports in the same way as the modules. Again, files of layout and monument coordinates will be carried on a laptop computer that controls the alignment procedure. Using a total station set up over a monument and inclinometers as control instruments, the supports will be tapped into position to an accuracy of a few millimeters. This is especially important for the C-frame supports, where a small roll displacement would have a large correlated horizontal (x) effect for the LER components. If not controlled, this type of support misalignment could easily exceed the adjustment mechanism range of individual components.

A secondary round of support alignment will also be performed on the C-frames. The bottom of a C-frame will support an HER dipole, while its top will support a raft in the LER. Elevations of the four HER dipole supports will be carefully adjusted to their ideal values so that the important dipole roll parameter is nearly perfect upon magnet installation. The horizontal positions of the dipole supports will be adjusted as well, to the 1-mm level, so that no horizontal magnet adjustments are required later. To preset the LER raft struts, a lightweight mock raft (with attachments and fiducials exactly like a real raft), will be mounted, surveyed, and adjusted into nominal position at each location. Raft sag induced by magnet weight will be determined and a correction applied to the raft layout coordinates.

5.3.2.4 Rough Alignment of Components. After the magnets are installed, they will be positioned relative to the traverse monuments to an accuracy of about 0.3 mm. This will be done with a two-step procedure:

(1) Bring the magnets to their ideal elevations and set their pitch and roll values to zero, using differential-leveling techniques

(2) Map the horizontal positions of quadrupole-sextupole pairs relative to the traverse points, using triangulation methods

The mapped positions will be compared with their ideal values to determine the required mechanical adjustments. The subsequent application of adjustments will be controlled using digital indicators. Experience with this alignment scenario indicates that two iterations should yield the desired accuracy. HER dipoles will be measured during the first iteration to confirm that the "stack-up" of supports and magnets went as anticipated. It is likely that a few will need adjustment. For the injection lines in the linac housing, traditional optical-tooling techniques will be used. The linac tooling reference holes will provide the necessary tunnel control after they have been mapped using the linac Fresnel lens alignment system.

Alignment of the matching sections, the barrel, and the detector will lend itself to the standard rough-alignment technique. Fiducials on the outermost magnets of the barrel will be visible from the aisle. These fiducials will be used to align the barrel.

5.3.2.5 Smoothing of Quadrupoles and Sextupoles. The global positioning accuracy obtained in the absolute positioning step is the quadratic sum of many random errors (surface network, penetration transfers, tunnel net, magnet fiducialization, etc.), plus the linear sum of any residual systematic errors (instrument calibration, centering, horizontal and vertical refraction, etc.). The typical absolute positioning error envelope (see Fig. 5-81) is cigar shaped; it is smallest at primary control points and reaches a maximum midway between primaries. The measured reference line oscillates somewhere within this error envelope. Its absolute position cannot be pinned down any more precisely than the size of the error envelope, and deviations within this envelope are statistically insignificant. However, within this absolute error envelope, the relative errors between adjacent magnets are much smaller. The major error sources tend to affect equally the positioning of adjacent components, with the result that relative alignment accuracies are much higher than absolute alignment accuracies.

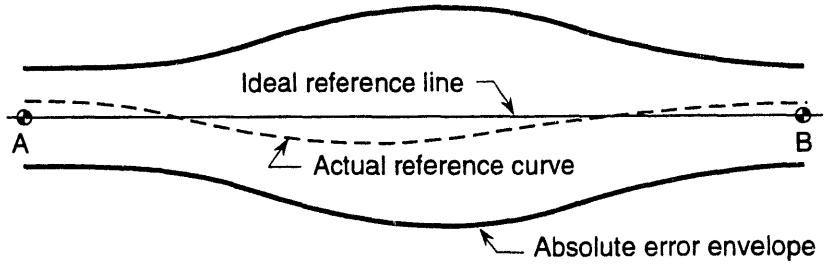

Fig. 5-81. Error envelope for absolute positioning. Points A and B denote primary control points.

Typically, some set of tunnel monument coordinates will be accepted as "errorless" for the purpose of absolute positioning. This effectively shrinks the absolute error envelope by ignoring some global factors, but the error envelope retains the same characteristics and shape. Logic and experience indicate that successive magnet surveys will define a reference line that wanders randomly within the absolute envelope. This implies that the absolute comparison of independent surveys is not meaningful when trying to evaluate differences smaller than the random wander. If attempts are made to achieve the final relative tolerances using an absolute alignment approach, successive rounds of survey and alignment will not converge. The magnitudes of the measured misalignments will not diminish. To overcome this problem, techniques known as "smoothing" have been developed. Smoothing separates the relative magnet displacements from the absolute trend curve.

The SLC arc magnet alignment task presented a compelling reason to devise a smoothing algorithm at SLAC, an algorithm now applied generally to other alignment projects. The complications of an irregularly shaped and complex beamline were eliminated by subtracting out the actual size and shape of the beamline, leaving a series of residual displacements (see Fig. 5-82), that is, the ideal fiducial coordinates are subtracted from the surveyed values. The correlation between horizontal and vertical error components remains, however. Therefore, a spatial fitting routine, principal curve analysis, was chosen to simultaneously pass a curve through the horizontal and vertical residual misalignments mapped out along the local Z axis (beam direction). This curve (see Fig. 5-83) passes through the middle of the data set such that the sum of the squared errors in all variables is minimized. The curve is nonparametric, with its shape suggested by the data. The processing is iterative, so the curve more and more closely fits the data set on each successive iteration. A smoothness criterion is applied to stop the process when the curve becomes too irregular.

The observation plan best suited for this method is a three-dimensional traverse measured directly over the components to be smoothed. Since this is impossible due to the vertical arrangement of the rings, observations will be carried out from the traverse stations.

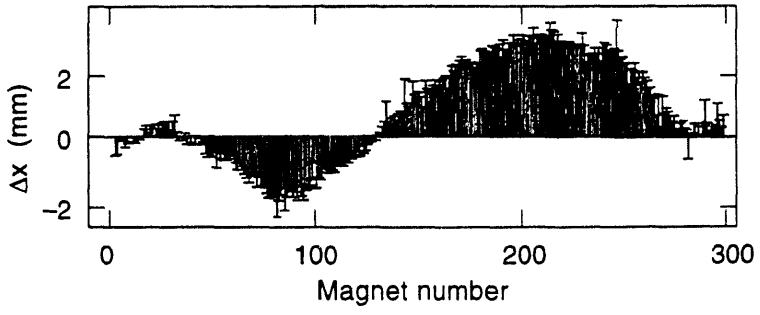

Fig. 5-82. Residual absolute positioning displacements rotated perpendicular to beamline, $\Delta x = x_{actual} - x_{ideal}$.

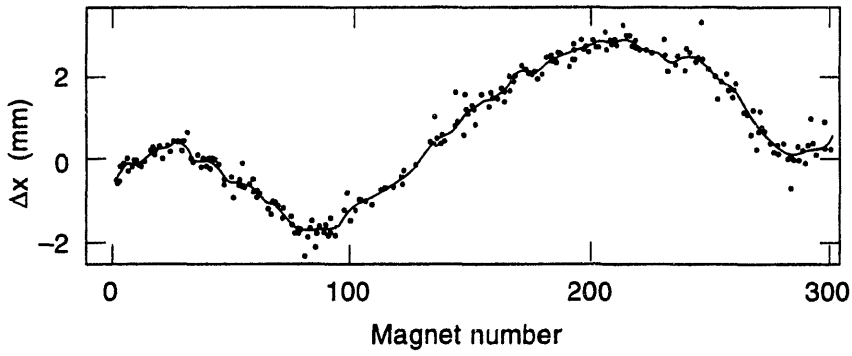

Fig. 5-83. Trend curve fitted to residual displacements.

From the aisle-side traverse stations, horizontal direction sets will be measured to the four nearest quadrupole-sextupole pairs. To strengthen the network, distances will be measured from station to station. Elevation differences from magnet to magnet will be measured via differential leveling. One important difference from the absolute positioning step described earlier is that the traverse stations will only be treated as tie points. This means that their "known" coordinate values will not be introduced into the least-squares adjustment, but rather treated as unknowns. Repeated test smoothings carried out in the SLC arcs and FFTB beamline have shown that 150-μm smoothness can be obtained in one iteration; a second iteration will improve this to better than 100 μm. (Note that this refers to the rms value of the residual magnet fiducial displacements relative to a smooth curve, without including any fiducialization error.) The matching sections and the detector barrel will be included in the smoothing procedure, as will the NIT and SIT parts of the injection lines. The alignment tolerances of the injection bypass lines (the injection transport lines in the linac tunnel) do not warrant smoothing.

5.3.2.6 Quality Control. After completing the final smoothing step, the positions of all components will be mapped one more time to confirm that the alignment tolerances have been met. These data will be recorded in the database for use in machine commissioning studies.

5.4 POWER SUPPLIES

In this section, we describe the power supplies required for PEP-II. For both the HER and the LER, many of the supplies are very similar in function. These are described together in Section 5.4.1. In the common IR of the two rings, there are a number of special magnets that serve to focus and to separate the two beams. Power systems for these magnets are discussed in Section 5.4.2. Finally, in Section 5.4.3, we discuss the power supplies required for the injection system. The power supplies have been sized for eventual operation at 12 GeV for the HER and 4 GeV for the LER. Magnet standardization will require briefly ramping the magnets to field levels corresponding to 13 GeV and 4.5 GeV for the HER and LER, respectively. Note that all magnet operating

currents and voltages shown in the tables in this section are listed at the nominal operating levels of 9 GeV for the HER and 3.1 GeV for the LER. Power supply ratings shown in the tables include an allowance for cable voltage drop.

5.4.1 HER and LER Power Supplies

The storage ring power supply systems are divided into a number of independent supply strings and individual power supplies, as listed in Table 5-29 for the HER and Table 5-30 for the LER. Because the strings for the two rings are identical in most respects, save only their detailed electrical characteristics, they are described together in the following paragraphs.

5.4.1.1 Bending Magnet Strings. The HER utilizes a single bending magnet string of 192 dipoles, plus 16 low-field bending magnets in the IR, connected in series (see Fig. 5-84) by existing water-cooled aluminum cables. The LER requires a similar string but, in this case, only 192 dipoles are on the main bus. The magnet connections consist of a supply cable and a return cable, with the turnarounds at IR-2 and the supplies at IR-8 (see Fig. 5-84). Supply and return cables are arranged to cancel the residual field resulting from the high cable currents. Supply and return cable connections alternate every half sector to minimize the voltage to ground and to cancel current differences in the bending magnets that would otherwise develop as a result of current leakage to ground through cooling hoses or stray capacitance. The HER bending magnets require a nominal operating current of 640 A, regulated to 0.01%; they are powered by two 500-V power supplies connected in series and located at IR-8. For the LER, the nominal operating current is 606 A, regulated to 0.01%; the main bending magnet string is powered by four 500-V power supplies, also connected in series and located at IR-8. All these supplies will be refurbished PEP chopper-type supplies, upgraded with new power hardware and controls.

5.4.1.2 Quadrupole Magnet Strings. The quadrupole magnets of both rings fall into three main functional groups: arc quadrupoles, dispersion-suppressor quadrupoles, and straight-section quadrupoles. The straight-section quadrupoles further subdivide into quadrupoles for "normal" straights, injection straights, phase trombone (or tune) straights, wiggler straights, and the collision straight.

Arc Quadrupoles. The two HER arc quadrupole strings (Fig. 5-85a) comprise 60 QF and 54 QD magnets. The LER (Fig. 5-85b) has 74 QF and 80 QD magnets connected in two magnet strings. The main quadrupole buses for the two strings in each ring will use existing aluminum cables. The two cables will be powered with current flowing in opposite directions to provide cancellation of stray magnetic fields. The main arc quadrupoles for both rings require an operational current of about 130 A, regulated to 0.01%, at a maximum of 500 V. These supplies will be refurbished PEP choppers, operating from the same DC power supply as the bending magnet supplies.

Table 5-29. HER power supplies. Currents tabulated for 9-GeV operation.

Magnet string name	Number of magnets	Current per magnet (A)	Voltage per magnet (V)	String voltage (V)	Number of supplies	Power supply rating[a]
HER Bends	192	640	3.6	691.2	2[b]	500V/950A
IR-2 soft bends	16	640	0.4		In bend string	
Normal quadrupoles QF	60	96	9.6	576.0	2[b]	500V/200A
Normal quadrupoles QD	54	128	10.5	567.2	2[b]	500V/200A
Straight quadrupoles QFO	16	154	11.1	90.0	2	200V/200A
Straight quadrupoles QDO	14	154	11.1	77.7	2	200V/200A
Injection quadrupoles QDOI	2	52	6.6	13.2	1	30V/200A
Injection quadrupoles QFOI	2	71	9.1	18.2	1	30V/200A
Injection quadrupoles QFI	2	33	4.3	8.6	1	30V/200A
Injection quadrupoles QDI	2	34	4.3	8.6	1	30V/200A
Suppressor quadrupoles QDS0	8	98	9.8	39.0	2	500V/200A
Suppressor quadrupoles QDS1	8	164	11.9	47.6	2	500V/200A
Suppressor quadrupoles QFS1	8	140	11.6	46.4	2	500V/200A
Suppressor quadrupoles QDS2	8	134	11.1	44.4	2	500V/200A
Suppressor quadrupoles QFS2	8	184	13.3	53.2	2	500V/200A
Suppressor quadrupoles QDS3	8	128	10.5	42.0	2	500V/200A
Suppressor quadrupoles QFS3	8	107	10.8	43.2	2	500V/200A
Suppressor quadrupoles QDS0	4	150	10.8	10.8	4	30V/200A
Suppressor quadrupoles QDS1	4	171	12.3	12.3	4	40V/300A
Suppressor quadrupoles QFS1	4	171	14.1	14.1	4	30V/200A
Suppressor quadrupoles QDS2	4	153	11.0	11.0	4	30V/200A
Suppressor quadrupoles QFS2	4	205	14.8	14.8	4	40V/300A
Suppressor quadrupoles QDS3	4	128	10.5	10.5	4	30V/200A
Suppressor quadrupoles QFS3	4	98	9.8	9.8	4	30V/200A
Tune quadrupoles QDP1	2	71	9.0	9.0	2	30V/200A
Tune quadrupoles QDP3	4	70/156	11.3	22.6	2	30V/200A
Tune quadrupoles QDP5	4	70/155	11.2	22.4	2	30V/200A
Tune quadrupoles QDP7	4	70/155	11.2	22.4	2	30V/200A
Tune quadrupoles QFP2	4	75	9.5	19.0	2	30V/200A
Tune quadrupoles QFP4	4	165	11.9	23.9	2	80V/250A
Tune quadrupoles QFP6	4	133	10.9	21.8	2	80V/250A
Tune quadrupoles QFP8	4	161	11.6	23.3	2	80V/250A

[a]Includes allowance for cable losses.

[b]Power supplies in series, one string.

Table 5-29. HER power supplies. Currents tabulated for 9-GeV operation (continued).

Magnet string name	Number of magnets	Current per magnet (A)	Voltage per magnet (V)	String voltage (V)	Number of supplies	Power supply rating[a]
Sextupoles SF	48	50	1.6	76.8	1	500V/200A
Sextupoles SD	48	95	3.0	144.0	1	500V/200A
Adjustable sextupoles SF	24	128	4.0	4.0	24	20V/200A
Adjustable sextupoles SD	24	178	5.6	5.6	24	20V/200A
Corrector vertical arcs	96	12	25.0	25.0	96	40V/12A
Corrector horizontal arcs	96	12	25.0	25.0	96	40V/12A
Corrector vertical straights	24	12	25.0	25.0	24	40V/12A
Corrector horizontal straights	24	12	25.0	25.0	24	40V/12A

[a]Includes allowance for cable losses.

Table 5-30. LER power supplies. Currents tabulated for 3.1-GeV operation.

Magnet string name	Number of magnets	Current per magnet (A)	Voltage per magnet (V)	String voltage (V)	Number of supplies	Power supply rating[a]
LER bends	192	606	7.4	1420	4[b]	500V/900A
Normal quadrupoles QF	74	122	5.7	423	1	500V/200A
Normal quadrupoles QD	80	121	5.6	452	1	500V/200A
Suppressor quadrupoles QFS1	6	112	5.3	5	6	40V/300A
Suppressor quadrupoles QDS1	4	150	7.1	7	4	40V/300A
Suppressor quadrupoles QFS2	4	118	5.5	6	4	30V/200A
Suppressor quadrupoles QDS2	6	133	6.3	6	6	30V/200A
Suppressor quadrupoles QFS3	6	130	6.1	6	6	40V/300A
Suppressor quadrupoles QDS3	4	111	5.2	5	4	30V/200A
Suppressor quadrupoles QFS4	4	128	6.0	6	4	40V/300A
Suppressor quadrupoles QDS4	6	122	5.7	6	6	30V/200A
Suppressor quadrupoles QFS5	2	122	5.7	6	2	30V/200A
Tune quadrupoles QFT1	4	132	6.2	12	2	30V/200A
Tune quadrupoles QDT1	4	108	5.1	10	2	30V/200A
Tune quadrupoles QFT2	4	130	6.1	12	2	30V/200A
Tune quadrupoles QDT2	4	94	4.4	9	2	30V/200A
Tune quadrupoles QFT3	4	111	5.2	11	2	30V/200A
Tune quadrupoles QDT3	4	96	4.5	9	2	30V/200A
Tune quadrupoles QFT4	4	88	4.2	8	2	30V/200A

[a]Includes allowance for cable losses.

[b]Power supplies in series, one string.

Table 5-30. LER power supplies. Currents tabulated for 3.1-GeV operation (continued).

Magnet string name	Number of magnets	Current per magnet (A)	Voltage per magnet (V)	String voltage (V)	Number of supplies	Power supply rating[a]
Tune quadrupoles QDT4	2	51	2.4	2	2	20V/100A
Injection quadrupoles QDOI	2	63	3.0	6	1	20V/100A
Injection quadrupoles QFOI	2	112	5.3	11	1	30V/200A
Injection quadrupoles QFI	2	40	1.9	4	1	20V/100A
Injection quadrupoles QDI	2	18	0.8	2	1	20V/100A
Wiggler quadrupoles QFW1	4	68	3.2	6	2	20V/100A
Wiggler quadrupoles QDW2	4	44	2.1	4	2	20V/100A
Wiggler quadrupoles QFW3	4	105	5.0	10	2	30V/200A
Wiggler quadrupoles QFW4	4	8	0.4	1	2	20V/100A
Wiggler quadrupoles QDW5	4	54	2.6	5	2	20V/100A
Wiggler quadrupoles QFW6	4	96	4.5	9	2	30V/200A
Wiggler magnets	2	827	206.7	207	2	610V/1500A
Wiggler bend magnets	8	518	20.0	80	2	80V/600A
Sextupoles SF	72	30	1.0	72	1	500V/200A
Sextupoles SD	72	54	1.7	122	1	500V/200A
Corrector vertical arcs	96	12	25.0	25	96	40V/12A
Corrector horizontal arcs	96	12	25.0	25	96	40V/12A
Corrector vertical straight bends	24	12	25.0	25	24	40V/12A
Corrector horizontal straight bends	24	12	25.0	25	24	40V/12A
Skew quadrupoles	16	103	2.5	3	16	30V/200A

[a]Includes allowance for cable losses.

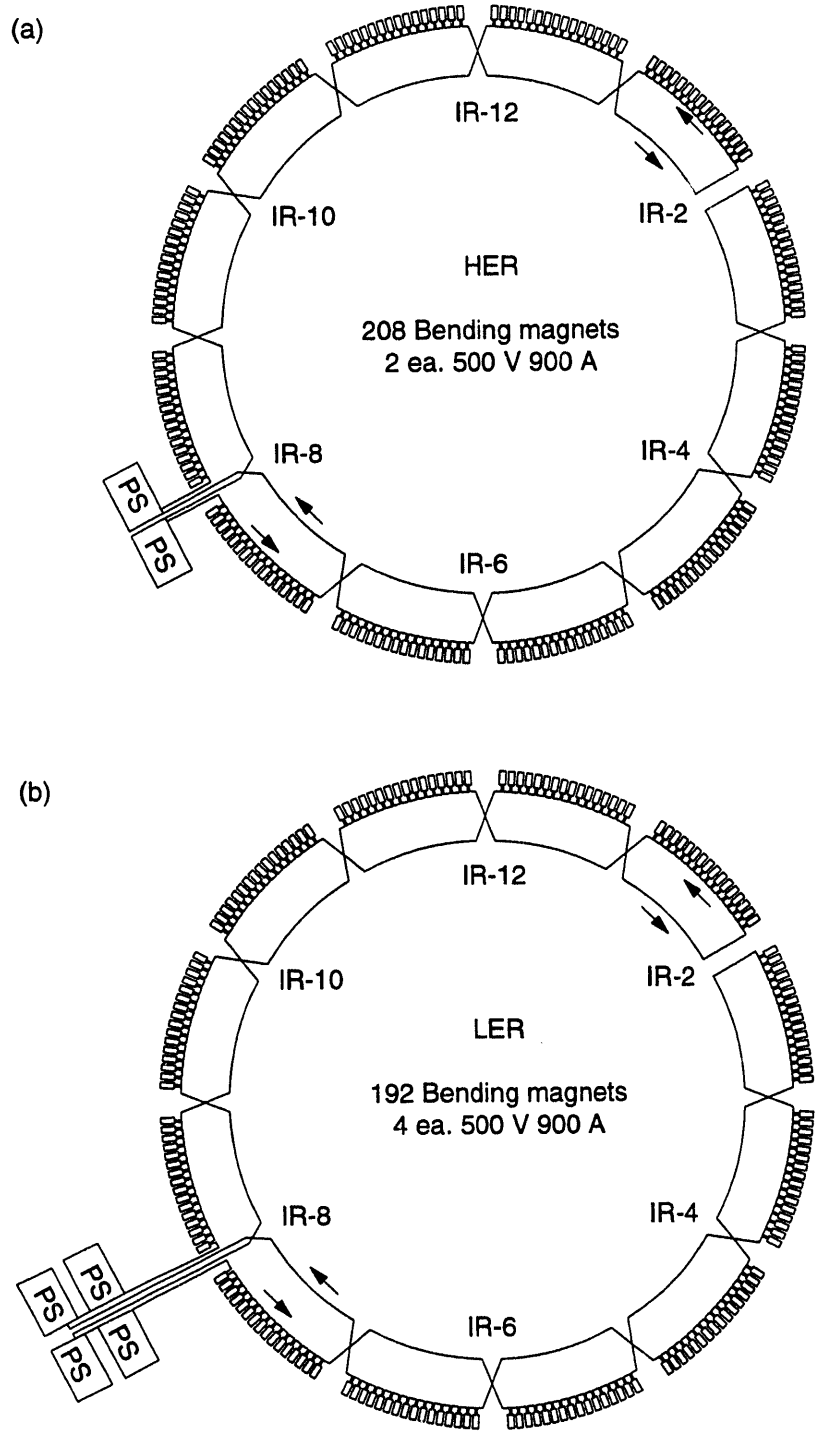

Fig. 5-84. Schematic of magnet and power supply connections for (a) the HER and (b) the LER bending magnet strings.

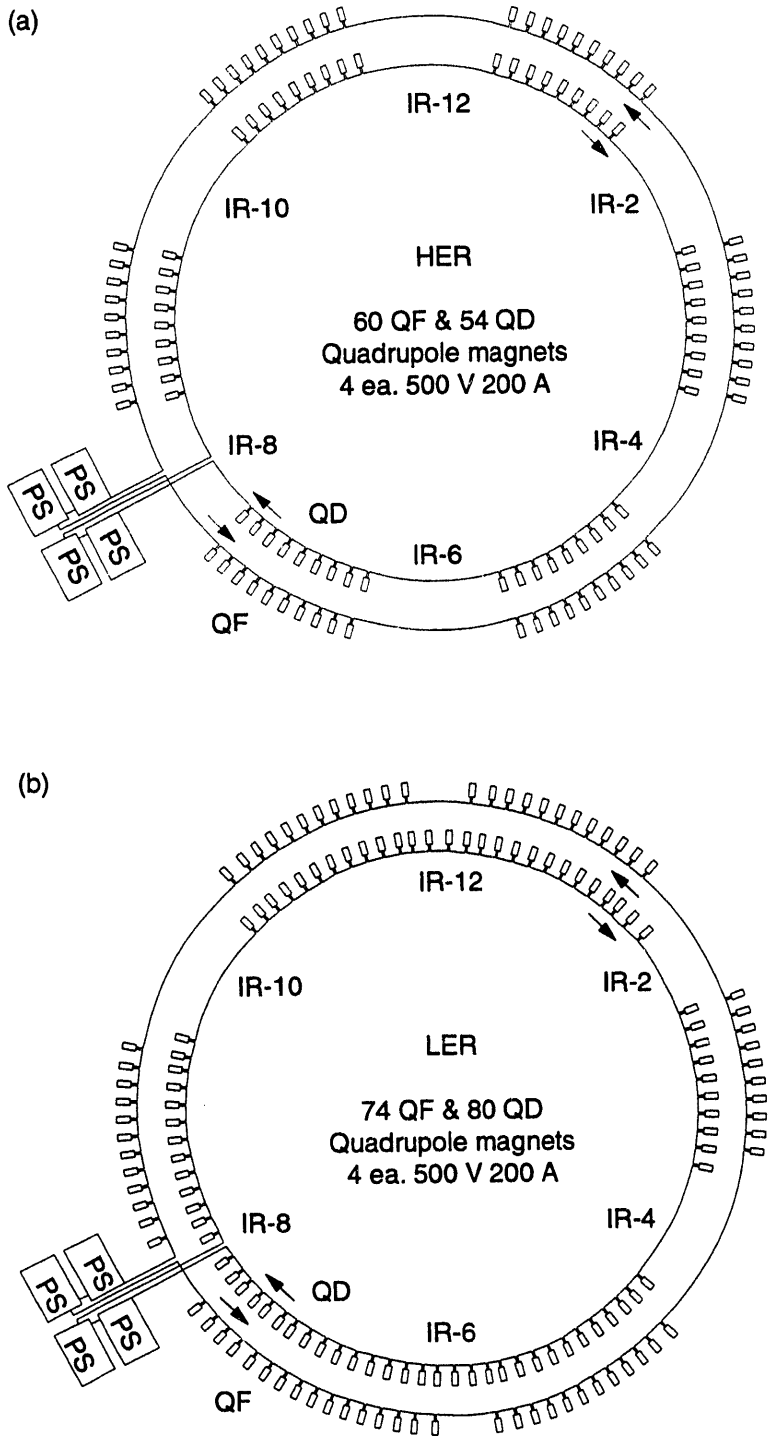

Fig. 5-85. Schematic of magnet and power supply connections for (a) the HER and (b) the LER arc quadrupole magnet strings.

Dispersion Suppressor Quadrupoles. For the HER (see Fig. 5-86a), the dispersion suppressors at both ends of each of the six arcs contain seven quadrupoles, four vertically focusing and three horizontally focusing, giving 48 QD and 36 QF quadrupoles in total. There are eight strings of four QD magnets in series and six strings of four QF magnets in series, connected by existing cables around the ring. Each string of four quadrupoles is powered by a refurbished PEP chopper rated at 500 V, 200 A. In addition, there are 12 QF and 16 QD magnets that are independently powered from supplies located in the adjacent interaction halls. In the LER, the dispersion suppressor quadrupoles, 22 QF and 20 QD magnets, are all driven from independent power supplies, similar to those in the HER, located in the adjacent interaction halls (see Fig.5-86b).

New cables will be installed for the independent power supplies, which are rated at either 30 V, 200 A or 40 V, 300 A.

Straight-Section Quadrupoles. The quadrupoles in the normal straight sections of the HER are arranged into FODO cells similar to those of the arcs (that is, the cells have the same length and phase advance, but the dipoles are absent). In the HER, normal straight sections are located in regions 12 and 4 (region 12 being a section where some of the RF cavities will be located). (The LER has no normal straight sections as such; every straight section is required for some special purpose.) The normal straight sections for the HER each utilize eight QF and seven QD quadrupoles (see Fig. 5-87a). The QF and QD magnets are both connected in two strings, each string powered in series from a supply having an operating current of 160 A, regulated to 0.01%, at a maximum of 120 V. These will be commercially procured, current-regulated supplies, installed in the IR-12 and IR-4 support buildings and connected by a new cable installation.

The injection straight sections are in region 10 (for the HER, Fig. 5-87a) and region 8 (for the LER, Fig. 5-87b), and are configured nearly identically for the two rings. Each is powered symmetrically about its center and consists of four groups of two magnets in series. Each string of two magnets in series will be powered by a commercially procured, current-regulated supply, regulated to 0.01%, that will be installed in the appropriate IR service building.

Each ring has two straight sections devoted to changing the betatron tunes of the machine. These "phase trombones" or tune sections are located in regions 6 and 8 for the HER, and in regions 4 and 10 for the LER. (The LER RF cavities will share region 4 with an LER tune section, and some of the HER RF cavities will share region 8 with an HER tune section.) The tune sections consist of regularly spaced quadrupoles, as in the normal straights. In each region, there are eight QF and seven QD magnets. These are connected pairwise, symmetrically about the center of the straight section (with the exception of the "odd" QD that is powered independently). Thus, each tune section uses 8 power supplies for its 15 quadrupoles, as shown in Figs. 5-88a and 5-88b. Each unit will be a commercially procured, current-regulated supply with a regulation of 0.01%.

In addition to the above functions, the LER has two straight sections (regions 6 and 12) dedicated to beam emittance and damping control via wiggler magnets. The quadrupoles in the wiggler straights are arranged symmetrically about its center, and comprise two groups of two QD magnets in series and four groups of two QF magnets in

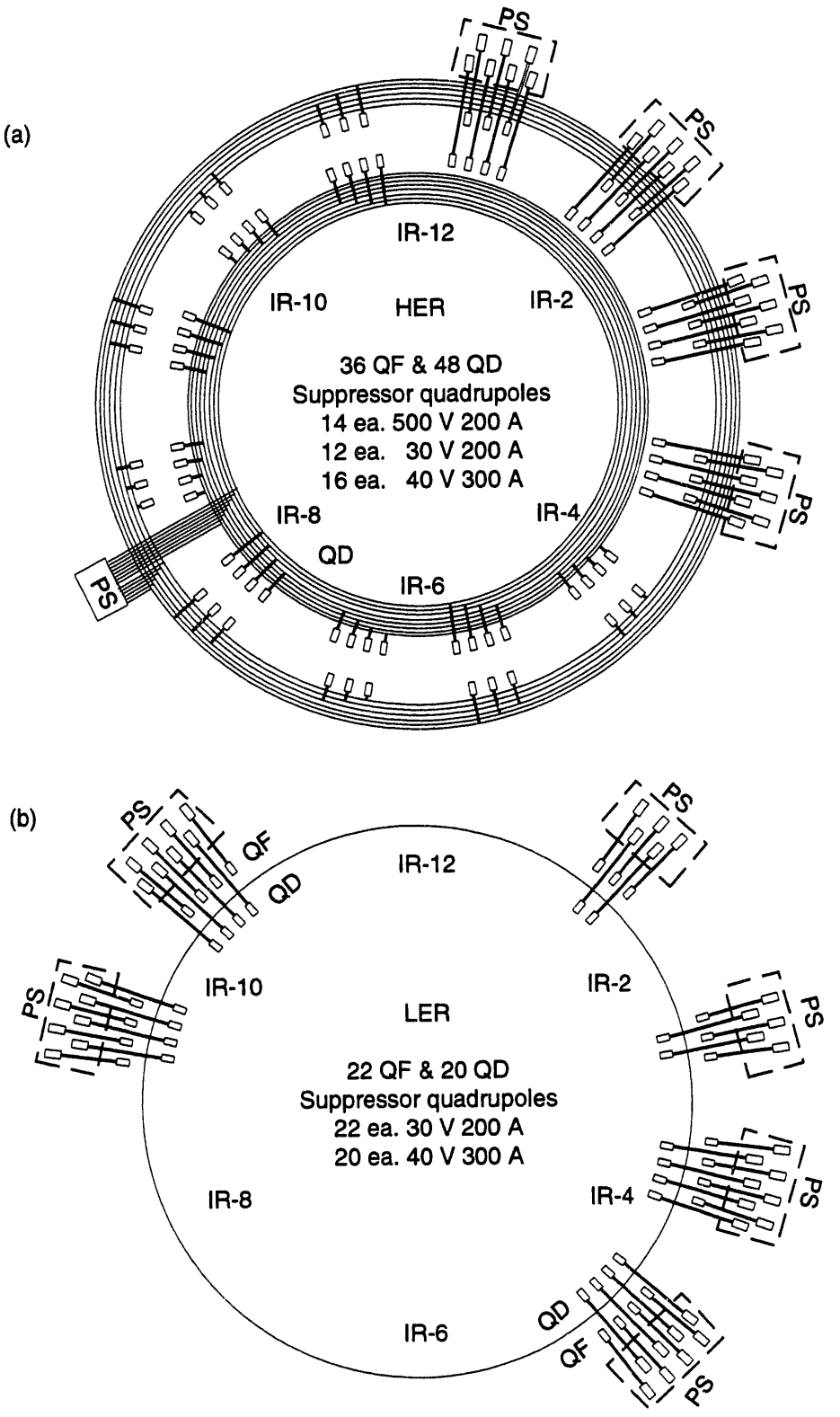

Fig. 5-86. Schematic of magnet and power supply connections for (a) the HER and (b) the LER suppressor quadrupole magnet strings.

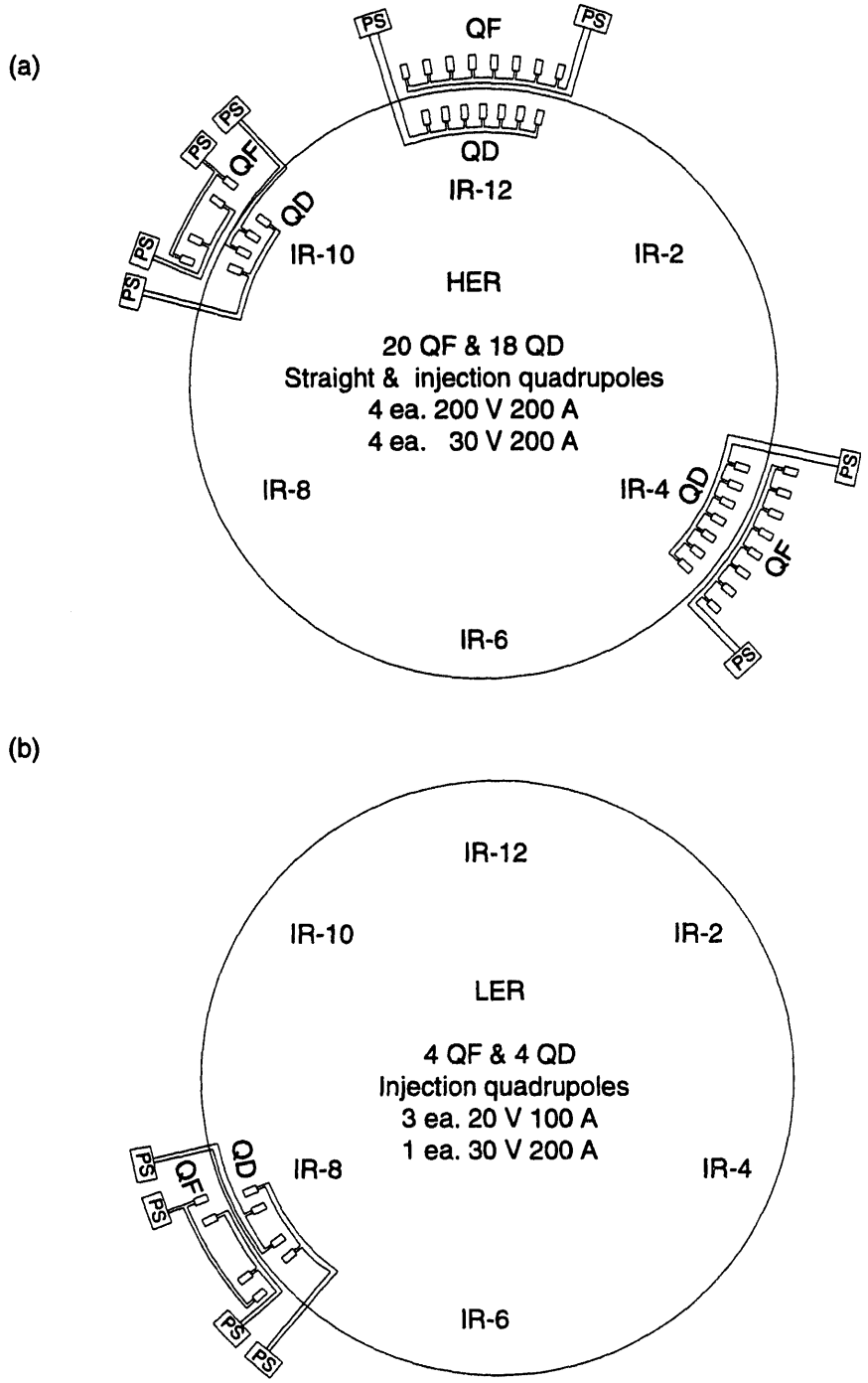

Fig. 5-87. Schematic of magnet and power supply connections for (a) the HER straight-section and injection quadrupole magnet strings and (b) the LER injection quadrupole strings.

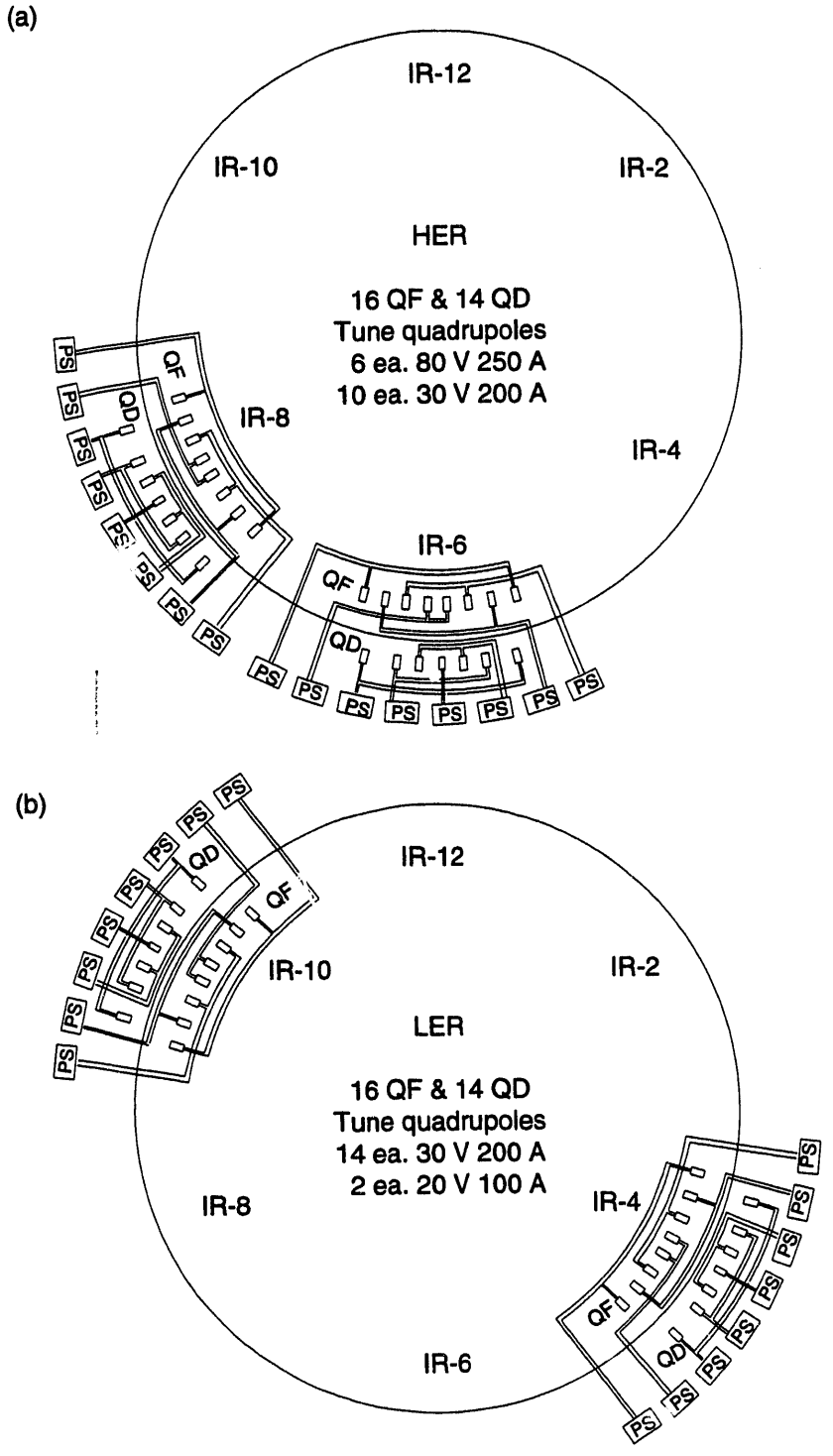

Fig. 5-88. Schematic of magnet and power supply connections for (a) the HER and (b) the LER tune control quadrupole magnet strings.

series (see Fig. 5-89). The resulting six independent quadrupole power supplies will be located in the corresponding interaction hall. As for the tune straights, the supplies will be commercially procured, current-regulated supplies.

5.4.1.3 Sextupole Magnet Strings. The ring sextupoles of the LER comprise two families of sextupoles, one of 72 focusing sextupoles and the other of 72 defocusing sextupoles; these are shown in Fig. 5-90. The sextupoles of the HER comprise four families of magnets: two families are distributed from IR-4 to IR-12, and the other two families are centered around the interaction region at IR-2. The larger group of sextupoles is connected in two strings, one with 48 focusing sextupoles and a second with 48 defocusing sextupoles, as shown in Fig. 5-91. The nominal operating current for these sextupole families is less than 72 A, regulated to 0.1%, at approximately 120 V per magnet string. The supplies will be refurbished PEP choppers operating from the same DC supply used for the bending magnets. The smaller group of sextupoles, located around the collision region in arcs 1 and 3, includes 24 focusing and 24 defocusing

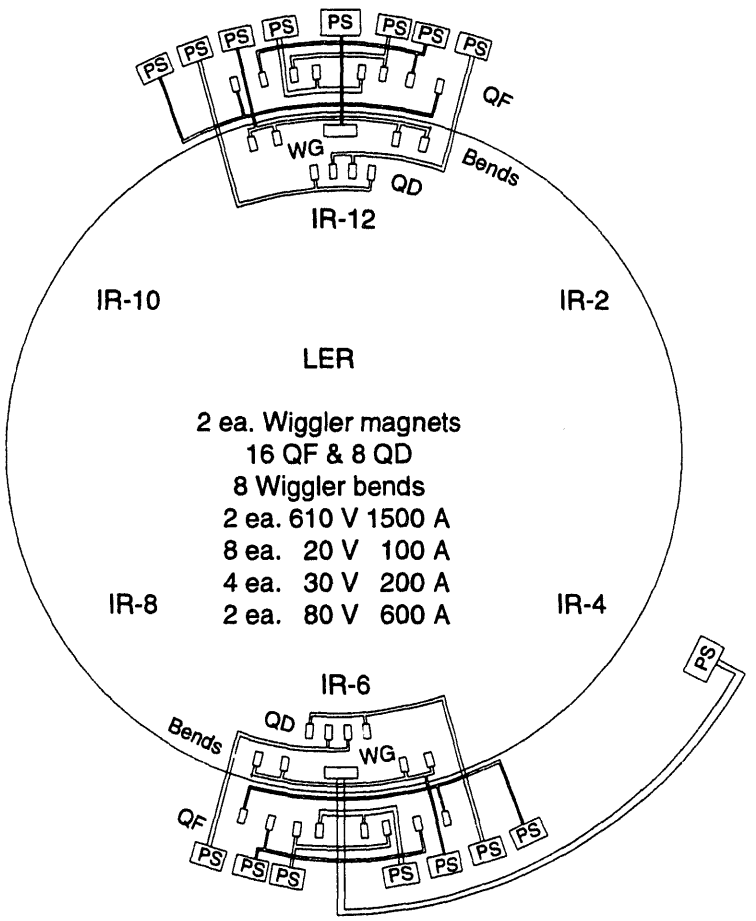

Fig. 5-89. Schematic of magnet and power supply connections for the LER wiggler, wiggler bending magnet, and wiggler quadrupole strings.

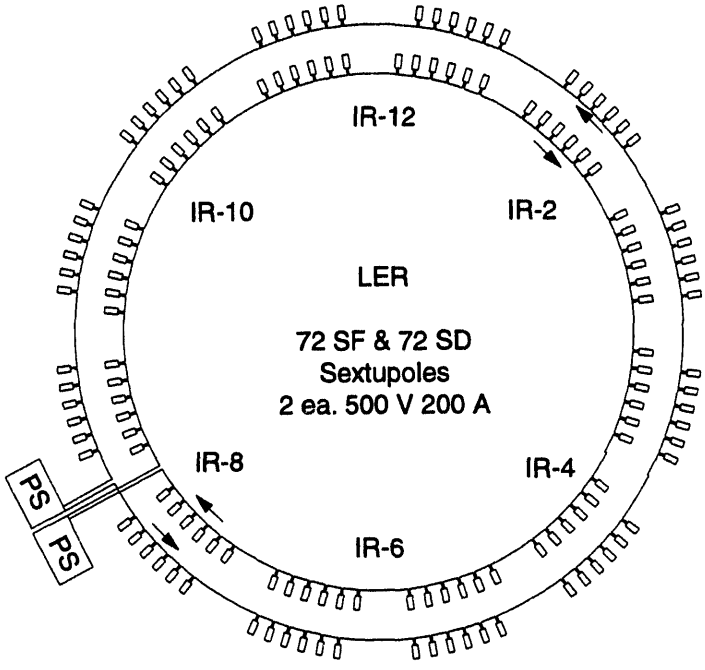

Fig. 5-90. Schematic of magnet and power supply connections for the sextupole magnet strings of the LER.

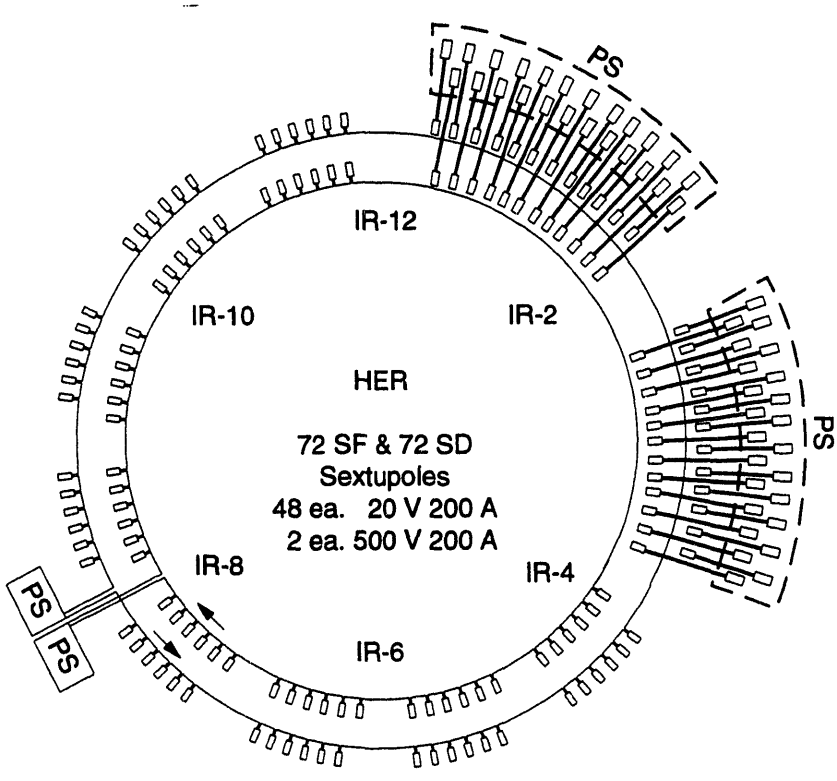

Fig. 5-91. Schematic of magnet and power supply connections for the sextupole magnet strings for the HER.

sextupole magnets, each powered by an independent power supply (see Fig. 5-91). Because the current requirements for these sextupoles are variable, the size of the supplies and new cable installation will be optimized to the nominal sextupole current and voltage requirements, that is, the units are rated at 20 V, 200 A and will be commercially procured, current-regulated supplies.

5.4.1.4 Corrector Magnets. Each of the HER bending magnets incorporates a backleg winding. Pairs of these (in the two bending magnets located adjacent to each QF) are powered together in the HER by 96 backleg-winding corrector power supplies for horizontal control (see Fig. 5-92). The power requirements for the backleg windings are less than 12 A, regulated to 0.1%, at approximately 25 V. There will be an induced voltage of not greater than 10 V on the backleg-winding corrector supplies when the bending magnets are energized or deenergized. There are also 96 vertical corrector magnets in the arcs and an additional 24 horizontal and 24 vertical corrector magnets in the straight sections of the HER. The LER also has 120 horizontal and 120 vertical corrector magnets distributed around the ring. The corrector supplies will be switching-type, bipolar two-quadrant supplies, mounted in groups of eight or more in the service buildings in which the existing PEP corrector cables are terminated. Additional cables will be needed to drive the LER correctors.

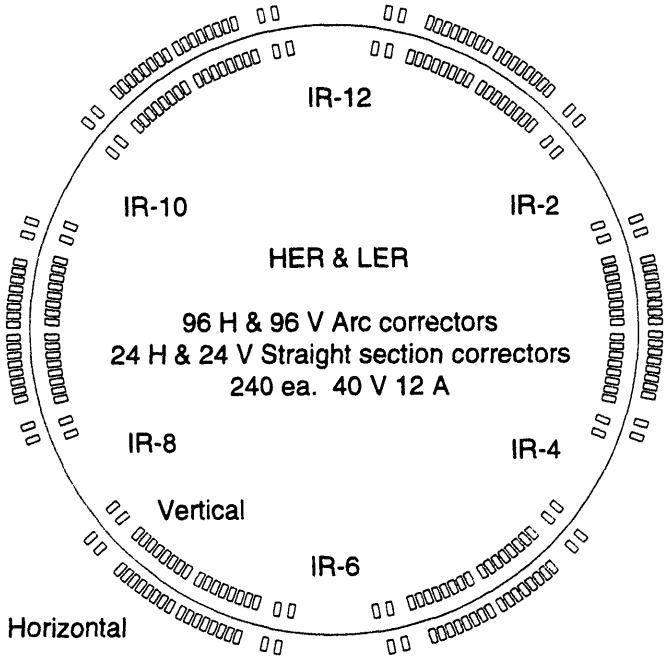

Fig. 5-92. Schematic of magnet and power supply connections for the corrector strings for both the HER and LER.

5.4.1.5 Wiggler Magnets. The LER will have two wiggler magnets located in IR-6 and IR-12. These magnets will require 830 A at 300 V (Fig. 5-89). The two existing booster supplies for the old PEP bending magnet string will be reworked in the same way as the bulk supplies for the choppers and used to power the wiggler magnets. The supplies are located in IR-12 and IR-4. Water-cooled aluminum cables will be used to bring power to the wigglers. Each wiggler section will also contain four bending magnets for creating a displaced orbit. These magnets in each region will be powered in series with a single power supply rated at 80 V, 600 A.

5.4.1.6 Refurbishing the PEP Chopper Supplies. The existing PEP chopper power system will be reworked for use in PEP-II. The 12-kV switchgear, rectifier transformers, and SCR-controlled DC converters will be totally reconditioned and then reused. All equipment will be thoroughly inspected and cleaned, connections will be remade, and all parts subject to aging will be replaced. The controls of the DC supplies will be redesigned and rebuilt. The chopper supplies themselves will be redesigned and refurbished to make them more reliable and accessible, and, where practical, they will be built with redundancy. The present SCR switches will be upgraded with modern switching devices, and the chopping frequency will be increased to improve the overall performance. Where practical, more than one chopper will be operated in parallel, designed, and rated such that a single-point failure of power equipment or controls will not result in equipment shutdown. In addition, new second-harmonic type transductors will be installed for each magnet string. As a means to improve the up-time of the supplies, the possibility of on-line replacement of failed equipment will be investigated to determine if it is practical and safe to incorporate this feature into the design. Improved EMI filtering will be incorporated into the supplies to reduce noise. The choppers will be redesigned with all-digital computer controls to enhance performance and flexibility. PEP-II requires two sizes of chopper—one rated at 500 V (maximum) at 950 A (maximum) for the bending magnets and a second rated at 500 V (maximum) at 200 A (maximum) for the quadrupoles and sextupoles.

5.4.1.7 Individual Supplies. There will be two types of individual supplies used, a standard commercial SCR-controlled unit for supplies over 50 kW and a switching-type unit for smaller supplies. The switching supplies will operate with a switching frequency greater than 20 kHz and will incorporate step-down transformers for magnet-ground isolation and protection. There will be more than one switching element operating in parallel in each supply, such that, in the event of a single-point failure, the supply will continue to operate without interruption. The supplies will be designed to be readily replaceable, to reduce down-time. All digital microcomputer controls will be connected to the PEP-II control system.

5.4.1.8 Corrector Supplies. The corrector switching-type power supplies will also be developed (see Fig. 5-92). The corrector supplies are bipolar, two-quadrant units rated for 12 A at 40 V. The corrector supplies operate from a DC supply of up to 120 V. The corrector supplies will be designed to operate with a switching frequency above 20 kHz and will incorporate an isolation step-down transformer for magnet-ground isolation. The corrector supplies will be installed in groups of eight or more and will be distributed

in the IR service buildings around the tunnel at locations selected to minimize cabling cost. Supplies will be mounted in cabinets that will service both the LER and the HER. Supply clusters will have DC breakers for DC source isolation and protection. The supplies will be plug-in types to allow easy replacement and thus reduce facility down-time. All digital microcomputer controls will be connected to the PEP-II control system for control and monitoring of the individual supplies.

5.4.2 Interaction Region Power Supplies

The magnetic devices at the heart of the IR are made of permanent magnet material and require no power supplies. To permit energy variations, however, there will be trim windings associated with these magnets (B1, Q1) that will require small supplies. The special quadrupoles of the HER (QD4 and QF5), which focus the high-energy beam, are powered from special high-current power supplies. The remaining IR power supply requirements for the HER are relatively straightforward. One supply will power the string of B4 weak bending magnets on each side of the IP. The string (see Fig. 4-10) will have four magnets. The remaining low-field bending magnets are powered from the main bending magnet string (see Section 5.4.1.1). Two supplies are needed for the individual QD6 and QF7 quadrupoles on each side of the IP (see Fig. 4- 12).

The LER requires power supplies for many IR quadrupole and dipole magnets, including the vertical bending magnets and the horizontal magnets to align the collision axis. The complete list of power supplies for the IR is shown in Table 5-31. Supplies will all be installed in the existing IR-2 service building, where sufficient AC power is available. With the exception of those for the correctors and trims, all supplies will be commercially obtained and will be regulated to 0.01%. Supplies will be controlled remotely from the PEP-II control system. The corrector supplies will be of the type described in Section 5.4.1.8, and will be installed in the service halls and controlled in the same manner.

5.4.3 Injection Power Supplies

The injection system for PEP-II utilizes the existing SLAC linac to produce positrons and electrons. We expect that no power supply modifications will be required to the present linac to accommodate the new injection system. Most of the linac power supplies were either installed or upgraded during construction of the SLC. Power supply requirements for the injection system are listed in Table 5-32. The majority of the power supplies will be commercial off-the-shelf units combined with several SLAC-designed types that have performed reliably in the SLC.

The PEP-II injection power supply system can be divided into five categories: electron extraction, positron extraction, electron and positron bypass lines, NIT and SIT lines, and the HER/LER injection systems. Power supplies installed in the klystron gallery will be controlled and operated by the SLC control system. Those for the storage ring magnets will be located in the IR-8 (LER) and IR-10 (HER) areas. Standard SLC

Table 5-31. Interaction region power supplies. HER and LER magnet currents correspond to 9- and 3.1-GeV operation, respectively.

Magnet string name	Number of magnets	Current per magnet (A)	Voltage per magnet (V)	String voltage (V)	Number of supplies	Power supply rating[a]
HER soft bends B4	4	71	0.5	2.0	1	20V/140A
HER corrector vertical	4	12	20.0	20.0	4	40V/12A
HER corrector horizontal	8	12	20.0	20.0	8	40V/12A
Bends B1 trims	2	203	19.0	19.0	2	40V/300A
LER bends B2H	2	76	1.1	2.2	1	20V/140A
LER bends B3H	4	378	6.3	25.1	1	80V/600A
LER bends B4V	2	314	4.5	9.0	1	80V/600A
LER bends B5H	2	564	13.3	26.6	1	40V/800A
LER bends B6H	4	564	13.3	53.2	1	80V/600A
LER bends B7V	2	354	12.0	24.0	1	80V/600A
LER bends B8V	2	79	0.8	1.5	1	20V/140A
LER bends B9H	2	356	25.8	51.7	1	80V/600A
Quadrupoles Q1 trims	2	203	19.0	19.0	2	40V/300A
Septum quadrupoles Q2	2	1367	27.0	53.1	1	80V/1400A
LER quadrupoles QD04	2	90	11.4	22.9	1	30V/200A
LER quadrupoles QD07	2	106	13.5	27.0	1	30V/200A
LER quadrupoles QD09	2	130	16.5	32.9	1	40V/300A
LER quadrupoles QD10	4	192	9.0	36.1	1	40V/300A
LER quadrupoles QD12	2	281	13.2	26.5	1	40V/300A
LER quadrupoles QD13	2	189	8.9	17.8	1	40V/300A
LER quadrupoles QD15	2	158	7.4	14.9	1	40V/300A
LER quadrupoles QD17	2	239	11.2	22.5	1	80V/600A
LER quadrupoles QF16	2	516	24.2	48.5	1	80V/600A
LER quadrupoles QF18	2	283	13.3	26.6	1	80V/600A
LER quadrupoles QF01	2	192	9.0	18.0	1	40V/300A
LER quadrupoles QF03	2	81	10.2	20.4	1	30V/200A
LER quadrupoles QF05	2	192	9.0	18.0	1	40V/300A
LER quadrupoles QF06	2	92	11.7	23.4	1	30V/200A
LER quadrupoles QF08	2	174	22.1	44.2	1	60V/300A
LER quadrupoles QF11	4	316	14.8	59.2	1	80V/600A
LER quadrupoles QF14	2	147	18.6	37.2	1	40V/300A
LER corrector quadrupoles	5	12	20.0	20.0	5	40V/12A
LER sextupoles SY	4	221	6.9	27.6	1	80V/600A
LER sextupoles SX	4	135	4.2	16.8	1	40V/300A

[a]Includes allowance for cable losses.

Table 5-31. Interaction region power supplies. HER and LER magnet currents correspond to 9- and 3.1-GeV operation, respectively (continued).

Magnet string name	Number of magnets	Current per magnet (A)	Voltage per magnet (V)	String voltage (V)	Number of supplies	Power supply rating[a]
HER quadrupoles QD4	2	600	11.0	21.8	1	40V/800A
HER quadrupoles QD6	2	138	18.0	35.3	1	40V/300A
HER quadrupoles QF5	2	600	11.0	21.8	1	40V/800A
HER quadrupoles QF7	2	104	13.1	26.3	1	30V/200A
HER corrector quadrupoles	6	12	20.0	20.0	6	40V/12A

[a]Includes allowance for cable losses.

interface electronics and programs will be used with the power supplies located in the klystron gallery.

5.4.3.1 Electron Extraction System. The electron extraction system consists of 2 pulsed bending magnets connected in series, a Lambertson septum, 18 quadrupole magnets that are independently powered, and 7 bend magnets. At the nominal energy of 9 GeV, the pulsed bending magnets require approximately 275 A at 3.3 kV, which will be provided by a SLAC-built power supply. The Lambertson septum operates at approximately 185 A at 11 V at nominal energy. The individually powered magnets and the series-string magnets will be powered by standard commercial power supplies operated through the SLC control system. Specifications for all of these 23 power supplies are listed in Table 5-32.

5.4.3.2 Positron Extraction System. The positron extraction system includes a splitter magnet to separate electrons and positrons that also serves as the first element of a four-dipole chicane to reinject the electrons back into the linac. The chicane uses independent power supplies for the first (splitter) and last dipole, with the two middle dipoles run in series. There are 21 independently powered quadrupoles. Specifications for this group of 26 power supplies are listed in Table 5-32.

5.4.3.3 Electron and Positron Bypass Lines. The electron-beam transport system requires two strings of 16 quadrupoles powered by two power supplies rated at 25 A, 100 V. The positron beam transport system, consisting of two strings of 22 quadrupoles connected in series, requires 5 A at 22 V per string. Available commercial power supplies rated at 15 A, 40 V and interfaced to the control system will be used. In addition, the beam transport systems include 197 individually controlled trim magnets, operating at 6 A maximum, at approximately 10 V. The necessary supplies are identical to corrector units now in use for the SLC, and they will be similarly interfaced to the control system; specifications are included in Table 5-32.

Table 5-32. Injection power supplies for e^+ at 3.1 GeV and e^- at 9 GeV.

Magnet string name	Number of magnets	Current per magnet (A)	Voltage per magnet (V)	String voltage (V)	Number of supplies	Power supply rating[a]
Electron extraction pulsed bends	2	275	1600	3200	1	Pulser 4 kV/350A
Electron ext. Lambertson septum	1	185	11	11	1	30V/333A
Electron extraction bends	4	318	15	60	1	120V/500A
Electron extraction bends	2	122	4	8	1	20V/250A
Electron extraction bends	1	254	15	15	1	40V/450A
Electron extraction quadrupoles	9	110	20	20	9	40V/250A
Electron extraction quadrupoles	6	15	3	3	6	30V/20A
Electron extraction quadrupoles	3	42	7	7	3	20V/90A
Positron extraction bends	2	211	8	8	2	20V/500A
Positron chicane	2	211	8	16	1	30V/333A
Positron extraction dipoles	3	290	15	30	2	30V/600A
Positron ext. quadrupoles	18	70	14	14	18	40V/125A
Positron ext. quadrupoles	3	32	6	6	3	20V/50A
Electron bypass quadrupoles	32	15	2	32	2	100V/25A
Positron bypass quadrupoles	44	5	1	22	2	40V/15A
Bypass trim dipoles	197	6	10	10	197	±24V/±12A
NIT matching bends	1	209	10	10	1	20V/500A
NIT matching bends	2	56	5	10	1	20V/90A
NIT matching bends	1	321	15	15	1	30V/600A
NIT matching bends	1	121	7	7	1	40V/250A
NIT matching bends	1	24	1	1	1	20V/50A
NIT matching quadrupoles	7	23	1	4	7	20V/50A
NIT matching quadrupoles	11	10	1	6	2	30V/20A
SIT matching bends	2	5	1	2	1	24V/12A
SIT matching bends	3	22	2	4	2	20V/50A
SIT matching bends	2	126	9	18	1	40V/250A
SIT matching quadrupoles	7	32	2	2	7	20V/50A
SIT matching quadrupoles	11	3	1	6	2	30V/20A
HER injection bends	2	705	138	138	2	220V/1100A
HER current sheet septum	1	790	1	1	1	20V/1200A
HER Lambertson septum	1	100	20	20	1	40V/250A
HER kickers	2	300	3000	3000	1	5kV/1000A[b]
HER bumps	4	120	50	100	2	200V/200A
LER injection bends	2	243	33	33	2	60V/500A
LER current sheet septum	1	370	1	15	1	30V/600A
LER Lambertson septum	1	50	15	15	1	60V/80A
LER kickers	2	200	2000	2000	1	5kV/1000A[b]
LER bumps	4	60	25	50	2	100V/100A

[a]Includes allowance for cable losses.

[b]Fast pulser.

5.4.3.4 NIT and SIT Lines. Matching the electron bypass line to NIT will require six bending magnets on five power supplies. Of the 18 quadrupoles required, 7 are independently powered quadrupoles, and the remaining 11 are powered in two series strings of 5 and 6 quadrupoles, respectively.

Matching the positron bypass line to SIT will require seven bending magnets on four power supplies. Of the 18 quadrupoles required, 7 are independently powered quadrupoles, and the remaining 11 are powered in two series strings of 5 and 6 quadrupoles, respectively.

The NIT and SIT lines will be electrically connected as they were for PEP. However, many of the original power supplies will be replaced with new commercial units. A small number of the NIT supplies now located in Buildings 685 and 705 will be relocated to Sector 30, so that all of the NIT and SIT supplies can be easily handled by the control system.

5.4.3.5 HER and LER Injection System. The injection system for each ring consists of two septa, two parallel-fed kicker magnets, and four bump magnets (see Section 6.5.1 for optics details).

The rise time for the kicker magnets must be less than 200 ns, and the fall time less than 1.3 μs. In each ring, the two kickers will be driven in parallel, at the same amplitude, from a single kicker modulator. The modulator will employ an FET array rather than a thyratron as the switching element, thereby guaranteeing extremely low timing jitter. The kicker modulator design uses a capacitor that is pulse-charged up to 6 kV, then discharged simultaneously into the two kicker magnets by use of the FET array. A terminating network is provided to damp the discharge and thus avoid ringing in the magnet. The kicker modulator will be connected to the magnet pair by parallel coaxial cables with an impedance of approximately 10 Ω.

5.5 RF SYSTEM

The design of the PEP-II RF system is governed by the requirement that the system be as conservative and reliable as possible, despite the increased demands associated with the high luminosity. In this section, we describe the design for the RF system and indicate the basis for our technical choices.

The PEP-II RF system must fulfill the following requirements:

- Provide sufficient voltage to maintain acceptable quantum lifetime and suitable bunch length
- Provide sufficient power to compensate for the losses due to synchrotron radiation and losses into higher-order modes (HOMs)
- Provide a suitable low-impedance environment for the beam

All of these requirements are common to every collider and storage ring RF system and do not in themselves drive us into uncharted territory as far as RF system design is concerned. The noteworthy difference in the case of PEP-II is associated with the very large beam current that must be supported—an order of magnitude higher than in present colliders.

The choice of frequency is driven by the need to produce short bunches and the availability of high-power RF sources. To minimize injection jitter, we have also specified that the storage ring RF systems be harmonically related to the 2856-MHz SLAC linac, which serves as the PEP-II injector. We selected a frequency of 476 MHz to meet these needs. This choice provides the required 1-cm bunches with moderate voltage and is a convenient subharmonic of the linac frequency. Moreover, klystrons capable of providing in excess of 1 MW of CW power are available, or can be easily modified to work at this frequency. Because the frequency range near 500 MHz is a common choice for storage rings, it is also a good starting point for the design of the RF cavity, as discussed below.

To provide adequate lifetime, the RF system momentum acceptance $\Delta p/p$ (the "bucket height") should be of the order of $10\sigma_E/E$. For our parameters (see Table 3-1), this calls for a bucket height of 0.6% in the HER and 0.8% in the LER. A more stringent voltage requirement arises from the need to provide short bunches, σ_ℓ = 1 cm, to avoid luminosity losses associated with the beam-beam interaction (for example, excitation of synchrobetatron resonances, as discussed in Section 4.4). This requires a voltage of 18.5 MV for the HER and 5.9 MV for the LER at our chosen frequency of 476 MHz.

The power requirements are most severe for the HER. Here, the energy loss per turn due to the emission of synchrotron radiation is 3.58 MeV. At the nominal operating current of 0.99 A, the total power that must be provided to the beam is 3.6 MW; miscellaneous losses, such as resistive-wall heating and HOM losses, add to this value. If the number of cavities were not a concern, the power could simply be distributed over sufficiently many RF cells that it did not become a technology issue.

Unfortunately, the RF cells contribute considerable impedance to the ring and can lead to either single-bunch or coupled-bunch instabilities, as discussed in Section 4.3. Although single-bunch instabilities are not predicted to limit the performance of PEP-II, HOMs of the RF cavities, driven by the intense beams, are expected to give rise to wakefields that cause potentially severe longitudinal and transverse coupled-bunch instabilities. This aspect could easily limit the performance of PEP-II and must be avoided, or at least mitigated, in the design of the RF system.

In practice, this means that the total impedance presented by the RF cavities should be kept as low as possible. To minimize the HOM impedance, we keep the number of cavities small and we adopt single-cell cavities, rather than multicell structures of the type used in PEP. (In multicell structures, the number of possible modes is increased by the coupling between cells as compared with the modes of a single cell.) In consequence, the single cells must operate at high accelerating fields to provide the required voltage and must provide high power to the beam. Even with these precautions, the cavity HOMs must be damped substantially to reduce their shunt impedance to acceptably low values, and a number of feedback systems must be employed to combat the effects of the coupled-bunch instabilities.

The PEP-II RF system could employ either room-temperature or superconducting cavities. Because about 60% of the RF power is delivered to the beam, only a minor reduction of installed RF power could be realized by using superconducting technology (at the cost of increased complexity associated with the required cryogenic systems). Furthermore, the technologies of providing a large input power and removing a large

HOM power in a superconducting environment are not yet in hand. For these reasons, and because the expertise at SLAC and LBL is mainly in conventional room-temperature RF systems, an approach using copper cavities was chosen.

The filling pattern adopted for our collider design places the beam bunches in every other RF bucket throughout 95% of the circumference, with a 5% gap in the bunch train to avoid trapping ions in the HER beam. Thus, out of the 3492 possible RF buckets in each ring, 1658 are filled with beam. The same filling pattern for both rings minimizes asymmetries in the beam-beam collisions, but it may be desirable to add bunches in the positron beam to equalize transients induced in the two RF systems by the beam gaps.

5.5.1 RF System Choices and Requirements

The design of the RF systems is based on the following input parameters for the HER and LER:

- The high luminosity of 3×10^{33} cm^{-2} s^{-1} requires high beam currents: 0.99 A (HER) and 2.14 A (LER)
- The lattice design and beam current determine the power to be delivered to the beam: 4 MW (HER) and 3.2 MW (LER)
- The low vertical beta functions of 2 cm (HER) and 1.5 cm (LER) at the interaction point require a bunch length of 1 cm, which, in turn, requires a large overvoltage

Two frequency regimes, 350 MHz and 500 MHz, were initially considered because CW klystrons delivering more than 1 MW are commercially available at these frequencies. Cavity designs also exist at both frequencies, including PEP, LEP, and APS cavities at 350 MHz and Daresbury, KEK, and ALS cavities at 500 MHz. Because the voltage required to achieve the design bunch length is reduced at higher frequencies, the higher-frequency regime was selected.

As mentioned above, to allow for stable injection with small phase deviations, 476 MHz, a subharmonic of the SLAC linac frequency, was established as the operating frequency for the RF systems of both rings. Contacts with klystron manufacturers indicate that the existing 500- or 508-MHz klystron designs can be easily modified to operate at 476 MHz.

The cavity design was strongly influenced by the requirement to load HOMs to a very low shunt impedance for beam stability reasons, while simultaneously maintaining a high shunt impedance for the fundamental mode. The scheme for loading the HOMs is a further development of that employed at Daresbury [Corlett, 1989; Corlett and Hill, 1989] and the ALS [Jacob et al., 1990] and analyzed by Conciauro and Arcioni [1990]. The technique consists of suitably positioning three waveguides on the wall of the cavity, with the waveguides dimensioned to be below cutoff for the fundamental mode while transmitting all unwanted HOMs into dissipative loads. This method of HOM impedance reduction does not restrict the cavity shape in other respects, leaving the designer free to maximize the shunt impedance of the fundamental mode (using a reentrant cavity shape). Thus, a cavity shape similar to the ALS cavity can be used, as shown in Fig. 5-93. The calculated shunt impedance of this ALS-type cavity is 5.3 MΩ, but, considering all the

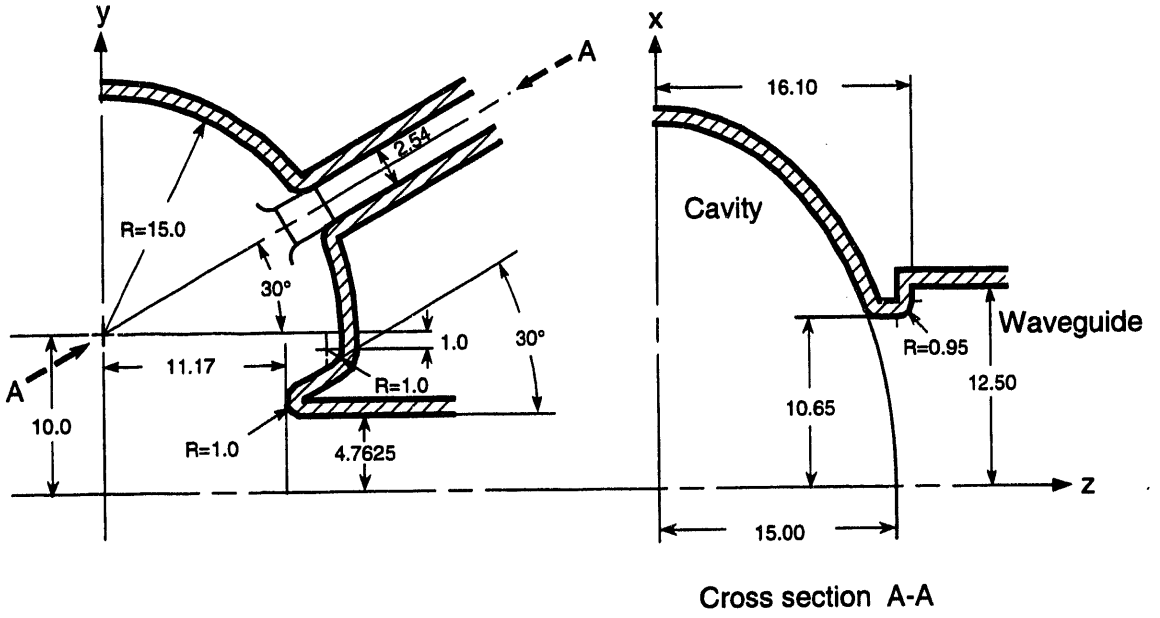

Fig. 5-93. Schematic of a quadrant of the PEP-II RF cavity. All dimensions are in cm.

ports and wall-heating effects, a lower value, say, 3.5 MΩ, is a more reasonably achievable fundamental-mode shunt impedance in an actual cavity.

The chosen RF system configuration requires a wall loss per cavity of 122 kW but is designed such that each cavity can handle a wall loss of up to 150 kW at an accelerating gradient of 4.5 MV/m. The design also requires the input window and coupling network for each cavity to carry a power load of about 400 kW. Both design requirements are challenging and will be discussed further in the context of the cavity description. The klystron output power is assumed to be 90% of saturated power to accommodate a capability for overdrive needed by some of the feedback circuits.

Based on the above considerations, the PEP-II RF system can meet all requirements with 10 klystron stations, driving 20 cavities, in the HER, and 5 klystron stations, driving 10 cavities, in the LER. The parameters for the RF systems for both rings are summarized in Table 5-33.

5.5.2 Cavity Design

The large synchrotron radiation losses mean that the RF cavities and conventional circuit components, such as windows and couplers, must deliver very high power throughput to the beam. In addition, the large circulating currents make it imperative to keep the HOM impedance as low as possible to avoid uncontrollable coupled-bunch instabilities. Thus, the number of cavities must be a compromise between their power-handling capability and the total beam impedance. The power-handling capability of existing (or reasonably extrapolated) window and coupler technology, and the problem of heat dissipation in the cavity walls and apertures, ultimately limit the power into each cell and thus determine the minimum number of cells that can be used reliably.

Table 5-33. RF system parameters for the PEP-II high- and low-energy rings. Parameters have been adjusted to take account of the 5% gap in the bunch trains.

Parameter	HER	LER
RF frequency, f_{RF} [MHz]	476	
Harmonic number, h	3492	
RF voltage, V [MV]	18.5	5.9
Beam current, I [A]	1.03	2.25
Energy loss/turn [MeV]	3.58	1.14
Synchrotron radiation power, P_{SR} [MW]	3.69	2.57
HOM power (est.) [MW]	0.15	0.45
Cavity wall loss, total [MW]	2.44	0.50
Klystron power, total [MW]	11.0	5.5
Number of klystrons	10	5
Klystron power, P [MW]	1.1	
Number of cavities	20	10
Shunt impedance/cavity,[a] R_s [MΩ]	3.5	
Gap voltage/cavity [MV]	0.925	0.590
Accelerating gradient [MV/m]	4.14	2.64
Wall loss/cavity [kW]	122	50
Coupling factor without beam, β	7.5	7.5
Unloaded Q of cavity	30,000	
Synchrotron frequency [kHz]	7.1	5.0
Natural bunch length, σ [cm]	1.0	1.0

[a] $R_s = V^2/2P$

5.5.2.1 Choice of Cavity Shape. Preliminary optimization of the cavity shape was done using the URMEL-T code (triangle mesh version). Initially, the mode patterns of open, or "bell-shaped" (Fig. 5-94a), and reentrant (Fig. 5-94b) cavities having the same beam pipe radius and fundamental-mode frequencies were compared. The results clearly demonstrate that, for conventional copper construction, there is no advantage to the open shape as far as the longitudinal HOM impedances are concerned—in fact quite the opposite. With this in mind, we adopted a reentrant cavity design with nose cones, patterned after those used at the Daresbury SRS, the KEK Photon Factory, and the ALS at LBL. (For superconducting cavities, where the fundamental-mode shunt impedance is very high in any case, there are other advantages to the smooth shape—for example, to reduce the problems of field emission and multipactoring.)

5.5.2.2 Cavity Parameters. URMEL calculates the transit-time-corrected shunt impedance R_s (= $V^2/2P$) for the basic reentrant geometry to be about 5.3 MΩ, with an unloaded Q of 45,000 and R_s/Q of 116 Ω. In a real cavity, this impedance is degraded by the addition of ports and damping waveguides and by the effect of increased temperature on the conductivity of the copper. Using MAFIA and ARGUS to compare the fundamental-mode properties with and without damping waveguides suggests a loss of about 10% in R_s and Q due to these structures, while R_s/Q stays about constant. Experience with other designs suggests a further 13% will be lost by the addition of the tuner, drive, and other ports, and from manufacturing imperfections.

The degradation due to thermal effects is determined by the effective wall temperature for the maximum power of 150 kW dissipated in the cavity. Extrapolation from existing designs (see Table 5-34), and studies using MAFIA output in a thermal model with the ANSYS code, suggest the average temperature rise may be as much as 45°C. This would give rise to an additional loss of about 10% in R_s and Q. Lowering the input water temperature by the use of chillers could reduce this, but may not be cost-effective. The result of these cumulative losses is to reduce the practical shunt impedance to about 3.5 MΩ, with a Q of about 30,000.

The coupling to the waveguide is such that the loaded Q is the same in both rings to match the transient response to the beam gap. This requires a coupling factor β of about 7.5 and results in a loaded quality factor, $Q_L = Q_0/(1 + \beta)$, of approximately 3500. Both loop and aperture couplers are under consideration. The loop coupler has the advantage that the coupling may be adjusted mechanically by rotating it, but it is a more complicated structure that must be water-cooled because of the very high surface-current density. An aperture coupler, on the other hand, has the advantages of simplicity and lower surface-current density but has a fixed coupling factor. The usual method of achieving a match with an aperture coupler is to use a tuning element in the waveguide, often a sliding short-circuit device. This could cause practical problems at high power, but fixed coupling could be set by interchangeable waveguide lengths. We plan to evaluate both types of coupler in a high-power test cavity.

Either coupling device requires the use of a vacuum window at some point. At lower power levels, previous designs have incorporated ceramic windows close to the cavity in the construction of the coupler (sometimes with disastrous results), either in the coaxial part of the loop or as a disk filling the coupling aperture. Neither of these designs is suitable for very-high-power applications, where it is necessary to locate the window well

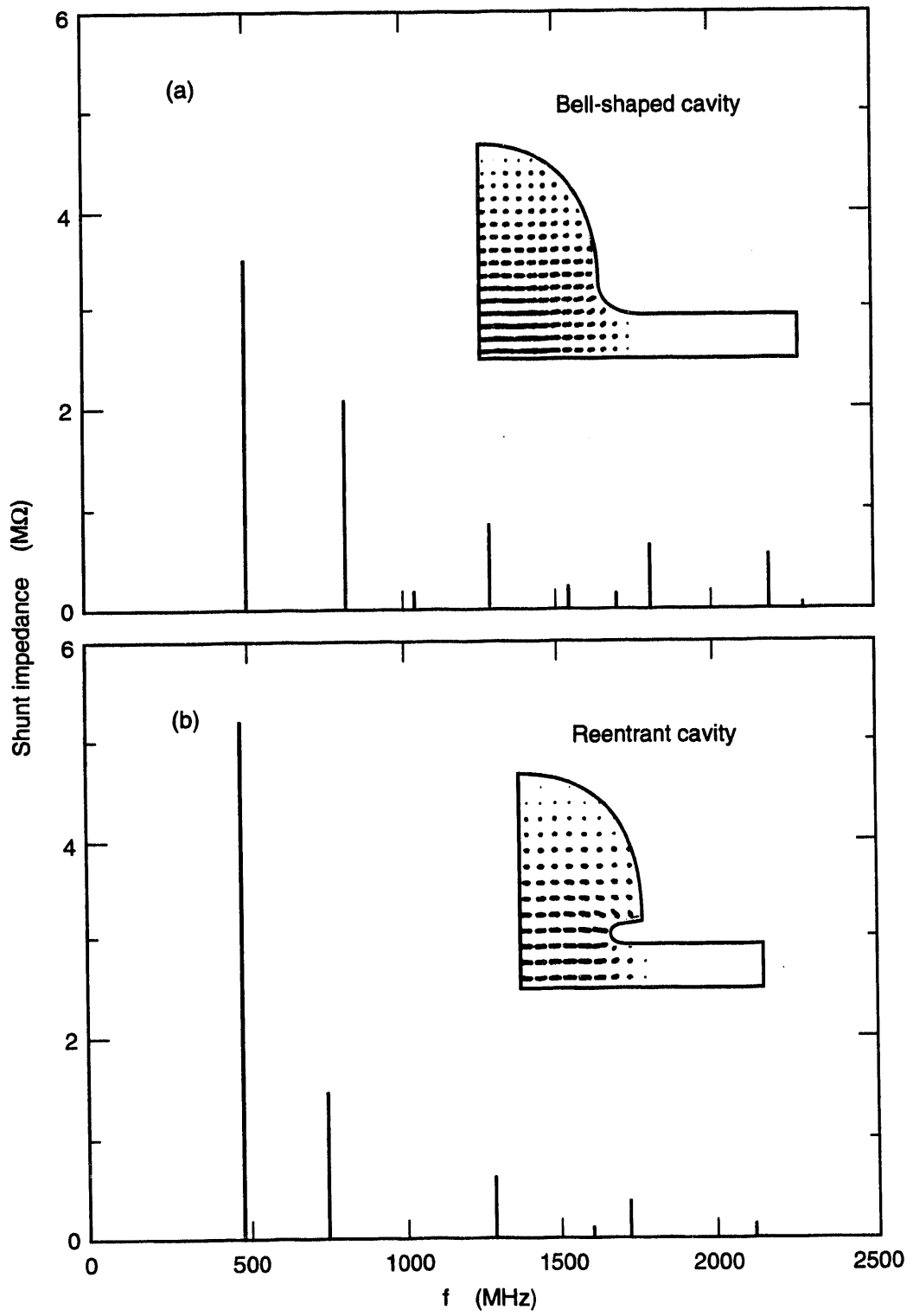

Fig. 5-94. Longitudinal mode spectrum calculated for (a) an open, or "bell-shaped," cavity and (b) a reentrant cavity shape.

Table 5-34. Temperature comparison of existing and proposed cavities.

System	Frequency (MHz)	Power (kW/cell)	T_{inlet} (°C)	$\Delta T(H_20)$ (°C)	ΔT(Cu) (°C)	ΔT(total) (°C)	R_s loss (%)
PETRA cavity[a]	500	24	45	10	18	53	23.3
PEP cavity (Al)	350	50	35	10	15	40	23.0
LEP cavity[b]	350	25	20	9	12	21	4.2
ALS cavity[c]	500	70	40	3	18	41	~9.0
PEP-II cavity	476	150	35	5	25	45	~10.0

[a]Gaede et al., 1980
[b]Henke and Wilson, 1981
[c]Taylor, 1990

away from the harmful heating of the cavity standing-wave fields. These may penetrate into the waveguide near the coupling point, so it is prudent to locate the window a safe distance away, possibly in the waveguide. Such a window then need only survive the heating due to the traveling wave that carries power to the cavity. Designs of this type are currently being developed by commercial sources and at SLAC. Remote location of the vacuum window requires that the waveguide adjacent to the cavity be part of the cavity vacuum system, which may lengthen the conditioning time and increase pumping requirements. The ceramic window must still be protected against multipactoring, which can be done by using a low-secondary-emission surface coating. It is also preferable to avoid direct exposure of the window to lost particles from the beam.

5.5.2.3 HOM Damping. The high beam currents, and therefore the potential for very high coupled-bunch instability growth rates, require that special attention be paid to the HOM impedances of the cavities. To reduce the growth rates to a level where they can be controlled by a technically (and economically) feasible feedback system required careful attention to the issue of HOM damping at an early point in the cavity design. Externally applied damping techniques using tuned couplers have not proved effective enough in existing applications to meet PEP-II requirements. Damping waveguides were therefore included in the initial design of the cavity. These waveguides are designed to propagate at the HOM frequencies and are positioned to offer the maximum coupling to the most troublesome HOMs, while being below cutoff and offering minimal perturbation at the fundamental-mode frequency.

Calculations of the damping effect of these waveguides were carried out with the three-dimensional codes MAFIA and ARGUS, making use of the Kroll-Yu method [Kroll and Yu, 1990]. This method involves calculating the frequencies of the cavity modes modified by waveguides having short-circuits placed at various lengths. This technique is necessary because neither code is capable of solving the complex eigenvalue problem that arises when losses are introduced into the model. Initially, the effect of the

size, shape, and locations of the coupling apertures on the modes of a simple pillbox cavity was calculated. The calculations were validated by measurements on a model of the pillbox geometry, with the results showing good agreement [Voelker et al., 1990]. Calculations were then carried out for a realistic cavity shape, having damping waveguides. URMEL was used to analyze the two-dimensional shape, and ARGUS and MAFIA, with the Kroll-Yu method, were used to estimate the damping in the fully three-dimensional cavity with loads.

The damping scheme for the PEP-II cavity uses shallow rectangular waveguides with a cutoff frequency of 600 MHz. This choice allows all of the HOMs to propagate while leaving the fundamental mode trapped in the cavity with its fields decaying rapidly with distance into the waveguides. The first and strongest longitudinal HOM is the TM011-like mode at about 770 MHz, and the cutoff frequency of the damping waveguides must be sufficiently far below this to allow for the frequency drop due to external loading. The choice of 600 MHz is conservative because it also allows the weak TE mode at 670 MHz to propagate. The waveguide width of 25 cm is reduced to 21 cm by means of an iris where it enters the cavity. This allows sufficient coupling to the HOMs while preserving as much as possible of the fundamental-mode impedance. Calculations showed strong damping for the worst HOMs with this scheme. A low-power test cavity was then fabricated to verify the predictions. The test cavity (see Fig. 5-95) has three damping

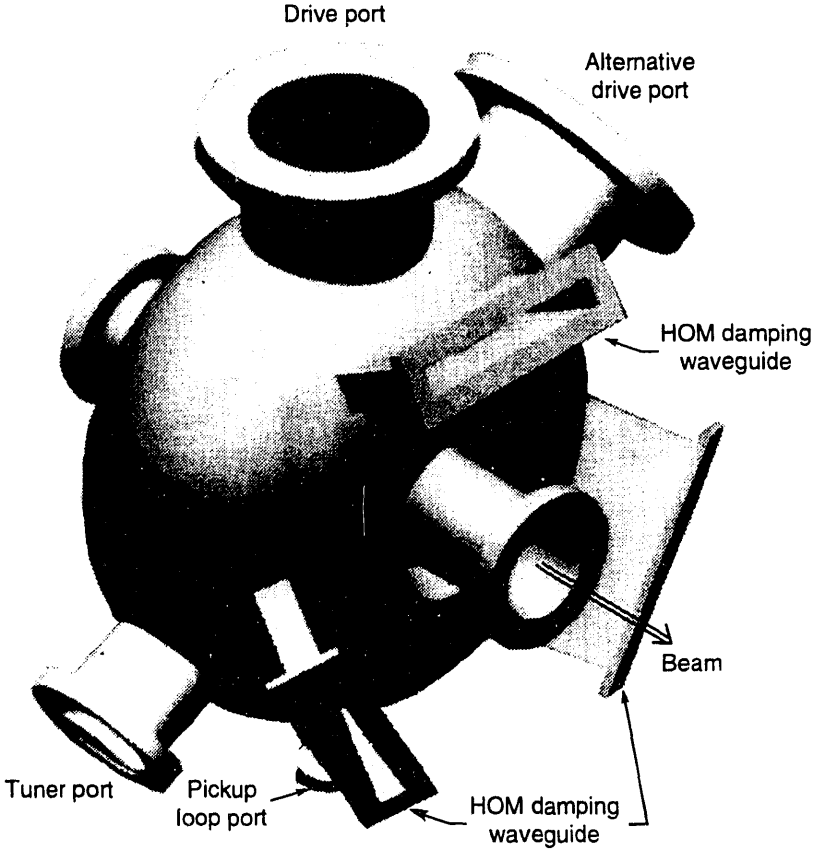

Fig. 5-95. Low-power test model of prototype PEP-II RF cavity.

waveguides, along with apertures for a PEP loop coupler (in two alternative positions), a PEP plunger tuner, and various sampling probes. To reduce its cost, the model was not made with the fine surface finish required of a real cavity, so, although good, it was not designed to be a test of the ultimate fundamental-mode Q. For the HOMs, of course, the Q factors are dominated by the coupling to the external loads, so the properties of the low-power test cavity were more than adequate.

The low-power test cavity was mounted in a fixture in the RF test lab at LBL (see Fig. 5-96) for measurement of its mode frequencies and investigation of its field profiles with an automated bead-perturbation system. With beam pipe extensions bolted on and all of the other ports blanked off, small electric-field antennas were introduced though the beam pipes to excite the cavity. The transmission response (S_{21}) between these probes was measured using an HP-8510C network analyzer. In this configuration, with no damping, the modes were visible as discrete resonances, and their frequencies were very close to the URMEL predictions, allowing all of the important modes below the beam pipe cutoff to be identified. Tables 5-35 and 5-36 list the observed modes and their

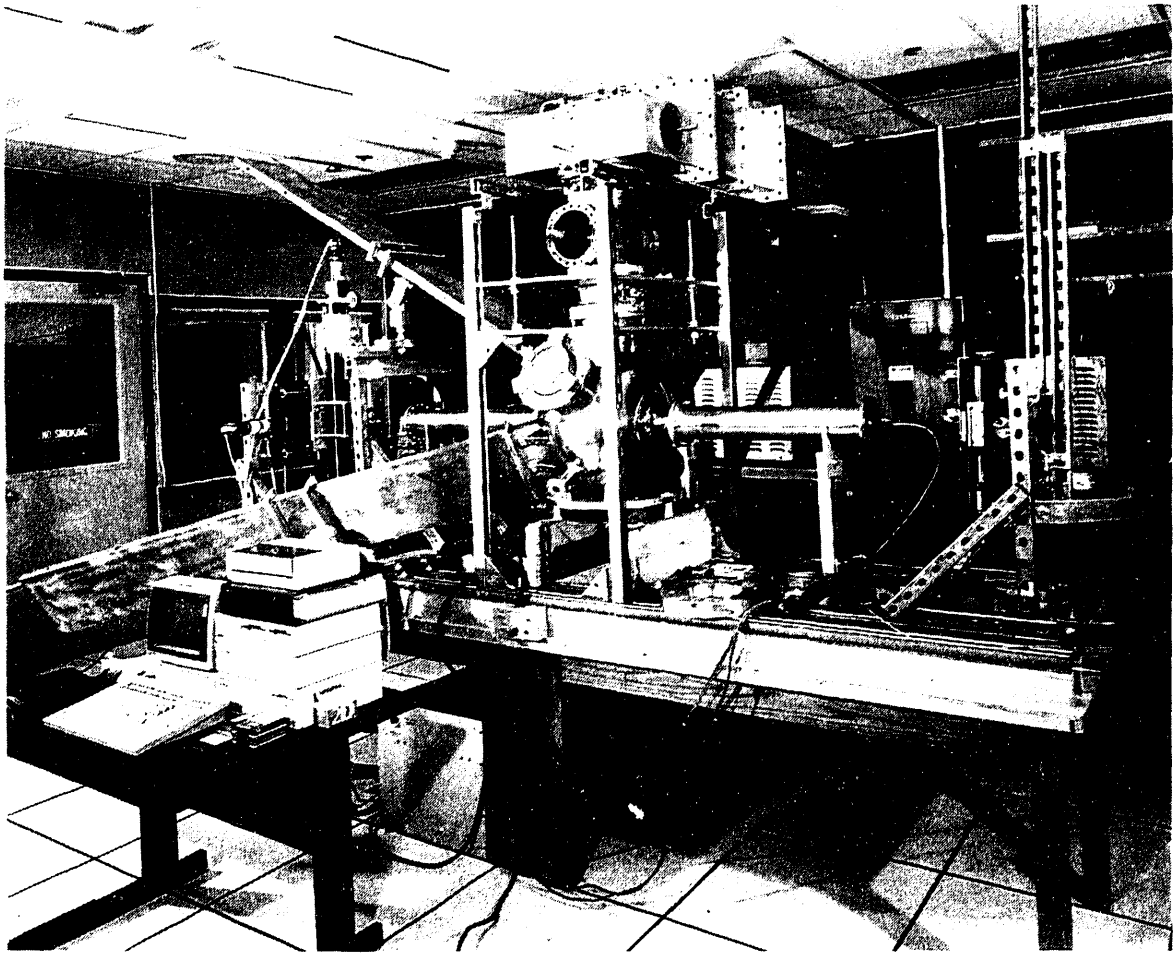

Fig. 5-96. Low-power test cavity in the RF measurement laboratory at LBL.

Table 5-35. Properties of the longitudinal (monopole) modes below the beam-pipe cutoff calculated by URMEL and measured in the low-power test cavity. The last column shows the effective impedance estimated from the calculated R/Q and the measured Q_L.

	Mode type	URMEL designation	f (MHz)	R/Q (Ω)	URMEL Q	R_s (MΩ)	f_L, calc. (MHz)	Q_L, calc.	f_L, meas. (MHz)	Q_L, meas.	$R/Q \times Q_L$ (kΩ)
A	TM010	0-EE-1	489.6	108.8	46306	5.036	479		484	31926[a]	3472.28
C	TM011	0-ME-1	769.8	44.97	39625	1.782	753	26	758	28	1.26
E	TM020	0-EE-2	1015.4	0.006	41383	0.0002	1004	169	1016	246	0.001
I		0-EE-3	1291.0	7.68	90188	0.692	1285	66	not visible after damping		
J	TM021	0-ME-2	1295.6	6.57	40326	0.265			1296	907	5.96
		0-EE-4	1585.5	5.06	42724	0.216			1588	178	0.90
		0-ME-3	1711.6	4.75	85135	0.404			not visible after damping		
		0-EE-5	1821.9	0.06	107874	0.006			1821	295	0.018
		0-ME-4	1891.0	1.68	44492	0.075			not visible after damping		
		0-EE-6	2103.4	3.52	66780	0.235			2109	233	0.82
		0-ME-5	2161.9	0.02	84386	0.002			2168	201	0.004
		0-EE-7	2252.2	1.21	55944	0.068			2253	500	0.61

[a]The test cavity as constructed is not designed to give the ultimate fundamental-mode Q.

Table 5-36. Properties of the deflecting (dipole) modes below the beam-pipe cutoff calculated by URMEL and measured in the low-power test cavity. The last column shows the effective transverse impedance estimated from the calculated R/Q at the beam-pipe radius, r_0, and the measured Q.

	Mode type	URMEL designation	f (MHz)	R/Q[a] (Ω)	$\frac{R}{Q}\left(\frac{1}{kr_0}\right)^{2}$ [a] (Ω)	URMEL Q	R/kr_0^2 (MΩ/m)	f_L, calc. (MHz)	Q_L, calc.	f_L, meas. (MHz)	Q_L, meas.	$\left(\frac{R}{Q}\right)\left(\frac{1}{kr_0^2}\right)Q_L$ (kΩ/m)
B	TE111	1-ME-1	679.6	0.001	0.002	47520	0.001	674	35	not visible after damping		
D	TM110	1-EE-1	795.5	9.876	15.263	61076	15.5	787	121	779	122	1.86
F		1-ME-2	1064.8	31.990	27.590	50048	30.8	1061	38	not visible after damping		
G		1-EE-2	1133.2	0.320	0.243	49771	0.287	1127	76	1141	112	0.65
H		1-ME-3	1208.2	0.385	0.258	87745	0.573	1205	2266	1203	1588	10.3
K		1-EE-3	1313.2	10.336	5.861	50189	8.09			1311	498	80.1
		1-ME-4	1429.0	5.999	2.873	38150	3.28			1435	3955	342.0
		1-EE-4	1541.0	2.065	0.850	102408	2.81			1554	59	1.62
		1-EE-5	1586.2	5.262	2.045	76118	5.17			1588	178	12.1
		1-EE-6	1674.2	14.732	5.140	36130	6.51			1674	2134	385.0
		1-ME-5	1704.4	0.285	0.096	52856	0.181			1704	444	1.52
		1-ME-6	1761.9	0.330	0.104	92516	0.355			1757	7129	27.3

[a]At $r_0 = 4.7625$ cm.

calculated and measured properties. Figure 5-97a shows the undamped response of the cavity up to 1.4 GHz. The peaks corresponding to the monopole and dipole modes are labeled and their unloaded impedances are listed for reference. (Note that the relative amplitudes of the peaks do *not* give a good indication of their relative impedances, because the network analyzer sweep of 801 data points may not accurately resolve the sharpest peaks in these wide spans and the antennas couple differently to the different modes due to their positions in the cavity and their own frequency response. For determination of the Q factors of the individual modes in subsequent measurements, much narrower frequency sweeps were used to properly resolve the peaks.)

Figure 5-97b shows the effect of adding the three HOM damping waveguides to the cavity. Apart from a small frequency shift, the fundamental mode A is not significantly

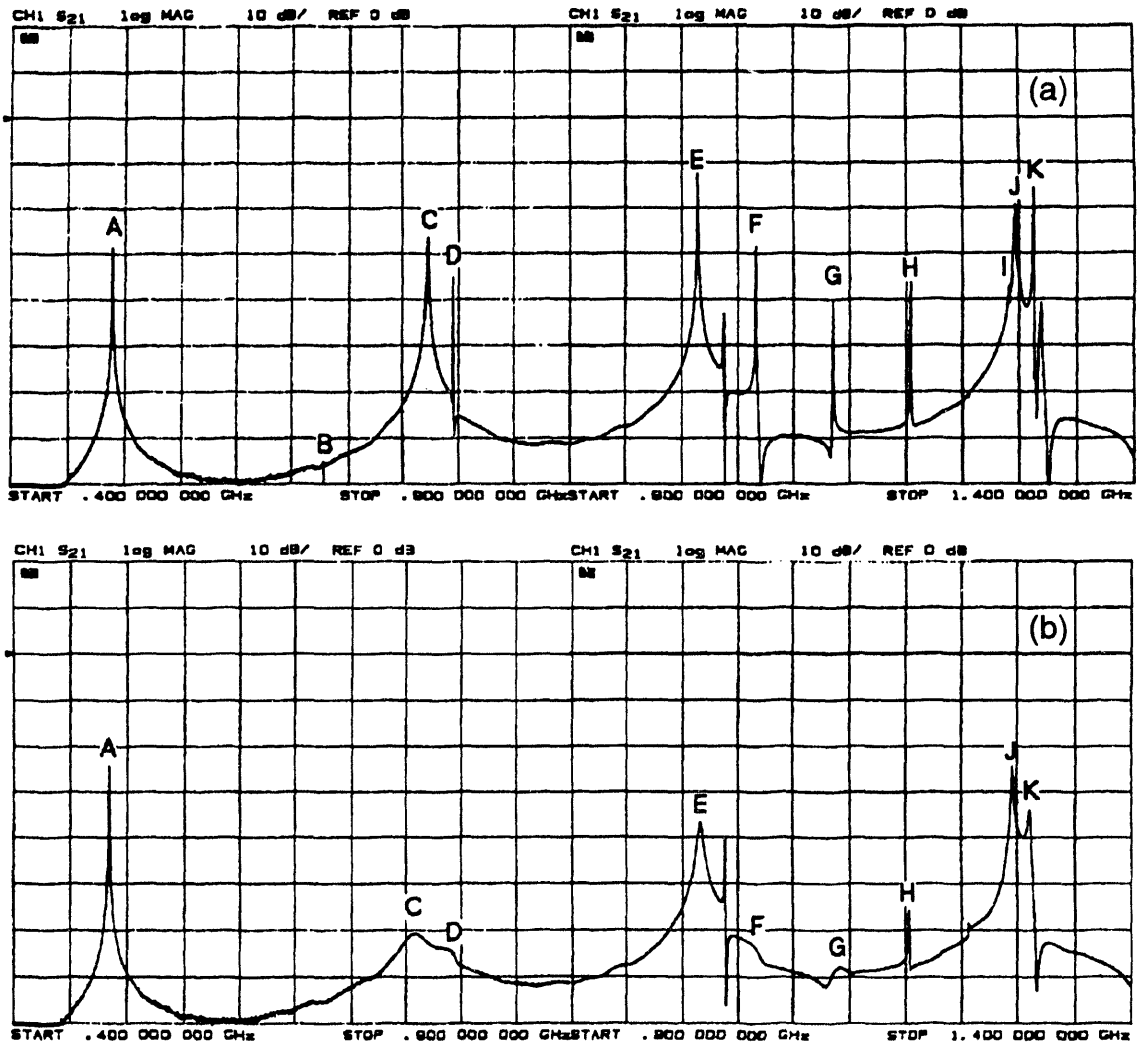

Fig. 5-97. Modes measured in the low-power test cavity from 0.4–1.4 GHz, (a) without damping, (b) with three damping waveguides. (Labels refer to modes in Tables 5-35 and 5-36).

changed but the first (and worst) monopole HOM, TM011 (C), is loaded to a Q of approximately 28 and a frequency of about 758 MHz. This Q, which is already a factor of two below the target value of 70 for the feedback system specification, represents a reduction of more than three orders of magnitude from the calculated unloaded Q_0 of >39600. Both orientations of the TM110 dipole mode (D) are strongly damped and are barely visible at the edge of the TM011 response.

All three waveguides were terminated in low-power test loads made of epoxy-ferrite mixture. The material was placed at the edges of the waveguides in the form of long tapers to provide low reflection over a wide frequency range. This arrangement simulates the high-power loads that will be used in the real cavities.

In Fig. 5-97b, the TM020 monopole mode (E) is still visible at 1016 MHz, but its Q is less than 250 and its residual impedance is very small, one thousandth of the target value at that frequency. The 1-ME-2 mode (F), which is the worst dipole HOM, along with the 1-EE-2 (G), 1-ME-3 (H), and 1-EE-3 (K) dipole modes are all damped to safe levels, the last being visible at 1311 MHz with $Q \approx 500$. The TM021-like 0-ME-2 monopole mode (J) is still visible at 1296 MHz with $Q = 907$. Simulations show that instabilities driven by this mode are within the capabilities of the proposed longitudinal feedback system (see Section 5.6). The results are similar for higher frequencies, all the way to the beam-pipe cutoff. The measurements are summarized in Table 5-35 for the longitudinal (monopole) modes and Table 5-36 for the deflecting (dipole) modes. Figure 5-98 shows the effective

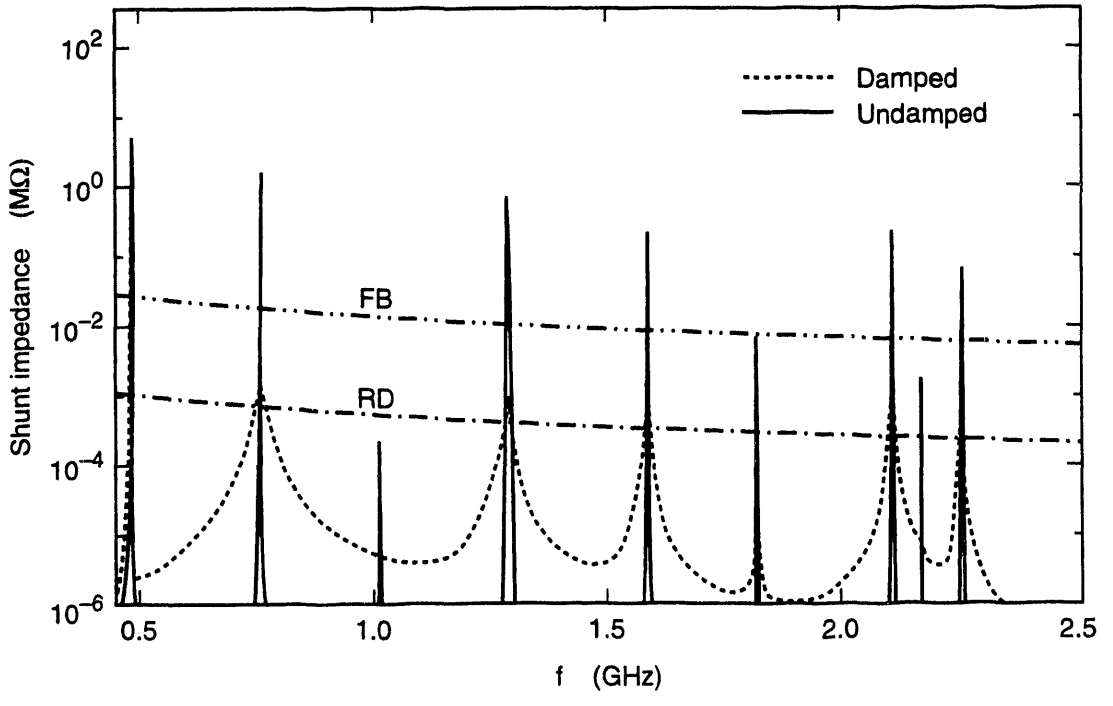

Fig. 5-98. Effective longitudinal impedance of the cavity modes before (solid line) and after (dashed line) damping. Also shown for reference are the radiation damping (RD) threshold and a tolerance from the longitudinal feedback system (FB) for a gain corresponding to 3 kV for a 5-mrad phase amplitude.

longitudinal impedance based on the calculated R/Q and Q values in the undamped cavity and the loaded Q values measured in the test cavity with the three damping waveguides attached. The worst longitudinal HOM is reduced by more than three orders of magnitude, and all other modes are within the capability of the broadband feedback system. Similarly, Fig. 5-99 shows the effective transverse impedance of the deflecting HOMs before and after damping. Additional damping may be possible through the drive port and pumping structure if need be.

The addition of the damping waveguides has implications for the mechanical design of the cavity; in particular, the apertures result in stress and surface-current concentrations at the ends of the irises. These issues are discussed in Section 5.5.2.4. Design of a high-power cavity, which will be tested to 150 kW on the klystron test stand at SLAC, is well under way.

Evanescent penetration of the cavity fundamental mode into the damping waveguides and other apertures gives rise to the possibility of multipactoring. Increasing the number of ports may therefore require a longer conditioning time before the cavity can take full power, and, in some places, the use of low-secondary-emission coatings may be appropriate.

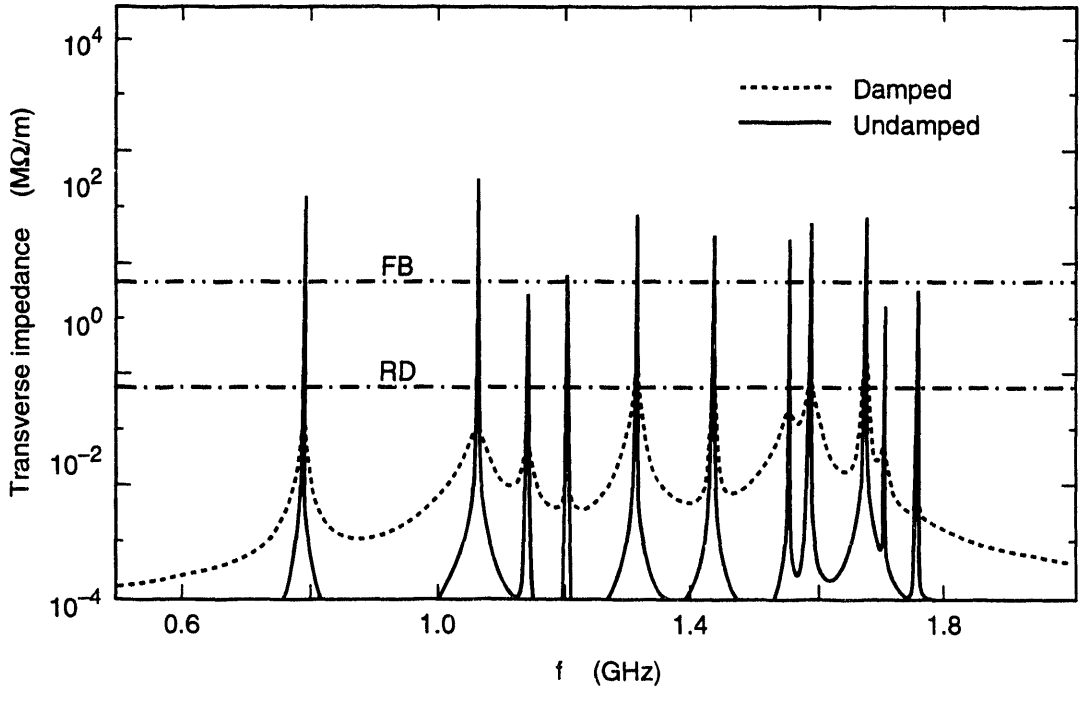

Fig. 5-99. Effective transverse impedance of the cavity modes before (solid line) and after (dashed line) damping. Also shown for reference are the radiation damping (RD) threshold and a tolerance from the transverse feedback system (FB) for a gain corresponding to 5 kV for a 0.5-mm transverse amplitude.

As discussed above, the RF cavities for PEP-II are designed with waveguides as high-pass filters coupling out the HOM power while perturbing the fundamental mode relatively lightly. In practice, this can only be achieved with a broadband, low-reflection load at the end of the waveguides. (A load that has high reflections could decrease the effectiveness of the HOM damping scheme and might result in higher Q values for the cavity HOMs.) The design requirements on the load are that it must

- work in vacuum
- have a VSWR (voltage standing-wave ratio) less than 2:1 over the frequency range from 700 to 2500 MHz for all propagating waveguide modes
- be capable of dissipating 10 kW

Using the time-domain module of MAFIA, various geometries for the HOM load have been investigated, and one has been found that can serve as the basis for a workable design. The load topology (Fig. 5-100) is a shaped alumina piece sandwiched between two tapered sheets of a lossy ceramic material (aluminum nitride with 7% glassy carbon) jointly developed at CEBAF and Ceradyne. Preliminary thermal calculations indicate that the load will be able to dissipate the of 10 kW specified as a design goal. Continued work will be directed at reducing the overall length of the load, investigating the bonding techniques required to build a load of this type with the lossy ceramic, and building a prototype.

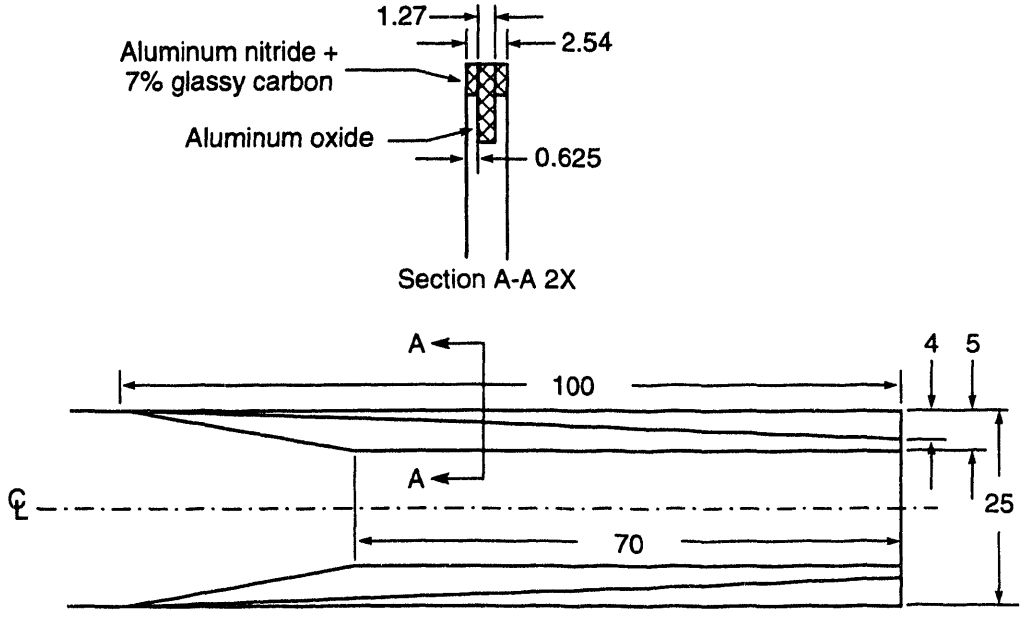

Fig. 5-100. HOM load design. All dimensions are in cm.

5.5.2.4 Mechanical Design. The success of the low-power test cavity gives us confidence in the electrical design of the cavity. A design for a high-power test cavity, using the same internal shape verified by the low-power test cavity, is being pursued vigorously.

The final configuration of the cooling-channel layout is being developed along with the fabrication details, but a complete cycle of thermal-mechanical analysis has been completed on a three-dimensional model of the high-power test cavity with a realistic cooling-channel layout.

General requirements of the cooling scheme are set by the expected dissipated RF power; the highest level of dissipated power is less than 130 kW for the HER cavities. In the engineering analysis, a power level of 150 kW was chosen as the design value of dissipated RF power to provide a safety margin. Using 150 kW as the input power and the (self-imposed) constraint of a 10°C bulk temperature rise of the cooling water, it is found that the cooling passages must be able to transport 57 gpm (3.6 kg/s) of water without an excessive pressure drop. Because of the relatively large size of the cavity and cooling channels, this is not a difficult criterion.

The surface heat flux F is calculated from the data generated by the three-dimensional electromagnetic codes by directly calculating the tangential magnetic field at the surface and converting this to surface heating via the relation

$$F = \frac{1}{2} R_s \mathbf{H}_{\tan}^2 \tag{5-37}$$

where

$$R_s = \left(\frac{\omega\mu}{2\sigma}\right)^{1/2} = 0.0057\ \Omega \tag{5-38}$$

for OFE copper at 476 MHz. This was then used as the input to thermal and mechanical finite-element analyses performed by Chalk River Laboratories [de Jong et al., 1993], using the computer codes MARC and MENTAT.

First a two-dimensional analysis was made to determine the basic layout of the cooling channels. The analysis assumed a water velocity of 5 m/s, resulting in a heat transfer coefficient of 21.2 kW/m^2/°C. The inlet water temperature was set at 35°C which, with the 10°C temperature rise of the water, results in an average water temperature in the cooling channels of 40°C. The calculated average temperature of the inside surface of the cavity was 52°C. This would cause a reduction in Q of 6.3% due to the increase in copper resistivity with temperature. The peak temperature, which occurred at the end of the nose cone, was only 60°C; the maximum calculated von Mises stress was 16 MPa, well below the yield point of OFE copper. The frequency shift caused by the deformation of the cavity from the combined effects of water pressure, vacuum, and thermal loading, was calculated to be –130 kHz.

Next, a three-dimensional model was made. The results for this baseline three-dimensional case, shown in Figs. 5-101 and 5-102, were an average surface temperature of about 60°C, a peak temperature of 97°C at the end of the iris, and a peak von Mises stress of 75 MPa (1 MPa = 145 psi) in the same region. It is noteworthy that the peak stress occurs in a very localized region and that it is compressive. A number of variations on the baseline case were analyzed in an effort to better understand how to optimize the cavity design. The variations included adding stiffening supports at various locations along the waveguides and other regions of the cavity, specifying the cooling water routing, etc. In one of these variations, the water velocity was reduced to 3.7 m/s, which led to a peak temperature at the end of the iris of 101°C. Using this *peak* temperature as an overall *average* temperature, the reduction in Q would be 14.5%; we take this as an upper bound on the reduction in Q. Combined with the more realistic estimate corresponding to the expected average temperature of 52°C, a reasonable estimate for the reduction in Q due to the increase in copper resistivity is 10%. An analysis incorporating all of the beneficial changes in cavity design resulted in a reduction of the peak stress by 16 MPa. The knowledge gained from these variations is being incorporated into the detailed design of the high-power test cavity.

The maximum stress in the waveguide iris region is predicted to be close to the yield point (69 MPa) of fully annealed OFE copper. If the stress in the high-power test cavity exceeds the yield point in this isolated region, the region will undergo a small inelastic deformation in the initial conditioning period and, from then on, will deform elastically. Because the region is small and localized, this should not be a problem for either the RF or the mechanical characteristics of the cavity. Considering cyclical fatigue, the predicted alternating stress, $s_a = (s_{max} + s_{min})/2$ is only slightly higher than $s_y/2 = 33$ MPa. The endurance limit of OFE copper, based on a lifetime of 10^6 cycles, is about 70 MPa, so the cavity has a good design margin.

5.5.2.5 Cavity Tuning. It is proposed that the tuning of the cavity be accomplished with a PEP-style tuner, that is, a 10-cm-diameter plunger with about 10 cm of travel (see Fig. 5-103). Tests of this type tuner on the low-power test cavity have shown that 2.6 MHz of tuning range can be achieved with the full travel range of 10 cm. Only ±500 kHz of tuning range is required to cover a temperature-related detuning of –200 kHz (for an operating temperature of 60°C), as well as a –200 kHz detuning to compensate for beam loading (or alternately a ±340 kHz detuning to park an idling cavity). Thus, a 1-MHz range, with less penetration of the plunger into the cavity will be chosen. This type tuner uses carbon brushes to prevent HOM power from entering the space of the bellows. The PEP tuner has been used at power levels of 60 kW; its suitability for the 150-kW power level needed for PEP-II will be verified by simulation and by tests in the high-power test cavity.

5.5.2.6 Input Coupler. Two different input coupling networks for 500-kW power transmission are now being designed and will be tested in the high-power test cavity.

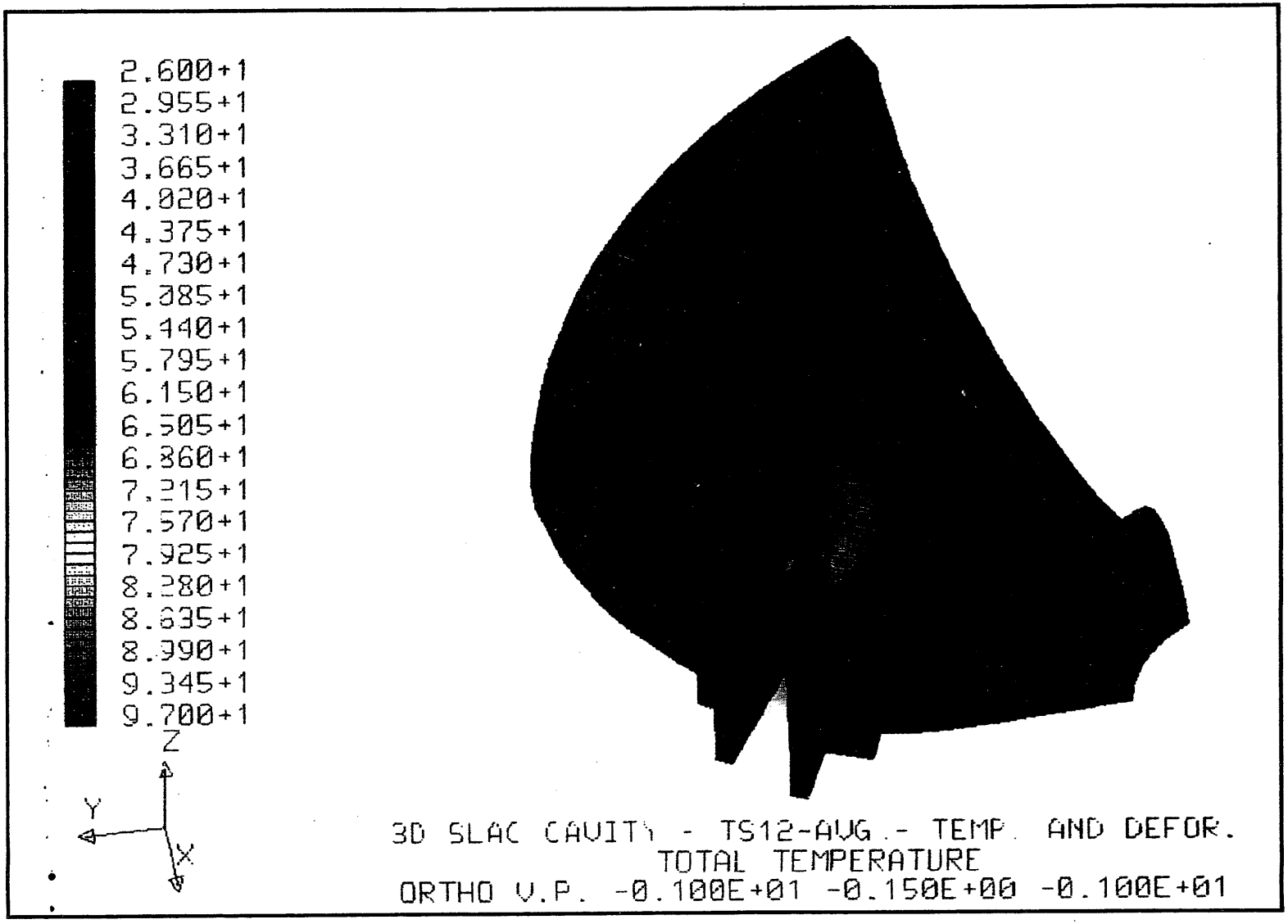

Fig. 5-101. Computed wall-temperature profile in the region of the HOM-loading waveguide ports for a PEP-II RF cavity at 150-kW wall dissipation.

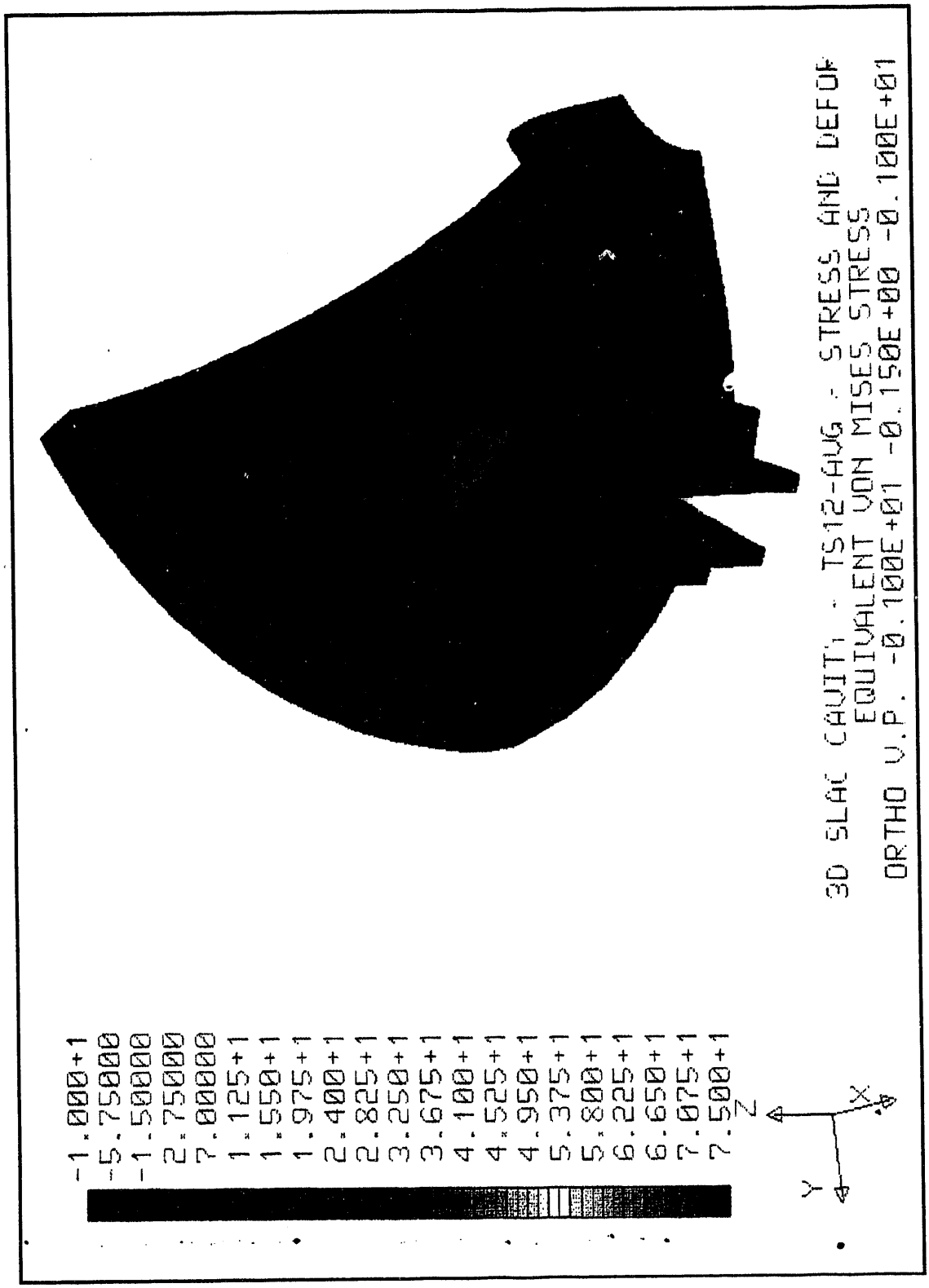

Fig. 5-102. Computed von Mises stress in the region of the HOM-loading waveguide ports for a PEP-II RF cavity at 150-kW wall dissipation.

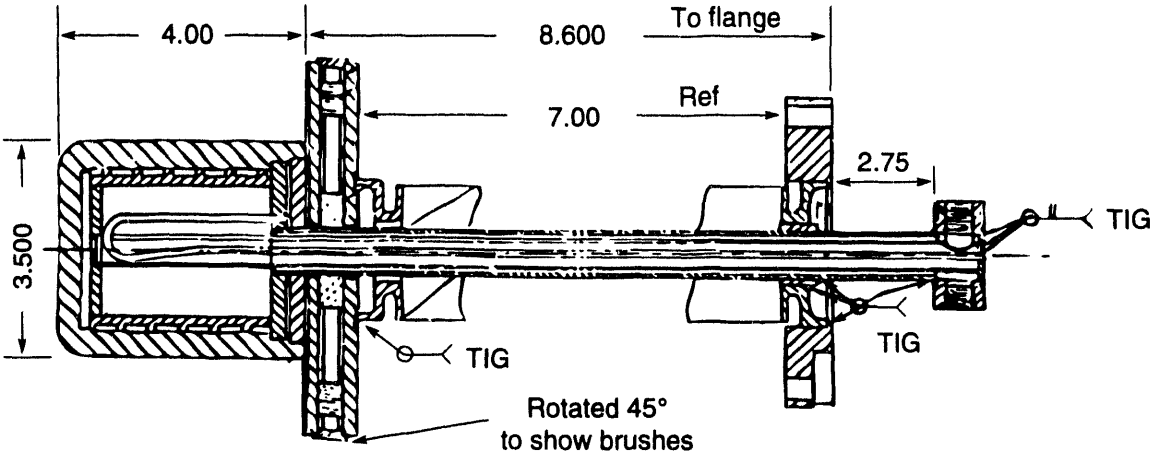

Fig. 5-103. Cross-sectional view of an all-copper PEP cavity tuner.

One uses a coupling loop in a 6.4-in. coaxial line similar to the PEP coupling loop (see Fig. 5-104). It will be the obvious choice if a coaxial window like the one developed for the 1.2-MW klystron is chosen for the PEP-II cavity. The coupling factor can be set between 0 and 10 by rotating the loop. To ensure that the window ceramic is shielded from the direct path of ions produced by the beam in the cavity, an effective shielding method is being developed. The correct loop penetration and associated frequency shift have been measured on the low-power test cavity using a PEP coupling loop.

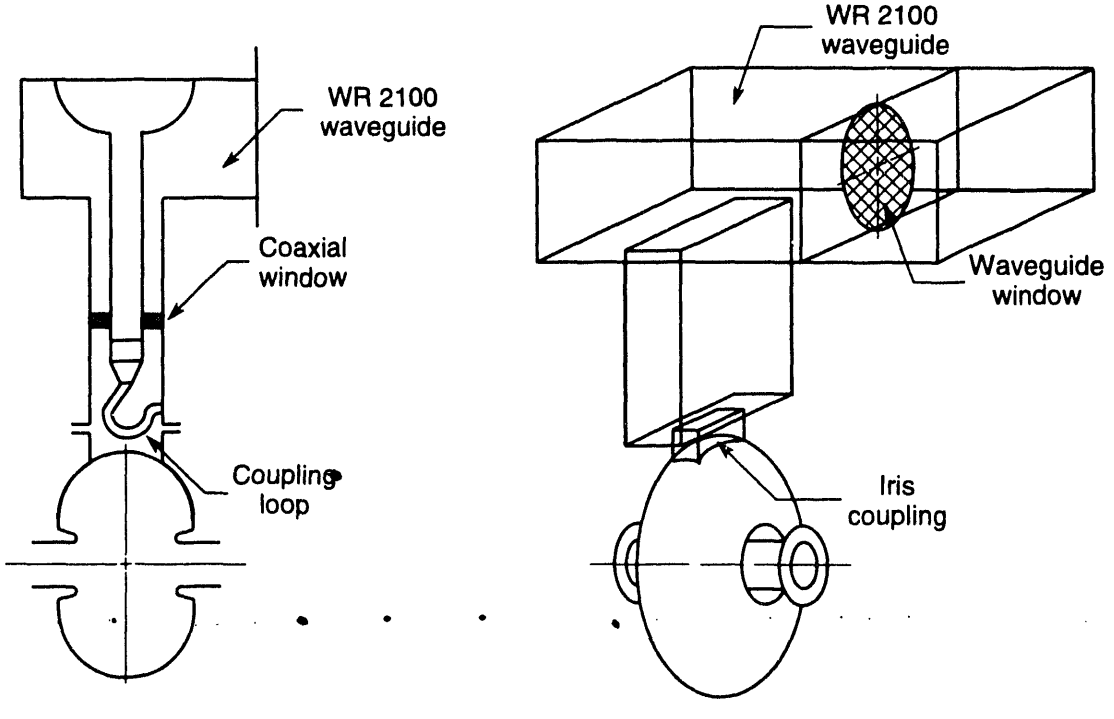

Fig. 5-104. Coaxial and waveguide coupling networks and windows.

The second coupling method utilizes iris coupling and a waveguide window (see Fig. 5-104). The coupling of a 5 × 20 cm iris, 10 cm deep, has been analyzed by calculating $Q_{external}$ via the Kroll-Yu method, using data from MAFIA calculations. The coupling factor can be varied between 3 and 10 by inserting quarter-wavelength transformers between the coupling iris and the waveguide (using exchangeable insert sections of waveguide). A commercial product, Helicoflex, was selected for use as a bakeable vacuum seal to join the waveguide coupling network. This product is used in large bakeable seals in industry, but it must be verified that it has the needed current-carrying capability to operate at a 500-kW input power level. Tests of this type seal using the existing 500-kW klystron are planned.

A vacuum pumping port to evacuate the cavity and window area will be provided at the input coupling network.

5.5.2.7 Cavity Window. The cavity window must transmit up to 500 kW of CW RF power to the cavity and must also handle considerable reflected power. Two configurations are being developed (see Fig. 5-104):

- *Coaxial window:* A coaxial ceramic disk window similar to the type used in commercial high-power klystrons is being developed at SLAC, both for the klystron and for possible use as a cavity window. It is being designed thermally to handle 2 MW of RF power. The peak electric field strength at the center conductor of this type of window is a comparatively high 2.4 kV/cm at 500 kW of transmitted power. As a result of this, the largest power dissipation in the ceramic also occurs close to the center conductor, where there is good thermal connection to the cooling channels. Mechanically, the coaxial window is a more complicated structure, compared with a waveguide window.
- *Ceramic disk in waveguide:* This approach inherently has a higher voltage due to the approximately 300 Ω characteristic impedance of a waveguide, compared with the 50 Ω impedance of a coaxial line. However, due to the larger dimension across the ceramic disk, its peak field is of the order of 1 kV/cm in the center. This lower peak field is an advantage over the coaxial approach, but this advantage is moderated by the fact that the loss occurs in the center of the disk, where the heat has to be removed through conduction in the ceramic and possibly air flow across one window face. Shielding of the window from ions produced by the beam can easily be accomplished by placing the window beyond a right-angle turn in the waveguide, away from the beam.

The window material choice for either style window is 99.5% pure alumina. This is the result of three requirements:

- low RF loss to minimize ΔT across the surface and internal stresses during operation
- availability of consistent processes in ceramic manufacture
- high-reliability joining technology for the window assembly

Most important for this window design is the ease of brazing, and 99.5% alumina has a long history of success in the microwave tube industry for joining to several different materials (copper, Kovar, and copper-nickel alloys). The sintering process for this alumina is optimized for consistency in shrinkage, and it can easily handle pieces twice as large as required for the PEP-II window design. Internal stresses will be minimized by the mechanical design of the window assembly; alumina is most attractive in this regard, too, because of its material strength. Windows of both designs, with power levels up to 1.2 MW, are being used in the klystron industry.

As far as reflected power is concerned, power levels up to 1 MW for few-μs time periods can be generated in the cavity under sudden beam-loss conditions. To avoid excessive stress on the window, it is placed a number of half-wavelengths away from the cavity detuned-short position. At these specific locations in the drive network, the field strength is closely tied to the field level in the cavity, which is stable unless driven hard. The window ceramic is most vulnerable to excessive fields, and in the proposed locations will always be exposed to field levels equivalent to 500 kW power flow into a matched load. One quarter-wavelength away, enormous field swings occur during fast turn-off of the RF or the beam.

Windows of each design will be tested. They will be run at a 500 kW power level into a load with two windows mounted back-to-back and an adjustable vacuum in between. By placing one window at a voltage-maximum point of a resonant line or in a resonant ring, higher field levels can be achieved and the windows thus tested to their breaking point. Extensive monitoring will be provided for these tests in the form of infrared detectors, arc detectors, etc.

5.5.3 RF Station

Each RF station consists of one klystron powering two cavities; a block diagram is shown in Fig. 5-105. A circulator is required to redirect reflected power coming toward the klystron and to guarantee stable klystron operation. Circulators with 1.2-MW CW power capability (both forward and reflected) have been produced in connection with 1.2-MW klystrons and are commercially available. A prototype has been ordered for evaluation and will be used in the high-power cavity tests. WR2100 waveguide was chosen because of its shorter delay for a given length, which benefits the feedback loops. After the circulator, the RF power is divided through a Magic Tee. Due to a deliberate path length difference of 90° in the arms to the two cavities, the reflected power from the cavities is directed towards the load of the Magic Tee; only imbalance power shows up at the load of the circulator. This shields the circulator from excessive overvoltages. Both circulator and Magic Tee loads are designed to handle 1.2 MW of CW power and 2 MW of peak power for short durations.

A 1.2-MW CW klystron is being developed jointly with an industrial partner under a Cooperative Research and Development Agreement (CRADA). The choice of parameters and the operating mode were guided by requirements of the feedback necessary to prevent coupled-bunch oscillations of the beam caused by the detuned fundamental resonance. The tube will have a 7-cavity design to give the large bandwidth and short group delay characteristics that are needed for the fast feedback stabilization. A

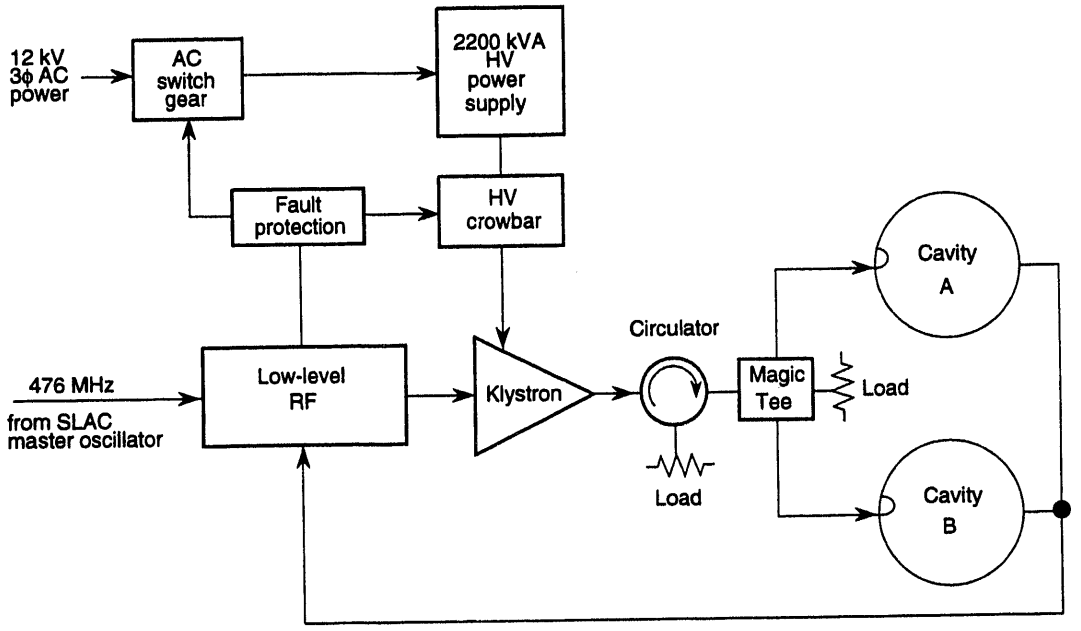

Fig. 5-105. Block diagram of a single PEP-II RF station.

multistage depressed-collector klystron is also being developed in parallel with the conventional-collector klystron. The depressed-collector klystron offers the potential advantage of much more efficient operation when running below saturation (as is required by feedback considerations). Klystron design parameters are summarized in Table 5-37.

Table 5-37. PEP-II klystron design parameters.

Operating frequency [MHz]	476
Output power at operating point [kW]	1100
Theoretical saturated output [kW]	1200
Beam voltage [kV]	83.5
Beam current [A]	24
Efficiency at operating point [%]	60
No. of cavities (incl. second harmonic)	7
Bandwidth at 1 dB [MHz]	8
Group delay [ns]	<100
Focusing magnetic field [G]	340
Type of output window	coaxial

With either collector, at least 10% overpower is required for amplitude modulation. Although a modulation anode design could be used on the conventional-collector klystron, we intend to use a conventional gun without a modulation anode to avoid the frequently observed instabilities associated with such electrodes. To protect the conventional collector from dissipating excessive power, the high voltage can be reduced through fast silicon-controlled rectifier (SCR) control on the power supply, and the associated large phase shift across the klystron can be compensated by a dedicated phase loop.

The high-voltage power supply for the conventional-collector klystron power supply will operate at 83.5 kV and 24 A. The supply is SCR regulated with inductive filtering in the primary to achieve a ripple of less than 1% at 720 Hz. A 1% high-voltage ripple causes 15° phase ripple in the klystron, which will be regulated out in a dedicated phase loop around the klystron. We intend to employ a novel scheme of filtering where no high currents from filtering capacitors have to be handled in the case of a high-voltage arc. With this approach, the high voltage can be shut down quickly with the primary SCRs and a relatively low-current SCR crowbar in the secondary. Such a power supply has been designed and a prototype will be built and evaluated on the 1.2-MW klystron test stand.

5.5.4 Low-Level Controls

The low-level RF system consists of a number of feedback loops, along with the usual controls, interlocks, and protection systems. The various low-level RF feedback loops are described functionally below and depicted schematically in Fig. 5-106.

Coupled-Bunch Mode Loops. Matching the klystron to the RF cavities, with their heavy beam loading, requires that the cavity be detuned to a frequency lower than its nominal operating frequency. This detuning is greatest in the LER, where the required frequency shift is more than one harmonic of the revolution frequency. Longitudinal coupled-bunch motions interacting with the real part of the detuned cavity impedance may either be damped or driven. Referring to Fig. 5-107, we illustrate how the effective impedance for each mode is calculated. At an upper synchrotron sideband, the impedance is driving; at a lower sideband, it is damping. Each mode appears at two sidebands, as labeled in Fig. 5-107. The difference between the driving and damping impedance for each mode, as given in Table 5-38, is the net stabilizing or destabilizing effect. We see that the unmodified cavity responses will strongly drive modes –1 and –2.

Using methods common in proton storage rings, a system composed of several loops working in concert has been shown by means of simulations to control the coupled-bunch modes driven by the fundamental cavity impedance. A baseband, time-domain simulation of the system, including nonlinear klystron saturation and beam-cavity effects, has been developed; Fig. 5-108 shows the elements of the simulation in block form.

Starting at the upper left, the voltage program provides the system with the RF reference, which tracks the transients in the cavity caused by the ion-clearing gap. This prevents the klystron from trying to correct for the change in cavity voltage and phase caused by the gap. This feature has worked well in simulation, keeping the klystron

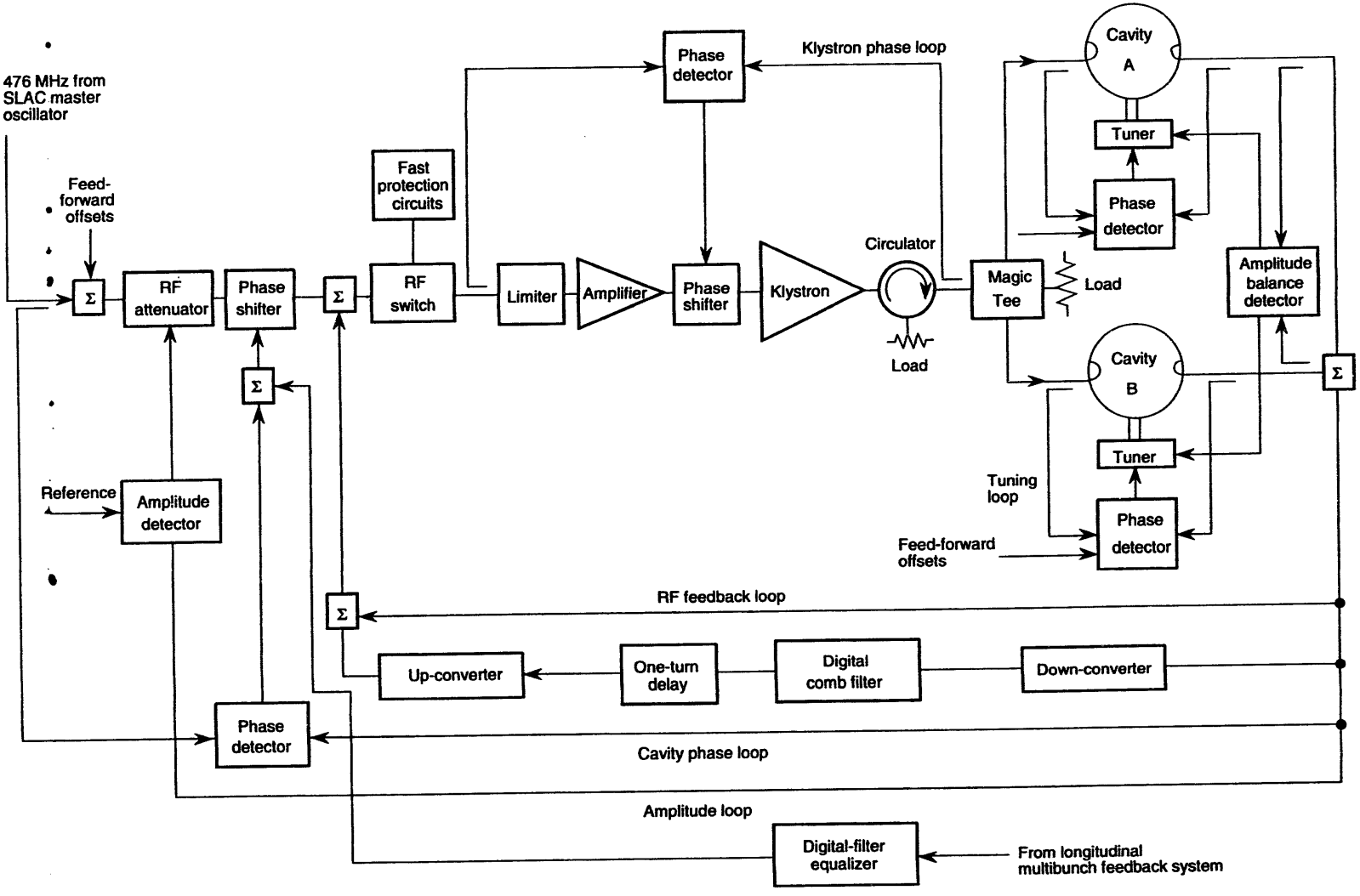

Fig. 5-106. Block diagram of the PEP-II low-level RF system.

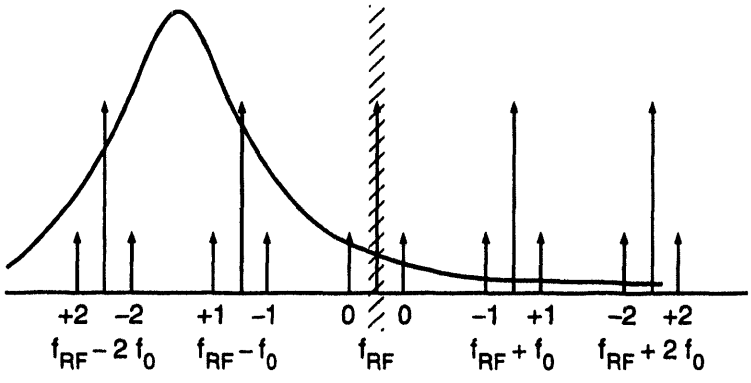

Fig. 5-107. Beam harmonics and cavity impedance.

power constant to within a few percent. To track changing ring conditions dynamically, the voltage program will be derived from an adaptive algorithm running on a digital signal processor (DSP).

The direct RF feedback loop vectorially subtracts a sample of the cavity voltage from the klystron drive, reducing the impedance seen by the beam. Unfortunately, while this loop reduces the magnitude of the driving impedance in the worst modes, it increases the impedance for some of the less strongly driven modes. (This undesired effect can be

Table 5-38. Coupled-bunch mode driving impedances.

Mode number	LER Re(Z) (kΩ)	HER Re(Z) (kΩ)
−5	5.7	1.6
−4	12.4	3.1
−3	36.3	7.4
−2	204.2	24.7
−1	178.7	151.7
0	−3.7	−42.3
1	−210.8	−122.4
2	−175.3	−21.3
3	−33.0	−6.7
4	−11.6	−2.9
5	−5.4	−1.5

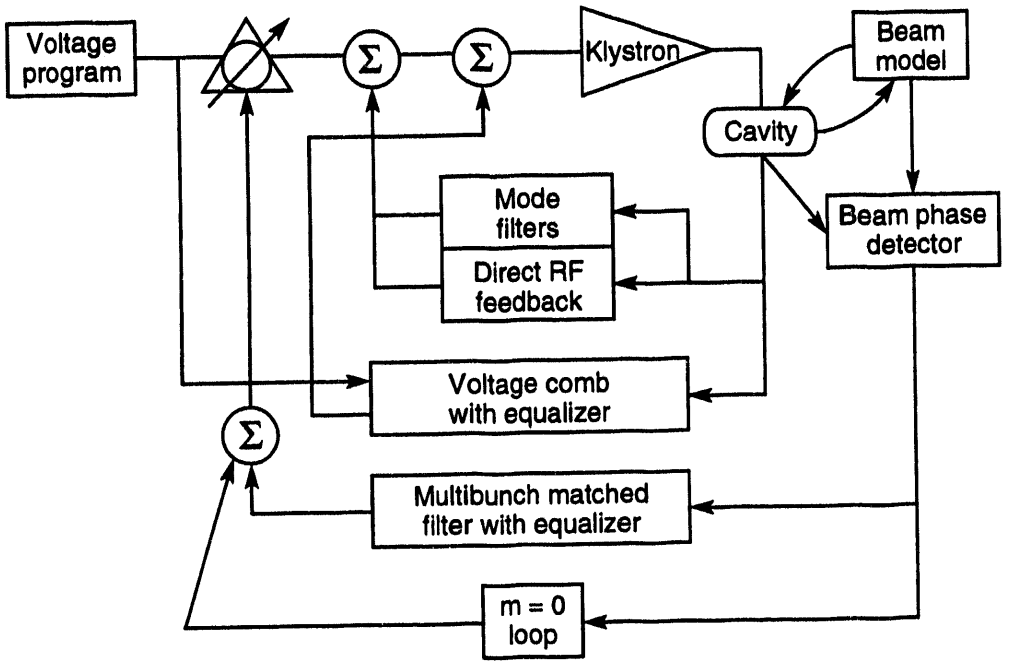

Fig. 5-108. Block diagram of RF feedback simulation.

reduced by minimizing the group delay around the loop, which is the basis for specifying a klystron with a low group delay.) This loop also helps to linearize the klystron-cavity response, benefiting the other feedback loops.

In parallel with the direct RF feedback loop is a narrow bandpass filter or mode filter. This class of filters is directed at upper synchrotron sidebands of the revolution harmonics, that is, at the sidebands responsible for driving the coupled-bunch oscillations. More gain may be applied here because the filter is narrow band, hence reducing the driving impedance more than the RF feedback loop alone. The present simulation uses only one modal filter, directed at the $m = -1$ mode.

The voltage loop that employs a comb filter avoids the problem of long group delay by taking a sample of the cavity voltage, filtering the data, then waiting until the next beam revolution before feeding the correction signal to the RF system. Because of the long delay needed, the filter in this loop is implemented digitally. The effect of the voltage-comb loop is to reduce the impedance seen by the beam at each of the synchrotron sidebands in the intermediate frequency (IF) bandwidth. The filter in the simulation uses a double-peaked response surrounding a notch at the revolution harmonic, as this allows greater loop gain. The first ± 10 revolution sidebands were handled by the comb-filter loop in the simulation.

As a comb-filter loop has a bandwidth of several MHz, it is necessary to correct for phase shifts through the klystron and cavity. A type of digital all-pass filter is used to add additional frequency-dependent group delay that wraps the phase back into the stable region. These filters can be implemented in several ways using DSP technology.

An important addition to the RF feedback system is the matched-filter loop. This loop is simply an extension of the broadband multibunch feedback system used to damp

all the other coupled-bunch modes. A sample of the wideband output from the multibunch system is low-pass filtered, phase equalized, and passed to the phase modulator in the klystron drive chain. By this means, the high-power RF system can be used as a very strong kicker for the multibunch feedback system. This augmented direct feedback of beam phase suppresses any mode growths driven by the net residual impedances of the RF cavity.

The last loop in the simulation is the $m = 0$ loop. This loop, which is a standard loop for many storage rings, measures beam phase, filters it, and phase-modulates the klystron. The simulation shows that this loop is not needed for stability, but it does improve the transient response of the $m = 0$ mode.

Tuning Loop. Two loops of this type, one per cavity, keep the cavities tuned by compensating for either detuning by the beam or temperature effects. Each loop measures phase across its cavity and moves the corresponding tuner. Bandwidth is limited by the stepping-motor response to 1 Hz.

Klystron Phase Loop. This is implemented to reduce the phase ripple of 15° introduced by the 1%, 720-Hz ripple on the klystron high-voltage power supply. Bandwidth of this loop can be as much as 10 kHz.

Cavity Phase Loop. This loop keeps the vector sum of the fields in the pair of cavities constant, compared with a reference signal (shifted by a station phase shifter) from the SLAC master oscillator. This will be a relatively slow loop, with a bandwidth of about 1 kHz, limited by the synchrotron frequency of the beam.

Cavity Amplitude Loop. In a similar fashion to the phase loop, the amplitude loop keeps the gap voltage constant by measuring the magnitude of the cavity field and comparing it to a reference voltage. The loop then adjusts a variable attenuator in the RF reference to the RF feedback loop to keep the gap voltage constant. Bandwidth of this loop will also be of the order of 1 kHz.

Cavity Balance Loop. In order to ensure that both cavities of one station contribute the same amount of power to the beam, a loop will be required to keep the field magnitude constant by differentially moving the tuners of both cavities.

If an RF station trips off, the circulating beam will induce a field in the cavities comparable to the normal operating field. This will not only produce similar wall losses in the cavities, it will also generate 1 MW of power traveling towards the Magic Tee to be absorbed by its load. In this case the beam will very likely become unstable (since the active feedback for this station is removed) and will have to be dumped. If the station cannot be brought back into operation, both cavities will be "parked" at ±340 kHz (±2.5 f_0) symmetrically around the operating frequency. This will reduce the beam-induced power to about 150 kW per cavity. A monitor will measure the beam-induced power and dump the beam should a potentially dangerous power level be reached in the idling cavities. (This could happen, for example, if, with klystron drive removed, a cavity were accidentally tuned to resonate at 476 MHz.)

Simulation Results. A simulation begins with an initial distribution of bunches whose centroids are not in their equilibrium positions and tracks their longitudinal position (measured in radians) as time progresses. The resulting time-domain history for each bunch is a damped harmonic oscillator, although some bunches retain some small oscillations. Results of a simulation run containing 60 current segments (macro-bunches) is shown in Fig. 5-109. Here a fast Fourier transform (FFT) of the bunch distribution around the ring was taken as a function of time to display the modal amplitudes. The first 100 turns are not displayed in order to show the final modal structure. The sense (±) of each mode is not distinguished here. The figure clearly shows that the ±10 modes that have feedback on them are successfully damped. The HOMs, which have only radiation damping, have some remaining amplitude present, but remain stable. The contrast between the modes handled by the feedback loops and the modes that are only radiation damped is dramatic and displays the effect of the feedback clearly.

With the simulation, we have demonstrated a successful feedback approach to the coupled-bunch mode problem caused by the fundamental cavity impedance. We plan to study other feedback topologies and simulate them as well. One possible alternative approach is based on digital modal filters. Figure 5-110 illustrates this concept. Here we mix each of the revolution harmonics requiring feedback down to IF. This may be a two-step process using analog mixing to IF, then digitally mixing to the revolution frequency. Next, the sideband associated with mode growth is bandpass filtered, mixed back up to 476 MHz, and vectorially subtracted from the klystron drive. This approach may be able to take advantage of the DSP modules developed for the multibunch feedback system (see Section 5.6) and would thus share the benefit of being programmable. Implementing

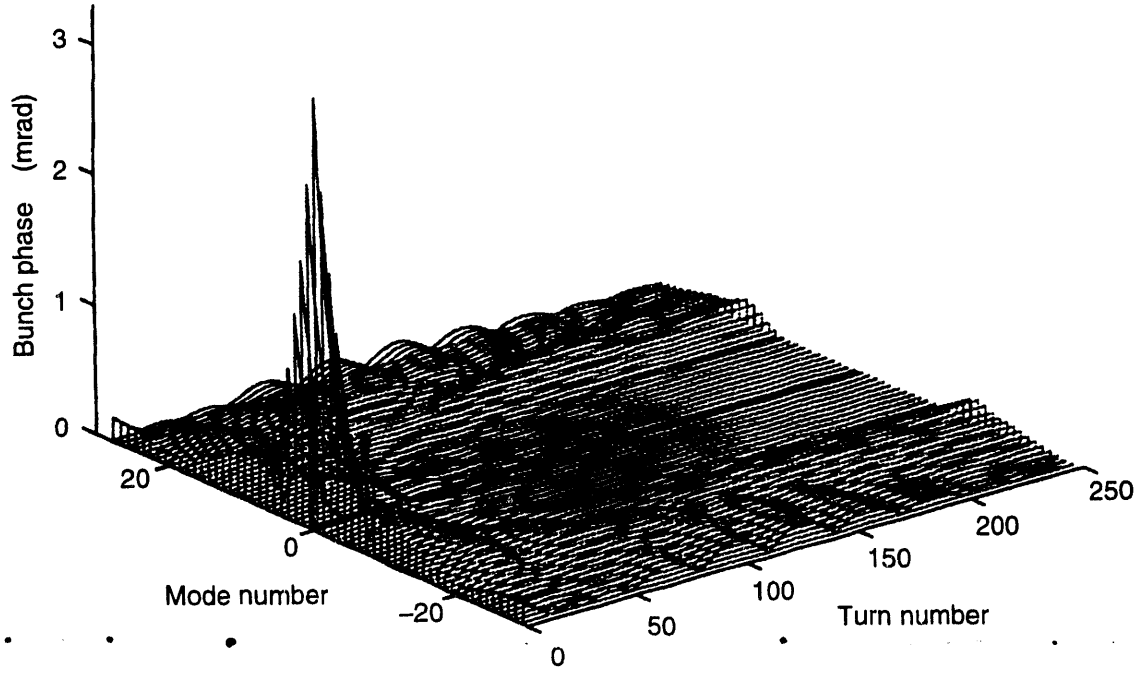

Fig. 5-109. Simulation result for 60 macro-bunches.

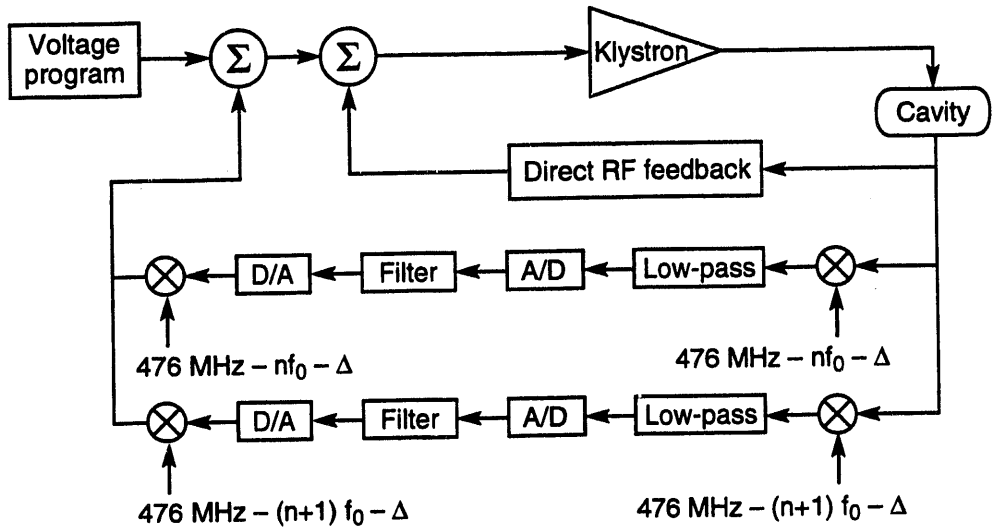

Fig. 5-110. Modal-filter approach to eliminate low-order coupled-bunch instabilities.

this approach with digital filters would allow incorporating features such as linear phase and adjustable phase shift (with no equalizers necessary). Other approaches will also be evaluated.

Hardware testing of the RF feedback loops is planned. These tests will use the existing 500-kW, 476-MHz klystron, the low-power test cavity, and the feedback electronics. Impedance-reduction techniques will be evaluated at each of the sideband frequencies, using a network analyzer; nonlinear effects of klystron saturation can also be evaluated.

5.5.5 General Layout

There are three RF buildings available at the PEP site, located in regions 4, 8, and 12 (Fig. 5-111). Each building can accommodate up to six RF stations, for a total of 18. For the initial operation of PEP-II, fifteen stations will be installed, five LER stations in region 4 and five HER stations each in regions 8 and 12. The RF building layout shown in Fig. 5-112 indicates how the klystrons, circulators, and control racks could be arranged. A profile view of an RF building and a section of the tunnel are shown in Fig. 5-113.

5.5.6 Design Margin and Expandability

RF parameters have been chosen to allow operation under normal conditions with some safety margin in power. This margin accommodates the possible operation of the machine with one station off in each ring. The only critical parameter reached would be a wall-power level of 150 kW in the remaining HER cavities.

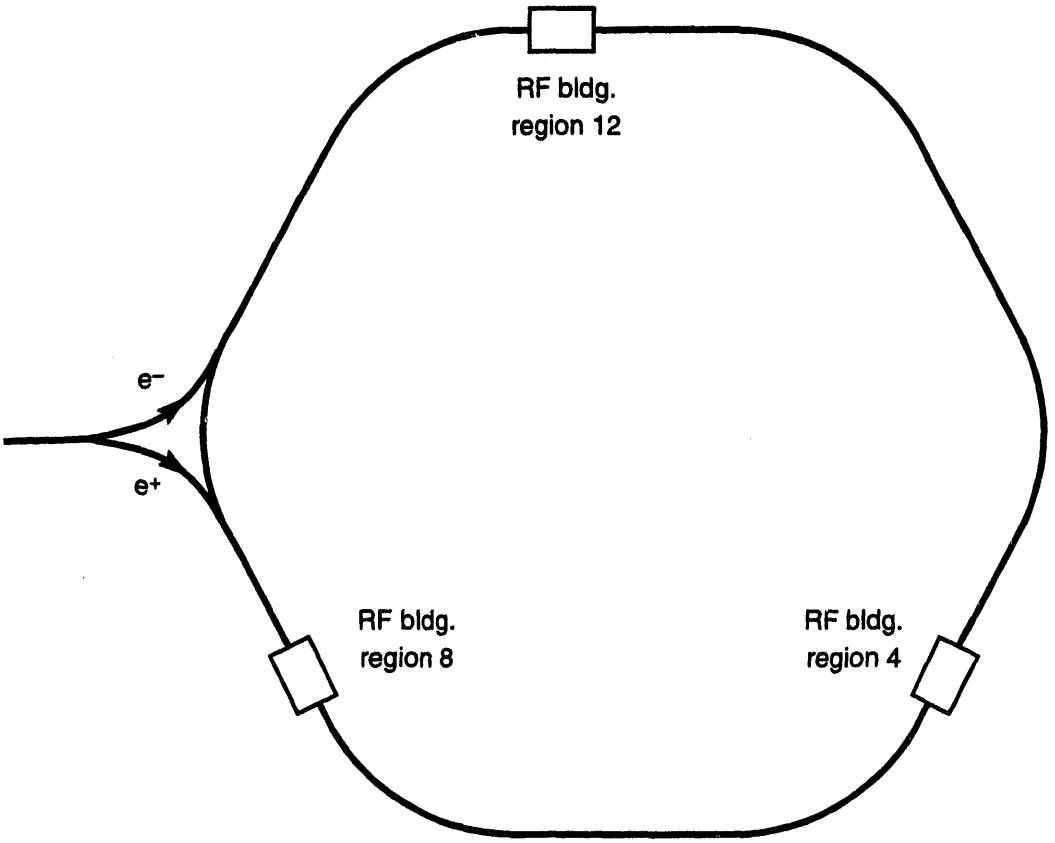

Fig 5-111. Layout of PEP-II, showing the locations of RF buildings.

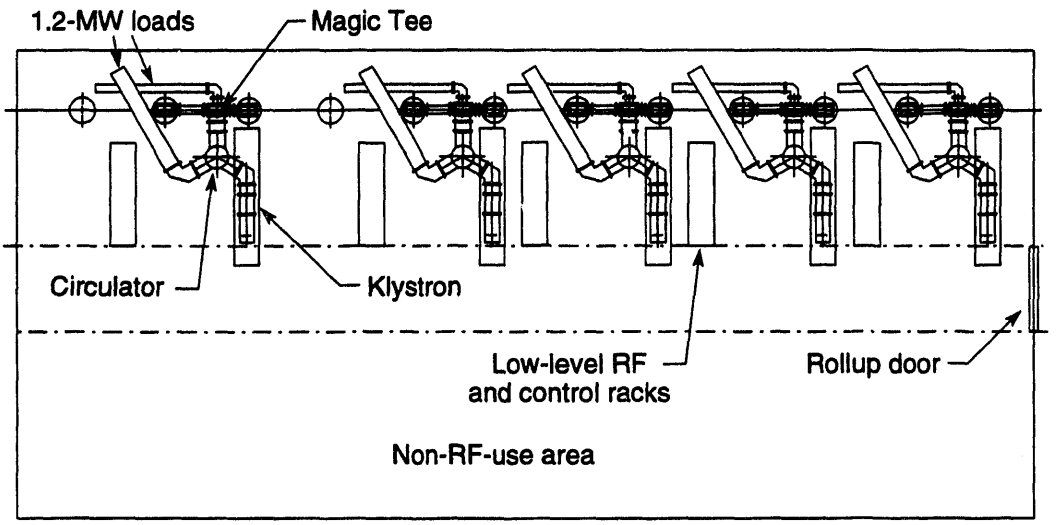

Fig. 5-112. Plan view of an existing RF building, showing the arrangement of five RF stations.

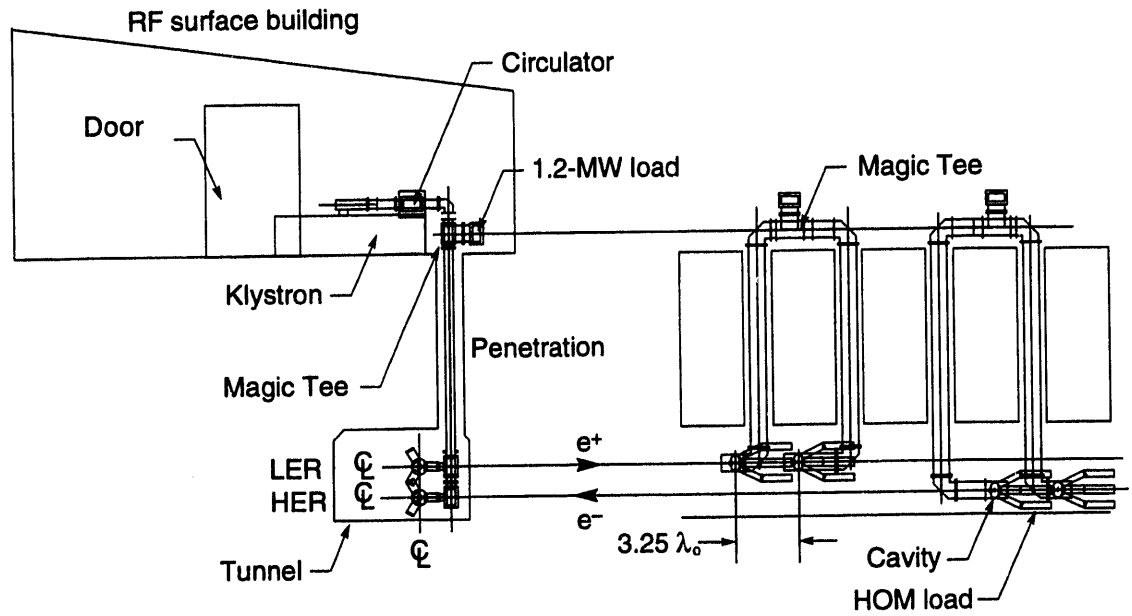

Fig. 5-113. Cross-sectional view showing an RF station and a section of the PEP tunnel. For purposes of illustration, we show both HER and LER cavities in the same straight section. In reality the LER and HER will be fed from different regions.

If the PEP-II current were increased to 3 A in each ring, three additional RF stations would be required for the HER; the number of cavities would increase to 26 in the HER and remain the same in the LER. The coupling factor for each cavity would have to be increased to 9.3, because more power must be delivered to the beam. The existing surface building could accommodate the three additional RF stations.

5.5.7 Summary

Considerable effort has gone into the choice and design of the PEP-II cavities. A cavity shape with nose cones provides a maximum shunt impedance at the cavity fundamental mode, while HOMs are heavily damped by three HOM-loading waveguides. The design specification of 150 kW of wall dissipation requires a careful design of the cavity cooling. A drive network with a window capable of delivering 500 kW of RF power to the cavity must also be developed. We believe the proposed designs to be within the realm of present-day technology, but further simulations, as well as actual tests under full power, will be conducted to verify their performance.

We chose an RF system design that uses two single-cell cavities for each 1.1-MW klystron. This combination can provide the required gap voltage and deliver the needed power to the beam using a relatively small number of cavities (20 in the HER and 10 in the LER).

The low-level RF controls provide matching of gap transients between the two rings and damping of beam-induced instabilities with direct RF feedback loops to reduce the effective impedance of the fundamental mode. The system has been simulated and shown to be stable.

The planned RF system for PEP-II has the advantage of being able to use existing conventional facilities and can be implemented without any structural changes. Furthermore, all components of the system can be used in a future upgrade to a 3-A machine with minor adjustments and the addition of a small number of RF stations.

5.6 FEEDBACK SYSTEMS

As pointed out in the discussion of beam instabilities (see Section 4.3), the high beam currents in the PEP-II rings can provide strong excitation of any resonator to which they can couple. The voltages that arise drive coupled-bunch instabilities, and active feedback systems are required to prevent the growth of longitudinal and transverse bunch oscillations. In practice, it is the high-Q resonators associated with the parasitic higher-order modes (HOMs) of the RF cavities that are the main culprits, hence the considerable effort to damp these modes, as described in Section 5.5.

To control the oscillations, the corrective kicks that the feedback system applies to the bunches must be at least as large as the induced resonator voltages minus the effective "voltage" due to the radiation damping. Because the induced voltages are proportional to the shunt impedances of the resonators, the technique of passive damping of HOMs in the RF cavities greatly reduces the feedback voltages required. On the other hand, a single HOM that has been broadened in frequency by damping can potentially cause instability in perhaps 100 coupled-bunch modes of the beam. Therefore, one expects many beam modes to require feedback stabilization.

In most operating accelerator rings, coupled-bunch damping has been applied selectively to the few observed unstable modes. The traditional method has been to extract the beam signal and feed it back at these few unstable mode frequencies. For PEP-II, damping must be provided to suppress many modes, and the systems must be designed in advance, before details of the particular modes that are unstable are known. For both these reasons, we have decided to damp bunch motions with systems that feed the signals detected from each oscillating bunch back to that same bunch. Such *bunch-by-bunch* feedback has the additional advantages of suppressing other disturbances, such as motions driven by the beam-beam interaction, and it is very effective in damping transients introduced by the injection of a small fraction of the stored beam. Systems of this type are now operating at PETRA [Heins et al., 1989].

Although we must deal with a relatively short bunch spacing of 4.2 ns, the electronics required for the prompt processing of such signals is now available. It is worth commenting that, for many-mode operation, the bandwidth required in the power amplifier and kicker would be the same for either mode-filtered or bunch-by-bunch feedback. Note that while the overall response must cover a band 119 MHz wide, the bandwidth requirements on individual components are greater. The nominal bunch spacing of 4.2 ns must be shared by kicker fill time, kicker transit time, and amplifier rise

time. This calls for a power-amplifier bandwidth of 350 MHz, which makes the power capability costly and emphasizes the importance of an efficient kicker design.

While instabilities driven by HOMs of the cavities are to be controlled by the bunch-by-bunch feedback, the unmodified response of the principal accelerating resonance (at 476 MHz) could drive some longitudinal coupled-bunch modes more strongly than the damping ability of the coupled-bunch feedback. There are three such modes in the HER and five in the LER. To reduce these driving impedances, local feedback loops around the cavity-klystron systems will be incorporated in the RF low-level controls (see Section 5.5.4). Where residual coupled-bunch driving impedances are still large, the RF cavities can be used in this narrow frequency range as strong supplemental "kickers" for coupled-bunch feedback.

5.6.1 Longitudinal Damping

The damping applied by the bunch-by-bunch feedback must be capable of opposing the shunt impedance of the strongest cavity HOM, at 750 MHz. As noted in Section 5.5, strong reduction of the Q of this HOM by passive damping has already been demonstrated. Although we have observed a reduction to $Q = 28$, we have specified a more conservative value of $Q = 70$ for the feedback system design described here. The various parameters that define the task of the longitudinal feedback system are given in Table 5-39 for both rings. In what follows, the HER will be used to illustrate the feedback system design and expected performance; extension of the design to the LER is straightforward.

Table 5-39. Parameters used for feedback system design.

	HER	LER
Average current, I_0 [A]	1.0	2.14
Number of cavities	20	10
Strongest HOM frequency [MHz]	750	
R/Q per cavity [Ω]	43	
Q	70	
Maximum mode amplitude [ps/rad]	10/0.03	
Injection scheme	1/5 bunch at 60 pps	
Assumed injection errors [$(\delta E/E)$/ps]	0.002/100	

The required system gain and kick amplitude are determined by the excitation of the strongest longitudinal resonance, a mode near 750 MHz having phase amplitude $\Delta\phi_0 = 0.03$ rad (at the RF frequency of 476 MHz). For short bunches this voltage is

$$V = j\, I_0\, R_s\, \frac{\omega_{\text{res}}}{\omega_{\text{RF}}}\, \Delta\phi_0 \tag{5-39}$$

where $R_s = 20\ (R/Q)Q = (20)\ (43)\ (70) = 60\ \text{k}\Omega$ for the HER. From Eq. 5-39 and the parameters of Table 5-39, we find that the damping voltage must be at least 2.8 kV/turn. Although radiation damping will provide about one-third of the required damping, we ignored this contribution in our design. That is, the contribution from radiation damping is considered a safety factor, and we have designed the feedback kickers to be capable of 3 kV/turn in the HER (and the same in the LER).

Errors in the energy and/or timing of the injected beam will combine to produce a phase error that is about 14 times as large as the 0.03-rad excitation considered from the 750-MHz HOM. However, the small quantity of charge injected with this large deviation can excite the resonators to less than 3 kV. Therefore, if the low-level circuits of the feedback system are designed to limit the kicker output to 3 kV in response to phase excursions greater than 0.03 rad, transients and growth at injection will still be controlled. This action is clearly illustrated by our numerical simulations, shown later in this section.

5.6.1.1 RF Feedback. For PEP-II, the usual practice of detuning the frequency of the cavity accelerating mode to compensate beam loading stabilizes the coupled-bunch mode $m = 0$ (Robinson damping), but leads to difficulties. This is because the detuning must be quite large to account for the beam loading, with the result that the detuned fundamental mode drives bunch modes $m = -1, -2$, etc., more strongly than can be counteracted by the damping provided by the bunch-by-bunch feedback system. To deal with this, these few particular modes will be damped by signals at the appropriate mode frequencies that are extracted from the detected beam phase signals and fed back through the RF amplifiers and cavities. To ensure that these mode can be damped in this manner, narrow-band active damping circuits around the cavities and drivers will be used to suppress the shunt impedance at the mode frequencies near 476 MHz. As described in Section 5.5.4, this suppression, combined with the amplified phase signals, will stabilize the coupled-bunch motions.

5.6.1.2 System Overview and Principle of Operation. The bunch-by-bunch feedback system will measure the instantaneous phase of each bunch with respect to the ring master oscillator and provide a correction voltage for each bunch via a kicker structure. The large number of bunches (1658) and the interbunch time interval of only 4.2 ns require a wideband processing system, with the front-end and power-amplifier stages operating at a 238-MHz clock rate. The processing of the phase information from each bunch can be performed at a lower rate. Our feedback system design therefore employs common wideband front-end and power-amplifier stages, with many processor channels operating in parallel, at a slower rate, to generate the correction signal for each bunch.

We decided upon a digital signal-processing approach to convert the bunch-phase information into a correction signal. This digital-filter approach permits the use of a

matched-filter feedback algorithm and takes advantage of recent commercial activity in the digital signal processing (DSP) field. The programmable nature of this scheme provides flexibility and allows us to implement compactly a nonlinear (soft-limiting) feedback system. It is also possible to program several operating modes into such a system—for example, to distinguish injected bunches from stored bunches, should this be necessary or desirable.

There are two possible approaches to the measurement of longitudinal motion: (i) direct measurement of the phase of each bunch and (ii) measurement of the transverse displacement of each bunch in a region of the storage ring with nonzero dispersion. The second approach requires signal processing to separate the betatron motion from the transverse displacement due to longitudinal motion, and can give problems with synchro-betatron coupling. Furthermore, this approach does not relax any of the timing or bandwidth constraints compared with a phase-measurement-based system. Therefore, we selected the direct phase-measurement approach for our design, which means that the phase of each bunch is our control variable.

5.6.1.3 System Design. Figure 5-114 presents a block diagram of the PEP-II longitudinal feedback system, showing its essential elements. The bunch phase signal is derived from a beam pickup structure, which generates a short coherent tone burst for each bunch passage. The phase of this burst is compared with a master oscillator synchronized to the ring RF system, and the phase-error signal is digitized at the bunch

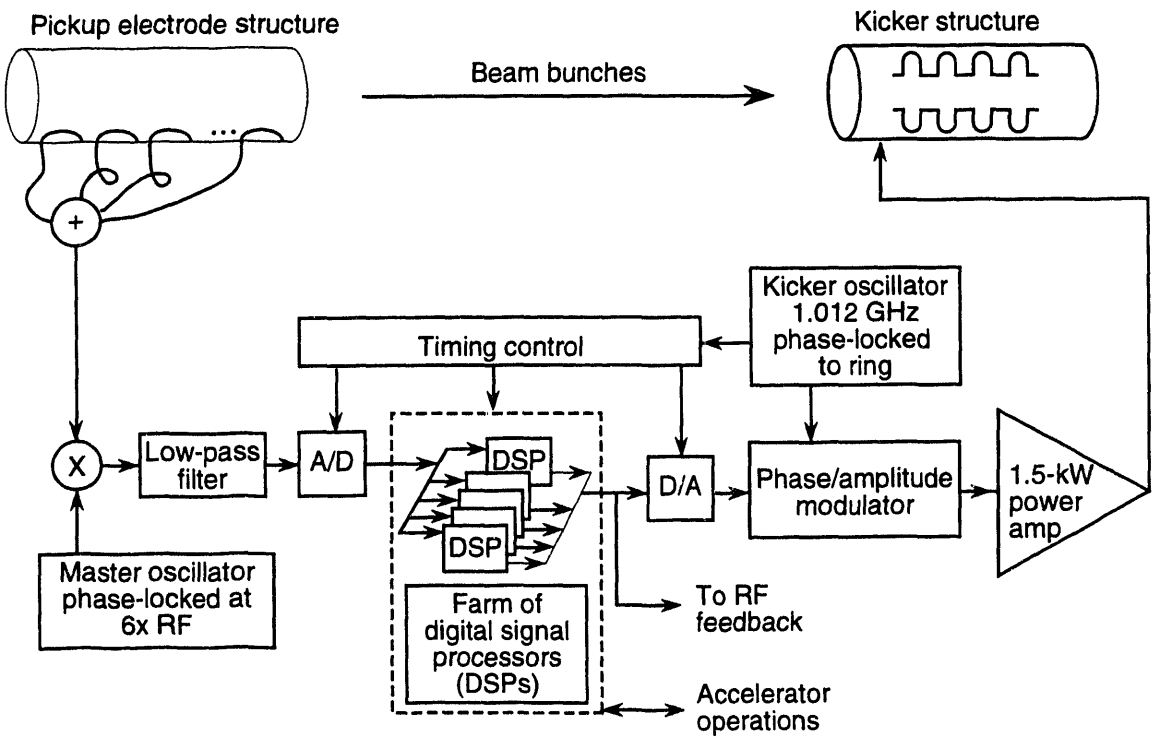

Fig. 5-114. Block diagram of the PEP-II longitudinal feedback system.

crossing rate. Digital processing of the phase-error signals is performed in an array of microprocessors (the DSP farm). This approach allows parallel processing of the phase-error signals and thus reduces the processing rate needed in each DSP block. The computed correction signals are recombined into a wideband correction signal and converted back to analog form. Finally, the feedback loop is closed via a power amplifier and a kicker structure that applies the correction voltage to each bunch. The constituents of the various functional units in Fig. 5-114 are described below.

Beam Pickup. The beam pickup generates a short (less than 4-ns) tone burst at the sixth-harmonic of the ring RF (that is, at 2856 MHz). We use a periodic coupler structure that generates a burst, rather than a tuned resonant structure, to avoid coupling between adjacent bunches. The burst of RF carrying the signature of the arrival time of the bunch can be generated in several different ways, using stripline pickups, power dividers and combiners, or delay lines. To simulate such a burst in the laboratory, we have performed measurements in which a narrow pulse is launched into a transmission line, coupled to an array of directional couplers evenly distributed along it, with all the coupler outputs added with a power combiner. As an alternative approach, we have also built another passive structure with periodically coupled microstrips. The advantage of this latter approach is that it minimizes the number of RF connections, and, for the case of a beam-coupled structure, it would also minimize the number of vacuum feedthroughs.

Figure 5-115a shows a stripline-type comb generator circuit. This periodic coupler is designed to generate a tone burst from a BPM electrode. The measured response of the comb generator is shown in Fig. 5-115b.

Phase Detector. Phase detection is implemented in a double-balanced mixer. A master oscillator, phase-locked to the ring RF, generates a stable 2856-MHz signal for the phase reference. A filter on the output of the mixer eliminates the 2ω term and limits the bandwidth of the signal for noise reduction.

The choice of a 2856-MHz operating frequency is a tradeoff between sensitivity and dynamic range. It allows a phase-processing range of $\pm 15°$ at the 476-MHz frequency of the RF system, with a phase measurement resolution of better than 0.5°. This value is adequate for the linear damping range of the system, but it is important that the phase detector limit smoothly for excursions greater than $\pm 15°$, because such a condition is likely at injection. Another attribute required in this block is an automatic gain control (AGC) loop to allow the system to operate over a wide range of beam currents. This loop will control an attenuator between the beam pickup and subsequent processing electronics.

Phase Digitizer. The digitizer converts the phase-error signal from the mixer into an 8-bit signal. It operates at the 238-MHz beam crossing rate and provides a unique measurement at each bunch crossing. Components are available commercially to implement this digitizer.

DSP Farm. The DSP farm includes fast digital functions to convert the sequential 238-MHz data stream into several slower parallel streams. An array of commercial

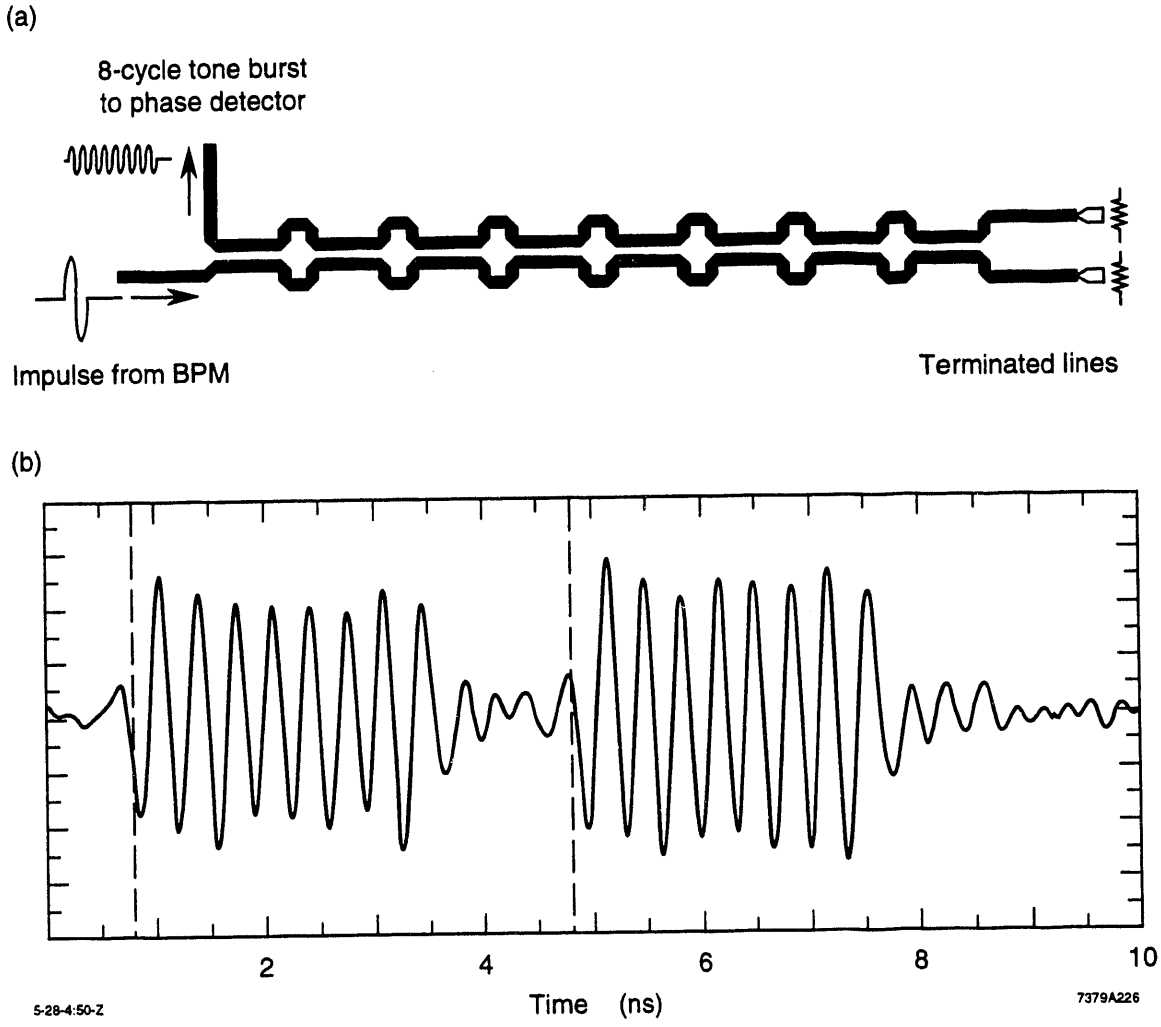

Fig. 5-115. (a) Eight-tap stripline comb generator circuit. (b) Measured time response of the comb generator for two simulated beam signals with 4.2-ns spacing.

digital signal processors accepts the digitized phase-error signals and produces an error-correction signal for each bunch. These processors (which are all identical and execute identical programs) treat each bunch as an individual oscillator and combine information from several sequential passages of a particular bunch to compute a correction signal to be applied to that bunch on subsequent turns.

The feedback algorithm selected is a finite-impulse-response (FIR) filter matched to the nominal synchrotron oscillation frequency. This filter generates the required 90° phase shift and also provides noise reduction (processing gain) on the raw error signals. In addition, the feedback filter algorithm incorporates the limiting functions and the special out-of-range condition handling mentioned earlier.

The front-end digitizer (A/D) produces a new sample from each bunch every 4.2 ns, and the kicker requires a correction signal at the same 4.2-ns interval. However, it is

possible to process the bunch error information at a rate slower than the 136-kHz revolution frequency, as the fundamental synchrotron frequencies in the PEP-II rings are only about 5–7 kHz, requiring roughly 20 orbit revolutions for a bunch to complete a single synchrotron oscillation. The continuous synchrotron oscillation can be reconstructed from as few as two samples per synchrotron period (Nyquist-limited sampling) as long as the original signal is bandwidth limited. It is the function of the feedback filter to reconstruct a correction sinusoid of the right amplitude, frequency, and phase from the input samples.

We have designed the DSP farm to operate as a down-sampled system in which the beam pickup information is used to compute a new correction signal for a particular bunch only every n turns (that is, n is the down-sampling factor). A digital hold-buffer memory is provided to hold a correction signal, for each bunch, for n turns. After n turns, the DSP farm computes a new kick value for each bunch. Note that in this architecture the kicker is still used efficiently, as it changes the energy of each bunch on *every* turn.

Figure 5-116 shows the essential components of the digital signal processing. The synchronous timing is used by the down-sampler to determine whether the data sample presented by the A/D will be passed to the digital farm and whether a calculated result will be read from the farm and placed into the hold buffer. The hold buffer is a dual-port memory that allows the held values to be read and presented to the D/A stage in synchronism with the bunches at the 238-MHz bunch repetition rate.

The architecture we have chosen is shown in Fig. 5-117. We have elected to package the phase detector, A/D, down-sampler and hold buffer, D/A, and amplitude modulator in a VXI mainframe, which offers good electromagnetic shielding, cooling, and system power. The VXI crate also has power for emitter-coupled logic (ECL) circuitry, and its 1.2-in. board spacing permits large analog components. With this choice, it is (conceptually) possible to package the front- and back-end processing for both rings in the same mainframe.

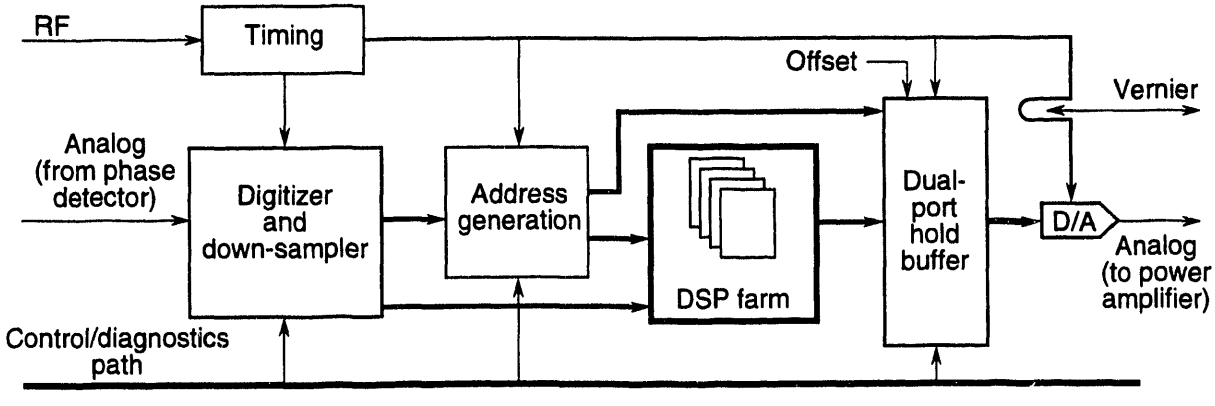

Fig. 5-116. Block diagram of the digital signal processing in the longitudinal feedback system.

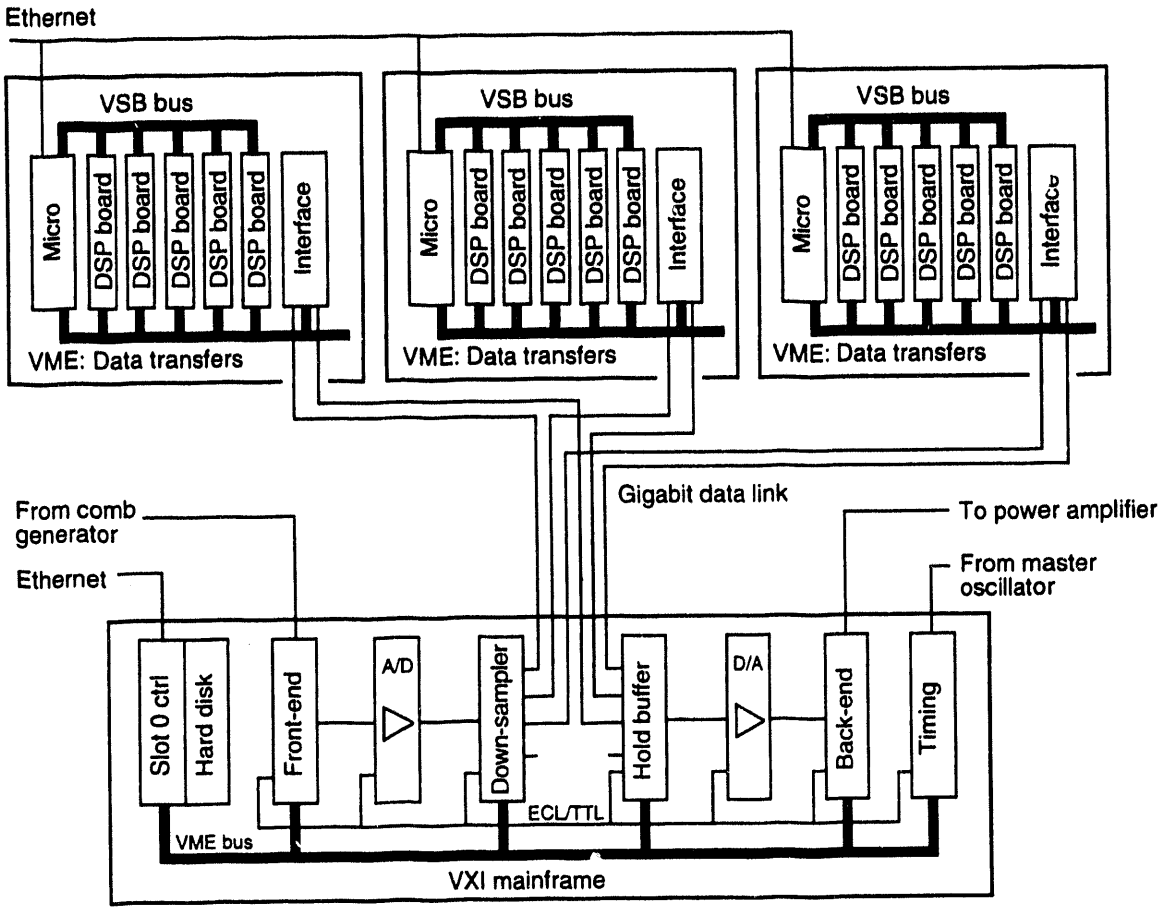

Fig. 5-117. Block diagram of the longitudinal feedback system architecture.

A DSP module in this design is structured as a four-processor VME board, as shown in Fig. 5-118. The VME bus, which has a computer architecture with 32-bit data and 24-bit-wide address buses, is well matched to the 8-bit-wide bunch and kicker data of our application. Therefore, each DSP on a board will treat the data for a subset of four consecutive bunches.

As will be demonstrated by the simulation results presented below, we have optimized the design for a down-sampling factor of $n = 4$, and thus an aggregate instruction rate of about 1×10^9 instruction cycles per second is required (including filter overhead). Such a computation rate can be obtained from roughly 60 DSPs having 25-ns instruction cycle time. Commercial processors from AT&T, Motorola, and Analog Devices are available; for PEP-II we chose the AT&T DSP1610 because of its speed, architecture, and ease of interfacing.

Digital processing for a 1658-bunch longitudinal feedback system requires 15 to 20 DSP modules. To avoid running at the bandwidth limit of the VME bus, only five DSP boards are plugged into a VME backplane. We envision two backplanes per VME chassis, so the longitudinal feedback for both rings can be packaged in four or five air-cooled chassis.

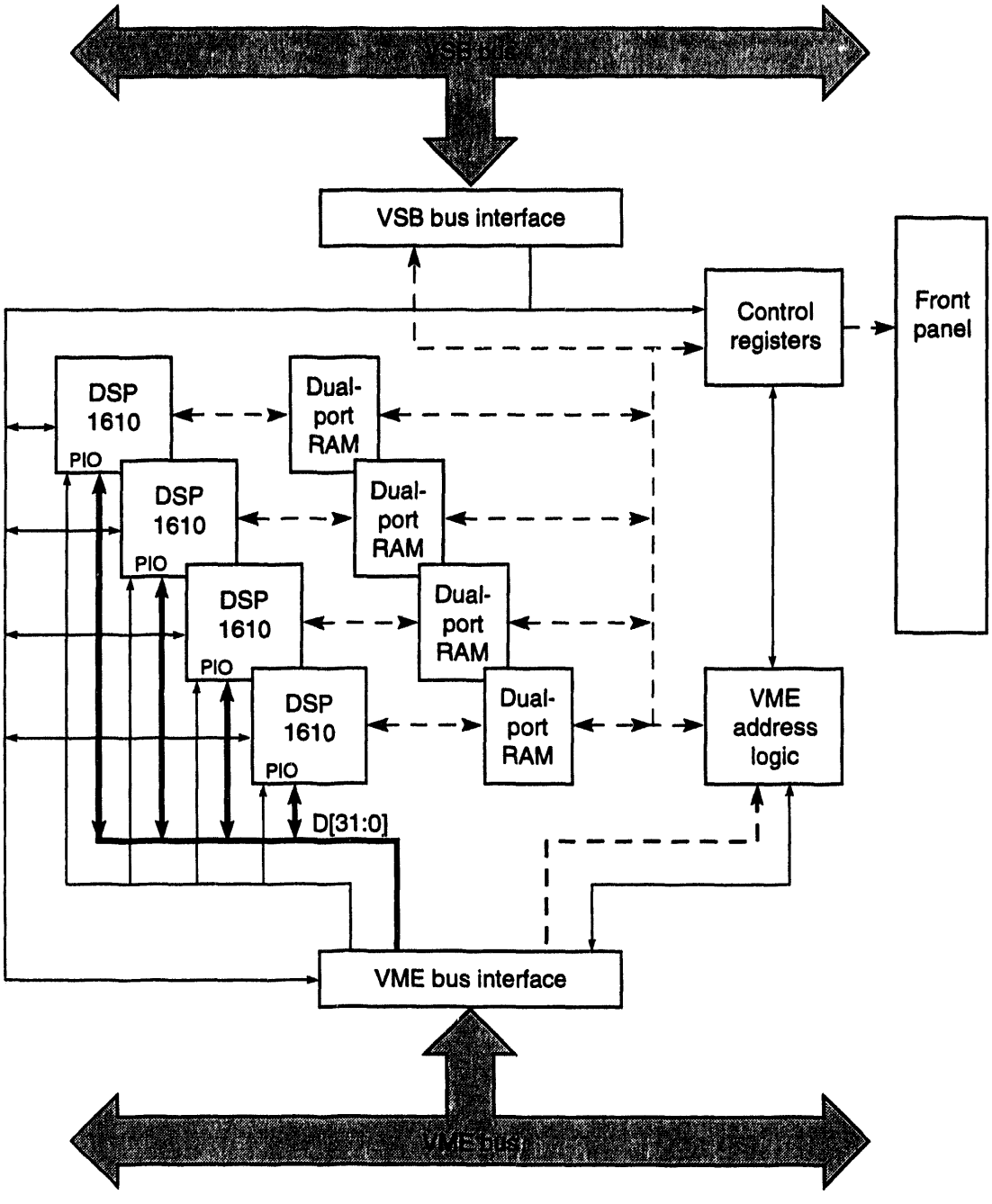

Fig. 5-118. Block diagram of a DSP module. The dashed lines indicate control paths and the solid lines data paths.

Loading code and coefficients into the DSPs, as well as system control and monitoring, can be performed at a low data rate of a few kHz over the VME subsystem bus, VSB. A master controller located in the VXI chassis communicates with local embedded VME/VSB microcomputers via Ethernet. Several high-performance real-time operating systems are currently available for this type of application, such as VxWorks from Wind River Systems. Such an operating system offers a development environment

for real-time applications, including a run-time system, testing and debugging facilities, and a UNIX cross-development package with networking facilities.

Because our design takes advantage of commercially available hardware and software, we expect that it will be a solid system that will be easy to bring up.

Output D/A and Modulator. This block converts (at a 238-MHz rate) the correction signal stream from the output multiplexer into an analog signal suitable for driving subsequent stages. The D/A is an 8-bit device.

Power Amplifier. The longitudinal feedback system uses commercial RF power amplifiers and modulators to provide the signal for the output kickers. The operating frequency is 1.012 GHz at a power level of 2.0 kW. The power amplifiers will be configured in a modular fashion. This allows a soft-failure mode, that is, operation at reduced power levels, should components fail.

Beam Kicker. The beam kicker converts the output signal from the power amplifier into a longitudinal E field to correct the energy of each bunch. A periodic coupler provides the bandwidth required to prevent bunch-to-bunch coupling, along with a small voltage gain. To reduce the broadband power required, three separate kickers are used in the HER to deliver the 3-kV (maximum) acceleration to the bunches. As illustrated in Fig. 5-119, each kicker consists of an array of four quarter-wavelength drift tubes, joined in series by half-wavelength delay lines (at the operating frequency of 1.012 GHz). The kicker is constructed as a transmission line (with a characteristic impedance of 25 Ω) made up of several segments in series and parallel. The transmission line is divided into two 50-Ω lines at the ends; these connect through vacuum feedthroughs to the driver at the downstream end and terminating loads upstream. Transitions between the drift tubes and the delay lines between them must be well matched to avoid reflections that will introduce losses and spurious responses. Initial modeling of series-electrode structures has verified the expected bandwidth; evaluation of the strength and some details of the response is under way.

Each kicker presents to the beam an impedance band that is about 250 MHz wide, with a maximum value of 400 Ω. Such an impedance is too broadband to drive coupled-bunch instabilities and contributes negligibly to the broadband impedance of the ring as well. The power this impedance extracts from the beam, about 800 W in the HER and 3 kW in the LER, is dissipated in the terminating loads.

To deliver a different voltage to each passing bunch, the allowed kicker length is limited by the combination of its filling time, the transit time of the passing bunch, and the rise time of the driving amplifier. The characteristics for each four-element kicker unit are summarized in Table 5-40. There are three of these kickers in each ring.

The 0.5-kW power amplifier required at the 1.012-GHz operating frequency is available from several commercial vendors. These solid-state amplifiers are modular and typically include low-level drive electronics and power supplies.

Digital Filter Algorithm. The proposed longitudinal feedback design is based on a general-purpose programmable system that uses a digital FIR filter to compute the

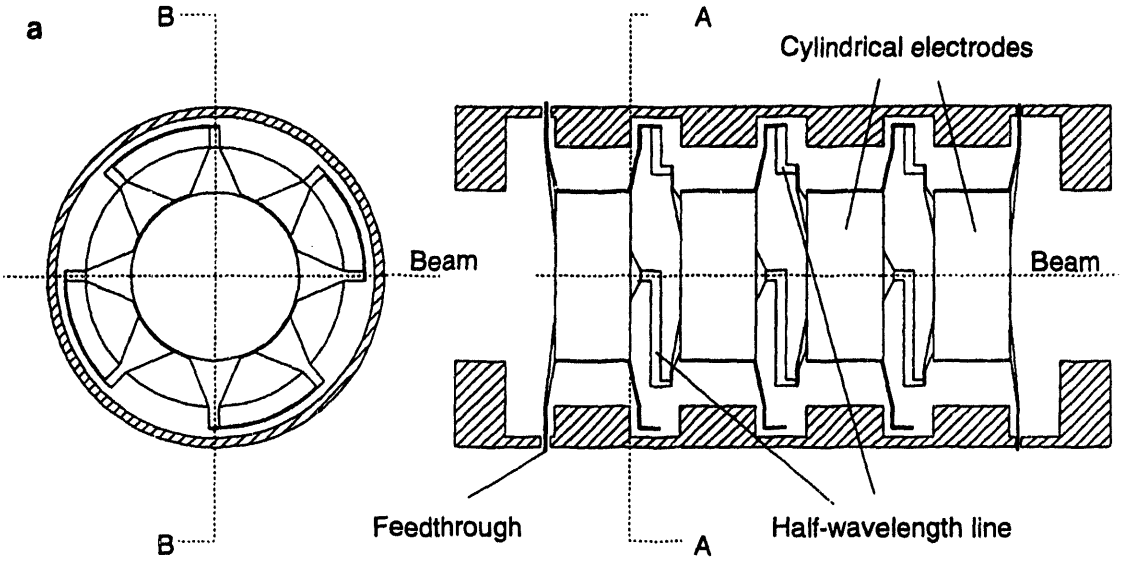

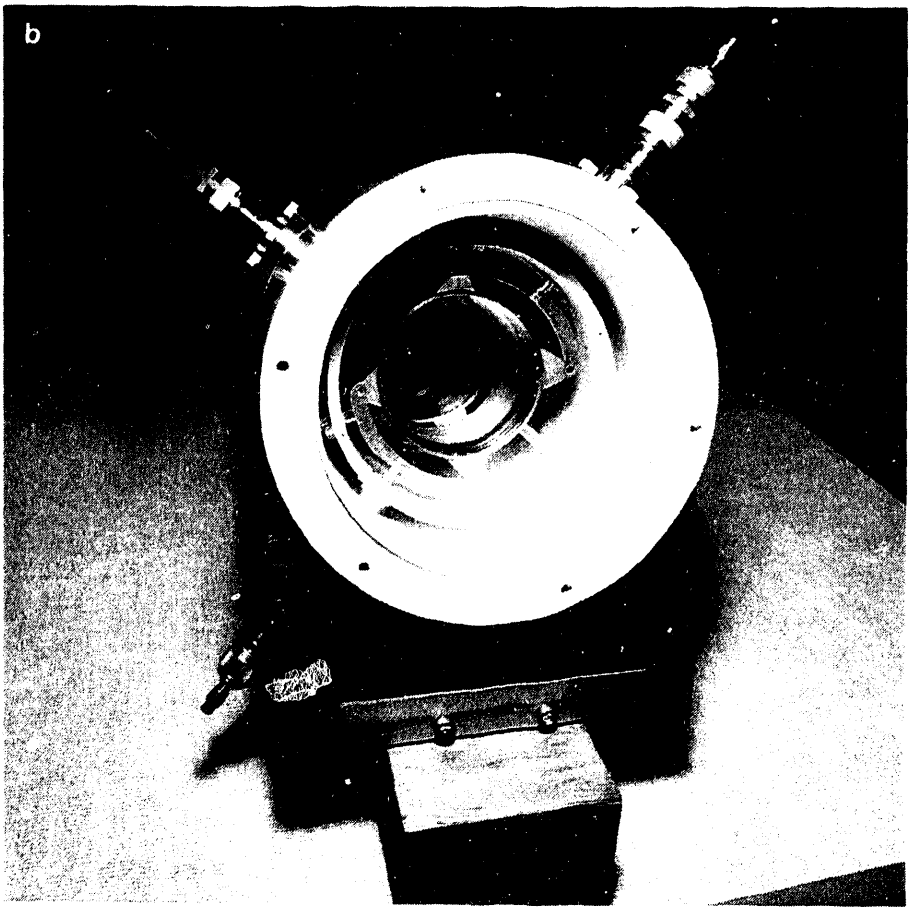

Fig. 5-119. (a) Beam kicker for longitudinal feedback. (b) End view into a series-electrode kicker used in the ALS at LBL. This device is a prototype for the PEP-II longitudinal kicker.

Table 5-40. Characteristics of longitudinal feedback kicker units.

Length [cm]	32
Frequency [GHz]	1.012
Kicker bandpass [MHz]	241
Driver bandwidth [MHz]	357
Shunt impedance [Ω]	1600
Power for 1 kV/unit [W]	313
Driver power rating [W]	500

correction signal to be applied (via a kicker) to each bunch. The output of such a filter is a convolution

$$Y_k = \sum_{n=0}^{m-1} C_n X_{k-n} \tag{5-40}$$

where Y_k is the output of our filter on turn k (sent to the kicker), n is an index that sums over each of the last m phase measurements of a particular bunch, C_n are the coefficients of our filter, and X_{k-n} are the digitized input bunch-phase values for the last m samples.

The coefficients C_n describe the impulse response of the filter. These coefficients reflect our prior knowledge of the pattern we seek in the input, namely a sinusoid at the synchrotron frequency. Our filter is specified such that, if the input is a sinusoid, the output is another sinusoid, proportional in amplitude to the input sinusoid and shifted 90° in phase. The filter has a frequency-dependent transfer function designed to pass the synchrotron frequency and reject other frequencies. In addition, our filter algorithm implements a limiting function that allows saturated operation of the system (for example, to handle injection transients).

We were led to the concept of down-sampled processing by considering the ratio of the synchrotron period to the sampling rate required to reconstruct the original continuous signal. In a down-sampled feedback system, the beam pickup information is used to compute a new correction signal only every nth turn, though we still apply a correction signal for a bunch on every turn. The basic concept is sketched in Fig. 5-120, which shows the relative phase of a bunch undergoing synchrotron oscillations and the associated sampling points. The result of applying the filter is shown in Fig. 5-121 for down-sampling factors of n = 1, 2, and 4. For each case we show the input to the processing filter (including 5% zero-mean noise) and the filter output, which demonstrates the proper 90° phase shift required for damping. We see that the down-sampled filters produce the correct phase shift despite the delay of the hold operations.

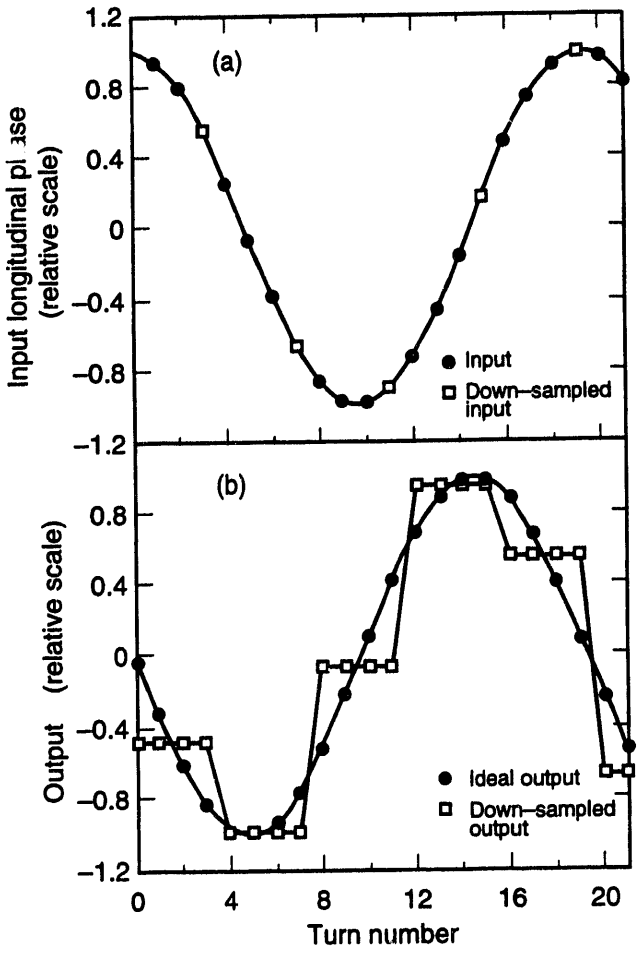

Fig. 5-120. Response of a down-sampled filter. In (a), the curve represents a sinusoid of unit amplitude, with a period of 19.3 turns. The data points indicate sampled values of the longitudinal oscillation, open squares indicating samples on every fourth turn and filled circles indicating the samples ignored in the down-sampling technique. In (b), the smooth curve represents the same sinusoid shown in (a), but with a 90° phase shift—the ideal longitudinal correction (in the limit that the damping time is very long). Here, the closed circles indicate the ideal correction to be applied on each turn and the squares indicate the approximation used in down-sampling by n = 4 such that the same correction is applied on four successive turns.

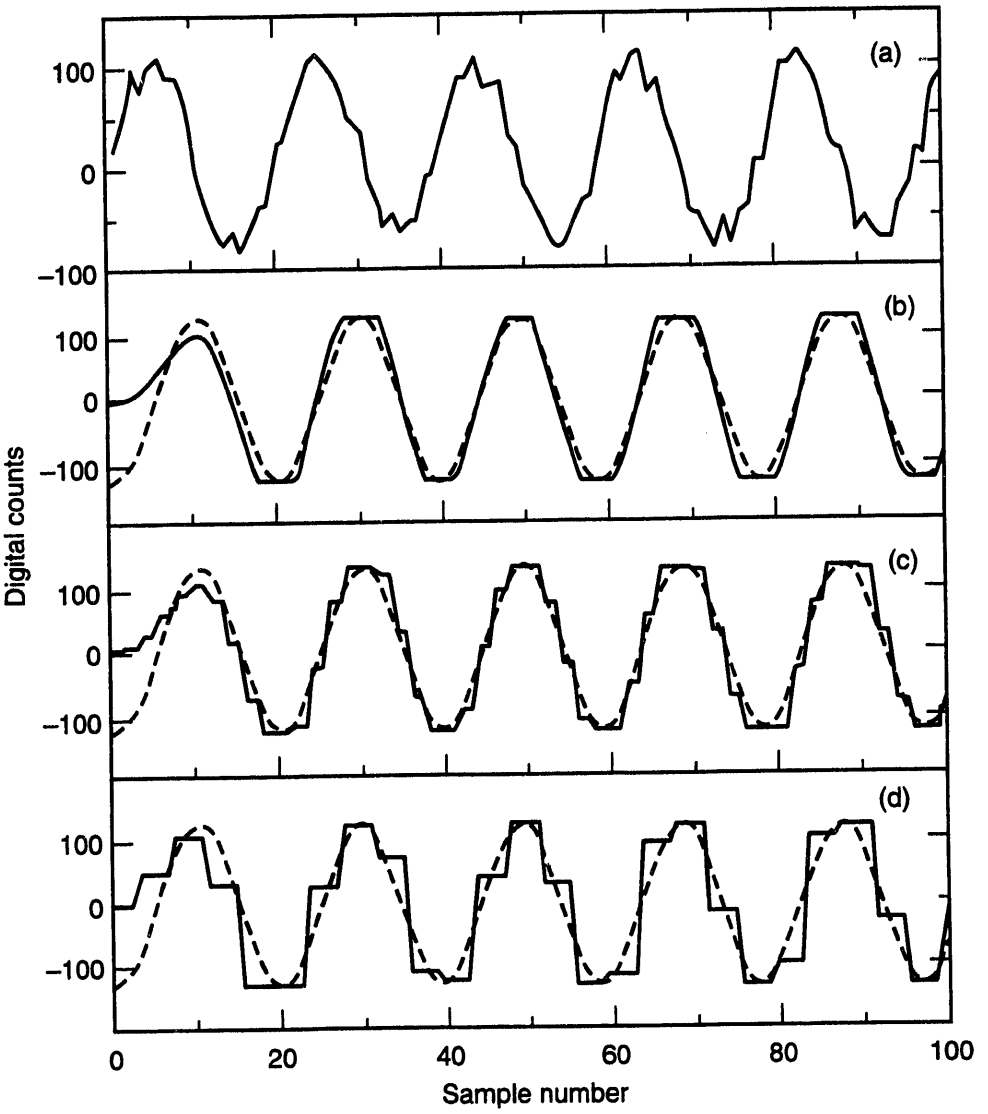

Fig. 5-121. Filter response for different down-sampling factors. The plots show (a) an input including 5% zero-mean noise, and the filter outputs for down-sampling factors of (b) n = 1, (c) n = 2, and (d) n = 4.

The down-sampled filters clearly produce a cruder, though still satisfactory, approximation to a pure sinusoid than does the $n = 1$ filter. Furthermore, because the simpler down-sampled filters have greater bandwidths than that of the $n = 1$ filter, their noise rejection decreases roughly as $1/\sqrt{n}$.

The impulse responses (tap weights) and frequency responses are shown in Figs. 5-122 and 5-123, respectively, for the $n = 1$ (20-tap) and $n = 4$ (5-tap) filters. These curves demonstrate the effective widening of the filter bandwidth with increased down-sampling. The down-sampled filters pass noise signals above the synchrotron frequency, or, alternatively, the filters can be considered to alias the noise signals down into the filter passband. With these graphs, we can also estimate the loss of system gain that would

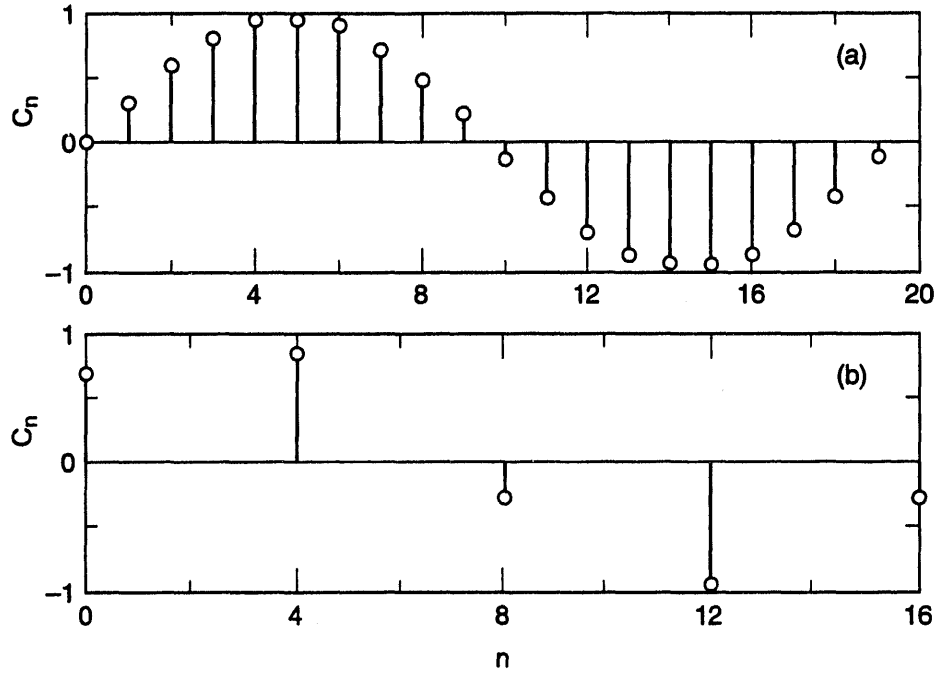

Fig. 5-122. Relative filter coefficients (and impulse responses) for down-sampling factor (a) n = 1 and (b) n = 4. For the n = 1 case, $C_0 = 0$; this condition ensures that no information from a beam measurement is used in a correction on the same turn (which corresponds to requiring a reasonable time for the computation of a correction signal). In the down-sampled cases, computed corrections are applied with a one-turn delay.

result if the synchrotron-oscillation frequency were not perfectly matched to the center frequency of the filter.

Our motivation to develop a down-sampled processing system is to simplify the electronics required to implement the feedback filter. (The raw computational throughput required of the filter convolution scales as $1/n^2$, that is, if we down-sample by a factor of two the filter convolution has half as many terms and produces output kicks at half the rate.) The total number of DSPs required scales linearly with the sum of the computational load plus some "overhead". Additional factors that influence the actual complexity of the filter hardware include the overhead associated with getting data into and out of each DSP and that associated with implementing any special functions (e.g., switching filter coefficients under various operating modes).

In an actual down-sampled feedback system, there are tradeoffs to be made among the issues of noise rejection, system complexity, and accelerator dynamics. We have used our accelerator feedback system simulation model to determine an appropriate down-sampling factor for our design, and to specify the feedback filter parameters. Results from these simulations are presented in Section 5.6.1.8.

5.6.1.4 System Summary. Table 5-41 provides a summary of the proposed technical specifications for the PEP-II longitudinal feedback system. Laboratory measurements of a prototype feedback system comprising a pickup, a fast front-end, a digitizer, and a

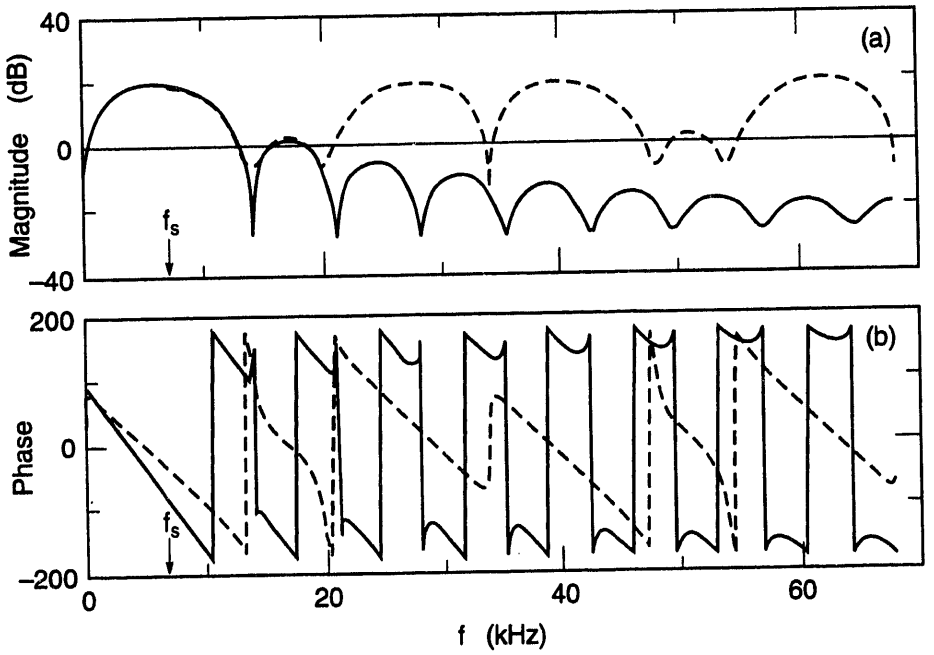

Fig. 5-123. Frequency responses in (a) magnitude and (b) phase. Solid lines show the n = 1 case and dashed lines the n = 4 case, as determined by the Fourier transform of the coefficients. In the simulation, the phase response is 90° at the synchrotron frequency for both cases, due to the delays in the hold buffer.

single-channel DSP module have demonstrated our ability to detect the phase of simulated bunches with a resolution of better than 0.2° (at 476 MHz) and with a coupling between bunches (separated by 4.2 ns) of –30 dB. The DSP-based 20-tap (n = 1) and 5-tap (n = 4) feedback filters have also been demonstrated to operate satisfactorily at the full design speed. A prototype kicker has been constructed, and measurements of its bandwidth are consistent with the bunch-spacing requirements. These laboratory efforts clearly validate the proposed longitudinal feedback system design and demonstrate the feasibility of achieving the level of performance needed for use at PEP-II.

Table 5-41. Longitudinal feedback system specifications.

RF frequency [MHz]	476
Bunch interval [ns]	4.2
Beam pickup central frequency [MHz]	2856
Phase detector dynamic range (at 476 MHz)	±15°
Phase detector resolution (at 476 MHz)	0.5°
Bunch-to-bunch signal isolation [dB]	–30
Kicker structure operating frequency [GHz]	1.012
Output power [kW]	1.5
FIR tap length, m	5
Down-sampling factor, n	4

5.6.1.5 Overview of the Simulation. We have studied the behavior of the proposed longitudinal bunch-by-bunch feedback system with a computer model of the HER. The simulation includes a ring model, along with an electronic model of the bunch-by-bunch feedback system shown in Fig. 5-114. The simulation code calculates the longitudinal motion of the bunches in the ring and their interactions with the RF cavities. It determines the bunch phase at the pickup electrode structure, adds the appropriate kick from the kicker structure (as determined by the electronic model), and propagates the bunches through the ring and cavities.

The electronic model of the transfer function of the feedback system includes:

- The feedback algorithm that processes the signals from the pickup electrode structure before sending them to the longitudinal kicker; this algorithm implements the down-sampled processing and includes a model of the DSP finite word length and arithmetic-saturation behavior
- The properties of the phase detector, the low-pass filter, the front-end A/D, the DSP farm, and the kicker (which is implemented as a phase-modulated RF kicker)
- Parameters to simulate input noise, gain and offset errors, bandwidth limitations, and the effects of the limited dynamic range of the analog components

The simulation model assumes that the measurement of bunch phase is independent of bunch charge. This corresponds to the case where the front-end circuits include an AGC loop or where a separate measurement of bunch charge is available for normalization. A propagation delay of at least one turn (7.33 μs) is enforced in the feedback transfer function.

5.6.1.6 Ring Simulation. In the ring simulation code, the bunch phases ϕ_i are taken with respect to the zero crossing of the RF waveform. We assume that a discrete kick is given to each bunch at a single point in the ring; that is, the system is modeled as though there were a discrete change in energy at a single point on each turn. This simplification is justified, because the synchrotron frequency is small compared with the revolution frequency. The motion of bunch i on one turn is divided into two parts:

- Propagation around the ring, outside the kick point:

$$\begin{aligned} \phi_i &\rightarrow \phi_i + T_0 \dot{\phi}_i \\ \dot{\phi}_i &\rightarrow \dot{\phi}_i \end{aligned} \tag{5-41}$$

- The kick given to the bunch at the kick location:

$$\begin{aligned} \phi_i &\rightarrow \phi_i \\ \dot{\phi}_i &\rightarrow \dot{\phi}_i + \Delta\dot{\phi}_i \end{aligned} \tag{5-42}$$

The kick given to bunch i includes several components, corresponding to the various contributions that produce an energy change in bunch i on one turn:

- The RF generator voltage in the cavity at the time bunch i passes through. We represent this as $\hat{V}_g \sin \phi_i + V^{\text{cav.fbk}}$, where the second term corresponds to the RF cavity feedback needed to control beam loading at the fundamental.
- The wakefields (both the fundamental mode and HOMs) ringing in the cavity.
- The synchrotron radiation loss per turn, U_0, which actually occurs throughout the ring, but is lumped into the kick in the simulation.
- The voltage V_i^{fdbk} applied to bunch i by the bunch-by-bunch feedback system.

The equation for the total kick is:

$$\Delta\dot{\phi}_i = -\frac{\alpha\omega_{\text{RF}}}{E_0/e}\left[\hat{V}_g \sin\phi_i + V^{\text{cav.fbk}} - \frac{U_0}{e} + V^{\text{wake}} + V_i^{\text{fdbk}}\right] - \frac{2T_0}{\tau_E}\dot{\phi}_i \qquad (5\text{-}43)$$

where α is the momentum compaction factor, E_0 is the nominal energy for a particle on the design orbit, ω_{RF} is the RF frequency, T_0 is the revolution period, and τ_E is the longitudinal radiation damping time.

Cavity Wakefield. In computing V^{wake}, we keep track of the (complex) wake voltage in each cavity mode k. This voltage gets a discontinuous increment each time a bunch passes through the cavity, and it rotates in phase and attenuates (since ω_k is complex) between bunch passages. Note that according to the fundamental theorem of beam loading, a bunch sees half the wake voltage it induces during its present passage.

Cavity Feedback. Because the beam loading in the fundamental cavity mode is very heavy, RF cavity feedback will be necessary to compensate it. The response at coupled-bunch frequencies that fall within the bandwidth of the fundamental mode will require special feedback. In simulations to date, we have assumed that the compensation is perfect, that is, that $V^{\text{cav.fbk}}$ exactly cancels the fundamental mode of the wakefield in the cavity. In reality, the situation is more complicated (involving the cavity phase loop, amplitude loop, tuning loop, localized impedance reduction, and bunch motion feedback), and the compensation will not be perfect. We are now studying an improved representation that includes the response of the cavity, the feedback of the phases of nearby beam modes, and the effect of the gap in the bunch train.

5.6.1.7 Simulation Parameters. We start a given simulation run with specified initial conditions ϕ_i and $\dot{\phi}_i$ for each bunch. A typical initial condition we have studied is that of an injected bunch with a relatively large offset from the average synchronous phase, while the remaining bunches are close to the synchronous phase. All bunches, including the injected bunch, begin at the nominal energy, and the charge in all bunches is taken to be equal and to remain constant. (Although not yet implemented, the simulation is structured such that it will be straightforward in the future to include the addition of charge to bunches during injection.)

When the simulation begins, there are no wakefields present in the cavities. As noted above, the present simulations then assume that the wakefield at the fundamental (accelerating) mode is fully compensated; that is, only the effect of the HOM wakefields

is included. The present simulations include two single dominant longitudinal HOMs above 750 MHz, whose properties are given in Table 5-36.

Parameters used in the simulation results shown below are as follows:

- Bunch charge $N_b = 4 \times 10^{10}$
- 1658 bunches (corresponding to a harmonic number of 3492, with every other bucket filled, except in a 5% gap)
- Total current of 1.48 A
- R/Q = 43 Ω per cavity for the strongest HOM (which is assumed to be damped to $Q = 70$)
- 20 RF cavities
- Starting phase for bunch #5 is $\phi_5 = 0.2915$ rad (that is, a 0.1-rad offset from the synchronous phase of $\phi_s = 0.1915$ rad); the remaining bunches start at the synchronous phase
- $U_0 = 3.52$ MeV/turn
- $\alpha = 0.00241$
- $\hat{V}_g = 18.5$ MV

(In some cases, these parameters are slightly different from those finally adopted for PEP-II, but the simulation results reported below are not strongly influenced by these minor differences.)

5.6.1.8 Simulation Results. Figure 5-124 plots the maximum bunch excursion ϕ_i achieved for the first 100 bunches in three cases: The first case is for 1000 turns, with no feedback; the second is for 3000 turns with no feedback; and the third is for 3000 turns, including feedback. Comparison of the first and second cases shows that, without feedback, an injection error on bunch #5 perturbs the following bunches, and the perturbations grow. (Note that the time between injection pulses is 1/60 second, which corresponds to about 2300 turns.) In 3000 turns, the perturbations of bunches #6 through #20 or #30 have grown to at least one-third of the original injection perturbation of bunch #5. In the absence of feedback, the disturbance would continue to grow in amplitude and would propagate further down the bunch train. In contrast, the third case shows that feedback suppresses the growth rate in subsequent bunches very effectively.

Next we focus on results that include the effects of bunch-by-bunch feedback. In these simulations, the kicker output is limited to 4 kV/turn; other parameters are summarized in Table 5-42. Only the first ten bunches after the gap are included, because the coupled-bunch excitation does not extend beyond a very few bunches with the feedback system turned on. These simulations were run for 4000 turns. The nominal gain of the PEP-II feedback system corresponds to reaching the 4-kV maximum kicker amplitude at a phase excursion of 30 mrad. Because the feedback system does not have a linear response at large amplitude (in order to saturate "gracefully"), however, we characterize the gain by quoting the slope in the *linear* (midband) region. The slope corresponding to reaching 4 kV at a 30-mrad excursion is then 110 V/mrad. In order to

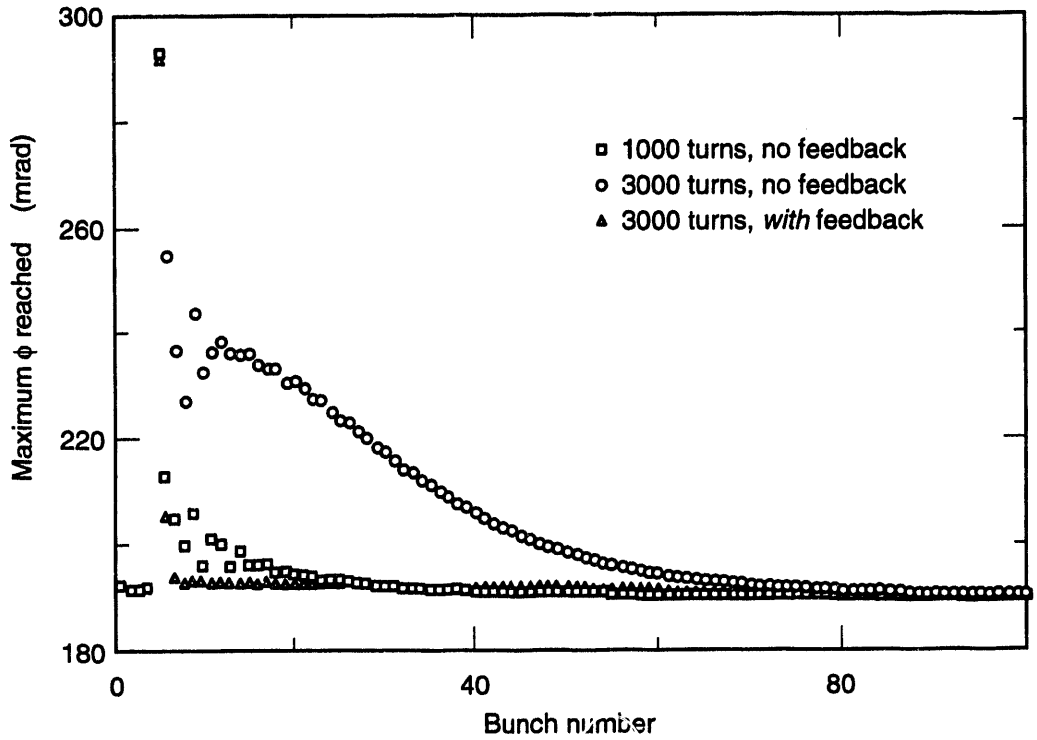

Fig. 5-124. Maximum bunch excursion for the first 100 bunches, with and without feedback. In the simulation, an injection error is introduced for bunch #5 on the first turn. No down-sampling was assumed.

observe the effect of the feedback system in fewer turns, some of the simulations were carried out with twice the linear gain (220 V/mrad), as noted in the appropriate figures.

Figure 5-125 shows the longitudinal phases of the injected bunch (#5) and the bunch immediately following (#6) vs turn number. The envelope of the phase of the injected bunch damps linearly because the kicker saturates, and the phase of the following bunch grows quickly to its maximum value near 1000 turns and then slowly damps. The system limits the excitation of the bunch following the injected bunch and strongly suppresses the excitation of subsequent bunches.

Table 5-42. Simulation system parameters.

Linear midband filter gain [V/mrad]	110
Input quantization size [mrad]	1.3
Output quantization size [V]	50
Input noise amplitude, rms [mrad]	8.3
Kicker saturation voltage [kV]	4

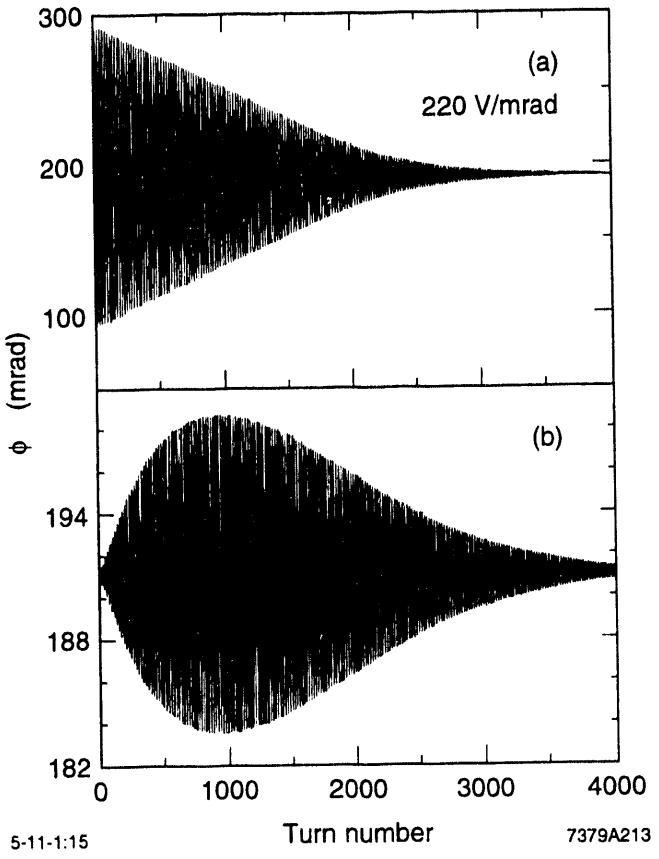

Fig. 5-125. Plots of the longitudinal phases of (a) the injected bunch (#5) and (b) the bunch immediately following (#6) vs turn number, in the presence of a longitudinal feedback system. Note the expanded vertical scale for (b).

Figure 5-126 exhibits the input and output of the DSP model for bunches #5 and #6 shortly after injection. The DSP outputs exhibit the jagged shape characteristic of the $n = 4$ down-sampling, but the filter outputs produce feedback signals with the correct 90° phase shift. We see that the DSP output saturates for bunch #5, but still maintains the proper 90° phase lag. Benign saturation behavior of this type is difficult to realize with conventional analog approaches.

Figure 5-127a shows the amplitude of the phase-space error vs turn number for the injected bunch (#5). (The phase-space error is defined as the result of adding the error in phase and the error in energy in quadrature, expressed in radians.) We see the amplitude decreasing linearly during the time when the kicker limits at ±4 kV per turn. After coming out of saturation, the amplitude of the injected bunch falls exponentially. The amplitude of the following bunch (#6) is plotted on the same scale. Figure 5-127b shows the behavior of the injected bunch as it leaves the regime of kicker saturation. The decrease in amplitude changes from linear to exponential. Note that the transition from saturation does not perturb the following bunch. Figure 5-127c shows the phase-space error amplitudes for the three bunches closely following the injected bunch. With bunch-

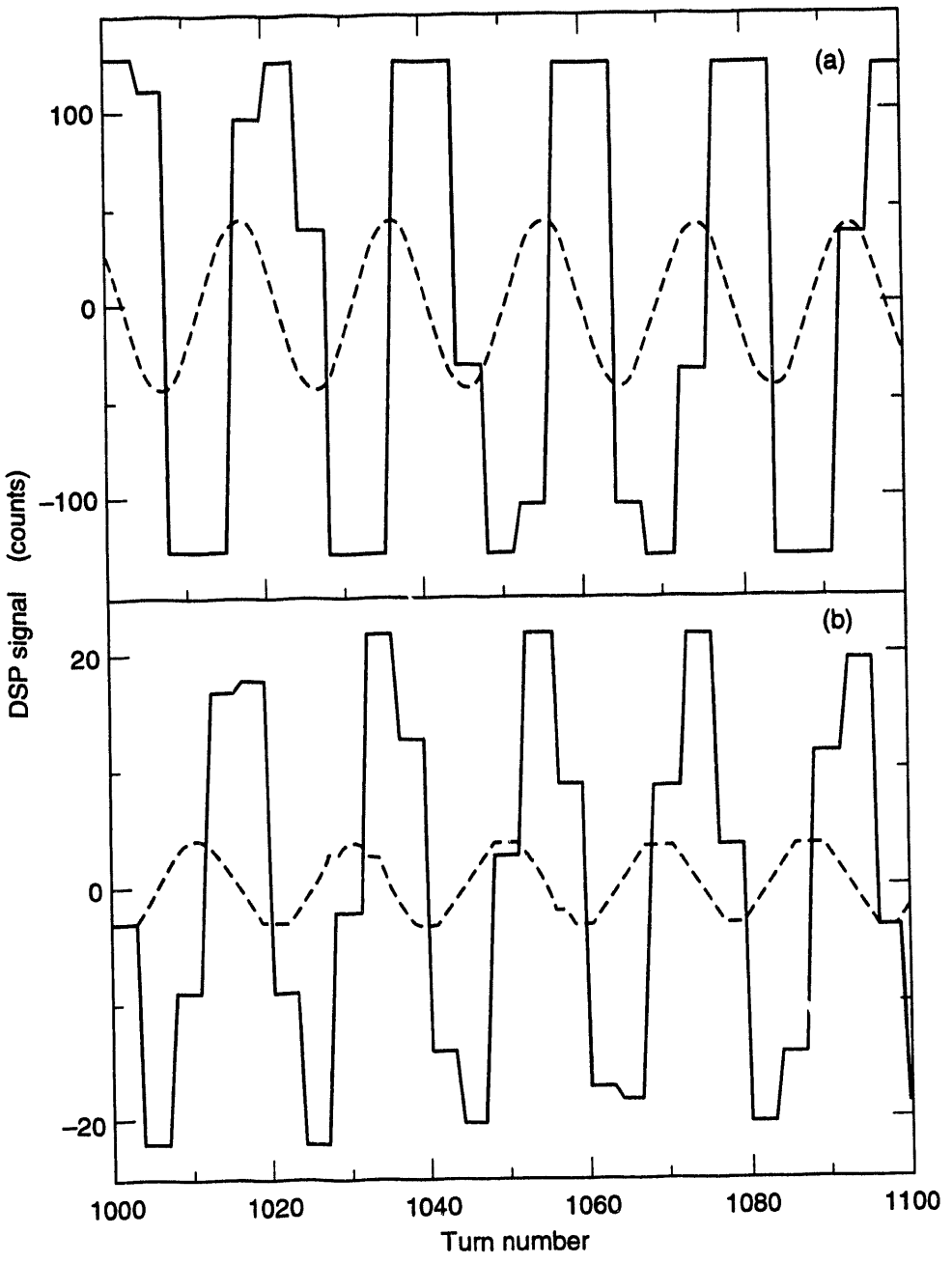

Fig. 5-126. Plots of the input and output of the DSP model for (a) bunch #5 and (b) bunch #6, shortly after the injection of bunch #5. The dashed lines indicate the inputs without down-sampling; the solid lines indicate outputs, with the down-sampling factor n = 4. Note that the output in (a) saturates benignly.

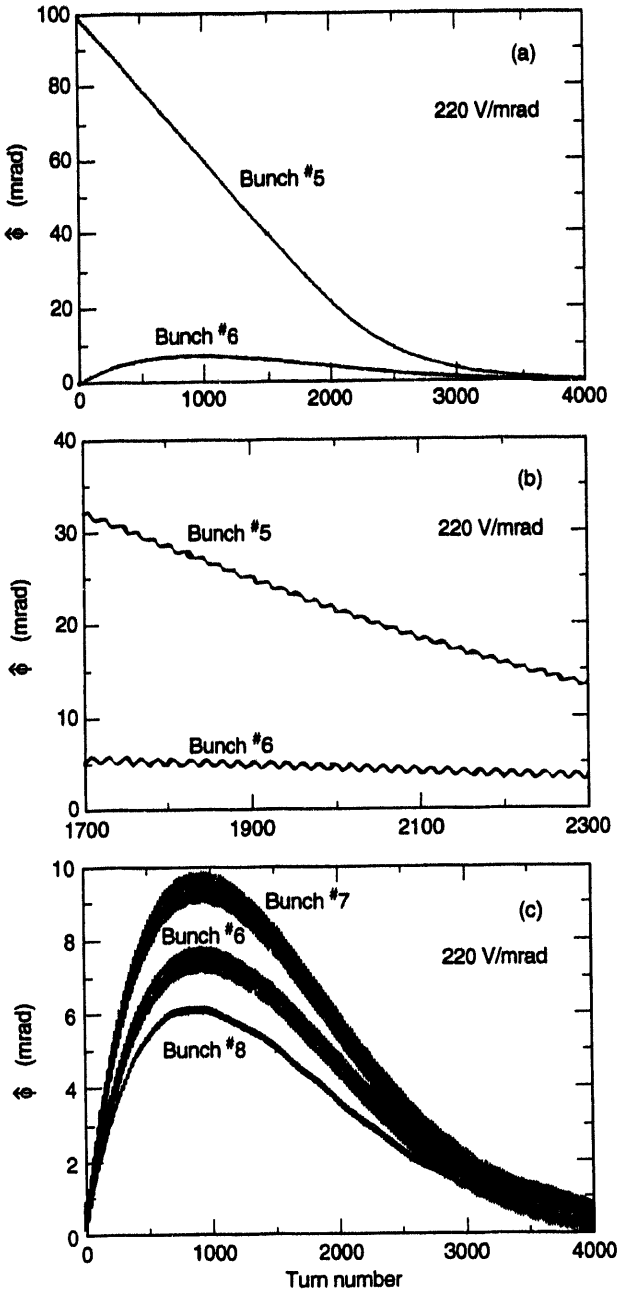

Fig. 5-127. Plots of the phase-space error amplitudes for (a) bunches #5 and #6 for the first 4000 turns, (b) bunches #5 and #6 in the region where the kicker comes out of saturation, and (c) bunches #6, #7, and #8 for the first 4000 turns. In (b), we see that the trailing bunch is undisturbed as the kicker comes out of saturation. The rise times shown in (c) agree with analytic calculations when no bunch-to-bunch coupling in the electronics is assumed. With the parameters indicated in Section 5.6.1.7, we find that bunch #5 drives bunch #7 most strongly.

to-bunch coupling in the electronics set to zero, the rates of rise agree with analytic calculations.

Figure 5-128a compares the amplitude of the injected bunch for two values of gain in the DSP model. As mentioned, the lower gain corresponds to our specified value of 4 kV at a phase excursion of 30 mrad. The higher gain, used for the simulations that produced Figs. 5-125 through 5-127, corresponds to doubling the nominal linear gain. Figure 5-128b shows the amplitude of the following bunch at each gain value. Lower gain results in larger excursions of amplitude and slower recovery, as expected. The only penalty of higher gain is a smaller linear regime.

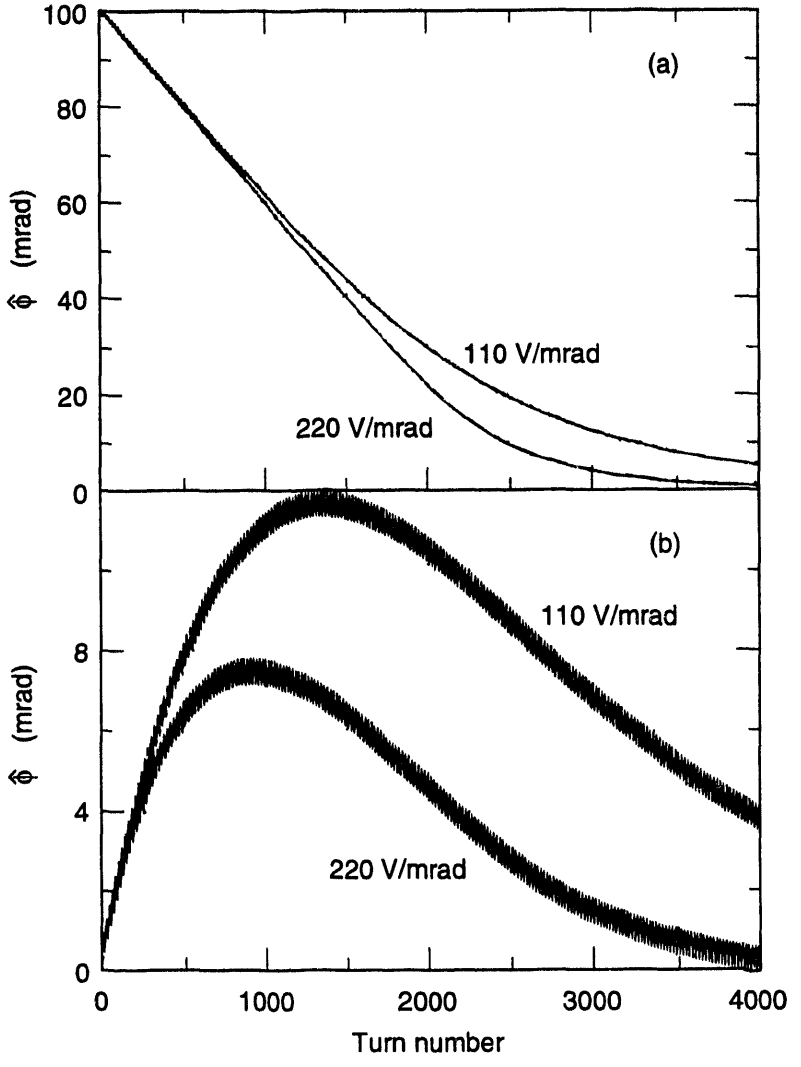

Fig. 5-128. Plots of the phase-space error amplitude over 4000 turns for (a) the injected bunch #5 and (b) the following bunch #6, for two values of gain: 220 V/mrad and 110 V/mrad. The lower gain corresponds to 4 kV at a 30-mrad phase excursion, which is roughly the PEP-II hardware specification. To reduce simulation time, the higher gain was used for the results shown in Figs. 5-125 through 5-127.

Figure 5-129 shows the amplitudes of the injected bunch (#5) and the three following bunches, with a 3% bunch-to-bunch coupling in the front-end electronics and a 10% coupling in the kicker. In this case, bunches #6 and #7 suffer a much greater excursion from equilibrium, but still damp. Bunch #8 suffers only slightly. We conclude from this that our system design is tolerant of a reasonable amount of bunch-to-bunch coupling in the analog components.

Down-sampling Parameter Study. As discussed in Section 5.6.1.3, we have used the longitudinal bunch-simulation code to quantify the performance of a down-sampled feedback system. Three figures-of-merit have been selected to evaluate system performance:

- Behavior during saturation, as measured by the slope of $\hat{\phi}$ (the amplitude of a phase oscillation), to quantify the overall gain and phase response
- Behavior in the unsaturated regime, as measured by the exponential decay time-constant of a disturbed bunch
- Quiescent behavior of the damped bunches, as measured by the steady-state rms phase value, to determine the noise-rejection properties of the filters

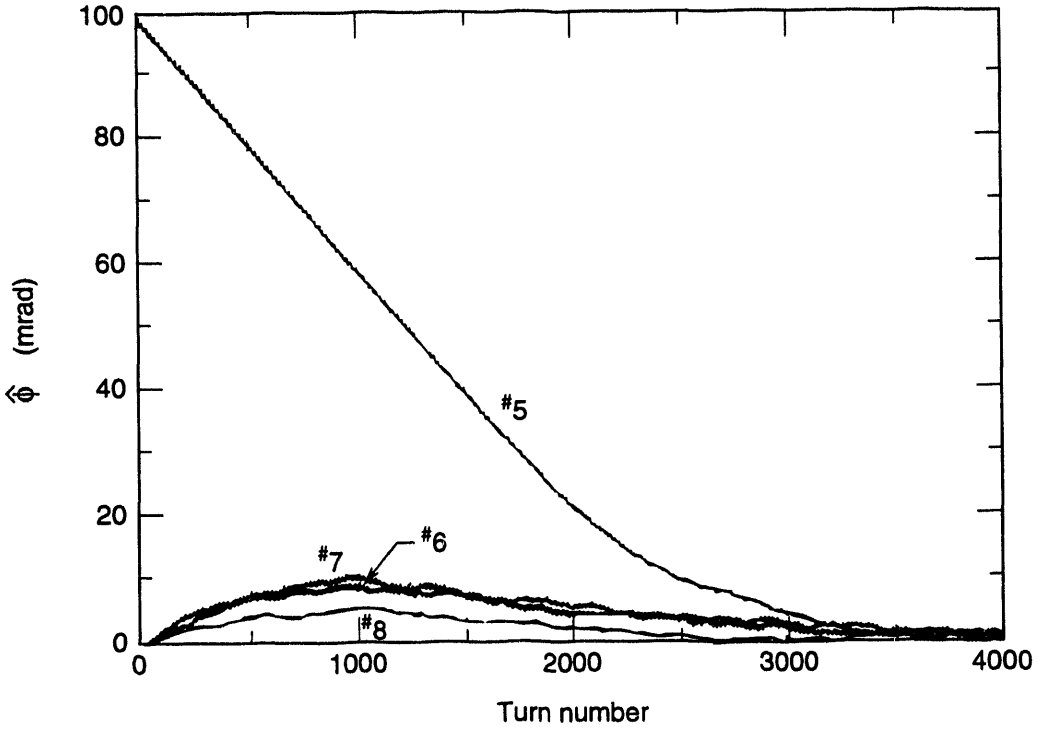

Fig. 5-129. Plot of the phase-space error amplitude for the injected bunch (#5) and the three following bunches, with 3% bunch-to-bunch coupling in the front-end electronics, 10% bunch-to-bunch coupling in the kicker (modulator, power amplifier and kicker structure), and 5% noise evaluated at the A/D input.

Figure 5-130 shows the damping of an injected bunch, with the three regimes indicated. These figures-of-merit have been used to compare the $n = 1$ (20-tap, no down-sampling), $n = 2$ (10-tap, down-sampled), and $n = 4$ (5-tap, down-sampled) feedback filters.

To make a fair comparison among the three filters, all were selected to have the same overall midband gain of 100 V/mrad, and all other system input and output gain parameters were kept as in Table 5-42. All simulations included zero-mean, Gaussian random noise injected at the phase detector quantizer, with a fixed 20-dB signal-to-noise ratio (referred to the full-scale input). The accelerator and RF system parameters used in this study are the same as those discussed above, with the exception that they were generated using only a single (dominant) longitudinal HOM.

Table 5-43 presents the measured values of the linear slope (in the saturated regime) and the exponential decay time-constant (in the unsaturated regime) for the three cases; we see that there is no significant variation among the three filters. (Recall that all three filters were chosen to have the same overall midband gain, 100 V/mrad, and were specified to produce a 90° phase shift, to within half a quantization level.) The essentially identical saturation slopes and exponential time-constants show that the down-sampled filters neither give additional phase shifts to the filter output nor reduce the effective kicker gain.

The noise rejection of the three filters under steady-state conditions is presented in Fig. 5-131a. Here, the simulation is run as for the transient studies and the rms equilibrium phases of selected bunches are plotted for the three filters, $n = 1$, 2, and 4.

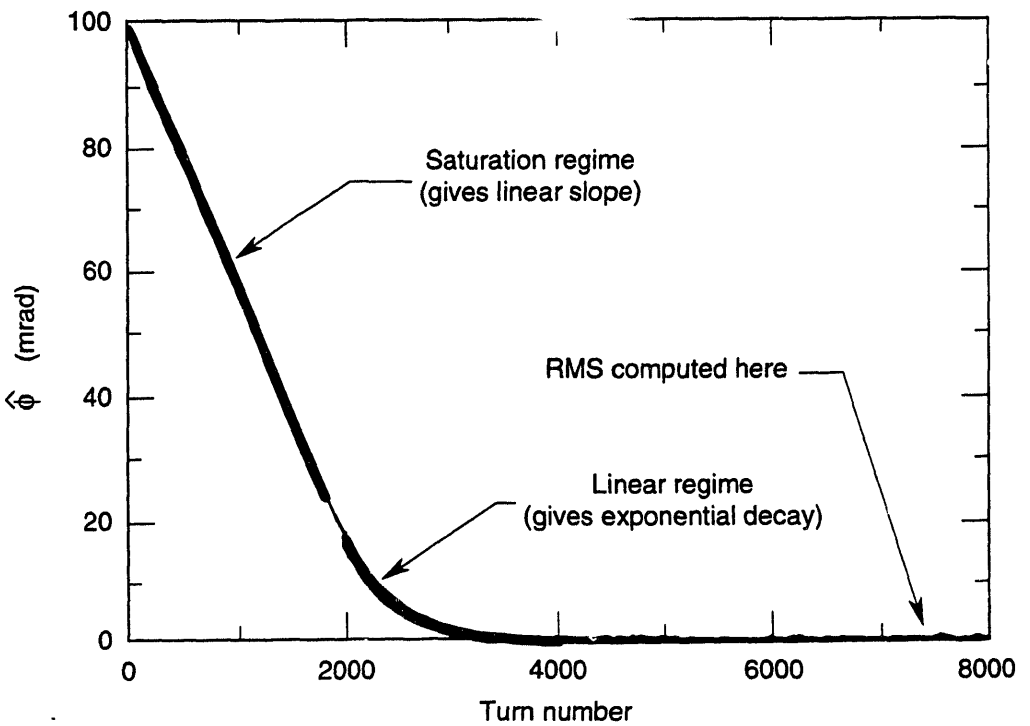

Fig. 5-130. Plot of the phase-space error amplitude for an injected bunch, indicating the operating regimes used to compare filters.

Table 5-43. Simulation saturation slopes and exponential decay time-constants.

	20-tap ($n = 1$)	10-tap ($n = 2$)	5-tap ($n = 4$)
Saturation slope [μrad/turn]	–41	–41	–38
Exponential time-constant [turns]	1098	1102	1111

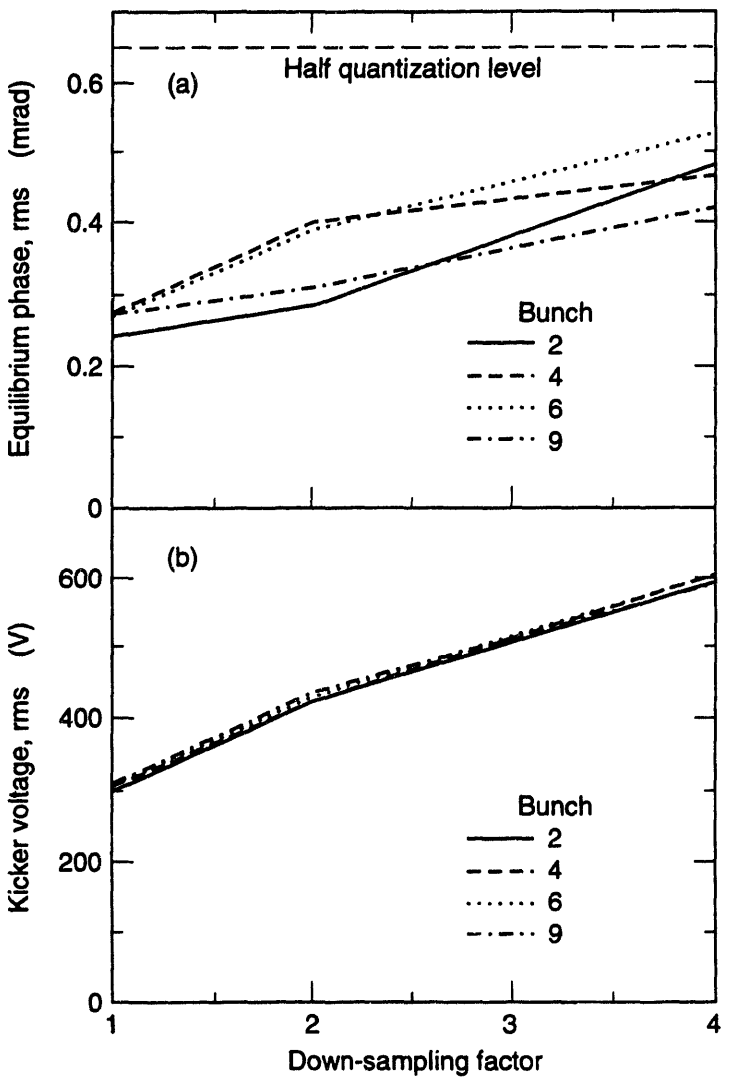

Fig. 5-131. Performance comparison, for several bunches, of the three filters ($n = 1, 2, 4$) in terms of (a) equilibrium rms phase noise and (b) rms applied kicker voltage. The noise in the rms phase and the applied kicker voltage increase with down-sampling, approximately as $n^{1/2}$.

We note that the down-sampled filters are noisier, having an rms equilibrium phase that grows approximately as $\sqrt{n}$. This can be viewed in terms of the wider passband of the down-sampled filters letting through more broadband noise power or, alternatively, in terms of the improved averaging allowed in the longer-tap filters reducing the noise fluctuations injected at the input. Note that while the rms broadband noise present at the input was set to 8.3 mrad, the filters reduce the rms noise to below 0.6 mrad. The rms noise level for the $n = 4$ down-sampled filter is of the same order as half the quantization level, whereas for the $n = 1$ filter the noise is about one-quarter of the quantization level. The noise rejection is illustrated in another way in Fig. 5-131b, which shows the rms kicker voltage for the various filters. Again, we see the approximate $\sqrt{n}$ scaling for noise power that appears at the kicker output.

The feedback system keeps the equilibrium input-phase fluctuations in a range bounded by $\pm 1/2$ the quantization level. In addition, because the feedback filters have been designed to minimize DC response, bunches that are riding on different DC synchronous phases (for example, due to the RF transient at the ion-clearing gap) are each restored to their own synchronous phase; the kicker does not attempt to restore all bunches to the *same* equilibrium phase.

Our system design goal for equilibrium rms phase noise is to restrict bunch-to-bunch motion to much less than the nominal rms bunch length. Given a 1-cm rms bunch length (100 mrad at 476 MHz), our ± 0.6 mrad quantization interval is less than 1% of the bunch length. Thus, we consider the performance of the down-sampled filters to be functionally identical to that of the 20-tap filter.

5.6.1.9 Conclusions of Simulation Study. In this simulation study of the PEP-II longitudinal bunch-by-bunch feedback, we have determined that the system proposed is a reasonable point of departure for a more detailed design effort. We have found that, for a 1.5-A beam current, 4 kV/turn is sufficient to damp both an injected bunch and the perturbed stored beam, in the presence of the expected HOM strength. We have set an upper bound on the number of DSPs required for bunch-by-bunch longitudinal feedback, and we have shown that the system performance is insensitive to nonidealities in the electronics. Finally, we have determined that the behavior of the feedback system using an $n = 4$ down-sampling factor easily meets the PEP-II performance requirements and allows considerable simplification of the digital processing system hardware. The simulation tools that have been developed for these studies can be adapted to further investigations.

5.6.2 Transverse Damping

A feedback system to stabilize transverse coupled-bunch motion is similar in concept to a longitudinal feedback system. The transverse feedback system must detect the transverse excursions of the beam, generate an error signal, and apply corrective kicks to the beam. Just as in the longitudinal case, the transverse feedback system must respond only to dynamic beam motion and not to static beam-orbit or pickup offsets.

Transverse oscillations are driven by resonators and by the resistive-wall impedance. With HOMs of the RF cavities damped to Q values of 70 or lower, the resistive-wall impedance becomes the dominant effect; it is most severe in the vertical direction.

Parameters used for the design of the vertical feedback system are summarized in Table 5-44.

Bunches oscillating with amplitude a in a coupled-bunch mode receive from the transverse beam impedance $R_\perp$ a maximum transverse voltage per turn of

$$\Delta V = I_0 a R_\perp \tag{5-44}$$

For the resistive wall, $R_\perp$ is largest at low frequency. At the frequency of interest for the resistive-wall instability, $f = (1 - \Delta\nu_y)f_0$, we find $R_\perp$ = 2.34 MΩ/m for the vertical plane. (For comparison, we see in Table 5-44 that the largest beam impedance from the cavity HOMs is below 1 MΩ/m.) Feedback to suppress growth of a 1-mm oscillation must at least cancel the corresponding ΔV per turn. The kickers will be located where $\beta_\perp$ is 20 m and will be capable of providing the required kicks (listed in Table 5-45).

5.6.2.1 Signal Processing. One important difference between the transverse and longitudinal feedback systems is that the beam executes 24 (HER) or 36 (LER) betatron oscillations per turn, whereas it takes 20 turns to complete a single synchrotron oscillation. A transverse feedback system that samples only once per turn is inherently an undersampled system (that is, it samples below the Nyquist frequency), and it processes the transverse motion signal at an aliased frequency. Another significant difference between the transverse and longitudinal systems is that, for the transverse case, a 90° phase shift of the betatron oscillation signal can be obtained in a straightforward fashion by detecting beam signals at two positions in the ring separated by 90° in betatron phase.

Table 5-44. Parameters used for transverse (vertical) feedback design.

	HER	LER
Average current, I_0 [A]	1.0	2.14
Vertical betatron tune, ν_y	23.64	34.64
Beam tube radius, b [cm]	2.40	
Lowest coupled-bunch mode frequency, f_{cb} [MHz]	0.049	
Resistive-wall impedance, $R_{\perp,RW}$ [MΩ/m]	2.34	
Resistive-wall growth time, τ_{RW} [ms]	4.4	1.1
No. of RF cavities	20	10
Frequency of strongest HOM, f_{HOM} [MHz]	1060	
$R_\perp/Q$ per cavity [Ω/m]	640	
Q	70	
Dominant HOM impedance, $R_{\perp,RF}$ [MΩ/m]	0.90	0.45
Growth time from HOM, τ_{HOM} [ms]	10.5	4.89
Maximum oscillation amplitude at cavities [mm]	1	
Injection scheme (vertical plane)	1/5 bunch per 1/60 s	
Injection error [mm]	10	

Table 5-45. Transverse kicker properties.

	HER		LER	
	Vertical	Horizontal	Vertical	Horizontal
Impedance at 10 kHz [kΩ]	57.9	38.3	57.9	38.3
Impedance at 119 MHz [kΩ]	23.5	15.5	23.5	15.5
Voltage kick [kV/turn]	2.34	1.55	5.01	3.32
Power required [W]	47.3	31.4	217	144

Additionally, the pickup signals from all of the circulating bunches have a common DC offset, allowing a single offset-rejection circuit. These essential differences permit a simpler signal processing scheme in the transverse case. Thus, we propose to base the transverse feedback system on quadrature processing channels with a one-turn delay. The essential components of such a system are shown in Fig. 5-132. Two beam pickups utilizing button electrodes are used to generate horizontal or vertical position signals from two points in the ring, separated by approximately 90° in betatron phase. The two pickups provide sine and cosine transverse oscillation signals that are the basis of the quadrature processing channel.

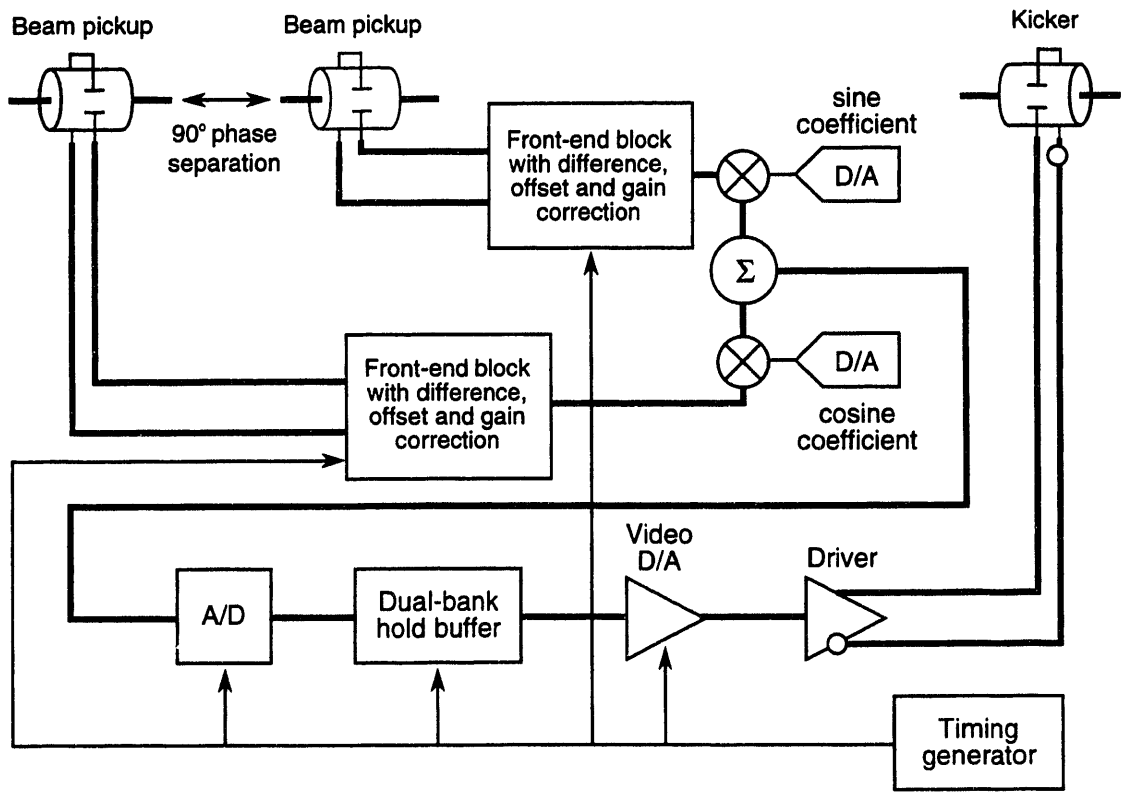

Fig. 5-132. Block diagram of the transverse feedback system for one plane.

The detailed functions required for each plane of a pickup electrode are shown in Fig. 5-133. The processing channel is designed to detect beam signals in a 250-MHz band around a 1.428-GHz carrier (the third harmonic of the ring RF). Transverse electrode signals are bandpass filtered around 1.428 GHz, scaled via two multiplying coefficients, subtracted in a difference (delta) hybrid, mixed down to baseband and filtered. A DC subtraction circuit measures average beam position over many oscillations and adjusts the multiplying coefficients to remove any DC component from the signal. (Such a system corrects fabrication or installation asymmetries of the pickup, and electronic component gain differences.) The required bandwidth for this DC-suppression loop is very modest because, in contrast to the longitudinal case, transverse offsets are the same for all bunches. Our approach also allows correction for any intensity-dependent gain via adjustments of the multiplying coefficients as a function of beam current. Values of the coefficients may be generated by either digital or analog means. The output signal from the transverse processing unit is a fast analog representation of the transverse position of each bunch.

The quadrature phase shifter shown in Fig. 5-132 is implemented using two bipolar quadrature coefficients to scale each of the pickup signals. These coefficients can be adjusted to allow the generation of an error signal at any arbitrary betatron phase with respect to the input signals. This approach allows the ring to be operated with any fractional tune by means of appropriate adjustments of the quadrature coefficients and, in

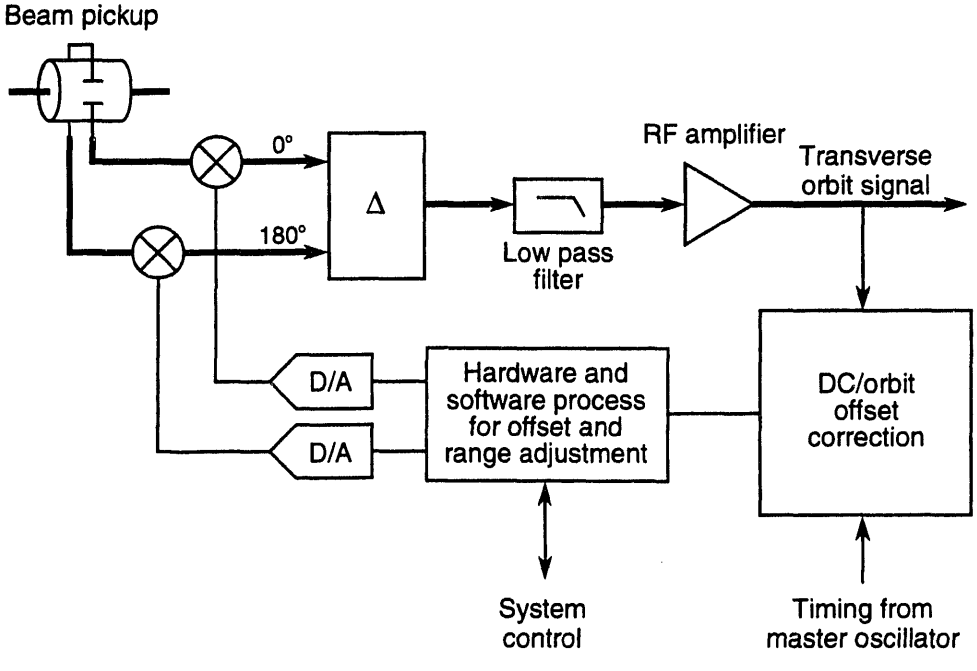

Fig. 5-133. Block diagram of the front-end block for the transverse feedback system. The output transverse position signal is multiplied by either the sine coefficient or the cosine coefficient, then summed to form a transverse correction applied one turn later.

addition, allows the kicker to be located at any convenient point in the ring. Fine tuning of the loop gain and phase are also made via the scaling coefficients.

The scaled sine and cosine terms are summed and digitized at the 238-MHz bunch repetition rate. A hold buffer is used to delay the sampled signal until the next revolution, at which time it is applied to the bunch via a D/A, a power amplifier, and the kicker (described below). Commercial power amplifiers operating in the 0.01–119 MHz band will be used to drive the transverse kicker structures.

We note that many components of the transverse feedback system will be identical to those of the longitudinal system described in Section 5.6.1.3. For example, both will use identical synchronous timing systems and very similar A/D and D/A processing. In addition, the hold buffers required for the one-turn delay in the transverse system are equivalent to those used for down-sampling in the longitudinal case, so a common design can be employed.

5.6.2.2 Kicker Structure. The shunt impedance of a stripline-pair transverse kicker electrode is given by

$$R_k = 2Z_L \left(g_\perp \frac{l}{b} \frac{\sin kl}{kl} \right)^2 \tag{5-45}$$

where $k = \omega/c = 2\pi f/c$. As Eq. 5-45 shows, such a kicker is most efficient at lower frequencies; this matches the need to oppose resistive-wall instabilities at the low end of the 0.01–119 MHz band. The length may be one-half the bunch spacing, which minimizes coupling at the bunch frequency. Each kicker unit consists of a pair of stripline electrodes; the electrodes form opposing sides of a 10 cm × 5 cm aperture. These electrodes have length 63 cm ($\lambda/4$ at 119 MHz) and have an electrical line impedance $Z_L = 50\ \Omega$. A vertical electrode pair will have a geometry factor of $g_\perp = 0.955$ and, using Eq. 5-45, we find the shunt impedance at 10 kHz, R_k, to be 57.9 kΩ. The horizontal electrodes are envisioned to be C-shaped, covering not only the sides of the rectangular aperture but extending over the top and bottom (to give enhanced coverage). For this geometry, the horizontal kicker is estimated to have $R_k = 38.3$ kΩ. Parameters of the kickers and power required for each ring are given in Table 5-45.

5.6.3 Experimental Verification of System Architecture

As a component of the PEP-II R&D effort, a laboratory prototype longitudinal feedback system has been developed. The prototype implements a full-speed (250-MHz) front-end phase detector, with digital signal processing, for a limited number of bunches. It incorporates an 8-tap stripline comb generator, a master phase reference oscillator that locks to the ring RF system, a phase detector, 250-MHz A/D and D/A stages, and a DSP microprocessor. Figure 5-134 shows photographs of the comb generator and the microwave and analog components of the front-end circuitry.

The prototype PEP-II longitudinal feedback system was tested in September 1992 using the SPEAR storage ring at SLAC. For this experiment, the beam was sensed via a button-type BPM electrode and processed by the prototype PEP-II front-end electronics.

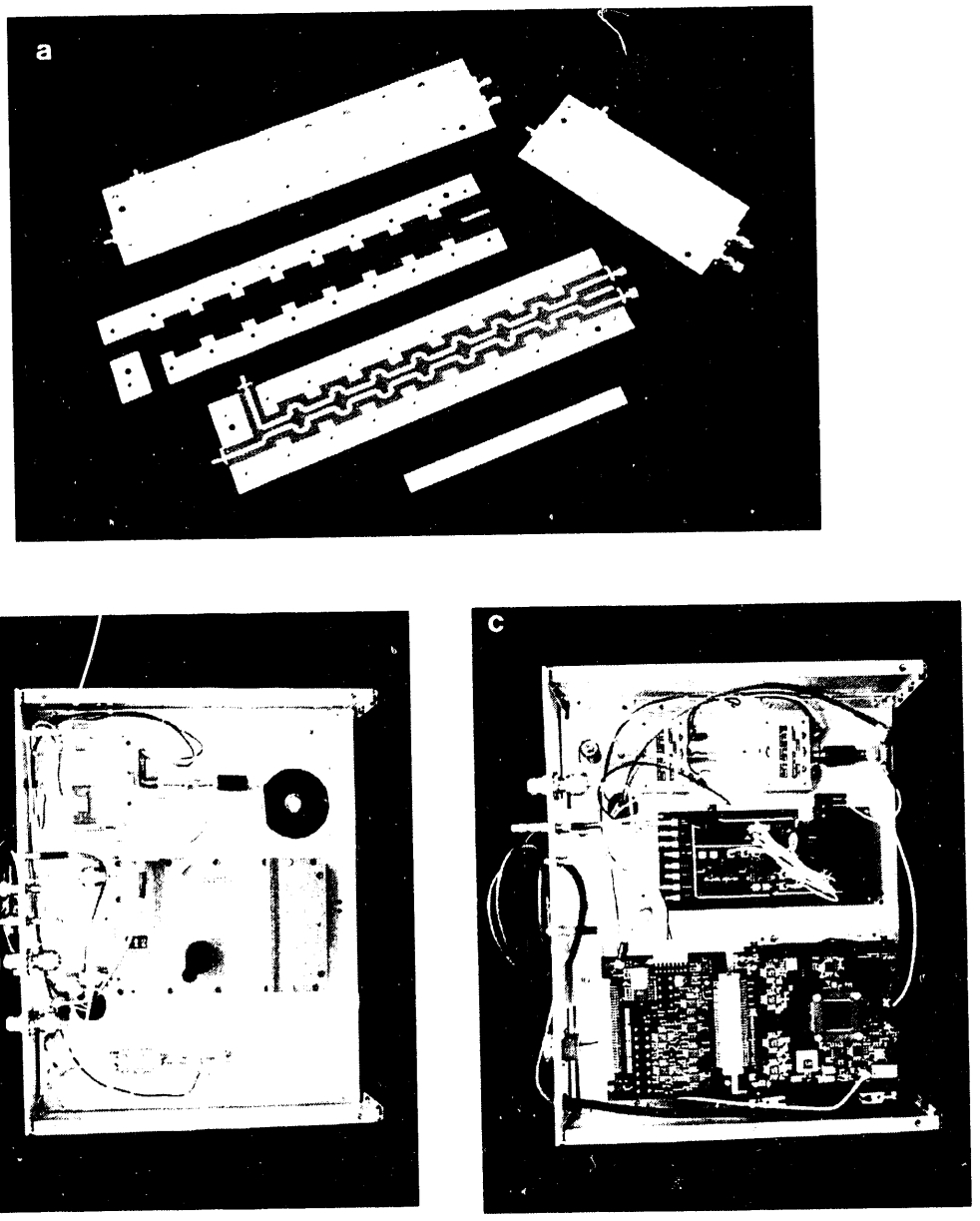

Figure 5-134. Photograph of the microstrip 8-tap comb generator (a) and the front-end circuitry (b, c).

The phase detector and phase-locked master oscillator were operated at eight times the SPEAR RF frequency (8 × 358 MHz = 2864 MHz) using the comb-generator circuits developed for the PEP-II prototype. The front-end digitizer was run at the nominal 4.2-ns digitizing cycle, and down-sampling circuits were provided to implement a programmable down-sampler and hold buffer for a single-bunch system. A single AT&T DSP 1610 processor was used to compute the feedback filter. The DSP feedback signal was used to control a phase shifter, acting on the RF cavity phase, which, in turn, acted upon the beam (through the RF cavity) to close the loop.

A series of frequency-domain and time-domain experiments were performed to evaluate the behavior of the accelerator and feedback system. Results were obtained for swept frequency-domain beam-transfer functions, for two types of time-domain transient studies, and for noise performance. The measured system performance has been compared with theoretical performance of a harmonic-oscillator model, as well as with the results of the numerical simulations of Section 5.6.1.8.

SPEAR parameters used during the experiment are summarized in Table 5-46. These parameters allow tests of the front-end circuitry under conditions similar to those of PEP-II. Feedback filters used in the experiments are the same type proposed for PEP-II. However, the SPEAR synchrotron frequency of 32 kHz requires a data rate in the feedback system approximately four times greater (per bunch) than for PEP-II, so a down-sampling factor of $n = 8$ was used to keep the number of samples per synchrotron period consistent with the PEP-II parameters.

Because the SPEAR storage ring does not have a wideband kicker of the type proposed for PEP-II, the experiment used one of the two main RF accelerating cavities to act back on the beam. As the bandwidth of the RF system is limited to roughly 40 kHz, it is not possible to implement a true multibunch feedback system. All of the closed-loop measurements were therefore performed using a single stored bunch. The test thus serves to demonstrate the behavior of a single bunch acted upon by a digital feedback system.

The experiments permitted the behavior of various filter parameters (tap length, down-sampling factor, etc.) to be studied with a real beam, and the performance of the front-end comb generators, digitizers, etc., to be measured under realistic conditions. An additional series of open-loop measurements was made while the ring was filled with multiple bunches, allowing multibunch coupling to be observed but not controlled.

5.6.3.1 Frequency-Domain Studies. Frequency domain measurements of the system were made by driving the beam via the RF cavity while observing the beam response as a function of frequency. Figure 5-135 shows the magnitude and phase responses of the beam transfer function for an open-loop configuration and for closed-loop gains of 18 and 28 dB. The open-loop response shows a weakly damped harmonic oscillator with a Q of

Table 5-46. SPEAR operating parameters for longitudinal feedback system tests.

Energy [GeV]	2.26
Single-bunch current [mA]	2.5
Particles per bunch	1.2×10^{10}
ν_s [kHz]	32
V_{RF} [MV]	1.9
ϕ_s [deg]	174
σ_ℓ [cm]	1.4

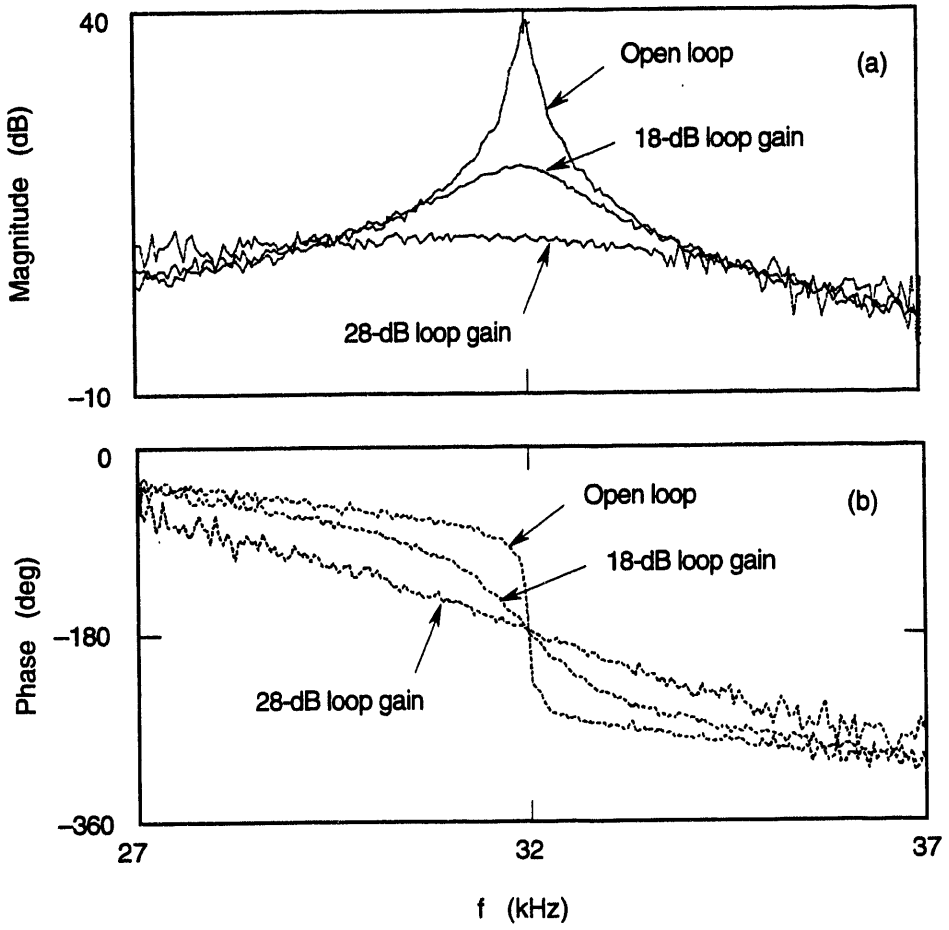

Figure 5-135. Magnitude (a) and phase (b) response for a single bunch for open-loop and for closed-loop gains of 18 and 28 dB. The associated Q factors are 200 (open-loop), 20 (18 dB), and 5 (28 dB).

roughly 200. The natural damping present in this case is due to Robinson damping as well as synchrotron radiation damping. We see in Fig. 5-135 the action of the feedback system to increase the damping and lower the Q of the harmonic oscillator. The configuration with a loop gain of 28 dB barely displays any resonant behavior ($Q = 5$), suggesting that the transient response of the combined system will damp in a few cycles.

5.6.3.2 Time-Domain Studies. The time response of the system can be observed in Fig. 5-136. In this measurement, the feedback loop was opened and a gated burst at the synchrotron frequency was applied via the RF cavity. (The excitation burst drives a growing synchrotron oscillation of the beam.) The excitation was then turned off and the feedback system loop closed. The damping transients of the beam could then be studied for various feedback filter parameters and overall loop gain. This transient excitation simulates an injection condition in which the feedback system must damp a large amplitude oscillation. In Fig. 5-136 we see the damping transient of such a gated burst for

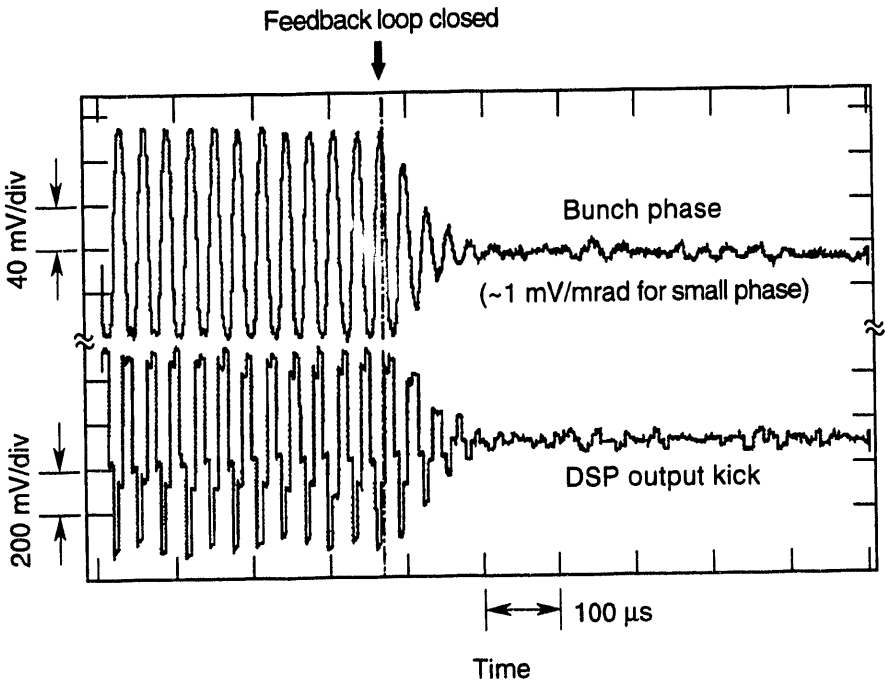

Figure 5-136. Time response of an excited bunch and the associated DSP filter output. The feedback loop is closed at the time of the dotted line in the figure.

a 33-dB loop gain, which provides damping in only a few cycles. The damping time-constant (*e*-folding time) is 2 ms in these experiments in the absence of feedback, while the external feedback damping reduces the damping time-constant to 40 μs. Figure 5-137 shows the damping transient on an expanded scale; the DSP output (down-sampled by a factor of 8) produces a distorted-sinusoid kick signal.

If the system is operated with increased DSP gain, the saturation behavior (output-limiting function) of the digital filter can be observed. To carry out this test, the DSP filter coefficients were multiplied by 16, which causes the DSP filter to saturate on moderate bunch motion. To keep the feedback loop gain (or damping time) consistent with the unsaturated measurements, the feedback error signal driving the cavity phase was divided by 16–24 dB attenuation in these measurements. Figure 5-138 shows such a transient with a saturated kick signal. We see in the figure the peak-limited kick signal during the saturated processing, followed by a very short linear processing interval. The beam completes damping in approximately three cycles, consistent with the damping time for the unsaturated filter at the same loop gain. This result replicates the behavior of the simulation study of Section 5.6.1.8, and shows that the saturated processing does not add extra phase shifts to the correction signal.

5.6.3.3 Noise Performance. To quantify the equilibrium noise performance of the damping system, the equilibrium rms bunch phase was measured at the completion of the damping transient, as was done in the simulation studies of Section 5.6.1.8. Figure 5-139a shows such a driven/damped excitation, while Fig. 5-139b presents the rms phase

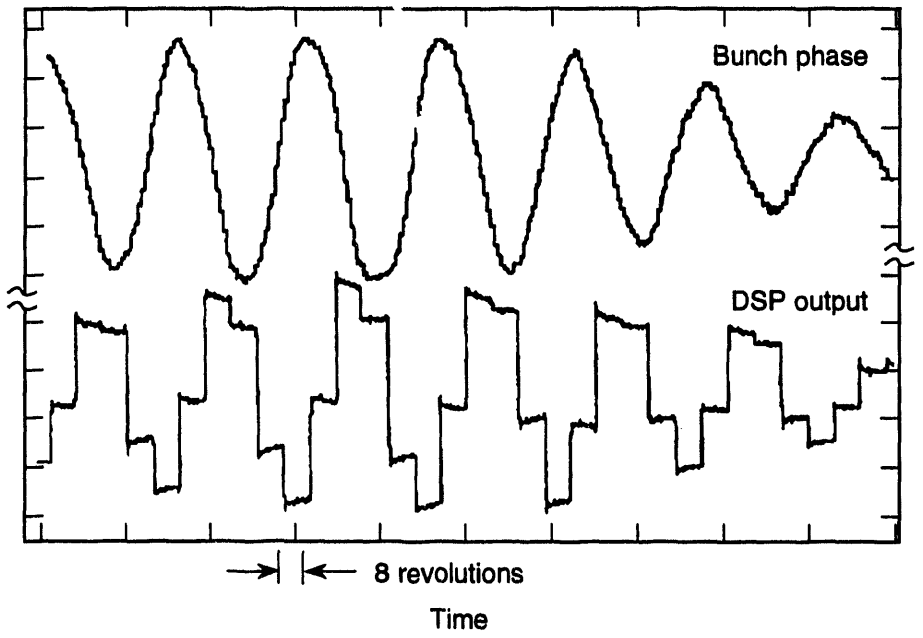

Figure 5-137. Filter input and output (on an expanded scale) during a damping transient for the n = 8 down-sampled filter.

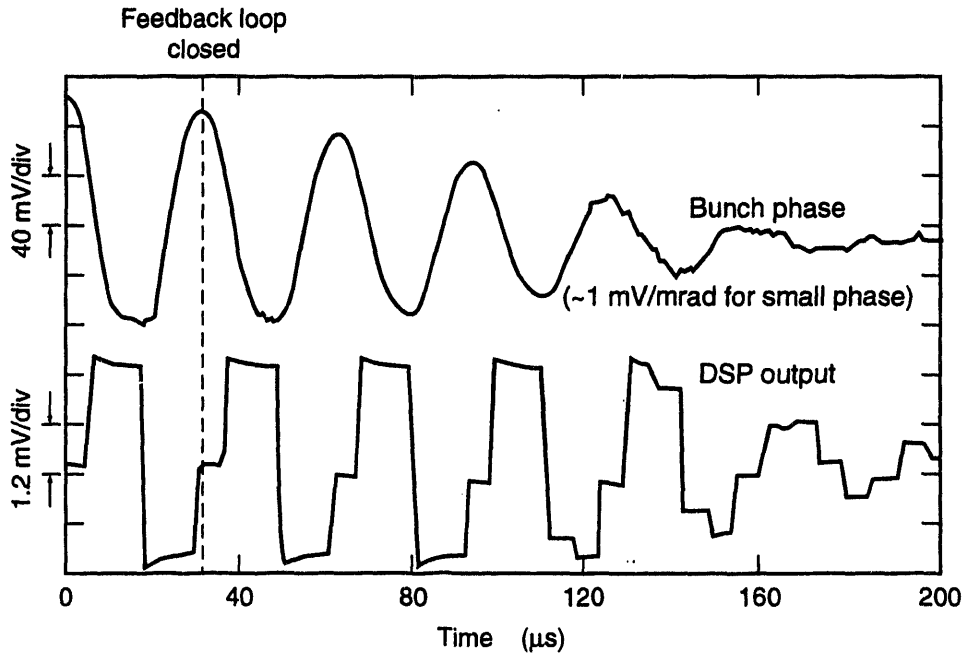

Figure 5-138. Filter input and output for the saturated-gain filter (coefficients multiplied by 16). The linear regime is visible in the last two cycles of the oscillation.

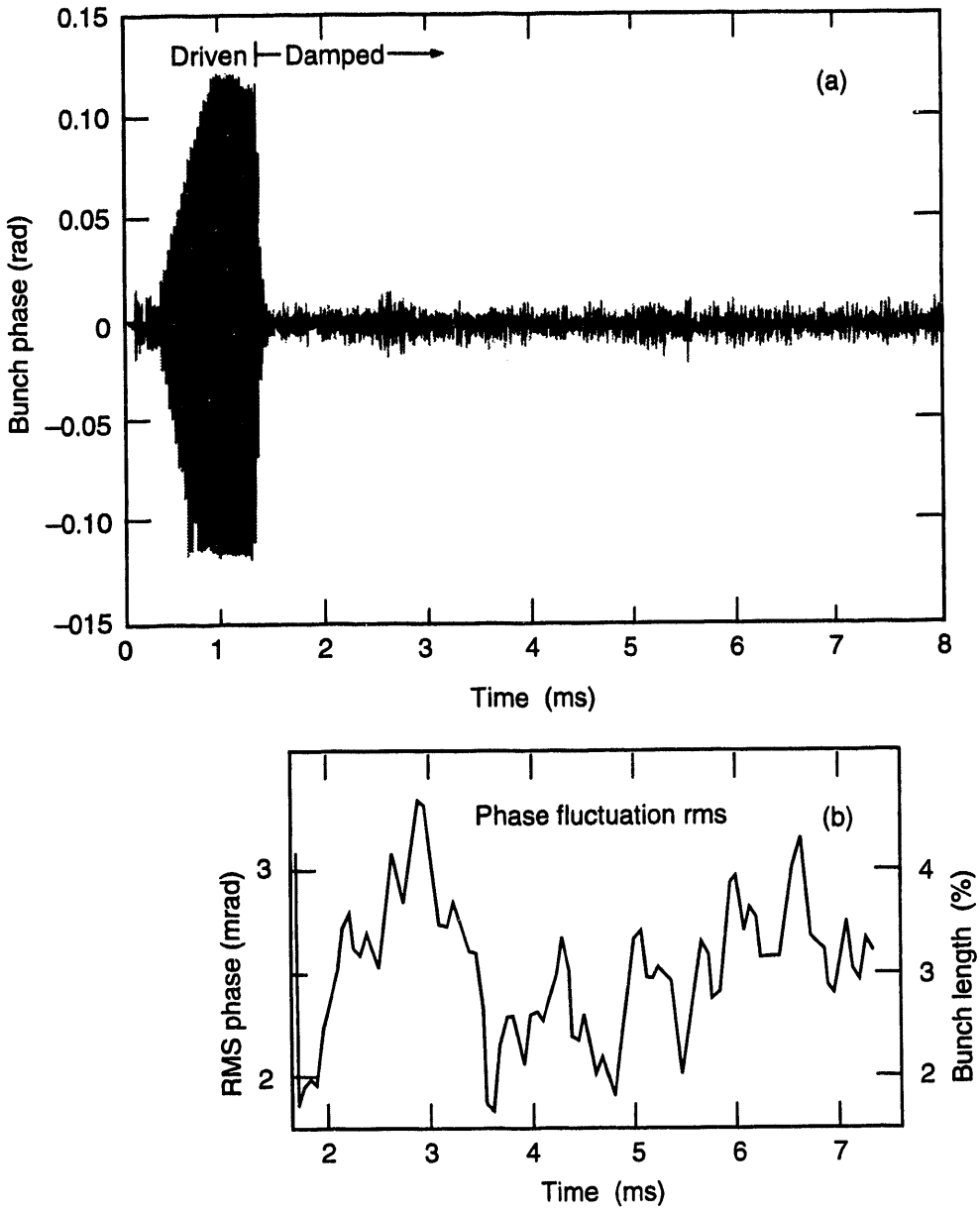

Figure 5-139. (a) Driven burst transient (33-dB loop gain) used to quantify the equilibrium noise of the system. (b) RMS residual noise on the beam for the case shown in (a).

fluctuations of the beam during the final portion of the time sequence. We note that the residual beam phase motion is roughly 2.5 mrad at 358 MHz (3% of the 1.4-cm bunch length), corresponding to a time jitter of 1 ps. The quantization interval for the system as configured at SPEAR was 2.7 mrad. Thus, we have demonstrated that the feedback system acted to damp excitations and noise to within the front-end quantization interval, as predicted by the simulation results.

5.6.3.4 Conclusions from the SPEAR Demonstration. These feedback system measurements, as well as a follow-on study performed on the ALS storage ring at LBL, show the operation of all the essential detection and processing components of the proposed PEP-II longitudinal feedback system. The fast front-end circuits have been demonstrated to operate with the required 4.2-ns bunch spacing, and the digital signal processing filter has been demonstrated for both the linear and the saturated regimes. The overall operation of the system has been shown to be as expected from the machine simulation studies. The measurements give important operating experience and will provide all the necessary information for a detailed design of the PEP-II feedback system components. Most importantly, the experiments validate the essential processing approach and provide a proof-of-principle demonstration of the feedback system performance required for PEP-II.

5.6.4 Conclusions

The proposed detection and processing system has been shown to damp excitations from off-energy injected bunches and from the excitation of HOM resonances in the accelerating cavities. Laboratory measurements of prototype front-end processing and kicker components, as well as operation of a prototype system at SPEAR, have demonstrated performance consistent with PEP-II requirements. The simulation tools we have developed and the simulation results already obtained provide a solid base for the detailed system design and optimization of the longitudinal and transverse damping systems. Finally, and most significantly, the feedback system output power requirements are relatively modest, and the electronics systems are based on existing commercial technology. We conclude, therefore, that PEP-II feedback systems based on the approach outlined here are entirely straightforward.

5.7 INSTRUMENTATION AND ELECTRONICS

Most storage rings are equipped with a standard package of instrumentation and electronics designed to speed up injection, optimize the lattice parameters, monitor the beams orbits, and improve the luminosity. The two rings of PEP-II will be no exception, and a full set of diagnostic tools is planned for each ring.

The injection transfer lines will be monitored with instrumentation similar to that currently used at PEP or at the SLC, namely, stripline position monitors, current monitors (resonant toroids), wire scanners, and injection screens (with TV transmission). Also similar to current PEP hardware will be the tune measurement system (with the addition of an X-Y pinger), a direct-current transformer, stoppers and scrapers, and profile monitors (UV telescope, vertical beam profile x-ray imaging system, and, for single-bunch operation, a streak camera). However, because of the very high bunch frequency, there will be some systems quite different from those now in operation at PEP. These are:

- Beam position monitors (BPMs; button type)

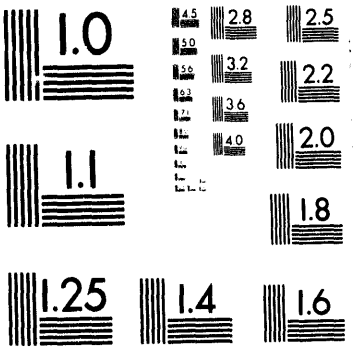
1.0
1.1
1.25
1.4
1.6
1.8
2.0
2.2
2.5
2.8
3.2
3.6
4.0
4.5
5.0
5.6
6.3
7.1

6 of 7

- Bunch-by-bunch current monitor system (for injection control)
- Feedback system to maintain the beams in collision

These last three systems, the third of which is unique to the operation of a two-ring collider such as PEP-II, are described below.

5.7.1 Beam Position Monitors

Each ring contains 144 BPMs, 16 in each of the six arcs and 8 in each of the six straight sections. Signal processing and digitization will be done locally with electronics in the tunnels for the arc BPMs and in the interaction region halls for the straight section BPMs. Each half-arc will contain a rack housing 16 sets of BPM electronics, 8 for each ring. Each half straight section will contain a rack housing 8 sets of BPM electronics, 4 for each ring. Buttons are connected to the processing electronics via matched sets of coaxial cable, the longest sets of which are approximately 60 m. Local processing preserves the signal bandwidth as well as saving on cable plant complexity and cost. PEP and SLC experience indicates that neither reliability nor radiation levels are a problem for such electronics in the tunnel.

The BPM system is required to measure the stored-beam orbit averaged over many turns to a resolution (short-term repeatability) of 20 μm and absolute accuracy of 100 μm in a measurement time of about 1 second. The absolute accuracy requirement is budgeted as 85 μm due to cable plant and electronics miscalibration (added in quadrature with 50 μm of mechanical offset). The resolution and accuracy specifications must be met for beam positions within a 1-cm radius of the center of the beam pipe. The system must be able to measure the orbit of a single small top-off bunch (2×10^9 e^-) injected into the machine with a resolution of 300 μm. Machine studies require that the position of the beam be followed over many successive turns. Therefore, the BPM electronics will be capable of making a position measurement of a particular bunch and storing it in local memory each turn (every 7.3 μs). The BPM electronics will have local memory and the intelligence to set up a measurement, carry it out, and ship the data to the control system when the measurement is complete.

PEP-II BPMs are designed around single-bunch measurements; the most stringent requirements on the BPM system arise from the needs of first-turn injection and of top-off injection. The single-bunch, single-turn mode implies wideband processing. The necessity of measuring one bunch in the presence of many nearby bunches implies fast gating by PIN-diode or GaAs-FET switches in the front-end electronics. Having met these requirements for single-bunch measurements, the stored-beam requirements are satisfied automatically.

The present design calls for independent processing of all BPMs in one ring but multiplexing the electronics between the HER and LER. We will investigate the possibility of multiplexing several sets of BPM signals to each BPM processor as part of the design optimization. Even in the multiplexed case, all buttons of a given BPM would be simultaneously processed so that each measurement corresponds to a single passage of a particular beam bunch.

5.7.2 Bunch-by-Bunch Current Monitor

There are two compelling reasons for wishing to operate each ring with an equal population in all its bunches (with the exception of an unpopulated gap for ion clearing). First, it is possible that the optimization of the beam-beam tune shift will be difficult in the event of nonuniform bunch currents (even though it is desirable to operate with different total currents in the individual rings). Second, equal bunch currents make it easier to control the stability of individual bunches.

This requirement places additional demands on the injection system (see Chapter 6) and suggests that a means of monitoring the intensity of individual bunches is necessary. The two key components of this monitoring system are a fast analog-to-digital converter and a programmable trigger delay generator (see Fig. 5-140). The ADC is a 500-megasample/s track-and-hold circuit, followed by an 8-bit flash converter; both units are now commercially available and sold as a single circuit board. We have evaluated this product in conjunction with the feedback system front-end (see Section 5.6). This circuit can be implemented in a straightforward fashion with 100K-series emitter-coupled logic. With both bunch intensity and bunch address data, the control system should be able to devise any injection pattern and monitor its orderly development by interrupting the injection process at the proper time and shifting the timing to aim at the next desired bucket. The master trigger generator of PEP will be redesigned to accommodate not only the new requirements of input-output address data, but also the new RF frequency.

For the bunch intensity measurement, we expect a resolution of about 1%. (Injection is planned in steps of 20% up to 80% of full intensity, followed by 5% steps; the residual

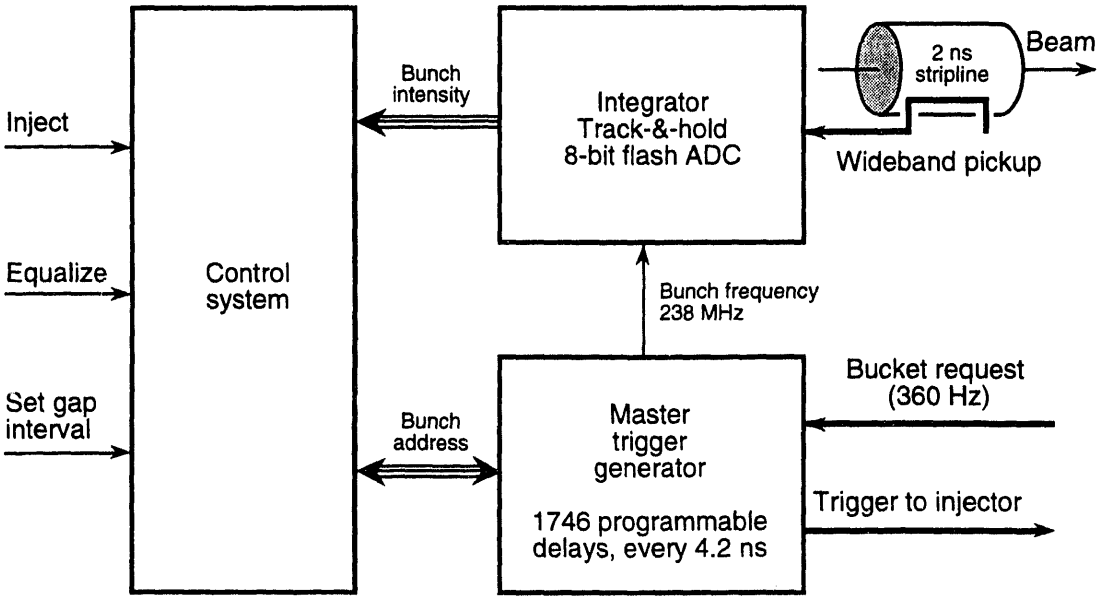

Fig. 5-140. Block diagram of the bunch-by-bunch current monitor. The injector trigger delay is programmed as a function of the bunch address.

imbalance in bunch population will be kept at the 2% level.) We anticipate injection trigger jitter of about 50 ps, comparable to that at PEP; this amounts to a phase error of less than 10° at the RF frequency.

5.7.3 Feedback System to Maintain the Beams in Collision

As part of the design effort for PEP-II, we have studied means of monitoring and controlling the beams in collision. Indeed, residual orbit shifts in both rings will have to be corrected with steering dipoles on each side of the interaction point, for each beam and in both planes. Figure 5-141 depicts an open-loop method of setting these steering dipoles. The hardware normally used for the measurement of the betatron tunes is connected so as to excite one beam and detect the response of the other to this excitation. We expect a strong coupling of the beams when they are colliding; however, this method does not lend itself to automatic control.

Alternatively, the scheme illustrated in Fig. 5-142, involving a rapid count of Bhabha events, could be implemented. Owing to the high luminosity of PEP-II and its relatively low beam energies (the cross section for Bhabha scattering is proportional to $1/E^2$), it should be possible to monitor changes of the order of 1% in luminosity in a few minutes (for instance, at $\mathcal{L} = 10^{31}\ \mathrm{cm}^{-2}\ \mathrm{s}^{-1}$ and a beam energy of 14 GeV, the count rate of the PEP luminosity monitor was of the order of 30 counts per second). We envision a system whereby the beams are brought into collision with the help of a raster scan excitation of the set of steering dipoles for one beam. After freezing the steering dipole settings, the system control is then turned over to a surveillance program. After the detection of a small drop in luminosity, a "miniscan" is initiated and the steering dipoles are reset to optimize the collision rate.

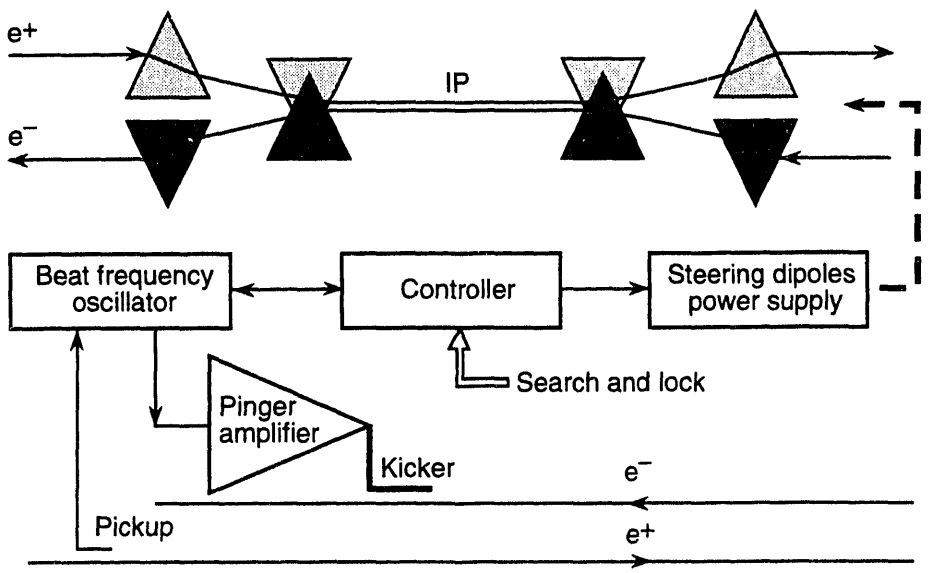

Fig. 5-141. Block diagram of a system for bringing beams into collision, based on the measurement of one beam's response to excitation of the other.

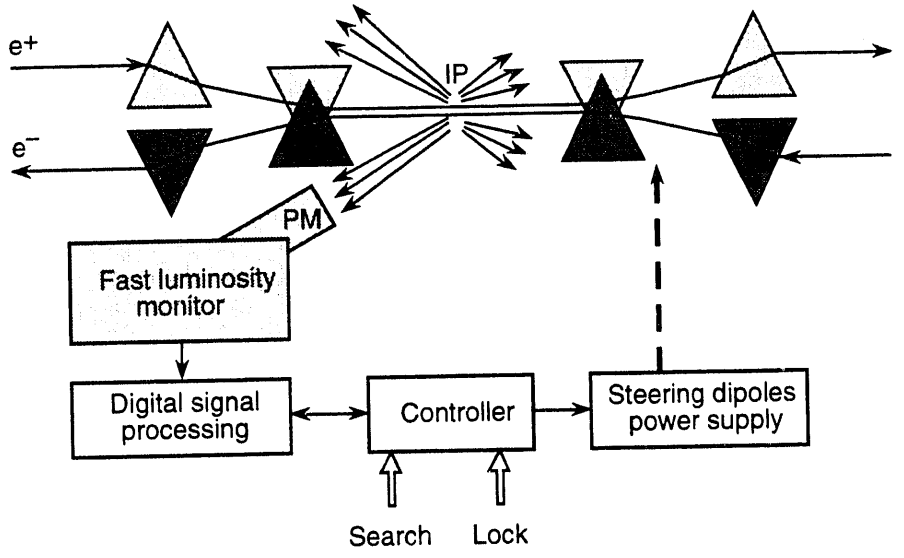

Fig. 5-142. Block diagram of a system for keeping the beams in collision, based on luminosity monitoring.

5.8 CONTROL SYSTEM

The control system for PEP-II comprises two separate systems, one for the linac injector and the other for the storage rings. The two systems are separate but closely integrated, owing to their common architecture and their hardware links.

Since the SLC linac will be used as the PEP-II injector, the control system currently running the SLC facility will be retained essentially unchanged. The two injection lines (for electrons and positrons) will be operated through the SLC control system, using an SLC control console.

The SLC control system distributes control functions among a supervisory mainframe, remote consoles for human interface, and remote microcomputers for actual hardware control. A more detailed discussion of the SLC control system can be found in Phinney [1985] and Phinney and Shoaee [1987].

The control system for the HER and LER will be new, but its design is envisioned to be patterned after the SLC control system (see Figs. 5-143 and 5-144). It consists of a multitiered distributed intelligence system. Supervisory control is provided by a pair of mainframes. Normally, one is used for on-line control and the other for software development and off-line monitoring. However, the second computer can be used as a backup should the primary mainframe go down. This redundancy has proved useful with the SLC and will be even more important in a facility serving as a particle "factory." Multiple workstation consoles, networked to the mainframe, provide the interface that allows operators and machine physicists to control and monitor the machine. Also connected to the mainframe is a group of microcomputers, linked by a separate, dedicated high-speed network. These microcomputers will be responsible for the actual machine-control and data-acquisition functions. The microcomputers will be logically organized

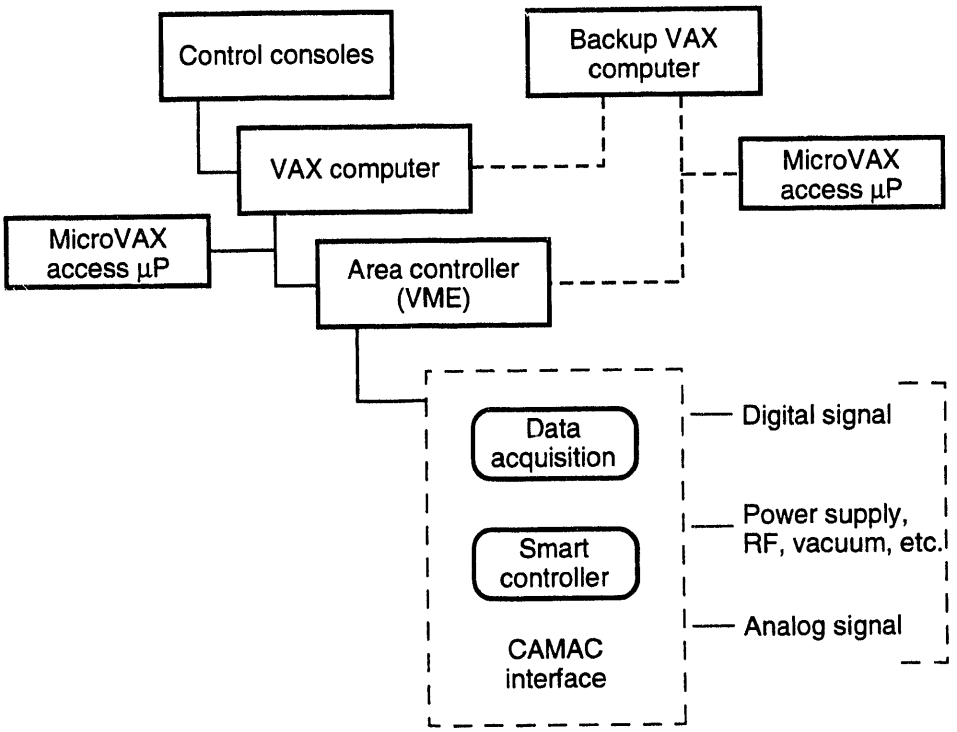

Fig. 5-143. Architecture of the PEP-II distributed control system.

on a geographical, rather than a functional, basis, thus reducing cabling costs and simplifying the software design, given the database structure described below.

The control systems for the injector and the storage rings are linked in two ways. First, the supervisory mainframes of both systems are networked to allow database exchange, hence streamlining coordination of the operating conditions of the two machines. Second, certain time-critical information will be passed directly from injector microcomputers to storage ring microcomputers via data paths already established for the SLC control system.

The storage ring control system will control and/or monitor the power supplies, vacuum system, RF system, beam position and luminosity monitors, machine protection system, and personnel protection system (status only). Based on experience at PEP, we expect this system to handle approximately 30,000 signals. The control of these functions will be governed by a run-time database in much the same way that the SLC control system now operates. The database will contain all the information needed to describe the machine, including control connections, device characteristics (for example, magnetization polynomial fits), and present configuration (for example, magnetic fields). This allows all devices of similar types to be controlled by the same software utilities, with references to different entries in the database. The database, managed by a standard relational database package, will be maintained by PEP-II operations staff.

The database-driven architecture of the control system will also facilitate the use of monitoring and analysis tools already available within the SLC control system. These

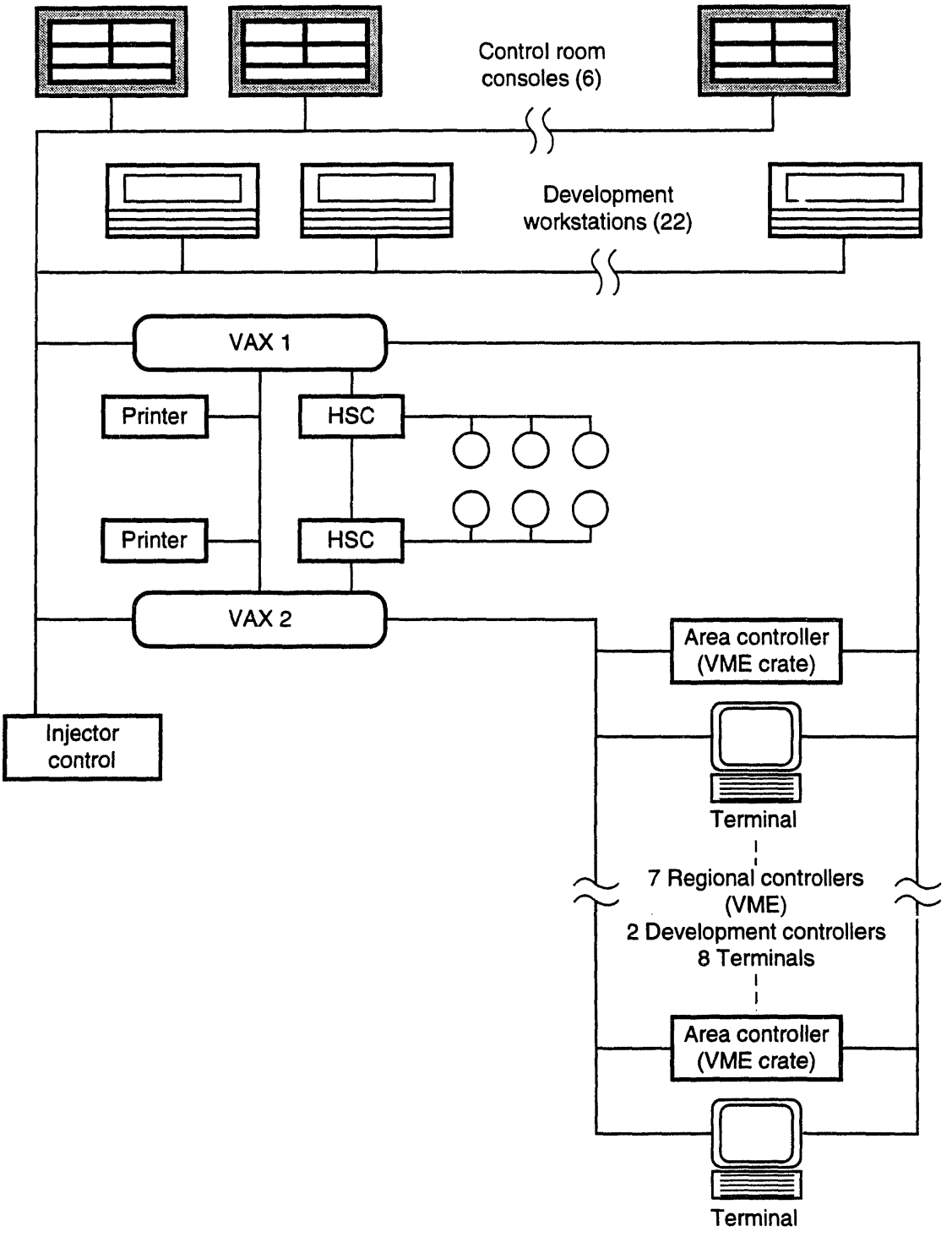

Fig. 5-144. Schematic layout for the PEP-II control center.

include historical data regarding machine conditions and correlation analyses of multiple machine parameters. These tools have proved very important in the commissioning and running of the SLC.

5.8.1 Control Center

5.8.1.1 Consoles and User Interface. The consoles in the control room will be developed in keeping with the philosophy that the operator interfaces must be easy and convenient to use, and must contain graphically presented information rather than a profusion of unprocessed data (see Fig. 5-145). Overview large-screen display systems having color and symbolic representations will be used to monitor machine operating parameters, operational processes and procedures, machine subfunctions, and safety systems.

These facilities will be implemented using industry standard X-Windows graphics systems, so as to separate software packages from the underlying hardware platforms. The hardware will support popular user-interface devices (track-ball, mouse, digitizing pad, etc.) and standard network and connectivity protocols, and will incorporate the flexibility needed to allow future, software-independent development.

The software will take advantage of the graphics facilities to provide symbolic representations of the machine and its elemental components. This approach guarantees that operators and other users get a visual image of the present state of the machine. These facilities will be integrated in such a way as to be independent of the underlying hardware.

The operator-control consoles will be implemented in such a way that multiple operators can work separately or in unison on the same or related machine subsystems

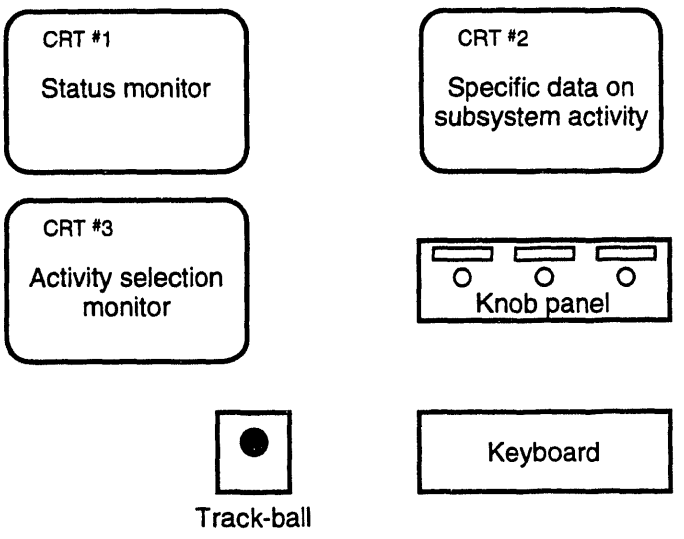

Fig. 5-145. Components of a PEP-II control console.

from identical consoles. This will require two- or three-screen consoles so that operators have a screen for data selection and one or more screens for data or status representation. In addition, summary status displays must be visible around the control room and in remote areas, so that all affected personnel are kept aware of information they need. Some consoles will be located in remote areas to aid commissioning and to provide emergency backup.

5.8.1.2 Database Facility. The database facility includes the data acquisition and control database that describes the characteristics and the operating parameters and limits for all real-time storage ring subsystems. It also includes the server functions that allow noncontrol software to collect and manipulate stored data. The database will be distributed such that local databases maintain and use local data to operate local equipment, whereas critical elements that must be available in multiple databases are broadcast across the entire computer system. This arrangement will minimize data-path bandwidth requirements between operating nodes, while maximizing local data availability, utilization, and manipulation.

These real-time databases will be built up and organized by a readily available relational database that draws on standardized device data structures and device characteristics. This approach will allow automated generation of run-time structures by personnel not familiar with the hardware and will ensure that the proper relationships exist among distributed elements of the database so as to provide updated real-time data to the right software applications on the correct hardware platforms.

5.8.1.3 Model Driver. Accelerator operation and performance will be very closely coupled to a real-time, on-line simulation model of the injector, transport lines, and accelerator optics. This has been done at the SLC, and the same model software can be adapted to the PEP-II environment. The model provides expected values when the machine parameters are changed and provides a diagnostic facility when expected and actual values differ.

5.8.1.4 Program Development Facility. The software development environment will be composed of a second large VAX processor, clustered with the primary control VAX and with limited but compatible access to machine networks and systems. The program development system will have access to the operational database and accelerator facilities via the cluster, and it makes available a backup processor to operate the accelerator if the primary computer fails. This secondary operations role requires that the development machine be of similar size to the on-line machine.

The software will be written in such a way as to be database-driven and layered so that elements of the code or hardware configurations can be changed without complex or extensive rework in the programming. To the extent possible, driver-style interfaces will be used to bridge the system to specific classes of devices or systems so that these elements can be upgraded to keep pace with advances in technology without unreasonable software modifications. Structured analysis and design tools will be used to improve the flexibility, modularity, and reusability of the code, so that generic software can be applied to a wider range of uses. These tools bridge well to modern structured languages, which provide greater software portability across hardware platforms.

Software development will be accomplished on workstations with VAX compatibility. This approach makes it possible to control, test, and debug hardware and software from workstations throughout the VAX systems.

5.8.2 Control Distribution

The control system will have its processes distributed spatially and functionally. The SLC injector will continue to use its own control system and will additionally control the injector beam transport lines, while the PEP-II control system will run the storage rings and their associated equipment. Functionally, the control processes will be distributed across the master VAX cluster, the remote microprocessors, and the smart controllers in the power supplies and RF systems. The VAX cluster will deal with the user interface, user analysis and data manipulation, network control, and the run-time database for all physical devices in the system. The remote microprocessors will be responsible for data acquisition and control forwarding. The smart device controllers will deal with functional control, backup safety monitoring, and calibration of the individual devices. The processors will be linked by standard networks or custom high-speed communication links, depending on their functions. This will allow functionality to be pushed down to the level where the actual control takes place or where data are manipulated.

5.8.2.1 Computers. The centralized computer will be a large VAX-cluster paired processor, with shadowed disks for redundancy and speed. This machine will be a multiple-processor machine with 100 megabytes of main memory. The remote microprocessors will be 32-bit diskless processors with hardware math support and approximately 4 megabytes of main memory. These units will be RAM based and will receive their systems and database-executable images from the centralized cluster or the network server, depending on the final detailed design. These units could be RISC- or CISC-based processor architectures, depending on the technology available at the time.

The device controllers will be relatively simple and can be implemented with highly integrated controller-oriented chips in either an 8- or 16-bit architecture. The controlling factor in this case will be the availability of software development and maintenance environments.

5.8.2.2 Networks. To the extent possible, general-purpose networks employed at the higher levels of the system will be standard "off-the-shelf" facilities to enhance connectivity and maximize flexibility. These networks, which could be implemented with Ethernet, are consistent with the notion that intelligence should be located where it can be useful, then laced loosely throughout a network.

Special-purpose networks will be required in some data paths, owing to particularly large data bandwidths or requirements for very fast response times. Systemwide networks will be implemented on fiber optics using standard T3 technology, while fast point-to-point links will be established with custom protocols on top of readily available transport hardware. These connections will exist at multiple levels: between large machines, between microcomputers, and between microcomputers and mainframes.

Standard networks utilize standard software, supported industry-wide across hardware platforms, and they are also layered so that the systems in general are extensible. Current technology provides a wide range of server and network-bridge functionality to permit the intelligence centers to operate at the subsystem level, without overloading the network bandwidth.

5.8.2.3 Device Interface. Device interfaces will be implemented around a layered, driver-oriented architecture, so that functional software can relate in a standard way to the driver, thus requiring no interaction or detailed familiarity with the actual physical devices. This approach will allow the use of more generic software and will allow the hardware specifics to change as the technology evolves. The system architecture will involve smart control nodes or clusters around the machine, tied to relatively less smart input-output facilities located adjacent to the equipment being controlled or monitored. Standard data conversion cards, bus structures, and communications facilities exist to support this approach.

5.8.2.4 Timing Systems and Synchronization. Software currently exists in the linac control system to operate the injector and the transport lines to the rings Synchronizing injector beams with the fill timing of the rings will be straightforward. The timing required for kickers and BPMs already exists. Although there is no need for timing and frequency control to ramp the energy of the rings during operation (because the beams are injected at full energy), provision must be made in the system design to allow slight energy changes to tune to the exact $\Upsilon(4S)$ energy. This capability requires a facility to synchronize the remote microprocessors and their associated control crates.

5.8.2.5 Access Procedures. Machine configuration changes, made before and after access is permitted to the machine structures and tunnels, will be controlled from the machine control rooms. This access control system will monitor and manage the hardware Personnel Protection Systems, although it will not supplant the hardware for that protection interlock system (see Chapter 8).

Specifically, the computer-controlled ring access control systems will manage the ramp-up, ramp-down, standardization, and calibration tasks associated with turning equipment off or returning it to ready status. These processes will also keep track of personnel in the tunnels during limited access periods to minimize the equipment restoration necessary for turn-on. The processor responsible for this function will be slaved to the database and control activator paths, but will be a separate physical processor, so that the main computer system can be repaired or tested without losing lockup security throughout the facility.

5.8.3 Special Control Zones

5.8.3.1 Injector. There will be two beam transport lines from the injector to the rings, one line for electrons and one for positrons. Both lines will require large numbers of quadrupole and trim magnets for optical changes and steering. All these will be controlled by existing microcomputers in the SLC control system.

5.8.3.2 Interaction Point. The interaction point requires controls to handle the focusing magnets and trim coils, as well as some fast-feedback control software to maintain the beam spots at the maximum luminosity. The feedback control loops will run on an interaction area microprocessor and will implement the beam-on-beam scans to measure the beam size, as well as control the beam wiggler magnets to keep the beams in collision at maximum luminosity.

5.8.4 Control System Functionality

5.8.4.1 Problem Reporting. Fault reporting and management will be configured so that the systems identify and report the specific device that failed or indicated an unsafe condition. These faults will be monitored by a separate machine protection system (MPS) that is capable of shutting down the system. Recovery from fault conditions will be automatic.

Diagnostic panels will display equipment or computer system problems through the MPS or computer error log system and will be linked to the run-time database, so that the device or system is correctly identified and located, and the faulty characteristic or parameter described. Such faults can be automatically logged into the existing CATER maintenance-reporting system as well. This system, developed for the SLC, will be responsible for logging and cataloging faults, the urgency of repair, and the responsible support groups. This system will help ensure that support and maintenance work is done on a priority basis and that problems are not lost, only to be rediscovered later.

5.8.4.2 Data Collection and Retention. As part of the PEP-II control system, history buffers will sample device status on a periodic basis, so that the configuration and status of the machine can be reviewed in detail later. Configurations can be archived for all or parts of the machine so that the machine can be restored to a known state and optimal orbits replicated.

5.8.4.3 Data Analysis. History plot facilities will be used to review trends or specific events over time. Such facilities are useful in correlating faults, detecting the onset of problems, and identifying optimal operational configurations. Correlation plot facilities will be used to correlate a wide range of data elements with one another to learn more about the interrelationships of machine parameters.

6.

INJECTION SYSTEM

THE basic method proposed to fill the PEP-II rings with electrons and positrons is to use the first two-thirds of the SLC linac, including its damping rings and positron source. Given that the PEP-II luminosity lifetime will be about two hours, our goal will be to top off both rings about once per hour, and to complete the top-off injection cycle for both electrons and positrons in about 3 minutes. As will be shown below, the SLC linac (with a few modifications and simplifications) is very well suited for this function.

By the time PEP-II is operational, it is envisioned that the SLC will have completed its Z^0 experimental program and thus will no longer be operated in its e^+e^- collider mode. It is probable that the linac will still be used for physics to supply 50-GeV e^- beams for fixed-target experiments in End Station A and/or for accelerator R&D for the Next Linear Collider (NLC), which involves the Final Focus Test Beam (FFTB) as well as other projects now in the planning stages. It is thus worth noting that the modifications discussed here for the PEP-II injection system do not preclude such uses. Furthermore, the so-called Nuclear Physics Injector (NPI), located at the beginning of linac Sector 25 and capable of producing 2- to 10-GeV e^- beams at the end of the linac, will be operable simultaneously with the PEP-II injection system on a noninterfering basis.

6.1 OVERALL APPROACH AND SPECIFICATIONS

The basic approach adopted for the PEP-II injection system is illustrated schematically in Fig. 6-1, and the overall injection specifications and relevant parameters are given in Table 6-1.

A fundamental simplification in operation compared with the SLC results from the use of two bypass lines—one for nominally 3.1-GeV positrons, the other for nominally 9-GeV electrons. These positron and electron bypass lines start at linac Sectors 4 and 8, respectively, and run to the end of the linac at Sector 30, where they connect to the existing South Injection Transport (SIT) and North Injection Transport (NIT) injection lines leading to the PEP-II tunnel. Because the beams are extracted at their correct energies from early points along the linac and never reenter it, problems of emittance

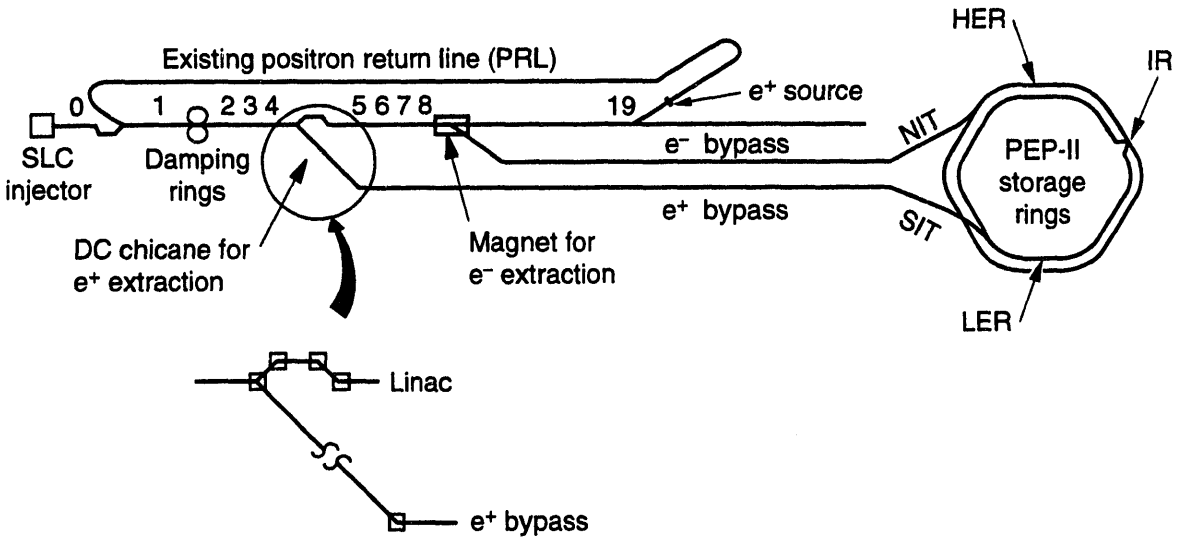

Fig. 6-1. Schematic of the PEP-II $e^{\pm}$ injection system, based on use of the SLC linac with bypass lines. The numbers along the linac indicate the location (not to scale) of each sector. Each of the 30 sectors is 100 m long.

growth and instabilities from wakefields in the disk-loaded waveguide structure are minimized and will not be an issue. An additional advantage of our approach is that it eliminates the need for a compromised transport lattice and for beam deceleration, unattractive features of the PEP injection process in the late 1980's, when PEP and SLC operations were interleaved. (The compromised lattice and beam deceleration were necessary in that scheme to maintain positron production with a 30-GeV beam at Sector 19.) In the PEP-II design, the linac is still used up to Sector 19 for positron production. That portion of the linac downstream of Sector 19 would still be available to provide high-energy beams for other uses, but will be turned off for normal PEP-II operation.

As discussed in Section 6.2, the two bypass lines (consisting of parallel and independent FODO arrays) are located above the existing linac, suspended in the tunnel just below the ceiling (much like the existing Positron Return Line, PRL, from Sector 19). The existing NIT and SIT lines will undergo only minor modifications (see Section 6.3). Injection into the high- and low-energy rings (HER and LER, respectively) will take place in the long straight sections (see Section 4.1) of IR-10 (e^-) and IR-8 (e^+). For both the HER and LER, injection will take place in the vertical plane, utilizing a combination of DC bumps and pulsed kickers. The decision to adopt vertical injection was a complex one; as discussed in Section 4.4, it was based on avoiding the increase in beam size that horizontal injection would produce due to the parasitic beam crossings near the IP. Because of the constraint from the parasitic crossings, there is more room for vertical injection than for horizontal. We note, however, that it is the low emittance of the damped SLC beam that is key to taking advantage of the vertical injection option.

The linac configuration proposed here was selected after considering other alternatives, including (i) using only the last one-third of the linac and building a new in-line positron source, (ii) using the NPI for electrons only, while using the SLC for positrons, and (iii) keeping a system very similar to the one previously used to fill PEP

Table 6-1. PEP-II injection specifications and parameters.

Beam energy	
High-energy ring (e^-) [GeV]	9 [range: 8–10][a]
Low-energy ring (e^+) [GeV]	3.1 [range: 2.8–4]
Beam current	
High-energy ring[A/10^{10} e^-]	0.99/4518
Low-energy ring [A/10^{10} e^+]	2.14/9799
Particles per bunch	
High-energy ring [10^{10} e^-]	2.7
Low-energy ring [10^{10} e^+]	5.9
Linac repetition rate [pps]	60 or 120
Linac current [10^{10} $e^\pm$ per pulse][b]	0.1–3
Invariant linac emittance [m·rad]	
Horizontal	4×10^{-5}
Vertical	0.5×10^{-5}
Normal filling time[c]	
Topping-off (80–100%) [min]	3
Filling time (0–100%) [min]	6
Ring circumference [m]	2199.318
Revolution period [μs]	7.336
Revolution frequency [kHz]	136.311
Bunch frequency [MHz]	476/2 = 238
Time between bunches [ns]	4.20
Harmonic number	3492
Number of bunches[d]	1746 – 5% = 1658
Vertical damping time	
High-energy ring [ms]	38
Low-energy ring, with wigglers [ms]	40
Low-energy ring, without wigglers [ms]	68
Nominal beam emittance [nm·rad][e]	
High-energy ring, horizontal/vertical	48/1.9
Low-energy ring, horizontal/vertical	64/2.6

[a]The present e^- extraction location has sufficient klystrons to provide a beam energy in excess of 12 GeV.

[b]The SLC routinely delivers 3×10^{10} e^+ and 3×10^{10} e^- per bunch on each linac pulse.

[c]Electron and positron bunches are injected on alternate pulses at 60 pps, in which case both rings can be topped-off in 3 minutes.

[d]For filling purposes, the rings will be divided into nine zones of equal length. The 5% gap leaves one zone partially unfilled.

[e]Storage ring emittances are quoted here, and elsewhere in this document, as unnormalized, or geometrical, values.

when its operation was interleaved with that of the SLC, where the low-energy $e^{\pm}$ beams (2.8–10 GeV) are obtained by deceleration downstream of Sector 19. Some of the reasons for ultimately rejecting these alternatives include:

- A new positron source would be very costly and would complicate the transmission of SLC-type beams to the Final Focus Test Beam or End Station A.
- NPI-type beams downstream of Sector 19 (electrons only) would either have bunch currents lower by two orders of magnitude (that is, about 10^8 electrons per bunch) or would require upgrading the NPI to SLC standards—a costly operation that would not, in any case, yield an SLC-quality beam emittance due to the absence of the damping rings in this scenario.
- Multibunch electron injection, that is, with a train of bunches 4.2 ns apart would only pay off if the linac were not operated with SLED, so that a long pulse train of at least 200 bunches (about 840 ns) could be accelerated and stored. This would require a costly move of the NPI to about Sector 20 to obtain the required electron energy and would mean tying up that entire part of the linac solely for this purpose. Furthermore, this approach would not permit single-bunch electron filling and would make the electron injection scheme very different from, and less flexible than, positron filling—an undesirable feature per se. Finally, this filling method is less desirable for the storage ring feedback systems, which benefit from a scheme in which the injected beam comes in small increments, as discussed in Section 5.6.
- Using the SLC in the interleaved "PEP-SLC" filling mode would have all the disadvantages of backphasing the latter part of the linac and simultaneously having to handle beams of 3.1 and 9 GeV of opposite charges. Such a scheme would not work for 3.1-GeV beams and is likely to be very marginal even at 9 GeV.

A slightly less costly implementation for the proposed bypass scheme might be to use a single, common line for both positrons and electrons beyond Sector 8. Such a scheme could be made to work with a weaker focusing system for the electrons but with twice as many correctors and beam position monitor (BPM) electronic processing systems. Moreover, it would require a second chicane at the Sector 9 junction point, larger aperture quadrupoles and BPMs, and a method of separating the unequal-energy beams at the end of the linac into the NIT and SIT lines. These complications would likely lead to operational difficulties arising from steering and instrumentation problems. The resulting compromises would almost inevitably lead to inefficiencies and an overall decrease in the robustness of the injection system.

After considering the various scenarios, we adopted the more flexible and reliable scheme described here, with independent bypass lines. As outlined in Section 6.7, the optimum injection pattern involves "topping-off" the rings approximately once every hour, so the operational benefits of having a robust injection scheme are extremely important for maintaining the high integrated luminosity required of PEP-II.

As shown in Table 6-1, the bypass lines are presently optimized for an energy range of 2.8–4 GeV for positrons and 8–10 GeV for electrons. When filled to the nominal operating point (corresponding to the design luminosity of 3×10^{33} cm^{-2} s^{-1}), the LER will have a current of 2.14 A, or roughly 6×10^{10} positrons per bunch, and the HER will have a current of 0.99 A, or about 3×10^{10} electrons per bunch. The normal topping-off

operation will consist of delivering roughly 10^{10} particles to each of the 1658 bunches in each ring. For each bunch, this will be accomplished in five (nonconsecutive) linac pulses, at a rate of 60 pps. At present, the SLC routinely delivers 3×10^{10} electrons and 3×10^{10} positrons per pulse to the arcs. It will be straightforward to deliver less than one-fifth of this charge per pulse to the PEP-II rings. At 60 pps (interleaved) and an overall 75% filling efficiency for both e^- and e^+, the filling operation should take $(1658/60) \times 5 \times (1/0.75) = 184$ seconds, or about 3 minutes.

When filling from zero current (empty rings), the linac will deliver roughly 10^{10} $e^{\pm}$ per pulse, and all of the 1658 bunches will be filled to about 80% of their final charge. This operation will also take about four or five linac pulses, or about 3 minutes, to fill both storage rings to 80% of design current; an additional 3 minutes will then be needed to top-off, giving a total filling time of about 6 minutes.

Another great simplification in the injection process results from choosing a storage ring RF frequency of 476 MHz (that is, exactly one-sixth of the 2856-MHz linac frequency). The drive system along the 3-km linac already operates at 476 MHz, and extending it to PEP-II (or vice versa) will be straightforward. With this choice, all the key RF frequencies (the damping rings at 714 MHz, the linac at 2856 MHz, and the two collider rings at 476 MHz) will be harmonically related. For proper spacing around the rings, every second RF bucket is filled, giving a bunch repetition frequency of 238 MHz (i.e., a 4.2-ns bunch separation). With a harmonic number of 3492 ($= 2^2 \times 3^2 \times 97$) and a 5% gap for ion control, there will be 1658 filled buckets. As explained later, for filling purposes each ring will be divided into nine equal "zones" (194 buckets per zone), one of which will be left half empty to avoid ion trapping in the HER. By filling the bunches in sequential zones, the time that elapses between each individual bucket fill will be 27.6 seconds. More importantly, with this scheme no injected bunch would again experience the full kick from the injection kickers for about 150 ms, allowing ample time for coherent injection oscillations to damp (see Section 6.6).

6.1.1 Injection Energy Spread and Beam Size

The momentum spectrum of the linac 3.1-GeV positron beam or 9.0-GeV electron beam depends on a number of factors:

- The charge distribution in the bunch extracted from the damping ring, including the effect of intensity-dependent bunch lengthening (due to longitudinal wakefields)
- The momentum spectrum of the beam extracted from the damping ring, including effects of longitudinal wakefields
- The adjustment of the bunch compressor, which reduces the bunch length and increases the uncorrelated energy spread by the same factor
- The average phase of the bunch relative to the RF in all linac sections in which the bunch is accelerated
- The short-range longitudinal wakefields in all the structures through which the beam passes (dominated by the wakefields in the accelerator structures)

- The phase and momentum jitter of the beams extracted from the damping rings
- The phase jitter of the compressor klystron and all of the klystrons used to accelerate the beam, which determines the pulse-to-pulse momentum jitter of the beams injected into the PEP-II storage rings

We have developed a program at SLAC for analyzing the longitudinal phase-space distributions of the SLC beams that simulates all of these contributions except for the phase jitters listed in the last two points above. This program has been used to simulate the spectra expected for PEP-II beams. We find that the spectrum of the positron beam is broader than that of the (higher-energy) electron beam, because the uncorrelated energy spread coming out of the bunch compressor is a larger fraction of the full energy spread. In order to minimize the energy spread of the e^+ beam, we have considered two possible adjustments of the phase of the positrons relative to the phase of the RF in the linac for the high-intensity case of 2×10^{10} particles per pulse.

Figure 6.2a shows the results of the first approach, which attempts to optimize the charge within a 1% full-width momentum spectrum. The result is a quite rectangular momentum spectrum that is about 1% wide (FWHM) and has 92% of the charge in ±1%. The trouble with this choice of optimization is that the transmitted charge will be quite sensitive to energy jitter. From SLC experience, we know that the energy jitter will be about 0.1%, dominated by the phase jitter of the compressor klystron. For this strategy, which optimizes the charge transmitted, a 0.1% energy jitter gives almost 10% intensity jitter.

This unpleasant result led to another optimization strategy. Figure 6-2b shows the result of moving the bunch closer to the accelerating crest. We find a more Gaussian-shaped momentum spectrum, for which 88% would be transmitted through a 1% momentum slit. Compared with the first approach, the intensity fluctuations due to energy jitter are reduced by about a factor of three.

Figure 6-3 shows the momentum spectrum for the electron beam. The 9-GeV electron beam shows only a minor intensity variation problem. This is because the adjustment for nearly maximum transmission through a 1% slit produces a double-spiked momentum spectrum having 0.7% FWHM and with 97% of the charge within a 1% full width.

To define the energy spread of the beam and the beam size from the linac, sets of energy and beam-size collimators will be installed in each of the transport lines. These collimators will shadow the ring acceptance apertures, thus preventing unnecessary beam loss in the rings themselves. A set of two energy-defining slits will be located 90° apart in phase in the dispersive region of the extraction lines, downstream of the BPMs that are used to measure, and control with feedback, the beam energy and initial trajectory launch into the extraction lines. A pair of *x-y* collimator jaws, again separated by 90° in phase, will be located in each transport line for the purpose of defining the transverse acceptance aperture of the ring injection system. A second pair of *x-y* collimators will be located downstream of the first set for the purpose of secondary collimation, that is, to clean up the halo generated by the primary energy and transverse collimators. The separation of these cleanup sets of collimators is again nominally 90° in phase. The existing energy-defining slits, located in the NIT and SIT lines, will be preserved and used for redundant

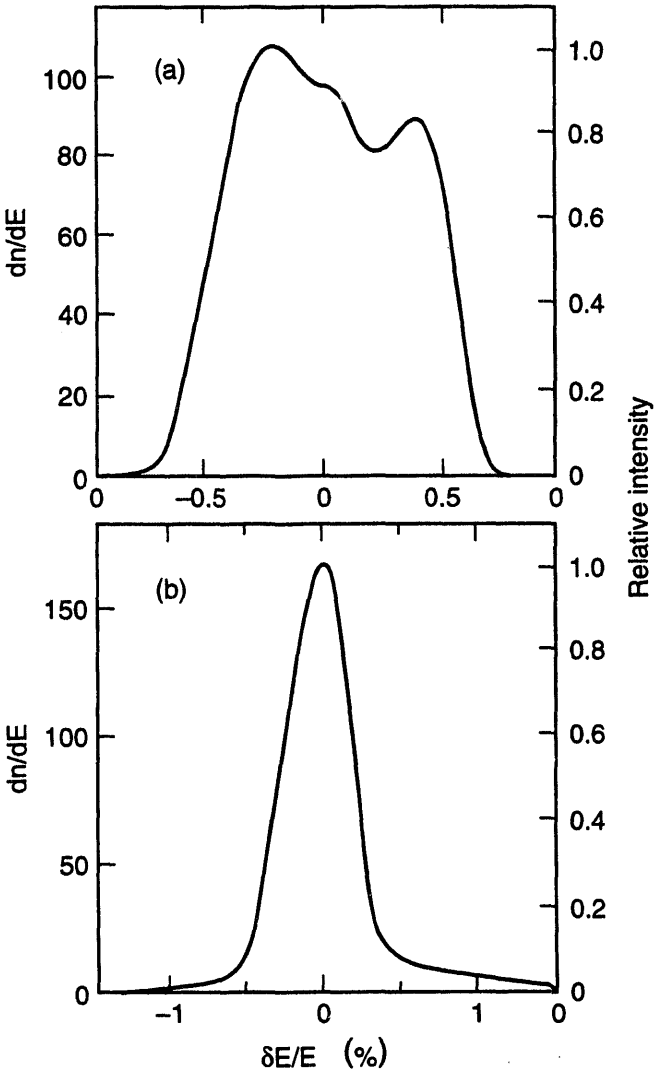

Fig. 6-2. (a) Momentum spectrum for the 3.1-GeV positron beam with $N_{e^+} = 2 \times 10^{10}$ per pulse, resulting from an attempt to optimize the charge within a 1% full-width momentum spectrum. This spectrum is 1% wide (FWHM) and has 92% of the charge in ±1% in momentum. For this spectrum, a 0.1% energy jitter gives almost 10% intensity jitter. (b) Momentum spectrum for the 3.1-GeV positron beam with $N_{e^+} = 2 \times 10^{10}$ per pulse, resulting from an approach that moves the bunch closer to the linac RF accelerating crest. A more Gaussian-shaped momentum spectrum results, for which 88% would be transmitted through a 1% slit. The intensity variation due to energy jitter is reduced by about a factor of three (to 3–4%) compared with the result in (a).

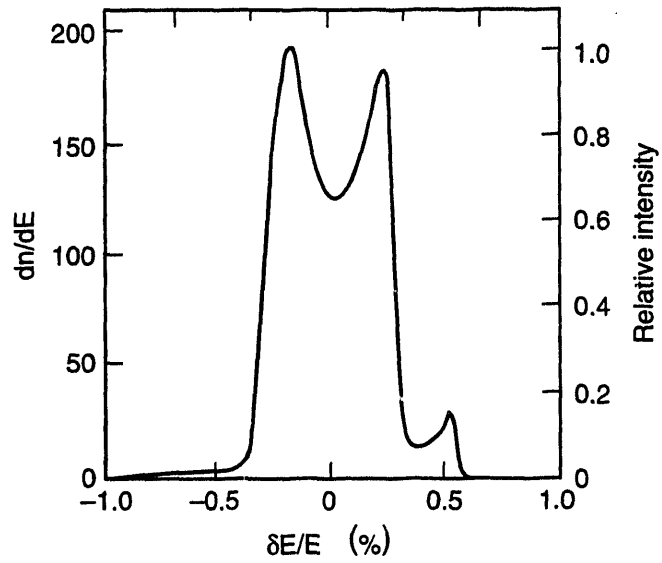

Fig. 6-3. Momentum spectrum for the 9.0-GeV e⁻ beam with $N_{e^-} = 2 \times 10^{10}$ per pulse, resulting from the adjustment of phase for almost maximum transmission through a 1% slit. This produces a double-spiked spectrum having 0.7% FWHM that contains 97% of the charge within a ±1% momentum aperture. The intensity variation due to energy jitter is a minor problem in this configuration.

energy collimation. In addition, this collimation is envisioned to be used in defining a so-called "pencil beam." The pencil-beam concept will be useful during the commissioning stages to aid in the diagnosis of potential ring acceptance issues.

All of the collimator jaws will be remotely adjustable with a repeatability of about 30 μm. The design of the adjustable SLC linac collimators is more than adequate for this job in terms of power-handling capability and adjustability/setability. An engineering study will be made to see if a simpler set of collimators could be adapted from the existing design. BPMs and steering dipoles will be incorporated into a standard launch-control feedback to stabilize the beam trajectory through the collimators.

6.1.2 Beam Dump

A pulsed beam dumper (kicker magnet and water-cooled dump) will be located near the end of each transport line. The availability of such a system allows suppression of beam injection into the rings while preserving the steady-state operation of the injection complex. This feature is required during tuneup and diagnosis of the injection beams and is also needed for the selective dumping of bunches during top-off mode. The system will also be used during automated filling to generate the ion-clearing gap in the stored bunch pattern and will be incorporated into the machine protection system. The present design calls for a 120-Hz pulsed magnet capable of deflecting a 10-GeV beam by about 40 mrad. The installations in both the electron and positron lines will be identical, even though the beam energies and beam power requirements are different, to reduce

engineering and fabrication costs and to ensure that required spare components will be suitable for either system.

In the following sections, we describe in more detail the elements of the proposed injection system.

6.2 LINAC EXTRACTION AND TRANSPORT TO NIT AND SIT

As illustrated in Fig. 6-1, positrons will be extracted from the linac near the beginning of Sector 4 and electrons near the beginning of Sector 8. These choices provide considerable latitude in obtaining the desired energies, as the linac can provide roughly 1.8 GeV per sector with SLED. When operating at the nominal PEP-II design energy, there will be eight spare klystrons in Sectors 2 and 3, and another eight spare klystrons in Sectors 4 through 8. At each extraction point, some accelerator waveguide sections will have to be removed to provide space for extraction magnets. The existing linac quadrupoles, which are spaced 6.4 and 12.7 m apart in Sectors 4 and 8, respectively, will not be disturbed. After extraction, the beam will traverse the length of either the positron or electron bypass line (2.6 and 2.2 km, respectively). The bypass lines will be connected at their downstream ends to the existing NIT and SIT lines, which transport the beams to the injection points of their respective rings.

6.2.1 Sequence of Operation and Extraction Methods

The method used to extract the desired beam from the linac will be different for positrons and electrons. In the positron case, the extraction method takes advantage of the opposite charges of the beams to provide differing transverse deflections in DC magnets, whereas, in the electron case, separation of the like-charge beams requires transverse deflection by means of a pulsed magnet (having a relatively slow rise time of several milliseconds).

To understand how these extraction methods fit in with the operation of the linac for PEP-II injection, it is helpful to understand how the linac currently operates for SLC and then how this operation will be modified for PEP-II.

The pulse sequence for the present SLC operation is shown in Fig. 6-4a. Two electron bunches and one positron bunch are accelerated during each linac macropulse. The first two bunches are used for the electron-positron collisions in the SLC arcs, while the trailing "scavenger" electron bunch is used to create the positron bunch for the next pulse. To accomplish this, at 60 or 120 pps, Sectors 2 through 30 are pulsed essentially simultaneously (with just enough delay to synchronize them with the 10-μs overall particle transit time) and Sectors 0 and 1, upstream of the damping rings, are pulsed roughly 12 μs later to receive the positrons generated at Sector 19, which return to the injector via the PRL.

At Sector 1, these returning positrons, along with two new electron bunches out of the gun, are accelerated up to 1.2 GeV, after which each bunch is injected into its appropriate damping ring (electrons to the north and positrons to the south). After a few milliseconds (the exact time depending upon the pulse rate), the bunches for the next pulse are extracted from the damping rings. Although there is only one positron bunch to be

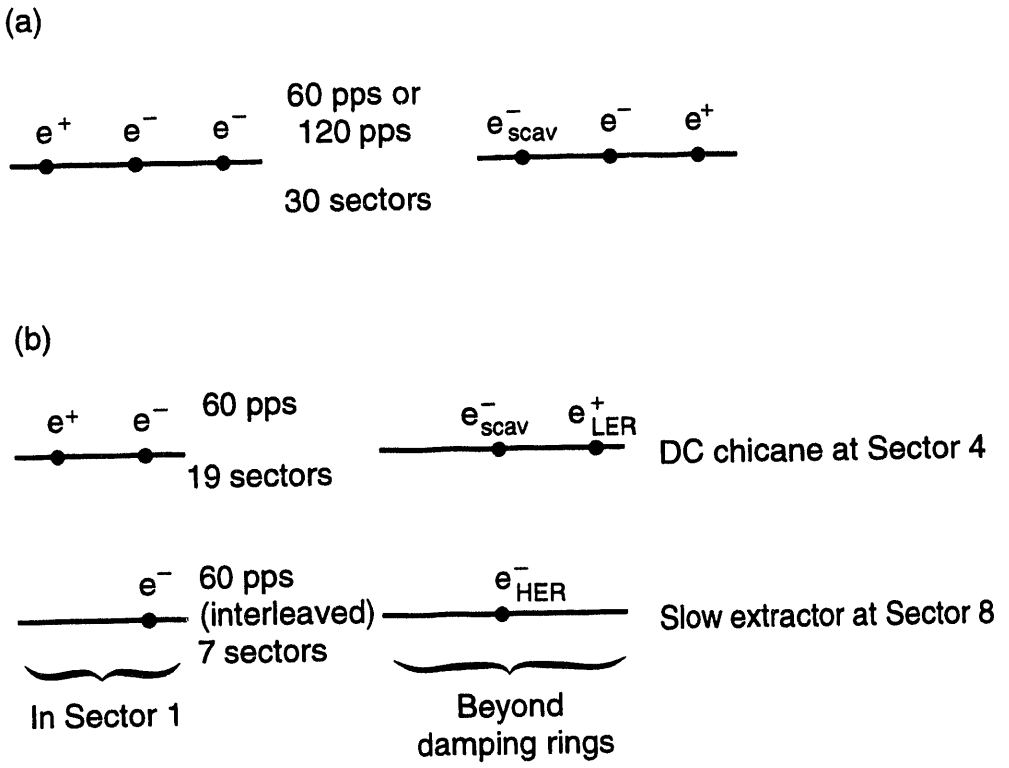

Fig. 6-4. Linac pulse and bunch sequence for (a) typical SLC operation and (b) injection into PEP-II.

extracted from the south damping ring, two bunches of electrons need to be extracted from the north damping ring; this leads to difficult kicker requirements—a fast rise time of a few nanoseconds coupled with a long flat-top. In Sectors 2 through 19, the positron bunch comes first, followed approximately 60 ns later by the first electron bunch and another 60 ns later by the second electron bunch. At Sector 19, the second electron bunch is redirected by a pulsed magnet (again having a very fast rise time of a few nanoseconds) and a Lambertson septum to the positron alcove, while the first electron bunch continues to be accelerated in the linac and eventually goes on to the SLC north arc.

In Sectors 0 and 1, the order of the bunches is inverted (for beam-loading reasons) and the newly generated electron bunches from the injector gun are placed ahead of the positron bunch returning from the positron source. The spacing between the three bunches is dictated by the almost diametrically opposite positions that they occupy in the damping rings and by the maximum appropriate distances at which they can ride on the SLED wave to acquire the proper energies in the linac.

The pulse sequence for filling PEP-II, shown in Fig. 6-4b, has been simplified vis-à-vis SLC operation. For PEP-II, a magnetic chicane at Sector 4 (see Fig. 6-1, and description below), set for a nominal energy of 3.1 GeV, extracts the positrons and reinjects the electrons into the linac. On one 60-pps time slot, the positron bunch comes first and the second bunch is the scavenger electron bunch, subsequently used to make new positrons. (We define a 60-pps "time slot" as a set of 60 pulses synchronized with one phase of the 60-Hz AC power line. When the accelerator runs at 120 pps, it uses two

such time slots, equally spaced in time.) Only one electron bunch is in the north damping ring at a time, and this considerably eases the difficulty of extraction compared with present SLC operation. To let the scavenger electron bunch reach Sector 19, the pulsed magnet at Sector 8 is turned off during this time slot. When the positron bunch returns via the PRL, only one new electron bunch is generated at the gun and stored in the north damping ring, while the positron bunch is stored in the south damping ring.

On the other time slot (8.3 ms, or 1/120 of a second, later), the electron bunch is ejected from the north damping ring and accelerated to Sector 8. This time, the extractor magnet is turned on and the electron bunch is launched into the electron bypass line. After 12 μs, the injector gun generates a new electron bunch that is stored in the north damping ring to become the next scavenger bunch (for the positron time slot 8.3 ms later). Subsequently, the entire pattern is repeated. Note that in this mode of injection there is no need for any new fast-pulsed magnet. The chicane has DC magnets and the magnet at Sector 8 need only be cycled on and off during successive pulses. Sectors 9 through 19 run at 60 pps, and Sectors 1 through 8 run at 120 pps.

6.2.2 Positron Extraction and the Chicane

The 3.1-GeV positron bunch is extracted at Sector 4 using DC magnets. These extraction magnets have a roll angle about the linac axis such that the plane of extraction for positrons is 59° from the vertical, as shown in Fig. 6-5. Also indicated in Fig. 6-5 are the orientation of the electron extraction plane (downstream at Sector 8, see below), which will be at 45° from the vertical, and the locations in the linac housing of the two new bypass lines (each more than 2 km in length) and the existing PRL.

Returning to the description of positron extraction, the electron bunches will undergo a local orbit excursion but will immediately be restored to their trajectories along the linac axis. This will be accomplished by a configuration of four dipole magnets (see Table 6-2), commonly referred to as a "chicane," that results in the bending sequence θ, $-\theta$, $-\theta$, θ. Note that the chicane consists entirely of DC magnets—an important feature when considering the stability of the extraction process. In the first magnet, both electrons and positrons enter coaxially and are deflected in opposite directions by 2.5°. This magnet will be less than 1 m long, with an integrated field of about 0.45 T·m. After drifting about 1 m, the electrons enter a second, C-type dipole that deflects them by 2.5° in the opposite direction, to a trajectory parallel to, but displaced from, the linac axis. A third dipole, identical to the second dipole then deflects the beam 2.5° (in the same sense as the second dipole) back towards the linac axis. When the electrons again cross the linac axis, a fourth dipole deflects them by 2.5° (in the opposite sense to dipoles 2 and 3) to make their trajectory again coaxial with the linac. For the electrons, the overall action of this chicane is independent of beam energy (except for slight flight-time variations), because it only affects the magnitude of the internal deflections and hence the orbit excursions. By utilizing a C-type dipole with a good-field region of reasonable size, and by fabricating a vacuum chamber with no obstructions between the linac axis and the maximum possible deflection (corresponding to the lowest energy accepted), the energy bandpass of the chicane can be made at least as large as 20%, and thus the chicane will be easy to operate. Aside from small edge-focusing effects, this region will be optically equivalent to a drift for the electrons.

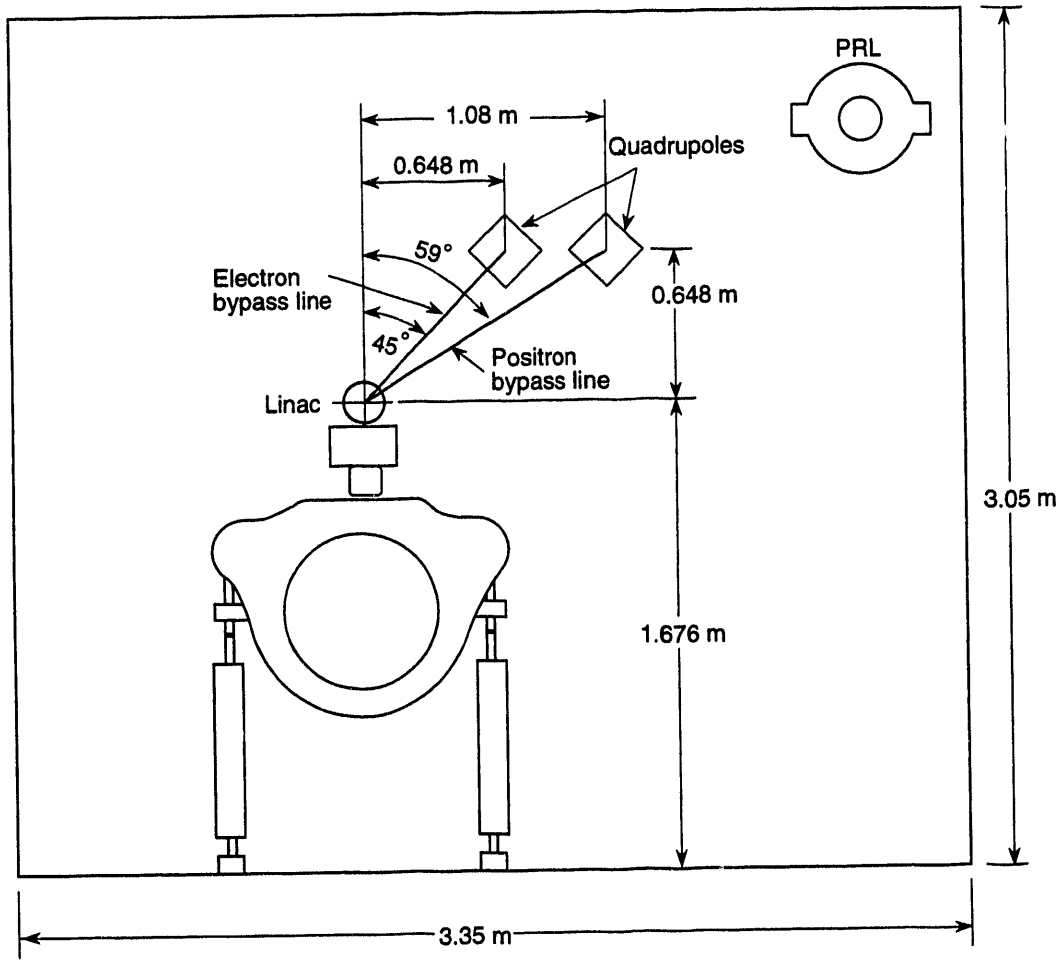

Fig. 6-5. Cross section of linac housing showing the locations of the electron and positron FODO array quadrupoles. Note the tilts of the extraction planes.

We now return our attention to the positron beam, which, after being deflected by the first dipole, will separate from the electron beam at a nominal angle of 5.0°. Because the strength of this first chicane magnet is always set by the requirement to deflect the positrons by a fixed angle of 2.5° for any energy selected for injection into the LER, the separation angle between positrons and electrons can vary. The nominal separation between the two beams at the entrance to the C-dipole (dipole 2) that deflects the electrons back towards the linac will be approximately 10 cm—a distance sufficient to allow good isolation of the positron beam from any adverse optical effects stemming from magnetic fringing fields. The positron bunch continues past this magnet for almost 6 m, at which point it will pass near the next quadrupole in the optical lattice of the linac. By the time the positron beam reaches this next linac quadrupole, it is offset transversely from the linac axis by nearly 25 cm and easily clears the quadrupole yoke. This is

Table 6-2a. Positron extraction line dipole parameters at 3.1 GeV. Coil material is copper for all magnets.

Magnet designation	2H24	2C24	2H24	2H24	2H24
Bending angle [deg]	2.5	2.5	2.5	2.5	1.122
Lattice designation	BS	Bchic.	BR	B1	B2
Number of magnets	1	2	1	2	2
Field @ 3.1 GeV [T]	0.752	0.752	0.752	0.752	0.338
Integrated field @ 3.1 GeV [T·m]	0.451	0.451	0.451	0.451	0.203
Pole width [in.]	8	8	8	8	8
Gap height [in.]	1	1	1	2	1
Core length [in.]	22.62	22.62	22.62	21.62	22.62
Magnetic length [in.]	23.62	23.62	23.62	23.62	23.62
Width of useful field, 0.1% [in.]	4.00	4.00	4.00	4.00	4.00
Lamination height [in.]	6.75	6 75	6.75	6.75	6.75
Lamination width [in.]	23	23	23	23	23
Packing factor, minimum [%]	96	96	96	96	96
Core weight [lb]	2,000	1,500	2,000	2,000	2,000
Amp·turns @ 3.1 GeV	7,598	7,598	7,598	15,197	9,548
Turns	36	36	36	36	36
Pancakes per pole	1	1	1	1	1
Conductor dimensions [in.]	0.34 × 0.34	0.34 × 0.34	0.34 × 0.34	0.34 × 0.34	0.34 × 0.34
Cooling hole diameter [in.]	0.1875	0.1875	0.1875	0.1875	0.1875
Conductor cross-sectional area [in.^{2}]	0.10	0.10	0.10	0.10	0.10
Conductor length/pole [ft]	211	211	211	205	211
Current @ 3.1 GeV [A]	211.06	211.06	211.06	422.13	265.23
Resistance @ 40°C [mΩ]	36.1	36.1	36.1	35.1	36.1
Power @ 3.1 GeV [kW]	1.61	1.61	1.61	6.25	2.54
Voltage drop @ 3.1 GeV [V]	7.6	7.6	7.6	14.8	9.6
Coil weight [lb]	154	154	154	149	154
Number of water circuits	2	2	2	2	2
Water flow rate, total [gpm]	1.3	1.3	1.3	1.3	1.3
Water pressure drop [psi]	150	150	150	150	150
Temperature rise [°C]	4.8	4.8	4.8	18.6	7.7
Total power (magnets and bus) [kW]	4.3	3.2	1.6	12.5	5.1
Total voltage (magnets and bus) [V]	49.2	25.2	17.6	39.6	26.7
Total system water requirements [gpm]	1.26	2.52	1.26	2.56	2.52

Table 6-2a. Positron extraction line dipole parameters at 3.1 GeV. Coil material is copper for all magnets (continued).

Magnet designation	2H60	2H80	2H60	2H60	2H60
Bending angle [deg]	0.162	0.824	3.731	0.646	0.162
Lattice designation	BH1	BV+	B02	B01	BH1
Number of magnets	2	1	2	2	1
Field @ 3.1 GeV [T]	0.019	0.074	0.449	0.078	0.019
Integrated field @ 3.1 GeV [T·m]	0.029	0.149	0.674	0.117	0.029
Pole width [in.]	8	8	8	8	8
Gap height [in.]	1	1	1	1	1
Core length [in.]	58.06	77.74	58.06	58.06	58.06
Magnetic length [in.]	59.06	78.74	59.06	59.06	59.06
Width of useful field, 0.1% [in.]	4.00	4.00	4.00	4.00	4.00
Lamination height [in.]	6.75	6.75	6.75	6.75	6.75
Lamination width [in.]	23	23	23	23	23
Packing factor, minimum [%]	96	96	96	96	96
Core weight [lb]	2,000	2,000	2,000	2,000	2,000
Amp·turns @ 3.1 GeV	197	751	4,536	785	197
Turns	36	36	36	36	36
Pancakes per pole	1	1	1	1	1
Conductor dimensions [in.]	0.34 × 0.34	0.34 × 0.34	0.34 × 0.34	0.34 × 0.34	0.34 × 0.34
Cooling hole diameter [in.]	0.1875	0.1875	0.1875	0.1875	0.1875
Conductor cross-sectional area [in.^{2}]	0.10	0.10	0.10	0.10	0.10
Conductor length/pole [ft]	424	542	424	424	424
Current @ 3.1 GeV [A]	5.47	20.87	126.00	21.82	5.47
Resistance @ 40°C [mΩ]	72.5	92.7	72.5	72.5	72.5
Power @ 3.1 GeV [kW]	0.00	0.04	1.15	0.03	0.00
Voltage drop @ 3.1 GeV [V]	0.4	1.9	9.1	1.6	0.4
Coil weight [lb]	308	394	308	308	308
Number of water circuits	2	2	2	2	2
Water flow rate, total [gpm]	0.9	0.8	0.9	0.9	0.9
Water pressure drop [psi]	150	150	150	150	150
Temperature rise [°C]	0.0	0.2	5.1	0.2	0.0
Total power (magnets and bus) [kW]	0.0	0.1	3.3	0.1	0.0
Total voltage (magnets and bus) [V]	1.9	6.0	43.1	7.5	1.5
Total system water requirements [gpm]	1.73	0.76	1.73	1.73	0.87

Table 6-2b. Electron extraction line dipole parameters at 9 GeV. Coil material is copper for all magnets.

Magnet designation	B2	B3	BP1	B2
Bending angle [deg]	2.511	1.031	0.25	2.511
Location	Extr./Septum	Extr.	Extr.	Extr.
Number of magnets	1	4	2	1
Field @ 9 GeV [T]	0.658	0.540	0.155	0.658
Integrated field @ 9 GeV [T·m]	1.3161	0.540	0.131	1.316
Pole width [in.]	8	8	8	8
Gap height [in.]	1	1.375	1.375	1.375
Core length [in.]	77.74	38.00	31.81	77.37
Magnetic length [in.]	78.74	39.37	33.19	78.74
Width of useful field, 0.1% [in.]	4.00	4.00	4.00	4.00
Lamination height [in.]	6.75	6.75	6.75	6.75
Lamination width [in.]	23	23	23	23
Packing factor, minimum [%]	98	98	98	98
Core weight [lb]	6,841	3,344	2,800	6,808
Amp·turns @ 9 GeV	6,646	15,282	4,396	9,138
Turns	36	48	36	36
Pancakes per pole	1	1	1	1
Conductor dimensions [in.]	0.34 × 0.34	0.34 × 0.34	0.34 × 0.34	0.34 × 0.34
Cooling hole diameter [in.]	0.1875	0.1875	0.1875	0.1875
Conductor cross-sectional area [in.^{2}]	0.08	0.08	0.08	0.08
Conductor length/pole [ft]	580	455	304	577
Current @ 9 GeV [A]	184.62	318.37	122.10	253.85
Resistance @ 40°C [mΩ]	116.1	91.1	60.9	115.6
Power @ 9 GeV [kW]	1.98	4.62	0.45	3.73
Voltage drop @ 9 GeV [V]	10.7	14.5	3.7	14.7
Coil weight [lb]	341.2	267.8	179.0	339.9
Number of water circuits	2	2	2	2
Water flow rate, total [gpm]	0.7	1.7	2.1	1.5
Water pressure drop [psi]	150	150	150	150
Temperature rise [°C]	10.3	10.5	0.8	9.7
Total power (magnets and bus) [kW]	2.0	18.5	0.9	3.7
Total voltage (magnets and bus) [V]	10.7	58.0	7.4	14.7
Total system water requirements [gpm]	1	7	4	1

Table 6-2b. Electron extraction line dipole parameters at 9 GeV. Coil material is copper for all magnets (continued).

Magnet designation	BHR3	BV+	BV–	BHL2
Bending angle [deg]	2.134	0.362	2.381	1.194
Location	Match	Match	Match	Match
Number of magnets	1	2	1	1
Field @ 9 GeV [T]	0.746	0.095	0.832	0.313
Integrated field @ 9 GeV [T·m]	1.1185	0.1897	1.2479	0.6258
Pole width [in.]	8	8	8	8
Gap height [in.]	1	1.375	1.375	1.375
Core length [in.]	58.06	77.37	57.68	77.37
Magnetic length [in.]	59.06	78.74	59.06	78.74
Width of useful field, 0.1% [in.]	4.00	4.00	4.00	4.00
Lamination height [in.]	6.75	6.75	6.75	6.75
Lamination width [in.]	23	23	23	23
Packing factor, minimum [%]	98	98	98	98
Core weight [lb]	5,109	6,808	5,076	6,808
Amp·turns @ 9 GeV	7,531	2,683	23,528	4,345
Turns	36	48	36	36
Pancakes per pole	1	1	1	1
Conductor dimensions [in.]	0.34 × 0.34	0.34 × 0.34	0.34 × 0.34	0.34 × 0.34
Cooling hole diameter [in.]	0.1875	0.1875	0.1875	0.1875
Conductor cross-sectional area [in.^{2}]	0.08	0.08	0.08	0.08
Conductor length/pole [ft]	461	770	459	577
Current @ 9 GeV [A]	209.20	55.89	653.55	120.71
Resistance @ 40°C [mΩ]	92.4	154.2	92.0	115.6
Power @ 9 GeV [kW]	2.02	0.24	19.64	0.84
Voltage drop @ 9 GeV [V]	9.7	4.3	30.1	7.0
Coil weight [lb]	271.7	453.2	270.4	339.9
Number of water circuits	2	2	2	2
Water flow rate, total [gpm]	0.8	1.3	1.7	1.5
Water pressure drop [psi]	150	150	150	150
Temperature rise [°C]	9.3	0.7	45.0	2.2
Total power (magnets and bus) [kW]	2.0	0.5	19.6	0.8
Total voltage (magnets and bus) [V]	9.7	8.6	30.1	7.0
Total system water requirements [gpm]	1	3	2	1

Table 6-2b. Electron extraction line dipole parameters at 9 GeV. Coil material is copper for all magnets (continued).

Magnet designation	BHR1	B2	B3
Bending angle [deg]	0.246	5.842	9.000
Location	Match	Extr.	Extr.
Number of magnets	1	1	1
Field @ 9 GeV [T]	0.086	1.177	0.898
Integrated field @ 9 GeV [T·m]	0.1289	3.0619	4.7171
Pole width [in.]	8	8	8
Gap height [in.]	1	1.375	1.375
Core length [in.]	58.06	101.00	205.43
Magnetic length [in.]	59.06	102.38	206.80
Width of useful field, 0.1% [in.]	4.00	4.00	4.00
Lamination height [in.]	6.75	6.75	6.75
Lamination width [in.]	23	23	23
Packing factor, minimum [%]	98	98	98
Core weight [lb]	5,109	8,888	18,078
Amp·turns @ 9 GeV	868	33,299	25,396
Turns	36	48	36
Pancakes per pole	1	1	1
Conductor dimensions [in.]	0.34 × 0.34	0.34 × 0.34	0.34 × 0.34
Cooling hole diameter [in.]	0.1875	0.1875	0.1875
Conductor cross-sectional area [in.^{2}]	0.08	0.08	0.08
Conductor length/pole [ft]	461	959	1346
Current @ 9 GeV [A]	24.12	693.73	705.44
Resistance @ 40°C [mΩ]	92.4	192.0	269.5
Power @ 9 GeV [kW]	0.03	46.21	67.06
Voltage drop @ 9 GeV [V]	1.1	66.6	95.1
Coil weight [lb]	271.7	564.5	792.3
Number of water circuits	2	2	2
Water flow rate, total [gpm]	0.8	1.1	0.9
Water pressure drop [psi]	150	150	150
Temperature rise [°C]	0.1	157.7	274.8
Total power (magnets and bus) [kW]	0.0	46.2	67.1
Total voltage (magnets and bus) [V]	1.1	66.6	95.1
Total system water requirements [gpm]	1	1	1

demonstrated in Fig. 6-6, where the quadrupoles for the linac and the bypass line are shown together with the S-band waveguide that feeds RF power to the linac.

While a large separation angle is desirable in order to clear the downstream components, it must be kept in mind that there are limits. If this angle becomes too large, then the rapid separation of the beams within the first magnet itself would require an excessively large good-field region. This, in turn, could lead to problems with available space and support structures due to excessive bulk of the magnet. Shortening the length and increasing the field strength of the first separation magnet is also not a good option, as this would increase the synchrotron-radiation-induced emittance growth. Estimates based upon these considerations indicate that there is a large range of comfortable design parameters and that a reasonable compromise can easily be found.

As mentioned earlier, for the present extraction design we have selected a separation dipole magnet with a bend angle of 2.5°. This angle gives sufficient separation of the two beams, leads to a reasonable design for the C-type dipoles required for the chicane, and provides adequate clearance for the required quadrupoles in both the linac and the extraction line. As described below, however, this choice also generated a geometrical problem for which a solution had to be found.

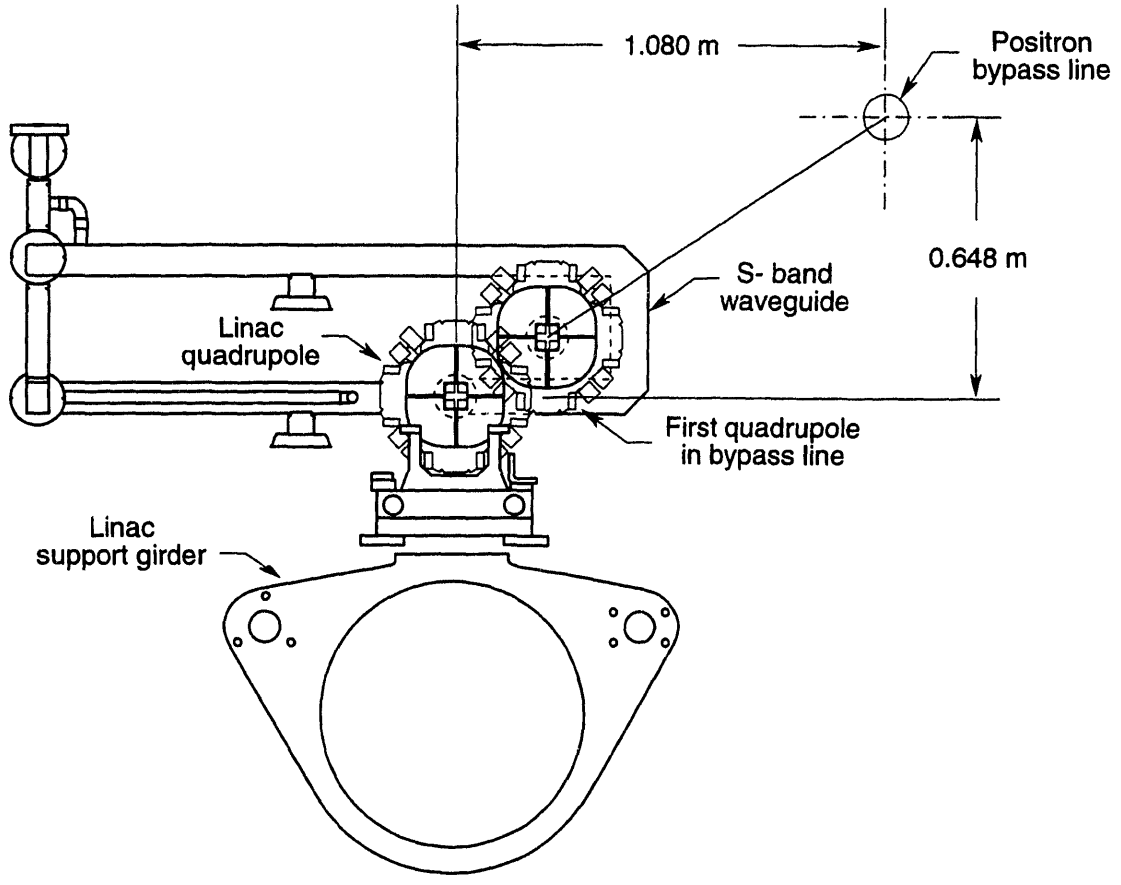

Fig. 6-6. Positron extraction line from linac, showing clearance at first downstream linac quadrupole.

6.2.3 Design of the Positron Extraction Line

The optical design of the positron extraction system is intended to satisfy the following requirements:

- Providing a good match to the beta functions of the linac lattice in both transverse planes
- Removing dispersion caused by the extraction dipoles
- Providing a region for monitoring and implementing feedback control of the positron energy
- Providing a region for optically matching to the bypass line
- Providing sufficient flexibility to match geometrically to the location of the bypass line, as required by engineering constraints

At the same time, it is advantageous to minimize disturbing the present linac structures. This strategy gives the option of early installation of some of the PEP-II injection hardware and the possibility of running beam tests prior to the cessation of the SLC experimental program.

Matching the beta functions and controlling dispersion are most easily managed by the simple expedient of using a FODO lattice with parameters closely matching those of the linac lattice. Our extraction line design is essentially an optical continuation of the linac lattice, and its cell length is very nearly that of the linac lattice (it has been slightly increased to longitudinally offset the first linac and extraction line quadrupoles downstream of the chicane for clearance purposes). For the extraction line, the phase advance per cell has been adjusted to be exactly 90° in both planes. In the linac lattice, the phase advance is kept near its optimum value of 76.5°, which maximizes the acceptance, though in practice the value of the phase advance is generally not carefully controlled and can vary.

The phase advance per cell of exactly 90° in the extraction line is necessary to provide an easy method for both controlling dispersion and matching to the desired geometry. The simplicity of matching results from the fact that four cells of such a lattice (phase advance of 2π) give an optical transfer matrix equal to the identity matrix. Thus, dispersion introduced by the 2.5° extraction magnet can be exactly canceled by a bend of equal strength, but in the opposite direction, placed four cells downstream. This use of equal but opposite bends, separated by a long drift, is ideal for the purpose of connecting two parallel beamlines. However, the desired large initial bend, coupled with the cell length of 12.7 m (50.8 m for four cells) as in the linac (needed for the beta function matching), would imply a transverse offset of more than 2 m from the linac; this would put the bypass at an awkward location in the linac tunnel. The obvious solution of simply decreasing the extraction angle is not acceptable, as it increases the difficulty of obtaining clearance for other components. Fortunately, the additional flexibility to match the geometry is easily provided by introducing two more dipoles (again of equal strength but of opposite sign and separated optically by the identity matrix). The first of these additional dipoles will bend in a direction opposite to that of the extraction dipole, but with less strength. We have determined that, with this scheme of using four magnets for

positron extraction, obstacles can be avoided and the design can be easily modified to optimize desired parameters or accommodate requested engineering changes.

The geometry of this extraction configuration is shown in Fig. 6-7, which indicates the location of key elements in elevation and in plan views (with the longitudinal scale

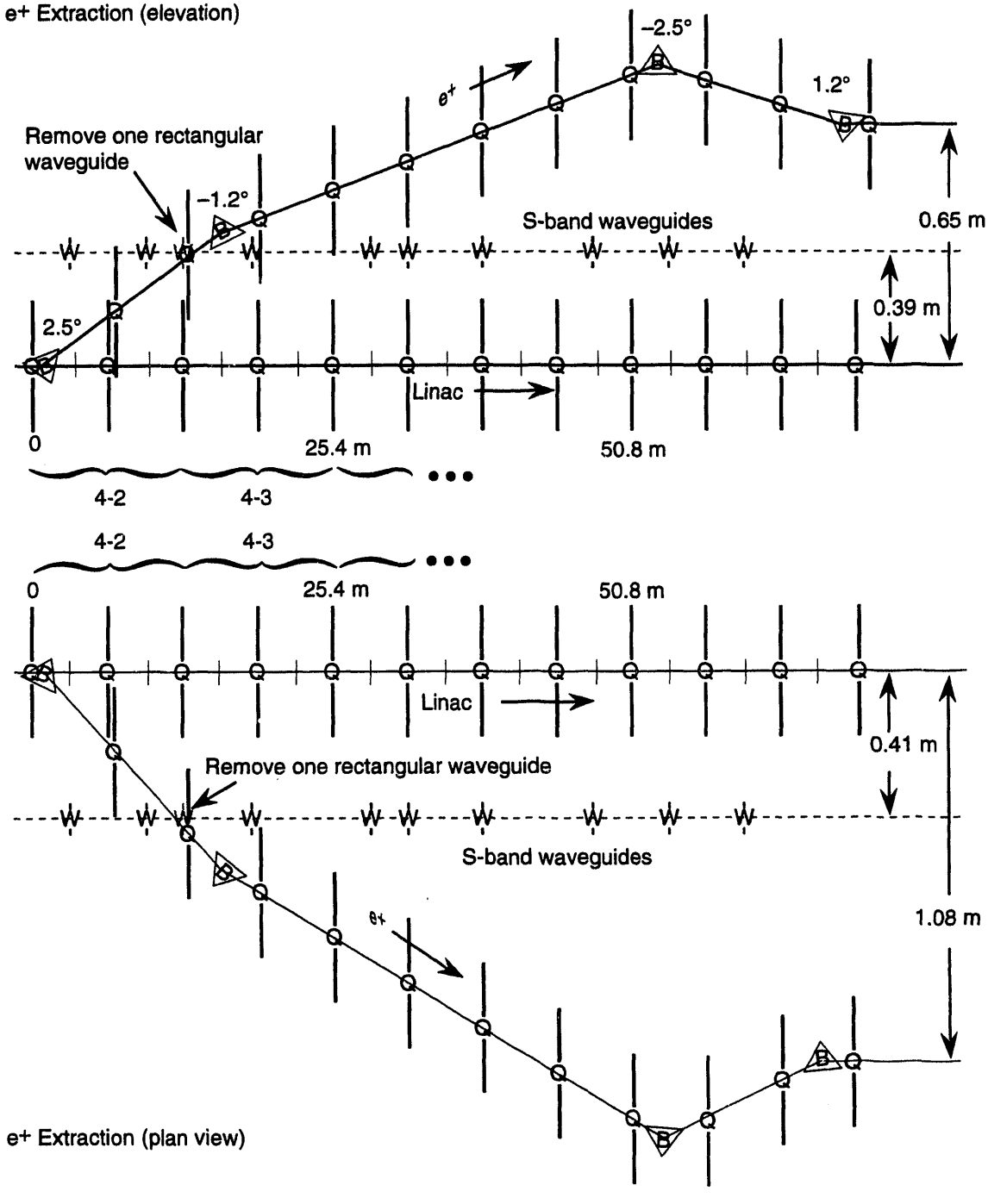

Fig. 6-7. Elevation and plan views of the positron extraction line. Linac quadrupole locations are marked Q, and the locations of S-band waveguides feeding power to the linac are marked W.

compressed). Also shown in this figure are the linac quadrupoles (indicated with Q) and the rectangular S-band waveguides (indicated with W), which we attempted to avoid. As can be seen, one such waveguide will have to be removed or rerouted.

The optical functions for this extraction configuration are shown in Fig. 6-8. The beta functions are almost a continuation of those of the linac, so the matching between the

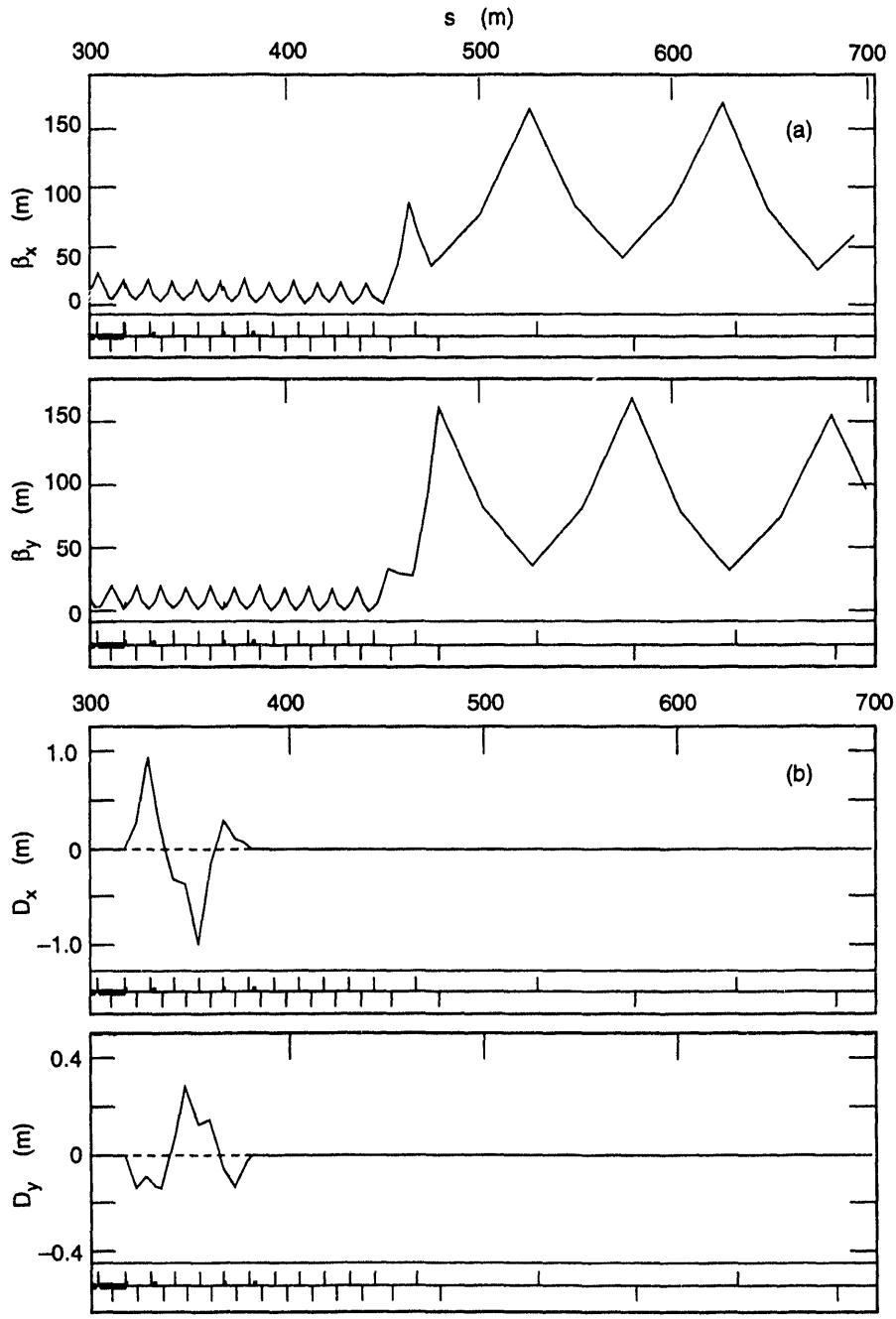

Fig. 6-8. Positron extraction line optical functions: (a) β_x and β_y; (b) D_x and D_y. The dispersion coupling results from not rolling the quadrupole axes to match the dipole roll angle.

lattices is easily achieved. In the optical configuration shown in Fig. 6-8, the quadrupoles are not rolled about the beam axis to match the roll angle of the dipoles. Although this preserves the matching of the beta functions, it means that the dispersion becomes coupled into both the vertical and horizontal planes. An alternative approach is possible, of course—to roll both quadrupoles and dipoles for uncoupled dispersion—but this would give both coupling and a large mismatch of the beta functions. Both options are under study and we will choose the one with the greatest tolerance for errors. In the example shown in Fig. 6-8, the energy resolution of the extraction line for an emittance-damped beam is approximately 1×10^{-3}, a value that matches the specification for the proposed energy feedback system.

Following the dispersive region is a dispersion-free region where the lattice continues with the same 90° phase advance per cell. This region will be used for beam diagnostics and for operational tuning of the optics to match into the bypass-line optics downstream. By maintaining an overall phase advance of 720°, this dispersion-free continuation also serves to preserve the option of rolling or not rolling the quadrupoles.

Following the continuation region is a short matching section, where four quadrupoles are used to match the beta functions to those of the bypass line optics.

6.2.4 Bypass Lines

Optical functions of the bypass lines are included in Fig. 6-8. The parameters of this FODO array have been adjusted such that there is exactly one cell per linac sector (L_{cell} = 101.6 m). A phase advance per cell of 76.5° has been chosen for this design, as that value maximizes the acceptance. Of course, the phase advance is not a fixed parameter and can be changed during operation. With the length L_{cell} and phase advance per cell μ determined, the values of the extrema for the matched beta function are given by the equation

$$\beta_{max,min} = \frac{L_{cell}}{\sin \mu}\left(1 \pm \sin \mu/2\right) \tag{6-1}$$

which gives β_{max} = 169 m and β_{min} = 40 m, as we see in Fig. 6-8. The required focal length f is given by

$$f = \frac{L_{cell}}{4 \sin \mu/2} = 41 \text{ m} \tag{6-2}$$

Achieving this value for the focal length will require only about 0.25 T of integrated gradient at 3.1 GeV.

These low-strength quadrupoles (two per sector, or 50.8 m apart) will be suspended from the ceiling of the linac housing, as suggested by Fig. 6-5. At each quadrupole, there is a BPM that measures either the horizontal or vertical position of the beam and one steering dipole that steers the beam in that same plane. Thus, each corrector is located at a point where the beta function in the plane in which it steers is a maximum, and there will be a phase advance between like correctors equal to that for one cell (76.5°).

As shown in Fig. 6-9, the bypass line vacuum chambers will be fabricated from 2-in.-diameter seamless stainless-steel tubing. This chamber aperture provides sufficient vacuum pumping conductance but, at each quadrupole (every 50.8 m), the chamber will be necked down to about 1-in. diameter to allow for small-bore quadrupoles and, more importantly, to reduce the cost of the line by the use of smaller flanges, bellows, and BPMs. For each line, there will be one 30-L/s pump every 101.6-m length (one FODO cell). Isolation valves are provided every third cell, and roughing connections are provided each cell, as indicated in Fig. 6-10.

Four independent power supplies will supply power to four strings of quadrupole magnets connected in series. All horizontally focusing quadrupoles will comprise one string, and all vertically focusing quadrupoles another string, in each of the two bypass lines. A parameter list for the injection system quadrupole magnets is given in Table 6-3.

Profile monitors and/or wire scanners will be used to check the beam emittance and beam shape at the launch point and before injection into the NIT and SIT lines. Intensity monitors will be placed near each end of the bypass lines and used to supplement the total charge information obtained from the BPM striplines.

The large maximum value of the beta function in the bypass line means that the transverse beam size will reach values as large as 0.5 mm rms for electrons and 0.75 mm rms for positrons. A series of four variable- (and overlapping-) jaw collimators in each beamline will serve to tailor the beam size and hence the emittance of the injected beam. These collimators will be placed 90° apart in phase advance in both the horizontal and vertical planes. In addition to these eight emittance-defining collimators, one or two collimators will be included in the dispersive region of the extraction line (downstream of the energy feedback devices) for the purpose of removing unwanted energy tails. Optimum locations for the variable-jaw collimators will be determined by further study. In addition to these controllable collimators, the existing energy-defining collimators in both the NIT and SIT beamlines will be used.

6.2.5 Electron Extraction

At Sector 8, the linac lattice has a cell length of 25.4 m (12.7-m spacing between quadrupoles). In order to provide the space for e^- extraction, it will be necessary to remove all of the disk-loaded accelerating structure corresponding to one klystron (a 12.7-m section).

As mentioned earlier, the electron extraction will take advantage of the temporal separation of about 8.3 ms between the scavenger bunch (used for positron production) and the electron bunch needed for injection into the HER. Because of this relatively large separation in time, the pair of pulsed magnets used at PEP to kick the electrons and positrons into the SIT and NIT lines are adequate for this purpose. These magnets (or perhaps newly designed equivalents) are each 0.843 m in length and have an integrated flux density of Bl = 0.14 T·m, sufficient to provide a total kick of 0.5° to the 9-GeV electron beam.

After a drift of 3 m following this kick, the beam will be sufficiently separated from the on-axis beam to be captured by a Lambertson septum magnet that will deflect the beam (by about 2.5°, orthogonal to the original deflection) sufficiently to avoid the first linac quadrupole. As was done in the positron extraction scheme (see Section 6.2.3),

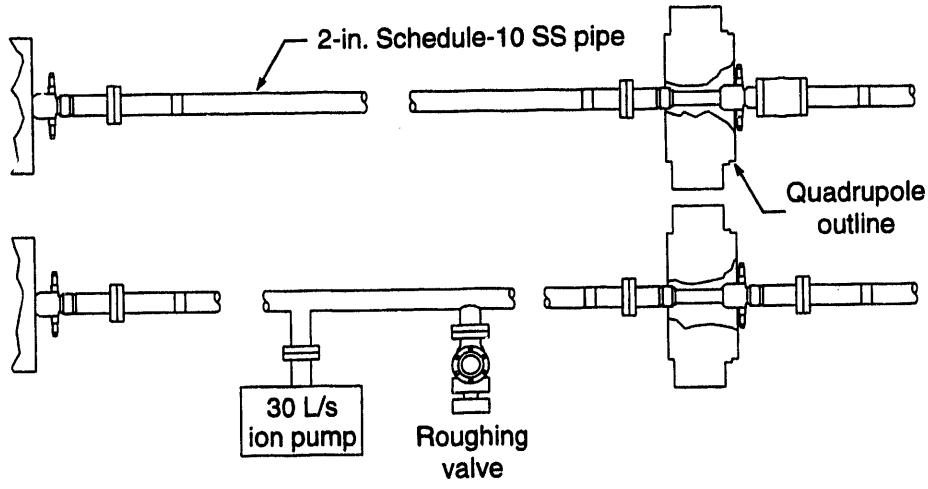

Fig. 6-9. Schematic layout of bypass lines.

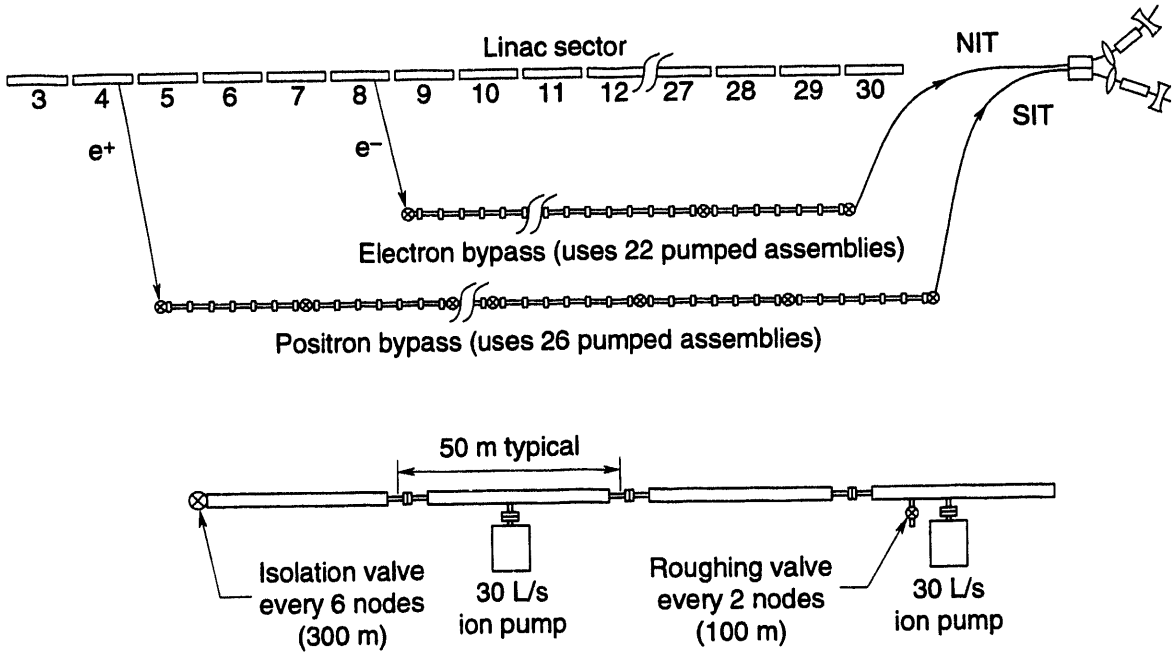

Fig. 6-10. Vacuum layout for bypass lines.

Table 6-3a. Positron injection line quadrupole parameters at 3.1 GeV. Coil material is copper for all magnets.

Magnet designation	2Q10	2Q10	2Q10	2Q10	2Q10	2Q10
Location	Extr.	Extr.	Extr.	Extr.	Extr.	Extr.
Lattice designation	QD	QF	QDI	QFI	QFM	QDM
Number of magnets	5	5	4	4	2	2
Operating gradient @ 3.1 GeV [T/m]	9.008	9.008	9.008	9.008	4.041	4.041
Pole-tip field @ operating gradient [T]	0.232	0.232	0.232	0.232	0.104	0.104
Gradient-length product [T]	2.25	2.25	2.25	2.25	1.01	1.01
Inscribed radius [in.]	1.015	1.015	1.015	1.015	1.015	1.015
Core length [in.]	9.34	9.34	9.34	9.34	9.34	9.34
Magnetic length [in.]	9.84	9.84	9.84	9.84	9.84	9.84
Lamination height [in.]	6.75	6.75	6.75	6.75	6.75	6.75
Lamination width [in.]	6.75	6.75	6.75	6.75	6.75	6.75
Packing factor, minimum [%]	98	98	98	98	98	98
Core weight [lb]	420	420	420	420	420	420
Amp·turns per pole @ 3.1 GeV	2381	2381	2381	2381	1068	1068
Turns per pole	34	34	34	34	34	34
Pancakes per pole	1	1	1	1	1	1
Conductor dimensions [in.]	0.2×0.2	0.2×0.2	0.2×0.2	0.2×0.2	0.2×0.2	0.2×0.2
Cooling hole diameter [in.]	0.11	0.11	0.11	0.11	0.11	0.11
Conductor cross-sectional area [in.^{2}]	0.022	0.022	0.022	0.022	0.022	0.022
Conductor length/pole [ft]	124	124	124	124	124	124
Current @ 3.1 GeV [A]	70	70	70	70	31	31
Resistance @ 40°C [mΩ]	198.5	198.5	198.5	198.5	198.5	198.5
Power @ 3.1 GeV [kW]	0.97	0.97	0.97	0.97	0.20	0.20
Voltage drop @ 3.1 GeV [V]	14	14	14	14	6	6
Coil weight [lb]	50	50	50	50	50	50
Number of water circuits	4	4	4	4	4	4
Water flow rate [gpm]	0.8	0.8	0.8	0.8	0.8	0.8
Water pressure drop [psi]	150	150	150	150	150	150
Temperature rise [°C]	4.5	4.5	4.5	4.5	0.9	0.9
Total power (magnets and bus) [kW]	4.9	4.9	3.9	3.9	0.4	0.4
Total voltage (magnets and bus) [V]	70	70	56	56	12	12
Total magnet water requirements [gpm]	4.9	4.9	3.9	3.9	0.4	0.4

Table 6-3a. Positron injection line quadrupole parameters at 3.1 GeV. Coil material is copper for all magnets (continued).

Magnet designation	2Q10	1Q4	1Q4	1Q4	1Q4	1Q4
Location	Extr.	Bypass	Bypass	Match	Match	Match
Lattice designation	QA2	QFBY	QDBY	QA2	QDSL	QFSL
Number of magnets	1	22	21	1	2	2
Operating gradient @ 3.1 GeV [T/m]	2.370	2.387	2.387	5.585	5.585	5.585
Pole-tip field @ operating gradient [T]	0.061	0.031	0.031	0.072	0.072	0.072
Gradient-length product [T]	0.59	0.25	0.25	0.59	0.59	0.59
Inscribed radius [in.]	1.015	0.5075	0.5075	0.5075	0.5075	0.5075
Core length [in.]	9.34	3.92	3.92	3.92	3.92	3.92
Magnetic length [in.]	9.84	4.17	4.17	4.17	4.17	4.17
Lamination height [in.]	6.75	6.75	6.75	6.75	6.75	6.75
Lamination width [in.]	6.75	6.75	6.75	6.75	6.75	6.75
Packing factor, minimum [%]	98	98	98	98	98	98
Core weight [lb]	420	176	176	176	176	176
Amp·turns per pole @ 3.1 GeV	626	158	158	369	369	369
Turns per pole	34	34	34	34	34	34
Pancakes per pole	1	1	1	1	1	1
Conductor dimensions [in.]	0.2×0.2	0.2×0.2	0.2×0.2	0.2×0.2	0.2×0.2	0.2×0.2
Cooling hole diameter [in.]	0.11	0.11	0.11	0.11	0.11	0.11
Conductor cross-sectional area [in.^{2}]	0.022	0.022	0.022	0.022	0.022	0.022
Conductor length/pole [ft]	93	93	47	47	47	93
Current @ 3.1 GeV [A]	18	5	5	11	11	11
Resistance @ 40°C [mΩ]	198.5	149.4	149.4	149.4	149.4	149.4
Power @ 3.1 GeV [kW]	0.07	0.00	0.00	0.02	0.02	0.02
Voltage drop @ 3.1 GeV [V]	4	1	1	2	2	2
Coil weight [lb]	50	37	37	37	37	37
Number of water circuits	4	4	4	4	4	4
Water flow rate [gpm]	0.8	1.0	1.0	1.0	1.0	1.0
Water pressure drop [psi]	150	150	150	150	150	150
Temperature rise [°C]	0.3	0.0	0.0	0.1	0.1	0.1
Total power (magnets and bus) [kW]	0.07	0.1	0.1	0.02	0.04	0.04
Total voltage (magnets and bus) [V]	4	22	21	2	4	4
Total magnet water requirements [gpm]	0.1	0.1	0.1	0.0	0.0	0.0

Table 6-3a. Positron injection line quadrupole parameters at 3.1 GeV. Coil material is copper for all magnets (continued).

Magnet designation	1Q4	1Q4	1Q4	1Q4	1Q4	1Q4
Location	Match	Match	Match	Match	Match	Match
Lattice designation	QA3	QMF	QMD	QEF	QED	QD
Number of magnets	1	2	2	4	4	1
Operating gradient @ 3.1 GeV [T/m]	4.115	8.182	8.182	0.818	0.818	0.818
Pole-tip field @ operating gradient [T]	0.053	0.105	0.105	0.011	0.011	0.011
Gradient-length product [T]	0.44	0.87	0.87	0.09	0.09	0.09
Inscribed radius [in.]	0.5075	0.5075	0.5075	0.5075	0.5075	0.5075
Core length [in.]	3.92	3.92	3.92	3.92	3.92	3.92
Magnetic length [in.]	4.17	4.17	4.17	4.17	4.17	4.17
Lamination height [in.]	6.75	6.75	6.75	6.75	6.75	6.75
Lamination width [in.]	6.75	6.75	6.75	6.75	6.75	6.75
Packing factor, minimum [%]	98	98	98	98	98	98
Core weight [lb]	176	176	176	176	176	176
Amp·turns per pole @ 3.1 GeV	272	541	541	54	54	54
Turns per pole	34	34	17	17	17	34
Pancakes per pole	1	1	1	1	1	1
Conductor dimensions [in.]	0.2×0.2	0.2×0.2	0.2×0.2	0.2×0.2	0.2×0.2	0.2×0.2
Cooling hole diameter [in.]	0.11	0.11	0.11	0.11	0.11	0.11
Conductor cross-sectional area [$in.^2$]	0.022	0.022	0.022	0.022	0.022	0.022
Conductor length/pole [ft]	93	93	47	47	47	93
Current @ 3.1 GeV [A]	8	16	32	3	3	2
Resistance @ 40°C [mΩ]	149.4	149.4	74.7	74.7	74.7	149.4
Power @ 3.1 GeV [kW]	0.01	0.04	0.08	0.00	0.00	0.00
Voltage drop @ 3.1 GeV [V]	1	2	2	0	0	0
Coil weight [lb]	37	37	19	19	19	37
Number of water circuits	4	4	0	0	4	4
Water flow rate [gpm]	1.0	1.0	0	0	1.4	1.0
Water pressure drop [psi]	150	150	0	0	150	150
Temperature rise [°C]	0.0	0.1	0	0	0.0	0.0
Total power (magnets and bus) [kW]	0.01	0.1	0.2	0.03	0.03	0.0
Total voltage (magnets and bus) [V]	1	4	4	0.01	0.01	0.0
Total magnet water requirements [gpm]	0.0	0.1	0	0	0.0	0.0

Table 6-3b. Electron injection line quadrupole parameters at 9 GeV. Coil material is copper for all magnets.

Magnet designation	1Q4	2Q9	2Q9	2Q9	2Q9
Location	Bypass	Extr.	Extr.	Extr.	Extr.
Lattice designation	QB	QD	QF1	QD2	QF3
Number of magnets	32	1	1	1	1
Operating gradient @ 9 GeV [T/m]	7.889	13.193	13.988	13.252	13.156
Pole-tip field @ operating gradient [T]	0.102	0.340	0.361	0.342	0.339
Gradient-length product [T]	0.84	3.30	3.50	3.31	3.29
Inscribed radius [in.]	0.5075	1.015	1.015	1.015	1.015
Core length [in.]	3.67	8.83	8.83	8.83	8.83
Magnetic length [in.]	4.17	9.84	9.84	9.84	9.84
Lamination height [in.]	6.75	6.75	6.75	6.75	6.75
Lamination width [in.]	6.75	6.75	6.75	6.75	6.75
Packing factor, minimum [%]	98	98	98	98	98
Core weight [lb]	93	222	222	222	222
Amp·turns per pole @ 9 GeV	521	3487	3697	3502	3477
Turns per pole	34	34	34	34	34
Pancakes per pole	1	1	1	1	1
Conductor dimensions [in.]	0.2×0.2	0.2×0.2	0.2×0.2	0.2×0.2	0.2×0.2
Cooling hole diameter [in.]	0.11	0.11	0.11	0.11	0.11
Conductor cross-sectional area [in.^{2}]	0.022	0.022	0.022	0.022	0.022
Conductor length/pole [ft]	92	121	121	121	121
Current @ 9 GeV [A]	15	103	109	103	102
Resistance @ 40°C [mΩ]	147.1	193.9	193.9	193.9	193.9
Power @ 9 GeV [kW]	0.03	2.04	2.29	2.06	2.03
Voltage drop @ 9 GeV [V]	2.3	19.9	21.1	20.0	19.8
Coil weight [lb]	36.78	48.48	48.48	48.48	48.48
Number of water circuits	0	4	4	4	4
Water flow rate [gpm]	0.0	0.2	0.2	0.2	0.2
Water pressure drop [psi]	0	150	150	150	150
Temperature rise [°C]	0.0	9.3	10.4	9.3	9.2
Total power (magnets and bus) [kW]	1.0	2.0	2.3	2.1	2.0
Total voltage (magnets and bus) [V]	73.6	19.9	21.1	20.0	19.8
Total magnet water requirements [gpm]	0	0.84	0.84	0.84	0.84

Table 6-3b. Electron injection line quadrupole parameters at 9 GeV. Coil material is copper for all magnets (continued).

Magnet designation	2Q9	2Q9	2Q9	2Q9	2Q9
Location	Extr.	Extr.	Extr.	Extr.	Extr.
Lattice designation	QD4	QF1	QD2	QF3	QD4
Number of magnets	1	1	1	1	1
Operating gradient @ 9 GeV [T/m]	13.304	12.396	13.132	13.228	13.080
Pole-tip field @ operating gradient [T]	0.343	0.320	0.339	0.341	0.337
Gradient-length product [T]	3.33	3.10	3.28	3.31	3.27
Inscribed radius [in.]	1.015	1.015	1.015	1.015	1.015
Core length [in.]	8.83	8.83	8.83	8.83	8.83
Magnetic length [in.]	9.84	9.84	9.84	9.84	9.84
Lamination height [in.]	6.75	6.75	6.75	6.75	6.75
Lamination width [in.]	6.75	6.75	6.75	6.75	6.75
Packing factor, minimum [%]	98	98	98	98	98
Core weight [lb]	222	222	222	222	222
Amp·turns per pole @ 9 GeV	3516	3276	3471	3496	3457
Turns per pole	34	34	34	34	34
Pancakes per pole	1	1	1	1	1
Conductor dimensions [in.]	0.2×0.2	0.2×0.2	0.2×0.2	0.2×0.2	0.2×0.2
Cooling hole diameter [in.]	0.11	0.11	0.11	0.11	0.11
Conductor cross-sectional area [in.^{2}]	0.022	0.022	0.022	0.022	0.022
Conductor length/pole [ft]	121	121	121	121	121
Current @ 9 GeV [A]	103	96	102	103	102
Resistance @ 40°C [mΩ]	193.9	193.9	193.9	193.9	193.9
Power @ 9 GeV [kW]	2.07	1.80	2.02	2.05	2.00
Voltage drop @ 9 GeV [V]	20.1	18.7	19.8	19.9	19.7
Coil weight [lb]	48.48	48.48	48.48	48.48	48.48
Number of water circuits	4	4	4	4	4
Water flow rate [gpm]	0.2	0.2	0.2	0.2	0.2
Water pressure drop [psi]	150	150	150	150	150
Temperature rise [°C]	9.4	8.2	9.2	9.3	9.1
Total power (magnets and bus) [kW]	2.1	1.8	2.0	2.1	2.0
Total voltage (magnets and bus) [V]	20.1	18.7	19.8	19.9	19.7
Total magnet water requirements [gpm]	0.84	0.84	0.84	0.84	0.84

Table 6-3b. Electron injection line quadrupole parameters at 9 GeV. Coil material is copper for all magnets (continued).

Magnet designation	1Q6	1Q6	1Q6	1Q6	1Q6
Location	Extr.	Extr.	Extr.	Extr.	Extr.
Lattice designation	QF	QALF	QDM	QFM	QDYB
Number of magnets	1	1	3	2	1
Operating gradient @ 9 GeV [T/m]	19.631	21.798	5.648	5.648	7.888
Pole-tip field @ operating gradient [T]	0.253	0.281	0.073	0.073	0.102
Gradient-length product [T]	3.30	3.66	1.41	1.41	1.97
Inscribed radius [in.]	0.5075	0.5075	0.5075	0.5075	0.5075
Core length [in.]	6.11	6.11	9.34	9.34	9.34
Magnetic length [in.]	6.61	6.61	9.84	9.84	9.84
Lamination height [in.]	6.75	6.75	6.75	6.75	6.75
Lamination width [in.]	6.75	6.75	6.75	6.75	6.75
Packing factor, minimum [%]	98	98	98	98	98
Core weight [lb]	154	154	234	234	234
Amp·turns per pole @ 9 GeV	1297	1440	373	373	521
Turns per pole	34	34	34	34	34
Pancakes per pole	1	1	1	1	1
Conductor dimensions [in.]	0.2×0.2	0.2×0.2	0.2×0.2	0.2×0.2	0.2×0.2
Cooling hole diameter [in.]	0.11	0.11	0.11	0.11	0.11
Conductor cross-sectional area [in.^{2}]	0.022	0.022	0.022	0.022	0.022
Conductor length/pole [ft]	106	106	124	124	124
Current @ 9 GeV [A]	38	42	11	11	15
Resistance @ 40°C [mΩ]	169.2	169.2	198.5	198.5	198.5
Power @ 9 GeV [kW]	0.25	0.30	0.02	0.02	0.05
Voltage drop @ 9 GeV [V]	6.5	7.2	2.2	2.2	3.0
Coil weight [lb]	42.31	42.31	49.63	49.63	49.63
Number of water circuits	4	4	4	4	4
Water flow rate [gpm]	0.2	0.2	0.2	0.2	0.2
Water pressure drop [psi]	150	150	150	150	150
Temperature rise [°C]	1.0	1.3	0.1	0.1	0.2
Total power (magnets and bus) [kW]	0.25	0.30	0.06	0.04	0.05
Total voltage (magnets and bus) [V]	6.5	7.2	6.6	4.4	3.0
Total magnet water requirements [gpm]	0.90	0.90	0.83	0.83	0.83

Table 6-3b. Electron injection line quadrupole parameters at 9 GeV. Coil material is copper for all magnets (continued).

Magnet designation	1Q6	1Q6	1Q6	1Q6	1Q9
Location	Extr.	Match	Match	Match	Match
Lattice designation	QFB1	QDSL	QFSL	QA2	QFM
Number of magnets	1	2	2	1	1
Operating gradient @ 9 GeV [T/m]	12.232	11.862	11.862	80.437	105.215
Pole-tip field @ operating gradient [T]	0.158	0.153	0.153	1.037	1.356
Gradient-length product [T]	2.06	1.99	1.99	13.51	26.30
Inscribed radius [in.]	0.5075	0.5075	0.5075	0.5075	0.5075
Core length [in.]	6.11	6.11	6.11	6.11	9.34
Magnetic length [in.]	6.61	6.61	6.61	6.61	9.84
Lamination height [in.]	6.75	6.75	6.75	6.75	6.75
Lamination width [in.]	6.75	6.75	6.75	6.75	6.75
Packing factor, minimum [%]	98	98	98	98	98
Core weight [lb]	154	154	154	154	234
Amp·turns per pole @ 9 GeV	808	784	784	5315	6952
Turns per pole	34	34	34	34	34
Pancakes per pole	1	1	1	1	1
Conductor dimensions [in.]	0.2×0.2	0.2×0.2	0.2×0.2	0.2×0.2	0.2×0.2
Cooling hole diameter [in.]	0.11	0.11	0.11	0.11	0.11
Conductor cross-sectional area [in.^{2}]	0.022	0.022	0.022	0.022	0.022
Conductor length/pole [ft]	106	106	106	106	124
Current @ 9 GeV [A]	24	23	23	156	204
Resistance @ 40°C [mΩ]	169.2	169.2	169.2	169.2	198.5
Power @ 9 GeV [kW]	0.10	0.09	0.09	4.14	8.30
Voltage drop @ 9 GeV [V]	4.0	3.9	3.9	26.5	40.6
Coil weight [lb]	42.31	42.31	42.31	42.31	49.63
Number of water circuits	4	4	4	4	4
Water flow rate [gpm]	0.2	0.2	0.2	0.2	0.2
Water pressure drop [psi]	150	150	150	150	150
Temperature rise [°C]	0.4	0.4	0.4	17.4	38.2
Total power (magnets and bus) [kW]	0.1	0.2	0.2	4.1	8.3
Total voltage (magnets and bus) [V]	4.0	7.8	7.8	26.5	40.6
Total magnet water requirements [gpm]	0.90	0.90	0.90	0.90	0.83

Table 6-3b. Electron injection line quadrupole parameters at 9 GeV. Coil material is copper for all magnets (continued).

Magnet designation	1Q20	1Q20	1Q20	1Q20
Location	Match	Match	Match	Match
Lattice designation	DEF	QED	QD	Q1
Number of magnets	5	5	1	1
Operating gradient @ 9 GeV [T/m]	4.852	4.852	4.852	5.391
Pole-tip field @ operating gradient [T]	0.063	0.063	0.063	0.069
Gradient-length product [T]	2.51	2.51	2.51	2.79
Inscribed radius [in.]	0.5075	0.5075	0.5075	0.5075
Core length [in.]	19.85	19.85	19.85	19.85
Magnetic length [in.]	20.35	20.35	20.35	20.35
Lamination height [in.]	6.75	6.75	6.75	6.75
Lamination width [in.]	6.75	6.75	6.75	6.75
Packing factor, minimum [%]	98	98	98	98
Core weight [lb]	497	497	497	497
Amp·turns per pole @ 9 GeV	321	321	321	356
Turns per pole	34	34	34	34
Pancakes per pole	1	1	1	1
Conductor dimensions [in.]	0.2×0.2	0.2×0.2	0.2×0.2	0.2×0.2
Cooling hole diameter [in.]	0.11	0.11	0.11	0.11
Conductor cross-sectional area [$in.^2$]	0.022	0.022	0.022	0.022
Conductor length/pole [ft]	184	184	184	184
Current @ 9 GeV [A]	9	9	9	10
Resistance @ 40°C [mΩ]	294	294	294	294
Power @ 9 GeV [kW]	0.03	0.03	0.03	0.03
Voltage drop @ 9 GeV [V]	2.8	2.8	2.8	3.1
Coil weight [lb]	73.46	73.46	73.46	73.46
Number of water circuits	4	4	4	4
Water flow rate [gpm]	0.2	0.2	0.2	0.2
Water pressure drop [psi]	150	150	150	150
Temperature rise [°C]	0.1	0.1	0.1	0.2
Total power (magnets and bus) [kW]	0.15	0.15	0.03	0.03
Total voltage (magnets and bus) [V]	14.0	14.0	2.8	3.1
Total magnet water requirements [gpm]	0.67	0.67	0.67	0.67

additional dipoles are placed downstream to increase the flexibility to match the desired geometry. The dispersion and bending angle from each of these dipoles are exactly canceled by placing a corresponding dipole, bending in the opposite direction, at its image point (four cells downstream in the 90° lattice). This extraction line lattice continues for approximately two sectors (203 m), beyond which a matching region with four quadrupoles will match the optics into the electron bypass line.

The electron bypass is optically the same as that for positrons (see Section 6.2.4) but will operate at a higher energy (9 GeV). The connections of the bypass lines to the NIT and SIT lines will be accomplished by using a general and flexible method (see Section 6-3).

6.3 UPGRADE OF THE NIT AND SIT BEAMLINES

The NIT and SIT beamlines were used to transport electrons and positrons, respectively, between the linac and the PEP ring. A schematic layout of both lines, including currently available instrumentation, is shown in Fig. 6-11. Except for a few minor modifications at the entrance and exit, the optics and geometry of these lines will not be changed. Each line is made up of three achromats comprising four cells with a phase advance of 90° per cell. Thus, the optical transfer matrix between any two points separated by a path length difference equal to the length of two cells is the negative of the identity matrix. This attribute of the achromats has been used extensively in the design of these beamlines to locate magnets and to roll whole sections in order to provide needed vertical deflections while simultaneously controlling the dispersion.

As an example, the dispersion induced by the first group of bending magnets, B1, B2, and B3, is canceled by the two dipoles B4 and B5. More subtle is the fact that dispersion induced by the vertically bending pulsed magnets 40PM1 and 40PM2 and the vertical magnet BVA is canceled by rolling the two downstream magnets. Therefore, it would be difficult to change any one region in these beamlines without significantly affecting the geometry and optics elsewhere. Because of this close coupling of optical and geometric parameters, it was decided to establish a matching point early in the beamline, beyond which all optical and geometrical parameters would remain fixed (that is, only upstream modifications would be allowed).

There are 14 such parameters in all: 8 optical parameters (β_x, β_y, α_x, α_y, D_x, D_y, D'_x, and D'_y) and 6 geometric parameters (X, Y, Z coordinates, the polar and azimuthal direction angles, and the roll angle of the curvilinear beam coordinate system). A workable solution for matching the bypass lines to the NIT and SIT lines has been found using a general method with great flexibility. The procedure is as follows:

- Extend the NIT or SIT optical lattice upstream as far as necessary (at least four cells); this continuation ensures an easy matching of the beta functions, once the geometry and dispersion are controlled by other means
- Modify the bending arrangement to obtain the desired geometry
- Add bending magnet configurations (some similar to the chicane described in Section 6.2.2) that allow independent adjustment of the dispersion while maintaining a desirable geometry

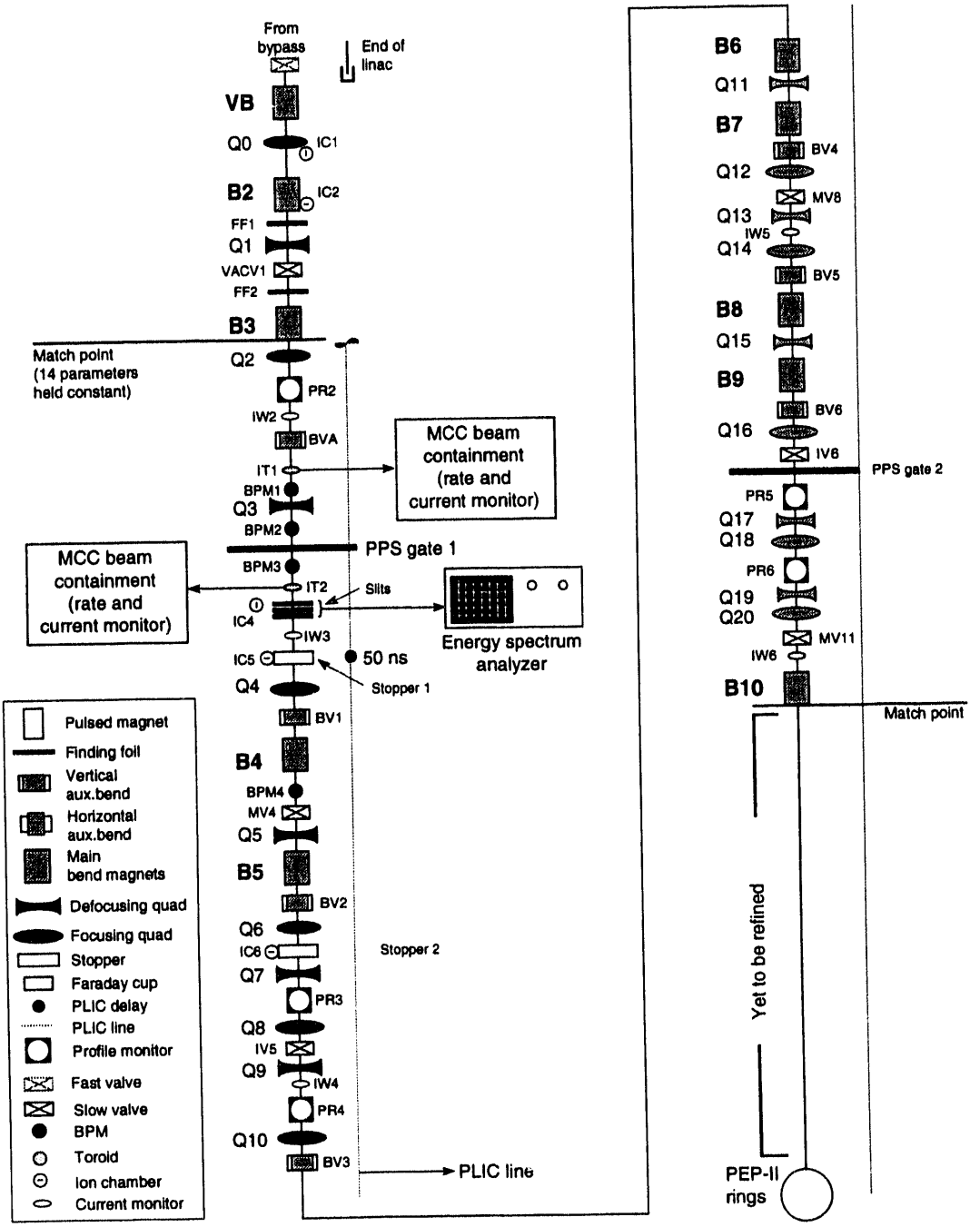

Fig. 6-11. Schematic layout of the identical NIT and SIT lines.

As described below, we have applied this method to optically connect the bypass lines to the NIT and SIT lines; the resulting solutions are shown in Fig. 6-12.

In the existing NIT and SIT beamlines, the separation of the electrons and positrons at the end of the linac is initiated by two vertically bending pulsed magnets that direct either beam into a downstream Lambertson septum dipole, B1. In this magnet, the beams are

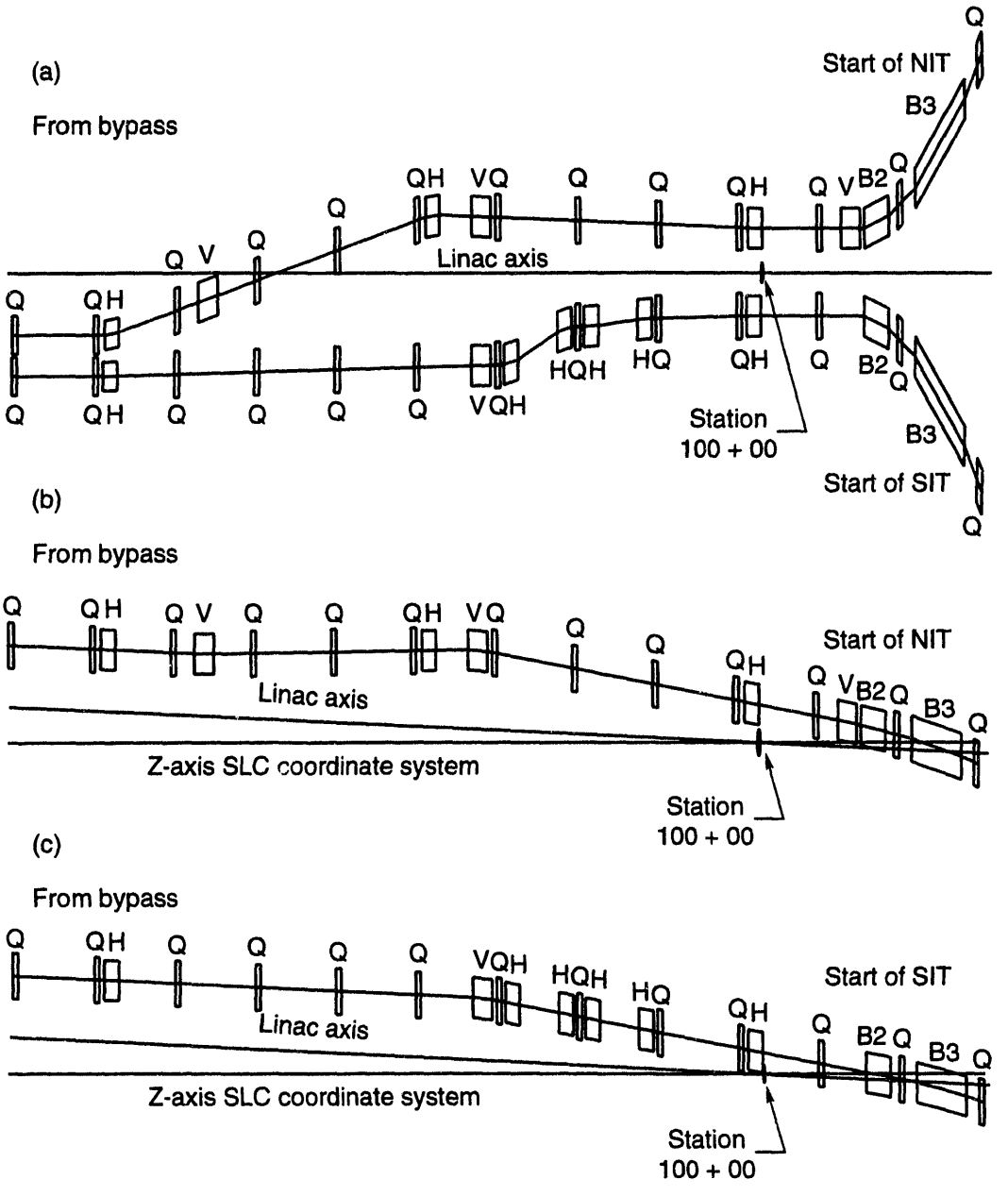

Fig. 6-12. Plan (a) and elevation (b, c) views of interfaces between the electron and positron bypass lines and the NIT and SIT lines, respectively. Vertically bending magnets are denoted with a V, and horizontally bending magnets are denoted with an H.

bent in opposite directions by 3.75° each. The two beamlines downstream of B1 are now independent; they are designed to be identical and are simply mirror images reflected about the linac axis. Two more bending magnets, B2 and B3, complete the horizontal deflection in this region, the first bending the beam by 3.75° and the second by 7.5°.

For the PEP-II injection optics, the downstream end of the B4 magnet was chosen as the matching point at which to hold fixed the 14 optical and geometric parameters while the geometry and optics upstream were changed (see Fig. 6-11). The first modifications were to increase the bend angle of B3 from 7.5° to 9° and to increase the bend angle of B2 from 3.75° to 6°. Thus, the total bend of 15° was maintained while eliminating magnet B1. These modifications resulted in a horizontal displacement of the input beam axi. (still parallel to the linac axis) by 47 cm at the end of the linac; this is shown in Fig. 6-12.

Next, the matching of the geometry and dispersion in the vertical plane are accomplished by utilizing small vertical bending magnet pairs having opposite strengths and placed four cells apart (that is, imaged by the optical identity). The strength of these magnets is adjusted to match the vertical height and direction of the positron bypass, thus connecting the beamlines and completing the geometrical match in the vertical plane. The vertical dispersion caused by these magnets nearly cancels because of their optical placement, but there remains a residual vertical dispersion that must be controlled to obtain the correct values of D_y and D_y' (both nonzero) at the matching point. This was accomplished by simultaneously rolling the magnet B4 (which changes vertical geometry and couples horizontal and vertical dispersion) and adjusting the strength of one additional small magnet to complete the vertical geometry and dispersion matching.

The same approach is applied to the horizontal plane but with added flexibility to match dispersion and geometry beyond that provided simply by using matched pairs of magnets. When the geometrical match is completed using only paired magnets, there remains residual dispersion to correct. This is done utilizing several differing configurations that can either change dispersion without changing the overall geometry (that is, the input and output are made coaxial) or offset the beam (that is, the input and output are made parallel but not coaxial), allowing an additional freedom of choice in the optimization of dispersion and geometry. For example:

- Use of four bending magnets in a chicane, placed symmetrically about a quadrupole. This will introduce dispersion and will have coaxial input and output beams. Two such chicanes, placed 90° apart in phase advance, provide control over the dispersion and its derivative.
- Use of two bending magnets of equal and opposite strength, placed either in a drift or at any two points in the lattice that are not separated by the negative identity matrix. This will introduce dispersion and simultaneously introduce a parallel offset.

Either of these two schemes can be used to adjust the geometry and dispersion without affecting the beta function matching. An example of one such configuration, which connects the electron and positron bypass lines to the NIT and SIT beamlines, is shown in Fig. 6-12.

With the geometry and dispersion matching between the bypass lines and NIT and SIT completed, it becomes a simple task to introduce a short optical section (consisting only of quadrupoles) to match the beta functions of the two lines.

Figures 6-13 and 6-14 show the optics for the completed positron and electron transport lines (including SIT and NIT), respectively, starting at the point where the beam from the damping ring is injected into Sector 2 of the linac and terminating at a point in the PEP tunnel near where the beam will be injected into its appropriate ring. In this optics calculation, the positron beam starts with an energy of 1.21 GeV (the design energy for the damping ring), is accelerated to 3.1 GeV in Sector 2, coasts through Sector 3 at constant energy, and is extracted at Sector 4. The electron beam also starts at 1.21 GeV but is accelerated to 9 GeV in Sectors 2–7 and extracted at Sector 8. The positron (electron) bypass line has 22 (18) cells and has been matched to the SIT (NIT) beamline as described above. The final segments of these beamlines, which will match to the parameters required for injection into the rings, are under design and will be completed soon. Because our design approach is quite flexible, it will easily accommodate any required engineering changes.

6.3.1 Coordinate System for the Injection Transport Lines

Before building the PEP-II injection lines, it is necessary to establish their coordinates and dimensions in the real world. The injection lines are longer than 3 km and undergo many elevation changes along their lengths. Furthermore, the lines cross the boundaries of regions where local coordinate systems and fiducial monuments have been previously defined and surveyed. Thus, three differing coordinate systems are needed for defining the positions of beamline components for installation and alignment purposes. The transformations required to ensure continuity across the regional boundaries are already well understood, though they will continue to be refined in surveys by the SLAC alignment group.

All work on the optical design of the injection lines has included the coordinates of components in their appropriate coordinate system; these have been checked for consistency at regional boundaries, as well as being checked with previous specifications (as with the NIT and SIT beamlines). Before describing these coordinate systems in detail, we note here that they are defined (and used in the optical codes) as right-handed coordinate systems. These same coordinate systems are often converted to left-handed systems by the SLAC alignment group. Fortunately, this conversion requires only a sign change of the X coordinate so this should not be a cause for confusion.

The three coordinate systems are depicted in Fig. 6-15, along with sufficient information to define all of the required coordinate transformations. The first coordinate system, that used in the linac housing, has as its origin the linac injector. The Z-axis for the linac coordinate system is along the linac central axis. This axis and the local gravity vector at the injector define a plane that is used to define the other two orthogonal directions. The X-axis is perpendicular to this plane, pointing north, and the Y-axis lies within this plane pointing upward (note that since the linac is sloped, the Y-axis is *not* along the local gravity vector). In this coordinate system, the coordinates (in meters) of the end of Sector n is given by (0, 0, 101.6n), so that the end of the last sector (Sector 30)

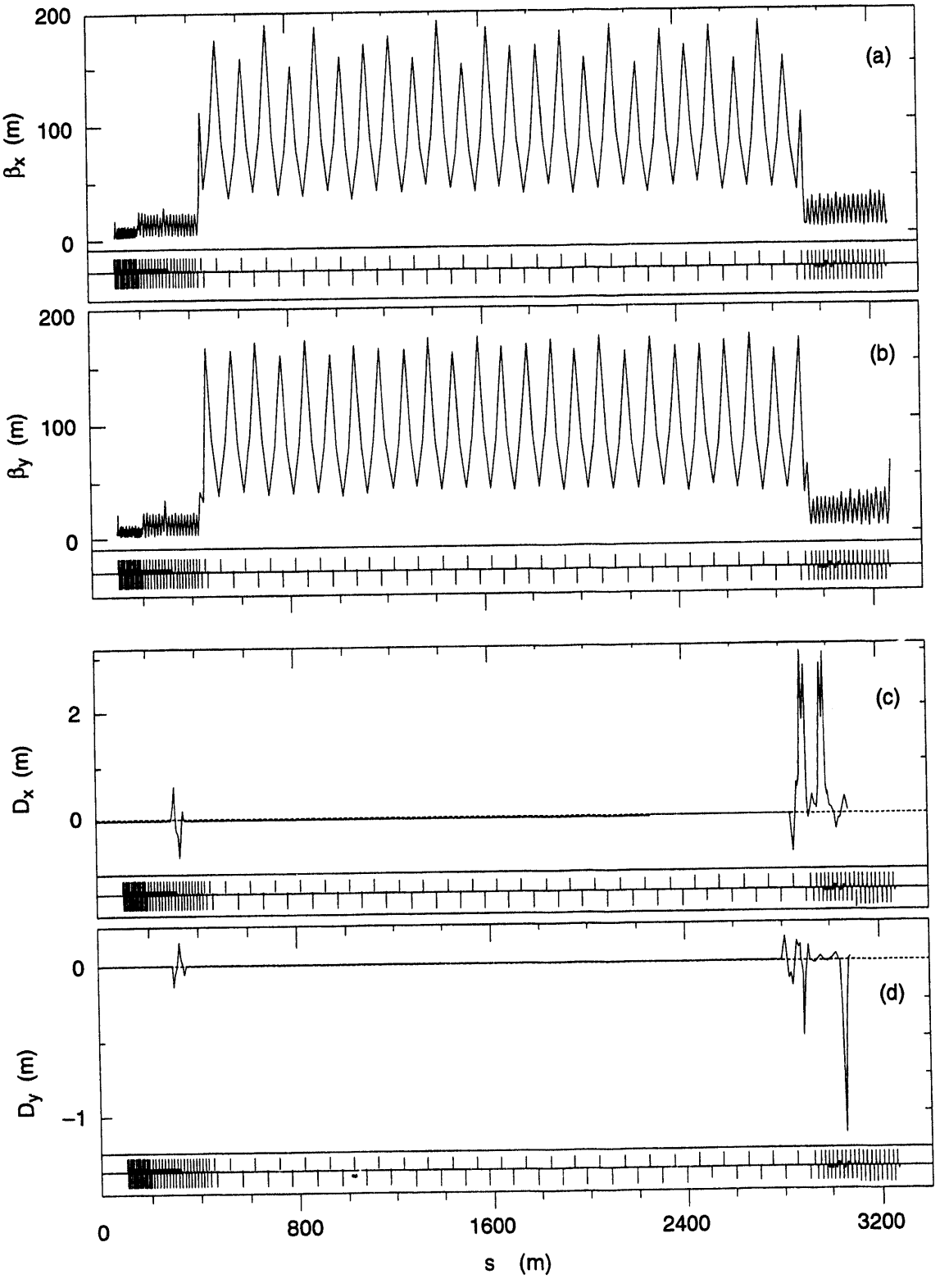

Fig. 6-13. Optics for the complete positron transport line.

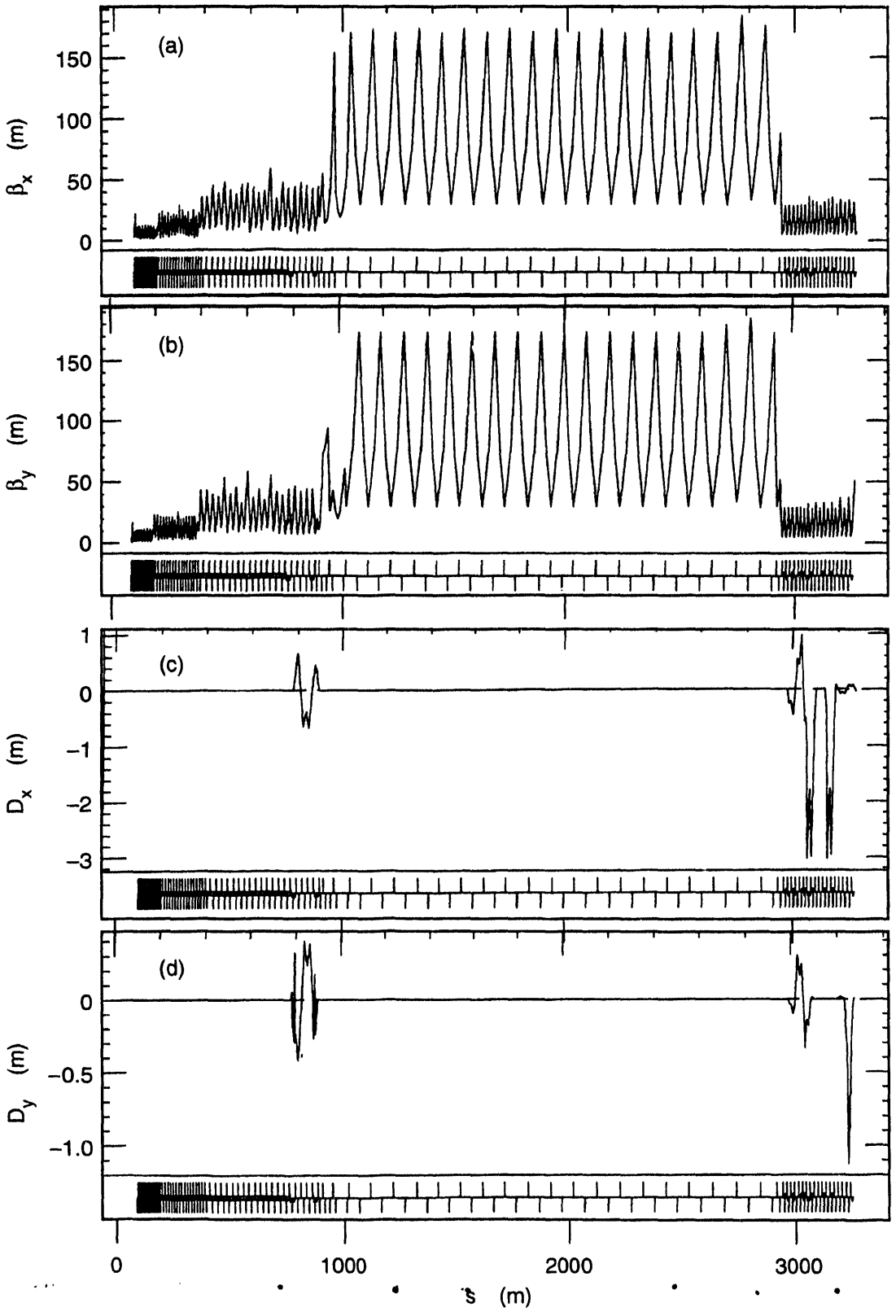

Fig. 6-14. Optics for the complete electron transport line.

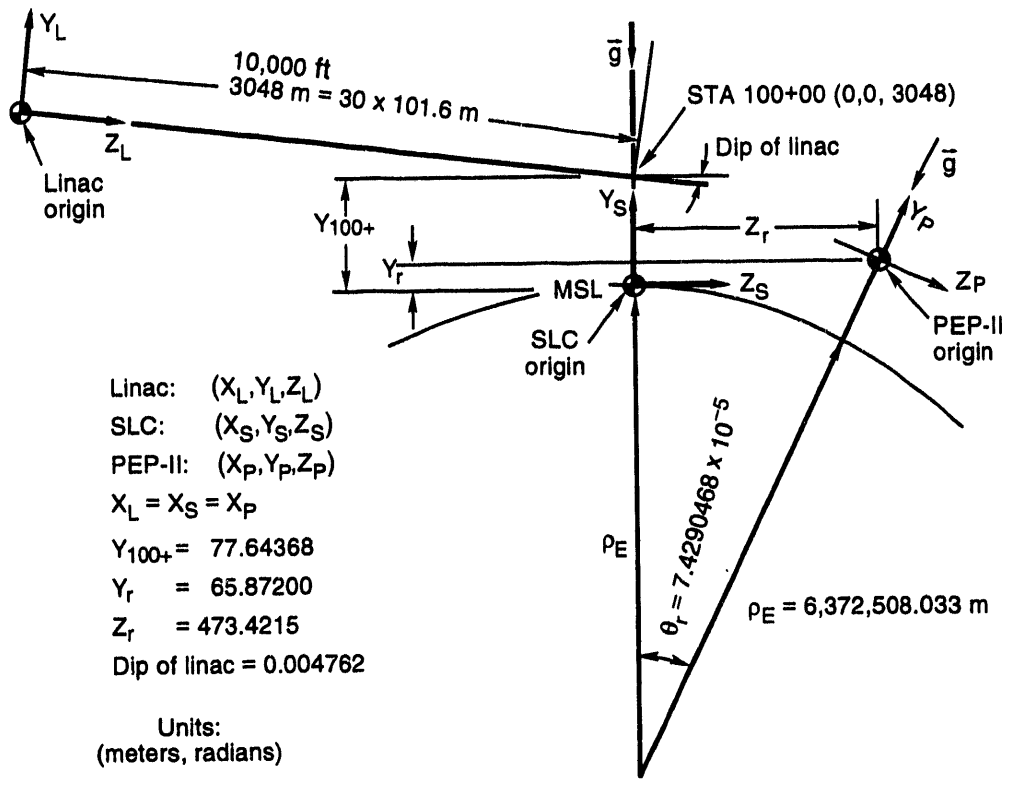

Fig. 6-15. Relationship among the various PEP-II coordinate systems. The coordinates Y_r, Z_r, and θ_r give the origin of the PEP-II coordinate system in the SLC coordinate system.

occurs at (0, 0, 3048), or exactly 10,000 feet from the origin. This point has been given a special name and is called "STA(tion) 100+ 00." We note it here because it leads us directly to the definition of the next coordinate system, which is the "SLC coordinate system."

The origin of the SLC coordinate system is at mean sea level (MSL), and its positive *Y*-axis is antiparallel to the local gravity vector and passes through the point on the linac axis denoted STA 100+ 00. The *Z*-axis of this coordinate system is perpendicular to the local gravity vector and is coplanar with this vector and those vectors defining the *Y*- and *Z*-axes for the linac coordinate system. Thus, we see that the *X* coordinate of a point in the SLC coordinate system has the same value as its *X* coordinate in the linac coordinate system. This turns out also to be true for the remaining coordinate system, the "PEP-II coordinate system," as the origins of all three of these systems are in a common vertical plane (that is, the plane of the paper in Fig. 6-15). The SLC coordinate system will be used for the alignment of the NIT and SIT beamlines.

The PEP-II coordinate system, which will be used for defining the locations of the ring components and the nearby components of the injection lines, has as its origin the center of the PEP-II HER. Its positive *Y*-axis is again antiparallel to the local gravity vector, and this vector, along with the orthogonal *Z*-axis, are coplanar with the linac axis

and the *Y*-axes of the other two coordinate systems. Information defining the translation and rotation transformation between this system and the other two is provided in Fig. 6-15. We note here that during alignment of the ring, it will be necessary to apply a correction to allow for the variation with ring azimuth of the difference between the *Y*-axis and the gravity vector at the ring perimeter. Furthermore, we note that the current computer model of the SIT beamline in this coordinate system has successfully reproduced alignment data for optical components that was last published in 1978.

6.4 FEEDBACK AND DIAGNOSTIC DEVICES

The PEP-II injection system must operate with very high reliability. To achieve this, diagnostic devices are needed to characterize and tune the beam so that filling of the rings can proceed efficiently. In addition, a fast feedback system is required to ensure that the injection system can be run in a routine fashion. Both the hardware and the software necessary to implement such a feedback system are therefore necessary.

Clearly, the injection transport lines will operate at maximum efficiency when the beams are of a specific energy for the rings, are of a specific size and shape, are injected at a specific location and angle, have the minimum possible energy spread, and do not suffer any unwanted losses. Hence, we must provide the hardware to measure the energy, phase-space distribution, trajectory, and energy spread, and to localize and measure beam losses. Considerable experience with the necessary devices has been gained during the operation of the SLC. That experience gives us high confidence that the PEP-II injection system is well matched to the hardware capability.

A generalized, database-driven fast feedback system has already been developed for the SLC [Rouse et al., 1991; Hendrickson et al., 1991; Rouse et al., 1992]. The system is designed to facilitate the implementation of new feedback loops. The hardware necessary to operate a particular fast feedback loop comprises only a distributed set of microprocessors and a communication link between them, as shown in Fig. 6-16. We intend to directly use the software and hardware already developed by the SLC in the PEP-II injection system. The following subsections will detail our specifications for the system. All of the comments should be interpreted to apply to both transverse planes of both the electron and positron transport lines.

6.4.1 Diagnostic Devices

In simplest terms, our diagnostic system must be able to measure beam positions, angles, and intensities, beam shape, beam energy and energy spread, and beam losses. We need the positions and angles to determine the beam trajectory. We must measure the trajectory reasonably precisely in order to steer the beam, determine its energy, and match it to the PEP-II rings. We need to determine the shape of the beam to ensure that we understand its phase-space area. (The transport lattice will operate at peak efficiency only over a limited range of beam energy and emittance values.) Finally, we must be able to localize beam losses to determine where we must resteer the beams.

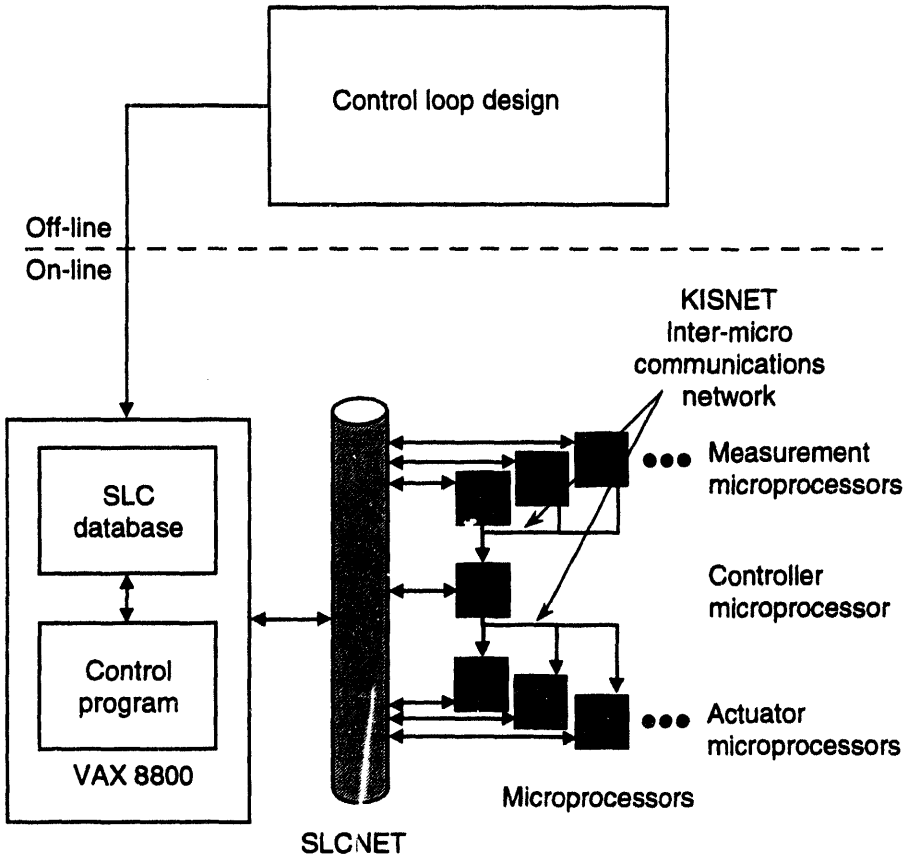

Fig. 6-16. Necessary hardware to implement a fast feedback loop for the injection system.

6.4.1.1 Injection Line BPMs. We will use BPMs to characterize the beam trajectory. Each quadrupole in the extraction, transport, and NIT/SIT parts of the injection line will have an x-y BPM (though only the two x strips or the two y strips will be connected to cables, depending on the quadrupole type—QFs having x readouts, QDs having y readouts). Near the ring injection point, we are dealing with devices (the kicker magnets and septum) that are best calibrated by use of the beam itself. Hence, we propose to add extra BPMs at this crucial location. A pair of BPMs will bracket each kicker magnet in the ring and three BPMs will be added in the region of the septum magnets. The BPMs may be either linac-style or FFTB-style devices. The electrodes will be slightly recessed in the beam pipe wall and will be rotated to be in the x and y directions, as only one plane will be read out for each quadrupole to reduce cabling and processing electronics costs.

BPM Electronics and Cabling. Where possible, a pair of cables will be run from each PEP-II injection line BPM to a nearby linac BPM. The cables will be coupled into the cables of the linac BPMs with 10-dB-loss couplers. To keep signals from the x and y plates the same relative size, four couplers must be installed together on any linac BPM. Thus, two injection BPMs can be connected to each linac BPM used. (This multiplexing

into existing cables and electronics has already been done successfully in the PRL.) An important restriction of this scheme is that, during one linac pulse, the BPM electronics module timing can only be set to look at one of the BPMs connected to its input. Care must also be taken to ensure that BPM pulses from the injection line positrons and linac scavenger electrons do not arrive too close together in time at the BPM electronics module. This time separation can be increased by always connecting the injection line BPMs to upstream linac BPMs.

In a similar fashion, the BPMs in the upstream NIT line will be multiplexed with those in the upstream SIT line, as the cables come back to the same service building. The downstream NIT BPMs, along with any used in the HER injection straight section, will come up in the IR-10 service building. It will not be possible to multiplex these with the downstream SIT and the LER injection BPMs, because these latter cables appear in the service building at IR-8.

For injection into the PEP-II rings, the smallest injected pulse is expected to contain 1/20 ($\sim 2 \times 10^9$ particles) of a full storage ring bunch ($3\text{–}6 \times 10^{10}$ particles). In the linac at present, the sum of the four strips in a 2.5-cm-diameter × 10-cm-long BPM can detect a minimum bunch intensity of 2×10^9 particles. We will design the BPMs to have an operating range of $0.1\text{–}3 \times 10^{10}$ particles (that is, the modules will have a dynamic range of 30:1). This is a factor of two increase in sensitivity compared with the BPMs of the linac (for which a bunch with lower charge will not reliably trigger the linac BPM module to convert). Because the 10-dB-loss coupler will introduce a factor of 3.2 loss in pulse height for the injection BPMs, and an additional factor of two loss results from the fact that only two strips will be summed (either the x or the y strips), the signal height must be increased by a factor of 13 compared with the linac BPMs in order to make use of the linac BPM electronics. This will be accomplished by increasing the length of the injection line BPMs and by having the strips cover a greater fraction of the beam pipe circumference.

BPM Position Resolution. The position resolution required of the injection line BPMs is dictated by our need to steer through apertures and to reliably and routinely match the position, angular, and energy acceptance of the PEP-II rings. If the BPM resolution is better than the rms beam sizes, σ_x and σ_y, everywhere in the injection line, then the beam position will clearly be sufficiently well known compared with the $>10\sigma$ apertures of the injection line. The smallest β_x or β_y at the injection line quadrupoles (where the BPMs are located) is $\beta \approx 40$ m. For an injection line emittance of 0.28 nm·rad, this corresponds to $\sigma = 0.1$ mm. In terms of spatial distance, the closest object to the injected beam is the septum at 3.5 mm. The energy aperture of the ring is ±0.5%, which corresponds to ±2 mm of horizontal motion in the dispersive region ($D_x \approx$ 0.4 m) at the beginning of the injection line (where the beam energy will be stabilized by a feedback loop). An rms resolution of 100 μm for all injection line BPM position measurements would be comfortably within these requirements. This 100 μm specification is for a pulse of 1×10^9 electrons, or about 1/40 of a full ring bucket. This is about half the smallest quantum of charge we contemplate injecting.

6.4.1.2 Energy Measurement. To measure and control the beam energy, we use BPMs to determine the incoming and outgoing beam angles from a calibrated dipole magnet [Abrams et al., 1987] in a dispersive region of each extraction line. One wire scanner will also be placed in the dispersive region in each line to measure the energy profile of the beam.

6.4.1.3 Beam Size and Shape Measurement. A wire scanner will be placed in a dispersion-free region of each extraction line. By varying a quadrupole strength, this scanner can be used to measure the beam phase-space ellipse, and thus the beam emittance. It is expected that such an emittance measurement will be done infrequently. An additional four wire scanners will be placed near the end of each injection line, again to measure the beam phase-space ellipse and emittance. These latter devices are expected to see more frequent use. Therefore, they are located so that measurements can be made during injection without having to vary a quadrupole. The injection lines will have a total of 12 wire scanners.

We intend to augment the wire-scanner measurements with observations from beam profile monitors (phosphorescent screens that can be viewed remotely via a television camera). Operators can insert the screens and directly view the beam shape. This information is not the quantitative equivalent of the wire-scanner information, but it is very useful operationally. We envision at least four screens for each beam—one to augment the measurement of the energy spread in the extraction line, one at the entrance to the NIT or SIT line, one at the exit of the NIT or SIT line, and one near the ring injection point.

6.4.1.4 Beam Loss Measurement. Lastly, we need a system to localize beam loss so that the operators can quickly isolate and correct any badly steered portions of the transport line. BPMs can be used to get an overall view of beam loss, but since the quadrupoles are approximately 50 m apart, this must be viewed as crude. We intend to augment the BPMs with a so-called PLIC (Panofsky Long Ion Chamber) cable strung along the entire length of the bypass lines. The ring injection areas are once again the most crucial locations. Fast ion chambers may be installed here to distinguish between beam losses at injection and beam losses in the ring. (A PLIC cable is already in place in the existing NIT and SIT lines.)

6.4.1.5 NIT and SIT Diagnostics. For the NIT and SIT lines, most of the instruments shown in Fig. 6-11 are satisfactory and will be used in the PEP-II injection system. The beam position systems in the NIT and SIT lines will be enhanced. Originally, beam position and shape were measured at 10 locations along each injection line, using scintillation screens. In the late 1980's, six additional SLC-type stripline BPMs, four of which are indicated in Fig. 6-11, were installed in each line. For PEP-II, new BPMs will be built so that there will be one BPM per quadrupole. As is the case elsewhere in the injection lines, the horizontal plates will be read out at QF locations and the vertical plates at QD locations.

The beam current is now measured by toroids installed in the NIT and SIT lines. The operation of these devices is satisfactory and they will be retained, though located in different places along the lines. The region after B10 is still in the process of refinement

and is not detailed in Fig. 6-11. In particular, the instrumentation in the critical region of the injection septa is not yet finalized. Section 6.4.2 discusses some of these issues.

6.4.2 Energy, Position, and Angle Feedback

For a generalized fast feedback system, the action of any closed feedback loop can be cast into a single matrix equation that can easily be implemented on a microprocessor. For the SLC system, the required matrices are designed off-line and downloaded via a database. The system is designed to run on a distributed set of microprocessors, so all routing and communication information is downloaded at startup time. All feedback loops use the same code except for nonlinear loops, for which a few special modules are needed. Currently, 18 such loops run on the SLC, with several more planned. It took about three months to implement all 18 loops.

Figures 6-17 and 6-18 show how the present feedback loops work on the SLC. The action of the energy feedback loop is displayed in Fig. 6-17. This loop modifies the phase of one klystron and keeps the energy constant to within 0.1%. Figure 6-18 shows the action of a steering loop. In this case, the beam upstream of the loop was perturbed and the effect on the position and angle were observed. Steady-state response is sufficient to steer the beam to within 15–20 μm and 1–2 μrad. Steering loops will constitute the majority of the loops for the PEP-II injection lines.

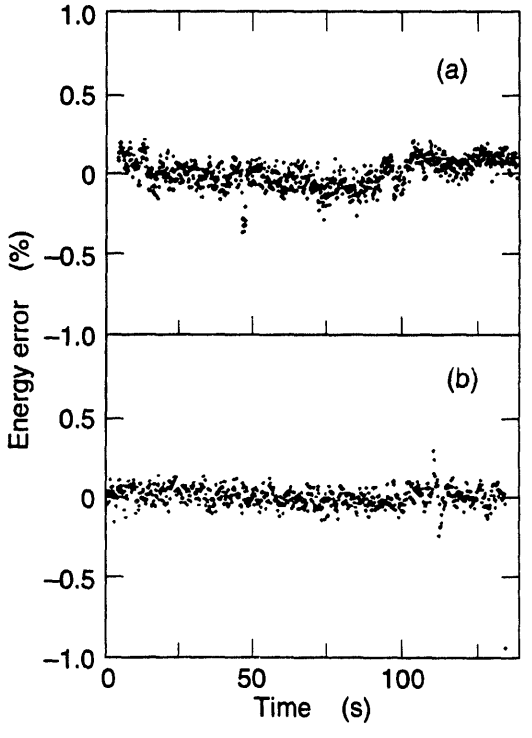

Fig. 6-17. SLC beam energy (a) without and (b) with energy feedback.

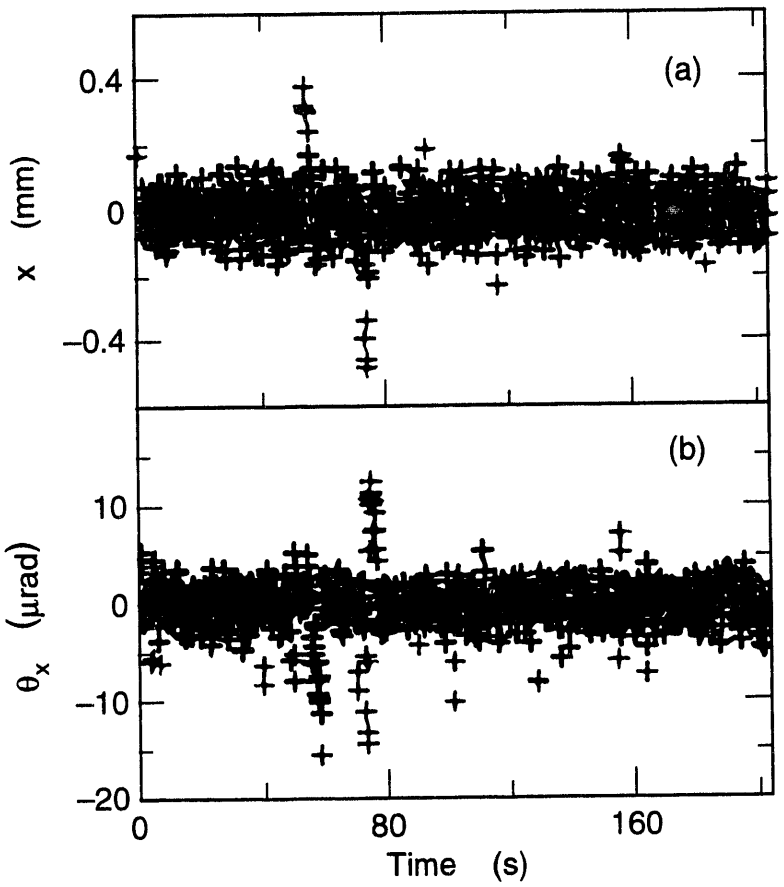

Fig. 6-18. Response of a typical steering feedback loop to an upstream beam perturbation.

Locations of the proposed steering and energy loops are indicated in Fig. 6-19. Steering loops will be placed at injection into the transport lines, at injection into the NIT and SIT tunnels, and at injection into the PEP-II rings. Instrumentation to measure the energy will be placed in the linac extraction area at the location with the highest precision for an energy measurement. The resultant information will then be sent to the microprocessor controlling a particular linac klystron assigned to adjust the energy. The magnets required to steer the beam for feedback will be located near the quadrupoles in the transport lines, as discussed earlier. The diagnostic devices listed above will perform the measurements. Phase shifters or drive amplitude control will be used on selected linac klystrons to change the energy of the beam.

Because we base the feedback and diagnostics for the PEP-II injection system entirely on the SLC, no new types of hardware or software need be developed; we use proven and reliable designs already built for the SLC. This gives us confidence that we can meet the goal of steering to within 15–20 μm and 2 μrad and can build a beam diagnostics system that can identify problems sufficiently to correct them in a timely manner. Our approach ensures that the injection system will always run at high efficiency.

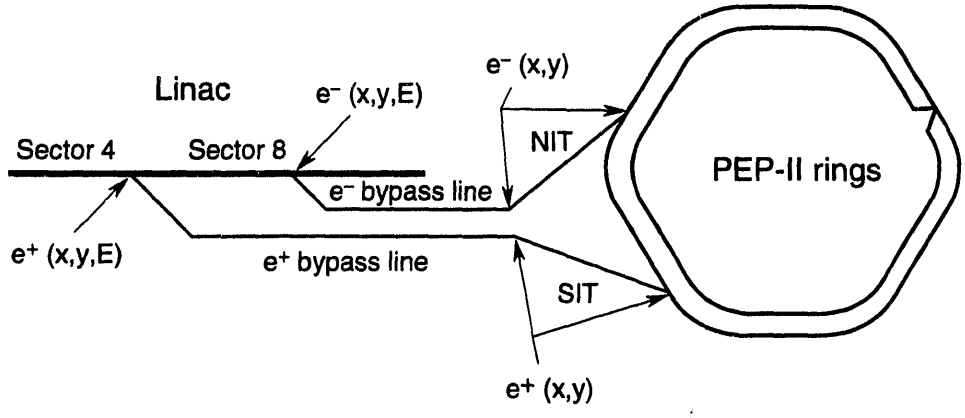

Fig. 6-19. Locations for steering and energy-correction feedback loops (schematic).

6.5 INJECTION INTO THE HER AND LER

Initially, we considered a horizontal injection scheme similar to that in PEP. Ultimately, however, we settled on a vertical injection scheme, which will be described below. The main potential advantage of horizontal over vertical injection is that the uncoupled horizontal emittance ε_x is twice the fully coupled vertical emittance ε_y. Thus, the rms horizontal beam size is at least 1.4 times the vertical beam size (for equal beta functions).

An injection septum in the horizontal case occupies a relatively smaller area in the available phase space, simply because the horizontal phase space is larger. In our case, however, a horizontally injected beam in one ring, which makes large oscillations before damping, will interact parasitically with the circulating beam in the other ring in the region where the two share the same pipe (i.e., near the IP). Beam-beam simulations (described in Section 4.4) show that significant blowup of the low-energy beam size is expected. Thus, in PEP-II, where the beams are separated horizontally, vertical injection is much more effective at reducing the parasitic beam-beam forces and leads to considerably less beam blowup. This was the strongest reason for choosing vertical injection.

There are also other considerations that favor vertical injection for PEP-II:

- Motion in the vertical plane is unaffected by synchrotron oscillations. This simplifies the problem of masking the detector from particles lost during injection. (If we injected in the horizontal plane, off-energy particles could miss the tight masking due to energy-related displacements in the arcs, where there is nonzero horizontal dispersion; vertical injection avoids this possibility.)
- Since there is essentially no bending in the vertical plane, vertical injection avoids the need to correct a nonlinear dispersion function. The nonlinear momentum dependence of the beta function (nonlinear chromaticity) will be slightly worse in the vertical than in the horizontal plane, but we have adopted a chromaticity correction scheme that provides adequate compensation for this.

The injection scheme envisioned for PEP-II is different from that used for PEP. In particular, the drift space constituting the injection straight in PEP-II is an optical section having three additional quadrupoles compared with PEP (for a total of five quadrupoles).

The scheme we have chosen has two significant advantages:

- The transport matrix element R_{12} between the first kicker, K1, and the injection point is large; the vertically defocusing second quadrupole adds to the total kick, thus reducing the burden on K1.
- It is possible to replace the septum kicker used in PEP—which kicked both the circulating and the injected beam and required a rather high voltage—with a DC septum that kicks only the injected beam. This avoids the jitter in the septum kicker that worsened the tracking between it and the other two injection kickers, and thus made it difficult to close the kicker bump in PEP.

The PEP-II injection optics is designed as a $-I$ transformer from the center of the first quadrupole to the center of the fifth quadrupole (180° phase shift). It has mirror symmetry around the central quadrupoles, QDI, with a 90° phase shift between the QDOI and QDI centers. Two slightly different implementations of the PEP-II injection straight section were considered. In the first, the central quadrupole, QDI, is a single element; two possible locations of the injection septum, S0, were investigated. In the second, QDI is split into two elements, with the injection septum centered between them. On comparing the three injection points, we noted two advantages of the split-quadrupole arrangement: (i) somewhat more phase space is available for injection, and (ii) a significantly smaller angular deflection is required from the current-sheet septum, S0, which reduces the current density needed. For these reasons, we selected the split-quadrupole solution.

Apart from the quadrupoles, the chosen injection optics uses two kickers driven in parallel for best tracking. The two kicks are identical and the resulting beam bump is always closed. Also required for the present injection scheme are two pairs of DC magnets, arranged in mirror symmetry with respect to the center of the QDI pair. Their function is to produce part of the bump required for injection and to give additional flexibility in tuning. The fields are always chosen so that the total DC bump is also closed. Finally, there are two septa, S0 and S1. The first of these, S0, is a current-sheet septum at the injection point. It is located inside the storage ring vacuum chamber to avoid the reduction in injected-beam acceptance that would result from providing an additional beam pipe wall. The second septum, S1, is a Lambertson septum designed such that the injected beam approaching its center horizontally from the outside (in the x-z plane) is kicked into the vertical plane for injection. Details of the injection optics are given in Section 6.5.1 below.

The criteria used in designing the injection region were as follows:

- The beam-stay-clear aperture of the circulating *unbumped* beam must be at least $12\sigma + 5$ mm.
- The beam-stay-clear aperture with the DC bump only must be at least 10σ.
- The fully bumped beam-stay-clear aperture must be at least 6σ.

- The vertical emittance used in calculating the beam size must be based on a fully coupled beam; it is $\varepsilon_y = 25$ nm·rad in the HER and $\varepsilon_y = 33$ nm·rad in the LER. (To accommodate a higher than normal β_y^* value in the HER, a larger vertical emittance value of $\varepsilon_y = 50$ nm·rad was used to define the beam-stay-clear aperture for the LER injection hardware.)

Figures 6-20 and 6-21 illustrate the injection straights, showing the paths of both the injected beam and the bumped circulating beam around the injection point of the HER and LER, respectively. Relevant angles and distances are noted. The local stored-beam orbits during the injection process are shown in Fig. 6-22.

The injected beam passes through a double window (two 0.5-mil stainless-steel foils), which isolates the ultrahigh vacuum needed in the storage ring from the poorer vacuum adequate for the injected-beam transport line. A small amount of helium gas is contained between the two windows to permit the detection of any leaks. The double window is placed at a point upstream of the thin septum where β_y of the injected beam is minimum and the phase ellipse is upright. This location minimizes the emittance growth due to multiple scattering in the window. Given the very small vertical emittance of the linac

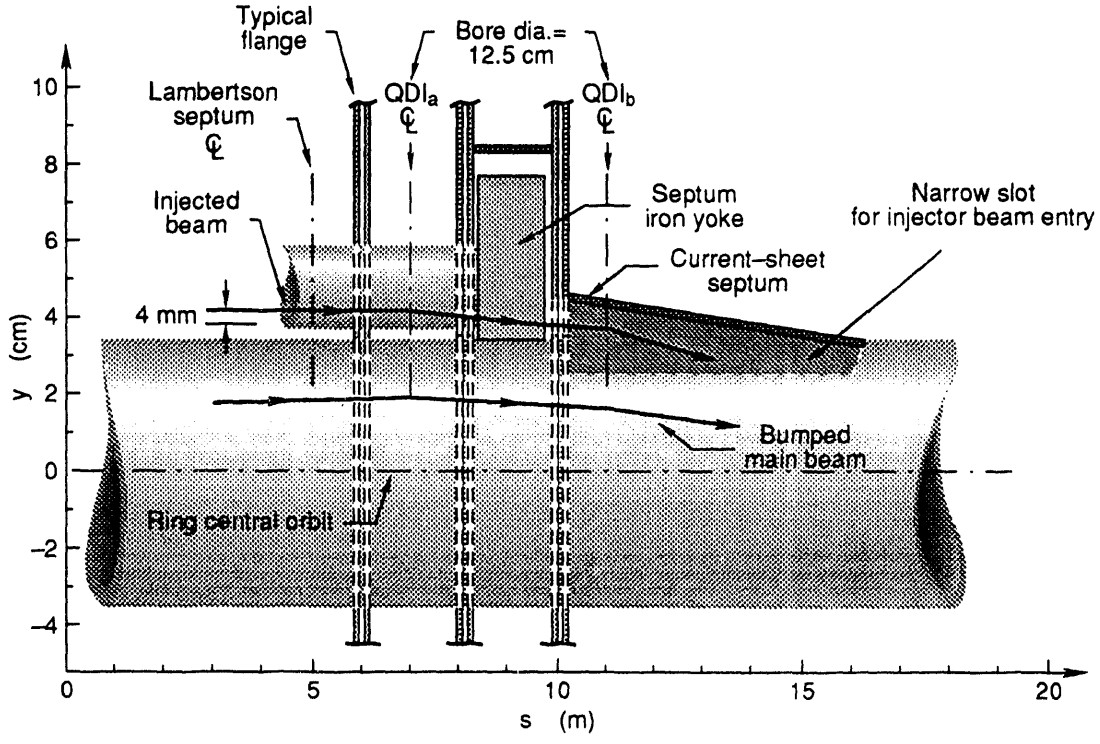

Fig. 6-20. Paths of injected beam and bumped circulating beam in the HER.

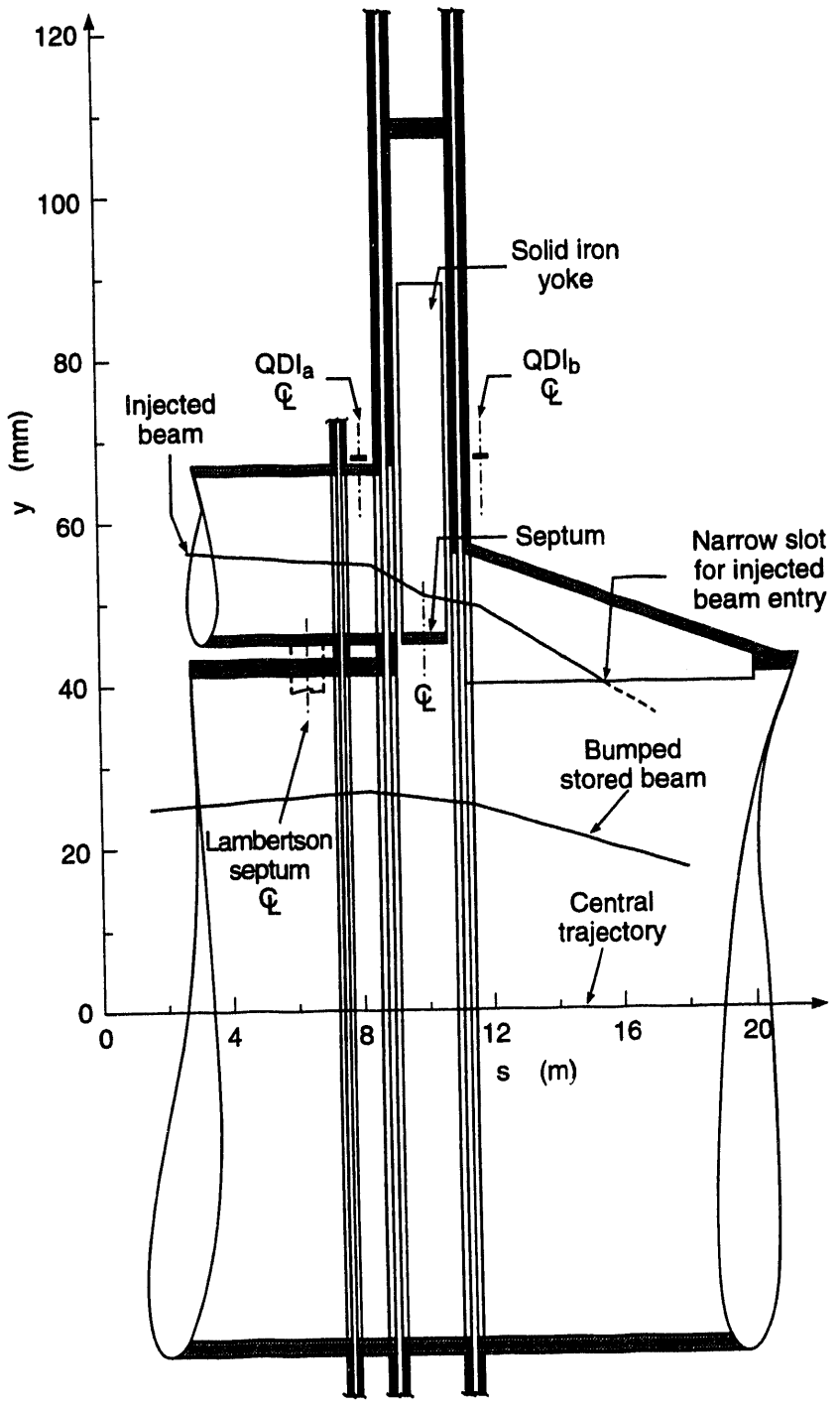

Fig. 6-21. Paths of injected beam and bumped circulating beam in the LER.

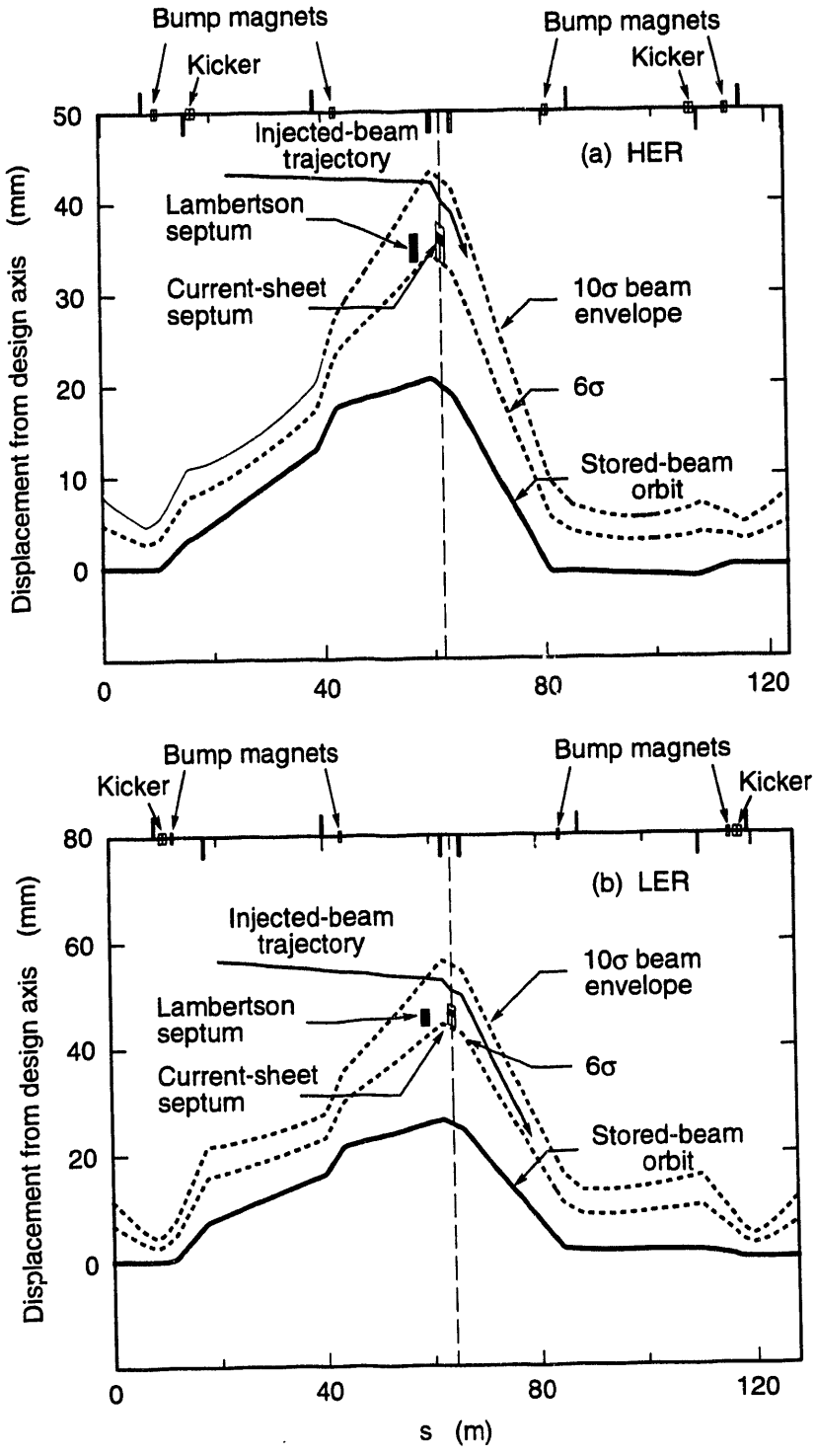

Fig. 6-22. Stored-beam orbit during the injection process, (a) HER and (b) LER.

beams, the actual emittance of the beam injected into the rings is dominated by multiple scattering in the windows. To control the beta functions in this region and to produce an upright phase ellipse at the injection point, two quadrupoles have been added to the injection line in the region between the window and the ring. Figure 6-23 shows the

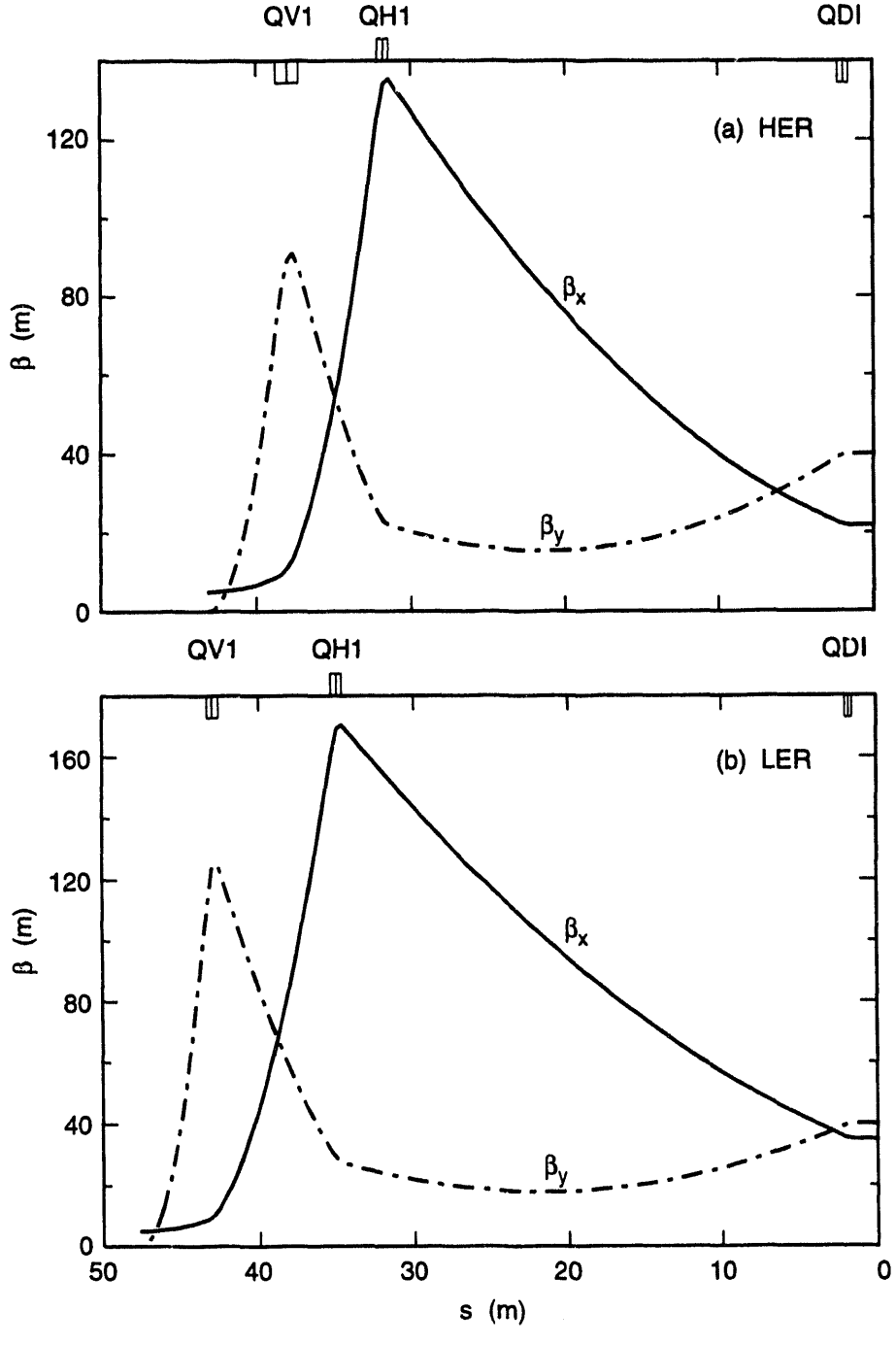

Fig. 6-23. Matching optics from vacuum isolation window to injection point, (a) HER and (b) LER.

resultant matching optics for each ring. The beta functions at the window locations will serve as an additional matching point for the upstream optics, as discussed in Section 6.3.

Figure 6-24 shows the 10σ phase-space ellipses of the HER and LER, indicating the septum (S0) location and the position and size of the injected beam. In both rings, the

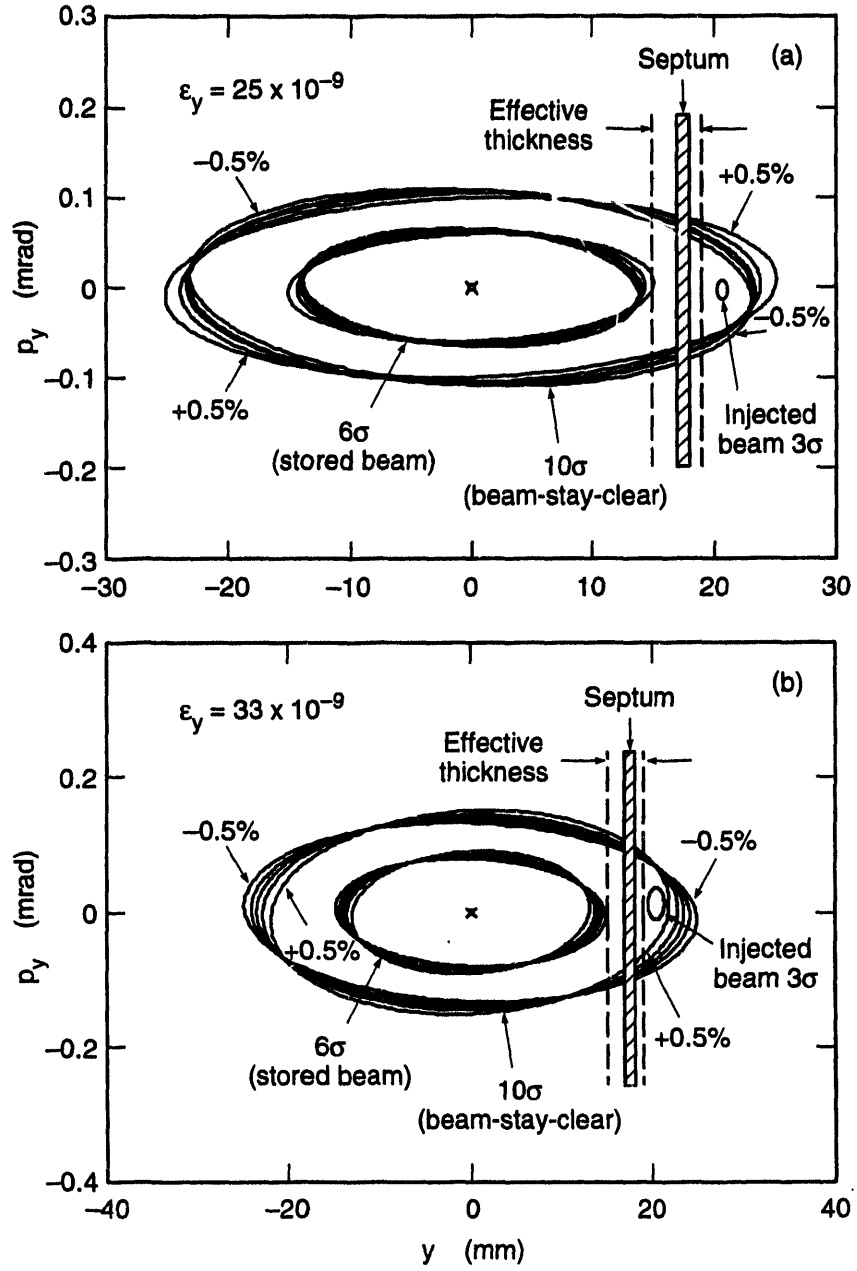

Fig. 6-24. Phase-space diagram of injection acceptance, (a) HER and (b) LER. The dashed lines indicate the effective thickness of the 1-mm septum. Injected beam sizes shown include the effects of multiple scattering in the isolation windows.

distance of S0 from the central orbit is 2 mm beyond that required to satisfy the beam-stay-clear criterion mentioned above, in order to allow for leakage field from the septum. This eliminates the possibility that the septum field might adversely influence the bumped circulating beam.

6.5.1 Ring Optics for Injection

A reasonably large value of the beta function in the plane of injection is needed at the injection septum. In essence, the requirement is that the septum appear to be thin relative to the sum of the injected and stored beam sizes at that point. The value of β at the injection point should not, however, be so large as to give rise to significant extra chromaticity.

Another important factor in the injection straight section design is to have the kickers very well matched to each other. This is especially important for PEP-II, because the bunch spacing is very small and many bunches will be affected by each firing of the kickers. As the filling proceeds, bunches already stored will see the rising and falling edges of the kicker waveform. To ensure well-matched kickers over their entire waveform, we select a system of two identical kickers, spaced 180° apart in betatron phase.

As discussed above, we chose to inject in the vertical plane and to make the optics almost identical for the HER and LER. Transverse dimensions of the LER orbit manipulations are simply scaled up from those of the HER due to the larger emittance of the LER beam.

The actual implementation of the injection scheme in both rings is shown in Fig. 6-25. At the center of the injection straight are two 90° cells. The injection kickers are placed toward the outside of these cells so as to have 180° of betatron phase between them. At each end of the injection straight, one straight-section cell (of length 15.419 m) is added, making the two center cells each 44.391 m in length. (The actual straight section length is somewhat greater than that given by the sum of these cell lengths, to accommodate the septum hardware.) These cells operate as quarter-wave transformers (from the normal cell beta functions to the beta functions at the center of the injection straight) that amplify the normal cell beta functions by a factor of $(44.391/15.419)^2 = 8.3$. Thus, we obtain a beta function of 215 m at the injection septum. In the LER, the quadrupoles must be shifted slightly to avoid interference with particular HER RF cavities in the same section of the tunnel. This changes the value of β_y at the injection point to 170 m for the LER, and requires the relocation of the LER kickers.

As mentioned earlier, the central quadrupole is split into two sections so that injection can occur at the center of the straight where $\alpha_x = \alpha_y = 0$. Four variable parameters (the strengths of quadrupoles QFI, QDI, QFOI, QDOI) ensure the ability to match to the lattice (i.e., to achieve $\alpha_x = \alpha_y = 0$ at the center of the straight section), to obtain 180° of betatron phase advance between the kickers, and to have fine control of the vertical beta function.

The vertical injection process occurs as shown schematically in configuration space and phase space in Figs. 6-26 and 6-27, respectively. The closed orbit of the stored beam is distorted by means of four DC bump magnets and two kickers. The stored beam is first

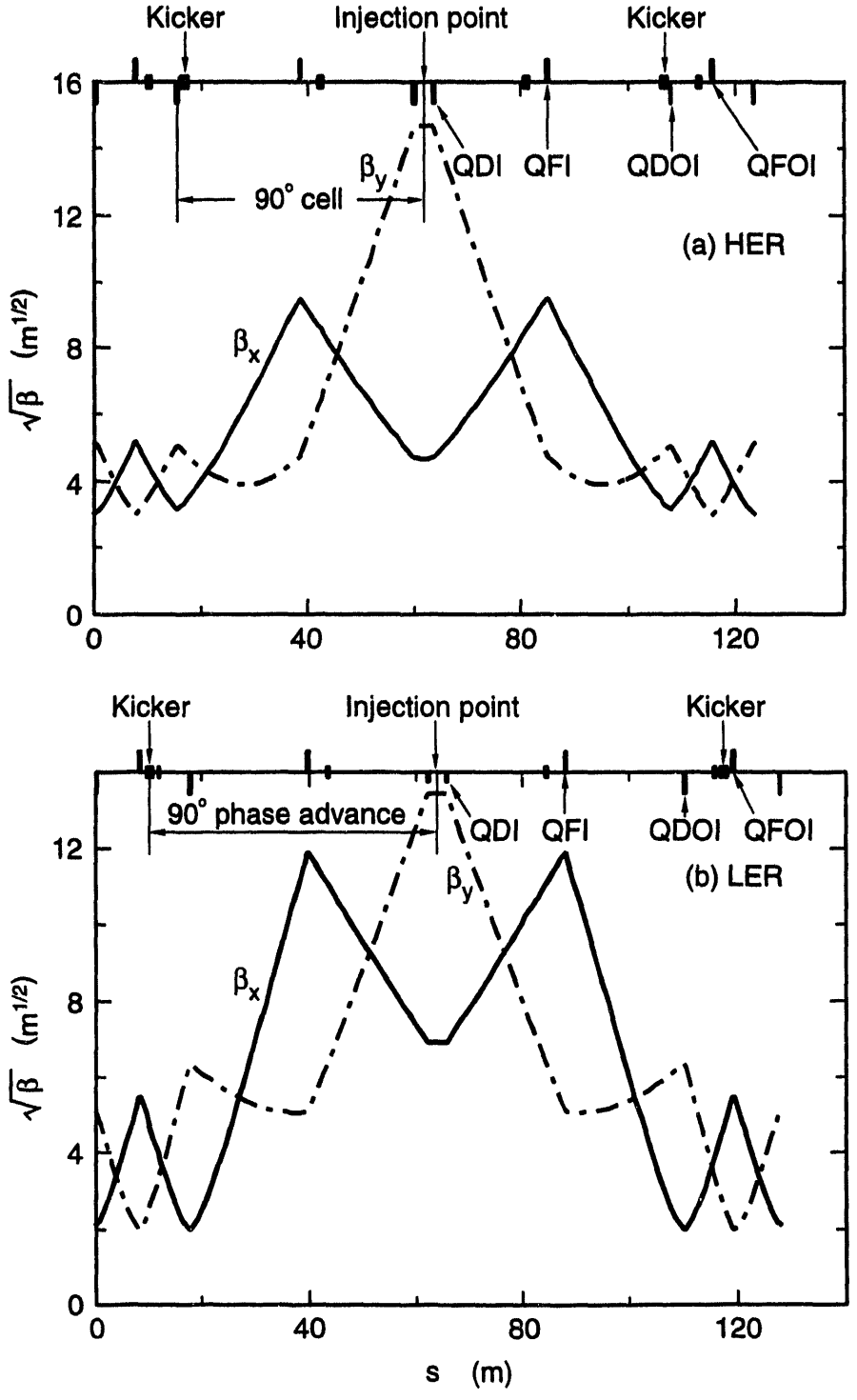

Fig. 6-25. Twiss parameters β_x and β_y in the injection straight section, (a) HER and (b) LER.

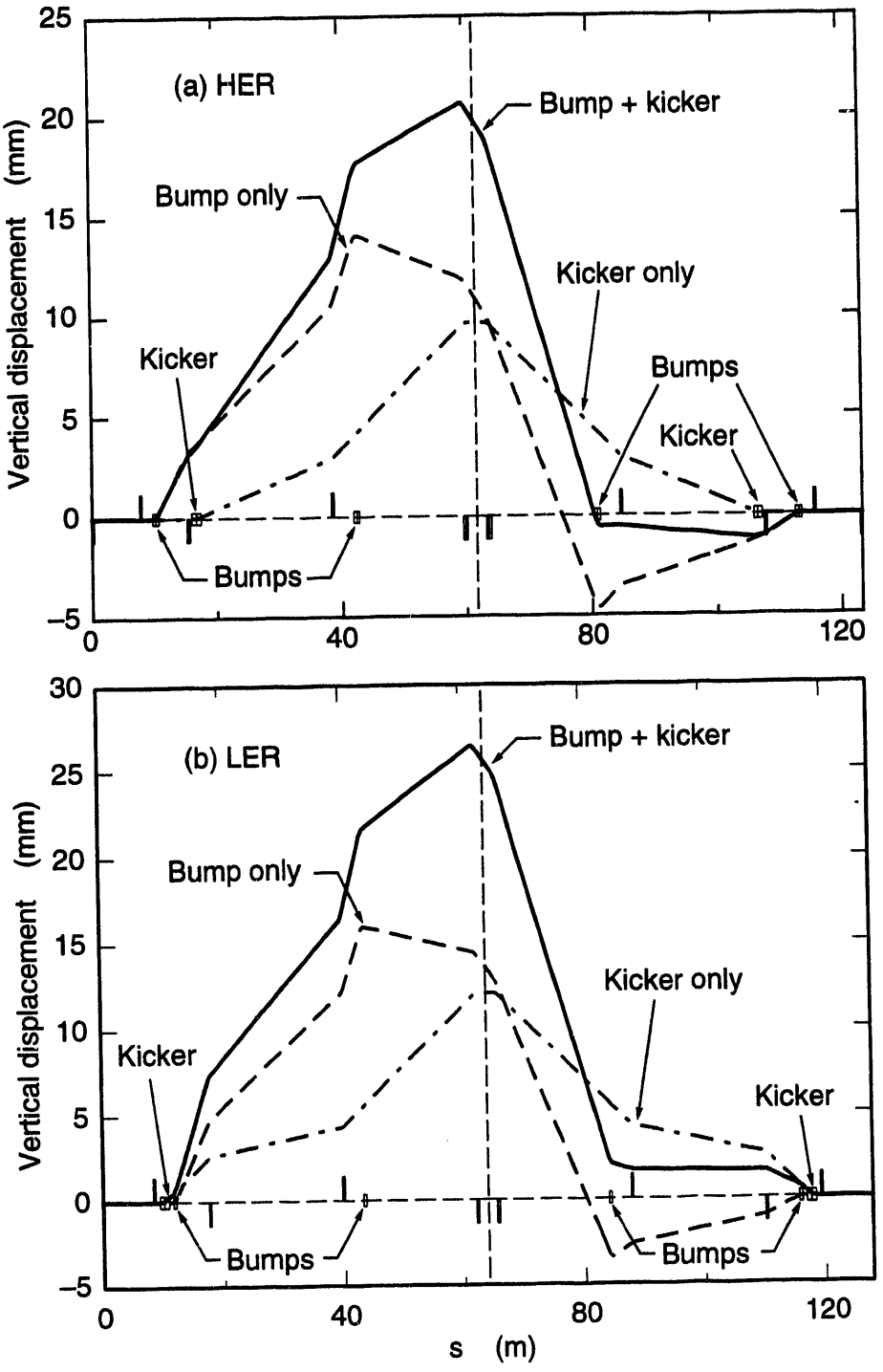

Fig. 6-26. Schematic of the vertical injection scheme, showing displaced orbits, (a) HER and (b) LER.

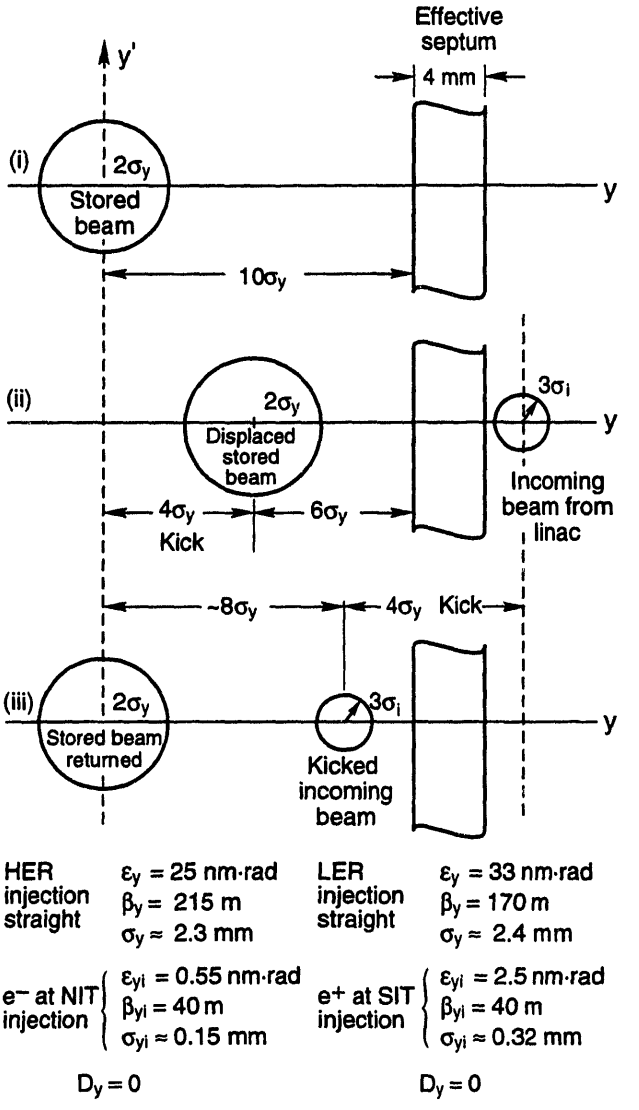

Fig. 6-27. Phase-space diagram of the vertical injection process.

moved to the DC bumped position, $10\sigma_y$ away from the inner edge of the septum. Although the physical thickness of the septum is only 1 mm, an allowance is made for regions of bad field on either side (1 mm on the injected-beam side and 2 mm on the stored-beam side). Then the stored beam is kicked to within $6\sigma_y$ of the effective inner edge of the septum; incoming beam from the transport line is tangent to the stored-beam orbit at this point and clears the effective outer edge of the septum. When the stored beam bunch returns to the injection region on subsequent turns, it is already back on its DC bumped orbit; the newly injected beam is also inside the beam-stay-clear aperture of the ring and inside the septum, ready to damp and merge with the stored beam.

If due care were not taken in correcting the nonlinear chromatic functions in the rings, the beta functions at the injection point would be strongly dependent on momentum. By taking these nonlinearities into account in the chromaticity correction scheme, we have

reduced the β_y variation at the injection point by a factor of 10. The corrected phase-space diagrams for the HER and LER are shown in Fig. 6-24. We see that the emittance of the injected beam (at the 3σ contour) fits easily into the acceptance of the ring. A virtue of the vertical injection scheme is that the nonlinear dispersion (which is confined to the horizontal plane) has much less importance than it would have if injection were in the horizontal plane.

Both the kicks and the bumps will produce a small dispersion function in the vertical plane. At the injection point, this dispersion function will be very nearly equal in magnitude to the orbit displacement there. For the HER, the dispersion function due to the bumps and kickers amounts to $D_y = 0.02$ m and, for a momentum spread of $\pm 0.5\%$, results in a displacement of 0.1 mm, which is negligible. For the LER, the equivalent displacement is 0.14 mm, again a negligible amount.

Because there are magnetic elements (quadrupoles) between the elements of the kicks and bumps, there will be a small residual dispersion function leaking out of the injection straight section. We find this residual dispersion to be entirely negligible.

6.5.2 Mechanical Design

6.5.2.1 Septum Magnets. In this section, we discuss the two septa, S0 and S1, for PEP-II. S1 is a standard Lambertson septum, which bends the injected beam 11 mrad horizontally into the vertical plane of the storage ring. The maximum field required in the gap (for the HER) is 0.4 T for a magnet length of 1 m. A cross section of this septum, suitable for both the HER and the LER, is shown in Fig. 6-28. For the chosen notch angle of 22°, the maximum field anywhere in the iron yoke is 1 T.

The current-sheet septum (S0), though simple in principle, requires a more detailed discussion. Essentially, it is a current loop with an iron flux return. A review of various types of septa and some useful practical considerations can be found in Fischer [1985], and a detailed discussion of dipole septum magnets can be found in Keizer [1974].

For a current-sheet septum, the current density J (in A/mm^2) is given by

$$J = \frac{10^4}{4\pi}\frac{B}{t} \tag{6-3}$$

where B is the magnetic field of the septum (in T) and t is the septum thickness (in mm). We obtain the required total current I (in A) from

$$\begin{aligned} NI &= \frac{Bg}{\mu_0} = 796\,Bg \\ &= JA \end{aligned} \tag{6-4}$$

where N is the number of turns in the loop ($N = 1$ for a current-sheet septum), g is the magnet gap (in mm), and A is the coil cross section (in mm^2).

Using the surface resistivity of copper ($\rho = 1.7 \times 10^{-6}$ Ω·cm), we obtain a power density in the conductor, P/A, in (W/mm^2) of

$$\frac{P}{A} = J^2R = J^2\rho L = 1.7 \times 10^{-4} J^2 L \tag{6-5}$$

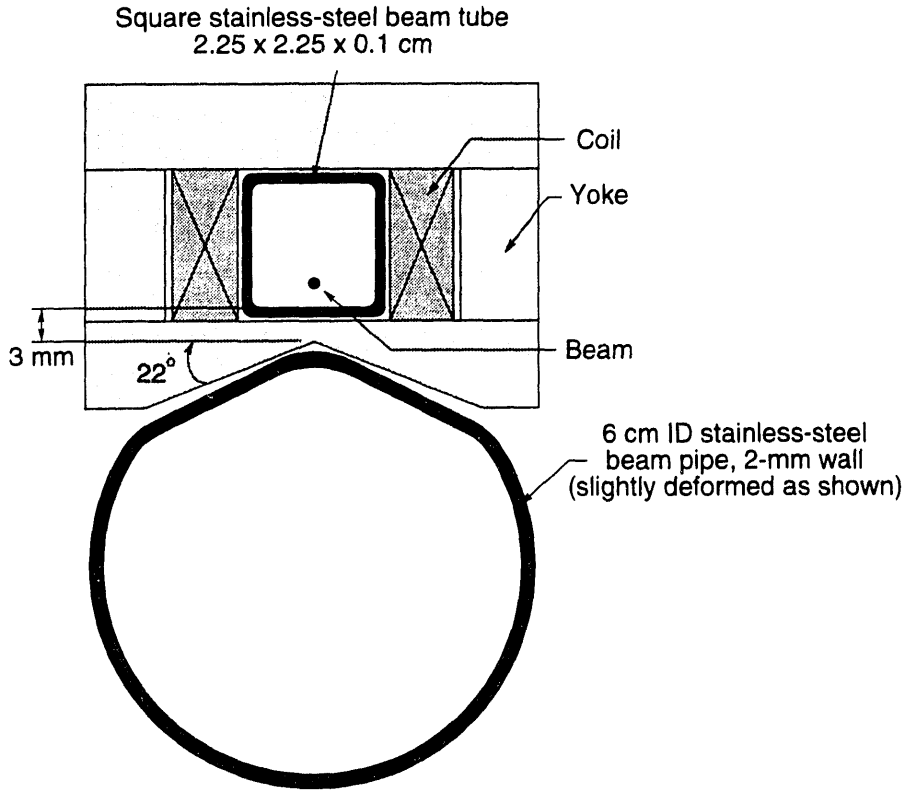

Fig. 6-28. Vacuum chambers and Lambertson septum magnet for both HER and LER.

where L is the conductor length (in cm). From this, we arrive at the total power dissipated in the conductor as

$$P = \frac{P}{A}(g \cdot t) = 1.7 \times 10^{-4} J^2 L(g \cdot t) \tag{6-6}$$

We have also estimated, in two ways, the power dissipated when 60 pulses of a 10-GeV beam with 5×10^9 e^- per pulse strike the septum. First, we ran the EGS code to examine the energy deposition from the shower generated in the initial interaction. Second, we scaled the energy deposition from the curves (also based on EGS) of Eckland and Nelson [1981]. In both cases, it was assumed that the incident beam enters perpendicular to the septum cross section, which is pessimistic in terms of the energy deposition. For the second case, we took the maximum value of $(1/E_0)\cdot(dE/dV)$ (roughly 0.1 E_0/cm^3) from the curves to make our evaluation. However, because the septum is only 1 mm thick, it intercepts just a fraction of the shower; the rest leaks away laterally. After a depth of 10 cm in copper, the radius of the shower is more than 1 cm, and the septum cross-sectional area is less than 5% of the shower area. Therefore, the volume of the septum where energy is deposited at the rate of 1 GeV/cm^3 is only about 2 cm^3. The

resulting estimates of the energy deposition per particle were 1.67 GeV (using EGS directly) or 2 GeV (using the scaled Eckland and Nelson curves).

Taking the more pessimistic value of 2 GeV, the energy deposition per particle is

$$(2 \times 10^{9}) \times (1.6 \times 10^{-19}) = 3.2 \times 10^{-10}\,\mathrm{J}$$

and the power in the septum from the shower due to 60 pulses is

$$(60\ \mathrm{s}^{-1}) \times (5 \times 10^{9}) \times (3.2 \times 10^{-10}\ \mathrm{J}) = 96\ \mathrm{W}.$$

The results of these estimates are collected in Table 6-4 for both rings. We designed both the HER and LER septum coil to safely dissipate 450 W. Figure 6-29 shows a cross section of the dipole septum and an isometric sketch of the coil. The length of the septum is 1 m. Its main features are:

- A yoke that extends beyond the septum at both ends by 5 cm, which helps to terminate the field longitudinally.
- A backleg winding to compensate for the finite permeability of the iron; with a modest number of ampere turns, the field outside the septum is reduced from 0.5 mT to less than 0.1 mT.
- Stainless-steel cooling tubes that carry a negligible fraction of the septum current. Magnetic-field maps showed that copper cooling tubes would carry a much larger portion of the current, leading to a significant distortion of the field in the gap and unacceptable leakage outside.

Cooling calculations show that the maximum rise in temperature anywhere in the septum is 3°C above the input cooling-water temperature (conservatively taken to be 30°C).

6.5.2.2 Ring Bump Magnets. Parameters for the bump magnets are summarized in Table 6-5. These magnets present no special problems since they are very weak. For diagnostic purposes, and for establishing the first-turn orbit, it is advantageous to be able to inject on-axis. To achieve this condition without increasing the kicker strength would require the strength of the bumps to increase by a factor of three. Alternatively, if the kicker strengths were doubled (as permitted by the design, see Section 6.5.2.3), then the bump magnet strengths need only be doubled to achieve on-axis injection.

Table 6-4. Parameters for the current-sheet septa at 10 and 4 GeV.

Ring	Nominal angle (mrad)	l (cm)	B (T)	J^a (A/mm^2)	Ohmic loss (W)	Beam loss (W)	Total (W)
HER	1.00	150	0.022	20.0	255	96	351
LER	1.32	150	0.012	10.0	65	96	160

[a] t = 1 mm, g = 25 mm.

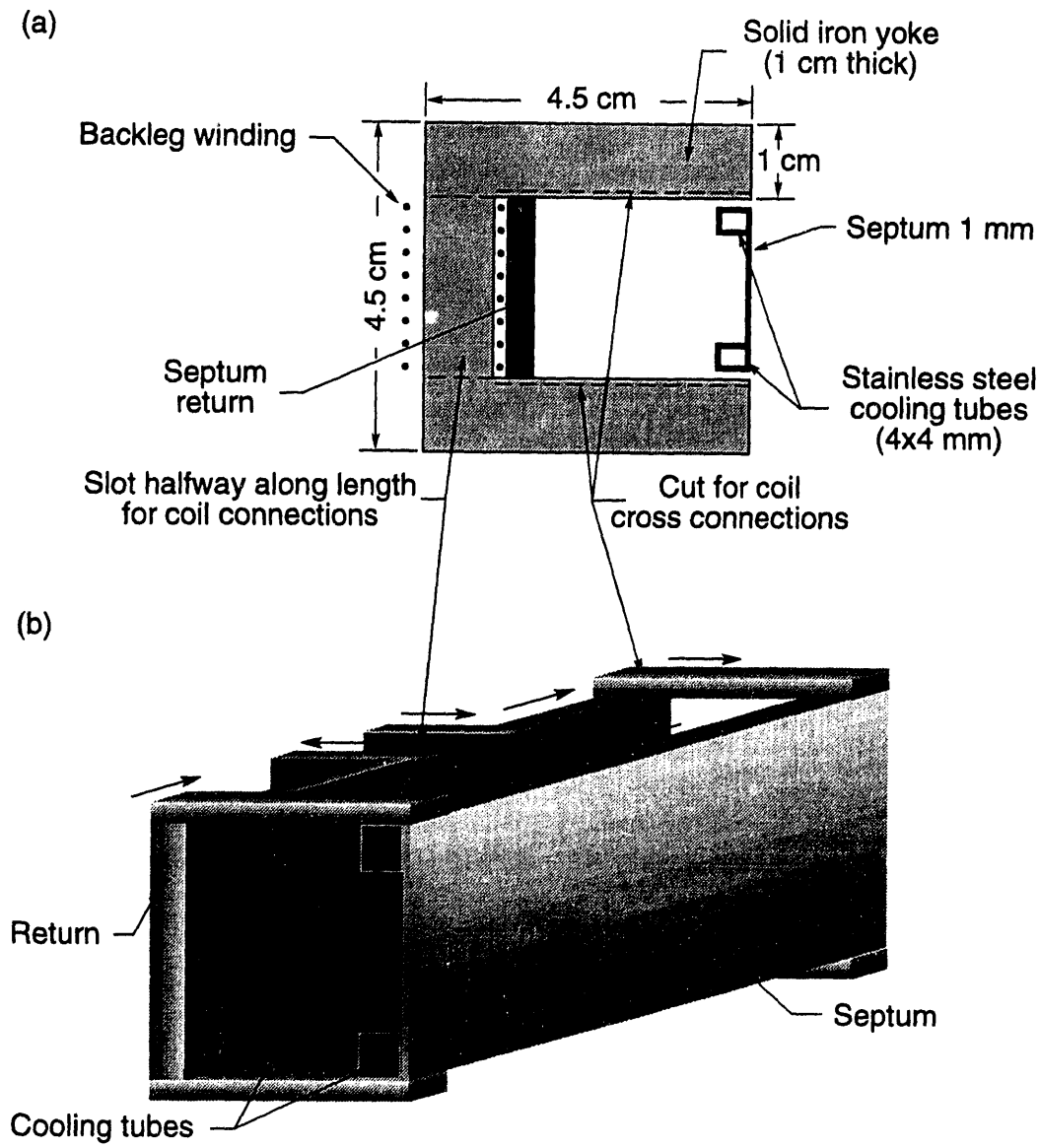

Fig. 6-29. Current-sheet septum for both HER and LER: (a) cross section, (b) isometric of coil.

6.5.2.3 Ring Kicker Magnets. We initially considered three different types of kicker:

- A current loop inside the ring vacuum
- A terminated transmission line inside the vacuum
- A ferrite magnet outside the vacuum

Details of the comparative study of these three types can be found in Bulos [1992]. Eventually, we chose the ferrite type, because it needs the lowest voltage and it avoids any penetration into the ring vacuum (as well as any additional metal surfaces inside the

Table 6-5. Bump magnet parameters at 10 and 4 GeV.

Magnet	Deflection angle (mrad)	Length (m)	Field (mT)	On-axis injection field (mT)
BM1L (HER)	–1.04	1.0	34.7	32.4
BM2L (HER)	0.61	1.0	20.4	33.4
BM1R (HER)	1.12	1.0	37.4	39.9
BM2R (HER)	–0.20	1.0	6.7	6.4
BM1L (LER)	–1.18	0.5	31.5	34.2
BM2L (LER)	0.91	0.5	24.3	44.0
BM1R (LER)	1.08	0.5	28.8	26.1
BM2R (LER)	–0.16	0.5	4.1	15.4

beam pipe, which can disturb the beam). Figure 6-30a shows a cross section of this magnet; the aperture satisfies the beam-stay-clear requirements for either the HER or the LER. The active magnetic length is 75 cm, and the ceramic beam pipe is 1 m long. The main features of this design are:

- A metallic coating on the inside of the ceramic beam pipe to carry the beam image current, as well as to shield against the electromagnetic field of the beam, while still allowing the magnetic field to penetrate the tube with minimal attenuation.
- An outside copper coating on the ceramic tube to permit external water channels to extract the ohmic heat generated by beam image currents in the coating and eddy currents from the magnetic field. The ferrite could also be cooled, if this were needed, in a similar fashion.

The calculation of the heat generated in the present design appears in Bulos [1992]; Table 6-6 lists the relevant kicker parameters.

As indicated by the simplified pulsing circuit of Fig. 6-30b, the two kickers in each ring are driven in parallel, using a common FET-switch pulser capable of delivering 6 kA at 6 kV. When the magnet is shorted at its output, it acts as an inductance, which can be turned into a pure resistance, as shown in Bulos [1992]. The magnet is fed by a cable of equal impedance and whatever length is required. This arrangement avoids any reflections.

6.5.2.4 Ring Quadrupoles. Although the ring quadrupoles in the injection straight have very modest strengths, there are a few special requirements. The two quadrupoles QDI (at the center of the straight) are required to have a large aperture, because here β_y is large and the orbit is sometimes displaced due to the injection bump. In addition, the upstream QFI quadrupole must have a small outer dimension on one side in order to provide clearance for the injection line beam pipe. Parameters for these magnets are included in Tables 5-2 and 5-5 for the HER and LER, respectively.

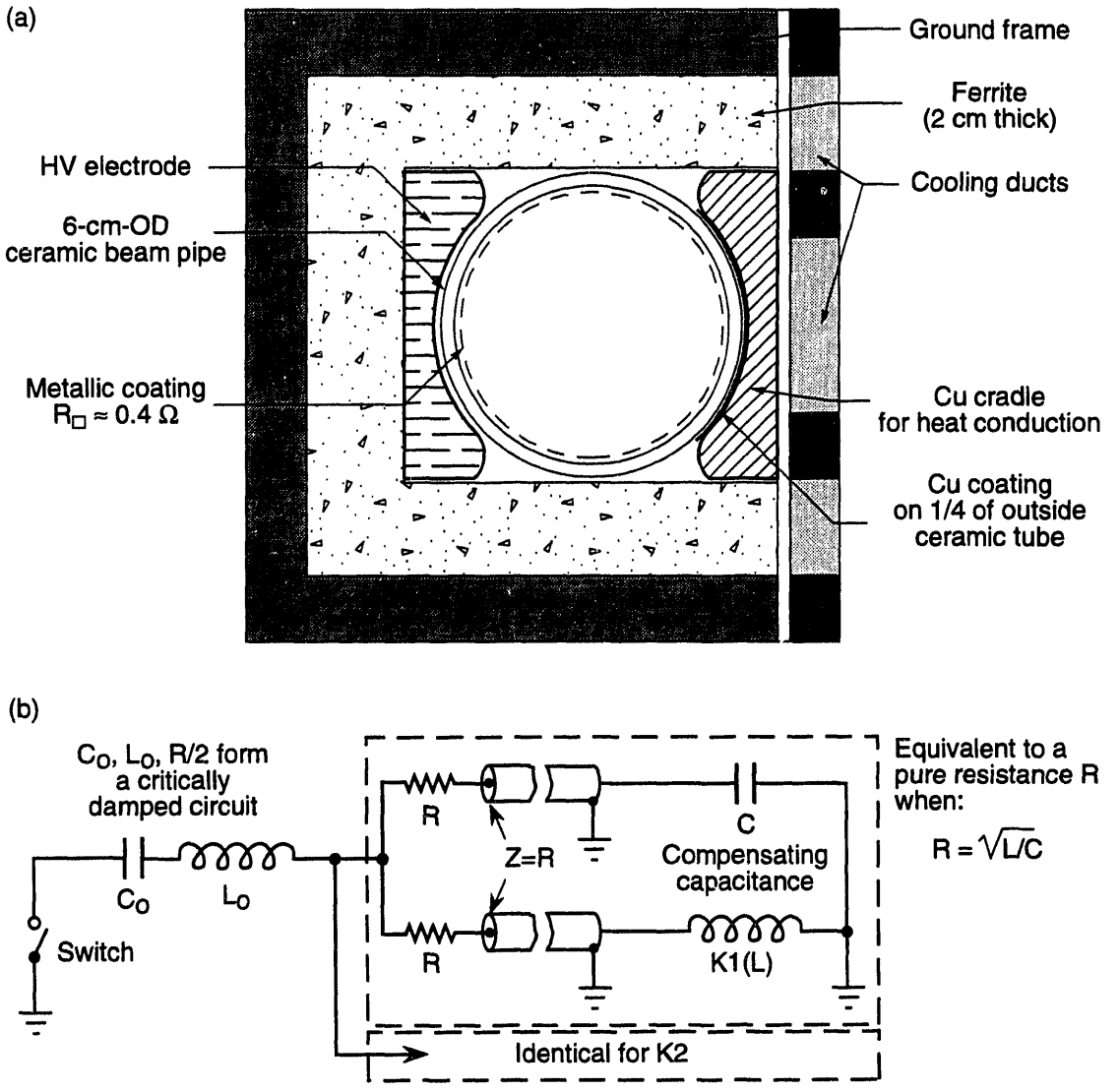

Fig. 6-30. (a) Cross section suitable for all HER and LER kickers; (b) pulsing circuit for fast kickers K1 and K2.

Table 6-6. Kicker parameters.

Ring	E_{max} (GeV)	Kick (mrad)	l (m)	B (mT)	L^a (μH)	R (Ω)	C (μF)	V (kV)	On-axis injection V (kV)
HER	10	0.13	0.75	5.8	1.0	6.6	0.023	4.0	6
LER	4	0.35	0.75	6.2	1.0	6.6	0.023	3.1	6

[a]Includes an estimate of the inductances of the leads and thyratron switch.

6.5.3 Protection of the Detector

The detector must be protected from the radiation caused both by particles lost from the stored beam and those lost due to injection inefficiencies. The relative magnitude of the problem for a high-luminosity collider may be appreciated by comparing some beam parameters of PEP-II with those of PEP and LEP (Table 6-7). Note that each time the HER and LER together lose their entire fills, 49 J/m will be deposited around the ring on average. (We refer to this circumferential average as the "fair-share" loss.) As an order-of-magnitude figure, depositing this 49 J/m into a silicon vertex detector near the beam pipe delivers about 75 rads (i.e., 0.75 J/kg). To be realistic in our estimates, we take here a 75% injection efficiency. We also assume that the 25% injection loss distributes itself around the ring evenly, so that the detector suffers its fair-share loss. In the standard injection mode, the ring will be filled roughly hourly, to bring the beam from 80% back to 100% intensity. Under these conditions, the vertex detector will receive a radiation dose of about 5 rads during each fill and an additional 15 rads associated with the beam loss between fills. Over an operating year (10^7 s), the integrated dose is thus

$$24 \text{ fills/day} \times 116 \text{ days/yr} \times 20 \text{ rad/fill} = 0.6 \times 10^5 \text{ rad/yr}$$

As 2×10^5 rads is the radiation-dose limit for the silicon vertex detector, collimators will be installed to decrease the annual dose below its fair-share amount by at least a factor of 100.

The detector must also be protected from an accident where the full injected beam is steered directly into the interaction region (IR) for any appreciable amount of time. As indicated in Table 6-7, in the case of the HER beam, the injector power (at a nominal 75% efficiency) is 650 W. Under this circumstance, the estimated radiation dose to the vertex detector would be due to 650 J/s (averaged, say, over 10 m), which corresponds to about 100 rad/s. We will deal with this possibility by installing an ionization detector (having a few-second integration time) near the IP. Exceeding a threshold of 0.1 rad/s during injection would be interlocked such that the injection rate would automatically drop from 60 to 10 pps. A manual override to 2 pps will also be possible.

Table 6-7. Comparison of stored and injected beam parameters in various machines.

	LEP	PEP	PEP-II
Charge stored in ring(s) [μC]	0.53	0.36	22.9
Energy stored in ring(s) [kJ]	24	5	108
Fair-share loss of a stored beam [J/m]	1	2	49
Injector power [W]	9	120	650[a]
Fair-share injector power [W/m]	0.003	0.05	0.3[a]

[a]HER only, assuming 1×10^{10} e^- per pulse, at 60 pps, with 75% efficiency.

As shown in Fig. 6-31, there will be three sets of IR protection collimators in each ring, located between the injection point and the detector. Details of the various collimators are summarized in Table 6-8 and discussed below. Note that a "graded-aperture" approach has been followed to protect the IR from particle losses—the aperture (in units of rms beam size) gradually increases as the IR is approached.

Collimator 1. This will be for momentum selection and beam dumping. It will consist of a pair of horizontal collimators, spaced 90° apart in betatron phase and located in a dispersive region. At the HER location shown in Fig. 6-31, $D_x = 1.2$ m and $\beta_x = 25.2$ m. A $\pm 10\sigma_x$ collimator aperture corresponds to a momentum acceptance of $\delta p/p = \pm 9 \times 10^{-3}$ for the stored HER beam.

Collimator 2. This will limit the amplitude of betatron oscillations to $10\sigma_x$ and $10\sigma_y$. Three horizontal collimators (denoted A, B, C in Fig. 6-31), spaced 60° apart in betatron phase, and three vertical collimators (A, B, C), also spaced 60° apart, are placed in a dispersion-free region. These sets of three collimators bound the 10σ beam ellipses in the two transverse planes, as shown in Fig. 6-32 (where the B and C collimators have been projected back in betatron phase to the position of the A collimator).

Collimator 3. This serves to catch any degraded particles that spray off the tips of collimator 2. It is a essentially a duplicate of the two collimator-2 sets, except that its aperture is 12σ.

As mentioned above, collimator 1 provides a momentum window that prevents a linac beam of the incorrect energy from going part way around the ring and possibly dumping near the detector. In addition, this collimator provides a place to dump the stored beam in the event of an RF trip, for example.

Due to the large stored energy (62 kJ in the HER and 46 kJ in the LER), the stored beam must be dumped in a controlled fashion. A typical ring failure might be an RF trip. The HER beam would then lose 3.6 MeV per turn and spiral into the small-aperture collimator 1 (located at a point of high dispersion) in about 20 turns. Since all other apertures are larger and are located in regions of similar or lower dispersion, the beam will be preferentially lost at collimator 1. (Even in the case of a general power failure, the magnets would maintain their fields long enough to duplicate the behavior of a simple

Table 6-8. Collimator properties.

		Horizontal collimators		Vertical collimators	
	Aperture	No.	Phase adv.	No.	Phase adv.
Injection	$12\sigma + 5$ mm	—	—	—	—
Collimator 1	10σ	2	90°	—	—
Collimator 2	10σ	3	60°	3	60°
Collimator 3	12σ	3	60°	3	60°
IR	$15\sigma + 2$ mm	—	—	—	—

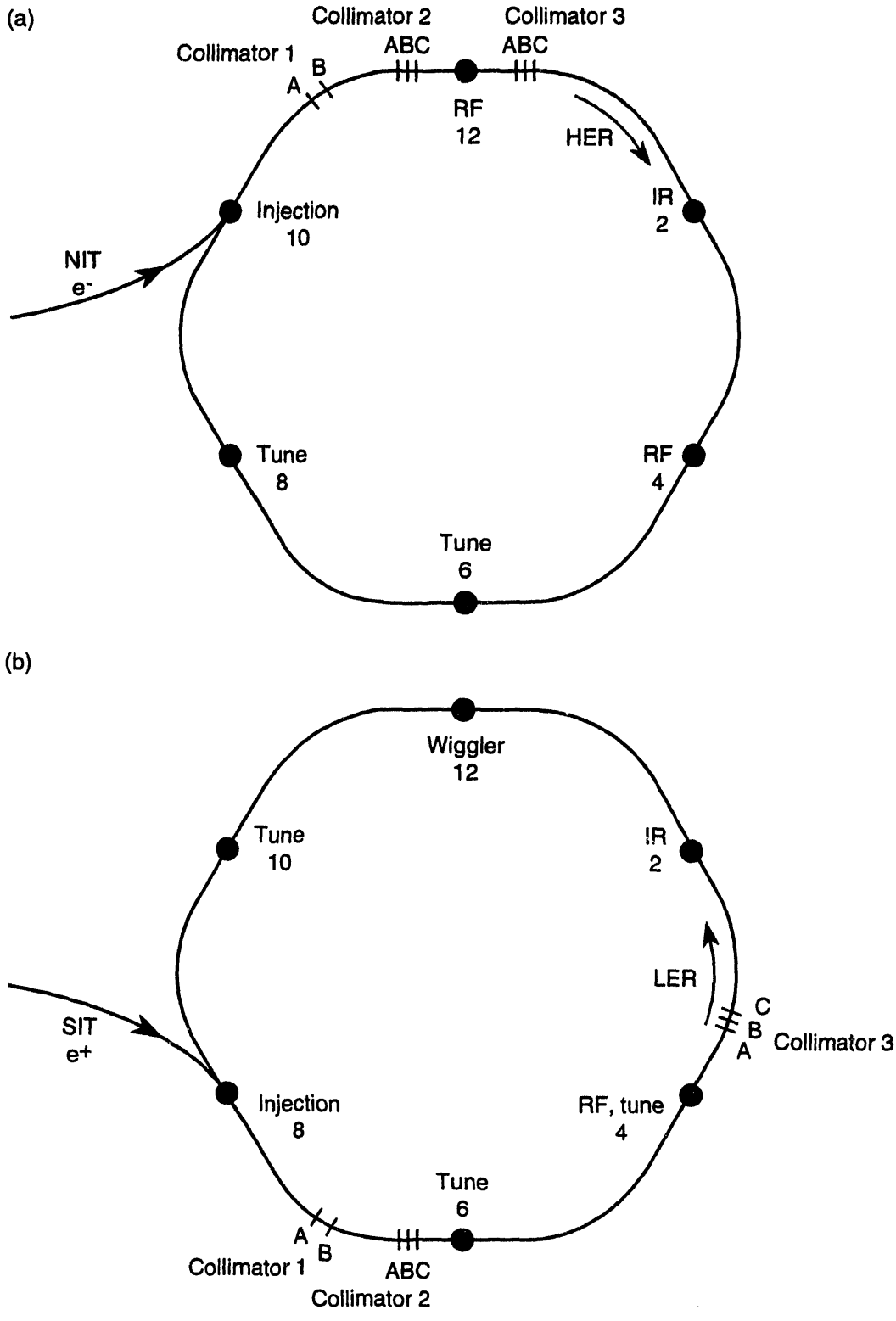

Fig. 6-31. Schematic layout of (a) the HER and (b) the LER, showing the placement of the collimator sets 1, 2, and 3.

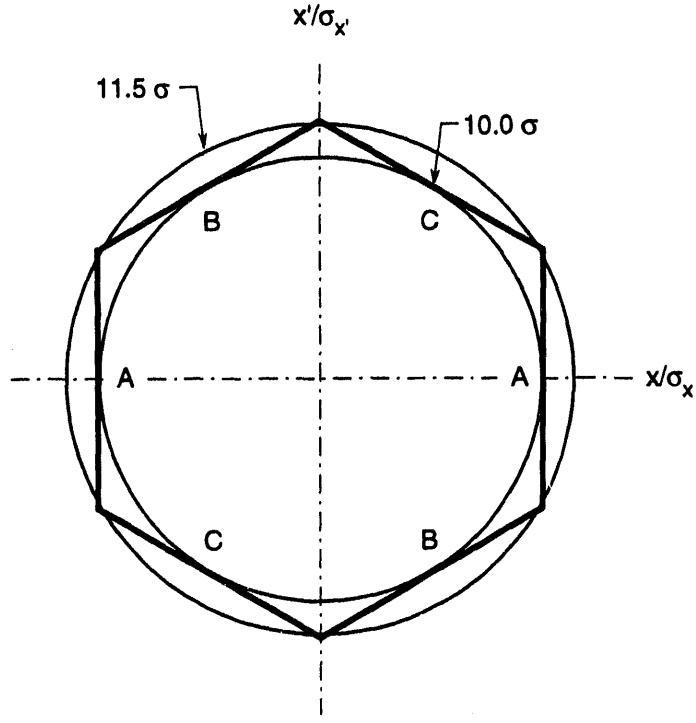

Fig. 6-32. Phase space at the location of collimator 2A. The horizontal and vertical axes have been scaled by σ and σ', respectively. The dark lines show the restrictions from collimators 2A, 2B, and 2C (the latter two projected back to the position of collimator 2A).

RF trip.) Another possible ring failure might involve one or a few steering magnets going sufficiently out of tolerance to steer the beam into something fragile. This will be protected against via the beam-loss monitors, which will detect such occurrences and purposely cause an RF trip.

To design the collimators described above, we must consider the energy deposition when the entire stored beam impinges on a single spot on the collimator (of typical beam-size dimensions) in one revolution (7.3 μs). The deposited energy will not diffuse significantly in this short time, and a very high local temperature will occur both at the surface of the struck material and more deeply inside where the shower has developed.

Figure 6-33 shows the result of an EGS calculation [Nelson, 1993] for the temperature rise of beryllium, carbon, and copper when hit by 9-GeV and 3-GeV pulses of 5×10^{10} electrons. The area of the PEP-II beam corresponds to a circular spot with $\sigma = 0.35$ mm, which is halfway between the $\sigma = 0.5$ mm and $\sigma = 0.2$ mm curves. The temperature rises shown in Fig. 6-33 must be multiplied by 900 for the HER and 1960 for the LER to scale to 4.5×10^{13} and 9.8×10^{13} particles, respectively. For the HER, Table 6-9 lists the maximum temperature reached as determined from the EGS calculation, as well as the entrance temperature due to *dE/dx* alone (that is, before the electrons have showered).

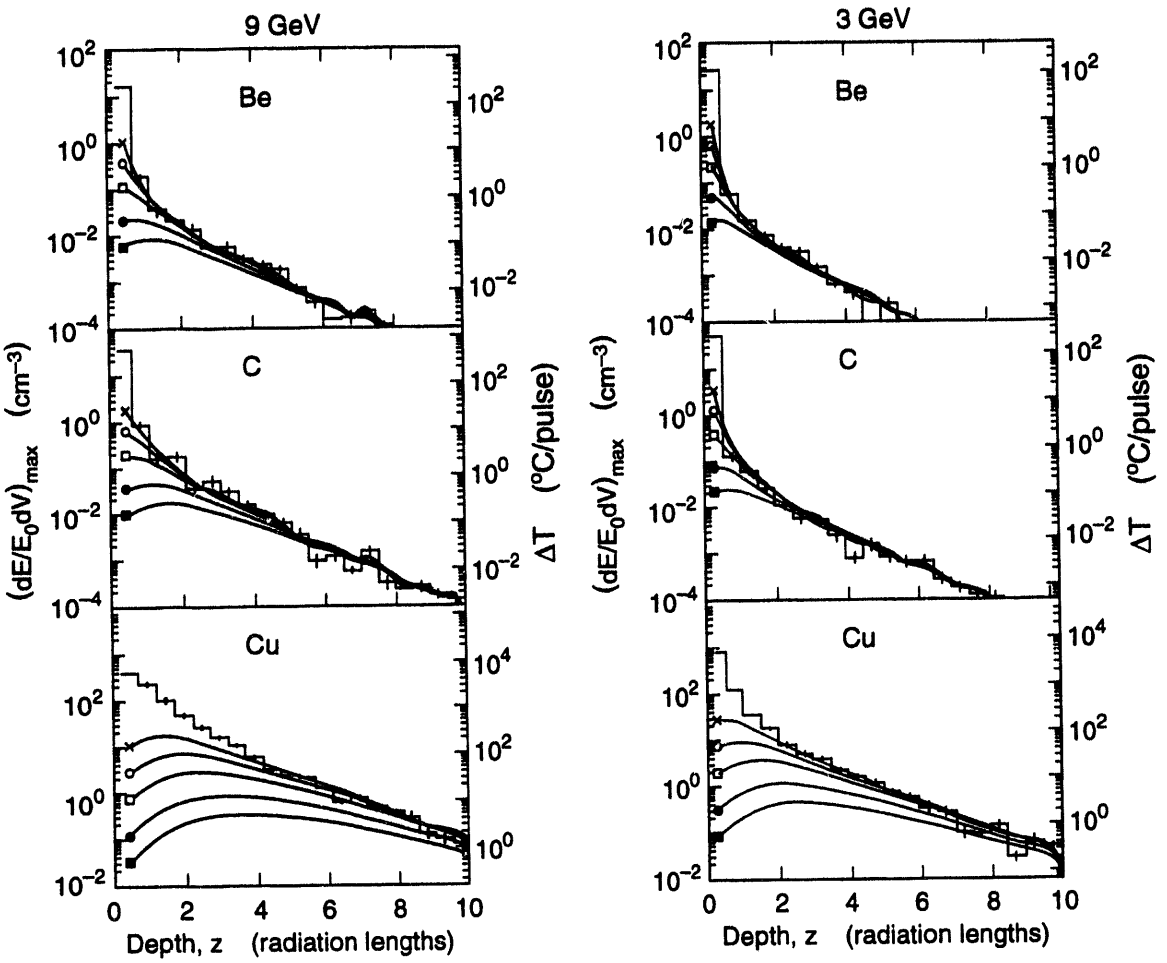

Fig. 6-33. An EGS calculation of the energy deposition and temperature rise, as a function of depth in Be, C, and Cu, for an incident pulse of 5×10^{10} electrons at 9 GeV (left column) and 3 GeV (right column). The various symbols correspond to circular bunch transverse rms size values of 0.0 (line), 0.05 (x), 0.10 (open circle), 0.20 (open box), 0.50 (filled circle), and 1.00 (filled box) mm. The area of the PEP-II beam corresponds to $\sigma = 0.35$ mm. Temperatures must be multiplied by 900 for the HER and 1960 for the LER to scale them to 4.5×10^{13} and 9.8×10^{13} stored particles, respectively.

Based on these estimates, we see that the only suitable material for the collimator (a material that will not melt in a localized dump of the ring) is carbon. A 20-radiation-length carbon collimator will be approximately 4 m long (plus some length to taper from the beam pipe diameter to the collimator hole diameter to minimize impedance and higher-order-mode losses). Movable jaws would be expensive and challenging. A simpler solution would be to have an elliptical hole through a block of carbon (machined along the length before two half-blocks were pushed together). The block could be moved out of the beam for machine physics. In the out position, the ring would be interlocked such that only a relatively small current could be stored.

Table 6-9. Predicted temperature rise from beam impact at a point. Columns 6 and 7 show the maximum temperature reached due just to dE/dx of 6.8×10^{13} electrons (9 GeV). The material begins at room temperature (27°C). Beam parameters used were $\varepsilon_x = 48$ nm·rad, $\varepsilon_y = 2$ nm·rad, $\beta_x = 8$ m, $\beta_y = 20$ m. This results in $\sigma_x = 0.6$ mm and $\sigma_y = 0.2$ mm, which is equivalent in area to a circular spot having $\sigma = 0.35$ mm. The maximum temperature reached deeper in the shower, based on an EGS calculation, is also included in column 8.

Z	A	Density (g/cm³)	dE/dx [a] (MeV·cm²/g)	dE/dx [b] (MeV·cm²/g)	Max. T [c] (°C)	Max. T [d] (°C)	Max. T [e] (°C)	Melting point (°C)
3	7	0.53	1.58	2.24	902	917	—	186
4	9	1.85	1.61	2.29	1175	1333	1100	1280
6	12	2.27	1.78	2.52	1702	2170	2200	3727
13	27	2.70	1.62	2.32	3523	3570	—	660
29	64	8.96	1.44	2.09	7468	7527	47000	1083
74	184	19.3	1.16	1.75	17946	18071	—	3410

[a]For minimum ionizing particles.
[b]Bethe-Bloch formula, $\delta = 0$.
[c]For $C_v = 6$ cal/mole-°K.
[d]For C_v from Debye theory estimate.
[e]Result from EGS calculation [Nelson, 1993].

If the decision were made to have nonadjustable collimators, then the horizontal and vertical collimators could be combined into a single cylinder, with an elliptical hole down the center. Nonadjustable collimators have the advantage of simplicity and will guarantee IR protection under all conditions—data taking, injection, accelerator physics running, and accidental beam dumps. However, there is a disadvantage in such an approach, because a decreased injection aperture will undoubtedly cause difficulties during commissioning and other nonstandard operating conditions. (This disadvantage will be partially mitigated by the enhanced capabilities of the ring BPM system, which can measure the trajectory of a single injected bunch during a single turn.)

6.5.4 Instrumentation and Control

In both the HER and LER, there will be one BPM per FODO cell (near the QD), for a total of 144 BPMs in each ring. This spacing provides roughly six orbit measurements per betatron wavelength in the HER and four per wavelength in the LER. The system

will be capable of following a single injected pulse around the ring for at least one turn. Desirable capabilities for the BPM system are:

- A particular stored or injected bunch can be followed for one turn, with each of the BPMs recording one reading
- A particular stored or injected bunch can be followed for as long as one transverse damping time (about 5000 turns); for each BPM, this requires a <7-μs ADC and a 5000-word buffer memory

To follow one particular bunch, a 4-ns analog gate or sample-and-hold circuit capable of rejecting signals from adjacent storage ring bunches is required. Because an injected pulse normally contains only 5–20% of the charge in a full bucket, the BPM and its associated electronics must be capable of measuring orbit-centroid shifts associated with currents in this range.

As shown in Figure 6-24, the injected beam must pass between the 8σ position of the septum and the 10σ aperture of the ring protection collimators. The injection line BPMs will permit the precise positioning of the injected beam in spatial coordinates and angle near the septum. The ring BPMs must be capable of determining the injected pulse position at the ring protection collimators. There is only about 1.8 mm ($2\sigma_y$, fully coupled), between the injected pulse and the collimator (at the extremes of motion). Our goal is to provide BPM sensitivity such that a single turn through a ring BPM provides a position resolution of ±0.3 mm (~1/5 of the $2\sigma_y$ injection aperture) for 5% of a full bunch charge (the minimum-size injected pulse expected). This corresponds to 0.015-mm resolution on a full ring bunch, even in the presence of adjacent bunches ±4 ns away. (If the ring BPMs were unable to accomplish this when all the bunches are approximately full, injection into the ring during top-off would be accomplished by initially filling an empty bucket in the beam gap from zero to fine-tune the injection setup.)

The dynamic range of the orbit-measuring system will be sufficient to measure from 5% of the full-bunch current (with 0.3-mm error) to twice the full-bunch current (with 0.015-mm error), or a dynamic range of 40:1. Usually, all BPM sample-and-hold circuits will be timed to look at the same bunch, but provision will be made to set the timing of individual BPMs separately so they can look at different bunches.

The horizontal position and angle at the injection point will be adjusted via the transport line optics to minimize any horizontal betatron oscillations in the ring. The vertical position and angle at the injection point will be adjusted to provide a good injection efficiency. During setup, the storage ring steering correctors will be adjusted as necessary to guide the injected beam through the center of the collimators. The ability to follow a bunch for many turns will allow an easy diagnosis of any timing mismatch between the injected bunch and the ring RF. In principle, the 144 BPMs turn the ring into a well-instrumented spectrometer that will—in conjunction with a computer model of the ring—allow the determination of the four transverse phase-space coordinates of an injected bunch.

For rapid and efficient injection, it is important that conditions for both the injected and stored beams be repeatable. Because the injection system will typically operate in top-off mode, where most of the stored beam continues to circulate in the rings, the orbits in the injection straights of the two rings can be measured and corrected back to a "golden orbit" for injection if need be. For example, the DC orbit bumps that shift the closed

orbit close to the injection septum will be adjusted to be free of residual field by automatic correction of difference orbits, in a manner similar to that used at PEP.

The lattice functions in the injection area will periodically be measured and adjusted as necessary to maintain exactly 180° of betatron phase advance between the injection kickers.

6.6 TIMING SYSTEM

For injection purposes, each ring is divided into nine "zones" of equal length. A zone has a length of about 244 m (or 815 ns) and contains 194 bunches. One of these zones in each ring will remain half empty to leave a gap for ion control. We describe here the process for filling the LER at a 60-pps rate; the HER is filled in a similar way. The transverse damping time for the HER is 37 ms. If the damping contribution of the wigglers in the LER is ignored—a worst-case situation in terms of injection—then the LER has a damping time of about 68 ms.

As shown in Fig. 6-34, the beginning of each zone is determined by the time onset of the kicker pulses. The two kickers are driven in parallel by a single pulser, consisting of a critically damped *RLC* circuit that rises and falls to practically zero within less than 1100 ns. The first bucket to be filled in zone n is located roughly 200 ns after the beginning of the kicker pulse so as to ride on the flat top, where sensitivity to time jitter is minimized. Since the rise time of the pulse is much shorter than the fall time, bunches recently stored in zone $n-1$ are unaffected. Bunches in zone $n+1$ (at least 815 ns later) are kicked slightly, but since they have been ng for the longest time, their orbits are almost fully damped, and, to the extent th ckers are matched, these bumps are closed. Thus, single buckets in zones 1 through 9 are filled in succession at a 60-pps rate, and then, 150 ms later (that is, two damping times in the LER in the absence of wigglers), the next adjacent buckets (4.2 ns later) in each zone are filled, and so on. With this method, damping in the LER, even without wigglers, is quite adequate.

Compared with previous experience with PEP injection, the timing and phase jitter from the SLC damping rings will be greatly reduced by using a frequency of 476 MHz (a subharmonic of the 2856-MHz linac frequency) for the PEP-II RF systems. Timing signals from PEP-II will be completely synchronized with the SLC timing system, enabling the electron gun to fill selected S-band buckets in the linac. Our design permits the beam in the damping rings to be phase shifted on a pulse-to-pulse basis. This gives several advantages. First, it allows completely interlaced e^+ and e^- injection (using two 60-pps time slots) without loss of beam pulses during bucket transitions, and second, it minimizes the timing jitter with respect to the power line zero-crossings. Before the beam is extracted from the damping ring, it will again be phase-locked to the linac RF reference and delivered to the PEP-II ring with a pulse-to-pulse timing jitter of less than a few picoseconds. Based on past experience, the diurnal drift in the phase-lock is expected to be less than ±100 ps; studies will be made to confirm this. Should the diurnal drift prove larger, a temperature-stabilized fiber optics timing cable could be installed, which would reduce the drifts to about ±10 ps.

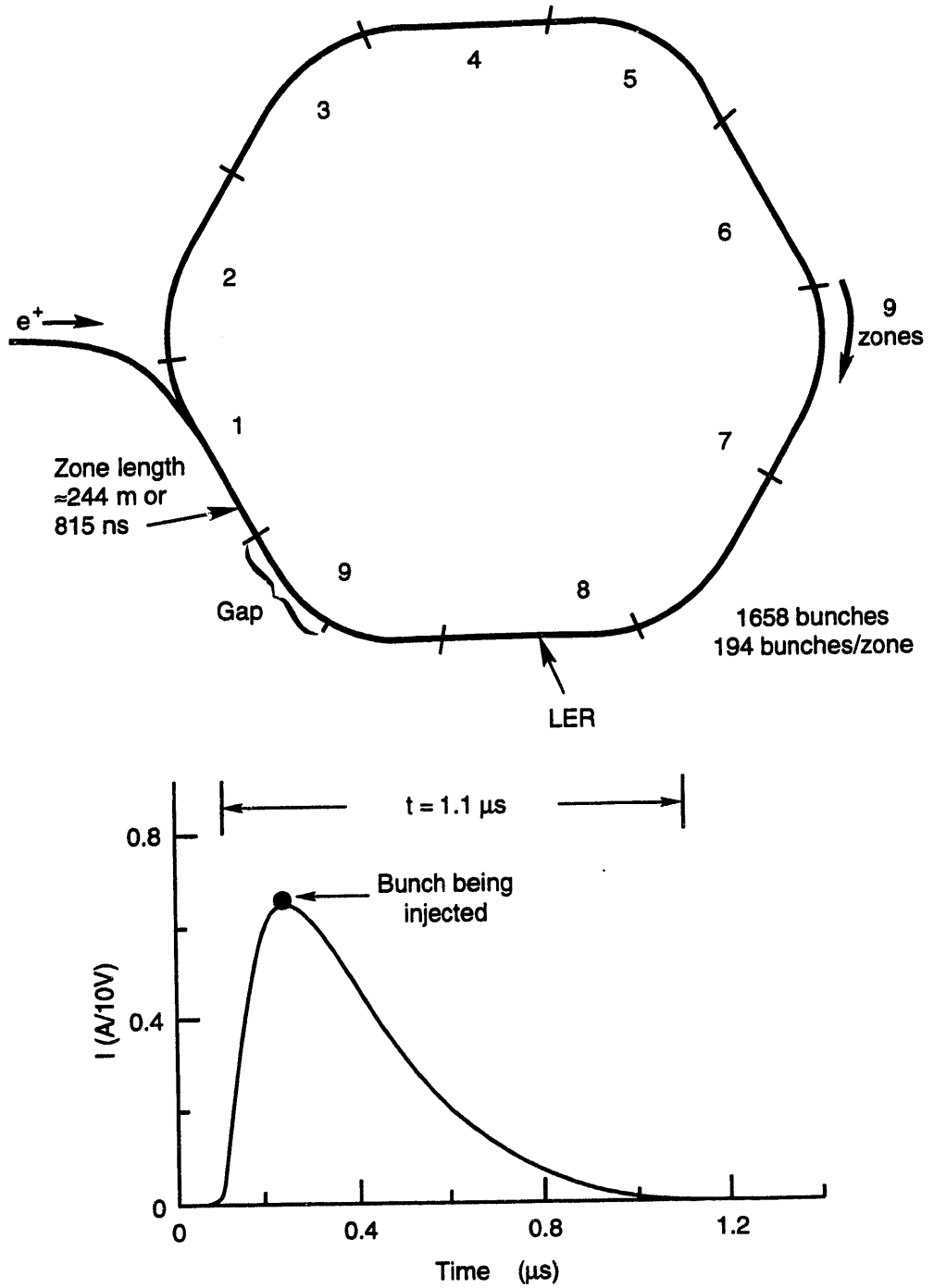

Fig. 6-34. Azimuthal zone filling sequence for the LER, showing nine zones. The kicker current pulse shown (equal for both kickers) was computed by assuming a charged, critically damped RLC circuit [$R = 2\,(L/C)^{1/2}$] in which the current reaches its maximum at $t = 2\,L/R$ after a FET-switch pulser is fired and allows the circuit to be discharged (see Fig. 6-30b).

Figure 6-35 shows schematically the layout of the injection timing system [Ronan et al., 1989]. This system transmits the linac 476-MHz reference signal from the master oscillator to the PEP-II control system, and it also sends the timing reference burst to the linac fiducial generator. Injection fiducials are transmitted to the S-band frequency dividers, the gun firing circuitry, and the damping rings. As shown in Fig. 6-36, the damping-ring phase-lock circuitry is reset by the PEP-II reference fiducial, causing a shift

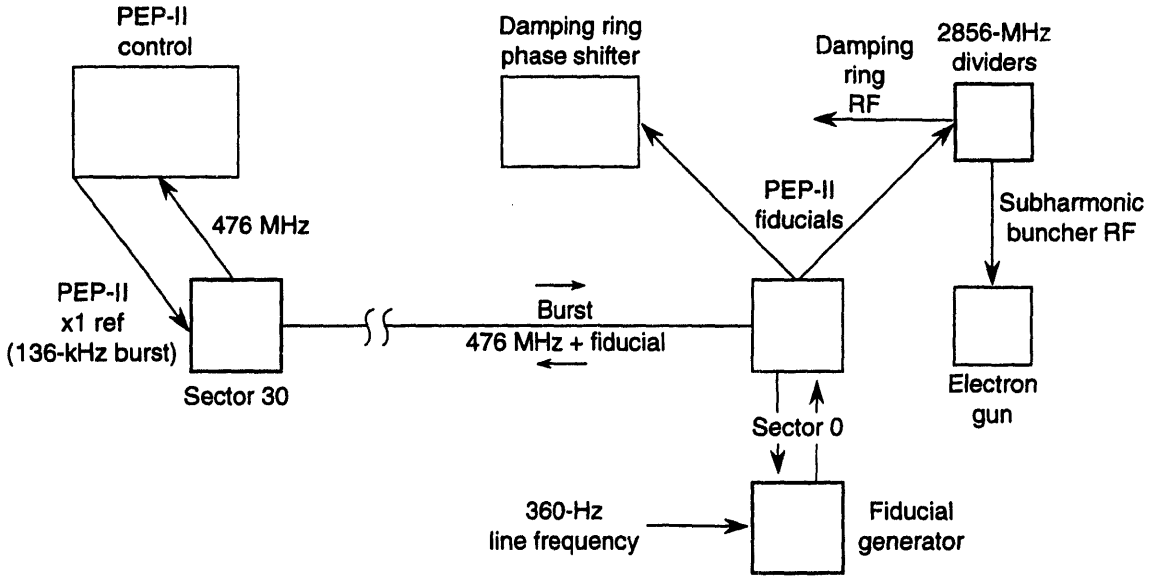

Fig. 6-35. Layout of injection timing and RF synchronization system.

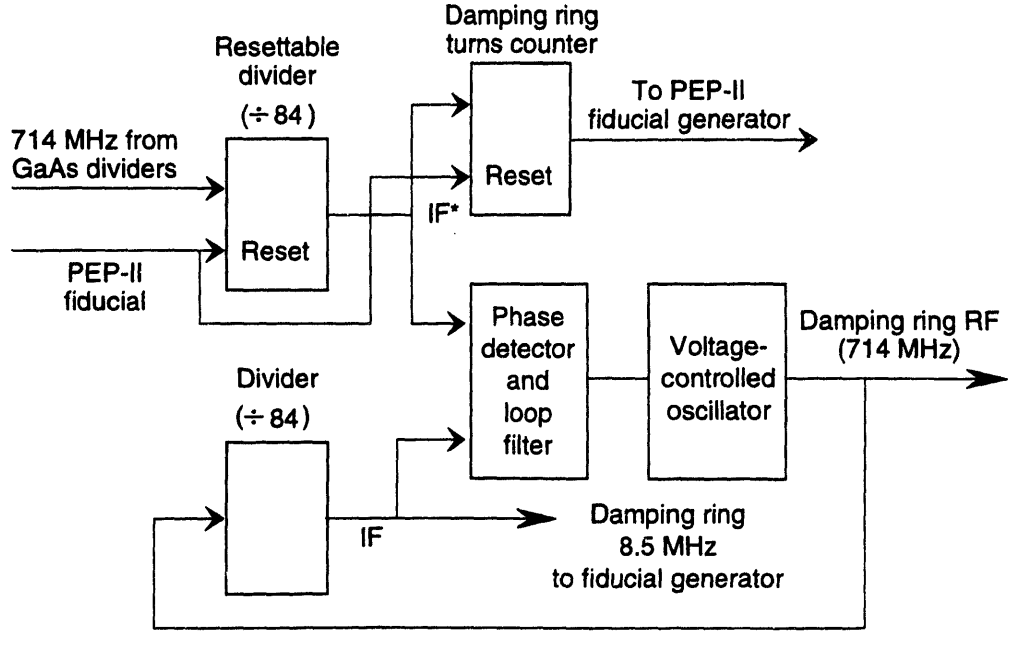

Fig. 6-36. Damping ring oscillator phase-shift circuitry.

in the revolution phase of the beam by up to half a damping-ring revolution period (or 42 damping-ring RF buckets) during an interpulse period of several milliseconds. This requires a 15-kHz shift in the damping ring frequency, which changes the orbit by only 0.1 mm—a negligible amount. The existing damping-ring phase ramp and bunch compressor maintain the phase of the extracted beam to within 0.25° at the 2856-MHz linac frequency.

The fully interlaced injection sequence is diagrammed in Fig. 6-37. When extracting $e^{\pm}$ beams from the damping rings for delivery to PEP-II, the storage ring RF bucket being filled, the bunch in the damping ring, and the damping-ring extraction kickers must all be locked to each other, as well as to the power line zero-crossing. After each delivered pulse, the PEP-II reference fiducial for the next e^+ or e^- bucket to be filled is used to reset the damping ring phase-lock circuitry, thus phasing the beam correctly for extraction on the next pulse. As the filling proceeds, e^+ and e^- bunches are continuously phase shifted for extraction and then phase-locked for delivery to the particular storage ring RF bucket being filled, thus decoupling the injection timing from the PEP-II bucket filling sequence. With this approach, the timing system places no restrictions on which bucket will be filled next, provided that the decision is made roughly 8 ms in advance. Toward the end of the filling process, the decision will be made on the basis of which buckets need more charge and on the time elapsed since they were last injected.

The entire filling sequence for the 1658 bunches will be computer controlled and automated. The selection of buckets within different zones will be done in a pattern that

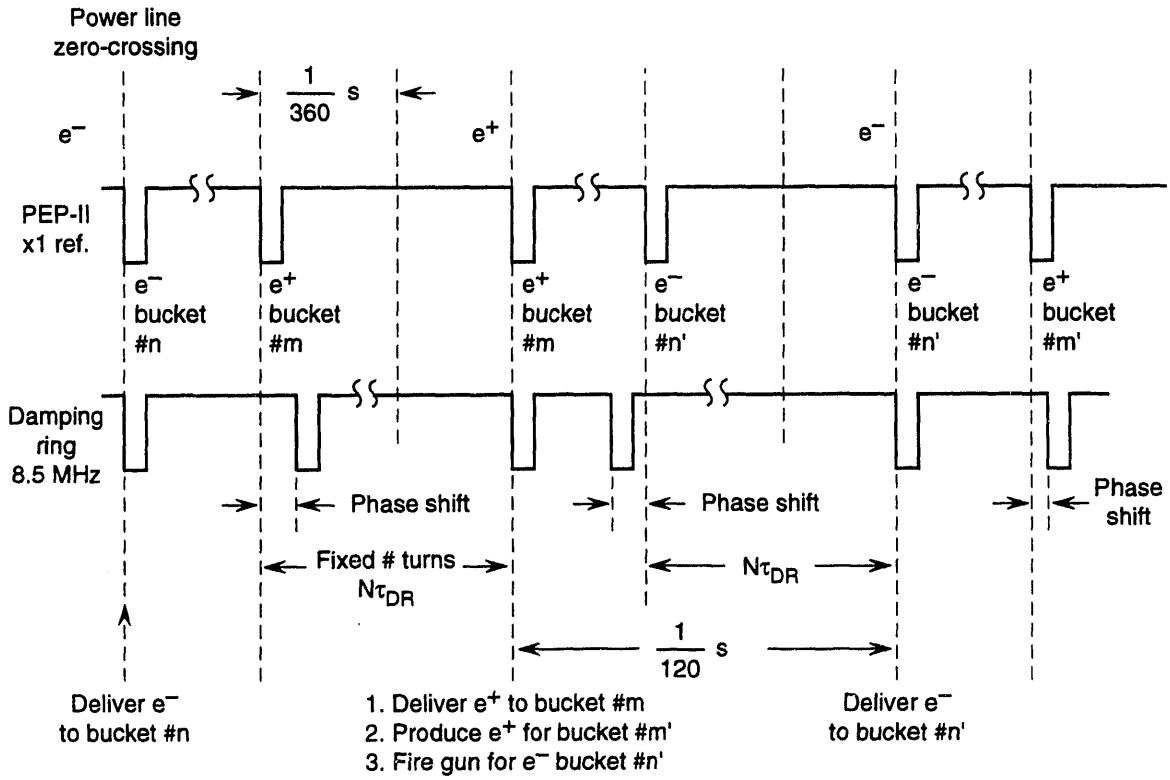

Fig. 6-37. PEP-II filling sequence.

minimizes effects due to kicker transients and allows sufficient damping time for newly injected bunches.

6.7 OPTIMUM TIME BETWEEN FILLS

As part of the design for the injection system, it is useful to estimate the optimal time between injection cycles (fills). By "optimal" we mean the filling pattern that maximizes the average luminosity. Clearly, this optimal value depends on the time course of the luminosity following injection, which will be determined to some extent by the details of storage ring operation. Still, it is useful here to get a sense of the likely interval between fills. Our assumptions, stated below, are intended to err on the side of conservatism, thus yielding a worst-case estimate (smallest val[illegible]this interval. In particular, we have taken a simple model in which the bunch s[illegible]ot vary with time. The appropriate luminosity formula is then

$$\mathcal{L}(t) = \frac{N_{b1}(t)N_{b2}(t)n_{bi}f_i}{2\pi\sqrt{(\sigma_{x1}^{*2} + \sigma_{x2}^{*2})(\sigma_{y1}^{*2} + \sigma_{y2}^{*2})}} \tag{6-7}$$

All time-dependent terms are indicated explicitly in Eq. 6-7. The σ_{xi}^* and σ_{yi}^* are the transverse rms spot sizes at the IP. We assume here that

- Bunches are distributed such that every bunch meets an opposing bunch at the IP. Thus, $n_{b1}f_1 = n_{b2}f_2$ is the bunch collision frequency, where f_i is the revolution frequency and n_{bi} is the number of bunches for beam i.
- All bunches in a given beam have the same number of particles (N_{bi} for beam i).
- Any modifications to the above formula from beam-beam considerations, finite bunch lengths, and nonzero crossing angles are independent of time.

To the extent that the individual beams decay according to exponential decay laws, the luminosity will also decay exponentially, and the desired optimization is straightforward. However, the beams are not expected to decay in a purely exponential way. For example, in beam-gas collision processes, the loss rate is proportional to the gas pressure, which in turn depends on the beam current. For the present calculations, we make the pessimistic assumption that the pressure does not decrease as the current decreases. Then beam-gas losses yield an exponential time dependence. In addition, beam-beam scattering losses, notably $e^+e^- \rightarrow e^+e^-\gamma$ do not give an exponential luminosity dependence. However, it can be shown [Porter, 1990] that if we make the exponential approximation, with a time constant given by the exact $1/e$ decay time, then the error is at most a few percent for times of interest to us. Thus, we start with a luminosity that depends on time according to

$$\mathcal{L}(t) = \mathcal{L}_0 e^{-t/\tau} \tag{6-8}$$

The decay time τ is dominated in the present design by the bremsstrahlung and Coulomb beam-gas scattering. Including these and additional losses due to beam-beam elastic

scattering and bremsstrahlung, and those due to Touschek scattering, gives $\tau = 1.5$ hr, with the assumptions discussed above.

The scenario we envision is that a data-taking period T for the experiment is long compared with the injection time and the stored-beam time (that is, there are many such fills in a data run). In this case, it is sufficient to replace the actual distribution of injection times with a single average injection time, which we call t_I. We further assume that we take data for a fixed time interval t_c following injection, prior to beginning the next injection, and that each fill begins with the same initial luminosity ($\mathcal{L}_0$). Finally, we assume that no useful data are accumulated during injection. Given this scenario, we wish to find the optimal value for t_c.

The total integrated luminosity accumulated during our data run is given by

$$\int_0^T \mathcal{L}\, dt = n \int_0^{t_c} \mathcal{L}_0 e^{-t/\tau}\, dt \tag{6-9}$$

where $n = T/(t_c + t_I)$ is the number of injection-coast cycles in the run. The ratio of the actual integrated luminosity to that obtained if the machine were capable of running the entire time at its peak luminosity is then

$$\frac{1}{\mathcal{L}_0 T} \int_0^T \mathcal{L}\, dt = \frac{\tau}{t_c + t_I}\left(1 - e^{-t_c/\tau}\right) \tag{6-10}$$

This quantity (and hence the actual integrated luminosity) is maximized when t_c is chosen to satisfy the condition

$$\frac{t_c + t_I}{\tau} = e^{t_c/\tau} - 1 \tag{6-11}$$

Thus, the maximum average luminosity possible is

$$\langle \mathcal{L} \rangle_{\max} = \mathcal{L}_0 e^{-t_c/\tau} \tag{6-12}$$

with t_c given by Eq. 6-11.

For simplicity, we assume that the injection time required is independent of the coast time t_c. For our parameters, this is a good approximation. Thus, we assume a fixed injection time of six minutes: approximately three minutes of overhead to change both accelerator and detector states between injection and stored-beam conditions, plus about three minutes for the actual top-off.

Solving Eq. 6-11 then gives an optimal coast time between fills of about 30 minutes. This yields an average luminosity of 71% of the peak luminosity. We note that the injection conditions are nearly optimum over a rather broad range; changing the stored-beam time from its optimal value of 30 minutes to 60 minutes reduces the average luminosity by only a few percent. Increasing the average injection time to 10 minutes reduces the average luminosity to 65% of its peak value.

6.8 SUMMARY AND CONCLUSIONS

One of the main requirements to be fulfilled by a high-luminosity $e^{\pm}$ collider designed to serve as a "factory" is that its design *average* luminosity be nearly as large as its design peak luminosity. To achieve such a high average luminosity, the machine must be endowed with an $e^{\pm}$ injector that can fill it rapidly and with minimal perturbation to the experimental program. Although a number of options could be considered for the PEP-II injection system, we believe our choice is the one that makes optimum use of the unique features of the SLC linac *without taxing its capabilities.* In particular, our chosen injection system

- Exploits the low invariant vertical emittance (0.5×10^{-5} m·rad) of the single bunches from the SLC damping rings (at intensities in the range of $0.2–3 \times 10^{10}$ $e^{\pm}$) to fill both PEP-II rings, on demand, in a few minutes
- Makes electron and positron bunches at the desired energies available to any of the individual 1658 buckets in the PEP-II rings, either from zero or in top-off mode, on interleaved 60-pps time slots
- Provides a 30-GeV electron beam for high positron production rates
- Permits bunches destined for PEP-II to spend only the minimum time in the linac before being directed to separate bypass lines, thereby minimizing dilution of their six-dimensional phase space
- Requires only one bunch at a time to be stored in each damping ring, a real simplification compared with SLC operation

In addition to the benefits to PEP-II, it is important to note that the injection system described here does not preclude the SLC linac from being used for other purposes at other times, nor does it prevent the last one-third of the linac from being used simultaneously, at lower energy, for test beams or for nuclear physics experiments.

In conclusion, we believe that the proposed injection system is powerful, efficient, and flexible, that it makes cost-effective use of existing SLAC facilities, and that it meets all of the requirements of PEP-II.

7.

CONVENTIONAL FACILITIES

SINCE PEP-II will occupy the existing PEP tunnel and make use of the existing SLC linac, no conventional construction is required. Modifications will be necessary to mechanical and electrical facilities, as described below. This chapter also describes necessary removals, including the steps to be followed in disassembling and refurbishing the PEP magnets. Finally, in Section 7.2.3, the installation procedure for the new facility is given in broad outline. All conventional facilities work will conform to applicable DOE, national, and state codes and regulations, including those portions of DOE 6430.1A that pertain to PEP-II.

7.1 SITE AND UTILITIES

7.1.1 PEP Buildings and Underground Structures

The PEP conventional facilities comprise all beam housings (bored and cut-and-cover tunnels), research halls, support buildings, roads, earthwork, fencing, landscaping, AC power, mechanical utilities, sewers, and drainage facilities (see Fig. 7-1). The only changes to these facilities that will be needed to accommodate PEP-II are modifications to the cooling water system, the tunnel drainage system, and the electrical distribution system.

An Environmental Impact Statement (EIS) for PEP was issued by the Energy Research and Development Administration in 1976. Only minor modifications to the existing PEP drainage facilities will be required to comply with current regulations.

The fact that PEP lies in close proximity to known earthquake faults required a conservative seismic design. For above-ground structures, equipment, and components, the basis for seismic design was a modification of the Uniform Building Code (1976 Edition), Section 2321, such that it equals or exceeds current seismic design practices.

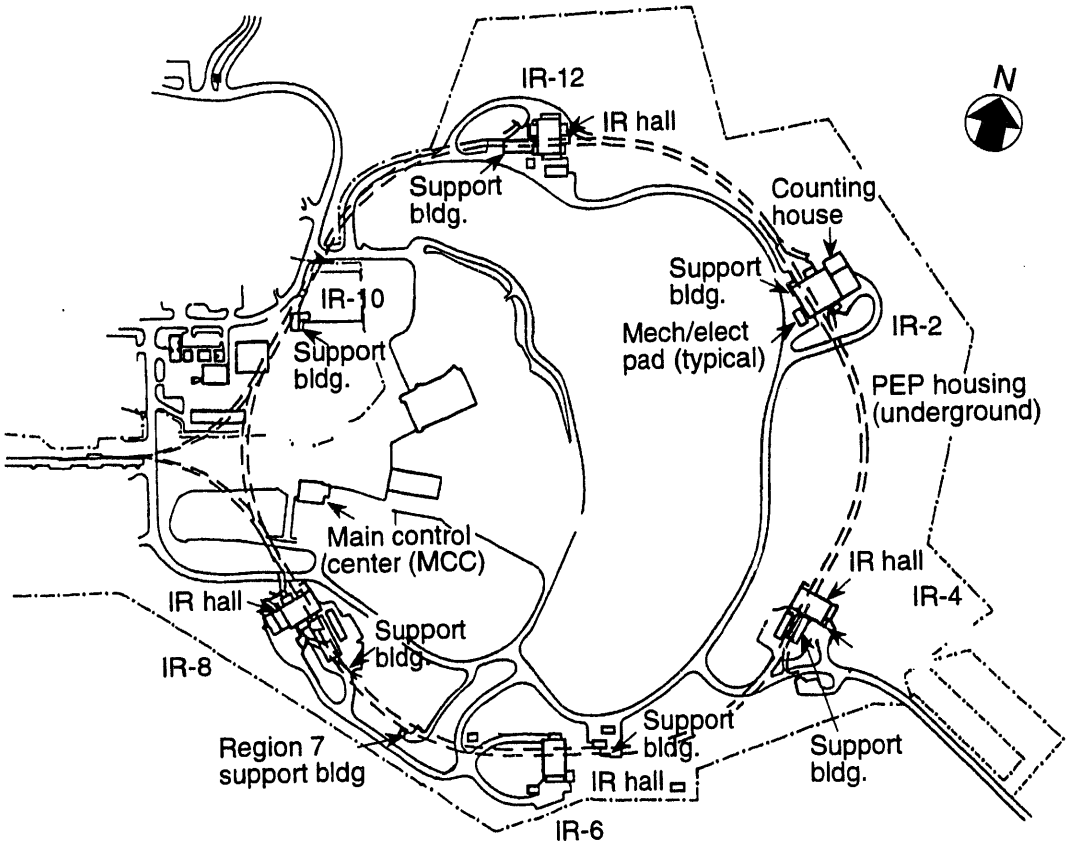

Fig. 7-1. Site map of the PEP facility.

7.1.1.1 Beam Housings. Beam housings include the PEP main ring tunnel, ring access tunnels, their junctions with the accelerator housing and the storage ring, and all penetrations into the tunnels. The underground structures were built with tunneling or cut-and-cover methods, depending on the depth underground. Beam housings are concrete lined, painted white, and have controlled ventilation. Telephone service is provided. The tunnels are protected from fire by detection and sprinkler systems. The fire-detection systems will be upgraded to current standards, as discussed in Chapter 8.

Water seepage into the PEP tunnel, primarily in regions 10 and 11, has been a problem since PEP was constructed. This water is high in mineral content, supports algae growth, and is corrosive to iron, aluminum, and some plastics. Deposits block drainage pipes, channels, and gutters. Because it was found to be uneconomical to stop the seepage, a water-management program was used consisting of equipment covers, diverting grooves, and routine maintenance of drainage systems.

A similar water-management system will be used for PEP-II. The affected areas will be thoroughly cleaned prior to installation of equipment and additional provisions for drainage will be installed where necessary. The discharge from the sumps will be routed to the sanitary sewer system to ensure long-term compliance with water-discharge regulations.

7.1.1.2 Support Buildings. Support buildings exist for instrumentation and controls (I&C) equipment at IR-2 and IR-6; for RF, I&C, and magnet power supplies at IR-4 and IR-12; and for RF, I&C, magnet power supplies, and overall operational control of the storage ring at IR-8. Additional special support buildings are located at region 7 and IR-10.

7.1.2 Mechanical Facilities

7.1.2.1 PEP Site Cooling Water. The machine components in the storage rings and the detector will be cooled by closed-loop, low-conductivity water (LCW) systems. These are, in turn, cooled by a cooling tower water (CTW) system. Existing PEP LCW water headers will be used for PEP-II; no additional headers are required.

A four-cell cooling tower is located near the Main Control Center (MCC) to provide circulating CTW to the PEP ring. The CTW is distributed to equipment pads at PEP interaction regions 2, 4, 6, 8, and 12. Each of these interaction regions has closed-loop cooling water systems including a heat exchanger to transfer the heat to the circulating CTW. Current PEP systems are designated for klystron tubes and ring magnets, RF cavities and vacuum chambers, and experimental systems.

The PEP-II heat load of 42.8 MW will need additional CTW flow, requiring all four existing pumps to operate. (This heat load is estimated assuming a conventional-collector klystron; the heat load would decrease to 37.1 MW with a depressed-collector klystron design.) One additional CTW pump will be installed to provide backup and facilitate maintenance.

The distribution of loads between the systems, both above and below ground (see Figs. 7-2 and 7-3), will be different from PEP. The heat exchangers will be replaced with suitably sized plate-type heat exchangers. The existing circulating pumps will be replaced with new appropriately sized pumps to match the PEP-II heat load distribution. The systems will be segregated such that copper and aluminum pipes are not present in the same loop.

The LCW systems will be connected to PEP-II loads as described in the following paragraphs. (The names used for the cooling systems below correspond to their current PEP functions.)

IR-2. The PEP-II detector will be installed at IR-2. The cooling water for the 3-MW detector magnet will be provided by the IR-2 experimental equipment cooling system.

IR-4. The RF-vacuum cooling system will supply cooling water to ten RF cavities, one-third of the vacuum chambers and a portion of the many magnet power supplies. The experimental equipment water systems will supply cooling to five klystron collectors. The klystron-magnet cooling system will supply cooling water to one-third of the magnets. A new closed-loop cooling system will be installed to cool the five circulators and Magic Tees.

IR-6. The experimental equipment water system will supply cooling water to one of the LER synchrotron radiation dumps.

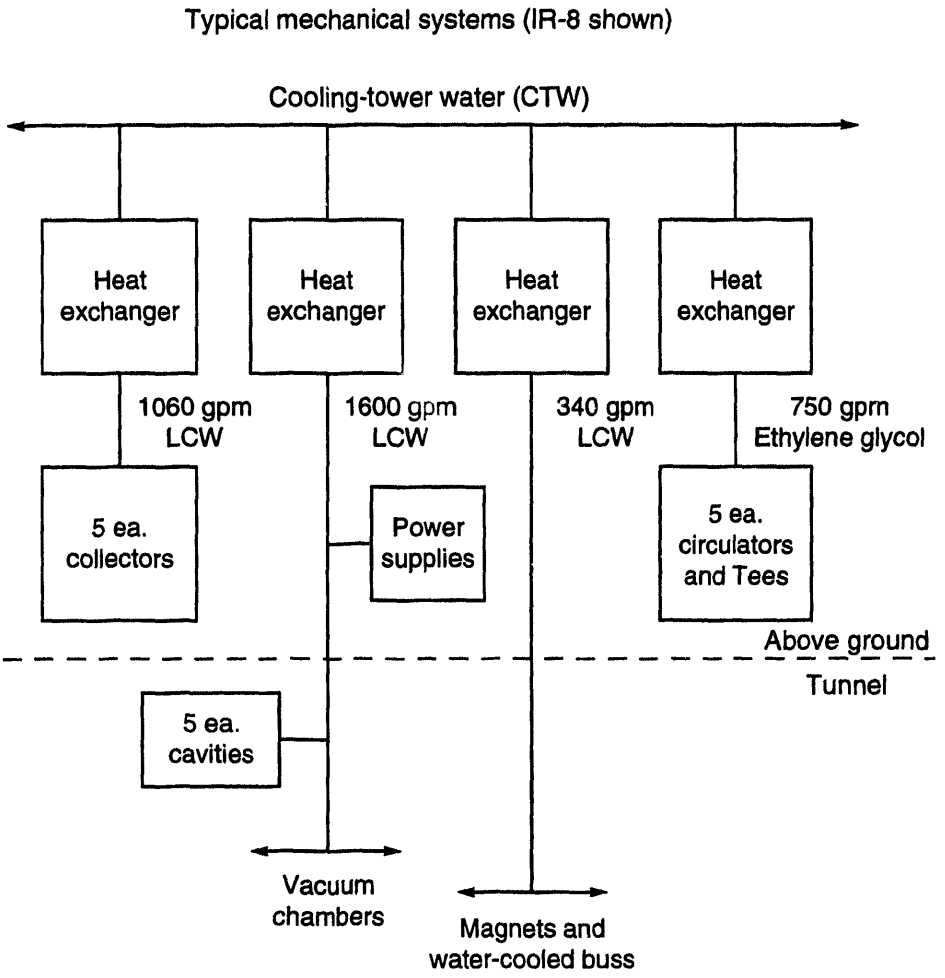

Fig. 7-2. Schematic of IR-8 cooling system.

IR-8. The RF-vacuum cooling system will supply cooling water to ten RF cavities, one-third of the vacuum chambers and some of the ring magnet power supplies. The experimental equipment water system will supply cooling to five klystron collectors. The klystron-magnet cooling system will supply cooling water to one-third of the magnets. A new closed-loop cooling system will be installed to cool the five circulators and Magic Tees.

IR-12. The RF-vacuum cooling system will supply cooling water to ten RF cavities, one-third of the vacuum chambers and the remaining ring magnet power supplies. The experimental equipment water system will supply cooling to five klystron collectors and one of the LER synchrotron radiation dumps. The klystron-magnet cooling system will supply cooling water to one-third of the magnets. A new closed-loop cooling system will be installed to cool the five circulators and Magic Tees.

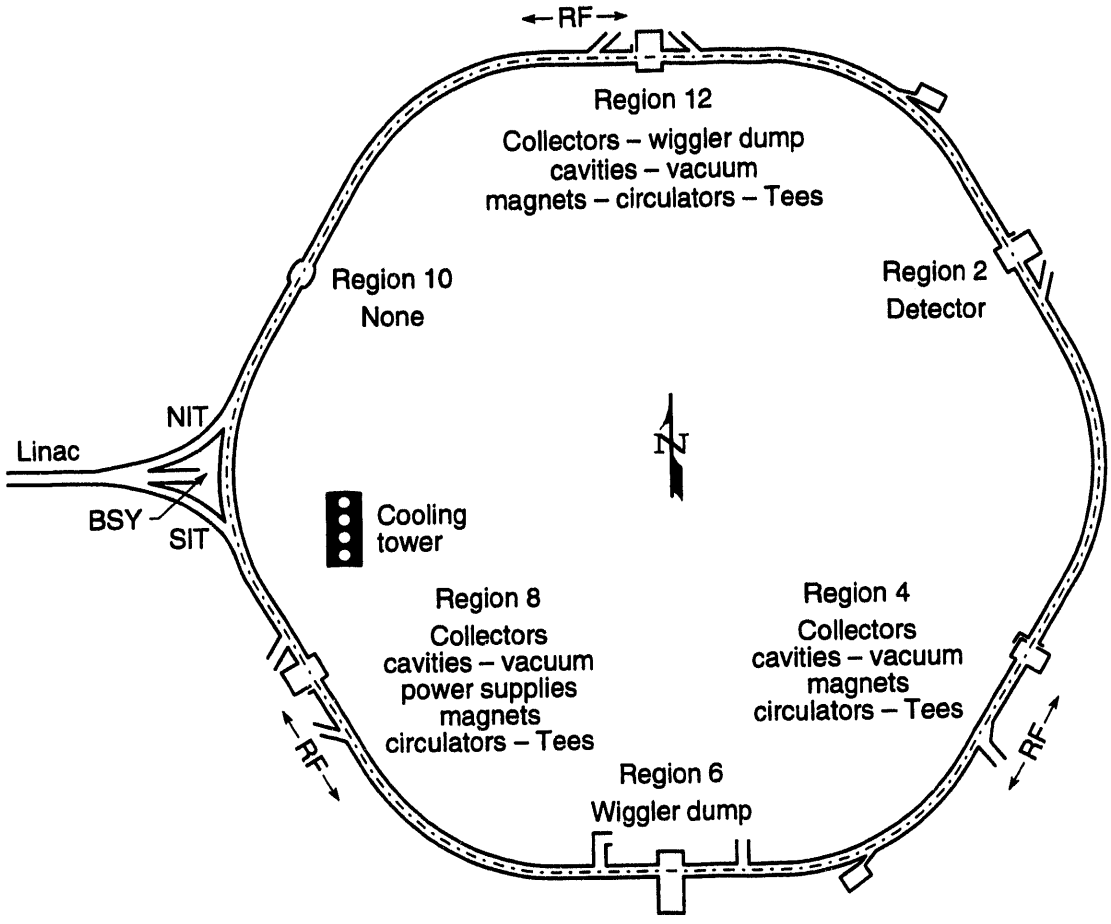

Fig. 7-3. Schematic of cooling system location.

7.1.2.2 Cooling Water for Injection System Components. The injection system magnets for PEP-II will be supplied with cooling water from existing headers in the accelerator housing and the NIT and SIT tunnels. Magnet power supplies will be located above ground and will be supplied with cooling water from existing headers.

7.1.3 Electrical Facilities

SLAC receives power from two sources: A 230-kV line with a 100-MW capacity and a standby 60-kV line with an 18-MW capacity. The two sources are asynchronous and cannot be operated in parallel. The master substation is located adjacent to Sector 30 on the south side of the linac. No expansion of the high-voltage feeders or the master substation is required for PEP-II.

The maximum electrical power demand for PEP-II will be 42.8 MW. The anticipated load is tabulated by region in Table 7-1. Electrical power to PEP-II will be distributed at 12.47 kV through the PEP duct bank to the six regional substations at regions 2, 4, 6, 8, 10, and 12.

Table 7-1. Anticipated electrical loads for PEP-II.

	Anticipated loads[a]	
Region	MW	MVA
2	4.9	6.2
4	10.9	15.2
6	1.4	1.8
8	13.3	18.0
10	0.4	0.5
12	11.9	16.5
Total	42.8	58.2

[a]Power estimated for conventional-collector klystrons. Total power would be 37.1 MW (49.2 MVA) with depressed-collector klystrons.

The PEP-II electrical power distribution system utilizes the underground duct banks of PEP. The cable capacity of this system will be increased to accommodate the higher loads of PEP-II.

7.1.4 Interaction Regions

PEP has five interaction halls designed for the assembly and operation of a large particle detector. To permit the reuse of equipment by other experimental programs, all experiments at PEP were removed. Equipment not identified for reuse has been stored for future use or salvaged in accordance with applicable ES&H guidelines. All five halls will be used for temporary storage during the disassembly of PEP and the installation of PEP-II.

Current plans are to install the detector for PEP-II in IR-2. The IR-2 experimental hall is 66 ft wide in the beam direction and 105 ft long. It is equipped with a 50-ton overhead crane. The beam height is 13.1 ft above the floor. The building can be divided into two spaces by a shielding-block wall, which makes it possible to work on a detector when it is off the beamline and beams are circulating. There is a two-story counting house on the north side of the experimental hall with 4,000 ft^2 of floor space. IR-2 has 5 MW of AC power available. The cooling water system will be expanded to handle this load by the addition of a heat exchanger.

7.2 REMOVALS AND INSTALLATIONS

7.2.1 Space Requirements

Construction of PEP-II requires that the PEP tunnel be cleared of all existing magnets and related components. Table 7-2 summarizes the components to be removed.

The covered storage and refurbishing space required for these and other components is shown in Table 7-3. The space used for PEP disassembly and HER assembly will be vacated by the time that the LER assembly space is needed. Recent tests, conducted throughout PEP, showed no residual radioactivity above background in the concrete rafts that currently support the PEP magnets. The rafts will therefore be disposed of in a conventional manner and will not require long-term covered storage. With the 40,000 ft^2 of crane-covered space already identified at SLAC (Table 7-4), no additional buildings will be required at SLAC during construction of PEP-II.

7.2.2 Disassembly and Removals

7.2.2.1 Main Tunnel. PEP disassembly will commence with the bending magnets in the water-affected area in regions 9 and 11 (see Fig. 7-1). The removal rate of these components will be two magnets or three rafts per day. At this rate, the PEP tunnel can be cleared in approximately nine months. Fixtures used for disassembly and removal will be designed to ensure that previously obtained alignment information for the bending magnet cores will be preserved.

Table 7-2. Summary of components to be removed from the PEP tunnel.

Component	Number	Weight (tons)
Bending magnets	192	1,416
Low-field bends	24	18
Quadrupoles	216	405
Insertion quadrupoles	24	207
Miscellaneous quadrupoles	48	60
Sextupoles	192	33
Concrete rafts	216	925
Miscellaneous supports	400	32
RF cavities	24	12
Vacuum chambers and components	>1,000	33
Total		3,141

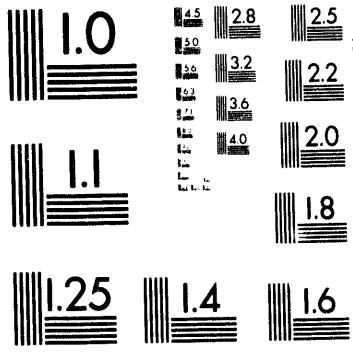
1.0
1.1
1.25
1.4
1.6
1.8
2.0
2.2
2.5
2.8
3.2
3.6
4.0
4.5
5.0
5.6
6.3

7 of 7

Table 7-3. Space required for preinstallation, PEP disassembly, and PEP-II component assembly.

Component	Space requirement (ft^2)
PEP disassembly	
Bending magnets	10,000
Quadrupole/sextupole pairs	2,500
Miscellaneous magnets	1,500
Miscellaneous supports	2,000
Vacuum components	2,000
Miscellaneous	1,000
Total	19,000
HER assembly	
Bending magnet assembly	1,000
Quadrupole assembly	600
Quadrupole fabrication	600
Sextupole fabrication	600
Sextupole assembly	600
Support assembly	600
Mechanical measurement	1,000
Mechanical alignment	1,000
Magnetic measurement	3,000
Coil storage	1,000
Hose factory	500
Miscellaneous storage	500
Total	11,000
LER assembly	
Bending magnet assembly	1,000
Quadrupole assembly	500
Sextupole assembly	500
Support assembly	500
Mechanical measurement	500
Mechanical alignment	750
Magnetic measurement	1,000
Coil storage	500
Miscellaneous storage	250
Total	5,500

Table 7-4. Crane-covered SLAC space available for PEP-II construction activities.

Area	Space available (ft^2)
Light assembly	11,500
Heavy fabrication (center bay)	7,500
IR-2	5,200
IR-4	2,700
IR-6	4,500
IR-8	4,500
IR-12	4,100
Total	40,000

Once removed from the tunnel, the main coils, trim coils, and other ancillary equipment will be removed from the cores. The coils will be inspected for possible radiation damage and will receive an approved water-sealing coating. The cores will be inspected for damage and will be repainted. New trim coils will be wound and installed, and the magnet then reassembled. To assure the magnetic quality of these refurbished magnets, each one will be mechanically checked for twist, roll, and gap. Previous measurements at SLAC using this technique have shown that magnetic measurements are necessary only on a sample basis, provided that mechanical measurements are completed on each magnet. This procedure will be followed for the refurbished magnets.

The quadrupole-sextupole raft structure will be removed after the main bending magnets. With the bending magnets removed, the unwanted aluminum vacuum chamber will be removed. Careful attention will be given to those components that can be reused, e.g., ion pumps, vacuum gauges, and isolation valves. After the quadrupole-sextupole pairs are removed from the tunnel, they will be transported to a refurbishing area where they will be opened and the vacuum components removed. Tests will be made to determine the extent of radiation damage to the coils. If undamaged, they will be removed from the cores and resealed. The cores will then be repainted prior to reassembly.

Since the quadrupole magnets underwent magnetic measurements prior to PEP installation, it may not be necessary to remeasure each magnet. Previous data have shown that the magnetic characteristics can be duplicated, provided good mechanical measurements are taken and specific reassembly techniques are used. With the previous PEP magnetic information at hand, sample tests can be performed to ensure that the magnetic properties are preserved. The refurbished magnets can then be mounted on a new support and rough-aligned using gauges and fixtures. When the vacuum chambers and beam position monitors become available, the cores will be opened and the chamber package installed. At this time, precision mechanical alignment will be accomplished. This alignment process will be completed in a temperature-controlled area, using

precision optical alignment docks to ensure that the beam position monitors and magnet components are aligned to within a few thousands of an inch.

Generally, much of the existing PEP cable plant will be used for the HER and LER. For example, all of the vacuum system cables will remain in place and will be connected to new equipment in locations nearby. In some instances, splicing and other means may be needed to make up the required lengths. Unneeded cabling will be removed and, in some cases, stored for later reuse.

To ensure adequate documentation and control during disassembly and subsequent reassembly, bar codes will be applied and travelers will be attached to each component for tracking. A database has been set up to ensure that other information regarding these components is readily available. Data taken during PEP construction regarding mechanical and magnetic measurements can be retrieved from the database in such a way as to allow comparison of these properties.

With the tunnel housing empty, the floor will be cleared of all attachments used for PEP. New support points for PEP-II rings will be accurately placed by an alignment team. Surveys are currently under way to determine what other equipment, such as utilities, must be modified and installed once the alignment process is complete in a given section of the tunnel.

Any unneeded materials will be disposed of in accordance with applicable ES&H guidelines (see Chapter 8).

7.2.3 Installation

7.2.3.1 High-Energy Ring. Installation of the HER components (Table 7-5) will begin after alignment teams have located support points. Anchor bolts will be installed for the bending magnet supports, which will be the first components to be reinstalled for PEP-II. After the supports are grouted and aligned, the bending magnets will be installed using

Table 7-5. Inventory of HER components.

Component	Quantity	Total weight (tons)
Bending magnets	212	1,433
Quadrupoles	272	514
Sextupoles	144	26
Bending magnet supports	192	36
Quadrupole/sextupole supports	192	8
Quadrupole supports	96	6
RF cavities	20	10
Vacuum chambers	~500	72
Total		2,105

new installation fixtures. Care will be taken to ensure that all magnets are handled in an approved manner. The quadrupole-sextupole pairs on their prealigned supports will be installed in a similar way. After this, the vacuum chamber will be placed in the bending magnets and the fixed flanges made up. The final connection will be the HER flexible bellows unit. During the entire installation process, quality control measures will be undertaken to ensure that each component is installed according to written procedures. Documentation regarding the installation, fabrication, and refurbishing process of PEP-II components will also be filed in the database according to written procedures.

7.2.3.2 Low-Energy Ring. The LER components (Table 7-6) will become available after the HER is installed, owing to the fact that they must all be fabricated. Accordingly, since these magnets are installed above the HER, they will be installed on the C-frame support structure as a prealigned unit. Quality control and documentation measurements will be taken, as described for the HER.

7.2.3.3 Injector. The injector installation commences with the electron and positron extraction sections at linac Sector 4 (for positrons) and linac Sector 8 (for electrons). Short stub-lines (which connect the extraction sections to the bypass lines) are installed next, followed by the two (long) bypass lines that carry the beams to NIT and SIT. The schedule for these installation phases must mesh with the SLC downtime schedule.

The NIT and SIT lines will be reused for PEP-II. To do so, they must be joined to the bypass lines at one end and to their respective rings (HER and LER) at the other end. This final step, which can be done while the SLC is running, will complete the injector installation. Table 7-7 summarizes the components to be installed for the injection complex. Quality control and documentation measurements will be taken, as described for the HER.

Table 7-6. Inventory of LER components.

Component	Quantity	Total weight (tons)
Bending magnets	208	227
Quadrupoles	298	289
Sextupoles	144	26
Dipole/quadrupole/sextupole supports	192	77
Quadrupole supports	96	17
RF cavities	10	5
Vacuum chambers	~500	25
Total		666

Table 7-7. Inventory of injector components.

Component	Quantity	Total weight (tons)
Bending magnets	32	57
Quadrupoles	110	21
Vacuum chambers	288	11
Total		89

7.2.3.4 Cable Plant Installation. Cables will run in 4-in.-deep steel cable trays, conduits, and wireways from points of origin to terminations. Instrumentation and DC cables will extend in the air from the cable trays to the devices served; long runs will be supported. Barriers in the cable trays or separate cable trays will be used to carry conductors for different functions (for example, DC, instrumentation, AC power). All raceways will be bonded for electrical continuity.

Existing cable trays in the PEP housing will be utilized for the new cable systems. Additional cable trays will be installed to carry cables for components in the interaction region halls and in the straight sections. An additional cable tray will be installed in the PEP tunnel and new cable trays will be installed in the RF areas of the support buildings to support the RF cable plant.

Large DC Cables. Existing DC circuits in the PEP ring are capable of supplying both the HER and LER high-current magnet circuits. There are twenty-one 1-in.-OD, PVC-jacketed, water-cooled aluminum cable circuits, extending completely around the ring, with taps to power supplies and the existing magnets. Air-cooled conductors bridge the gap between the water-cooled conductors and the magnets. In addition, six air-cooled 350-MCM aluminum cables run through the same route. Existing circuits will be modified to reach the new magnet locations. Modifications will consist of jumpers in locations no longer served and taps from existing cables to new magnet locations.

Many of the existing power supplies will be reassigned or removed. Changes to the existing large DC cables will be made as appropriate.

Power supplies for HER and LER high-current magnet circuits will remain in the various IR areas. To minimize cable lengths to the magnets, power supplies for lower-current magnet circuits in the straight sections will be located in accessible areas inside the interaction halls. DC-DC converters for HER sextupole power supplies will be located in the arcs; taps from DC busses will supply these magnets.

Power supplies for the injection system magnets will be located in the RF support buildings. Cables will run in cable trays through vertical penetrations to the accelerator housing, where they will be routed to the magnets served. Additional raceways will be installed in the vertical penetrations, as needed. Cable grips will support the vertical load of cables at the entry points to raceways in the vertical penetrations.

Trim and Steering Circuits. Existing trim and steering cables will be disconnected from PEP magnets and tied back for use in the new HER circuits. For the LER trim and

steering magnets, new circuits will be run from new power supplies located at IR-2, -4, -6, -8,-10, and -12. As with the large DC cables, trim and steering cables for the injection lines will originate at power supplies in the RF support buildings.

Instrumentation and Control Cables. A wide variety of cable types will be utilized for these systems. Where practical, cables will be preassembled with connectors as complete units. In other cases, cable connectors will be installed in the field. Multiconductor instrumentation and control cables will be type TC (tray cable) and will be provided with an overall shield. Safe High-Voltage (SHV) connectors will be utilized where required. High-voltage circuits will be run separately from other circuits.

New instrumentation and control cables in the injection system will be routed through cable trays in the RF buildings to vertical penetrations, then to cable trays in the PEP-II tunnel, and thence to the instruments served.

AC Circuits. The existing AC distribution system for ring components, removed to allow the dismantling of the PEP ring, will be reinstalled in appropriate locations. Rigid steel conduits or cable trays will be used for 480-V circuits; 208Y/120-V circuits will be run in EMT or other suitable raceways. Wireways will be used for 480-V and 208Y/120-V circuits where required.

Grounding. All elements of the new rings, the IR, and the injection beamlines will be grounded to the existing SLAC ground system. Connections will be made by clamp-type connectors, for easy removal. The grounding connectors will be torqued to specifications.

8.

ENVIRONMENT, SAFETY, HEALTH, AND QUALITY ASSURANCE

SLAC has numerous environment, safety, and health (ES&H) and quality assurance (QA) programs already in place. From the ES&H and QA standpoints, PEP-II does not present any significant new challenges. All of the anticipated hazards are ones that SLAC has successfully faced during previous construction and/or experimental activities.

Installation of PEP-II in the existing PEP tunnel at SLAC will take advantage of a number of existing, mature programs, as well as proven safety features and systems. The fact that these features are already operational in the tunnel will provide an extra measure of safety during the disassembly of PEP and the installation and commissioning of PEP-II.

The SLAC programs in ES&H and QA will ensure that all aspects of the design, installation, testing, and operational phases of the project are properly managed. As appropriate, the cognizant SLAC safety committees, including the Safety Overview Committee, the Hazardous Experimental Equipment Committee, the Radiation Safety Committee, the Fire Protection Safety Committee, the Hoisting and Rigging Committee, the ALARA Committee, the Electrical Safety Committee, the Non-Ionizing Radiation Safety Committee, and the Earthquake Safety Committee [SLAC Environment and Safety Office, 1987] will review and approve various aspects of the project. All aspects of the project will conform to the applicable DOE, national, and state codes and regulations, including those aspects of DOE 6430.1A that pertain to PEP-II.

Peer and expert review have been heavily utilized to optimize the component designs and to ensure the use of best engineering practices. Ease of maintenance and reliable operation for the facility have been an integral part of the engineering design criteria.

8.1 FIRE SAFETY

The existing fire safety system in the PEP tunnel and experimental areas will remain operational throughout the installation, commissioning, and operation of PEP-II. All

areas are classified as Ordinary Hazard, Group I. The tunnel sections, interaction region (IR) halls, and support buildings are protected by automatic wet sprinkler systems and smoke detectors. The sprinkler systems are designed for a coverage of 0.15 gpm/ft^2 over 1500 ft^2. The ring is divided into twelve zones, each with its separate water supply. Six of these zones supply water to the centers of the curved (arc) sections of the tunnel. The remaining six supply water to the interaction regions. The counting houses and control room are protected by pre-action, air-supervised sprinklers activated by a smoke detection system. The support buildings in regions 4, 8, and 12 are protected by deluge sprinkler systems activated by heat-detection systems. The existing smoke detectors are of a high-voltage type that is no longer manufactured; these will be replaced with a VESDA-type detection system. This will eliminate the beam-radiation-induced false-alarm problem associated with ionization and photoelectric-type detectors. The fire alarm panels will also be replaced with improved technology.

With the exception of regions 8 through 12, each curved section of the PEP tunnel has three fans: two intake and one exhaust. Owing to the presence of above-ground structures above regions 8 through 12, the ventilation configuration there is somewhat different, with a total of five fans: two intake and three exhaust, including one double-volume exhaust fan. The fans automatically stop operating when the fire alarm sounds. The Fire Department then has the option of restarting any of the fans to provide fresh air or to exhaust smoke. The controls for this system are located on above-ground pedestals.

SLAC subcontracts with the Palo Alto Fire Department to operate an on-site fire station and to provide emergency response services. The Palo Alto Fire Department also provides ongoing fire safety inspections of SLAC facilities, as well as training of personnel.

8.2 RADIATION SAFETY

The design and operation of all facilities at SLAC are governed by the ALARA (as low as reasonably achievable) policy. Thus, SLAC has always maintained radiation dose limits below the maximum allowed by regulation.

8.2.1 Radiation Shielding

Shielding for PEP-II will conform to the Design and Control section of DOE Order 5480.11, Section 9(J) [*SLAC Radiological Control Manual*, 1993, Article 131]. The design criterion will be 1 rem/yr at 30 cm from the shield surface for normal beam losses. This assumes a 2000-hr working year and an occupancy factor of 1. In addition, SLAC internal design criteria require that (i) the boundary dose be limited to 5 mrem/yr for 7200-hr beam operation and (ii) the maximum radiation dose at 30 cm from the outer surface of the shield from an accidental beam loss not exceed 3 rem.

The PEP tunnel was originally designed for 200-GeV protons. As the shielding requirements for protons are far more stringent than those for electrons, present shielding was more than adequate for PEP operation with 18-GeV electrons and will also be adequate for PEP-II operation at its maximum values for energies and currents.

The IRs in PEP were originally designed for about 20 kW of injected power at 18 GeV, though injection was always limited to 1 kW. Radiation has never been a problem at these low power levels. The PEP-II design calls for injection power levels of less than 3.2 nC/pulse × 60 pps × 10 GeV = 1.9 kW, well below the original design criterion for the IRs. (Even at the highest conceivable injection power of 8 nC/pulse × 120 pps × 10 GeV = 9.6 kW, there is a factor-of-two safety margin compared with the original PEP shielding design.) Thus, we expect little or no radiation from these areas during normal PEP-II operation.

The loss of the circulating beams in the case of the thinnest shielding (that is, a curtain wall in an IR) would result in an integrated dose-equivalent of less than 50 mrem. Since the total energy of the two circulating beams, at their maximum allowable currents of 3 A, is only 308 kJ, the potential for activating air, ground, or beamline components is very low. Operational experience with PEP and SPEAR indicates that air, ground, and beamline component activation are not significant radiological problems.

8.2.2 Personnel Protection System

The Personnel Protection System (PPS) currently in place in the PEP tunnel is designed to protect personnel from radiation, electrical, and RF hazards. This is accomplished through a system of electronically interlocked gates, lights, alarms, and operator displays and controls [Constant et al., 1977; Smith and Constant, 1981]. (See below for further discussion of electrical and RF safety considerations.) With installation of PEP-II in the tunnel, the PPS will undergo necessary upgrades and enhancements to address the new facility and operating conditions, but will remain largely the same in terms of its overall design and function. The five existing access states, as shown in Table 8-1, will be retained, as will the lighting controls and audio signals that alert personnel to a change in access state.

Because the PEP-II high- and low-energy rings (HER and LER) will be assembled within the existing PEP housing structure, and because their injection lines will occupy the existing north and south injection transport (NIT and SIT) lines, the present PPS perimeter control and interlock facility can be utilized with some modifications and upgrades. The perimeter access points into the housing tunnels from all the IR halls and the personnel and equipment tunnel access gates can be fully utilized as part of an upgraded distributed PPS system. All displays and remote control functions available in the PEP control room will be retained. In addition to interfacing with the existing hardware panels, the upgraded system will provide software-driven CRT displays and touch-panels from a dedicated distributed PPS controller system. The new upgraded system will be able to read personnel badges and grant access only to those individuals whose badges are encoded as authorized for access to the area.

The PPS stopper logic will be modified to accommodate the new HER, LER, NIT, and SIT configurations. The emergency-off button configuration will remain the same. In general, the new configurations will not impose any major new PPS logic requirements. Tone loop systems will be reconfigured to be compatible with the upgraded distributed controller logic.

Table 8-1. Access states of the current PEP Personnel Protection System [SLAC Radiological Control Manual, 1993].

NO ACCESS	Beam on or potential for beam to be on.
RESTRICTED ACCESS	Similar to CONTROLLED ACCESS, but electrical hazards and x-rays from the RF system may be present. Because of additional hazards, access is allowed only as necessary to knowledgeable persons.
CONTROLLED ACCESS	Beam off. Electrical and RF hazards off. Zone has been searched. Persons are identified, are logged in and out, and must carry a key from the keybank.
IN SEARCH	Beam off. Electrical and RF hazards off. Doors electrically locked until search completed.
PERMITTED ACCESS	Assurance that beam and RF hazards cannot come on. All door releases are enabled (doors are "open").

Existing doors and gates will be upgraded to ensure reliability over the 15-year PEP-II lifetime. The current system provides seven complete access modules located at or near the five IR halls. Each entry module includes keybanks, video cameras, and direct voice communications via intercom and telephone. In addition, five equipment/personnel entry points are located around the periphery of the PEP ring, together with 13 additional key-operated personnel access/egress points. All of these points can be "crashed" for emergency exit.

There are 15 zone barrier gates in the PEP tunnel that require "access state" compatibility to allow passage in either direction. These zones will be retained for PEP-II, and logic requirements will not change. RF areas will continue to be located at the IR halls 4, 8, and 12. The four NIT/SIT barrier gates between the beam switchyard and the PEP tunnels will also remain.

The current PPS safety system interface (SSI) provides for electrical and RF hazard safety interlocks distributed throughout the PEP ring and at IR halls 4, 8, and 12. The input interface to this system will be expanded to accommodate additional RF and magnet power supply requirements, and the control logic will be upgraded to a distributed control interface that will be compatible with the PPS technology.

8.2.3 Beam Containment System

The redesigned NIT/SIT lines will be monitored by toroid current monitors located at their entry portals and will be instrumented in much the same way as are the existing beamlines [Constant et al., 1977]. Each beamline (NIT and SIT) will have two toroids that feed wideband balanced-input preamps located near the beamlines. The preamps

will drive fan-out distribution amplifiers in the main control room area. These, in turn, will distribute the beam-induced current signals to average-current monitors, repetition-rate monitors, and pulse-to-pulse peak-current monitors. Each current-monitoring device will generate test signals between beam pulses that will be redistributed to the beamline toroids and fed back to the processing electronics to provide a closed-loop test capability.

These beamlines will also be monitored by Protection Ion Chambers (PICs), in the same manner as is presently done in other SLAC beamlines. Other protection devices may also be needed. Protection systems will turn off beams via the existing Beam Containment System (BCS) shutoff paths.

Because the existing BCS is primarily analog in nature, it requires many careful setup adjustments to achieve the operational protection limits required by these beamlines. We are therefore exploring the possibility of upgrading the present BCS, utilizing digital-processing techniques to capture beam-pulse information and generate the necessary interlocks. The upgrade would include the use of state-of-the-art wideband preamps, flash A/Ds, serial data links, digital discrimination logic, and intelligent processors. Use of such techniques would provide rapid setup, flexibility, and improved reliability.

8.2.4 Radiation Safety Training

In accordance with SLAC's implementation plan for DOE Order 5480.11 (Radiation Protection for Occupational Workers) and the *SLAC Radiological Control Manual* [Reference Document SLAC-I-720-0A05Z-001], all SLAC employees and any persons who work at the laboratory longer than one month must receive training in radiation fundamentals through General Employee Radiological Training. In addition, those workers whose assignments make it likely that they will receive a total occupational radiation dose greater than 100 mrem in one year receive more extensive radiation safety training and are classified as Radiation Workers. Both classes of workers must be recertified every two years.

8.3 NONIONIZING RADIATION SAFETY

The RF system for PEP-II will incorporate all the safety measures that are currently in place at PEP [Allen and Karvonen, 1978]. These include the use of pressurized waveguides and strict procedures for mechanical assembly and inspection.

Each waveguide network will be pressurized with regulated 0.25-psig instrument air. Since the volumetric supply rate is limited, a leak in the waveguide will cause a drop in pressure, actuation of a pressure switch, and shutdown of the rings. After the leak is repaired, a field measurement will be made to check for RF leakage. Normal ring operation may resume when the pressure in the waveguide is restored and the RF field survey is completed.

Pressurization guards mainly against operation with a missing piece of waveguide or an improperly assembled flanged joint. Although the most likely cause of RF leakage under operating conditions is that a waveguide joint has been left open, it is possible that the system could be gas-leak-tight and not RF-leak-tight. This could occur, for example,

if the flange bolts are not tightened enough to fully compress the rubber gas seal. Thus, proper torquing of the flange bolts is necessary to prevent possible RF leakage at the flange joint.

During assembly and installation of the waveguide components, all flange bolts will be torqued and all field-assembled waveguide joints will be tested by pressurization and checked for bubbles. Joints must be free of visible bubbles. After installation, an inspector will measure the torque on a minimum of six bolts chosen at random on each flange. If the torques exceed specified levels, the inspector will then initial and date the flange joint, thus indicating that the joint is acceptable. If the joint is not acceptable, all the bolts on the flange must be retorqued and remeasured.

After the requirements for gas-leak checking and bolt torquing are satisfied, a check for RF leakage around each accessible flanged joint will be made. If the test is satisfactory, an adhesive label with the inspector's initials and the date will be applied across each joint. An intact and signed label on each waveguide joint is always a prerequisite to operational transmission of RF through a waveguide network. The coaxial connectors at the final drive amplifier and at the input to the klystron will also be surveyed for possible leakage.

When a klystron is disconnected from the waveguide between the klystron and the circulator, a cover will be bolted over the open end of the waveguide on the cavity side. The cover will be inspected and labeled, and the waveguide pressurized, before any beam can be stored in the ring. Also, a pressure switch interlock in the waveguide close to the klystron will prevent high voltage from being applied to a klystron when it is disconnected from the waveguide feeding its cavities.

PEP-II operations staff will conduct RF radiation hazard surveys periodically to ensure that the RF leakage level is less than 1 mW/cm^2.

8.4 ELECTRICAL SAFETY

It is SLAC policy that every necessary precaution is taken in the performance of work to protect all persons on the site from the risk of electrical shock and to minimize the probability of damage to property due to electrical accidents. This policy is implemented by assigning responsibility and adhering to basic safety principles, as stated in the *Environment, Safety, and Health Manual,* Chapter 8 [Reference Document SLAC-I-720-70100-100], and by complying with regulations and procedures appropriate to each operation. Appropriate electrical safety training courses are provided by the Laboratory for those workers who are likely to be exposed to high-voltage hazards.

Several PEP-II subsystems, such as the large ring power supplies, will employ high voltages. The controls and work procedures necessary to ensure safe work on these systems are well understood. The provisions for locking of these systems will utilize SLAC's established procedures for lockout and tagout. Energized equipment will be worked on only under very limited and controlled conditions, and only qualified employees will perform such work. All work will be performed in accordance with safe work practices and in accordance with OSHA 1910, Subpart S.

Special procedures are in place to permit authorized personnel to occupy areas adjacent to energized hazardous magnets. These procedures are called RASK, for

"Restricted Access Safety Key." Under these procedures, a special RASK authorization form must be filled out to obtain a key that enables the hazardous supply under test. Testing is done in accordance with written procedures. The emergency-off buttons remain active and will crash off the power supply when pushed. The RASK system will remain operational during construction of PEP-II. Thus, we will have the advantage of having this safety system in place during installation and testing of the magnets.

During the life of the PEP tunnel, there has been some damage to junction boxes and conduit due to water seepage near IR-10. Owing to the difficulty in obtaining a tight water seal in the shotcrete-lined tunnel, water flow has been managed through a series of efforts, including covering vulnerable equipment and installing drainage gutters to channel the flow of water [Weidner, 1990; see also Section 7.1.1]. No electrical accidents have occurred as a result of the water seepage. To address this continuing problem over the life of PEP-II, additional improvements to the drainage system are planned, as described in Chapter 7. Further, the entire electrical distribution system now in place will be inspected, and any elements of the system that are damaged or vulnerable to damage will be replaced and maintained in a manner that will ensure safe operation. All new electrical installations will be in accordance with current applicable codes and requirements.

8.5 CONSTRUCTION

The line organization acting through the subcontract administrator has primary responsibility for overseeing safety compliance by construction subcontractors. This responsibility includes:

- Apprising subcontractors of SLAC and DOE safety criteria prior to construction
- Conducting periodic inspections of subcontractor construction areas to evaluate the quality of the subcontractor's safety compliance program
- Receiving subcontractor accident reports and compiling information for reporting to DOE

The Quality Assurance and Compliance Department of the ES&H Division oversees the *QACD Subcontractor Oversight Program* [Reference Document SLAC-I-770-0A17A-001-R001].

8.6 EMERGENCY PREPAREDNESS

Like all experimental equipment at SLAC, PEP-II will be designed, constructed, and operated in a manner that minimizes the risk of injury to property or personnel as a result of a natural disaster or other emergency situation. In the event of any abnormal condition, the interlock system will automatically shut the machine down until the situation is diagnosed and corrected. The formal emergency planning system described in the *SLAC Emergency Preparedness Plan* [Reference Document SLAC-I-720-70000-105] will help to ensure a logical, organized, and efficient response to any emergency. It

sets forth specific steps to deal with various emergency conditions, identifies the appropriate personnel to act as resources, and provides a chain of command for responding to unplanned events.

The emergency situation most likely to arise at SLAC is an earthquake. SLAC structures are designed to withstand the effects of a major earthquake. In addition, all mechanical components of PEP-II will be secured to protect persons working nearby. This will be assured by a review of the design and installation of the experimental equipment by the SLAC Earthquake Committee, as mandated by the SLAC Safety Program. Further, as with all activities at SLAC, operation of PEP-II will be covered by the *SLAC Emergency Preparedness Plan* [1991], which outlines the procedures to be followed in the event of an earthquake severe enough to cause possible structural damage or personal injury.

8.7 ENVIRONMENTAL PROTECTION

8.7.1 Disposal of PEP Components

Disassembling PEP and making room in the tunnel for installation of PEP-II will require the removal of 925 tons of concrete rafts and hundreds of tons of other materials. The concrete rafts have been surveyed and found to be free of radioactivity other than background activity from radon (^{214}Bi, ^{214}Pb) and ^{40}K. The concrete may therefore be disposed of as nonhazardous waste. All other items will be surveyed before they are removed from the tunnel and will be handled in a manner appropriate to the level of residual radioactivity present, if any. Those materials that may be reused in PEP-II will be held in a secure area until they are reinstalled. All scrap will be disposed of in accordance with approved procedures.

8.7.2 Ongoing Environmental Protection Activities

Construction and operation of PEP-II is not expected to cause any adverse impact on the groundwater. Preservation of groundwater quality will be ensured through the implementation of the Groundwater Management Program that SLAC is currently preparing to comply with DOE Order 5400.1.

8.8 HAZARDOUS MATERIAL ISSUES

In accordance with 29 CFR 1910.1200 (the OSHA hazard communication standard), SLAC has developed a *SLAC Hazard Communication Program* [Reference Document SLAC-I-720-0A06Z-001, 1992]. Under this program, SLAC directs Department Heads and Group Leaders to conduct regular inventories of hazardous materials, to make Material Safety Data Sheets (MSDSs) available to all employees, to ensure appropriate labeling of hazardous materials, to train employees to identify and control hazards in the

workplace, and to inform users, subcontractors, and temporary employees of the hazards that may be encountered at SLAC.

8.9 DETECTOR SAFETY ISSUES

A separate Conceptual Design Report and safety evaluation will be prepared and submitted for the PEP-II detector. This discussion is intended merely to summarize the safety and environmental hazards posed by the detector and to describe the means proposed to mitigate them.

The detector for PEP-II will be similar, from a safety point of view, to particle physics detectors at many other storage rings. It is therefore possible to evaluate with some confidence potentially hazardous conditions that must be protected against. The detector systems may employ gases with a small but significant flammable component. This is also a standard situation. Safety procedures in this case involve (i) the proper venting of gases in such a way as to prevent the accumulation of explosive concentrations, (ii) the placement and proper maintenance of flammable-gas detectors on the detector itself and in the regions of gas storage and mixing, (iii) the proper siting and installation of pressure vessels, (iv) the interlocking of high voltages so as to prevent sparks that could ignite the mixture, and (v) the training of operators regarding proper safety procedures.

The final potential safety hazard is the cryogenic system associated with a superconducting solenoidal magnet if it were adopted (which presently is considered unlikely). This system must handle liquid helium to cool the magnet. Safety considerations here mainly involve prevention of spills of cryogens (liquid helium and liquid nitrogen), which could cause injury by freezing or by creating an oxygen-deprived atmosphere upon evaporation. This will be done by engineering the system such that large liquid spills can be prevented, even in the event of a major line rupture; by the installation of low-oxygen detectors; by the proper engineering of pressure vessels and attendant systems; and by extensive training of the system operators and maintenance personnel. If superconducting IR magnets were utilized for the PEP-II rings, these measures would be applied to them as well. Of course, the volume of cryogens would be much smaller for the ring magnets.

8.10 QUALITY ASSURANCE

The PEP-II project management will provide funding, staffing, thought, and time to ensure that PEP-II meets its short- and long-term performance goals. It is the responsibility of management to maintain the project's direction and to make decisions that encourage quality assurance (QA) considerations. At all levels, project management will communicate high expectations and concrete goals for the attainment of quality, and make decisions to ensure that performance objectives for both construction and operation are met. Project management will also seek out and use, as applicable, modern quality assurance, manufacturing, and reliability approaches. The project management will develop management systems that ensure that the long-term reliability, availability, and

maintainability (RAM) objectives for the entire PEP-II project (not just the individual subsystems) are attained and optimized, and that PEP-II conforms to its intended safe, functional, and environmentally-sound design. The PEP-II quality assurance strategy is described below.

Project management has used a policy of peer and expert review to monitor and guide all phases of the PEP-II design and its related R&D program. This process has been used extensively to ensure that the highest quality engineering and design practices are followed, as well as to verify that optimal technical decisions are being made. Following each review, a written report is prepared. The report is kept on file and is available for public inspection and use. Emphasis is always placed on securing the most qualified reviewers available—when local experts are not available, reviewers have been brought to SLAC from Europe and/or Japan. For example, in late 1990 four separate review teams, with experts drawn from the international community, were assembled to review the technical choices and implementation schemes for the major accelerator areas of vacuum, RF and feedback, lattice, and interaction region design. Improvements and modifications determined from the various design and R&D reviews have been incorporated, as appropriate, to optimize the PEP-II design. PEP-II management will continue this tradition of expert reviews throughout the life of the construction project.

PEP-II management is keenly aware that the "factory" nature of this project demands highly efficient operation and ease of maintenance. To ensure these goals, efficient operation and maintainability have been stressed as integral requirements for all systems. A budget for operational availability has been defined (see Section 3.4) that provides a clear target for operational efficiency for the design team.

Reporting directly to the project management, a QA manager for the PEP-II project will assist in implementing the QA effort. The QA manager will work closely with project management and subsystem managers to develop and implement the overall QA program. In accordance with the *SLAC Institutional Quality Assurance Program Plan* [Reference Document SLAC-I-770-0A17M-001] and DOE Order 5700.6C, *Quality Assurance,* the QA manager will develop a Quality Implementing Procedure (QIP) for the PEP-II project. This QIP will delineate the roles of the project management, the QA manager, the subsystem managers, and others involved in the project. The QIP will include:

- Description of the QA program (its purpose, scope, organization, and responsibilities)
- Personnel training and qualifications
- Quality improvement teams
- Documentation and records
- Work processes
- Design
- Procurement
- Inspection and testing

- Management assessments
- Independent reviews

Previous experience with other accelerators indicates that managing drawings, personnel, and administrative activities using traditional paper-based methods is slow, difficult, and labor intensive. In response to this challenge, a major effort has been under way at SLAC for over a year to develop a computerized solution. Significant progress has been made in developing a database system for managing the drawings, personnel, and administrative activities associated with the design, construction, maintenance, and operation of PEP-II. This system is very similar to a computerized approach that was successfully incorporated into the LEP project at CERN. On-line configuration control, on-line drawing availability, on-line component fabrication and operational history, and an extensive database of project personnel are all features of the application.

Although project management leads the quality assurance process and the QA manager facilitates the process, individual subsystem managers and engineers play a significant role in implementing QA objectives, including RAM objectives (see Section 3.4), for PEP-II. To foster involvement in QA of all those concerned, two types of training are planned:

(1) General QA training for the project management, subsystem managers, and engineers

(2) Specific training in quality planning, primarily for subsystem managers and engineers

The general QA training will provide an overview of modern QA principles, case studies of successfully applied techniques, and a common language to facilitate communication among all project members throughout the project's phases.

In an effort to incorporate quality assurance planning at the subsystem level, the QA program will include the use of QA milestones in project schedules. In the past, separate documents describing quality assurance issues for each subsystem have been used. The major drawback of this approach is that the documents suggest QA actions but do not provide a way for project management to verify that specified actions have been taken. The approach for PEP-II will overcome this difficulty by integrating QA milestones directly into project schedules. For example, a typical project schedule might have the following QA milestones with assigned dates and responsibilities:

- Develop drawings for the subsystem
- Review design for the subsystem
- Obtain drawing approval for the subsystem
- Submit drawings to the PEP-II database
- Develop an inspection plan
- Inspect the subsystem dimensionally
- Review dimensional inspection results

- Test the subsystem for environmental stability
- Review results of environmental stability testing
- Verify that the actual reliability of the subsystem is consistent with the reliability goals for the subsystem
- Commission the subsystem

The subsystem manager will work with project management, the QA manager, and, in some cases, other subsystem managers to develop a schedule with QA milestones. Some QA milestones, such as documentation of safety-related systems by project management, will be mandatory for all subsystems, while other QA milestones will be applicable to only a few specific subsystems. The QIP developed for PEP-II will distribute between the QA manager and subsystem managers the responsibility for determining that QA milestones have been met.

The budget presented in Chapter 9 includes the salary for the full-time QA manager, as well as funds for engineers to perform QA tasks for each subsystem. The budget includes funds for QA inspections both on site and at potential and actual vendor facilities. Detailed budgets for subsystems include funds to develop drawings, to build test fixtures, and to maintain the quality and RAM objectives of the PEP-II project.

As stated earlier, project management is committed to an ongoing process of subsystem review. Reviews will be performed by a combination of in-house and outside personnel. Reviewers will provide technical input throughout all phases of the project and ensure that best engineering practices are adhered to. Reviewers will also ensure that proper standards of not only quality but also environment, safety, and health are incorporated into designs. Since the RAM characteristics of the PEP-II project are largely a function of subsystem design, reviewers will verify that RAM-related issues have been properly considered in subsystem design.

9.

COST AND SCHEDULE

THE PEP-II project involves an upgrade of the SLAC accelerator complex. This upgrade includes construction of the PEP-II high- and low-energy rings in the existing PEP tunnel and construction of bypass lines for the electrons and positrons in the existing linac enclosure. Many PEP components will be reused in the construction of the storage rings. Although no conventional construction is required, minor modifications to the electrical and cooling-water systems are included in the project scope.

9.1 COST ESTIMATE

The PEP-II construction cost estimate was generated, and will be subsequently monitored, through a work breakdown structure (WBS), described in Section 9.3. The total construction cost in FY 1993 dollars, including contingency, is $157.4 million. This estimate is presented in Table 9-1; the associated schedule (presented in Section 9.2) assumes a "technology limited" profile, though the actual schedule may be constrained by funding limitations.

Contingency is an explicit line item that was determined after a detailed analysis of each of the major subsystems. The contingency percentage varies from system to system, depending upon the complexity of the particular system, the details of our understanding, and the status of our R&D activities. In those cases where PEP components are being duplicated, we feel justified in assigning a lower-than-average contingency. The percentage of contingency ranges from 15% (for a well-defined and well-understood magnet system) to 50% (for the less-well-defined interaction region components). The overall contingency for the project is 24%. Table 9-1 includes the individual contingency assigned to each subsystem.

9.2 CONSTRUCTION SCHEDULE

Major project milestones are listed in Table 9-2. The corresponding schedule, shown in Fig. 9-1, is based on a technology-limited funding profile. If funds are not available to

Table 9-1. Estimated cost, in FY 1993 dollars, of the PEP-II Asymmetric B Factory.

WBS code	System	Cost (FY1993 K$)	Contingency (%)	Contingency (FY1993 K$)	Total (FY1993 K$)
1	**PEP-II Asymmetric B Factory**	**127278**	**24**	**30090**	**157368**
1.1	**High-Energy Ring**	**55021**	**23**	**12690**	**67711**
1.1.1	Magnets	2705	17	459	3164
1.1.2	Power Conversion	3038	29	873	3911
1.1.3	RF	18528	28	5181	23709
1.1.4	Vacuum	18356	19	3564	21920
1.1.5	Feedback	2246	24	544	2790
1.1.6	Diagnostics	2531	20	502	3033
1.1.7	Installation	5303	23	1220	6523
1.1.8	Alignment	1072	15	161	1233
1.1.9	Supports & Stands	1242	15	186	1428
1.2	**Low-Energy Ring**	**40422**	**24**	**9837**	**50259**
1.2.1	Magnets	7084	20	1417	8501
1.2.2	Power Conversion	3017	28	854	3871
1.2.3	RF	9274	28	2594	11868
1.2.4	Vacuum	12910	25	3198	16108
1.2.5	Feedback	1336	25	331	1667
1.2.6	Diagnostics	1359	20	267	1626
1.2.7	Installation	2323	24	557	2880
1.2.8	Alignment	426	15	64	490
1.2.9	Supports & Stands	2693	21	555	3248
1.3	**Interaction Region**	**4489**	**32**	**1454**	**5943**
1.3.1	Magnets	1001	39	390	1391
1.3.2	Power Conversion	985	23	229	1214
1.3.4	Vacuum	1007	27	270	1277
1.3.6	Diagnostics	314	50	157	471
1.3.7	Installation	871	37	324	1195
1.3.9	Supports & Stands	311	27	84	395
1.4	**Injector**	**9883**	**22**	**2141**	**12024**
1.4.1	Magnets	1649	29	475	2124
1.4.2	Power Conversion	2423	17	407	2830
1.4.4	Vacuum	1301	21	272	1573
1.4.6	Diagnostics	1307	22	285	1592
1.4.7	Installation	2226	23	501	2727
1.4.8	Alignment	395	23	91	486
1.4.9	Stands and Supports	582	19	110	692

Table 9-1. Estimated cost, in FY 1993 dollars, of the PEP-II Asymmetric B Factory (continued).

WBS code	System	Cost (FY1993 K$)	Contingency (%)	Contingency (FY1993 K$)	Total (FY1993 K$)
1.5	**Control System**	**8540**	**25**	**2140**	**10680**
1.5.1	HER Controls	5150	25	1265	6415
1.5.2	LER Controls	3390	26	875	4265
1.6	**Utilities**	**4867**	**20**	**991**	**5858**
1.6.1	Electrical	2607	20	522	3129
1.6.2	Mechanical	2110	20	421	2531
1.6.3	Site Work	150	32	48	198
1.7	**Safety & Protection**	**515**	**25**	**129**	**644**
1.7.1	Accelerator	515	25	129	644
1.8	**Management**	**3540**	**20**	**708**	**4248**
1.8.1	Administration	3540	20	708	4248

maintain this schedule, the project will take longer. Note that the associated schedule for preconstruction R&D has been incorporated into the overall project schedule. That is, the schedule presented in Fig. 9-1, while based on a technology-limited scenario, takes proper account of the time required for R&D activities prior to detailed design and component fabrication.

Table 9-2. PEP-II project milestones. Q1 refers to quarter 1 of the indicated fiscal year.

Schedule	Milestone
Q1 1994	PEP-II project start
Q3 1996	Inject into first sextant - HER
Q1 1997	Inject into first sextant - LER
Q3 1997	HER complete (installed capability 1 A, 9 GeV)
Q4 1997	LER complete (installed capability 2.1 A, 3.1 GeV)
Q4 1997	Project complete
Q1 1998	Colliding-beam operation begins

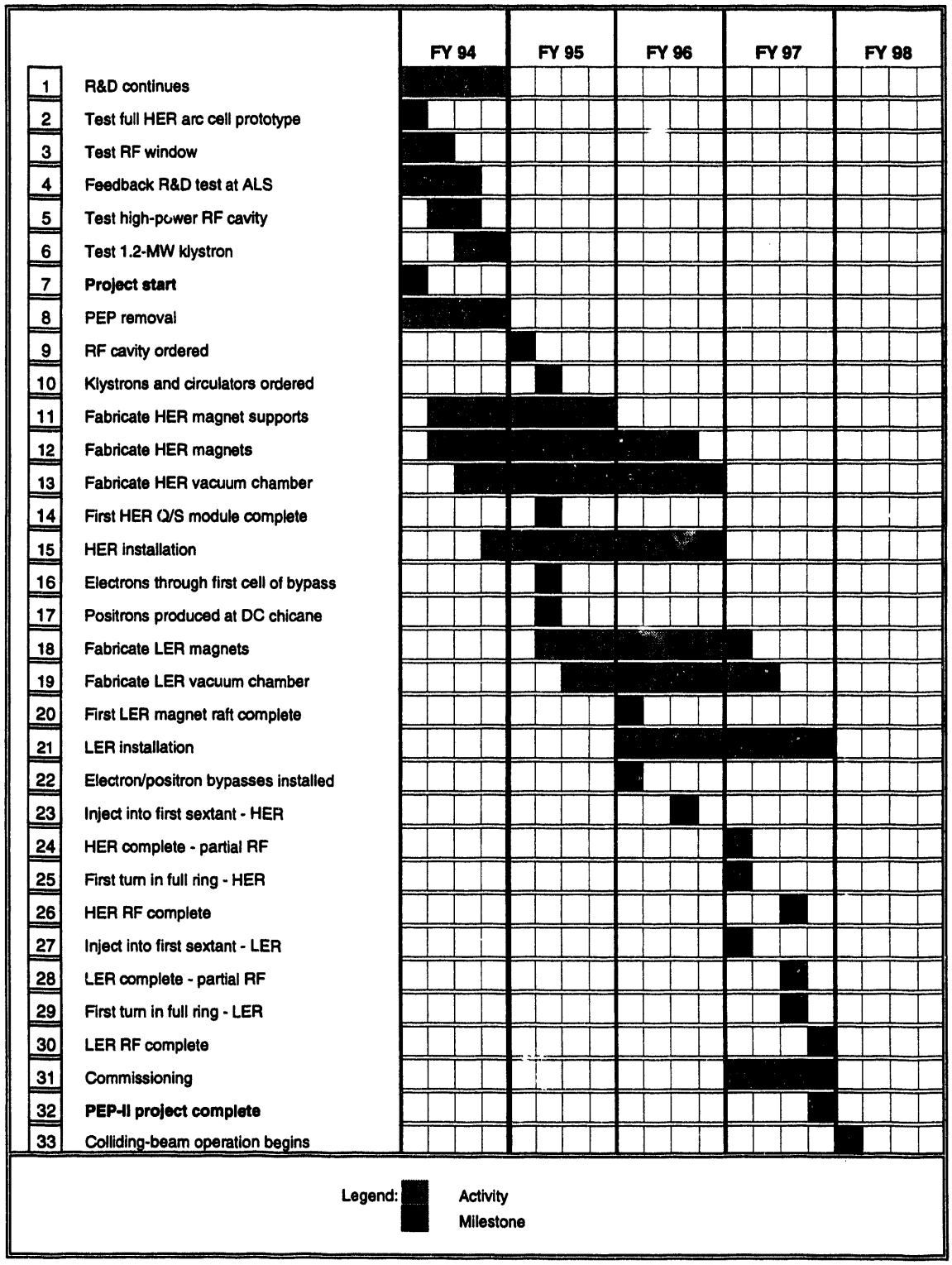

Fig. 9-1. Project schedule and construction milestones for PEP-II.

9.3 WORK BREAKDOWN STRUCTURE

The work breakdown structure was designed to be consistent with project management's need to track detailed costs of all PEP-II subsystems. It conforms to the structure used by the SLAC Accounting Office for reporting costs and commitments to PEP-II management. The levels are defined as follows:

- Level 1 = x *PEP-II*
- Level 2 = x.x *Major systems*
- Level 3 = x.x.x *Subsystems*
- Level 4 = x.x.x.x *Subsystem detail*

Definitions for levels two and three of the PEP-II WBS are given below.

1.1 High-Energy Ring (HER). PEP-II utilizes a reconfigured and refurbished PEP storage ring as the high-energy storage ring. Its nominal operating energy is 9 GeV.

1.1.1 HER Magnets. The existing PEP magnets will be refurbished and reconfigured in the PEP tunnel. Additional quadrupoles will be added to maintain the beam focusing in the long straight sections.

1.1.2 HER Power Conversion. The existing PEP large power supplies will be refurbished; additional supplies will be acquired as needed for new magnets. Monitoring systems will be constructed.

1.1.3 HER RF. New high-power, low-impedance copper cavities, driven by 1.2-MW klystrons, will be designed and fabricated or purchased. The PEP-II RF system will operate at a higher frequency (476 MHz) than the original PEP RF system (353 MHz).

1.1.4 HER Vacuum. The high circulating currents of PEP-II result in high synchrotron radiation power on the vacuum chamber wall. The existing PEP vacuum chamber will be replaced with a new copper chamber to provide the appropriate low pressure and thermal management. Costs of installation of the chamber are included here.

1.1.5 HER Feedback. To control coupled-bunch instabilities in the high-energy ring, one longitudinal and two transverse feedback systems will be employed. These will be wideband, bunch-by-bunch systems, designed and built primarily in-house but using commercially obtained power amplifiers.

1.1.6 HER Diagnostics. Beam position monitors, profile monitors, and various other beam diagnostic devices will be designed and fabricated.

1.1.7 HER Installation. The existing PEP storage ring will be disassembled, refurbished, and reassembled into its new configuration as the PEP-II HER. Mechanical, electrical, and RF installation are included here.

1.1.8 HER Alignment. The reinstallation of the PEP ring in its new configuration will require a realignment of all components.

1.1.9 HER Supports and Stands. New supports for the HER are required to lower the ring in order to accommodate the LER. These supports also incorporate the C-frame supports for the LER rafts.

1.2 Low-Energy Ring (LER). The PEP-II LER is a completely new ring having a circumference of 2200 m, to be located atop the HER in the PEP tunnel. Its nominal operating energy is 3.1 GeV.

1.2.1 LER Magnets. The LER magnet system is modeled after that of the HER, with the lengths of some of the components reduced because of the lower energy. Designs and fabrication techniques closely follow those used successfully in the construction of the PEP magnets.

1.2.2 LER Power Conversion. The bulk of the power supplies required for the LER are existing, refurbished PEP supplies.

1.2.3 LER RF. New high-power, low-impedance 476-MHz RF cavities, driven by 1.2-MW klystrons, will be fabricated or purchased for the LER. No additional penetrations or surface buildings will be required.

1.2.4 LER Vacuum. The LER vacuum system utilizes a copper beam pipe in those regions where the photon flux is high (the areas just downstream from the dipoles) and a stainless-steel beam pipe elsewhere.

1.2.5 LER Feedback. The feedback demands of the LER are comparable to those of the HER. These bunch-by-bunch feedback systems will be capable of damping both transverse and longitudinal instabilities.

1.2.6 LER Diagnostics. Beam position monitors, current monitors, profile monitors and other beam-monitoring devices and their associated electronics are included here.

1.2.7 LER Installation. The LER magnetic components will be installed on preassembled and prealigned rafts. The supports for these rafts are an extension of the HER supports. Mechanical, electrical, and RF installation are all included here.

1.2.8 LER Alignment. Conventional optical alignment tooling, already available at SLAC, will be modified to align the LER.

1.2.9 HER Supports and Stands. The magnetic elements of the LER (dipoles, quadrupoles, and sextupoles) will be prealigned on rafts in the shop.

1.3 Interaction Region (IR). PEP-II will have one interaction region, located at IR-2.

1.3.1 IR Magnets. As PEP-II consists of two separate rings, special magnets are necessary to bring the beams into collision and then to return them to their respective rings. Included here are the septum quadrupoles, as well as the permanent-magnet bending and focusing elements and their trim windings.

1.3.2 IR Power Conversion. Power supplies, as well as current-monitoring equipment are required for the septum quadrupoles, and also for some

conventional quadrupoles located in this area. Power for the permanent magnet trim windings is also included here.

1.3.4 IR Vacuum. This comprises all vacuum chamber elements in the IR, including the special thin-walled beryllium beam pipe for the detector, radial ion pumps, masks, etc.

1.3.6 IR Diagnostics. Special care must be taken to monitor the beam position and measure the luminosity in the interaction region both to maximize the luminosity and to avoid background problems.

1.3.7 IR Installation. This entry includes the costs associated with the electrical and mechanical installation of PEP-II final focusing elements, including alignment costs. The IR components will be prealigned in a support barrel to ensure proper relative alignment through the detector.

1.4 Injection System (INJ). The injector for PEP-II is the SLC linac. Separate bypass beamlines for positrons and electrons will be provided in the linac housing. These beams will be delivered to the NIT and SIT tunnels that supplied beams to PEP, and then transported to the HER and LER injection straight sections.

1.4.1 INJ Magnets. New magnets are required for the transport lines from linac Sector 4 to the SIT line (for positrons) and from linac Sector 8 to the NIT line (for electrons). Both the NIT and SIT lines will be upgraded at their entrance and exit ends.

1.4.2 INJ Power Conversion. The existing NIT and SIT line bending magnet and quadrupole power supplies will be refurbished. New trim dipole power supplies will be added, and the power supply control and monitoring equipment will be upgraded. The positron and electron bypass lines will use existing bending magnet power supplies and new quadrupole supplies. Magnet control and monitoring equipment will be all new.

1.4.4 INJ Vacuum. Roughing lines and necessary valving and piping for the bypass lines and the NIT and SIT lines are included here, as are ion pumps and their controllers.

1.4.6 INJ Diagnostics. New beam position monitors, profile monitors, and wire scanners will be installed in both the bypass lines and the NIT and SIT lines.

1.4.7 INJ Installation. Two new beam transfer lines will be installed, bypassing the linac, to transport electrons to the NIT line and positrons to the SIT line. The NIT and SIT lines will be extended and partially rebuilt to accommodate vertical injection for PEP-II.

1.4.8 INJ Alignment. The two new bypass lines must be aligned and matched to the extraction optics from the linac and the injection optics into either the NIT or the SIT line. The NIT and SIT lines require realignment, as do their injection lines into the HER and LER.

1.5 Control System. The control system for PEP-II is modeled after the existing control system at the SLC.

1.5.1 HER Controls. This entry represents costs necessary to develop control software and hardware to operate the PEP-II HER.

1.5.2 LER Controls. This entry represents costs necessary to develop control software and hardware to operate the PEP-II LER.

1.6 Utilities. PEP-II utilizes the existing PEP facility. No new conventional construction is required. The PEP electrical distribution system will be modified to accommodate the new load distribution of PEP-II. Similarly, the water system will be upgraded to replace some parts and slightly reconfigured to reflect the new PEP-II loads.

1.6.1 Electrical Utilities. This entry represents the costs of reconfiguring the PEP electrical distribution system to match PEP-II requirements.

1.6.2 Mechanical Utilities. This entry represents the costs associated with the replacement of all the PEP LCW pumps and heat exchangers, and the modifications to the linac LCW system to accommodate the injector bypass lines. It also includes a modification to the RF cooling system to include an ethylene glycol loop.

1.6.3 Site Work Utilities. This involves improving the water management within the PEP tunnel. A small portion of the tunnel will be cleaned and water-diverting hardware will be installed.

1.7 Safety and Protection. Included here are costs associated with upgrading the fire-protection system and the rework of the personnel protection system. The salary of a full-time safety inspector will also be covered.

1.8 Management. This entry reflects the costs associated with the overall management of the project, i. e., effort that is not otherwise included in any of the various subsystem costs. (Salaries for lead engineers are associated with the costs of their respective subsystems.) Included are such things as project administration, quality control and quality assurance activities, planning and scheduling, and budget-related activities.

10.

SUMMARY

IN this report, we have described an updated conceptual design for the high-luminosity Asymmetric *B* Factory (PEP-II) to be built in the PEP tunnel on the SLAC site. This proposal, a collaborative effort of SLAC, LBL, and LLNL, is the culmination of more than four years of effort aimed at the design and construction of an asymmetric e^+e^- collider capable of achieving a luminosity of $\mathcal{L} = 3 \times 10^{33}\ cm^{-2}\ s^{-1}$. All aspects of the conceptual design were scrutinized in March 1991 by a DOE technical review committee chaired by Dr. L. Edward Temple. The design was deemed feasible and capable of achieving its physics goals. Furthermore, the cost estimate, schedule, and management plan for the project were fully endorsed by the committee. This updated conceptual design report captures the technical progress since the March 1991 review and reflects the lower cost estimate corresponding to the improved design. Although the PEP-II design has continued to evolve, no technical scope changes have been made that invalidate the conclusion of the DOE review.

The configuration adopted utilizes two storage rings, an electron ring operating at 9 GeV and a positron ring at 3.1 GeV, each with a circumference of 2200 m. The high-energy ring is an upgrade of the PEP storage ring at SLAC; all PEP magnets and most power supplies will be reused. The upgrade consists primarily of replacing the PEP vacuum chamber and RF system with newly designed versions optimized for the high-current environment of PEP-II. The low-energy ring will be newly constructed and will be situated atop the high-energy ring in the PEP tunnel. Utilities already installed in the PEP tunnel are largely sufficient to operate the two PEP-II storage rings.

Siting an asymmetric *B* factory at SLAC offers a number of important advantages. The existing 2200-m-circumference PEP tunnel provides sufficient space to construct the two-ring collider, and it permits a flexible design with conservative parameters. The bending radius accommodated by the arc sections, 165 m, allows the use of low-field bending magnets, thereby keeping the synchrotron radiation power density to reasonable levels (only 3.3 kW/m at the design current for the high-energy ring). The availability of six long (120-m) straight sections increases the flexibility of the design and easily accommodates the requirements for beam separation, emittance and tune control, injection, and the detector. Because the PEP tunnel was originally sized to house two rings, space is also fully adequate for the addition of the PEP-II low-energy ring. Indeed, no conventional

construction will be necessary for PEP-II, saving both cost and time in making it operational. The tunnel is adequately shielded against the additional radiation that results from high-luminosity operation, and the IR hall is sufficient to accommodate the envisioned detector and its ancillary equipment.

A unique advantage of the SLAC site is the availability of the most powerful positron injection system in the world—the SLC linac. This feature is crucial for the operation of the collider as a "factory," because maintaining a high average luminosity depends strongly on achieving rapid injection. The linac injection system is also the ideal choice in terms of the requirements of the storage ring feedback systems, because it provides a small amount of charge per injection shot, thus ensuring that the feedback systems are not overloaded by injection transients.

The design approach followed here has focused on achieving the performance goals of PEP-II in a reliable manner. This has meant designing the hardware from the outset with sufficient operating margin, as well as providing good diagnostics as part of the design. Where possible, we have adopted parameters consistent with established collider practice. For example, the required beam currents of 0.99 A and 2.14 A in the high- and low-energy rings, respectively, are split into 1658 bunches. Therefore, the single-bunch parameters (length, current, emittance, beam-beam tune shift) are all conventional and do not require any extrapolation from the operating experience of present machines.

Our choice of many low-intensity bunches, as opposed to fewer high-intensity bunches, avoids difficulties associated with single-bunch instabilities, though it does not change the need for a state-of-the-art feedback system to manage coupled-bunch instabilities. In our approach, the design challenges for PEP-II are restricted to a few selected areas. These areas, listed below, are all amenable to attack by standard engineering approaches and, though demanding, can be handled by applying and extending existing techniques in a reasonably well-understood manner.

Based on our studies, we have concentrated the design effort on those aspects where the most difficult technical challenges exist. These include

- Vacuum system
- RF system
- Multibunch feedback system
- Beam separation and detector masking system

For each of these areas, careful and systematic design work has been undertaken to identify the problems (associated mainly with the required high beam currents) and then to solve them. To ensure that our solutions are effective and appropriate, international experts in each of the above areas were brought to SLAC or LBL to review and validate our design concepts. In each case, the outcome of this process was favorable, thereby verifying the basic soundness of our design. Overall technical feasibility was subsequently confirmed by the March 1991 DOE technical review.

For the vacuum system, we have adopted a copper vacuum chamber patterned after the HERA design. Copper exhibits good thermal properties and a low rate of photon-induced gas desorption, thus ensuring a low pressure in the face of 1–2 A of beam current in each ring. Detailed estimates of photon desorption and two- and three-dimensional thermal calculations of the chamber have demonstrated that the approach is an effective one. The

required photodesorption properties of the copper adopted for fabrication have been verified at the National Synchrotron Light Source at Brookhaven National Laboratory.

The RF system is based on a standard room-temperature cavity design that includes waveguides to damp the unwanted higher-order modes of the structure. This approach has been shown (by means of three-dimensional electromagnetic calculations) to reduce the Q factors of higher-order modes to very low values that are favorable for the stabilization of coupled-bunch motions. Furthermore, experiments have been performed on a prototype PEP-II cavity that confirm the results of the calculations and demonstrate the capability of reaching, or even exceeding, the required amount of damping.

The multibunch feedback system is based on a bunch-by-bunch approach. Extensive simulations have shown that the system will perform effectively under either injection or colliding-beam conditions. The feedback system makes use of commercially available wideband power amplifiers and requires a power level of 1.5 kW for the longitudinal case and even less for the transverse case. An advantage of our approach is that the feedback system will deal with any form of bunch motion, whatever the cause. Thus, even coherent disturbances arising from the beam-beam interaction can potentially be controlled. A prototype longitudinal system has been successfully tested at both SPEAR and the ALS.

We have carefully designed a beam separation scheme to minimize detector backgrounds, and we have invested substantial effort in detailed simulations of the effects on detector background of both synchrotron radiation photons and lost electrons. This aspect is a challenge for PEP-II because we must achieve the same level of background typically found in today's colliders, but at a beam current an order of magnitude higher. Our masking design gives a factor of 84 safety margin with respect to synchrotron radiation background limitations and a factor of 20 margin with respect to lost particles. We have also shown the system to be stable against reasonable changes in our design assumptions by examining misalignments of magnets and masks.

The construction of PEP-II is an ambitious and exciting project, both as an extension of the accelerator builder's art and as a contributor to our understanding of one of the most fundamental questions in our Universe—the origin of CP violation. The SLAC site, with its large-circumference tunnel and the world's most powerful positron injector, is an ideal base from which to launch such a project. Moreover, the combination of the three participating laboratories, SLAC, LBL, and LLNL, offers a pool of accelerator physics, high-energy physics, and engineering expertise unmatched anywhere—a team fully capable of dealing with the challenges presented by a high-luminosity asymmetric B factory. There is, in addition, a large community of physicists worldwide who eagerly await the exceptional physics opportunities afforded by PEP-II.

The time is at hand to begin the construction of this frontier facility for high-energy physics research. Based on a four-year construction schedule, PEP-II could begin operation at the end of FY 1997. Thereafter, we envision a vigorous research effort that will last for at least 15 years and will address with unique efficacy some of the crucial problems in high-energy physics today.

ACKNOWLEDGMENTS

THIS document marks the culmination of several years of intensive R&D and design activity in support of the PEP-II project. Its technical content is a result of the high-quality work of many dedicated scientists, engineers, and designers, without whom the design of PEP-II could not have been done; computer support from the NERSC played an important role in the design work. The cooperation of the technical staff in providing the raw materials for this report did much to smooth the work of creating it. It is a great pleasure to be a member of such a team; the PEP-II Project Leader, Jonathan Dorfan from SLAC, deserves much of the credit for creating such a good working environment. Preparation of a large technical document such as this is a yeoman task in its own right and takes many people "behind the scenes." The efforts of Sylvia MacBride and Terry Anderson of the SLAC Publications Department were crucial in creating more than 300 excellent drawings. It is a pleasure to thank them for their skill and their dedication to getting the job done quickly and well. Help and advice from Vani Bustamante and Effie Clewis of the SLAC Publications Department, especially in sorting out the references, and organizational help from Bernie Lighthouse were also important. Connie Silva and Jean Wolslegel of the LBL Technical Information Department provided word-processing support for portions of the document. Their ability to quickly and accurately type difficult sections of a report is unequaled. Production of the report relied on the excellent support from members of the LBL Technical Information Department. Marilee Bailey, Alice Ramirez, and Ralph Dennis spent many hours doing the layout, and Jimmy Lovato and his crew at the LBL printing plant produced the required copies smoothly and promptly. Doug Vaughan from LBL supervised the document preparation at LBL. His editing skills and attention to detail did much to improve the contents and the presentation of the report. Coordination and transportation of the document between SLAC and LBL were cheerfully and reliably handled by Nina Adelman-Stolar and Juanita O'Malley. It is a special pleasure to thank the small "core group" of individuals, Loretta Lizama from LBL and Andrea Chan from SLAC, who together turned the many independent technical inputs into a cohesive report on the PEP-II project. Loretta organized and edited the myriad figures and spent many weeks "camped out" at SLAC to guide the document-preparation process. Her dedication and editorial prowess are noteworthy—but even more noteworthy are her good cheer and good spirit. Creating this report might well have been impossible without Loretta's help, and it certainly would have been less fun! Andrea Chan also played a crucial role, serving as production editor for the document, doing much of the technical typing, and generally making sure that the work was done promptly and properly. Her unrelenting insistence on doing things right shows up throughout the report and is one of the main reasons for its high quality. Working with people of this caliber is both an experience and an opportunity, and I would not have missed it for the world.

Michael Zisman
Berkeley, California
June 1, 1993

REFERENCES

Abrams, G., et al., 1987. Fast Energy and Energy Spectrum Feedback in the SLC Linac, in *IEEE Particle Accelerator Conference Proceedings*, Washington, D.C., p. 1258.

Albrecht, M., et al., 1987. *Physics Letters* **192B,** 245.

Alexandrov, A., A. Hutton, and P. Logatchev, 1990. *Synchrotron Radiation Power Calculations and Bending Radius Choice for the LER*, SLAC ABC-13.

Allen, M., and L. Karvonen, 1978. *Precautions against RF Radiation Leakage in PEP*, SLAC–PTM–177.

Altarelli, G., and F. Buccella, 1964. *Nuovo Cimento* **34**, 6385.

Bane, K. L., 1988. *The Calculated Longitudinal Impedance of the SLC Damping Ring*, SLAC–PUB–4618.

Bane, K. L. 1991. SLAC-PUB-5549.

Barletta, W. A., and A. Garren, 1990. *Radiation from Wigglers in the Low Energy Ring of an Asymmetric B-Factory*, SLAC-ABC NOTE 30 and LLNL Internal Report.

Barton, E., G. Eigen, D. Hitlin, and X. Liang, 1991. Private communication.

Bassetti, M., and G. A. Erskine, 1980. *Closed Expression for the Electric Field of a Two-Dimensional Gaussian Charge,* CERN–ISR–TH/80–06; see also lectures by E. Keil and G. H. Rees in *Theoretical Aspects of the Behaviour of Beams in Accelerators and Storage Rings*, CERN 77–13.

Bengtsson, T., 1992. Private communication.

Berz, M., 1989. *Particle Accelerators* **24**, 109.

Billing, M., 1993. Private communication.

Biscari, C., 1992. *Lectures at the Joint US-CERN School on Particle Accelerators*, Benalmádena, Spain, October 29–November 4, 1992.

Blinov, A. E., et al., 1988. Nuclear Instruments and Methods **A273**, 31.

Bowden, G., 1985. SLAC CN 314.

Bowden, G., 1991. *Fringe Field Representations of IP Magnets*, SLAC-ABC NOTE-46.

Bowden, G., 1993. "Permanent Magnet Quadrupole Field Errors," SLAC-PEP-II ME NOTE 4-93.

Bowden, G., and G. Putallaz, 1985. *A Positioning System for the Final Quadrupole Triplet*, Final Focus memo.

Browder, T., and M. Witherell, 1991. *Limits on Backgrounds for the B Factory Detectors*, BaBar Note-65 Rev.

Brown, K. L., et al., 1977. *TRANSPORT,* SLAC-91.

Bulos, F., 1992. PEP-II AP NOTE, 5-92.

Byrd, J. M., 1993. "Resistive Wall Instability at the PEP–II B Factory." SLAC–PEP II–AP–NOTE–9–93.

Byrd, J. M., 1993. "Study of Coupled Bunch Collective Effects in the PEP–II B Factory," SLAC–PEP II–AP–NOTE–10–93.

Carey, D. C., et al., 1982. *DECAY TURTLE,* SLAC-246.

Caspers, F., et al., 1988. *EPA Beam Vacuum Interaction and Ion Clearing System,* EPAC, Rome, Vol 2, 1324 (1988).

CERN 85-02, 1985.

CERN SL/91-29 (AP), 1991.

Chao, A. W., and J. Gareyte, 1976. *Scaling Law for Bunch Lengthening in SPEAR–II,* SLAC Note SPEAR–197, PEP–224.

Chin, Y. H., 1988. *Program MOSES, Mode-Coupling Single-Bunch Instability in Electron Storage Rings, Version 2.0,* CERN/LEP–TH/88–05.

Chin, Y. H., 1989. LBL-27665.

Chin, Y. H., 1990. "Symmetrization of the Beam-Beam Interaction," in *Beam Dynamics Issues of High Luminosity Asymmetric Collider Rings,* A. M. Sessler, ed., *AIP Conf. Proc.* **214**, 424.

Chin, Y. H., 1991a. "Parasitic Crossing at an Asymmetric B Factory, APIARY," in *IEEE Particle Accelerator Conference Proceedings*, San Francisco, CA, p. 213.

Chin, Y. H., 1991b. *Beam-Beam Dynamics During the Injection Process at the SLAC/LBL/LLNL B-Factory,* ABC-51/LBL-31434/ESG-158.

Chin, Y. H., 1992. "Effects of Parasitic Beam-Beam Interaction During the Injection Process at the PEP-II B Factory," LBL-32468, in *Proceedings of the International Conference on B Factories: The State of the Art in Accelerators, Detectors, and Physics*, Stanford, California, April 6–10, 1992, p.130.

Christenson, J., et al., 1964. *Physical Review Letters* **13,** 138.

Conciauro, G., and P. Arcioni, 1990. "A New HOM-free Accelerating Resonator," in *Proceedings of the 2nd European Particle Accelerator Conference*, Nice, France.

Constant, T. N., et al., 1977. *Operational Experience with SLAC's Beam Containment Electronics,* SLAC–1901.

Corlett, J. N., 1992. *Higher-Order Mode and Parasitic Losses to the B Factory RF Cavities,* SLAC-ABC NOTE 70.

Corlett, J. N., 1989. "Higher-Order Modes in the SRS 500 MHz Accelerating Cavities," in *Proceedings of the 1989 IEEE Particle Accelerator Conference*, Chicago, IL, p. 211.

Corlett, J. N., and S. F. Hill, 1989. *Measurement of the Damping of Higher-Order Modes in the Cavity by Waveguide Filters,* SRS/APN/89/96.

Coupal, D. P., and C. Hearty, 1990. "Detector Backgrounds from Scattered Beam Particles in the SLAC B Factory Design," in *Proceedings of the Workshop on Physics and Detector Issues for a High-Luminosity Asymmetric B Factory,* D. Hitlin, ed., SLAC-373.

de Jong, M. S., et al., 1993. *Mechanical Design Development of a 476 MHz Cavity for the PEP-II Asymmetric B Factory;* Mise au Point de La Conception Mecanique Diune Cavité A Champ de RF de 476 MHz de L'Accelerateur du Project PEP-II B Factory, AECL-10782.

Eckland, S., and G. Nelson, 1981. SLAC Collider Note CN-135 (unpublished).

Eden, J. R., and M. A. Furman, 1992a. "Assessment of the Beam-Beam Effect for Various Operating Scenarios in APIARY 6.3D," ABC-62/ESG Tech. Note 186.

Eden, J. R., and M. A. Furman, 1992b. "Further Assessment of the Beam-Beam Effect for PEP-II Designs APIARY 6.3–D and APIARY 7.5," PEP-II/AP Note 2-92/ESG Tech. Note 210.

Eden, J. R., and M. A. Furman, 1993a. "Simulation of the Beam-Beam Interaction for PEP-II with Unequal Beam-Beam Parameters," PEP-II/AP Note 6-92, ESG Tech Note 216.

Eden, J. R., and M. A. Furman, 1993b. "Simulation of the Beam-Beam Interaction with Tune Compensation," PEP-II/AP Note 4-92/ESG Tech Note 213.

Fischer, G. E., 1985. "Iron Dominated Magnets," SLAC–PUB–3726.

Fischer, G. E., 1989. *SLAC Site Geology, Ground Motion and Some Effects of the October 17, 1989 Earthquake*, SLAC–358.

Foerster, C. L., et al., 1990. *Journal of Vacuum and Science Technology A* **8**(3), 2856.

Foerster, C. L., et al., 1992. Desorption Measurements of Copper and Copper Alloys for PEP-II, in *Proceedings of the 12th International Vacuum Congress.*

Forest, E., 1993. Private communication.

Forest, E., J., Bengtsson, and M. Reusch, 1992. "DESPOT Uses n-step 'Symplectic Integrators for Thick Elements," private communication.

Forest, E., M. Berz, and J. Irwin, 1989. "Normal Form Methods for Complicated Periodic Systems: A Complete Solution Using Differential Algebra and Lie Operators," *Particle Accelerators* **24**, 91.

Funakoshi, F., et al., 1990. "Asymmetric B-Factory Project at KEK," in *Beam Dynamics Issues of High-Luminosity Asymmetric Collider Rings*, A. M. Sessler, ed., *AIP Conf. Proc.* **214,** 575.

Furman, M. A., 1991a. *The Hourglass Reduction Factor for Asymmetric Colliders*, ABC–21/ESG–161 (rev. 8/91); "Hourglass Effects for Asymmetric Colliders," in *IEEE Particle Accelerator Conference Proceedings,* San Francisco, CA, p. 422.

Furman, M. A., 1991b. *Luminosity Formulas for Asymmetric Colliders with Beam Symmetries,* ABC–25/ESG–0163.

Furman, M. A., 1993. *Beam-Beam Simulations with Displaced Beams for PEP-II*, PEP-II/AP Note 14-93/CBP Tech Note-011, revised.

Garren, A., et al., 1989. "An Asymmetric B-Meson Factory at PEP," in *Proceedings of the 1989 IEEE Particle Accelerator Conference,* Chicago, IL, p. 1847.

Glaser, W., 1956. "Electron and Ion Optics," in *Handbuch der Physik* XXXIII, S. Flügge, ed., p. 123.

Goddard, B., et al., 1992. *Measurement of Minimum Pretzel Separation as a Function of Energy*, SL-MD Note 67.

Gröbner, O., et al., 1983. *Vacuum* **33**, 397.

Halama, H. J., and Y. Guo, 1990. "Non-Evaporable Getter Investigation at the National Synchrotron Light Source," in *Proceedings of the Second Topical Conference on Vacuum Design of Synchrotron Light Sources*, Argonne National Laboratory.

Halbach, K., 1981a. *Nuclear Instruments and Methods* **187,** 107.

Halbach, K., 1981b. *Perturbation Effects in Segmented Rare-Earth Cobalt Multipole Magnets*, Lawrence Berkeley Laboratory report LBL-13221 (unpublished).

Hartill, D., 1990. "CESR B," invited talk at the International Workshop on Accelerators for Asymmetric B-Factories, KEK, October 4–6.

Hartwig, H., and J. S. Kouptsidis, 1974. "A New Approach for Computing Diode Sputter-Ion Pump Characteristics," *Journal of Vacuum and Science Technology* **11,** 1154. These design rules give satisfactory agreement with the measured performance of SLAC radial ion pumps.

Hearty, C., 1991. *OBJEGS Users' Manual*, BaBar Note 73.

Heifets, S., 1990. *Preliminary Estimate of the B Factory Impedance*, SLAC/AP–84.

Heifets, S., 1990a. *HOM Losses at the IR of the B Factory*, SLAC Note ABC-14/AP-81.

Heifets, S., 1990b. *Preliminary Estimate of B Factory Impedance*, SLAC Note ABC-21.

Heifets, S., 1991. *Broadband Impedance of the B Factory*, ABC-60.

Heins, D. et al., 1989. *Wideband Multibunch Feedback Systems for PETRA*, DESY 89-157.

Hendrickson, L., et al., 1991. *Generalized Fast Feedback System in the SLC*, SLAC-PUB-5693, presented at the International Conference on Accelerators and Large Experimental Physics Control Systems, Tsukuba, Japan.

Henke, H., and I. Wilson, 1981. *Thermal Analysis and Loss in Shunt Impedance of the LEP Accelerating Cell,* LEP Note 309.

Herb, S. W., 1985. "Field Quality and Stability of Permanent Magnet Quadrupoles," *IEEE Transactions on Nuclear Science* **NS-32**, p. 3578.

Herb, S. W., 1989. *IEEE Transactions on Nuclear Science* **NS34**, 1434.

Hermann, W., and W. Szyszko, 1989. *IEEE Transactions on Magnetics* **25**, 3278.

Hirata, K., 1990. "The Beam-Beam Interaction: Coherent Effects," in Beam Dynamics Issues of High-Luminosity Asymmetric Collider Rings, A. M. Sessler, ed., *AIP Conf. Proc.* **214,** 175.

Hitlin, D., 1989. SLAC–353/LBL PUB–5245/CALT–68–1588.

Hitlin, D., ed., 1991. *Proceedings of the Physics and Detector Issues for a High Luminosity Asymmetric B Factory Workshop* at SLAC, January–June 1990. SLAC-373/LBL PUB–30097/CALT–68–1697.

Hitlin, D., ed., 1992. *B Factories: The State of the Art in Accelerators, Detectors and Physics.*, SLAC-400.

Irwin, J., 1990. "The Application of Lie Algebra Techniques to Beam Transport Design," *Nuclear Instruments and Methods* **A298**, 460.

Irwin, J., 1992. "Simulation of Tail Distributions in Electron-Positron Circular Colliders," SLAC-PUB-5743.

Iselin, F. C., 1991. *The MAD Program (Methodical Accelerator Design) Version 8.4: User's Reference Manual*, CERN-SL-90-13-AP-REV.2, 120 (1991).

Jacob, A., G. R. Lambertson, and W. Barry, 1989. "Impedance Measurements on Button Electrodes," presented at the *IEEE Particle Accelerator Conference*, Chicago, IL, May 20–23, 1989.

Jacob, A. F., G. R. Lambertson, and W. Barry, 1990. "Higher-Order Mode Damping in an ALS Cavity," in *Proceedings of the 2nd European Particle Accelerator Conference*, Nice, France, p. 928.

Jackson, G., 1990. "Dispersive Crab Crossing: An Alternative Crossing Angle Scheme," *AIP Conf. Proc.* **214**, 327.

Jenkins, T. M., W. R. Nelson, and N. Ipe, 1990. *Synchrotron Radiation Leakage from the B-Factory Beam Pipe*, SLAC ABC Note 17.

Jurow, J., 1976. *Hot Water Bakeout Station*, PEP–Note 76-7.

Kadyk, J., 1991. *Nuclear Instruments and Methods* **A300**, 436.

Keizer, R. L., 1974. *Dipole Septum Magnet*, CERN 74-13 Laboratory I Proton Synchrotron Machine Division.

Kim, K.-J., 1986. "Angular Distribution of Undulator Power," *Nuclear Instruments and Methods* **A246**.

Ko, K., 1990. Private communication.

Krishnagopal, S., and R. H. Siemann, 1990. "A Comparison of Flat Beams with Round," in *Beam Dynamics Issues of High-Luminosity Asymmetric Collider Rings*, A. M. Sessler, ed., *AIP Conf. Proc.* **214**, 278.

Krishnagopal, S., and R. Siemann, 1990a. *Physical Review* **D41**, 2312.

Krishnagopal S., and R. Siemann, 1990b. *Physical Review* **D41**, 1741.

Krishnagopal S., and R. Siemann, 1991. *Field Calculation Algorithm for General Beam Distributions*, LBL–31094; SLAC/AP–90.

Kroll, N., and D. Yu, 1990. *Computer Determination of the External Q and Resonant Frequency of Waveguide Loaded Cavities,* SLAC–PUB–5171.

Kurennoy, S. S., 1991. *On the Coupling Impedance of a Hole or Slot*, LBL PUB-5263, SLAC-359, CALT-68-1622, March 1990.

Laslett, L. J., S. Caspi, and H. Helm, 1987. *Particle Accelerators* **22**, 1.

Laurent, J. M., 1992. Private communication.

LBL, 1986. *1-2 GeV Synchrotron Radiation Source: Conceptual Design Report,* 1986. LBL PUB–5172 Rev.

LBL, 1989. *Feasibility Study for an Asymmetric B Factory Based on PEP,* 1989. LBL PUB–5244/SLAC–352/CALT–68–1589.

LBL, 1990. *Investigation of an Asymmetric B Factory in the PEP Tunnel.* LBL PUB-5263/SLAC-359/CALT-68-1622.

Lightbody, J. W., Jr., and J. S. O'Connel, 1988. "Modeling Single-Arm Electron Scattering and Nucleon Production from Nuclei by GeV Electrons," *Computers in Physics,* May/June, p. 57.

Lisin, A., 1993. *Synchrotron Radiation Absorbers Near the IP*, PEP–II ME 3–93.

Luna, H. B., et al., 1989. *Nuclear Instruments and Methods* **A285**, 349.

Mathewson, A. G., et al., 1990. "Comparison of Synchrotron Radiation Induced Gas Desorption from Al, Stainless Steel and Cu Chambers," submitted to the Second Topical Conference on Vacuum Design of Synchrotron Light Sources, Argonne National Laboratory, November 1990.

Nelson, W. R., 1993. Unpublished results.

Nelson, W. R., G. J. Warren, and R. C. Ford, 1975. *Radiation Dose to Coil Windings and Production of Nitric Acid and Ozone from PEP Synchrotron Radiation*, PEP Note PEP–109.

Nelson, W. R., H. Hirayama, and D. W. O. Rogers, 1985. *The EGS4 Code System,* SLAC–265.

Nir, Y., et al., 1990a. *Nuclear Physics* **B345,** 301.

Nir, Y., et al., 1990b. *Nuclear Physics* **D42,** 1473.

Nir, Y., et al., 1990c. *Physics Review* **D42,** 1477.

Oddone, P. J., 1987. In Proceedings of the UCLA Workshop: Linear Collider $B\bar{B}$ Factory Conceptual Design, p. 243.

Padamsee, H., et al., 1990. "Superconducting Cavities for a B Factory—Interim Progress Report," in *Beam Dynamics Issues of High-Luminosity Asymmetric Collider Rings*, A. M. Sessler, ed., *AIP Conf. Proc.* **214**, 508.

PEP Design Handbook, 1977. Stanford Linear Accelerator Center and Lawrence Berkeley Laboratory, H. Wiedemann, ed.

Phinney, N., 1985. *Report on the SLC Control System,* SLAC-3668.

Phinney, N., and H. Shoaee, 1987. *The SLC Controls System—Status and Development,* SLAC-4215.

Porter, F., 1990. CALT–68–1611; to be published in *Nuclear Instruments and Methods A.*

Rice, D., 1989. Presentation at Third Advanced ICFA Beam Dynamics Workshop on Beam-Beam Effects in Circular Accelerators, Akademgorodok, Novosibirsk, USSR.

Rice, D., 1990. "Beam–Beam Interaction: Experimental," in *Beam Dynamics Issues of High Luminosity Asymmetric Collider Rings*, A. M. Sessler, ed., *AIP Conf. Proc.* **214**, 219.

Rivkin, L., 1987. "Collective Effects in PEP," in *Proceedings of the Workshop on PEP as a Synchrotron Radiation Source*, October 20–21, 1987, p. 139.

Rivkin, L., 1990. "B-Meson Factory in the CERN–ISR Tunnel," in *Beam Dynamics Issues of High-Luminosity Asymmetric Collider Rings*, A. M. Sessler, ed., *AIP Conf. Proc.* **214,** 536.

Rogers, D. W. O., 1984. *Health Physics* **46**, 891.

Roman, R. R., 1965. "Fabrication Techniques of Several Coils in the Zero Gradient Synchrotron Complex," in *Proceedings of the International Symposium on Magnet Technology*, Stanford, CA., p. 356.

Ronan, M. T., et al., 1989. "Timing and RF Synchronization for Filling PEP/SPEAR with the SLC Damping Rings," in *IEEE Particle Accelerator Proceedings*, Chicago, IL, p. 1577.

Rouse, F. R., et al., 1991. "A Generalized, Database Driven Fast Feedback System for the Stanford Linear Collider," in *IEEE Particle Accelerator Proceedings*, San Francisco, CA, p. 1419.

Rouse, F. R., et al., 1992. *A Database Driven Fast Feedback System for the Stanford Linear Collider*; submitted to Nuclear Instruments and Methods.

Sagan, D., R. Siemann, and S. Krishnagopal, 1990. Cornell Report CLNS 90/1001.

Sagan, D., and J. J. Welch, 1992. "The Effect of the Leakage Electrostatic Fields from the DIP on the Electron and Positron Beams," CBN 92–01.

Sands, M., 1970. *Physics of Electron Storage Rings—An Introduction*, SLAC–121.

Sands, M., 1977. *Energy Loss from Small Holes in the Vacuum Chamber*, PEP–253.

Savage, W. P., 1990. *Potential Earthquake Effect on B-Factory at PEP*, SLAC report.

Seeman, J. T., 1985. "Nonlinear Dynamics Aspects of Particle Accelerators," in *Proceedings of the Joint US–CERN School on Particle Accelerators*, Sardinia, Italy, J. M. Jowett, M. Month, and S. Turner, eds., *Springer-Verlag Lecture Notes in Physics* **247**, p. 121.

Siemann, R., 1993. unpublished results.

SLAC, 1991. *An Asymmetric B Factory Based on PEP: Conceptual Design Report,* 1991. LBL PUB–5303/SLAC-372/CALT–68-1715/UCRL–ID–106426/UC-IIRPA-91–01, (1991).

SLAC Earthquake Emergency Plan, 1987.

SLAC Emergency Preparedness Plan, 1991.

SLAC Emergency Preparedness Plan, SLAC-I-720-70000-105.

SLAC Environment and Safety Office, 1987. *SLAC Safety Program.*

SLAC Environment, Safety, and Health Manual, I-720-70100-100.

SLAC Hazard Communication Program, 1992, SLAC-I-720-0A06Z-001.

SLAC Institutional Quality Assurance Program Plan, SLAC-I-770-0A17M-001.

SLAC QACD Subcontractor Oversight Program, SLAC 1-770-0A17A-001-R001.

SLAC Radiological Control Manual, 1993. SLAC-I-720-0A05Z-001.

SLAC Radiological Control Manual, 1993. Article 131.

Smith, H., and T. Constant, 1981. *Radiation and Electrical Safety Systems for PEP,* SLAC-2675.

Spencer, J. E., 1985. SLAC-PUB 3647.

Tavares, P. F., 1992. *Transverse Distribution of Ions Trapped in an Electron Beam*, CERN-PS/92–55 (LP).

Taylor, B., 1990. Private communication.

Tennyson, J. L., 1989. "TRS," undocumented code, unpublished.

Tennyson, J. L., 1990. "The Beam-Beam Limit in Asymmetric Colliders: Optimization of the B-Factory Parameter Base," in *Beam Dynamics Issues of High Luminosity Asymmetric Collider Rings*, A. M. Sessler, ed., *AIP Conf. Proc.* **214**, 130.

Tennyson, J. L., 1991a. *Long-Range Forces in APIARY–6*, ABC Note 28.

Tennyson, J. L., 1991b. *Choosing the APIARY-6 Tunes: Luminosity Considerations*, ABC Note 29.

Ueda, S., et al., 1990. "Photodesorption from Stainless-Steel, Aluminum Alloy, and Oxygen-Free Copper Test Chambers," submitted to Proceedings of Second Topical Conference on Vacuum Design of Synchrotron Light Sources, Argonne National Laboratory.

Van Bibber, K., 1989. *Nuclear Instruments and Methods* **B40/41,** 436.

Villevald, D., 1993. *Ion Trapping in the SLAC B Factory High Energy Ring.* SLAC PEP-II AP Note 18-93.

Voelker, F., et al., 1990. "Techniques for Beam Impedance Measurements Above Cutoff," in the *Proceedings of the European Particle Accelerator Conference,* Nice, France, June 12–16, LBL-28190.

Voelker, F., G. Lambertson, and R. Rimmer, 1991. "Higher Order Mode Damping in a Pill Box Cavity," *US Particle Accelerator Physics Conference Proceedings*, San Francisco, CA, May 6–9, p. 687.

Walker, N., 1993. Private communication.

Warnock, R., and R. Ruth, 1992. "Long-term Bounds on Nonlinear Hamiltonian Motion," *Physica D* **56**, 188. See also J. Berg, R. Warnock, R. Ruth, and E. Forest, *Construction of Sympletic Maps for Nonlinear Motion of Particles in Accelerators*, SLAC–PUB–6037 and LBL–34035, 1993.

Weaver, J. N., 1981. *Measuring, Calculating and Estimating PEP's Parasitic Mode Loss Parameters*, PEP-Note-342.

Weidner, H., 1990. *Seepage into PEP Tunnel,* SLAC-ABC-10.

Winch, T.R., 1977. *Bakeout Tests for 14 m Chamber*, PEP–Note 77–3.

Zholents, A. A., 1990. "Novosibirsk B Factory," in *Beam Dynamics Issues of High-Luminosity Asymmetric Collider Rings*, A. M. Sessler, ed., *AIP Conf. Proc.* **214,** 592.

Zisman, M. S., 1990a. In *Beam Dynamics Issues of High-Luminosity Asymmetric Collider Rings*, A. M. Sessler, ed., *AIP Conf. Proc.* **214**, 81.

Zisman, M. S., 1990b. *Influence of Collective Effects on the Performance of High Luminosity Colliders*, ABC Note 8.

Zisman, M. S., et al., 1988. *Study of Collective Effects for the PEP Low-Emittance Optics*, LBL-25582, SSRL ACD Note-59.

Zisman, M. S., S. Chattopadhyay, and J. Bisognano, 1986. *ZAP User's Manual*, LBL-21270.

APPENDIX A: PARAMETERS

THIS appendix contains a summary of the PEP-II accelerator parameters. It is intended to give a self-consistent snapshot of the machine design. As such, values are often given to more precision than would ultimately be relevant (or even measurable) in an operating accelerator. We start with a few specific comments on the tables to follow:

General Machine Parameters. As is conventional, we quote the luminosity at zero bunch length, constrained by design to be 3.00×10^{33} cm^{-2} s^{-1}. If we take into account the geometric effect of a nonzero bunch length, the luminosity is reduced by about 7% to 2.80×10^{33} cm^{-2} s^{-1}.

The $1/e$ luminosity decay time is estimated under the conservative assumption that the spot sizes remain constant, i.e., that the luminosity goes like the product of the two beam currents. It includes beam loss estimates from $e^+e^- \rightarrow e^+e^-$, $e^+e^- \rightarrow e^+e^-\gamma$, beam-gas bremsstrahlung, beam-gas Coulomb scattering, and Touschek intrabeam scattering. These estimates are made for a ten-standard-deviation limiting transverse aperture (for an uncoupled beam horizontally and a fully coupled beam vertically).

Lattice Cell Parameters. There are four "standard straights" in the HER and two in the LER. These include the two phase-control straights in each ring. In addition, there is an "injection straight" and an "IR straight" in each ring, and two "wiggler straights" in the LER.

TABLES

TABLE A–1

General Machine Parameters

Parameter	Symbol	HER	LER	Units
Center-of-mass energy	$E_{\text{c.m.}}$	10.580		GeV
Beam energy	E	9.000	3.109	GeV
Peak luminosity	$\mathcal{L}$	3.00×10^{33}		$\text{cm}^{-2}\text{s}^{-1}$
$1/e$ luminosity decay time	$\tau_{\mathcal{L}}$	1.55		hr
Number of populated bunches	k_B	1658	1658	
Number of empty bunches	k_B(gap)	88	88	
Bunch spacing	s_B	1.2596		m
Machine circumference	L	2199.318	2199.318	m
Horizontal tune	ν_x	24.570	36.570	
Vertical tune	ν_y	23.640	34.640	
Momentum compaction	α_p	.00241	.00131	
Natural energy spread	σ_E	5.51	2.51	MeV
Natural fractional energy spread	δ_E	6.1×10^{-4}	8.1×10^{-4}	
Natural bunch length	σ_ℓ	1.00	1.00	cm
Circulating current	I	0.986	2.140	A
Number of particles/bunch	N_b	2.723×10^{10}	5.911×10^{10}	
Horizontal damping time	τ_x	36.8	40.4	ms
Horizontal emittance	ϵ_x	48.24	64.32	nm·rad
Vertical emittance	ϵ_y	1.93	2.57	nm·rad
Natural chromaticity, horizontal	ξ_x	−42.640	−63.840	
Natural chromaticity, vertical	ξ_y	−45.690	−77.750	
Horizontal damping partition number	J_x	1.0031	0.9883	
Vertical damping partition number	J_y	1.0000	1.0001	
Longitudinal damping partition number	J_E	1.9969	2.0116	
Energy variation of J_x	$dJ_x/d\ln E$	−297.4	−147.6	
Energy Variation of J_y	$dJ_y/d\ln E$	0	−129.4	
Energy Variation of J_E	$dJ_E/d\ln E$	297.4	277.0	

TABLE A–2

Interaction Region Parameters

Parameter	Symbol	HER	LER	Units
Horizontal beta function at IP	β_x^*	50.00	37.50	cm
Vertical beta function at IP	β_y^*	2.00	1.50	cm
Horizontal dispersion at IP	D_x^*	0.000	0.000	m
Vertical dispersion at IP	D_y^*	0.000	0.000	m
Horizontal spot size at IP	σ_x^*	155	155	μm
Vertical spot size at IP	σ_y^*	6.2	6.2	μm
Beam cross half-angle	θ_x	0.0		mrad
Beam-beam linear tune shift	$\Delta\nu_x$	0.030	0.030	
Beam-beam linear tune shift	$\Delta\nu_y$	0.030	0.030	
$e^+e^- \rightarrow e^+e^-\gamma$ beam lifetime	τ_{Br}	14.8	34.4	hr
$e^+e^- \rightarrow e^+e^-\gamma$ luminosity lifetime	τ_{Br}	12.6		hr
Beam pipe inner radius at IP	r^*	2.50		cm
IP to first magnet distance	d_f	0.200		m
Detector solenoid field	B_{sol}	1.00		T
Detector solenoid length	L_{sol}	4.00		m

TABLE A–3

RF System Parameters

Parameter	Symbol	HER	LER	Units
Circulating current	I	0.986	2.140	A
Natural bunch length	σ_ℓ	1.00	1.00	cm
RF frequency	$f_{\rm RF}$	476.0	476.0	MHz
Harmonic number	h	3492	3492	
Synchrotron tune	ν_s	0.0516	0.0371	
Synchrotron frequency	f_s	7.0	5.1	kHz
Number of klystrons	$N_{\rm klys}$	10	5	
Power/klystron	$P_{\rm klys}$	1.10	1.10	MW
Number of cavities	$N_{\rm Cavity}$	20	10	
Shunt impedance	R_s	3.5	3.5	MΩ
Gap voltage	V_g	0.91	0.60	MV
Accelerating gradient	$\mathcal{E}$	4.09	2.70	MV/m
Wall loss/cavity	$P_{\rm Wall}$	0.122	0.050	MW
Coupling factor, no beam	β	7.5	7.5	
Unloaded Q	Q	30000	30000	
Energy loss per turn	U_0	3.57	1.14	MeV
Synchrotron radiation power	$P_{\rm SR}$	3.52	2.44	MW
HOM power (est.)	$P_{\rm HOM}$	0.15	0.45	MW
Cavity wall loss total	$P_{\rm Wall}$	2.44	0.50	MW
Total RF power	$P_{\rm RF}$	6.11	3.39	MW
Klystron power total	$P_{\rm tot\,Klys.}$	11.00	5.50	MW
RF voltage	$V_{\rm RF}$	18.29	6.03	MV
Synchronous phase angle	ϕ_s	168.2	167.0	deg
Fractional energy RF aperture	f_E(RF)	0.0105	0.0139	
Fractional energy aperture ($10\sigma_E$)	f_E	0.0061	0.0081	

TABLE A–4

Instrumentation and Feedback

Parameter	Symbol	HER	LER	Units
Number of BPMs	N_{BPM}	144	144	
Resolution (short-term repeatability)	σ_{BPM}	20	20	μm
Absolute accuracy		100	100	μm
Bunch intensity resolution		1	1	%
Bunch spacing	t_B	4.202		ns
Bunch frequency	f_B	238.0		MHz
RF frequency	f_{RF}	476.0	476.0	MHz
Luminosity	Bhabha scattering monitor			
Longitudinal feedback system				
Beam pickup central frequency		2856	2856	MHz
Down-sampling factor		4	4	
Linear phase range correction		$\pm$15.0	$\pm$15.0	deg
Phase detector resolution		0.50	0.50	deg
Bunch-to-bunch signal isolation		-30	-30	dB
Kicker structure operating frequency	f_{kick}	1012	1012	MHz
Number of kicker units	N_{kick}	3	3	
Kicker length	L_{kick}	0.32	0.32	m
Kicker bandpass		241	241	MHz
Driver bandwidth		357	357	MHz
Kicker shunt impedance	Z_{kick}	1600	1600	Ω
Installed power/unit		500	500	W
Power for 1 kV/unit		313	313	W
Maximum voltage/turn		3	3	kV

TABLE A–4 (continued)

Instrumentation and Feedback

Parameter	Symbol	HER	LER	Units
Transverse feedback system				
Detection central frequency		1428	1428	MHz
Detection bandwidth		250	250	MHz
Kicker length	L_{kick}	0.63	0.63	m
Impedance at 10 kHz (vertical)		57.9	57.9	kΩ
Impedance at 10 kHz (horizontal)		38.3	38.3	kΩ
Impedance at 119 kHz (vertical)		23.5	23.5	kΩ
Impedance at 119 kHz (horizontal)		15.5	15.5	kΩ
Voltage kick/turn (vertical)		2.34	5.01	kV
Voltage kick/turn (horizontal)		1.55	3.32	kV
Power required (vertical)		47.3	217	W
Power required (horizontal)		31.4	144	W
Beta function at kicker	$\beta_{\perp}$	20	20	m

TABLE A–5

Vacuum Parameters

Parameter	Symbol	HER	LER	Units
Vacuum (3A design goal, N_2 equivalent):				
Arcs		≤ 10		nTorr
Straights		3		nTorr
IR straight		1		nTorr
Wigglers			10	nTorr
Value assumed for lifetime		5	6	nTorr
Horizontal chamber aperture	a_x	± 4.5	± 4.5	cm
Vertical chamber aperture	a_y	± 2.5	± 2.5	cm
Dipole critical energy	ϵ_{crit}	9.8	4.8	keV
Beam-gas brems. cross section	$\sigma_{eZ\gamma}$	7.42×10^{-32}	6.96×10^{-32}	cm^2
Beam-gas brems. lifetime	τ_{BGbrem}	7.8	6.9	hr
Average horizontal beta	$\langle\beta_x\rangle$	24.8	18.5	m
Average vertical beta	$\langle\beta_y\rangle$	20.2	17.5	m
Horiz. angular aperture	$\theta_{\text{min}\,x}$	0.4498	0.6015	mrad
Vert. angular aperture	$\theta_{\text{min}\,y}$	0.3526	0.4374	mrad
Beam-gas Coul. cross section	σ_{eZ}	2.05×10^{-32}	1.06×10^{-31}	cm^2
Beam-gas Coulomb lifetime	τ_{BGcoul}	28.2	4.6	hr
Nominal desorption for Cu	η_{Cu}	2×10^{-6}		$\frac{\text{molecules}}{\text{photon}}$
Pumping speed in arc cell		2000 130	780 50	L/s L/s/m
Pumping speed in straight section cell		540 35	440 29	L/s L/s/m

TABLE A–6

Lattice Cell Summary

Parameter	Symbol	HER	LER	Units
Standard arc cells				
Cell Layout		QF-B-QD-B		
Cell length	L_{cell}	15.200	15.191	m
Phase advance	ϕ_c	60.0	90.0	deg
Dipole magnetic length	L_B	5.400	0.450	m
Dipole field at E_{des}	B_B	0.1819	0.7540	T
Bend radius	ρ	165.012	13.751	m
Dispersion suppressor cells				
Cell Layout		QF-B-QD-B		
Cell length	L_{cell}	15.200	15.191	m
Phase advance	ϕ_c	~ 90	~ 90	deg
Dipole magnetic length	L_B	5.400	0.450	m
Dipole field at E_{des}	B_B	0.1819	0.7540	T
Bend radius	ρ	165.012	13.751	m
Standard straight cells				
Cell Layout		QF-O-QD-O		
Cell length	L_{cell}	15.419	16.030, 14.608	m
Phase advance	ϕ_c	~ 60	~ 90	deg

TABLE A-7

Conventional Dipole Physical Parameters

Designation	Number	$L_{magnetic}$ (in., m)	Pole width (in., cm)	Gap height (in., cm)
2C24	2	23.62, 0.600	8, 20.3	2, 5.08
2.8C212	192	212.60, 5.400	8.425, 21.4	2.787, 7.08
2H24	6	23.62, 0.600	8, 20.3	1.0, 2.54
2H60	7	59.06, 1.500	8, 20.3	1.0, 2.54
2H80	1	78.74, 2.000	8, 20.3	1.0, 2.54
2.8H12	2	11.81, 0.300	8, 20.3	2.8, 7.11
2.8H17	4	17.72, 0.450	7.5, 19.1	2.787, 7.08
2.8H18	192	17.72, 0.450	8, 20.3	2.87, 7.29
2.8H24	4	23.62, 0.600	8, 20.3	2.8, 7.11
2.8H29	4	29.53, 0.750	8, 20.3	2.8, 7.11
2.8H49	2	49.21, 1.250	8, 20.3	2.8, 7.11
2.8H59	2	59.06, 1.500	8, 20.3	2.8, 7.11
2.8H80	4	78.74, 2.000	8, 20.3	2.8, 7.11
2.8H98	2	98.43, 2.500	8, 20.3	2.8, 7.11
5.8H80	8	78.56, 1.995	5.9, 15.0	5.875, 14.92
5.8H85	8	84.96, 2.158	5.9, 15.0	5.875, 14.92
BMH (HER bump)	4	39.37, 1.000		
BML (LER bump)	4	19.69, 0.500		

TABLE A-8

Conventional Dipole Operating Parameters at E_{design}

Transport	Designation	Number	B (T)	$\int B d\ell$ (T-m)	Bend angle (deg)
HER ($E_{\text{design}} = 9$ GeV)					
B	2.8C212	192	0.1819	0.9824	1.875
Injection bump					
BM1L	BMH	1	0.031	0.0312	0.060
BM2L	BMH	1	0.018	0.0183	0.035
BM1R	BMH	1	0.034	0.0336	0.064
BM2R	BMH	1	0.006	0.0060	0.011
IR bends					
B2	5.8H80	8	0.0216	0.0431	0.082
B3	5.8H85	8	0.0216	0.0466	0.089
B4	2.8H17	4	0.0904	0.0407	0.078
LER ($E_{\text{design}} = 3.109$ GeV)					
B	2.8H15	192	0.754	0.339	1.875
Wiggler chicane					
BD+,BD-	2.8H80	4	0.226	0.452	2.50
Injection bump					
BM1L	BML	1	0.024	0.0122	0.068
BM2L	BML	1	0.017	0.0085	0.047
BM1R	BML	1	0.023	0.0114	0.063
BM2R	BML	1	0.004	0.0019	0.010
IR vertical bends					
B4	2.8H23	2	0.400	0.240	1.329
B7	2.8H23	2	0.451	0.271	1.5
B8	2.8H12	2	0.100	0.030	0.166
B9	2.8H60	2	1.209	1.814	10.048
IR horizontal bends					
B3	2.8H30	4	0.481	0.361	2.0
B5	2.8H100	2	0.500	1.250	6.925
B6	2.8H50	2	0.718	0.898	4.973

TABLE A–8 (continued)

Conventional Dipole Operating Parameters at E_{design}

Transport	Designation	Number	B (T)	$\int B d\ell$ (T-m)	Bend angle (deg)
Positron extraction					
Bs	2H24	1	0.752	0.451	2.5
Bch	2C24	2	0.752	0.451	2.5
BRec	2H24	1	0.752	0.451	2.5
B1	2H24	2	0.752	0.451	2.5
B2	2H24	2	0.338	0.203	1.122
BH1	2H60	2	0.019	0.029	0.162
BVup	2H80	1	0.074	0.149	0.842
B02	2H60	2	0.449	0.674	3.731
B01	2H60	2	0.078	0.117	0.646
BH1	2H60	1	0.019	0.029	0.162

TABLE A–9

Conventional Quadrupole Physical Parameters

Designation	Number	L_{magnetic} (in., cm)	Inscribed diameter (in., cm)
Injector			
1Q4	94	4.17, 10.6	1.015, 2.58
1Q6	14	6.61, 16.8	1.015, 2.58
1Q10	1	9.84, 25.0	1.015, 2.58
1Q20	12	20.35, 51.69	1.015, 2.58
2Q9	9	9.84, 25.0	2.030, 5.16
2Q10	23	9.84, 25.0	2.030, 5.16
Rings			
4Q17	282	16.93, 43.0	3.936, 10.0
4Q18	70	17.72, 45.0	3.936, 10.0
4Q22	94	21.65, 55.0	3.936, 10.0
4Q29	82	28.74, 73.0	3.936, 10.0
4Q40	36	39.37, 100.0	3.936, 10.0

TABLE A–10

HER Conventional Quadrupole Operating Parameters at 9 GeV

Lattice	Designation	Number	Gradient (T/m)	B_{poletip} (T)	$\int G d\ell$ (T)	$k = G/B\rho$ (m^{-2})
QD	4Q22	54	7.33	0.366	4.03	0.244
QF	4Q29	60	5.48	0.274	4.00	0.183
Dispersion suppressor						
QFS11	4Q22	1	9.48	0.474	5.22	0.316
QFS12	4Q22	1	9.48	0.474	5.22	0.316
QFS1L	4Q22	1	9.76	0.488	5.37	0.325
QFS1R	4Q22	1	9.80	0.490	5.39	0.326
QFS21	4Q18	1	11.77	0.588	5.30	0.392
QFS22	4Q18	1	11.75	0.588	5.29	0.391
QFS2L	4Q18	1	11.68	0.584	5.26	0.389
QFS2R	4Q18	1	11.74	0.587	5.28	0.391
QFS31	4Q29	1	5.61	0.280	4.10	0.187
QFS32	4Q29	1	5.62	0.281	4.10	0.187
QFS3L	4Q29	1	5.61	0.281	4.10	0.187
QFS3R	4Q29	1	5.62	0.281	4.10	0.187
QDSOL	4Q18	1	8.61	0.430	3.87	0.287
QDSOR	4Q18	1	8.61	0.430	3.87	0.287
QDSO1	4Q29	1	5.33	0.266	3.89	0.178
QDSO2	4Q29	1	5.35	0.267	5.35	0.178
QDS11	4Q18	1	8.61	0.430	3.87	0.287
QDS12	4Q18	1	9.79	0.489	4.41	0.326
QDS1L	4Q22	1	7.98	0.399	4.39	0.266
QDS1R	4Q22	1	8.01	0.400	4.41	0.267
QDS21	4Q22	1	7.19	0.359	3.95	0.239
QDS22	4Q22	1	7.17	0.358	3.94	0.239
QDS2L	4Q18	1	8.68	0.434	3.90	0.289
QDS2R	4Q18	1	8.76	0.438	3.94	0.292

TABLE A–10 (continued)

HER Conventional Quadrupole Operating Parameters at 9 GeV

Transport	Designation	Number	Gradient (T/m)	B_{poletip} (T)	$\int G d\ell$ (T)	$k = G/B\rho$ (m^{-2})
Dispersion suppressor (continued)						
QDS31	4Q22	1	7.33	0.366	4.03	0.244
QDS32	4Q22	1	7.33	0.366	4.03	0.244
QDS3L	4Q22	1	7.33	0.366	4.03	0.244
QDS3R	4Q22	1	7.33	0.366	4.03	0.244
QFS11E	4Q22	4	8.06	0.403	4.43	0.268
QFS12E	4Q22	4	8.08	0.404	4.44	0.269
QFS21E	4Q18	4	10.55	0.527	4.75	0.351
QFS22E	4Q18	4	10.53	0.526	4.74	0.351
QFS31E	4Q29	4	6.16	0.308	4.49	0.205
QFS32E	4Q29	4	6.16	0.308	4.50	0.205
QDSO1E	4Q29	4	5.62	0.281	4.10	0.187
QDSO2E	4Q29	4	5.66	0.283	4.13	0.189
QDS11E	4Q18	4	9.37	0.468	4.22	0.312
QDS12E	4Q18	4	9.41	0.470	4.24	0.313
QDS21E	4Q22	4	7.72	0.386	4.25	0.257
QDS22E	4Q22	4	7.71	0.385	4.24	0.257
QDS31E	4Q22	4	7.33	0.366	4.03	0.244
QDS32E	4Q22	4	7.33	0.366	4.03	0.244

TABLE A–10 (continued)

HER Conventional Quadrupole Operating Parameters at 9 GeV

Transport	Designation	Number	Gradient (T/m)	$B_{poletip}$ (T)	$\int G d\ell$ (T)	$k = G/B\rho$ (m^{-2})
Straight section						
QFO	4Q18	16	8.83	0.441	3.97	0.294
QDO	4Q18	14	8.83	0.441	3.97	0.294
Phase trombone						
QDP1	4Q40	2	4.06	0.203	4.06	0.135
QFP2	4Q40	4	4.29	0.214	4.29	0.143
QDP3R6	4Q40	2	4.02	0.201	4.02	0.134
QDP3R8	4Q18	2	8.94	0.447	4.02	0.298
QFP4	4Q18	4	9.46	0.473	4.26	0.315
QDP5R6	4Q40	2	4.00	0.200	4.00	0.133
QDP5R8	4Q18	2	8.89	0.444	4.00	0.296
QFP6	4Q22	4	7.61	0.380	4.19	0.253
QDP7R6	4Q40	2	3.99	0.199	3.99	0.133
QDP7R8	4Q18	2	8.88	0.444	3.99	0.296
QFP8	4Q18	4	9.22	0.461	4.15	0.307
Injection						
QFOI	4Q40	2	4.08	0.204	4.08	0.136
QDOI	4Q40	2	2.98	0.149	2.98	0.099
QFI	4Q40	2	1.92	0.096	1.92	0.064
QDI	4Q40	2	1.95	0.097	1.95	0.065
IR						
QD6	4Q40	2	7.89	0.394	7.89	0.263
QF7	4Q40	2	5.96	0.298	5.96	0.199

TABLE A-11

LER Conventional Quadrupole Operating Parameters at 3.1 GeV

Transport	Designation	Number	Gradient (T/m)	$B_{poletip}$ (T)	$\int G d\ell$ (T)	$k = G/B\rho$ (m^{-2})
QD	4Q17	80	4.50	0.226	1.93	0.434
QF	4Q17	74	4.55	0.227	1.96	0.439
Dispersion suppressor, IR						
QF1	4Q17	2	7.07	0.354	3.04	0.682
QD2	4Q17	2	6.33	0.316	2.72	0.610
QF3	4Q17	2	5.18	0.259	2.23	0.499
QD4	4Q17	2	3.46	0.173	1.49	0.334
QF5	4Q17	2	4.55	0.227	1.98	0.439
Dispersion suppressor, tune regions 3,5,9,11						
QF1,QF1A	4Q17	4	4.16	0.208	1.79	0.401
QD1,QD1A	4Q17	4	5.58	0.279	2.40	0.538
QF2,QF2A	4Q17	4	4.38	0.219	1.88	0.422
QD2,QD2A	4Q17	4	4.95	0.247	2.13	0.477
QF3,QF3A	4Q17	4	4.84	0.242	2.08	0.467
QD3,QD3A	4Q17	4	4.12	0.206	1.77	0.397
QF4,QF4A	4Q17	4	4.77	0.239	2.05	0.460
QD4,QD4A	4Q17	4	4.55	0.227	1.96	0.439
RF/Tune straights						
QDT4,QDT4A	4Q17	2	1.88	0.094	0.81	0.181
QFT4,QFT4A	4Q17	4	3.29	0.165	1.42	0.317
QDT3,QDT3A	4Q17	4	3.57	0.179	1.53	0.344
QFT3,QFT3A	4Q17	4	4.14	0.207	1.78	0.399
QDT2,QDT2A	4Q17	4	3.48	0.174	1.50	0.336
QFT2,QFT2A	4Q17	4	4.83	0.242	2.08	0.466
QDT1,QDT1A	4Q17	4	4.04	0.202	1.74	0.390
QFT1,QFT1A	4Q17	4	4.90	0.245	2.11	0.472

TABLE A–11 (continued)

LER Conventional Quadrupole Operating Parameters at 3.1 GeV

Transport	Designation	Number	Gradient (T/m)	B_{poletip} (T)	$\int G d\ell$ (T)	$k = G/B\rho$ (m^{-2})
Injection straight						
QDI	4Q17	2	0.66	0.033	0.28	0.064
QFI	4Q17	2	1.47	0.074	0.63	0.142
QDOI	4Q17	2	2.34	0.117	1.01	0.226
QFOI	4Q17	2	4.17	0.208	1.79	0.402
Wiggler straight section						
QFW1,QFW1A	4Q17	4	2.52	0.126	1.08	0.243
QDW2,QDW2A	4Q17	4	1.64	0.082	0.70	0.158
QFW3,QFW3A	4Q17	4	3.92	0.196	1.69	0.378
QFW4,QFW4A	4Q17	4	0.28	0.014	0.12	0.027
QDW5,QDW5A	4Q17	4	2.02	0.101	0.87	0.195
QFW6,QFW6A	4Q17	4	3.58	0.179	1.54	0.345
IR straight						
IQF1	4Q17	2	7.12	0.356	3.06	0.687
IQD2	4Q40	2	5.04	0.252	5.04	0.486
IQF3	4Q40	2	4.53	0.226	4.529	0.437
IQD4	4Q40	2	5.05	0.253	5.05	0.487
IQF5	4Q17	2	10.35	0.517	4.45	0.998
IQF6	4Q40	2	5.20	0.260	5.20	0.501
IQD7	4Q40	2	5.98	0.299	5.98	0.577
IQF8	4Q40	2	9.80	0.490	9.80	0.945
IQD10	4Q17	4	7.12	0.366	3.06	0.687
IQF11	4Q17	4	11.76	0.587	5.05	1.134
IQD12	4Q17	2	10.46	0.523	4.50	1.009
IQD13	4Q17	2	7.04	0.352	3.03	0.679
IQF14	4Q40	2	8.25	0.413	8.25	0.795
IQD15	4Q17	2	5.87	0.293	2.52	0.566
IQF16	4Q17	2	19.21	0.960	8.26	1.852
IQD17	4Q17	2	10.54	0.527	4.53	1.016
IQF18	4Q17	2	8.89	0.444	3.82	0.857

TABLE A–12

Injector Conventional Quadrupole Operating Parameters at E_{design}

Transport	Designation	Number	Gradient (T/m)	B_{poletip} (T)	$\int G d\ell$ (T)	$k = G/B\rho$ (m^{-2})
e^- (9 GeV)						
QD ext	2Q9	1	13.193	0.340	3.30	0.439
QF1 ext	2Q9	1	13.988	0.361	3.50	0.466
QD2 ext	2Q9	1	13.252	0.342	3.31	0.441
QF3 ext	2Q9	1	13.156	0.339	3.29	0.438
QD4 ext	2Q9	1	13.304	0.343	3.33	0.443
QF1 ext	2Q9	1	12.396	0.320	3.10	0.413
QD2 ext	2Q9	1	13.132	0.339	3.28	0.437
QF3 ext	2Q9	1	13.228	0.341	3.31	0.441
QD4 ext	2Q9	1	13.080	0.337	3.27	0.436
QF ext	1Q6	1	19.631	0.253	3.30	0.654
QAlf	1Q6	1	21.798	0.281	3.66	0.726
QDM	1Q6	3	5.648	0.073	1.41	0.188
QFm ext	1Q6	2	5.648	0.073	1.41	0.188
QDyB ext	1Q6	1	7.888	0.102	1.97	0.263
QFB1 ext	1Q6	1	12.232	0.158	2.06	0.407
QDSL match	1Q6	2	11.862	0.153	1.99	0.395
QFSL match	1Q6	2	11.862	0.153	1.99	0.395
QA2 match	1Q6	1	80.437	1.037	13.51	2.679
QFM match	1Q10	1	105.215	1.356	26.30	3.505
DEF match	1Q20	5	4.852	0.063	2.51	0.162
QED match	1Q20	5	4.852	0.063	2.51	0.162
QD match	1Q20	1	4.852	0.063	2.51	0.162
Q1 match	1Q20	1	5.391	0.069	2.79	0.180

TABLE A–12 (continued)

Injector Conventional Quadrupole Operating Parameters at E_{design}

Transport	Designation	Number	Gradient (T/m)	$B_{poletip}$ (T)	$\int G d\ell$ (T)	$k = G/B\rho$ (m^{-2})
e^+ (3.1 GeV)						
Extraction	2Q10	18	9.008	0.232	2.25	0.869
Extraction	2Q10	4	4.041	0.104	1.01	0.390
Extraction	2Q10	1	2.370	0.061	0.59	0.229
Bypass	1Q4	43	2.387	0.031	0.25	0.230
30 match	1Q4	5	5.585	0.072	0.59	0.539
30 match	1Q4	1	4.115	0.053	0.44	0.397
30 match	1Q4	4	8.182	0.105	0.87	0.789
30 match	1Q4	9	0.818	0.011	0.09	0.079

TABLE A–13

Sextupole Physical Parameters

Parameter	Value	Units
Magnet designation	4.5S10	
Number in HER	144	
Number in LER	152	
Inscribed radius	2.362, 5.999	in., cm
Core length	8.071, 20.500	in., cm
Magnetic length	10.041, 25.504	in., cm

TABLE A–14

Sextupole Operating Parameters at E_{design}

Transport	Number	Gradient (T/m^2)	$B_{poletip}$ (T)	Integrated strength (T/m)
HER (E_{design} = 9 GeV)				
SD	48	79.654	0.143	10.40
SF	48	42.029	0.076	4.49
SD1	2	104.863	0.189	13.70
SF1	2	5.674	0.010	0.74
SD1A	2	130.921	0.236	17.10
SF1A	2	17.952	0.032	2.34
SD2,SD4	4	105.073	0.189	13.72
SF2	2	78.654	0.142	10.27
SD2A,SD4A,SD6A	6	150.104	0.270	19.60
SF2A	2	86.190	0.155	11.28
SD3,SD3A,SD5,SD5A	8	60.042	0.108	7.84
SF3	2	90.272	0.162	11.79
SF3A	2	90.062	0.162	11.76
SF4	2	11.618	0.021	1.52
SF4A	2	13.659	0.025	1.78
SF5	2	54.908	0.099	7.17
SF5A	2	107.835	0.194	14.08
SD6	2	61.903	0.111	8.08
SF6	2	96.006	0.173	12.54
SF6A	2	75.742	0.136	9.89
LER (E_{design} = 3.109 GeV)				
SF	72	25.62	0.046	7.53
SD	72	45.60	0.082	13.40
SX	4	113.75	0.205	33.43
SY	4	186.13	0.335	54.70

TABLE A-15

IR Permanent-Magnet Parameters

Parameter	Symbol	Value	Units
Magnetic material	Sm_2Co_{17} – R26HS		
Remanent field	B_r	1.050	T
Temperature dependence	$\frac{dB_r}{dT}$	−0.03	%/°C
Curie point	T_C	1093	K
Density	ρ	8.4	g/cm^3

Parameter	Symbol	HER	LER	Units
B1: First separation dipole				
Nominal field	B_{B1}	0.675		T
Integrated field	$\int B d\ell$	0.3375		T-m
Bend angle at E_{des}		0.64	1.86	deg
Length	L_{B1}	0.500		m
Inner diameter	ID_{B1}	7.5–12.0		cm
Outer diameter	OD_{B1}	10.2–25.1		cm
Magnet weight	W_{B1}	220		lb
Trim range (air core coil)		±3		%
QD1: IR quadrupole				
Gradient	G_Q	10.64		T/m
Pole tip field	B_Q	0.890		T
Length	L_Q	1.200		m
Inner diameter	ID_Q	0.0875		m
Outer diameter	OD_Q	0.166		m
Magnet weight	W_Q	1393		lb
Trim range (air core coil)		±3		%
BH1: Steering for background (HER)				
Field	B	0.15		T
Integrated field	$\int B d\ell$	0.060		T-m
Bend angle at E_{des}		0.11		deg
Length	L_B	0.40		m

TABLE A–16

IR Septum Quadrupoles

Parameter	Symbol	Value	Units
Q2: First septum quadrupole (LER)			
Technology	conventional warm iron		
Number of magnets	N_{Q2}	2	
Distance from IP	d_{Q2}	2.800	m
Beam-beam spearation at d_{Q2}		8.69	cm
Beam-beam stay clear separation at d_{Q2}		3.00	cm
Magnetic length	L_{Q2}	0.50	m
Gradient	G_{Q2}	11.5	T/m
Pole tip bore radius		4.23	cm
Q4: First septum quadrupole (HER)			
Technology	conventional warm iron		
Number of magnets	N_{Q4}	2	
Distance from IP	d_{Q4}	3.7	m
Beam-beam spearation at d_{Q4}		13.7	cm
Beam-beam stay clear separation at d_{Q4}		6.7	cm
Magnetic length	L_{Q4}	1.5	m
Gradient	G_{Q4}	−7.74	T/m
Aperture		13.8	cm
Q5: Second septum quadrupole (HER)			
Technology	conventional warm iron		
Number of magnets	N_{Q5}	2	
Distance from IP	d_{Q5}	5.95	m
Beam-beam spearation at d_{Q5}		25.2	cm
Beam-beam stay clear separation at d_{Q5}		14.5	cm
Magnetic length	L_{Q5}	1.5	m
Gradient	G_{Q5}	7.27	T/m
Aperture		19.8	cm

TABLE A–17

Injection Septum Dipoles

Parameter	Symbol	HER	LER	Units
Technology		Current sheet		
Designation		S0	S0	
Number		1	1	
Magnetic length	L_{mag}	1.5	1.5	m
Field at E_{design}	B	0.018	0.008	T
Bend angle		1.0	1.3	mrad
Technology		Lambertson		
Designation		S1	S1	
Number		1	1	
Magnetic length	L_{mag}	1.0	1.0	m
Field at E_{design}	B	0.30	0.10	T
Bend angle		11	11	mrad
Aperture		2.25×2.25	2.25×2.25	cm^2

TABLE A–18

Injection Kickers

Parameter	Symbol	HER	LER	Units
Number		2	2	
Technology		Ferrite		
Length	L_k	0.75		m
Aperture		6×6		cm^2
Kick angle		0.13	0.43	mrad
Field at E_{design}	B	5.2	4.8	mT
Voltage at E_{design}	V	3.6	2.4	kV
Inductance	L	1		μH
Stability at peak		2		%
Beam pipe				
Material		Ceramic		
Coating resistance	R_a	0.4		Ω/sq
Length	L_{pipe}	1.0		m
Thickness	t_{pipe}	2.5		mm
Outside diameter	OD_{pipe}	6		cm

TABLE A–19

Wiggler Parameters (Low-energy ring)

Parameter	Symbol	Value	Units
Number of wiggler arrays	N_W	2	
Wiggle plane	Horizontal		
Total length of wigglers	L_W	32	m
Total magnetic length		19.2	m
Energy loss/turn at E_{design}	$U_{0,W}$	0.43	MeV
Wiggler segments per array	N_S	4	
Segment length	L_S	4	m
Periods/segment		6	
Dipole length		0.20	m
Drift space		0.133	m
Fill factor		60	%
Wiggler period		0.666	m
Dipole field at E_{design}	B_W	1.35	T
Critical energy at E_{design}	E_{crit}	8.7	keV

TABLE A-20

Injection Parameters

Parameter	Symbol	HER	LER	Units
Injection energy	E	9.000	3.109	GeV
Injection energy range		8–10	2.8–4	GeV
Number of populated bunches	k_B	1658	1658	
Number of empty buckets	k_B(gap)	88	88	
Bunch spacing	t_B	4.202		ns
Revolution frequency	f_0	136.312	136.312	kHz
Circulating current	I	0.986	2.140	A
Number of particles/bunch	N_b	2.723×10^{10}	5.911×10^{10}	
Horizontal emittance	ϵ_x	48.24	64.32	nm·rad
Vertical emittance	ϵ_y	1.93	2.57	nm·rad
Vertical damping time	τ_y	37.0	39.9	ms
Linac repetition rate		60		s^{-1}
Linac current ($e^{\pm}$/bunch/pulse)		$(0.1 - 3) \times 10^{10}$		
Linac invariant emittance (horiz.)	$\epsilon_{N\,\mathrm{linac}}$	4.0×10^{-5}		m·rad
Linac invariant emittance (vert.)		0.5×10^{-5}		m·rad
Ring kicker pulse length	t_{kick}	≤ 300		ns
Injection top-off time from 80%		3.0		min
Injection time from zero		6.0		min
Fractional energy spread		0.007	0.005	FWHM
Fractional energy jitter	$\delta E/E$	0.001		

TABLE A–21

Parameters Relevant to Experiment Design

Parameter	Symbol	HER	LER	Units
Horizontal spot size at IP	σ_x^*	155	155	μm
Vertical spot size at IP	σ_y^*	6.2	6.2	μm
Natural bunch length	σ_ℓ	1.00	1.00	cm
Beam cross half-angle	θ_x	0.0		mrad
Natural energy spread	σ_E	5.51	2.51	MeV
Natural C.M. energy spread	$\sigma_{E_{\rm c.m.}}$	5.36		MeV
Beam pipe inner radius at IP	r^*	2.50		cm
Beam pipe outer radius at IP	$r^*_{\rm out}$	2.82		cm
IP to first magnet distance	d_f	0.200		m
Detector solenoid field	$B_{\rm sol}$	1.00		T
Detector solenoid length	$L_{\rm sol}$	4.00		m
Beam pipe thickness	$X_{0;\rm pipe}$	0.0053		X_0
Support tube ID	$\rm ID_{tube}$	39.00		cm
Support tube OD	$\rm OD_{tube}$	43.00		cm
Support tube thickness at IP	$X_{0;\rm tube}$	0.0047		X_0
Support tube length	$\rm L_{tube}$	4.20		m
Minimum acceptance angle	$\theta_{\rm min}$	0.300	0.300	rad
cos(min. acceptance angle in C.M.)	$\cos\theta^*_{\rm min}$	0.876	0.984	

DATE
FILMED
2/18/94
END